

Springer Series on Polymer and Composite Materials

Igor E. Uflyand
Gulzhian I. Dzhardimalieva

Nanomaterials Preparation by Thermolysis of Metal Chelates

 Springer

Springer Series on Polymer and Composite Materials

Series editor

Susheel Kalia, Army Cadet College Wing, Indian Military Academy, Dehradun,
India

More information about this series at <http://www.springer.com/series/13173>

Igor E. Uflyand · Gulzhian I. Dzhardimalieva

Nanomaterials Preparation by Thermolysis of Metal Chelates

 Springer

Igor E. Uflyand
Department of Chemistry
Southern Federal University
Rostov-on-Don
Russia

Gulzhian I. Dzhardimalieva
Institute of Problems of Chemical Physics
Russian Academy of Sciences
Chernogolovka, Moscow Region
Russia

ISSN 2364-1878 ISSN 2364-1886 (electronic)
Springer Series on Polymer and Composite Materials
ISBN 978-3-319-93404-4 ISBN 978-3-319-93405-1 (eBook)
<https://doi.org/10.1007/978-3-319-93405-1>

Library of Congress Control Number: 2018943387

© Springer International Publishing AG, part of Springer Nature 2018

This work is subject to copyright. All rights are reserved by the Publisher, whether the whole or part of the material is concerned, specifically the rights of translation, reprinting, reuse of illustrations, recitation, broadcasting, reproduction on microfilms or in any other physical way, and transmission or information storage and retrieval, electronic adaptation, computer software, or by similar or dissimilar methodology now known or hereafter developed.

The use of general descriptive names, registered names, trademarks, service marks, etc. in this publication does not imply, even in the absence of a specific statement, that such names are exempt from the relevant protective laws and regulations and therefore free for general use.

The publisher, the authors and the editors are safe to assume that the advice and information in this book are believed to be true and accurate at the date of publication. Neither the publisher nor the authors or the editors give a warranty, express or implied, with respect to the material contained herein or for any errors or omissions that may have been made. The publisher remains neutral with regard to jurisdictional claims in published maps and institutional affiliations.

Printed on acid-free paper

This Springer imprint is published by the registered company Springer International Publishing AG part of Springer Nature
The registered company address is: Gewerbestrasse 11, 6330 Cham, Switzerland

Preface

Among the existing condensation pathways for the production of nanomaterials, the thermolysis of metal compounds is one of the simplest and inexpensive methods for obtaining nanoparticles with a narrow size distribution, low crystalline defects, and tunable shapes. It is known as a general method for the synthesis of a wide range of nanomaterials, including metals, metal oxides, mixed oxides, metal sulfides, non-oxide ceramics, carbon materials. Its undoubted advantages include economy and environmental friendliness, high yields, the possibility of large-scale production, control of synthesis conditions, as well as the purity, size, and morphology of the particles. In addition, thermolysis allows to avoid special equipment, complex technological processes, and heavy synthesis conditions. It should be emphasized that the central component of any successful synthesis of nanomaterials using thermolysis is the initial choice of precursors in combination with rational thermolysis conditions. Among the most well-known examples of precursors, metal chelates occupy a special place, the undeniable advantages of which include ease of synthesis, stability with respect to moisture and atmospheric oxygen at room temperature, safety, and, in many cases, greater economy compared to, for example, multicomponent systems. In addition, good scalability and controllability of the process of obtaining nanomaterials by thermolysis of metal chelates are attractive. Currently, coordination chemistry is an extensive library of metal chelates, which are potential precursors for nanomaterials.

This book is devoted to obtaining nanomaterials by thermolysis of metal chelates. We believe that this is the first comprehensive analysis of this field of science, so we tried to fully consider this problem, and we hope that missed problems are not fundamental. It should be specially noted that this monograph is mainly devoted to the logic of research and the internal methodological and scientific interrelations in this field. It reflects the current state of the problems under consideration, and many ideas are still being developed.

We are very pleased to present this book to English-speaking readers. Any author is satisfied with his book, published by the world-famous Springer publishing house, in which the most fundamental scientific works are published. This is also important for us, because this book is a continuation of already published monographs in

the Springer series in the field of materials science from our laboratory: A. D. Pomogailo and V. N. Kestelman, *Metallopolymer Nanocomposites* (Springer, Berlin, Heidelberg, New York, 2005), A. D. Pomogailo, G. I. Dzhardimalieva and V. N. Kestelman, *Macromolecular Metal Carboxylates and Their Nanocomposites* (Springer, Berlin, Heidelberg, 2010), A. D. Pomogailo and G. I. Dzhardimalieva, *Nanostructured Materials Preparation via Condensation Ways* (Springer, Dordrecht, Heidelberg, New York, London, 2014).

Who is our potential reader? The preparation of nanomaterials by the thermolysis of metal chelates, like any interdisciplinary field of science and technology, is rapidly developing, and the intensive accumulation of experimental data in this area confuses not only novices, but also experienced researchers working in this field. First of all, this book can be useful for a wide range of scientists and engineers of research institutes and industry. After 25 years of our own research in this field and analysis of the literature, we believe in the necessity of the appearance of this book, which summarizes the accumulated data on all aspects of *Nanomaterials Preparation by Thermolysis of Metal Chelates*.

Chernogolovka, Moscow Region, Russia
Rostov-on-Don, Russia Federation
January 2018

Gulzhian I. Dzhardimalieva
Igor E. Uflyand

Contents

1	General Introduction	1
	References	15
2	General Characteristics of the Methods of Thermolysis of Metal Compounds	25
2.1	Thermogravimetric Methods	27
2.1.1	Volumetric Methods	33
2.1.2	Linear Pyrolysis Method	37
2.1.3	Thermolysis Induced by High-Energy Radiation	39
2.1.4	Spray Pyrolysis	40
2.1.5	Chemical Vapor Deposition	44
2.1.6	Kinetic Approaches to the Investigation of Thermolysis of Metal Chelates	49
	References	63
3	Thermolysis of Low Molecular Weight Metal Chelates	71
3.1	Metal Carboxylates	71
3.1.1	Metal Formates	73
3.1.2	Metal Acetates	76
3.1.3	Metal Oleates	84
3.1.4	Other Metal Monocarboxylates	95
3.1.5	Metal Oxalates	97
3.1.6	Metal Malonates	101
3.1.7	Metal Succinates	104
3.1.8	Metal Phthalates	105
3.2	Metal Acetylacetonates	107
3.2.1	Nickel Acetylacetonate	107
3.2.2	Aluminum Acetylacetonate	108
3.2.3	Copper Acetylacetonate	109
3.2.4	Cobalt Acetylacetonates	111

3.2.5	Zirconium Acetylacetonate	111
3.2.6	Zinc Acetylacetonate	112
3.2.7	Manganese Acetylacetonate	112
3.2.8	Iron Acetylacetonates	114
3.2.9	Cadmium Acetylacetonate	117
3.2.10	Gold Acetylacetonate	117
3.2.11	Platinum Acetylacetonate	120
3.2.12	Palladium Acetylacetonate	121
3.2.13	Ruthenium Acetylacetonates	122
3.2.14	Indium Acetylacetonate	125
3.3	Metal Chelates Based on Other O,O-Donor Ligands	127
3.3.1	Metal Salicylaldehydates	127
3.3.2	Metal 2-Hydroxyacetophenone	130
3.3.3	Metal 2-Hydroxy-1-Naphthaldehydates	131
3.3.4	Metal Glycerolates	133
3.3.5	Metal Cupferronates	133
3.4	Metal Chelates with N,N-Containing Ligands	134
3.4.1	2,2'-Diamino-5,5'-Dimethyl-4,4'-Bithiazole	135
3.4.2	2,2'-Bipyridine	138
3.4.3	Ethylenediamine and Related Ligands	140
3.4.4	1,10-Phenanthroline and Related Ligands	145
3.4.5	Aminoiminates	149
3.4.6	Pyridine Carboxamides	151
3.4.7	Dimethylglyoxime	151
3.5	Azomethine Metal Chelates	151
3.5.1	Metal Chelates Based on 2-Hydroxyacetophenonimine	152
3.5.2	Metal Chelates of Salicylaldimine Type	153
3.5.3	Salen Chelates	156
3.5.4	Salphen Chelates	161
3.5.5	Metal Chelates Based on Tridentate Azomethine Ligands	163
3.5.6	Metal Chelates with Other Azomethine Ligands	163
3.6	Metal Chelates with N,O-Donor Ligands	167
3.7	Metal Chelates with S,O-Donor Ligands	171
3.7.1	Metal Chelates with N,S (Se, Te)-Donor Ligands	175
3.8	Metal Dichalcogenides	180
3.9	Mixed-Ligand Metal Chelates	202
3.10	Polynuclear Metal Chelates	208
3.11	Multicomponent Precursors Based on Metal Chelates	217
	References	234

4 Thermolysis of Polymeric Metal Chelates	247
4.1 Synthesis of Carbon Nanomaterials	250
4.2 Preparation of Metal and Metal Oxide–Carbon Nanocomposites	255
4.3 Preparation of Metal Oxide Nanomaterials	274
4.3.1 Transition Metal Oxides	276
4.3.2 Main Group Metal Oxides	301
4.3.3 Rare Earth Metal Oxides	309
4.3.4 Preparation of Metal Nanomaterials	310
4.4 Preparation of Mixed-Oxide Nanocomposites	315
4.5 Preparation of Metal Sulfide Nanomaterials	323
4.6 Preparation of Polymer-Derived Non-oxide Nanocomposites	325
References	336
5 The Conjugate Thermolysis—Thermal Polymerization of Metal Chelate Monomers and Thermolysis of Polymers Formed In Situ	351
5.1 General Characteristics of Metal Chelate Monomers Used in Conjugated Thermolysis	352
5.2 Thermal Polymerization of Metal Chelate Monomers	364
5.3 Overall Scheme of Conjugated Thermolysis	370
5.3.1 Dehydration	373
5.3.2 Polymerization	376
5.3.3 Decarboxylation	378
5.4 The Composition of Gaseous and Solid Products of Conjugated Thermolysis	387
5.4.1 Gaseous and Condensed Products	387
5.4.2 The Composition of the Solid-Phase Products	390
5.5 Kinetic Schemes and Reactions of Thermal Transformation of Metal Chelate Monomers	406
5.5.1 General Kinetic Scheme and Ways of Decomposition of Metal Chelate Monomers	407
5.5.2 Transformation Pathways of Cobalt Acrylate	409
References	418
6 Thermolysis of Metal Chelates in Polymer Matrices	425
References	453
7 Application of Nanomaterials Prepared by Thermolysis of Metal Chelates	459
7.1 Fuel Cells	459
7.2 Supercapacitors	487
7.3 Lithium-Ion Batteries	497
7.4 Nanocatalysis	507

7.4.1	Catalytic Hydrogenation	508
7.4.2	Oxidation Reactions	513
7.4.3	Ullmann-Type Amination Coupling Reaction	516
7.4.4	Suzuki–Miyaura Coupling Reaction	517
7.4.5	Fischer–Tropsch Synthesis	518
7.4.6	Enantioselective Catalysis	518
7.4.7	Photocatalysis	520
	References	527
	Conclusions and Future Prospects	543
	Index	545

About the Authors



Prof. Igor E. Uflyand, Dr. Sci. (Chem.) is the head of Chemistry Department, Southern Federal University, Rostov-on-Don, Russia. He was born in 1956 and graduated from the Rostov State University, Department of Physical and Colloid Chemistry. He received his Ph.D. in 1981 and his Doctorate in chemistry in 1996 from the Rostov State University. He received the title of professor in 1996. The scope of his scientific interest is: coordination and organometallic chemistry, metal chelate monomers and polymers on their basis, catalysis by metal complexes, tribochemistry, and nanomaterials. He is the author of over 150 scientific papers, 10 patents, and 4 books.



Gulzhian I. Dzhardimalieva, Dr. Sci. (Chem.), Ph.D. is the head of Laboratory, Institute of Problems of Chemical Physics, Russian Academy of Sciences, and the professor of the Department of Applied Mechanics, Moscow Aviation Institute (National Research University). She received her Ph. D. in 1987 from the Institute of Problems of Chemical Physics RAS in Moscow and her Doctorate in chemistry in 2010 from the Institute of Problems of Chemical Physics RAS in Chernogolovka. The scope of her scientific interest is: metal-containing monomers and polymers on their base, macromolecular metal carboxylates, coordination polymers, and metallopolymer nanocomposites, and nanomaterials. She is the author of about 150 articles and 5 monographs. She was an invited researcher at Auburn University, USA (2001), Warsaw Technology University, Poland (2002, 2011),

Bremen University, Germany (2007), Turin University, Italy (2008), and Institute of Composite and Biomedical Materials, CNR, Neapol, Italy (2011, 2013). She was an issue editor of *Journal of Inorganic and Organometallic Polymers and Materials* (2016, vol. 26, 6) and a member of the Organizing Committee of the International Conference on Macromolecular Metal Complexes MMC-17 (Tokyo, Japan, August, 2017).

Abbreviations

3DGN	Three-dimensional graphene network
4,4'-bipy	4,4'-Bipyridine
4-bpdh	2,5-Bis(4-pyridyl)-3,4-diaza-2,4-hexadiene
AACVD	Aerosol-assisted chemical vapor deposition
AAO	Anodic alumina oxide
Ac	Acetate
ACA	1-Adamantane carboxylic acid
acac	Acetylacetonate anion
Acr	Acrylate
ADC	Acetylenedicarboxylate
AFM	Atom force microscopy
ALD	Atomic layer deposition
Am	N,N'-Bis(trimethylsilyl)phenyl amidinate
APS	Average particles size
ATI	N,N'-Diisopropyl-aminotroponimate
ATRP	Atom transfer radical polymerization
BDC	1,4-Benzenedicarboxylate
BET	Brunauer–Emmett–Teller
BINAP	2,2'-bis(diarylphosphino)-1,1'-binaphthyl
bpy	2,2'-Bipyridine
BSE SEM	Backscattered electron scanning electron microscopy
BTC	1,3,5-Benzene-tricarboxylate
CBD	Chemical bath deposition
CdDEX	Cadmium diethylxanthate
CE	Coulomb efficiency
CIS	Copper indium xanthate CuInS ₂
CNP	Carbonated nanoparticle
CNRod	Carbon nanorods
CNT	Carbon nanotube
-co-	Copolymer

COD	1,5-Cyclooctadiene
COP	Covalent organic polymer
CoP-CMP	Cobalt porphyrin-based conjugated mesoporous polymer
CP	Coordination polymer
CPM	Crystalline porous material
CPP	Coordination polymer particle
CR	Congo red
CV	Cyclic voltammogram
CVD	Chemical vapor deposition
<i>cyclam</i>	1,4,8,11-Tetraazacyclotetradecane
dabco	1,4-Diazabicyclo[2.2.2]octane
DEA	Dielectric thermal analysis
DIL	Dilatometry
DIOP	2,3- <i>O</i> -Isopropylidene-2,3-dihydroxy-1,4-bis(diphenylphosphino)butane
DMA (DMTA)	Dynamic mechanical analysis
DMF	Dimethylformamide
DMSO	Dimethylsulfoxide
DNC	Dendritic nanocube
DSC	Differential scanning calorimetry
DTA	Differential thermal analysis
dtc	Dithiocarbamate
DTG	Differential thermogravimetry
DTPA	Diethylenetriamine pentaacetic acid
$E_{1/2}$	Half-wave potential
EC	Electrochemical capacitor
ED	Electronic diffraction
EDL	Electrical double layer
EDLC	Electrochemical double-layer capacitor
EDS	Energy-dispersive X-ray spectroscopy
EDTA	Ethylenediaminetetraacetic acid
ee	Enantiomeric excess
EELS	Electron energy loss spectroscopy
EGA	Evolved gas analysis
EI-MS	Electron ionization mass spectrometry
EIS	Electrochemical impedance spectroscopy
EM	Electron microscopy
en	Ethylene diamine
FA	Folic acid
FASP	Flame-assisted spray pyrolysis
FESEM	Field emission scanning electron microscopy
FFT	Fast Fourier transform
FP	Frontal polymerization
FSP	Flame spray pyrolysis
FTIR	Fourier transformation infrared spectroscopy

GC	Glassy carbon
GC-MS	Gas chromatography–mass spectroscopy
GMA	Glycidyl methacrylate
GNRib	Graphene nanoribbons
GO	Graphene oxide
GRAILS	Gas reducing agent in liquid solution
H3ABTC	Azobenzene-3,5,4'-tricarboxylic acid
H3NTA	Nitrilotriacetic acid
HDA	Hexadecylamine
HER	Hydrogen evolution reaction
HF	High frequency
hfac	Hexafluoroacetylacetonate
HMDA	Hexamethylenediamine
HOR	Hydrogen oxidation reaction
HP + SD	High-pressure polymerization under shear deformation
HPC	Hierarchical porous carbons
HRTEM	High-resolution transmission electron microscopy
ITO	Indium tin oxide
K-L	Koutecky–Levich linear plots
L	Ligand
LFA	Laser flash analysis
LF-FSP	Liquid-feed flame spray pyrolysis
LIB	Lithium-ion battery
LP	Linear pyrolysis
LP-MOCVD	Low-pressure metal–organic chemical vapor deposition
LSV	Linear sweep voltammetry
M	Metal
Macr	Methacrylate
MAcr _n	Metal acrylate
MAT	Mesoporous anatase TiO ₂
MB	Methylene blue
MCM	Metal chelate monomer
MEH	Poly(2-methoxy-5-(2'-ethyl-hexyloxy))
MFum _n	Metal fumarates
MIac _n	Metal itaconates
MMacr	Metal methacrylate
MMal _n	Metal maleate
MO	Metal oxide
MOCVD	Metal–organic chemical vapor deposition
MOF	Metal–organic framework
MPC	Microporous carbon
MRI	Magnetic resonance imaging
MS	Metal sulfide
MS	Mass spectrometry
MWCNT	Multiwalled carbon nanotube

MX _n	Metal compound
NCF	Nitrogen-doped carbon microfiber
NCNT	N-doped carbon nanotube
NDC	2,6-Naphthalenedicarboxylate
NED	Nanoelectron diffraction
NGPC	N-doped graphite porous nanocarbon
NMP	Nitroxide-mediated polymerization
NP	Nanoparticle
NPC	Nanoporous carbon
OA	Oleic acid
OAm	Oleylamine
ODE	1-Octadecene
OER	Oxygen evolution reaction
OI	Oleate
OLED	Organic light-emitting diode
OM	Optical microscopy
ORR	Oxygen reduction reaction
ORTEP	Oak Ridge Thermal Ellipsoid Plot
ox	Oxalate
P3EEET	Poly(3-[(2'-(2-ethoxy)ethoxy) ethoxy]-thiophene)
P3HT	Poly(3-hexylthiophene)
P4VP	Poly-4-vinylpyridine
PBPFO	Poly[9,9-bis(3,5-di-tert-butylphenyl)-9H-fluorene]
PCE	Power conversion efficiency
PCN	Porphyritic conjugated network
PCP	Porous coordination polymer
PDC	Polymer-derived ceramics
PDI	Polydispersity index
PE	Polyethylene
PEDOT	Poly(3,4-ethylenedioxythiophene)
PEG	Polyethylene glycol
PEI	Polyethylene imine
PEMFC	Proton exchange membrane fuel cell
phen	1,10-Phenanthroline
pip	Piperidine
PMC	Polymeric metal chelate
PMMA	Poly(methyl methacrylate)
PP	Polymeric product
PPV	Poly(<i>para</i> -phenylenevinylene)
PS	Polystyrene
PSS	Polystyrene sulfonate
PTCDA	Perylene-3,4,9,10-tetracarboxylic dianhydride
PVA	Polyvinyl alcohol
PVD	Physical vapor deposition
PVp	Poly(vinylpyrrolidone)

Py	Pyridine
QD	Quantum dot
RAFT	Reversible addition–fragmentation chain transfer
RAPET	Reaction under Autogenic Pressure at Elevated Temperature
RB	Regularly band
RB	Rose Bengal
RDE	Rotating disk electrode
RGO	Reduced graphene oxide
RhB	Rhodamine-B
RHE	Reversible hydrogen electrode
ROP	Ring-opening polymerization
RRDE	Rotating ring-disk electrode
SADP	Selected area diffraction pattern
SAED	Selected area electron diffraction
salen	N,N'-bis(salicylaldehyde)ethylenediamine
salphen	N-N'-bis(salicylaldehyde)-1,2-phenylenediamine
SBU	Secondary building block
SCE	Saturated calomel electrode
SD	Size distribution
SEGPPOS	5,5'-Bis(diphenylphosphino)-4,4'-bi-1,3-benzodioxole
SEM	Scanning electron microscopy
SGA	Self-generated atmosphere
SPR	Surface plasmon resonance
SSP	«Single-source» precursors
TA	Thermal analysis
TEG	Triethylene glycol
TEM	Transmission electron microscopy
TG	Thermogravimetry
TGA	Thermogravimetric analysis
THF	Tetrahydrofuran
thq	Tetrahydroquinoline
TMA	Thermomechanical analysis
TOA	Trioctylamine
TOF	Turnover frequency
TON	Turnover number of the catalyst
TOP	Trioctylphosphine
TOPO	Trioctylphosphine oxide
TPP	Triphenylphosphine
TTA	Thenoyl-trifluoro-acetylacetone

USP	Ultrasonic spray pyrolysis
VAFS	Vapor-fed aerosol flame synthesis
XPS	X-ray photoelectron spectroscopy
XRD	X-ray diffraction
YSZ	Yttrium-stabilized zirconia

Chapter 1

General Introduction



Advances in the chemistry and technology of nanomaterials whose sizes are less than 100 nm in at least one dimension led to exponential development in many fields of science and industry [1–19]. They find wide applications in chemistry, physics, and biology, including energy conversion and storage [20–24], image generation [25, 26], biomedicine [27, 28], highly sensitive gas sensors for leak detection [29], optical applications [25, 30], nanofluids for enhanced heat transfer [31], extinguishing powder for high-profile fire [32], catalytic reactors [33], catalysis [34–36], magnetism [37], optics [38–41], sensors [42–44], biosensing [44–47], medical diagnostics [48, 49], data storage [50, 51], and others.

Nanomaterials are of interest in academic research and technical applications due to various unique physical, chemical, and biological properties, which are induced by their nanometric size and which are different from those of molecular species and bulk materials [52–64]. Size- and shape-associated properties of nanomaterials include the small-size effect, surface and interface effect, quantum size effect, and macroscopical quantum tunnel effect [65–70]. In particular, the quantization of electronic states becomes apparent leading to very sensitive size-dependent effects such as optical and magnetic properties [71]. In addition, the high surface-to-volume ratio leads to a high number of potential active sites at their surface.

It is now generally accepted that the properties of nanomaterials, as well as final productivity and applications, are largely determined by the structure, morphology, phase, shape, size, distribution, and spatial arrangement of the nanoparticles (NPs) [72, 73]. Since synthetic methodologies and preparing conditions have an obvious effect on the morphology, size, and surface properties of NPs, it is vital to find reasonable and suitable approaches to the preparation of monodisperse NPs [74–78]. The synthesis of nanomaterials has become a major interdisciplinary area of research over the past 20 years, because nanotechnology is demanding high-quality materials in industrial scale with facile, green, efficient, and economically feasible processing methods [79]. The ability to prepare nanomaterials of high quality (uniform size and shape, no defects except those desired, designed surface, etc.) is a key point in the area of nanoscience, and also interesting in its

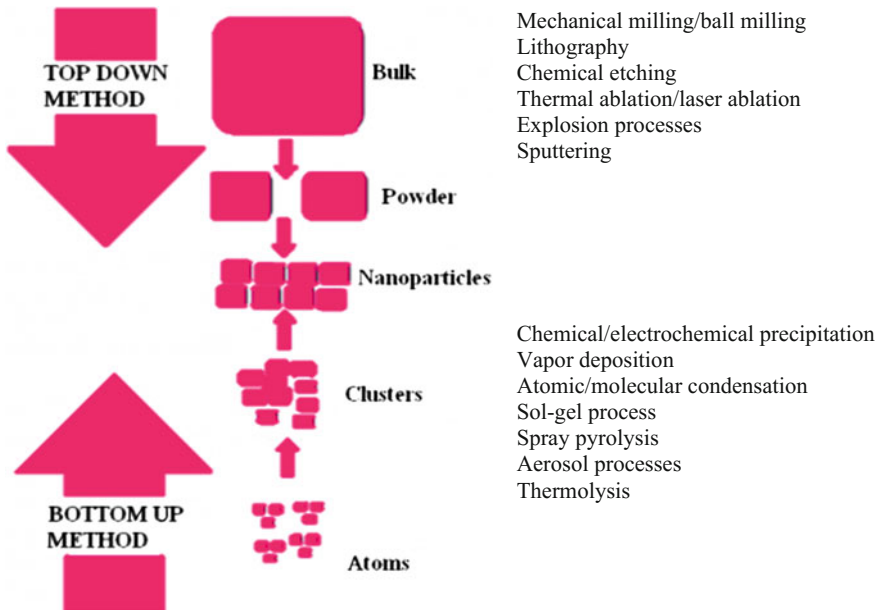


Fig. 1.1 Schematic of various NP syntheses

own right. The design and controlled synthesis of nanomaterials with different sizes, shapes, and morphologies is very important from the viewpoint of both basic science and technology [80–83].

Most techniques for the synthesis of nanomaterials, including physical, chemical, or biological methods, are still limited to laboratory scale, while a number of methods have found wide application in industry. It was found that, despite the many methods of production of nanomaterials, the entire versatility of synthetic approaches to the preparation of NPs and their self-assembly can be reduced to two fundamentally different ways (Fig. 1.1): “top-down” (descending way) and “bottom-up” (ascending way) [84–88].

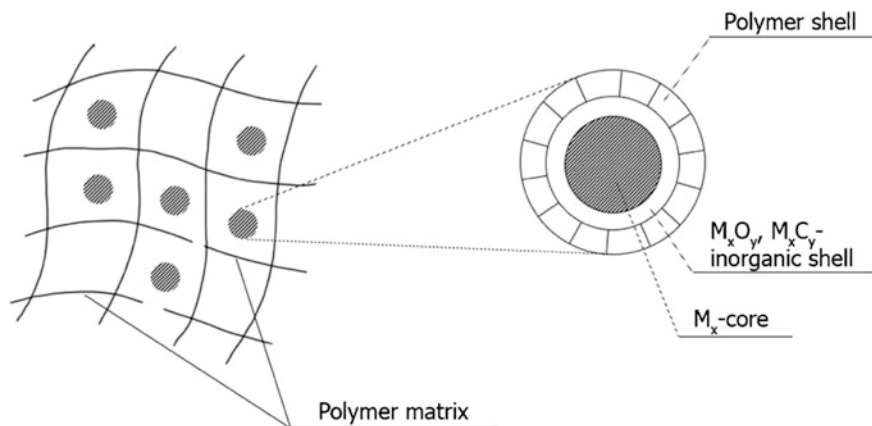
In the former method, NPs can be obtained by such techniques as milling or lithography which generates small particles from the corresponding bulk materials [89]. By nature, this method is not cheap and quick to manufacture, not suitable for large-scale production, and has high requirements on experiment condition including clean room, vacuum, etc. The bottom-up approach of nanomaterial synthesis first forms the nanostructured building blocks (NPs) and then assembles these into the final material [90]. The latter method is low cost and highly efficient and is more widely used due to its variability and potential abilities than the dispersion method. A researcher can predict in advance properties of obtained NPs: He can choose composition and properties of initial components, stabilizing agents, can estimate their role, predict conditions of nucleation and growth of the NPs at each stage, thus constructing targeted nanomaterials.

It should be noted the biosynthesis of nanomaterials, for example, the production of nanoparticles under the influence of microorganisms, bio-templates, plant extracts, etc. [91–95].

The most general kinetic principle of the NP formation is based on the combination of the high rate of the metal-containing phase origin and the low rate of its growth. These fundamental kinetic parameters of the NP synthesis determine the dimension of the formed NPs and are of particular importance for technology. The developed interphase surface and the excessive quantity of surface atoms with respect to the bulk material promote extremely high chemical activity of the NPs formed [96–98]. This peculiarity is further enhanced in case of NPs with hollow or porous core [99–102]. Therefore, “energy saturated” NPs which are formed under strongly non-equilibrium conditions interact vigorously with the components of the reaction medium. Sometimes such high chemical activity of the NPs is useful, but more often one needs to solve the problems of their stabilization for safe storage and transport. In this regard, the search for effective methods of chemical passivation of the NPs is of particular importance. The stabilization of highly dispersed and active particles is one of the basic problems in the physical chemistry of the ultradispersed state based on the competition of formation and growth of produced particles on one hand and stabilization of readily reacting particles on the other [103].

Currently, various methods for stabilizing NPs are available [104]. In particular, in order to stabilize and avoid aggregation of NPs, their surface is usually coated with desired functional polymers or surfactants. The surfactant, while limiting the particle growth, also plays important role in the nucleation process. Therefore, the choice of the stabilizing agent maybe fundamental as it will influence the growth, stability, and surface chemistry of the nanostructures that are of high importance for any target application [105–107]. The various functional organic molecules [108–110], surfactants [111], polymers [112], dendrimers [113, 114], ionic liquids [115, 116], etc., are used for this purpose. For example, metal-containing NPs with a core–shell structure (Scheme 1.1) in which polymers [117–122] can be used as surface layers (shells) have become the objects of many studies.

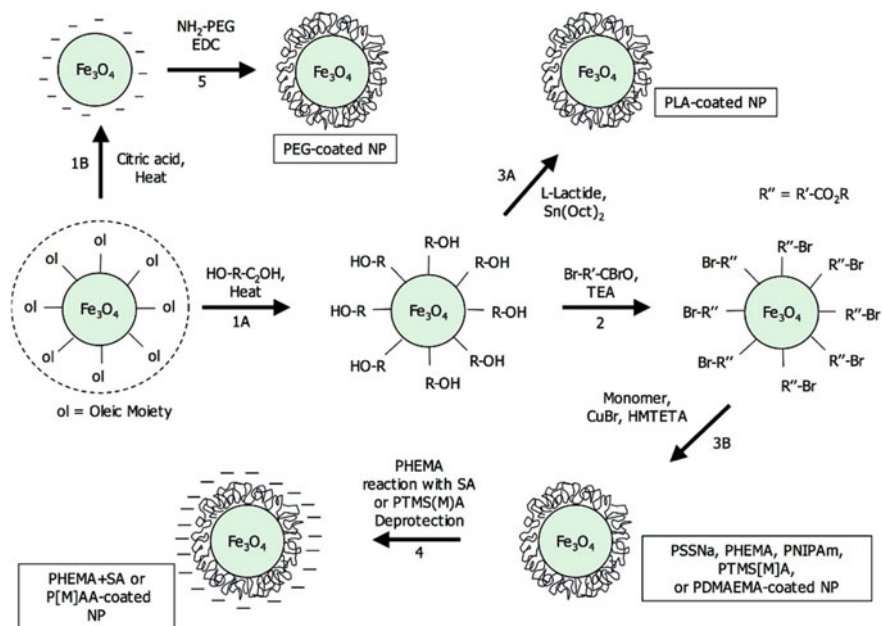
Interest to metal-containing polymeric nanocomposites is caused by a unique combination of properties of metal, metal oxide, and chalcogenide NPs, and by mechanical, film-forming, and other characteristics of polymers with opportunities of their use as magnetic materials for record and storage of information, as catalysts and sensors, in medicine and biology [123–125]. The advantages of metal–polymer nanostructures over other types of nanomaterials are based on the flexibility with which their structures can be modified to produce materials of different compositions, morphologies, sizes, and surface properties, with the possibility of hierarchical assembly of several nanomaterials of various components into one design. The solution of the problem is facilitated in many respects by the high adsorption capability of the NPs toward macromolecules. The full NP protection by polymers is achieved due to the formation of structured adsorption-solvate layers, which serve as structural–mechanical barriers preventing their aggregation [126]. The aggregation stability of NPs is determined, on the one hand, by both the stability of



Scheme 1.1 Proposed core-shell structure of the nanocomposite. Reproduced with permission from Ref. [122]. Copyright (2012) John Wiley and Sons

such structures and their ability to recover, as well as the properties of the formed nanocomposites, on the other hand. There are two basic approaches to the formation of these hybrid structures [127]: grafting-onto method, in which the macromolecules of a polymer interact with a modified surface of a NP via their terminal functional groups [128–130] and grafting-from method, in which polymer chain propagation begins directly from the NP surface coated with the monolayer, which contains a polymerization initiator [131]. The former method is very flexible because different types of polymers and copolymers can be grafted, and thus, it can be effectively used with large particles. However, in the case of very small NPs, there is a high probability of grafting the polymer chain simultaneously to several particles, which leads to the formation of clusters. In addition, the grafting-onto method usually requires particles with a bare surface and is, therefore, most efficiently adopted to stabilize particles during their nucleation phase. In order to obtain a polymer shell, a NP surface is commonly modified with certain functionalities, which are subsequently used to bind a polymer; in another case, the role of a modifier is played by initiator molecules that are involved in graft polymerization [132]. For these purposes, ROP (ring-opening polymerization) [133–136] and various living radical polymerization methods, for example ATRP (atom transfer radical polymerization) [137–141] are widely used, which allows the development of polymer shells with homogeneous structures and controlled thickness.

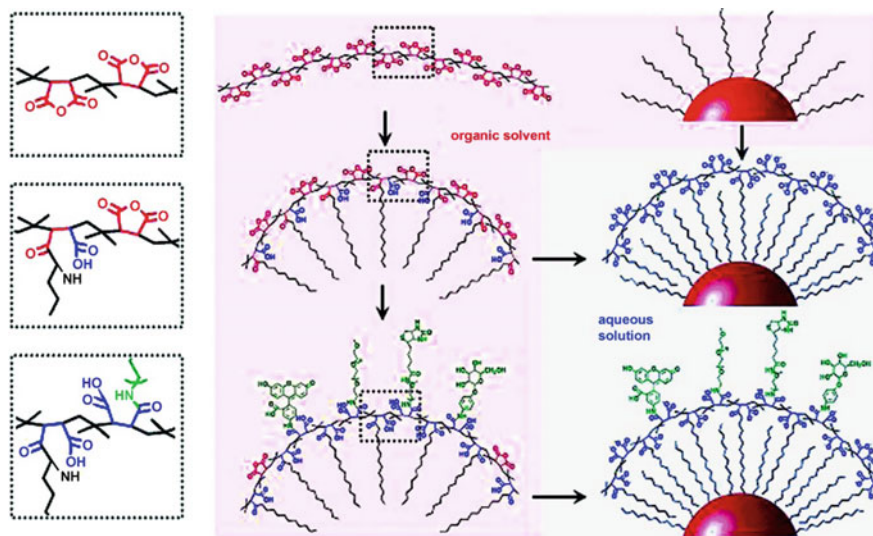
As a typical example, we note surface modification of the NPs with hydrophilic and biocompatible polymers such as polyethylene glycol (PEG), polylactic acid, and poly(lactic-co-glycolic acid) (Scheme 1.2) [142]. The oleic acid (OA) and oleylamine (OAm) moieties initially present on the NP surface are replaced with other ligands that possess high affinity for the NP surface, provide direct solubility in water, and expose functional hydroxyl groups. The hydroxyl groups have been used both to initiate catalyzed ROP from the particle surfaces and coat the particles



Scheme 1.2 Scheme of procedure for the functionalization of magnetic NPs. Steps 1A and 1B: ligand exchange reactions. Step 2: acylation of hydroxyl groups to obtain surface ATRP initiators. Step 3A: surface-initiated ROP of L-lactide. Step 3B: surface-initiated ATRP. Step 4: deprotection or additional reaction after polymerization. Step 5: grafting of the terminal functionalized PEG chains onto the NP surface using amidation chemistry. Reproduced with permission from Ref. [142]. Copyright (2007) American Chemical Society

with a layer of polylactic acid or have been reacted with a powerful acylating agent to form esters that can be used as initiators for ATRP polymerization. A notable feature of the proposed strategy is that by appropriate selection of a ligand, particles can be obtained that are soluble either in organic solvents (both non-polar and highly polar) or in water, which allows for greater flexibility in the choice of monomers and polymerization conditions. It should be noted that many polyelectrolytes, both anionic and cationic, were grown from the NP surface. With pH-sensitive polymers, aggregation of the particles was caused by a change in pH conditions, and in almost all cases, the aggregation behavior could be reversed by switching back to the pH conditions that ensured the presence of charges on the particle surfaces.

Polymer coatings of PEG, polyvinyl alcohol, and poly(acrylic/methacrylic acid) are simple polymeric coatings for NPs [143]. These polymers are selected to provide stability by preventing agglomeration and enhancing the hydrophilicity of NPs for waterborne applications. Typically, the coating process is carried out by suspending NPs in solution with the polymer. However, grafting-through and grafting-to techniques allow for a more unique polymer functionalization of NPs. It is of interest to use poly(maleic anhydride) as a polymer coating for magnetic NPs.



Scheme 1.3 Scheme for synthesis of amphiphilic polymer and NP coating. The central column shows the synthesis of an amphiphilic polymer. To the polymer backbone, poly(isobutylene-*alt*-maleic anhydride) (top line), the alkylamine chains are linked by direct amidation between maleic anhydride and an amino-ligand (middle line). In an additional step, the functional groups (drawn in green) with an amino-terminal group are also linked to the polymer (bottom line). In the left column, the amide linkage between amino ligands and anhydride rings is shown in detail. NPs with a hydrophobic capping (right column, top line) are coated with an amphiphilic polymer by a hydrophobic interaction between the alkyl chains of the polymer and the surfactant molecules at the NPs (middle line). This works similarly for polymers with (bottom) and without (middle) embedded functional molecules. Solubility in water is provided by opening the anhydride rings (drawn in red) for the carboxylic groups (drawn in blue), which introduce a negative charge on the surface of the particles and lead to electrostatic repulsion between the particles. Reproduced with permission from Ref. [144]. Copyright (2008) John Wiley and Sons

For example, this polymer was used to functionalize several NPs (Scheme 1.3), including iron oxide NPs [144]. The binding of poly(maleic anhydride) to the surface of NPs is due to the fact that the ring opening of the maleic anhydride groups with amines generates a grafting point for the amide, along with the formation of a carboxylic acid that can participate in aqueous and electrostatic interactions. Addition of PEG, biotin and fluorescein together with long-chain alkylamines to the polymer was carried out, which could then be used to coat the NPs via hydrophobic interactions. In neutral water, carboxylic acid groups are deprotonated, yielding particles of pure negative charge, which minimizes aggregation.

Glycidyl methacrylate (GMA) is a promising choice for grafting-through and grafting-to methodologies, as the epoxide can react with native $-OH$ groups on the outside of metal oxide NPs. For example, poly(methacryloxyethyl trimethylammonium chloride)-coated Fe_3O_4 NPs were produced by coating them with GMA,

then polymerizing in solution the corresponding polymer and GMA with an azo initiator [145]. It should be noted the synthesis of a polystyrene (PS) shell on nanoparticles by polymerization with a reversible addition-fragmentation chain transfer (RAFT) using 2-[(dodecylsulfanyl)-carbonothioyl] sulfanylpropanoic acid as the RAFT agent [146]. The PS has carboxylic end groups that can undergo ligand exchange with smaller ligands on iron oxide to yield NPs coated with a PS brush. It is noteworthy that polymer brushes are efficient stabilizers at high grafting densities [147] and lead to brush coated NPs with low aggregation behavior [148]. ATRP was used to grow polymer from chloropropionic acid-coated MnFe_2O_4 NPs [149]. In this early case, the coating generated was PS. However, more interesting coatings such as activated esters [124], antibacterial quaternary amines [150], and poly-2-(dimethylamino) ethyl methacrylate (capable of gene delivery) [151] have also been prepared. In particular, ATRP and click chemistry were combined to make FA-functionalized NPs (FA is folic acid) that target tumor cells while maintaining low immuno-recognition [152]. Other controlled polymerization techniques like nitroxide-mediated polymerization (NMP) or ROP are also amenable to grafting-from polymerization for magnetic NP surfaces [153, 154].

Of interest are ferromagnetic magnetite nanocubes which were coated with poly-2-(dimethylamino) ethyl methacrylate, a water-soluble, biodegradable, and pH-responsive polymer, in order to produce good drug carriers with excellent dispersity in biological buffer, low cytotoxicity, and controllable drug release [155]. The polymer coating was performed using ATRP.

The synthesis of nanomaterials described in the many studies is based on the formation of NPs in polymeric matrix as reaction medium. The multistage synthetic procedure usually involves the following sequential steps: The synthesis of the proper polymeric support; addition of metal precursor into the polymeric matrix either from the gaseous or from liquid phases (more rarely by mixing the components in the solid phase); formation of NPs followed by the removal of undesired (unbound) chemical products and solvents. However, many of these methods are multistage and quite laborious.

Among the wide variety of existing ways for the nanomaterials preparation, the thermolysis of their metal compounds is one of the simplest and most inexpensive methods for preparing NPs with narrow size distribution, low crystalline defects, and tunable shapes [1–7, 86, 156–179]. Thermolysis is known as general method to synthesize a wide range of nanomaterials including metals (M), metal oxides (MOs), metal sulfides (MSs), etc. Thermolysis technique is a chemical process in which chemical precursors decompose under suitable thermal treatment into one solid compound and unwanted by-products evaporate or can be removed by washing with solvents. Thermolysis has a number of advantages, primarily related to its economy and environmental friendliness [180, 181]. In addition, thermolysis methods are very promising [182–184], since they allow to regulating the synthesis conditions, particle size, and morphology, and also their purity [185–188]. Of no small importance is the fact that thermolysis requires a short time and has high yields, low cost, and low power consumption. Using thermolysis leads to the NPs with various morphologies, for example, nanorods [189], nanoflowers [190],

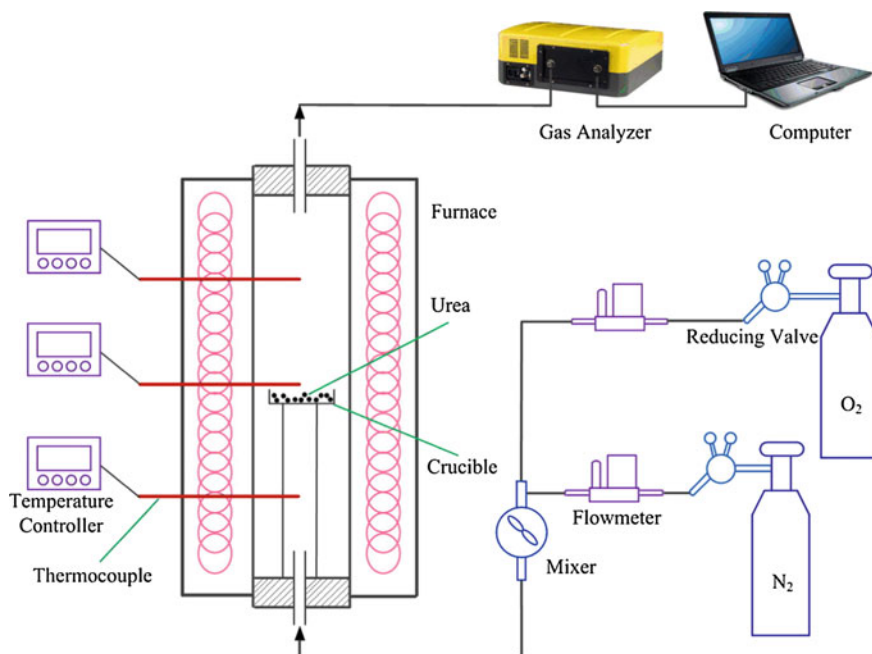


Fig. 1.2 Schematic of the experimental setup for the thermolysis of a precursor

nanoplastics [191], and also provides the possibility of large-scale production [192, 193]. Therefore, it is considered as an easily accessible and economical way of obtaining NPs of controlled sizes and shapes in large quantities [191, 194–196]. It is important that thermolysis not only allows to avoiding special equipment, complex technological processes, and heavy synthesis conditions, but also providing a good control of the composition, homogeneity, purity, phase, and microstructure of the produced nanomaterials [197–212].

The synthesis of nanomaterials can be implemented by two main methods: “dry” and “wet.” The dry method is characterized by the complete elimination of a solvent from the technological process (Fig. 1.2). In the thermolysis without solvent, precursor decomposes at high temperature. The atmosphere of the reaction can affect the type of NPs. For instance, MO NPs and metal NPs are formed in air and inert atmosphere, respectively. The choice of the precursor is paramount in the dry method of thermolysis. The thermolysis temperature of the precursor should not be too high, since an increase in the reaction temperature results in the formation of larger particles with a wide particle size distribution. During this procedure, some other chemicals are also added to the system to produce the final product with the desired morphology. Due to the poor solubility of the components, and in some cases of their chemical instability, as well as the difficulties in the subsequent removal of certain solvents, including environmental aspects, a “dry” process for the production of nanomaterials is preferred.

The wet process is characterized by one component (or at least one stage of a multistage process) used as a solution or dispersion in solution. Water or an organic solvent is used as the solvent, the first being the best among all the decomposing media. A remarkable advantage of the hydrothermal technology for the production of nanomaterials is the preparation of monodisperse NPs with complete control of their shape and size, as well as chemical homogeneity (Fig. 1.3) [65]. Thus, a significant number of advanced nanomaterials, NPs, and nanocomposites with conductive and semiconducting properties, including compounds of elements II–VI and III–V groups, silicates, sulfides, hydroxides, tungstates, titanates, carbon, zeolites, ceramics, composites, etc., has been synthesized using a hydrothermal process. Despite all the advantages, there are some disadvantages in hydrothermal technology, such as low safety, high pressure, and temperature; in addition, there is always the danger of an autoclave explosion [65].

Thermal degradation of precursor in organic solvents is another kind of thermolysis method (Fig. 1.4) [180]. Thermolysis in organic solvents is less aggressive than dry method, because the associated decomposition rate is more controlled than thermal treatment. In this method, to obtain more dispersed particles with a smaller size, there are many parameters that can be optimized, such as solvent, reaction temperature and time. To reduce the rate of thermolysis, some other chemicals, such

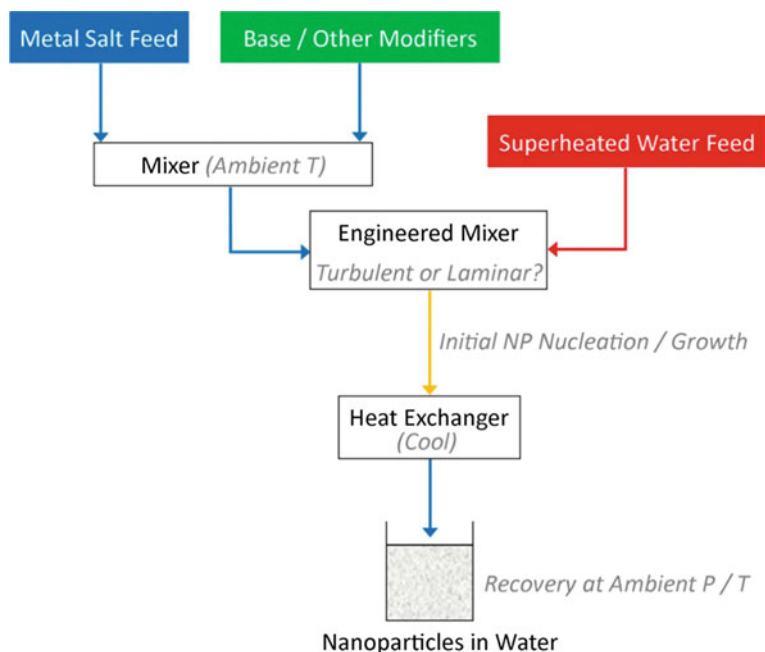
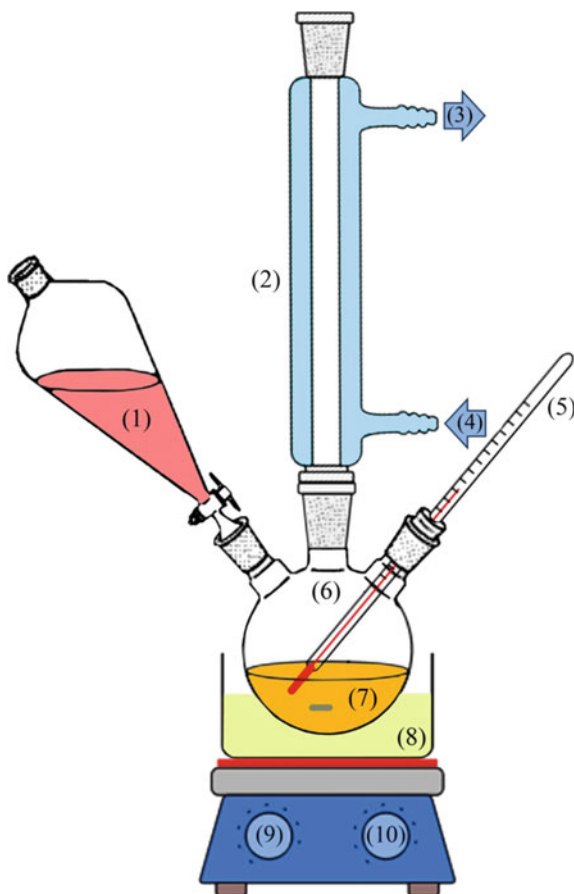


Fig. 1.3 Simplified process flow of a continuous hydrothermal flow synthesis type process for the synthesis of NPs in an engineered mixer under high pressure. Reproduced with permission from Ref. [65]. Copyright (2017) American Chemical Society

Fig. 1.4 Schematic diagram of the experimental setup for thermolysis: (1) surfactant/reducer solution; (2) water condenser; (3) water outlet; (4) water inlet; (5) thermometer; (6) three-neck flask; (7) precursor solution; (8) oil bath; (9) heat control; (10) speed control. Reproduced with permission from Ref. [180]. Copyright (2017) Elsevier



as surfactants or capping agents, are used additionally. By reducing the rate of thermolysis, the size, particle size distribution, and shape of the NPs are more governable. According to this method, special NPs can be easily synthesized for a specific application.

Regarding the critical role of thermal energy, various thermal sources, including furnaces, lasers, ultrasonic equipment, electric discharge, microwave, plasma, and many other thermal resources were used to decompose the precursors. For this purpose, any individual method can provide uniform or temporary thermal energy. Some thermal sources can even supply energy in picoseconds or nanoseconds in a very small space.

For the synthesis of NPs by thermolysis, various types of chemical compounds, including carbonyls, nitrates, carboxylates (such as acetates, oleates, oxalates, phthalates), acetylacetonates, polymers, and complex coordination compounds are suitable precursors. These precursors are able to decompose into solid substances, NPs, and other volatile by-products. It should be noted that the choice of precursors

is an important step in the thermolysis method, since it determines the size of the final particles and their size distribution.

Thermolysis usually requires metallic precursors with certain properties such as high purity, easy handling, facile storage, non-toxicity, low temperature decomposition [213–216]. Depending on the synthetic route chosen to convert these precursors into nanomaterials, some additional properties are also required, such as improved stability, solubility, or volatility. Bi- and multimetallic nanomaterials can be prepared using either a mixture of precursors or a “single-source” precursor (SSP) containing all the necessary elements in one molecule, the latter providing better homogeneity at the molecular level. Nevertheless, then the correct stoichiometry corresponding to the final materials is required. The use of precursor chemistry makes it possible to control the chemical and phase composition, crystallinity, morphology, porosity, and surface characteristics of the nanomaterials obtained.

Some of the most important precursors are metal complexes [217–224]. It should be emphasized that the central component of any successful synthesis of nanomaterials using thermolysis is the initial choice of metal complexes with a corresponding ligand environment in combination with rational thermolysis conditions [2, 6, 7, 97–101, 180, 225–227].

It is well known that in coordination chemistry, the ligand environment in metal complexes determines their overall thermodynamic and kinetic stability. Among the most well-known examples, mention should be made of chelating ligands that provide thermodynamic stabilization of metal complexes by chelating or macrocyclic effect [228, 229]. Chelation is the type of binding of ligands to metal ions. It involves the formation or the presence of two or more separate coordination or coordination and covalent bonds between a polydentate (multiply connected) ligand and one central metal atom. According to the classical definition, the chelate effect is the enhanced affinity of the chelating ligands to the metal ion compared to the affinity of a set of similar non-chelating (monodentate) ligands for the same metal. Ligands that contain more than one binding site for the metal ion are called chelating ligands (from the Greek word $\chi\eta\lambda\acute{\iota}$, $ch\acute{e}l\acute{e}$, which means “claw”). As the name suggests, chelating ligands have a high affinity for metal ions with respect to ligands with only one binding group (called monodentate = “single tooth”) ligands. The macrocyclic effect follows the same principle as the chelate effect, but the effect is further enhanced by the cyclic conformation of the ligand. Macrocyclic ligands are not only multidentate but also covalently bounded by their cyclic form, which allows for less conformational freedom. It is believed that the chelating ligand is “pre-organized” for binding, and to wrap it around the metal ion, there is a slight restriction of entropy. The strategy of using chelating ligands helps in achieving many of the aforementioned properties of the precursors.

The classification of metal chelates adopted in this monograph includes four types of compounds: molecular metal chelates, intracomplex compounds, macrocyclic complexes, and polynuclear chelates of metals. In metal chelates of molecular type, chelation of metal ions occurs only through coordination bonds. The binding of the metal ion by both covalent and coordination bonds is characteristic

for intracomplex compounds. Chelating of metals with ligands containing macrocyclic groups leads to macrocyclic complexes. Finally, polynuclear metal chelates contain two or more metal ions and at least one of them must be part of the metallocycle. In the future, metal chelates are classified depending on the nature of the donor atoms (N,N-, N,O-, N,S-, O,O-, etc.).

The unquestionable advantages of metal chelates include the ease of synthesis, stability with respect to moisture and atmospheric oxygen at room temperature, safety, and in many cases more cost-effective than, for example, multicomponent systems. In addition, good scalability and controllability of the process of obtaining nanomaterials by means of thermolysis of metal chelates are also attractive. Currently, coordination chemistry provides an extensive library of potential metal chelates, which are regarded as precursors for nanomaterials. Possible roles of chelating ligands in the preparation of nanomaterials by thermolysis of metal chelates are as follows [180, 225–227]:

- regulation of kinetic and thermodynamic stability of precursors by metal chelation,
- increase in colloidal stability by coordinating the chelating ligand with NP surface,
- determination of the direction of growth of the nanocrystal into the targeted forms by coordinating the chelating ligand with NP surface,
- use of a ligand as a reducing agent and/or a capping agent.

As an interesting example, we note the influence of the structure of the metal chelate precursor on the characteristics of the produced NPs. In particular, the change in the geometry of the precursor affects the morphology of NPs from spherical to pyramidal when the precursor geometry changes from octahedral to square pyramidal, respectively [230].

The growing interest in the thermolysis of metal chelates in the condensed phase is associated with the possibility of obtaining a variety of materials possessing a nanoscale spatial organization: Metal-containing particles form a core stabilized by a polymer shell consisting of the chelating ligand decomposition products [5, 122, 181, 231–233]. This synthetic technique is an example of a bottom-up approach for assembling NP from individual atoms (or ions and then reducing them) to an NP of the required size in the presence of a precursor of a polymer stabilizing matrix. It is important that the properties of the nanostructured materials obtained can be controlled by changing the composition and properties of the metal chelate precursors [234, 235].

The synthetic technique for obtaining nanostructured materials is often also based on the thermolysis of metal chelates like SSP in a hot organic solvent with a high-boiling point. It is important that this method does not require the use of a reducing agent, which is one of the most attractive advantages of this approach. In some cases, the solvent itself acts as a reducing agent depending on the electropositivity of the metal cation used. Very often, a surfactant is added to the solvent to reduce the coalescence between the NPs, increasing their mutual

repulsion. This method is widely used because it leads to a narrow NP size distribution and provides significant control over the shape of NPs for various metals [25, 40, 180, 227, 236].

It should also be noted the use of precursors consisting of several metal chelates for the purposeful synthesis of bi- and polymetallic nanostructured materials [34, 57, 237–239]. Despite the wide usage of such approaches, including two or more precursors, they have significant limitations, since the formation of the targeted nanomaterial often depends on the relative reactivity of each component, their stability, etc.

In the field of hybrid materials science [240, 241], thermolysis is a challenging technique for the manufacture of metal–polymer nanocomposites.

The use of concepts and methods for the chemistry of metal chelates provided significant advances in the development of well-defined nanomaterials, indicating the key roles of both metal chelates and stabilizing agents (polymers, dendrimers, ionic liquids, ligands, etc.) in three main stages of nanostructure formation: release of metal atoms, nucleation, and growth [242]. It is now recognized that the interaction between a metal chelate and a stabilizing agent can generate intermediate complexes in a reactive medium that can change the course of the reaction. In addition, the coordination of the chelating ligand on growing seeds is recognized as an important factor affecting the growth of nanostructures. Finally, coordination of the chelating ligand on the surface of nanostructures can cause a change in their physical and chemical properties by adjusting the electron density and steric hindrances on their surface.

The idea that a metal surfactant complex can act both as the metal ion source as well as NP protector opens up a new method for nanosynthesis while eliminating the need for any stabilizing or capping agents.

It should be noted that the use of metallosurfactants as SSPs for the synthesis of NPs is a relatively simple and highly effective way to high-quality crystalline nanostructures with good yields. This “one-pot” synthetic route allows you to effectively control the size and shape of the NPs by simply changing the reaction conditions [243, 244]. Because metal-surfactant complex can act both as a source of metal ions and as NP protector, this method for the synthesis of nanomaterials eliminates the need for any stabilizing or capping agents.

In this book, we analyze all types of metal chelates used as precursors for the fabrication of nanomaterials via thermolysis. In particular, of special interest are polymeric metal chelates (PMCs), in which the metal is chemically bound to the polymer, containing active chelating fragments. The characteristic features allowing to reliably identifying PMCs as a specific class of chemical compounds are the presence of the polymer chains and metallochelatate cycles [245]. PMCs are a promising field of coordination chemistry because of their specific properties and high thermal stability in comparison with conventional polymeric complexes. In addition, PMCs are located at the intersection of the border areas of science, polymer, and coordination chemistry. The combination of metal chelates and polymers in a single chemical facility is a rather complex path, where in each case it is necessary to use their own methods of synthesis and research. PMCs are very

interesting materials that combine typical polymer features with properties of metal chelates. The polymer chain in PMCs allows them in many cases to behave like ordinary macromolecular compounds, and the presence of a metal ion in the chain is responsible for a number of properties characteristic of a given metal ion.

The extended hybrid crystalline complex compounds formed by organic ligands (also called spacers) and metal ions expanding in one, two or three dimensions due to the formation of a metal–ligand (M-L) coordination bond are called coordination polymers (CPs) [246–253]. CPs refer to a special class of PMC containing a metal in the backbone, the feature of which is the destruction of the polymer chain after metal removal. For the first time, the term “coordination polymer” was used in 1964 [254]. In the first stage of the studies, CPs were obtained by simply mixing the components or using a template method, resulting in insoluble substances whose exact structure could not be determined. A great leap forward in the directed synthesis of CPs was made in the 1990s due to the wide introduction of new methods for the production of such materials, primarily the solvothermal method [255, 256], which made it possible to obtain pure substances suitable for X-ray investigation. Controlling the process of molecular self-assembly of CPs, it is possible to obtain new crystalline functional materials with specified practical properties. Because they contain large voids in the crystal structure, they were called porous CPs or metal–organic frameworks (MOF). This term MOF was popularized around 1995 [257, 258], and it highlights their similarity to traditional structure of solids, in particular, zeolite framework materials, and thus characterizes reliability and porosity. MOFs are characterized by an interesting architecture, crystalline state, capable of surface modification and have potential applications in the areas of storage of gaseous fuel, catalysis, magnetism, and separation. The emergence of MOFs became a real outbreak in science and served as a powerful catalyst for the intensive development of CP chemistry.

It should be noted the development of PMC studies as precursors of nanomaterials, since they serve not only as a starting material for the design of sizes, shapes, and the chemical composition of the final product, but also for the stabilization of the formed NPs [1, 2, 4, 6, 7, 123, 259–265]. In addition, the use of PMCs makes it possible to obtain nanomaterials with low crystal defects, a narrow size distribution, and tunable shapes under high-temperature thermolysis [156, 261]. From the point of view of designing functional nanomaterials, solid-state thermolysis of PMCs with a wide variety of structures, compositions, and architectures provides a simple and efficient method for the synthesis of new nanostructured materials. Of considerable interest is the development of many important concepts, such as size distribution focusing, selective adhesion shape control, and branching to describe the thermolysis process [3, 5, 261, 266]. Thermolysis of PMCs under various conditions has been extensively studied for obtaining metal-containing nanostructures with target morphologies and sizes [1, 2, 4, 6, 7, 123, 157, 158, 160, 259, 267–270]. It is important that various nanomaterials, such as metals, metal oxides, metal sulfides, and metal halides, can be obtained using PMCs or their precursors.

Recently, a new approach has been developed [122], based on the use of metal chelate monomers (MCMs) as precursors. These monomers contain metal chelate cycle and multiple bonds to polymerization or functionality that may be involved in the polycondensation [271–278]. It is important that the undoubted advantage of MCMs is the increased stability compared to unchelated counterparts due to the chelate or macrocyclic effect [258]. This method involves thermal polymerization of the MCM with the formation of corresponding metal-containing polymer and its controlled thermolysis, resulting in NPs with the structure “core–shell.” Thus, the MCM polymerization and synthesis of metal NPs occur simultaneously during the thermal transformation.

This book covers the major advances in the nanomaterials preparation by thermolysis of metal chelates and includes chapters devoted general characteristics of the methods of thermolysis of metal compounds, thermolysis of low molecular weight metal chelates and PMCs, the conjugate thermolysis—thermal polymerization of MCMs and thermolysis of polymers formed in situ, as well as applications of nanomaterials prepared by thermolysis of metal chelates. We focused on emphasizing achievements and problems in this interesting field, which will be periodically filled with new experimental and theoretical results, thus creating a complete pattern.

References

1. A.D. Pomogailo, A.S. Rozenberg, I.E. Uflyand, *Nanochastitsy metallov v polimerakh (Metal Nanoparticles in Polymers)* (Khimiya, Moscow, 2000)
2. A.D. Pomogailo, G.I. Dzhardimalieva, V.N. Kestelman, *Macromolecular Metal Carboxylates and Their Nanocomposites* (Springer, Heidelberg, 2010)
3. G.I. Dzhardimalieva, A.D. Pomogailo, *Russ. Chem. Rev.* **77**, 259 (2008)
4. A.D. Pomogailo, G.I. Dzhardimalieva, *Monomeric and Polymeric Metal Carboxylates* (Fizmatlit, Moscow, 2009)
5. A.D. Pomogailo, A.S. Rozenberg, G.I. Dzhardimalieva, *Russ. Chem. Rev.* **80**, 257 (2011)
6. A.D. Pomogailo, G.I. Dzhardimalieva, *Nanostructured Materials Preparation via Condensation Ways* (Springer, Dordrecht, 2014)
7. A.D. Pomogailo, G.I. Dzhardimalieva, *Metallopolymeric Hybride Nanocomposites* (Nauka, Moscow, 2015)
8. Z. Abdullaeva, *Nano- and Biomaterials: Compounds, Properties, Characterization, and Applications* (Wiley, Weinheim, 2017)
9. V.K. Tewary, Y. Zhang (eds.), *Modeling, Characterization, and Production of Nanomaterials: Electronics, Photonics and Energy Applications* (Elsevier, Amsterdam, 2015)
10. M.A. Shah, J.P. Davim, M.A. Bhat, *Nanotechnology Applications for Improvements in Energy Efficiency and Environmental Management* (IGI Global, Pennsylvania, US, 2015)
11. M.V. Kovalenko, L. Manna, A. Cabot, Z. Hens, D.V. Talapin, C.R. Kagan, V.I. Klimov, A.L. Rogach, P. Reiss, D.J. Milliron, P. Guyot-Sionnest, G. Konstantatos, W.J. Parak, T. Hyeon, B.A. Korgel, C.B. Murray, W. Heiss, *ACS Nano* **9**, 1012 (2015)
12. G. Cao, Y. Wang (eds.), *Nanostructures and Nanomaterials: Synthesis, Properties, and Applications*, 2nd edn. (World Scientific, New Jersey, 2011)

13. D. Vollath, *Nanomaterials: An Introduction to Synthesis, Properties and Applications*, 2nd edn. (Wiley, Weinheim, 2013)
14. S. Logothetidis (ed.), *Nanostructured Materials and Their Applications* (Springer, Heidelberg, 2012)
15. D. Shi, *Nanomaterials and Devices*, 1st edn. (Elsevier, Amsterdam, 2014)
16. Z.P. Aguilar, *Nanomaterials for Medical Applications* (Elsevier, Amsterdam, 2013)
17. O. Manasreh, *Introduction to Nanomaterials and Devices* (Wiley, Weinheim, 2012)
18. G. Schmid (ed.), *Nanoparticles: From Theory to Application*, 2nd edn. (Wiley, Weinheim, 2010)
19. A. Iqbal, K. Iqbal, B. Li, D.Y. Gong, W.W. Qin, J. Nanosci. Nanotechnol. **17**, 4386 (2017)
20. S.-I. Lee, J. Kim, J.-W. Son, J.-H. Lee, B.-K. Kim, H.-J. Je, H.-W. Lee, H. Song, K.J. Yoon, J. Power Sources **250**, 15 (2014)
21. A. Sakunthala, M.V. Reddy, S. Selvasekarapandian, B.V.R. Chowdari, P.C. Selvin, Electrochim. Acta **55**, 4441 (2010)
22. K. Saravanan, V. Ramar, P. Balaya, J.J. Vittal, J. Mater. Chem. **21**, 14925 (2011)
23. S. Ko, J.-I. Lee, H.S. Yang, S. Park, U. Jeong, Adv. Mater. **24**, 4451 (2012)
24. G. Wang, L. Zhang, J. Zhang, Chem. Soc. Rev. **41**, 797 (2012)
25. K. Mahendraprabhu, P. Elumalai, J. Sol-Gel Sci. Technol. **73**, 428 (2015)
26. M. Bañobre-López, C. Bran, C. Rodríguez-Abreu, J. Gallo, M. Vázquez, J. Rivas, J. Mater. Chem. B **5**, 3338 (2017)
27. X. Gu, H. Wang, J.P. Camden, Chem. Sci. **8**, 5902 (2017)
28. E. Aşık, Y. Akpınar, N.T. Güray, M. İşcan, G.Ç. Demircigil, M. Volkan, Toxicol. Res. **5**, 1649 (2016)
29. E. Palazzi, F. Curro, A. Reverberi, B. Fabiano, Process Saf. Environ. Prot. **92**, 357 (2014)
30. Y. Zhang, R. Huang, X. Zhu, L. Wang, C. Wu, Chin. Sci. Bull. **57**, 238 (2012)
31. O.A. Alawi, N.A.C. Sidik, H.A. Mohammed, S. Syahrullail, Int. Commun. Heat Mass Transfer **56**, 50 (2014)
32. C. Vianello, B. Fabiano, E. Palazzi, G. Maschio, J. Loss, Prev. Process Ind. **25**, 718 (2012)
33. B. Fabiano, F. Pistrutto, A. Reverberi, E. Palazzi, Clean Technol. Environ. Policy **17**, 1261 (2015)
34. Y. Liu, G. Zhao, D. Wang, Y. Li, Natl. Sci. Rev. **2**, 150 (2015)
35. K. Zhou, Y. Li, Angew. Chem. Int. Ed. **51**, 602 (2012)
36. L. Jin, B. Liu, S.S. Duay, J. He, Catalysts **7**, 44 (2017)
37. K.T. Arul, E. Manikandan, P.P. Murmu, J. Kennedy, M. Henini, J. Alloys Compd. **720**, 395 (2017)
38. G. Leahu, E. Petronijevic, A. Belardini, M. Centini, R. Li Voti, T. Hakkarainen, E. Koivusalo, M. Guina, C. Sibilila, Sci. Rep. **7**, 2833 (2017)
39. S. Yuan, F. Ge, X. Yang, S. Guang, J. Fluoresc. **26**, 2303 (2016)
40. I.B. Burgess, N. Abedzadeh, T.M. Kay, A.V. Shneidman, D.J. Cranshaw, M. Lončar, J. Aizenberg, Sci. Rep. **6**, 19542 (2016)
41. A. Bansal, S.S. Verma, Phys. Lett. A **379**, 163 (2015)
42. H. Tian, H. Fan, J. Ma, Z. Liu, L. Ma, S. Lei, J. Fang, C. Long, J. Hazard. Mater. **341**, 102 (2018)
43. W. Lu, X. Qin, Y. Luo, G. Chang, X. Sun, Microchim. Acta **175**, 355 (2011)
44. Y.B. Hahn, R. Ahmad, N. Tripathy, Chem. Commun. (Camb.) **48**, 10369 (2012)
45. C. Toccafondi, S. Thorat, R. La Rocca, A. Scarpellini, M. Salerno, S. Dante, G. Das, J. Mater. Sci. Mater. Med. **25**, 2411 (2014)
46. C.H. Lai, G.A. Wang, T.K. Ling, T.J. Wang, P.K. Chiu, Y.F. Chou Chau, C.C. Huang, H.P. Chiang, Sci. Rep. **7**, 5446 (2017)
47. J.T. Dias, G. Svedberg, M. Nystrand, H. Andersson-Svahn, J. Gantelius, Sci. Rep. **7**, 6837 (2017)
48. B. Kang, B. Cha, B. Kim, S. Han, M.-K. Shin, E. Jang, H.-O. Kim, S.R. Bae, U. Jeong, I. Moon, H.Y. Son, Y.-M. Huh, S. Haam, Anal. Chem. **88**, 1078 (2016)

49. R.D. Brohi, L. Wang, H.S. Talpur, D. Wu, F.A. Khan, D. Bhattarai, Z.U. Rehman, F. Farmanullah, L.J. Huo, *Front. Pharmacol.* **8**, 606 (2017)
50. P. Hashemi, H. Bagheri, A. Afkhami, S. Amidi, T. Madrakian, *Talanta* **176**, 350 (2018)
51. L.G. Astafyeva, V.K. Pustovalov, W. Fritzsche, *Photonics Nanostruct. Fundam. Appl.* **26**, 35 (2017)
52. R. Narayanan, *Molecules* **15**, 2124 (2010)
53. A. Umar, *Metal Oxide Nanostructures and Their Applications* (American Scientific Publishers, Valencia, 2009)
54. A. Ugulava, Z. Toklikishvili, S. Chkhaidze, S. Kekutia, *Phys. B Condens. Matter* **513**, 77 (2017)
55. H.B. Bohidar, K. Rawat, *Design of Nanostructures: Self-Assembly of Nanomaterials* (Wiley, Weinheim, 2017)
56. J.A. Rodriguez, M. Fernandez-Garcia (eds.), *Synthesis, Properties and Applications of Oxides Nanomaterials* (Wiley, Hoboken, 2007)
57. Y.M. Li, G. Somorjai, *Nano Lett.* **10**, 2289 (2010)
58. R. Richards, R. Koodali, K. Klabunde, L. Erickson (eds.), *Nanoscale Materials in Chemistry: Environmental Applications* (ACS Publications, Washington, DC, 2011)
59. A. Ali, H. Zafar, M. Zia, I. Haq, A.R. Phull, J.S. Ali, A. Hussain, *Nanotechnol. Sci. Appl.* **9**, 49 (2016)
60. K. Philippot, P. Serp (eds.), *Concepts in Nanocatalysis* (Wiley-VCH, Weinheim, 2013)
61. K.N. Trohidou (ed.), *Magnetic Nanoparticle Assemblies* (CRC Press, Pan Stanford, Boca Raton, 2014)
62. H. Montaseri, S. Alipour, M.A. Vakilnezhad, *Res. Pharm. Sci.* **12**, 274 (2017)
63. L. Wang, Z. Zhang, X. Han, *NPG Asia Mater.* **5**, e40 (2013)
64. H.B. Mantravadi, *J. Clin. Diagn. Res.* **11**, DC37 (2017)
65. J.A. Darr, J. Zhang, N.M. Makwana, X. Weng, *Chem. Rev.* **117**, 11125 (2017)
66. K. Logaranjan, A.J. Raiza, S.C.B. Gopinath, Y. Chen, K. Pandian, *Nanoscale Res. Lett.* **11**, 520 (2016)
67. M.H. Rashid, S.F. Ralph, *Nanomaterials (Basel)* **7**, 99 (2017)
68. D. Liu, X. Xu, Y. Du, X. Qin, Y. Zhang, C. Ma, S. Wen, W. Ren, E.M. Goldys, J.A. Piper, S. Dou, X. Liu, D. Jin, *Nat. Commun.* **7**, 10254 (2016)
69. F. Zhang, L. Qi, *Adv. Sci.* **3**, 1600049 (2016)
70. S. Chawla, K. Jayanthi, Z.H. Khan, J. Shah, R.K. Kotnala, *Mater. Des.* **31**, 1666 (2010)
71. A.V. Zhukhovitskiy, M.J. MacLeod, J.A. Johnson, *Chem. Rev.* **115**, 11503 (2015)
72. Y. Du, X. He, Y. Zhan, S. Li, Y. Shen, F. Ning, L. Yan, X. Zhou, *ACS Catal.* **7**, 3607 (2017)
73. T.H. Noh, O.-S. Jung, *Acc. Chem. Res.* **49**, 1835 (2016)
74. H. Goesmann, C. Feldmann, *Angew. Chem. Int. Ed.* **49**, 1362 (2010)
75. A. Schatz, O. Reiser, W.J. Stark, *Chem. Eur. J.* **16**, 8950 (2010)
76. Z. Zhuang, Q. Peng, Y. Li, *Chem. Soc. Rev.* **40**, 5492 (2011)
77. A. Lassenberger, T.A. Grünewald, P.D.J. van Oostrum, H. Rennhofer, H. Amenitsch, R. Zirbs, H.C. Lichtenegger, E. Reimhult, *Chem. Mater.* **29**, 4511 (2017)
78. V.V. Krisyuk, I.A. Baidina, N.A. Kryuchkova, V.A. Logvinenko, P.E. Plyusnin, I.V. Korolkov, G.I. Zharkova, A.E. Turgambaeva, I.K. Igumenov, *Dalton Trans.* **46**, 12245 (2017)
79. I. Iavicoli, V. Leso, W. Ricciardi, L.L. Hodson, M.D. Hoover, *Environ. Health* **13**, 78 (2014)
80. T. Abeywickrama, N.N. Sreeramulu, L. Xu, H. Rathnayake, *RSC Adv.* **6**, 91949 (2016)
81. M. Ramanathan, S.M. Kilbey II, Q. Ji, J.P. Hill, K. Ariga, *J. Mater. Chem.* **22**, 10389 (2012)
82. K. Ariga, T. Mori, J.P. Hill, *Adv. Mater.* **24**, 158 (2012)
83. Q. Li, S. Sun, *Nano Energy* **29**, 178 (2016)
84. A. Abedini, A.R. Daud, M.A.A. Hamid, N.K. Othman, E. Saion, *Nanoscale Res. Lett.* **8**, 474 (2013)
85. S.G. Kwon, T. Hyeon, Kinetics of colloidal chemical synthesis of monodisperse spherical nanocrystals, in *Nanoscale Materials in Chemistry*, 2nd edn., ed. by K.J. Klabunde, R.M. Richards (Wiley, Hoboken, 2009), pp. 127–153

86. B.G. Rao, D. Mukherjee, B.M. Reddy, Novel approaches for preparation of nanoparticles, in *Nanostructures for Novel Therapy. Synthesis, Characterization and Applications* (Elsevier, Amsterdam, 2017), pp. 1–36
87. S.-Z. Qiao, J. Liu, G.Q. Max Lu, Synthetic chemistry of nanomaterials, in *Modern Inorganic Synthetic Chemistry*, 2nd edn., ed. by R. Xu, Y. Xu (Elsevier, Amsterdam, 2017), pp. 613–640
88. P.M. Visakh, M.J.M. Morlanes (eds.), *Nanomaterials and Nanocomposites: Zero- to Three-Dimensional Materials and Their Composites* (Wiley, Weinheim, 2016)
89. J. Marques-Hueso, R. Abargues, J. Canet-Ferrer, J. Valdes, J. Martinez-Pastor, *Microelectron. Eng.* **87**, 1147 (2010)
90. M.J. Madou, *Fundamentals of Microfabrication and Nanotechnology: From MEMS to Bio-MEMS and Bio-NEMS: Manufacturing Techniques and Applications* (CRC Press Inc, Boca Raton, 2011)
91. M. Rai, C. Posten (eds.), *Green Biosynthesis of Nanoparticles: Mechanisms and Applications* (CRC Press, Boca Raton, 2017)
92. W. Cai, F. Chen (eds.), *Hybrid Nanomaterials: Design, Synthesis, and Biomedical Applications* (CAB International, 2013)
93. Z. Abdullaeva, *Synthesis of Nanoparticles and Nanomaterials. Biological Approaches* (Springer, Switzerland, 2017)
94. O.V. Kharissova, H.V. Rasika Dias, B.I. Kharisov, B. Olvera Pérez, V.M. Jiménez Pérez, *Trends Biotechnol.* **31**, 240 (2013)
95. N.I. Hulkoti, T.C. Taranath, *Colloids Surf. B Biointerfaces* **121**, 474 (2014)
96. P. Liu, R. Qin, G. Fu, N. Zheng, *J. Am. Chem. Soc.* **139**, 2122 (2017)
97. I. Karadjova, I. Dakova, T. Yordanova, P. Vasileva, *J. Anal. At. Spectrom.* **31**, 1949 (2016)
98. S. Zhang, R. Geryak, J. Geldmeier, S. Kim, V.V. Tsukruk, *Chem. Rev.* **2017** (Article ASAP)
99. F. Tao, L. Nguyen, S. Zhang, in *Metal Nanoparticles for Catalysis: Advances and Applications*, RSC Catalysis Series, no. 17, ed. by F. Tao (RSC, London, 2014)
100. G. Prieto, H. Tüysüz, N. Duyckaerts, J. Knossalla, G.-H. Wang, F. Schüth, *Chem. Rev.* **116**, 14056 (2016)
101. X. Wang, J. Feng, Y. Bai, Q. Zhang, Y. Yin, *Chem. Rev.* **116**, 10983 (2016)
102. L. Zhou, Z. Zhuang, H. Zhao, M. Lin, D. Zhao, L. Mai, *Adv. Mater.* **29**, 1602914 (2017)
103. Y. Wang, J. He, C. Liu, W.H. Chong, H. Chen, *Angew. Chem. Int. Ed.* **54**, 2022 (2015)
104. A.D. Pomogailo, *Russ. Khim. Zh. (Mendeleev Chem. J.)* **46**, 64 (2002)
105. B.R. Cuenya, *Thin Solid Films* **518**, 3127 (2010)
106. L. Pan, M. Gu, G. Ouyang, C.Q. Sun, *Key Eng. Mater.* **444**, 17 (2010)
107. D. Uzio, G. Berhault, *Catal. Rev. Sci. Eng.* **52**, 106 (2010)
108. S. Nath, S. Jana, M. Pradhan, T. Pal, *J. Colloid Interface Sci.* **341**, 333 (2010)
109. S. Mourdikoudis, L.M. Liz-Marzain, *Chem. Mater.* **25**, 1465 (2013)
110. D.-Y. Kim, M. Kim, S. Shinde, R.G. Saratale, J.-S. Sung, G. Ghodake, *ACS Sustain. Chem. Eng.* **5**, 7678 (2017)
111. E.G. Bilé, E. Cortelazzo-Polisini, A. Denicourt-Nowicki, R. Sassine, F. Launay, A. Roucoux, *ChemSusChem* **5**, 91 (2012)
112. N. Yan, J. Zhang, Y. Yuan, G.-T. Chen, P.J. Dyson, Z. Li, Y. Kou, *Chem. Commun.* **46**, 1631 (2010)
113. V.S. Myers, M.G. Weir, E.V. Carino, D.F. Yancey, S. Pande, R.M. Crooks, *Chem. Sci.* **2**, 1632 (2011)
114. D. Astruc, A.K. Diallo, C. Ornelas, in *Nanomaterials and Catalysis*, ed. by P. Serp, K. Philippot (Wiley-VCH, Weinheim, 2013), ch. 3, p. 101
115. J. Dupont, J.D. Scholten, *Chem. Soc. Rev.* **39**, 1780 (2010)
116. J.D. Scholten, M.G. Precht, J. Dupont, *Handbook of Green Chemistry*, vol. 8 (Wiley-VCH-Verlag, Weinheim, 2012), p. 1
117. C. Yang, Q. Li, C. Cai, J. Lin, *Langmuir* **32**, 6917 (2016)
118. S.H. Jo, H.W. Kim, M. Song, N.J. Je, S. Oh, B.-Y. Chang, J. Yoon, J.H. Kim, B. Chung, S.I. Yoo, *ACS Appl. Mater. Interfaces* **7**, 18778 (2015)

119. N. Yan, H. Liu, Y. Zhu, W. Jiang, Z. Dong, *Macromolecules* **48**, 5980 (2015)
120. J. Song, B. Duan, C. Wang, J. Zhou, L. Pu, Z. Fang, P. Wang, T.T. Lim, H. Duan, *J. Am. Chem. Soc.* **136**, 6838 (2014)
121. L. Wan, Z. Chen, C. Huang, X. Shen, *TrAC Trends Anal. Chem.* **95**, 110 (2017)
122. A.D. Pomogailo, G.I. Dzhardimalieva, *Macromol. Symp.* **317–318**, 198 (2012)
123. A.D. Pomogailo, V.N. Kestelman, *Metallopolymer Nanocomposites* (Springer, Berlin, 2005)
124. A. Tokarev, J. Yatvin, O. Trotsenko, J. Locklin, S. Minko, *Adv. Funct. Mater.* **26**, 3761 (2016)
125. A. Walter, A. Garofalo, P. Bonazza, F. Meyer, H. Martinez, S. Fleutot, C. Billotey, J. Taleb, D. Felder-Flesch, S. Begin-Colin, *ChemPlusChem* **82**, 647 (2017)
126. J.L. Daniels, T.M. Crawford, O.A. Andreev, Y.K. Reshetnyak, *Biochem. Biophys. Rep.* **10**, 62 (2017)
127. L. Mei, X. Zhang, Polymer-silver nanocomposites: preparation, characterisation and antibacterial mechanism, in *Silver Nanoparticles for Antibacterial Devices. Biocompatibility and Toxicity*, ed. by H. Cao (Routledge, London, 2017), pp. 111–132
128. L.M. Foster, A.J. Worthen, E.L. Foster, J. Dong, C.M. Roach, A.E. Metaxas, C.D. Hardy, E.S. Larsen, J.A. Bollinger, T.M. Truskett, C.W. Bielawski, K.P. Johnston, *Langmuir* **30**, 10188 (2014)
129. N.K. Maurya, P. Kushwaha, A. Mandal, *J. Taiwan Inst. Chem. Eng.* **70**, 319 (2017)
130. S.M. Louie, R.D. Tilton, G.V. Lowry, *Environ. Sci. Nano* **3**, 283 (2016)
131. K. Babu, R. Dhamodharan, *Nanoscale Res. Lett.* **4**, 1090 (2009)
132. R.G. Chaudhuri, S. Paria, *Chem. Rev.* **112**, 2373 (2012)
133. N.D. Burrows, W. Lin, J.G. Hinman, J.M. Dennison, A.M. Vartanian, N.S. Abadeer, E.M. Grzincic, L.M. Jacob, J. Li, C.J. Murphy, *Langmuir* **32**, 9905 (2016)
134. Z. Ferjaoui, R. Schneider, A. Meftah, E. Gaffet, H. Alem, *RSC Adv.* **7**, 26243 (2017)
135. G. Nie, G. Li, L. Wang, X. Zhang, *Polym. Chem.* **7**, 753 (2016)
136. B. He, L. Zhou, *RSC Adv.* **5**, 97764 (2015)
137. P. Chmielarz, J. Yan, P. Kryszewski, Y. Wang, Z. Wang, M.R. Bockstaller, K. Matyjaszewski, *Macromolecules* **50**, 4151 (2017)
138. Z. Zhang, P. Zhang, Y. Wang, W. Zhang, *Polym. Chem.* **7**, 3950 (2016)
139. J.O. Zoppe, N.C. Ataman, P. Mocny, J. Wang, J. Moraes, H.-A. Klok, *Chem. Rev.* **117**, 1105 (2017)
140. C.-W. Chu, Y. Higaki, C.-H. Cheng, M.-H. Cheng, C.-W. Chang, J.-T. Chen, A. Takahara, *Polym. Chem.* **8**, 2309 (2017)
141. C.S. Park, H.J. Lee, A.C. Jamison, T.R. Lee, *ACS Appl. Mater. Interfaces* **8**, 5586 (2016)
142. M. Lattuada, T.A. Hatton, *Langmuir* **23**, 2158 (2007)
143. J. Pellico, J. Ruiz-Cabello, I. Fernández-Barahona, L. Gutiérrez, A.V. Lechuga-Vieco, J.A. Enríquez, M.P. Morales, F. Herranz, *Langmuir* **33**, 10239 (2017)
144. C.-A.J. Lin, R.A. Sperling, J.K. Li, T.-Y. Yang, P.-Y. Li, M. Zanella, W.H. Chang, W.J. Parak, *Small* **4**, 334 (2008)
145. Y. Yong, Y. Bai, Y. Li, L. Lin, Y. Cui, C. Xia, *J. Magn. Magn. Mater.* **320**, 2350 (2008)
146. Y. Jiao, P. Akcora, *Macromolecules* **45**, 3463 (2012)
147. J.M. Hart, S.M. Kimani, L.R. Hutchings, I. Grillo, A.V. Hughes, N. Clarke, V. Garcia-Sakai, S.E. Rogers, B. Mendis, R.L. Thompson, *Macromolecules* **49**, 1434 (2016)
148. W.J. Brittain, S. Minko, *J. Polym. Sci. A Polym. Chem.* **45**, 3505 (2007)
149. F. Jiang, Y. Zhang, Z. Wang, W. Wang, Z. Xu, Z. Wang, *ACS Appl. Mater. Interfaces* **7**, 10563 (2015)
150. H. Dong, J. Huang, R.R. Koepsel, P. Ye, A.J. Russell, K. Matyjaszewski, *Biomacromolecules* **12**, 1305 (2011)
151. A.P. Majewski, U. Stahlschmidt, V. Jérôme, R. Freitag, A.H.E. Müller, H. Schmalz, *Biomacromolecules* **14**, 3081 (2013)
152. C. Huang, K.G. Neoh, E.-T. Kang, *Langmuir* **28**, 563 (2012)
153. M. Kobayashi, R. Matsuno, H. Otsuka, A. Takahara, *Sci. Technol. Adv. Mater.* **7**, 617 (2006)

154. P.B. Zetterlund, S.C. Thickett, S. Perrier, E. Bourgeat-Lami, M. Lansalot, *Chem. Rev.* **115**, 9745 (2015)
155. P. Ajikdkarn, P. Ritprajak, W. Injumba, T. Pornaveetus, N. Insin, *J. Magn. Magn. Mater.* **427**, 235 (2017)
156. A.P. Reverberi, N.T. Kuznetsov, V.P. Meshalkin, M. Salerno, B. Fabiano, *Theor. Found. Chem. Eng.* **50**, 59 (2016)
157. B.I. Kharisov, O.V. Kharissova, U.O. Méndez, *J. Coord. Chem.* **66**, 3791 (2013)
158. O. Carp, Materials obtained by solid-state thermal decomposition of coordination compounds and metal-organic coordination polymers, in *Reactions and Mechanisms in Thermal Analysis of Advanced Materials*, ed. by A. Tiwari, B. Raj (Scrivener Publishing LLC, Salem, Massachusetts, 2015)
159. M.A. Malik, P. O'Brien, *Organometallic and Metallo-Organic Precursors for Nanoparticles. Precursor Chemistry of Advanced Materials* (Springer, Berlin, 2005)
160. B.I. Kharisov, H.V. Rasika Dias, O.V. Kharissova, V.M. Jiménez-Pérez, B.O. Pérez, B.M. Flores, *RSC Adv.* **2**, 9325 (2012)
161. G.A. Seisenbaeva, V.G. Kessler, *Nanoscale* **6**, 6229 (2014)
162. R.S. Devan, R.A. Patil, J.-H. Lin, Y.-R. Ma, *Adv. Funct. Mater.* **22**, 3326 (2012)
163. Y. Eom, M. Abbas, H.Y. Noh, C.G. Kim, *RSC Adv.* **6**, 15861 (2016)
164. M. Hosseinifard, L. Hashemi, V. Amani, A. Morsali, *J. Struct. Chem.* **54**, 396 (2013)
165. T.P. Hernandez, G.A.H. Flores, O.E.C. Lopez, M.E.M. Sanchez, I.V. Arreola, E.G. Vergara, M.A.M. Rojas, *Inorg. Chim. Acta* **392**, 277 (2012)
166. L.R. Gonsalves, S.C. Mojumdar, V.M.S. Verenkar, *J. Therm. Anal. Calorim.* **108**, 859 (2012)
167. L.R. Gonsalves, S.C. Mojumdar, V.M.S. Verenkar, *J. Mater. Sci.* **100**, 789 (2010)
168. L.R. Gonsalves, S.C. Mojumdar, V.M.S. Verenkar, *J. Therm. Anal. Calorim.* **104**, 869 (2011)
169. F. Davar, M. Salavati-Niasari, Z. Fereshteh, *J. Alloys Compd.* **496**, 638 (2010)
170. M. Tanveer, C. Cao, I. Aslam, Z. Ali, F. Idrees, W.S. Khan, M. Tahir, S. Khalid, G. Nabi, A. Mahmood, *New J. Chem.* **39**, 1459 (2015)
171. Y. Li, J. Scott, Y.-T. Chen, L. Guo, M. Zhao, X. Wang, W. Lu, *Mater. Chem. Phys.* **162**, 671 (2015)
172. S.K. Maji, N. Mukherjee, A.K. Dutta, D.N. Srivastava, P. Paul, B. Karmakar, A. Mondal, B. Adhikary, *Mater. Chem. Phys.* **130**, 392 (2011)
173. S.H. Chaki, M. Deshpande, J.P. Taylor, *Thin Solid Films* **550**, 291 (2014)
174. J. Lee, S. Zhang, S. Sun, *Chem. Mater.* **25**, 1293 (2013)
175. L.T. Lu, N.T. Dung, L.D. Tung, C.T. Thanh, O.K. Quy, N.V. Chuc, S. Maenosono, N.T.K. Thanh, *Nanoscale* **7**, 19596 (2015)
176. R. Hufschmid, H. Arami, R.M. Ferguson, M. Gonzales, E. Teeman, L.N. Brush, N.D. Browning, K.M. Krishnan, *Nanoscale* **7**, 11142 (2015)
177. K.S. Rejitha, S. Mathew, *J. Therm. Anal. Calorim.* **106**, 267 (2011)
178. K.S. Rejitha, T. Ichikawa, S. Mathew, *J. Therm. Anal. Calorim.* **103**, 515 (2011)
179. R.A. Mereu, A. Mesaros, T. Petrisor, M. Gabor, M. Popa, L. Ciontea, T. Petrisor, *J. Anal. Appl. Pyrol.* **104**, 653 (2013)
180. Z. Fereshteh, M. Salavati-Niasari, *Adv. Colloid Interface Sci.* **243**, 86 (2017)
181. M.M. Al Majthoub, *J. Comput. Theor. Nanosci.* **13**, 7014 (2016)
182. K. Motevalli, Z. Zarghami, M. Panahi-Kalamuei, *J. Mater. Sci. Mater. Electron.* **27**, 4794 (2016)
183. M. Madkour, Y.K. Abdel-Monem, F. Al Sagheer, *Ind. Eng. Chem. Res.* **55**, 12733 (2016)
184. M. Malathy, R. Jayasree, R. Rajavel, *Smart Sci.* **5**, 100 (2017)
185. D. Ling, T. Hyeon, *Small* **9**, 1450 (2013)
186. F. Davar, M.R. Loghman-Estarki, M. Salavati-Niasari, M. Mazaheri, *J. Clust. Sci.* **27**, 593 (2016)
187. M. Al-Shakban, P.D. Matthews, G. Deogratias, P.D. McNaughten, J. Raftery, I. Vitorica-Yrezabal, E.B. Mubofu, P. O'Brien, *Inorg. Chem.* **56**, 9247 (2017)

188. A. Santhoshkumar, H.P. Kavitha, R. Suresh, *Asian J. Chem.* **29**, 239 (2017)
189. B.M. Abu-Zied, S.M. Bawaked, S.A. Kosa, W. Schwiager, *Appl. Surf. Sci.* **351**, 600 (2015)
190. Q. Yan, X. Li, Q. Zhao, G. Chen, *J. Hazard. Mater.* **209–210**, 385 (2012)
191. S. Farhadi, K. Pourzare, S. Bazgir, *J. Alloys Compd.* **587**, 632 (2014)
192. F.B. Effenberg, R.A. Couto, P.K. Kiyohara, G. Machado, S.H. Masunaga, R.F. Jardim, L.M. Rossi, *Nanotechnology* **28**, 115603 (2017)
193. S.E. Hunyadi Murph, K.J. Coopersmith, G.K. Larsen, *Synthetic strategies for anisotropic and shape-selective nanomaterials*, in *Anisotropic and Shape-Selective Nanomaterials*, ed. by S.E. Hunyadi Murph, G.K. Larsen, K.J. Coopersmith (Springer, Switzerland, 2017), pp. 29–77
194. M. Ghiasi, A. Malekzadeh, H. Mardani, *Mater. Sci. Semicond. Process.* **42**, 311 (2016)
195. S. Kitabayashi, N. Koga, *J. Phys. Chem. C* **119**, 16188 (2015)
196. V. Bartůněk, Š. Huber, D. Sedmidubský, Z. Sofer, P. Šimek, O. Jankovský, *Ceram. Int.* **40**, 12591 (2014)
197. A. Hosseinian, S. Jabbari, H.R. Rahimipour, A.R. Mahjoub, *J. Mol. Struct.* **1028**, 215 (2012)
198. F. Mohandes, F. Davar, M. Salavati-Niasari, *J. Magn. Magn. Mater.* **322**, 872 (2010)
199. M.G. Babashkina, D.A. Safin, M.P. Mitoraj, F. Sagan, M. Bolte, A. Klein, *Cryst. Growth Des.* **16**, 3287 (2016)
200. M.Y. Nassar, A.S. Attia, KhA Alfallous, M.F. El-Shahat, *Inorg. Chim. Acta* **405**, 362 (2013)
201. M.Y. Nassar, T.Y. Mohamed, I.S. Ahmed, *J. Mol. Struct.* **1050**, 81 (2013)
202. S. Farhadi, K. Pourzare, *Mater. Res. Bull.* **47**, 1550 (2012)
203. S. Farhadi, J. Safabakhsh, *J. Alloys Compd.* **515**, 180 (2012)
204. I.J. Plante, T.W. Zeid, P. Yang, T. Mokari, *J. Mater. Chem.* **20**, 6612 (2010)
205. D.C. Onwudiwe, P.A. Ajibade, *Int. J. Mol. Sci.* **12**, 5538 (2011)
206. K. Thangavelu, K. Parameswari, K. Kuppusamy, Y. Haldorai, *Mater. Lett.* **65**, 1482 (2011)
207. S. Farhadi, K. Pourzare, S. Sadeghinejad, *J. Nanostruct. Chem.* **3**, 1 (2013)
208. H.M. Aly, M.E. Moustafa, M.Y. Nassar, E.A. Abdelrahman, *J. Mol. Struct.* **1086**, 223 (2015)
209. O.B. Ibrahim, M.A. Mohamed, M.S. Refat, *Can. Chem. Trans.* **2**, 108 (2014)
210. F. Behnoudnia, H. Dehghani, *Polyhedron* **56**, 102 (2013)
211. S. Yousef Ebrahimipour, I. Sheikhsheoie, J. Castro, W. Haase, M. Mohamadi, S. Foro, M. Sheikhsheoie, S. Esmaeili-Mahani, *Inorg. Chim. Acta* **430**, 245 (2015)
212. Y. Haldorai, J. JinShim, *Mater. Lett.* **116**, 5 (2014)
213. L.G. Bloor, C.J. Carmalt, D. Pugh, *Coord. Chem. Rev.* **255**, 1293 (2011)
214. M.A. Malik, M. Afzal, P. O'Brien, *Chem. Rev.* **110**, 4417 (2010)
215. S. Mishra, S. Daniele, *Chem. Rev.* **115**, 8379 (2015)
216. M. Iacob, C. Racles, C. Tugui, G. Stiubianu, A. Bele, L. Sacarescu, D. Timpu, M. Cazacu, *Beilstein J. Nanotechnol.* **7**, 2074 (2016)
217. A. Khansari, M. Enhessari, M. Salavati-Niasari, *J. Clust. Sci.* **24**, 289 (2013)
218. A.D. Khalaji, *J. Clust. Sci.* **24**, 209 (2013)
219. A.D. Khalaji, *J. Clust. Sci.* **24**, 189 (2013)
220. F.S. Sangsefidi, M. Sabet, M. Salavati-Niasari, *J. Mater. Sci. Mater. Electron.* **27**, 8793 (2016)
221. M. Salavati-Niasari, N. Mir, F. Davar, *J. Alloys Compd.* **493**, 163 (2010)
222. F. Motahari, M.-R. Mozdianfard, F. Soofivand, M. Salavati-Niasari, *Synth. React. Inorg. Met.-Org. Nano-Met. Chem.* **45**, 1449 (2015)
223. M. Salavati-Niasari, A. Sobhani, F. Davar, *J. Alloys Compd.* **507**, 77 (2010)
224. S. Sabbaghi, H. Orojlu, M.R. Parvizi, S. Saboori, M. Sahooi, *Int. J. Nano Dimens.* **3**, 69 (2012)
225. C. Amiens, B. Chaudret, D. Ciuculescu-Pradines, V. Collière, K. Fajerweg, P. Fau, M. Kahn, A. Maisonnat, K. Soulantica, K. Philippot, *New J. Chem.* **37**, 3374 (2013)
226. M. Ghiasi, A. Malekzadeh, *Superlattices Microstruct.* **77**, 295 (2015)
227. N. Ortiz, S.E. Skrabalak, *Langmuir* **30**, 6649 (2014)

228. L.M. Blanco, A.D. Garnovskii, D.A. Garnovskii, B.I. Kharisov, M.A. Mendez-Rojas, I.S. Vasilchenko, *Synthetic Coordination and Organometallic Chemistry* (Marcel Dekker, New York-Basel, 2003)
229. F.A. Cotton, G. Wilkinson, C.A. Murillo, M. Bochmann, *Advanced Inorganic Chemistry*, 6th edn. (Wiley-Interscience, New York, 1999)
230. A.D. Pomogailo, A.S. Burlov, N.D. Golubeva, L.A. Petrova, S.A. Mashchenko, S.I. Pomogailo, G.I. Dzhardimalieva, A.D. Garnovskii, *Inorg. Mater.* **47**, 876 (2011)
231. A.S. Rozenberg, G.I. Dzhardimalieva, A.D. Pomogailo, *Dokl. Akad. Nauk* **356**, 66 (1997)
232. A.D. Pomogailo, G.I. Dzhardimalieva, A.S. Rozenberg, D.N. Muraviev, *J. Nanopart. Res.* **5**, 497 (2003)
233. A.S. Rozenberg, G.I. Dzhardimalieva, N.V. Chukanov, A.D. Pomogailo, *Colloid J.* **67**, 57 (2005)
234. A.D. Pomogailo, A.S. Rozenberg, G.I. Dzhardimalieva, *Russ. Khim. Zh. (Mendeleev Chem. J.)* **53**, 140 (2009)
235. V.I. Irzhak, *Rev. J. Chem.* **6**, 370 (2016)
236. J. Watt, S. Cheong, R.D. Tilley, *Nano Today* **8**, 198 (2013)
237. Y. Kumar, P.M. Shirage, *J. Mater. Sci.* **52**, 4840 (2017)
238. L. Wu, J.P. Olivier, B. David, I. Wayne, N. Alshakim, Z. Huiyuan, Z. Sen, S. Shouheng, *Nano Lett.* **14**, 3395 (2014)
239. Y.S. Yu, A. Mendoza-Garcia, B. Ning, S.H. Sun, *Adv. Mater.* **25**, 3090 (2013)
240. V. Pascariu, O. Avadanei, P. Gasner, I. Stoica, A.P. Reverberi, L. Mitoseriu, *Phase Transitions* **86**, 715 (2013)
241. L. Nicole, C. Laberty-Robert, L. Rozes, C. Sanchez, *Nanoscale* **6**, 6267 (2014)
242. C. Amiens, D. Ciuculescu-Pradines, K. Philippot, *Coord. Chem. Rev.* **308**, 409 (2016)
243. N. Revaprasadu, S.N. Mlondo, *Pure Appl. Chem.* **78**, 1691 (2006)
244. R. Kaur, S.K. Mehta, *Coord. Chem. Rev.* **262**, 37 (2014)
245. A.D. Pomogailo, I.E. Uflyand, *Makromolekulayrnye Metallokhelaty (Macromolecular Metal Chelates)* (Khimiya, Moscow, 1991)
246. K.D. Karlin, D.T.D. Lili, C.L. Cahill, *Coordination Polymers of the Lanthanide Elements* (Wiley, Weinheim, 2008)
247. S.R. Batten, D.R. Turner, M.S. Neville, *Coordination Polymers: Design, Analysis and Application* (RSC, Cambridge, 2009)
248. K. Naka, Metal organic framework (MOF), in *Encyclopedia of Polymeric Nanomaterials*, ed. by S. Kobayashi, K. Müllen (Springer, Berlin, 2015)
249. M.C. Hong, L. Chen (eds.), *Design and Construction of Coordination Polymers* (Wiley, Weinheim, 2009)
250. J. Jiang (ed.), *Metal-Organic Frameworks: Materials Modeling towards Engineering Applications* (CRC, Boca Raton, 2015)
251. L.R. MacGillivray (ed.), *Metal-Organic Frameworks: Design and Application* (Wiley, Weinheim, 2010)
252. L.R. MacGillivray, C.M. Lukehart (eds.), *Metal-Organic Framework Materials* (Wiley, Weinheim, 2014)
253. O.L. Ortiz, L.D. Ramirez, *Coordination Polymers and Metal Organic Frameworks: Properties, Types, and Applications* (Nova Science Publishers, NY, 2012)
254. J.C. Bailar, Jr., in *Preparative Inorganic Reactions*, vol. 1, ed. by W.L. Jolly (Interscience, NY, 1964)
255. Y. Zhao, K. Li, J. Li, *Z. Naturforsch.* **65b**, 976 (2010)
256. W. Xuan, C. Zhu, Y. Liu, Y. Cui, *Chem. Soc. Rev.* **41**, 1677 (2012)
257. O.M. Yaghi, G. Li, H. Li, *Nature* **378**, 703 (1995)
258. O.M. Yaghi, H. Li, *J. Am. Chem. Soc.* **117**, 10401 (1995)
259. M.Y. Masoomi, A. Morsali, *Coord. Chem. Rev.* **256**, 2921 (2012)
260. H.D. Mai, K. Rafiq, H. Yoo, *Chem. Eur. J.* **23**, 1 (2017)
261. W.L. Leong, J.J. Vittal, *Chem. Rev.* **111**, 688 (2011)
262. R. Das, P. Pachfule, R. Banerjee, P. Poddar, *Nanoscale* **4**, 591 (2012)

263. K. Akhbari, N.B. Bahman, A. Morsali, P. Retailleau, J. Iran. Chem. Soc. **13**, 165 (2016)
264. F.S. Shirazi, K. Akhbari, Inorg. Chim. Acta **436**, 1 (2015)
265. P. Saravanan, R. Gopalan, V. Chandrasekaran, Def. Sci. J. **58**, 504 (2008)
266. H. Liu, J. Owen, A.P. Alivisatos, J. Am. Chem. Soc. **129**, 305 (2007)
267. Y. Song, X. Li, L. Sun, L. Wang, RSC Adv. **5**, 7267 (2015)
268. J.-K. Sun, Q. Xu, Energy Environ. Sci. **7**, 2071 (2014)
269. M. Ramazani, A. Morsali, Ultrason. Sonochem. **18**, 1160 (2011)
270. G.I. Dzhardimalieva, I.E. Uflyand, RSC Adv. **7**, 42242 (2017)
271. U.S. Schubert, A. Winter, G.R. Newkome (eds.), *Terpyridine-based Materials. For Catalytic, Optoelectronic and Life Science Applications* (Wiley-VCH, Weinheim, 2011)
272. A.S. Abd-El-Aziz, P.O. Shipman, B.N. Boden, W.S. McNeil, Prog. Polym. Sci. **35**, 714 (2010)
273. A.S. Abd-El-Aziz, E.A. Strohm, Polymer **53**, 4879 (2012)
274. G.I. Dzhardimalieva, I.E. Uflyand, J. Coord. Chem. **70**, 1468 (2017)
275. A.C.W. Leung, M.J. MacLachlan, J. Inorg. Organomet. Polym. **17**, 57 (2007)
276. W.K. Chan, Coord. Chem. Rev. **251**, 2104 (2007)
277. A. Wild, A. Winter, F. Schlutter, U.S. Schubert, Chem. Soc. Rev. **40**, 1459 (2011)
278. G.I. Dzhardimalieva, I.E. Uflyand, J. Inorg. Organomet. Polym. **26**, 1112 (2016)

Chapter 2

General Characteristics of the Methods of Thermolysis of Metal Compounds



The study of thermolysis of metal-containing compounds can be carried out in closed or open systems both under isothermal and non-isothermal conditions using external and internal heating sources. Depending on the tasks, different approaches allow controlling the degree of conversion and determining the choice of equipment for the experimental study of thermolysis of compounds [1–14]. Weight (thermogravimetry, TG) or volumetric (volumetry) methods are the most common. Although the development of experimental facilities for the study of thermolysis kinetics began in the first quarter of the twentieth century, the current state of TA can be characterized as diverse and dynamic. In particular, improved tools, methods, and applications are constantly appearing on the market and in scientific research. It should be noted that practically any compound in a solid, semi-solid, or liquid state can be analyzed and characterized by thermal analysis (TA) methods. In recent years, integrated (synchronous) devices have begun to appear that combine several methods for analyzing the conversion of matter with automation and using the capabilities of modern computers in a single approach. In this chapter, we will consider the features of the basic methods used to study the kinetics of thermolysis of metal-containing compounds.

Theoretically, various methods can be used to detect effects caused by a change in temperature. All TA methods are based on measuring some characteristic of the material (e.g., its weight, volume.) or on changing its behavior in comparison with the reference substance. This, in turn, allows access to information about macroscopic theories of matter, including equilibrium and irreversible thermodynamics and kinetics [1]. Although there are numerous analytical methods, they differ from one another in measurable properties (Table 2.1).

Table 2.1 Common TA methods and the properties measured

Method	Abbreviation	Measured characteristics	Application
<i>Common methods</i>			
Dielectric thermal analysis	DEA	Dielectric permittivity and loss factor (dielectric constant)	Phase changes, changes in polymers
Differential thermal analysis	DTA	Temperature difference versus temperature or time (temperature difference between the reference and the tested compound)	Phase transitions (temperature and heat) and chemical reaction (heat capacity)
Differential scanning calorimetry	DSC	Heat flow changes versus temperature or time (enthalpy)	Phase transitions (temperature and heat) and chemical reaction (heat capacity)
Dilatometry	DIL	Volume changes with temperature change	Progress of chemical reactions, the rate of phase changes, thermal expansion
Dynamic mechanical analysis	DMA or DMTA	Measures storage modulus (stiffness) and loss modulus (damping) versus temperature, time and frequency (deformation)	Glass transition temperature of the material and its composition
Evolved gas analysis	EGA	Analysis of gases evolved during heating of a material, usually decomposition products	Thermal degradation processes (oxidation, thermolysis), chemical reactions, characterization of starting materials and end products
Laser flash analysis	LFA	Thermal diffusivity and thermal conductivity	Progress of chemical reactions, characterization of starting materials and end products
Thermogravimetric analysis	TGA	Weight change versus temperature or time	Phase destruction, dehydration, oxidation
Thermomechanical analysis	TMA	Dimensional changes versus temperature or time (deformation)	Mechanical changes, deformations
Thermo-optical analysis	TOA	Optical properties	Phase changes, surface reactions, color changes
<i>Specific methods</i>			
Synchronous thermal analysis		Combines two or more methods of sample investigation	
Thermal analysis with a specified process rate		The rate of the change of sample properties is maintained constant	

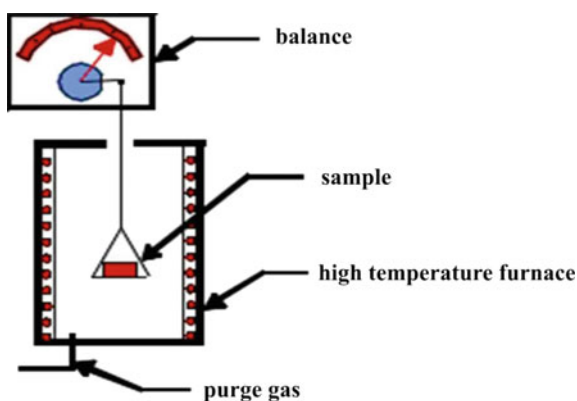
2.1 Thermogravimetric Methods

Various chemical changes (e.g., thermal decomposition, oxidation.) and some physical processes (desorption of solvent or water, evaporation, sublimation, etc.) can occur when the substance is heated with subsequent changes in the weight of the sample. The study of these processes is the task of thermogravimetric analysis (TGA). TGA is the TA method in which changes in the physical and chemical properties of substances are measured with increasing temperature (with a constant heating rate) or with time (constant temperature and/or constant weight loss). TGA provides information on physical phenomena such as second-order phase transitions, including evaporation, sublimation, adsorption, and desorption, as well as chemical phenomena, including chemisorption, desolvation (especially dehydration), decomposition, and solid–gas reactions (e.g., oxidation or reduction).

TGA is based on a high degree of accuracy in measuring the weight and temperature as a function of time. Therefore, the main instrumental components of the TGA are the exact balance, the pan loaded with the sample, and the programmable furnace (Fig. 2.1). The furnace can be programmed either for a constant heating rate, or for heating, which allows you to obtain a constant weight loss with time. In addition to controlling the temperature of the sample, it is also important to monitor its environment (e.g., the atmosphere). Measurements can be carried out in the air or under an inert gas (e.g., nitrogen or helium). Modern thermobalance continuously (automatically) determines the change in sample weight (Δm) as a function of time or temperature. TGA is a traditional non-isothermal version of the linear heating method. Several experimental factors, such as the heating rate and furnace atmosphere, furnace geometry and sample holder, the speed of the recording device, the amount of sample, the particle size, the heat of reaction, the compactness of the sample, affect the course and nature of the TGA curves.

Measurements of changes in the weight of the sample with temperature are carried out using a thermobalance, sometimes called a thermogravimetric analyzer [8, 15]. Thermobalance consists of a suitable electronic microbalance, furnace,

Fig. 2.1 Schematic principle of TGA measurement



temperature programmer, and computer for control, which allows you to simultaneously weigh and heat or cool the sample, as well as obtain data on weight, time, and temperature. The balance should be in a properly closed system so that the nature and pressure of the atmosphere around the sample can be controlled.

When heat is applied to the sample, processes accompanied by a change in enthalpy can occur, which is not necessarily related to changes in weight (crystallographic changes, melting, etc.) [16]. These processes are the subject of a differential thermal analysis (DTA) study in which the temperature difference between a sample and a reference material is controlled in time or temperature, while the temperature of the sample in a given atmosphere is programmed. The principle involves measuring the potential difference between two thermocouples in the test sample and a thermally inert material in a bridge circuit with a galvanometer as zero-instrument (Fig. 2.2). The deflection of a galvanometer, which is proportional to the temperature difference between the sample and the reference material, is plotted against the temperature. This curve is a differential thermoanalytic curve.

In addition to X-ray and spectroscopic methods, TA measurements make it possible to obtain a more complete characterization of the substance by studying the thermally induced mechanisms of decomposition [18–20].

In particular, it was found that the thermal behavior of azomethine metal chelates is determined by the nature of the metal, the composition and structural features of the chelating ligands, the nature of the metal–ligand bond, and, in general, the stability of the metal chelate [21–23]. Here, we carry out a comparative analysis of various azomethine metal chelates to determine the influence of the ligand environment on their thermal stability. The thermal characteristics of azomethine metal chelates are given in Table 2.2.

As expected, the thermal stability of azomethine metal chelates depends on the type of chelating ligand. For example, among nickel chelates **Ni1–Ni4**, the following regularities can be noted. Firstly, the melting point is the maximum for the

Fig. 2.2 Block diagram of DTA. Reproduced with permission from Ref. [17]. Copyright (2011) Springer Nature

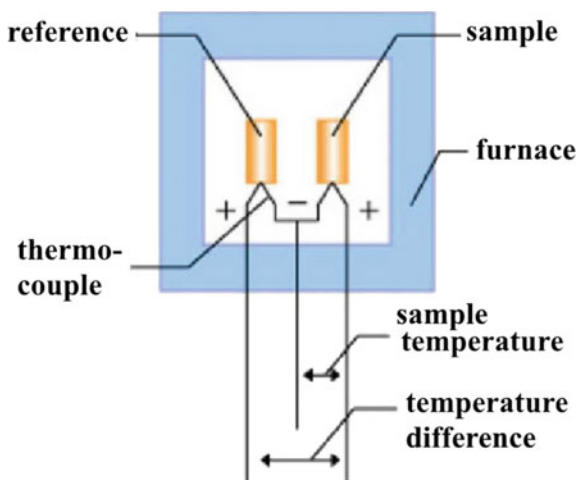
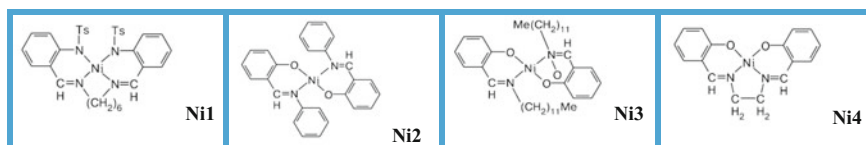


Table 2.2 Thermal properties of azomethine chelates

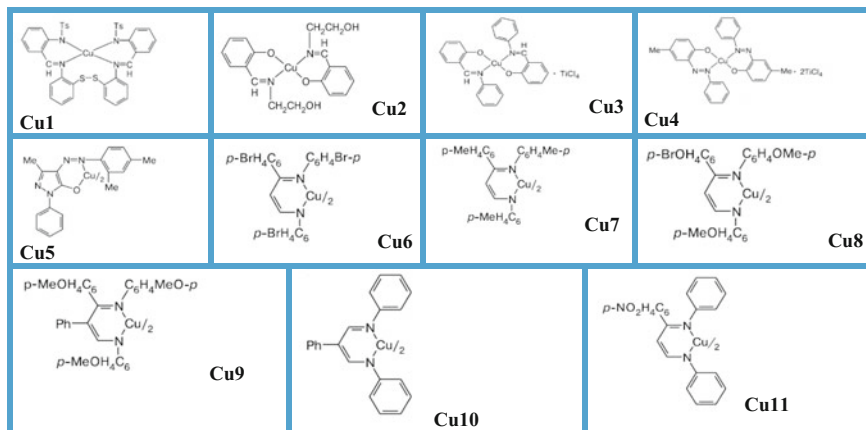
Chelate	Temperature, K				Weight loss in full decomposition, %
	Melting	Decomposition onset	Decomposition at 50%	Decomposition end	
Ni1	— ^a	623	663	1023	70.8
Ni2	— ^a	498	708	1013	62.5
Ni3	365.8	593	663	823	79.9
Ni4	638.2	653	–	1053	35.7
Cu1	498	543	–	1033	40.4
Cu2	450	463	565	973	67.8
Cu3	383	598	–	963	45.8
Cu4	413	373	–	973	47.4
Cu5	518	533	695	933	60.2
Cu6	–	558	993	1053	53.3
Cu7	–	538	1053	1063	50.1
Cu8	–	473	–	1003	46.0
Cu9	561	473	675	893	68.9
Cu10	591.3	603	648	1003	84.6
Cu11	–	483	–	1013	37.0
Co1	411.1	596	–	833	48.8
Co2	624.9	628	–	1003	35.2
Co3	464	493	–	973	42.7

^aPrior to the decomposition onset the melting is not observed

Ni4 chelate; secondly, the temperature of the onset of decomposition increases in the series **Ni3** < **Ni2** < **Ni1** < **Ni4**; and, thirdly, the weight loss at 1073 K is minimal for the **Ni4** chelate. This allows us to conclude that the metal chelates **Ni1** and **Ni4** based on tetradentate azomethine ligands are much more stable than the metal chelates based on bidentate azomethines, and the introduction of allyl fragments into the aldehyde and amine parts leads to a significant decrease in the melting point. It should also be noted the thermal behavior of the **Ni4** chelate: up to 663 K, an increase in weight is observed at 3.6%, which, apparently, is due to the oxidation process; at 723 K the sharp drop in weight continues to 31%, then this process slows down, and at 1073 K, the weight loss is 43%.



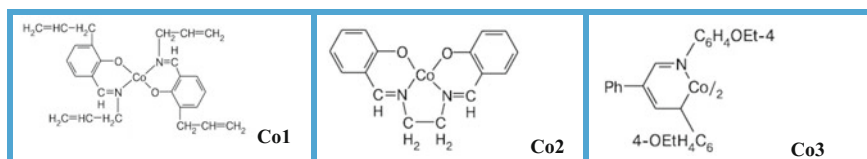
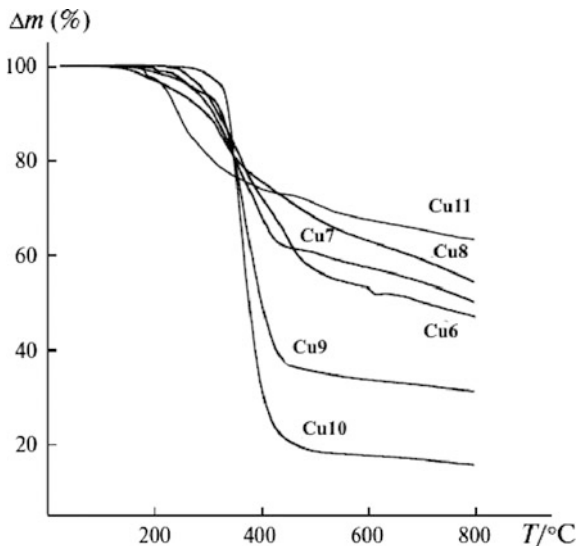
Similar results were obtained in the study of copper azomethine metal chelates. For example, the **Cu1** chelate based on the tetradentate ligand has the highest melting point. It is important that the introduction of alcohol fragments into the amine part of the **Cu2** chelate leads to a decrease in the melting point. In addition, heterometallic complexes based on chelates **Cu3** and **Cu4** are less stable and already begin to melt at 383 and 413 K, respectively (see Table 2.2). It should be noted that in the case of **Cu6–Cu9** and **Cu11** chelates, the introduction of methyl- and methoxy-groups in the phenyl ring lowers the melting point from 495 to 464 K. For chelates **Cu9** and **Cu10**, the introduction of alkoxy-groups in the benzene rings of amine fragments also results in a decrease in the melting point in comparison with unsubstituted analogs.



In most cases, copper chelates are more heat resistant than nickel chelates: for them, weight loss at 773 K, as determined by TA, is not more than 50% by weight (Fig. 2.3) [22].

Cobalt chelate **Co1** is a stable substance up to 473 K and its weight loss is 21.8% to 583 K, then the process slows down, and the total weight loss resulting from thermolysis to 1073 K is 48.8%. The melting peak corresponds to 411.1 K with heat absorption of 50.67 J g^{-1} , and at 596.2 K an exothermic process is observed with heat absorption of 258 J g^{-1} . Above 823 K, the chelate decomposes. Among the studied cobalt chelates, **Co2** is the most stable: Its melting point is 624.9 K, and the loss of **Co2** during thermolysis to 1073 K is only 35.2% (see Table 2.2). As in the case of nickel chelates, allyl substituents reduce the melting point in comparison with aryl substituents. It should be noted that the **Co2** chelate, based on the tetradentate salen ligand, has a significantly higher melting point ($>573 \text{ K}$) as compared with chelates of bidentate ligands.

Fig. 2.3 TGA data for azomethine copper(II) chelates [22]



With programmable heating rates, concepts such as the temperature of the onset of decomposition, the decomposition stage, the temperature ranges of stability of intermediate compounds, which are the kinetic characteristics of the process, are important [24, 25]. Taking into account the peculiarities of exo- and endothermic reactions, as well as the influence of heat transfer parameters (heat transfer coefficient, heating rate, reaction heat, sample weight, etc.) allows us to conclude that the method used to determine the kinetic data is correct.

The development of DTA in the direction of increasing the accuracy of the quantitative determination of thermal effects led to the development of TA method called differential scanning calorimetry (DSC) [26–28]. The main difference between DTA and DSC methods is that the former measures the difference in temperature, while the second, in principle, allows measuring the change in the enthalpy of chemical reactions [29]. DSC is a method in which the difference in heat flow rate in a sample and a reference material is measured. It provides a simple way to obtain thermodynamic parameters of chemical compounds, in particular, free Gibbs energy, enthalpy, and entropy.

Simultaneous TA involves the use of TGA and DSC to the same sample in a single instrument. It is important that the test conditions are absolutely identical for

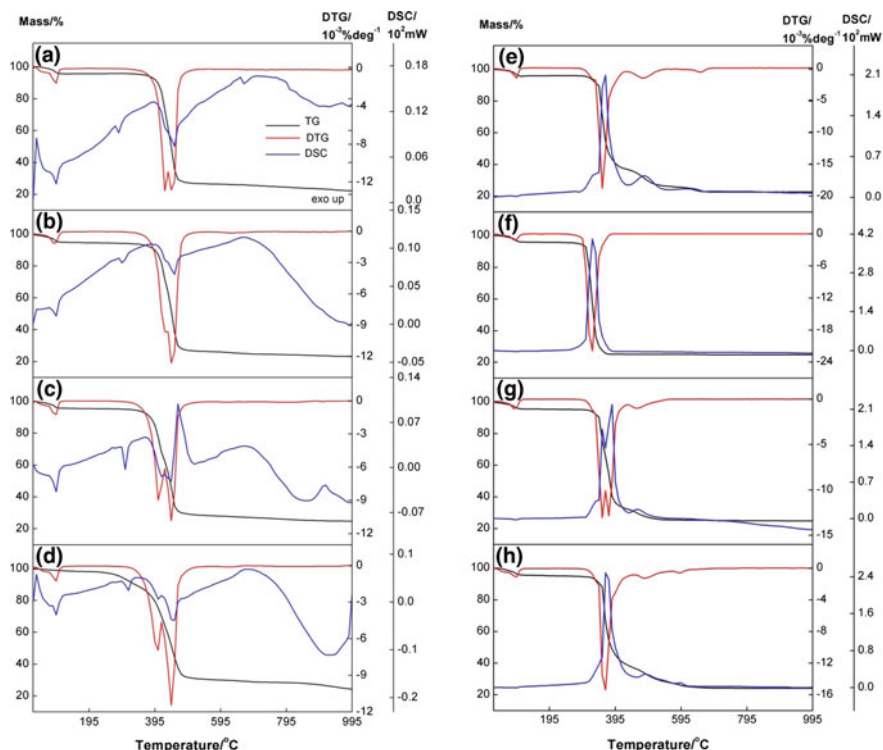


Fig. 2.4 Simultaneous TG/DTG–DSC curves of the compounds in N_2 : **a** La–L, **b** Ce–L, **c** Pr–L, **d** Nd–L and in air: **e** La–L, **f** Ce–L, **g** Pr–L, **h** Nd–L. Reproduced with permission from Ref. [30]. Copyright (2017) Elsevier

the TGA and DSC signals (the same atmosphere, gas flow rate, sample vapor pressure, heating rate, thermal contact with crucible and sample sensor, radiation effect, etc.).

TA approaches, including TGA/DTA and DSC, are becoming increasingly important for the study of kinetic and thermodynamic parameters, as well as the thermal stability of metal chelates [6, 7].

As a typical example, let us consider binuclear complexes of La(III), Ce(III), Pr(III), and Nd(III) ions with N-phenylanthranilic acid (L) of the general formula $Ln_2(L)_5(OH) \cdot nH_2O$ [30]. The detailed TG/DTG–DSC analysis (Fig. 2.4) made it possible to obtain information on the thermal behavior of these binuclear compounds in an atmosphere of nitrogen and air. In particular, TGA indicates that thermolysis processes are multistage, and dehydration is the first stage of thermolysis. The calculated enthalpies of dehydration are low for all the complexes studied; thus, it can be concluded that the dehydration is connected with the release of weakly bonded water molecules. It is important that the thermal stability and the thermolysis mechanism of these compounds depend on the nature of the metal ions and the atmosphere used.

In another interesting example, the simultaneous TG/DTG–DTA method was used to analyze the thermolysis of cobalt(II) complexes with 2,2'-dipyridylamine (L) and substituted salicylaldehyde ligands (X-saloH, where X = 5 - NO₂, CH₃, Br, and Cl) with the general formula [Co(X-salo)₂(L)] in an inert atmosphere [31]. It turned out that their thermolysis pathways are of a multistage nature, accompanied by the release of molecules of the salicylaldehyde ligand. In addition, the thermolysis kinetics analyzed using Vyazovkin's advanced isoconversional method and associated with the elimination of ligand molecules in the 473–673 K range confirmed the stability order estimate obtained only on the basis of thermolysis temperatures. It is important that the comparison of the TG/DTG–DTA curves showed a significant effect of the nature of the substituent at the 5-position of both salicylaldehyde rings on the thermal behavior of the tested complexes.

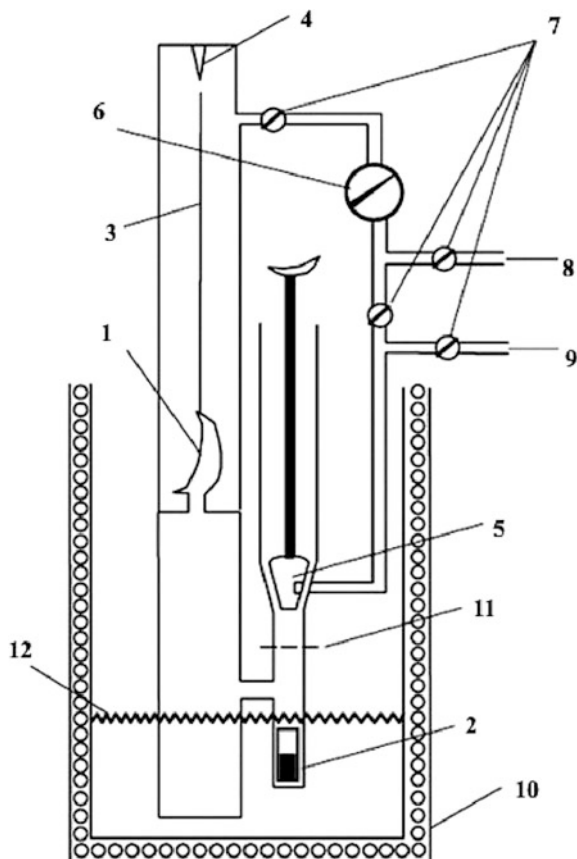
Of great interest is the connection of TGA with chemometrics as a new analytical tool using TA for the characterization of metal compounds [32]. This approach includes a multivariate statistical analysis of the TG curves, which allows one to identify significant differences in the thermal profile of the test sample. In some cases, small sample-to-sample differences may cause very small differences in TG profile. This means that the resulting TG data depend simultaneously on more than one variable and, therefore, are multidimensional. Therefore, chemometric approach based on multifactor analysis becomes very useful.

2.1.1 Volumetric Methods

Volumetric methods are used to study the early stages of thermolysis and to detect the decomposition of a small amount of matter. Evolved gas analysis (EGA), including the study of the dependence of the volume of the evolved gas $[V(t)]$, can be carried out either discretely or continuously. The main disadvantage of manometers is a direct contact of evolved gaseous products, which can be chemically aggressive, with corrosive metal parts and mercury, is. Therefore, it is more attractive to use manometers, such as a glass membrane, where there are no metal parts. They have a short response time, which allows one to study the rates of fast processes in a closed reactor space using a Bourdon membrane-type manometer (Fig. 2.5). The evolution of gas during thermolysis occurs in a self-generated atmosphere (SGA). The reaction volume proceeds under static isothermal conditions and is completely thermostatic. The pressure created in the reaction chamber deforms the membrane **1** and this causes the bend rod **3** to flex to it. If the compensating gas is supplied to the compensation chamber through the valve **8** at a pressure equal to the pressure of the gases released from the sample, the rod **3** returns to its original position, which is detected by the pointer **4**.

This reactor, made of quartz glass and having a sealed reaction chamber, is suitable for studying the kinetics of thermolysis of metal compounds at sufficiently high temperatures (1270–1470 K) under completely isothermal conditions, as well as for analyzing and interrupting gas evolution at any stage of thermolysis.

Fig. 2.5 Schematic diagram of the reaction vessel with a Bourdon manometer for kinetic measurements. (1) Quartz crescent-shaped membrane, (2) tested compound, (3) rod, (4) zero indicator (zero reader), (5) vacuum valve, (6) recording mercury manometer, (7) valves, (8) compensating gas inlet, (9) pumping out, (10) high-temperature thermostat, (11) vacuum sealing-off position, (12) position of the reaction vessel relative to the thermostat in the non-isothermal scheme



The number of moles of the evolved heated gas (n_{exp}), reduced by the number of moles (n_{Σ}) of gas released at room temperature (T_r), is found from equation:

$$n_{\text{exp}}/n_{\Sigma} = (V_{\text{exp}}/V_{\Sigma})(T_r/T_{\text{exp}}) \quad (2.1)$$

Typically, the reactor is constructed in such a way that the ratio of the heated volume (V_{exp}) to the total volume of the reactor (V_{Σ}) is 1–5%.

Recently, this method was called RAPET (Reaction under Autogenic Pressure at Elevated Temperature) [33]. This method has a number of significant advantages, as it is a simple, reproducible, effective, safe, non-aqueous approach without the use of templates, surfactants, or solvents. In addition, it allows the production of well-crystalline, stoichiometric materials with high yields and is applicable to hazardous or carcinogenic materials (e.g., carbonyls) with the prospect of scaling up to mass production. RAPET is not an analog of the solvothermal process, since a complete thermolysis of the chemical takes place, and then a nanomaterial is formed.

For example, the RAPET method was used to fabricate magnetic NPs with or without using an external high magnetic field (10 T) [34].

A continuous real-time analysis of the weight loss and gas evolution can be obtained by combining mass spectrometry with thermogravimetry (TG-MS) [35–40]. One of the advantages of the TG-MS method is that it avoids the multistage preparation of the sample and provides more detailed information on the decomposition of metal complexes by identifying fragment ions at different temperatures [41, 42].

In a typical example, the EGA-MS method was used to determine the thermolysis steps of the Cd(II), Mn(II), and Zn(II) biomimetic complexes with the 1,1-diaminobutane-Schiff base [43]. EGA-MS confirmed the release of two water molecules by detecting fragments at $m/z = 17$ and 18 (Fig. 2.6, left) regardless of the nature of the atmosphere (air or Ar). The presence of fragments at $m/z = 28$ and 29 (see Fig. 2.6, left) and the calculated percentage weight loss indicate a rupture of the ligand ring (Fig. 2.6, right), and a temporary subsequent rearrangement. The final thermally induced step leads to the complete decomposition of the residual compound to produce a metal oxide.

In another interesting example, the EGA-MS method was used to characterize metal complexes with a polycarboxylate ligand, imidazole-4,5-dicarboxylic acid [44]. This method allowed to confirming for the complexes the expected stages of thermolysis, calculated by the percentage weight loss. In particular, only peaks with $m/z = 18$ (H_2O^+) and $m/z = 17$ (OH^+) were detected in the temperature range 473–543 K, which confirms the release of water molecules. In the temperature range corresponding to the second main stage of thermolysis, $m/z = 46$ (HCOOH^+) and $m/z = 29$ (H_2CNH^+) were found, which are caused by the rupture of the imidazole ring. EGA, associated with the fourth and final stage of thermolysis, showed fragments that are characteristic for the release of CO_2 due to the decomposition of the metal carbonate to the metal oxide. Based on the results of TA and EGA, the general decomposition mechanism for all complexes, irrespective of the metal ion, is graphically generalized in Fig. 2.7.

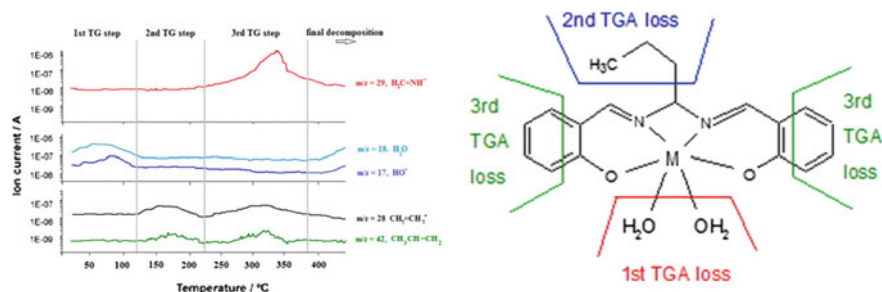


Fig. 2.6 (left) Evolved gas analysis by mass spectrometry: m/z traces as a function of the temperature, (right) General thermolysis mechanism of complexes with N,N' -bis(2-hydroxybenzylidene)-1,1-diaminobutane ligand. Reproduced with permission from Ref. [43]. Copyright (2017) Springer Nature

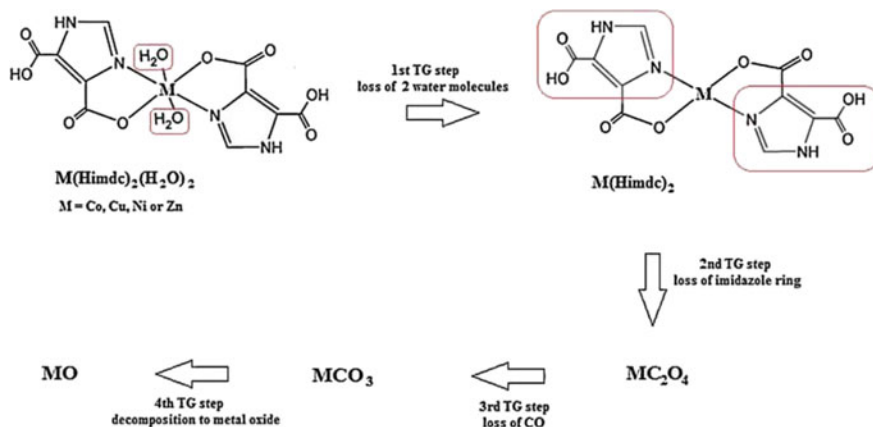


Fig. 2.7 Scheme of the mechanism of thermolysis of the analyzed complexes. Reproduced with permission from Ref. [44]. Copyright (2014) Elsevier

It should be noted the use of the EGA-MS method to describe the thermolysis of the Co(II), Cu(II), and Ni(II) complexes with the 2-aminomethylbenzimidazole (L) ligand (Fig. 2.8, left) [45]. Their thermolysis is based on three main stages. In the temperature range 403–453 K, $m/z = 36$ was detected for chloride complexes, which corresponds to the release of HCl, while $m/z = 79$ (HBr) was detected for bromide complexes. Thus, the first thermally induced process is the removal of the anion. In the temperature range corresponding to the second main stage of thermolysis, ions with $m/z = 118$, 91 and 63 were detected, as expected for the typical fragmentation of the benzimidazole molecule. At the last stage of thermolysis, metal oxide forms.

The possibility of online combination of TA with Fourier transformation infrared (FTIR) or MS spectroscopies makes it possible to correctly characterize the thermolysis stages [46–52] and propose its mechanisms for metal complexes [53, 54]. This method can also be used to conduct additional analysis of the released gases during the thermal treatment of polymers, which facilitates the determination of the structure and composition of polymeric metal complexes. In particular, EGA during thermolysis of PMCs based on thiourea–formaldehyde resin was conducted for thermolysis up to 1073 K, using both online TG-FTIR and simultaneous TG-MS [55]. The total weight loss resulting from thermolysis of PMC-Cu(II) at 1043 K was 73.26, and 44.02% of the initial weight was lost at 498–598 K. Based on the results of TG-FTIR-MS, the main volatile products obtained during thermolysis were carbon disulfide (CS_2), ammonia (NH_3), sulfur dioxide (SO_2), carbonyl sulfide (COS), hydrogen cyanide (HCN), cyanamide (H_2NCN), and isothiocyanic acid (HNCS). Comparison of the results obtained with TG-FTIR and TG-MS methods indicate some differences due to the change in residence time caused by experimental devices and the uncertainty of some gases with FTIR, such as H_2 and Cl_2 .

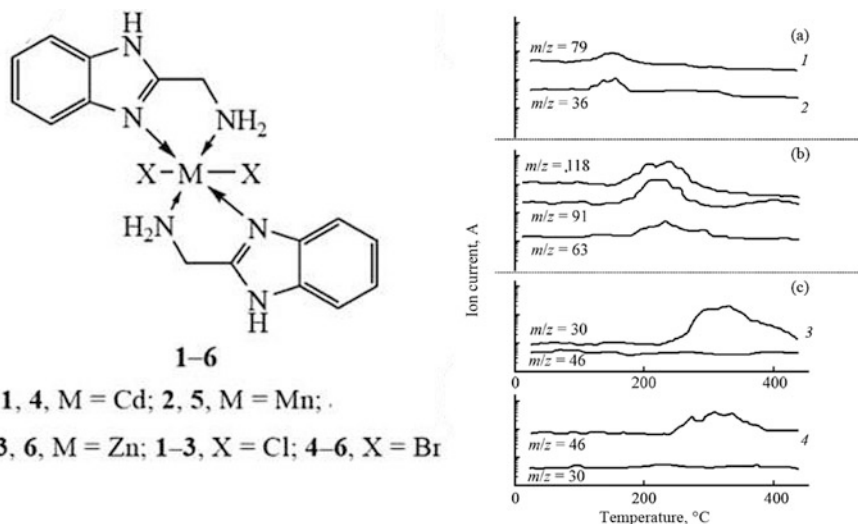


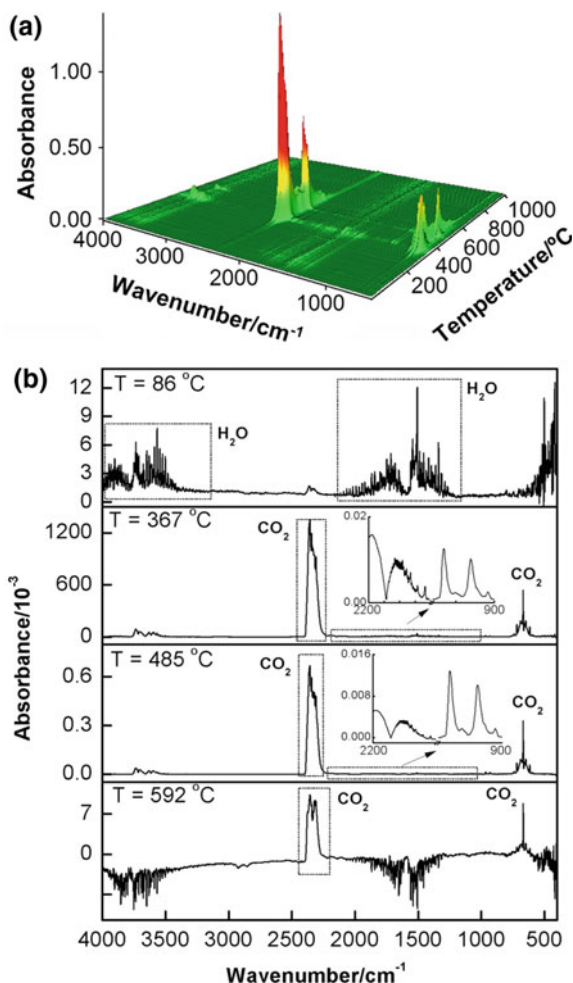
Fig. 2.8 (left) Structure of complexes; (right) EGA-MS *m/z* traces for the (a) first [(1) bromide complexes and (2) chloride complexes], (b) second, and (c) third [(3) TGA nitrogen flow and (4) TGA air flow] thermolysis steps of complexes as functions of temperature. Reproduced with permission from Ref. [45]. Copyright (2017) Springer Nature

Of interest are the 3D contour maps of the IR spectra of the thermolysis products (Fig. 2.9a) and IR spectra made at different temperatures for the gaseous products evolved during the thermolysis of the neodymium complex with N-phenylanthranilic acid in nitrogen atmosphere (Fig. 2.9b) [30]. In the temperature range of 303–423 K, only *m/z* 17 and 18 (see Fig. 2.9a) are detected corresponding to the release of OH⁺ and H₂O⁺ species. The FTIR spectrum recorded at 361 K shows characteristic bands at 3550–3200, 1630–1600, and 600–400 cm⁻¹ which correspond to asymmetric and symmetric O–H stretching, and HOH bending and rotational oscillations of water molecules, respectively. Thus, the first step of thermolysis corresponds only to the removal of water molecules.

2.1.2 Linear Pyrolysis Method

Linear pyrolysis (LP) is a stationary one-dimensional propagation of the reaction front of thermolysis in a condensed matter, when heat is supplied from an external source [56]. Depending on the relationship between the parameters, LP can occur in either of two modes: kinetic, when the pyrolysis macrokinetics coincides with the true kinetics of decomposition and $E_{\text{eff}} \approx E_{\text{tr}}$ or the regime of internal diffusion

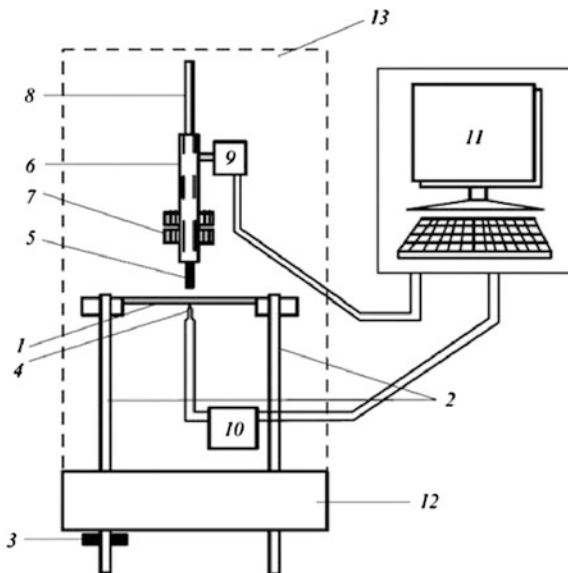
Fig. 2.9 EGA-FTIR for the Nd(III) complex in a nitrogen atmosphere: **a** a stacked plot of the FTIR spectra of the evolved gases; **b** FTIR spectra of the evolved gases formed at different temperatures (ν —stretching vibrations, π —deformation out-of-plane vibrations). Reproduced with permission from Ref. [30]. Copyright (2017) Elsevier



(with heating), when $E_{\text{eff}} \approx E_{\text{tr}}/2$. The development of this method was caused by the need to study the kinetics of fast high-temperature processes in condensed media, where transition from one temperature region to another is accompanied by a change in the rate-limiting step of the reaction.

The principle of operation of the devices based on LP-method (Fig. 2.10) is that a sample of the test compound is constantly pressed upon the surface of the heating plate at a constant temperature. During the experiment, the surface temperature of the heater (T_0) and the migration rate of the sample (U) equal to the linear rate of decomposition are recorded. When the LP rate associated with the experiment parameters is below a certain limiting value (as is true for most real conditions), the surface temperature of a hot sample can be considered to be T_0 without significant errors. For a condensed substance with low thermophysical characteristics, the LP is fast enough.

Fig. 2.10 Schematic diagram for LP. (1) Heater plate, (2) conducting planes, (3) current lead, (4) thermocouple, (5) sample, (6) sliding piston, (7) ring loads, (8) guide bar, (9) photodiode block for process rate recording, (10) control and heater plate temperature recording block, (11) computer block with a monitor, (12) massive vinyl plastic plate, (13) cover



Under conditions of low heat exchange with the environment, its rate is determined (for a zero-order reaction) by the Merzhanov relation [56]:

$$U = \sqrt{\frac{ak_0RT_s^2 \exp(-E/RT_s)}{E[(T_s - T_0) \pm Q/2c]}} \quad (2.2)$$

where a and c are the temperature conductivity and the heat capacity of the compound, respectively, k_0 is the pre-exponential factor in the Arrhenius equation, T_s is the temperature of the environment and of the opposite surface of the sample, Q is the reaction heat.

2.1.3 Thermolysis Induced by High-Energy Radiation

The thermal methods considered above are based on external heating of the test sample. High-frequency (HF) electric field can be used as an alternative heating source [57–61]. The essence of the HF method is that, on the one hand, polar groups and fragments of the organic parts of metal complexes (dielectric material) placed in an alternating electric field are oriented in accordance with a change in its polarity. On the other hand, thermal motion, as well as other groups and molecules, hinder such orientation. The energy expended in overcoming the disorientation of the material dissipates in the material and heats it. The intensity of heating increases with increasing frequency and electric field strength. The main advantage of HF heating is that the heating occurs without contact throughout the entire volume of the test sample.

A promising approach is the thermal treatment of metallopolymer materials under the action of lasers or accelerated electrons [62].

2.1.4 *Spray Pyrolysis*

By its nature and design, spray pyrolysis differs from the methods described above. This is an aerosol process, which is an effective alternative method for obtaining metallic and oxide NPs, ceramics, nanostructured materials [63, 64]. Widely used are ultrasonic, laser and plasma pyrolysis, as well as flame spray pyrolysis [65–67]. The method of aerosol spray pyrolysis is a promising strategy for increasing both surface area and crystallinity, which ensures consistent, easy, and large-scale production of nanomaterials [68–74].

Spray pyrolysis includes five main stages. In the first stage, the liquid precursor is sprayed using an appropriate droplet generator. It is interesting to note that under certain conditions it is possible to observe processes of self-assembly caused by evaporation or the formation of micelles, which leads to highly organized structures [75]. Then, it is followed by spray transport with air or an inert gas stream during which the solvent evaporates. The next step is the precipitation of the solute after the critical limit of supersaturation is reached in the drops. A combination of sol–gel synthesis and spray pyrolysis methods is rarely used. The main stage is the thermolysis of the precipitated substance, leading to nanoporous particles, followed by their calcination to obtain dense materials. The process of extracting particles from the gas stream completes the process. The methods of gas–particle conversion and liquid–solid-phase transformations with subsequent thermolysis and grinding have advantages related to the purity of the resulting material, its homogeneous chemical composition, the narrow particle size and shape distribution, the ability to synthesize multicomponent systems, the simplicity and scalability of the process.

Although some stages of spray pyrolysis [76] continue to develop (e.g., the formation of droplets [77], evaporation and drying [78], spraying through various devices—sprays, atomizers, ultrasonic generators, etc.), there is still no deep understanding of the effect of changes in reaction conditions (concentration, flow rate, evaporation–precipitation stage of thermolysis) on the mechanism and the possibility of controlling the uniform formation of NPs. By now, it is generally accepted that temperature has the most significant effect on the formation of nanocrystals. It should be noted that nanocomposites based on metal oxides obtained by spray pyrolysis are described in sufficient detail (see, for example, [79–86]).

Depending on the state of the precursor (based on water, solvent, or vapor) and the conditions of thermolysis, the methods for the synthesis of flame aerosols is divided into three general groups [87, 88]: (a) the synthesis of an aerosol flame with a vapor phase (VAFS) into which a metal precursor is supplied in the form of vapor, such as SiCl_4 and TiCl_4 , for the manufacture of the most advanced ceramic products [89]; (b) flame aerosol spray pyrolysis (FASP), where the feed is supplied in a state

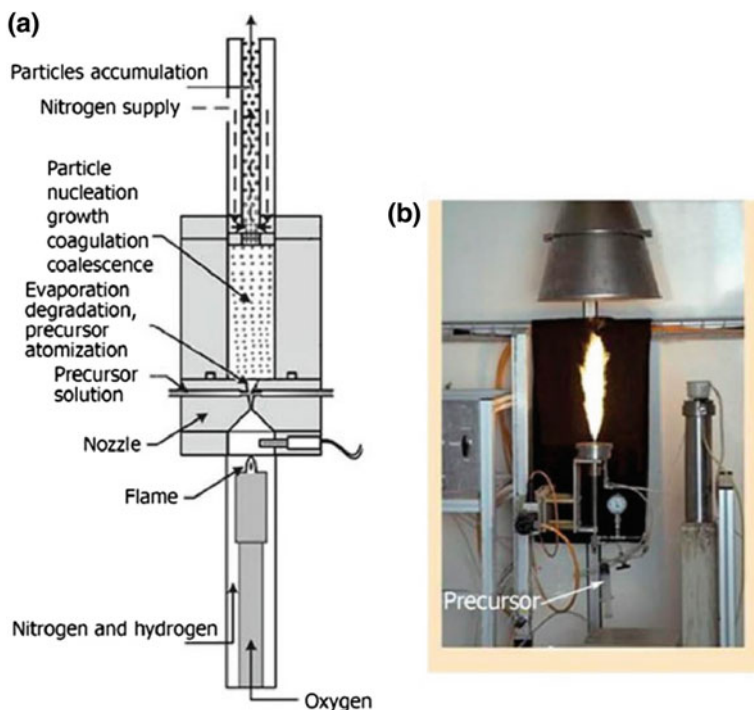


Fig. 2.11 A scheme of FSP (a) and a view of the high-temperature stream reactor (b)

with a low enthalpy (<50% of the total thermolysis energy), usually in an aqueous solvent, and therefore an auxiliary hydrogen or hydrocarbon flame is necessary for its combustion [90] and (c) flame spray pyrolysis (FSP), where the precursor is also in liquid form, but with a significantly higher combustion enthalpy (>50% of the total energy of combustion), usually in an organic solvent [91]. FSP, which is the youngest of the three processes, has important technological elements such as self-sustaining flame, the use of liquid feeds and less volatile precursors, proven scalability, high-temperature flame and large temperature gradients. It has also been most actively used in the recent years for the production of complex and functional nanomaterials [92–96]. As a typical example, we note FSP synthesis of nanostructured ZnO (particle diameter 10–20 nm), which can be represented by a schematic diagram (Fig. 2.11) [97, 98].

FSP allows the production of nano-oxide powders from highly volatile gaseous metal chlorides that decompose/oxidize in a hydrogen–oxygen flame [94, 99–104]. However, products derived from the FSP vapor-phase process are limited to Al, Ti, Zr, and Si oxides from their metal chlorides.

Interest in the production of more complex materials required a new methodology called liquid-feed flame spray pyrolysis (LF-FSP) [105–107]. LF-FSP method can be used to produce mixed and single MOs easily from low-cost starting

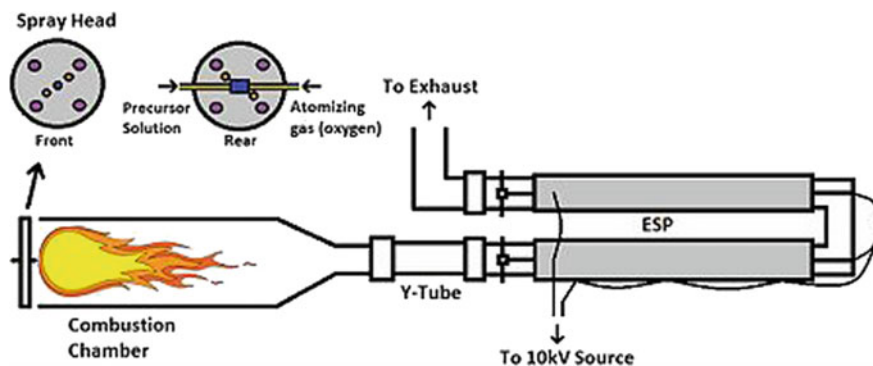


Fig. 2.12 Schematic of LF-FSP device. In spray head, purple, orange, and blue correspond to auxiliary oxygen, ignition torch, and aerosol generator, respectively

materials in a single step without forming harmful by-products [104, 108–110]. A LF-FSP device has five parts: aerosol generator with fluid feed and reservoir, cylindrical quartz combustion chamber, Y-shaped quartz tube, four wire-in-cylinder (electrostatic precipitators) connected in parallel-series, and exhaust piping (Fig. 2.12).

Typically, the solvent acts as a fuel, so ethanol or other “inexpensive” alcohols are used to dissolve the precursors. The oxygen/alcohol aerosol undergoes rapid combustion for milliseconds, oxidizing all organic components at temperatures up to 2273 K, leaving only the MOs in the gas phase [111]. The formed particles form clusters and, finally, particles up to 100 nm in size, as shown in Fig. 2.13.

As a typical example, we note the preparation of submicron-sized mesoporous nickel ferrite (NiFe_2O_4) spheres by an aerosol spray pyrolysis method using Pluronic F127 as a structure-directing agent (Fig. 2.14) [112].

It should be also noted that spray pyrolysis has been applied to deposit a wide variety of thin films [113, 114]. Thin-film deposition, using the spray pyrolysis technique, involves spraying a metal salt solution onto a heated substrate (Fig. 2.15). Droplets impact on the substrate surface, spread into a disk-shaped structure, and undergo thermal decomposition. The substrate surface temperature is the most critical parameter as it influences film roughness, cracking, crystallinity, etc.

Of interest is ultrasonic aerosol pyrolysis (USP), widely used for the synthesis of the nanomaterials, especially metals and metal oxides, various morphologies [115–121]. It is important that higher reaction temperatures give a larger APS, which increases coalescence and NP growth [122]. NPs exhibit depressive melting points in comparison with their bulk analog, which is another important factor for the fusion and growth of the particles [123, 124]. The range of materials that can be obtained with ultrasound is dramatically increased due to the diversification of precursors with the inclusion of solid-phase reactants, such as metal acetates [125, 126]. Control over the particle size and aggregation state in the aerosol can be

Particle Formation of a Single-Phase System

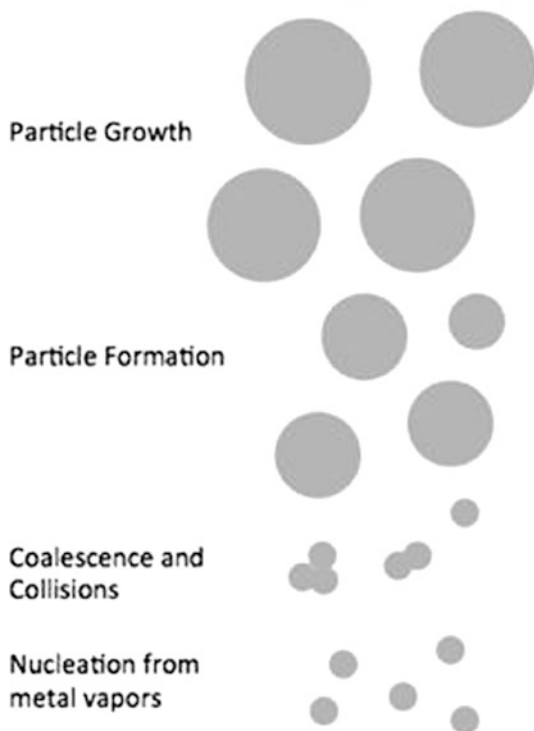


Fig. 2.13 Formation route of a single phase ceramic via LF-FSP



Fig. 2.14 Synthesis of NiFe_2O_4 via LF-FSP. Reproduced with permission from Ref. [112]. Copyright (2014) American Chemical Society

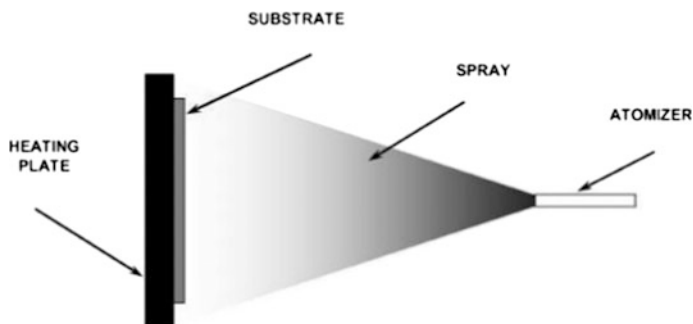


Fig. 2.15 Schematic diagram of spray pyrolysis equipment. Reproduced with permission from Ref. [113]. Copyright (2017) American Chemical Society

achieved by a reasonable choice of process parameters [127–132]. The crystalline phase, the degree of oxidation, the morphology and size of particles strongly depend on the synthesis process and, in addition, the precursor used for metallic NPs [133]. USP technology has shown better control over the synthesis of nano-materials, leading to target dimensions, spherical morphology, and high purity [134–138].

2.1.5 Chemical Vapor Deposition

Chemical vapor deposition (CVD) is a chemical process used to produce high quality, high performance, solid materials, as well as thin films [139–142]. In typical CVD process, the wafer (substrate) is exposed to one or more volatile precursors, which react and/or decompose on the substrate surface to produce the targeted material (Fig. 2.16) [143]. Frequently, volatile by-products are also produced, which are removed by gas flow through the reaction chamber.

In the CVD process, solids are grown in the form of polycrystalline, epitaxial, or amorphous films, depending on the materials and conditions of the reactor [144, 145]. The CVD process is determined by chemical reactions on the surface and in the gas phase, so parameters such as temperature, pressure, input concentration and reaction flow rate, substrate material, morphology and coating material, thickness and uniformity of the film, availability of precursors, and their cost are important [146, 147].

The principle of the CVD process includes the following consecutive stages:

- (1) The precursors are transported in the gas phase, in which gas-phase reactions occur;
- (2) Adsorption and transport of precursors on the surface;
- (3) Supply of energy (thermal, plasma, light) for the destruction of precursor molecules and the formation of a film;

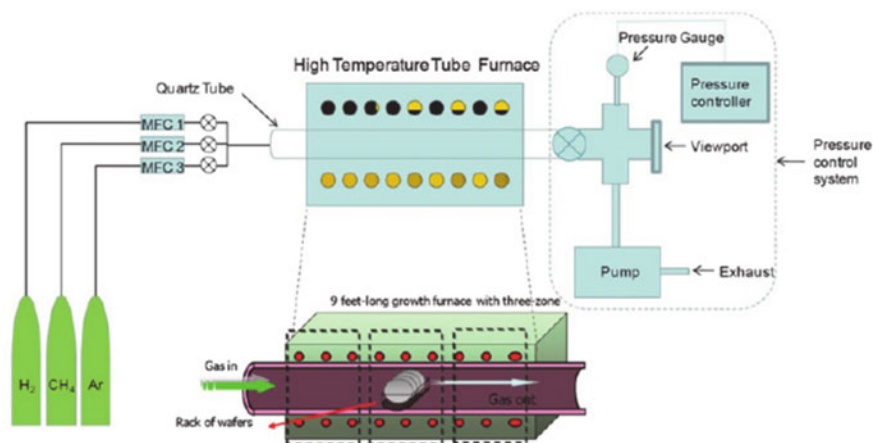


Fig. 2.16 Complete apparatus setup for CVD [143]

- (4) Transportation and desorption of by-products from the surface;
- (5) Transport of the gas phase and evacuation of by-products in the gas phase [148].

As a typical example, the reaction pathways for the fragmentation of the ruthenium chelate molecule with trifluoroacetylacetone are shown in Fig. 2.17 [149], of which the following conclusions follow:

- (1) Ru chelate provides most of the oxygen in the RuO_2 film and the reaction is unimolecular.
- (2) The growth rate exponentially changes with the temperature of the substrate. Nevertheless, the growth rate of the film increases with decreasing partial pressure and it saturates at high partial pressures. This indicates that the kinetics of the reaction follows the adsorption isotherm of Langmuir.
- (3) Water vapor is required to precipitate thin ruthenium films, since water molecules destabilize the precursors by partial protonation of the ligands.

Various variants of CVD technology are commonly used to produce metal-polymer nanocomposite materials [150, 151]. Their essence lies in the joint or sequential deposition of metallic and organic components and the formation of metallic NPs in a growing film. The volume fraction of metallic NPs in the resulting film is controlled by deposition rates of metallic and organic components [152].

It should be noted that metal oxide nanomaterials are one of the most frequently compounds obtained using CVD methods [153–156].

Methods of metal-organic chemical vapor deposition (MOCVD) are widely used to produce a variety of film nanomaterials [157–159]. The use of metal chelates in gas-phase processes for the production of nanocomposite materials has a

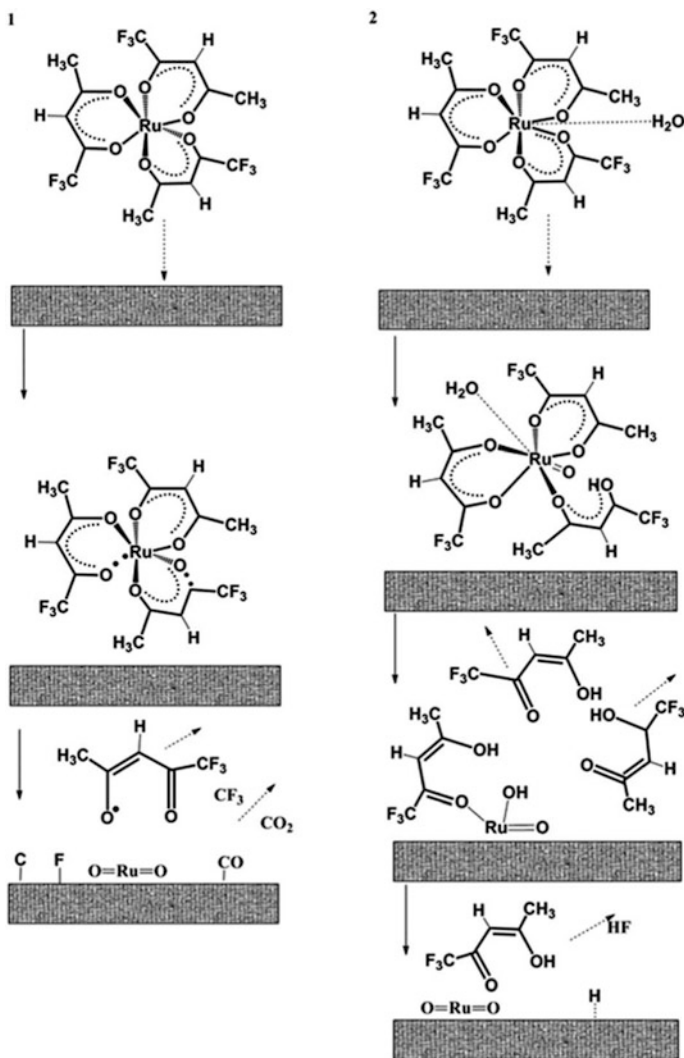


Fig. 2.17 Reaction mechanism of the Ru chelate precursor molecule at the substrate surface. (1) Thermolysis with the formation of highly reactive radicals, without water. (2) Volatile reaction by-products formation by protonation of the ligands in the presence of water. Reproduced with permission from ref. 149. Copyright (2000) John Wiley and Sons

number of advantages, since the presence of strongly bound components makes it possible to obtain qualitative products without defects with stoichiometric composition [160], including thin-film materials based on cadmium [161, 162], iron [163, 164], sulfides of antimony and bismuth [165], etc. The advantages of the MOCVD method are the control of thickness, precise doping, large deposition area, and morphological diversity.

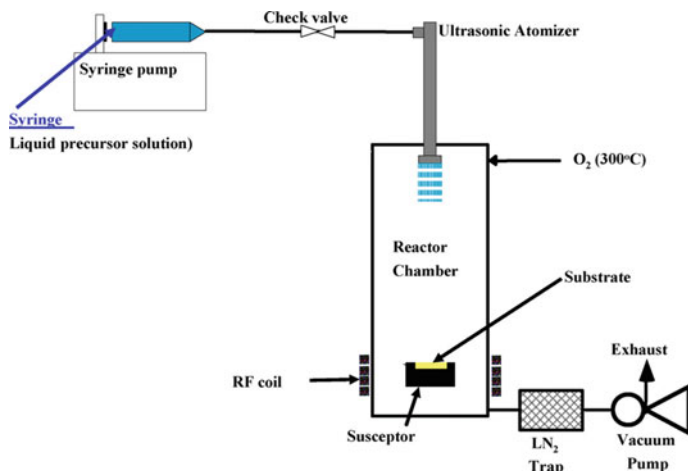


Fig. 2.18 Schematic of the MOCVD reactor utilizing aerosol-assisted liquid delivery and a vertical cold-wall stagnation plane flow injector. Reproduced with permission from Ref. [166]. Copyright (2009) Elsevier

Of interest is the use of MOCVD as an effective means for manufacturing yttria-stabilized zirconia (YSZ) for thermal barrier coating [166]. The precursors of MOCVD were $Y(L)_3$ and $Zr(L)_4$ ($L = 2,2,6,6$ -tetramethyl-3,5-heptanedianato). The maximum deposition rate of YSZ was $14.2 \pm 1.3 \mu\text{m h}^{-1}$ at 1000 K, which provided a microstructure of the layered coating. The growth rate was the first order with a temperature below 1000 K with an apparent activation energy of $50.9 \pm 4.3 \text{ kJ mol}^{-1}$, and the coating efficiency was a maximum of about 10% at the highest growth rates. MOCVD method was also used with aerosol-assisted liquid delivery system (Fig. 2.18) [166].

It should be noted that different CVD methods are often used to obtain nanomaterials because of their advantages over physical vapor deposition (PVD) methods [167]. In particular, CVD methods include atmospheric pressure [168], hot filament [169], microwave plasma [170], plasma enhanced [171] types, and so on. As an example, Fig. 2.19 shows schematic images of the methods of microwave plasma (a) and hot filament (b).

CVD experiments with pulsed spray evaporation (PSE-CVD) of liquid solutions of Ni and Co acetylacetonates in ethanol as precursors were used for production of deposited Ni and Co metal films [172]. It turned out that addition of water improves growth of a metallic Ni film and reduces carbon contamination, while in the case of $\text{Co}(\text{acac})_2$, even smallest amounts of water promote complete oxidation of the deposited film.

Of interest is also the method of atomic layer deposition (ALD), which is the widespread replacement of the conventional bubbler evaporator with a direct liquid

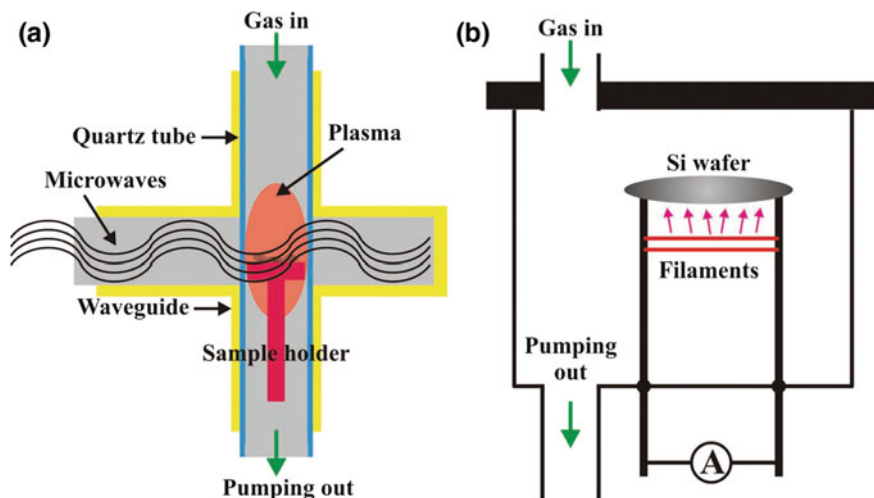
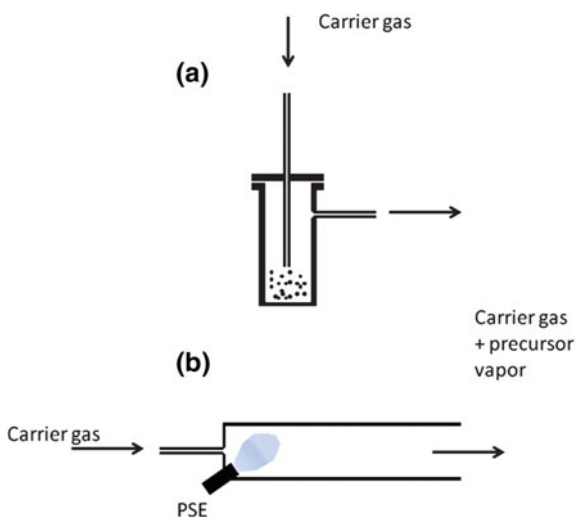


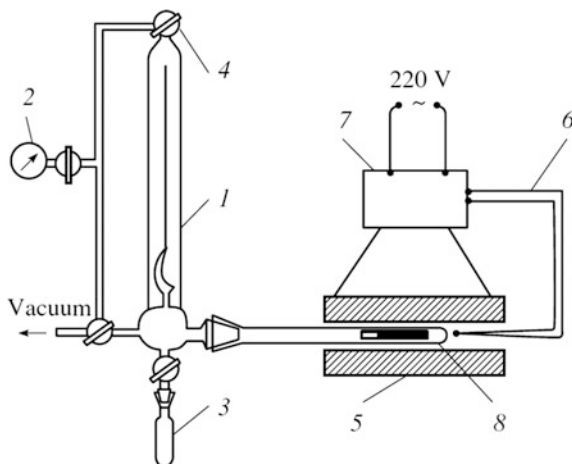
Fig. 2.19 Schematic diagram of the **a** microwave-plasma and **b** hot-filament CVD techniques. Reproduced with permission from Ref. [167]. Copyright (2012) John Wiley and Sons

Scheme 2.1 Delivery strategies: **a** bubbler evaporator, **b** direct liquid delivery using a pulsed spray evaporator (PSE). Reproduced with permission from Ref. [173]. Copyright (2011) Royal Society of Chemistry



delivery as schematically shown in Scheme 2.1 [173]. In ALD method, either liquid precursors or liquid feedstocks are introduced into the heated evaporation chamber under vacuum in the form of a fine spray. The precursor is dissolved in a reactive or inert solvent that provides a fine control of the composition and places less stringent demands on the thermal stability of the precursors.

Fig. 2.20 Scheme of a unit for kinetic studies of thermolysis of test compounds: (1) a reaction vessel, (2) a vacuum gauge, (3) a sampling vessel for gaseous products, (4) a vacuum cock, (5) a calcination furnace, (6) thermocouple, (7) a heat regulator and (8) an ampoule with a substance [175]



2.1.6 Kinetic Approaches to the Investigation of Thermolysis of Metal Chelates

Kinetic approaches to studies of the thermolysis of metal chelates are very promising as a tool for understanding the mechanisms of physical and chemical processes that occur in each stage for relatively slow processes at temperatures below 1370 K. Kinetic analyses of thermolysis processes are of interest for many researchers because it is inherently bound with the thermolysis mechanisms. The knowledge of the mechanism allows postulating the kinetic equations or vice versa, kinetics is the starting point for postulating thermolysis mechanisms [174]. Isothermal kinetic studies are performed by recording the gas evolution in static non-isothermal reactor (Fig. 2.20) using a zero-manometer [175].

It should be noted that any thermal process is to some extent accompanied by a change in the internal heat content of the system, i.e., absorption or release of heat. At low-temperature thermolysis of the majority of condensed systems, the conversion rates are relatively small, and the temperatures for sufficiently intense heat transfer are rather low. Such processes, regardless of the magnitude of the thermal effect, are spatially isothermal in time, i.e., the temperature of the surface of the condensed sample (T_a) coincides with the temperature of the surrounding medium (T_s) [56]. In this case, it is possible to use isothermal methods of classical chemical kinetics, and the process conditions are formulated from the requirements of its scaling, in particular from the ratio of the characteristic times of heating (τ_h) and transformation (t_r).

In general, most methods of kinetic analysis of TA data begin with the Arrhenius' equation,

$$K(T) = A \exp(-E_a/RT), \quad (2.3)$$

where A is the pre-exponential factor (s^{-1}), E_a is the apparent activation energy (kJ mol^{-1}), T is the absolute temperature (K), and R is the gas constant.

The kinetics of thermolysis of metal chelates in general form is described by the macrokinetic equation:

$$W(T, \eta) = k(T)\varphi(\eta), \quad (2.4)$$

where $W(T, \eta)$ is the reaction rate (s^{-1}), $k(T)$ is the temperature-dependent rate constant of the reaction (s^{-1}), determined by its mechanism, and $\varphi(\eta)$ is the kinetic function. The latter depends on the reaction mechanism and reflects the ratio between the concentrations of the unreacted and reacted substances:

$$\varphi(\eta) = (1-\eta)^n \quad (2.5)$$

where n is the order of the reaction, η is the degree of conversion varying from 0 to 1.

The kinetic function assumes different mathematical forms depending on the reaction mechanism [176].

Then the characteristic reaction time

$$\tau_r \approx W(T, \eta)^{-1} \quad (2.6)$$

Since the transformations take place in the condensed phase, it is advisable to use the characteristic sample heating time for τ_h as macrokinetics [177]:

$$\tau_h = d^2/a, \quad (2.7)$$

where d is the diameter of the sample, and a is its temperature conductivity. In this case, in order to obtain reliable kinetic results, the following conditions must be fulfilled:

$$\tau_h < < \tau_p \quad (2.8)$$

As a rule, thermolysis of metal chelates is a multistep process. When studying its mechanism, various types of kinetic models are used. In a pseudo-one-component model, the sample is regarded as an ordered single-component one, and to describe the loss of weight, the kinetics of the solid-phase or gas-phase reaction is studied in the entire temperature range [178]. However, such a model does not describe possible changes in the kinetics and mechanism with increasing thermolysis temperature.

A pseudo-multicomponent composite model analyzes the sample as consisting of various pseudo-components, each of which represents a separate real component or a mixture of several ones, and the thermolysis of the metal chelate is modeled by a superposition of the decomposition of these components. However, this approach significantly complicates the kinetic studies of thermolysis.

In particular, PMCs are characterized by a wide variety of thermal transformations. For example, thermolysis of Cu-PMCs based on polyacrylamidoxime fibers [179] includes three temperature-separated stages: at 398–603 K (weight loss by 14.3%), 603–715 K (10.8%), and 715–965 K (68.6%). It can be seen that the main weight loss occurs at the final stage of the thermolysis, which is somewhat lower than in the case of the chelating polymer ligand. One possible reason for this may be the catalytic effect of copper ions on the process of thermal decomposition of a polymer, especially as its rate increases with an increase in the content of copper ions.

A pseudo-two-component stepwise-separated first-order model treats the sample as being decomposable in two temperature regions, which are described by different kinetic models. The temperature corresponding to the minimum on the derivatogram is the point of separation between the two stages of weight loss. This method is greatly complicated when two peaks are not completely separated, but overlap with each other.

A non-isothermal method is widely used to describe the kinetics and mechanism of reactions in the condensed phase. Since the rate of thermolysis depends on temperature, the change in weight of the sample can be represented as a function:

$$\frac{d\eta}{dt} = k(T)\varphi(\eta) = A\exp\left(-\frac{E_a}{RT}\right)\varphi(\eta) \quad (2.9)$$

However, due to the complexity of the kinetic description concerning the solid state thermolysis processes it is usually assumed that the activation energy is not a constant value but depends on η [180–182].

When the temperature of the sample is controlled by a constant heating rate β ($\beta = dT/dt$), this equation becomes:

$$\frac{d\eta}{dt} = \frac{A}{\beta}\exp\left(-\frac{E_a}{RT}\right)(1-\eta)^n \quad (2.10)$$

In integral form, expression (2.9) looks like this:

$$\varphi(\eta) = \int_0^\eta \frac{d\eta}{(1-\eta)^n} = \frac{A}{\beta} \int_0^T \exp\left(-\frac{E_a}{RT}\right) dT = \frac{AE_a}{\beta R} P(x) \quad (2.11)$$

and

$$\ln\left[\frac{\varphi(\eta)}{T^2}\right] = \ln\frac{AR}{\beta E_a} - \frac{E_a}{RT} \quad (2.12)$$

For the special case $n = 1$,

$$\ln \left[-\ln \frac{1-\eta}{T^2} \right] = \ln \frac{AR}{\beta E_a} - \frac{E_a}{RT} \quad (2.13)$$

For $n \neq 1$ in the most cases expression (2.12) is solved numerically.

In the case of metal chelates, the thermolysis process follows either a sigmoidal function or a deceleration (acceleration) function. Table 2.3 shows expressions of $\varphi(\eta)$ for the different solid-state mechanisms [183].

Equations (2.11) and (2.12) are the fundamental expressions for calculating the kinetic parameters from TG data. These are analyzed using the different methods in the differential and integral forms [184–187]. $P(x)$ has no analytical solution but has many approximations, among of which we consider the most commonly used. These methods allow to calculating values of A , E , and n from a single curve or from a series of curves recorded at different heating rates.

Coats-Redfern method

This method [188] is an integral method and involves the thermolysis mechanism. The following equation can be obtained with using an asymptotic approximation for solution of Eq. (2.11):

$$\ln \left[\frac{\varphi(\eta)}{T^2} \right] = \ln \left[\frac{AR}{\beta E_a} \left(1 - \frac{2RT}{E_a} \right) \right] - \left(\frac{E_a}{RT} \right) \quad (2.14)$$

Coats-Redfern method supposes that $\left(1 - \frac{2RT}{E_a} \right) \rightarrow 0$ for the Doyle approximation [189], obtaining in natural logarithmic form:

$$\ln \varphi(\eta) \cong \ln \left[\frac{AR}{\beta E_a} \right] - \frac{E_a}{RT} \quad (2.15)$$

A straight line can be obtained from the relationship $\ln (\varphi(\eta)/T^2)$ versus $1000/T$. The slope of the line gives $-E_a/R$.

van Krevelen method

The integral method used by van Krevelen [190] is expressed as:

$$\ln \varphi(\eta) = \ln \left(\frac{A(0.368/T_m)^{\frac{E_a}{RT_m}}}{\beta \left(\frac{E_a}{RT_m} + 1 \right)} \right) + \left(\frac{E_a}{RT_m} + 1 \right) \ln T \quad (2.16)$$

where T_m is the temperature at the maximum rate of weight loss. Therefore, E can be obtained from the slope of a plot of $\ln \varphi(\eta)$ versus $\ln T$.

MacCallum-Tanner method

The method by MacCallum and Tanner [191] provides an approximation integrated from the rate of thermolysis as a function of temperature. The rate of thermolysis can be expressed by:

Table 2.3 Algebraic expressions for the most frequently used mechanisms of solid state process

No	Mechanisms	Symbol	Differential form, f (η)	Integral form, $\varphi(\eta)$
<i>Sigmoidal curves</i>				
1	N and G ($n = 1$)	A_1	$(1 - \eta)$	$[-\ln(1 - \eta)]$
2	N and G ($n = 1.5$)	$A_{1.5}$	$(3/2)(1 - \eta)[- \ln(1 - \eta)]^{1/3}$	$[-\ln(1 - \eta)]^{2/3}$
3	N and G ($n = 2$)	A_2	$2(1 - \eta)[- \ln(1 - \eta)]^{1/2}$	$[-\ln(1 - \eta)]^{1/2}$
4	N and G ($n = 3$)	A_3	$3(1 - \eta)[- \ln(1 - \eta)]^{2/3}$	$[-\ln(1 - \eta)]^{1/3}$
5	N and G ($n = 4$)	A_4	$4(1 - \eta)[- \ln(1 - \eta)]^{3/4}$	$[-\ln(1 - \eta)]^{1/4}$
<i>Deceleration curves</i>				
6	Diffusion, 1D	D_1	$1/(2\eta)$	η^2
7	Diffusion, 2D	D_2	$1/(\ln(1 - \eta))$	$(1 - \eta)\ln(1 - \eta) + \eta$
8	Diffusion, 3D	D_3	$1.5/[(1 - \eta)^{-1/3} - 1]$	$(1 - 2\eta/3) - (1 - \eta)^{2/3}$
9	Diffusion, 3D	D_4	$[1.5(1 - \eta)^{2/3}]/[1 - (1 - \eta)^{1/3}]^{-1}$	$[1 - (1 - \eta)^{1/3}]^2$
10	Diffusion, 3D	D_5	$(3/2)(1 + \eta)^{2/3}/[(1 + \eta)^{1/3} - 1]^{-1}$	$[(1 + \eta)^{1/3} - 1]^2$
11	Diffusion, 3D	D_6	$(3/2)(1 - \eta)^{4/3}/[(1 - \eta)^{1/3} - 1]^{-1}$	$[[1/(1 - \eta)^{1/3} - 1]^2]$
12	Contracted geometry shape (cylindrical symmetry)	R_2	$3(1 - \eta)^{2/3}$	$1 - (1 - \eta)^{1/3}$
13	Contracted geometry shape (sphere symmetry)	R_3	$3(1 - \eta)^{2/3}$	$1 - (1 - \eta)^{1/3}$
<i>Acceleration curves</i>				
14	Mample power law	P_1	1	η
15	Mample power law ($n = 2$)	P_2	$2\eta^{1/2}$	$\eta^{1/2}$
16	Mample power law ($n = 3$)	P_3	$(1.5)\eta^{2/3}$	$\eta^{1/3}$
17	Mample power law ($n = 4$)	P_4	$4\eta^{3/4}$	$\eta^{1/4}$
18	Mample power law ($n = 2/3$)	$P_{3/2}$	$2/3(\eta)^{-1/2}$	$\eta^{3/2}$
19	Mample power law ($n = 3/2$)	$P_{2/3}$	$3/2(\eta)^{1/3}$	$\eta^{2/3}$
20	Mample power law ($n = 4/3$)	$P_{3/4}$	$4/3(\eta)^{-1/3}$	$\eta^{3/4}$

$$\log \varphi(\eta) = \log \frac{AE_a}{\beta R} - 0.4828E^{0.4351} - \left(\frac{0.449 + 0.217E_a}{10^{-3}T} \right) \quad (2.17)$$

A plot of $\log \varphi(\eta)$ versus $1/T$ can give E from the slope, and A is calculated from the intersection with the Y axis.

Broido model

This method [192] is based on the following equation:

$$\ln \varphi(\eta) = \ln[A/\beta \times (R/E)T_{\max}^2] - (E/R) \times 1/T \quad (2.18)$$

The activation energy, E , and the frequency factor, A , were computed from the slope and the intercept of a plot of $\ln \varphi(\eta)$ versus $1/T$ after linear regression of the data.

As an example, we consider thermolysis of PMCs–Cu(II) based on the chelating resins synthesized by condensing a phenolic Schiff base derived from 4,4'-diaminodiphenylmethane and *o*-hydroxyacetophenone with formaldehyde (ligand I) or furfuraldehyde (ligand II) [193]. The TG data were fitted into different models and subjected to computational analysis to calculate the kinetic parameters (Table 2.4). It should be noted that the Coats and Redfern model does not involve T_{\max} in the expression. This model was used to evaluate the kinetic parameters in the entire range (403–883 K). On the other hand, the Van Krevelen and Broido models involve T_{\max} in the expressions and, hence, were used to calculate the kinetic parameters for different thermolysis stages using the relevant T_{\max} value of each stage. The entropy of activation, ΔS (cal K⁻¹ mol⁻¹) was calculated using the relation $A = (kT_{\max}/h) \cdot (e^{\Delta S/R})$, where k is the Boltzmann constant and h is Planck's constant. Data analysis of activation energy shows that both ligands were less stable than their respective PMCs–Cu(II).

In another interesting example, the reaction order, n , the apparent activation energies of thermolysis, E_a , entropies, ΔS^* , enthalpy change, ΔH^* , free energy change, ΔG^* , pre-exponential factor, A , and the linearization curves of the thermolysis of oligo-2-[(4-bromophenylimino) methyl] phenol and its PMC–Co, –Ni,

Table 2.4 Kinetic parameters

Compound	Temperature range (K)	T_{\max} (K)	Method ^a	E (kcal)	A (s ⁻¹)	ΔS (cal K ⁻¹ mol ⁻¹)
Ligand I	403–883	–	CR	13.862	1.52E + 04	–41.470
		843.33	vK	6.666	2.09E + 00	–59.150
		843.33	BR	5.445	6.06E – 01	–61.608
PMC–Cu	403–883	–	CR	4.848	1.00E + 02	–51.220
		748.01	vK	19.115	2.61E + 05	–35.582
		748.01	BR	16.522	3.82E + 04	–39.405
Ligand II	403–883	–	CR	9.062	2.90E + 03	–44.720
		823.2	vK	9.952	1.26E + 02	–50.948
		823.2	BR	6.954	2.35E + 00	–58.866
PMC–Cu	403–883	–	CR	23.155	1.82E + 10	–13.045
		620.67	vK	20.508	1.58E + 07	–27.053
		620.67	BR	20.740	2.85E + 07	–25.887

^aCR Coats–Redfern, vK Van Krevelen, BR Broido

Table 2.5 Thermodynamic and kinetic parameters obtained by the different methods^a

Materials	Stage ^b	Methods	<i>n</i>	<i>E_a</i>	ln <i>A</i>	Δ <i>S</i> *	Δ <i>H</i> *	Δ <i>G</i> *	<i>r</i>
Ligand	I (453–581 K)	MC	0.9	105.4	28.07	–16.51	100.9	109.9	0.99701
		vK	0.9	107.4	28.71	–11.20	102.9	109.0	0.99665
		CR	0.9	96.31	19.53	–87.52	91.76	139.6	0.99654
PMC–Co	I (475–590 K)	MC	0.1	47.22	14.37	–130.3	42.69	113.6	0.99656
		vK	0.2	45.14	10.11	–165.8	40.61	130.8	0.99519
		CR	0.2	39.84	5.811	–201.6	35.31	145.0	0.99439
	II (626–977 K)	vK	0.8	39.29	6.052	–203.9	31.70	217.6	0.99733
		MC	0.6	35.91	9.694	–173.6	28.32	186.6	0.99655
		CR	0.9	31.34	0.693	–248.4	23.75	250.3	0.98027
PMC–Cu	I (502–626 K)	MC	0.5	110.2	26.89	–27.17	105.2	121.6	0.99899
		vK	0.5	112.3	24.53	–46.79	107.3	135.4	0.99809
		CR	0.5	100.2	18.16	–99.75	95.29	155.2	0.99876
	II (626–977 K)	MC	0.9	76.51	15.48	–125.1	69.17	179.5	0.99528
		CR	1.0	65.36	6.327	–201.3	57.96	235.5	0.99347
		vK	0.1	78.05	10.81	–164.0	70.71	215.3	0.99055
PMC–Ni	I (530–656 K)	MC	0.7	65.18	14.41	–131.3	59.90	143.1	0.99756
		vK	0.8	60.83	12.08	–150.7	55.55	151.1	0.99568
		CR	0.8	62.04	6.476	–197.3	56.76	181.9	0.98792
	II (656–899 K)	vK	0.4	57.79	12.59	–147.7	51.63	160.9	0.99701
		MC	0.4	58.95	15.89	–120.3	52.79	141.8	0.99567
		CR	0.4	48.81	6.823	–195.7	42.65	187.5	0.99421

^a*E_a* is measured in kJ mol^{–1}, *A* in s^{–1}, Δ*S** in kJ mol^{–1}, Δ*H** in kJ mol^{–1}, Δ*G** in kJ mol^{–1}, *r* is the correlation coefficients of the linear plot, and *n* is the order of reaction

^bI and II are the temperature regions of initial and 50% weight loss

and –Cu have been calculated from the TGA curves by the Coats-Redfern method (CR), MacCallum-Tanner method (MC), and van Krevelen method (vK) (Table 2.5) [194]. The results indicate that the values of all methods are comparable and the values of correlation coefficients of ligand and PMCs are approximately 1.00. In this case, the values of the apparent activation energy of thermolysis of oligomer metal chelates change in the following order Cu > Ni > Co.

Madhusudanan-Krishnan-Ninan method

In the Madhusudanan method [195], the equation used has the form:

$$\ln \frac{\varphi(\eta)}{T^{1.9206}} = -\ln \frac{AR}{\beta E} + 3.7678 - 1.9206 \ln E - 0.1240 \frac{E}{RT} \quad (2.19)$$

WanJun-Yuwen-Hen-Cunxin method

WanJun et al. [196] proposed another approximate formula for the Arrhenius temperature integral, which gives the following linear equation:

$$\ln \frac{\varphi(\eta)}{T^{1.8946}} = -\ln \frac{AR}{\beta E} + 3.6350 - 1.8946 \ln E - 1.0014 \frac{E}{RT} \quad (2.20)$$

Horowitz-Metzger method

The Horowitz-Metzger method [197] introduced a characteristic temperature T_m and a parameter θ as follows:

$$\theta = T - T_m. \quad (2.21)$$

If the reaction order is 1, T_m is defined as the temperature at which $(1 - \eta)_m = 1/e = 0.368$ and the final expression becomes:

$$\ln \varphi(\eta) = \frac{E\theta}{RT_m^2} \quad (2.22)$$

If the reaction order is unknown, T_m is defined for the maximum heating rate. When $\theta = 0$, $(1 - \eta) = (1 - \eta)_m$ and $(1 - \eta)_m = n^{1/1-n}$ and

$$\ln \left[\frac{1 - (1 - \eta)^n}{(1 - n)} \right] - \ln \frac{ART_m^2}{\beta E} - \frac{E}{RT_m} + \frac{E\theta}{RT_m^2} \quad (2.23)$$

Activation energy can be calculated from the line drawn between $\ln \varphi(\eta)$ versus θ .

Criado-Malek-Ortega method

If the value of the activation energy is known, the kinetic model of the process can be determined by Criado-Malek-Ortega method [198], which can accurately determine the reaction mechanism in a solid-phase reaction process. This is defined by a $z(\eta)$ type function:

$$z(\eta) = \frac{\left(\frac{d\eta}{dt}\right)}{\beta} \pi(x)T, \quad (2.24)$$

where $x = E_a/RT$, and $\pi(x)$ is an approximation of the temperature integral, which cannot be expressed in a simple analytical form. In this case, the fourth rational expression of Senum and Yang [199] is used. Combining a rate expression $\frac{d\eta}{dt} = k\varphi(\eta)$ and Eq. (2.10), we can obtain:

$$z(\eta) = \varphi(\eta)F(\eta) \quad (2.25)$$

Equation (2.25) is used to represent the experimental curve. By comparing these two curves, the type of mechanism involved in the thermolysis can be identified.

Tang Method

Using a suitable approximation to solve Eq. (2.11), when it is taken logarithm each side, the following equation can be obtained [200]:

$$\ln\left(\frac{\beta}{T^{1.894661}}\right) = \ln\left(\frac{AE_a}{R\varphi(\eta)}\right) + 3.635041 - 1.894661 \ln E_a - \frac{1.001450E_a}{RT} \quad (2.26)$$

Plots of $\ln(\beta T^{1.894661})$ versus $1/T$ give a group of straight lines. The activation energy E can be obtained from the slope ($-1.001450E/R$) of the regression line calculated for the same thermolysis values at different heating rates.

Kissinger–Akahira–Sunose Method

This method [201] is an isoconversional method like Tang method and the following equation can be obtained:

$$\ln\left[\frac{\beta}{T^2}\right] = \ln\left[\frac{AR}{E_a\varphi(\eta)}\right] - \frac{E_a}{RT} \quad (2.27)$$

Activation energy can be calculated using the following equation without knowing the solid state thermolysis reaction mechanism.

$$\ln\left(\frac{\beta}{T_{\max}^2}\right) = \left\{ \ln\frac{AR}{E_a} + \ln\left[n(1 - \varphi_{\max})^{n-1}\right] \right\} - \frac{E_a}{RT_{\max}} \quad (2.28)$$

T_{\max} is temperature related to maximum reaction rate; α_{\max} is maximum degradation fraction. The dynamic parameter of thermolysis under linear heating is determined from the modified Kissinger equation at T_{\max} , i.e., the temperature corresponding to the maximum conversion in the TG curves. The Kissinger method assumes that $\ln(1 - \eta_m)^n$ is independent of the heating rate. It also assumes that the reaction order remains constant, and is nearly equal to unity. The straight-line plot $\ln(\beta/T_{\max}^2) - 1000/T_{\max}$, calculated for the same η values at different heating rates β , is used to calculate the activation energy and the pre-exponential factor.

Flynn–Wall–Ozawa method

This is the simplest method for determining activation energies directly from weight loss against temperature obtained at several heating rates. This technique assumes that A , $(1 - \eta)^n$ and E_a are independent of T ; A and E_a are independent of η . The Flynn–Wall–Ozawa [202, 203] plot is obtained by using the following expression:

$$\log \varphi(\eta) = \log \frac{AE_a}{R} - \log \beta + \log p \left(\frac{E_a}{RT} \right) \quad (2.29)$$

If $E_a/RT < 20$, Doyle approximation [189] is used and the following equation can be obtained:

$$\log \beta = \log \frac{AE_a}{R} - \log \varphi(\eta) - 2.315 - 0.4567 \frac{E_a}{RT} \quad (2.30)$$

Therefore, for different heating rates (β) and a given degree of conversion (η), a linear relationship is observed by plotting $\log \beta$ versus $1/T$, and the E_a is obtained from the slope of the straight line. This method cannot give the other kinetic parameters except for the activation energy.

Friedman Method

The differential isoconversional method suggested by Friedman [204] is based on following expression:

$$\ln \left(\frac{d\eta}{dt} \right) = \ln(A) + n \ln(1 - \eta) - \frac{E_a}{RT} \quad (2.31)$$

This is the simplest method and it assumes that thermolysis process is independent of temperature and depends only on the instantaneous weight of the material. The plot of $\ln(d\eta/dt)$ versus $1/T$ should be linear with the slope E_a/R , from which E_a can be obtained.

Kim–Park Method

The Kim–Park method [205] assumes that η_m (the weight loss at the maximum thermolysis rate) is independent of the heating rate β , activation energy E_a , and a pre-exponential factor A .

$$\ln \beta = \ln A + \ln \left(\frac{A}{R} \right) + \left[1 - n + \left(\frac{n}{0.9440} \right) \right] - 5.3305 - 1.0516 \left(\frac{E_a}{RT_m} \right) \quad (2.32)$$

Activation energy can be determined from the slope of $\ln \beta$ versus $1/T_m$. Since the conversion factor is taken as unity, this method can be considered as more accurate than the other methods.

Unfortunately, these methods have severe restrictions due to the procedure used that need a separation of variables: the $\varphi(\eta)$ function (and therefore the values of both Arrhenius parameters) must be constant at constant temperature within the whole range of η [206]. To overcome this problem, Vyazovkin developed a method that provides results with a highest accuracy [207–209] by minimizing the following function:

$$\varphi(E_\eta) = \sum_{i=1}^n \sum_{j \neq i}^n \{J[E_\eta, T_i(t_\eta)]/J[E_\eta, T_j(t_\eta)]\}, \quad (2.33)$$

being $J[E_\eta, T(t_\eta)] = \int_0^{T_\eta} \exp[-E_\eta/RT(t)]dT$. Minimization of the function $\varphi(\eta)$ is achieved at each value of η , thus providing a conversion dependency of activation energy.

Several kinetic methods were used to investigate the thermolysis of chromium polyacrylate complexes [210, 211]. Under comparable conditions, the initial temperatures for the ligand and the PMC were 628 and 591 K, respectively, and the final temperatures were 806 and 813 K; the temperature peaks in the derivatogram were observed at 713 and 690 K, the weight losses (%) were 53.40 and 65.56, and the activation energies of thermolysis (at $0.05 < \eta < 0.90$) were 187.8 and 122.5 kJ mol⁻¹. The orders of reaction differed from unity for all of the thermolysis models. These parameters depend to some extent on the storage time of the aged (for 1–5 weeks) PMC.

Thermal treatment considerably changes the structure and properties of a polymeric material. This is due, first of all, to the physical and chemical processes that accompany the polymer destruction. The processes of physical destruction (crystallization, recrystallization, etc.) are usually reversible and do not lead to cleavage or cross-linking of polymer chains. The chemical processes are irreversible and are accompanied by chemical bond cleavage, cross-linking of macromolecules, changes in the chemical structure, or decrease/increase in the molecular weight [212, 213].

For the design of metallopolymer systems, the thermal stability of polymer matrices is important. It can be estimated from the strength of the bond between atoms. According to the Boltzmann law, the bond strength is determined by the expression $S = E_b/RT^2$, where E_b is the bond energy (in kJ mol⁻¹). The dependence of S on $\gamma = (E_{X-Y} - E_{C-C})/E_{C-C}$, i.e., the change in the bond energy between the atoms X and Y (E_{X-Y}) relative to the average energy of carbon–carbon bond (E_{C-C}) inorganic polymer, shows that organic homo- and heterochain polymers are least thermally stable. Inorganic matrices (clays, hexagonal boron nitride, silicate glasses, zeolites, etc.) having no carbon backbone and graphite are distinguished by enhanced thermal stability and mechanical strength. The bond energies between most typical atoms of the organic and inorganic matrices are summarized in Table 2.6 [214, 215]. Polymeric compounds have especially strong Si–O, B–N and B–O bonds (note that the probability of chemical bond cleavage depends also on temperature).

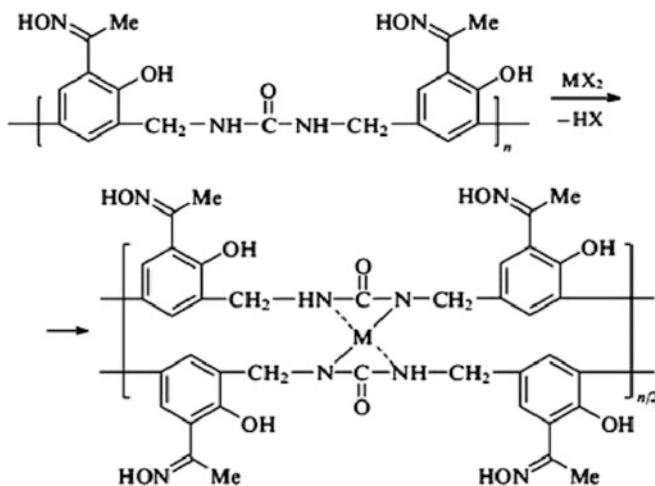
Table 2.6 Bond energy between the atoms in the polymer matrices

Bond	Bond energy, kJ mol ⁻¹	Bond	Bond energy, kJ mol ⁻¹
<i>Carbon-containing matrices</i>			
C–C	336	C–B	372
C–O	327	Al–N	363
C–N	277	Si–O	364
C–Si	241	B–O	500
C–Al	258	B–N	387
<i>Inorganic polymer matrices</i>			
C–Al	715 ^a	Ti–O	933
Al–O	1027.6	B–O	1047
Al–N	1121	B–N	1289
Si–O	586		

^aFor crystalline graphite

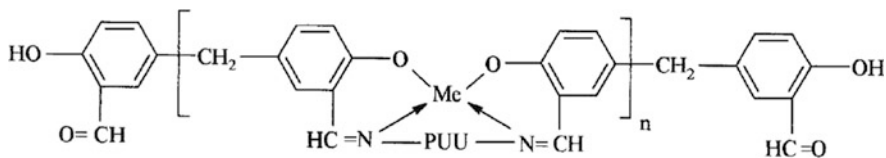
A different kinetic picture is observed at relatively high temperature. In the case of high-temperature thermolysis, the time τ_r related to the temperature T_a decreases and τ_h does not depend on T_a and remains constant. Then in the case of exothermic reaction at $\tau_h \approx \tau_r$, thermal explosion is possible, and at $\tau_h \gg \tau_r$, the ignition occurs long before the test compound was heated and had time to react in the area adjacent to the hot surface [56]. In the case of fast endothermic reactions, self-ignition does not occur after the increase in T_a , and the temperature profile for the test compound is not spatially isothermal. It depends on both the reaction coordinate and time, and the temperature assignment of the detected conversion is undefined. Hence, the classical isothermal methods are inapplicable to the kinetics of fast high-temperature processes. These processes are to be studied using the approaches of non-isothermal chemical kinetics [56].

Of interest are the PMCs formed by the interaction of MX_n , where $M = \text{Cu(II), Ni(II), Co(II), Zn(II), Mn(II), VO(II), UO(II), Zr(IV), Ti(IV)}$, with chelating polymers containing amino-, hydroxyamino- and hydroxyl groups [216]. It turned out that the thermal stability of PMCs falls in the row $\text{Ni} > \text{Zn} > \text{Mn} > \text{Co} > \text{Cu} > \text{Ti} > \text{UO} > \text{Zr} > \text{VO}$; moreover, the initial polymer is characterized by the highest thermal stability. Similar regularities have been found in the series of diaminoalkane copolymers with Schiff's base of 5,5'-methylene-bis (3-bromosalicylaldehyde) [217, 218].



The change in the ratio of comonomers and metal nature has a significant effect on the thermal behavior of PMC–Cu(II) and PMC–Co(II) based on poly (*N*-phenylmaleimide-*co*-acrylic acid) in the temperature range 473–1073 K [219]. In particular, it has been found that an increase in the amount of *N*-phenylmaleimide units in the copolymer chain increases T_g and the thermal stability of the PMCs. Nevertheless, this increase is not as significant as expected, for example, it is optimally from 623 to 646 K, and in the case of a number of copolymer compositions it even decreases to 488 K.

In the case of copper(II), cobalt(II), and nickel(II) chelates with polymer synthesized from 5,5'-methylene-bissalicylaldehyde and polyurethane-urea (PUU) prepolymer based on polyethylene adipate diol, hexamethylene diisocyanate and ethylene diamine, the initial temperatures of thermolysis are in the range between 458 and 500 K, which is lower than the parent ligand [220]. This result indicates that the metal acts as a catalyst and facilitates the first stage of thermolysis. All the PMCs show multiple-stage thermolyses. According to the values of activation energy of thermolysis, it can be concluded that the thermal stability decreases in the following order: Ni > Cu > Co which corresponds to the decrease of metal electronegativity.



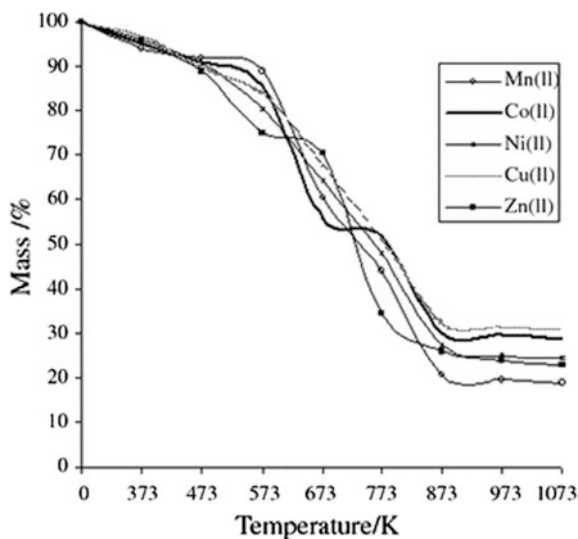


Fig. 2.21 TG curves of polyester complexes. Reproduced with permission from Ref. [221]. Copyright (2011) Springer Nature

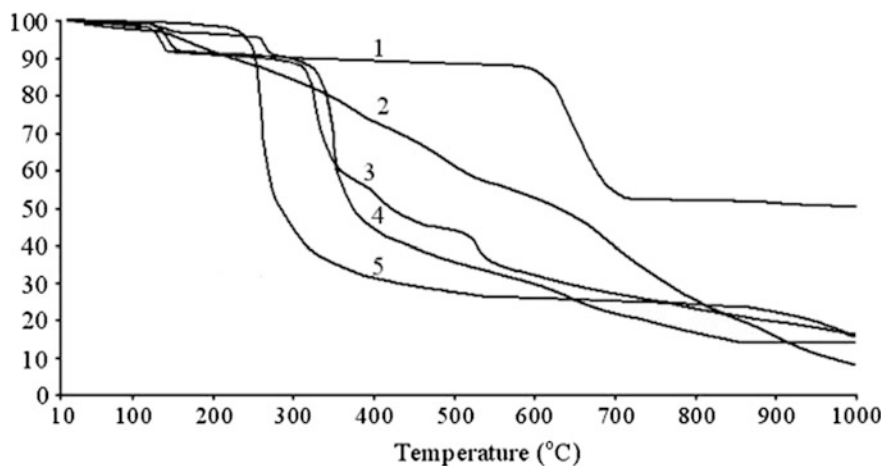


Fig. 2.22 TG curves of PMCs (1—Mn, 2—Cd, 3—Co, 4—Ni, 5—Cu). Reproduced with permission from Ref. [222]. Copyright (2007) John Wiley and Sons

The order of stability of PMCs based on polyesters according to TG results appeared to be $\text{Zn(II)} < \text{Cu(II)} > \text{Co(II)} > \text{Ni(II)} > \text{Mn(II)}$ (Fig. 2.21) [221]. This order matched with Irving–Williams order of stability of the complexes of divalent metal ions.

PMC–Mn demonstrated also higher thermal stability among azomethine PMCs [222]. The initial thermolysis temperature and the temperature after 53.82% weight loss of PMC–Mn were found to be 430 and 1273 K, respectively. According to TG curves (Fig. 2.22), high thermal stability of PMCs may indicate the formation of covalent metal-oxygen and coordination metal-nitrogen linkages between the oligomeric ligand and metal ions.

References

1. A.D. Pomogailo, G.I. Dzhardimalieva, *Nanostructured Materials Preparation via Condensation Ways* (Springer, Dordrecht, 2014)
2. A.D. Pomogailo, G.I. Dzhardimalieva, *Metallopolymeric Hybrid Nanocomposites* (Nauka, Moscow, 2015)
3. J.D. Menczel, R.B. Prime (eds.), *Thermal Analysis of Polymers. Fundamentals and Applications* (Wiley, London, 2009)
4. D. Emadi, L.V. Whiting, S. Nafisi, R. Ghomashchi, *J. Therm. Anal. Calorim.* **81**, 235 (2005)
5. S. Farahany, A. Ourdjini, M.H. Idris, *J. Therm. Anal. Calorim.* **109**, 105 (2012)
6. P. Gabbott (ed.), *Principles and Applications of Thermal Analysis* (Wiley-Blackwell, 2007)
7. J. Šesták, P. Hubík, J.J. Mareš (eds.), *Thermal Physics and Thermal Analysis. From Macro to Micro, Highlighting Thermodynamics, Kinetics and Nanomaterials* (Springer, Berlin, 2017)
8. M.E. Brown (ed.), *Introduction to Thermal Analysis: Techniques and Applications* (Kluwer Academic Publishers, NY, Boston, Dordrecht, London, Moscow, 2001)
9. S. Gaisford, V. Kett, P. Haines (eds.), *Principles of Thermal Analysis and Calorimetry*, 2nd edn. (RSC, Cambridge, 2016)
10. P.J. Haines, *Thermal Methods of Analysis* (Blackie Academic and Professional, London, 1995)
11. S.Z.D. Cheng, C.Y. Li, B.H. Calhoun, L. Zhu, W.W. Zhou, *Thermochim. Acta* **355**, 59 (2000)
12. D.Q.M. Craig, M. Reading, *Thermal Analysis of Pharmaceuticals* (CRC Press, Boca Raton, 2007)
13. C. Kuo-Chung, Y. Cheng-Bin, G. Wenjeng, W. Sea-Fue, T.H. Chuang, Y.H. Lin, *Carbohydrate Polym.* **87**, 1119 (2012)
14. P. Phansi, K. Danchana, V. Cerdà, *TrAC Trends. Anal. Chem.* **97**, 316 (2017)
15. B. Wunderlich, *Thermal Analysis of Polymeric Materials* (Springer, 2005)
16. S. Loganathan, R.B. Valapa, R.K. Mishra, G. Pugazhenthii, S. Thomas, *Thermogravimetric Analysis for Characterization of Nanomaterials*, in *Thermal and Rheological Measurement Techniques for Nanomaterials Characterization*, eds. by S. Thomas, R. Thomas, A.K. Zachariah, R.K. Mishra (Elsevier, 2017), pp. 67–108
17. R. Sah, S.K. Dutta, *Trans. Indian Inst. Met.* **64**, 583 (2011)
18. S. Materazzi, R. Risoluti, *Appl. Spectrosc. Rev.* **49**, 635 (2014)
19. S. Materazzi, S. Vecchio, *Appl. Spectrosc. Rev.* **48**, 654 (2013); **46**, 261 (2011); **45**, 241 (2010)
20. S. Materazzi, A. Gentili, R. Curini, *Talanta* **69**, 781 (2006)
21. A.D. Pomogailo, A.S. Burlov, N.D. Golubeva, L.A. Petrova, S.A. Mashchenko, S.I. Pomogailo, G.I. Dzhardimalieva, A.D. Garnovskii, *Inorg. Mater.* **47**, 876 (2011)
22. A.D. Pomogailo, G.I. Dzhardimalieva, S.I. Pomogailo, N.D. Golubeva, G.V. Shilov, E.A. Dzhevadyan, A.S. Burlov, S.A. Mashchenko, D.A. Garnovskii, *Russ. Chem. Bull.* **65**, 139 (2016)

23. B.A. Komarov, A.T. Kapasharov, E.A. Dzhavadyan, V.A. Lesnichaya, G.I. Dzhardimalieva, A.S. Burlov, A.I. Uraev, S.A. Mashchenko, D.A. Garnovskii, A.D. Pomogailo, *Russ. Chem. Bull.* **64**, 936 (2015)
24. V.A. Logvinenko, F. Paulik, I. Paulik, *Kvaziravnovesnaya Termogravimetriya v Sovremennoi Neorganicheskoi Khimii (Quasi-equilibrium Thermogravimetry in Modern Inorganic Chemistry)* (Nauka, Novosibirsk, 1989)
25. J. Paulik, F. Paulik, *Therm. Acta* **100**, 23 (1986)
26. G. Hohne, W.F. Hemminger, H.J. Flammersheim, *Differential Scanning Calorimetry*, 2nd edn. (Springer, NY, 2003)
27. P. Gill, T.T. Moghadam, B. Ranjbar, *J. Biomol. Techn.* **21**, 167 (2010)
28. S.L. Simon, *Thermochim. Acta* **374**, 55 (2001)
29. S. Yu, S. Wang, M. Lu, L. Zuo, *Front. Mech. Eng.* (2017). <https://doi.org/10.1007/s11465-017-0451-0>
30. L. Zapała, M. Kosńska, E. Wóznicka, Ł. Byczyński, W. Zapała, J. Kalembkiewicz, *J. Anal. Appl. Pyrolysis* **123**, 1 (2017)
31. C. Papadopoulos, B. Cristóvão, W. Ferenc, A. Hatzidimitriou, S. Vecchio Cipriotti, R. Risoluti, M. Lalia-Kantouri, *J. Therm. Anal. Calorim.* **123**, 717 (2016)
32. S. Materazzi, G. Gullifa, M.A. Fabiano, P. Frati, A. Santurro, M. Scopetti, V. Fineschi, R. Risoluti, *J. Therm. Anal. Calorim.* **130**, 549 (2017)
33. S.V. Pol, V.S. Pol, A. Gedanken, *Chem. Eur. J.* **10**, 4467 (2004)
34. V.G. Pol, S.V. Pol, A. Gedanken, *J. Phys. Chem. C* **112**, 6627 (2008)
35. S. Hoffmann, M. Schmidt, S. Scharsach, R. Kniep, *Thermochim. Acta* **527**, 204 (2012)
36. T. Arii, Y. Sawada, K. Iizumi, K. Kudaka, S. Seki, *Thermochim. Acta* **352–353**, 53 (2000)
37. S. Materazzi, R. Risoluti, A. Napoli, *Thermochim. Acta* **606**, 90 (2015)
38. S. Materazzi, J. Finamore, R. Risoluti, A. Napoli, S. D'Arienzo, *Int. J. Mass Spectrom.* **365–366**, 372 (2014)
39. S. Materazzi, J. Finamore, R. Risoluti, A. Napoli, *Microchem. J.* **115**, 27 (2014)
40. R. Risoluti, G. Gullifa, M.A. Fabiano, S. Materazzi, *Russ. J. Gen. Chem.* **85**, 2374 (2015)
41. Q. Guo, X. Zhang, C. Li, X. Liu, J. Li, *J. Hazard. Mater.* **209–210**, 443 (2012)
42. J. Madarasz, S. Kaneko, M. Okuya, G. Pokol, *Thermochim. Acta* **489**, 37 (2009)
43. R. Risoluti, M.A. Fabiano, G. Gullifa, L.W. Wo, S. Materazzi, *Russ. J. Gen. Chem.* **87**, 564 (2017)
44. S. Materazzi, C. Foti, F. Crea, R. Risoluti, J. Finamore, *Thermochim. Acta* **580**, 7 (2014)
45. R. Risoluti, G. Gullifa, M.A. Fabiano, L.W. Wo, S. Materazzi, *Russ. J. Gen. Chem.* **87**, 300 (2017)
46. A. Napoli, D. Aiello, G. Aiello, M.S. Cappello, L. Di Donna, F. Mazzotti, S. Materazzi, G. Sindona, *J. Proteome Res.* **13**, 2856 (2014)
47. S. Materazzi, R. Risoluti, J. Finamore, A. Napoli, *Microchem. J.* **115**, 27 (2014)
48. Y. Liu, V. Kravtsov, R.D. Walsh, P. Poddar, H. Srikanthc, M. Eddaoudi, *Chem. Commun.* **2806** (2004)
49. S. Materazzi, S. Vecchio, S. De Angelis, Curtis, *J. Therm. Anal. Calorim.* **112**, 529 (2013)
50. S. Materazzi, A. Napoli, J. Finamore, R. Risoluti, S. D'Arienzo, *Int. J. Mass Spectrom.* **365/366**, 372 (2014)
51. V. Migliorati, P. Ballirano, L. Gontrani, S. Materazzi, F. Ceccacci, R. Caminiti, *J. Phys. Chem. B* **117**, 7806 (2013)
52. S. Materazzi, S. De Angelis Curtis, S. Vecchio Cipriotti, R. Risoluti, J. Finamore, *J. Therm. Anal. Cal.* **116**, 93 (2014)
53. G. Crea, C. Foti, O. Giuffrè, S. Materazzi, *New J. Chem.* **38**, 3973 (2014)
54. S. Vecchio, S. Materazzi, L.W. Wo, S. De Angelis, Curtis, *Thermochim. Acta* **568**, 31 (2013)
55. S.M. Alshehri, A. Al-Fawaz, T. Ahamad, *J. Anal. Appl. Pyrolysis* **101**, 215 (2013)
56. A.S. Shteinberg, *Fast Reactions in Energetic Materials, High-Temperature Decomposition of Rocket Propellants and Explosives* (Springer, Berlin, Heidelberg, 2008)

57. J.Q. Sun, X.P. Shen, L.J. Guo, K.M. Chen, Q. Liu, *Phys. E. Low Dimens. Syst. Nanostr.* **41**, 1527 (2009)
58. J.Q. Sun, X.P. Shen, K.M. Chen, Q. Liu, W. Liu, *Solid. State Comm.* **147**, 501 (2008)
59. M. Bowtell, *Adhes. Age* **40**, 62 (1997)
60. B.V. L'vov, *Thermal Decomposition of Solids and Melts: New Thermochemical Approach to the Mechanism, Kinetics and Methodology* (Springer, 2007)
61. G.P. Shveikin, I.V. Nikolaenko, *Theor. Found. Chem. Eng.* **43**, 553 (2009)
62. F. Antolini, A. Ghezlbash, C. Esposito, E. Trave, L. Tapfer, B.A. Korgel, *Mater. Lett.* **60**, 1095 (2006)
63. Y.C. Kang, S.B. Park, I.W. Lenggoro, K. Okuyama, *J. Mater. Res.* **14**, 2611 (1999)
64. I.W. Lenggoro, T. Hata, F. Iskandar, *J. Mater. Res.* **15**, 733 (2000)
65. H.K. Kammler, L. Mädler, S.E. Pratsinis, *Chem. Eng. Technol.* **24**, 583 (2001)
66. E.K. Athanassiou, R.N. Grass, W.J. Stark, *Nanotechnology* **17**, 1668 (2006)
67. M.T. Swihart, *Curr. Opin. Colloid. Interf. Sci.* **8**, 127 (2003)
68. C. Boissiere, D. Grosso, A. Chaumonnot, L. Nicole, C. Sanchez, *Adv. Mater.* **23**, 599 (2011)
69. C.-K. Tsung, J. Fan, N. Zheng, Q. Shi, A.J. Forman, J. Wang, G.D. Stucky, *Angew. Chem. Int. Ed.* **47**, 8682 (2008)
70. T.A. Ostomel, Q. Shi, C.-K. Tsung, H. Liang, G.D. Stucky, *Small* **2**, 1261 (2006)
71. L. Li, C.-K. Tsung, Z. Yang, G.D. Stucky, L.D. Sun, J.F. Wang, C.H. Yan, *Adv. Mater.* **20**, 903 (2008)
72. Y. Lu, H. Fan, A. Stump, T.L. Ward, T. Rieker, C.J. Brinker, *Nature* **398**, 223 (1999)
73. A.K.P. Mann, S.E. Skrabalak, *Chem. Mater.* **23**, 1017 (2011)
74. S. Areva, C. Boissiere, D. Grosso, T. Asakawa, C. Sanchez, M. Linden, *Chem. Commun.* 1630 (2004)
75. J.B. Pang, J.N. Stuecker, Y.B. Jiang, A.J. Bhakta, E.D. Branson, P. Li, J. Cesarano, D. Sutton, P. Calvert, C.J. Brinker, *Small* **4**, 982 (2008)
76. D.S. Jung, S.B. Park, Y.C. Kang, *Korean J. Chem. Eng.* **27**, 1621 (2010)
77. J.-C. Lin, J.W. Gentry, *J. Aerosol Sci.* **31**, 797 (2000)
78. N. Reuge, B. Caussat, *Comput. Chem. Eng.* **31**, 1088 (2007)
79. I.W. Lenggoro, Y. Itoh, K. Okuyama, T.O. Kim, *J. Mater. Res.* **19**, 3534 (2004)
80. W.-N. Wang, A. Purwanto, K. Okuyama, in *Handbook of Atomization and Sprays*, ed. by N. Ashgriz (Springer Science Business Media, LLC, 2011)
81. Y.C. Kang, Y.S. Chung, S.B. Park, *J. Am. Ceram. Soc.* **82**, 2056 (1999)
82. K. Okuyama, I.W. Lenggoro, *Chem. Eng. Sci.* **58**, 537 (2003)
83. W.-N. Wang, I.W. Lenggoro, Y. Terashi, T.O. Kim, K. Okuyama, *Mat. Sci. Eng. B* **123**, 194 (2005)
84. Y.C. Kang, S.B. Park, *Mater. Res. Bull.* **35**, 1143 (2000)
85. W.-N. Wang, I.W. Lenggoro, Y. Terashi, Y.C. Wang, K. Okuyama, *J. Mater. Res.* **20**, 2873 (2005)
86. I.W. Lenggoro, Y. Itoh, N. Iida, K. Okuyama, *Mater. Res. Bull.* **38**, 1819 (2003)
87. R.M. Laine, T. Hinklin, G. Williams, S.C. Rand, *Mater. Sci. Forum* **343–346**, 500 (2000)
88. A. Camenzind, R. Strobel, S.E. Pratsinis, *Chem. Phys. Lett.* **415**, 193 (2005)
89. A. Camenzind, R. Strobel, F. Krumeich, S.E. Pratsinis, *Adv. Powder Technol.* **18**, 5 (2007)
90. D. Dosev, B. Guo, I.M. Kennedy, *J. Aerosol Sci.* **37**, 402 (2006)
91. T.R. Hinklin, J. Azurdia, M. Kim, J.C. Marchal, S. Kumar, R.M. Laine, *Adv. Mater.* **20**, 1270 (2008)
92. P. Milani, L.G. Bettini, Nano- and Micromanufacturing with Nanoparticles Produced in the Gas Phase: An Emerging Tool for Functional and Length-Scale Integration, in *Gas-Phase Synthesis of Nanoparticles*, ed. by Y. Huttel (Wiley, Weinheim, 2017)
93. G. Solero, *Nanoscience and Nanotechnology* **7**, 21 (2017)
94. R. Strobel, S.E. Pratsinis, *J. Mater. Chem.* **17**, 4743 (2007)
95. W.Y. Teoh, R. Amal, L. Mädler, *Nanoscale* **2**, 1324 (2010)
96. G.A. Kelesidis, E. Goudeli, S.E. Pratsinis, *Proc. Comb. Inst.* **36**, 29 (2017)

97. H.H. Nersisyan, J.H. Lee, J.-R. Ding, K.-S. Kim, K.V. Manukyan, A.S. Mukasyan, *Prog. Energy Comb. Sci.* **63**, 79 (2017)
98. T. Tani, L. Madler, S.E. Pratsinis, *J. Nanopart. Res.* **4**, 337 (2002)
99. R. Riedel, A. Gurlo, E. Ionescu, *Chem. unserer Zeit* **44**, 208 (2010)
100. A. Purwanto, I.W. Lenggoro, H.W. Chang, K. Okuyama, *J. Chem. Eng. Jpn* **39**, 68 (2006)
101. B. Thiébaud, *Platinum Metals Rev.* **55**, 149 (2011). <https://doi.org/10.1595/147106711X567680>
102. R. Strobel, A. Alfons, S.E. Pratsinis, *Adv. Powder Tech.* **17**, 457 (2006)
103. K. Wegner, S. Vinati, P. Piseri, A. Antonini, A. Zelioli, E. Barborini, C. Ducati, P. Milani, *Nanotechnology* **23**, 185603 (2012)
104. L. Mädler, H.K. Kammler, R. Mueller, S.E. Pratsinis, *J. Aerosol Sci.* **33**, 369 (2002)
105. A.T. Hinklin, B. Toury, C. Gervais, F. Babonneau, J.J. Gislason, R.W. Morton, R.M. Laine, *Chem. Mater.* **16**, 21 (2004)
106. M. Kim, T.R. Hinklin, R.M. Laine, *Chem. Mater.* **20**, 5154 (2008)
107. R. Baranwal, M.P. Villar, R. Garcia, R.M. Laine, *J. Am. Ceram. Soc.* **84**, 951 (2001)
108. J. Marchal, T. Hinklin, R. Baranwal, T. Johns, R.M. Laine, *Chem. Mater.* **16**, 822 (2004)
109. M. Szutkowska, *J. Mater. Proc. Tech.* **153–154**, 868 (2004)
110. Y. Jia, Y. Hotta, K. Sato, K. Watari, *J. Am. Ceram. Soc.* **89**, 1103 (2006)
111. W.J. Stark, S.E. Pratsinis, *Powder Technol.* **126**, 103 (2002)
112. D. Hong, Y. Yamada, M. Sheehan, S. Shikano, C.-H. Kuo, M. Tian, C.-K. Tsung, S. Fukuzumi, *ACS Sustain. Chem. Eng.* **2**, 2588 (2014)
113. G. Benetti, C. Caddeo, C. Melis, G. Ferrini, C. Giannetti, N. Winkelmanns, S. Bals, M.J. Van Bael, E. Cavaliere, L. Gavioli, F. Banfi, *J. Phys. Chem. C* **121**, 22434 (2017)
114. D. Perednis, L.J. Gauckler, *J. Electroceram.* **14**, 103 (2005)
115. M.T. Hay, Y. Hashimoto, N. Momose, K. Ito, *J. Cryst. Growth* **311**, 4499 (2009)
116. M.A. Montero, M.R.G. Chialvo, A.C. Chialvo, *J. Mater. Chem.* **19**, 3276 (2009)
117. U. Alver, T. Kilinc, E. Bacaksiz, S. Nezir, *Mater. Chem. Phys.* **106**, 227 (2007)
118. H. Zhang, M.T. Swihart, *Chem. Mater.* **19**, 1290 (2007)
119. S.E. Skrabalak, K.S. Suslick, *J. Am. Chem. Soc.* **127**, 9990 (2005)
120. P. Majeric, R. Rudolf, I. Anzel, J. Bogovic, S. Stopic, B. Friedrich, *Mater. Technol.* **49**, 75 (2015)
121. J.J. Hinman, K.S. Suslick, *Top. Curr. Chem. (Z)* **375**, 12 (2017)
122. D. Mott, J. Yin, M. Engelhard, R. Loukrakpam, P. Chang, G. Miller, I.-T. Bae, N. Chandra Das, C. Wang, J. Luo, C.-J. Zhong, *Chem. Mater.* **22**, 261 (2009)
123. D. Mott, J. Galkowski, L. Wang, J. Luo, J.C. Zhong, *Langmuir* **23**, 5740 (2007)
124. Z. Xu, C. Shen, Y. Hou, H. Gao, S. Sun, *Chem. Mater.* **21**, 1778 (2009)
125. S.D. Bakrania, T.A. Miller, C. Perez, M.S. Wooldridge, *Combust. Flame* **148**, 76 (2007)
126. S.D. Bakrania, C. Perez, M.S. Wooldridge, *Proc. Combust. Inst.* **31**, 1797 (2007)
127. L. Mangolini, E. Thimsen, U. Kortshagen, *Nano Lett.* **5**, 655 (2005)
128. E. Thimsen, P. Biswas, *AIChE J.* **53**, 1727 (2005)
129. E. Thimsen, N. Rastgar, P. Biswas, *J. Phys. Chem.* **112**, 4134 (2005)
130. P. Biswas, E. Thimsen, *Aerosol Measurements*, 3rd ed. (Wiley-VCH, New York, 2011). (Ch. 33)
131. R. Rudolf, B. Friedrich, S. Stopic, I. Anzel, S. Tomic, M. Colic, *J. Biomater. Appl.* **26**, 595 (2012)
132. J. Dokic, R. Rudolf, S. Tomic, S. Stopic, B. Friedrich, B. Budic, I. Anzel, M. Colic, *J. Biomed. Nanotechnol.* **8**, 528 (2012)
133. M. Afzal, P.K. Butt, H. Ahmad, *J. Therm. Anal.* **37**, 1015 (1991)
134. S. Stopic, R. Rudolf, J. Bogovic, P. Majeric, M. Colic, S. Tomic, M. Jenko, B. Friedrich, *MTAEC9* **47**, 557 (2013)
135. S. Stopic, B. Friedrich, H.U. Fritsching, K. Raic, *Synthesis of Metallic Nanosized Particles by Ultrasonic Spray Pyrolysis*, IME Metallurgische Prozesstechnik and Metallrecycling, RWTH Aachen, Germany, 1st ed (Shaker Verlag, 2015)

136. P. Majeric, D. Jenko, B. Budic, S. Tomic, M. Colic, B. Friedrich, R. Rudolf, *Nanosci. Nanotechnol. Lett.* **7**, 1 (2015)
137. P. Majeric, B. Friedrich, R. Rudolf, *Mater. Technol.* **49**, 791 (2015)
138. D.M. Dobkin, M.K. Zuraw, *Principles of Chemical Vapor Deposition* (Kluwer Academic Publishers, Dordrecht, The Netherlands, 2003)
139. K.R. Johnson, P.A. Rodriguez, C.R. Brewer, J.A. Brannaka, Z. Shi, *J. Chem. Phys.* **146**, 052816 (2017)
140. R. Gaur, L. Mishra, M.A. Siddiqi, B. Atakan, *RSC Adv.* **4**, 33785 (2014)
141. J. Jeschke, S. Möckel, M. Korb, T. Rüffer, K. Assim, M. Melzer, G. Herwig, C. Georgi, S.E. Schulz, H. Lang, *J. Mater. Chem. C* **4**, 2319 (2016)
142. R. Rudolf, P. Majeric, S. Tomic, M. Shariq, U. Fercec, B. Budic, B. Friedrich, D. Vucevic, M. Colic, *J. Nanomater.* (2017). <https://doi.org/10.1155/2017/9365012>
143. L.G. De Arco, Y. Zhang, C. Zhou, Large Scale Graphene by Chemical Vapor Deposition: Synthesis, Characterization and Applications, in *Nanotechnology and Nanomaterials: Graphene—Synthesis, Characterization, Properties and Applications*, ed. by J.R. Gong (InTech, 2011)
144. M. Schwander, K. Partes, *Diamond Relat. Mater.* **20**, 1287 (2011)
145. P.M. Martin, *Handbook of Deposition Technologies for Films and Coatings: Science, Applications and Technology*, 3rd edn. (Elsevier, 2010)
146. J.R. Creighton, P. Ho, Introduction to Chemical Vapor Deposition (CVD), in *Chemical Vapor Deposition*, eds. by J.H. Park, T.S. Sudarshan (ASM International, Materials Park, OH, 2001)
147. *Chemical vapor deposition* (Surface engineering series), eds. by J.H. Park, T.S. Sudarshan (ASM International, 2001)
148. A.C. Jones, P. O'Brien, *General Materials Science, CVD of Compound Semiconductors: Precursor Synthesis, Development and Applications* (VCH, 2008), pp. 1–352
149. P. Hones, F. Lévy, T. Gerfin, M. Grätzel, *Chem. Vap. Deposition* **6**, 193 (2000)
150. H. Biederman, in *Plasma Polymer Films* (Imperial College Press, London, 2004)
151. A. Biswas, Z. Marton, J. Kanzow, J. Kruse, V. Zaporojtchenko, F. Faupel, T. Strunskus, *Nano Lett.* **3**, 1 (2003)
152. H. Takele, H. Greve, C. Pochstein, V. Zaporojtchenko, F. Faupel, *Nanotechnology* **17**, 3499 (2006)
153. C.N.R. Rao, S.R.C. Vivekchand, K. Biswasa, A. Govindaraj, *Dalton Trans.* 3728 (2007)
154. D.A. Boyd, L. Greengard, M. Brongersma, M.Y. El-Naggar, D.G. Goodwin, *Nano Lett.* **6**, 2592 (2006)
155. E. Alarcón-Lladó, S. Estradé, J.D. Prades, F. Hernandez-Ramírez, J. Arbiol, F. Peiró, J. Ibáñez, L. Artúsa, J.R. Morante, *CrystEngComm* **13**, 656 (2011)
156. J. Lee, M.C. Orilall, S.C. Warren, M. Kamperman, F.J. DiSalvo, U. Wiesner, *Nat. Mater.* **7**, 222 (2008)
157. D. Barreca, A. Gasparotto, C. Maragno, E. Tondello, C. Sada, *Chem. Vap. Deposition* **10**, 229 (2004)
158. K. Ramasamy, M.A. Malik, P. O'Brien, J. Raftery, *Dalton Trans.* **39**, 1460 (2010)
159. W.I. Park, D.H. Kim, S.-W. Jung, G.-C. Yi, *Appl. Phys. Lett.* **80**, 4232 (2002)
160. D. Barreca, A. Gasparotto, C. Maragno, R. Seraglia, E. Tondello, A. Venzo, V. Krishnan, H. Bertagnolli, *Appl. Organometal. Chem.* **19**, 129 (2005)
161. S. Mlowe, L.D. Nyamen, P.T. Ndifon, M.A. Malik, J. Raftery, P. O'Brien, N. Revaprasadu, *Inorg. Chim. Acta* **434**, 181 (2015)
162. S. Mlowe, D.J. Lewis, M.A. Malik, J. Raftery, E.B. Mubofu, P. O'Brien, N. Revaprasadu, *New J. Chem.* **38**, 6073 (2014)
163. R. Morrish, R. Silverstein, C.A. Wolden, *J. Am. Chem. Soc.* **134**, 17854 (2012)
164. V.G. Bessergenev, R.J.F. Pereira, A.M.B. do Rego, *Surf. Coat. Technol.* **201**, 9141 (2007)
165. R.K. Sharma, G. Kedarnath, V.K. Jain, A. Wadawale, M. Nalliath, C.G.S. Pillai, B. Vishwanadh, *Dalton Trans.* **39**, 8779 (2010)

166. V.G. Varanasi, T.M. Besmann, R.L. Hyde, E.A. Payzant, T.J. Anderson, *J. Alloys Compd.* **470**, 354 (2009)
167. R.S. Devan, R.A. Patil, J.-H. Lin, Y.-R. Ma, *Adv. Funct. Mater.* **22**, 3326 (2012)
168. L. Liu, H. Zhou, R. Cheng, Y. Chen, Y.-C. Lin, Y. Qu, J. Bai, I.A. Ivanov, G. Liu, Y. Huang, X. Duan, *J. Mater. Chem.* **22**, 1498 (2012)
169. J. Tavares, E.J. Swanson, S. Coulombe, *Plasma Process. Polym.* **5**, 759 (2008)
170. M.L. Hitchman, A.C. Jones, *Chemical Vapor Deposition: Precursors, Processes and Applications* (RSC, 2009)
171. G. Luo, P. Zhu, P. Chen, Z. Liu, H. Lin, P. Qian, *Vacuum* **59**, 927 (2000)
172. T. Weiss, V. Zielasek, M. Bäumer, *Sci. Rep.* **5**, 18194 (2015)
173. N. Bahlawane, K. Kohse-Höinghaus, P.A. Premkumar, D. Lenoble, *Chem. Sci.* **3**, 929 (2012)
174. J.A. Conesa, A. Marcilla, J.A. Caballero, R. Font, *J. Anal. Appl. Pyrol.* **58/59**, 617 (2001)
175. A.S. Rozenberg, G.I. Dzhardimalieva, N.V. Chukanov, A.D. Pomogailo, *Colloid J.* **67**, 51 (2005)
176. X. Gao, D. Chen, D. Dollimore, *Thermochim. Acta* **223**, 75 (1993)
177. R. Skorpá, T.J.H. Vlught, D. Bedeaux, S. Kjelstrup, *J. Phys. Chem. C* **119**, 12838 (2015)
178. W. Shurong, D. Gongxin, Y. Haiping, L. Zhongyang, *Progr. Energy Combust. Sci.* **62**, 33 (2017)
179. G. Moroi, D. Bilba, N. Bilba, C. Ciobanu, *Polym. Degrad. Stabil.* **91**, 535 (2006)
180. S. Vyazovkin, C.A. Wight, *Ann. Rev. Phys. Chem.* **48**, 125 (1997)
181. A.K. Galwey, M.E. Brown, *Thermal Decomposition of Ionic Solids* (Elsevier, Amsterdam, 1999)
182. S. Vyazovkin, W. Linert, *J. Solid State Chem.* **114**, 392 (1995)
183. I. Kaya, F. Dogan, A. Bilici, *Polym. Int.* **58**, 570 (2009)
184. H.S. Khaudeyer, Z.N. Kadhim, W.S. Hanoosh, *Res. J. Sci. Tech.* **7**, 183 (2015)
185. R.G. Chaudhary, P. Ali, N.V. Gandhare, J.A. Tanna, H.D. Juneja, *Arab. J. Chem.* <https://doi.org/10.1016/j.arabjc.2016.03.008>
186. F. Dogan, I. Kaya, A. Bilici, M. Sacak, *J. Appl. Polym. Sci.* **118**, 547 (2010)
187. F. Dogan, *Polym. Eng. Sci.* **54**, 992 (2014)
188. A.W. Coats, J.P. Redfern, *Nature* **201**, 68 (1964)
189. C.D. Doyle, *J. Appl. Polym. Sci.* **6**, 1033 (1970)
190. D.W. Van Krevelen, C. van Heerden, F.J. Huntjens, *Fuel* **5**, 285 (1961)
191. J.R. MacCallum, J. Tanner, *Eur. Polym. J.* **30**, 253 (1951); **6**, 1033 (1970)
192. A. Broido, *J. Polym. Sci. A-2. Polym. Lett.* **7**, 1761 (1969)
193. S. Samal, S. Acharya, R.K. Dey, A.R. Ray, *J. Appl. Polym. Sci.* **88**, 570 (2003)
194. I. Kaya, A. Solguntekin, *J. Appl. Polym. Sci.* **113**, 1994 (2009)
195. P.M. Madhusudanan, K. Krishnan, K.N. Ninan, *Thermochim. Acta* **221**, 13 (1993)
196. T. Wanjun, L. Yuwen, Z. Hen, W. Zhiyong, W.J. Cunxin, *J. Therm. Anal. Calorim.* **74**, 309 (2003)
197. H.H. Horowitz, G. Metzger, *Anal. Chem.* **35**, 1464 (1963)
198. J.M. Criado, J. Malek, A. Ortega, *Thermochim. Acta* **147**, 377 (1989)
199. G.I. Senum, K.T. Yang, *J. Therm. Anal.* **11**, 445 (1977)
200. W. Tang, Y. Liu, C.H. Zhang, C. Wang, *Thermochim. Acta* **408**, 39 (2003)
201. H.F. Kissinger, *Anal. Chem.* **29**, 1702 (1957)
202. J. Flynn, L. Wall, *J. Polym. Sci. A-2. Polym. Lett.* **4**, 323 (1966)
203. T. Ozawa, *Bull. Chem. Soc. Jpn* **38**, 1881 (1965)
204. H.L. Friedman, *J. Polym. Sci., Part C: Polym. Lett.* **7**, 41 (1969)
205. S.D. Kim, J.K. Park, *Thermochim. Acta* **264**, 137 (1995)
206. P. Simon, *J. Therm. Anal. Calorim.* **74**, 123 (2004)
207. S. Vyazovkin, *J. Comput. Chem.* **18**, 393 (1997)
208. S. Vyazovkin, *J. Comput. Chem.* **22**, 178 (2001)
209. S. Vyazovkin, D. Dollimore, *J. Chem. Inf. Comput. Sci.* **730**, 42 (1996)
210. Ö.F. Öztürk, D.A. Köse, A.N. Ay, B. Zumreoglu-Karan, *J. Appl. Polym. Sci.* **98**, 490 (2005)

211. F. Doğan, Ö.F. Öztürk, M. Yürekli, A.N. Ay, D.A. Köse, *J. Appl. Polym. Sci.* **106**, 1129 (2007)
212. G.E. Zaikov, A. Jiménez (eds.), *Polymer Analysis, Degradation, and Stabilization* (Nova Science Publication, New York, 2005)
213. N.C. Billingham, Degradation and Stabilization of Polymers, in *Materials Science and Technology*. 469–507 (2013)
214. S.S. Batsanov, A.S. Batsanov, *Introduction to Structural Chemistry* (Springer, Dordrecht, 2012)
215. L.L. Andreeva V.A. Molochko, *Constants of Inorganic Substances. A Handbook* (Begell House Publishers Inc., U.S., 1995)
216. D. Wohrle, A.D. Pomogailo, *Metal Complexes and Metals in Macromolecules* (Wiley-VCH, Weinheim, 2003)
217. M.N. Patel, V.J. Patel, *Indian J. Chem. A* **28**, 428 (1989)
218. M.N. Patel, D.H. Sutaria, G.J. Patel, *Synth. React. Inorg. Metal-Org. Chem.* **24**, 401 (1994)
219. O.G. Marambio, G.C. del Pizzaro, M. Jeria-Orell, M. Huerta, C. Olea-Azar, W.D. Habicher, *Polym. Chem.* **43**, 4933 (2005)
220. S. Vlad, A. Vlad, *Mater. Plastice* **45**, 172 (2008)
221. N. Nishat, S. Hasnain, T. Ahmad, A. Parveen, *J. Therm. Anal. Calorim.* **105**, 969 (2011)
222. I. Kaya, A. Bilici, *J. Appl. Polym. Sci.* **105**, 1356 (2007)

Chapter 3

Thermolysis of Low Molecular Weight Metal Chelates

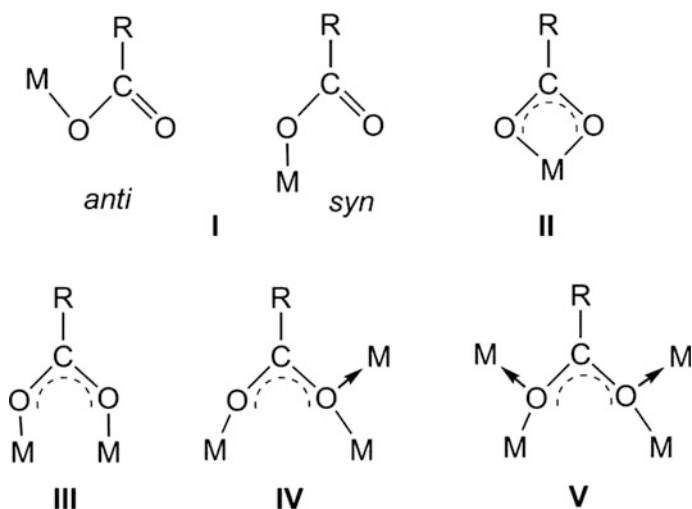


Knowledge of the effect of the chemical structure of SSP and the nature of its constituent ions on the efficiency of NP formation provides the possibility of a purposeful change in the functional characteristics of the nanomaterials prepared. At the present time, the problem of the influence of the nature of the chelating ligand on the physicochemical properties and architecture of nanomaterials is being actively studied with a view to predicting possible directions for their application. This problem, like many other problems in the nanomaterial chemistry, it is advisable to investigate based on individual classes of SSPs. In this chapter, we discuss using well-defined and unambiguously characterized metal chelates as SSPs for the preparation of nanomaterials by thermolysis. We are not attempting to give an exhaustive analysis of the entire array of experimental data to date. The main attention will be paid to the specifics of preparing nanomaterials by thermolysis of metal chelates with the most typical and in detail studied ligands.

3.1 Metal Carboxylates

Metal carboxylates refer to promising classes of SSPs for the NP preparation, because they are commercially available, easy to handle, and low toxic. Of great importance is the fact that metal carboxylates act as the main intermediates in certain NP growth processes. This is because they can be formed in situ by using a long-chain carboxylic acid as a NP stabilizer, thus leading to a complete or partial modification of the initial metal complex.

Metal carboxylates are a wide range of metal complexes containing carboxylate functionality with a diverse type of coordination with the metal atom, including by chelation (Scheme 3.1) [1–4]. Most often the RCOO^- carboxylate group is coordinated with the metal in the form of a monodentate (I) *anti*- and *sin*-configuration, bidentate cyclic (chelating) (II), bidentate bridged (III), tridentate (IV), and tetradentate ligand (V).



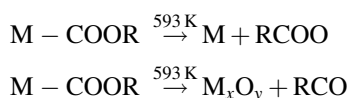
Scheme 3.1 Scheme of diverse bonding modes of metal carboxylates [2]

Among this variety of modes for coordinating the carboxylate group, the basic ones are bidentate chelate or bridge coordination [2, 3, 5–7]. It should be noted that the formation of four-membered chelate cycles involving a carboxyl group requires a large deformation of the valence angles of the metal atom. The least deformation occurs in compounds of rare earth elements, and therefore, the probability of cyclic chelate coordination increases. This is probably also facilitated by an increase in the polarity of the metal–ligand (M–L) bond and the high coordination numbers of the rare earth metals. In addition, the using mixed-ligand metal chelates, which include, in addition to the carboxylate group, auxiliary chelating donor ligands, such as 2,2'-bipyridine (bpy), 1,10-phenanthroline (phen), mono-, di-, and triethanolamine, are also widespread.

The thermolysis of metal mono- and dicarboxylates has been extensively studied for the preparation of metal and MO NPs of technological importance [2, 3, 8–17]. Among the basic requirements for metal carboxylates as SSPs of nanomaterials, we note the following [7]:

- They must be either commercially available or easily synthesized and purified.
- They must have a well-defined molecular structure and belong to high purity materials.
- They must be air-stable to facilitate processing.
- The metal content in them must be high to prevent a significant decrease in volume during thermolysis.
- They should be characterized by high solubility in the chosen solvent.
- Decomposition of the SSP should not lead to the formation of volatile metal-containing intermediates, melts, carbon contamination, and toxic gases. This particularly applies to carboxylates containing heteroatoms, for example, nitrogen, sulfur, or fluorine in the chain, which often lead to highly toxic gases during thermolysis.

The thermolysis mechanism of metal carboxylates based on saturated carboxylic acids has been studied in detail in a wide series of works. Without going into the details of the well-studied mechanism of this process, it should be noted that metal carboxylates are usually monohydrates, the dehydration of which is characterized by a phase transformation and a significant loss of crystallinity at a temperature T_1 (>383 K) [18, 19]. After reaching the temperature T_2 , which decreases exponentially after increasing the number of carbon atoms in the carboxylate fragment, they begin to decompose over a wide temperature range exceeding 573 K. The process of thermolysis of metal carboxylates involves two separate stages: the nucleation and growth of a crystal. In particular, it has been suggested that during the thermolysis of hydrated iron carboxylate, nucleation initiates the thermal generation of free radicals from the metal carboxylate [20]:



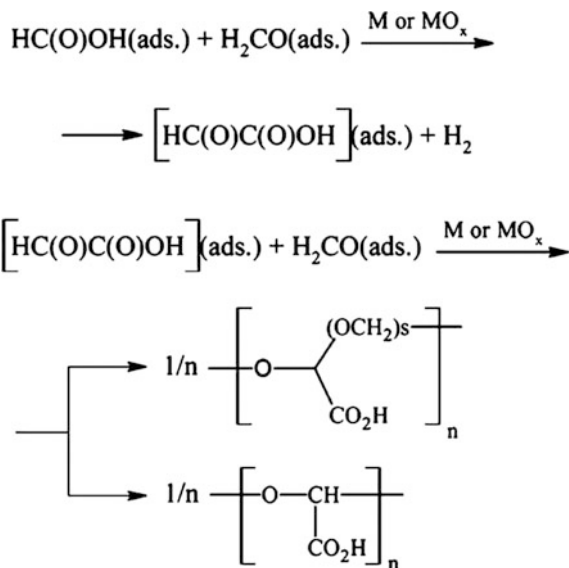
In the following, free radicals formed can recombine or form volatile products, for example, CO, CO₂, H₂O, ethers.

3.1.1 Metal Formates

In general case, the mechanism of thermolysis of metal formates corresponds to the above scheme and includes a series of successive temperature-separated processes. Thus, thermolysis of formates Fe(II), Fe(III), Ni(II), Cu(II), Co(II), and Pb(II) with the general formula $\text{M}(\text{HCOO})_n$ includes dehydration and subsequent thermolysis of anhydrous carboxylate [21]. The kinetics of their isothermal decomposition in SGA is determined by such parameters as the temperature, the rate of previous dehydration, and the ratio of the sample weight to the volume of the reaction vessel.

Among the gaseous products of thermolysis of anhydrous metal formates, it should be noted H₂, CO, CO₂, water vapor, which also evaporates in the dehydration stage, as well as CH₃OH, CH₃COOH, and thermolysis products of formic acid. It is important that the block structure of the crystals of the starting compounds is retained in the solid products of thermolysis. Blocks having sufficient porosity are “attached” to the crystal by a polymer substance with the formula $[-\text{CH}(\text{R})-\text{O}-]_s-$ $[-\text{CH}(\text{COOH})-\text{O}-]_r-$, where $r \ll s$. Apparently, the metals or MOs formed during the thermolysis catalyze the formation of such a polymer under SGA conditions by catalytic thickening (polymerization) of gaseous products of thermolysis CO₂, H₂, CO, H₂O, HCOOH (Scheme 3.2) [21].

As the results of the investigation of electron microscopy (EM) show, the thermolysis of metal formates results in zero-valence metal and/or MO NPs of less than 100 nm in size with a narrow size distribution (Table 3.1) [22] and an almost spherical shape.



Scheme 3.2 Formation of polymer products during the thermolysis of metal formates [21]

Table 3.1 Average particle size (APS) and thickness of the polymeric shell for thermolysis products of metal carboxylates

Compound	T_{ex} , K	D_s^f , nm ^a	d_{EM} , nm ^b	ΔL_{shell} , nm ^c	Product ^d
$\text{Fe}(\text{HCOO})_2 \cdot 2\text{H}_2\text{O}$	543	27.0	20.0	3–5	Fe_3O_4
$\text{Fe}(\text{HCOO})_3$	543	~ 25.0	–	–	Fe_3O_4
$\text{Ni}(\text{HCOO})_2 \cdot 2\text{H}_2\text{O}$	483	~ 30.0	50.0	~ 4.0	Ni
$\text{Cu}(\text{HCOO})_2$	413	~ 30.0	~ 30.0	–	Cu
$\text{Cu}(\text{HCOO})_2 \cdot \text{L}^e$	398	–	69–75	–	Cu
$\text{Cu}(\text{N}_2\text{H}_3\text{COO})_2 \cdot 2\text{H}_2\text{O}^f$	393	–	200–300	–	Cu
$\text{Pb}(\text{HCOO})_2$	493	~ 150.0	~ 3000.0	–	Pb
$\text{Pb}(\text{HCOO})_2 \cdot \text{L}$	525	–	~ 3000.0 (~ 46.0) ^g	–	Pb

^aParticle diameter calculated from the specific surface area data for the solid products at the end of thermolysis

^bAverage particle diameter calculated from EM data

^cPolymer shell thickness

^dPowder X-ray diffraction (XRD) and electron diffraction data

^eL is monoethanolamine

^fHydrazinocarboxylate

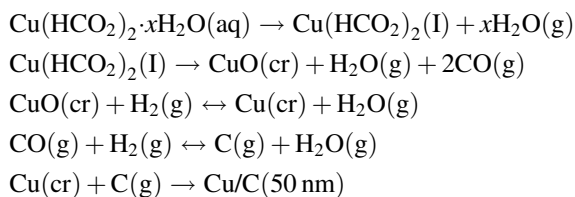
^gAfter ultrasonic treatment

In addition, in the process of thermolysis, a less electron-dense passivation polymeric shell is formed on the surface of the electron-dense NPs formed. It is important that the thickness of the polymeric shell is 3–5 nm, while the size of the NPs is 1.5–2.5 nm, and the rate of shell formation competes with the growth rate of the NPs.

The formation of NPs with a similar “core–shell” structure was also observed during thermolysis of bismuth monocarboxylates with different alkyl chain lengths [23]. This process occurs progressively: Firstly, bismuth NPs (1–2 nm) are formed in ordered layered structures with an interlayer distance of ~ 5 nm, which are subsequently converted into core–shell structures with sizes up to 50 nm. It should be noted that in the air various polymorphs of bismuth oxide or their mixture with the metal were prepared, whereas a nanocrystalline bismuth powder is formed in a vacuum, an inert medium- or a high-boiling (423–523 K) organic solvent (e.g., benzyl alcohol).

The complex multichannel nature of the thermolysis is confirmed by studying the composition of volatile products formed during high vacuum pyrolysis of copper formate in the cavity of the mass spectrometer [24] under conditions that exclude secondary reactions. It turned out that in the early stages of the thermolysis, to the degree of conversion $\chi_{\Sigma} \sim 0.5$, where χ_{Σ} represents the fraction of the total intensity of the main mass peaks at the end of the thermolysis and Σ includes summation over all components, the main gaseous products (CO_2 , CO , H_2O , and HCO_2H) are formed simultaneously. It is worth noting the established relationship between the thermolysis products $\chi\text{CO}_2 > \chi\text{H}_2\text{O} \approx \chi\text{CO} > \chi\text{HCO}_2\text{H}$, and furthermore, the accumulation of H_2O and CO practically stops.

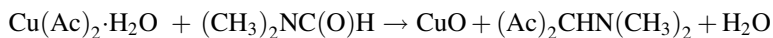
It is of interest to study the flame pyrolysis of a solution of copper formate in an excess of hydrogen, which leads to the formation of copper NPs coated with carbon according to the following scheme [25]:



It should be noted the preparation of mixed cubic FeO – Fe_3O_4 NPs by thermolysis of iron formates in the presence of OA as a surfactant and trioctylamine (TOA) as a solvent and cosurfactant at elevated temperatures (about 643 K) under an inert atmosphere [26]. It is important that, depending on the reaction parameters (type and concentration of the SSP, surfactant concentration, water concentration, thermolysis time, and temperature), various NPs (spheres, hexagons, and cubes) are obtained. In particular, it has been established that nanocubes are single crystal Fe_xO (wüstite) with small amounts of Fe_3O_4 (magnetite).

3.1.2 Metal Acetates

As a typical example of the thermolysis of metal acetates (Ac), we shall note the preparation of CuO NPs by colloid-thermal synthesis via thermolysis of Cu(II) acetate monohydrate as a SSP in the presence of dimethylformamide (DMF) as a solvent [27]. The synthesis of CuO NPs with dimensions of approximately 3–5 nm can be described by the following equation [28, 29]:



Numerous studies have been devoted to the thermolysis of nickel acetate tetrahydrate ($\text{Ni}(\text{Ac})_2 \cdot 4\text{H}_2\text{O}$), which also proceeds stepwise with the release of water at ca. 393 K at the first stage [30]. It is assumed that an intermediate is the basic nickel acetate with the formula $0.86 \text{Ni}(\text{Ac})_2 - 0.14 \text{Ni}(\text{OH})_2$ with the subsequent stage of its dehydration at ca. 613 K. The thermolysis products are either NiO or Ni in air or in H_2 atmosphere, respectively. Relatively, large nickel NPs were prepared by thermolysis of the same SSP in OAm in the presence of 1-adamantane carboxylic acid (ACA) and trioctylphosphine oxide (TOPO) [31]. It is important that high crystalline **hcp** NPs of different sizes were prepared at 563 K, whereas at relatively low temperatures **fcc** NPs are predominant. The particle size varied from 50 to 150 nm by properly adjusting the proportion of the capping ligands. In the absence of surfactants, pure OAm inhibits the growth of Ni NPs, size of which does not exceed 5.5 nm (Fig. 3.1a). This is probably due to the dense coating and strong binding of linear OAm molecules on the Ni NPs surface, as well as the formation of the Ni–OAm complex, which increases the energy requirement for decomposition and retards the growth stage. At the same time, the addition of ACA causes a significant increase in the size of Ni NPs reaching 110 nm (Fig. 3.1b). In this case, a large volume of ACA molecules increases the percentage of the unoccupied surface of Ni NPs, which leads to the growth of larger particles. It should be also

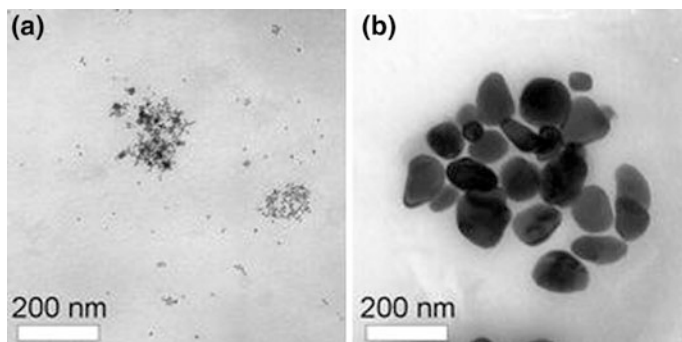


Fig. 3.1 Transmission electron microscopy (TEM) images of Ni NPs obtained in the presence of inclusive OAm (a) or ACA (b). Reproduced with permission from Ref. [31]. Copyright (2010) Springer Nature

noted the preparation of Ni NPs by thermolysis of nickel acetate tetrahydrate in the presence of long-chain amines, which act as solvents and reducing agents [32]. In this process, the **hcp** or **fcc** crystal structures of Ni NPs can be synthesized by controlling the thermolysis temperature. In particular, higher temperatures contribute to the formation of the **hcp** structure. The thermolysis of the SSP in the presence of hexadecylamine (HDA) used as solvent, reducing agent, and stabilizing agent made it possible to obtain nickel NPs with a diameter of 7 nm and a product purity of 74.3% [33, 34]. Interestingly, in some cases, intermediate products, in particular, Ni₃C nanocrystals were identified. Alkylphosphine surfactants, in particular, TOP (trioctylphosphine) and TOPO, are quite effective for controlling the crystalline phase, morphology, particle size, and size distribution of Ni NPs [35]. Thus, for example, using TOP as a surfactant, **hcp** structures of Ni NPs were obtained, which have a spherical shape with APS of 6.5 ± 0.6 nm.

Of interest are a promising one-pot solvent-, catalyst-, and template-free synthesis of a single-phase crystalline hexagonal luminescent europium oxycarbonate Eu₂O₂·CO₃ consisting of nanoplates by europium acetate thermolysis at 923 K for 3 days in the SGA [36].

Using a similar process, zinc acetate was converted to pencil-shaped luminescent ZnO with micro- or nanoscale diameters [37]. It is important that the SSP thermolysis leads to carbon sphere-decorated ZnO micropencils under autogenic pressure or uniformly carbon-coated ZnO nanopencils under released pressure (Fig. 3.2).

It should be noted the preparation of homogenous high-quality thin ZnO films having a controlled morphology of wurtzite on Si(111) substrates by USP of zinc acetate solutions [38]. At the same time, the thermolysis of the same SSP on a silicon substrate by a modified CVD at relatively low temperature (473–523 K) leads to the formation of NPs, nanowires, and nanowalls [39]. In particular, quasi-spherical ZnO NPs with diameters of 100 nm were obtained on silicon

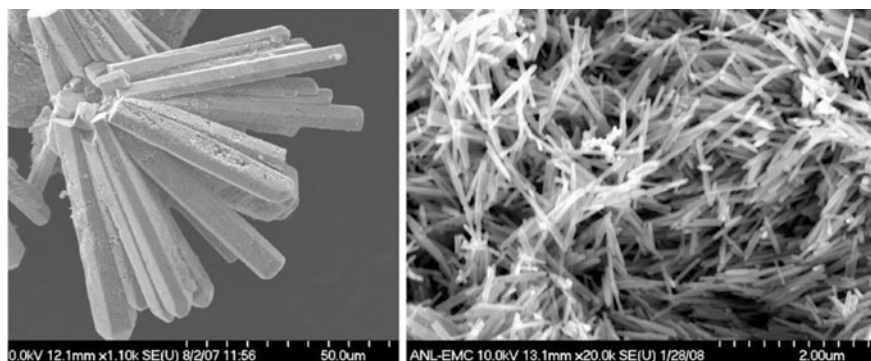


Fig. 3.2 Scanning electron microscopy (SEM) images of ZnO micropencils (left) and ZnO nanopencils (right). Reproduced with permission from Ref. [37]. Copyright (2008) American Chemical Society

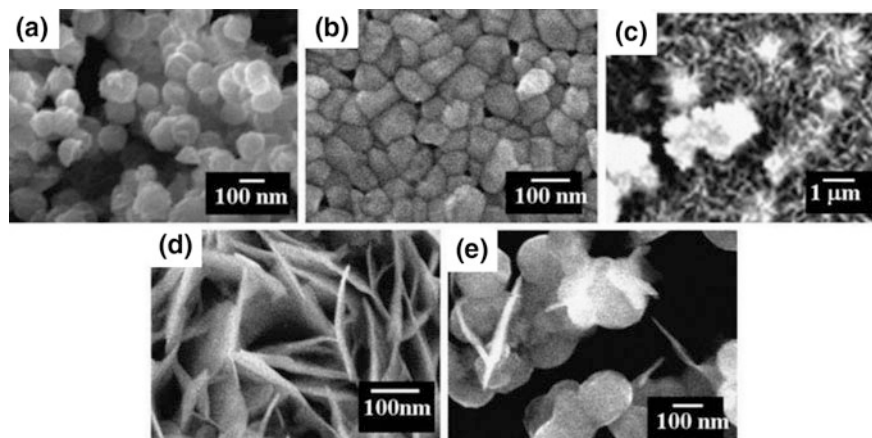


Fig. 3.3 SEM images of as-synthesized ZnO diverse nanostructures: NPs synthesized on substrate A (a), nanostructured films synthesized on substrate B (b), low magnification image of nanowalls synthesized on substrate C (c), high magnification image of as-synthesized nanowalls (d), nanowires/NPs synthesized on substrate D. Reproduced with permission from Ref. [39]. Copyright (2008) Springer Nature

substrate A with a local temperature of 473 K in the downstream region of the quartz tube (Fig. 3.3a). A flat ZnO nanostructured films with diameters in the range of 80–120 nm were formed on silicon substrate B with a local temperature of 673 K in the downstream region of the quartz tube (Fig. 3.3b). ZnO nanowalls formed on ZnO particles were synthesized on silicon substrate C with a local temperature of 523 K in the upstream region of the quartz tube (Fig. 3.3c). The thickness of the nanowalls was around 20 nm (Fig. 3.3d). Finally, ZnO nanostructures were prepared on silicon substrate D with a local temperature of 503 K in the upstream region of the quartz tube (Fig. 3.3e). In particular, several nanowires were grown on NPs, and their diameter and length are around 20 and 200 nm, respectively.

Of interest is the synthesis of PbS nanocrystals of various forms by thermolysis of lead acetate and sulfur sources: star-shaped nanocrystals in the presence of thioacetamide [40, 41], dendritic hierarchical nanostructures with amino acids [42–44], as well as nanotubes and dendrites using thiourea [45]. A wide variety of PbS micro- and nanostructures with different morphologies, for example, stars, dendrites, hexapods, and cubes, was also prepared by thermolysis of lead acetate by varying the synthesis parameters, such as $[\text{Pb}^{2+}]:[\text{S}^{2-}]$ ratio, thermolysis temperature, time, and sulfur source (Table 3.2) [45].

In particular, sample 1 (prepared using a 1:1 ratio) has a symmetrical hexapod-like morphology with smooth edges (Fig. 3.4a). With an increase in this ratio to 1:2 (sample 2), star-shaped dendrites are formed (Fig. 3.4b). For the micro-/nanostructure of PbS (ratio 1:4, sample 3), well-developed dendrites are typical

Table 3.2 Reaction conditions for the synthesis of various PbS micro- and nanostructures with their morphologies

Sample	Reactants	Reaction conditions	Morphology
1	Pb(Ac) ₂ + thiourea (1:1)	393 K, 5 min	Hexapods (microstructures)
2	Pb(Ac) ₂ + thiourea (1:2)	393 K, 5 min	Star-shaped nanostructures
3	Pb(Ac) ₂ + thiourea (1:4)	393 K, 5 min	Dendrites
4	Pb(Ac) ₂ + thiourea (1:6)	393 K, 5 min	Dendrites with elongated arms
5	Pb(Ac) ₂ + thiourea (1:8)	393 K, 5 min	Dendrites with elongated arms and small NPs
6	Pb(Ac) ₂ + thiourea (1:2)	323 K, 60 min	Irregular nanostructures
7	Pb(Ac) ₂ + thiourea (1:2)	353 K, 60 min	Underdeveloped hexapods (microstructures)
8	Pb(Ac) ₂ + thiourea (1:2)	393 K, 60 min	Dendrites
9	Pb(Ac) ₂ + thiourea (1:2)	423 K, 60 min	Dendrites with flattened arms
10	Pb(Ac) ₂ + thiourea (1:2)	453 K, 60 min	Broken hexapods
11	Pb(Ac) ₂ + thiourea (1:2)	493 K, 60 min	Broken arms of hexapods
12	Pb(Ac) ₂ + thiourea (1:1)	393 K, 5 min	Hexapods
13	Pb(Ac) ₂ + thiourea (1:1)	393 K, 30 min	Hexapods with ridges in arms
14	Pb(Ac) ₂ + thiourea (1:1)	393 K, 60 min	Hexapods with deep ridges in arms
15	Pb(Ac) ₂ + thiourea (1:1)	393 K, 90 min	Broken arms
16	Pb(Ac) ₂ + thiourea (1:1)	393 K, 120 min	Truncated nanocubes
17	Pb(Ac) ₂ + thiourea (1:1)	393 K, 180 min	Truncated microcubes
18	Pb(Ac) ₂ + thiourea (1:2)	393 K, 5 min	Star-shaped dendrites
19	Pb(Ac) ₂ + thiourea (1:2)	393 K, 30 min	Dendrites
20	Pb(Ac) ₂ + thiourea (1:2)	393 K, 60 min	Dendrites with flattened arms
21	Pb(Ac) ₂ + thiourea (1:2)	393 K, 90 min	Dendrites with flattened arms
22	Pb(Ac) ₂ + thiourea (1:2)	393 K, 120 min	Micro-hexapods and small NPs
23	Pb(Ac) ₂ + thiourea (1:2)	393 K, 180 min	Nanocubes
24	Pb(Ac) ₂ + thioacetamide (1:1)	393 K, 5 min	Irregular nanoplatelets
25	Pb(Ac) ₂ + thioacetamide (1:2)	393 K, 5 min	Irregular nanoplatelets

(Fig. 3.4c). Finally, a subsequent increase in this ratio leads to an increase in the length of the sub-branches (Fig. 3.4d, e) to 150 nm (ratio 1:6, sample 4) and 200 nm (ratio 1:8, sample 5).

The thermolysis of manganese acetate in a mixture of OA and TOA at 473 K leads to an interesting metastable MnO having a 2D structure with a size $(10.2 \pm 0.6) \text{ nm} \times (6.8 \pm 0.4) \text{ nm}$ (Fig. 3.5a) [47, 48]. Controlled chemical oxidation can ensure the preparation of Mn₃O₄ nanocrystals from MnO. Interestingly, by varying the post-treatment procedure and the polarity of the dispersants, the resulting nanoplates are aligned to form self-assembling nanoarrays either in

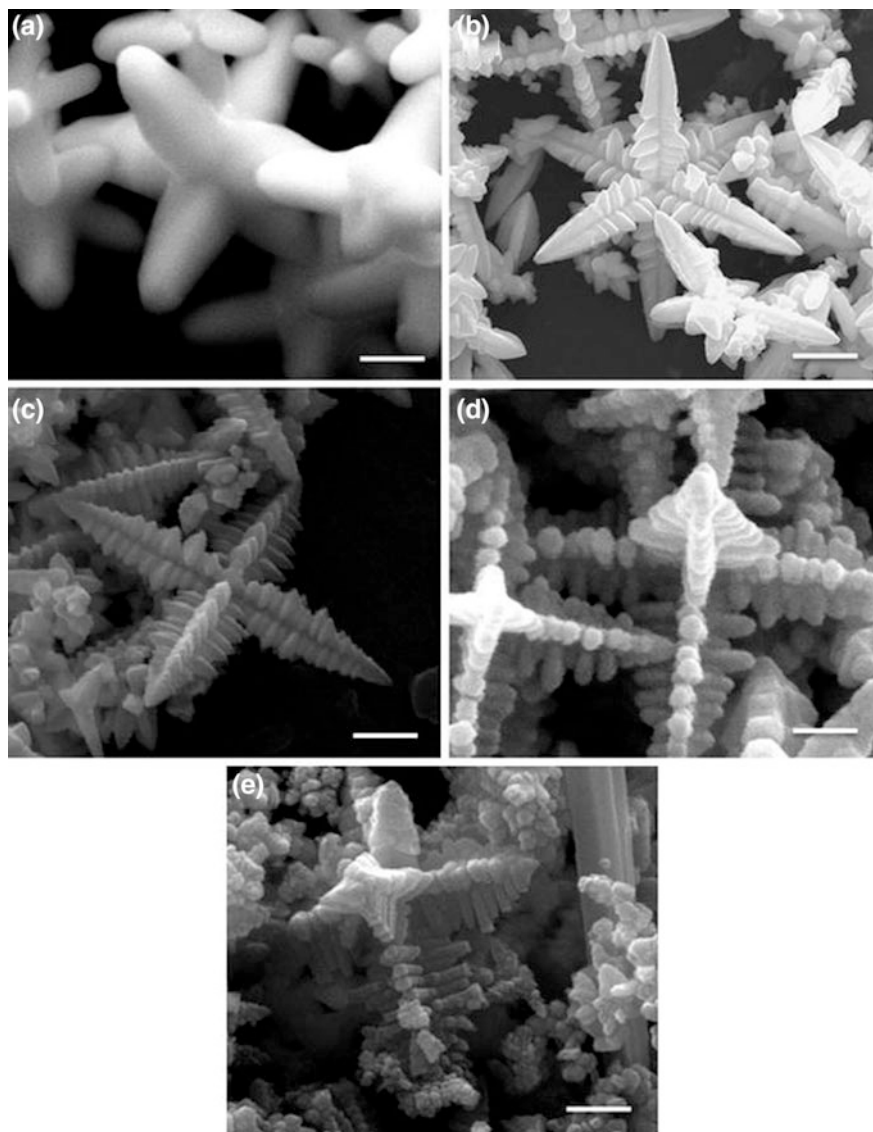


Fig. 3.4 Field emission scanning electron microscopy (FESEM) images of PbS micro-nanostructures prepared using different $[\text{Pb}^{2+}]:[\text{S}^{2-}]$ molar ratios (thermolysis time = 5 min and temperature = 393 K): **a** 1:1 (1), **b** 1:2 (2), **c** 1:4 (3), **d** 1:6 (4), and **e** 1:8 (5). Scale bar 200 nm. Reproduced with permission from Ref. [46]. Copyright (2016) Springer Nature

“side-to-side” or “face-to-face” form. For example, using a mixture of toluene/hexane as a dispersant allows to the locating the MnO nanoplates on their bottom surfaces, forming a “side-to-side” pattern (Fig. 3.5b). Adding a certain amount of ethanol to the toluene/hexane mixture leads to a change in the orientation of the

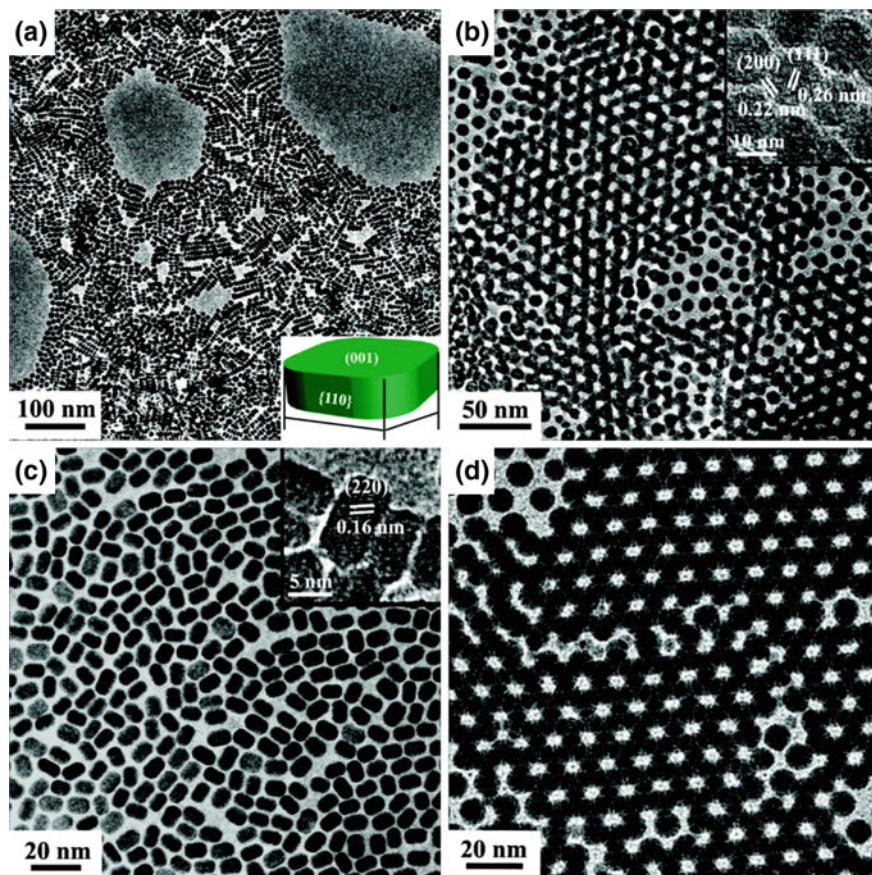


Fig. 3.5 **a** TEM image of MnO nanoplates, the lower inset shows the schematic diagram of a nanoplate. **b** “Side-to-side” self-assembly nanoarrays and high-resolution transmission electron microscopy (HRTEM) (inset) images of MnO nanoplates. **c** “Face-to-face” self-assembly nanoarrays and HRTEM (inset) images of MnO nanoplates. **d** TEM image of highly ordered MnO nanoplate arrays with 3D superlattice in some parts of TEM grids. Reproduced with permission from Ref. [48]. Copyright (2009) American Chemical Society

nanoplates to form a “face-to-face” pattern (Fig. 3.5c). It should be noted that the MnO nanoplates prepared are single crystalline and are enclosed by {100} and {110} planes (inserts in Fig. 3.5b and c). In addition, a highly ordered 3D superlattice of MnO nanoplates precipitated from a concentrated dispersion of nanocrystals is formed in some sections of the TEM grid (Fig. 3.5d).

Among the other interesting examples, we note the controlled thermolysis of $\text{Fe}_3(\text{Ac})_6(\text{OH})_2(\text{Ac})$ in a closed reactor under an inert atmosphere at 973 K, which gives ferromagnetic octahedra Fe_3O_4 with an average edge length of about 6–10 μm without using a solvent or catalyst (Fig. 3.6a) [49]. It is important that only carbon dioxide, oxygen, iron (Fig. 3.6b), and Fe_3O_4 octahedra of high purity were

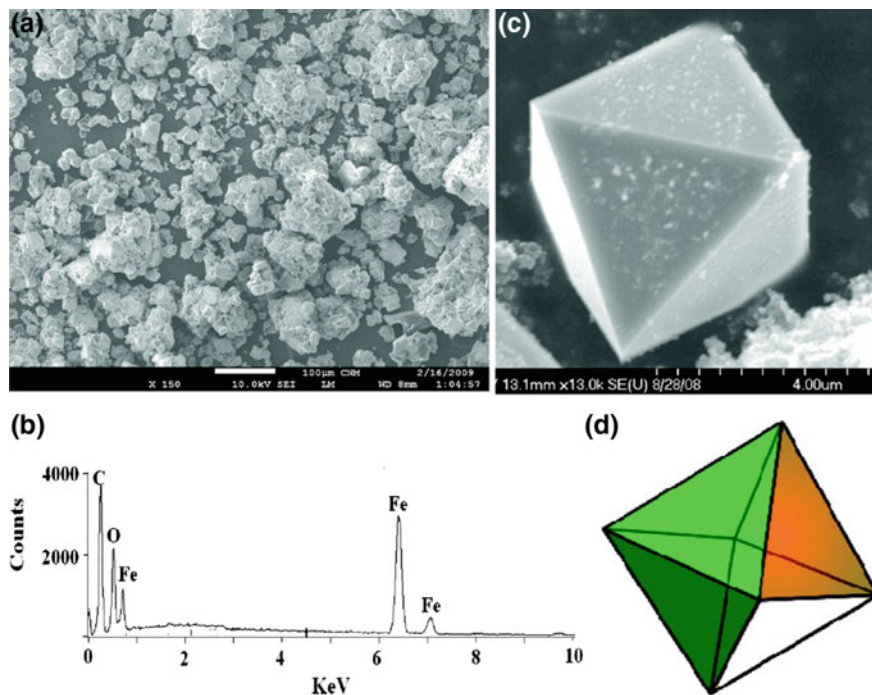


Fig. 3.6 **a** Low-resolution SEM of Fe_3O_4 octahedra, **b** energy-dispersive X-ray spectroscopy (EDS) of bulk Fe_3O_4 octahedra, **c** high-resolution SEM of Fe_3O_4 octahedron, and **d** colored sketch of octahedral. Reproduced with permission from Ref. [49]. Copyright (2010) American Chemical Society

detected. In addition, the octahedral particles were in situ decorated with small carbon particles (Fig. 3.6c). It should be noted that a regular octahedron is a platonic solid composed of eight equilateral triangles, four of which meet at each vertex (Fig. 3.6d).

It is of interest to obtain polycrystalline CdO thin films onto a hot glass substrate at 673 K by spray pyrolysis from an aqueous cadmium acetate solution [50]. The pure phase of fcc CdO quantum dots (QDs) was obtained by thermolysis of γ -irradiated anhydrous cadmium acetate at 673 K for three hours in the presence and absence of benzyl alcohol as a surfactant [51]. It turned out that the thermolysis without benzyl alcohol led to the mesoporous structure of CdO NPs (Fig. 3.7, left), whereas the presence of benzyl alcohol surfactant allows preparing the cauliflower-like mesoporous structure of CdO (Fig. 3.7, right).

The thermolysis of cobalt acetate was used to produce Co NPs with dimensions of 8–200 nm [52]. It is important that the use of various combinations of TOP, OAm, and OA as surfactants allows controlling the particle size.

Of interest is using thermolysis of silver acetate in an inert atmosphere as a promising method for the preparation of highly dispersed silver [53]. The same

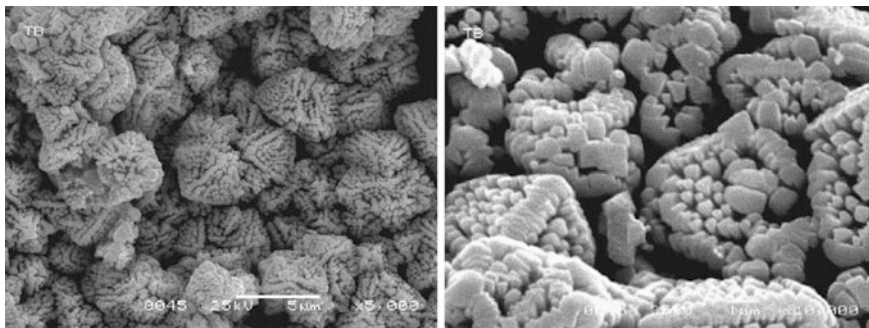


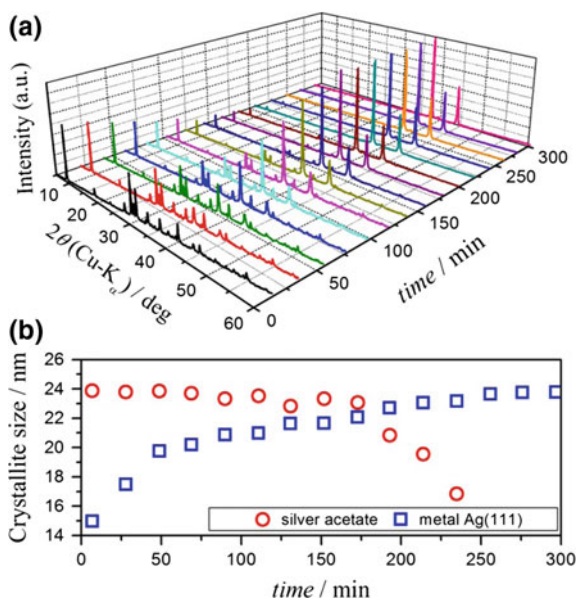
Fig. 3.7 (left) SEM images of CdO NPs synthesized by thermolysis of γ -irradiated cadmium acetate for three hours at 673 K; (right) SEM images of CdO NPs synthesized in presence of benzyl alcohol as surfactant-free [51]

process in diphenyl ether as a solvent in the presence of OA and OAm as surfactant leads to the formation of silver NPs [54]. The overall kinetic scheme of the thermolysis of silver acetate including two partially overlapping reaction steps was proposed using systematic kinetic and morphological analyses [55]. The apparent activation energies of these steps were comparable (approximately 75 kJ mol^{-1}); however, the first reaction step was regulated by the first-order law because of the consumption of reactive sites on the end surfaces of columnar crystals, whereas the second reaction step is advanced by shrinkage of the side surfaces of the crystals with an accelerating linear shrinkage rate, leading to slimming of the crystals. The time-dependent XRD pattern points out to the attenuations of the XRD peaks of silver acetate and gradual growth of those that belong to metallic Ag (Fig. 3.8a). The changes in the size of the crystallites of silver acetate and metallic Ag (Fig. 3.8b) clearly indicate the formation of Ag NPs, which gradually increase from 15 to 24 nm as the reaction progresses.

At a very early stage of the reaction ($\alpha = 0.05$), spherical NPs are observed on the end surfaces of the columnar crystals (Fig. 3.9a, b). As the overall reaction advances, the Ag NP aggregates start to appear on the side surfaces of the reactant crystals (Fig. 3.9c, $\alpha = 0.49$). The time lag of the reaction initiations on the end and side surfaces is associated with the different nucleation rates in each surface. The initially formed spherical Ag NP aggregates grow gradually to submicron-sized spherical particles, and these are positioned on certain parts of the reactant surface (Fig. 3.9d). The resulting product forms a chain of Ag NP aggregates along with the original columnar crystals of the reactant (Fig. 3.9e). Finally, the chain is formed by the sintering of aggregates of submicron-sized spherical particles (Fig. 3.9f).

It should be also noted the formation of Au NPs by the rapid and violent fragmentation of reactant particles during the thermolysis of gold(III) acetate [56].

Fig. 3.8 Changes in XRD pattern during isothermal heating of silver acetate at 443 K in flowing N_2 ($100 \text{ cm}^3 \text{ min}^{-1}$): **a** changes in XRD pattern with time and **b** changes in the crystallite sizes of silver acetate and metallic Ag as the reaction advances. Reproduced with permission from Ref. [55]. Copyright (2016) American Chemical Society



3.1.3 Metal Oleates

The products of the thermolysis of metal–oleate (M–OI) complexes are metal nanocrystals, MOs, and metal sulfides [57]. The general synthetic procedure used for the ultralarge-scale preparation of monodisperse nanocrystals by thermolysis of M–OI complex has been represented in Scheme 3.3 [58].

Among the M–OI complexes, the thermolysis of iron oleate has been studied most thoroughly, since it is an effective way for relatively large monodisperse iron oxide nanocrystals with an accurate narrow size distribution and multiple shapes [8, 20, 59–63]. The undoubted advantage of iron oleate complexes as an iron precursor by thermolysis is the possibility to ultralarge-scale obtaining iron oxide NPs with wide range of sizes by varying reaction conditions (Scheme 3.4).

As a typical example, we note thermolysis of anhydrous iron oleate at 573 K leading to superparamagnetic iron oxide particles [8, 35, 64]. The particle size of the iron oxide NPs is easily controlled by using solvents with different boiling points [65]. In particular, NPs with accurate sizes of 5, 9, 12, 16, and 22 nm were prepared by varying the boiling points of each solvent, such as 1-hexadecene (b.p. 547 K), octyl ether (b.p. 560 K), 1-octadecene (b.p. 590 K), 1-eicosene (b.p. 603 K), and TOA (b.p. 638 K) [8]. Controlled modification of the iron oleate thermolysis method made it possible to obtain faceted iron oxide NPs with octahedral shape [66, 67]. The basis of this approach is the formation in situ of trioctylammonium bromide through decomposition of quaternary ammonium salts. The presence of both metallic iron and iron oxide within the nano-octahedra was shown.

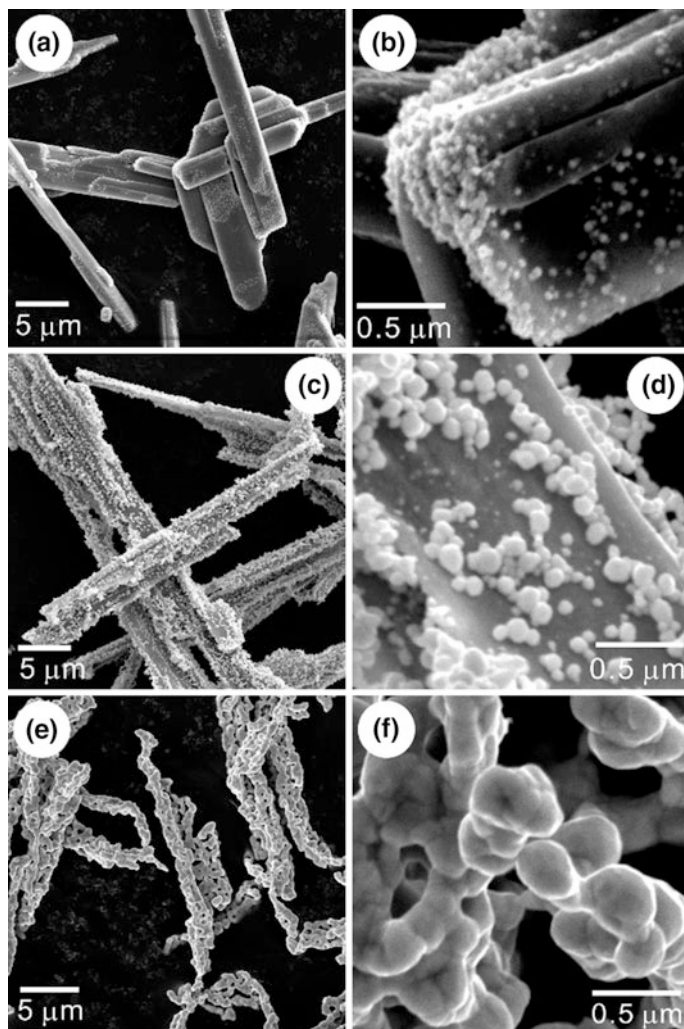
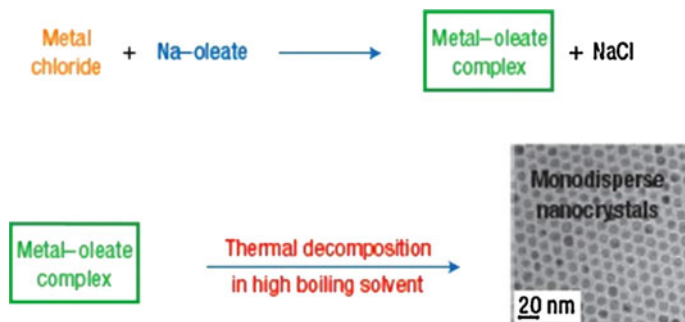
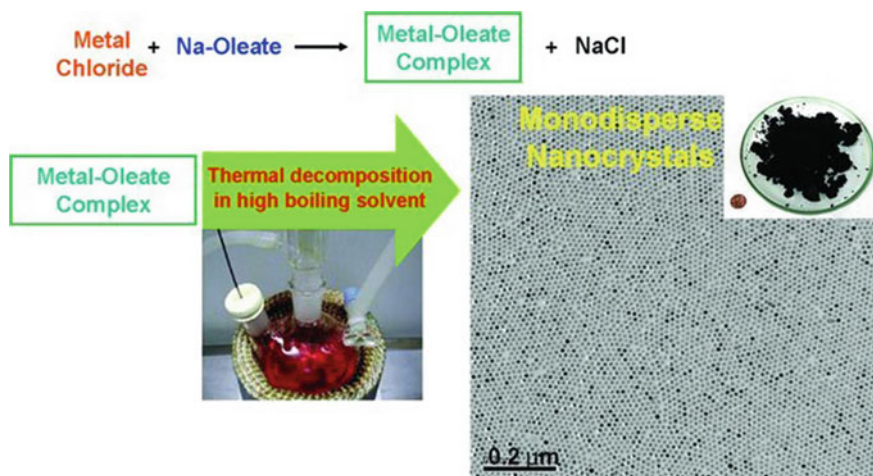


Fig. 3.9 Typical SEM images of partially decomposed silver acetate obtained by heating the sample to different temperatures at $\beta = 5 \text{ K min}^{-1}$ in flowing N_2 ($80 \text{ cm}^3 \text{ min}^{-1}$): **a, b** $\alpha = 0.05$ (453 K), **c, d** $\alpha = 0.49$ (468 K), and **e, f** $\alpha = 1.00$ (573 K). Reproduced with permission from Ref. [55]. Copyright (2016) American Chemical Society

Of interest is the synthesis of metal nanocrystals of a highly crystalline structure by the very easy, economical, and nontoxic thermolysis method under low pressure at about 593 K without any solvent (Scheme 3.5) [68]. The prepared nanocrystals were controlled by the thermolysis time and vacuum pressure. It is important that TEM images of products showed the 2D assembly of nanocrystals with the particle size of $10.6 \pm 1.2 \text{ nm}$ for iron and $9.5 \pm 0.7 \text{ nm}$ for silver.

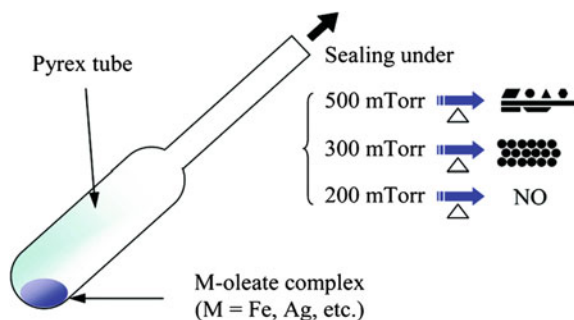


Scheme 3.3 Overall scheme for the ultralarge scale synthesis of monodisperse nanocrystals. Reproduced with permission from Ref. [58]. Copyright (2002) Royal Society of Chemistry



Scheme 3.4 Overall scheme for the ultralarge-scale synthesis of monodisperse iron oxide NPs. M-OI precursors were prepared from the reaction of metal chloride and NaOI. The thermolysis of the M-OI precursors in high-boiling solvent produced monodisperse nanocrystals. The TEM image clearly demonstrates that the nanocrystals are highly uniform in particle size distribution. Inset is a photograph showing a petri dish containing 40 g of the monodisperse magnetite nanocrystals, and a US one cent coin for comparison. Reproduced with permission from Ref. [8]. Copyright (2004) Springer Nature

It should be noted that the thermolysis of metal oleates in high-boiling solvents of 1-octadecene (ODE) type is the most widespread (see, for example, [8]). Thus, the thermolysis of the solution of Fe(III)-OI in ODE or docosane led to the formation of a clear black solution containing iron oxide nanocrystals [20]. The magnetite nanocrystals present spherical dots with very narrow size distributions, typically 5–10% (Fig. 3.10). It is important that the nanocrystal average diameter increased with the reaction time and the molar ratios of OA to FeO(OH).



Scheme 3.5 A procedure for synthesizing nanocrystallites using M-OI complex (M = Ag⁺, Fe²⁺, etc.). Reproduced with permission from Ref. [68]. Copyright (2008) American Chemical Society

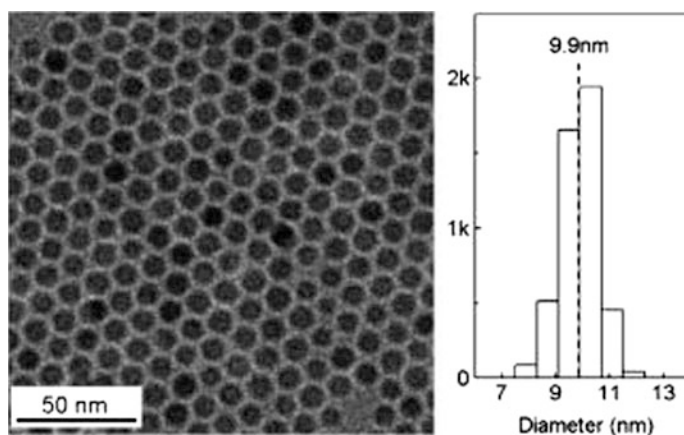


Fig. 3.10 TEM micrograph (left) and histogram (right) of the as-prepared magnetite nanocrystals. The y-axis of the histogram represents the number of particles (1 k ~ 1000). Reproduced with permission from Ref. [20]. Copyright (2004) Royal Society of Chemistry

In particular, NPs with 6.4-, 7.7-, and 9.0-nm diameter were obtained when the reaction time was 35, 45, and 60 min, respectively.

Magnetic iron oxide ($\text{Fe}_{3-x}\text{O}_4$) nanoplates with a high aspect ratio (lateral size/thickness ratio of >50) were synthesized via a facile hydrothermal treatment of an iron oleate precursor [69]. Representative TEM images of the $\text{Fe}_{3-x}\text{O}_4$ nanoplates (Fig. 3.11a, b) show hexagonal nanoplates with flat surfaces and lateral size of ca. 50–500 nm. The clear facet of a well-defined crystalline lattice is observed (Fig. 3.11c). The lattice spacing distance is ca. 2.9 Å and corresponds to the (220) plane of inverse spinel iron oxide. The fast Fourier transform (FFT) pattern of the nanoplate (Fig. 3.11c, inset) indicates the (111) plane of the $\text{Fe}_{3-x}\text{O}_4$, and the diffraction spots are regularly aligned indicating a single crystal.

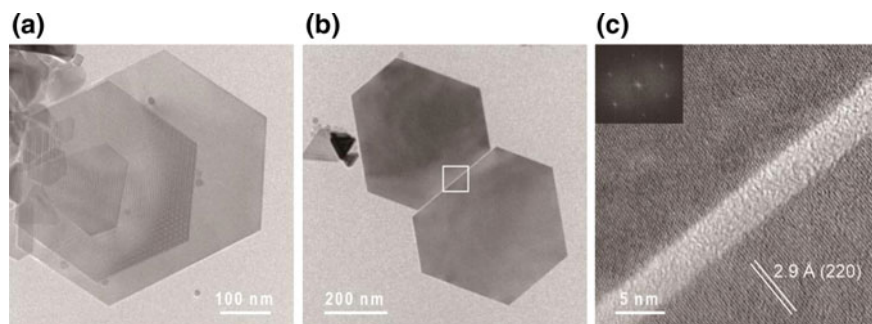


Fig. 3.11 **a, b** Representative TEM images of the $\text{Fe}_{3-x}\text{O}_4$ nanoplates. **c** HRTEM image of the marked area in **(b)**. Inset shows the corresponding FFT pattern. Reproduced with permission from Ref. [69]. Copyright (2017) Elsevier

Additionally, the thermolysis method is a promising way to prepare iron oxide NPs with different shapes, such as 0D nanocubes [61, 70–75] and nano-bipyramids (Fig. 3.12a–c) [76, 77]. In particular, it was shown that spherical iron oxide NPs are formed using OA as surfactant, and cubic iron oxide NPs are obtained by replacing the OA with oleate salt (NaOl or K–Ol). Besides, the sizes of both spherical and cubic iron oxide NPs increase with temperature (Fig. 3.12d–f). It is interesting that bipyramidal iron oxide NPs are synthesized by decreasing the molar ratio of Ol/Fe–Ol (Fig. 3.12g).

Of interest is the comparative analysis of using hydrated and non-hydrated iron oleate complexes as SSPs for iron oxide NPs by thermolysis [64]. In these compounds, iron ions coordinate with dimeric Ol ligands in both bidentate and bridging modes without water or ethanol molecules (Scheme 3.6).

In particular, the reaction of metal nitrate and carboxylic acid at 393 K was used to synthesize the non-hydrated iron oleate complexes with subsequent thermolysis of iron oleate at 573 K in non-coordination solvent to form the in situ-prepared superparamagnetic iron oxide NPs. The diameter of obtained NPs can be regulated by changing molar ratios of Fe–Ol/OA from 1:1 to 1:5 at fixed reaction temperature (593 K) and time (30 min). Using molar ratio of 1:1, the NP (sample 1) with different morphologies, such as triangle, cubic, spherical, and irregular shapes was synthesized (Fig. 3.13a). With increasing OA concentration, the size of NPs was increased, and the morphology of NPs changes to hexagonal in sample 2 and sample 3, cubic in sample 4, and spherical in sample 5. It is interesting that the most intense lattice fringes are observed from the {220} to {311} planes in sample 4 (Fig. 3.13f, inset). The average diameters of the NPs in samples 1–5 were equal to 8.4, 11.1, 12.3, 15, and 10 nm, respectively (Fig. 3.13g). It should be noted that the particle size increases by increasing the OA molar ratio from 1:1 to 1:4 and then decreases when OA molar ratio is raised to 1:5.

It was shown that the thermolysis of iron oleate proceeds stepwise: First, one Ol ligand is released at 473–513 K, and then the remaining two Ol moieties are released at ~ 573 K [59]. The NPs were not prepared at 583 K, whereas the

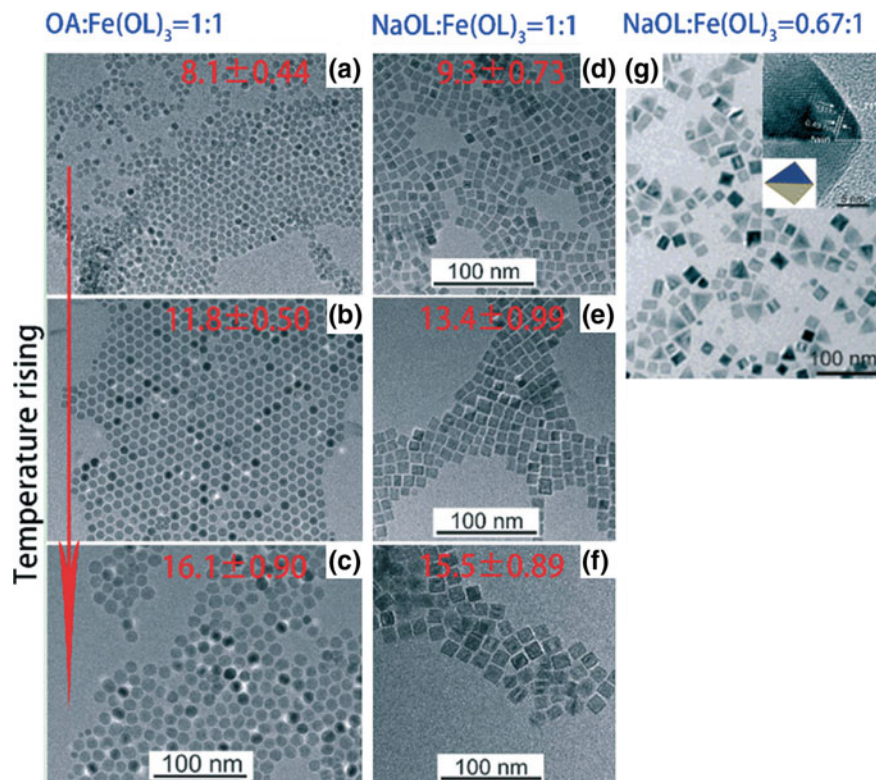
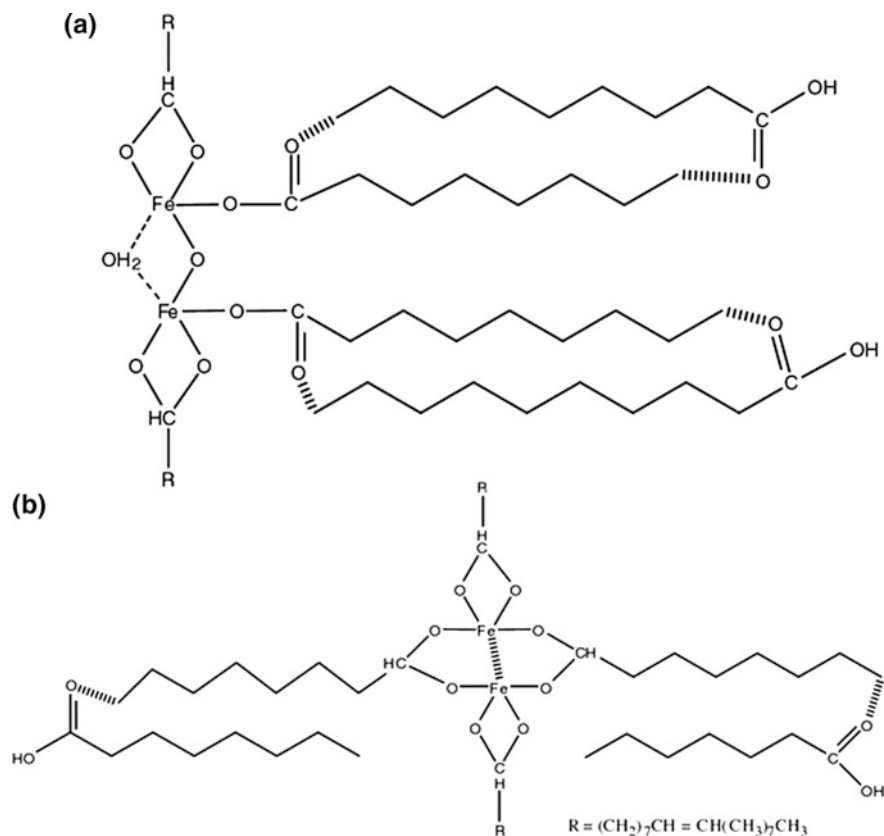


Fig. 3.12 TEM images of monodisperse spherical (a–c), cubic (d–f), and bipyramidal (g) Fe_3O_4 NPs with different particle sizes. These Fe_3O_4 NPs with different morphologies are obtained by changing the stabilizer and the ratio of oleate/Fe–Ol. Fe_3O_4 NPs with different sizes are obtained by changing the temperature. Reproduced with permission from Ref. [76]. Copyright (2007) American Chemical Society

relatively uniform NPs in size range of 8–11 nm are formed at 593 K (Fig. 3.14). The formation of monodisperse NPs of 12 nm size is observed in the samples taken after aging at 593 K for 10, 20, and 30 min.

Of interest is a solvent-free technique to synthesize highly crystalline and monodisperse Fe_3O_4 NPs [78]. This process was carried out at room temperature instead of refluxing temperatures (~ 538 – 623 K) by solid-state reaction of Fe(II)– and Fe(III)–Ol complexes with NaOH to form monodisperse and highly crystalline Fe_3O_4 nanocrystals in a self-assembled, 2D, and uniform periodic array (Scheme 3.7).

It should be noted the study the influence of reaction conditions and the chain length on the NP size and morphology in the case of thermolysis of long-chain iron carboxylates such as Fe(III) oleate, palmitate, and myristate [79]. Besides the usually forming spherical NPs, a number of interesting morphologies are observed



Scheme 3.6 Structure of Fe–OI complex: **a** hydrated iron oleate complex and **b** non-hydrated iron oleate. Reproduced with permission from Ref. [64]. Copyright (2012) Springer Nature

in some “extreme” conditions. In particular, iron oxide nanostars are prepared in eicosane at the high Fe–OI/OA ratio (Fig. 3.15). At the same time, the cubic NPs with flat facets are prepared by thermolysis of iron palmitate, and, finally, elliptical NPs are formed from Fe myristate with the most well-defined structure.

Of interest is the study of effect of the temperature, the nature of organic solvent, heating rate, and the mode of the heating on the thermolysis process of Fe–OI dried at 303 and 443 K in high-boiling organic solvents [80]. It turned out that heating on wood alloy with simultaneous bubbling of argon through the reaction mixture versus the heating on mantle with magnetic stirring is a promising route to improve the monodispersity of the resulting NPs (Fig. 3.16). It is important that the heating mode and rate are additional factors affecting the kinetic separation of nucleation and NP growth processes.

It should be noted the preparation of the hematite nanocubes by iron oleate thermolysis (Fig. 3.16) [81]. The nanocubes are highly uniform in terms of size and

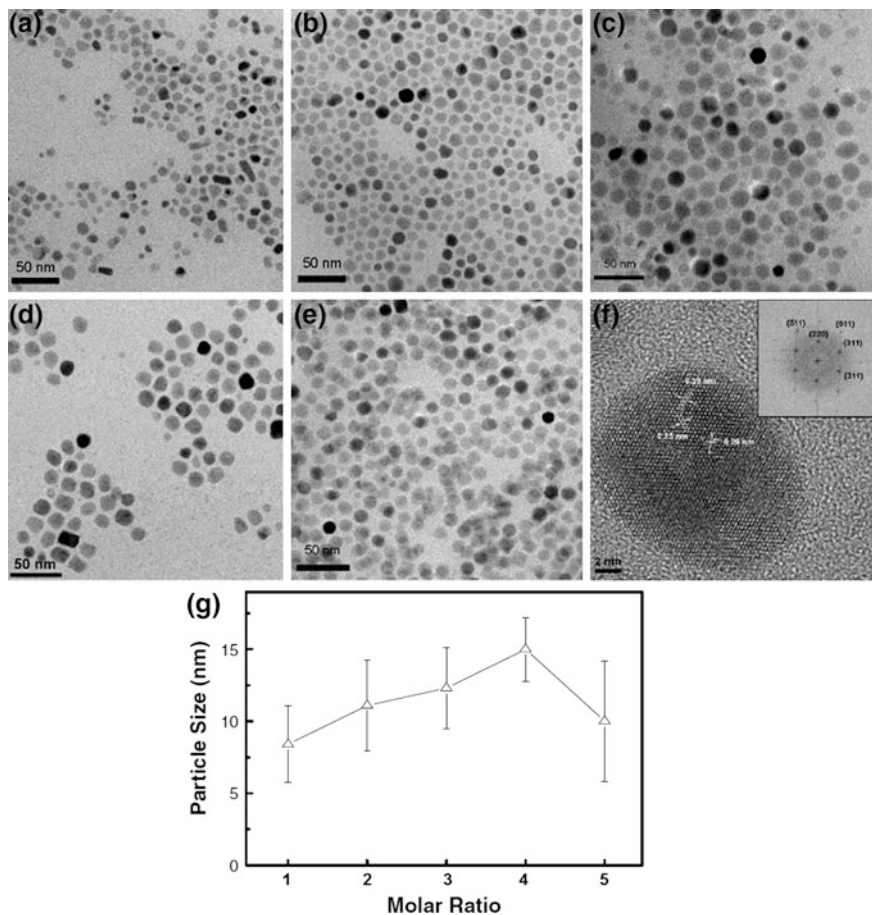


Fig. 3.13 TEM images of sample 1–5 prepared by thermolysis at 593 K for 30 min in ODE (a–e), HRTEM image of sample 4 (f), and the variation of magnetic particle size depending on molar ratio (indicated by sample numbers) of metal ion and OA (g). Reproduced with permission from Ref. [76]. Copyright (2007) American Chemical Society

shape, and their cyclohexane-dispersed colloidal solution is red (the color turns deeper with increasing the NP concentration) and usually stable for months under ambient conditions (Fig. 3.17a, inset). By controlling the solvent evaporation rate and the concentration of nanocubes, a superlattice structure can be prepared from these nanocubes (Fig. 3.17b). The edges of the nanocubes have a mean size of 14.7 nm and an interparticle distance estimated at ca. 4.3 nm. The single nanocube has a well-defined shape and highly crystalline nature (Fig. 3.17b, inset).

To obtain homogeneous hexagonal nanocrystalline ZnO, thermolysis of Zn–OI complex was used [82]. In particular, the thermolysis starts at 523 K and ends at 763 K, and the size of nanocrystallites depends on time (from 1 to 10 h) and temperature of thermolysis, as well as a solvent nature (Fig. 3.18).

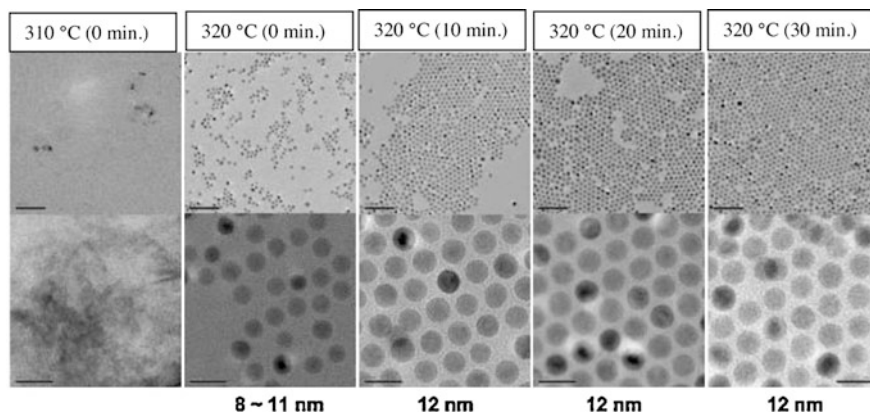
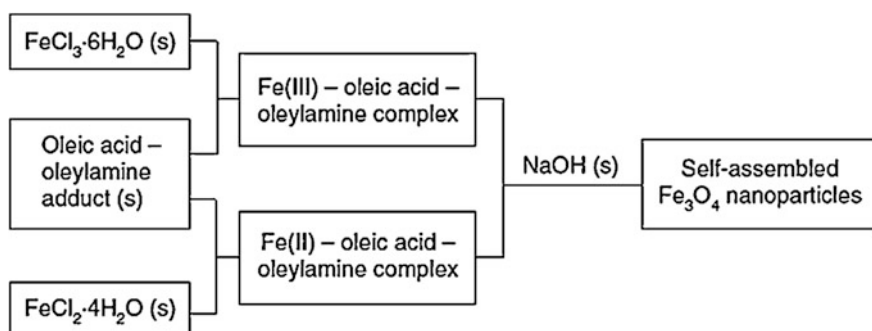


Fig. 3.14 TEM images (upper: low magnification; bottom: higher magnification) of the iron oxide NPs at various reaction time intervals. Reproduced with permission from Ref. [59]. Copyright (2014) Elsevier



Scheme 3.7 Overall scheme for synthesis of monodisperse Fe_3O_4 NPs. Reproduced with permission from Ref. [59]. Copyright (2014) Elsevier

Co-OI complexes were used for the preparation of Co NPs by thermolysis [83]. It is important that the NPs need to be coated with organic surfactants to prevent them from irreversible aggregation and to form ordered 2D or 3D self-assembled superlattices [84]. It should be noted the synthesis of uniformly sized, pencil-shaped CoO nanorods with an extraordinary wurtzite ZnO crystal structure by the thermolysis of a Co-OI complex [85]. These uniformly sized nanorods self-assembled to form both horizontal parallel arrangements and perpendicular hexagonal honeycomb superlattice structures. The diameters and lengths of the CoO nanorods could be controlled by varying the synthetic conditions, such as the monomer concentration, heating rate, and aging time (Fig. 3.19). In particular, when a reaction mixture composed of Co-OI complex and ODE was heated to 593 K at a rate of 3.1 deg min^{-1} , CoO nanorods with dimensions $23 \text{ nm (base edge)} \times 28 \text{ nm}$

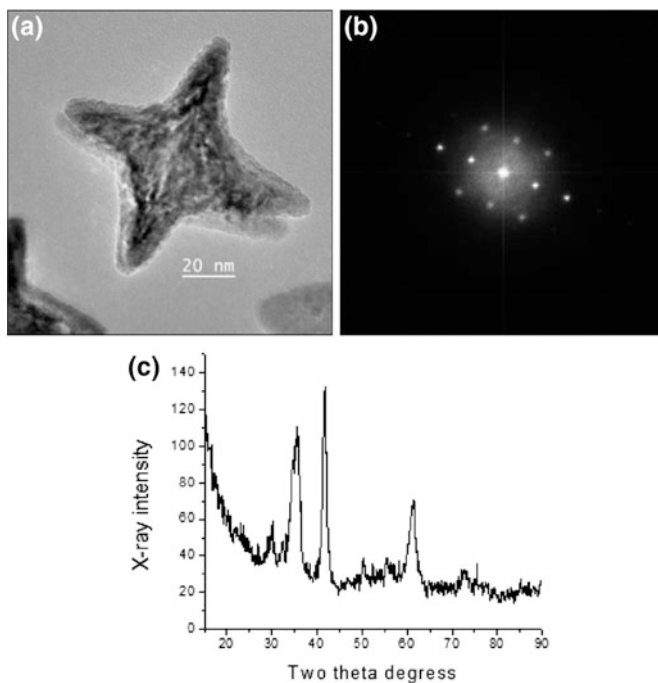


Fig. 3.15 HRTEM image of a star-like NP (a), its FFT image (b), and XRD profile (c). Reproduced with permission from Ref. [79]. Copyright (2011) American Chemical Society

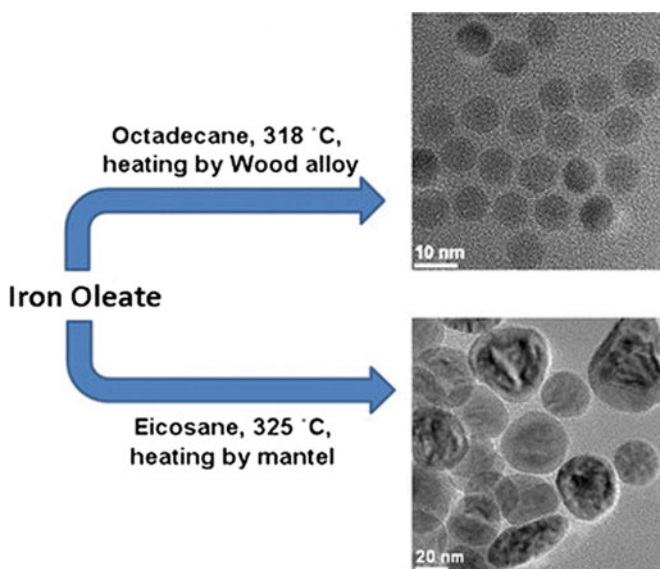


Fig. 3.16 TEM images of the iron oxide spherical, monodisperse 22-nm-sized particles synthesized in octadecane (top) and microphotographs of the iron oxide NPs with an increased polydispersity synthesized in eicosane (bottom). Reproduced with permission from Ref. [80]. Copyright (2016) Springer Nature

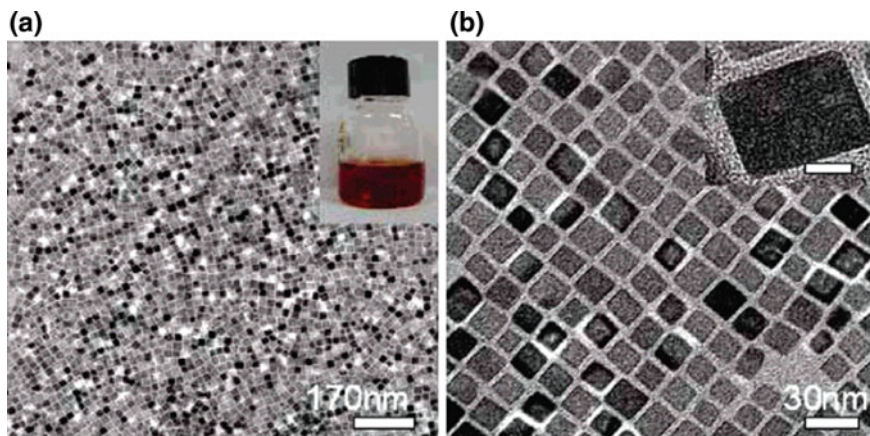


Fig. 3.17 **a** General view of hematite nanocubes. The inset shows the sample photograph; **b** a typical self-assembled monolayer of hematite nanocubes. *Inset* HRTEM image of single nanocube, bar 8 nm. Reproduced with permission from Ref. [81]. Copyright (2007) American Chemical Society

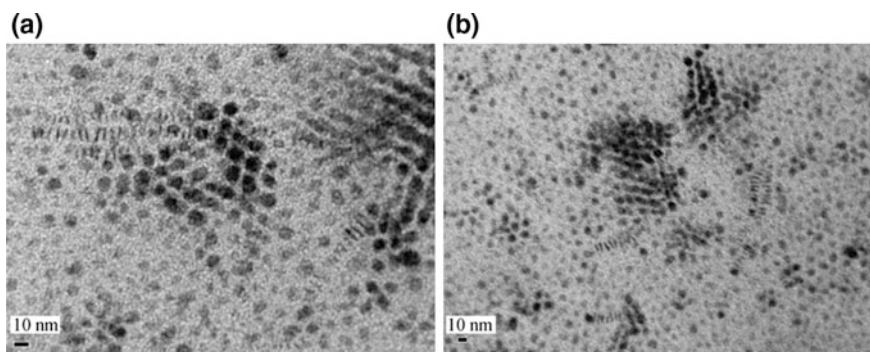


Fig. 3.18 (top) TEM micrographs of ZnO nanocrystals: **a** synthesized in ODE medium; **b** synthesized in octyl ether medium, (down) SEM micrographs of ZnO nanocrystals: **a** synthesized in ODE medium; **b** synthesized in octyl ether medium. Reproduced with permission from Ref. [82]. Copyright (2008) Springer Nature

(height) were obtained (Fig. 3.19a). At the same time, when the heating rate was decreased to 1.9 and 1.0 deg min⁻¹, 12 nm × 19 nm (Fig. 3.19b) and 8 nm × 26 nm (Fig. 3.19c) CoO nanorods were prepared, respectively. The overall size of the nanorods was also increased by increasing the amount of Co–OI complex while keeping the other experimental conditions unchanged. For example, when the amount of the Co–OI complex was increased to 10 and 15 mM, CoO nanorods with dimensions 9 nm × 28 nm (Fig. 3.19d) and 20 nm × 38 nm (Fig. 3.19e) were prepared, respectively. The size of the CoO nanorods was further controlled by

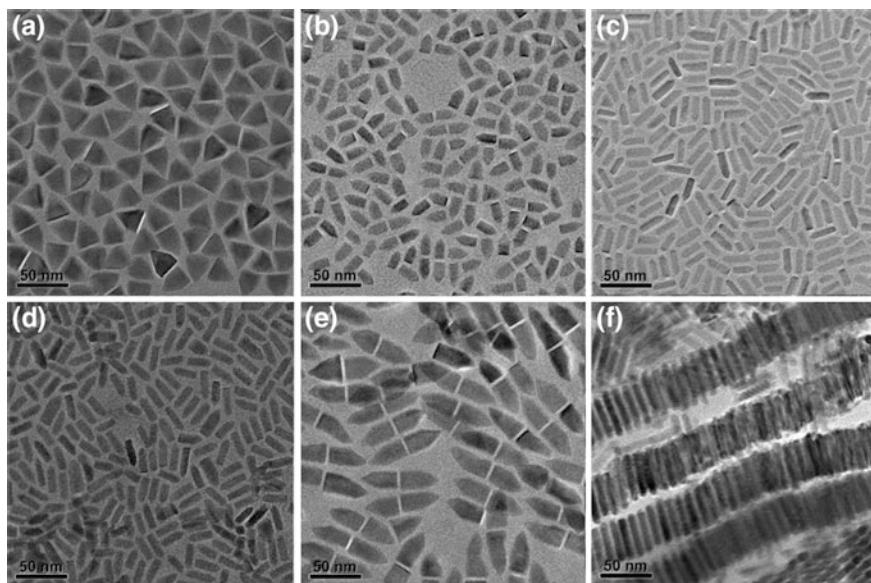


Fig. 3.19 TEM images of pencil-shaped CoO nanorods obtained using various synthetic conditions. CoO nanorods with dimensions of 23 nm (base edge) \times 28 nm (height) (a), 12 nm \times 19 nm (b), and 8 nm \times 26 nm (c), synthesized at heating rates of 3.1, 1.9, and 1.0 deg min⁻¹, respectively, with the same Co–Ol concentration of 5 mM. CoO nanorods with dimensions of 9 nm \times 28 nm (d) and 20 nm \times 38 nm (e) were synthesized using 10 and 15 mM of Co–Ol with the same heating rate of 1.9 deg min⁻¹. f 9 nm \times 46 nm CoO nanorods were synthesized using the Co–Ol concentration of 5 mM and a heating rate of 1.9 deg min⁻¹, but an increased aging time of 1 h. Reproduced with permission from Ref. [85]. Copyright (2007) American Chemical Society

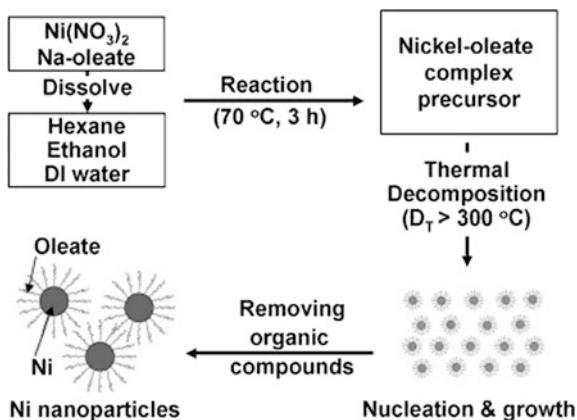
varying the aging time. When the aging time was increased from 30 min to 1 h, the length of the nanorods was increased from 19 nm (see Fig. 3.19b) to 46 nm (Fig. 3.19f), while their diameter was decreased slightly.

Of interest is thermolysis of Ni–Ol complex under inert gas flow leading to Ni NPs (Scheme 3.8) [86]. The mean particle sizes of the cubic-phase Ni NPs prepared at 623, 653, and 673 K were 5.1, 5.5, and 6.6 nm, respectively.

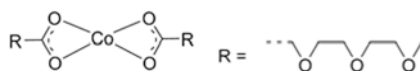
3.1.4 Other Metal Monocarboxylates

Among the other metal monocarboxylates, we note ethylene glycol-functionalized Co(II) carboxylate [Co(CO₂CH₂(OC₂H₄)OMe)₂] used as an SSP for preparing Co₃O₄ NPs by solid-phase thermolysis in air [87]. It is important that NPs with

Scheme 3.8 Schematic diagram of the synthesis of Ni NPs using thermolysis. Reproduced with permission from Ref. [86]. Copyright (2009) Elsevier



different chemical composition (including Co_3O_4 , CoO , and Co) and with particle sizes from 9 to 18 nm are formed depending on the time of thermolysis. For example, APS of Co_3O_4 NPs was equal 18 ± 1 , 14 ± 1 , and 16 ± 1 nm after 10, 20, and 30 min, respectively.

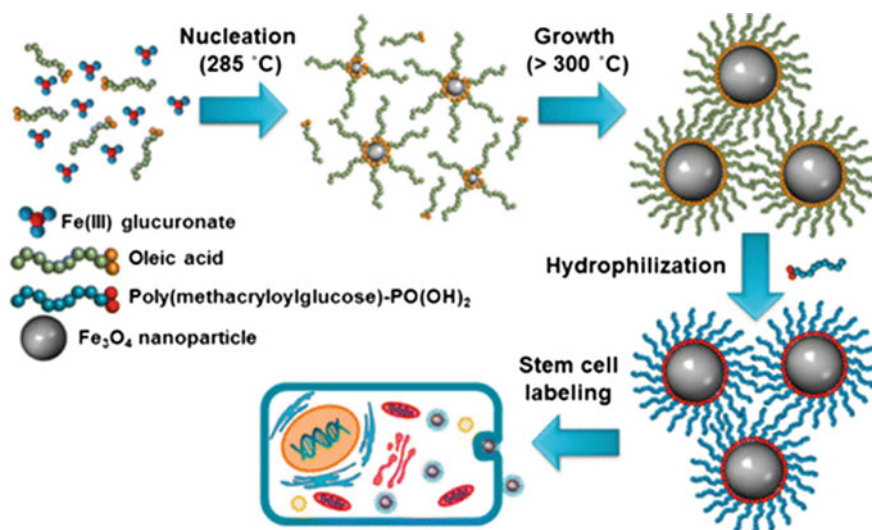


Thermolysis of Fe(III) glucuronate led to monodisperse superparamagnetic Fe_3O_4 NPs coated with OA (Scheme 3.9) [88]. It turned out that the size, shape, and particle size distribution can be regulated by varying the reaction parameters, in particular, the reaction temperature, concentration of the stabilizer, and type of high-boiling-point solvents. In order to obtain the Fe_3O_4 NPs dispersible in water, the NP surface was treated with α -carboxyl- ω -bis(ethane-2,1-diyl) phosphonic acid-terminated poly(3-*O*-methacryloyl- α -D-glucopyranose).

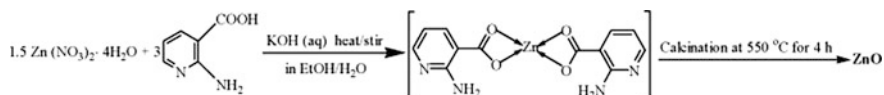
Thermolysis of the complex $\text{EuL} \cdot 6\text{H}_2\text{O}$, where H_3L is 1,3,5-benzene tricarboxylic acid, resulted to 1D Eu_2O_3 nanorods of 10–20 nm thick with 50–100 nm width, and a length ranging from hundreds nanometers to several micrometers [89–91].

Of interest is also thermolysis of ZnL_2 ($\text{HL} = 2$ -aminonicotinic acid) at 823 K for 4 h leading to the formation of a pure ZnO with a hexagonal wurtzite structure and various morphologies (Scheme 3.10) [92].

Hollow microblocks of ZnL_2 (Fig. 3.20a, c) are converted to porous microbricks that comprise ZnO NPs with a size of ~ 30 nm (Fig. 3.20d, f). The prepared products possess a mesoporous structure with a surface area of $8.13\text{ m}^2\text{ g}^{-1}$ and a pore size of 22.6 nm (Fig. 3.20g, i).



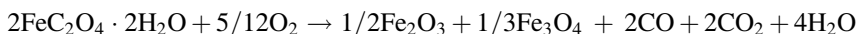
Scheme 3.9 Scheme of the preparation of Fe₃O₄ NPs dispersible in water. Reproduced with permission from Ref. [88]. Copyright (2016) American Chemical Society



Scheme 3.10 Formation reaction for the zinc complex and for zinc oxide. Reproduced with permission from Ref. [92]. Copyright (2015) Elsevier

3.1.5 Metal Oxalates

The solid-state thermolysis of metal complexes of dicarboxylic acids, in particular, oxalates (ox) showing the wide variety of coordination modes predominantly gives MOs and mixed oxides as intermediates and end products. It has been investigated for a long time (see, for example, [93–95]). Prehistory (temperature and duration of thermolysis, aging, morphology) affects essentially the structure of a thermolysis product as, for example, in case of the most thoroughly studied iron oxalate. In particular, thermolysis in air results to hematite (α -Fe₂O₃), and deficiency of oxygen at 773–973 K leads to the formation of Fe₃O₄ NPs of 35–55 nm of size:



In the case of thermolysis of Fe(III) oxalate tetrahydrate in a dynamic inert atmosphere, the main products are FeO (wustite), α -Fe, magnetite, and small amounts of superparamagnetic Fe(III) oxide [96]. At the same time, thermolysis in

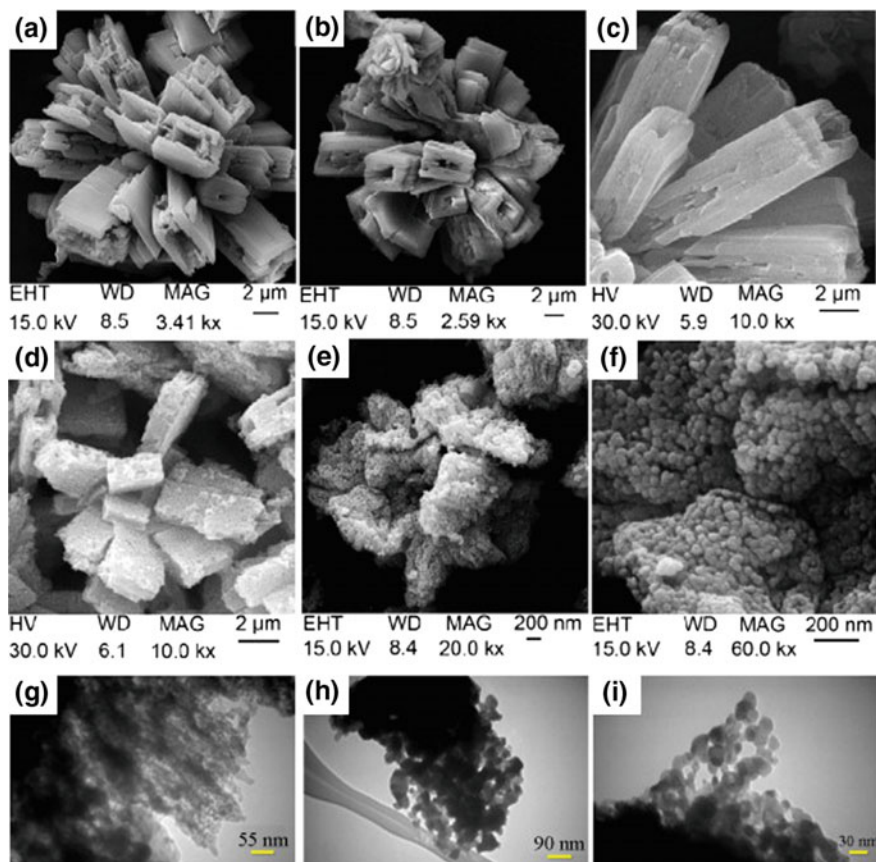
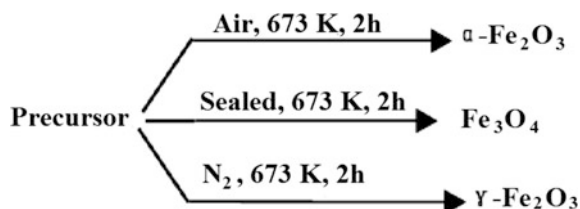


Fig. 3.20 SEM images of hollow microblocks of the ZnL₂ in **a**, **b** a wide and **c** a close-up window and **d**, **e** ZnO microbricks containing **f** ZnO NPs; TEM images (**g**–**i**) of the mesoporous structure of the ZnO NPs. Reproduced with permission from Ref. [92]. Copyright (2015) Elsevier

Scheme 3.11 Products formed during thermolysis of ferrous oxalate dihydrate depending on experimental conditions



an oxidative atmosphere consists of dehydration, reduction to Fe(II), and the subsequent decarboxylation to hematite.

The numerous studies of the thermolysis of ferrous oxalate dihydrate Fe(ox)·2H₂O showed that experimental conditions such as reaction atmosphere and duration or temperature of thermolysis influence the formation of the final products (Scheme 3.11) [94, 97–99].

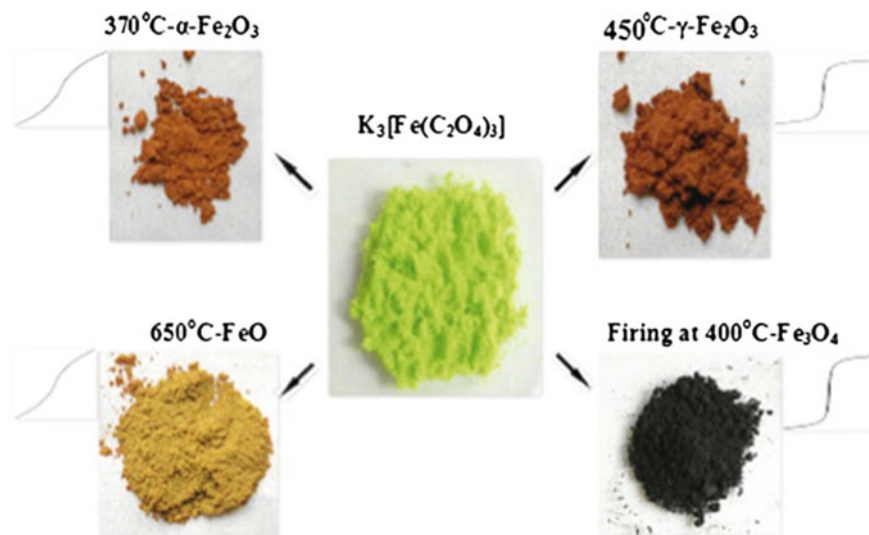


Fig. 3.21 α - Fe_2O_3 , γ - Fe_2O_3 , Fe_3O_4 , and FeO obtained from the $\text{K}_3[\text{Fe}(\text{ox})_3]$ precursor using different thermolysis temperatures. Reproduced with permission from Ref. [104]. Copyright (2015) Elsevier

In particular, it was well established that the final product of thermolysis of ferrous oxalate in air is hematite, α - Fe_2O_3 [94, 96, 97, 100–102]. It is important that the morphology of the oxalate crystals is preserved during thermolysis; the oxalates are transformed into spinel particle aggregates of similar size (40 or 55 nm) and shape [94]. The detailed investigation of intermediate and final products by XRD measurements performed simultaneously with the thermolysis process of $\text{Fe}(\text{ox}) \cdot 2\text{H}_2\text{O}$ nanorod sample has shown that diffraction peaks characteristic of ferrous oxalate disappeared at $T = 453$ K [103]. At the next stage of the thermolysis, the poorly crystalline Fe_2O_3 phase is formed, which was stable in the whole temperature interval. In the last stage, the final product was identified as bulk hematite α - Fe_2O_3 .

Of interest is solid-state thermolysis of a chiral, 3D anhydrous potassium tris(oxalato)ferrate(III) ($\text{K}_3[\text{Fe}(\text{ox})_3]$) precursor in air to form the four iron oxide polymorphs: iron oxide NPs hematite (α - Fe_2O_3), maghemite (γ - Fe_2O_3), magnetite (Fe_3O_4), and wustite (FeO) (Fig. 3.21) [104].

Thermolysis of the copper oxalate at 573 K for 1 h leads to the products containing Cu, Cu_2O (cuprite), as well as CuO (tenorite) depending on temperature and includes the following stages: $[\text{Cu}] \rightarrow \text{Cu} + \text{Cu}_2\text{O}$ (458–573 K), $0.5\text{Cu}_2\text{O} + 2\text{CuO}$ (573–618 K), 3CuO (618–673 K) [105–107].

Thermolysis of $\text{Co}(\text{ox}) \cdot 2\text{H}_2\text{O}$ proceeds in two steps: dehydration to anhydrous oxalate and subsequent decomposition to Co and CoO in two parallel reactions [93]. It should be noted that both reactions obey Avrami–Erofeev equations. In particular, for the first reaction leading to metallic cobalt, parameter n and

activation energy are equal to 2 and $97 \pm 14 \text{ kJ mol}^{-1}$, accordingly. At the same time, the thermolysis to CoO includes two stages. First stage proceeds with $n = 2$ and activation energy $251 \pm 15 \text{ kJ mol}^{-1}$, while second stage proceeds with $n = 1$ and activation energy $203 \pm 21 \text{ kJ mol}^{-1}$. Similar kinetic regularities were obtained during a study on kinetics of isothermal thermolysis of cobalt oxalate at six different temperatures between 568 and 643 K in reducing ($\text{He} + 15 \text{ vol\% H}_2$) atmosphere [108]. The powder size was less than 100 nm at the thermolysis temperatures below 643 K (Fig. 3.22). At the same time, thermolysis at 823 K for 30 min was found to be optimum condition preparing fine size, non-pyrophoric, and spherical powder in larger scale of preparation.

1D array of Co_3O_4 NPs was prepared via the thermolysis of cobalt oxalate nanorods [109, 110]. By using the combinations of TPP and OAm as surfactants, the morphology of the particles can be regulated (Scheme 3.12).

The diameters of the prepared Co_3O_4 nanorods are 20 nm, and the average lengths are around 500 nm. Due to the whiskers-like structure, very thin arrays of Co_3O_4 NPs are observed (Fig. 3.23a). It is important that the formed NPs consist of a large number of the nanorods (Fig. 3.23b).

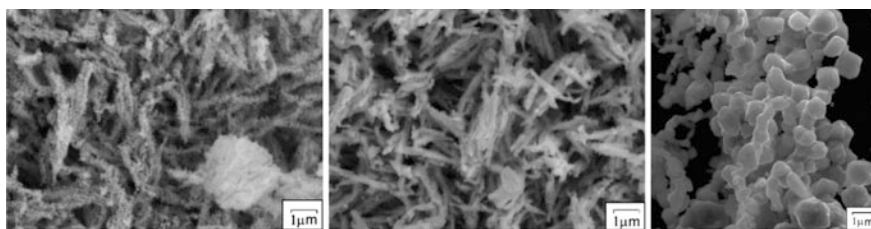
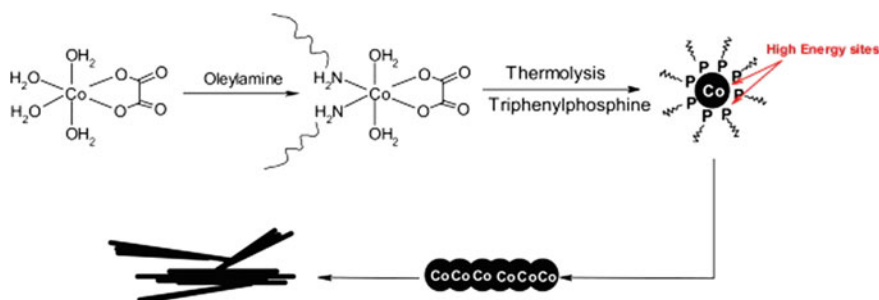


Fig. 3.22 (left) SEM image showing nanosized cobalt powder formation at 613 K, (middle) SEM image showing nanopowder chain formation at 643 K, (right) micron size cobalt powder produced after decomposition at 823 K for 30 min. Reproduced with permission from Ref. [108]. Copyright (2008) Elsevier



Scheme 3.12 Overall synthetic procedure of the formation Co_3O_4 nanorods and view of the growth rod-like shapes by thermolysis. Reproduced with permission from Ref. [110]. Copyright (2009) Elsevier

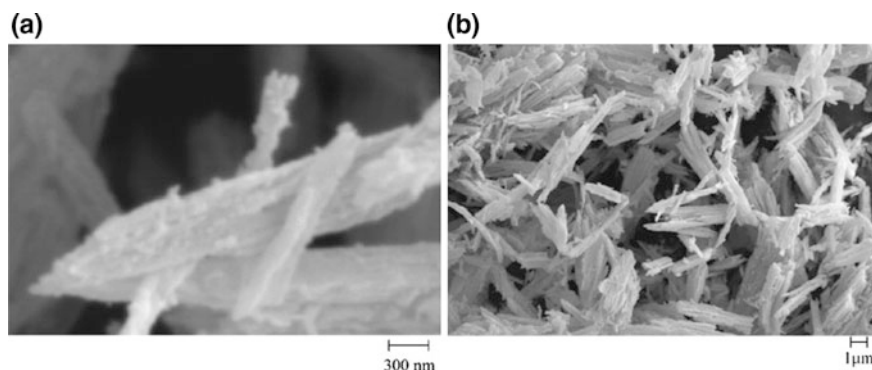


Fig. 3.23 SEM images of Co_3O_4 nanorods. Reproduced with permission from Ref. [110]. Copyright (2009) Elsevier

It is interesting that particle size of initial cobalt oxalate plays a crucial role in determining the size of prepared oxide particles [111]. In particular, cobalt oxalate particles with sizes of ~ 60 and 30 nm were prepared with (sample S_P) and without surfactant (sample S_A), respectively (Fig. 3.24a, b). As a thermolysis result, the Co_3O_4 NPs with sizes of ~ 60 nm and 25 nm for first and second samples were obtained (Fig. 3.24c, d).

It should be noted that thermolysis of manganese oxalate and its ethylene glycol crystal solvate having quasi-unidimensional structure leads to Mn_3O_4 and Mn_2O_3 nanowhiskers in air and MnO in an inert gas environment [112]. It is important that thermolysis of these compounds completely conserves their initial crystal shape. In particular, manganese oxalate trihydrate forms needles about $1 \mu\text{m}$ in diameter (Fig. 3.25a), while its solvate crystallizes as thinner needles and fibers that tend to longitudinally intergrowth (Fig. 3.25b). Thermolysis of the solvate in air and in an inert gas environment leads to the separation of the initial crystals into thinner extended aggregates of Mn_2O_3 and MnO , respectively (Fig. 3.25c, d).

3.1.6 Metal Malonates

Of interest are kinetic and thermodynamic studies of the non-isothermal decompositions of nickel and cobalt malonates dihydrate and nickel and cobalt hydrogen malonates dihydrate [113], isothermal and non-isothermal decomposition of zinc malonates [114], and thermolysis of transition metal malonates [14]. The binding of the carboxylate group to the metal is chelating bidentate and/or bridging in these compounds. This conclusion is supported (at least in the case of the Cu and Zn compounds) by the results of the crystal structure determination of Cu malonate trihydrate [115] and Zn malonate dihydrate [116]. The thermolysis of metal malonates occurred preferentially with the release of carbon dioxide due to decarboxylation and oxidation of organic part.

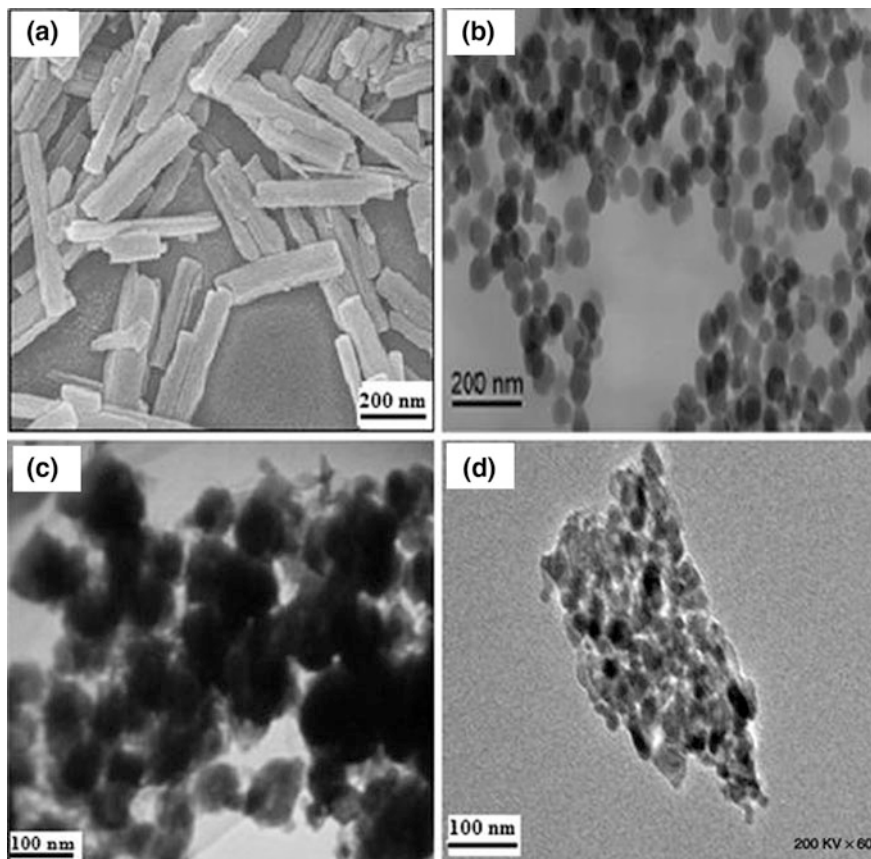


Fig. 3.24 TEM images of $\text{Co(ox)}\cdot 2\text{H}_2\text{O}$: S_P (a), S_A (b) and Co_3O_4 : **c** produced from S_P , **d** produced from S_A . Reproduced with permission from Ref. [111]. Copyright (2015) Springer Nature

It should be also noted thermolysis of copper malonate $[\text{CuCH}_2\text{C}_2\text{O}_4\cdot 2\text{H}_2\text{O}]$ with surfactant OAm and triphenylphosphine (TPP) as capping agent leading to copper NPs (Scheme 3.13) [117]. It is important that CuO instead of Cu is formed as a result of thermolysis of copper malonate without using surfactants. However, thermolysis with OAm and TPP as surfactants gives pure Cu NPs with diameter of ~ 35 nm, because the surfactants inhibit oxygen diffusion to the NP surface and prevent from oxidation.

The study of thermolysis of transition metal malonates $\text{MCH}_2\text{C}_2\text{O}_4\cdot n\text{H}_2\text{O}$ ($\text{M} = \text{Mn(II)}, \text{Fe(II)}, \text{Co(II)}, \text{Ni(II)}, \text{Cu(II)}, \text{Zn(II)}$) showed that the dehydration and the thermal decomposition of the anhydrous compounds occur in one step [118]. The final residue of thermolysis at 608 (Mn), 673 (Fe), 613 (Co), 623 (Ni), 793 (Cu), and 723 K (Zn) is Mn_3O_4 , Fe_2O_3 , Co_3O_4 , NiO, CuO, and ZnO, respectively.

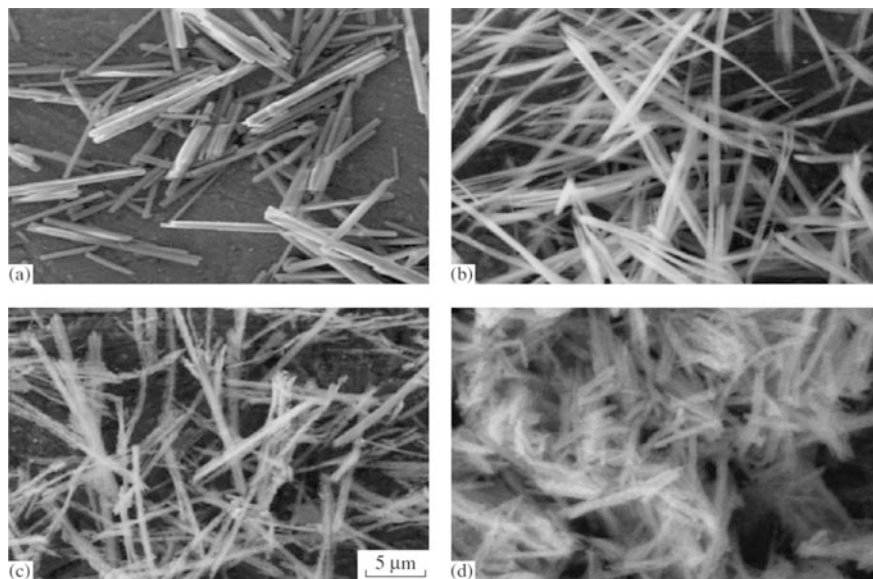
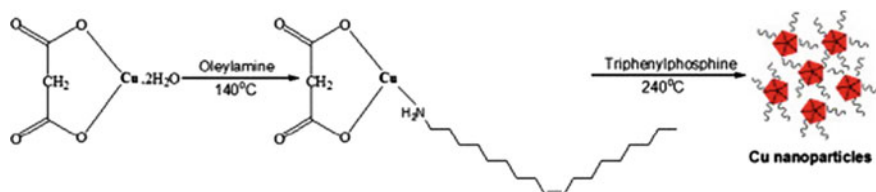


Fig. 3.25 SEM images ($\times 2500$) of **a** $\text{Mn(ox)}\cdot 3\text{H}_2\text{O}$, **b** $\text{Mn(ox)(HOCH}_2\text{CH}_2\text{OH)}$, **c** product of thermolysis of the solvate in air at 723 K, **d** product of thermolysis in a helium atmosphere at 873 K. Reproduced with permission from Ref. [112]. Copyright (2009) Springer Nature



Scheme 3.13 Illustration of the formation of Cu NPs by copper malonate as a Cu precursor. Reproduced with permission from Ref. [117]. Copyright (2013) Elsevier

Thermolysis of cadmium malonate led to CdO nanoplatelets, which are randomly agglomerated **fcc** structures with the APS of 40–50 nm [119]. Thermolysis of cadmium malonate hydrates was studied in dynamic helium and air atmospheres [120]. It turned out that the mechanism of thermolysis of cadmium malonate strongly depends on the amount of water in the initial sample. In particular, the degree of decomposition of dehydrated malonate obtained from sample with 1.4 hydration water molecules is greater than the degree of decomposition of the dehydrated malonate obtained from samples with 0.2 hydration water molecules at the same temperature. The initial temperature of decomposition of anhydrous malonate for all

the samples is in the range 518–523 K which can indicate the same mechanism of decomposition. The primary solid product of thermolysis is metallic cadmium both in air and in helium, and the gaseous products are acetone, isobutylene, propyne, CO_2 , and H_2O . In helium, metallic cadmium evaporates at the temperature of decomposition. In air, cadmium immediately oxidizes and forms CdO .

3.1.7 Metal Succinates

Copper and copper oxide NPs with the sizes of 50 nm are the products of thermolysis of Cu(II) succinate with OAm as a capping agent [121]. A procedure has been proposed for the preparation of copper/polymer composites through $\text{Cu}(\text{C}_4\text{H}_4\text{O}_4)\cdot\text{H}_2\text{O}$ succinate thermolysis [122]. Three types of copper NPs have been incorporated into a fibrous carbon–polymer matrix of the composite: cubic (350×350 nm) and needle-like (40–80 nm in diameter and 4.5–5.5 μm in length) crystals and spherical copper particles ranging in size from 5 to 45 nm (Fig. 3.26).

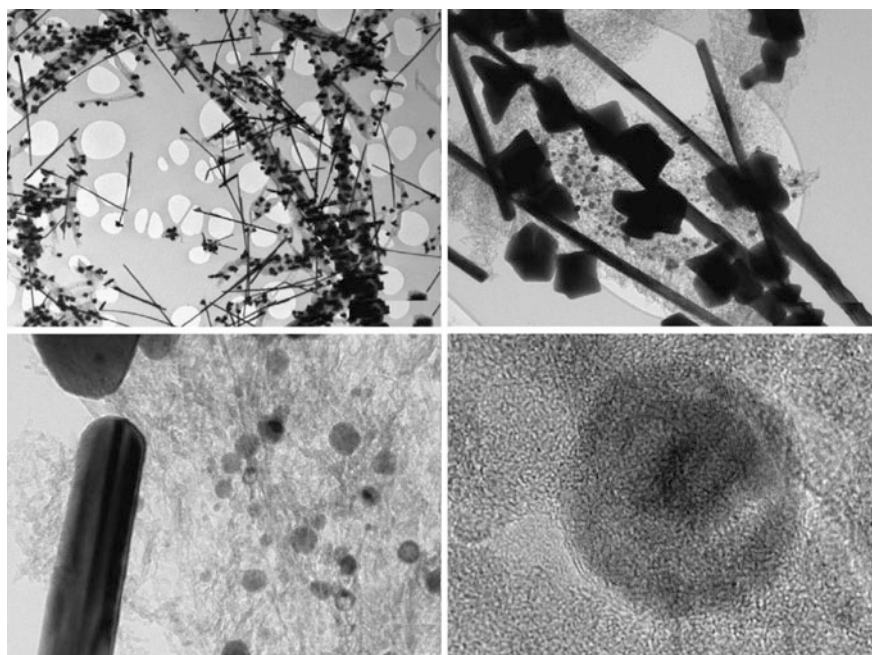


Fig. 3.26 TEM micrographs of the composite prepared through copper(II) succinate thermolysis. Reproduced with permission from Ref. [122]. Copyright (2014) Springer Nature

3.1.8 Metal Phthalates

Metal phthalates are the promising candidates for the thermolysis process. Phthalic acid (H_2L), an aromatic dicarboxylic acid, can be used to bind two acid groups with metal atoms. The simultaneous interaction of two carboxylate groups of the H_2L with one metal ion leads to the lower thermal stability of phthalate complexes in comparison with isophthalate and terephthalate ones. The obtained structure is a seven-member metal chelate cycle which stabilizes the complex, increases the intermolecular interactions, and decreases the intermolecular bonds leading to a consequent decrease in the thermal stability. Thus, for example, the thermolysis of *ortho*- $[Ni(H_2O)_2(L)](H_2O)_2$, $[Cu(H_2O)(L)]$, and acid $[M(H_2O)_6](HL)_2$ ($M = Fe(II)$, $Co(II)$, and $Ni(II)$), $[Cu(H_2O)_2(HL)_2]$ phthalates gives the nanocomposites with NPs embedded in carbon-polymer matrices [123]. It is interesting that nickel/copper composites consist only of metal NPs, and in iron/cobalt polymer nanocomposites there are metal NPs with oxide NP impurities. In addition, the copper-based composite matrix contains spherical conglomerates (50–200 nm) with numerous spherical Cu NPs (5–10 nm), while nickel NPs with the diameters of 6–8 nm are covered with disordered graphene layers.

The mechanism of thermolysis of phthalate complexes has well been studied in the absence of surfactants [124, 125]; however, surfactants optimize particle size, morphology, and synthesis methods of nanomaterials. For example, the chain-like Mn_2O_3 NPs were obtained via thermolysis of manganese phthalate SSPs in the presence of OA and TPP as stabilizer and capping agent at 493 K [126]. It is important that OA and TPP could not react with the surface Mn_2O_3 atoms, but in the thermolysis process metal ions could be capped by OA and TPP [127]. The chain-like structures are composed of nano-sized (approximately 35–40 nm) primary particles (Fig. 3.27, left). It should be noted the preparation of pure tin dioxide (SnO_2) NPs by thermolysis of tin phthalate in the presence of OA as solvent (Fig. 3.27, right) [128].

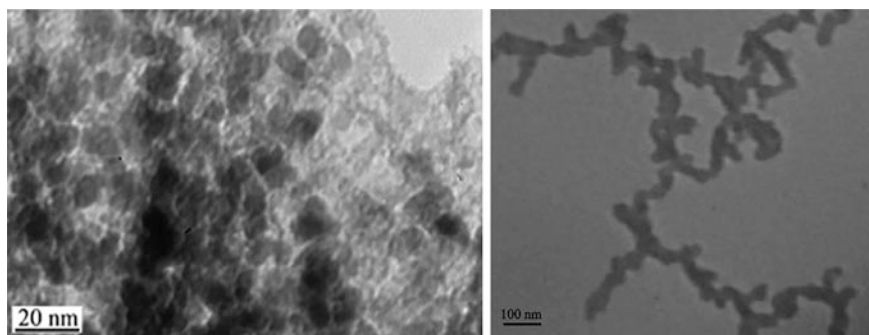


Fig. 3.27 (left) TEM images of SnO_2 obtained from $[Sn(L)(H_2O)]_n$. Reproduced with permission from Ref. [128]. Copyright (2010) Elsevier; (right) TEM image of Mn_2O_3 nanostructures. Reproduced with permission from Ref. [126]. Copyright (2009) Elsevier

Of interest is synthesis of NiO NPs by solid-state thermolysis of layered coordination nickel phthalate SSPs [129]. The smaller particle size and lower agglomeration level were obtained when the molar ratio of ligand to metal increased and thermolysis temperature decreased. Thermolysis of $[\text{Ni}(\text{L})(\text{H}_2\text{O})_2]$ complex at 773 K leads to the formation of spherical particles with a maximum diameter of about 25 nm (Fig. 3.28). At the same time, uniform spherical NiO NPs with particle size of about 10–15 nm were obtained by thermolysis of NiL_2 complex at 773 K.

Thermolysis of Co-phthalate with OA as a surfactant along with TPP as a modulating additive led to highly dispersed Co_3O_4 NPs with APS of about 20–30 nm. It was shown that OA is chemisorbed via a carboxylate fragment onto the NPs in a bidentate mode. In addition, TPP is an appropriate surfactant which provides greater steric hindrance than the straight-chained alkyl group; therefore, TPP reduces growth rate of the NPs during the reaction and results in producing much smaller NPs (Fig. 3.29) [130].

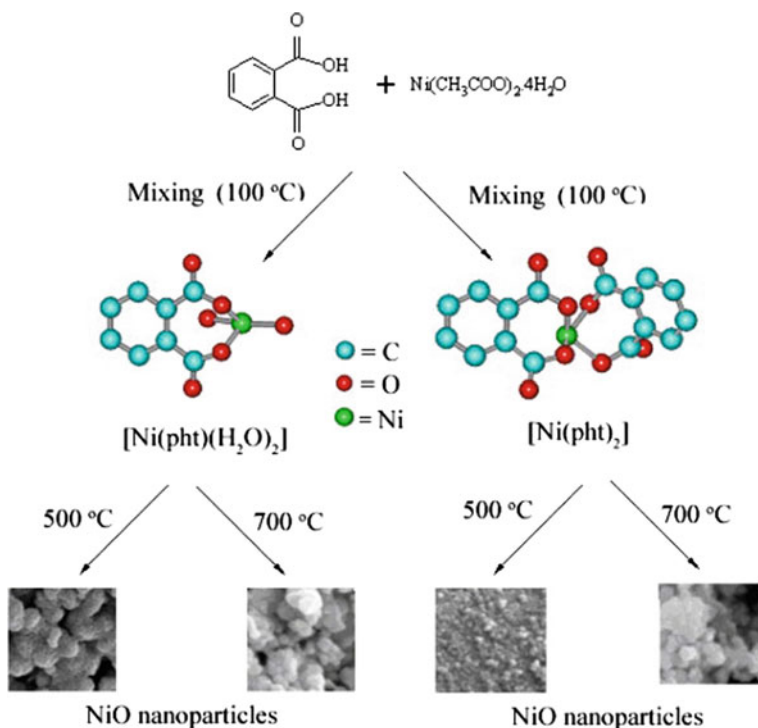


Fig. 3.28 Scheme of the synthesis and thermolysis of $[\text{Ni}(\text{L})(\text{H}_2\text{O})_2]$ and NiL_2 . Reproduced with permission from Ref. [129]. Copyright (2009) Elsevier

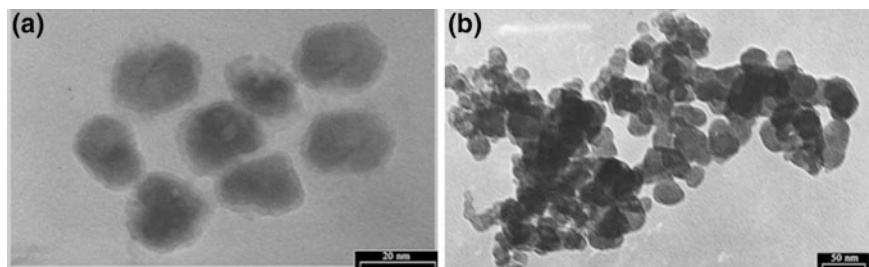


Fig. 3.29 **a** TEM images of Co_3O_4 NPs obtained in the presence of OA and TPP and **b** TEM image of Co_3O_4 NPs obtained in the presence of OA without TPP. Reproduced with permission from Ref. [130]. Copyright (2010) Elsevier

3.2 Metal Acetylacetonates

The acetylacetonate anion (acac) interacts with many metal ions to form the metal chelates containing a six-membered chelate cycle. These SSPs are one of the most promising compounds in nanomaterials preparation by thermolysis [131, 132]. The β -diketonate bidentate ligands coordinate to the metal center strongly and are believed to provide for more controlled reaction rates than monodentate ligands in the synthesis of metal oxide NPs. In the presence of surfactants, for example, OA or OAm, which form intermediate complexes with $\text{M}(\text{acac})_2$, thermolysis of these compounds leads to the formation of evenly shaped monodisperse NPs. Long-chain amines, thiols, carboxylic acids, and phosphine oxides are efficient stabilizing agents of metal NPs in different solvents, because they prevent aggregation of NPs formed during thermolysis.

3.2.1 Nickel Acetylacetonate

Nickel acetylacetonate was thermolyzed in OAm under inert atmosphere to form nanocrystals of two cubic phases and a hexagonal phase (Fig. 3.30, left) [133]. It was shown that one cubic phase was fcc metallic nickel, the other cubic phase was novel cubic nickel carbide, and the hexagonal phase was nickel carbide. It is interesting that the $\text{Ni}(\text{acac})_2 \cdot n\text{H}_2\text{O}$ released its hydrated water at ~ 373 K, then it decomposed above 509 K, and the weight steeply decreased up to 554 K (Fig. 3.30, right).

Spherical Ni NPs (23–114 nm in diameter) were prepared by thermolysis of $\text{Ni}(\text{acac})_2$ with OA and OAm both as surfactant and as solvent [61]. All samples are single-phase with fcc structure, and APS of the prepared Ni NPs increases with increasing reaction temperature (Fig. 3.31). It is important that perfect cubic symmetry can be clearly identified for the polycrystalline Ni NPs (Fig. 3.31a, inset). In addition, the HRTEM image (Fig. 3.31b) shows the granular morphology and the surface nature of magnetically dead layer.

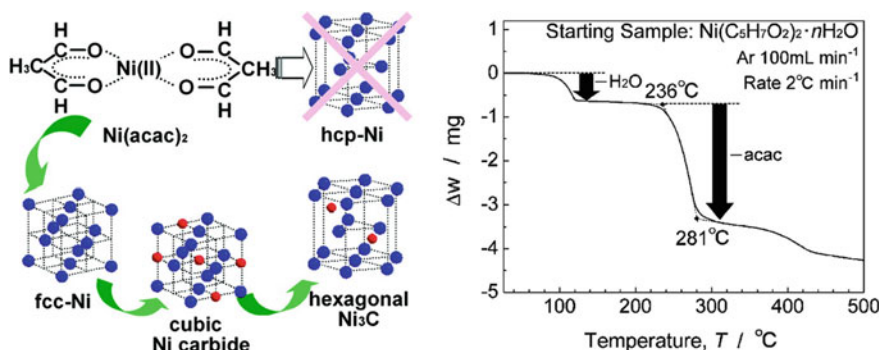


Fig. 3.30 (left) Scheme of thermolysis of Ni acetylacetonate and (right) the result of TG analysis of Ni acetylacetonate in flowing Ar gas. Reproduced with permission from Ref. [133]. Copyright (2008) American Chemical Society

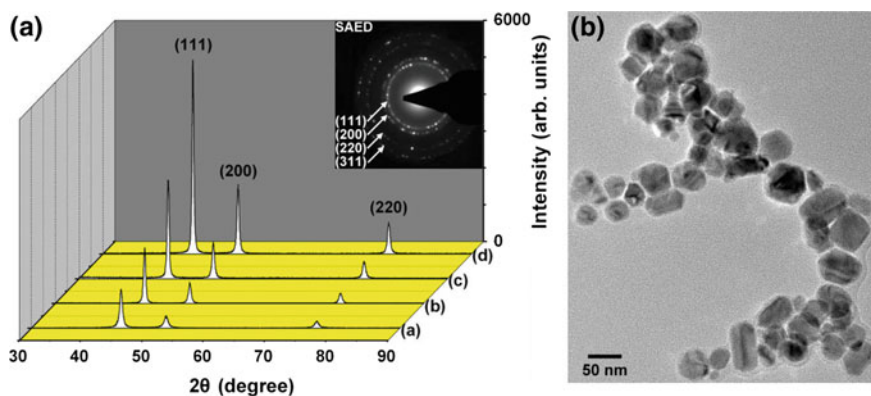


Fig. 3.31 XRD patterns (a) and HRTEM image (b). Ni NPs formed at a 513 K, b 528 K, c 543 K, and d 558 K. Selected area electron diffraction (SAED) pattern and HRTEM image relative to Ni NPs formed at 528 K. Reproduced with permission from Ref. [61]. Copyright (2004) American Chemical Society

Ni NPs were synthesized by the thermolysis of Ni acetylacetonate in OAm at 493 K with TOP as the capping agent [134]. It is important that an increase in the TOP/Ni ratio resulted in the NP size decrease.

3.2.2 Aluminum Acetylacetonate

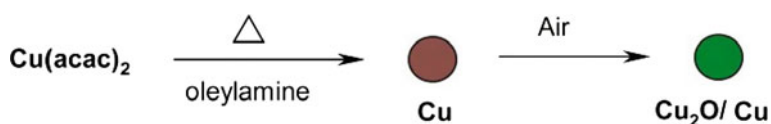
NPs of α -Al₂O₃ were prepared by thermolysis of Al(acac)₃ at 1273 K for 2 h [135]. It should be noted that the key factor for the formation of α -Al₂O₃ nanopowders is the volumetric ratio (alumina to acetylacetonate) of the SSP solutions. In addition, the

prepared nanomaterials can be modified from segregated NP to NP aggregates by reducing the volume ratio of alumina to acac from 8:2 to 5:5 in the SSP solutions.

3.2.3 Copper Acetylacetonate

Of interest are uniform Cu_2O -coated Cu NPs prepared by the thermolysis of $\text{Cu}(\text{acac})_2$ in OAm followed by air oxidation (Scheme 3.14) [136].

The prepared products are uniform 15-nm-sized copper NPs and have the polycrystalline nature (Fig. 3.32a, b). After exposure to air, the color of the NP solution changed to blue, showing the formation of copper oxide Cu_2O (Fig. 3.32c).



Scheme 3.14 Synthetic procedure for Cu_2O -coated Cu NPs. Reproduced with permission from Ref. [136]. Copyright (2004) Royal Society of Chemistry

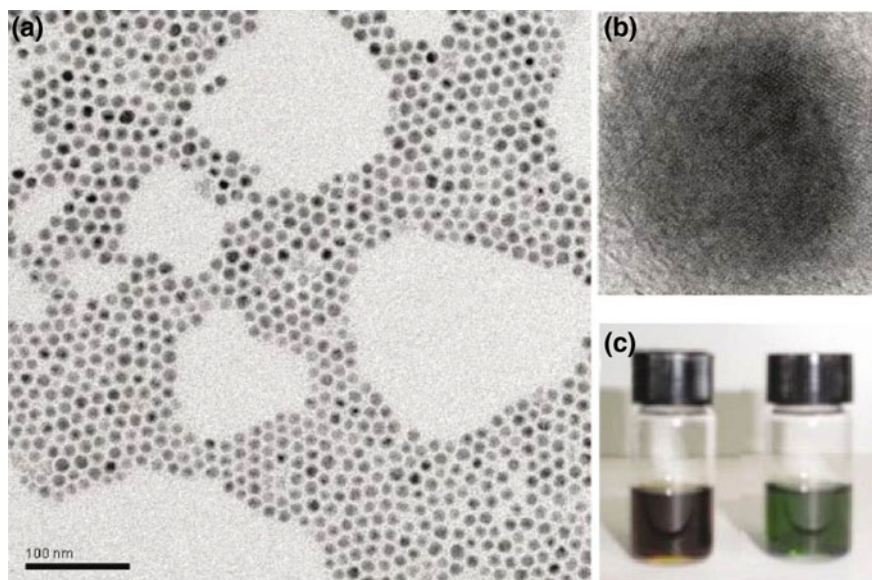


Fig. 3.32 **a** TEM and **b** HRTEM images of 15-nm Cu_2O -coated Cu NPs. **c** Photographs of the colloidal solution containing Cu NPs (left) and Cu_2O -coated Cu NPs (right). Reproduced with permission from Ref. [136]. Copyright (2004) Royal Society of Chemistry

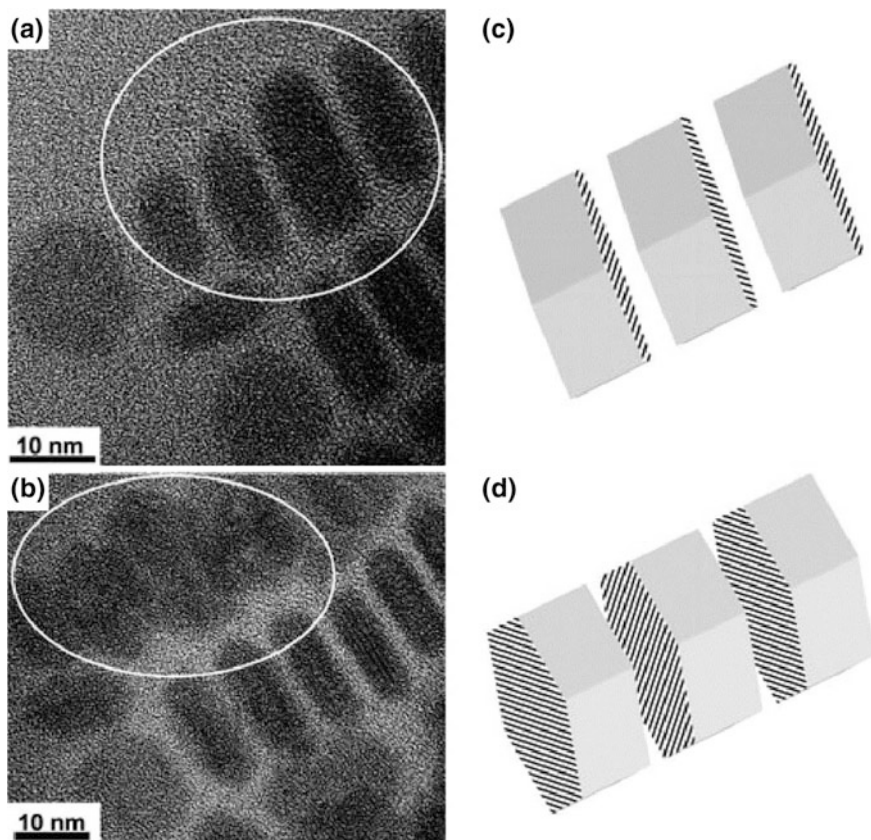
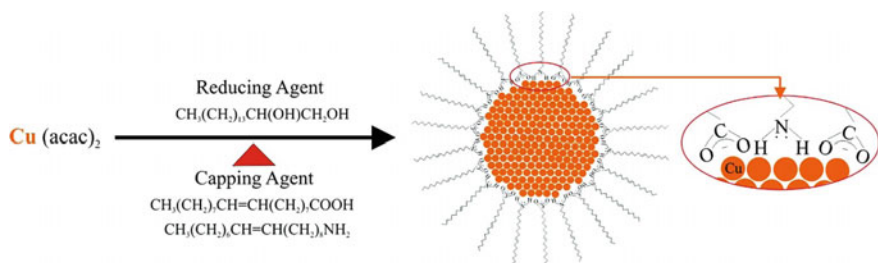


Fig. 3.33 TEM images of a row of stacked CuS nanodisks imaged at different tilt angles: **a** +18.5° and **b** -18.5° in the x direction. **c, d** Schematic illustration of the nanodisk morphology and how their overlap affects the image. Reproduced with permission from Ref. [137]. Copyright (2005) American Chemical Society

Of interest is synthesis of CuS nanodisks with APS of 15 nm by the reaction of $\text{Cu}(\text{acac})_2$ with elemental sulfur in *o*-dichlorobenzene using OAm and octanoic acid as the surfactant at 455 K for 60 min [137]. It is important that the disks lie flat on their hexagonal faces and look spherical (or hexagonal) when isolated on a substrate. At the same time, they look like rods when stacked together. In addition, tilting of the stacked disks (Fig. 3.33) confirms their disk shape.

It should be noted an interesting approach to the synthesis of size-controllable and potentially shape-controllable molecularly capped copper NPs by thermolysis of $\text{Cu}(\text{acac})_2$ [138]. It involved the regulation of reaction temperature for the synthesis of copper NPs in organic solvents in the presence of amine and acid capping agents (Scheme 3.15). Control of the reaction temperature and capping molecules allows to preparing copper NPs ranging from 5 to 25 nm with different shapes such as rods and cubes.



Scheme 3.15 Schematic illustration of the synthesis of copper NPs in the presence of capping agents in organic solvent. Reproduced with permission from Ref. [138]. Copyright (2007) American Chemical Society

3.2.4 Cobalt Acetylacetonates

The precursor $\text{Co}(\text{acac})_2$ has been thermolyzed in the presence of OA and TOP to form Co NPs (~ 3 nm) [139]. At the same time, using $\text{Co}(\text{acac})_3$ as SSP at 408 K under an Ar atmosphere allows to preparing the interesting wurtzite-type hexagonal CoO nanocrystals [140]. It is important that cubic CoO nanocrystals were prepared under similar synthetic conditions using longer reaction time at 408 K. In addition, size and shape of the CoO NPs can be regulated by changing the SSP concentration. For example, using a solution with 1:200 molar ratio of $\text{Co}(\text{acac})_3$ to OAm leads to rod-shaped CoO nanocrystals with 11 ± 1.7 nm in width and 40 ± 7.3 nm in length (Fig. 3.34a), which can be well indexed to the wurtzite structure (Fig. 3.34b). Hexagonal pyramid-shaped CoO nanocrystals of 47 ± 4.6 nm inside edge length and 24 ± 2.4 nm in basal edge length (Fig. 3.34d) were synthesized using a solution of 1:100 molar ratio of $\text{Co}(\text{acac})_3$ and OAm. It should be noted that similar shaped with larger nanocrystals of 83 ± 9.2 nm inside edge length and 42 ± 4.5 nm in basal edge length (Fig. 3.34e) was grown from a 1:50 molar ratio solution.

3.2.5 Zirconium Acetylacetonate

Pure zirconium oxide nanocrystals were successfully prepared via thermolysis of precursor $[\text{Zr}(\text{acac})_3(\text{H}_2\text{O})_2](\text{NO}_3)$ in coordinating solvent of OA or PEG and TPP [141].

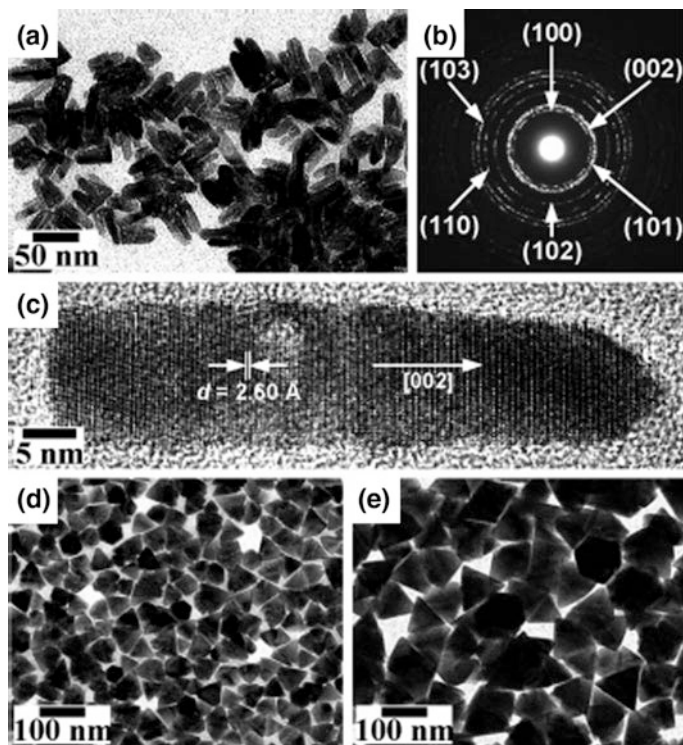


Fig. 3.34 TEM micrographs of hexagonal CoO nanocrystals: **a** TEM image, **b** SAED pattern, and **c** HRTEM image of rod-shaped nanocrystals with average width of 11 ± 1.7 nm and average length of 40 ± 7.3 nm. TEM images of hexagonal pyramid-shaped nanocrystals with average side edge lengths of **d** 47 ± 4.6 nm and **e** 83 ± 9.2 nm. Reproduced with permission from Ref. [140]. Copyright (2005) American Chemical Society

3.2.6 Zinc Acetylacetonate

$\text{Zn}(\text{acac})_2$ was used as SSP to prepare ZnO NPs by thermolysis with the different combinations of TPP and OAm as surfactants to control the NP size (Fig. 3.35, left) [142]. The synthesized ZnO NPs have a hexagonal zincate structure with diameter in the range of 12–20 nm (Fig. 3.35, right).

3.2.7 Manganese Acetylacetonate

Thermolysis of $\text{Mn}(\text{acac})_2$ in OAm leads to size-controlled nanocrystals of two different manganese oxides, Mn_3O_4 and MnO [143]. The product shows nearly monodisperse spherical NPs of 10 nm in diameter (Fig. 3.36a) having the highly

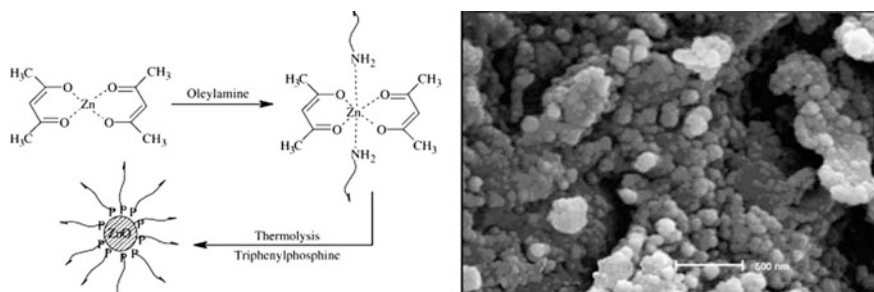


Fig. 3.35 (left) Synthesis of ZnO NPs by thermolysis of $\text{Zn}(\text{acac})_2$ and (right) SEM image of ZnO NPs. Reproduced with permission from Ref. [142]. Copyright (2008) Elsevier

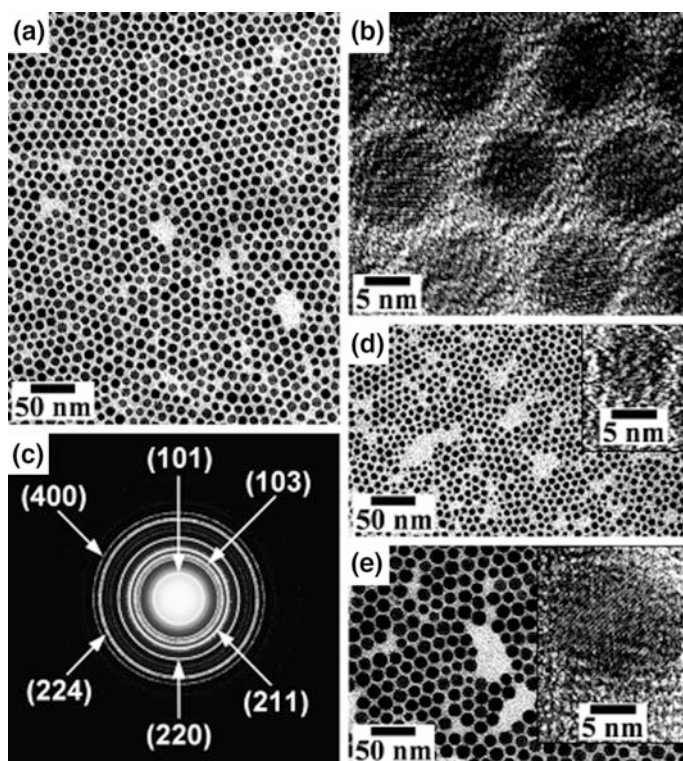


Fig. 3.36 TEM micrographs of Mn_3O_4 NPs: **a** TEM image, **b** HRTEM image, and **c** an SAED pattern of 10 nm NPs. TEM images of **d** 6 nm and **e** 15 nm NPs. HRTEM images are shown in the insets. Reproduced with permission from Ref. [143]. Copyright (2004) John Wiley and Sons

crystalline nature (Fig. 3.36b). It is important that the particle size can be easily regulated by a change in the thermolysis temperature. For example, smaller NPs of 6 nm in diameter were prepared at 423 K (Fig. 3.36d) and larger NPs of 15 nm in

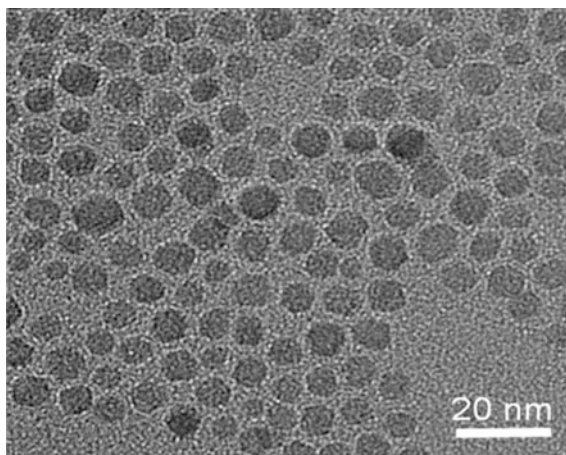
diameter were synthesized at 523 K (Fig. 3.36e). An interesting observation was made during adding water to the reaction slurry of $\text{Mn}(\text{acac})_2$ in OAm (1:24 molar ratio). As a result, only pure cubic MnO was prepared without contamination by Mn_3O_4 .

It should be noted the preparation of an ordered (predominantly cubic) 3D array of monodispersed Mn_3O_4 NPs (diameter ca. 8 nm) with the core-shell structure by thermolysis of $\text{Mn}(\text{acac})_2$ in OAm [144]. It is interesting that these particles have a highly crystalline Mn_3O_4 core encapsulated within a thin shell of MnO_2 , which is capped by OAm.

3.2.8 Iron Acetylacetonates

Highly monodisperse iron oxide NPs with high crystallinity and uniform size distribution were synthesized on a large scale by thermolysis of $\text{Fe}(\text{acac})_3$ in a hot surfactant solution [145–155]. Thermolysis of $\text{Fe}(\text{acac})_3$ with 1,2-hexadecanediol in the presence of OA and OAm leads to monodisperse magnetite (Fe_3O_4) NPs with a cubic spinel structure, whose diameter can be tuned from 3 to 20 nm by a change of thermolysis conditions or by seed-mediated growth [156]. It is important that the hydrophobic NPs can be converted into hydrophilic ones by adding bipolar surfactants. Water-dispersible magnetite NPs were directly obtained using thermolysis of $\text{Fe}(\text{acac})_3$ in triethylene glycol (TEG), which plays a triple role as high-boiling solvent, reducing agent, and stabilizer, as well as can prevent from interparticle aggregation [157]. Fe_3O_4 NP sizes prepared from $\text{Fe}(\text{acac})_3$ via solvent-free thermolysis method increase with increasing temperature and reaction time [157]. Monodisperse 8-nm Fe_3O_4 NPs (Fig. 3.37) were synthesized by the thermolysis of $\text{Fe}(\text{acac})_3$ in OAm and then were deposited onto *n*-type silicon wafer [158].

Fig. 3.37 A representative TEM image of Fe_3O_4 NPs. Reproduced with permission from Ref. [158]. Copyright (2016) Elsevier



Thermolysis of $\text{Fe}(\text{acac})_3$ in the presence of OA, OAm, and a series of alcohols was shown to be economically attractive alternative for the synthesis of iron oxide NPs without compromising their size and shape control [159]. It is important that the relative cost for the preparation of Fe_3O_4 NPs is reduced to only 21% and 9% of the original cost when using 1,2-octanediol and cyclohexanol, respectively. It should be noted that the thermolysis carried out in the presence of OAm, as the only one stabilizing agent, led to a material with a poor morphology and size control, while in the presence of OA, as the only one stabilizing agent, a material with better dispersion was obtained. The same synthesis with a mixture of OA and OAm (without 1,2-alkanediol) gives a product with quite a uniform size distribution of NPs, which shows faceted NPs with a mean diameter of 9.0 nm. It is interesting that the thermolysis in the presence of OA, OAm, and 1,2-octanediol resulted in reproducible products with well-dispersed spherical-shaped NPs of 5.5 nm with narrow size distribution.

Of interest is a low-cost route for synthesis of NPs with sizes from 7 to 10 nm by thermolysis of $\text{Fe}(\text{acac})_3$ at temperature as low as 443 K in dibenzyl ether and OAm (Fig. 3.38a) [160]. The NP size was tunable by varying the volumetric ratio of benzyl ether and OAm (Fig. 3.38b, c).

It should be noted the preparation of Fe_3O_4 nanoflowers with diameters of 42 ± 8 , 30 ± 5 , and 19 ± 3 nm (Fig. 3.39a–c) by thermolysis of the mixture of $\text{Fe}(\text{acac})_3$, PEG bis(carboxymethyl) ether, OAm, and phenyl ether in solution [161]. It is important that Fe_3O_4 nanoflowers consist of clusters connected in three dimensions (Fig. 3.39d) and the average diameters of the primary Fe_3O_4 NPs in the nanoflowers are approximately 4.3 nm (42-nm Fe_3O_4 nanoflowers), 4.8 nm (30-nm Fe_3O_4 nanoflowers), and 4.5 nm (19-nm Fe_3O_4 nanoflowers), respectively.

Large iron oxide nanocubes from 20 to 160 nm were obtained by the thermolysis of $\text{Fe}(\text{acac})_3$ in the presence of OA and benzyl ether at 563 K [162]. The prepared nanocubes have a uniform edge length of 79 nm (Fig. 3.40a) and the highly crystalline nature (Fig. 3.40a, inset). It is important that the dimensions of the nanocubes could be regulated by a change of the thermolysis conditions, for example, the amount of benzyl ether. Thus, reducing the amount of benzyl ether to 5.2 g and increasing the reaction time to 1 h led to ~ 110 -nm-sized particles composed of truncated cubes and truncated octahedra (Fig. 3.40b). At the same time, when the thermolysis time increased to 1.5 and 2 h, the particles grew to a larger size and more perfect cubic shape with edge dimensions of 150 nm (Fig. 3.40c) and 160 nm (Fig. 3.40d), respectively. In addition, using 4-biphenylcarboxylic acid and OA at keeping all the other thermolysis conditions, the smaller 22-nm-sized nanocubes were obtained (Fig. 3.40e). The overall evolution of NP shapes is illustrated in Fig. 3.40f.

Among the other interesting examples, we note the preparation of single crystalline iron oxide NPs with few defects and similar physical properties by introducing molecular oxygen as one of the reactive species in the thermolysis process [163]. Of interest is also the preparation of nanosized iron(III) oxide by thermolysis of $\text{Fe}(\text{acac})_3$ using diphenyl ether as a dispersion medium [164]. In particular, it has been shown that at low-temperature thermolysis (453 K) the obtained particles

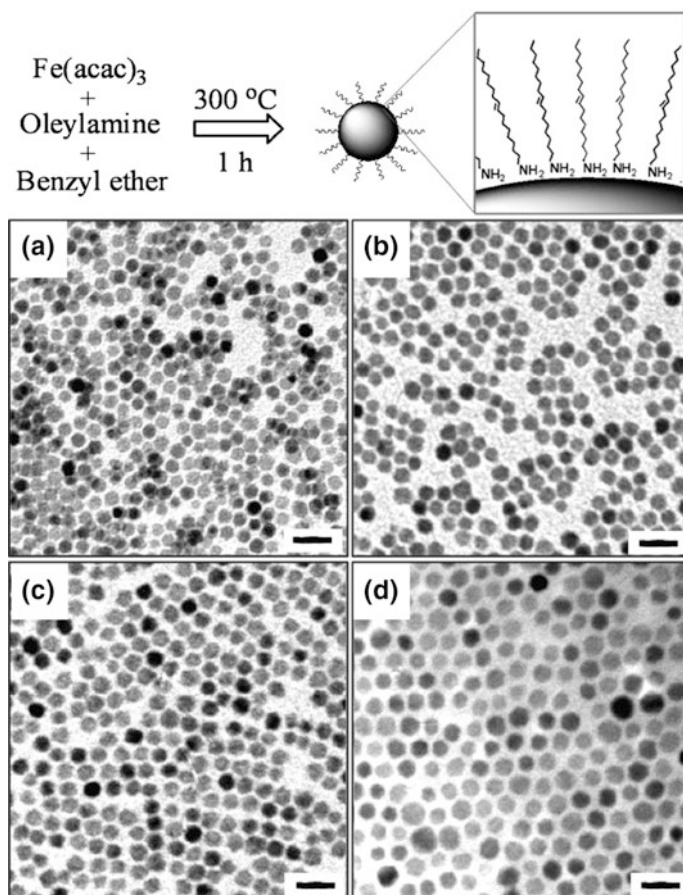


Fig. 3.38 (top) Schematic illustration of the synthetic process. (down) TEM images of Fe_3O_4 NPs: **a** 7 ± 0.5 nm, **b** 8 ± 0.4 nm, **c** 9 ± 0.6 nm, and **d** 10 ± 0.8 nm. Scale bar is 20 nm. Reproduced with permission from Ref. [160]. Copyright (2009) American Chemical Society

differ in form and there is a trend to form particles of triangle shape with APS of 12–15 nm (Fig. 3.41a). Increase in thermolysis temperature leads not only to decrease of APS but also formation of particles of uniform shape (Fig. 3.41b). In addition, increasing thermolysis temperature from 453 to 523 K provides more than twofold decrease of APS of iron(III) oxide particles (Fig. 3.41c).

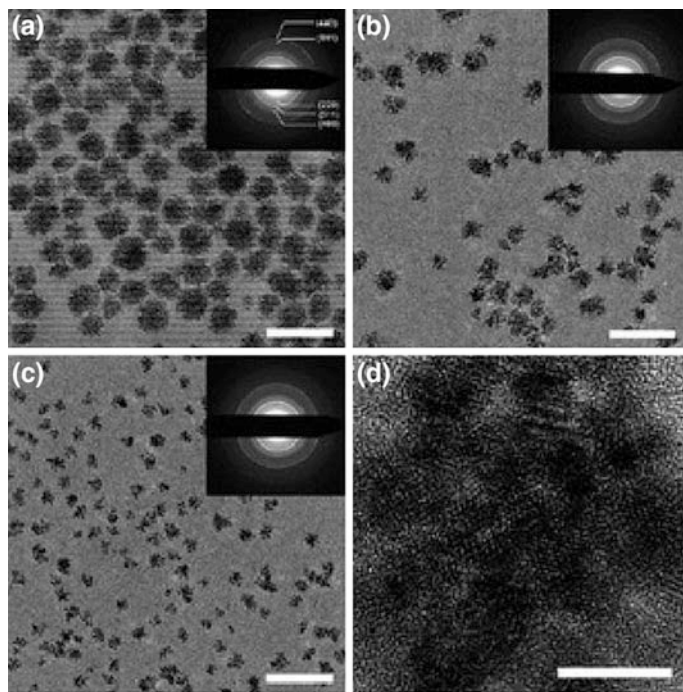


Fig. 3.39 a–c TEM images of a 42 nm, b 30 nm, and c 19 nm Fe_3O_4 nanoflowers. Insets are electron diffraction patterns. Scale bar 100 nm. d HRTEM image of 30 nm Fe_3O_4 nanoflowers. Scale bar 10 nm. Reproduced with permission from Ref. [161]. Copyright (2010) Royal Society of Chemistry

3.2.9 Cadmium Acetylacetonate

Of interest is the formation of CdO thin films by thermolysis of cadmium hexafluoroacetylacetonate dihydrate [165, 166]. This process was carried out in a low-pressure horizontal hot-wall reactor on optically transparent SiO_2 substrates. The prepared products consist of highly oriented cubic crystals.

3.2.10 Gold Acetylacetonate

The gold NPs of variable sizes were obtained by thermolysis of gold(I) complexes, such as $\text{Au}(\text{acac})\text{PPh}_3$, in coordinating solvents [167]. The advantage of this method is the control of the NP's growth rate by selection of the SSP, the stabilizer, the thermolysis temperature, and time. In particular, a time-dependent growth of gold NPs was observed during the thermolysis of $\text{Au}(\text{acac})\text{PPh}_3$ in the presence of HDA and TOPO in diphenyl ether (Fig. 3.42, left). When the as-prepared NPs have diameters less than 15 nm, they are relatively monodisperse in size (Fig. 3.42, right).

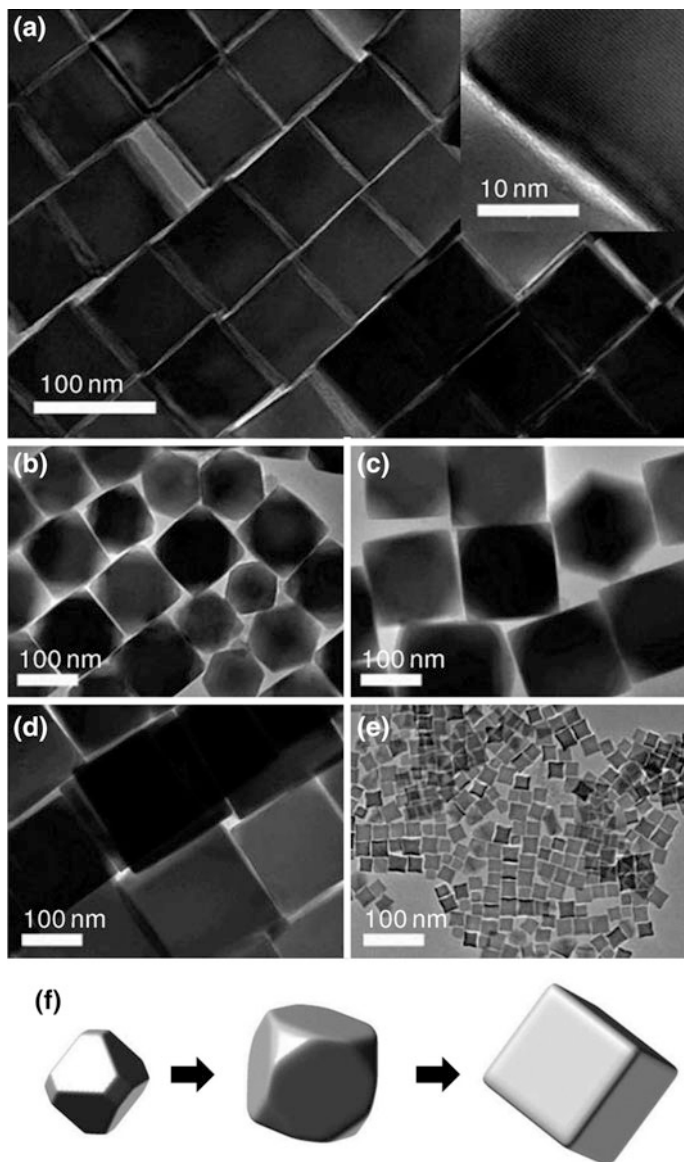


Fig. 3.40 TEM images of **a** 79-nm-sized Fe_3O_4 nanocubes (*inset* HRTEM image); **b** mixture of truncated cubic and truncated octahedral NPs with an average dimension of 110 nm; **c** 150-nm-sized truncated nanocubes; **d** 160-nm-sized nanocubes; **e** 22-nm-sized nanocubes. **f** Schematics showing the overall shape evolution of the Fe_3O_4 NPs. Reproduced with permission from Ref. [162]. Copyright (2008) American Chemical Society

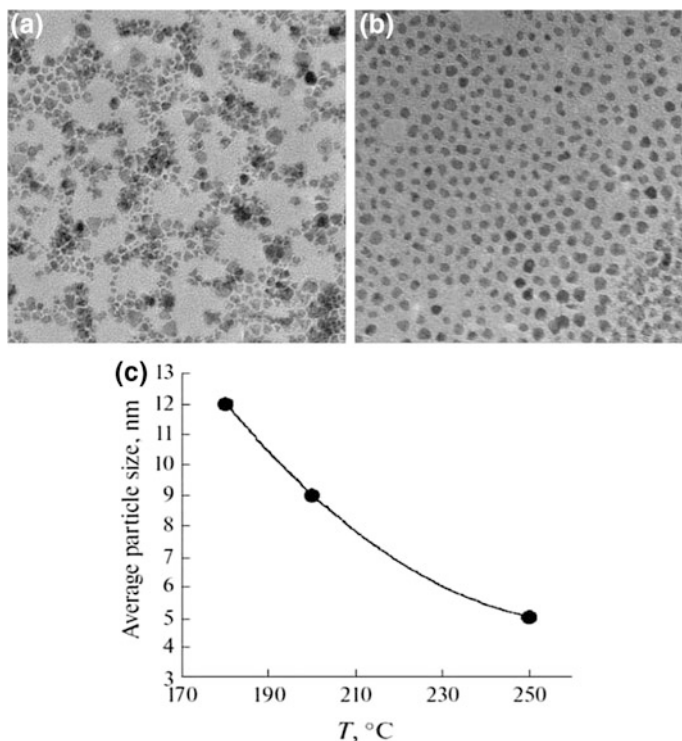


Fig. 3.41 TEM image of nano-Fe₂O₃: **a** thermolysis at 453 K, **b** thermolysis at 523 K, dependence of APS on thermolysis temperature (c). Reproduced with permission from Ref. [164]. Copyright (2016) Springer Nature

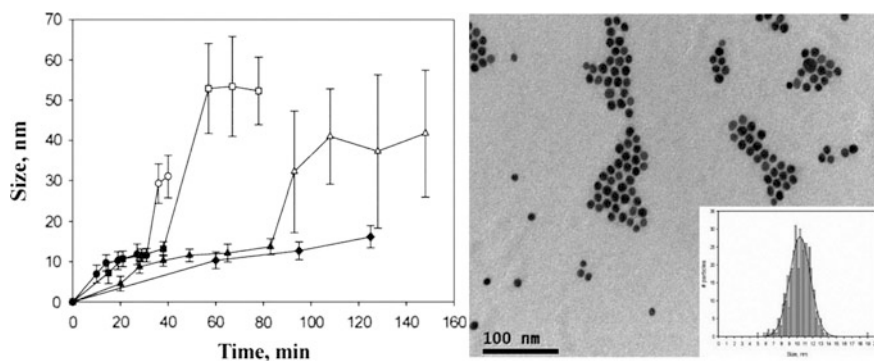


Fig. 3.42 (left) Evolution of APS over time for samples containing 0% (dot), 25% (filled square), 50% (filled triangle), and 75% (filled diamond) TOPO. Size increases until about 15 nm (closed symbols), at which point particles become destabilized and aggregation occurs (open symbols). At this point, particle dispersities also dramatically increase, (right) Representative TEM image of Au NPs removed from a 50:50 mixture of TOPO and HDA after 38 min. Particle size was calculated to be 10.2 ± 1.4 nm. The inset shows a histogram calculated from 465 particles measured from different areas on the TEM grid. Reproduced with permission from Ref. [167]. Copyright (2004) American Chemical Society

3.2.11 Platinum Acetylacetonate

Pt nanocubes were synthesized from the thermolysis of $\text{Pt}(\text{acac})_2$ in the organic phase with gaseous CO [168]. In this process, CO is capable of serving as both a reducing agent and a capping agent for structure control. In particular, the presence of CO may account for the expression of $\{100\}$ facets and nanocube formation. The similar results were obtained during the study of the thermolysis of $\text{Pt}(\text{acac})_2$ in OAm and OA when tungsten hexacarbonyl $\text{W}(\text{CO})_6$ served as the source of CO [169].

It should be noted that the GRAILS method (gas reducing agent in liquid solution) is a common method for the formation of metallic nanocrystals with a controlled shape [170]. For example, $\text{Pt}(\text{acac})_2$ was reduced by CO and saturated in a solution containing dodecylamine, OA, and $\text{Y}(\text{acac})_3$ as a cocapping agent to form the Pt icosahedra (Fig. 3.43a) [171]. It is interesting that without CO, hyperbranched Pt structures are formed (Fig. 3.43b). At the same time, maintaining a CO atmosphere with simultaneous slowing the nucleation process via temperature control facilitated the formation of single crystalline Pt octahedra or cuboctahedra (Fig. 3.43c) whereas incomplete degassing prior to CO addition led the formation of Pt octapods (Fig. 3.43d).

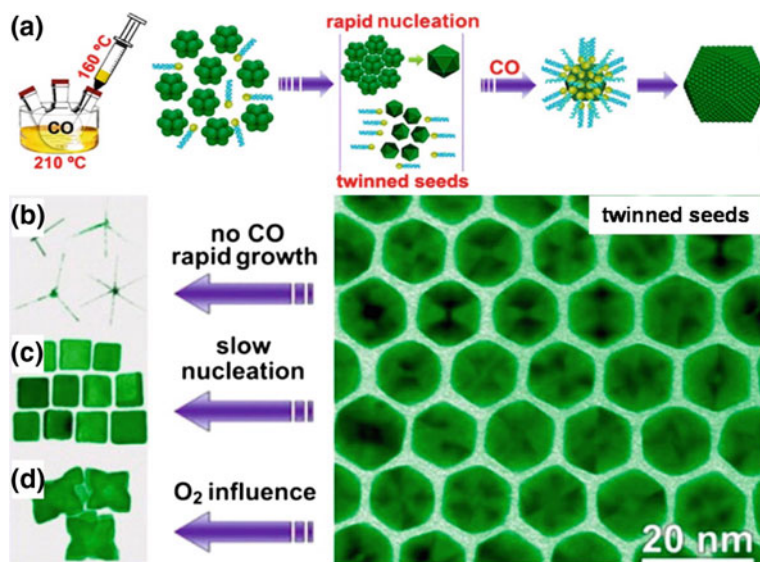
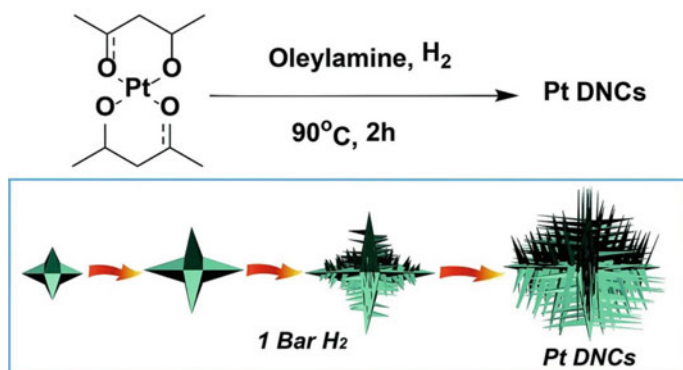


Fig. 3.43 a Schematic of the monodisperse Pt icosahedra synthesis using GRAILS and the corresponding TEM image (bottom right). TEM images of (b) hyperbranched Pt nanostructures synthesized with the omission of CO, c Pt nanocubes synthesized by slowing the nucleation process but maintaining a CO atmosphere, and d Pt octapods synthesized under conditions in which degassing prior to CO addition was incomplete. Reproduced with permission from Ref. [171]. Copyright (2011) American Chemical Society



Scheme 3.16 Illustration of the formation of Pt dendritic nanocubes (DNCs). Reproduced with permission from Ref. [172]. Copyright (2015) Royal Society of Chemistry

Pt dendritic nanocubes were successfully synthesized in OAm under a 1 bar H₂ atmosphere via thermolysis of Pt(acac)₂ (Scheme 3.16) [172].

3.2.12 Palladium Acetylacetonate

Of interest is the study of the formation of Pd nanostructures using palladium acetylacetonate and palladium hexafluoroacetylacetonate as SSPs in OAM to evaluate the role of the local ligand environment [173–177]. During thermolysis, all SSPs gave polycrystalline Pd nanodendrites formed via the aggregation of smaller, single crystalline Pd NPs (Fig. 3.44a). Adding softer ligands (phosphines) to the Pd (acac)₂–OAM system [173] leads to a significant morphology change as single crystalline quasi-spherical Pd NPs are produced rather than polycrystalline Pd nanodendrites (Fig. 3.44b). A more stable complex is formed by coordination to the Pd(II) center, and nucleation is delayed by 22 h.

The different shapes of palladium NPs were obtained by thermolyzing a mixture of OAM, formaldehyde, and Pd(acac)₂ in an autoclave at 373 K for 8 h (Fig. 3.45) [176]. In particular, the formation of the icosahedron (an edge length of 8.8 ± 0.6 nm), decahedron (an edge length of 10.3 ± 0.8 nm), octahedron (an edge length of 6.6 ± 0.5 nm), tetrahedron (an edge length of 12.9 ± 1.4 nm), and triangular plate (an edge length of 17.3 ± 4.1 nm) was shown.

It should be noted the thermolysis of Pd(acac)₂ with OAM as both the capping agent and solvent in an argon atmosphere at 403 K [178]. In this case, Pd nanostructures with branched morphology 10–20 nm across and composed of smaller spherical crystallites with diameters of about 4 nm were prepared (Fig. 3.46a–c). It is important that APS was equal to 4.37 nm, and the discrete Pd particles were formed in the early stages of the thermolysis.

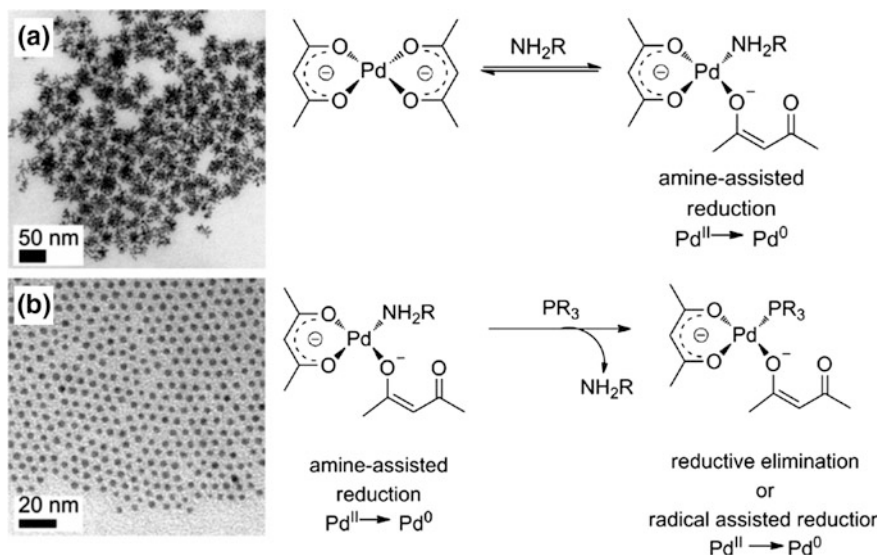
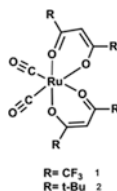


Fig. 3.44 **a** TEM image of dendritic Pd structures generated from heating $\text{Pd}(\text{acac})_2$ in OAm, which serves as a reducing agent, capping agent, and solvent. The amine-assisted reduction to Pd (0) is facilitated by the coordination of OAm to the SSP, and the subsequent weak binding of OAm to the generated quasi-spherical 5 nm subunits facilitates larger branched structures via aggregation. **b** TEM image of sub-10-nm spherical Pd NPs formed upon addition of an extraneous ligand, TOP, in the presence of $\text{Pd}(\text{acac})_2$ and OAm. Reproduced with permission from Ref. [173]. Copyright (2012) John Wiley and Sons

3.2.13 Ruthenium Acetylacetonates

Ruthenium acetylacetonates are the promising SSPs in CVD for the formation of different ruthenium films [179]. As a typical example, we consider the acetylacetonates **1–2** as CVD precursors [180].



The complexes **1** and **2** were used as SSPs for preparing ruthenium thin film at temperatures of 623–723 K under H_2 atmosphere or at temperatures of 548–673 K using a 2% mixture of O_2 in argon as carrier gas. It is interesting that using complex **1** under 100% O_2 atmosphere, conductive RuO_2 thin films with the lowest resistivity ($156 \mu\Omega \text{ cm}$) were deposited at a preferred (200) orientation at 623 K. In addition, the controlled partial pressure of oxygen (i.e., 2%) and accurate control of

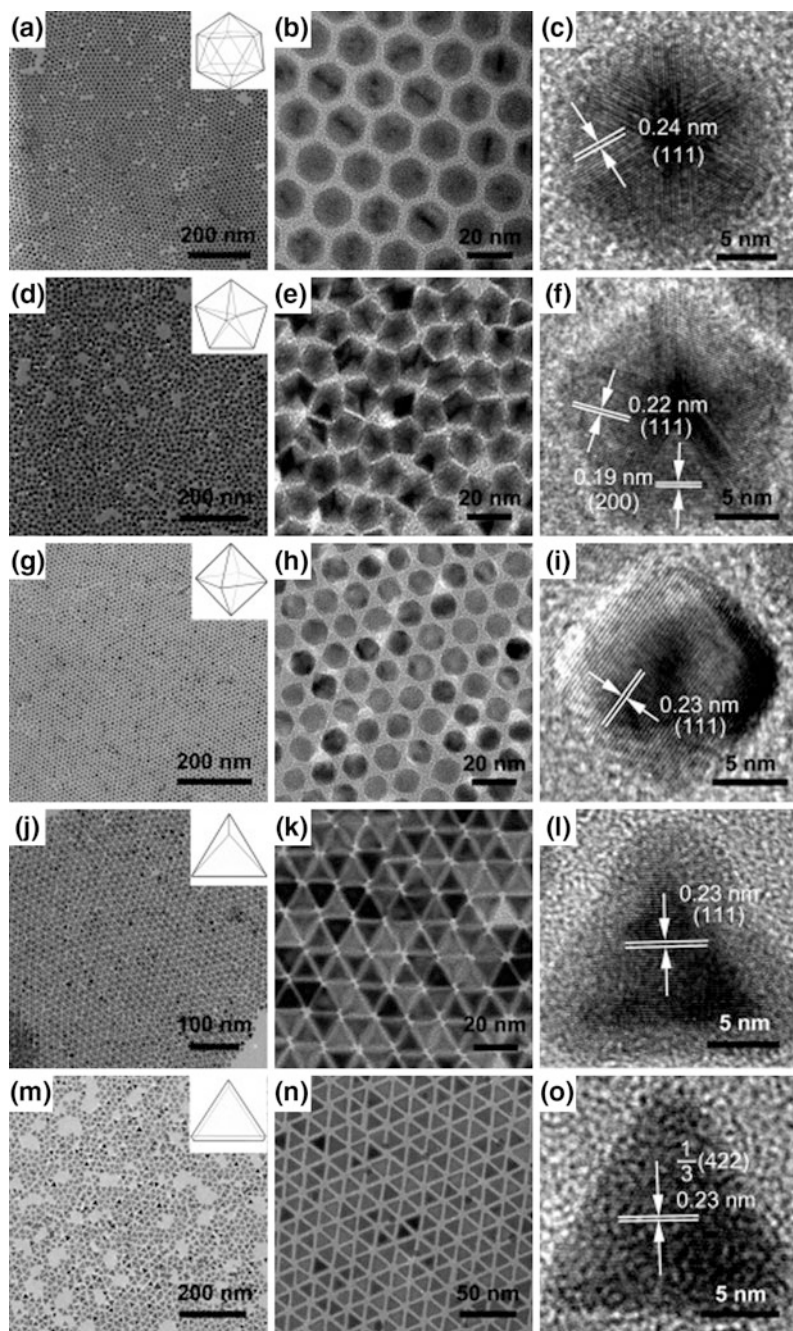


Fig. 3.45 TEM images of Pd NPs with different shapes: **a–c** icosahedron, **d–f** decahedron, **g–i** octahedron, **j–l** tetrahedron, and **m–o** triangular plate. Reproduced with permission from Ref. [176]. Copyright (2011) John Wiley and Sons

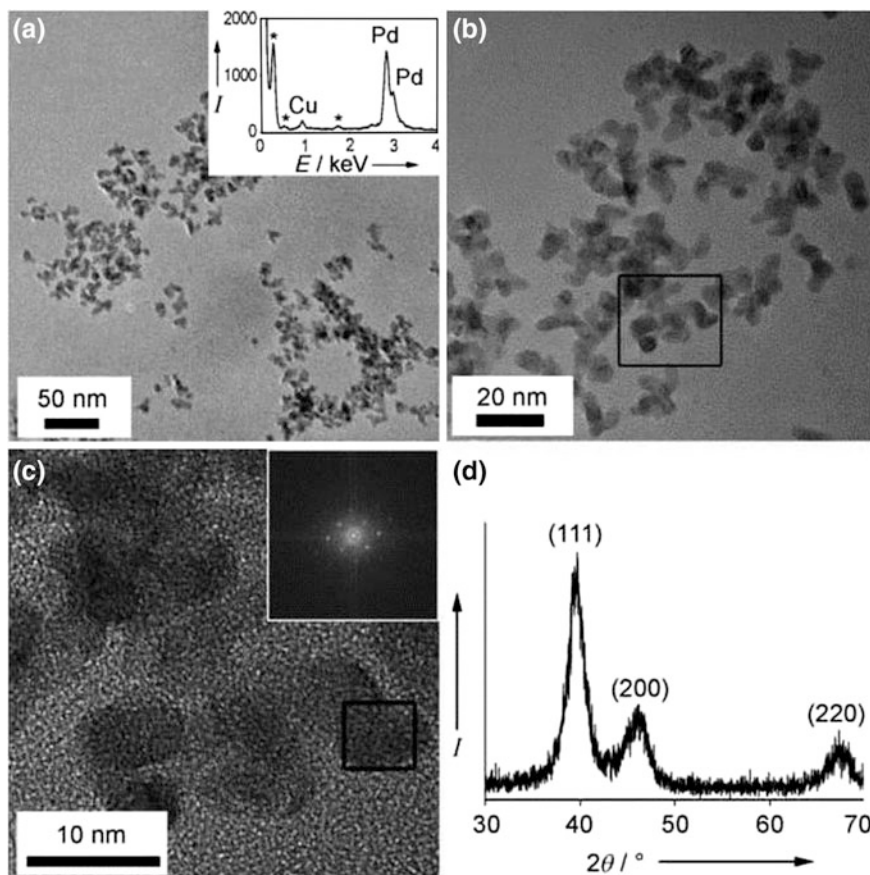


Fig. 3.46 Characterization of Pd nanodendrites synthesized by the thermolysis of $\text{Pd}(\text{acac})_2$ in the presence of OAm: **a** TEM image and corresponding EDX analysis (inset); the Cu signal arises from the TEM grid, and * denotes signals from the sample holder; **b** higher magnification TEM image of (a); **c** HRTEM image of the selected area denoted in (b), with FFT of the selected area (inset) in (c); and **d** powder XRD pattern of Pd nanodendrites. Reproduced with permission from Ref. [178]. Copyright (2014) American Chemical Society

the deposition temperature are key factors for the formation of pure thin films. In particular, a higher partial pressure of O_2 and higher temperature lead to a mixture of Ru and RuO_2 thin films (Table 3.3) [180].

Of interest is the study of the initial growth of Ru on Si (100) surfaces from Ru $(\text{L})_2(\text{CO})_2$, where L is hexafluoroacetylacetonate anion, in a temperature range of $548 \leq T \leq 623$ K [181]. It turned out that the nucleation rate increases with increasing substrate surface termination sites and the Volmer–Weber growth dominates the initial stage of the deposition of the growing film. The nuclei

Table 3.3 Experimental data of CVD experiments

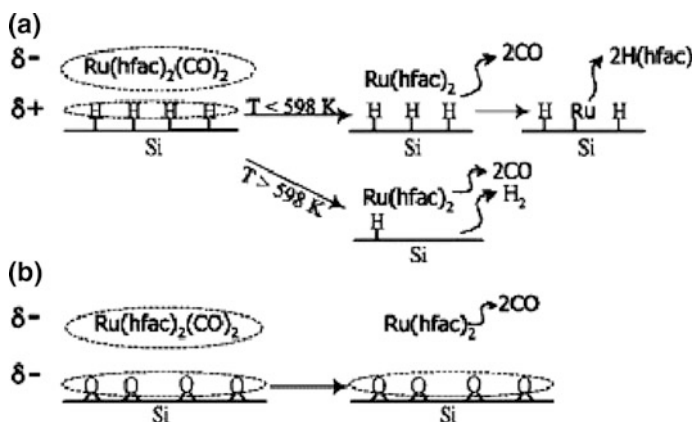
Source	CGFR (sccm)	T_s (K)	T_D / K	P_s (Torr)	Thickness (Å)	D rate (Å min ⁻¹)	Resistivity ρ ($\mu\Omega$ cm)
1	H ₂ (20)	28	623	5	1600	23	618
1	H ₂ (20)	28	673	5	3200	46	39
1	H ₂ (20)	28	723	5	4800	69	26
1	O ₂ (2%)/Ar (10)	50	573	5	600	12	34
1	O ₂ (2%)/Ar (10)	50	623	5	1450	28	15
1	O ₂ (2%)/Ar (10)	50	673	5	5000	96	37
2	O ₂ (2%)/Ar (10)	80	548	1	1400	31	206
2	O ₂ (2%)/Ar (10)	80	598	1	1600	36	111
2	O ₂ (2%)/Ar (10)	80	648	1	3000	67	24
1	O ₂ (10)	25	573	5	1600	80	218
1	O ₂ (10)	25	623	5	4800	240	156
1	O ₂ (10)	25	673	5	5400	270	170

CGFR carrier gas flow rate, T_s source temperature, T_D deposition temperature, P_s initial system pressure, D rate deposition rate

formation process proceeds with lower activation energy on H-terminated surface (5 kcal mol⁻¹) than on the oxide surface (11 kcal mol⁻¹). In addition, the deposition is controlled by L dissociation step due to high dissociation energy for Ru-L (241 kcal mol⁻¹) compared to Ru-CO (57 kcal mol⁻¹). The proposed surface chemistry mechanism is shown in Scheme 3.17.

3.2.14 Indium Acetylacetonate

It should be noted the preparation of colloidal, highly crystalline, and size-controlled indium oxide NPs by thermolysis of the In(acac)₃ in the presence of OAm as a stabilizing surfactant [182]. Using a 1:12 molar ratio of In(acac)₃/OAm, nearly monodisperse spherical NPs with diameter of 6 nm were obtained (Fig. 3.47a). The In₂O₃ NPs formed have the highly crystalline nature (Fig. 3.47b). It is interesting that a 3D close-packed In₂O₃ superlattice is observed in the case a sample obtained with a concentrated dichloromethane solution of In₂O₃ NPs (Fig. 3.47c). In addition, the SAED of the NPs is consistent with cubic In₂O₃ with strong ring patterns (Fig. 3.49d).



Scheme 3.17 Reaction mechanism proposed for $\text{Ru}(\text{L})_2(\text{CO})_2$ on both **a** H-terminated and **b** OH-terminated $\text{Si}(100)$ surfaces. Reproduced with permission from Ref. [181]. Copyright (2005) Elsevier

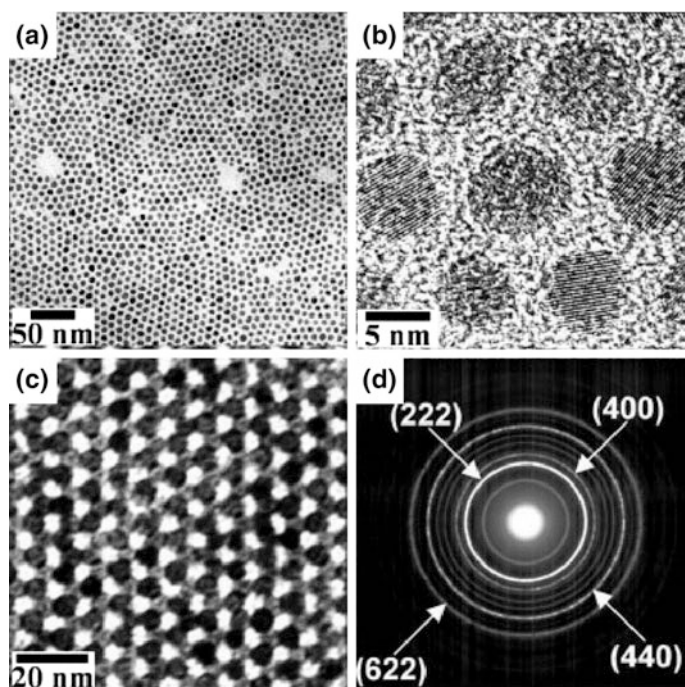


Fig. 3.47 TEM micrographs of 6-nm In_2O_3 NPs: **a** TEM image of a monolayer assembly, **b** HRTEM image, **c** TEM image of a 3D superlattice, **d** SAED pattern. Reproduced with permission from Ref. [182]. Copyright (2003) John Wiley and Sons

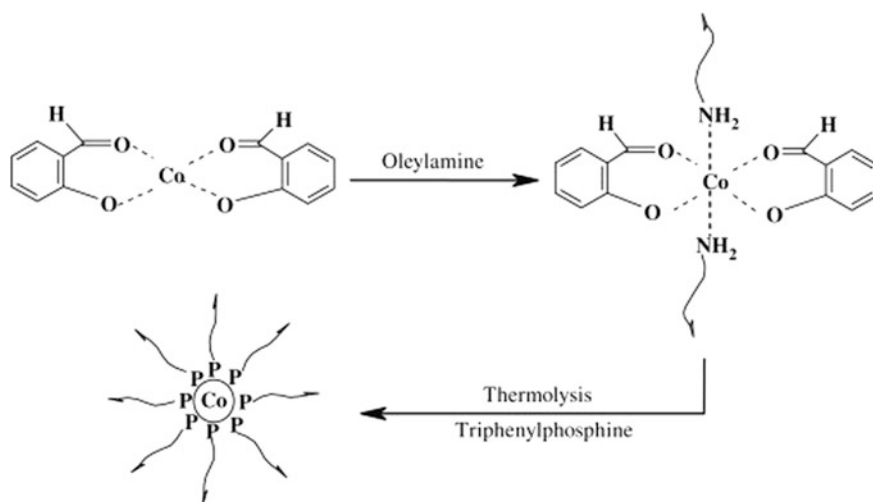
3.3 Metal Chelates Based on Other O,O-Donor Ligands

In addition to the metal carboxylates and acetylacetonates considered above, a number of other metal chelates with O,O-donor ligands were used as SSPs for the thermolysis. We consider the most typical examples.

3.3.1 Metal Salicylaldehydates

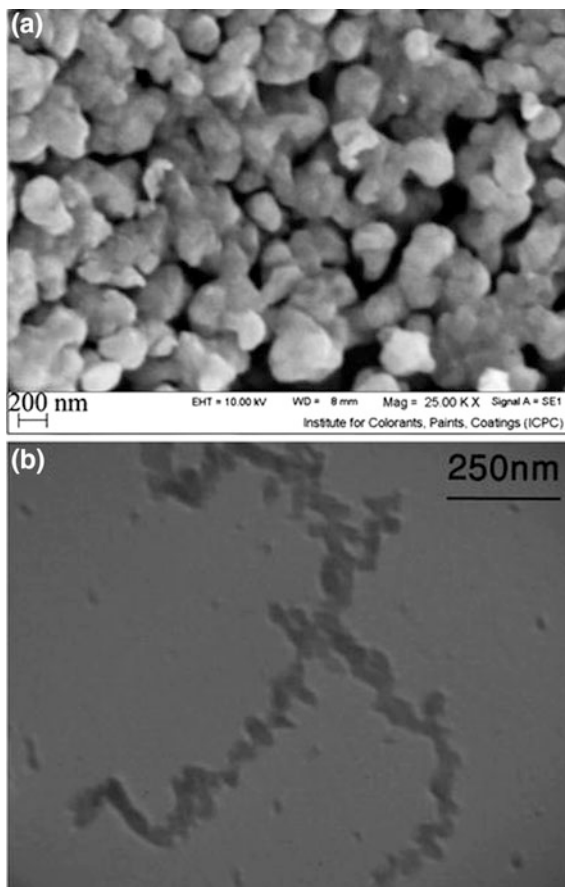
Cobalt NPs of diameter 25–35 nm were prepared by thermolysis of CoL_2 , where HL is salicylaldehyde, without any additional reducing agents [183]. The use of different combinations of TPP and OAm as surfactants allows to tuning the particle size (Scheme 3.18). It is interesting that the addition of TPP into the mixture of OAm and CoL_2 as an additional surfactant reduced the particle size and resulted in uniform size distribution. In its turn, OAm as a ligand binds tightly on the metal NPs surface accompanied by TPP, thus providing a more profound effect than that of individual contribution. The morphology of cobalt NPs was spherical in shape, and primary NPs were single crystals of nearly uniform size.

In another interesting example, cubic-phase Co_3O_4 NPs with the size of mostly 20–30 nm were produced by thermolysis of the CoL_2 in air at 773 K for 5 h [184]. The diameter of the quasi-spherical NPs is 25 nm. It is important that the prepared particles were dense agglomerates with uniform size (Fig. 3.48).



Scheme 3.18 Overall synthetic procedure for Co NP synthesis. Reproduced with permission from Ref. [183]. Copyright (2008) Elsevier

Fig. 3.48 **a** SEM and **b** TEM images of Co_3O_4 NPs. Reproduced with permission from Ref. [184]. Copyright (2012) Springer Nature



It should be noted the preparation of Mn_3O_4 NPs by thermolysis of MnL_2 [185]. Depending on thermolysis conditions, the Mn_3O_4 NPs were formed with different size distribution and morphologies. In particular, mixing and heating MnL_2 and OAm led to the Mn_3O_4 NPs (10–15 nm), and the obtained NPs were irregular, but not monodispersed. At the same time, to obtain the monodispersed Mn_3O_4 NPs, TPP, as a stabilizing agent, was injected into the solution at 373 K for 90 min. Uniform-shaped Mn_3O_4 NPs were prepared with APS of 20–30 nm (Fig. 3.49).

Of interest is the preparing CdS NPs by thermolysis of CdL_2 with elemental sulfur in OAm [186]. This method allows to obtaining different morphologies of CdS, including NPs, long, and short nanorods. It is important that shape and size of the prepared nanomaterials were changed by increasing the SSP concentration (Table 3.4).

Thermolysis of $[\text{Zr}(\text{L})_3(\text{H}_2\text{O})_2](\text{NO}_3)$ in OAm was used for obtaining single-phase ZrO_2 ceramics with a cubic shape (Scheme 3.19) [187].

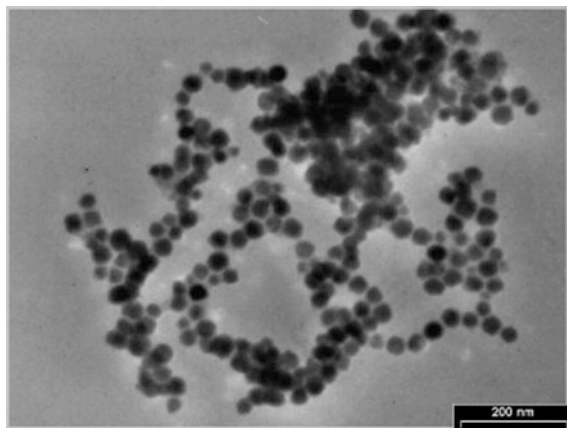
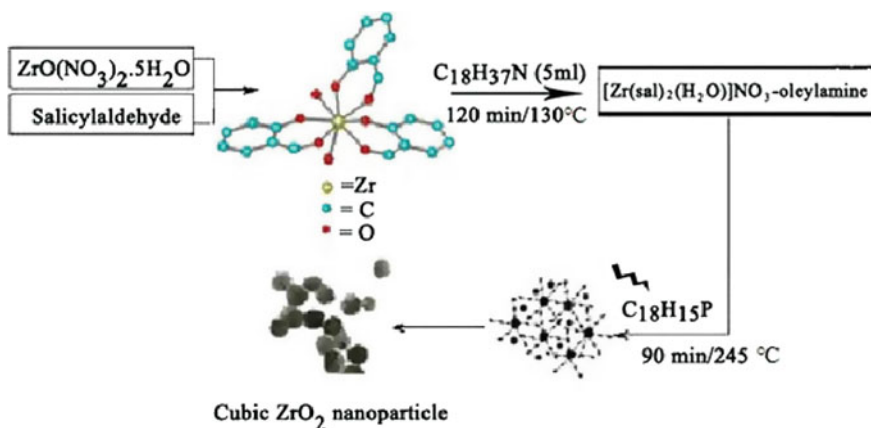


Fig. 3.49 TEM image of Mn_3O_4 NPs. Reproduced with permission from Ref. [185]. Copyright (2008) Elsevier

Table 3.4 Nanomaterials synthesized in [186]

Type of nanomaterials	Concentration (mmol)	Temperature ($^{\circ}\text{C}$)	Size (nm)
CdS nanoparticles	0.05	383	10–15
CdS long nanorods	0.1	383	20×300
CdS short nanorods	0.2	403	5×20



Scheme 3.19 Synthetic procedure for ZrO_2 NPs. Reproduced with permission from Ref. [187]. Copyright (2012) Springer Nature

Table 3.5 Preparation of ZnO under different conditions

Sample	Capping agent	Temperature (K)	Time	Morphology and particles size
1	–	873	4 h	Irregular shape and size
2	OAm	518	90 min	Quasi-spherical (30 nm)
3	TPP	518	90 min	No product
4	OAm + TPP	518	90 min	Spherical (25 nm)

Under certain conditions, ZrO₂ NPs of the quasi-spherical shape and about 30 nm of size are formed. To control the particle size, combination of OAm and TPP as surfactants was applied (Table 3.5) [187]. It is important that the OAm and TPP play a key role in preventing aggregation of ZrO₂ nanocrystals.

Covellite (hexagonal structure of CuS) NPs were obtained by low-temperature thermolysis using (CuL₂)–OAm complex and sulfur as the Cu²⁺ source and S source, respectively [188]. It turned out that the shape, size, and phase of CuS nanostructures is determined by thermolysis parameters, such as the copper:sulfur molar ratio, the thermolysis temperature, and time. In particular, the covellite with APS between 20 and 45 nm was prepared with the Cu:S molar ratio of 1:3 at 378 K for 60 min. At the same time, non-stoichiometric Cu_{1.65}S with APS of 25–50 nm was obtained by increasing the thermolysis temperature from 378 to 473 K due to the different existing states of the released Cu²⁺ ions from the (CuL₂)–OAm complex.

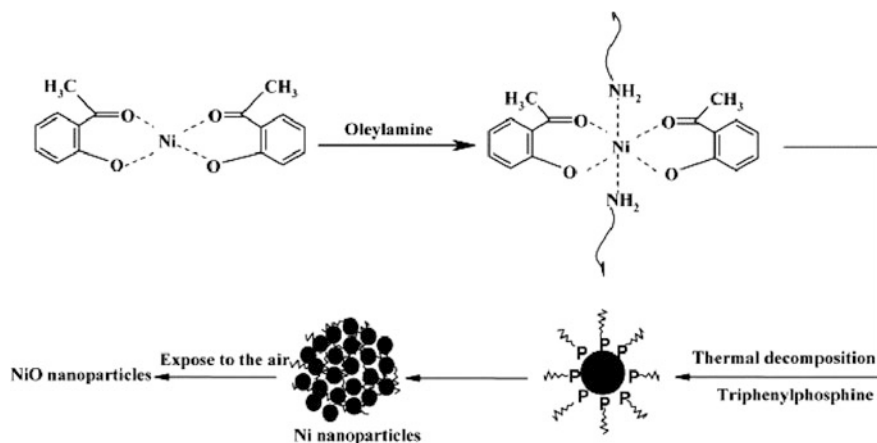
3.3.2 Metal 2-Hydroxyacetophenone

Metal chelates based on 2-hydroxyacetophenone (HL) are promising SSPs for the synthesis of MO NPs via thermolysis (Table 3.6) [189–194].

The overall synthetic procedure of the preparation of MO NPs is shown in Scheme 3.20 using NiL₂ as an example [192]. It is important that the different combinations of TPP and OAm were used as surfactants to tuning the particle size. The TEM images of these NPs are shown in Fig. 3.50.

Table 3.6 Summary of the researches carried out with 2-hydroxyacetophenone as ligand for the synthesis of NPs

Metal	<i>T</i> (K)	Time (min)	Size (nm)	Reference
SnO ₂	493	40	15–20	[189]
Co/ Co ₃ O ₄	513	60	13–25	[190]
ZnO	503	60	15–25	[191]
Ni/NiO	508	45	14–22	[192]
Cu/CuO	518	35	2–4	[193]
ZrO ₂	523	90	30–40	[194]



Scheme 3.20 Schematic diagram illustrating the formation of NiO NPs. Reproduced with permission from Ref. [192]. Copyright (2009) Elsevier

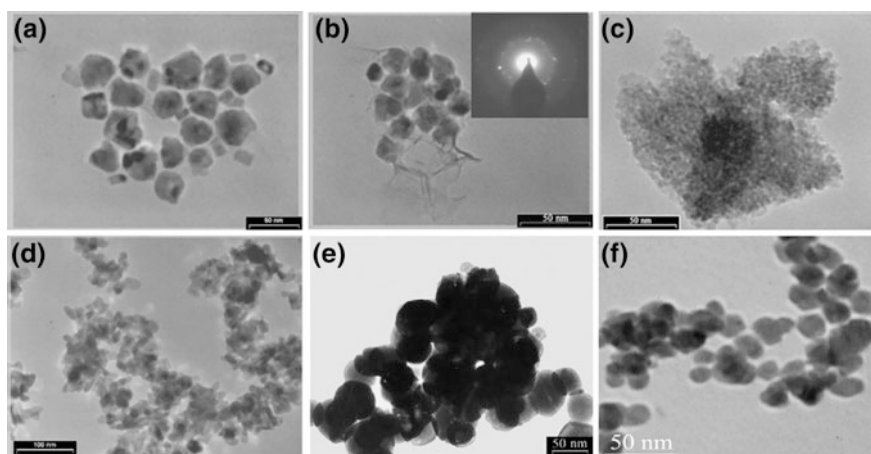


Fig. 3.50 TEM images of **a** Co NPs. Reproduced with permission from Ref. [190]. Copyright (2009) Elsevier, **b** Ni NPs (the inset shows the electronic diffraction (ED) pattern). Reproduced with permission from Ref. [192]. Copyright (2009) Elsevier, **c** Cu nanocrystals. Reproduced with permission from Ref. [193]. Copyright (2009) Elsevier, **d** ZnO nanocrystals. Reproduced with permission from Ref. [191]. Copyright (2011) Elsevier, **e** ZrO₂ NPs. Reproduced with permission from Ref. [194]. Copyright (2009) Elsevier, and **f** SnO₂ NPs. Reproduced with permission from Ref. [189]. Copyright (2010) Elsevier

3.3.3 Metal 2-Hydroxy-1-Naphthaldehydates

Cu NPs were obtained by thermolysis of CuL₂, where HL is 2-hydroxy-1-naphthaldehyde, in the OAm as a capping agent and solvent in order to completely protect the metallic NPs [195]. Two different approaches were used, including thermolysis in presence and absence of protecting agent (Table 3.7) [195].

Table 3.7 Two different approaches for the synthesis of metallic Cu NPs

Sample	Capping agent	T (K)	Time (min)	Results
1	OAm	518	65	30 nm metallic Cu particles
2	OAm + TPP	518	65	No products
3	–	673	300	CuO NPs
4	–	773	300	Agglomerated CuO particles
5	–	873	300	Agglomerated CuO particles

Table 3.8 Comparison of particle size of metal and MO synthesized by thermolysis of [bis(2-hydroxy-1-naphthaldehydato)metal(II)] complex

Metal	Product	Size (nm)	Reference
Cu	Cu/CuO	20–35	[195]
Ni	NiO	15–20	[196]
Mn	Mn ₃ O ₄	9–24	[198]

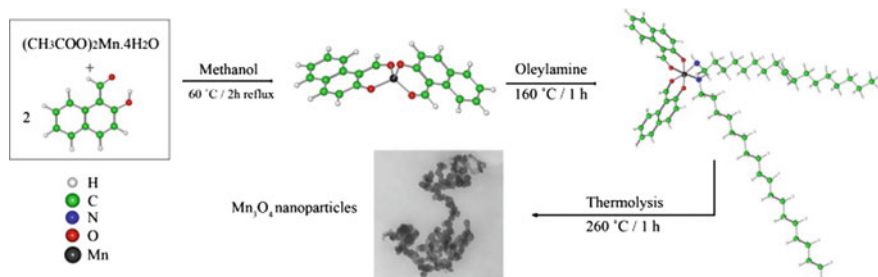
It is interesting that Cu NPs were not prepared without capping agent, and CuO particles were synthesized. In addition, increasing the thermolysis temperature led to enhancing the size and density of products. Aggregated nanostructures are formed at 673 K, but when temperature increased, the NPs have grown and turned into bulk structures.

NiO nanocrystals were also obtained via thermolysis of NiL₂ [196]. When both OAm and TPP were used as capping agents, no product was precipitated after washing with organic solvents. In addition, the combination of OAm and TPP resulted in a narrow size distribution [197]. When increasing the temperature, agglomerated NPs are formed at 773 K while their separation is observed at 873 K.

It should be also noted the preparation of Mn₃O₄ NPs by thermolysis of MnL₂ [198]. It is interesting that at 673 K NPs with the smallest size were prepared. At higher temperature (773 K), the small NPs grow; however, further increase in thermolysis temperature up to 873 K causes agglomeration of the particles with string shapes (Table 3.8).

Complex bis(2-hydroxy-1-naphthaldehydato) manganese(II) was used as SSP in the presence of OAm as both surfactant and solvent to control the size of resulting NP (Scheme 3.21). Synthesized manganese oxide NPs have a tetragonal structure with APS of 9–24 nm.

Of interest is the synthesis of ZnO and CdO NPs using ZnL₂ and CdL₂ via thermolysis technique using TOPO as a capping agent. The spherical NPs of ZnO and CdO revealed the fcc phase in both materials [199]. It should be noted using CdL₂ as SSP for the synthesis of CdO NPs via thermolysis method at various temperatures (393, 433, and 473 K) using HDA as a stabilizing agent, as well as CdO thin films onto the glass substrates by spin coating and consequent thermolysis at 523, 573, and 623 K, respectively [200].



Scheme 3.21 Schematic diagram illustrating the formation of Mn_3O_4 NPs. Reproduced with permission from Ref. [198]. Copyright (2010) Elsevier

3.3.4 Metal Glycerolates

As an example of such metal chelates, we note the preparation of CoO and Co_3O_4 NPs with tunable sizes by thermolysis of a cobalt glycerolate complex at different temperatures and atmospheres [201]. Thermolysis of this SSP was carried out in a controlled oxygen/nitrogen atmosphere for 1 h at the temperature range from 723 to 923 K. It turned out that under pure nitrogen atmosphere NPs of CoO were obtained, while the oxygen atmosphere led to a formation of Co_3O_4 NPs (Fig. 3.51). Co_3O_4 NPs with sizes ranging from 14.2 to 24.6 nm and CoO NPs from 8.4 to 21.6 nm were obtained only by changing the thermolysis temperature of cobalt oxides precursors. The smallest NPs were obtained at 723 K and the largest ones at 923 K.

3.3.5 Metal Cupferronates

The interesting results were obtained during study of thermolysis of metal chelates based on cupferron (Cup: *N*-nitrosophenylhydroxylamine, $\text{C}_6\text{H}_5\text{N}(\text{NO})\text{O}^-$) with the metal ion coordinated via the oxygen atoms of the cup ligand in a bidentate manner [202]. Thermolysis of respective metal cupferron complexes in the presence of a hot coordinating solvent allows to synthesizing magnetic oxide NPs including $\gamma\text{-Fe}_2\text{O}_3$, Fe_3O_4 , and Co_3O_4 and semiconductor NPs such as ZnO and ZnS . Thus, for example, $\gamma\text{-Fe}_2\text{O}_3$ NPs were synthesized from the direct decomposition of FeCup_3 (Fig. 3.52a) [203]. The NPs were generated by the rapid injection of a FeCup_3 solution into a TOA solution at high temperature under vigorous stirring (Fig. 3.52b). It is interesting that the obtained product forms a stable suspension consisting of MO NPs, and NP has core-shell structure. In addition, NPs with uniform size distribution ($s < 7\%$) can be achieved through size-selective precipitation steps and the organic monolayer coordinating each NP surface enables to self-assemble into NP superlattices under controlled conditions.

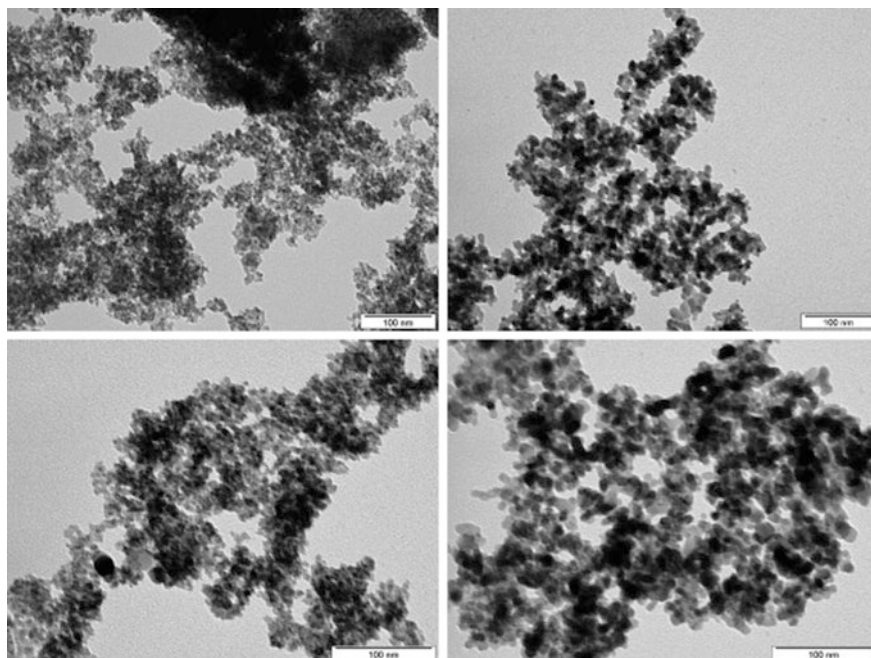


Fig. 3.51 TEM images of CoO NPs (both on the left) and Co₃O₄ NPs (both on the right) prepared at 923 K. Reproduced with permission from Ref. [201]. Copyright (2014) Elsevier

At the same time, Fe₃O₄ particles were synthesized by thermolysis of cupferronates in H₂ atmosphere [204]. It is interesting that the 2D assembly of OAm-capped Co₃O₄ and dodecylamine-capped Fe₃O₄ occurred spontaneously on the copper TEM grids after the evaporation of the solvents, indicating the regular shapes and narrow size distribution of these NPs. It should be also noted the preparation of OAm-capped ZnO and ZnS NPs by thermolysis of zinc cupferron complex under Ar and H₂S atmosphere, respectively (Fig. 3.53) [205].

3.4 Metal Chelates with N,N-Containing Ligands

Metal complexes with N,N-chelating ligands are the wide class of the compounds used as SSPs for thermolysis process.

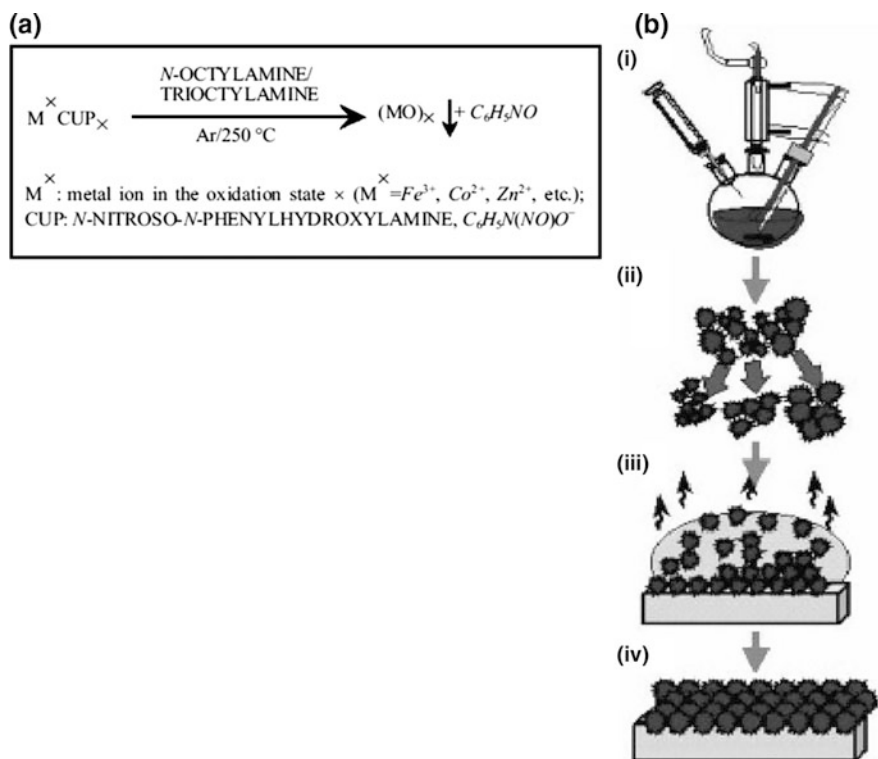


Fig. 3.52 **a** Reaction scheme for the preparation of MO NPs, and **b** schematic representation of steps involved in obtaining ordered NP assemblies: (i) synthesis of NPs by thermolysis, (ii) narrowing the NP sample by size-selective precipitation, (iii) deposition of NP dispersions to self-assemble, and (iv) ordered NP assemblies (superlattices) [202]

3.4.1 2,2'-Diamino-5,5'-Dimethyl-4,4'-Bithiazole

NPs and single crystals of an azido Co(II) complex $[CoL_2(N_3)_2]_{0.25}CH_3OH$ were obtained by the reaction of cobalt chloride, sodium azide, and 2,2'-diamino-5,5'-dimethyl-4,4'-bithiazole ligand (L) using sonochemical and heat gradient methods, respectively, (Scheme 3.22) [206]. The coordination number of cobalt in the compound was six with spatial structure of distorted octahedron, CoN_6 . In this compound, L acts as bidentate ligand to form five-membered chelate rings with different internal angles in coordination polyhedron.

Co_3O_4 NPs of spinel structure with APS of 32 nm were obtained by the thermolysis of the metal chelate at 723 K under air (Fig. 3.54).

Of interest is the preparation of an oxide sulfide nanocomposite CdO–CdS with APS of 43 nm by thermolysis of $[CdL_3](ClO_3)_2$ [207]. At the same time, CdS NPs were prepared by thermolysis of Cd(II) complex $[CdL_2(NO_2)_2]$ (Fig. 3.55, left) as

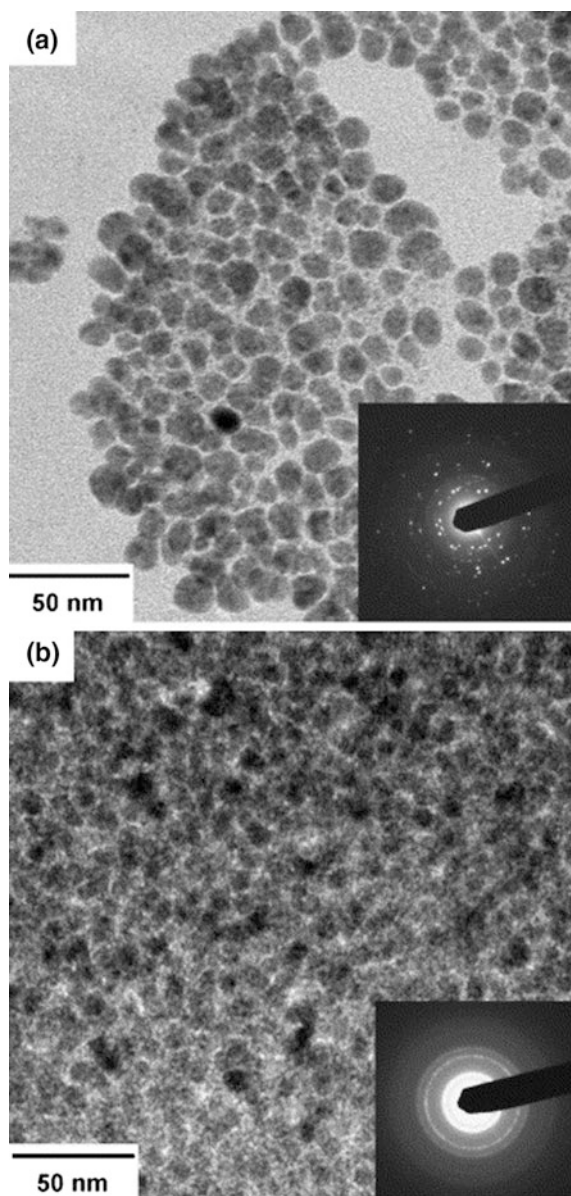
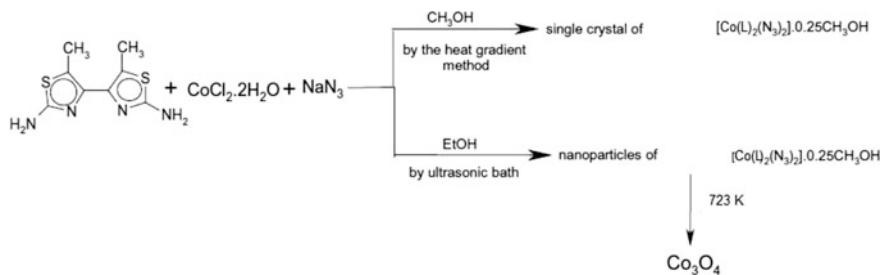


Fig. 3.53 TEM micrographs of OAm-capped: **a** ZnO and **b** ZnS semiconductor NPs (*insets* SAED patterns). Reproduced with permission from Ref. [205]. Copyright (2004) Elsevier



Scheme 3.22 Scheme of the reaction between Co(II) chloride, NaN_3 , and L to form single crystal or NPs of metal chelate, in two different conditions, and the preparation of Co_3O_4 . Reproduced with permission from Ref. [206]. Copyright (2012) Elsevier

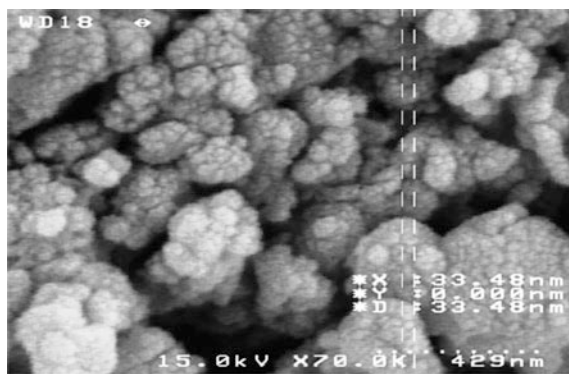


Fig. 3.54 SEM photographs of Co_3O_4 NPs prepared from direct thermolysis of nanosized metal chelate. Reproduced with permission from Ref. [206]. Copyright (2012) Elsevier

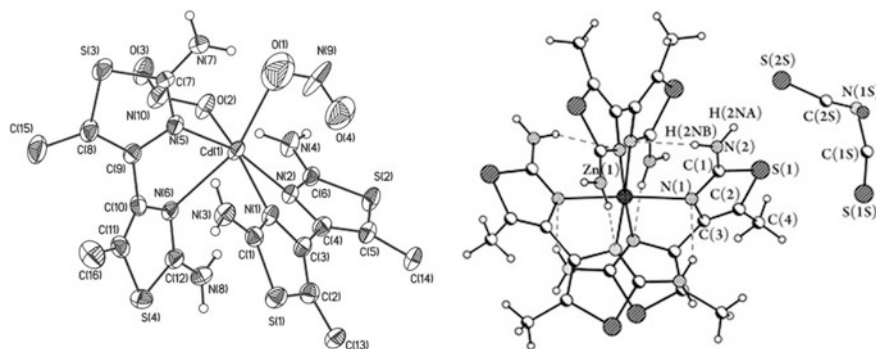


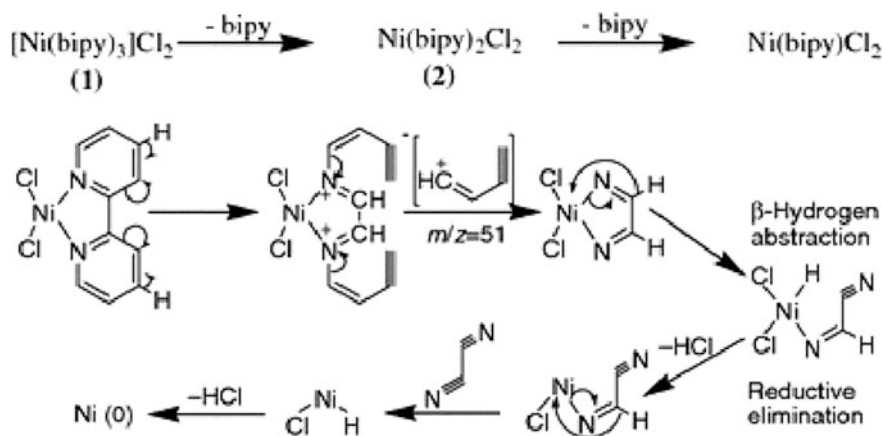
Fig. 3.55 (left) Oak Ridge Thermal Ellipsoid Plot (ORTEP) drawing of $[\text{CdL}_2(\text{NO}_2)_2]$ showing the atom-labeling scheme and 50% probability level displacement ellipsoids. Reproduced with permission from Ref. [208]. Copyright (2011) Elsevier. (right) ORTEP drawing of $\{[\text{ZnL}_3(\text{SCN})_2 \cdot 4\text{H}_2\text{O}]_n\}$ showing the atom-labeling scheme and 50% probability level displacement ellipsoids. Reproduced with permission from Ref. [209]. Copyright (2014) Elsevier

SSP [208]. It should be noted using NPs and single crystals of a tris-chelate Zn(II) compound, $[\text{ZnL}_3](\text{SCN})_2 \cdot 4\text{H}_2\text{O}$ (Fig. 3.55, right), synthesized by sonochemical and branched tube methods, respectively, as SSPs for thermolysis [209]. The process at 673 K under argon atmosphere led to ZnS wurtzite nanostructures with APS of 50 nm.

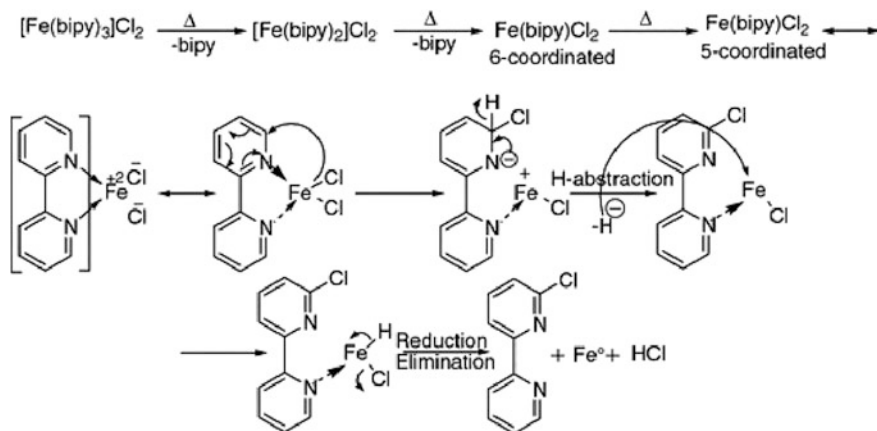
3.4.2 2,2'-Bipyridine

2,2'-Bipyridine is one of the most popular ligands for the synthesis of metal chelates used as SSPs for thermolysis [21]. The different mechanisms of thermolysis of SSPs based on bpy metal chelates are postulated on the assumption of the composition and structure of the resulting products [210–217]. First of all, it concerns bpy complexes Zn(II) and Cd(II) [210, 211] as well as Fe(II) [218] and Ni(II) [219]. Thus, for example, thermolysis of the tris(bpy)nickel(II) chloride (**1**) and bis(bpy)nickel(II) chloride (**2**) [219] proceeds at 723 K for 24 h in an argon stream, resulting to **fcc** phase of Ni NPs of 3.5–5.0 nm in size. Their clean thermolysis pathway to zero-valent nickel was shown (Scheme 3.23). Such parameters as heating rate and argon gas flow rate affect purity, particle size, and shape of the formed NPs.

The same way, thermolysis mechanism of tric(bpy)iron(II) dichloride in an argon stream comprises of two stage of the ligand removing with the formation of coordinatively unsaturated iron centers. This process is facilitated by the H detachment in the pyridine cycle with subsequent attaching the chlorine ion and reduction of Fe(II) ion to Fe(0) NPs of 50–72 nm in size (Scheme 3.24).



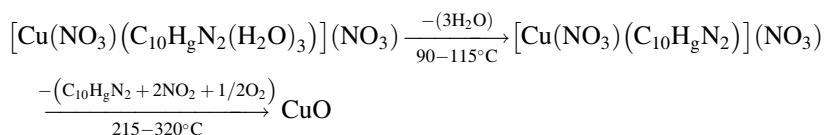
Scheme 3.23 Proposed mechanism for thermolysis of complexes (1) and (2) to Ni(0) NPs. Reproduced with permission from Ref. [219]. Copyright (2013) Springer Nature



Scheme 3.24 Mechanism of thermolysis of tric(bpy)iron(II) dichloride to Fe(0) in an inert atmosphere. Reproduced with permission from Ref. [218]. Copyright (2012) Springer Nature

The study of bipyridine complexes has shown that their stability is changed in the next row: bpy > 4,4'-bipyridine > 2,4'-bipyridine. The higher stability of bpy is attributed to its ability to form five-membered metal chelate ring [212].

The difference in thermolysis patterns of the bipyridine metal chelates was attributed to the presence of different anions. Thus, for example, nickel and copper nitrate complexes with bpy as an N-donor ligand and nitrate and water as O-donor ligands of the general formula $[\text{M}(\text{NO}_3)(\text{bpy})(\text{H}_2\text{O})_3](\text{NO}_3)$, where M = Ni and Cu, were used as SSPs for thermolysis [220]. In the case of Ni chelate, the resulting product is a mixture of Ni and NiO. At the same time, thermolysis of copper chelate led to CuO according to the following scheme:



It should be noted thermolysis of two Zn(II) chelates Zn(6,6'-dimethyl-bpy)Cl₂ (**1**) and Zn(6,6'-dimethyl-bpy)I₂ (**2**) at two different temperatures [221]. ZnO NPs with APS of 50 nm and 60 nm were obtained from chelates **1** and **2**, respectively, (Fig. 3.56, left). In addition, the higher temperature (873 K) leads to an increasing agglomeration and thus small and spherical ZnO NPs with good separation were obtained by the thermolysis of compound **1** at 453 K by using surfactant (Fig. 3.56, right).

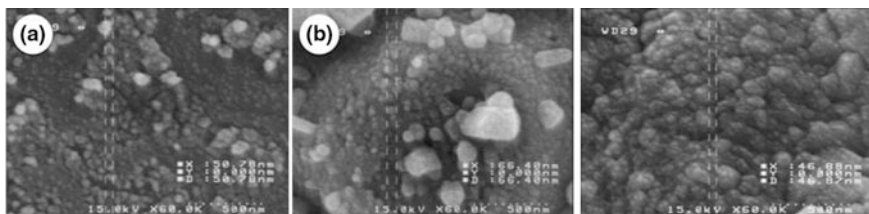


Fig. 3.56 (left) SEM photograph of ZnO NPs produced by thermolysis of **a** precursor **1** and **b** precursor **2** at 873 K, and (right) SEM image of ZnO nanostructure prepared by the thermolysis of compound **1** with OA as a surfactant at 453 K. Reproduced with permission from Ref. [221]. Copyright (2013) Springer Nature

No constant pattern of thermolysis was observed in the case of $[M(\text{bpy})_3]\text{Br}_2$, where $M = \text{Mn}(\text{II}), \text{Co}(\text{II}),$ and $\text{Zn}(\text{II})$. In addition, the thermolysis of hydrated and anhydrous complexes shows various thermolysis patterns at different temperatures. It should be noted that in the case of transition metal perchlorate complexes with bpy such as $[\text{Mn}(\text{bpy})_2(\text{H}_2\text{O})(\text{ClO}_4)]\text{ClO}_4$, $[\text{Cu}(\text{bpy})(\text{ClO}_4)_2(\text{H}_2\text{O})_2]$, $[\text{Zn}(\text{bpy})_2(\text{H}_2\text{O})](\text{ClO}_4)_2$, the Mn and Cu chelates are thermolyzed in one stage whereas thermolysis of Zn chelate proceeds in two steps [222]. For these chelates, the explosion delay and activation energy decrease in the next row: $\text{Zn} > \text{Cu} > \text{Mn}$. In dimeric complexes of type $[\text{LnL}_3(\text{bpy})]_2$, where $\text{Ln} = \text{Tb}$ and Dy , $L =$ cinnamic acid, the thermolysis proceeds by elimination of bpy and acid ligand to form MO NPs [215]. At the same time, thermolysis of $\text{W}(\text{bpy})\text{Cl}_4$ chelate under argon atmosphere in the presence of excess of bpy leads to the formation of tungsten carbides WC and W_2C . It is interesting that the formation of the zero-valent metal is possible in samples where bpy is present in small amounts owing to its evaporation during heating before decomposition [216]. Thermolysis of $[\text{Rh}(\text{bpy})_3]^{3+}$ gave metallic Rh irrespective of the type of halide atom present [223]. It is important that the formed planar 2D NPs have core-shell structure including ruthenium metal stabilized in the carbon matrix. In these Ru@C composites, ruthenium particles of sizes 1.5–2.0 nm with the interplanar distance of 0.21 nm are observed (Fig. 3.57). In addition, the metal NPs are uniformly distributed in the carbon matrix consisting of mutually disordered carbon layers with the interlayer distance of 0.35 nm, which is characteristic of a turbostratic graphite-like carbon structure.

3.4.3 Ethylenediamine and Related Ligands

It should be noted the numerous examples of the thermolysis of metal chelates with such interesting ligands as ethylene diamine (en) [224, 225], propylenediamine [226, 227], 1,4-diaminobutane [228, 229], 1,6-diaminohexane [230, 231]. In particular, high energy thermolysis of nitrate complexes of bis-ethylenediamine $[\text{M}(\text{en})_2](\text{NO}_3)_2$ ($M = \text{Cu}, \text{Co}, \text{Ni}$ and Zn) is investigated in detail [224]. Their

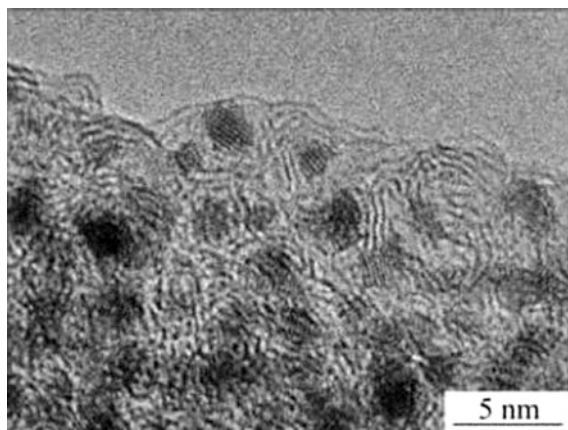
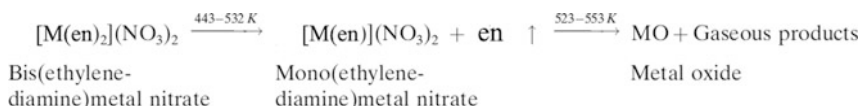


Fig. 3.57 TEM image of the Ru@C composite. Reproduced with permission from Ref. [223]. Copyright (2009) Springer Nature

thermolysis occurs in two stages involving the separation of one molecule of ethylenediamine and formation of mono (ethylene diamine) complex, and then obtaining high-dispersed MOs. The following mechanism of thermolysis has been proposed:



Of interest is the thermolysis of such metal chelates as Ni(formate)₂(en)₂ at 523 or 573 K [232], as well as [Ni(saccharinate)₂(en)₂]en [233], [Ni(en)₃](ox) [234], Ni(succinate)(en) [235], and Ni(en)₃SO₄ [236] at 573, 598, 683, and 739 K, respectively. It is important that in helium atmosphere, [Ni(en)₃](ox) gives nickel as the product, whereas the thermolysis of Ni(en)₃SO₄ leads to a mixture of nickel and nickel sulfide phases as the final product [237]. However, thermolysis of both chelates gives NiO as a final product in air. The comparison of tris(ethylenediamine)nickel(II) oxalate dihydrate, intermediates isolated at different temperatures and the residue in air has shown that the initial chelate and the dehydrated amine complex have an elongated morphology (Fig. 3.58). In the case of mono (ethylenediamine) nickel(II) oxalate, there is an apparent change in morphology and a reduction of the size. The resulting product NiO appears as very small rods.

In the case of tris(ethylenediamine)nickel(II) sulfate, the initial chelate has a rod-like structure and NiO product is agglomerated (Fig. 3.59).

Of interest is the formation of nanocrystalline nickel (18.1 nm) at the controlled thermolysis of chelate [Ni(en)₂(H₂O)₂](NO₃)₂ [238]. It is important that under static

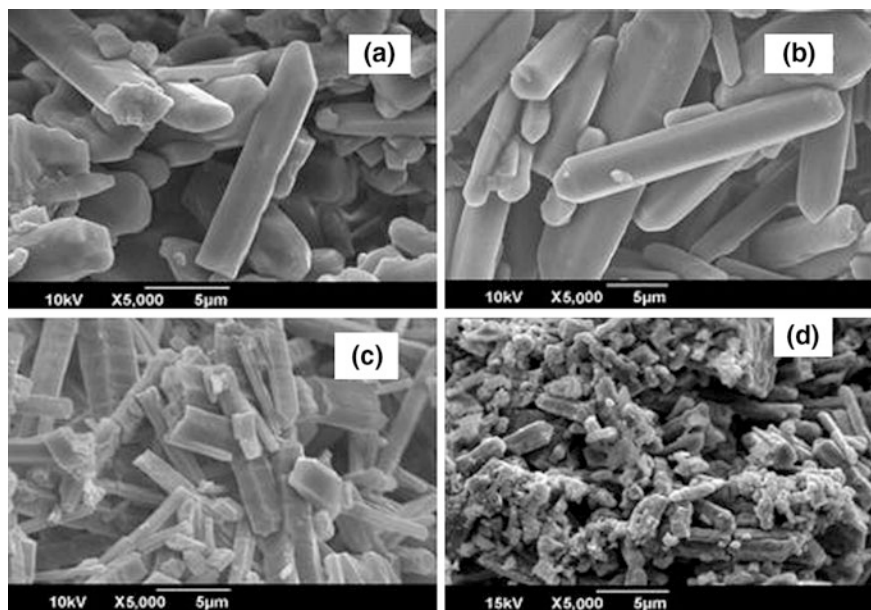


Fig. 3.58 SEM pictures of **a** $[\text{Ni}(\text{en})_3](\text{ox}) \cdot 2\text{H}_2\text{O}$, **b** $[\text{Ni}(\text{en})_3](\text{ox})$, **c** $\text{Ni}(\text{en})(\text{ox})$, and **d** NiO . Reproduced with permission from Ref. [234]. Copyright (2010) Springer Nature

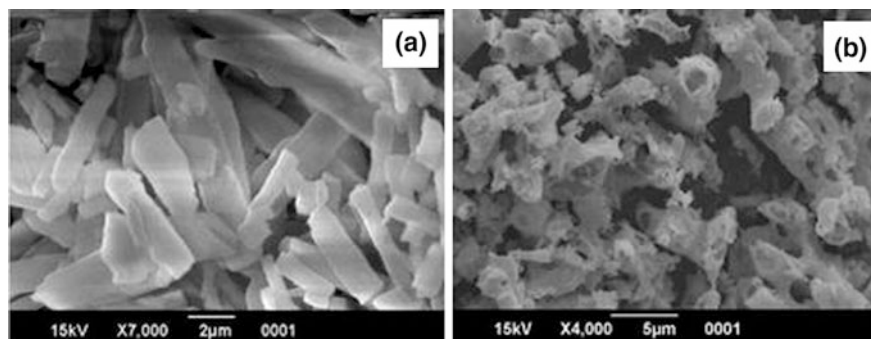


Fig. 3.59 SEM pictures of **a** $[\text{Ni}(\text{en})_3]\text{SO}_4$ and **b** NiO . Reproduced with permission from Ref. [234]. Copyright (2010) Springer Nature

conditions an autogenic thermolysis proceeds at 473 K, and its kinetics follows the Johnson–Mehl–Avrami mechanism with the activation energy of $135.1 \text{ kJ mol}^{-1}$. In addition, the formed product is stable and not oxidized up to 623 K. NiO NPs with size about 13 and 15 nm were also synthesized by solid-state thermolysis of octahedral $[\text{Ni}(\text{en})_3](\text{NO}_3)_2$ complex for 1 h in the temperature range of 473–673 K, respectively, [239].

Important direction of the application of thermolysis is the preparation of supported nickel catalysts by thermolysis of Ni-en chelates [240–242]. This approach is based on the thermolysis of catalyst precursors (the support and the nickel chelate) in an inert atmosphere. For example, 1.5 Ni wt%/Al₂O₃ catalysts have been prepared by incipient wetness impregnation using [Ni(diamine)_x(H₂O)_{6-2x}]₂Y₂ precursors (diamine = en and *trans*-1,2-cyclohexanediamine; *x* = 0, 1, and 2; Y = NO₃⁻ and Cl⁻) to avoid the formation, during thermolysis, of difficult-to-reduce nickel aluminate (Fig. 3.60) [241]. After treatment of [Ni(en)₂(H₂O)₂]₂Y₂ chelates at 503 K, Ni(II) ions were grafted to the alumina via two O–Al bonds and en ligands still remain coordinated to the grafted nickel ions but monodentate way. Temperature-programmed reduction leads to the metallic state at 773 K, in contrast with the aluminate obtained when the preparation is carried out from [Ni(H₂O)₆]²⁺, which is reduced only partly at 1223 K. In addition, a total self-reduction of nickel chelates leading to 2–5-nm metal NPs proceeds upon thermal treatment via the hydrogen released by a hydrogen-rich ligand such as *trans*-1,2-cyclohexanediamine. It is important that an appropriate choice of the ligand and the counterion allows then to preparing selectively Ni(II) ions or the dispersed phase of the reduced nickel.

In another interesting example, a 15 Ni wt%/Al₂O₃ catalyst is obtained by impregnation by [Ni(en)₂(H₂O)₂](NO₃)₂ as SSP [242]. The use of metal chelate is effective to obtain nickel NPs by a one-stage thermolysis at 773 K in argon, leading to a complete autoreduction of the chelates. It should be noted that small monodisperse nickel NPs (2–5 nm) are obtained after decomposition of the larger [Ni(en)₂(H₂O)₂](NO₃)₂ crystals formed during impregnation.

Important observation was made during the study of the thermolysis of Cd nitrate en chelate and thiourea to the preparation of CdS nanorods [243]. It turned out that the chelating ability of en with Cd²⁺ provides the growth of CdS nanorods along *c* axis. For this process, an accordion-like folding mechanism was proposed.

Cd(II) chelates in dicationic form with general formula [Cd(dien)₂]₂CdBr₄ (**1**), where dien is diethylenetriamine, and [Cd(dipn)₂]₂CdBr₄ (**2**), where dipn is dipropylenetriamine, (Scheme 3.25) are the promising SSPs [244].

In particular, thermolysis of complex **1** revealed the formation of a cubic regular spherical CdO NPs with the ~60-nm APS (Fig. 3.61). For complex **1**, particles were irregular before thermolysis, while after thermolysis regular spherical NPs were collected, confirming that tridentate organic ligands play de-structure role during thermolysis process.

Cadmium bromide chelate based on dien was used as SSP for preparation of CdO NPs by thermolysis (Scheme 3.26) [245].

The resulting product has fcc structure of CdO NPs with the high crystallinity. APS of CdO NPs of spherical shape is about 25.5 nm (Fig. 3.62).

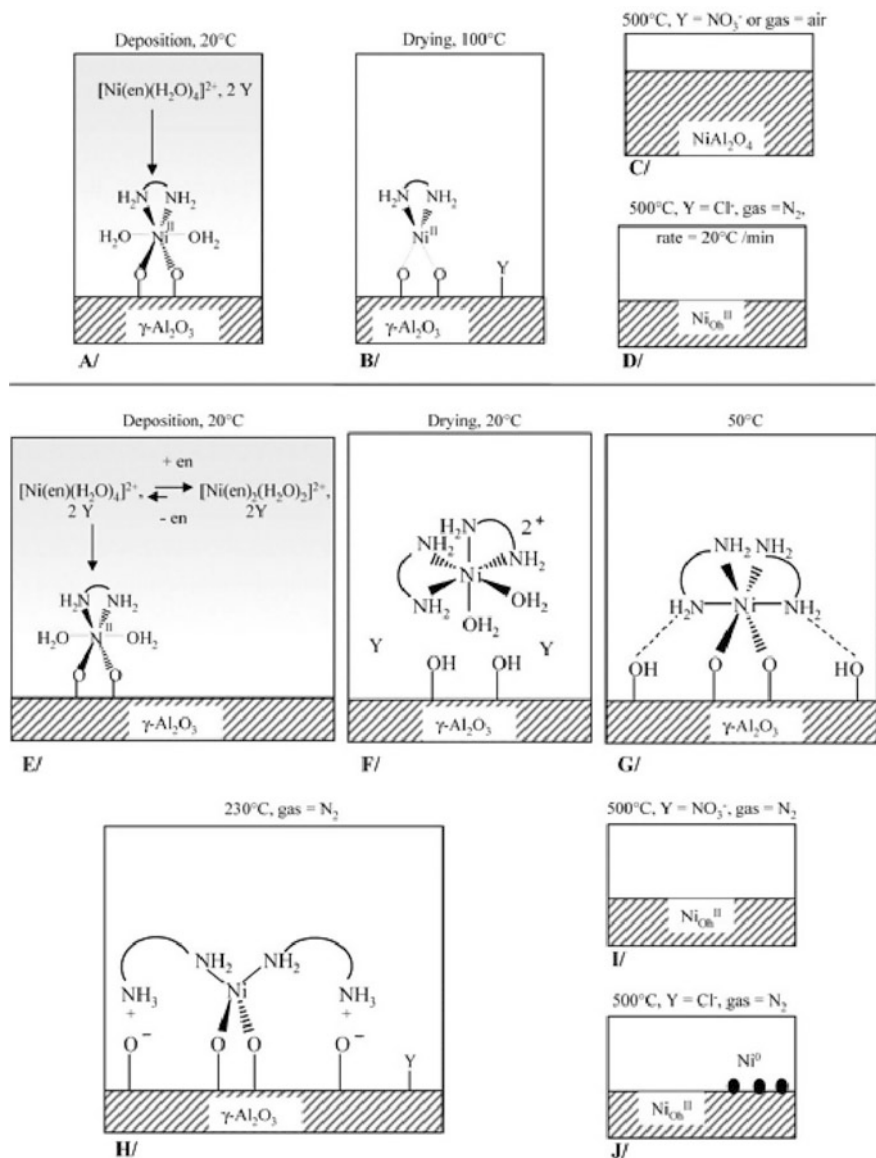
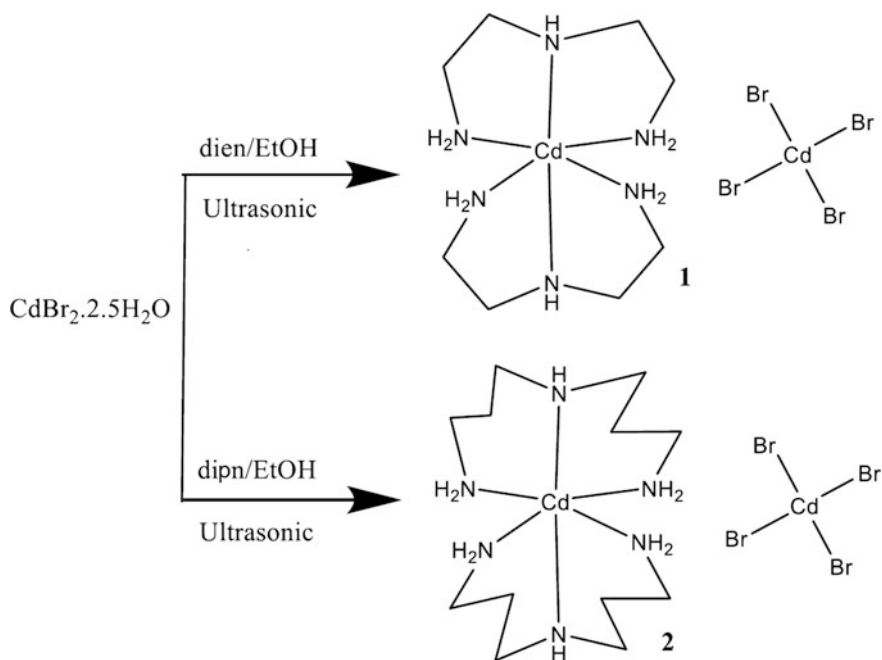


Fig. 3.60 Speciation of nickel on alumina during the history of the preparation of catalysts Ni(en)Y (a-d) and Ni(en)₂Y (e-j). Reproduced with permission from Ref. [241]. Copyright (2005) American Chemical Society



Scheme 3.25 Synthesis of the desired complexes [244]

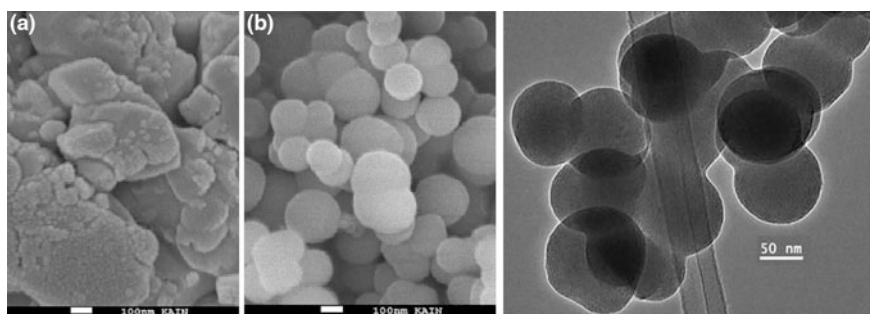
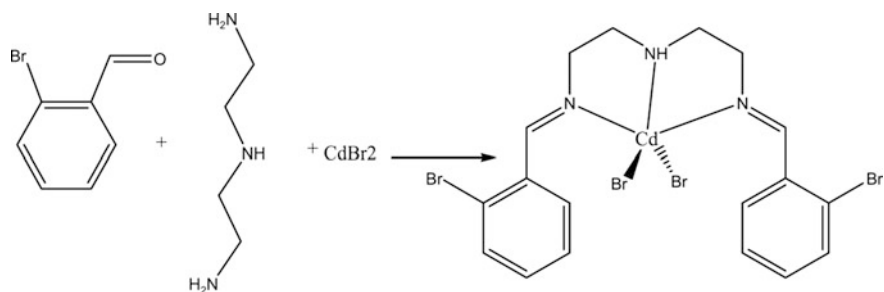


Fig. 3.61 (left) SEM image of complex 1 (a) before and (b) after thermolysis to produce CdO NPs and (right) TEM image of CdO NPs of an average diameter of ~ 60 nm [244]

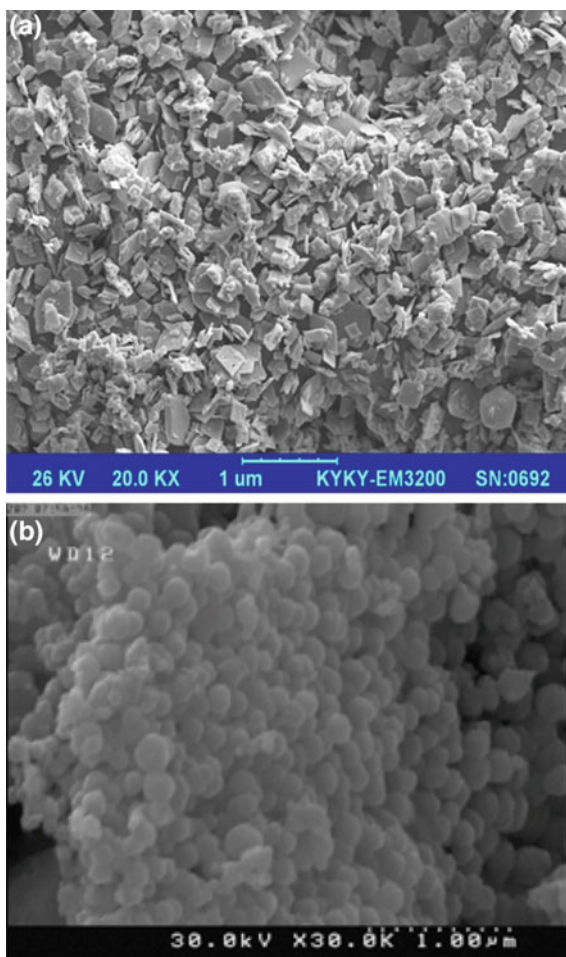
3.4.4 1,10-Phenanthroline and Related Ligands

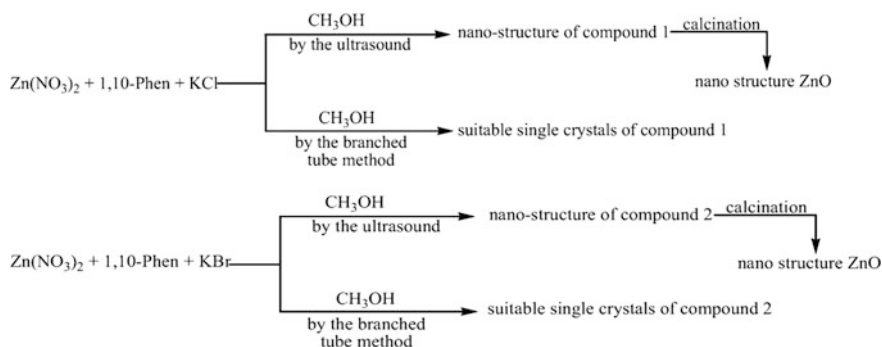
In the synthesis of NiO NPs, a $[\text{Ni}(\text{phen})_2]^{2+}$ chelate was used as a SSP in solid-state thermolysis process at air at 773 K [246]. Synthesized NiO microstructures have a cubic phase with APS of 56 nm through NPs, which exist on the surface of a



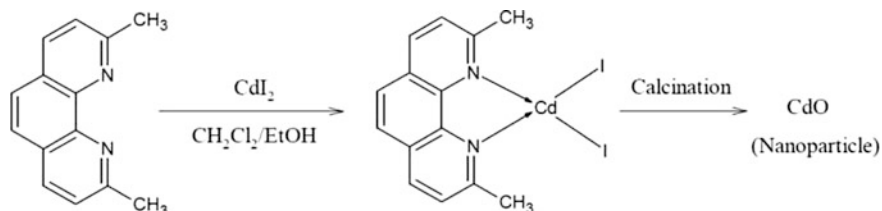
Scheme 3.26 Synthesis of the cadmium bromide chelate. Reproduced with permission from Ref. [245]. Copyright (2017) Elsevier

Fig. 3.62 **a** SEM image of CdLBr_2 complex prepared by sonochemical process. **b** SEM image of cadmium oxide NPs. Reproduced with permission from Ref. [245]. Copyright (2017) Elsevier





Scheme 3.27 Materials produced and synthetic methods. Reproduced with permission from Ref. [248]. Copyright (2017) Elsevier



Scheme 3.28 Synthesis of the desired *cis*-[(2,9-dimethyl-phen)-CdI₂] chelate and CdO NP [249]

pyramidal microstructure. ZnO NPs of the typical zincate structure have been prepared by thermolysis of two Zn(II) chelates, [Zn(phen)Cl₂] (**1**) and [Zn(phen)Br₂] (**2**), at 773 K [247]. It is interesting that the formation of NPs or single crystals of these chelates depends on process conditions (Scheme 3.27) [248].

It should be noted CdO NPs derived from *cis*-[(2,9-dimethyl-phen)-CdI₂] chelate via a one-step thermolysis at 1073 K for 120 min (Scheme 3.28) [249].

The CdO NPs have regular spherical or elliptical shape and uniform size, with APS of 50 nm and some coalesced NPs with a size of about 100 nm (Fig. 3.63).

[NiCl₂(2,9-dimethyl-phen)(H₂O)] chelate was subjected to thermolysis at low temperature of 673 K in an open atmosphere for preparing pure NiO NPs with uniform spherical shape of *fcc* phase [250]. APS of the NiO NPs was equal to 16 nm, and particles had crystalline nature. The powder of the initial complex included very large block crystals of different sizes (Fig. 3.64a). At the same time, the shape and size of the particles obtained are significantly different from the SSP (Fig. 3.64b). In particular, the product consisted of extremely thin hemispherical particles that were poorly aggregated.

Of interest are the Ni(II) chelates [Ni(L)₂](ClO₄)₂ (**1**) and [Ni(L)₂(NO₃)₂] (**2**), where L is the ligand of 4,5,9,13,14-pentaaza-benzo[*b*] triphenylene, (Scheme 3.29) [251]. NPs of chelate (**1**) were synthesized using sonochemistry (**3**) and solvothermal (**4**) methods, thermolysis of which in air at 773 K resulted in NiO NPs.

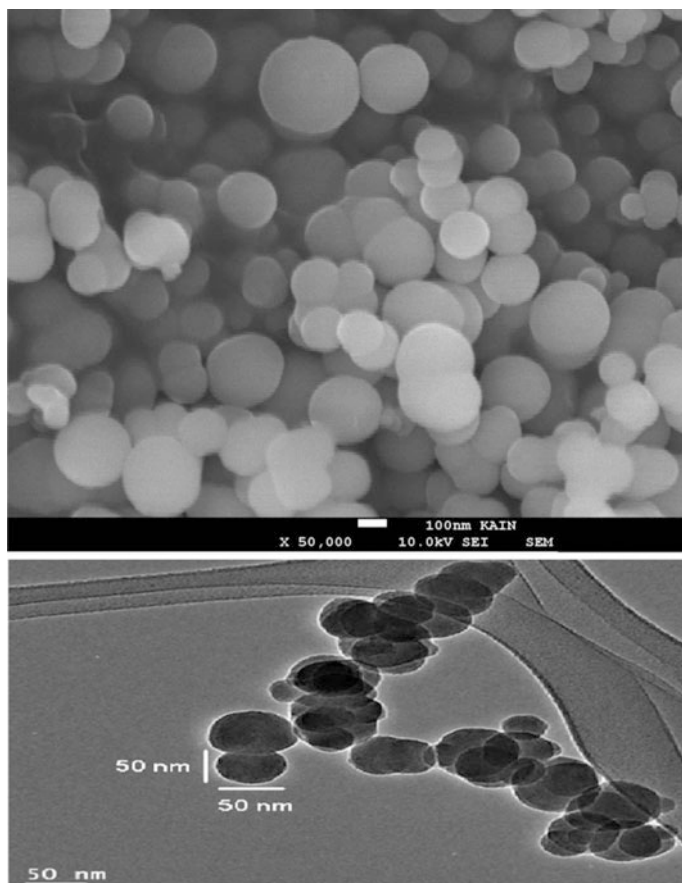


Fig. 3.63 (left) SEM image of CdO NPs of an average diameter of 40–100 nm and (right) TEM image of CdO NPs of an average diameter of 50 nm [249]

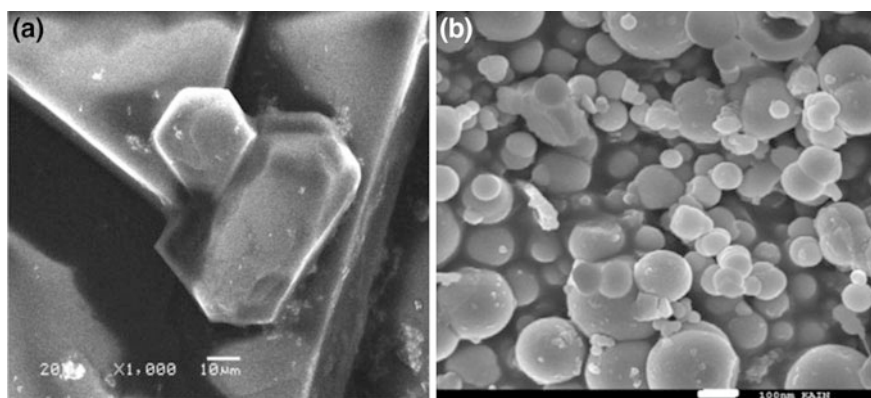
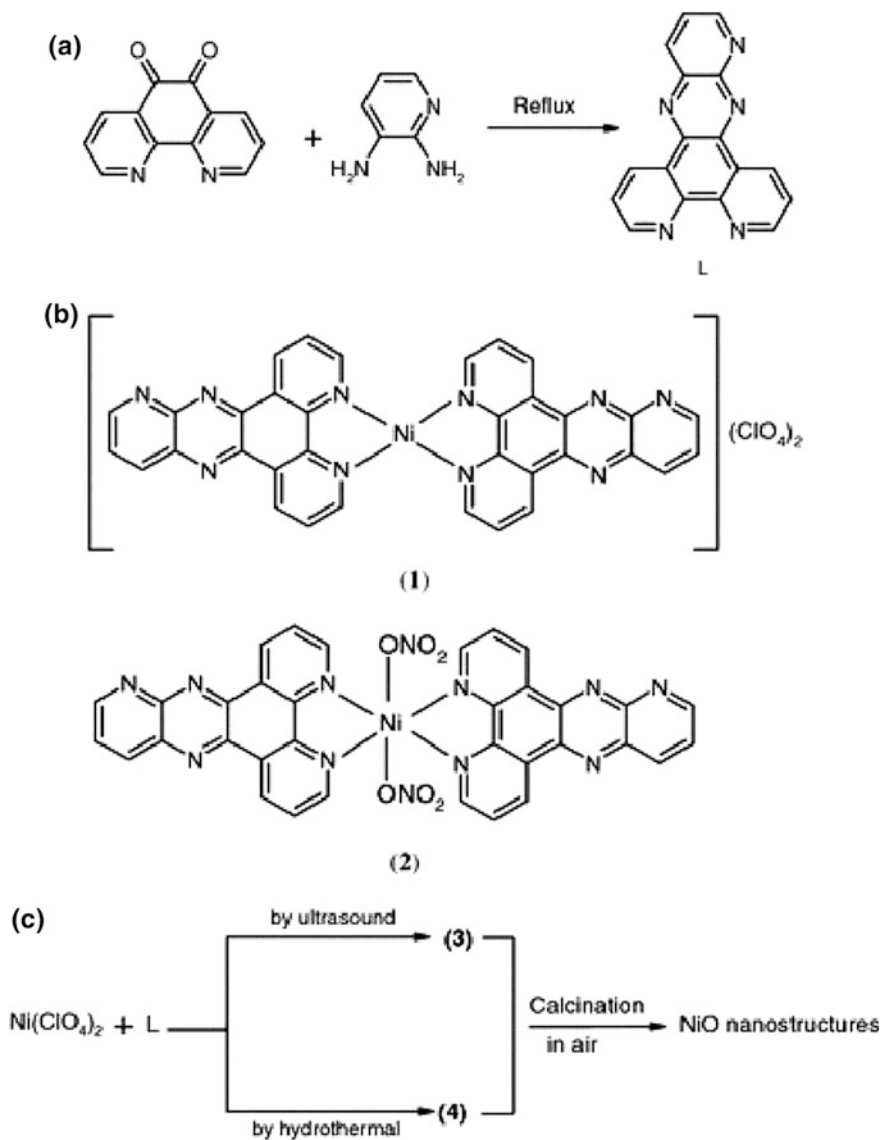


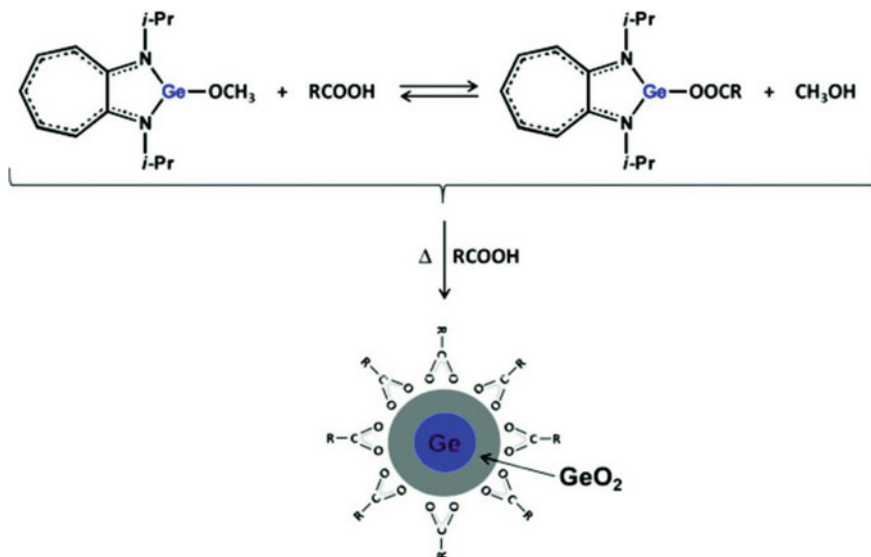
Fig. 3.64 SEM micrographs **a** $\text{NiCl}_2(2,9\text{-dimethyl-phen})\cdot\text{H}_2\text{O}$ chelate and **b** NiO NPs [250]



Scheme 3.29 a Syntheses and structure of the L ligand. b Suggested structures of Ni(II) chelates. c The formation of nanocompounds and synthetic methods. Reproduced with permission from Ref. [251]. Copyright (2010) Springer Nature

3.4.5 Aminoiminates

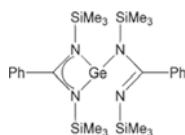
It should be noted the thermolysis of the metal chelate SSPs based on two other N, N-donor ligands: N,N'-diisopropyl-aminotroponimate (ATI) and N,N'-bis

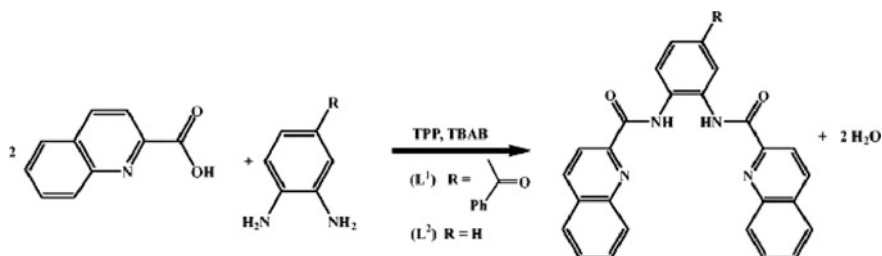


Scheme 3.30 Mechanism of Ge/GeO₂ NP formation by thermolysis of (ATI)GeOMe. Reproduced with permission from Ref. [252]. Copyright (2015) Royal Society of Chemistry

(trimethylsilyl)phenyl amidinate (Am) [252]. In particular, the preparation of Ge/GeO₂ NPs with core-shell structure with a mean diameter close to 5 nm with a narrow size distribution (<15%) was reached by using the aminoiminato Ge(II) (ATI)GeZ chelate, where Z = OMe or NPh₂ (Scheme 3.30). In this process, OA has an important role in the establishment of the equilibrium between the initial metal chelate and formed intermediate (ATI)GeOI even at room temperature during mixing (ATI)GeOMe with an acid. It is interesting that substitution of OA by HDA or its mixture with OA as well as using separately obtained (ATI)GeOI complex does not lead to the NPs formation. Apparently, the presence of the initial chelate (ATI)GeOMe in the system is necessary for the nucleation process, while the OA promotes the decoordination of a strong chelating ATI ligand under the influence of an acidic proton. Whereas the high temperatures (>573 K) classically reported in the literature for the preparation of Ge-based NPs, the use of a weaker chelating ligand as amidinate can significantly reduce (up to 433 K) operating temperatures of the synthesis of germanium NPs.

It should be emphasized that the lower reactivity of (ATI)GeZ (for which the concomitant use of high temperature and acidic reagent is required) was explained in terms of lower ring strain compared to the case of bis(amidinato)germylene (Am)₂Ge.





Scheme 3.31 Synthesis of carboxamide ligands L¹ and L². Reproduced with permission from Ref. [253]. Copyright (2017) Springer Nature

3.4.6 Pyridine Carboxamides

Cobalt oxide NPs have been synthesized by thermolysis of [Co(L¹)] and [Co(L²)] chelates at 773 K for 2 h (Scheme 3.31) [253]. The morphology of these oxides is influenced by the difference in the structure of {3,4-bis(2-quinolinecarboxamido)benzophenone (L¹) and {bis(2-quinolinecarboxamido)-1,2-benzen} (L²), differing only by a benzoyl substituent. The size of NPs is 30 and 33 nm, respectively. The NPs obtained from first SSP are agglomerated and polymorphic, with a non-uniform distribution of sizes and shape. At the same time, the Co₃O₄ NPs obtained from thermolysis of the second SSP are mostly crystalline with a narrow shape and size distribution forming chains of well-ordered NPs.

3.4.7 Dimethylglyoxime

The cubic-phase NiO NPs with APS of 12 nm and a high specific surface area of 88.5 m² g⁻¹ were easily prepared via the thermolysis of the complex Ni(dmgh)₂ (Fig. 3.65, left) [254]. The NiO powder is a crystalline aggregate of NPs (Fig. 3.65, right). The particles possess a narrow size distribution in a range from 8 to 16 nm (inset of Fig. 3.65b, right).

3.5 Azomethine Metal Chelates

In recent years, special attention is paid to preparing new bi- and tridentate azomethine ligands with oxygen-, nitrogen-, sulfur-containing chelating fragments and their metal chelates [255–259]. Undoubted advantages of these metal chelates are the possibility of a wide variation of heteroligand environment of the metal, their high thermal and chemical stability, relatively simple synthetic schemes, and the availability of the initial reagents. This allows to considering azomethine metal

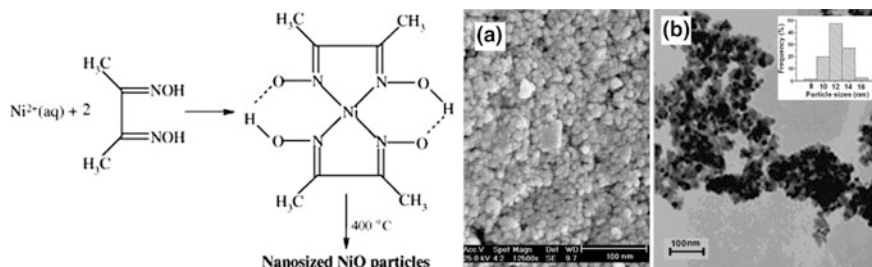


Fig. 3.65 (left) Scheme of synthesis of metal chelate and NPs; (right) SEM (a) and TEM (b) images of the NiO NPs. Reproduced with permission from Ref. [254]. Copyright (2011) Elsevier

chelates as promising SSPs for obtaining a wide range of metal–polymer nano-materials including the specific polymer (oligomer) shell is formed from ligand decomposition products.

3.5.1 Metal Chelates Based on 2-Hydroxyacetophenimine

Such complexes are typical representatives of azomethine metal chelates. As an example, we note the surfactant-free thermolysis of praseodymium metal chelate $[\text{PrL}(\text{NO}_3)_2]\text{NO}_3$, where L is N,N'-bis(2'-hydroxyacetophenimine)-*o*-dipropylene triamine), which was carried out at different temperatures 573–1073 K (Scheme 3.32) [260]. Thermolysis product is praseodymium oxide with very uniform sphere-like shape, small grain size, and pure cubic phase.

In another interesting example, Cd(II) chelate $[\text{CdL}_{0.5}(\text{NO}_3)(\text{H}_2\text{O})]$, where L = N,N'-bis(2'-hydroxyacetophenone) ethylene diamine, has been synthesized as single crystal and nano size [261]. The latter was used as SSP to obtain CdO NPs having 40–60 nm range sizes and perfect morphology at 673 K by direct thermolysis.

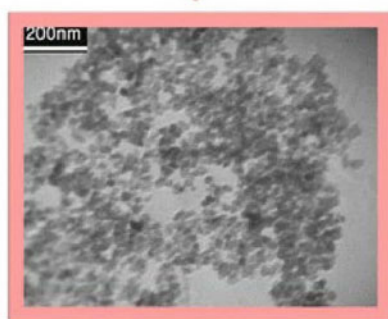
It should be noted azomethine metal chelates with the general formulae NiL , CuL , and VOL , where H_2L means S-ethyl-N1-(2-hydroxyacetophenone)-N4-(saliicylidene) isothiosemicarbazide (Scheme 3.33) [262]. It is important that the chelates have similar thermolysis patterns. In the first stage of the thermolysis of Ni(II) and VO(IV) chelates, the S-ethyl and methyl fragments are removed, while these fragments are removed in two stages for Cu(II) chelate. In the second step of thermolysis of Ni(II) and VO(IV) chelates, and the third step of thermolysis of Cu(II) chelate, the remainder of the organic moiety is removed completely. The NPs of NiO, CuO, and V_2O_5 , with APS of 27, 22, and 39 nm, are formed as the final products.

Praseodymium nitrate + *N,N*-bis(2'-hydroxyacetophen-onimine)-
o-dipropylene triamin

Ethyl acetate
Chloroform

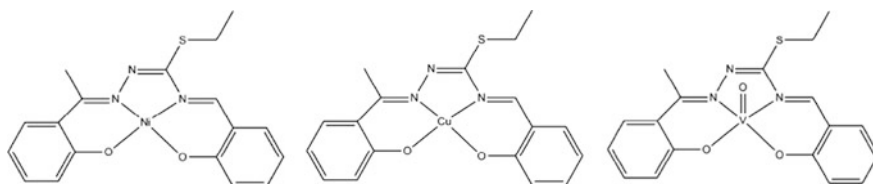


Calcination at 600 °C
for 5 h



Pr_6O_{11} nanoparticles

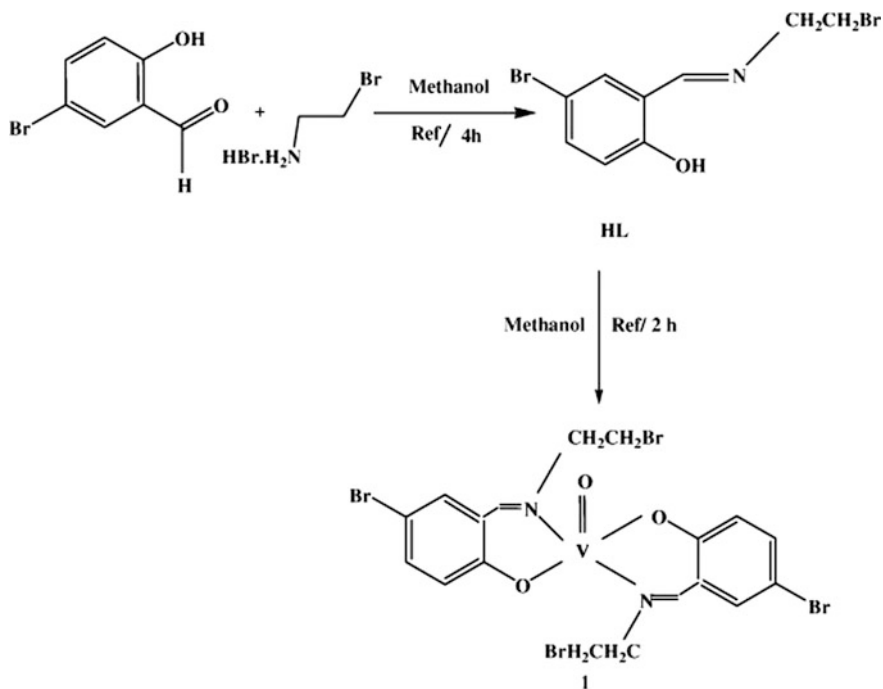
Scheme 3.32 Schematic diagram of the Pr_6O_{11} NPs preparation. Reproduced with permission from Ref. [260]. Copyright (2016) Springer Nature



Scheme 3.33 Structures of azomethine metal chelates. Reproduced with permission from Ref. [262]. Copyright (2014) Elsevier

3.5.2 Metal Chelates of Salicylaldimine Type

As a typical example of these chelates, we note VO(IV) azomethine chelate (**1**) containing an ethyl bromide pendant group which was synthesized by the reaction of the bidentate N,O-ligand (**HL**) and VO(acac)₂ in a 2:1 ratio in methanol, under reflux conditions (Scheme 3.34) [263]. The vanadium center in this chelate has a



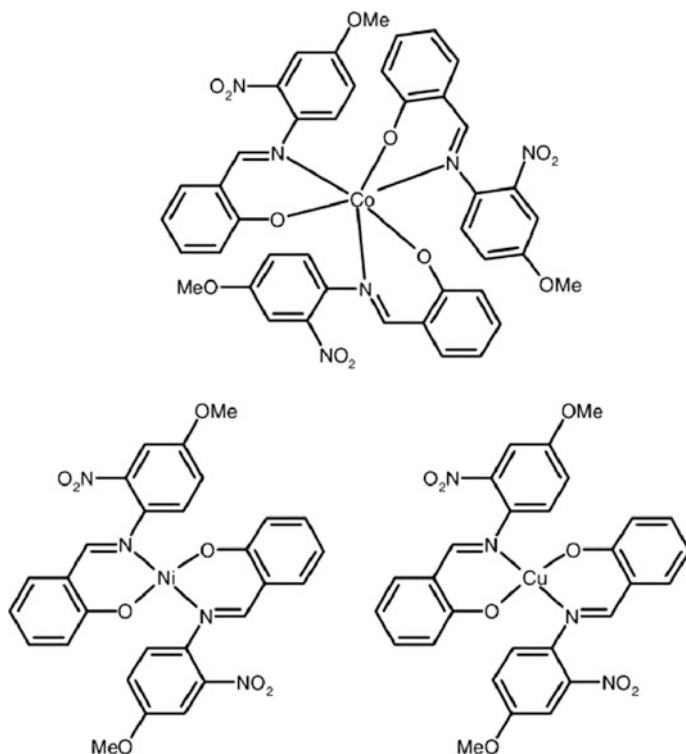
Scheme 3.34 Preparation procedures of **HL** and its vanadyl(IV) chelate **1**. Reproduced with permission from Ref. [263]. Copyright (2014) Elsevier

distorted tetragonal pyramidal N_2O_3 coordination sphere with a six-membered chelating ring. Chelate **1** thermolyzed in air at 933 K to form V_2O_5 NPs with APS of 57 nm. It should be noted that in this case thermolysis of the chelate **1** proceeds in two stages.

Co(III) , Ni(II) , and Cu(II) chelates based on asymmetric bidentate azomethine ligand 2-[(4-methoxy-2-nitrophenyl) iminomethyl] phenol (Scheme 3.35) have been used for the preparation of corresponding MO NPs by controlled aerobic thermolysis at 773 K [264].

The size and shape of the NPs depended on the type of SSP. In particular, the NPs of Co_3O_4 are hexagonal, NiO are plate, and CuO are both spherical and cubic (Fig. 3.66).

It should be noted a bidentate azomethine ligand *N*-(4-amino-2-chlorophenyl)-2-hydroxybenzaldehyde (L) and its octahedral Mn(III) chelate MnL_3 [265]. It turned out that this chelate is SSP for the facile preparation of Mn_3O_4 NPs of hausmannite structure via solid-state thermolysis under aerobic conditions at a temperature of *ca.* 723 K. In addition, the nanoplate shape of the rather monodisperse crystalline Mn_3O_4 NPs, with an average diameter of *ca.* 10 nm, is observed.



Scheme 3.35 Structures of Co(III), Ni(II), and Cu(II) chelates. Reproduced with permission from Ref. [264]. Copyright (2014) Springer Nature

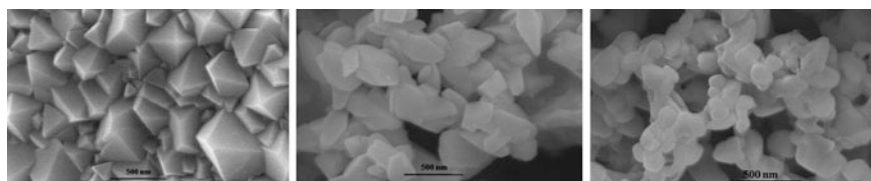
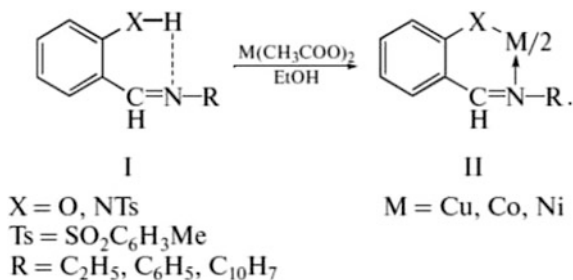


Fig. 3.66 SEM images of Co_3O_4 NPs (left), NiO NPs (middle), and CuO NPs (right). Reproduced with permission from Ref. [264]. Copyright (2014) Springer Nature

The controlled thermolysis of metal chelates with azomethine ligands, containing oxygen, nitrogen, and sulfur atoms in the chelate rings, allows to prepare the various nanocomposites including metals, metal carbides, or sulfides [266]. Thermolysis (643 and 873 K) of metal chelates of this type in the condensed phase, apparently, is a multistep process, the total scheme of which can be represented as follows (Scheme 3.36) [267].

Scheme 3.36 Thermolysis of azomethine metal chelates [267]



The thermolysis products of azomethine metal chelates are core-shell-structured metallopolymer nanocomposites: A metal compound (or metal) is surrounded by a shell of ligand decomposition products. The core consists of small NPs (2–3 nm in size), which form larger aggregates (10–20 nm or more in size).

It is important that the products of the thermolysis are matrix-stabilized NPs which are homogeneously distributed in size and in the space of a matrix. In particular, the size of cobalt NPs in the thermolysis product of azomethine cobalt chelate ($T = 873$ K) was ~ 15 nm. For different metal chelates, the formation of self-organized nanocomposites are based on crystalline cobalt sulfide clusters Co₉S₈ (thermolysis at 593 K) and Co₆S₅ (thermolysis at 873 K), Ni₃S₂ and NiC, nanocrystalline copper with structure core-shell [268].

It should be noted that azomethine metal chelates are effective SSPs for the fabrication of self-organized nanocomposites stabilized by the thermolysis products of the ligand environment to prevent further aggregation. Thermolysis optimization of these chelates (Table 3.9), the possibility of the formation of alloys based on heterometallic complexes, along with the identification of the thermolysis mechanism and detailed characteristic of the properties of emerging products will promote further progress of modern nanochemistry toward effective fabrication of composite nano-materials [269].

3.5.3 Salen Chelates

The main component of such chelates is salen—N,N'-bis(salicylaldehyde) ethylenediamine. As a typical example of these chelates, we note using Ni(salen) as SSP for the preparation of NiO NPs via thermolysis [270]. Ni(salen) has been synthesized via two methods: solid-state reaction in absence solvent and coprecipitation reaction in presence of propanol as solvent, respectively. The formed NPs with APS between 15 and 30 nm have a spherical shape, and their distribution is not uniformed. It is important that varying molar ratio of metal salt to ligand resulted in morphological changes in NPs (Fig. 3.67).

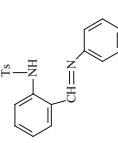
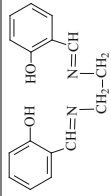
The interesting results were obtained during study of the ZnO NPs synthesized by thermolysis at 773 K for 5 h of Zn(salen) chelates prepared by using the

Table 3.9 Azomethine metal chelates as SSP of the nanostructured materials

SSP	Chelating ligand	Thermolysis conditions	Phase composition, NP shape, and sizes	Reference
Bis[(2- <i>N</i> -tosylaminobenzylidene) benzoylhydrazonato]dicopper(II)		Solid-phase thermolysis, SGA, 873 K	Cu, 40–70 nm	[266]
Bis[(2-hydroxy-5-methoxybenzylidene)-2'-mercaptophenyliminato]dicopper(II)		Solid-phase thermolysis, SGA, 873 K	Cu, 20 nm	[266]
Bis[(2-hydroxybenzylidene) phenylimino]copper (II)		Solid-phase thermolysis, SGA, 873 K	Cu	[267]
Bis[(2- <i>N</i> -tosylaminobenzylidene) phenylimino]cobalt(II)		Solid-phase thermolysis, SGA, 593 K, 873 K	Co ₉ S ₈ (593 K); Co ₆ S ₅ (873 K)	[267]

(continued)

Table 3.9 (continued)

SSP	Chelating ligand	Thermolysis conditions	Phase composition, NP shape, and sizes	Reference
Bis[(2- <i>N</i> -tosylaminobenzylidene) phenylimino] nickel(II)		Solid-phase thermolysis, SGA, 873 K	Ni ₃ S ₂ , NiC	[267]
<i>N,N'</i> -Bis[(2-hydroxybenzylidene)-1,2-diaminoethane]cobalt(II)		Solid-phase thermolysis, SGA, 873 K	Co, ~15 nm	[268]

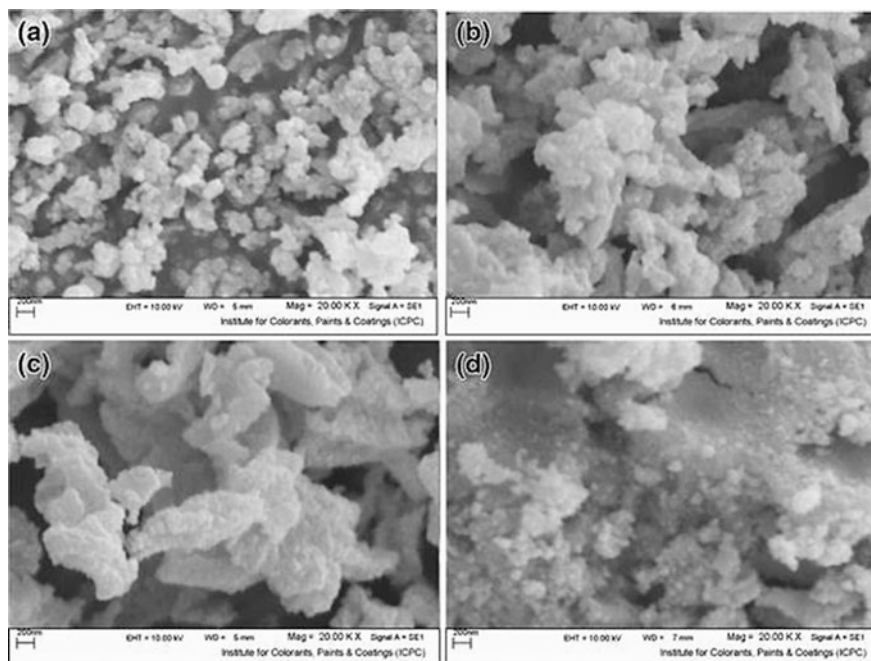


Fig. 3.67 SEM images of NiO NPs prepared from Ni(salen) in a molar ratio 1:1 (a), 1:2 (b), 1:3 (c), and 1:4 (d) by the thermolysis of Ni(salen) at 773 K for 5 h. Reproduced with permission from Ref. [270]. Copyright (2013) Springer Nature

solid-state method at the $\text{Zn}(\text{Ac})_2 \cdot 2\text{H}_2\text{O}$ to salen molar ratios of 1:1, 1:2, and 1:3, respectively (Fig. 3.68) [271]. In particular, it was shown that APS of ZnO NPs decreased with decreasing $\text{Zn}(\text{Ac})_2 \cdot 2\text{H}_2\text{O}$ to salen molar ratio. In addition, the aggregation of NPs is observed that points out to a quasi-spherical morphology of ZnO NPs. It is important that NPs are uniform in both morphology and particle size, which averages 10–20 nm.

Mononuclear azomethine Ni(II) chelates based on *N,N'*-bis(salicylaldehyde)-1,4-diaminobutane (**1**) or 2,2-dimethylpropylenediamine (**2**) were employed as SSPs in solid-state thermolysis (Scheme 3.37) [272]. The synthesized NiO NPs of the spinel structure have **fcc** phases with an average diameter of around 5–15 nm.

Of interest are 2,3-bis-[(3-ethoxy-2-hydroxybenzylidene)amino]but-2-enedinitrile azomethine ligand and its corresponding copper/nickel chelates used as SSPs for the formation of irregular Cu and Ni NPs with APS of 25 nm and 28 nm, respectively, (Fig. 3.69) [273].

It is important that the surface area of the obtained Ni NPs and Cu NPs and commercial Raney Ni samples were determined to be 42, 33, and 35 $\text{m}^2 \text{g}^{-1}$, respectively, (Table 3.10) [273]. In addition, the volume of pores for the obtained Ni NPs was significantly greater than that of commercial Raney Ni, while the value of pore diameter in the obtained Ni NPs is smaller than that found in the commercial Raney Ni.

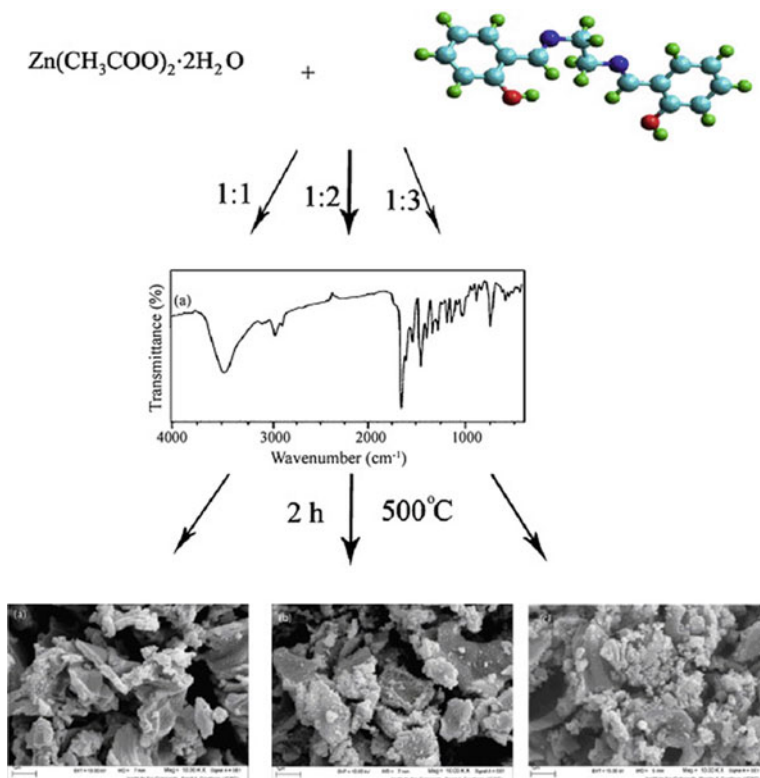
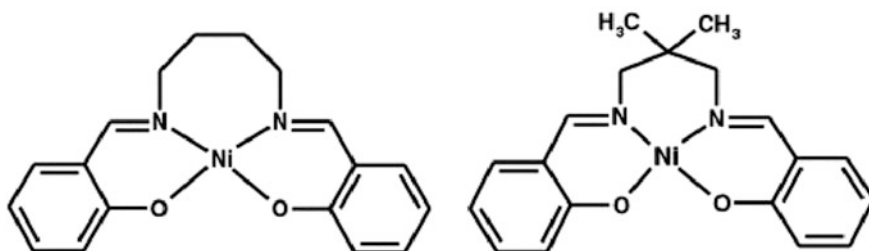


Fig. 3.68 A diagram illustrating the formation of ZnO nanostructures and SEM images of ZnO NPs prepared from Zn(salen) in molar ratios of (left) 1:1, (middle) 1:2, and (right) 1:3, by thermolysis of SSP at 773 K for 5 h. Reproduced with permission from Ref. [271]. Copyright (2012) Elsevier



Scheme 3.37 Chemical structures of the chelates (1) and (2) [272]

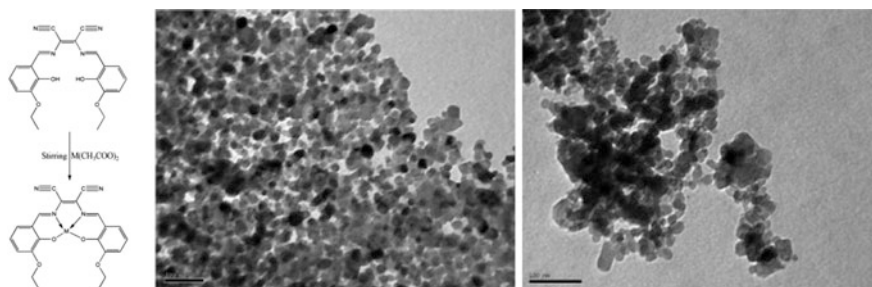


Fig. 3.69 (left) Synthesis of 2,3-bis-[(3-ethoxy-2-hydroxybenzylidene) amino] but-2-enedinitrile metal complex (ML), TEM micrograph of obtained Ni NPs (middle) and Cu NPs (right). Reproduced with permission from Ref. [273]. Copyright (2014) Elsevier

Table 3.10 Surface area and porosity of Cu NPs, commercial Raney Ni, and Ni NPs

Sample	S_{BET} ($\text{m}^2 \text{g}^{-1}$)	V_{p} ($\text{cm}^3 \text{g}^{-1}$)	R (\AA)
Cu	33	0.140	11.00
Ni	42	0.190	7.00
Commercial Raney Ni	35	0.072	53

S_{BET} is BET surface area, V_{p} is the total pore volume, and R is the mean pore radius

3.5.4 Salphen Chelates

Another interesting type of azomethine metal chelates is metal complexes based on *N-N'*-bis(salicylaldehyde)-1,2-phenylenediamine (salphen). For example, Co(salphen) was used as SSP for the preparation of pure single crystalline cubic-phase Co_3O_4 NPs by thermolysis in air at 773 K for 5 h (Fig. 3.70) [274]. The Co_3O_4 NPs obtained have a spherical shape, and their distribution is not uniform (30–50 nm). It is important that the increase of thermolysis temperature resulted in obvious size growth of the NPs.

Of interest is the preparation of NiO NPs from chelates Ni(salphen) and Ni(Me-salphen) (Scheme 3.38) by solid-state thermolysis at 823 K for 3.5 h [275]. It turned out that the NiO NPs have uniform shape with APS between 35 and 70 nm.

It should be noted that the choice of metal chelates as SSPs is a key step in the preparation of NiO NPs (Table 3.11).

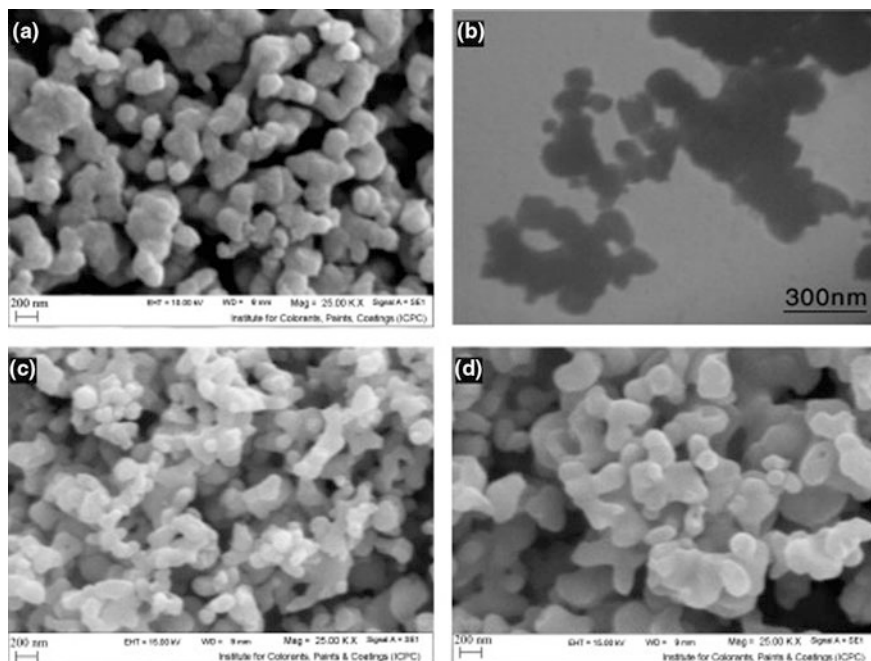
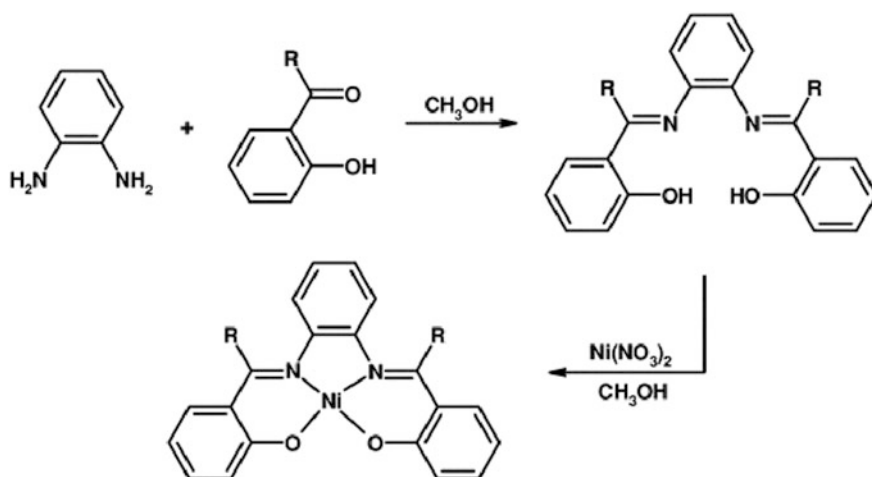


Fig. 3.70 a SEM, b TEM image of Co_3O_4 NPs obtained at 773 K for 5 h, SEM images of obtained Co_3O_4 at c 873 K and d 973 K for 5 h. Reproduced with permission from Ref. [274]. Copyright (2009) Elsevier



Scheme 3.38 Synthesis and chemical structure of Ni(II) azomethine chelates Ni(salphen) ($\text{R}=\text{H}$) and Ni(Me-salphen) ($\text{R}=\text{CH}_3$). Reproduced with permission from Ref. [275]. Copyright (2013) Springer Nature

Table 3.11 Comparison of particle size of NiO NPs prepared by thermolysis method of Ni(II) azomethine chelates

Sample	Precursor	T (K)	Reaction time (h)	Particle size (nm) according to XRD results	Reference
1	Ni(salen)	773	5	15-20	[270]
2	Ni chelate ^a	823	3.5	55	[272]
3	Ni(salphen)	823	3.5	35	[273]
4	Ni(Me-salphen)	823	3.5	70	[273]

^aIt is shown in Scheme 3.39

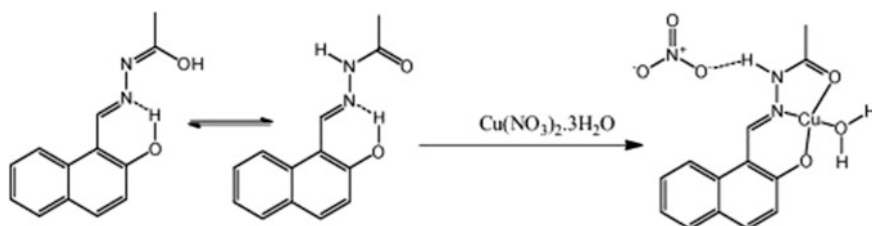
3.5.5 Metal Chelates Based on Tridentate Azomethine Ligands

As a typical example of these chelates, we note cationic Cu(II) complex [Cu(L)(H₂O)]NO₃ based on a tridentate ONO ligand (E)-N'-((2-hydroxynaphthalen-1-yl)methylene) acetohydrazide (HL), which was used as SSP for the preparation of nanocrystalline CuO with APS of 23 nm via thermolysis (Scheme 3.39) [276]. It is interesting that the obtained CuO NPs was in a monoclinic phase.

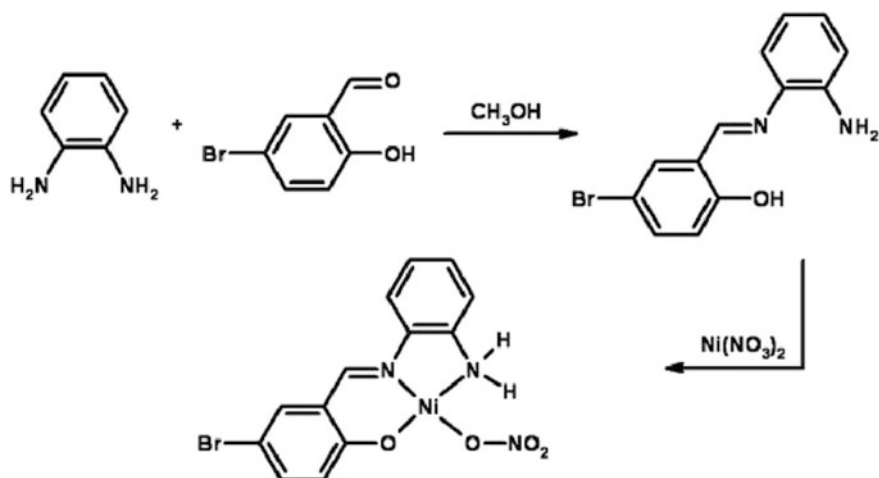
Ni(II) chelate based on *N*-(5-bromosalicylaldehyde)-1,2-phenylenediamine, whose thermolysis at 823 K for 3.5 h led to NiO NPs of cubic phase with the diameter of 45 nm (Scheme 3.40), is of interest [277].

3.5.6 Metal Chelates with Other Azomethine Ligands

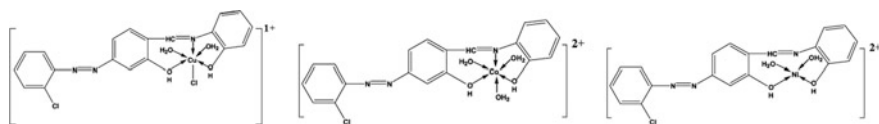
We note also a number of other azomethine metal chelates. For example, Cu(II), Co(II), and Ni(II) chelates of 2-[(5-*o*-chlorophenylazo-2-hydroxybenzylidene) amino]-phenol azomethine ligands (Scheme 3.41) were used as SSPs for the preparation of single phases of CuO, CoO, and NiO NPs via a solid-state thermolysis procedure [278]. APS for the cobalt and nickel NPs thus obtained was 51 and 29 nm, respectively.



Scheme 3.39 Schematic diagram for chelation process. Reproduced with permission from Ref. [276]. Copyright (2015) Elsevier

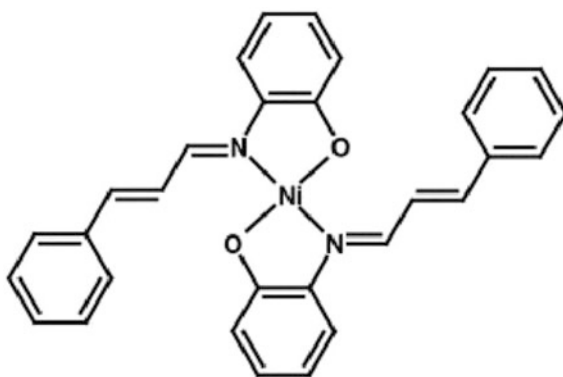


Scheme 3.40 Synthesis and chemical structure of Ni(II) chelate. Reproduced with permission from Ref. [277]. Copyright (2013) Springer Nature



Scheme 3.41 Structures of Cu(II), Co(II), and Ni(II) chelates. Reproduced with permission from Ref. [278]. Copyright (2013) Elsevier

Scheme 3.42 Chemical structure of nickel(II) chelate. Reproduced with permission from Ref. [279]. Copyright (2016) Springer Nature



Of interest is the preparation of Ni/NiO nanocomposite using solid-state thermolysis of bis(*N*-(2-hydroxyphenyl) cinnamaldimine) nickel(II) at 673, 773, and 873 K (Scheme 3.42) [279].

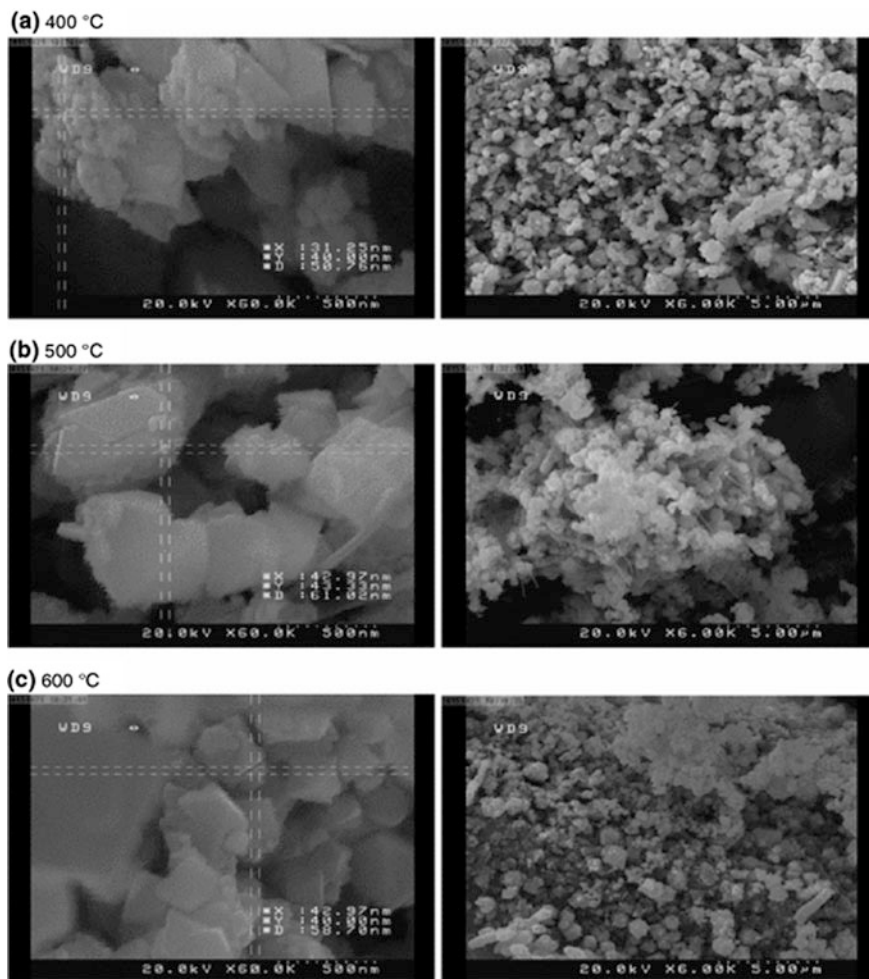
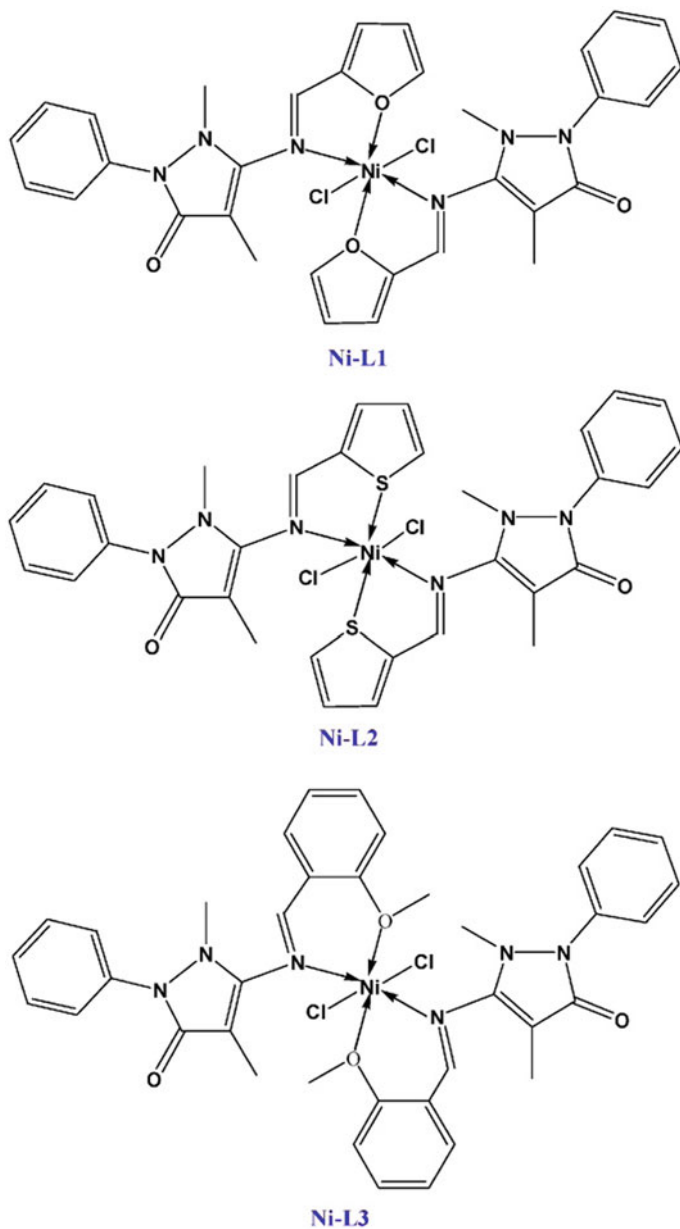


Fig. 3.71 SEM image of Ni/NiO nanocomposites prepared at 673 (a), 773 (b), and 873 K (c). Reproduced with permission from Ref. [279]. Copyright (2016) Springer Nature

It is important that the composites were a mixture of Ni and NiO and they were almost similar morphology. In addition, upon increasing the temperature from 673 to 873 K in air atmosphere, the amount of metallic Ni decreased due to transformation to NiO. In particular, the weight ratio between Ni and NiO prepared at 673, 773, and 873 K is decreasing in order of 10:90, 8:92, and 4:96%, respectively. High temperature for preparation increases the agglomeration of NPs with non-uniform morphology (Fig. 3.71).

It should be noted azomethine metal chelates derived from 4-amino antipyrine with 2-furaldehyde, 2-thiophene carboxaldehyde, and 2-methoxybenzaldehyde (Scheme 3.43) [280]. In these chelates, azomethine ligands are coordinated to the



Scheme 3.43 Speculated structures of Ni(II) complexes. Reproduced with permission from Ref. [280]. Copyright (2016) Elsevier

Ni(II) ions by bidentate ON and NS fashion with the 2-furaldehyde, 2-methoxybenzaldehyde, and 2-thiophene carboxaldehyde, respectively. These chelates were used as SSPs to prepare NiO NPs by thermolysis in static air.

3.6 Metal Chelates with N,O-Donor Ligands

Using thermolysis of the Cu(II) precursor $[\text{Cu}(\text{OCH}(\text{Me})\text{CH}_2\text{NMe}_2)_2]$ synthesized by reacting Cu(II) methanolate with the corresponding aminoalcohol in a hot coordinating solvent without further reducing agents allows to obtaining highly monodispersed capped copper metal NPs of good quality [281]. The formation of copper nanomaterial as well-defined, spherical particles with a diameter of about 7.5 nm is observed (Fig. 3.72). The size and shape of the nanocrystals are very uniform, and the individual NPs are separated by about 2 nm due to the repulsion of their shells of surfactant from neighboring particles. Apparently, the small NP size leads to the formation of hexagonally 2D ordered lattices of free-standing copper colloids.

Thermolysis in TOPO allows to obtaining mostly spherical particles of different sizes ranging from 50 to 3.7 nm (Fig. 3.73, left). Thus, the use of TOPO leads to

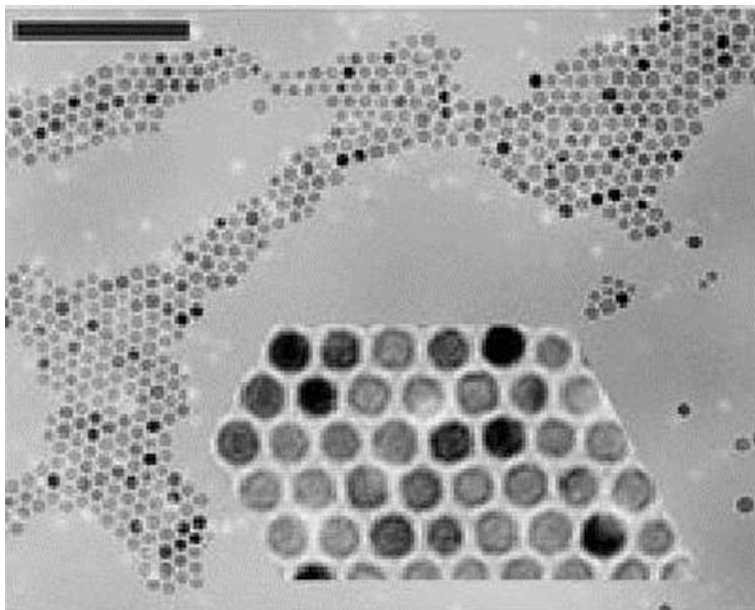


Fig. 3.72 TEM image of individual copper metal NPs showing a tendency toward 2D ordering. The nanocrystals were deposited from a toluene dispersion onto a carbon support film on an Au grid; bar = 110 nm. Reproduced with permission from Ref. [281]. Copyright (2002) Royal Society of Chemistry

the particles that are larger by a factor of at least 10 compared to the thermolysis in HDA. When a solution of metal chelate in tri-*n*-butylphosphine is injected into hot TOPO, the diameter of NPs decreases and various copper NP shapes are observed: spherical, oval, elongated, and cylindrical (Fig. 3.73, right). Their sizes range from 8 to 60 nm for spherical NPs and 15–40 (short axis) and 50–100 nm (long axis) for the elongated NPs, respectively.

Single crystal Fe₃O₄ nanosheets with average edge length in the range of 80–100 nm and thickness of about 30 nm were obtained on a large scale via thermolysis of iron complex with ethylenediaminetetraacetic acid (EDTA) [282]. The product has a highly symmetrical lattice, which reveals the single crystalline nature of the obtained Fe₃O₄ nanosheets. It is important that the morphology of the products is strongly affected by the thermolysis temperature. In particular, during thermolysis at 673 K for 6 h, sheet-like structured Fe₃O₄ with average edge length of 90 nm appeared (Fig. 3.74a). With increasing temperature to 773 K, Fe₃O₄ nanosheets with average edge length of 100 nm (Fig. 3.74b) were also obtained. Finally, when temperature increases to 873 K, irregular structures (Fig. 3.74c) appeared.

A silver complex, Ag(PPh₃)₂(L)·0.5H₂O·0.5C₂H₅OH (Fig. 3.75, left), where L is 2-pyridinecarboxylic acid, was used as a SSP for the preparation of silver NPs with APS of 60 nm and spherical morphology by thermolysis at 623 K in the presence of OA as a surfactant (Fig. 3.75, right) [283]. It is interesting that bulk silver particles of a granulated shape were obtained instead of silver NPs when thermolysis of the silver complex was carried out in the absence of OA.

Of interest is the Zn(II) chelate, [pydaH]⁺²[Zn(L)₂]²⁻{(pydaH)⁺ = pyridine-2,6-diaminium, (L)²⁻ = pyridine-2,6-dicarboxylate}, obtained by sonochemical

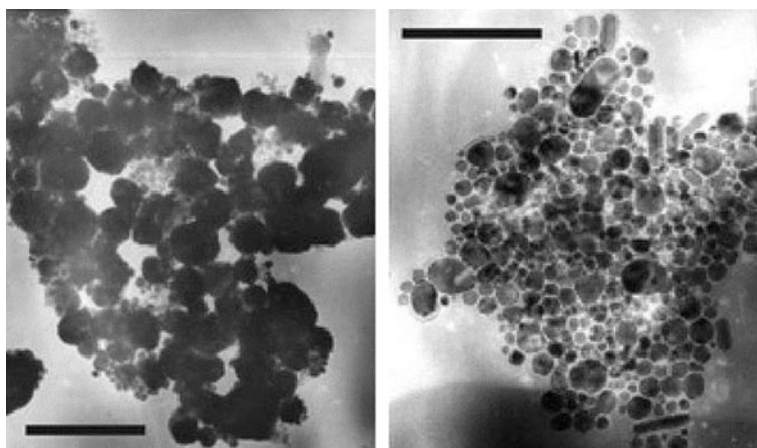


Fig. 3.73 Image of insoluble copper NPs synthesized (left) by thermolysis of SSP in hot TOPO: bar = 200 nm. (right) by thermolysis of a solution of SSP (in tri-*n*-butylphosphine) in hot TOPO: bar = 950 nm. Reproduced with permission from Ref. [281]. Copyright (2002) Royal Society of Chemistry

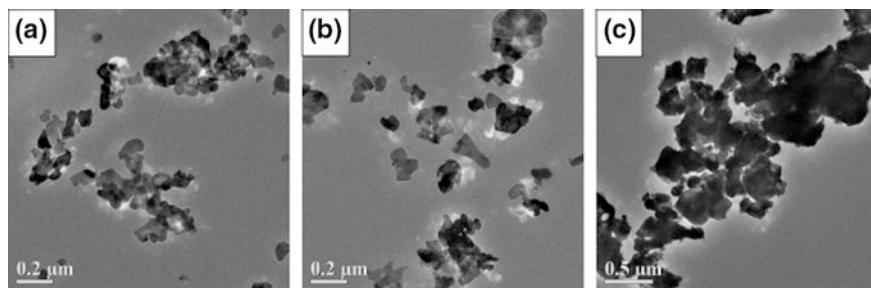


Fig. 3.74 TEM images of the products at **a** 673, **b** 773, and **c** 823 K for the same reaction time of 6 h. Reproduced with permission from Ref. [282]. Copyright (2010) Elsevier

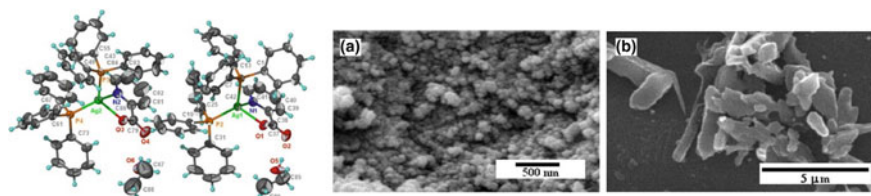
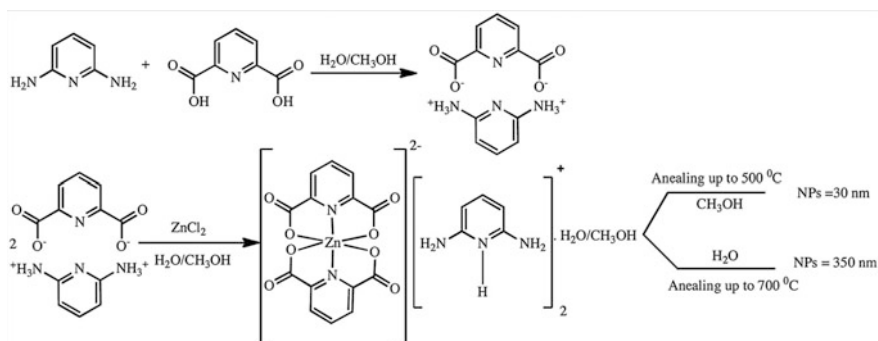


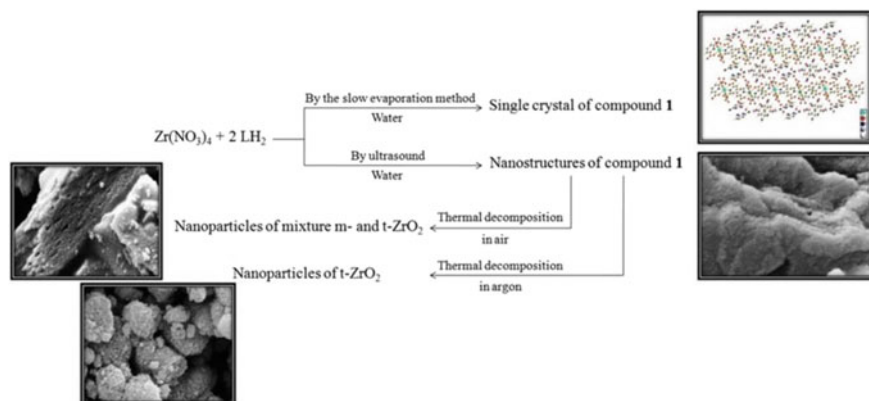
Fig. 3.75 ORTEP diagram of $\text{Ag}(\text{PPh}_3)_2(\text{L})$ (left), SEM micrographs of silver NPs obtained from heat treatment of the silver complex, $\text{Ag}(\text{PPh}_3)_2(\text{L})$, in the presence (middle) and absence (right) of OA. Reproduced with permission from Ref. [283]. Copyright (2013) Springer Nature



Scheme 3.44 Schematic diagram illustrating the formation of ZnO NPs. Reproduced with permission from Ref. [284]. Copyright (2016) Elsevier

method in two different solvents [284]. It turned out that thermolysis of chelates obtained in dry methanol and deionized water as solvents led to two different kinds of ZnO NPs with the APS of about 30 and 350 nm, respectively, (Scheme 3.44).

Zirconia (ZrO_2) nanopowders were obtained by the thermolysis of the similar nanostructured Zr(IV) chelate, $(\text{pydaH})_2[\text{Zr}(\text{L})_3] \cdot 5\text{H}_2\text{O}$ (Scheme 3.45) [285].



Scheme 3.45 Schematic diagram illustrating the formation of chelate and ZrO_2 nanopowders. Reprinted by permission from Springer Nature: Iran. J. Sci. Technol. Trans. Sci., advance online publication, 02 August 2016 (<https://doi.org/10.1007/s40995-016-0069-9>)

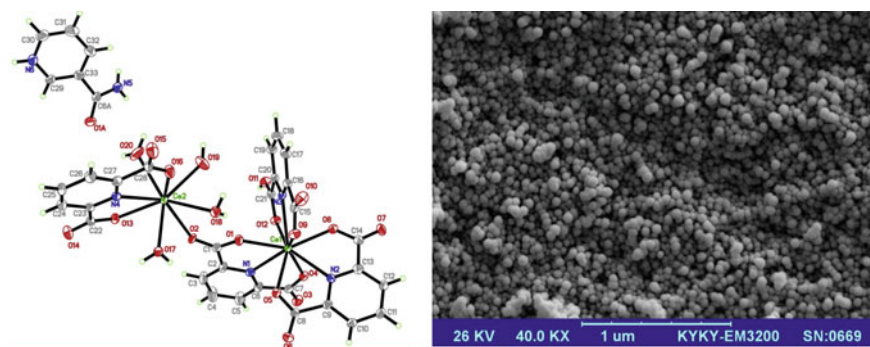
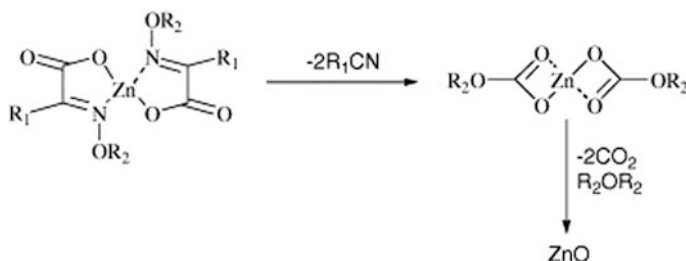


Fig. 3.76 Coordination environment of Ce(III) cations in chelate (left) and SEM image of CeO_2 NPs, prepared by thermolysis of chelate at 1073 K. Reproduced with permission from Ref. [286]. Copyright (2016) Elsevier

The sizes of the nanostructures were approximately 50 nm. It is interesting that thermolysis of chelate under argon and air atmospheres provided two different kinds of crystal systems of zirconia, tetragonal, and mixture of monoclinic and tetragonal with APS about 35 and 28 nm, respectively.

It should be noted Ce(III) chelate with the same ligand, $(\text{XH}^+)_2[\text{Ce}_4(\text{L})_6(\text{HL})_2(\text{H}_2\text{O})_8] \cdot 8\text{H}_2\text{O}$, where $\text{X} = \text{nicotinamide}$ [286]. Its structure consists of tetranuclear building units that extend into a 3D supramolecular network via non-covalent interactions mainly H bonding (Fig. 3.76, left). Ceria NPs were prepared upon the thermolysis of chelate at 1073 K under atmospheric air for 2.5 h (Fig. 3.76, right).

The promising SSPs were obtained by the reaction of Cd(II), Pb(II), and In(III) salts with in situ generated pyruvic acid oxime (ketoacidoximate) of the type



Scheme 3.46 Scheme of the thermolysis of zinc complexes of pyruvic and glyoxylic acid oximes. Reproduced with permission from Ref. [288]. Copyright (2005) Elsevier

$[\text{O}_2\text{CC}(\text{R}) = \text{NOH}]^-$ ($\text{R} = \text{CH}_3$ or $-\text{CH}_2-\text{C}_6\text{H}_5$) [287]. The mononuclear In(III) and dinuclear, μ_2 -oxo-bridged Cd(II), Pb(II) complexes undergo thermolysis below 483 K to the corresponding MOs. It is interesting that the thermal stability of ketoacidoximate complexes of zinc is dependent on the substituents present on the chelating ligand. In particular, ZnO in the form of thin films and particles were prepared by taking advantage of the flexibility in tuning the thermolysis behavior of ketoacidoximate complexes of zinc. APS of the oxides decreases in the order $\text{In}_2\text{O}_3 < \text{CdO} < \text{PbO}$ and is 10–20 nm, 50–150 nm and several microns for In_2O_3 , CdO, and PbO, respectively.

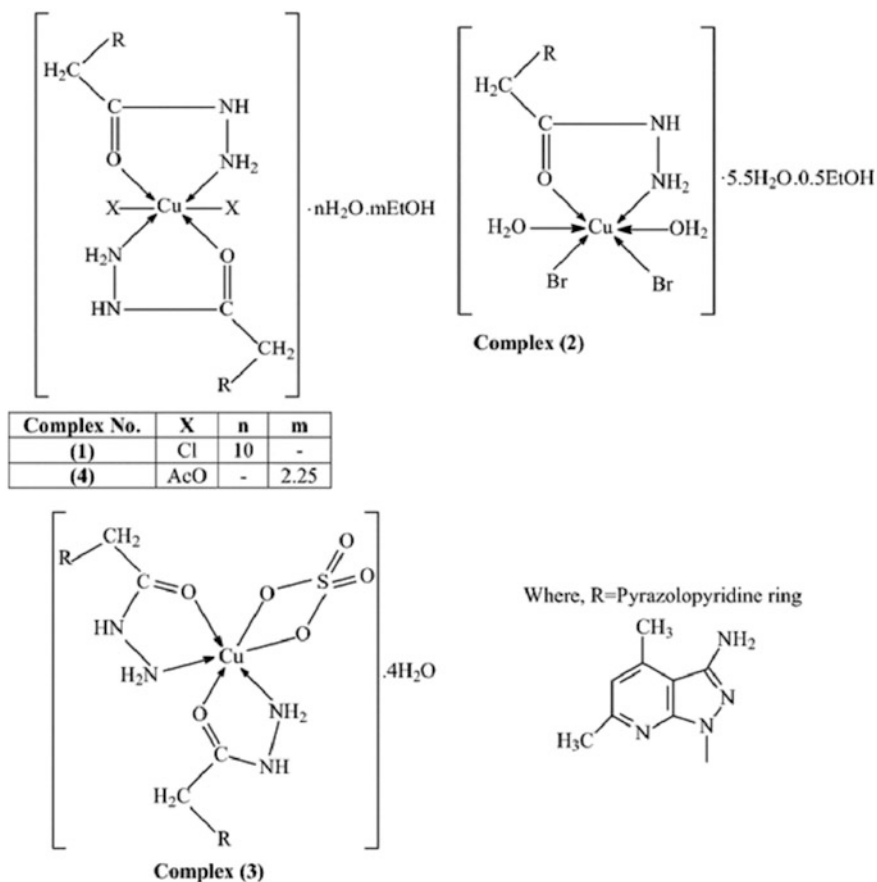
It should be noted the low-temperature thermolysis of different metal oximate complexes leading to a large variety of MO particles [288–292]. For example, zinc complexes of pyruvic and glyoxylic acid oximes are potential SSPs for single-source chemical vapor deposition (SSCVD) of ZnO thin films (Scheme 3.46).

Of interest are the complexes 1–4 derived from reaction of Cu(II) salts (Cl^- , Br^- , CH_3COO^- , and SO_4^{2-}) with 2-(3-amino-4,6-dimethyl-1H-pyrazolo[3,4-b]pyridin-1-yl) acetohydrazide used as SSPs for the preparation of CuO NPs with 15.5 nm of particle size via solid-state thermolysis (Scheme 3.47) [293].

The randomly distributed CuO grains with small size, agglomeration of particles, and slight distortion are observed (Fig. 3.77). In addition, the uniform, nearly spherical ball-like shapes CuO NPs in the form of clusters are formed, and their surfaces are for the most part homogeneous.

3.7 Metal Chelates with S,O-Donor Ligands

As a typical example of the metal chelates with S,O-donor ligands, we note Zn(II) cysteine complex $[\text{ZnI}_2(\text{L})]_n$ (L is 2-amino-3-mercaptopropanoic acid) used as SSP of the hexagonal microcrystalline ZnO by thermolysis at 873 K for 2 h (Scheme 3.48) [294]. It is interesting that nanocrystals with APS about 54 nm are formed, and after hydrothermal treatment in an autoclave their size reduced up to about 38 nm.



Scheme 3.47 Proposal structures of Cu(II) complexes of hydrazide ligand. Reproduced with permission from Ref. [293]. Copyright (2017) Springer Nature

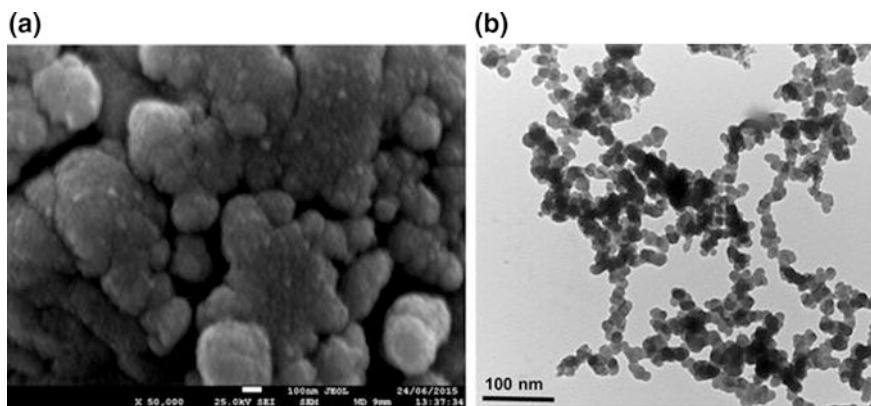
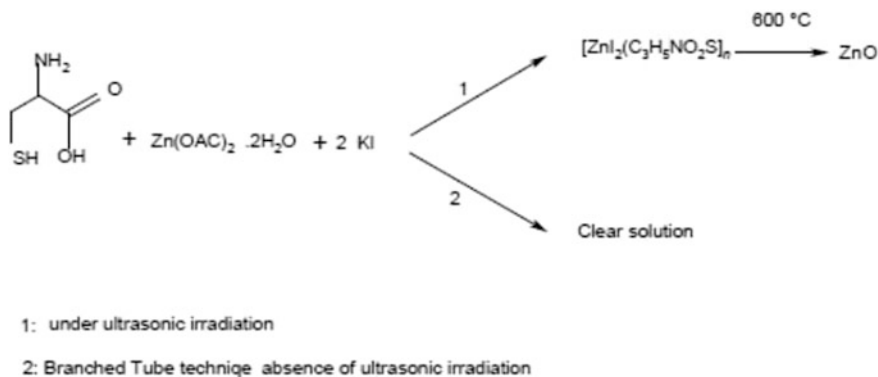
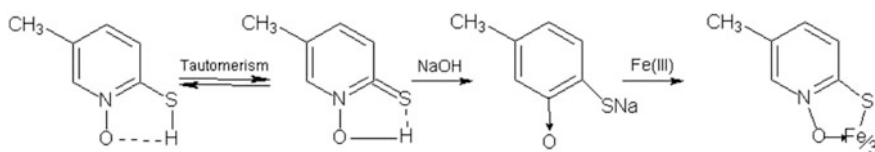


Fig. 3.77 **a** SEM; **b** TEM photographs of CuO NPs. Reproduced with permission from Ref. [293]. Copyright (2017) Springer Nature



Scheme 3.48 Materials produced and synthetic methods [294]



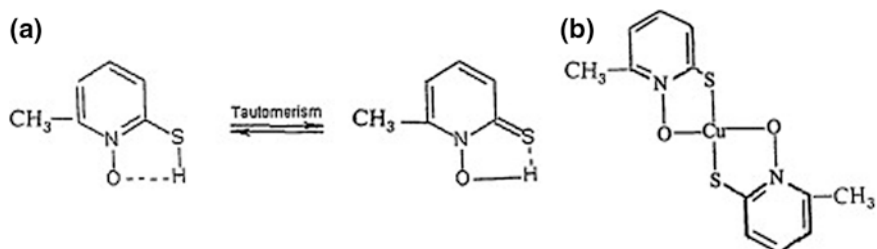
Scheme 3.49 Stages for the preparation of iron(III) chelate. Reproduced with permission from Ref. [295]. Copyright (2011) John Wiley and Sons

Another interesting example is Fe(L)_3 chelate based on 2-mercapto-5-methylpyridine-*N*-oxide (L) obtained accordingly to Scheme 3.49 [295]. The thermolysis of this chelate at 623 K yielded highly pure reddish-brown $\gamma\text{-Fe}_2\text{O}_3$ nanocrystallites with APS of 6.2 nm and a specific surface area of $51.5 \text{ m}^2 \text{ g}^{-1}$. The undoubtable advantages of producing nano- $\gamma\text{-Fe}_2\text{O}_3$ by thermolysis of this metal chelate are a high purity and low particle size of the product, a high specific surface area due to the formation of considerable amounts of volatile materials in the thermolysis process, using aqueous media and, therefore, the possibility of commercial production.

It should be noted copper chelate CuL (Scheme 3.50), where L is 2-mercapto-6-picoline-*N*-oxide, used as SSP for the preparation of CuO NPs (APS of 6.8 nm) via thermolysis [296].

CdS NPs with different shapes and sizes (rods and spheres) were obtained by thermolysis of complex $[\text{Cd}(\text{SOCPh})_2\text{Lut}_2]$ (Fig. 3.78), where Lut = 3,5-dimethylpyridine (lutidine), using structure-directing solvents such as en, dimethylsulfoxide (DMSO) and ammonia [297].

It is important that different morphologies (cubic, and hexagonal phases) and the sizes of CdS can be obtained from the same SSP, depending on the reaction parameters (Table 3.12) [297]. For example, the obtained CdS NPs looks like rod (hexagonal crystallite) when en was used as the solvent (393 K for 15 min).



Scheme 3.50 **a** 2-Mercapto-6-picoline-*N*-oxide (L); **b** Cu(II)-bis(2-thio-6-picoline-*N*-oxide) (CuL). Reproduced with permission from Ref. [296]. Copyright (2013) Elsevier

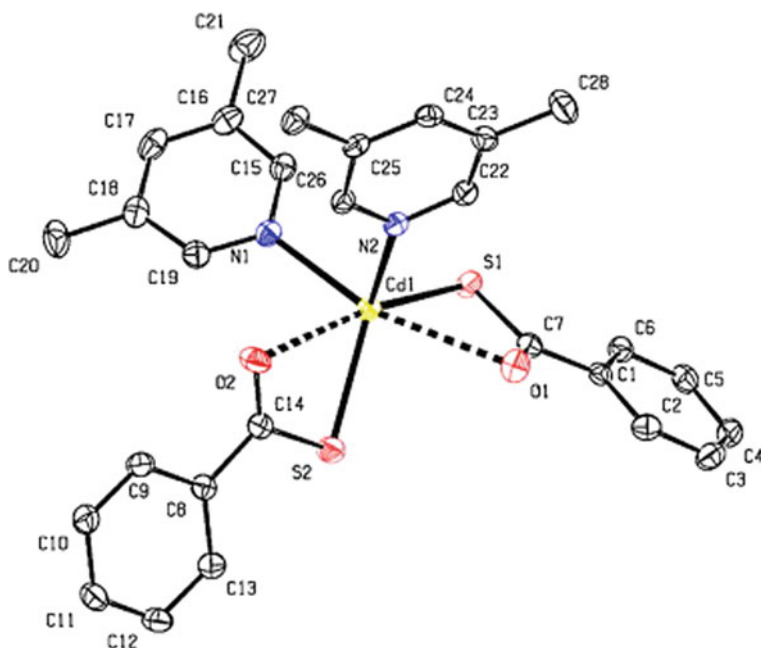


Fig. 3.78 ORTEP diagram of the complex $[Cd(SOCPh)_2Lut_2]$. Reproduced with permission from Ref. [297]. Copyright (2012) Elsevier

Using DMSO and NH_3 as solvents (393 K for 15 min and 300 K for 12 h) allows to obtaining the CdS NPs showing spherical morphology (hexagonal crystallite). In addition, direct thermolysis of the SSP gives nanospheres of larger size than that of DMSO and NH_3 , with cubic crystallite.

Thermolysis of the similar precursor $[Pb(SCOPh)_2]$ led to PbS [298].

Table 3.12 Summary of reaction conditions and experiments results

Reactants	Temp (K)	Time	Shape	Average size (nm)		Average pore diameter (nm)	Specific surface area (m ² g ⁻¹)
				XRD	TEM		
Precursor	673	1 h	Spherical	6.7	10	4.5	57.3
Precursor + en	393	15 min	Rod	5.1	$D = 6^a$, $L = 25\text{--}100^b$	3.8	43.2
Precursor + DMSO	393	15 min	Sphere	3.8	4	2.9	33.1
Precursor + NH ₃	300	12 h	Sphere	3.86	4	2.2	26.6

^aDiameter^bLength

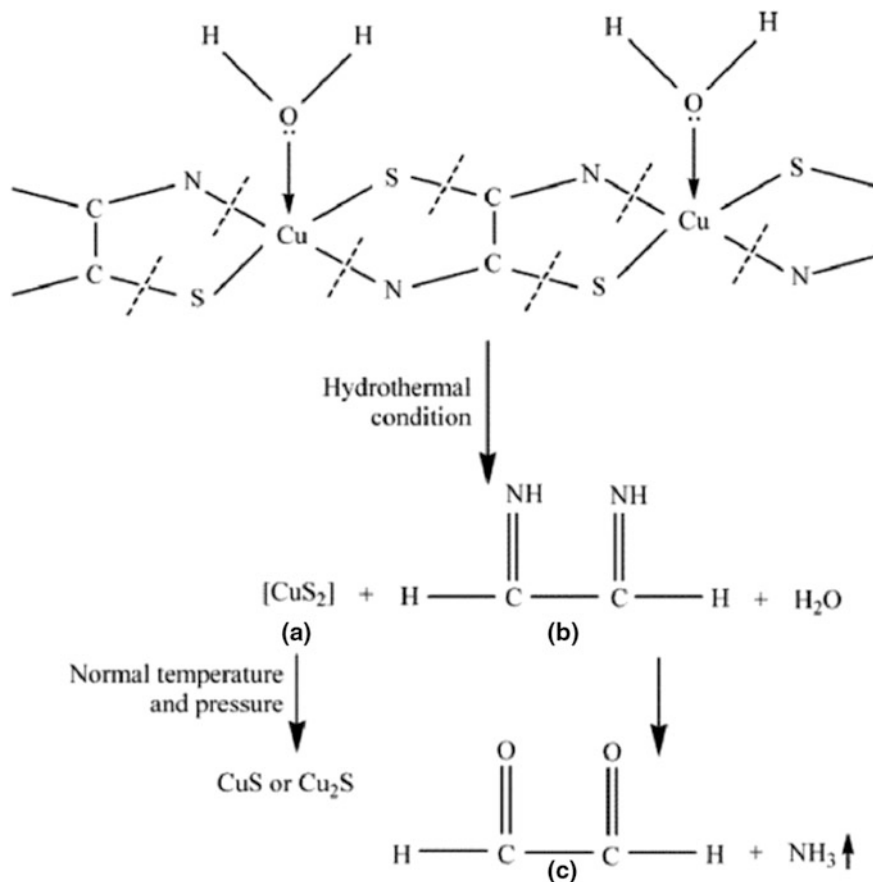
3.7.1 Metal Chelates with N,S (Se, Te)-Donor Ligands

Metal complexes with N,S (Se, Te)-chelating ligands are paid wide attention due to the possibility of synthesis of semiconductor nanomaterials such as CdSe, CdS, ZnS, and PbS [299–303]. It is anticipated that the size and shape of such nanomaterials entirely depend upon the crystal structures of the initial SSPs. As a typical example, we note the preparation of CuS nanowires from Cu-dithiooxamide by a hydrothermal method at 393 K for 24 h (Scheme 3.51) [304]. It is important that the nanowires are 40–80 nm in diameter and up to a few microns long. In addition, reaction temperature, duration, and solvents have substantial effect on the formation of a covellite form of CuS having a hexagonal phase.

Of interest are the thiosemicarbazide complexes [Cd(NH₂CSNHNH₂)Cl₂]·H₂O (complex A) and [Cd(NH₂CSNHNH₂)₂Cl₂] (complex B) which are effective SSPs for the preparation of CdS nanomaterials (Fig. 3.79) [305, 306].

Their thermolysis in HDA results in the formation of nanorods of different dimensions (Fig. 3.80). It is interesting that in both cases there is a predominance of anisotropic material. However, while the aspect ratios of the materials are approximately the same, there is a significant difference in the widths of the rods. Complex A gave rods with widths approaching the Bohr radius of 6.0 ± 1.5 nm, whereas complex B results in rods with significantly smaller widths of 3.0 ± 0.5 nm.

It should be noted using of thiosemicarbazide complexes of lead bromide as SSPs for the preparation of a cubic phase of galena by thermolysis (Scheme 3.52) [307]. It turned out that the nature of the chelate utilized in the synthesis of PbS via SSP method has a significant impact on the properties of the NPs. In particular, smaller cubic shapes and QDs were yielded from cinnamaldehyde thiosemicarbazide and benzophenone thiosemicarbazide complexes due to larger ligands and the symmetrical position of the thiosemicarbazide group in benzophenone chelate. At the same time, relatively larger NPs were obtained from acetophenone



Scheme 3.51 Thermolysis of Cu-dithioamide complex under hydrothermal conditions. Reproduced with permission from Ref. [304]. Copyright (2006) American Chemical Society

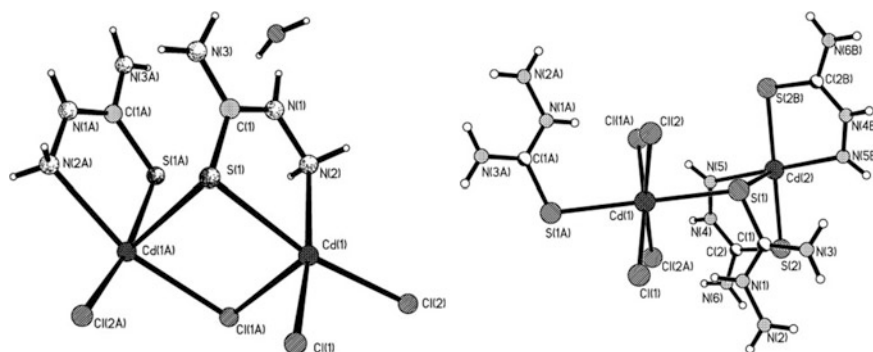


Fig. 3.79 Structures of $[\text{Cd}(\text{NH}_2\text{CSNHNH}_2)\text{Cl}_2]\cdot\text{H}_2\text{O}$ (left) and $[\text{Cd}(\text{NH}_2\text{CSNHNH}_2)_2\text{Cl}_2]$ (right). Reproduced with permission from Ref. [306]. Copyright (2009) Elsevier

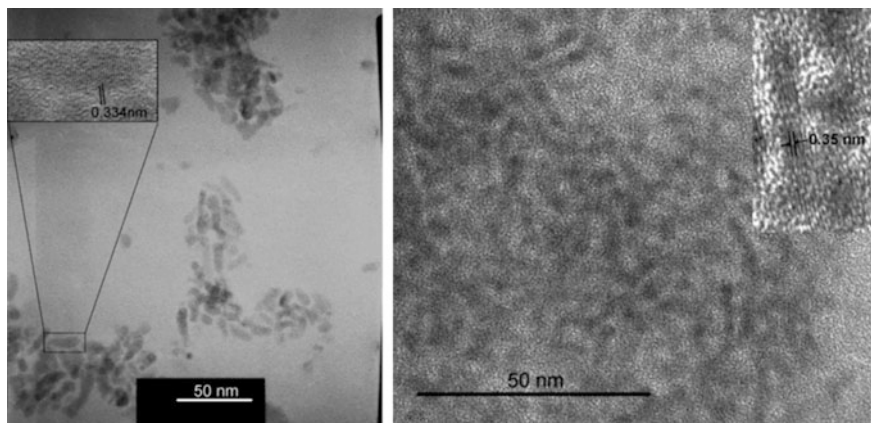
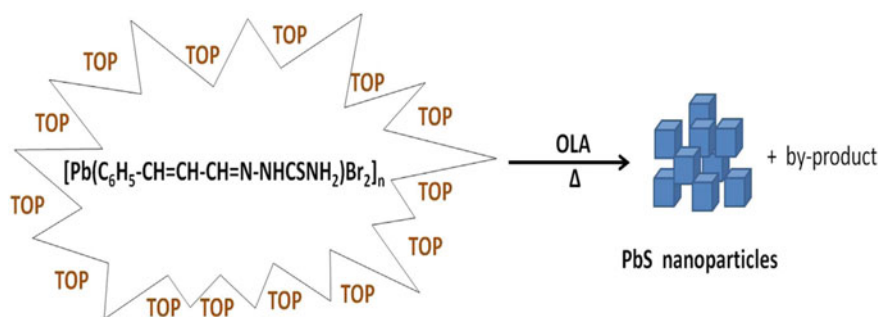


Fig. 3.80 TEM of nanorods prepared from complex A (left) and complex B (right) at 453 K in HAD. Reproduced with permission from Ref. [306]. Copyright (2009) Elsevier



Scheme 3.52 Scheme of synthesis of PbS NPs by thermolysis of thiosemicarbazide chelates [307]

thiosemicarbazide complex. In addition, the shape and size of PbS NPs also depend on the temperature of synthesis.

Cd(II) thiosemicarbazone chelates were used as SSPs for the synthesis of OAm-capped CdS NPs by solvothermal decomposition [308]. It is important that CdS NPs in the form of cubes/spheres/rods and nanodendrite structures were obtained from CdCl₂ and CdI₂ thiosemicarbazone chelates, respectively. In this process, the size, morphology, and shape of the NPs depend on the temperature of formation.

Nanoflowers and nanospheres of palladium sulfide Pd₄S were obtained from a SSP [PdCl₂(PhS-CH₂CH₂CH₂-NH₂)] by its one-pot thermolysis at 468 K [309]. Thermolysis of 3-phenylsulfonylpropylamine chelate of palladium chloride (Fig. 3.81, left) at 468 K in OAm leads to the formation of flower-shaped NPs, whereas Pd₄S nanospheres (size in the range ~23–38 nm and 15–28 nm,

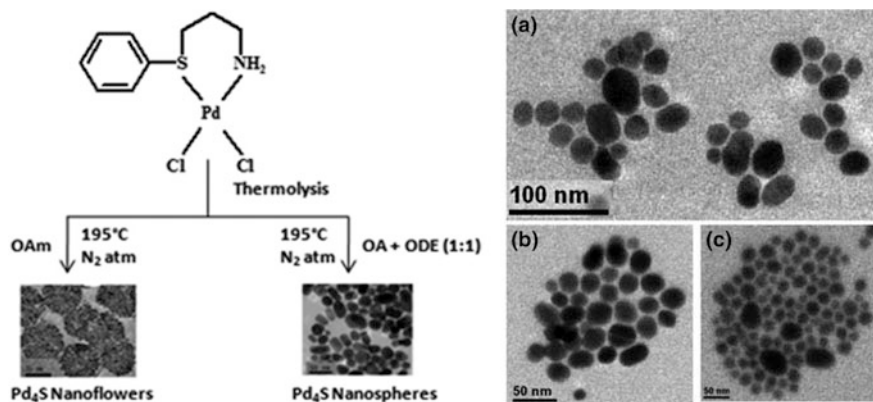
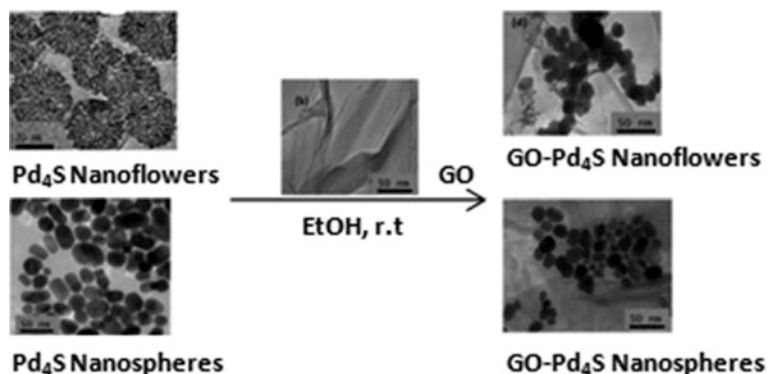


Fig. 3.81 (left) The scheme for obtaining NPs of palladium sulfide from precursor $[\text{PdCl}_2(\text{PhS-CH}_2\text{CH}_2\text{CH}_2\text{-NH}_2)]$ and (right) HRTEM images of the synthesized Pd_4S nanoflowers at different reaction times; **a** 10 min (scale bar 100 nm), **b** 20 min (scale bar 50 nm), and **c** 30 min (scale bar 50 nm). Reproduced with permission from Ref. [309]. Copyright (2014) Royal Society of Chemistry



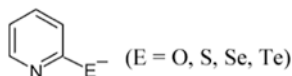
Scheme 3.53 Synthesis of nanocomposite $\text{GO-Pd}_4\text{S}$ nanoflowers and nanospheres. Reproduced with permission from Ref. [309]. Copyright (2014) Royal Society of Chemistry

respectively) are formed in OA and ODE mixture (1:1). Apparently, the flower shape of the obtained NPs is determined by the stronger complexing and reducing properties of OAm [147, 292]. This can be appreciated easily on monitoring the thermolysis carried out in OAm at 10, 20, and 30 min intervals by recording the TEM of the NPs formed (Fig. 3.81, right).

These NPs were grafted on graphene oxide (GO) at room temperature to form nanocomposite materials, $\text{GO-Pd}_4\text{S}$ (Scheme 3.53). It is interesting that the shape of the resulting NPs is not changed during their attachment to the GO as a carrier and has a significant influence on the catalytic properties of these nanocomposites in

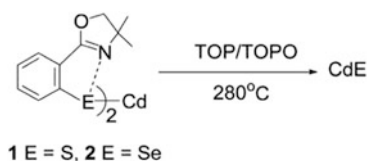
Suzuki–Miyaura coupling reactions. In particular, the catalytic efficiency follows the order GO–Pd₄S-nanoflowers > GO–Pd₄S-nanospheres > Pd₄S nanoflowers > Pd₄S nanospheres.

It should be noted that one of the most interesting families of chelating ligands for the synthesis of SSP is chalcogenopyridines:

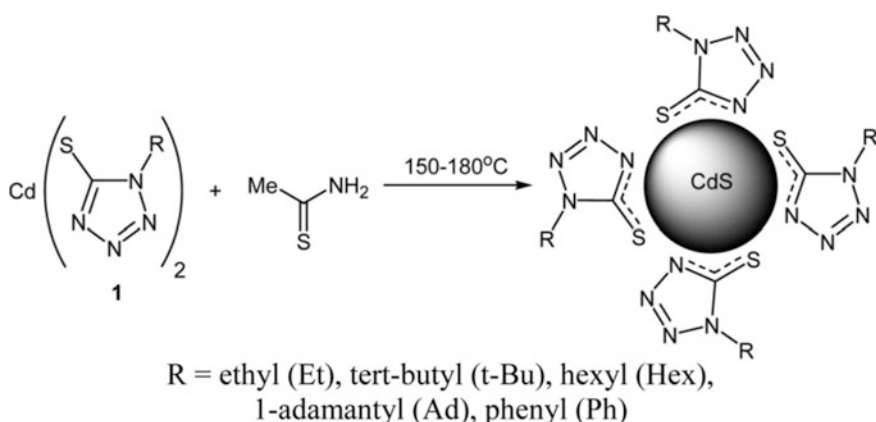


Metal chelates of 2-thio and 2-selenopyridines are well known, while the coordination chemistry of 2-telluriumpyridines is just beginning to develop. For example, thermolysis of [M(Te-Py)₂] in a furnace or in coordinating solvents such as HDA/TOPO at 623 and 433 K, respectively, gave MTe NPs [310].

Interestingly, thermolysis of Cd[E(L)]₂ [E = S, Se; L = 2-(4,4-dimethyl-2-oxazoliny) benzene] in TOPO medium at 553 K led to CdS or CdSe NPs with a sufficiently large size up to 200 nm according to the following scheme [311]:



CdS NPs capped with 1-R-5-thiotetrazoles were obtained using two different synthetic schemes: solution-phase (Scheme 3.54) and solventless single precursor



Scheme 3.54 Solution-phase synthesis of CdS NPs capped with 1-R-5-thiotetrazoles. Reproduced with permission from Ref. [312]. Copyright (2008) American Chemical Society

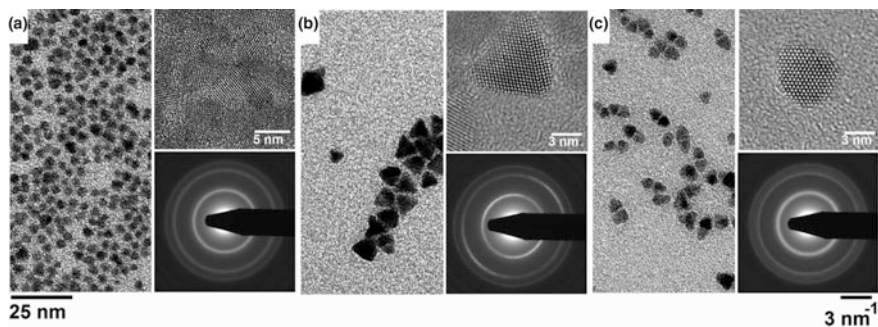


Fig. 3.82 TEM images of CdS NPs as-synthesized by solution-phase approach using 1-R-5-thiotetrazolates **a** R = Et, **b** R = Hex, and **c** R = *t*-Bu. Reproduced with permission from Ref. [312]. Copyright (2008) American Chemical Society

approaches [312]. It is important that in both synthetic procedures cadmium thiotetrazolates were used as cadmium precursors and sources of surfactant.

The monodisperse 3.7 ± 0.3 -nm-diameter CdS NPs were synthesized from cadmium 1-ethyl-5-thiotetrazolate at 423 K (Fig. 3.82a). At the same time, under heating at 453 K CdS NPs with different shapes and sizes are formed depending on the nature of substituent R. In particular, with R = Et or Ad spherical NPs were prepared, and R = Hex led to tetrahedral NPs with ~ 8 nm edge (Fig. 3.82b). However, in the case of R = *t*-Bu both spherical and tetrahedral NPs were prepared (Fig. 3.82c).

3.8 Metal Dichalcogenides

Currently, a wide variety of metal chelates with dichalcogen-containing ligands such as the metal dithio/diselenocarbamates [313–318], xanthates [319, 320], dialkylchalcogenephosphates, dichalcogeneimidophosphates [321–323], and imino-bis(diisopropylphosphine)selenides [324] are used as SSPs for the synthesis of CdS, CdSe, ZnS, ZnSe, and other NPs. The possibility of a wide selection of solvents and surfactant molecules and varying the synthesis conditions allow to tuning the properties of the resulting products and to preparing nanomaterials with targeted characteristics.

Up to now, many ligands from dithiocarbamate (dtc) compounds are used as SSP for metal sulfide production [325, 326]. In particular, metal chelates based on dimethyl-dtc [327], diethyl-dtc [313, 328–337], *N*-alkyl-*N*-cyclohexyl-dtc [338], *N*-methyl-*N*-phenyl-dtc [339], ethylbutyl-dtc [340] are the typical representatives of such SSPs. In thermolysis process with OA and OAm as surfactants, metal sulfides such as 0D Ag₂S, ZnS and CdS QDs, 1D CdS nanorods and ZnS ultrathin nanowires, 2D SnS nanosheets, Bi₂S₃ and Fe₇S₈ nanoplates were obtained. For example,

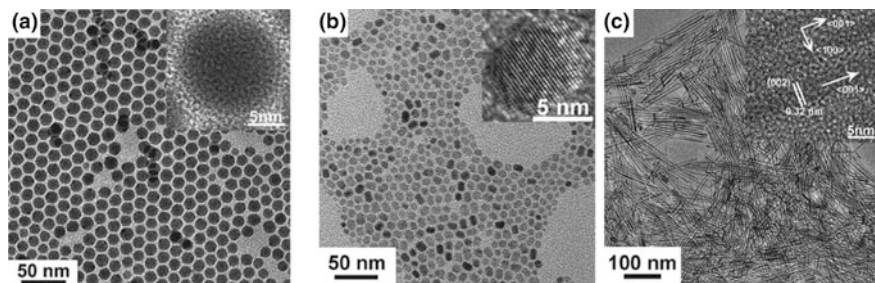


Fig. 3.83 (left) a TEM image of Ag_2S QDs. Insets in (a) are the HRTEM images of a typical Ag_2S QD. Reproduced with permission from Ref. [341]. Copyright (2011) Royal Society of Chemistry; (right) TEM images and XRD patterns of ZnS QDs (a) and nanowires (b). Reproduced with permission from Ref. [342]. Copyright (2010) Royal Society of Chemistry

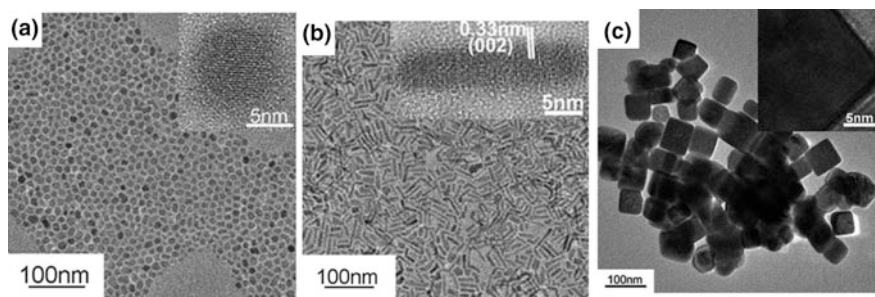


Fig. 3.84 (left) TEM images of CdS QDs (a) and nanorods (b); (right) TEM image (a) of PbS nanocubes. Reproduced with permission from Ref. [341]. Copyright (2011) Royal Society of Chemistry

single crystalline Ag_2S QDs, with a size of 10.2 ± 0.4 nm, were prepared by the thermolysis of $\text{Ag}(\text{diethyl-dtc})$ (Fig. 3.83, left) [341]. Single crystalline ZnS QDs with a size of 9.5 nm were also obtained (Fig. 3.83a, right) by the thermolysis of $\text{Zn}(\text{diethyl-dtc})_2$ in the presence of OA, OAm, and ODE [342]. In addition, the size and shape of the same metal sulfides could be simply controlled by changing the type of surfactants and solvents. Thus, ultrathin crystalline ZnS nanowires, with a diameter of 4.4 nm and length of 300 nm, were prepared from the reaction with OAm as surfactant in ODE solvent. At the same time, under these conditions, ZnS nanocrystals were able to grow along $\langle 001 \rangle$ direction due to the selective adsorption of OAm onto the $\{100\}$ crystal planes and the inhibition of isotropic growth (Fig. 3.83b, right).

In a similar way, CdS QDs with a diameter of 7.5 nm and CdS nanorods with a diameter of 5.7 nm and length of 16 nm were obtained (Fig. 3.84a, b, left) [341, 343]. It should be noted the preparation of PbS nanocubes with APS of 50 nm in the OAm/ODE system in addition to 0D QDs and 1D nanowires (Fig. 3.84a, right).

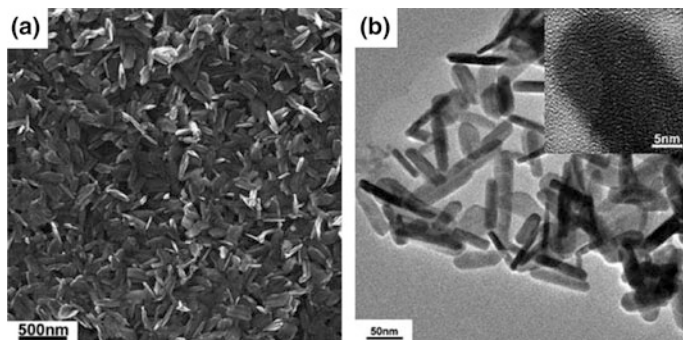


Fig. 3.85 **a** SEM image and **b** TEM image of Bi_2S_3 nanoplates. Reproduced with permission from Ref. [341]. Copyright (2011) Royal Society of Chemistry

CdS flower-like nanostructures were synthesized through facile hydrothermal decomposition of the cadmium diethyl-dtc SSP solution. The morphologies of the nanostructures can be controlled by manipulating the precursor concentration and the reaction time [341]. Bi_2S_3 nanoplates with a diameter of 16 nm and length of 80 nm were also obtained (Fig. 3.85).

SnS rectangular nanosheets were synthesized under low concentration of SSP with OAm as capping ligand (Fig. 3.86a–c) [344]. The prepared nanosheets represent a uniform size of 7000 nm \times 3000 nm \times 20 nm and have the highly crystalline nature (inset in Fig. 3.86b).

When using $\text{Fe}(\text{diethyl-dtc})_3$ as SSP and carrying out the thermolysis in the mixture of OAm and ODE, Fe_3S_4 NPs were obtained. These NPs with sizes in the range of 30–200 nm have the tendency to form aggregates (Fig. 3.87, left, a, b) [345]. In addition, the as-synthesized Fe_3S_4 NPs are single crystal with a cubic-phase structure (inset in Fig. 3.87, left, b). Solvents also play an important role in controlling the composition of metal sulfides. When $\text{Cu}(\text{diethyl-dtc})_2$ was thermolyzed in dodecanethiol at 493 K, Cu_2S QDs with a uniform size of 6.5 nm were obtained (Fig. 3.87, right, a).

The formation of cuprous sulfide (Cu_2S) and lead sulfide (PbS) nanomaterials directly on substrates by the thermolysis of SSPs, $\text{Cu}(\text{diethyl-dtc})_2$ and $\text{Pb}(\text{diethyl-dtc})_2$, was shown [313]. The final morphology and arrangement of the nanomaterials may be controlled through the concentration of the dissolved SSPs and choice of solvent. 1D morphologies may also be grown onto substrates with the addition of a metal catalyst layer through solution–liquid–solid growth.

Core–shell microspheres (Fig. 3.88) can be made from hexagonal CuS by thermolysis of $\text{Cu}(\text{octyl-dtc})_2$ precursors at 403–453 K under N_2 flow for 0.5 h [346].

Nature of ligand of the metal chelate SSP could be used in the modification of the size and shape of the NPs. For example, variation of the alkyl groups on the dtc ligand led to the particles with non-spherical morphologies [318]. It was also shown that SSP with shorter alkyl group yields larger rods of Bi_2S_3 [347]. Nanorods of

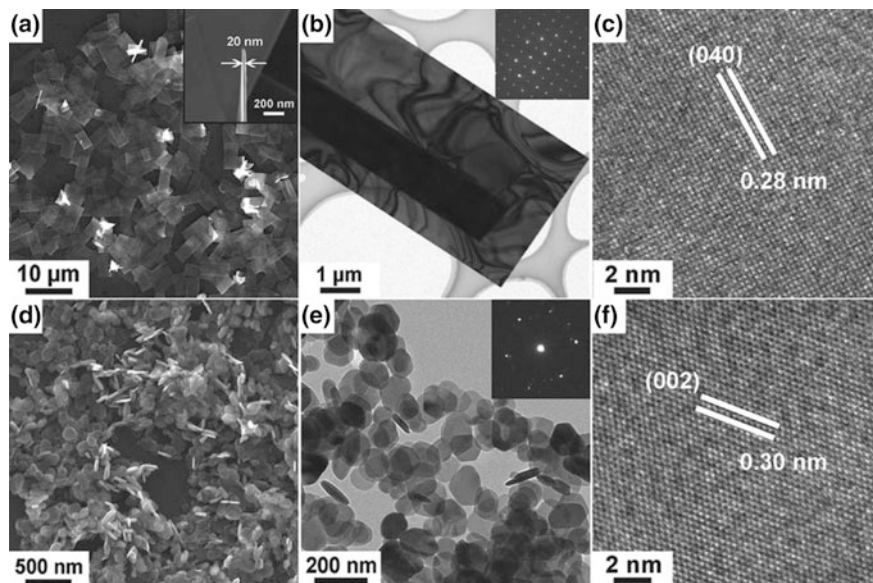


Fig. 3.86 SEM, TEM, and HRTEM images of SnS nanosheets (a–c) and SnS₂ nanoplates (d–f). Reproduced with permission from Ref. [344]. Copyright (2011) Royal Society of Chemistry

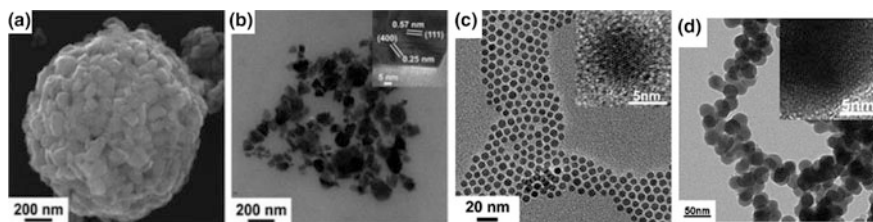


Fig. 3.87 (left) As-obtained Fe₃S₄ NPs. **a** SEM image; **b** TEM and HRTEM (inset) images, obtained at room temperature (300 K). Reproduced with permission from Ref. [345]. Copyright (2010) Royal Society of Chemistry; (right) **c** TEM image of CuS QDs. **d** TEM image of Cu₇S₄ NPs. Reproduced with permission from Ref. [346]. Copyright (2014) Royal Society of Chemistry

bismuth sulfide were prepared by thermolysis of Bi(*N*-ethyl cyclohexyl dtc)₂ (Scheme 3.55) at different thermolysis duration [348].

At 673 K, SSP was fully thermolyzed to orthorhombic bismuth sulfide after 2 h of thermolysis, while a mixture of short and long nanorods of Bi₂S₃ was obtained after thermolysis from 2 to 6 h (Fig. 3.89). It is important that different thermolysis duration does not affect the morphology of the sample except for a slight change in the particle size. Bi₂S₃ nanorods with an average width ranging from 29 to 36 nm were obtained. Different sizes of Bi₂S₃ are observed due to the non-uniform

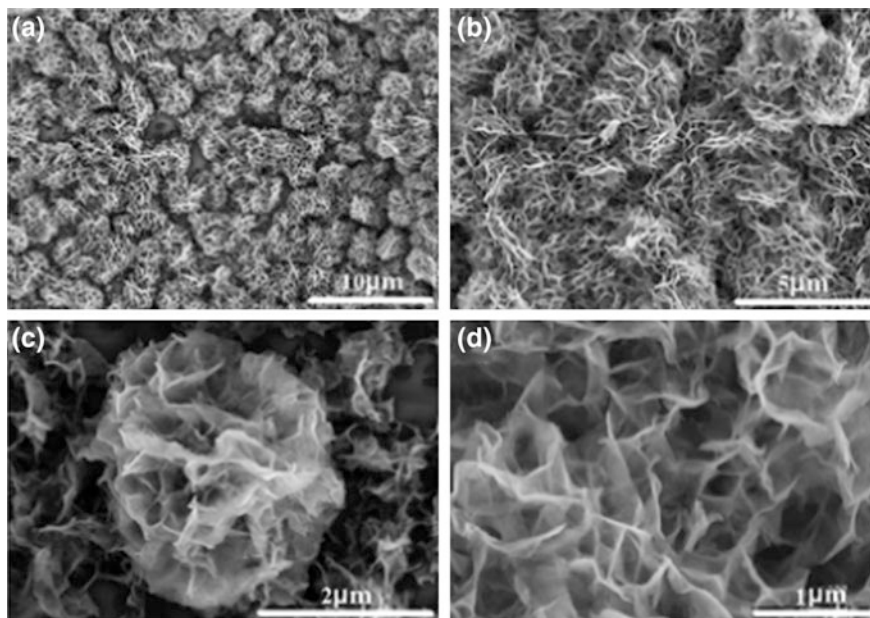


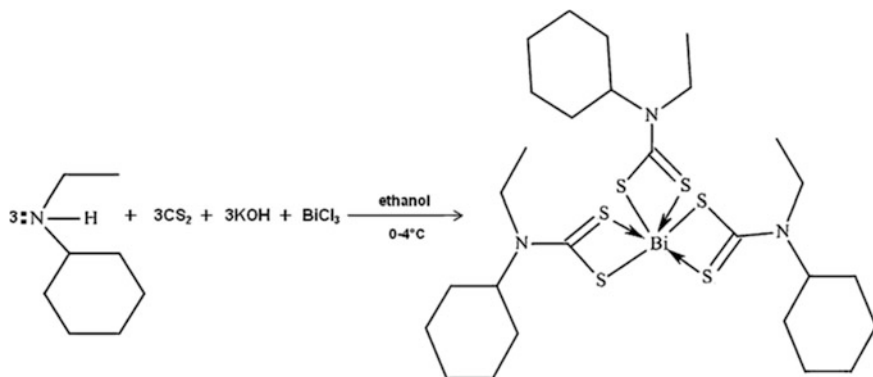
Fig. 3.88 a–d SEM images of CuS hierarchical microflowers. Reproduced with permission from Ref. [346]. Copyright (2014) Royal Society of Chemistry

formation of Bi_2S_3 and overlapping of particles caused by agglomeration. Besides, the particle may compose of two or more individual crystallites. Increment in thermolysis duration has resulted in the formation of larger size Bi_2S_3 nanorods.

The similar $\text{Zn}(N\text{-ethyl cyclohexyl dtc})_2$ precursor (Scheme 3.56) was thermolyzed to hexagonal ZnS after 2–6 h of thermolysis duration at 673 K [349]. The sizes of ZnS NPs were about 6–11 nm. The existence of the hexagonal wurtzite ZnS phase is not affected by the thermolysis duration, while only a slight difference in the crystallinity and crystallite size of ZnS is observed. Pure ZnS can be prepared at a temperature of 673 K, which is about three times smaller than that of bulk ZnS phase transition temperature (1293 K).

ZnS NPs were prepared via two approaches, involving the thermolysis of the SSP, $\text{Zn}(N,N\text{-diallyl dtc})_2$, in a furnace and by solvothermal process in the presence of hexadecylamine (HDA–ZnS) [313]. HDA–ZnS are spherical and monodispersed with APS of 4.5 nm. It should be noted that the ZnS NPs prepared by thermolysis have the hexagonal wurtzite phase, whereas the HDA–ZnS NPs showed a mixture of wurtzite and cubic phase with the cubic phase being dominant.

Hexagonal CuS NPs were prepared by thermolysis of $\text{Cu}(\text{but-dtc})_2$ as SSP at two different temperatures [350]. Particles are almost spherical in shapes with APS of 21–38 nm for CuS1 prepared at 453 K and 3–7 nm for CuS2 prepared at 393 K. This confirms that the choice of thermolysis temperature allows to controlling the crystallite sizes of the NPs. Both CuS1 and CuS2 are spherically shaped NPs



Scheme 3.55 General reaction of bismuth dithiocarbamate. Reproduced with permission from Ref. [348]. Copyright (2016) Elsevier

(Fig. 3.90, left, a and b). The topographical view of the NPs (Fig. 3.90, right) indicated that the as-prepared NPs were rich in dents and irregular surfaces. The room temperature square roughness (R_q) for CuS1 is 29.3 nm with average roughness (R_a) of 21.3 nm. For CuS2, the R_q and R_a values are 155 and 130 nm, respectively.

It should be also noted using Ni(II) dtc complexes as SSPs to prepare HDA-capped NiS nanocrystals with cubic crystalline phases [351]. TEM images showed spherical and close-to-spherical nanocrystals with the size in the range 12–38 nm for NPs from nickel(II) anisidine dtc complex, 8–11 nm for NPs from nickel(II) dibenzyl dtc complex, and 9–16 nm for NPs from nickel(II) butyl dtc complex.

Among dtc SSPs, the substantial place is heterocyclic derivatives of dtc, in particular piperidine-dtc (pip-dtc) and tetrahydroquinoline-dtc (thq-dtc) chelates (Scheme 3.57) [352].

For example, Cd chelates based on these ligands were thermolyzed in HDA to form HDA-capped CdS NPs. A combination of close to spherical, rod, bipods, and tripods was obtained by varying the thermolysis parameters such as SSP concentration and temperature (Table 3.13) [352].

It should be noted that Cd(thq-dtc)₂ was also used as SSP for the synthesis of large faceted hexagonal and close to cubic-shaped HDA-capped CdS NPs [353]. In this case, crystalline NPs of stable wurtzite phase in the shape of a hexagon are clearly observed.

Zn(pip-dtc)₂ and Zn(thq-dtc)₂ thermograms show a single-stage weight loss corresponding to thermal decomposition of the organic ligand with the endothermic peak on the DSC curves at 614.9 K ($\Delta H = 214.3 \text{ J g}^{-1}$) and 567.5 K ($\Delta H = 188.0 \text{ J g}^{-1}$), respectively, [354]. At the same time, a two-stage decomposition is observed with a weight loss at 483 (15.6%) and 577 K (65.5%) in the case of Fe(pip-dtc)₃ [355]. According to the proposed mechanism based on TA and gas chromatography–mass spectroscopy (GC-MS), the detachment of one of the three dtc ligands (m/z 160) proceeds initially to form a four-coordinated intermediate and

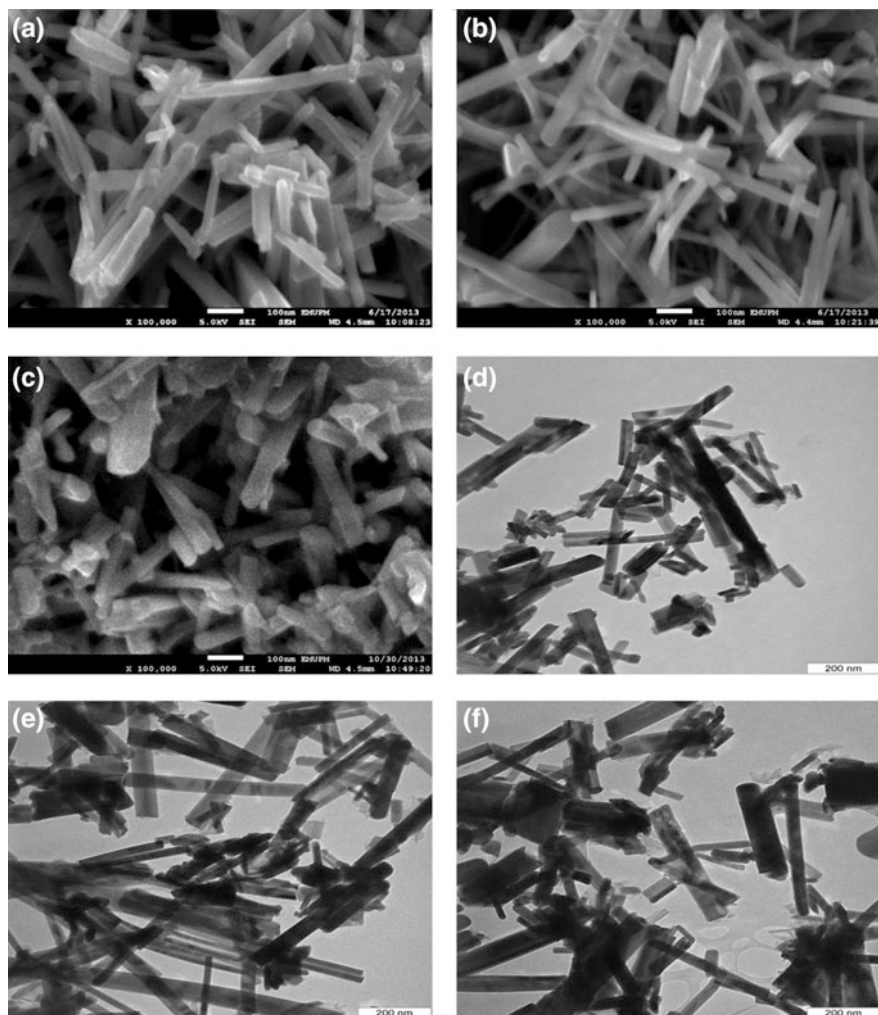
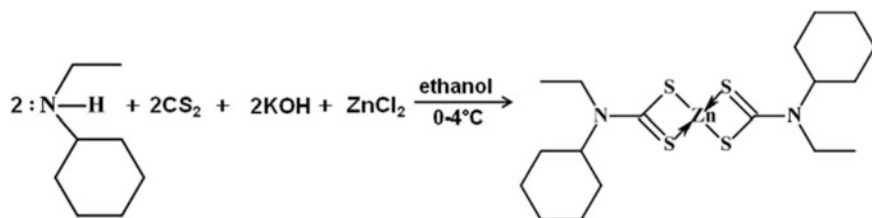


Fig. 3.89 EM images of bismuth sulfide prepared at 673 K and different thermolysis duration: **a** 2 h (FESEM), **b** 4 h (FESEM), **c** 6 h (FESEM), **d** 2 h (TEM), **e** 4 h (TEM), and **f** 6 h (TEM). Reproduced with permission from Ref. [348]. Copyright (2016) Elsevier



Scheme 3.56 General reaction of zinc dithiocarbamate. Reproduced with permission from Ref. [349]. Copyright (2016) Elsevier

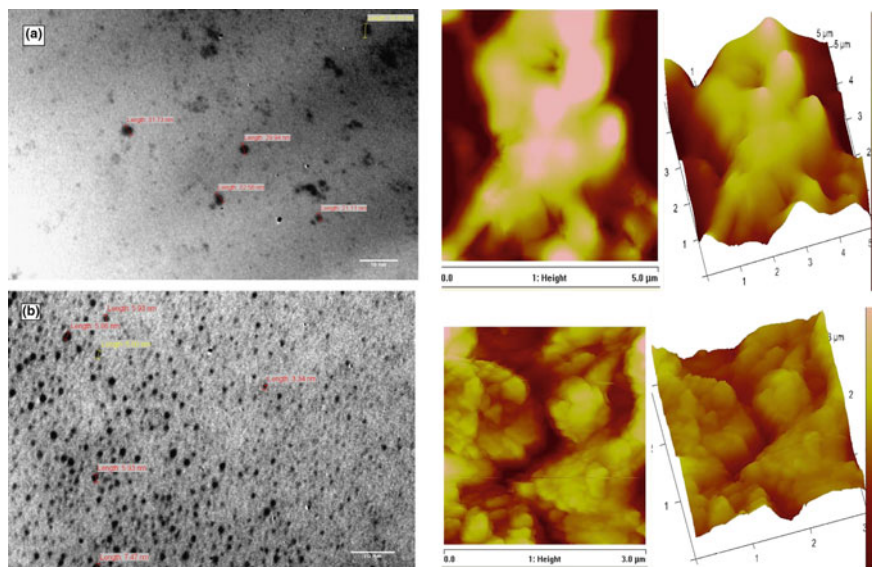
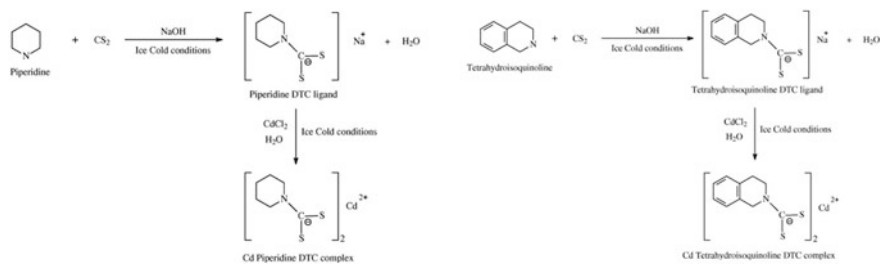


Fig. 3.90 (left) TEM images of CuS1 (a) and CuS2 (b) NPs; (right) AFM and 3D topographical images of the CuS NPs. Reproduced with permission from Ref. [350]. Copyright (2016) Elsevier



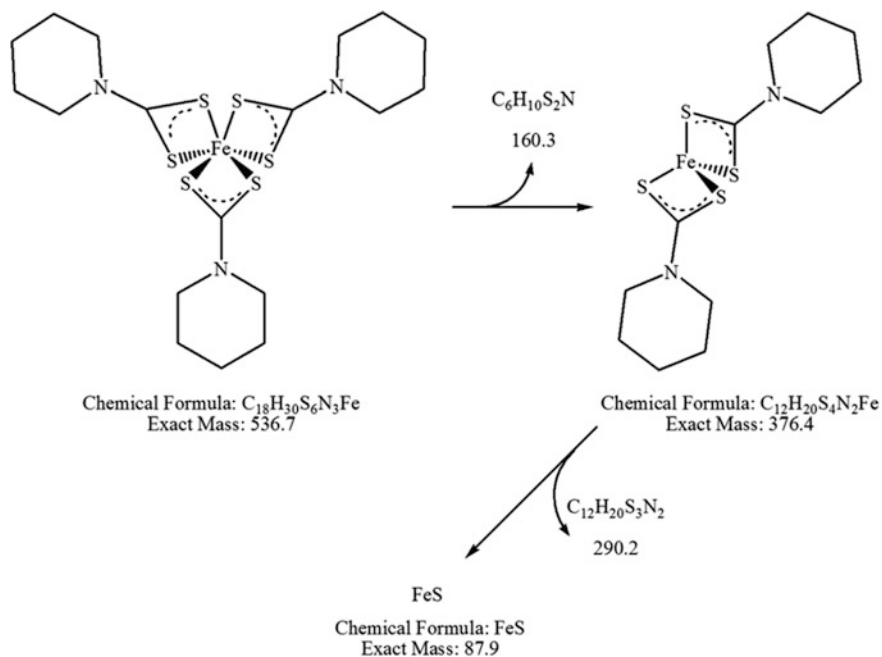
Scheme 3.57 Reaction scheme for the synthesis of Cd pip-dtc complex (left) and Cd thq-dtc complex (right). Reproduced with permission from Ref. [352]. Copyright (2009) Elsevier

then a final removal of organic components (m/z 290) leads to the resulting FeS (m/z 86) product (Scheme 3.58).

The interesting observations were made during the deposition of iron sulfide thin films by aerosol-assisted chemical vapor deposition (AACVD) using $\text{Fe}(\text{pip-dtc})_3$ and $\text{Fe}(\text{thq-dtc})_3$ as SSPs [355]. Iron sulfide films from both complexes are flakes/leaves/sheets, spherical granules, and nanofibres. The sizes and shapes of these crystallites depended on the nature of the SSP, temperature, solvent, and the amount of *tert*-butyl thiol used. Iron sulfide films deposited using $\text{Fe}(\text{pip-dtc})_3$ in toluene (solvent) show the growth of sheet-like structures at 623 K and nanoleaf-/flake-like

Table 3.13 CdS nanocrystals synthesized with Cd(pip-dtc)₂ and Cd(thq-dtc)₂ with HDA at 313 and 353 K

Cd chelate	Mass of HDA (g)	Thermolysis temp. (K)	Particle shape	Particle size (nm)
Cd (pip-dtc) ₂	3.0	313	Oblate	Diameter = 7.9 ± 0.9
	6.0	313	Rods	Length = 14.1 ± 2.1 Breadth = 4.1 ± 0.65
	3.0	353	Dots	19.71 ± 3.24
	6.0	353	Rods Bipods Tripods	Length = 19.35 ± 2.98 Breadth = 5.80 ± 0.78
Cd (thq-dtc) ₂	3.0	313	Rods	Length = 9.99 ± 1.38 Breadth = 5.31 ± 0.9
	6.0	313	Rods Bipods tripods	Length = 18.18 ± 2.10 Breadth = 4.82 ± 0.77
	3.0	353	Dots	Diameter = 20.61 ± 4.72
	6.0	353	Rods Bipods tripods	Length = 20.91 ± 2.96 Breadth = 6.13 ± 1.02

**Scheme 3.58** Scheme of the thermolysis of Fe(pip-dtc)₃ [355]

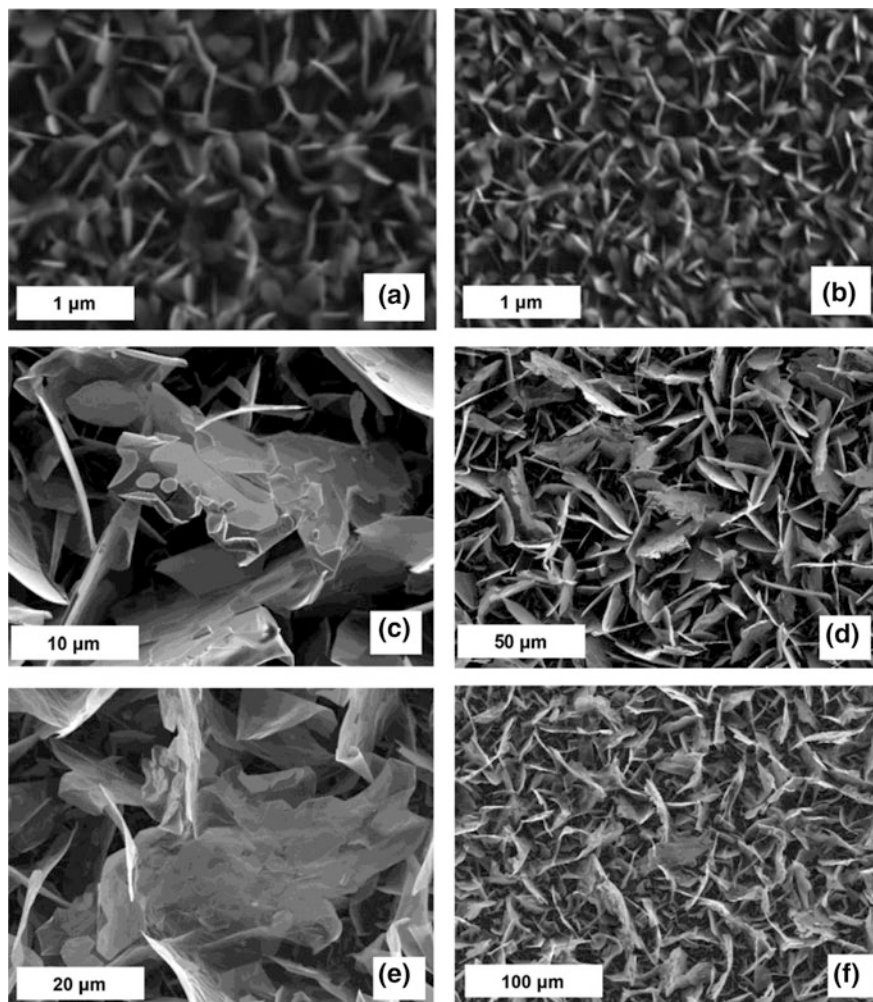


Fig. 3.91 Representative secondary electron SEM images of the iron sulfide thin films deposited at (a, b) 623, 673 (c, d), and (e, f) 723 K using $\text{Fe}(\text{pip-dtc})_3$ [355]

crystallites at 673 and 723 K (Fig. 3.91). The film size increased from 0.6 to 1.0 μm with an increase in deposition temperature from 673 to 723 K.

A similar trend was observed when $\text{Fe}(\text{thq-dtc})_3$ was used as the SSP to deposit a pyrrhotite film (Fig. 3.92a, b). The backscattered electron scanning electron microscopy (BSE SEM) image (which provide Z contrast) of iron sulfide films shows small particles with bright contrast embedded into flakes of darker contrast. Point scanning EDX spectroscopy revealed that the white spots (chunks) were S-rich (Fe 53.7% and S 46.3%), while the opposite is observed for the black spots (flakes) which are Fe-rich (Fe 66.9% and S 33.1%) (Fig. 3.92c). This phenomenon

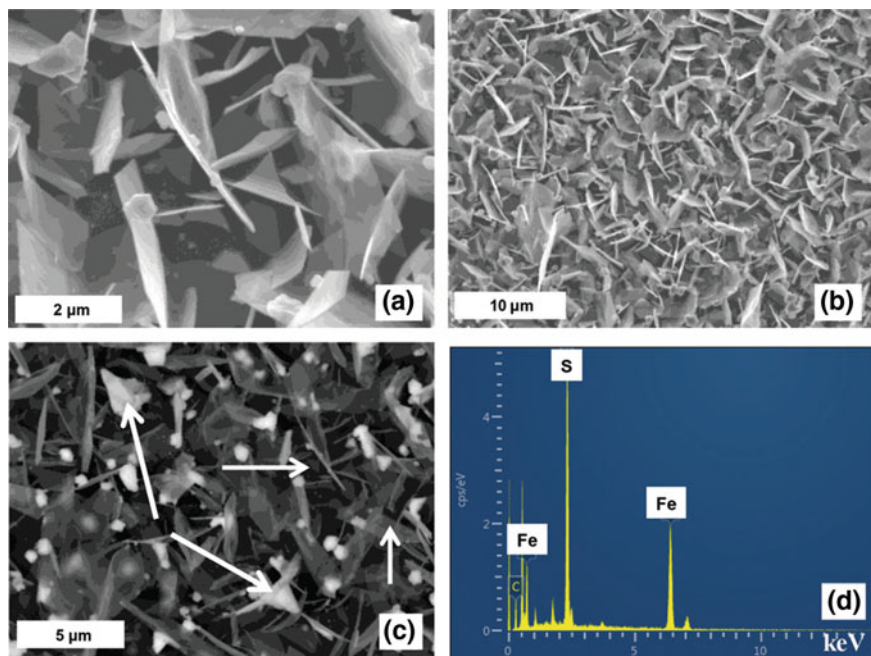


Fig. 3.92 Representative secondary electron SEM images of the iron sulfide thin films deposited at (a, b) 723 K and a BSE SEM image (c) and a representative EDX spectrum (d) when $\text{Fe}(\text{thq-dtc})_3$ was used [355]

validates that Fe and S atoms in an iron sulfide thin film are unevenly distributed on a substrate.

Of interest is the preparation of CdS NPs by the thermolysis of $\text{Cd}(\text{pip-dtc})_2$ or $\text{Cd}(\text{thq-dtc})_2$, and their growth is effectively controlled using capping agents of HDA and TOPO of various concentrations [356]. The thermolysis conditions such as the amount of capping group and thermolysis temperature have an effect on the properties and morphology of the NPs. In particular, elongated CdS particles in the form of rods, bipods, and tripods were obtained for the HDA-capped CdS whereas spherical particles were observed when TOPO was used as the capping material (Fig. 3.93).

It should be noted the using $\text{Cd}(\text{pip-dtc})_2$ or $\text{Cd}(\text{thq-dtc})_2$ as SSPs to deposit CdS films on glass substrates at 623, 673, and 723 K via the AACVD method [357]. APS is in the range between 50–110 nm and 100–220 nm for first and second chelate, respectively. It is important that the morphology, size, and composition of the films are influenced by the deposition temperature.

NP synthesis temperature plays also an important role in the structural-phase transformations. For example, for CdS NPs it is demonstrated that the hexagonal phase is the predominant one at high thermolysis temperatures [358, 359]. During CdS NP preparation by thermolysis of $\text{Cd}(\text{pip-dtc})_2$ in castor oil at 463, 503, 543,

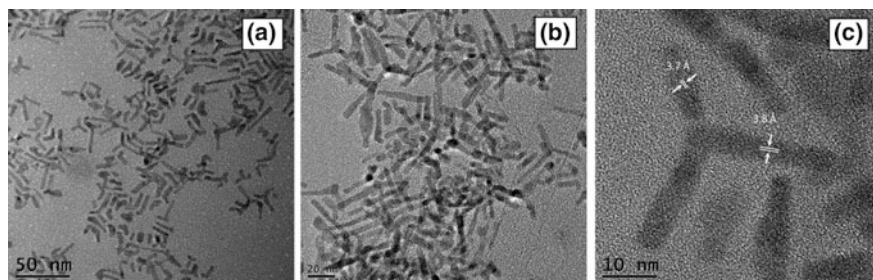


Fig. 3.93 TEM (a, b) and HRTEM (c) CdS NPs images obtained by thermolysis of Cd(pip-dtc)₂ at temperatures 413 (a) and 453 K (b, c) in HAD. Reproduced with permission from Ref. [356]. Copyright (2011) Royal Society of Chemistry

Table 3.14 Morphology and phase composition of the iron sulfide thin films obtained at different reaction conditions

Precursor	Conditions	Morphology	Phase composition
Fe (pip-dtc) ₃	Toluene, 623–723 K, 2 h	Leaf, flake, sheet	Hexagonal (Fe _{0.975} S), marcasite (FeS ₂)
	Chloroform, 623–723 K, 30 min	Fiber	Hexagonal (Fe _{0.975} S), smythite (Fe ₃ S ₄)
	<i>tert</i> -Butyl thiol, 723 K, 2 h	Flower, spherical–globular	Greigite (Fe ₃ S ₄)
Fe (thq-dtc) ₃	Toluene, 623–723 K, 2 h	Leaf, flake, sheet	Pyrrhotite (Fe _{0.95} S _{1.05}), hexagonal (Fe _{0.975} S)
	Chloroform, 623–723 K, 30 min	Fiber	Hexagonal (Fe _{0.975} S)
	<i>tert</i> -Butyl thiol, 723 K, 2 h	Spherical and flake	Greigite (Fe ₃ S ₄)

and 573 K, hexagonal phase was formed at all temperatures, while during the Cd (thq-dtc)₂ thermolysis at 463 and 503 K, metastable cubic phase was formed, and thermodynamically stable hexagonal phase was observed at 543 and 573 K [360]. In contrast, thermolysis of these SSPs in the ricinoleic acid at all temperatures leads to the cubic-phase formation. It should be noted that the occurrence of CdS metastable cubic phase also indicates the quantum confinement effect, because the cubic phase is only characteristic of CdS nanocrystal unlike the hexagonal form which is characteristic of both nanocrystalline and the bulk material [361].

The wide variation in morphology and the phase composition of thin films of iron sulfide from dtc Fe(III) complexes is observed when the conditions change during AACVD process, e.g., temperature, the precursor nature, the solvent type (Table 3.14) [362].

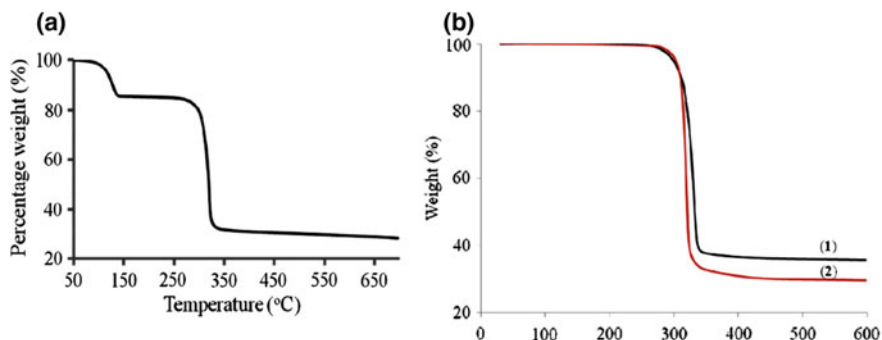


Fig. 3.94 TG curves for complexes of (left) [Cd(pip-dtc)₂Py] [314] and (b) Cd(pip-dtc)₂ (1) and Cd(thq-dtc)₂ (right) [367]

Of interest is the preparation of nanocrystals of SnS by thermolysis of metal diethyl-dtc in OAm at 443 K [363].

The nitrogen-containing ancillary ligands like pyridine (Py) have a significant effect on the thermal stability and volatility of the chalcogenide metal complexes [364–366]. In particular, two stages of thermolysis at temperatures of 403 and 593 K are typical for the pyridine adduct of Cd(pip-dtc)₂, the first of which corresponds to a loss of Py ligand (Fig. 3.94, left) [314]. In contrast, dtc Cd(II) complexes, which does not contain donor adducts, are decomposed in a single step at 604 and 593 K with weight loss of 64.9 and 70.9% for the Cd(pip-dtc)₂ and Cd(thq-dtc)₂ complexes, respectively, (Fig. 3.94, right) [367]. The nonvolatile residues represent 35.1 and 29.1% that is slightly higher than the estimated values of CdS (33.4 and 27.3%), obtained from these complexes.

The same SSP was used for the synthesis of hexagonal CdS NPs by thermolysis in HDA at different temperatures in the range 463–543 K and CdS thin films by AACVD method [367].

It is important that CdS NPs obtained by [Cd(pip-dtc)₂Py] thermolysis at 463 K had rod form with a length of 64.38 ± 4.62 nm and a width of 5.20 ± 0.98 nm with an aspect ratio of 12.38 (Fig. 3.95) [314]. At 503 K, nanorods had a size of 24.84 ± 4.42 nm in length and 6.58 ± 1.02 nm in width, whereas oval-shaped NPs with a diameter of 16.8–23.3 nm along with rod shape NPs are formed at 543 K.

Complexes *catena*-(μ_2 -nitrate-*O,O'*)bis(pip-dtc) bismuth(III) (1) and tetrakis(μ -nitrate)tetrakis[bis(thq-dtc) bismuth(III)] (2) were used as SSPs for the synthesis of dodecylamine-, HDA-, OAm-, and TOPO-capped orthorhombic Bi₂S₃ NPs at different temperatures [368]. High-quality, crystalline, long, and short Bi₂S₃ nanorods were obtained depending on the thermolysis temperature, which was varied from 463 to 543 K. A general trend of increasing NP breadth with increasing thermolysis temperature and increasing length of the carbon chain of the amine (capping agent) is shown (Table 3.15).

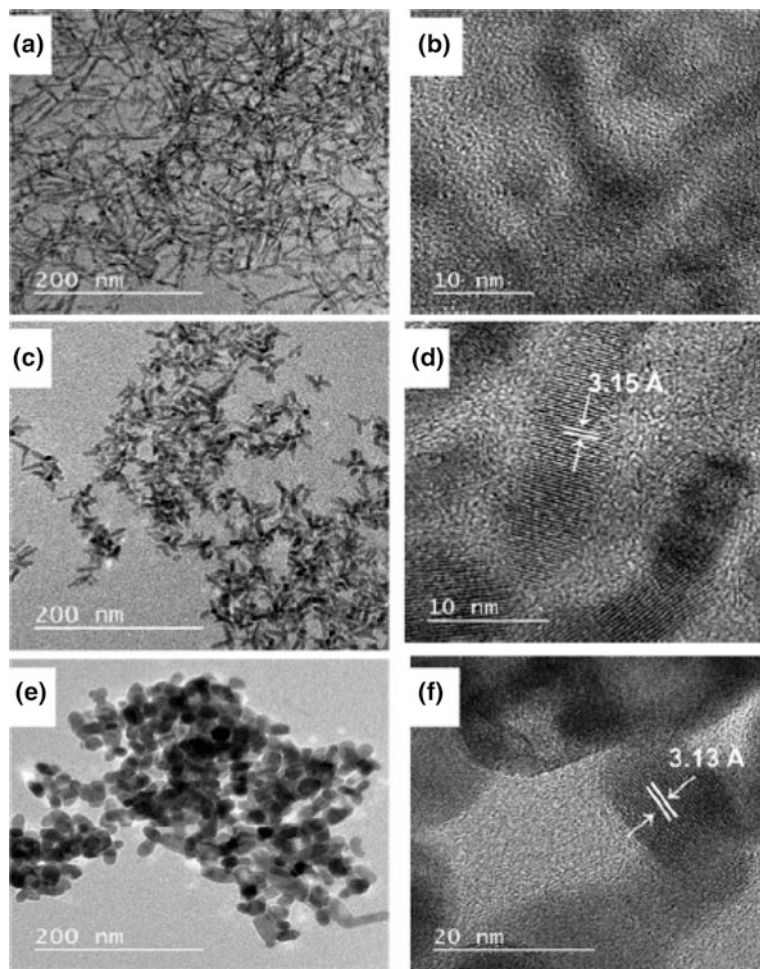
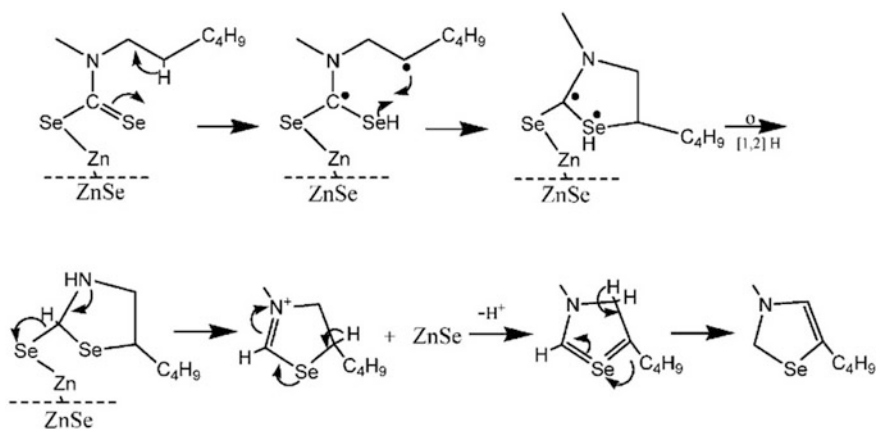


Fig. 3.95 TEM and HRTEM images of HDA-capped CdS NPs obtained by thermolysis of [Cd(pip-dtc)₂Py] at 463 (a, b), 503 (c, d), and 543 K (e, f) [314]

It should be noted that depending on the nature of the substituent on the nitrogen atom, the symmetrical diselenocarbamate complexes produced selenium clusters during the thermolysis, while metal selenides are formed in the case of asymmetric diselenocarbamates [369]. By mass spectrometry with electron ionization (electron ionization mass spectrometry EI-MS) and high-resolution pyrolysis GC-MS analysis, it is shown that slight differences in the alkyl substituents on the nitrogen atom of the diselenocarbamate ligand of $\text{Zn}(\text{Se}_2\text{CNET}_2)_2$ and $\text{Zn}(\text{Se}_2\text{CNMe}^n\text{Hex})_2$ complexes are responsible for the two routes of their thermolysis. In the first case, Se_n clusters ($n = 1-7$) are formed from the intermediate diethyldiselenide EtSe_2Et , whereas stable five-membered intermediate dihydroselenazole $\text{Zn}(\text{Se}_2\text{CNMe}^n\text{Hex})_2$

Table 3.15 Lengths (L) and widths (W) of the Bi₂S₃ nanorods synthesized from **1** with various reaction parameters

Capping agent	T, K	L, nm	W, nm	Aspect ratio (± 0.1)
Dodecylamine	463	161.9 \pm 0.3	16.5 \pm 0.1	9.8
Dodecylamine	503	154.7 \pm 0.4	22.7 \pm 0.1	6.8
Dodecylamine	543	76.1 \pm 0.5	23.9 \pm 0.1	3.2
HDA	463	236.9 \pm 0.2	20.3 \pm 0.1	11.7
HDA	503	217.2 \pm 0.1	24.4 \pm 0.1	8.9
HDA	543	193.5 \pm 0.3	49.9 \pm 0.2	3.9
OAm	463	252.6 \pm 0.2	31.2 \pm 0.1	8.1
OAm	503	221.5 \pm 0.2	36.4 \pm 0.2	6.1
OAm	543	194.2 \pm 0.4	38.3 \pm 0.2	5.1
TOPO	463	182.3 \pm 0.2	29.2 \pm 0.2	6.2
TOPO	503	106.6 \pm 0.1	42.8 \pm 0.2	2.4
TOPO	543	95.4 \pm 0.3	44.1 \pm 0.2	2.1

**Scheme 3.59** Thermolysis mechanism of bis(hexyl(methyl)diselenocarbamato)zinc. Reproduced with permission from Ref. [369]. Copyright (1999) Royal Society of Chemistry

is formed in the latter case, which completely removed from system, and the final product of the thermolysis is metal selenide (Scheme 3.59).

Of interest is using bis(hexylmethyl)diselenocarbamato)cadmium(II)/zinc(II) ($(\text{Se}_2\text{CNMe}^n\text{Hex})_2$ [$M = \text{Zn}, \text{Cd}$]) as SSPs for the preparation of TOPO-capped CdSe and ZnSe NPs [370]. The NPs were of high quality, close to monodispersed, spherical particles. Two samples of CdSe ($t = 10$ min and $t = 24$ h) show well-defined, monodispersed, spherical TOPO-capped CdSe particles (Fig. 3.96).

Thin films of several zinc or cadmium selenides have been deposited on glass substrates by low-pressure MOCVD (LP-MOCVD) using SSPs,

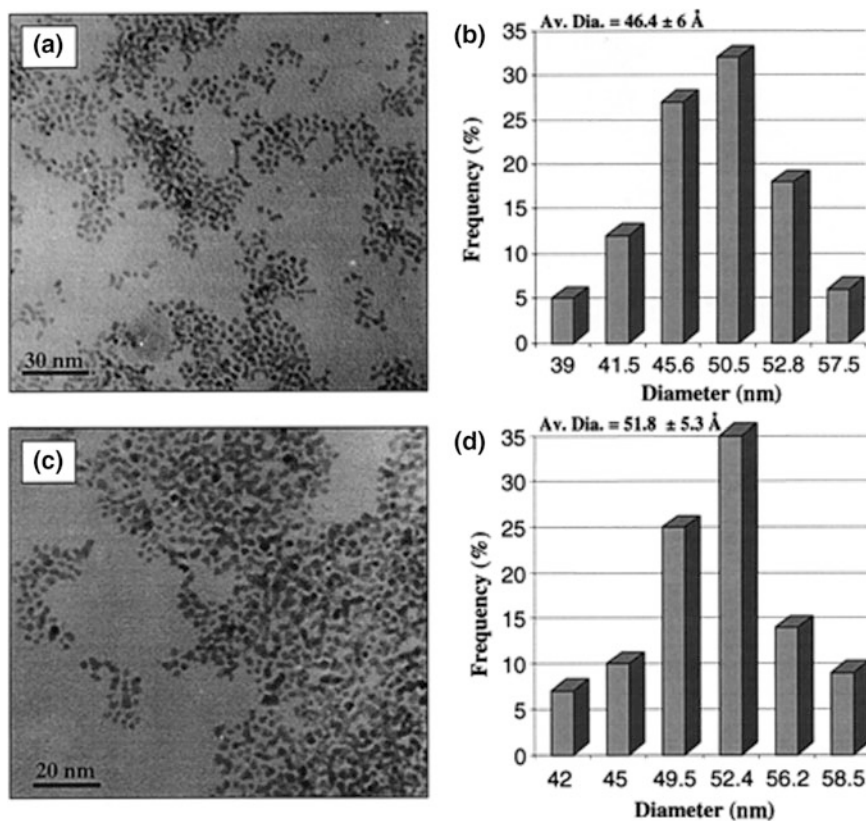


Fig. 3.96 CdSe NPs: **a** TEM image of ($t = 10$ min) and **b** corresponding particle size distribution; **c** TEM of ($t = 24$ h) and **d** corresponding particle size distribution. Reproduced with permission from Ref. [370]. Copyright (2001) American Chemical Society

$[M\{(SeP^iPr_2)_2N\}_2]$, where $M = Cd(II), Zn(II)$ [322]. The morphology of film deposited at 698 and 723 K consists of randomly oriented domains of compacted thin acicular crystallites with ca. $1.75 \mu\text{m}$ in thickness (Fig. 3.97, top). The surface of the film deposited at 748 K consists of globules ranging in size $0.25\text{--}1.25 \mu\text{m}$. Cross-sectional SEM image of the film indicates columnar growth for ZnS, and the growth rate is equal to ca. $1 \mu\text{m h}^{-1}$ (Fig. 3.97, bottom).

$[Cd(Se_2P^iPr_2)_2]$ was used as SSP in OAm for the synthesis of CdSe NPs in a microcapillary reactor (Fig. 3.98) [315]. The different reaction parameters (SSP concentration, growth temperature and residence time) have substantial effect on the size and the optical properties of the NPs.

Of interest is approach to the one-step synthesis of CdSe QDs using the air-stable complex cadmium imino-bis(diisopropylphosphine selenide) (Scheme 3.60) [324]. The prepared QDs are of comparable quality with those

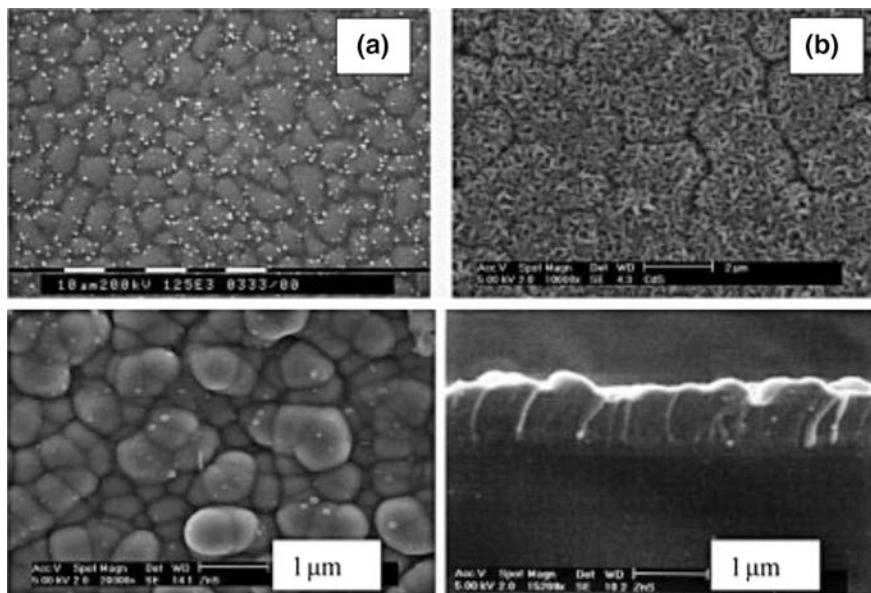
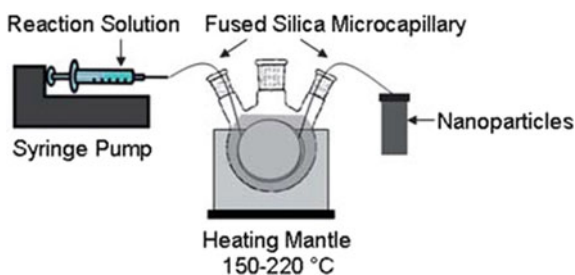


Fig. 3.97 (top) SEM images of CdS films from $[\text{Cd}\{(\text{SP}^i\text{Pr}_2)_2\text{N}\}_2]$ deposited at **a** 698 K and **b** 723 K; (bottom) SEM images of ZnS films deposited at 748 K from $[\text{Zn}\{[\text{SP}^i\text{Pr}_2)_2\text{N}\}_2]$ by LP-MOCVD. Reproduced with permission from Ref. [322]. Copyright (2004) John Wiley and Sons

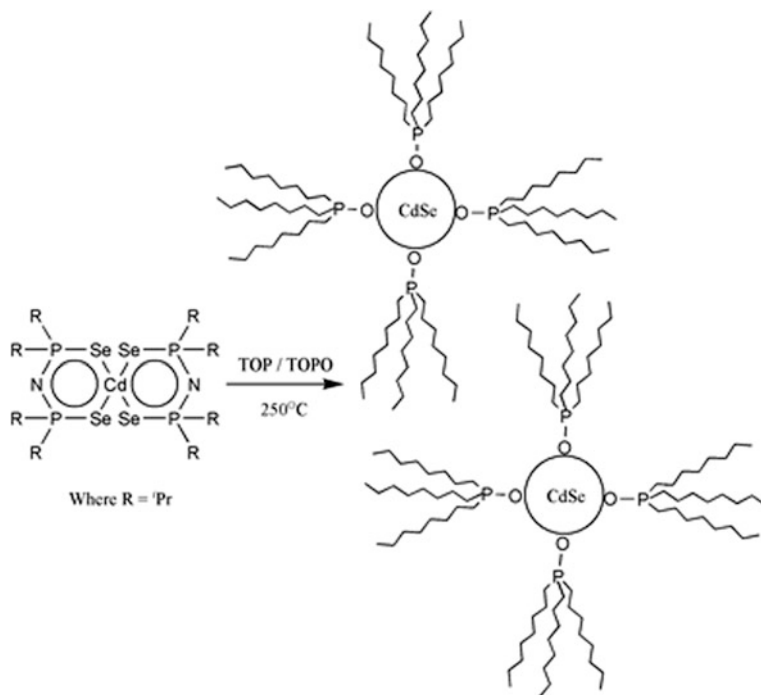
Fig. 3.98 Illustration of the experimental setup using the microcapillary reactor. Reproduced with permission from Ref. [315]. Copyright (2011) Royal Society of Chemistry



obtained by conventional methods, and the QD sizes derived from $\text{Cd}[\text{N}(\text{SeP}^i\text{Pr}_2)_2]_2$ can be precisely controlled by the reaction time.

It should be noted the preparation of nanowires and nanorods of Sb_2Se_3 by thermolysis of $[\text{Sb}\{\text{Se}_2\text{P}(\text{O}^i\text{Pr})_2\}_3]$ at 373–423 K [371].

As a typical example of the preparation of CdTe NPs, we note AACVD using $[\text{Cd}\{(\text{TeP}^i\text{Pr}_2)_2\text{N}\}_2]$ at substrate temperatures between 648 and 748 K [372]. The compounds $[\text{M}(\mu\text{-Te})\text{N}(\text{Pr}_2\text{P}^i\text{Te})_2]_3$ ($\text{M} = \text{In}, \text{Ga}$) were used to deposit M_2Te_3 films onto glass and Si(100) substrates at deposition temperatures between 598 and 748 K [373]. The indium SSP gave cubic In_2Te_3 exclusively, whereas the gallium complex generated a mixture of cubic Ga_2Te_3 , monoclinic GaTe , and hexagonal Te .

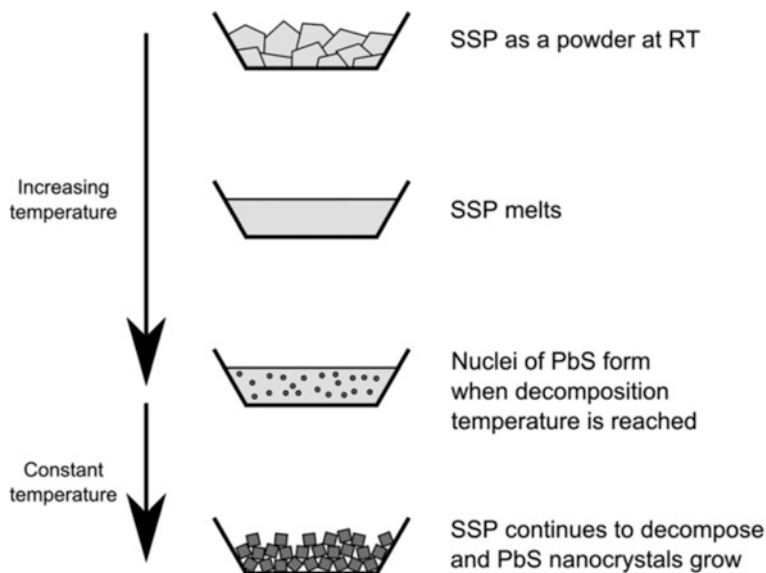


Scheme 3.60 Synthesis of CdSe QDs from cadmium imino-bis(diisopropylphosphine selenide). Reproduced with permission from Ref. [324]. Copyright (2003) Royal Society of Chemistry

Of interest is using metal xanthates as SSPs for the preparation NPs and thin films of metal sulfides [374–376]. As an example, melt reaction synthesis of PbS nanomaterials from Pb(II) alkylxanthates, $[\text{Pb}(\text{S}_2\text{COR})_2]$, is shown in Scheme 3.61 [377].

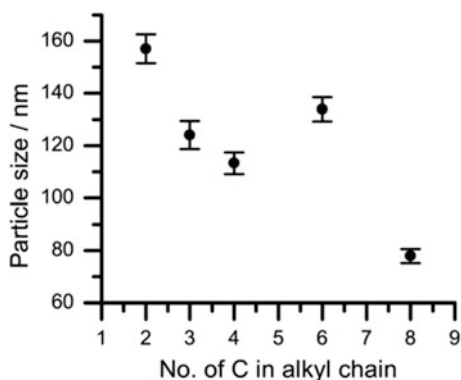
Metal xanthates breakdown via Chugaev elimination produces volatile by-products that should be removed at the reaction temperature [377–380]. The study of the thermolysis of Pb(II) alkylxanthates, $[\text{Pb}(\text{S}_2\text{COR})_2]$ (R = ethyl, *n*-propyl, *n*-butyl, *n*-hexyl or *n*-octyl), showed that the choice of SSP has an influence on nanocrystal size. In particular, thermolysis of SSPs with longer alkyl chains results in smaller cubic nanocrystals (Fig. 3.99). In addition to cubes, anisotropic growth was observed during decomposition of xanthate. It is important that with increasing alkyl chain length the TGA patterns change from a single-step to a two-step thermolysis and in parallel the crystal structures show an increased difference in bonding modes between the two xanthate ligands. The change in bonding modes may be responsible for changes in the thermolysis pathways leading to the appearance of a two-step thermolysis indicating the decomposition of one ligand before the other.

The similar results were obtained during thermolysis of copper(I) xanthate SSPs $[(\text{PPh}_3)_2\text{Cu}(\text{S}_2\text{COR})]$ (R = *iso*-butyl, 2-methoxyethyl, 2-ethoxyethyl,



Scheme 3.61 Solventless thermolysis of lead(II) xanthates to form PbS nanocrystals. Reproduced with permission from Ref. [377]. Copyright (2016) Royal Society of Chemistry

Fig. 3.99 Mean particle edge length from SEM against length of alkyl chain for decomposition at 423 K. Standard errors for the size measurements are displayed ($n = 55$). Reproduced with permission from Ref. [377]. Copyright (2016) Royal Society of Chemistry



1-methoxy-2-propyl, 3-methoxy-1-butyl, and 3-methoxy-3-methyl-1-butyl) [381]. In particular, it turned out the width of the obtained rods is dependent on the length of the xanthate chain. The longer chain xanthates lead to the formation of rods of decreased width. At long thermolysis times, heavily aggregated Cu_2S is formed, while short times result in $\text{Cu}_{1.74}\text{S}$ nanorods.

A Lewis base solvent is used to achieve a low thermolysis temperature of 323–423 K, usually in air [382]. The precise control over the particle size (by regulating the temperature or the concentration) was shown on example of the preparation of CdS. It is important that CdS/ZnS core-shell particles are prepared using the same

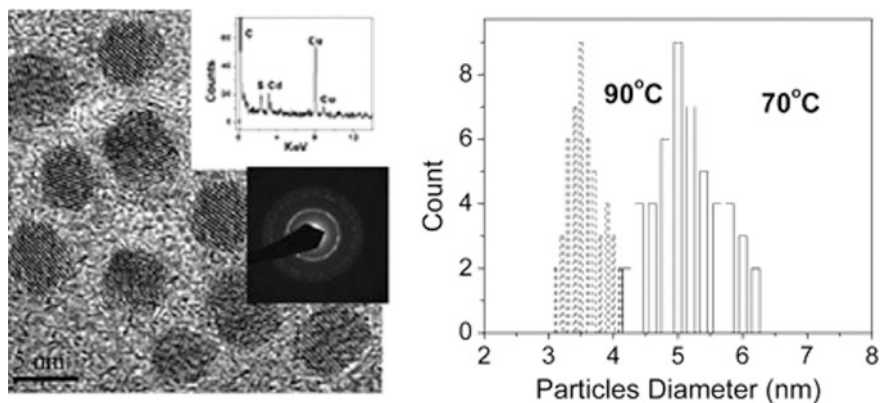
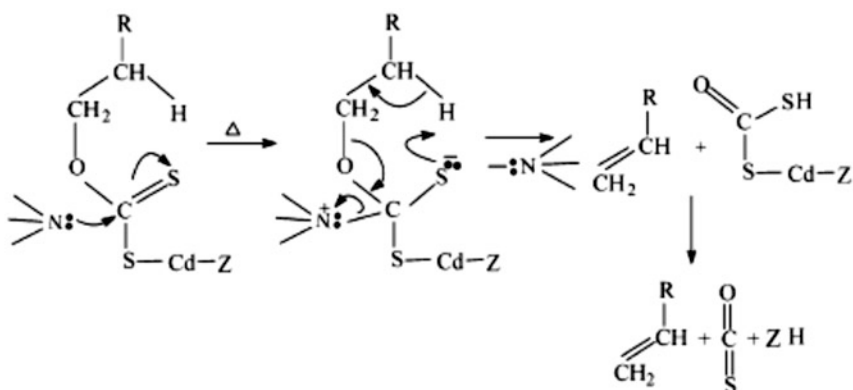


Fig. 3.100 TEM of CdS NPs produced in HDA at 343 K. (Top insert) EDS spectrum; (bottom insert) diffraction pattern. Size distribution histograms of particles grown at 343 and 363 K (both thermolyzed at 393 K). Reproduced with permission from Ref. [382]. Copyright (2003) American Chemical Society

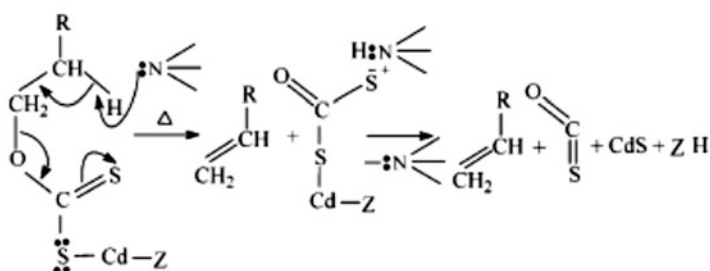
SSP. Nearly monodisperse CdS NPs are observed with average diameters of 5.2 (± 0.6) and 3.5 (± 0.4) nm when thermolysis proceeds with HAD at 343 and 363 K, respectively, (Fig. 3.100).

In another interesting example, Lewis base alkylamine solvents promoted the thermolysis of metal alkyl xanthates at low temperatures (from below room temperature up to ~ 423 K) [383]. By this method, monodisperse crystalline size- and shape-tunable NPs were prepared. This tunability is achieved by controlling parameters such as the thermolysis temperature and time, the concentration of the SSP, and the alkyl chain length. Core-shell structures are synthesized with the same method, using the same SSPs, applying either a single-stage or a dual-stage process. In this process, first, the solvent might activate the O-C-S₂Cd group, moving charge density from the C-S bond toward the S-Cd bond (Scheme 3.62a). Second, the Lewis base solvent can serve as a protonated intermediate and facilitate the proton transfer required in the reaction (Scheme 3.62b). Third, it can link the cadmium (Scheme 3.62c), weakening at least one CdS bond in the dixanthate, activating it as a convenient leaving group and thus facilitating the formation of a full CdS bond. Finally, the solvent can stabilize the particles (and the intermediate embryo cores) by forming a capping layer, as well as the xanthic acid. All these effects depend on the nature of Lewis base solvent.

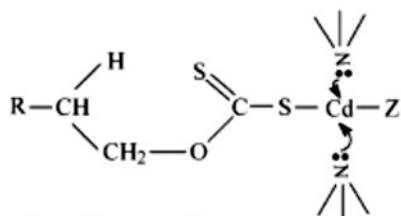
It should be noted the shape- and phase-controlled synthesis of ZnS nanocrystals (nanorods and nanodots) by the selection of ligand molecules with a simple method of thermolysis of SSP-zinc ethylxanthate with OAm or TOP as solvents [384]. In HDA + OAm system, diameter- and aspect-ratio-tunable hexagonal wurtzite ZnS nanorods were obtained in the temperature range of 423–523 K, and the nanorods self-assembled into 2D aligned arrays. While in the HDA + TOP system, a shape changes from rod to spherical particle and a phase transition from wurtzite to



(A) Nucleophilic attack on the (thio) carbonyl center



(B) Protonated intermediates



(C) Ligand stabilization of the metal center

Scheme 3.62 Possible ways of involvement of a Lewis base in the thermolysis of Cd-xanthate ($Z = \text{xanthate}$). Reproduced with permission from Ref. [383]. Copyright (2003) American Chemical Society

sphalerite simultaneously occurred with the increase of TOP content in the solution, and sphalerite nanodots were prepared in high TOP content or in TOP (or TOA) solution without HDA. In addition, the ordered arrays of the nanorods and nanodots were obtained on a relatively large scale. For example, at 423 K and thermolysis for 10 h, the ZnS nanorods with an average 200 nm in length and 2.5 nm in width were prepared, and the ZnS nanorods were aggregated into bundles (Fig. 3.101a). At

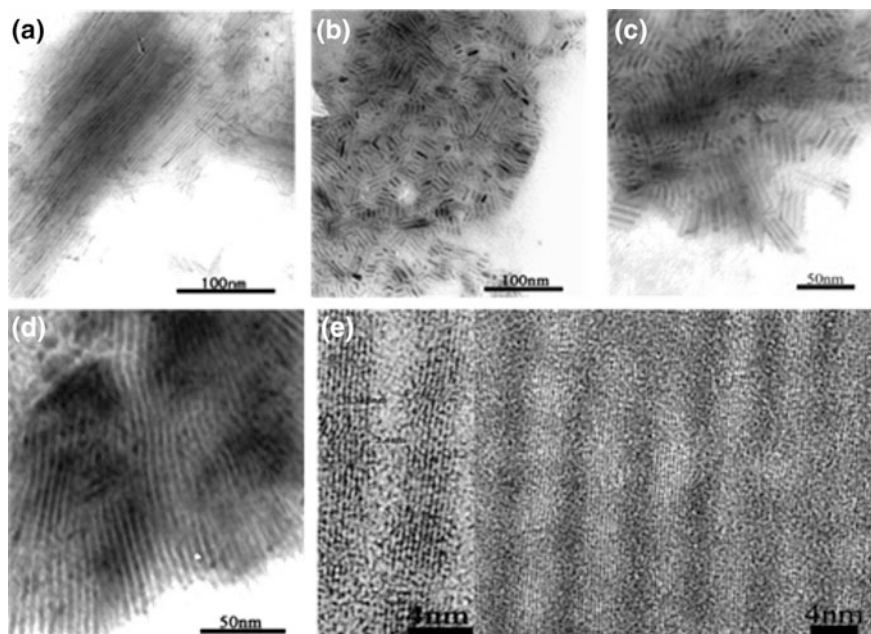


Fig. 3.101 TEM images of the ZnS nanorods prepared in the solution of HDA + OA with different reaction conditions: **a** at 423 K, 0.35 g of SSP, and for 10 h; **b** at 473 K, 0.2 g of SSP, and for 6 h; **c** at 523 K, 0.35 g of SSP, and for 4 h; **d** at 523 K, 0.5 g of SSP, and for 4 h; **e** large area HRTEM images for **(d)** (the inset (left side) is a magnified HRTEM image). Reproduced with permission from Ref. [384]. Copyright (2004) American Chemical Society

473 K and thermolysis for 6 h, the resultant ZnS nanorods were an average 25 nm in length and 3.5 nm in width (Fig. 3.101b). At 523 K and thermolysis for 4 h, the formed nanorods were an average 35 nm in length and 4.5 nm in width, and a few spherical particles also appeared (Fig. 3.101c), while at the same conditions but higher SSP concentration, the longer nanorods with an average 50 nm in length and 4.5 nm in width were formed, and the nanorods self-assembled into 2D ordered array (Fig. 3.101d). Most rods are parallelly arranged with a distance of an average 2.4 nm (one to the other), and each rod is a single crystal with the interplanar distances of 0.338 nm which is consistent with that of wurtzite ZnS (Fig. 3.101e).

Of interest is the thermolysis of cadmium ethylxanthate in hot HDA solution leading to CdS nanocrystals including nanorods and faceted NPs [319]. It is important that under the conditions of high SSP concentration and adequate thermolysis time (3 h), long multiarmed nanorods were prepared dominantly when the thermolysis temperature was not higher than 473 K, while at high temperature (533 K), the formation of short single-armed nanorods was preferred. When the SSP concentration was low, spherical-shaped nanocrystals were mainly obtained. By optimal combination of the thermolysis temperature, SSP concentration, and thermolysis time, size- and aspect-ratio-tunable 1D CdS nanorods and

hexagonal-like CdS nanocrystals which self-assembled into superlattice arrays were obtained.

CdS NPs capped with TOPO were prepared by a thermolysis using cadmium ethylxanthate as a SSP [319]. The product is hexagonal with a calculated particle size of 3.9 nm. $M(S_2COCH(CH_3)_2)_2$ ($M = Zn, Cd$) were used as SSPs for the preparation of nanostructured $Zn_xCd_{1-x}S$ ($0 \leq x \leq 1$) thin films by CVD method on SiO_2 substrates [385]. The method of preparation used consisted in the sequential deposition of single-phase MS coatings ($M = Zn, Cd$) at 573 K in a N_2 flow, followed by ex situ annealing in an inert atmosphere at various temperatures in the range 673–973 K. Irrespective of the annealing conditions, all the obtained films were contaminant-free and nanophasic ($\phi \approx 25$ nm) and possessed a hexagonal crystal structure, the lattice parameters of which decreased linearly with increasing zinc molar fraction.

Thermolysis of calcium isopropylxanthate and bis(triphenylphosphine) copper 2-methoxyethylxanthate with barium isopropylxanthate leads to the clean formation of complex alkaline earth metal copper sulfide ($CaCu_2S_2$, β - $BaCu_2S_2$, and β - $BaCu_4S_3$) thin films [386]. The alkaline earth metal copper sulfides consist of conjoined spheres 0.1–0.5 mm in diameter.

The complex $[PdPh(S_2COPr^i)(PMe_2Ph)]$ has been used to deposit thin film of tetragonal Pd_4S on glass by AACVD method [387]. It should be also noted the utility of $Pd(S_2COR)_2$ as SSPs for PdS NPs and thin films [388]. AACVD generated PdS films with matted, needle-like, or granular morphologies depending on temperature and substrate. Solvothermal (ethylene glycol) decomposition led to sulfur-rich PdS NPs with diameters 120–400 nm. When dodecanethiol was employed as a capping agent, $PdS_{1.75}$ NPs < 10 nm were obtained from SSP.

Thus, chalcogenide metal chelates are effective SSPs for the preparation of the nanocomposites, stabilized against further aggregation by shell from thermolysis products of ligands (Table 3.16).

3.9 Mixed-Ligand Metal Chelates

The interesting SSPs are metal complexes in which one metal ion is connected with two or more different chelating ligands. As an example, we consider SSPs formed by the interaction of metal dtc complexes with chelating bpy and phen ligands (Scheme 3.63).

Thus, when using $Fe(diethyl-dtc)_2(phen)$ as SSP for thermolysis with OAm and ODE, Fe_7S_8 hexagonal nanoplates with sizes ranging from 500 to 1000 nm and thicknesses from 20 to 55 nm were obtained (Fig. 3.102a, b) [345].

By increasing the concentration of $Fe(diethyl-dtc)_2(phen)$ precursor and adding OA to the mixture of OAm and ODE, $Fe_{1.2}S$ nanoribbons with a width of 15 nm and length up to several microns were prepared (Fig. 3.103a, b) [345].

In similar way, CdS nanorods with diameter ca. 7 nm and length 50–75 nm were prepared by thermolysis of $[Cd(thq-dtc)_2(phen)]$ in diethylenetriamine at 372 K for

Table 3.16 Chalcogenide metal chelates as SSP of the nanostructured materials

SSP	Thermolysis conditions	Phase composition, NP shape and dimensions	Reference
Metal alkyl (R = ethyl, decyl, hexadecyl) xanthates M = Cd, Zn, Pb, Hg, Cu, Ni, Mn	HDA, decylamine, TOA, 393–413 K	CdS, ZnS (4.5 nm), spherical, CdS rods (5-nm width, 20-nm length), CdS/ZnS, CuS, NiS, MnS (spherical, rods), PbS, and HgS (r.t., decylamine)	[360]
Cd(pip-dtc) ₂	623–723 K (AACVD)	CdS, thin film, 57.37 nm (623 K), 63.57 nm (673 K), 72.97 nm (723 K)	[365]
Cd(pip-dtc) ₂	TOP, HDA, 453 K	CdS, rods, bipods, tripods (19.11 ± 7.29 nm length, 3.64 ± 0.78 breadth)	[366]
Cd(pip-dtc) ₂	TOP/TOPO, 513 K	CdS, spheres, 3.97 ± 0.69 nm, 4.33 ± 0.59 nm	[366]
Fe(pip-dtc) ₃	AACVD, chloroform, toluene, 623–723 K	Fe _{0.975} S, FeS ₂ (623, 673 K), FeS, hexagonal phase (723 K); sheet-like (623 K), nanoleaf-/flake-like (673, 723 K)	[342]
Zn(pip-dtc) ₂	HDA, TOP, TOPO, 453, 543 K	ZnS (spherical to elongated), 4.74 ± 0.64 nm (453 K), 6.43 ± 0.60 nm (543 K)	[353]
Cd(thq-dtc) ₂	623–723 K (AACVD)	CdS, thin film, 160–220 nm, cubic to spherical	[365]
Cd(thq-dtc) ₂	TOP, HDA, 453 K	CdS, rods, bipods (21.61 ± 6.08-nm length, 4.55 ± 1.04 breadth)	[366]
Cd(thq-dtc) ₂	Castor oil, ricinoleic acid, 463–473 K, N ₂ , 30 min–2 h	CdS (castor oil), spherical, short rods, and oval, 15.53 ± 3.18 nm (503 K), 15.6 ± 3.74 nm (543 K), 17.96 ± 1.95 nm (573 K); CdS (ricinoleic acid) 21.12 ± 3.57 nm (543 K), 22.67 ± 3.58 nm (573 K)	[349]
Cd(thq-dtc) ₂	Castor oil, ricinoleic acid, 463–573 K, N ₂ , 30 min–2 h	CdS, oval rod, 13.36 ± 1.82 nm (543 K), spherical 15.7 ± 1.73 nm (573 K)	[349]
Fe(thq-dtc) ₃	AACVD, chloroform, toluene, 623–723 K	FeS, hexagonal (623, 673 K), nanosheet-like;	[342]

(continued)

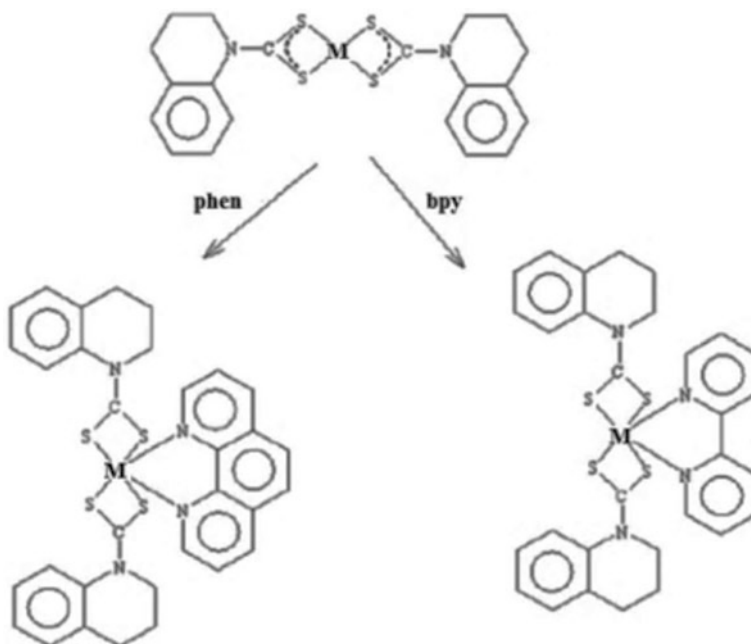
Table 3.16 (continued)

SSP	Thermolysis conditions	Phase composition, NP shape and dimensions	Reference
		Fe _{0.95} S _{1.05} , hexagonal pyrrhotite (723 K)	
Zn(thq-dtc) ₂	HDA, TOP, TOPO, 453, 543 K	ZnS, spherical, 5.94 ± 0.25 nm (543 K)	[353]
[Cd(pip-dtc) ₂ Py]	HDA, TOP, 463 K; thin films, chloroform, (AACVD, 623, 673, 723 K)	CdS, rods, 64.38 ± 4.62 nm length, 5.20 ± 0.98 nm width (463 K), 24.84 ± 4.42 nm length, 6.58 ± 1.02 nm breadth (503 K), oval, 16.8–23.3 nm; CdS, thin film	[355]
Metal <i>N</i> -hexadecyl-dtc M = Cd, Zn, Pb, Hg, Cu, Ni, Mn	HDA, 443–473 K	CdS, ZnS (spherical), ZnS/CdS (343–443 K)	[361]
Metal hexadecyltrithiocarbamate M = Cd, Zn, Pb, Hg, Cu, Ni, Mn	HDA, 453–473 K	CdS (5 nm)	[361]
Cd(II) butyl amine-dtc	TOP, HDA, 453–393 K, 60 min, N ₂	CuS, spherical, 15.8 nm (453 K), 6.61 nm (393 K)	[248]
Zn(II) diethyldiselenocarbamate	Thermolysis GC-MS, 553 K	Se _n , <i>n</i> ~ 1 ± 7, ZnSe	[343]
Cd(II) diethyldiselenocarbamate	Thermolysis GC-MS, 553 K	Se _n , <i>n</i> ~ 1 ± 7, CdSe	[343]
Zn(II) bis[methyl(<i>n</i> -hexyl)-diselenocarbamate]	Thermolysis GC-MS, 553 K	ZnSe	[343]
Cd(II) bis[methyl(<i>n</i> -hexyl)-diselenocarbamate]	Thermolysis GC-MS, 553 K	CdSe	[343]

2 min [316] and ZnS nanosheets of 75–225 width and 90–375 nm length were obtained by thermolysis of Zn(thq-dtc)₂(bpy) in triethylenetetraamine [317].

It should be noted the preparation of high surface area (86.7 m² g⁻¹) NiO NPs through thermolysis of [Ni(L)(bpy)]·CH₃OH chelate, where L = racemic-1,1'-bi-2-naphtholate, as SSP [389]. The mixed-ligand chelate was obtained by the reaction of *rac*-Na₂(L) with Ni(II) ion coordinated to bpy ligand in alcoholic solution to form yellow-brown colored solid (Scheme 3.64).

APS of the NiO was 8.9 nm. The as-synthesized NiO NPs consisted of homogeneous, uniform, and spherical NPs with narrow size distribution of 15–30 nm (Fig. 3.104, left). The used synthetic route is facile and economic that makes it suitable for large-scale preparation of pure NiO NPs.



Scheme 3.63 Scheme of the formation of $[M(\text{thq-dtc})_2]$ complexes with additional chelating ligands phen or bpy

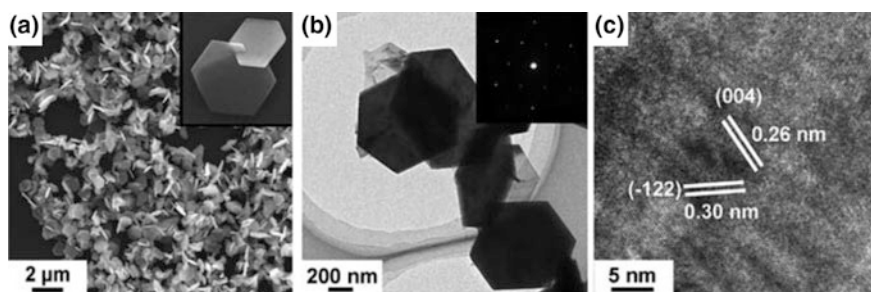


Fig. 3.102 As-obtained Fe_7S_8 nanoplates. **a** SEM image, **b** TEM image, and **c** HRTEM image. Reproduced with permission from Ref. [345]. Copyright (2010) Royal Society of Chemistry

Of interest are nanorods of the mixed-ligand chelate of $\text{Cd}(\text{II})$ fluorine-substituted β -diketonate with bpy, $[\text{Cd}(\text{bpy})(\text{L})_2]$, where $\text{L} = 4,4$ -difluoro-1-phenyl-1,3-butandion, obtained by a sonochemical method [390]. Regularly shaped cubic CdO NPs with the diameter 35 nm (Fig. 3.104, right) were obtained by thermolysis of this SSP at 453 K in air with OA as a surfactant.

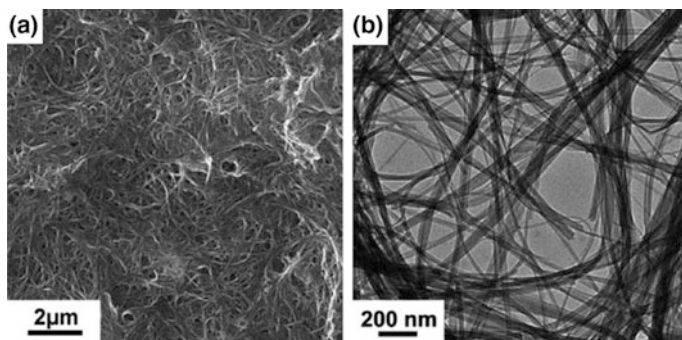
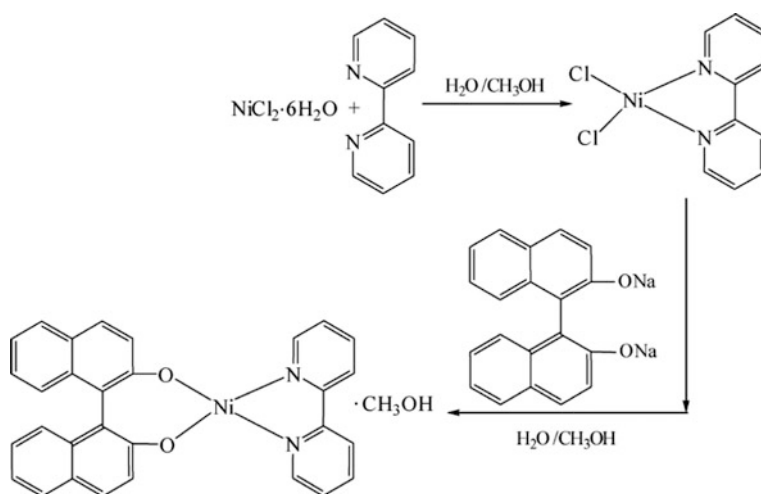


Fig. 3.103 As-obtained $\text{Fe}_{1.2}\text{S}$ nanoribbons. **a** SEM image and **b** TEM image. Reproduced with permission from Ref. [345]. Copyright (2010) Royal Society of Chemistry



Scheme 3.64 Synthetic scheme of mixed-ligand chelate $[\text{Ni}(\text{L})(\text{bpy})]\cdot\text{CH}_3\text{OH}$. Reproduced with permission from Ref. [389]. Copyright (2016) Springer Nature

The cubic CdO NPs were also prepared by thermolysis of another mixed-ligand chelate of Cd(II) fluorine-substituted β -diketonate, $[\text{Cd}(2,9\text{-dimethyl-phen})(\text{TTA})_2]$ (Fig. 3.105, left), where TTA is thenoyl-trifluoro-acac, at 453 K in air with OA as the surfactant [391]. The bulk powder of SSP gave regularly shaped CdO NPs with a diameter of about 35 nm (Fig. 3.105, right).

It should be noted the preparation of the cubic CdO NPs (45 nm) by thermolysis of another mixed-ligand chelate $[\text{Cd}(\text{phen})(\text{TTA})_2]$ at 453 K in air with OA as a surfactant [392]. After thermolysis at 673 K of nanosized flower-like Cd(II) chelate, $[\text{Cd}(\text{bpy})(\text{L})_2]_n$ (L = furoyltrifluoroacetate), pure phase cubic CdO NPs were

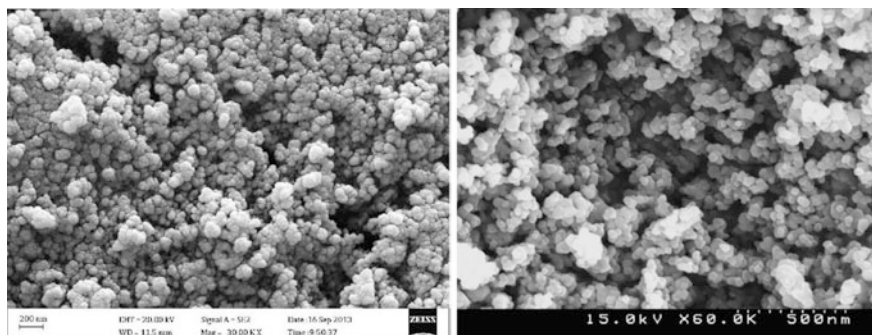


Fig. 3.104 (left) SEM image for NiO NPs. Reproduced with permission from Ref. [389]. Copyright (2016) Springer Nature; (right) SEM images of CdO NPs produced by thermolysis of $[\text{Cd}(\text{bpy})(\text{L})_2]$ using OA as surfactant at 453 K. Reproduced with permission from Ref. [390]. Copyright (2012) Springer Nature

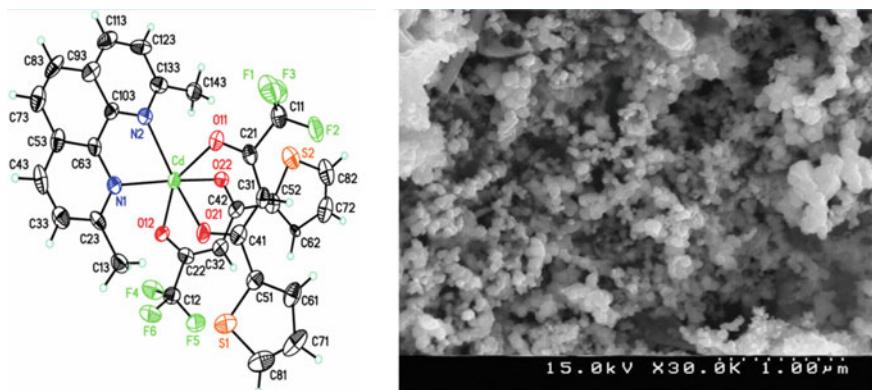


Fig. 3.105 ORTEP view of complex $[\text{Cd}(2,9\text{-dimethyl-phen})(\text{TTA})_2]$ (left) and SEM photographs of CdO NPs produced by the thermolysis of SSP using OA as the surfactant at 453 K (right). Reproduced with permission from Ref. [391]. Copyright (2012) Springer Nature

produced [393]. These NPs show a high degree of crystallinity. The CdO NPs obtained from thermolysis of the SSP at 673 K in air have a diameter distribution of 20–35 nm and an average diameter of about 25 nm (Fig. 3.106). At higher temperatures (823 K), agglomeration occurs and the particles formed have a larger size. It is important that the size of the SSP correlates to the particle size of the CdO NPs, and the nanosized SSP produces smaller particles of CdO.

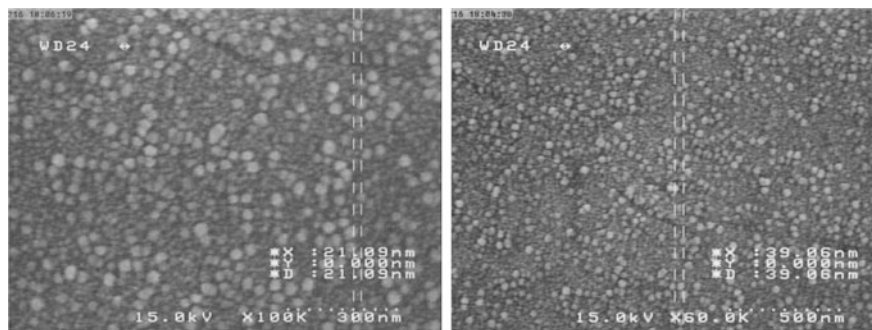
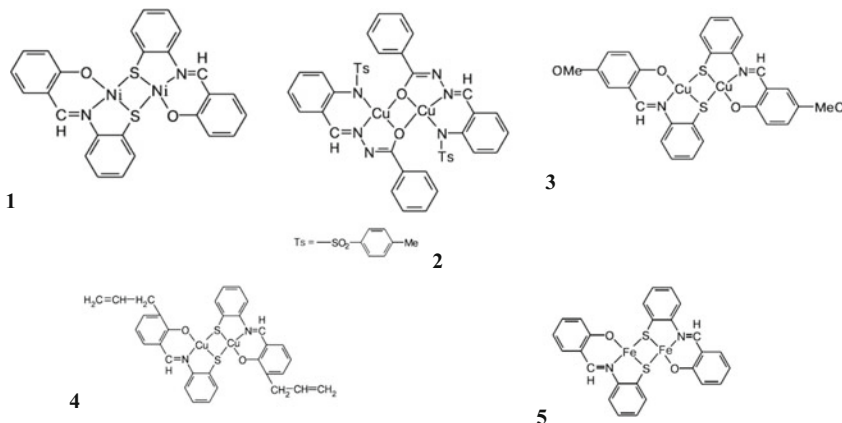


Fig. 3.106 SEM photographs of CdO nanopowders produced by thermolysis of nanoflowers of the SSP at 673 (left) and 823 K (right). Reproduced with permission from Ref. [393]. Copyright (2012) Springer Nature

3.10 Polynuclear Metal Chelates

In recent years, considerable attention has been paid to the study of SSPs based on polynuclear metal chelates, which allow purposefully to obtaining the desired nanomaterials with a given ratio of metals. First, we will consider homometallic polynuclear complexes. As a typical example, we note binuclear complexes of Ni(II), Cu(II), and Fe(II) with azomethine ligands **1–5** containing oxygen, nitrogen, and sulfur atoms in the chelate rings allowing to examine the effect of the ligand environment on the thermal stability and composition of the resulting nanoproducts [266]. Binuclear nickel complex **1** is stable below 453 K, and heating up to 623 K is accompanied by a small weight loss (4.19%). At 733 K, the complex loses weight abruptly (to 57%). Consequent heating up to 1073 K results in a 7% weight loss, and the total weight loss is 64.0%. The DSC curve shows endothermic peaks at 495.6 and 595.6 K; the complex decomposes above 993 K. At the same time, binuclear copper complex **2** is stable below 578 K but loses weight rapidly when heated to 653 K (by 57.4%). The total weight loss at 1073 K is 64.6%. For this compound, the DSC analysis revealed melting at 581 K; the complex decomposes above 1013 K. Complex **3** is stable below 483 K and then incurs a stepwise weight loss: by 1.55% at 543 K and by 6.43% at 553 K. Further heating is accompanied by a more monotonic decrease in the weight (by 35% at 673 K). The process slows down more strongly above 673 K. The weight loss at 1073 K is 44.65%. In this case, the DSC curve shows an endothermic peak at 542.9 K and the complex decomposes above 948 K. Binuclear copper complex **4** with the azomethine ligand containing allyl substituents is stable below 423 K and then loses weight (by 0.96% at 533 K). Consequent heating increases the thermolysis rate; the weight loss at 1073 K is 40.81%. The DSC curve shows an exothermic peak at 514 K and an endothermic peak at 561 K. Binuclear iron complex **5** is stable below 373 K and then loses weight in a stepwise manner: by 3.17% at 423 K, by 4.23% at 463 K, by 2.55% at 601 K, and by 4.66% at 623 K. The total weight loss at 1073 K is

54.67%. For this chelate, the DSC curve shows exothermic peaks at 420.3, 441.8, and 474.1 K; the complex decomposes above 743 K. Consequently, the binuclear chelates are stable up to >473 K.



It is important that the nature of the chelating ligands and, as a consequence, the formed stabilizing shell on their basis, has a significant effect on the sizes of the NPs obtained and the nature of their size distribution, exemplified by the thermolysis products of the binuclear copper(II) chelates **2** and **3** (Fig. 3.107).

Of interest is SSP based on a binuclear Ni(II) chelate from a hexadentate imine ligand $(\text{NNO})_2$ prepared via condensation of 9-hexyl-9H-carbazole-3,6-dicarbaldehyde or 2-amino-3,5-dibromobenzaldehyde and 5-bromo-2-hydroxyaniline using an ultrasonic method (Fig. 3.108, top) [394]. NPs of NiO (32 nm) were produced from the SSP by a thermolysis method. The morphology evolution of the prepared NiO NPs showed spherical shapes, aggregated with APS of 53 nm (Fig. 3.108, bottom). The agglomeration of particles was related to many factors such as shape factor, surface area, porosity, and density.

MO NPs were obtained via solid-state thermolysis of binuclear chelates of Ni(II), Co(II), and Cu(II) based on a symmetric tetradentate Schiff base ligand, *N,N'*-bis(5-bromosalicylaldehyde)-1,3-phenylenediamine, as SSPs (Scheme 3.65) [395, 396].

Solid-state thermolysis of the Ni(II) SSP was carried out at 723 K for 3 h to form NiO NPs with the square shape between 10 and 15 nm. The Co(II) and Cu(II) SSPs are thermolyzed in the electrical furnace at 873 K leading to the formation of the Co_2O_3 and CuO NPs. Co_2O_3 NPs are plate-like, while CuO NPs are almost spherical (Fig. 3.109).

It should be noted the thermolysis of the homobinuclear Co(II) complex $[\text{Co}_2(\text{L})_2(\text{H}_2\text{O})_5] \cdot 2\text{H}_2\text{O}$, where H_2L is pyridine-2,6-dicarboxylic acid, to form CoO NPs [397] and Zn(II) azomethine chelate, $[\text{Zn}(\text{HL})\text{NO}_3]_2$ (Scheme 3.66), where

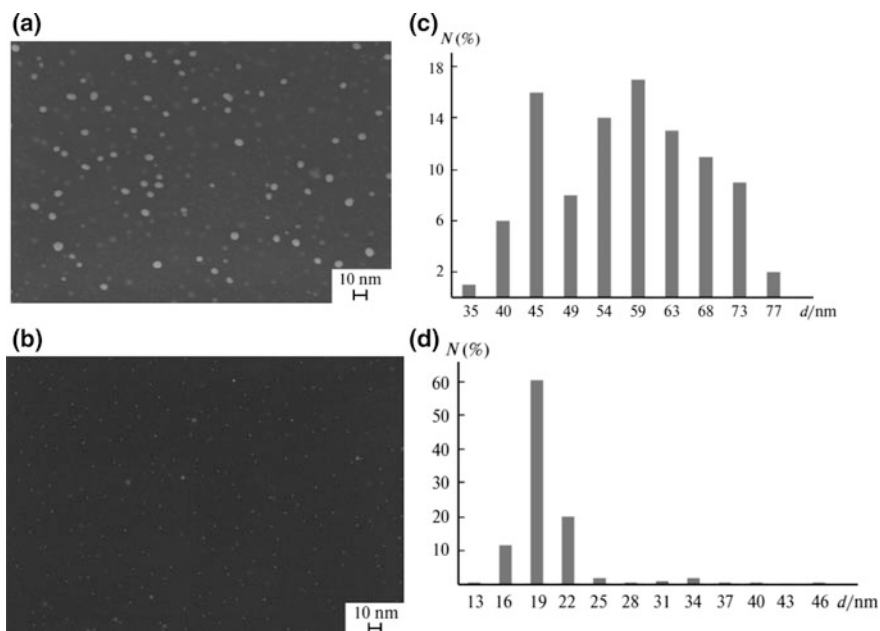


Fig. 3.107 SEM images (a, b) and histograms showing the size distribution of NPs (c, d) for the thermolysis products (873 K) of Cu chelates **2** (a, c) and **3** (b, d) [266]

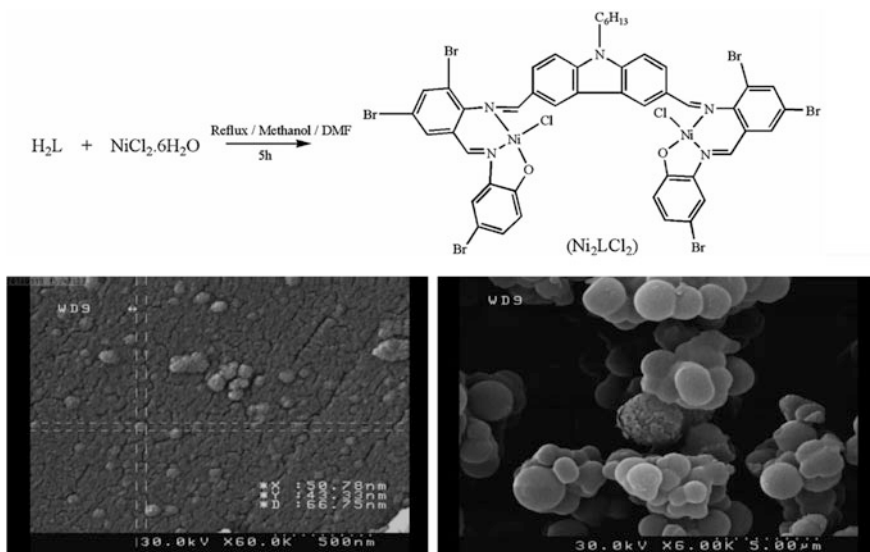
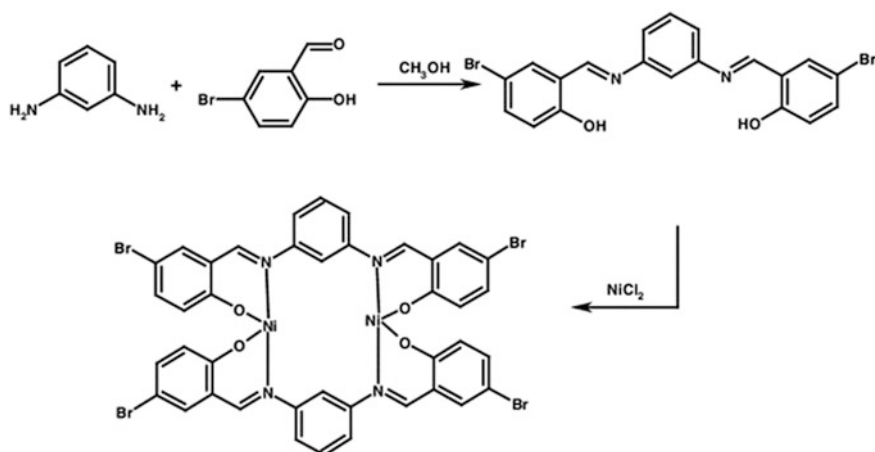


Fig. 3.108 (top) Synthesis of the SSP, (bottom) SEM images of the SSP (left) and NiO nanostructure (right). Reproduced with permission from Ref. [394]. Copyright (2016) Royal Society of Chemistry



Scheme 3.65 Synthesis of binuclear chelates. Reproduced with permission from Ref. [396]. Copyright (2013) Springer Nature

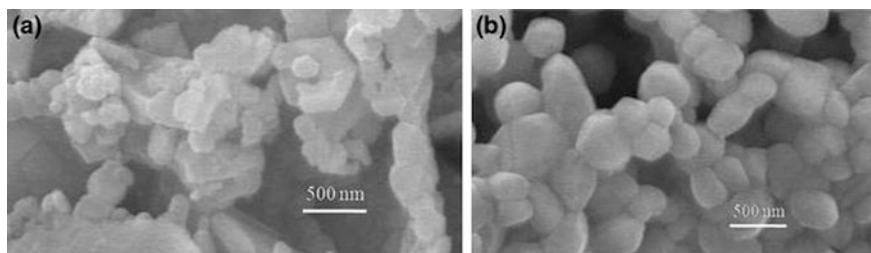


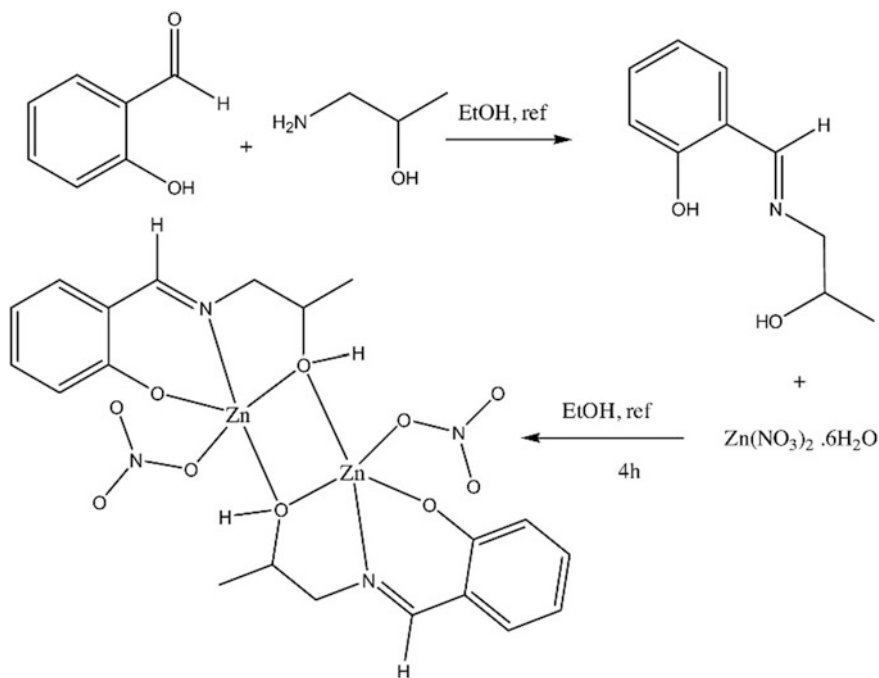
Fig. 3.109 SEM images of **a** Co₂O₃ and **b** CuO NPs obtained from thermolyzed metal chelates at 873 K. Reproduced with permission from Ref. [396]. Copyright (2013) Springer Nature

H₂L = 2-[(2-hydroxy-propylimino) methyl] phenol, synthesized using solvothermal method [398].

Hexagonal ZnO NPs were simply synthesized by solid-state thermolysis of the SSP at 973 K in air atmosphere. The ZnO products have uniform morphology (Fig. 3.110a), and their diameter is varying between 15 and 20 nm with APS of 17 nm (Fig. 3.110b).

Two double-helical binuclear Cu(II) chelates of N,O-bidentate azomethine ligands bis (3-methoxy-*N*-salicylidene-4,4'-diaminodiphenyl) sulfone (**L**¹) and bis (5-bromo-*N*-salicylidene-4,4'-diaminodiphenyl) sulfone (**L**²) were used as SSPs to form the CuO NPs by thermolysis in solid state at 793 K for 3 h (Scheme 3.67) [399]. The prepared CuO NPs of a similar shape were very small with an APS of about <50 nm.

Binuclear Cu(II) chelates with azomethine ligands based on 3-substituted-4-amino-5-mercapto-1,2,4-triazole and dibenzoylmethane (Scheme 3.68) were used



Scheme 3.66 Schematic representation of the synthesis of $[Zn(HL)NO_3]_2$. Reproduced with permission from Ref. [398]. Copyright (2016) Elsevier

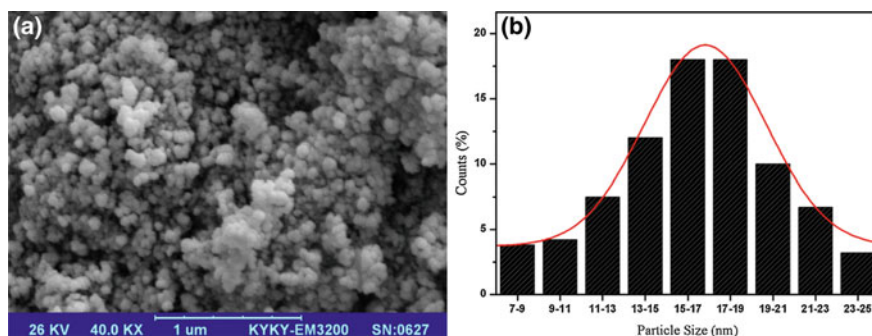
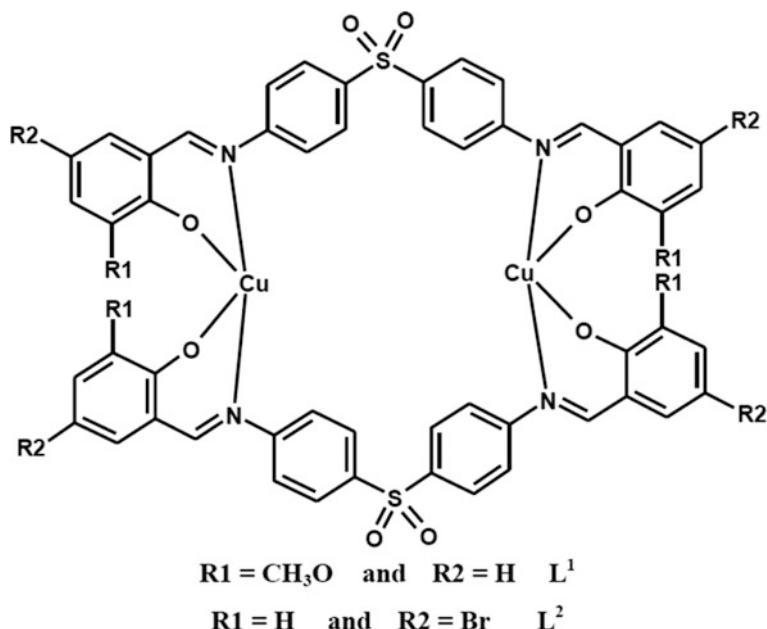


Fig. 3.110 **a** SEM images of ZnO NPs prepared by direct thermolysis of the SSP; **b** the particle size distribution of ZnO NPs. Reproduced with permission from Ref. [398]. Copyright (2016) Elsevier

as SSPs for CuO NPs [400]. The estimated crystal sizes of CuO samples from Cu (II) complexes of HL1, HL2, and HL3 were 35.60, 34.47, and 28.28 nm, respectively.

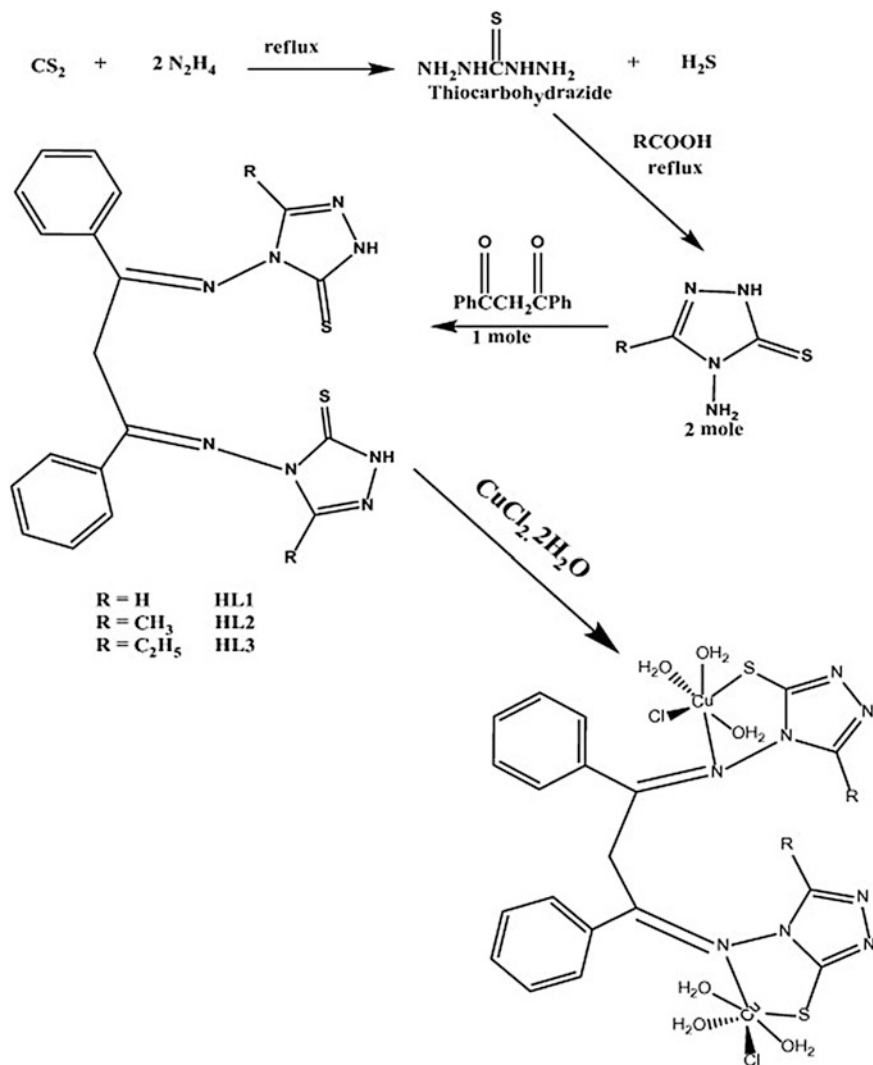


Scheme 3.67 Chemical structure of Schiff base double-helical binuclear Cu(II) chelates [399]

A convenient solvothermal single-source route at a relatively low temperature was developed for the bulk synthesis of CdS nanorods using stable in air dimeric Cd(II) chelate of *S*-benzylthiocarbamate $\text{PhCH}_2\text{SC}(=\text{S})\text{NHNH}_2$ (L), $[\text{Cd}(\text{L})\text{Cl}_2]_2$ [401]. The thermolysis of the SSP was carried out by heating at 433 K in hexamethylenediamine (HMDA) to give amine-capped CdS nanocrystals (rods). The rod morphology with lengths in the range 18–22 nm and diameters in the range 3.5–5.0 nm as well as the clear crystallinity of CdS NPs with lattice fringe spacing 3.33 Å, corresponding to the (002) planes, was shown.

It should be noted heterobimetallic SSPs $[\text{Ti}_4(\text{L})_6(i\text{-OH})(i\text{-O})_6\text{Cu}_6(\text{OAc})_9\cdot\text{H}_2\text{O}]$ (**1**) and $[\text{Zn}_7(\text{OAc})_{10}(i\text{-OH})_6\text{Cu}_5(\text{L})_4\text{Cl}_4]$ (**2**) [L = (*N,N*-dimethylamino)ethanolate] for the deposition of MO thin films of $\text{Cu}_6\text{Ti}_4\text{O}_{12}$ (Cu_3TiO_4 , TiO_2) and $\text{Cu}_5\text{Zn}_7\text{O}_{12}$ (ZnO , CuO) [402]. SSPs **1** and **2** are easily thermolyzed at 573 and 733 K to form thin films of Cu/Ti and Cu/Zn mixed MOs, respectively. An oxide thin film deposited from complex **1** has film morphology with small crystallites evenly distributed with no preferred orientation and grains with a variable shape without well-defined boundaries. At the same time, an oxide thin film deposited from complex **2** has compact and smooth film morphology with homogeneously dispersed particles and grains that are well-defined with distinct boundaries.

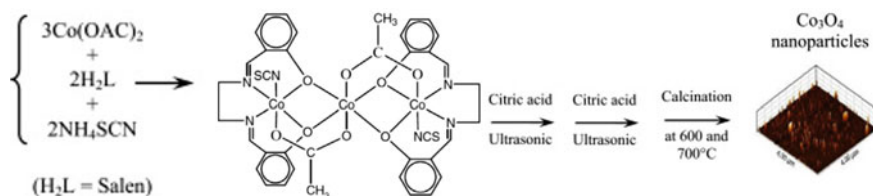
Of interest also are heterobimetallic SSPs based on the same ligand L $[\text{Co}_2(\text{acac})_2(i\text{-OH})_2\text{Cu}_4(\text{L})_4\text{Cl}_4]$ and $[\text{Ni}_2(\text{acac})_2(\mu\text{-OH})_2\text{Cu}_4(\text{L})_4\text{Cl}_4]$ for the deposition of mixed oxide thin films [403]. Both complexes are thermolyzed at 723 K to give impurity-free crystalline mixed oxide films with APS ranging from 0.55 to



Scheme 3.68 Synthesis of binuclear Cu(II) chelates. Reproduced with permission from Ref. [400]. Copyright (2015) Elsevier

2.0 μm . In these complexes, each metal center is coordinatively saturated with oxygen atoms of the chelating acac and L ligands, which eliminates the need for additional oxygen to form oxides.

Cubic Co_3O_4 NPs were synthesized via thermolysis in air, using $[Co^{II}\{(m-L)(m-OAc)Co^{III}(NCS)\}_2]$, where $H_2L = \text{salen} = 1,6\text{-bis}(2\text{-hydroxyphenyl})\text{-}2,5\text{-diazahexa-}1,5\text{-diene}$, as SSP (Scheme 3.69) [404]. The temperature of thermolysis and citric acid, as an emulsifier, has a significant effect on the phase



Scheme 3.69 Synthesis procedure for Co₃O₄ NPs. Reproduced with permission from Ref. [404]. Copyright (2016) Elsevier

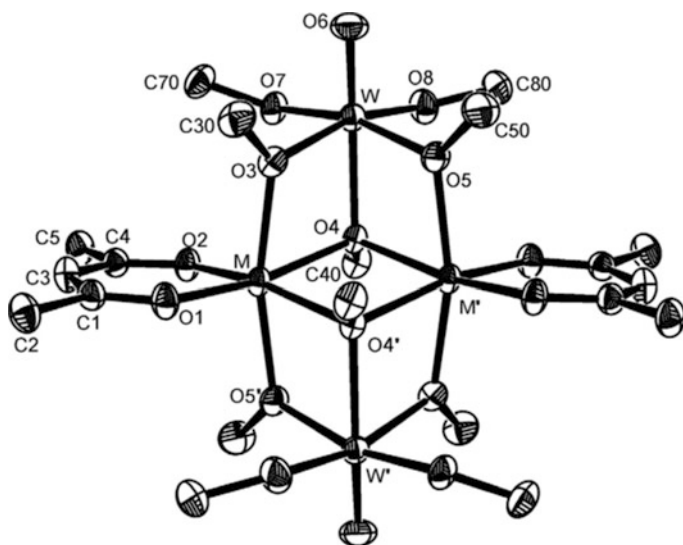


Fig. 3.111 Asymmetric unit of M = Co (**1**), Mg (**3**) showing the labeling scheme used; thermal ellipsoids are at the 50% probability level. Reproduced with permission from Ref. [405]. Copyright (2013) Elsevier

formation and the distribution of product particles in size. In particular, thermolysis of SSP at 873 K in the presence of citric acid leads to the formation of CO₃O₄ NP with APS ~ 13 nm.

The thermolysis of M₂W₂(O)₂(acac)₂(OMe)₁₀ involving two metals in the same molecule (Fig. 3.111) [M = Co (**1**), Mg (**3**)] as SSP led to metal tungstates MWO₄ [405].

When the thermolysis is carried out under an autogenic pressure (RAPET) at 973 K, complex **1** forms monoclinic CoWO₄ NPs together with WO_x-filled carbon nanotubes and amorphous carbon (Fig. 3.112), while complex **3** forms MgWO₄ NPs and rods, although the latter do not have a carbonaceous shell and are much shorter in length.

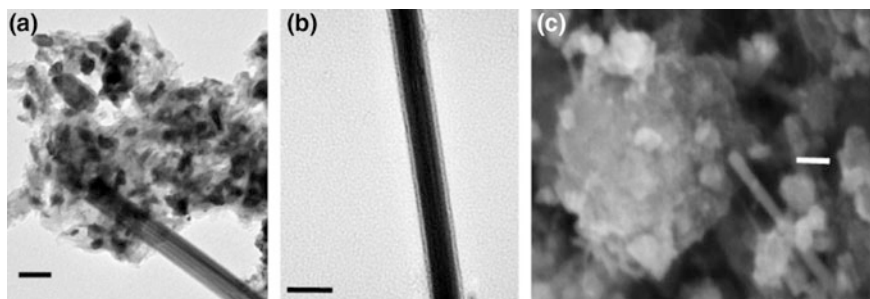


Fig. 3.112 EM images of the products of the thermolysis of **1** under RAPET conditions at 973 K: **a, b** TEM, bar = 50 nm, and **c** SEM, bar = 100 nm. Reproduced with permission from Ref. [405]. Copyright (2013) Elsevier

Table 3.17 Composition of the precursors and properties of the materials obtained by their thermolysis under nitrogen at different temperatures

Sample	Precursor	Atomic ratios in solution		Atomic ratios in the solid		T (K)	XRD phases	S_{BET} ($\text{m}^2 \text{g}^{-1}$)
		Co/Mo	C/(Co + Mo)	Co/Mo	C/(Co + Mo)			
1	Co (acac) ₂	1	15	0.99	3.5	823	Co	–
						923	Co ₃ Mo ₃ N, ϵ Co	120
						1073	Co ₃ Mo ₃ N	–
2	Co (acac) ₂	1	30	1	5.8	923	Co, Mo ₂ C, Co ₃ Mo ₃ N	39
						1073	Co ₃ Mo ₃ C, Co ₃ Mo ₃ N	–

Bimetallic nitrides and carbides Co–Mo were obtained from the thermolysis of heterometallic chelates based on ammonium heptamolybdate ((NH₄)₆Mo₇O₂₄·4H₂O), cobalt acetylacetonate hydrate (Co(acac)₂·xH₂O), and hexamethylenetetramine (L) under inert atmosphere [406]. During the thermolysis, L acts at once as a reducing agent and as a source of carbon and nitrogen. The composition of SSPs and the thermolysis conditions are the key parameters that affect the nature of the phases obtained. Chemical composition of the products depends on Co/Mo and C/(Co + Mo) ratios in the solutions (Table 3.17) [406]. Complexes with a Co/Mo ratio of 1 were of primary interest, since SSPs with such Co/Mo would result in pure bimetallic nitrides. Thermolysis of SSP at 1023 K gave Co₃Mo₃N as a single phase. However, the thermolysis at a lower temperature (923 K) led to a mixture of metallic cobalt and bimetallic nitride Co₃Mo₃N.

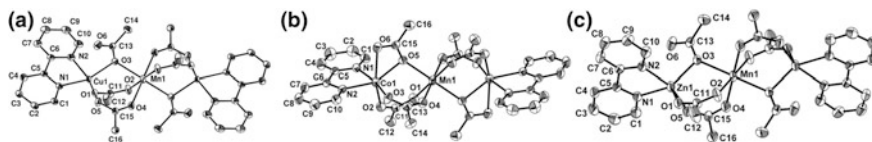


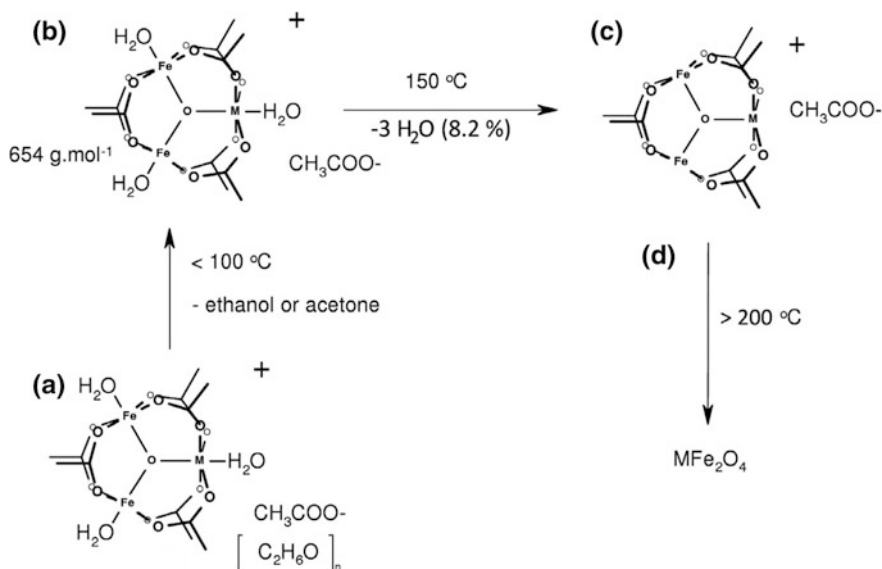
Fig. 3.113 Labeled ORTEP plots of the molecular structures of **1** (a), **2** (b), and **3** (c). The ellipsoids of the hydrogen atoms have been drawn at the 40% probability level with H atoms omitted for clarity. Reproduced with permission from Ref. [410]. Copyright (2010) Elsevier

It should be noted that use of heterometallic carboxylate complexes as SSPs of fine-dispersed mixed MOs and metal/oxide systems has some advantages over thermolysis of multicomponent systems, mainly due to precise control of stoichiometry and the potential ability to obtain the most uniform distribution of metals caused by the initial presence of covalent M1–O–M2 bridge in a polynuclear metal chelate. In addition, using heterometallic metal chelates with readily decomposable ligands can reduce the thermolysis temperature to 483 K [407]. It is important that Zn/Mn and Cu/Mn heterometallic complexes can be obtained using a simple one-pot synthetic procedure (the so-called direct synthesis [408]), starting with cheap and conventional reagents with good reproducibility and high yield. The thermolysis of such SSPs, for example, $[M_2Mn(OAc)_6(bpy)_2]$, where M = Cu (**1**), Co (**2**), Zn (**3**), at 623 K leads to the formation of solids from nano- to microdimensional dispersion levels (Fig. 3.113) [409–412]. In particular, by selectively converting these heterometallic carboxylate complexes with bpy by thermolysis, either a well-defined spinel $ZnMn_2O_4$ over ZnO or well-dispersed copper particles surrounded by manganese oxide (Mn_3O_4) in a core–shell like structure [413] can be obtained.

Fe(II), Co(II), and Ni(II) ferrite NPs in the range of 9–25 nm were synthesized by thermolysis of trimetallic acetate complex SSPs $MFe_2O(CH_3COO)_6(H_2O)_3$ (M = Fe, Co, Ni) in benzyl ether in the presence of OA and OAm, using 1,2-dodecanediol as the reducing agent (Scheme 3.70) [413]. Compared to spinel ferrites NPs prepared from stoichiometric mixtures of metal acetate metal acetylacetonate, ferrite NPs were more uniform and had a narrower size distribution when trimetallic complexes were used as SSPs.

3.11 Multicomponent Precursors Based on Metal Chelates

Simultaneous thermolysis of multicomponent precursors leads to the formation of zero-valent metal atoms, which are nucleated and grow together to form polymetallic NPs [414]. The difference in thermolysis rates can be regulated by controlling the relative precursor concentrations and/or by introducing additional chemicals (e.g., catalysts or other ligands). The reaction at temperatures below the thermolysis temperature of the less stable metal precursor consists in the formation



Scheme 3.70 Series of reactions proposed for thermolysis of the heterometallic acetate complexes ($M = \text{Co(II)}, \text{Ni(II)}$). Reproduced with permission from Ref. [413]. Copyright (2011) Elsevier

of monometallic NPs, the second metal precursor still intact in the solution. Newly formed NPs can catalyze the thermolysis of a second metal precursor and serve as active centers (or seeds) for heterogeneous nucleation. As an example, we note the preparation of Pd@Ni core-shell NPs through the successive thermolysis of Pd(acac)₂ and Ni(acac)₂ precursors [415]. In the first step, the Ni-TOP complex is thermolyzed at a lower temperature than Pd-TOP. Finally, the temperature was slowly increased to 508 K, at which the Pd-TOP complex was decomposed, forming the Pd shells on the already formed Ni NPs.

It is of interest to synthesize uniform 9-nm Pt-Ni octahedra from Pt(acac)₂ and Ni(acac)₂ using OAm and OA as surfactants and W(CO)₆ as a source of CO which can contribute to the formation of {111} faces in the presence of Ni [416]. The introduction of benzyl ether as a solvent is possible to reduce the coverage of both surfactants on the surface of the Pt-Ni octahedra formed, while the octahedral form was still attained. The resulting Pt-Ni octahedral with an average edge length of 9 nm indicates the formation of an octahedral form with a high degree of purity along with good uniformity in size (Fig. 3.114a). The d-spacing for neighboring lattice fringes was $2.25 \pm 0.05\text{ \AA}$, which is less than that (2.27 \AA) of the {111} planes of fcc bulk Pt (Fig. 3.114b, c). It should be also noted that the particle is inhomogeneous (Fig. 3.114d). The amine group of OAm can be coordinated with Pt(acac)₂ at the initial stage of synthesis. This so-called ligand effect slowed the reduction of the Pt precursor, which led to a higher Pt content in the peripheral region of NP.

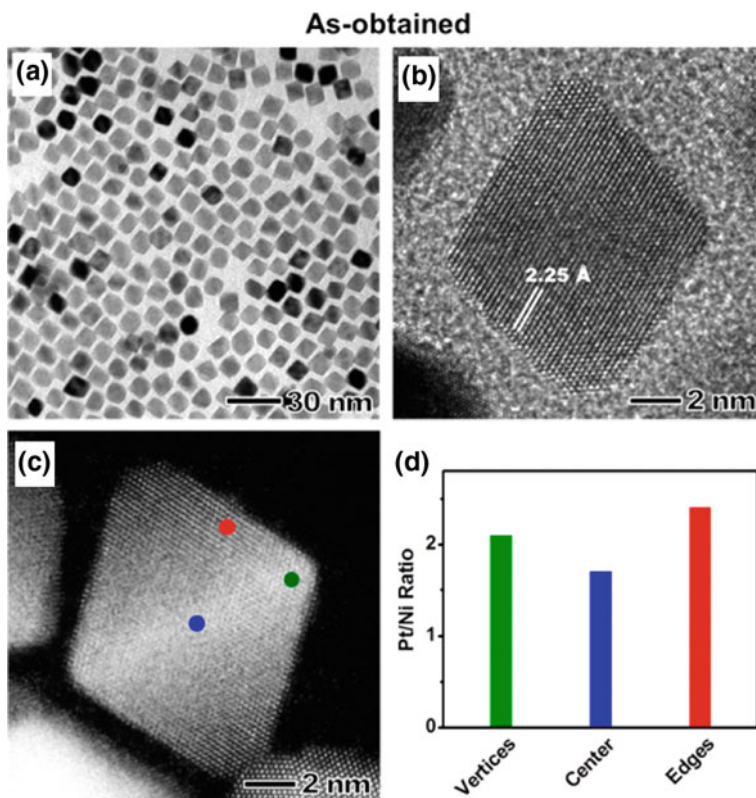


Fig. 3.114 **a** TEM and **b** HRTEM images of as-obtained Pt–Ni octahedra with 9-nm edge length synthesized in benzyl ether containing OAM and OA at low concentrations. **c** Scanning TEM-high angle annular dark-field image and **d** EDS spot analysis for elemental distribution of Pt/Ni ratios at different positions of the as-obtained Pt–Ni octahedron. Reproduced with permission from Ref. [416]. Copyright (2013) American Chemical Society

It should be noted a wet chemical approach to the production of monodisperse Pt_3Ni nanooctahedra and nanocubes ending with $\{111\}$ and $\{100\}$ facets, respectively, by thermolysis of $\text{Pt}(\text{acac})_2$ and $\text{Ni}(\text{acac})_2$ in the presence of OAM and OA with the addition of tungsten hexacarbonyl ($\text{W}(\text{CO})_6$) at 503 K (Fig. 3.115) [417]. Due to the high uniformity both in size and shape, Pt_3Ni nanooctahedra can be assembled into a multilayer superlattice with characteristic dimensions on the order of micrometers.

It is of interest to use the GRAILS method to produce various Pt–M alloy ($M = \text{Co}, \text{Fe}, \text{Ni}, \text{Pd}$) nanocrystals with cubic and octahedral morphology under the same conditions (Fig. 3.116) [171]. For example, cubic Pt–Ni alloys were homogeneous, and the typical edge length was 10–20 nm. It is important that the GRAILS method allows obtaining uniform shapes and composition-controlled nanocrystals of Pt alloys.

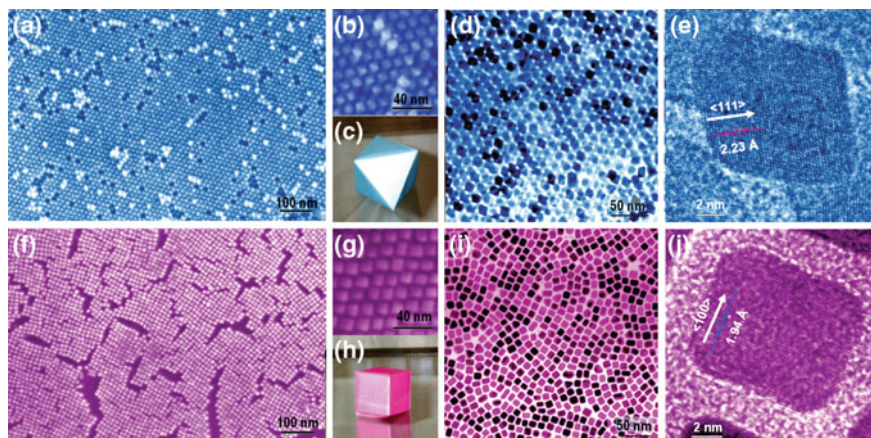
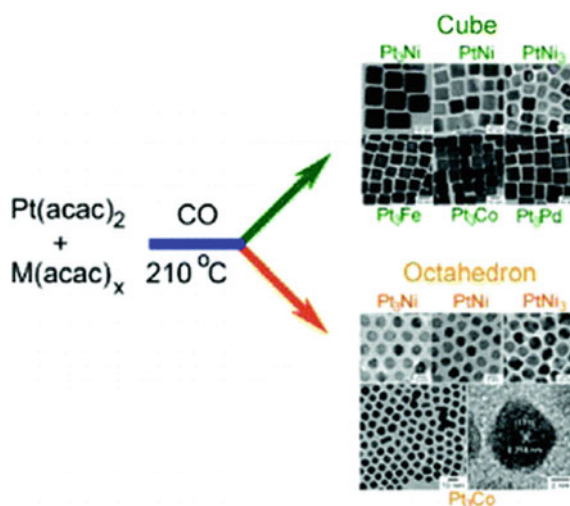


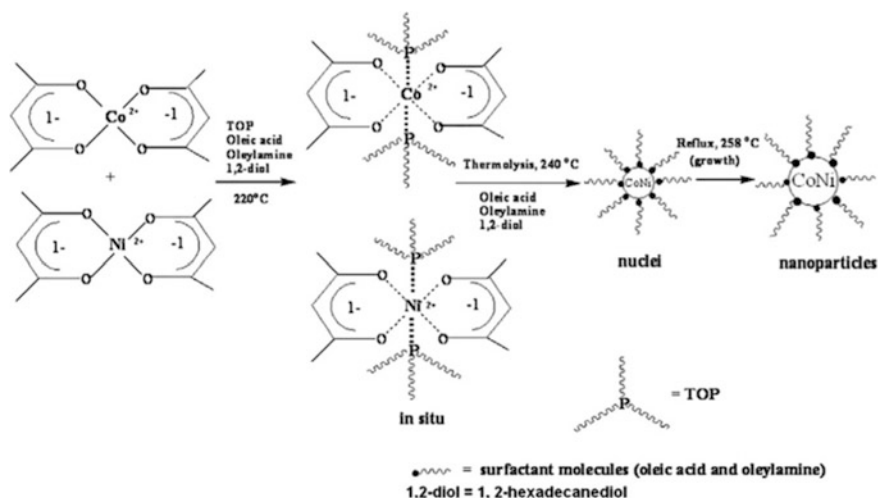
Fig. 3.115 a–e Images for Pt₃Ni nanooctahedra. f–j Images for Pt₃Ni nanocubes. a, f Field-emission SEM images. b, g High-resolution SEM images. c 3D image of an octahedron. d, i TEM images. e, j HRTEM images of single nanocubes. h 3D image of a cube. Reproduced with permission from Ref. [416]. Copyright (2013) American Chemical Society

Fig. 3.116 Scheme of the preparation of Pt–M alloy (M = Co, Fe, Ni, Pd) nanocrystals with cubic and octahedral morphologies. Reproduced with permission from Ref. [171]. Copyright (2011) American Chemical Society



It should be noted using Co(acac)₂ and Ni(acac)₂ as precursors for the synthesis of Co–Ni NPs [418]. The proposed reaction mechanism is shown schematically in Scheme 3.71. Interestingly, a higher atomic percentage of Ni leads to a larger size of Co–Ni NPs that is explained by the different rates of thermolysis of Ni–TOP and Co–TOP complexes.

Monodisperse spherical Fe–Co NPs were synthesized by thermolysis of Fe(acac)₃ and Co(acac)₂ in the presence of surfactants and 1,2-hexadecanediol [419].



Scheme 3.71 Reaction mechanism of the synthesis of alloy Co–Ni. Reproduced with permission from Ref. [418]. Copyright (2010) Elsevier

The particle size can be controlled by varying the surfactants. The presence of surfactants on the surface of the nanocrystal protects them from surface oxidation. Synthesized Fe–Co NPs can be obtained air-stable by thermolysis at 773 K for 30 min without sintering the particles. The formation of Fe–Co NPs with an average diameter of 20 nm is shown (Fig. 3.117).

High-temperature thermolysis of $\text{Fe}(\text{acac})_3$ and $\text{M}(\text{acac})_2$ (Fig. 3.118) with 1,2-hexadecanediol, OA, and OAm in a high-boiling ether solvent allows to preparing monodisperse MFe_2O_4 NPs ($\text{M} = \text{Fe}, \text{Co}, \text{Mn}, \text{Mg}, \text{etc.}$) [145, 156, 414]. The composition of the particles can be controlled by the initial molar ratio of $\text{Fe}(\text{acac})_3$ and $\text{M}(\text{acac})_2$, and the particle diameter can be adjusted from 3 to 20 nm by changing the conditions of thermolysis or seed-mediated growth. It is important that hydrophobic NPs can be converted to hydrophilic ones by the addition of bipolar surfactants, and therefore, an aqueous dispersion of NPs can be easily prepared (Fig. 3.119).

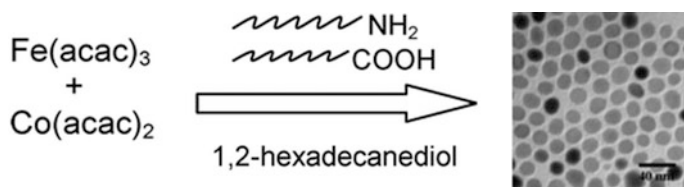


Fig. 3.117 TEM bright-field image of the Fe–Co NPs. Reproduced with permission from Ref. [419]. Copyright (2007) American Chemical Society

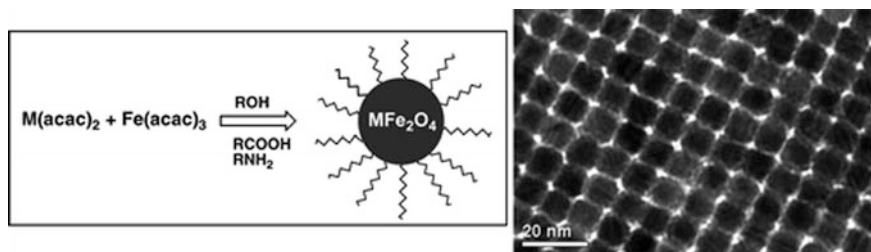


Fig. 3.118 Solution-phase thermolysis of $\text{Fe}(\text{acac})_3$ and $\text{M}(\text{acac})_2$ and TEM image of MFe_2O_4 NPs. Reproduced with permission from Ref. [156]. Copyright (2004) American Chemical Society

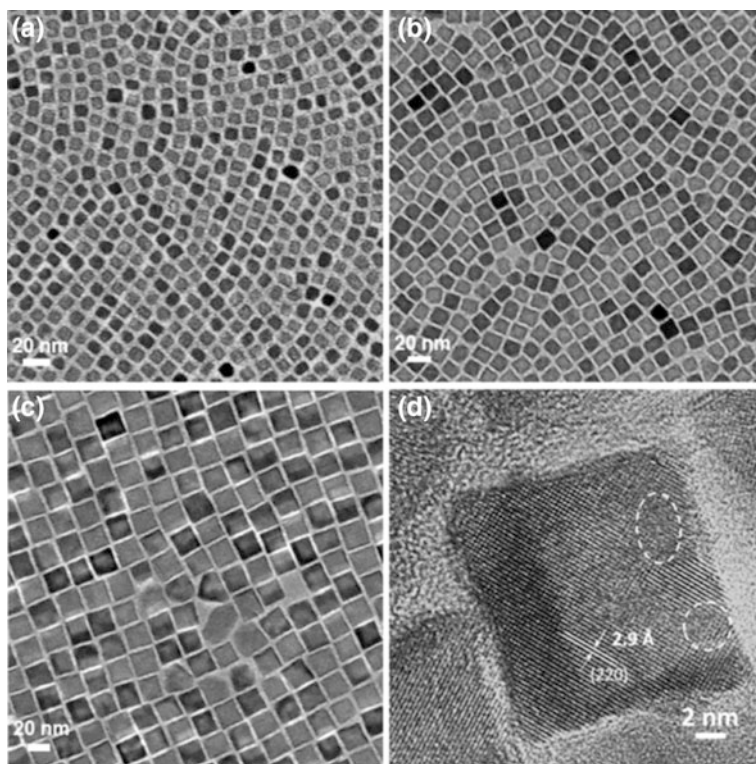


Fig. 3.119 TEM images of the as-synthesized **a** 10 nm, **b** 15 nm, and **c** 20 nm $\text{Co}_{0.6}\text{Fe}_{2.4}\text{O}_4$ nanocubes; (D) HRTEM image of a single 20-nm nanocube. Reproduced with permission from Ref. [420]. Copyright (2014) American Chemical Society

The thermolysis of $\text{Fe}(\text{acac})_3$ and $\text{Co}(\text{acac})_2$ in benzyl ether with OA and NaOI as surfactants at 563 K for 1 h leads to monodisperse $\text{Co}_x\text{Fe}_{3-x}\text{O}_4$ nanocubes with x and then adjusted the molar ratio of $\text{Co}(\text{acac})_2/\text{Fe}(\text{acac})_3$ [420]. Synthesized NPs deposited on an amorphous carbon-coated Cu grid have an average edge size of

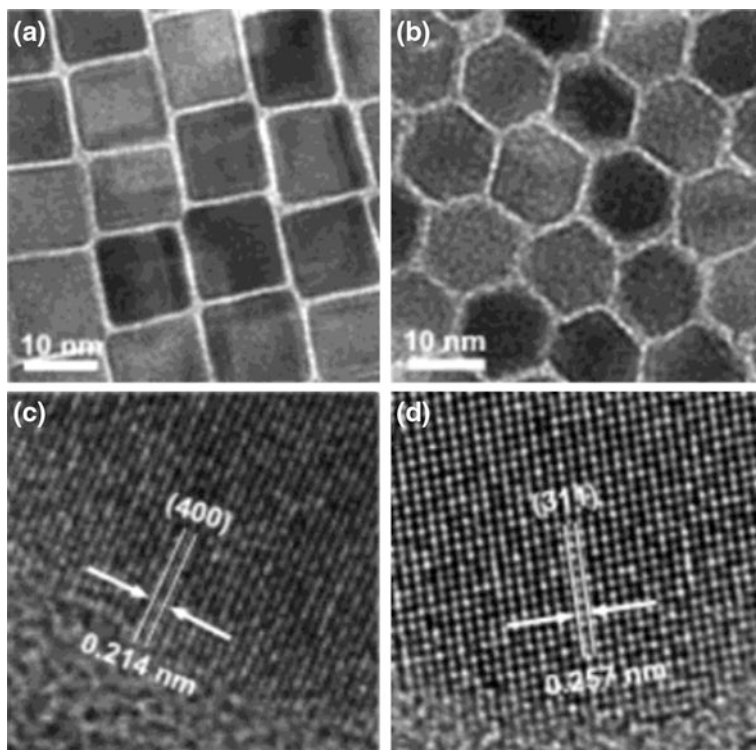


Fig. 3.120 TEM images of the as-synthesized **a** 12-nm cube-like and **b** 12-nm polyhedron-shaped MnFe_2O_4 NPs. HRTEM images of a part of a single **c** cube-like and **d** polyhedron-shaped MnFe_2O_4 NPs. Reproduced with permission from Ref. [72]. Copyright (2004) American Chemical Society

10 ± 0.7 nm (Fig. 3.120a). Larger nanocubes with a size of 15 ± 0.6 nm and 20 ± 1 nm were obtained by increasing the amount of $\text{Fe}(\text{acac})_3$ and $\text{Co}(\text{acac})_2$ while maintaining other parameters unchanged (Fig. 3.120b).

Monodisperse MnFe_2O_4 NPs with cube-like (Fig. 3.120a) and polyhedron shapes (Fig. 3.120b) were prepared by thermolysis of $\text{Fe}(\text{acac})_3$ and $\text{Mn}(\text{acac})_2$ with 1,2-hexadecanediol, OA, and OAm [72]. In a single cube-like MnFe_2O_4 NP, the interfringe distance is 0.214 nm (Fig. 3.120c), and in the case of a polyhedron-shaped particle (Fig. 3.120d) the interfringe distance is 0.257 nm. It is important that controlled evaporation of the dispersion of particles allows the production of superlattices of NPs.

In another interesting example, $\text{Co}(\text{acac})_2$ and $\text{Fe}(\text{acac})_3$ were thermolyzed in benzyl ether in the presence of OA and OAm to produce CoFe_2O_4 NPs [421]. The composition of $\text{Co}_x\text{Fe}_{3-x}\text{O}_4$ NPs was regulated either by thermolysis conditions or by the $\text{Co}(\text{acac})_2/\text{Fe}(\text{acac})_3$ molar ratio, and the NPs size was controlled by the amounts of OA and OAm added or the thermolysis temperature. In particular, NPs

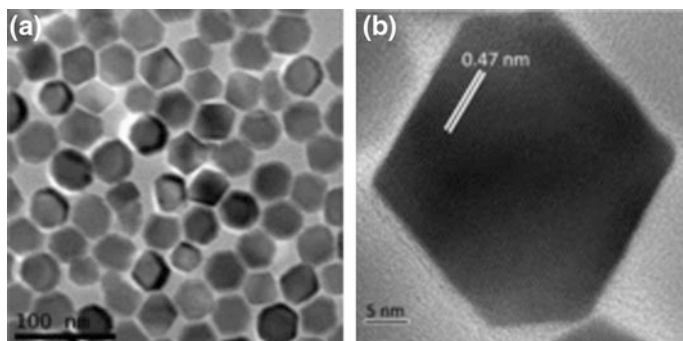


Fig. 3.121 a) TEM image of the 35-nm $\text{Co}_{0.6}\text{Fe}_{2.4}\text{O}_4$ NPs synthesized at 563 K for 1 h. b) HRTEM image of a representative NP shown in (a). Reproduced with permission from Ref. [421]. Copyright (2013) John Wiley and Sons

obtained from 0.5 to 1 h of thermolysis had compositions of $\text{Co}_{0.6}\text{Fe}_{2.4}\text{O}_4$, but those separated after 2 h of thermolysis showed a total composition reaching $\text{Co}_{0.9}\text{Fe}_{2.1}\text{O}_4$. However, in both cases, the size and morphology of the NPs were almost identical (Fig. 3.121a). NP is in a single crystal state and has a lattice fringe of 0.47 nm, close to the spacing of the (111) planes in the inverse spinel structured fcc CoFe_2O_4 (0.48 nm) (Fig. 3.121b).

It is of interest to easily synthesize monodisperse ferromagnetic $\text{Co}_x\text{Fe}_{3-x}\text{O}_4$ nanocubes (Fig. 3.122a) by thermolysis of $\text{Fe}(\text{acac})_3$ and $\text{Co}(\text{acac})_2$ in the presence of OA and NaOH [422, 423]. The sizes of the nanocubes vary from 10 to 60 nm. The size and morphology of the NPs are successfully regulated by thermolysis parameters, such as the thermolysis temperature, the amount of OAm as the reducing agent, and the amount of benzyl ether as solvent. Statistical size analysis of the prepared CoFe_2O_4 NPs showed APS of 28.0 nm and a standard deviation of 1.32 nm (Fig. 3.122b). The SAED image (Fig. 3.122c) has a clear diffraction circle in the (220), (311), and (400) CoFe_2O_4 crystal planes. There is a lattice fringe with an interfringe distance in single NPs at 0.25 nm, which is confirmed by the lattice spacing of (311) planes at 0.25 nm in the reverse spinel CoFe_2O_4 (Fig. 3.122d).

It is important that CoFe_2O_4 NPs had a cubic morphology, a uniform size distribution, and a pure phase structure. The crystallite sizes for the CoFe_2O_4 NPs obtained at different temperatures are 26.45, 32.67, 35.83, and 38.60 nm (Fig. 3.123a). In addition, the lattice parameter increases with thermolysis temperature (Fig. 3.123b), which indicates the redistribution of Co^{2+} ions from the octahedral to the tetrahedral site with increasing thermolysis temperature.

It should be noted the synthesis of CoFe_2O_4 NPs by thermolysis of $\text{Fe}(\text{acac})_3$ and $\text{Co}(\text{acac})_2$ compounds in organic solvents in the presence of OA/OAm as surfactants and 1,2-hexadecanediol (HDD) or octadecanol (OCD-ol) as an accelerating agent [424]. The thermolysis parameters, such as thermolysis time, temperature, surfactant concentration, solvent, precursor ratio, and accelerating agent, were studied in detail to determine the best conditions for the synthesis of the

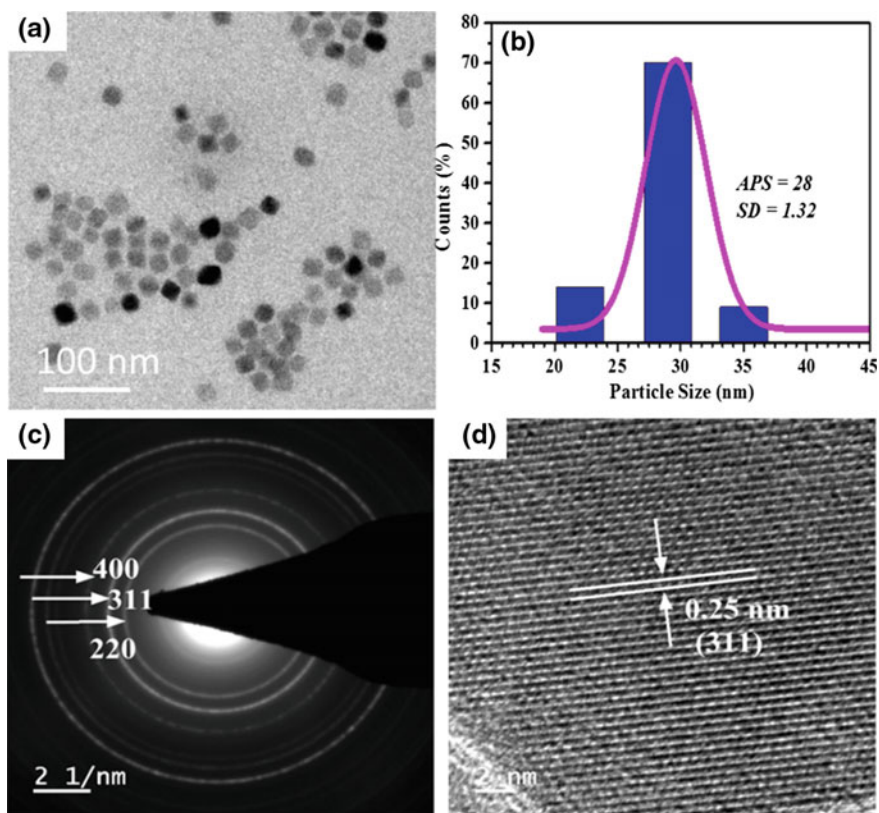


Fig. 3.122 **a** TEM image of the as-prepared, **b** size histogram with log-normal fitting curve (solid line), **c** SAED pattern of CoFe₂O₄ NPs, and **d** HRTEM image of single NPs. Reproduced with permission from Ref. [423]. Copyright (2017) Springer Nature

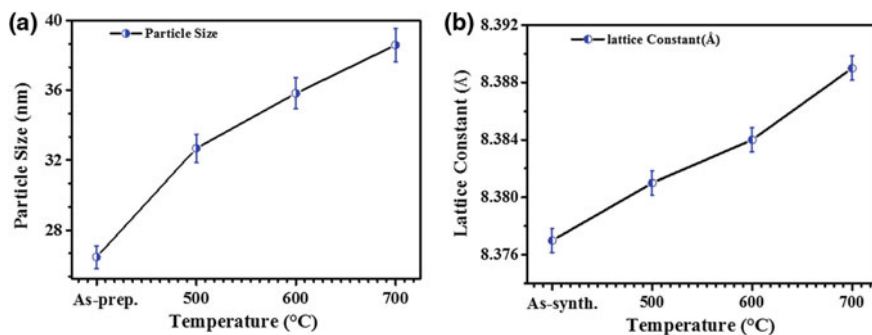


Fig. 3.123 **a** Particle size and **b** lattice parameter variation of the CoFe₂O₄ NPs at different temperatures. Reproduced with permission from Ref. [423]. Copyright (2017) Springer Nature

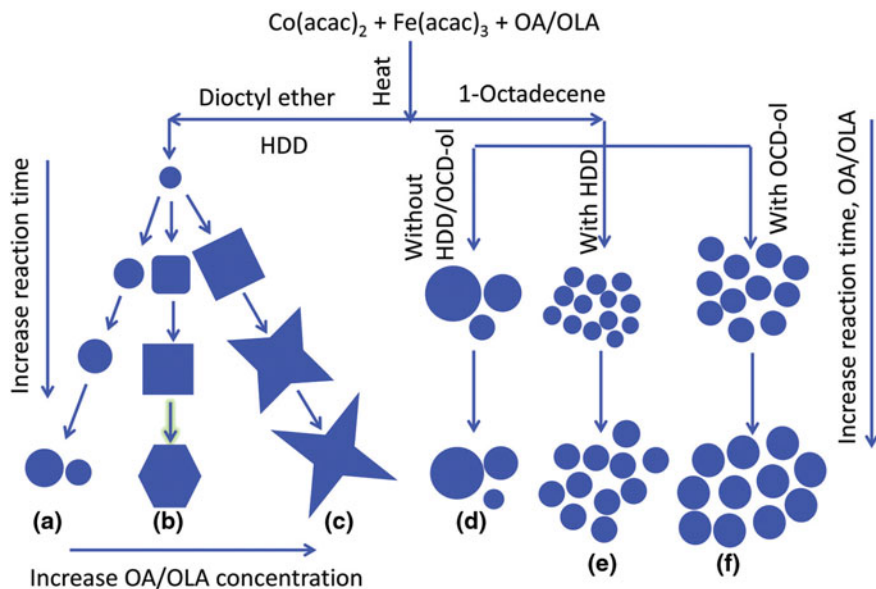


Fig. 3.124 Schematic diagram of morphological evolution of NPs under different synthetic conditions: **a–c** in diethyl ether with HDD at different reaction times and low (**a**), medium (**b**), and high concentrations of OA and OLA (**c**); **d–f** in octadecene at different reaction times and concentrations of OA and OLA without HDD/OCD-ol (**d**), with HDD (**e**), and OCD-ol (**f**) [424]

CoFe_2O_4 NPs. As a result, a schematic diagram of the evolution of the morphology of NPs with respect to solvents, reducing agents, surfactant concentrations, and thermolysis time was proposed (Fig. 3.124). At a low concentration of surfactants throughout the thermolysis process, NPs were obtained only with a spherical shape (Fig. 3.124a, d–f). However, in the future, the development of the initial spheres proceeded in different morphologies including rounded cubes, cubes, and faceted NPs (Fig. 3.124b) or cubes and stars at higher surfactant concentrations in the case of diethyl ether as the solvent (Fig. 3.124c). Increasing the time of thermolysis and concentration of surfactants led to large NPs (Fig. 3.124e, f). In similar synthetic conditions, the NPs formed with OCD-ol were larger than those prepared with the HDD, which is due to the difference in the reducing ability between HDD and OCD-ol.

The morphology-controlled synthesis of highly crystalline CoFe_2O_4 NPs by thermolysis with $\text{Fe}(\text{acac})_3$ and $\text{Co}(\text{acac})_2$ as precursors, as well as OA and OAm used as solvents, stabilizers, and reducing agents, is of interest [425]. NPs have well-defined shapes of different size, and their morphology can be varied by adjusting the time of thermolysis, solvent, and temperature. In particular, monodisperse sphere-like shapes of 6.41-nm size of CoFe_2O_4 NP were prepared using 40 mL of benzyl ether and 3 mL of each OA and OAm for 45 min of thermolysis time (Fig. 3.125a). However, a highly crystalline nanocube with an

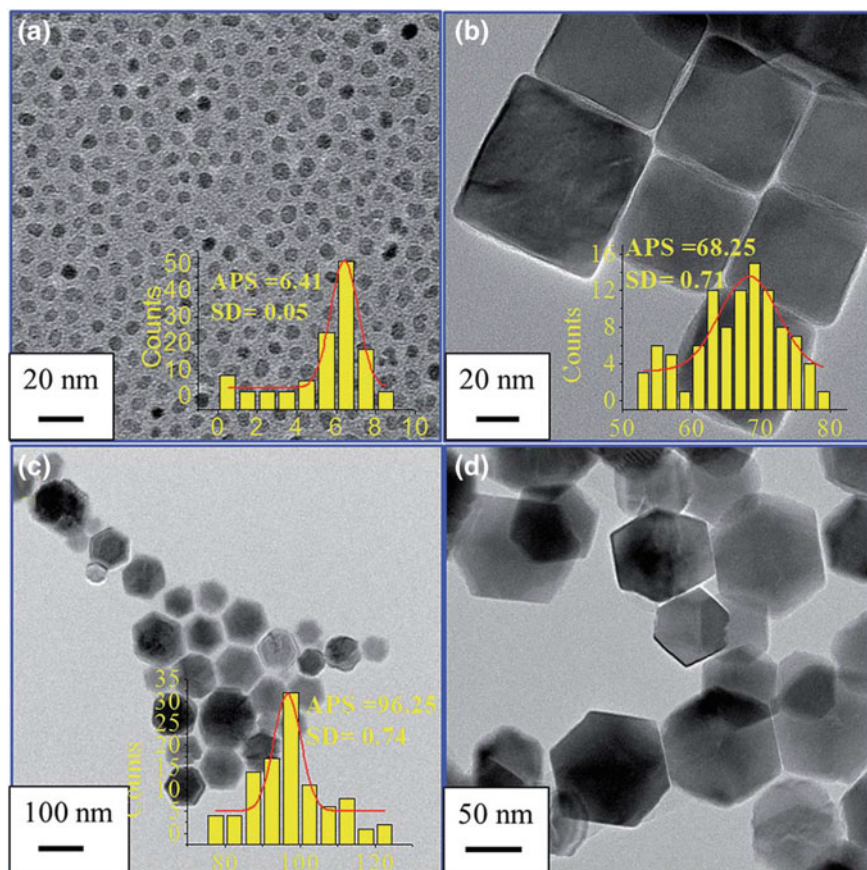


Fig. 3.125 TEM images of CoFe_2O_4 NPs with different shapes (a) sphere shape, (b) cube shape, and (c, d) hexagonal shape. The inset is a statistical analysis of the NPs including APS and SD. Reproduced with permission from Ref. [425]. Copyright (2016) Royal Society of Chemistry

APS of 68.25 nm was obtained by reducing the amount of solvent to 20 mL and using OA as the sole reducing agent in a 30-min thermolysis time (Fig. 3.125b). It should be noted that the subsequent decrease in the amount of solvent to 15 mL and the increase in the thermolysis time to 90 min led to the fact that the shape of the nanocubes was hexagonal with an APS of 96.65 nm (Fig. 3.125c, d). The evolution of the NPs shape is mainly due to the determining role of the surfactant and the thermolysis time.

An effective method for the preparation of composite oxide NPs such as magnetic MFe_2O_4 ($\text{M} = \text{Fe}, \text{Co}, \text{Mg}, \text{Zn}$ or Mn) using thermolysis is shown by changing bimetal precursors in a certain molar ratio. In particular, CoFe_2O_4 and MnFe_2O_4 spinel ferrite NPs with a diameter of ~ 10 nm were obtained, which formed 2D patterns on TEM grids and showed good uniformity (Fig. 3.126) [426].

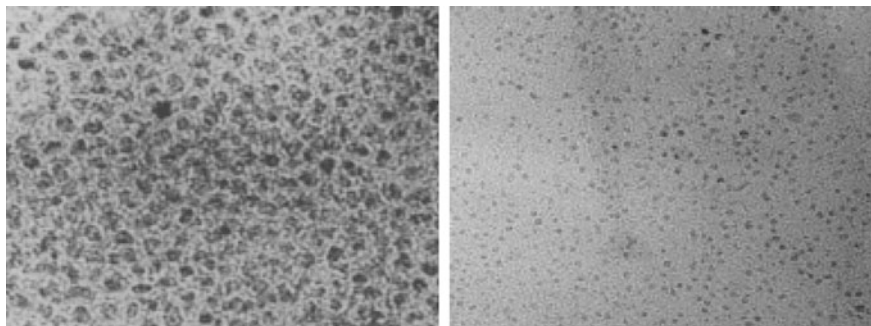


Fig. 3.126 TEM micrographs of *n*-octylamine capped magnetic spinel ferrite NPs: (left) CoFe_2O_4 and (right) MnFe_2O_4 . Reproduced with permission from Ref. [426]. Copyright (2002) Springer Nature

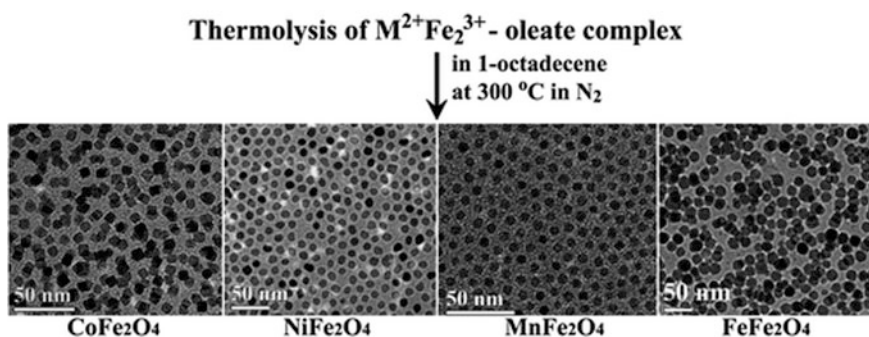


Fig. 3.127 Thermolysis of $\text{M}^{2+}\text{Fe}_2^{3+}$ -OI complex and TEM images of MFe_2O_4 NPs. Reproduced with permission from Ref. [428]. Copyright (2007) American Chemical Society

It should be noted using liquid-feed flame spray pyrolysis (LF-FSP) for the synthesis of Mg–Fe-containing nanopowders in the $(\text{MgO})_x(\text{Fe}_2\text{O}_3)_{1-x}$ system from bimetallic precursors [427]. In a typical example, the iron propionate $\text{Fe}(\text{O}_2\text{CCH}_2\text{CH}_3)_3$ and $\text{Mg}(\text{acac})_2 \cdot 2\text{H}_2\text{O}$ precursors were dissolved in ethanol, aerosolized with oxygen and thermolyzed at 1773 K, and then quickly quenched. The resulting nanopowders were un-aggregated and had APS < 45 nm with a specific surface area of 40–65 $\text{m}^2 \text{g}^{-1}$. It is important that the powders with different compositions ($x = 0.30, 0.45, 0.50, 0.65, 0.75, \text{ and } 0.90 \pm 0.02$) were obtained and their particle size generally increased with increasing proportion of MgO.

Monodisperse ternary ferrite (MFe_2O_4 , M = Co, Ni, Mn, and Fe) nanocrystals were prepared using thermolysis of an intimately mixed binary $\text{M}^{2+}\text{Fe}_2^{3+}$ -OI complex with a similar thermolysis temperature of the constituents (Fig. 3.127) [428].

Bimetallic nanocrystals can also be prepared by combining thermolysis with reduction. As a typical example, we note the synthesis of Fe–Pt nanocrystals

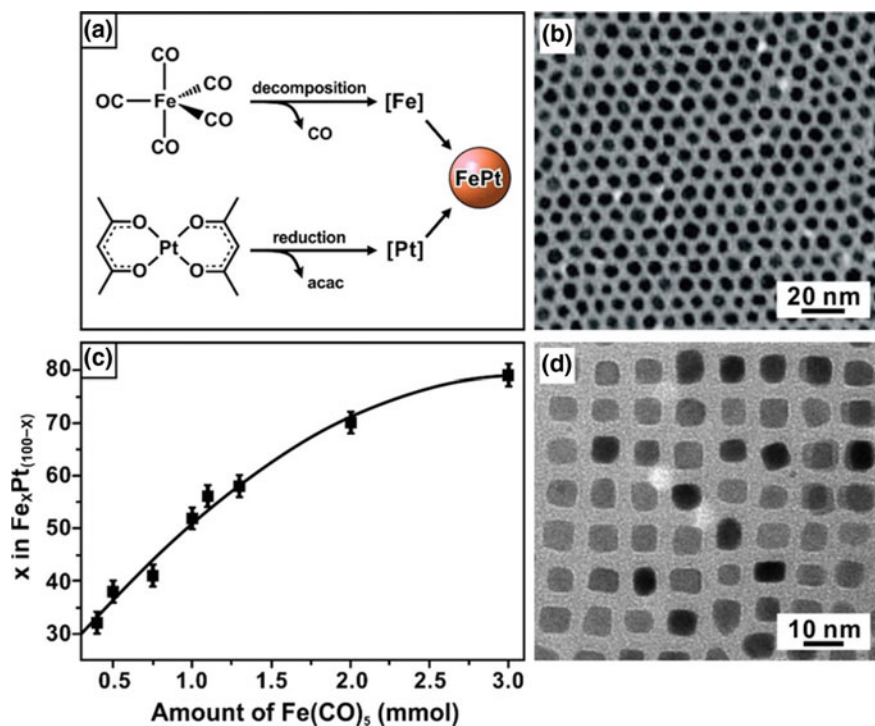


Fig. 3.128 a Schematic illustration showing the formation of Fe–Pt nanocrystals via simultaneous thermolysis of $\text{Fe}(\text{CO})_5$ and chemical reduction of $\text{Pt}(\text{acac})_2$. b TEM image of a representative sample of the Fe–Pt spherical nanocrystals. c Correlation between the amount of $\text{Fe}(\text{CO})_5$ used and the x in $\text{Fe}_x\text{Pt}_{(100-x)}$ based on the use of 0.5 mM of $\text{Pt}(\text{acac})_2$. d TEM image of Fe–Pt nanocubes obtained from a synthesis that involved the introduction of OA in the initial stage of the reaction. Reproduced with permission from Ref. [433]. Copyright (2006) American Chemical Society

through the simultaneous reduction of $\text{Pt}(\text{acac})_2$ and thermolysis of $\text{Fe}(\text{CO})_5$ in the presence of OA and OAm stabilizers (Fig. 3.128a) [429–431]. In this case, $\text{Fe}(\text{CO})_5$ decomposes to Fe^0 and CO at high temperature while the $\text{Pt}(\text{acac})_2$ is reduced to Pt^0 and acac by the polyol. The combination of Fe and Pt results in Fe–Pt spherical nanocrystals of equal size (Fig. 3.128b). The nucleation rate greatly influences the overall size and element uniformity; in particular, slower rates generate nanocrystals of larger sizes and nonhomogeneous compositions while the more rapid nucleation rates resulted in smaller, more homogeneous nanocrystals [432]. The Fe–Pt particle composition is easy to control by changing the $\text{Pt}(\text{acac})_2$ to $\text{Fe}(\text{CO})_5$ ratio, and the size is tunable from 3- to 10-nm diameter with a standard deviation (SD) less than 5% (Fig. 3.128c). Interestingly, these NPs self-assemble into 3D superlattices. In addition, the thermolysis converts the chemically disordered fcc FePt into chemically ordered fct FePt, and the annealed assembly shows a strong (001) texture in the directions parallel and perpendicular to the substrate. It is

important that composition, size, and shape of the nanocrystals were controlled by changing the synthetic parameters, including the molar ratio of stabilizer to metal precursor, the sequence of adding the stabilizers and metal precursors, heating profile and temperature, and duration of synthesis [431]. For example, highly faceted Fe–Pt nanocubes were formed by simultaneous thermolysis of $\text{Fe}(\text{CO})_5$ and reduction of $\text{Pt}(\text{acac})_2$ after the reaction temperature was reduced from 573 to 478 K, and also by the addition of OA first in the reaction solution (Fig. 3.128d) [433].

This general approach is also applicable to other metal precursors. In particular, monodisperse, highly crystalline CoPt_3 nanocrystals were obtained by simultaneously reducing and thermolysis of $\text{Pt}(\text{acac})_2$ and $\text{Co}_2(\text{CO})_8$ in the presence of ACA in different compositions [434]. The APS can vary from 1.5 to 7.2 nm by controlling the reaction conditions and the type of precursors. Synthesized CoPt_3 particles represent single crystal domains and have chemically disordered fcc structure. Interestingly, nearly spherical CoPt_3 nanocrystals assemble in 2D and 3D structures. Slow precipitation led to the formation of faceted colloidal crystals with sizes up to 20 μm (Fig. 3.129).

Monodisperse 4 nm Fe–Pt magnetic NPs were prepared by superhydride reduction of FeCl_2 and $\text{Pt}(\text{acac})_2$ in the presence of OA, OAm, and 1,2-hexadecanediol at high temperature, and thin assemblies of Fe–Pt NPs with controlled thickness were formed through polymer-mediated self-assembly (Scheme 3.72) [435]. It is important that the final Fe–Pt composition of the particles was readily tuned. In addition, the adsorption of a layer of polyethylene imine (PEI) and Fe–Pt NPs on a solid substrate led to the NP assemblies with tunable thickness. Thermolysis induced internal changes in the structure of the particles from chemically disordered fcc to chemically ordered fct and transformed the thin assembly from superparamagnetic to ferromagnetic.

Controlled reduction of $\text{Pt}(\text{acac})_2$ and thermolysis of $\text{Fe}(\text{CO})_5$ in a mixture of OAm and ODE leads to Fe–Pt nanowires and nanorods with a diameter of 2–3 nm [436]. The length of the nanowires/nanorods is tunable from over 200 nm to 20 nm simply by controlling the volume ratio of OAm and ODE. For example, for Fe–Pt nanowires with length of 200 nm, using 0.15 mL $[\text{Fe}(\text{CO})_5]$ led to about 55%Fe in the final product, while using 0.1 mL $[\text{Fe}(\text{CO})_5]$ resulted in approximately 45% of Fe (Fig. 3.130). The interfringe distance was measured equal to 0.214 nm, which is close to the lattice spacing of the (111) planes (0.22 nm) in the fcc FePt structure. It should be noted that Co–Pt nanowires can also be obtained by reduction of $\text{Pt}(\text{acac})_2$ and thermolysis of $\text{Co}_2(\text{CO})_8$ under similar reaction conditions.

Of interest is polyol reduction of $\text{Pt}(\text{acac})_2$ precursor together with the thermolysis of $\text{Fe}(\text{CO})_5$ and $\text{Co}_2(\text{CO})_8$ for the preparation of hard magnetic alloys of the type Fe–Pt or Co–Pt NPs [437]. In another interesting example, polyol reduction of $\text{Sm}(\text{acac})_3$ was used in association with the thermolysis of $\text{Co}_2(\text{CO})_8$ to prepare SmCo_5 NPs [438]. It should be also noted thermolysis of MnCl_2 , $\text{Fe}(\text{acac})_3$ OAc, OAm dioctyl ether and CoCl_2 , $\text{Fe}(\text{acac})_3$ OAc, OAm dioctyl ether [439], as well as ZnCl_2 , $\text{Fe}(\text{acac})_3$ OAc, OAm dioctyl ether [440].

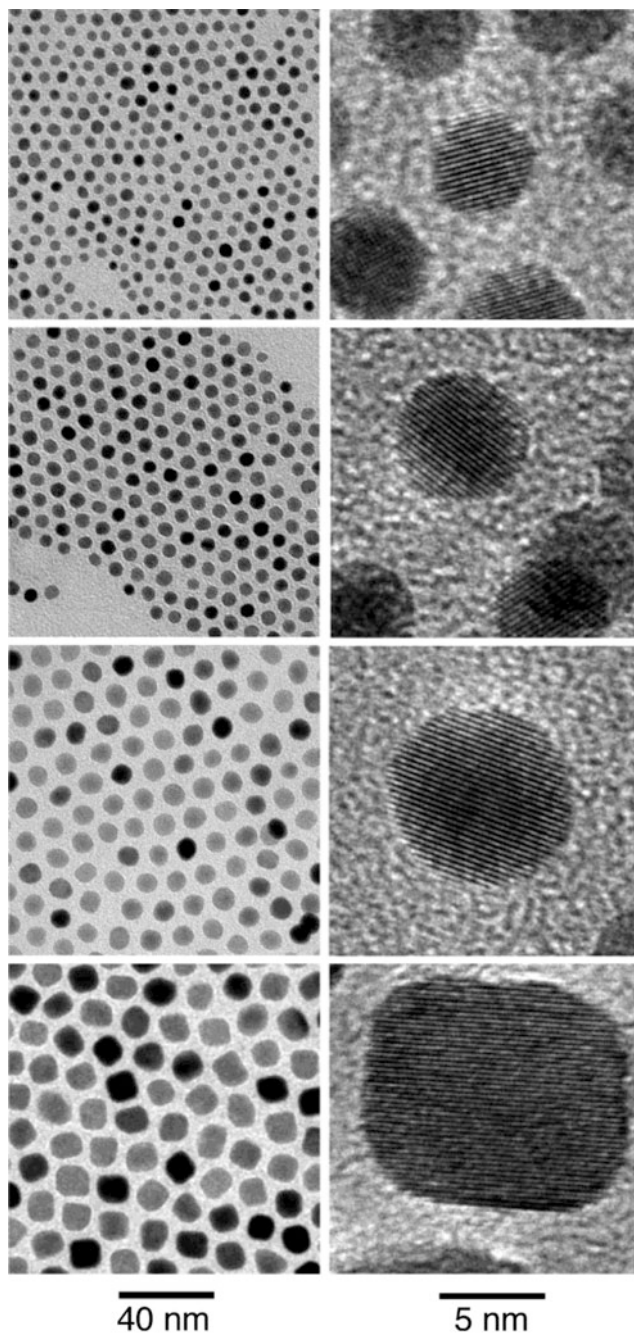
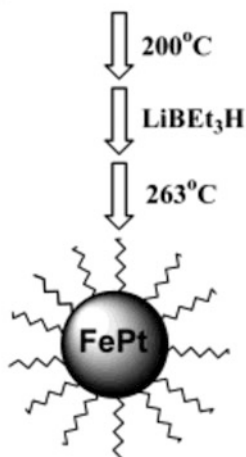
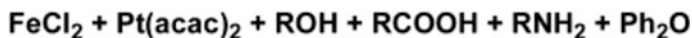


Fig. 3.129 TEM and HRTEM images showing the effect of the reaction temperature on the mean size and SD of 3.7, 4.9, 6.3, and 9.3 nm CoPt_3 nanocrystals prepared at 493, 473, 343, and 318 K and annealed at 553 K for 1 h. Molar ratio of Pt:Co:ACA is 1:3:6 for all samples. Reproduced with permission from Ref. [434]. Copyright (2002) American Chemical Society



Scheme 3.72 Schematic illustration of Fe–Pt NP synthesis by superhydride reduction of FeCl_2 and $\text{Pt}(\text{acac})_2$ in the presence of OA, OAm, and 1,2-hexadecanediol. Reproduced with permission from Ref. [435]. Copyright (2003) American Chemical Society

It is important that during thermolysis were allocated a large amount of gas that led to the formation of NPS with high surface area. It turned out that the temperature and time of thermolysis have a significant impact on reducing the size of the particles.

Pure greenish-blue cobalt chromite (CoCr_2O_4) NPs with a narrow particle range of 4.1 ± 1.9 nm and the surface area of the $78.2 \text{ m}^2 \text{ g}^{-1}$ were obtained by the thermolysis of mixed chelates of corresponding metals using 2-mercaptopyridine *N*-oxide sodium salt as chelating agent (Scheme 3.73) [441]. It is important that during thermolysis, a large amount of gas was emitted that led to the formation of NPs with high surface area. It turned that the temperature and time of thermolysis have a significant impact on reducing the size of the particles.

It should be noted the preparation of cobalt ferrite (CoFe_2O_4) NPs in two ways. The first method is based on the thermolysis of metal complexes with α -nitroso- β -naphthol [442]. In the second method, a template-free sonochemical treatment of mixed cobalt and iron chelates of α -nitroso- β -naphthol is used. The products prepared with first method were spherical, with a high specific surface area ($54.39 \text{ m}^2 \text{ g}^{-1}$) and small APS of 13 nm. However, the CoFe_2O_4 NPs prepared by the second method were in random shapes, with a wide range of crystal sizes and low specific surface area of $25.46 \text{ m}^2 \text{ g}^{-1}$ though highly pure.

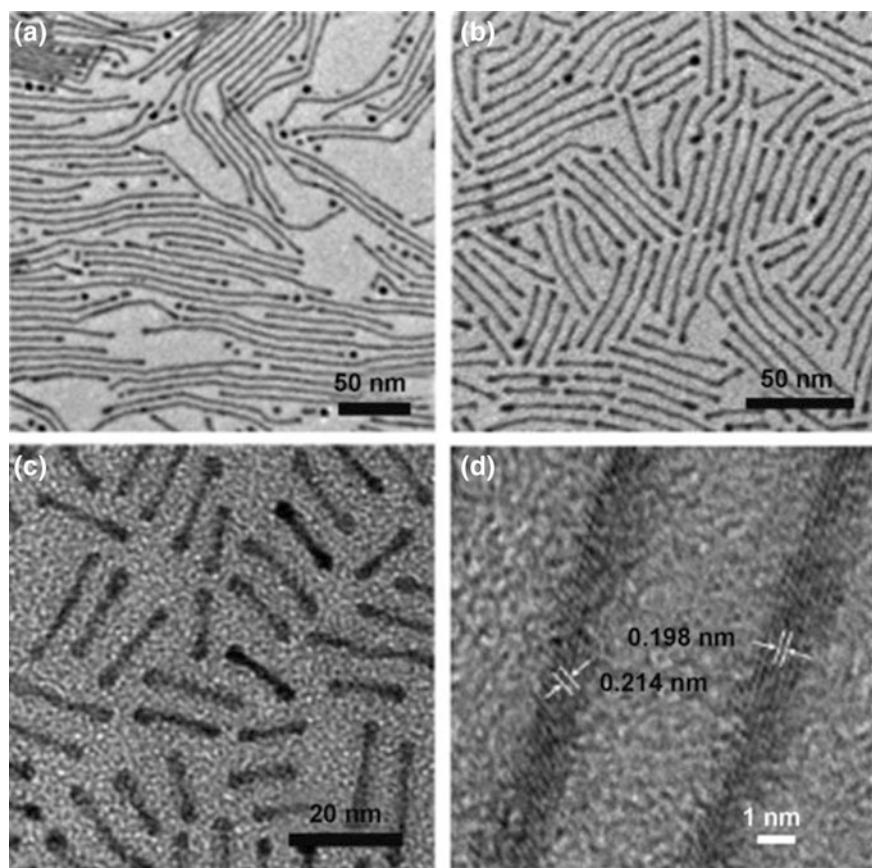
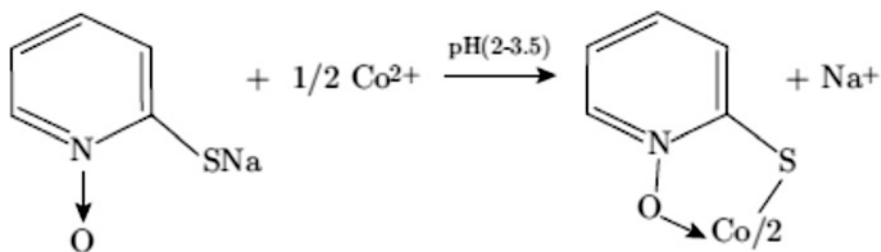


Fig. 3.130 a–c TEM images of $\text{Fe}_{55}\text{Pt}_{45}$ nanowires with a length of 200 nm (a), 50 nm (b), and 20 nm (c). **d** HRTEM image of portions of two single 50-nm $\text{Fe}_{55}\text{Pt}_{45}$ nanowires. Reproduced with permission from Ref. [436]. Copyright (2007) John Wiley and Sons



Scheme 3.73 Scheme of synthesis of Co(II) chelate with 2-mercaptopyridine *N*-oxide [441]

References

1. A.D. Pomogailo, A.S. Rozenberg, I.E. Uflyand, *Nanochastitsy metallov v polimerakh (Metal Nanoparticles in Polymers)* (Khimiya, Moscow, 2000)
2. A.D. Pomogailo, G.I. Dzhardimalieva, V.N. Kestelman, *Macromolecular metal carboxylates and their nanocomposites* (Springer, Heidelberg, 2010)
3. G.I. Dzhardimalieva, A.D. Pomogailo, Russ. Chem. Rev. **77**, 259 (2008)
4. S. Mishra, S. Daniele, Chem. Rev. **115**, 8379 (2015)
5. T. Bala, B.L.V. Prasad, M. Sastry, M.U. Kahaly, U.V. Waghmare, J. Phys. Chem. A **111**, 6183 (2007)
6. T.J. Boyle, R. Raymond, D.M. Boye, L.A.M. Ottley, P. Lu, Dalton Trans. **39**, 8050 (2011)
7. T. Schneller, D. Griesche, Carboxylate based precursor systems, in *Chemical Solution Deposition of Functional Oxide Thin Films*, ed. by T. Schneller, R. Waser, M. Kosec, D. Payne (Springer, Wien, 2013)
8. J. Park, K. An, Y. Hwang, J.G. Park, H.J. Noh, J.Y. Kim, J.H. Park, N.M. Hwang, T. Hyeon, Nat. Mater. **3**, 891 (2004)
9. N.V. Petrochenkova, B.V. Bukvetskii, A.G. Mirochnik, V.E. Karasev, Russ. J. Coord. Chem. **28**, 64 (2002)
10. N. Deb, J. Therm. Anal. Calorim. **81**, 61 (2005)
11. X. Li, Y.-Q. Zou, J. Chem. Cryst. **35**, 351 (2005)
12. M. Badea, R. Olar, D. Marinescu, G. Vasile, J. Therm. Anal. Calorim. **80**, 683 (2005)
13. S.R. Ghodake, U.A. Ghodake, S.R. Sawant, S.S. Suryavanshi, P.P. Bakare, J. Magn. Magn. Mater. **305**, 110 (2006)
14. B.S. Randhawa, K. Gandotra, J. Therm. Anal. Calorim. **85**, 417 (2006); **90**, 887 (2007)
15. B.S. Randhawa, M. Kaur, J. Therm. Anal. Calorim. **89**, 251 (2007)
16. S.G. Kwon, Y. Piao, J. Park, S. Angappane, Y. Jo, N.M. Hwang, J.G. Park, T. Hyeon, J. Am. Chem. Soc. **129**, 12571 (2007)
17. B.S. Randhawa, M. Kaur, K. Gandotra, J. Radioanal. Nucl. Chem. **269**, 69 (2006)
18. A. Valor, E. Reguera, E. Torres-Garcia, S. Mendoza, F. Sanchez-Sinencio, Thermochim. Acta **389**, 133 (2002)
19. A. Valor, E. Reguera, F. Sanchez-Sinencio, Powder Diffr. **17**, 13 (2002)
20. W.W. Yu, J.C. Falkner, C.T. Yavuz, V.L. Colvin, Chem. Commun. 2306 (2004)
21. A.D. Pomogailo, G.I. Dzhardimalieva, *Nanostructured Materials Preparation via Condensation Ways* (Springer, Dordrecht, 2014)
22. A.S. Rozenberg, G.I. Dzhardimalieva, A.D. Pomogailo, Dokl. Akad. Nauk **356**, 66 (1997)
23. B.B. Bokhonov, Y.M. Yukhin, Russ. J. Inorg. Chem. **52**, 922 (2007)
24. A.S. Rozenberg, V.R. Stepanov, Russ. Chem. Bull. **45**, 1336 (1996)
25. W.J. Scharmach, R.D. Bucher, V. Papavassiliou, P. Pacouloute, M.T. Swihart, Aerosol. Sci. Technol. **44**, 1083 (2010)
26. C. Hofmann, I. Rusakova, T. Ould-Ely, D. Prieto-Centurion, K.B. Hartman, A.T. Kelly, A. Luttge, K.H. Whitmire, Adv. Funct. Mater. **18**, 1661 (2008)
27. D.I. Son, C.H. You, T.W. Kim, Appl. Surf. Sci. **255**, 8794 (2009)
28. R.V. Kumar, Y. Diamant, A. Gedanken, Chem. Mater. **12**, 2301 (2000)
29. C.C. Li, M.H. Chang, Mater. Lett. **58**, 3903 (2004)
30. J.C. De Jesus, I. Gonzalez, A. Quevedo, T. Puerta, J. Mol. Catal. A: Chem. **228**, 283 (2005)
31. A. Kotoulas, M. Gjoka, K. Simeonidis, I. Tsiaoussis, M. Angelakeris, O. Kalogirou, C. Dendrinou-Samara, J. Nanopart. Res. **13**, 1897 (2011)
32. S. Mourdikoudis, K. Simeonidis, A. Vilalta-Clemente, F. Tuna, I. Tsiaoussis, M. Angelakeris, J. Magn. Magn. Mater. **321**, 2723 (2009)
33. J. Park, E. Kang, S.U. Son, H.M. Park, M.K. Lee, J. Kim, K.W. Kim, H.-J. Noh, J.-H. Park, C.J. Bae, J.-G. Park, T. Hyeon, Adv. Mater. **17**, 429 (2005)
34. H. Wang, X. Jiao, D. Chen, J. Phys. Chem. C **112**, 18793 (2008)
35. X. Luo, Y. Chen, G. Yue, D. Peng, X. Luo, J. Alloys Compd. **476**, 864 (2009)

36. V.G. Pol, M. Popa, S. Acharya, K. Ariga, P. Thiyagarajan, *Inorg. Chem.* **48**, 5569 (2009)
37. V.G. Pol, J.M. Calderon-Moreno, P. Thiyagarajan, *Langmuir* **24**, 13640 (2008)
38. V.V. Kireev, L.N. Demyanets, L.E. Li, V.V. Artemov, *Inorg. Mater.* **46**, 154 (2010)
39. R.-C. Wang, C.-C. Tsai, *Appl. Phys. A* **94**, 241 (2009)
40. T. Huang, Q. Zhao, J. Xiao, L. Qi, *ACS Nano* **4**, 4707 (2010)
41. N. Zhao, L. Qi, *Adv. Mater.* **18**, 359 (2006)
42. S. Liu, S. Xiong, K. Bao, J. Cao, Y. Qian, *J. Phys. Chem. C* **113**, 13002 (2009)
43. S. Shao, G. Zhang, H. Zhou, P. Sun, Z. Yuan, B. Li, T. Chen, *Solid State Sci.* **9**, 725 (2007)
44. J. Xiang, H. Cao, Q. Wu, S. Zhang, X. Zhang, *Cryst. Growth Des.* **8**, 3935 (2008)
45. B. Ding, M. Shi, F. Chen, R. Zhou, M. Deng, M. Wang, H. Chen, *J. Cryst. Growth* **311**, 1533 (2009)
46. R. Gaur, P. Jeevanandam, *J. Nanopart. Res.* **18**, 80 (2016)
47. M. Yin, S. O'Brien, *J. Am. Chem. Soc.* **125**, 10180 (2003)
48. Y.-P. Du, Y.-P. Du, Y.-W. Zhang, L.-D. Sun, C.-H. Yan, *J. Phys. Chem. C* **113**, 6521 (2009)
49. V.G. Pol, L.L. Daemen, S. Vogel, G. Chertkov, *Ind. Eng. Chem. Res.* **49**, 920 (2010)
50. M.D. Uplane, P.N. Kshirsagar, B.J. Lokhande, C.H. Bhosale, *Mater. Chem.* **64**, 75 (2000)
51. R.M. Mahfouz, G.A.-W. Ahmed, T. Al-Rashidi, *Cogent Chem.* **2**, 1215233 (2016)
52. H. Shao, Y. Huang, H. Lee, Y.J. Suh, C.O. Kim, *J. Magn. Magn. Mater.* **304**, e28 (2006)
53. V. Logvinenko, O. Polunina, Yu. Mikhailov, K. Mikhailov, B. Bokhonov, *J. Therm. Anal. Calorim.* **90**, 813 (2007)
54. P. Jeevanandam, C.K. Srikanth, S. Dixit, *Mater. Chem. Phys.* **122**, 402 (2010)
55. M. Nakano, T. Fujiwara, N. Koga, *J. Phys. Chem. C* **120**, 8841 (2016)
56. S.D. Bakrania, G.K. Rathore, M.S. Wooldridge, *J. Therm. Anal. Calorim.* **95**, 117 (2009)
57. T. Hyeon, Y. Chung, J. Park, S.S. Lee, Y.W. Kim, B.H. Park, *J. Phys. Chem. B* **106**, 6831 (2002)
58. T. Hyeon, *Chem. Commun.* 927 (2003)
59. R. Kaur, S.K. Mehta, *Coord. Chem. Rev.* **262**, 37 (2014)
60. J. Liu, Z. Wu, Q. Tian, W. Wu, X. Xiao, *CrystEngComm* **18**, 6303 (2016)
61. N.R. Jana, Y. Chen, X. Peng, *Chem. Mater.* **16**, 3931 (2004)
62. L. Zhang, J. Wu, H. Liao, Y. Hou, S. Gao, *Chem. Commun.* 4378 (2009)
63. D. Ling, T. Hyeon, *Small* **9**, 1450 (2013)
64. M.M. Lin, D.K. Kim, *J. Nanopart. Res.* **14**, 688 (2012)
65. X. He, W. Zhong, C.-T. Au, Y. Du, *Nanoscale Res. Lett.* **8**, 446 (2013)
66. A. Shavel, B. Rodrigues-Gonzalez, J. Pacifico, M. Spasova, M. Farle, L.M. Liz-Marzan, *Chem. Mater.* **21**, 1326 (2009)
67. Y. He, Y. Sahoo, S. Wang, H. Luo, P.N. Prasad, M.T. Swihart, *J. Nanopart. Res.* **8**, 335 (2006)
68. H.G. Cha, D.K. Lee, Y.H. Kim, C.W. Kim, C.S. Lee, Y.S. Kang, *Inorg. Chem.* **47**, 121 (2008)
69. Y. Kamei, K. Wakayama, Y. Makinose, Y. Endo, N. Matsushita, *Mater. Sci. Eng., B* **223**, 70 (2017)
70. F.X. Redl, C.T. Black, G.C. Papaefthymiou, R.L. Sandstrom, M. Yin, H. Zeng, C.B. Murray, S.P. O'Brien, *J. Am. Chem. Soc.* **126**, 14583 (2004)
71. H. Yang, T. Ogawa, D. Hasegawa, M. Takahashi, *J. Appl. Phys.* **103**, 07D526 (2008)
72. H. Zeng, P.M. Rice, S.X. Wang, S. Sun, *J. Am. Chem. Soc.* **126**, 11458 (2004)
73. A. Ahniyaz, Y. Sakamoto, L. Bergstroem, *Proc. Natl. Acad. Sci. U.S.A.* **104**, 17570 (2007)
74. G. Salazar-Alvarez, J. Qin, V. Sepelak, I. Bergmann, M. Vasilakaki, K.N. Trohidou, J.D. Ardisson, W.A.A. Macedo, M. Mikhaylova, M. Muhammed, M.D. Baro, J.J. Noguees, *J. Am. Chem. Soc.* **130**, 13234 (2008)
75. L. Wang, L. Gao, *J. Phys. Chem. C* **113**, 15914 (2009)
76. M.V. Kovalenko, M.I. Bodnarchuk, R.T. Lechner, G. Hesser, F. Schaffler, W. Heiss, *J. Am. Soc. Chem.* **129**, 6352 (2007)
77. L.M. Bronstein, X. Huang, J. Retrum, A. Schmucker, M. Pink, B.D. Stein, B. Dragnea, *Chem. Mater.* **19**, 3624 (2007)

78. X.R. Ye, C. Daraio, C. Wang, J.B. Talbot, S. Jin, *J. Nanosci. Nanotechnol.* **6**, 852 (2006)
79. L.M. Bronstein, J.E. Atkinson, A.G. Malyutin, F. Kidwai, B.D. Stein, D.G. Morgan, J.M. Perry, J.A. Karty, *Langmuir* **27**, 3044 (2011)
80. A. Stepanov, A. Mustafina, R.G. Mendes, M.H. Rümmele, T. Gemming, E. Popova, I. Nizameev, M. Kadirov, *J. Iran. Chem. Soc.* **13**, 299 (2016)
81. S.B. Wang, Y.L. Min, S.H. Yu, *J. Phys. Chem. C* **111**, 3551 (2007)
82. C.S. Li, Y.N. Li, Y.L. Wu, B.S. Ong, R.O. Loutfy, *Sci. China Ser. E-Technol. Sci.* **51**, 2075 (2008)
83. D.K. Lee, Y.H. Kim, X.-L. Zhang, Y.S. Kang, *Curr. Appl. Phys.* **6**, 786 (2006)
84. V.F. Puentes, K.M. Krishnan, A.P. Alivisatos, *Science* **291**, 2115 (2001)
85. K. An, N. Lee, J. Park, S.C. Kim, Y. Hwang, J.G. Park, J.Y. Kim, J.H. Park, M.J. Han, J. Yu, T. Hyeon, *J. Am. Chem. Soc.* **128**, 9753 (2006)
86. S. Kim, Y. Terashi, A. Purwanto, K. Okuyama, *Colloid Surf. A.* **337**, 96 (2009)
87. K. Assim, S. Schulze, M. Pügner, M. Uhlemann, T. Gemming, L. Giebeler, M. Hietschold, T. Lampke, H. Lang, *J. Mater. Sci.* **52**, 6697 (2017)
88. V. Patsula, L. Kosinova, M. Lovrić, L.F. Hamzić, M. Rabyk, R. Konefal, A. Paruzel, M. Šlouf, V. Herynek, S. Gajović, D. Horak, *ACS Appl. Mater. Interfaces* **8**, 7238 (2016)
89. K. Liu, H. You, G. Jia, Y. Zheng, Y. Song, M. Yang, Y. Huang, H. Zhang, *Cryst. Growth Des.* **9**, 3519 (2009)
90. B.L. Chen, Y. Yang, F. Zapata, G.N. Lin, G.D. Qian, E.B. Lobkovsky, *Adv. Mater.* **19**, 1693 (2007)
91. J.R. William, M.L. Kathryn, H.Y. An, W.L. Lin, W.B. Lin, *J. Am. Chem. Soc.* **128**, 9024 (2006)
92. K. Bijanzad, A. Tadjarodi, O. Akhavan, *Chin. J. Catal.* **36**, 742 (2015)
93. B. Małecka, E. Drożdż-Cieśla, A. Małecki, *J. Therm. Anal. Calorim.* **68**, 819 (2002)
94. A. Angermann, J. Topfer, *J. Mater. Sci.* **43**, 5123 (2008)
95. O. Carp, L. Patron, G. Marinescu, G. Pascu, P. Budrugu, M. Brezeanu, *J. Therm. Anal. Calor.* **72**, 263 (2003)
96. P. Hermankova, M. Hermanek, R. Zboril, *Eur. J. Inorg. Chem.* **2010**, 1110 (2010)
97. W. Zhou, K. Tang, S. Zeng, Y. Qi, *Nanotechnology* **19**, 065602 (2008)
98. N. Koga, Y. Sato, *J. Phys. Chem. A* **115**, 141 (2011)
99. M. Hermanek, R. Zboril, M. Mashlan, L. Machala, O. Schneeweiss, *J. Mater. Chem.* **16**, 1273 (2006)
100. M. Hermanek, R. Zboril, I. Medrik, J. Pechousek, C. Gregor, *J. Am. Chem. Soc.* **129**, 10929 (2007)
101. R. Zboril, L. Machala, M. Mashlan, M. Hermanek, M. Miglierini, A. Fojtík, *Phys. Status Solidi C* **1**, 3583 (2004)
102. M. Popa, J.M. Calderon-Moreno, D. Crisan, M. Zaharescu, *J. Therm. Anal. Calorim.* **62**, 633 (2000)
103. M. Perovic, V. Kusigerski, A. Mrakovic, V. Spasojevic, J. Blanus, V. Nikolic, O. Schneeweiss, B. David, N. Pizúrová, *Nanotechnology* **26**, 115705 (2015)
104. A. Saritha, B. Raju, D. Narayana Rao, A. Roychowdhury, D. Das, K.A. Hussain, *Adv. Powder Technol.* **26**, 349 (2015)
105. B. Donkova, D. Mehandjiev, *J. Mater. Sci.* **40**, 3881 (2005)
106. K. Sarada, K.R. Vijisha, K. Muraleedharan, *J. Anal. Appl. Pyrol.* **120**, 207 (2016)
107. E. Lamprecht, G.M. Watkins, M.E. Brown, *Thermochim. Acta* **446**, 91 (2006)
108. S. Majumdar, I.G. Sharma, A.C. Bidaye, A.K. Suri, *Thermochim. Acta* **473**, 45 (2008)
109. X. Wang, X.Y. Chen, L.S. Gao, H.G. Zheng, Z. Zhang, Y.T. Qian, *J. Phys. Chem. B* **108**, 16401 (2004)
110. M. Salavati-Niasari, N. Mir, F. Davar, *J. Phys. Chem. Solids* **70**, 847 (2009)
111. M.N.H. Hamed, R. Kamal, *J. Therm. Anal. Calorim.* **123**, 675 (2016)
112. O.I. Gyrdasova, V.N. Krasil'nikov, G.V. Bazuev, *Russ. J. Inorg. Chem.* **54**, 1035 (2009)
113. M.A. Mohamed, A.K. Galwey, S.A. Halawy, *Thermochim. Acta* **346**, 91 (2000)
114. M.A. Mohamed, S.A. Halawy, *J. Anal. Appl. Pyrol.* **80**, 238 (2007)

115. P. Naumov, M. Ristova, B. Soptrajanov, M.G.B. Drew, S.W. Ng, *Croat. Chem. Acta* **75**, 701 (2002)
116. Z.L. Wang, L.H. Wei, J.Y. Niu, *Acta Cryst. E* **61**, 1907 (2005)
117. C.R. Bhattacharjee, D.D. Purkayastha, N. Das, *Mater. Lett.* **94**, 108 (2013)
118. F.J. Cairnes, L.S. Lima, C.T. Carvalho, R.J. Giagio, M. Ionashiro, *Thermochim. Acta* **497**, 35 (2010)
119. K. Giribabu, R. Suresh, R. Manigandan, A. Stephen, V. Narayanan, *J. Iran. Chem. Soc.* **10**, 771 (2013)
120. B. Malecka, A. Łacz, A. Małeck, *J. Anal. Appl. Pyrol.* **80**, 126 (2007)
121. A.D. Karthik, K. Geetha, *Int. J. Nano Dimens.* **5**, 321 (2014)
122. L.I. Yudanov, V.A. Logvinenko, N.F. Yudanov, N.A. Rudina, A.V. Ishchenko, P.P. Semyannikov, L.A. Sheludyakova, N.I. Alferova, I.V. Korol'kov, *Inorg. Mater.* **50**, 945 (2014)
123. L.I. Yudanov, V.A. Logvinenko, N.F. Yudanov, N.A. Rudina, A.V. Ishchenko, I.V. Korol'kov, P.P. Semyannikov, L.A. Sheludyakova, N.I. Alferova, *Russ. J. Phys. Chem. A* **90**, 1206 (2016)
124. J.T. Sun, L.J. Yuan, K.L. Zhang, D.L. Wang, *Thermochim. Acta* **343**, 105 (2000)
125. D. Zhan, X.W. Zhou, Y. Zhang, J.H. Hong, K.L. Zhang, *Thermochim. Acta* **428**, 47 (2005)
126. M. Salavati-Niasari, F. Mohandes, F. Davar, K. Saberyan, *Appl. Surf. Sci.* **256**, 1476 (2009)
127. H.T. Yang, C.M. Shen, Y.G. Wang, Y.K. Su, T.Z. Yang, H.J. Gao, *Nanotechnology* **15**, 70 (2004)
128. F. Davar, F. Mohandes, M. Salavati-Niasari, *Polyhedron* **29**, 3132 (2010)
129. M. Salavati-Niasari, F. Mohandes, F. Davar, M. Mazaheri, M. Monemzadeh, N. Yavarinia, *Inorg. Chim. Acta* **362**, 3691 (2009)
130. F. Mohandes, F. Davar, M. Salavati-Niasari, *J. Magn. Magn. Mater.* **322**, 872 (2010)
131. R.K. Sodhi, S. Paul, *Catal. Surv. Asia* **1** (2017). <https://doi.org/10.1007/s10563-017-9239-9>
132. Z. Fereshteh, M. Salavati-Niasari, *Adv. Coll. Interface. Sci.* **243**, 86 (2017)
133. Y. Goto, K. Taniguchi, T. Omata, S. Otsuka-Yao-Matsuo, *Chem. Mater.* **20**, 4156 (2008)
134. T. Ishizaki, K. Yatsugi, K. Akedo, *Nanomaterials* **6**, 172 (2016)
135. J. Chandradass, K.H. Kim, *Mater. Manuf. Processes* **24**, 541 (2009)
136. S.U. Son, I.K. Park, J. Park, T. Hyeon, *Chem. Commun.* **778** (2004)
137. A. Ghezelbash, B.A. Korgel, *Langmuir* **21**, 9451 (2005)
138. D. Mott, J. Galkowski, L. Wang, J. Luo, C.-J. Zhong, *Langmuir* **23**, 5740 (2007)
139. N.S. Gajbhiye, S. Sharma, A.K. Nigam, R.S. Ningthoujam, *Chem. Phys. Lett.* **466**, 181 (2008)
140. W.S. Seo, J.H. Shim, S.J. Oh, E.K. Lee, N.H. Hur, J.T. Park, *J. Am. Chem. Soc.* **127**, 6188 (2005)
141. M. Salavati-Niasari, M. Dadkhah, F. Davar, *Inorg. Chim. Acta* **362**, 3969 (2009)
142. M. Salavati-Niasari, F. Davar, M. Mazaheri, *Mater. Lett.* **62**, 1890 (2008)
143. W.S. Seo, H.H. Jo, K. Lee, B. Kim, S.J. Oh, J.T. Park, *Angew. Chem. Int. Ed.* **43**, 1115 (2004)
144. F. Jiao, A. Harrison, P.G. Bruce, *Angew. Chem. Int. Ed.* **46**, 3946 (2007)
145. S.H. Sun, H. Zeng, *J. Am. Chem. Soc.* **124**, 8204 (2002)
146. Y.L. Hou, Z.C. Xu, S.H. Sun, *Angew. Chem. Int. Ed.* **46**, 6329 (2007)
147. J. Xie, S. Peng, N. Brower, N. Pourmand, S.X. Wang, S. Sun, *Pure Appl. Chem.* **78**, 1003 (2006)
148. M. Lattuada, T.A. Hatton, *Langmuir* **23**, 2158 (2007)
149. P. Guardia, J. Perez-Juste, A. Labarta, X. Batlle, L.M. Liz-Marzan, *Chem. Commun.* **46**, 6108 (2010)
150. X. Liu, M. Atwater, J. Wang, Q. Dai, J. Zou, J.P. Brennan, Q. Huo, *J. Nanosci. Nanotechnol.* **7**, 3126 (2007)
151. C.A. Crouse, A.R. Barron, *J. Mater. Chem.* **18**, 4146 (2008)
152. M. Klokkenburg, J. Hilhorst, B.H. Erne, *Vib. Spectrosc.* **43**, 243 (2007)

153. I.O. Perez De Berti, M.V. Cagnoli, G. Pecchi, J.L. Alessandrini, S.J. Stewart, J.F. Bengoa, S.G. Marchetti, *Nanotechnology* **24**, 175601 (2013)
154. A.G. Roca, M.P. Morales, C.J. Serna, *IEEE Trans. Magn.* **42**, 3025 (2006)
155. V.B. Barbeta, R.F. Jardim, P.K. Kiyohara, F.B. Effenberger, L.M. Rossi, *J. Appl. Phys.* **107**, 073913 (2010)
156. S. Sun, H. Zeng, D.B. Robinson, S. Raoux, P.M. Rice, S.X. Wang, G. Li, *J. Am. Chem. Soc.* **126**, 273 (2004)
157. D. Maity, S.N. Kale, R. Kaul-Ghanekar, J.M. Xue, J. Ding, *J. Magn. Magn. Mater.* **321**, 1259 (2009); **321**, 3093 (2009)
158. A.R. Deniz, Z. Caldıran, O. Metin, K. Meral, S. Aydogan, *J. Colloid Interface Sci.* **473**, 172 (2016)
159. F.B. Effenberger, R.A. Couto, P.K. Kiyohara, G. Machado, S.H. Masunaga, R.F. Jardim, L.M. Rossi, *Nanotechnology* **28**, 115603 (2017)
160. Z. Xu, C. Shen, Y. Hou, H. Gao, S. Sun, *Chem. Mater.* **21**, 1778 (2009)
161. F.Q. Hu, K.W. MacRenaris, E.A. Waters, E.A. Schultz-Sikma, A.L. Eckermann, T.J. Meade, *Chem. Commun.* **46**, 73 (2010)
162. D. Kim, N. Lee, M. Park, B.H. Kim, K. An, T. Hyeon, *J. Am. Chem. Soc.* **131**, 454 (2008)
163. M. Unni, A.M. Uhl, S. Savliwala, B.H. Savitzky, R. Dhavalikar, N. Garraud, D.P. Arnold, L.F. Kourkoutis, J.S. Andrew, C. Rinaldi, *ACS Nano* **11**, 2284 (2017)
164. A.S. Lyadov, A.A. Kochubeev, L.D. Koleva, O.P. Parenago, S.N. Khadzhev, *Russ. J. Inorg. Chem.* **61**, 1387 (2016)
165. A. Gulino, F. Castelli, P. Dapporto, P. Rossi, I. Fragala, *Chem. Mater.* **14**, 704 (2002)
166. A. Gulino, P. Dapporto, P. Rossi, I. Fragala, *Chem. Mater.* **14**, 1441 (2002)
167. D.A. Fleming, M.E. Williams, *Langmuir* **20**, 3021 (2004)
168. Y.J. Kang, X.C. Ye, C.B. Murray, *Angew. Chem. Int. Ed.* **49**, 6156 (2010)
169. Y. Wang, X. Yang, G. Xiao, B. Zhou, B. Liu, G. Zou, B. Zou, *CrystEngComm* **15**, 5496 (2013)
170. W. Zhou, J. Wu, H. Yang, *Nano Lett.* **13**, 2870 (2013)
171. J. Wu, A. Gross, H. Yang, *Nano Lett.* **11**, 798 (2011)
172. R. Xie, Y. Pan, H. Gu, *RSC Adv.* **5**, 16497 (2015)
173. N. Ortiz, S.E. Skrabalak, *Angew. Chem. Int. Ed.* **51**, 11757 (2012)
174. S.-W. Kim, J. Park, Y. Jang, Y. Chung, S. Hwang, T. Hyeon, Y.W. Kim, *Nano Lett.* **3**, 1289 (2003)
175. V. Mazumder, S. Sun, *J. Am. Chem. Soc.* **131**, 4588 (2009)
176. Z. Niu, Q. Peng, M. Gong, H. Rong, Y. Li, *Angew. Chem. Int. Ed.* **50**, 6315 (2011)
177. Z. Yang, K.J. Klabunde, *J. Organomet. Chem.* **694**, 1016 (2009)
178. N. Ortiz, S.E. Skrabalak, *Langmuir* **30**, 6649 (2014)
179. R. Gaur, L. Mishra, M.A. Siddiqi, B. Atakan, *RSC Adv.* **4**, 33785 (2014)
180. Y.-H. Lai, Y.-L. Chen, Y. Chi, C.-S. Liu, A.J. Carty, S.-M. Peng, G.-H. Lee, *J. Mater. Chem.* **13**, 1999 (2003)
181. W.-Y. Cheng, L.-S. Honga, J.-C. Jianga, Y. Chib, C.-C. Lin, *Thin Solid Films* **483**, 31 (2005)
182. W.S. Seo, H.H. Jo, K. Lee, J.T. Park, *Adv. Mater.* **15**, 795 (2003)
183. M. Salavati-Niasari, F. Davar, M. Mazaheri, M. Shaterian, *J. Magn. Magn. Mater.* **320**, 575 (2008)
184. A. Khansari, M. Salavati-Niasari, A.K. Babaheydari, *J. Clust. Sci.* **23**, 557 (2012)
185. M. Salavati-Niasari, F. Davar, M. Mazaheri, *Polyhedron* **27**, 3467 (2008)
186. F. Davar, M. Salavati-Niasari, M. Mazaheri, *Polyhedron* **28**, 3975 (2009)
187. M. Salavati-Niasari, M. Dadkhah, M.R. Nourani, A.A. Fazl, *J. Clust. Sci.* **23**, 1011 (2012)
188. F. Davar, M.R. Loghman-Estarki, M. Salavati-Niasari, M. Mazaheri, *J. Clust. Sci.* **27**, 593 (2016)
189. F. Davar, M. Salavati-Niasari, Z. Fereshteh, *J. Alloys Compd.* **496**, 638 (2010)
190. M. Salavati-Niasari, Z. Fereshteh, F. Davar, *Polyhedron* **28**, 1065 (2009)
191. M. Salavati-Niasari, F. Davar, A. Khansari, *J. Alloys Compd.* **509**, 61 (2011)

192. F. Davar, Z. Fereshteh, M. Salavati-Niasari, *J. Alloys Compd.* **476**, 797 (2009)
193. M. Salavati-Niasari, Z. Fereshteh, F. Davar, *Polyhedron* **28**, 126 (2009)
194. M. Salavati-Niasari, M. Dadkhah, F. Davar, *Polyhedron* **28**, 3005 (2009)
195. M. Salavati-Niasari, N. Mir, F. Davar, *Appl. Surf. Sci.* **256**, 4003 (2010)
196. M. Salavati-Niasari, N. Mir, F. Davar, *J. Alloys Compd.* **493**, 163 (2010)
197. M. Salavati-Niasari, N. Mir, F. Davar, *Polyhedron* **28**, 1111 (2009)
198. F. Davar, M. Salavati-Niasari, N. Mir, K. Saberyan, M. Monemzadeh, E. Ahmadi, *Polyhedron* **29**, 1747 (2010)
199. T. Xaba, M.J. Moloto, N. Moloto, *Asian J. Chem.* **28**, 1015 (2016)
200. T. Xaba, M.J. Moloto, M.A. Malik, N. Moloto, *J. Nanotechnol.* **2017**(Article ID 8317109), 11 p (2017)
201. V. Bartůňek, Š. Huber, D. Sedmidubský, Z. Sofer, P. Šimek, O. Jankovský, *Ceram. Int.* **40**, 12591 (2014)
202. P. Saravanan, R. Gopalan, V. Chandrasekaran, *Defence Sci. J.* **58**, 504 (2008)
203. J. Rockenberger, E.C. Scher, A.P. Alivisatos, *J. Am. Chem. Soc.* **121**, 11595 (1999)
204. P. Saravanan, S. Alam, G.N. Mathur, *J. Mater. Sci. Lett.* **22**, 1283 (2003)
205. P. Saravanan, S. Alam, G.N. Mathur, *Mater. Lett.* **58**, 3528 (2004)
206. A. Hosseinian, S. Jabbari, H.R. Rahimpour, A.R. Mahjoub, *J. Mol. Struct.* **1028**, 215 (2012)
207. A. Hosseinian, A.R. Mahjoub, M. Movahedi, *Int. J. Nano Dim.* **1**, 65 (2010)
208. A. Hosseinian, A.R. Mahjoub, *J. Mol. Struct.* **985**, 270 (2011)
209. A. Hosseinian, H.R. Rahimpour, H. Haddadi, A.A. Ashkarran, A.R. Mahjoub, *J. Mol. Struct.* **1074**, 673 (2014)
210. D. Czakis-Sulikowska, J. Radwanska-Doczekalska, M. Markiewicz, M. Pietrzak, *J. Therm. Anal. Calor.* **93**, 789 (2008)
211. D. Kumar, I.P.S. Kapoor, G. Singh, N. Geol, U.P. Singh, *J. Therm. Anal. Calor.* **107**, 325 (2012)
212. D. Czakis-Sulikowska, A. Malinowska, M. Markiewicz, *J. Therm. Anal. Calorim.* **60**, 151 (2000)
213. D. Czakis-Sulikowska, J. Kaluzna, J. Radwańska-Doczekalska, *Polish J. Chem.* **74**, 607 (2000)
214. D. Czakis-Sulikowska, A. Czyłkowska, *J. Therm. Anal. Calorim.* **74**, 349 (2003)
215. A. Czyłkowska, M. Markiewicz, *J. Therm. Anal. Calorim.* **100**, 717 (2010)
216. L. Tian, N. Ren, J.J. Zhang, H.M. Liu, S.J. Sun, H.M. Ye, K.Z. Wu, *J. Therm. Anal. Calorim.* **99**, 349 (2010)
217. S. Wanner, L. Hilaire, P. Wehrer, J.P. Hindermann, G. Maire, *Appl. Catal. A Gen.* **203**, 55 (2000)
218. R. Nazir, M. Mazhar, T. Wakeel, M.J. Akhtar, M. Siddique, M. Nadeem, N.A. Khan, M.R. Shah, *J. Therm. Anal. Calor.* **110**, 707 (2012)
219. N. Parveen, R. Nazir, M. Mazhar, *J. Therm. Anal. Calor.* **111**, 93 (2013)
220. D. Kumar, I.P.S. Kapoor, G. Singh, R. Fröhlich, *Thermochim. Acta* **545**, 67 (2012)
221. M. Hosseinifard, L. Hashemi, V. Amani, A. Morsali, *J. Struct. Chem.* **54**, 396 (2013)
222. G. Singh, I.P.S. Kapoor, D. Kumar, U.P. Singh, N. Goel, *Inorg. Chim. Acta* **362**, 4091 (2009)
223. N.B. Shitova, P.G. Tsyrułnikov, D.A. Shlyapin, P.S. Barbashova, D.I. Kochubei, V.I. Zaikovskii, *J. Struct. Chem.* **50**, 268 (2009)
224. G. Singh, D.K. Pandey, *Propellant. Explor. Pyrotech.* **28**, 231 (2003)
225. G. Singh, P.S. Felix, D.K. Pandey, *Thermochim. Acta* **411**, 61 (2004)
226. G. Singh, D.K. Pandey, *Combust. Flame* **135**, 135 (2003)
227. G. Singh, D.K. Pandey, *J. Therm. Anal. Calorim.* **82**, 253 (2005)
228. G. Singh, C.P. Singh, S.M. Mannan, *J. Hazard. Mater.* **122**, 111 (2005)
229. G. Singh, C.P. Singh, S.M. Mannan, *Thermochim. Acta* **437**, 21 (2005)
230. G. Singh, C.P. Singh, S.M. Mannan, *J. Hazard. Mater.* **A135**, 10 (2006)
231. G. Singh, A.K. Shriamal, I.P.S. Kapoor, C.P. Singh, D. Kumar, S.M. Manan, *J. Therm. Anal. Calorim.* **103**, 149 (2011)

232. K.X. Steirer, R.E. Richards, A.K. Sigdel, A. Garcia, P.F. Ndione, S. Hammond, D. Baker, E.L. Ratcliff, C. Curtis, T. Furtak, D.S. Ginley, D.C. Olson, N.R. Armstrong, J.J. Berry, *J. Mater. Chem. A* **3**, 10949 (2015)
233. H. Icbudak, T.K. Yazicilar, W.T. Yilmaz, *Thermochim. Acta* **335**, 93 (1999)
234. K.S. Rejitha, S. Mathew, *J. Therm. Anal. Calorim.* **102**, 931 (2010)
235. V.T. Yilmaz, S. Demir, O. Andac, W.T.A. Harrison, *J. Coord. Chem.* **55**, 863 (2002)
236. K.S. Rejitha, S. Mathew, *J. Therm. Anal. Calorim.* **93**, 213 (2008)
237. P.R. Ponminiessary, A. Vasudevan, M. Sebastian, U.A. Chennampilly, K.M.Y. Karukapadath, *J. Therm. Anal. Calor.* **100**, 733 (2010)
238. L.R. Gonsalves, S.C. Mojumdar, V.M.S. Verenkar, *J. Mater. Sci.* **100**, 789 (2010)
239. S. Farhadi, Z. Roostaei-Zaniyani, *Polyhedron* **30**, 971 (2011)
240. S. Schimpf, C. Louis, P. Claus, *Appl. Catal. A: General.* **318**, 45 (2007)
241. F. Negrier, E. Marceau, M. Che, J.M. Giraudon, L. Gengembre, A. Lofberg, *J. Phys. Chem. B.* **109**, 2836 (2005)
242. F. Negrier, E. Marceau, M. Che, D. de Caro, *C. R. Chimie* **6**, 231 (2003)
243. J. Yang, J. Zeng, S. Yu, L. Yang, G. Zhou, Y. Qian, *Chem. Mater.* **12**, 3259 (2000)
244. I. Warad, F. Al-Rimawi, A. Barakat, S. Affouneh, N. Shivalingegowda, N.K. Lokanath, I.M. Abu-Reidah, *Chem. Centr. J.* **10**, 38 (2016)
245. S.G. Niyaky, M. Montazerzohori, A. Masoudiasl, J.M. White, *J. Mol. Struct.* **1131**, 201 (2017)
246. R. Mehdizadeh, S. Sanati, L.A. Saghatforoush, *Synth. React. Inorg. Metal-Org. Nano-Metal Chem.* **43**, 466 (2013)
247. H.K. Liu, G.X. Wang, Z.P. Guo, J.Z. Wang, K. Konstantinov, *J. New Mater. Electrochem. Syst.* **10**, 101 (2007)
248. M.J.S. Fard, P. Hayati, A. Firoozadeh, J. Janczak, *Ultrason. Sonochem.* **37**, 286 (2017)
249. A.S. Aldwayyan, F.M. Al-Jekhedab, M. Al-Noaimi, B. Hammouti, T.B. Hadda, M. Suleiman, I. Warad, *Int. J. Electrochem. Sci.* **8**, 10506 (2013)
250. A. Barakat, M. Al-Noaimi, M. Suleiman, A.S. Aldwayyan, B. Hammouti, T.B. Hadda, S.F. Haddad, A. Boshala, I. Warad, *Int. J. Mol. Sci.* **14**, 23941 (2013)
251. L.A. Saghatforoush, R. Mehdizadeh, F. Chalabian, *Transit. Met. Chem.* **35**, 903 (2010)
252. D. Matioszek, W.-S. Ojo, A. Cornejo, N. Katir, M. El Ezzi, M. Le Troedec, H. Martinez, H. Gornitzka, A. Castel, C. Nayral, F. Delpech, *Dalton Trans.* **44**, 7242 (2015)
253. S. Meghdadi, M. Amirnasr, M. Zhiani, F. Jallili, M. Jari, M. Kiani, *Electrocatalysis* **8**, 122 (2017)
254. S. Farhadi, M. Kazem, F. Siadatnasab, *Polyhedron* **30**, 606 (2011)
255. G.I. Dzhardimalieva, I.E. Uflyand, *J. Coord. Chem.* **70**, 1468 (2017)
256. G.I. Dzhardimalieva, I.E. Uflyand, *J. Inorg. Organomet. Polym.* **26**, 1112 (2016)
257. I.S. Vasil'chenko, I.G. Borodkina, A.S. Burlov, N.V. Karpova, G.M. Abakarov, K.A. Lyssenko, G.S. Borodkin, I.E. Uflyand, A.D. Garnovskii, V.I. Minkin, *Russ. Chem. Bull.* **62**, 1809 (2013)
258. T.O. Shmakova, D.A. Garnovskii, K.A. Lysenko, E.P. Ivakhnenko, V.I. Simakov, I.S. Vasil'chenko, A.I. Uraev, A.S. Burlov, M.Yu. Antipin, A.D. Garnovskii, I.E. Uflyand, *Russ. J. Coord.Chem.* **35**, 657 (2009)
259. G.I. Dzhardimalieva, N.N. Volkova, V.A. Shershnev, N.D. Golubeva, A.S. Burlov, L.D. Popov, *Int. J. Nanomech. Sci. Technol.* **8**, 334 (2017)
260. S. Zinatloo-Ajabshir, M. Salavati-Niasari, M. Hamadani, *J. Mater. Sci.: Mater. Electron.* **27**, 998 (2016)
261. Z.R. Ranjbar, I. Sheikhshoae, Z. Bagheri, *Int. J. Nano Dimens.* **5**, 409 (2014)
262. M. Ahmadi, A. Fasihizad, B. Machura, R. Kruszynski, T. Barak, *Polyhedron* **81**, 115 (2014)
263. G. Grivani, V. Tahmasebi, A.D. Khalaji, *Polyhedron* **68**, 144 (2014)
264. A.D. Khalaji, M. Nikoogar, D. Das, *J. Therm. Anal. Calorim.* **115**, 409 (2014)
265. A.D. Khalaji, M. Nikoogar, C. Charles, S. Triki, F. Thetiot, D. Das, *J. Clust. Sci.* **25**, 605 (2014)

266. A.D. Pomogailo, G.I. Dzhardimalieva, S.I. Pomogailo, N.D. Golubeva, G.V. Shilov, E.A. Dzhavadyan, A.S. Burlov, S.A. Mashchenko, D.A. Garnovskii, *Russ. Chem. Bull.* **65**, 139 (2016)
267. A.D. Pomogailo, A.S. Burlov, N.D. Golubeva, L.A. Petrova, S.A. Mashchenko, S.I. Pomogailo, G.I. Dzhardimalieva, A.D. Garnovskii, *Inorg. Mater.* **47**, 876 (2011)
268. B.A. Komarov, A.T. Kapasharov, E.A. Dzhavadyan, V.A. Lesnichaya, G.I. Dzhardimalieva, A.S. Burlov, A.I. Uraev, S.A. Mashchenko, D.A. Garnovskii, A.D. Pomogailo, *Russ. Chem. Bull.* **64**, 936 (2015)
269. S.P. Gubin, N.A. Kataeva, *Russ. J. Coord. Chem.* **32**, 849 (2006)
270. A. Khansari, M. Enhessari, M. Salavati-Niasari, *J. Clust. Sci.* **24**, 289 (2013)
271. A.K. Babaheydari, M. Salavati-Niasari, A. Khansari, *Particuology* **10**, 759 (2012)
272. A.D. Khalaji, D. Das, *Int. Nano Lett.* **4**, 117 (2014)
273. E.S. Azam, W.A. El-Said, *Bioorg. Chem.* **57**, 5 (2014)
274. M. Salavati-Niasari, A. Khansari, F. Davar, *Inorg. Chim. Acta* **362**, 4937 (2009)
275. A.D. Khalaji, *J. Clust. Sci.* **24**, 209 (2013)
276. S.Y. Ebrahimipour, I. Sheikhshoae, J. Castro, W. Haase, M. Mohamadi, S. Foro, M. Sheikhshoae, S. Esmaeili-Mahani, *Inorg. Chim. Acta* **430**, 245 (2015)
277. A.D. Khalaji, *J. Clust. Sci.* **24**, 189 (2013)
278. M.S. Refat, M.Y. El-Sayed, A.M. Adam, *J. Mol. Struct.* **1038**, 62 (2013)
279. A.D. Khalaji, G. Grivani, S. Izadi, *J. Therm. Anal. Calorim.* **126**, 1105 (2016)
280. S.M. El-Megharbel, A.S. Megahed, M.S. Refat, *J. Mol. Liq.* **216**, 608 (2016)
281. J. Hambrock, R. Becker, A. Birkner, J. Weiß, R.A. Fischer, *Chem. Commun.* 68 (2002)
282. L. Chen, C. Zhao, Y. Zhou, H. Peng, Y. Zheng, *J. Alloys Compd.* **504**, L46 (2010)
283. M.M. Amini, O. Sadeghi, S.W. Ng, *J. Inorg. Organomet. Polym.* **23**, 826 (2013)
284. M. Ranjbar, S.A. Mozaffari, E. Kouhestanian, H.S. Amoli, *J. Photochem. Photobiol. A: Chem.* **321**, 110 (2016)
285. M. Ranjbar, M. Yousefi, *Iran. J. Sci. Technol. Trans. Sci.* (2016). <https://doi.org/10.1007/s40995-016-0069-9>
286. P.G. Derakhshandeh, J. Soleimannejad, *Ultrason. Sonochem.* **31**, 122 (2016)
287. J. Khanderi, B. Davaasuren, A. Rothenberger, *ChemistrySelect* **1**, 1897 (2016)
288. M.R. Hill, A.W. Jones, J.J. Russell, N.K. Roberts, R.N. Lamb, *Inorg. Chim. Acta* **358**, 201 (2005)
289. J. Patzsch, I. Balog, P. Krau, C.W. Lehmann, J.J. Schneider, *RSC Adv.* **4**, 15348 (2014)
290. Z. Zhang, R. Liu, M. Zhao, Y. Qian, *Mater. Chem. Phys.* **71**, 161 (2001)
291. Y.S. Wang, P.J. Thomas, P. O'Brien, *J. Phys. Chem. B* **110**, 4099 (2006)
292. M. Pashchanka, R.C. Hoffmann, O. Burghaus, B. Corzilius, G. Cherkashinin, J.J. Schneider, *Solid State Sci.* **13**, 224 (2011)
293. Y.K. Abdel-Monem, S.M. Emam, H.M.Y. Okda, *J. Mater. Sci.: Mater. Electron.* **28**, 2923 (2017)
294. M. Ranjbar, N. Shahsavan, M. Yousefi, *Am. Chem. Sci. J.* **2**, 111 (2012)
295. M. Edrissi, M. Soleymani, *Chem. Eng. Technol.* **34**, 991 (2011)
296. M. Edrissi, H. Roohollahi, *Mater. Res. Bull.* **48**, 961 (2013)
297. S.K. Maji, A.K. Dutta, S. Dutta, D.N. Srivastava, P. Paul, A. Mondal, B. Adhikary, *Appl. Catal. B: Environ.* **126**, 265 (2012)
298. Z. Zhuhua, S.H. Lee, J.J. Vittal, W.S. Chin, *J. Phys. Chem. B* **110**, 6649 (2006)
299. M.S. Bakshi, G.K. Ahluwalia, Nanostructured chalcogenides, in *Applications of Chalcogenides: S, Se, and Te*, ed. by G.K. Ahluwalia (Springer, Berlin, 2017)
300. S.I. Sadovnikov, A.I. Gusev, A.A. Rempel, *Russ. Chem. Rev.* **85**, 731 (2016)
301. S.I. Sadovnikov, A.A. Rempel, A.I. Gusev, Nanostructured silver sulfide Ag₂S. In: *Nanostructured Lead, Cadmium, and Silver Sulfides* (Springer, Cham, 2018)
302. N. Revaprasadu, S.N. Mlondo, *Pure Appl. Chem.* **78**, 1691 (2006)
303. P. Roy, S.K. Srivastava, *CrystEngComm* **17**, 7801 (2015)
304. P. Roy, S.K. Srivastava, *Cryst. Growth Des.* **6**, 1921 (2006)

305. P.S. Nair, T. Radhakrishnan, N. Revaprasadu, G.A. Kolawole, P. O'Brien, *J. Chem. Soc., Chem. Commun.* **564** (2002)
306. S.N. Mlondo, N. Revaprasadu, P. Christian, P. O'Brien, *Polyhedron* **28**, 2097 (2009)
307. K.P. Mubiayi, N. Revaprasadu, S.S. Garje, M.J. Moloto, *J. Saudi Chem. Soc.* **21**, 593 (2017)
308. A.S. Pawar, S.C. Masikane, S. Mlowe, S.S. Garje, N. Revaprasadu, *Eur. J. Inorg. Chem.* **366** (2016)
309. V.V. Singh, U. Kumar, S.N. Tripathi, A.K. Singh, *Dalton Trans.* **43**, 12555 (2014)
310. G. Kedarnath, V.K. Jain, A. Wadawale, G.K. Dey, *Dalton Trans.* **8378** (2009)
311. K. Kandasamy, H.B. Singh, S.K. Kulshreshtha, *J. Chem. Sci.* **121**, 293 (2009)
312. S.V. Voitekhovich, D.V. Talapin, C. Klinke, A. Kornowski, H. Weller, *Chem. Mater.* **20**, 4545 (2008)
313. D.C. Onwudiwe, P.A. Ajibade, *Int. J. Mol. Sci.* **12**, 5538 (2011)
314. S. Mlowe, D.J. Lewis, M.A. Malik, J. Raftery, E.B. Mubofu, P. O'Brien, N. Revaprasadu, *New J. Chem.* **38**, 6073 (2014)
315. A.L. Abdelhady, M. Afzaal, M.A. Malik, P. O'Brien, *J. Mater. Chem.* **21**, 18768 (2011)
316. N. Srinivasan, S. Thirumaran, S. Ciattini, *J. Mol. Struct.* **1026**, 102 (2012)
317. N. Srinivasan, S. Thirumaran, S. Ciattini, *Spectrochim. Acta. Part A: Mol. Biomol. Spectr.* **102**, 263 (2013)
318. A.A. Memon, M. Afzaal, M.A. Malik, C.Q. Nguyen, P. O'Brien, J. Raftery, *Dalton Trans.* **4499** (2006)
319. Y. Li, X. Li, C. Yang, Y. Li, *J. Mater. Chem.* **13**, 2641 (2003)
320. P.S. Nair, T. Radhakrishnan, N. Revaprasadu, G.A. Kolawole, P. O'Brien, *J. Mater. Chem.* **12**, 2722 (2002)
321. G. Kedarnath, V.K. Jain, S. Ghoshal, G.K. Dey, C.A. Ellis, E.R.T. Tiekink, *Eur. J. Inorg. Chem.* **2007**, 1566 (2007)
322. M. Afzaal, D. Crouch, M.A. Malik, M. Motevalli, P. O'Brien, J.H. Park, J.D. Woollins, *Eur. J. Inorg. Chem.* **2004**, 171 (2004)
323. S.S. Garje, J.S. Ritch, D.J. Eisler, M. Afzaal, P. O'Brien, T. Chivers, *J. Am. Chem. Soc.* **128**, 3120 (2006)
324. D.J. Crouch, P. O'Brien, M.A. Malik, P.J. Skabara, S.P. Wright, *J. Chem. Soc., Chem. Commun.* **1454** (2003)
325. S.H. Sohrabnezhad, A.J. Pourahmad, *J. Alloys Compd.* **505**, 324 (2010)
326. A. Pourahmad, S.H. Sohrabnezhad, M.S. Sadjadi, K. Zare, *Mater. Lett.* **62**, 655 (2008)
327. E.Y.M. Lee, N.H. Tran, R.N. Lamb, *Appl. Surf. Sci.* **241**, 493 (2005)
328. I.J. Plante, T.W. Zeid, P. Yang, T. Mokari, *J. Mater. Chem.* **20**, 6612 (2010)
329. G. Xie, Z.P. Qiao, M.H. Zeng, X.M. Chen, S.L. Gao, *Cryst. Growth Des.* **4**, 513 (2004)
330. R. Romano, O.L. Alves, *Mater. Res. Bull.* **41**, 376 (2006)
331. H. Yin, *Polyhedron* **27**, 663 (2008)
332. T. Zhai, Z. Gu, Y. Ma, W. Yang, L. Zhao, J. Yao, *Mater. Chem. Phys.* **100**, 281 (2006)
333. G.S. Sivagurunathan, K. Ramalingam, C. Rizzoli, *Polyhedron* **72**, 96 (2014)
334. S.T. Breviglieri, E.T.G. Cavalheiro, G.O. Chierice, *Thermochim. Acta* **356**, 79 (2000)
335. D.C. Menezes, G.M. de Lima, A.O. Porto, C.L. Donnici, J.D. Ardisson, *Polyhedron* **23**, 2103 (2004)
336. M. Hrubaru, D.C. Onwudiwe, E. Hosten, *J. Sulfur Chem.* **37**, 37 (2016)
337. S. Acharya, M. Dutta, S. Sarkar, D. Basak, S. Chakraborty, N. Pradhan, *Chem. Mater.* **24**, 17679 (2012)
338. N. Awang, I. Baba, B.M. Yamin, *World Appl. Sci. J.* **12**, 630 (2011)
339. D.C. Onwudiwe, P.A. Ajibade, *Int. J. Mol. Sci.* **12**, 1964 (2011)
340. K.W. Seo, S.H. Yoon, S.S. Lee, I. Shim, *Bull. Korean Chem. Soc.* **26**, 1582 (2005)
341. S. Shen, Y. Zhang, L. Peng, B. Xu, Y. Du, M. Deng, H. Xub, Q. Wang, *CrystEngComm* **13**, 4572 (2011)
342. Y. Zhang, H. Xub, Q. Wang, *Chem. Commun.* **46**, 8941 (2010)
343. C. Song, Y. Zhang, L. Jiang, D. Wang, *Sci. Adv. Mater.* **4**, 1096 (2012)
344. Y. Zhang, J. Lu, S. Shen, H. Xu, Q. Wang, *Chem. Commun.* **47**, 5226 (2011)

345. Y. Zhang, Y. Du, H. Xu, Q. Wang, *CrystEngComm* **12**, 3658 (2010)
346. M. Tanveer, C. Cao, I. Aslam, Z. Ali, F. Idrees, W.S. Khan, M. Tahir, S. Khalid, G. Nabi, A. Mahmood, *New J. Chem.* **39**, 1459 (2015)
347. Y. Wang, J. Chen, P. Wang, L. Chen, Y. Chen, L. Wu, *J. Phys. Chem. C* **113**, 16009 (2009)
348. N.H. Abdullah, Z. Zainal, S. Silong, M.I.M. Tahir, K.-B. Tan, S.-K. Chang, *Thermochim. Acta* **632**, 37 (2016)
349. N.H. Abdullah, Z. Zainal, S. Silong, M.I.M. Tahir, K.-B. Tan, S.-K. Chang, *Mater. Chem. Phys.* **173**, 33 (2016)
350. N.L. Botha, P.A. Ajibade, *Mater. Sci. Semicond. Process.* **43**, 149 (2016)
351. A. Nqombolo, P.A. Ajibade, *J. Chem.* **2016** (Article ID 1293790), 9 p (2016)
352. T. Mthethwa, V.S.R. Rajasekhar Pullabhotla, P.S. Mdluli, J. Wesley-Smith, N. Revaprasadu, *Polyhedron* **28**, 2977 (2009)
353. V.S.R. Rajasekhar Pullabhotla, M. Scriba, N. Revaprasadu, *J. Nanosci. Nanotechnol.* **11**, 1201 (2011)
354. L.D. Nyamen, A.A. Nejo, V.S.R. Pullabhotla, P.T. Ndifon, M.A. Malik, J. Akhtar, P. O'Brien, N. Revaprasadu, *Polyhedron* **67**, 129 (2014)
355. S. Mlowe, D.J. Lewis, M.A. Malik, J. Raftery, E.B. Mubofu, P. O'Brien, N. Revaprasadu, *Dalton Trans.* **45**, 2647 (2016)
356. L.D. Nyamen, V.S.R. Pullabhotla, A.A. Nejo, P. Ndifon, N. Revaprasadu, *New J. Chem.* **35**, 1133 (2011)
357. S. Mlowe, L.D. Nyamen, P.T. Ndifon, M.A. Malik, J. Raftery, P. O'Brien, N. Revaprasadu, *Inorg. Chim. Acta* **434**, 181 (2015)
358. M. Kim, H. Kim, S. Lee, S. Sohn, *Mol. Cryst. Liq. Cryst.* **564**, 162 (2012)
359. J. Xiao, B. Wen, R. Melnik, Y. Kawazoe, X. Zhanga, *Phys. Chem.* **16**, 14899 (2014)
360. G.B. Shombe, E.B. Mubofu, S. Mlowe, N. Revaprasadu, *Mater. Sci. Semicond. Process.* **43**, 230 (2016)
361. R. Banerjee, R. Jayakrishnan, P. Ayyub, *J. Phys.: Condens. Matter* **12**, 10647 (2000)
362. E.S. Raper, *Coord. Chem. Rev.* **165**, 475 (1997)
363. D.S. Koktysh, J.R. McBride, S.J. Rosenthal, *Nanoscale Res. Lett.* **2**, 144 (2007)
364. N. Srinivasan, S. Thirumarana, S. Ciattini, *J. Mol. Struct.* **936**, 234 (2009)
365. D.C. Onwudiwe, C.A. Strydom, *Spectrochim. Acta: Mol. Biomol. Spectrosc.* **135**, 1080 (2015)
366. K. Ramasamy, M.A. Malik, P. O'Brien, J. Raftery, *Dalton Trans.* **39**, 1460 (2010)
367. D. Barreca, A. Gasparotto, C. Maragno, E. Tondello, C. Sada, *Chem. Vap. Depos.* **10**, 229 (2004)
368. W.N. Kun, S. Mlowe, L.D. Nyamen, P.T. Ndifon, M.A. Malik, O.Q. Munro, N. Revaprasadu, *Chem. Eur. J.* **22**, 13127 (2016)
369. M. Chunggaze, M.A. Malik, P. O'Brien, *J. Mater. Chem.* **9**, 2433 (1999)
370. M.A. Malik, N. Revaprasadu, P. O'Brien, *Chem. Mater.* **13**, 913 (2001)
371. H.-W. Chang, B. Sarkar, C.W. Liu, *Cryst. Growth Des.* **7**, 2691 (2007)
372. S.S. Garje, J.S. Ritch, D.J. Eisler, M. Afzaal, P. O'Brien, T. Chivers, *J. Mater. Chem.* **16**, 966 (2006)
373. S.S. Garje, M.C. Copey, M. Afzaal, P. O'Brien, T. Chivers, *J. Mater. Chem.* **16**, 4542 (2006)
374. K. Ramasamy, M.A. Malik, N. Revaprasadu, P. O'Brien, *Chem. Mater.* **25**, 3551 (2013)
375. M. Al-Shakban, Z. Xie, N. Savjani, M.A. Malik, P. O'Brien, *J. Mater. Sci.* **51**, 6166 (2016)
376. P.D. Matthews, M. Akhtar, M.A. Malik, N. Revaprasadu, P. O'Brien, *Dalton Trans.* **45**, 18803 (2016)
377. P.D. McNaught, S.A. Saah, M. Akhtar, K. Abdulwahab, M. Azad Malik, J. Raftery, J.A.M. Awudzaa, P. O'Brien, *Dalton Trans.* **45**, 16345 (2016)
378. M. Afzaal, M.A. Malik, P. O'Brien, *J. Mater. Chem.* **20**, 4031 (2010)
379. M. Kemmler, M. Lazell, P. O'Brien, D.J. Otway, J.H. Park, J.R. Walsh, *J. Mater. Sci.: Mater. Electron.* **13**, 531 (2002)

380. E.A. Lewis, P.D. McNaughter, Z. Yin, Y. Chen, J.R. Brent, S.A. Saah, J. Raftery, J.A.M. Awudza, M.A. Malik, P. O'Brien, S.J. Haigh, *Chem. Mater.* **27**, 2127 (2015)
381. M. Al-Shakban, P.D. Matthews, G. Deogratias, P.D. McNaughter, J. Raftery, I. Vitorica-Yrezabal, E.B. Mubofu, P. O'Brien, *Inorg. Chem.* **56**, 9247 (2017)
382. N. Pradhan, S. Efrima, *J. Am. Chem. Soc.* **125**, 2050 (2003)
383. N. Pradhan, B. Katz, S. Efrima, *J. Phys. Chem. B* **107**, 13843 (2003)
384. Y. Li, X. Li, C. Yang, Y. Li, *J. Phys. Chem. B* **108**, 16002 (2004)
385. I.W. Lenggoro, Y. Itoh, N. Iida, K. Okuyama, *Mater. Res. Bull.* **38**, 1819 (2003)
386. M. Al-Shakban, P.D. Matthews, P. O'Brien, *Chem. Commun.* **53**, 10058 (2017)
387. K.R. Chaudhari, S. Dey, A.P. Wadawale, V.K. Jain, *J. Organomet. Chem.* **813**, 119 (2016)
388. Y.S. Tan, S.N.A. Halim, K.C. Molloy, A.L. Sudlow, A. Otero-de-la-Roza, E.R.T. Tiekink, *CrystEngComm* **18**, 1105 (2016)
389. A. Salehirad, *Russ. J. Appl. Chem.* **89**, 63 (2016)
390. Y. Hanifehpour, S.M. Asl, B. Mirtamizdoust, S.W. Joo, *J. Inorg. Organomet. Polym.* **22**, 923 (2012)
391. Y. Hanifehpour, B. Mirtamizdoust, S.W. Joo, *J. Inorg. Organomet. Polym.* **22**, 816 (2012)
392. Y. Hanifehpour, B. Mirtamizdoust, S.W. Joo, *Z. Anorg. Allg. Chem.* **638**, 357 (2012)
393. Y. Hanifehpour, B. Mirtamizdoust, S.W. Joo, *J. Inorg. Organomet. Polym.* **22**, 549 (2012)
394. Z. Parsaee, K. Mohammadi, M. Ghahramaninezhad, B. Hosseinzadeh, *New J. Chem.* **40**, 10569 (2016)
395. A.D. Khalaji, M. Nikookar, D. Das, *Res. Chem. Intermed.* **41**, 357 (2015)
396. A.D. Khalaji, D. Das, *J. Therm. Anal. Calorim.* **114**, 671 (2013)
397. D. Li, G.-Q. Zhong, Z.-X. Wu, *J. Serb. Chem. Soc.* **80**, 1391 (2015)
398. S. Saeednia, P. Iranmanesh, M.H. Ardakani, M. Mohammadi, Gh Norouzi, *Mater. Res. Bull.* **78**, 1 (2016)
399. A.D. Khalaji, D. Das, *J. Ultrafine Grained Nanostruct Mater.* **48**, 93 (2015)
400. H.M. Aly, M.E. Moustafa, M.Y. Nassar, E.A. Abdelrahman, *J. Mol. Struct.* **1086**, 223 (2015)
401. P. Bera, C.H. Kim, S.I. Seok, *Solid State Sci.* **12**, 532 (2010)
402. M. Hamid, A.A. Tahir, M. Mazhar, M. Zeller, A.D. Hunter, *Inorg. Chem.* **46**, 4120 (2007)
403. M. Hamid, A.A. Tahir, M. Mazhar, M. Zeller, K.C. Molloy, A.D. Hunter, *Inorg. Chem.* **45**, 10457 (2006)
404. M. Ghiasi, A. Malekzadeh, H. Mardani, *Mater. Sci. Semicond. Proc.* **42**, 311 (2016)
405. H. Choujaa, A.L. Johnson, G. Kociok-Köhn, K.C. Molloy, *Polyhedron* **59**, 85 (2013)
406. S. Chouzier, P. Afanasiev, M. Vrinat, T. Cseri, M. Roy-Auberger, *J. Solid State Chem.* **179**, 3314 (2006)
407. D. Domide, O. Hübner, S. Behrens, O. Walter, H. Wadepohl, E. Kaifer, H.-J. Himmel, *Eur. J. Inorg. Chem.* **2011**, 1387 (2011)
408. V.G. Makhankova, *Glob. J. Inorg. Chem.* **2**, 265 (2011)
409. J. Barrault, V.G. Makhankova, O.V. Khavryuchenko, V.N. Kokozay, P. Ayrault, *J. Solid State Chem.* **187**, 291 (2012)
410. V.G. Makhankova, O.V. Khavryuchenko, V.V. Lisnyak, V.N. Kokozay, V.V. Dyakonenko, O.V. Shishkin, B.W. Skelton, J. Jezierska, *J. Solid State Chem.* **183**, 2695 (2010)
411. T. Fukunaga, N. Ryumon, N. Ichikuni, S. Shimazu, *Catal. Commun.* **10**, 1800 (2009)
412. N.D. Subramanian, J. Moreno, J.J. Spivey, C.S.S.R. Kumar, *J. Phys. Chem. C* **115**, 14500 (2011)
413. K.P. Naidek, F. Bianconi, T.C. Rizuti da Rocha, D. Zanchet, J.A. Bonacin, M.A. Novak, M. das Graças Fialho Vaz, H. WinnischoferNovak, *J. Colloid Interface Sci.* **358**, 39 (2011)
414. K.D. Gilroy, A. Ruditskiy, H.-C. Peng, D. Qin, Y. Xia, *Chem. Rev.* **116**, 10414 (2016)
415. S.U. Son, Y. Jiang, J. Park, H.B. Na, H.M. Park, H.J. Yun, J. Lee, T. Hyeon, *J. Am. Chem. Soc.* **126**, 5026 (2004)
416. S.-I. Choi, S. Xie, M. Shao, J.H. Odell, N. Lu, H.-C. Peng, L. Protsailo, S. Guerrero, J. Park, X. Xia, J. Wang, M.J. Kim, Y. Xia, *Nano Lett.* **13**, 3420 (2013)
417. J. Zhang, H. Yang, J. Fang, S. Zou, *Nano Lett.* **10**, 638 (2010)

418. S. Sharma, N.S. Gajbhiye, R.S. Ningthoujam, *J. Colloid Interface Sci.* **351**, 323 (2010)
419. G.S. Chaubey, C. Barcena, N. Poudyal, C.B. Rong, J.M. Gao, S.H. Sun, J.P. Liu, *J. Am. Chem. Soc.* **129**, 7214 (2007)
420. L. Wu, J.P. Olivier, B. David, I. Wayne, N. Alshakim, Z. Huiyuan, Z. Sen, S. Shouheng, *Nano Lett.* **14**, 3395 (2014)
421. Y.S. Yu, A. Mendoza-Garcia, B. Ning, S.H. Sun, *Adv. Mater.* **25**, 3090 (2013)
422. W. Yang, Y. Yu, L. Wang, C. Yang, H. Li, *Nanoscale* **7**, 2877 (2015)
423. Y. Kumar, P.M. Shirage, *J. Mater. Sci.* **52**, 4840 (2017)
424. L.T. Lu, N.T. Dung, L.D. Tung, C.T. Thanh, O.K. Quy, N.V. Chuc, S. Maenosono, N.T.K. Thanh, *Nanoscale* **7**, 19596 (2015)
425. Y. Eom, M. Abbas, H.Y. Noh, C.G. Kim, *RSC Adv.* **6**, 15861 (2016)
426. P.J. Thomas, P. Saravanan, G.U. Kulkarni, C.N.R. Rao, *Pramana J. Phys.* **58**, 371 (2002)
427. S. Kumar, J.A. Azurdia, R.M. Laine, *J. Ceram. Proc. Res.* **11**, 517 (2010)
428. N. Bao, L. Shen, Y. Wang, P. Padhan, A. Gupta, *J. Am. Chem. Soc.* **129**, 12374 (2007)
429. S.H. Sun, C.B. Murray, D. Weller, L. Folks, A. Moser, *Science* **287**, 1989 (2000)
430. S. Sun, E.E. Fullerton, D. Weller, C.B. Murray, *I.E.E.E. Trans, Magn.* **37**, 1239 (2001)
431. S. Sun, *Adv. Mater.* **18**, 393 (2006)
432. M. Chen, J.P. Liu, S. Sun, *J. Am. Chem. Soc.* **126**, 8394 (2004)
433. M. Chen, J. Kim, J.P. Liu, H.Y. Fan, S.H. Sun, *J. Am. Chem. Soc.* **128**, 7132 (2006)
434. E.V. Shevchenko, D.V. Talapin, H. Schnablegger, A. Kornowski, Ö. Festin, P. Svedlindh, M. Haase, H. Weller, *J. Am. Chem. Soc.* **125**, 9090 (2003)
435. S.H. Sun, S. Anders, T. Thomson, J.E.E. Baglin, M.F. Toney, H.F. Hamann, C.B. Murray, B.D. Terris, *J. Phys. Chem. B* **107**, 5419 (2003)
436. C. Wang, Y.L. Hou, J.M. Kim, S.H. Sun, *Angew. Chem. Int. Ed.* **46**, 6333 (2007)
437. N.A. Frey, S. Peng, K. Cheng, S. Sun, *Chem. Soc. Rev.* **38**, 2532 (2009)
438. H. Gu, B. Xu, J. Rao, R.K. Zheng, X.X. Zhang, K.K. Fung, C.Y.C. Wong, *J. Appl. Phys.* **93**, 7589 (2003)
439. J.H. Lee, Y.M. Huh, Y. Jun, J. Seo, J. Jang, H.T. Song, S. Kim, E.J. Cho, H.G. Yoon, J.S. Suh, J. Cheon, *Nat. Med.* **13**, 95 (2007)
440. J.T. Jang, H. Nah, J.H. Lee, S.H. Moon, M.G. Kim, J. Cheon, *Angew. Chem. Int. Ed.* **48**, 1234 (2009)
441. M. Edrissi, A.R. Keshavarz, *Nano-Micro Lett.* **4**, 83 (2012)
442. J. Tavana, M. Edrissi, *Mater. Res. Express* **3**, 035009 (2016)

Chapter 4

Thermolysis of Polymeric Metal Chelates



Solid-state thermolysis of various metal chelates is a simple and rational way of synthesizing new nanostructured materials characterized by a narrow size distribution, low crystal defects, and controlled forms [1–11]. Target thermolysis of PMCs in different conditions allows obtaining nanomaterials with desired dimensions and morphologies [12–29]. It should be noted that PMCs are not only a starting materials, but also stabilizers of the NPs formed [1–6, 24, 25, 30].

Usually, PMCs are used as templates or sacrificial templates for the production of targeted nanomaterials [31]. In the first case, the initial chelate is first converted into a nanoform and then nanomaterials are made from it. It is important that in this approach, the morphology of the PMC precursor will determine the shape of the nanomaterials produced. With this approach, it became possible to obtain a wide variety of nanomaterials with improved and more interesting properties [12, 32, 33], as well as different morphologies from different precursors of PMC [7, 34–37]. In the sacrificial template approach, insoluble macroscopic crystalline materials are used, and in this case, the original crystal structure of PMC will determine the form and size of the NPs formed [7, 17, 38–47].

Of particular note is the use of 1D, 2D, and 3D PMCs in the synthesis of a wide range of nano- and microarchitectures [48–66]. It is important that the carbon and nitrogen components of these PMCs are easily oxidized to the gases that are released during thermolysis leading to the formation of a porous nanoframework preserving the shape of the precursor [67–69].

Thermolysis of PMCs for the production of nanomaterials is a method with interesting advantages [70–73], for example:

- the simplicity of the process and the lack of the need for the use of special equipment;
- the relationship between the architectures of the final materials and the starting compounds;
- the possibility of phase control of products;
- easy regulation of process conditions;

- the ability to control the size, structure, and purity of the final NPs;
- decrease in the probability of interparticle collisions;
- economic efficiency and potential for large-scale production.

Additional advantages arise when using metal–organic frameworks (MOFs) as precursors, which are a specific subclass of PMCs, in particular:

- a large number of MOFs has been received so far in the most diverse compositions, morphologies, and architectures;
- the possibility of penetration and polymerization of additional precursors inside the pores of MOF, similar to mesoporous silicas and zeolites;
- easy regulation of MOF pore size and structure;
- target design of MOFs, which allows to obtaining nanomaterials with desired topologies and properties;
- well-defined MOF morphologies are important for manufacturing anisotropic nanomaterials that are difficult to obtain using conventional approaches [74];
- structural stability of MOF, which avoids undesirable aggregation or structural breakdown of the framework during thermolysis.

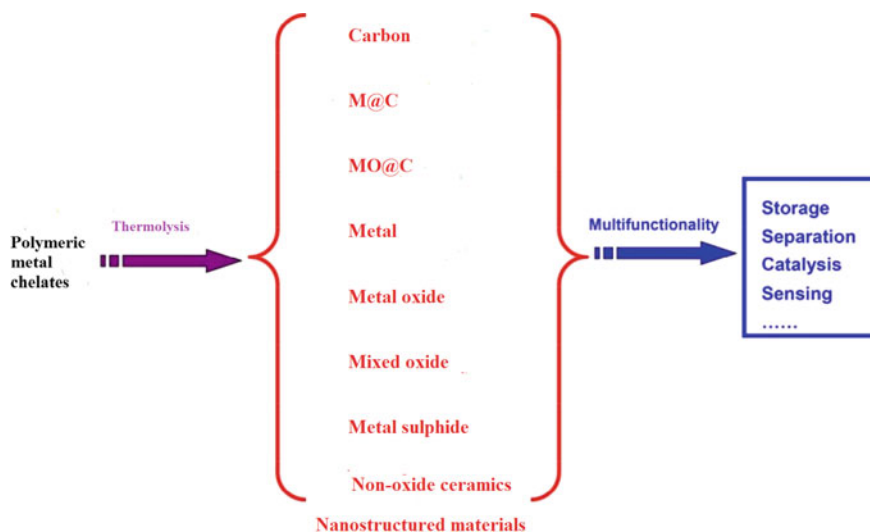
The undoubted advantage of PMC thermolysis is also the possibility of obtaining nanomaterials that cannot be prepared in the usual way [7].

It should be specially emphasized that the target synthesis of the desired nanomaterials with uniform dimensions and controlled structures is of paramount importance for the regulation of their chemical and physical properties. This is due to the fact that most of the parameters of these nanomaterials, for example, electronic structure, surface energy, coupling and chemical reactivity, are uniquely related to their surface morphology. It is important that thermolysis of PMCs as precursors allows obtaining nanomaterials with target forms, in particular, nanowires, nanorods, NPs, microplates, nanolayers, spongy forms, hollow, and coraloid nanostructures, etc. Such a design is possible by controlling both the thermolysis conditions, for example, the thermolysis temperature and time, and the precursors.

We also note the production of hybrid nanomaterials (e.g., nanosized bi- or multimetal oxides), which often show interesting chemical and physical properties that are not characteristic of each individual component, which is connected, apparently, with their synergistic effects [21, 75]. It is important that materials including such multicomponent formulations or heteroatomic dopants obtained on the basis of purposefully synthesized PMCs often exhibit excellent characteristics, for example, in catalysis and energy storage.

Since PMCs are formed from inorganic metal particles and organic ligands, their thermolysis under various conditions can lead to a wide variety of products including nanoporous carbon (NPC), metal, metal oxides, metal sulfides, metals and metal oxides decorated with carbon compositions M/MO@C, etc. (Scheme 4.1) [7, 17, 20, 27, 40, 41, 53, 76–106].

Target production of various nanostructured materials is possible by adjusting the thermolysis conditions, for example, temperature, gas atmosphere, post-synthetic treatment, etc. In particular, we note that thermolysis of PMC in an



Scheme 4.1 Use of PMCs as templates and/or precursors to prepare nanostructured functional materials

inert atmosphere (N_2 , Ar) usually leads to M/C hybrids. To obtain nanomaterials with a high NPC content, additional removal of the metal forms present in the carbon is necessary. Thermolysis in an atmosphere of air or oxygen gives the nanostructured MO as main products, since at high temperatures various forms of carbon are oxidized with formation of carbon oxides. It is important that each type of nanomaterials derived from PMCs demonstrates promising applications in various fields.

It is necessary to emphasize the superiority of nanomaterials obtained by thermolysis of PMCs over similar materials prepared by traditional methods [107, 108]. It is important that the use of PMC for the synthesis of nanostructured materials improves their practical application on an experimental and industrial scale [75, 109]. The potential use of these nanomaterials for nanotechnological applications is very extensive, from heterogeneous catalytic reactions, including electrocatalysis, organocatalysis, and photocatalysis, to lithium storage, electrical energy storage, sensors, sorbents and remediation agents, magnetic applications, supercapacitors, and drug delivery [8, 85, 104–106, 110, 111]. First of all, this is due to the fact that nanomaterials demonstrate new interesting physical and chemical properties depending on the size, which cannot be observed in their bulk analogue [112, 113].

4.1 Synthesis of Carbon Nanomaterials

It should be noted that the use of carbon nanomaterials is largely determined by their internal characteristics, for example, pore structure and micromorphology, which in turn depend on the method of obtaining them. In this regard, it is very promising to synthesize NPCs with hierarchical pore structures that allow to significantly expanding the use of carbon materials [114]. The main advantages of hierarchical carbons compared to the 1D porous carbon associated with increasing mass transport through macro- or mesopores, as well as increasing of specific surface area through small meso- or micropores.

Numerous studies have shown that thermolysis of PMCs is an easy and perspective way to NPC materials [38, 45, 76, 77, 104, 107, 115–144]. PMCs are used as effective templates and/or precursors for preparing NPCs and nanostructured functional materials based on them due to their unique characteristics, such as high surface area, controlled high porosity, wide variability of structures and compositions, as well as metal-containing units in their frameworks [42, 104, 118, 119, 145]. Long-range ordering in PMC structures is also of great importance. The main parameters that exert a decisive influence on the structure of the carbon nanomaterials formed are the heating rate, the thermolysis time, and the nature of metal and chelating fragments in the PMCs [104, 122, 146–148]. It is important that the PMC pore structure plays a key role in determining the texture of the pores of the NPC-forming materials. The use of PMCs with a variety of metal-containing units allows to obtaining new types of NPC materials with promising applications.

The NPC is obtained by thermolysis of the PMCs in an inert atmosphere using two methods. In the first method, PMC is used as a sacrificial template and precursor with addition of an additional carbon source, for example, furfuryl alcohol [38, 76, 120], phenolic resin, carbon tetrachloride, or ethylenediamine (en) [145] in the reaction system. Due to the presence of large cavities in the PMC architecture, an additional source penetrates into these cavities, which allows to significantly improving the technological characteristics of the obtained nanomaterials, in particular, surface area and porosity. The most widely used for this method are Zn- or Al-based MOFs. The synthesis procedure consists of successive stages of PMC impregnation with an additional source of carbon and its polymerization within the PMC micropores. The subsequent thermolysis of PMCs containing an additional carbon source allows to obtaining NPC materials.

The second method of obtaining NPC materials is based on direct thermolysis of PMC without additional use of other carbon sources [75, 76, 107, 120, 121, 146, 149], since they themselves contain a significant amount of organic fragments and can act as precursors of carbon. During process, the thermolysis of PMC and the formation of a NPC network occur simultaneously. In other words, PMCs are both sacrificial templates and secondary carbon sources. Since the PMC includes a large number of metal ions that are an integral part of the whole polymer architecture, it is necessary to remove these metallic species from the products of thermolysis in order to obtain high surface area of carbon materials. Therefore, at the final stage of

the thermolysis, the prepared product is thoroughly washed with an acid solution to remove the metal NPs, or the metal is evaporated to remove from the reaction system at higher temperatures (up to 1273 K). However, this method allows to producing carbon materials with a low surface area, even after post-synthetic treatment of the thermolysis product. One method of increasing the surface area ($>2000 \text{ m}^2 \text{ g}^{-1}$) is to heat the mixture of the product obtained and potassium hydroxide at high temperatures, followed by acid treatment to remove impurities [150, 151]. However, more promising is the approach in which thermolysis of PMC and the removal of metal particles are carried out simultaneously. For example, thermolysis of Zn-PMC precursor in an inert atmosphere leads to the formation of ZnO, which is very difficult to remove at relatively low temperatures (1173–1223 K), since it has a very high-boiling point (2633 K) compared to Zn (1181 K). At the same time, thermolysis of PMC also results in the formation of carbon, which effectively reduces ZnO to Zn at 1173 K [38, 152]. The subsequent evaporation of Zn made it possible to obtain a pure carbon material with a high surface area of $3447 \text{ m}^2 \text{ g}^{-1}$ (Fig. 4.1) [147].

This method was extended by using an oxygen-abundant Zn-MOF-74 to produce NPCs of exceptional quality with high yield (Scheme 4.2) [153]. In this case, the obtained ZnO is reduced by carbon with the formation of metallic Zn, which is removed by evaporation, when the temperature reaches its boiling point (about 1181 K) that leads to the formation of a metal-free NPC. In addition, the high

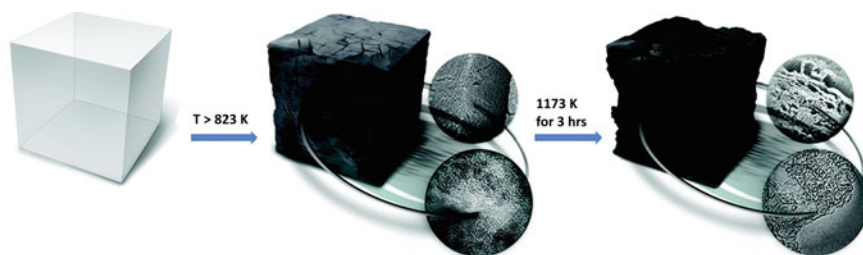
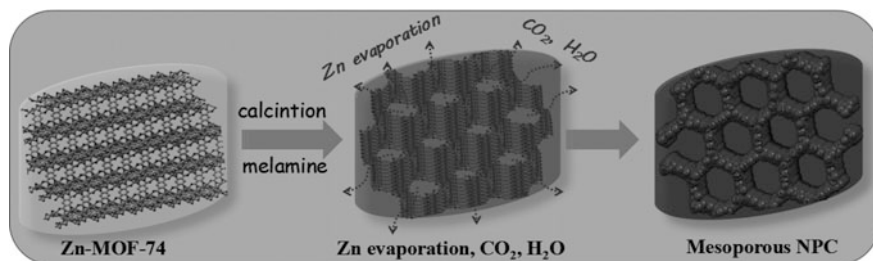


Fig. 4.1 Structural changes of PMC with heat treatment to yield PMC-derived carbon: schematic view. Reproduced with permission from Ref. [147]. Copyright (2012) American Chemical Society



Scheme 4.2 Process of preparation of the nitrogen-doped NPC. Reproduced with permission from Ref. [153]. Copyright (2017) John Wiley and Sons

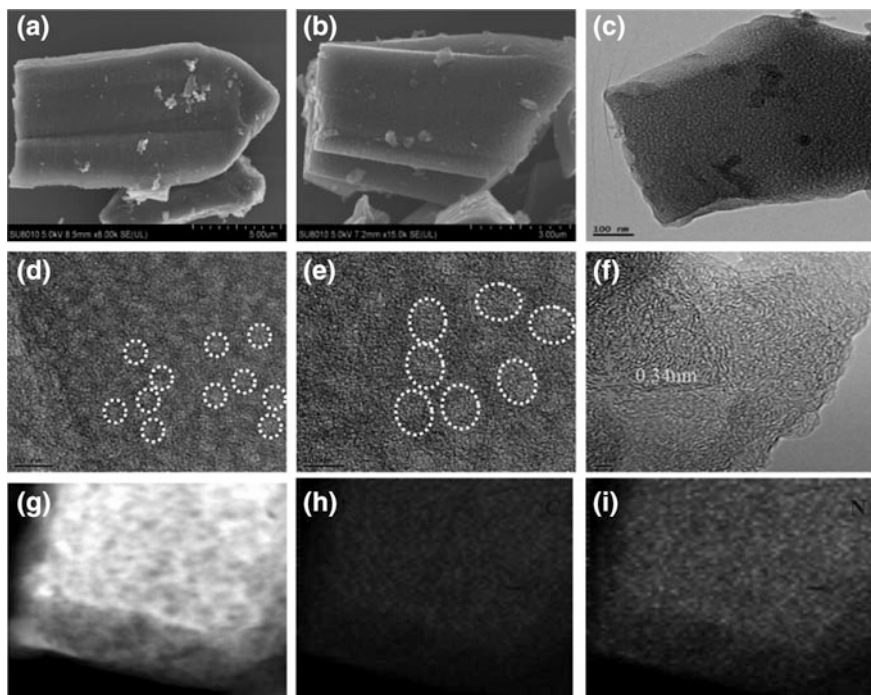


Fig. 4.2 SEM of **a** Zn-MOF-74, **b** NPC-1273, **c–e** TEM and **f** HRTEM of NPC-1273, **g–i** the elemental mapping of NPC-1273. Reproduced with permission from Ref. [153]. Copyright (2017) John Wiley and Sons

oxygen content of Zn-MOF-74 promotes the formation of more gaseous products, in particular, CO_2 and H_2O , which allows to producing nanomaterials with large pore sizes.

NPC-1273 obtained at the thermolysis temperature of 1273 K has a similar shape and size as the original Zn-MOF-74, thus confirming the preservation of the morphology of Zn-MOF-74 during thermolysis (Fig. 4.2a, b). At the same time, NPC-1273 shows a rougher surface with the appearance of some observable pores and the absence of the Zn element, which is evidence of the removal of Zn via high-temperature evaporation. In addition, the pores in the NPC-1273 have an average pore diameter of about 10–12 nm (Fig. 4.2c–e) and an interplanar crystalline space of 0.34 nm, indicating the formation of graphic carbon (Fig. 4.2f) [153]. It is important that the nitrogen element is uniformly doped in NPC-1273 (Fig. 4.2g–i).

Thermolysis products may contain metallic species at lower thermolysis temperatures or for PMCs based on metals having higher boiling points than Zn (in particular, Fe, Co, Cu, etc.). To remove them, post-synthetic acid treatment is carried out, which will make it possible to obtain pure NPC materials with tailored nanostructures and functions [121].

It should be emphasized that by varying the structure of the initial PMC and thermolysis conditions, it is possible to obtain various forms of carbon nanomaterials ranging from 0D to 3D. As an example of 0D carbon, we note carbon nanodots with an APS of 2.2 nm prepared by MOF thermolysis at a mild temperature (773 K) [154]. By thermolysis of Fe-, Co-, and Ni-PMCs, carbon nanotubes, which are a typical 1D material, were obtained. In this process, metallic Fe, Co, or Ni NPs are first formed, which then catalyze the formation of carbon nanotubes on the surface. Of interest is the production of 1D carbon nanorods [155] as well as multiwalled carbon nanotubes (MWCNT) by thermolysis of Ni-MOF in a conventional tubular furnace at 773 K for 20 h without additional catalyst or carrier gas [156]. The similar non-hollow (solid) carbon nanorods are the basis for the synthesis of two- to six-layered graphene nanoribbons using a sonochemical methodology with post-synthetic chemical activation. 2D carbon materials, for example, graphene-like carbon nanosheets, were also obtained by thermolysis of PMCs under an Ar atmosphere at 1223 K for 5 h [123]. The PMC-derived 3D NPCs showed a hierarchically porous structure and a high surface area ($1820 \text{ m}^2 \text{ g}^{-1}$) [157]. It should be also noted using PMC thermolysis to preparing NPCs with special morphologies, for example, cube, polyhedron, etc. [158–162]. These examples demonstrate the importance of choosing proper PMC for targeted synthesis of PMC-derived carbon nanomaterials.

It is of interest to synthesize hybrids of nitrogen-doped graphitic NPCs and carbon nanotubes by thermolysis of typical MOF and urea as precursors of carbon and nitrogen with the participation of nickel, which acts as a catalyst for graphitization [163]. The resulting hybrids showed interesting catalytic properties due to the synergistic contributions of the components of their hybrid architecture, high nitrogen content, significant degree of graphitization, and large surface area.

The usual process of obtaining NPC materials by thermolysis of typical Al-MOFs purified by removal of Al_2O_3 a solution of HF was modified by double-template method (Fig. 4.3) [164]. In this method, PMC is used as a template and a precursor, and an additional metal ion (Cu^{2+}) is introduced as a second template. It is important that the particle size of Al_2O_3 is determined by the amount of reintroduced Cu^{2+} ions before thermolysis, which allows to producing the NPC with a hierarchical pore structure and controlled pore parameters (pore size, surface area, and pore volume) after removing metal particles from the resulting carbons.

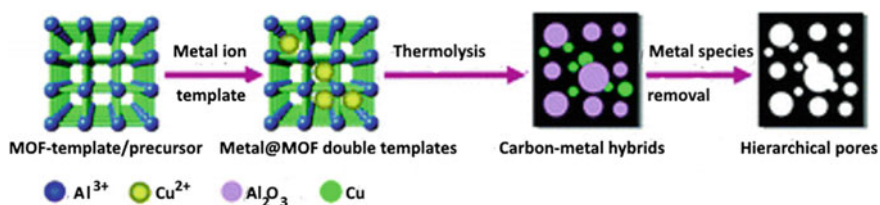


Fig. 4.3 Schematic representation of double-template method. Reproduced with permission from Ref. [164]. Copyright (2014) Royal Society of Chemistry

It should be noted that the temperature of thermolysis of MOFs templates is difficult to affect the characteristics of the obtained carbon material. For example, 3D framework structure of aluminum naphthalenedicarboxylate (Al-PCP where PCP is porous coordination polymer) contains two types of pores which is square in shape, in particular, the large and small channels with dimensions 7.7×7.7 and $3.0 \times 3.0 \text{ \AA}^2$, respectively (Fig. 4.4, left) [130]. Apparently, the structure of the coordination template in conditions of direct thermolysis at 1073 K promotes formation of NPC (Fig. 4.4, right) with an extremely high surface area ($5500 \text{ m}^2 \text{ g}^{-1}$) [121]. But during thermolysis over 1173 K specific surface area decreases to $200 \text{ m}^2 \text{ g}^{-1}$ due to the collapse of the structure caused by the graphitization of the product. In such cases, additional sources of carbon are required for the preservation of the porous structure in the system, such as the use of typical carbon precursor, for example, furfuryl alcohol.

An interesting example is MOF-5 having a 3D interconnected system of channels with 18 \AA cavities [165]. NPC obtained at 803 K has the largest surface area ($3040 \text{ m}^2 \text{ g}^{-1}$), and with a further increase in temperature from 923 to 1073 K-specific surface area decreased from 1521 to $1141 \text{ m}^2 \text{ g}^{-1}$. But if the thermolysis temperature exceeds 1173–1273 K, then again there is an increase in the specific surface area from 1647 to $2524 \text{ m}^2 \text{ g}^{-1}$ is again observed, which may be associated with the evaporation of Zn at temperatures above 1073 K. In the process of thermolysis at a temperature of 1273 K under a flow of argon MOF-5 decomposes with the formation of NPC with a specific surface area and pore volume $2872 \text{ m}^2 \text{ g}^{-1}$ and $2.06 \text{ cm}^3 \text{ g}^{-1}$. It is important that the MOF-5 is characterized by mesoporous structure, while the nature of the curves of adsorption–desorption isotherms indicates the presence of macropores along with a low content of micropores (Fig. 4.5) [115].

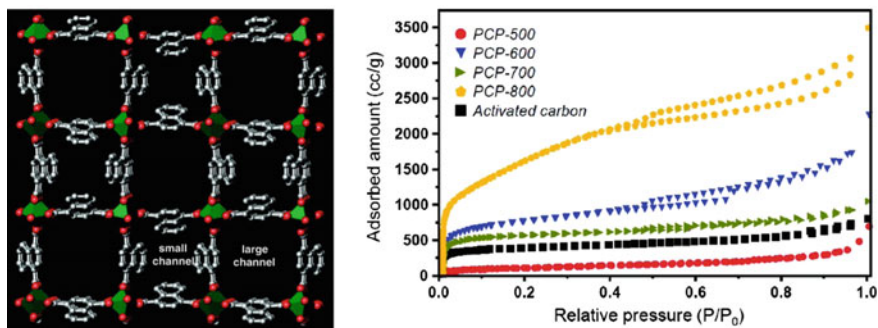


Fig. 4.4 (left) Crystal structure of Al-PCP. Reproduced with permission from Ref. [130]. Copyright (2008) American Chemical Society. (right) The adsorption–desorption N_2 isotherms for carbonization products of coordination polymer Al-PCP at different temperatures. Reproduced with permission from Ref. [121]. Copyright (2012) American Chemical Society

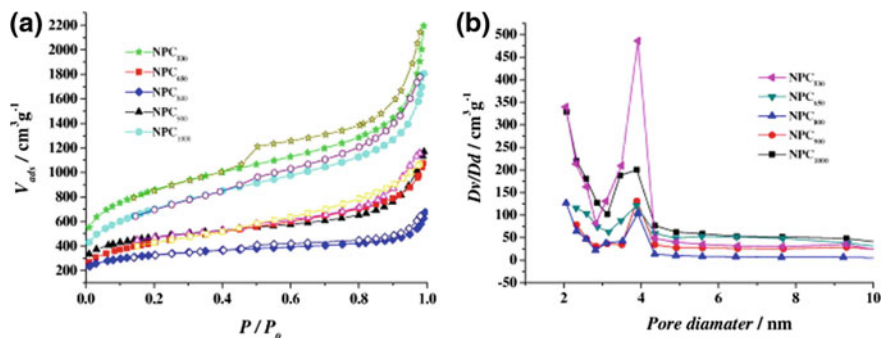


Fig. 4.5 Nitrogen adsorption–desorption isotherms (a) and pore size distribution (b) of thermolysis products for MOF-5 obtained at various temperatures. Reproduced with permission from Ref. [115]. Copyright (2010) Elsevier

Over the past ten years, numerous studies on the synthesis of NPC materials by PMC thermolysis have been carried out, but the influence of the nature of PMC precursors on the structure and properties of the resulting NPC materials remains unclear.

4.2 Preparation of Metal and Metal Oxide–Carbon Nanocomposites

Various types of nanostructured materials, such as metal/carbon (M@C), metal oxides/carbon (MO@C), and metal/metal oxides/carbon (M/MO@C), can be obtained by thermolysis of PMCs that are their SSPs [41, 104, 120, 166–175]. They allow to improving the properties of NPC materials by the introduction of functional NPs in the matrix of NPC, graphene, or carbon nanotube due to the synergistic effect of combining two or more components [176–193].

During PMC thermolysis, metal-containing units are converted to metal or metal oxide NPs and organic fragments form porous carbon structures with controlled pore sizes. Ultimately, this results in a variety of M/MO@C nanomaterials without removing metallic sites [38, 194–197]. Among the most interesting examples, we note nanomaterials containing MnO_2 [198–200], RuO_2 [201–203], SnO_2 [204–206], cobalt oxides [207, 208], and iron oxides [209–212]. It is important that PMCs are thermolysis precursors for the production of nanomaterials with a homogeneous distribution of metallic NPs and in situ formed metal-free NPC layers [105, 178, 213].

The spindle-like monodisperse nanosized Fe-MOFs, MIL-88B- NH_3 ($\text{Fe}_3\text{O}(\text{L})_3$, $\text{L} = 2\text{-aminoterephthalic acid}$) with uniform diameters of ~ 50 nm and lengths of ~ 140 nm (Fig. 4.6a) were thermolyzed in NPs at 1173 K in Ar for 6 h [135]. It is important that the shape and size of NPs are preserved after the thermolysis process

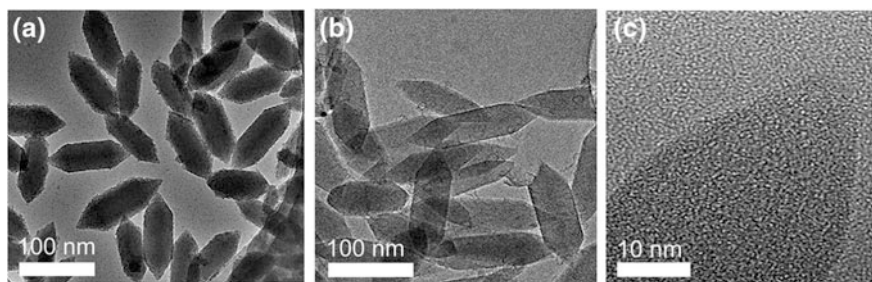
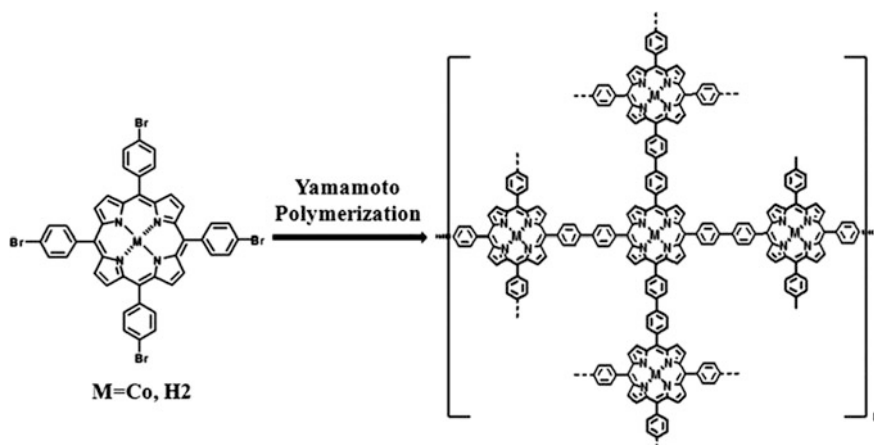


Fig. 4.6 a, b TEM images of nanosized MIL-88B-NH₃ and NPs formed; c HRTEM image of NPs formed. Reproduced with permission from Ref. [135]. Copyright (2014) American Chemical Society



Scheme 4.3 Schematic representation of the chemical synthesis of metalporphyrin-based conjugated mesoporous polymer frameworks (M = Co). Reproduced with permission from Ref. [214]. Copyright (2014) John Wiley and Sons

(Fig. 4.6b). The obtained NPs have an increased porosity of $326 \text{ m}^2 \text{ g}^{-1}$ with uniform pore sizes of about 3.8 nm, but the arrangement of the pores inside the NPs is disordered (Fig. 4.6c).

Numerous studies are devoted to the thermolysis of porphyrin-containing PMC [214, 215]. For example, nanomaterials obtained by the template-free thermolysis of conjugated mesoporous polymer frameworks based on cobalt porphyrin (Co-PMC) [214] are of considerable interest. Co-PMC frameworks (Scheme 4.3) were synthesized by Yamamoto polycondensation of 5,10,15,20-tetrakis(4'-bromophenyl) porphyrin-Co(II) catalyzed by Ni(COD)₂ (COD is cyclooctadiene) and bpy in dry dioxane.

Co-PMC frameworks, having a rigid conjugated matrix with a 3D cross-linked architecture, proved to be promising SSPs for obtaining nitrogen-enriched NPCs

with inclusion of cobalt NPs by thermolysis at 873, 1073, and 1273 K. Obtained nanomaterials are characterized by a number of interesting features, for example, high surface area, a ribbon-shaped morphology, and mesoporous structure (4–20 nm). In particular, such a conventional ribbon-like monolithic morphology has a length of up to tens of micrometers and a width from hundreds of nanometers to micrometers (Fig. 4.7a). In addition, this highly porous ribbon-like monolith is characterized by interconnected framework constructed of densely entangled nanofibers with a length of tens to hundreds of nanometers and a width from 10 to 30 nm (Fig. 4.7b). It is important that the nanomaterials contain uniformly distributed cobalt NPs embedded in nitrogen-enriched carbon framework (Fig. 4.7c) and fully encapsulated in graphitic carbon nanoshells (Fig. 4.7d).

Interesting SSPs for the synthesis of nanomaterials by thermolysis are such PMCs as CPM-99X (CPM = crystalline porous material, X = Zn, Co, Fe). They have a binodal cubic network consisting of 12-connected $Zr_6O_4(OH)_4$ cuboctahedra (Fig. 4.8b) connected by tetrakis(4-carboxybiphenyl) porphyrin (Fig. 4.8a) [215]. It should be noted that the 3D framework consists of large cubic cages with an edge length of up to 2.5 nm (Fig. 4.8c), and nanocubic cavities enclosed in a primitive cubic lattice (Fig. 4.8d). It is important that black cube-shaped crystals (Fig. 4.8e),

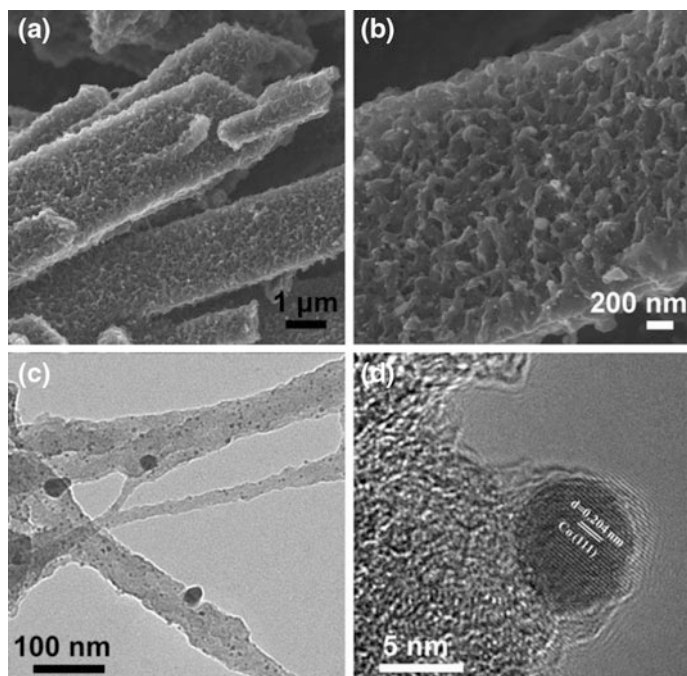


Fig. 4.7 **a** Low- and **b** high-magnification SEM images of cobalt NPs embedded in a nitrogen-enriched NPC, **c** TEM and **d** HRTEM images of cobalt NPs embedded in a nitrogen-enriched NPC. Reproduced with permission from Ref. [214]. Copyright (2014) John Wiley and Sons

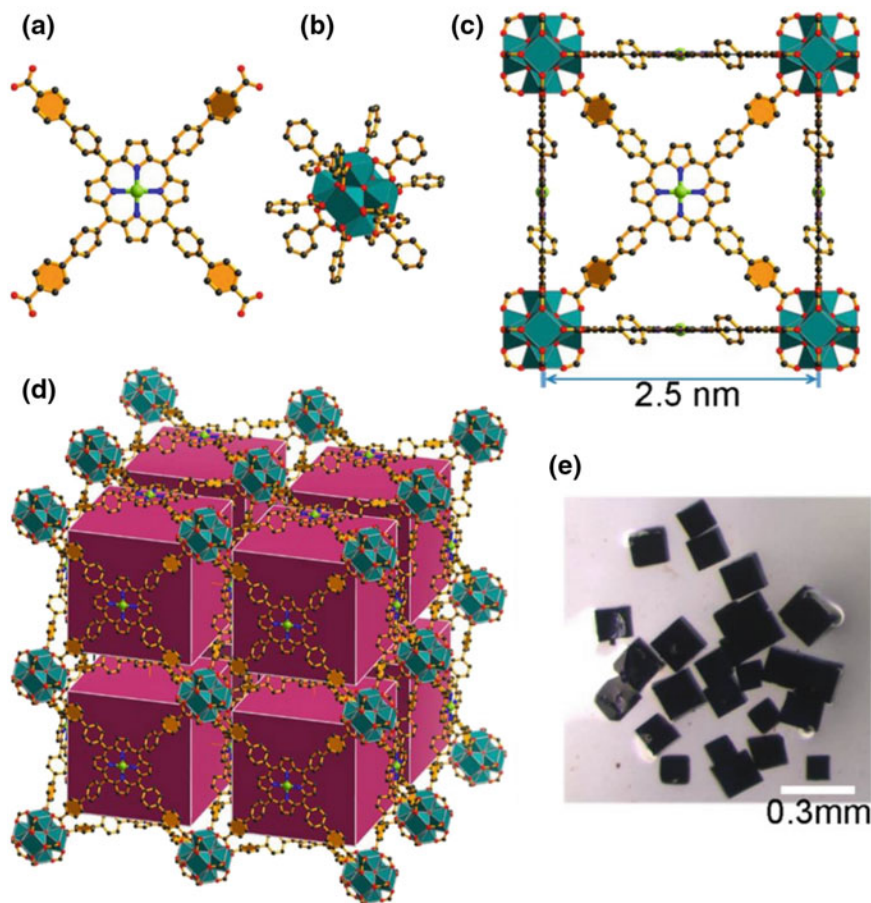


Fig. 4.8 **a** Augmented tetracarboxylic porphyrinic linkers ($X = \text{Zn}, \text{Co}, \text{Fe}$). **b** 12-connected $\text{Zr}_6(\mu_3\text{-O})_4(\mu_3\text{-OH})_4(\text{O}_2\text{C})_{12}$ cluster. **c** Cubic cage with 2.5 nm edge length. **d** The 3D network with Zr_6 clusters shown as polyhedra and 3D cubic-cavity packing in CPM-99Fe. Color scheme: Zr (teal); Fe (lime); O (red); N (blue); C (gray). **e** Photograph of CPM-99Fe. Reproduced with permission from Ref. [215]. Copyright (2014) American Chemical Society

having a size of ~ 0.20 mm, made it possible to determine the structure of the PMC by the single crystal X-ray method.

Thermolysis of PMCs at the optimum temperature of 973 K allows to obtaining (metallo)porphyrinic carbons, denoted as CPM-99X/C ($X = \text{Zn}, \text{Co}, \text{Fe}$), containing also cubic ZrO_2 . Removal of ZrO_2 was achieved by leaching with dilute HF. It should be noted that the obtained CPM-99X/C retain the cubic morphology of the original precursors (Fig. 4.9).

Fe-PMC is easily thermolyzed into Fe/N-codoped hierarchical NPCs (C-Fe/N-X, where X is thermolysis temperature) at various temperatures (973–1173 K) and

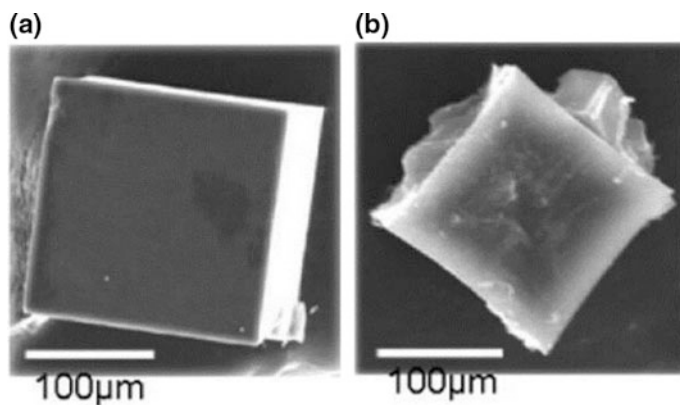
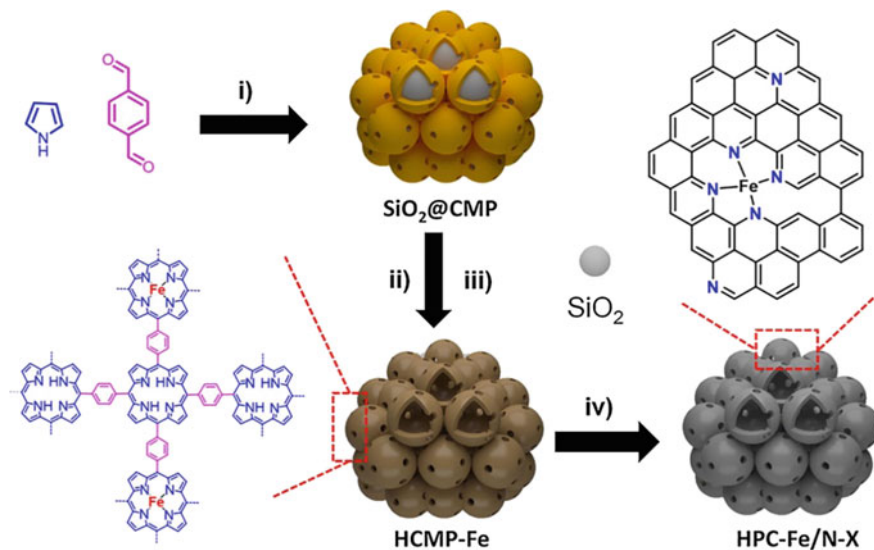


Fig. 4.9 a, b SEM images for CPM-99Fe and CPM-99Fe/C. Reproduced with permission from Ref. [215]. Copyright (2014) American Chemical Society



Scheme 4.4 Overall synthetic procedure of C–Fe/N–X. (i) silica nanosphere, 1,4-phthalaldehyde and pyrrole in CH_2Cl_2 at room temperature for 12 h, then *p*-chloranil at 323 K for 12 h; (ii) etching of SiO_2 templates in NaOH solution; (iii) coordinated with $\text{FeCl}_2 \cdot 4\text{H}_2\text{O}$ in DMF at 423 K for 12 h; (iv) thermolysis of Fe-PMC under N_2 at different temperatures and etching in HCl solution to produce C–Fe/N–X ($X = 973, 1073$ and 1173 K). Reproduced with permission from Ref. [216]. Copyright (2017) Elsevier

by etching (Scheme 4.4) [216]. The obtained NPCs are characterized by high specific surface areas up to $518 \text{ m}^2 \text{ g}^{-1}$ and a content of N and Fe up to 3.28 at% and 0.85 wt%, respectively.

In contrast to the N 1s core-level spectrum of the original Fe-PMC (Fig. 4.10a), samples of the nanomaterials obtained have more than one type of nitrogen, with the exception of pyrrole-type nitrogen, which passes into other types of nitrogen during thermolysis. The total nitrogen content of C-Fe/N-973, -1073 and -1173 is 3.28, 2.71 and 2.01 at%, respectively, including a pyridinic nitrogen content of 1.54, 1.16, and 0.56 at%, respectively (Fig. 4.10b). It is interesting that when the temperature of thermolysis increases, the content of graphitic nitrogen remains constant, while the content of pyridinic nitrogen decreases significantly, indicating that this type of nitrogen is less stable at high temperatures. It should be noted that the Fe content is 0.85, 0.88, and 0.90 wt% for C-Fe/N-973, -1073, and -1173, respectively (Fig. 4.10c).

Thermolysis of the porous PMCs based on a catechol-substituted porphyrin [*meso*-tetrakis(3,4-dihydroxyphenyl)-porphyrin] with nanorod morphology leads to the NPCs with large surface areas (up to $800 \text{ m}^2 \text{ g}^{-1}$), containing MO NPs (Scheme 4.5) [217]. After thermolysis at 1073 K, the nanorod-like morphology was to some extent retained although random structures also emerged probably due to the destruction of the crystals during thermolysis.

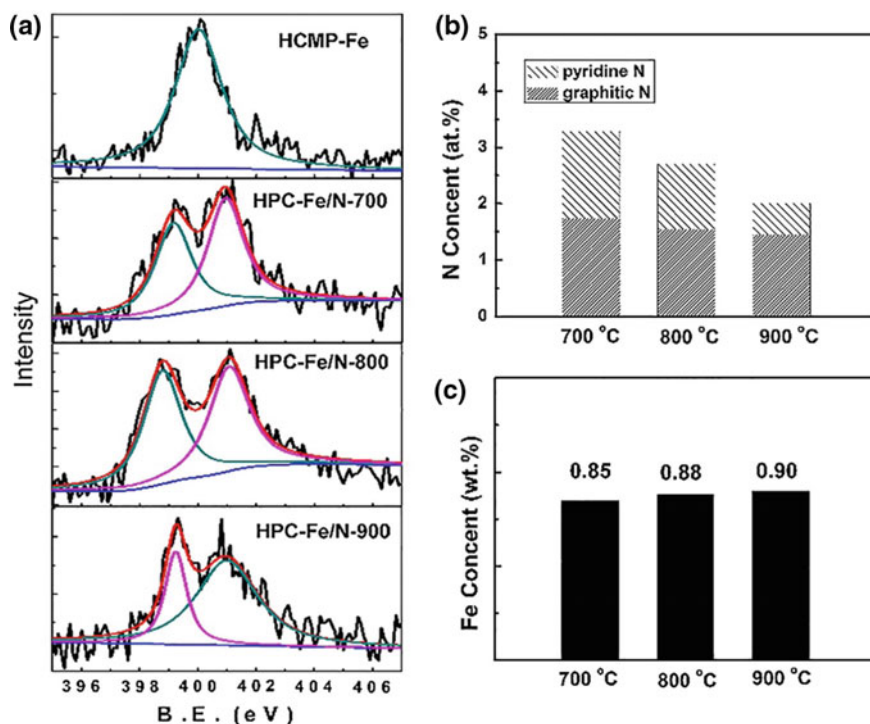
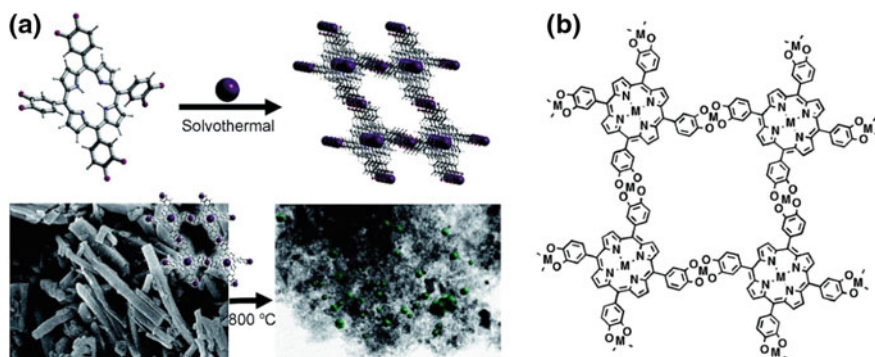


Fig. 4.10 a High-resolution N 1s spectra of Fe-PMC, C-Fe/N-973, C-Fe/N-1073, and C-Fe/N-1173; N content (b) and Fe content (c) of C-Fe/N-973, C-Fe/N-1073 and C-Fe/N-1173, respectively. Reproduced with permission from Ref. [216]. Copyright (2017) Elsevier



Scheme 4.5 **a** Schematic illustration of the preparation of MO@C hybrid materials from porphyrin PMCs. Purple sphere: metal cation; green sphere: metal oxide NP; **b** Model structure of PMC. Reproduced with permission from Ref. [217]. Copyright (2016) Royal Society of Chemistry

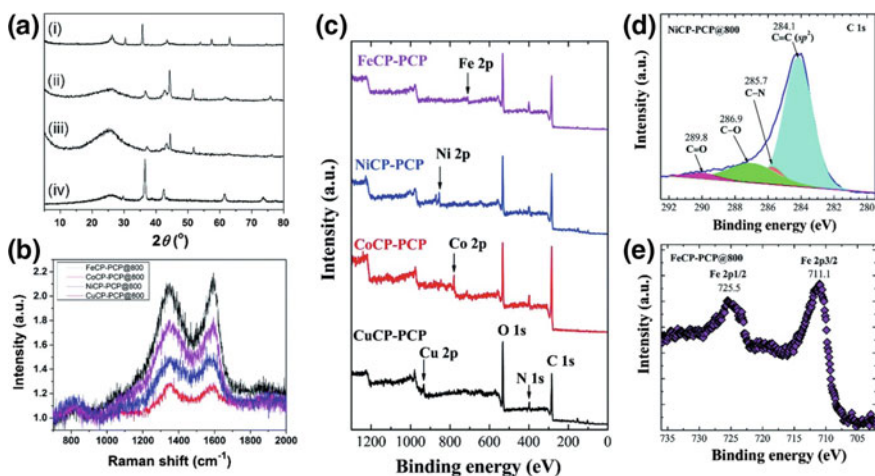
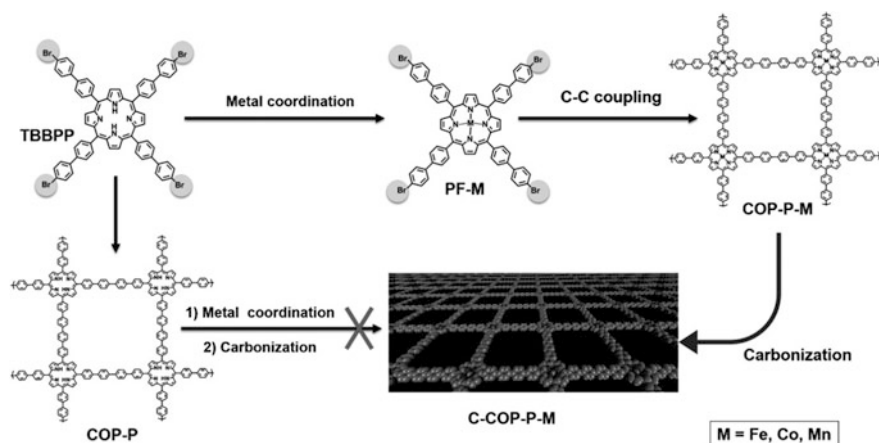


Fig. 4.11 **a** Power XRD profiles of samples M/MO@C: (i) Fe₂O₃@C; (ii) CoO/Co@C; (iii) NiO/Ni@C; (iv) Cu₂O@C. **b** Raman spectra of PMCs after thermolysis. **c** XPS survey scans for PMCs. **d, e** Representative XPS spectra of M/MO@C for NiO/Ni@C (carbon 1s region) and Fe₂O₃@C (Fe 2p region). Reproduced with permission from Ref. [217]. Copyright (2016) Royal Society of Chemistry

Powder XRD patterns confirm the formation of γ -Fe₂O₃, CoO/Co, NiO/Ni, and Cu₂O contained in the carbonized matrix (Fig. 4.11a). It should be noted that the observed Raman peaks at 1337 and 1589 cm⁻¹ (Fig. 4.11b) refer to the D and G bands of amorphous graphitic carbon in the nanomaterials obtained. In addition, X-ray photoelectron spectroscopy (XPS) shows the formation of hybrid materials in these systems (Fig. 4.11c for PMC before thermolysis, Fig. 4.11d, e for M/MO@C). It is important that in the process of thermolysis, an increase in the



Scheme 4.6 Scheme for synthesizing PMCs and their thermolysis. Reproduced with permission from Ref. [219]. Copyright (2014) John Wiley and Sons

carbon content from 65 to 80 wt% is observed with a simultaneous decrease in the oxygen content. Thermolysis also leads to an increase in the metal content, in particular, up to 6 wt% for Fe_2O_3 and NiO, and about 12 wt% for CoO and Cu_2O .

The poor solubility of the porphyrin-based polymers in most common solvents does not allow to preparing the PMCs; therefore, they were prepared by polycondensation of metal chelate monomers (MCMs) based on 5,10,15,20-tetrakis(4'-bromobiphenyl) porphine (Scheme 4.6) [218, 219]. The subsequent thermolysis of the PMCs at optimized temperature of 1223 K leads to M@C nanomaterials (M = Fe, Co, or Mn).

The presence of a strong G band and a one-peak 2D band in Raman spectra (Fig. 4.12a) indicates a multilayered graphitic structure for all M@C samples. In addition, TEM images show the porous texture of Fe@C nanomaterials (Fig. 4.12b, c). In accordance with the elemental mapping on the TEM unit (Fig. 4.12d), carbon (Fig. 4.12e), iron (Fig. 4.12f) and cobalt atoms are homogeneously dispersed over the carbon matrix. We note also that the corresponding high-resolution N1s peaks present in the XPS spectrum (Fig. 4.12g) refer to pyrrole N and metal-coordinated N atoms. The results show that the porphyrin rings in the main framework of PMC precursors are retained after high-temperature thermolysis, and all M@C samples have high thermal stability with a weight loss of less than 20% even at 1073 K.

Even more attractive is the scheme for synthesizing polymetallic porphyrinic conjugated networks (PCNs) by polycondensation of the Sonogashira–Hagihara type of two different-metal porphyrin monomers (Fig. 4.13) [220]. As a result of such processes, a series of PMCs with three different combinations of metals (MM = FeCo, FeFe, CoCo) was obtained. Subsequent thermolysis allowed to producing heterometalloporphyrin carbons.

It should be noted the study of the effect of air impurities on the thermolysis process of MOF based on copper porphyrin. The systematic structural characteristic

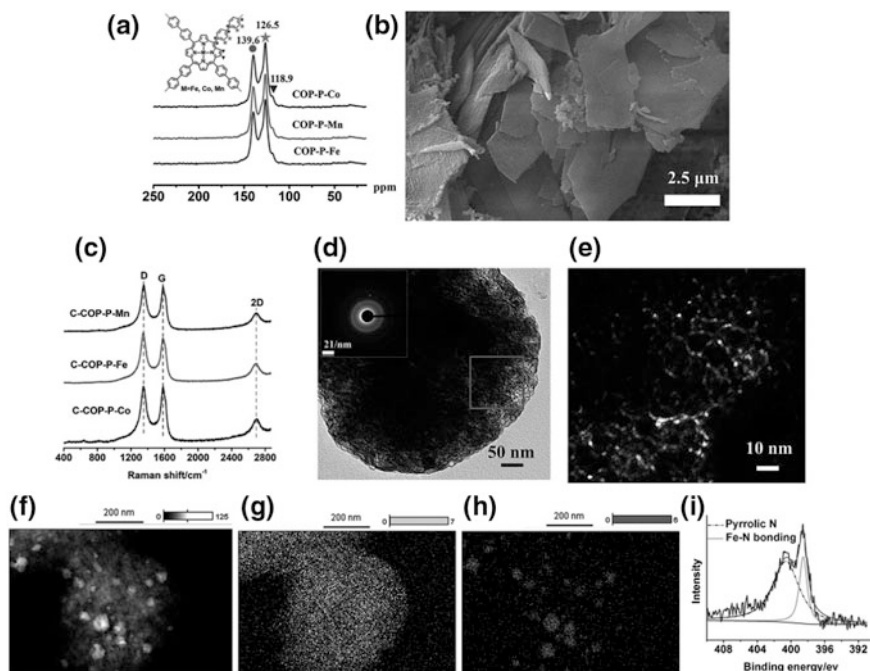


Fig. 4.12 **a** Solid-state ^{13}C NMR spectra of COP–P–M (M = Fe, Co, and Mn). **b** SEM image of COP–P–Fe. **c** Raman spectra of C–COP–P–M (M = Fe, Co, or Mn). **d** TEM image of C–COP–P–Fe. *Inset* The selected-area electron diffraction (SAED) pattern. **e** An enlarged view of the area within the square in **(d)**. **f** TEM image of C–COP–P–Fe for element mapping. **g** Carbon atom mapping of the C–COP–P–Fe sample. **h** Iron atom mapping of the C–COP–P–Fe sample. **i** XPS N 1s spectrum of the C–COP–P–Fe. The N 1s peak can be fitted with two Lorentzian peaks corresponding to Fe–N (398.7 eV) and pyrrolic N (400.6 eV), respectively. Reproduced with permission from Ref. [219]. Copyright (2014) John Wiley and Sons

of copper- and nitrogen-doped carbon materials showed that partial etching of carbon by air leads to an increased porosity of the samples, which consequently has a much larger surface area (Fig. 4.14) [221].

Of interest is a low-temperature and gram-scale approach to synthesizing iron phthalocyanine-embedded 2D carbon sheets by thermolysis at 723 K [222]. It is important that such process of the preparation of Fe–N–C-based carbon nanomaterials is useful for maintaining the Fe–N–C structure while enhancing coupling with carbon.

Particular attention should be paid to the strategy of synthesis of a wide range of metals and metal oxide NPs, such as Cu/CuO, Co/Co₃O₄, ZnO, Mn₂O₃, MgO, and CdS/CdO, embedded in the carbon matrix through controlled thermolysis of the MOFs [17]. This strategy is based on the use of the metal reduction potential in the design of the nanomaterial obtained. In particular, if the metal reduction potential is -0.27 V or higher, metal NPs are the final products of thermolysis. At the same

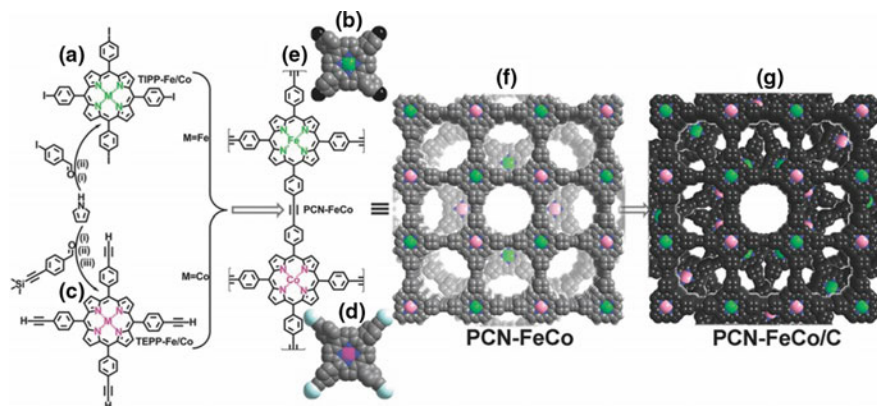
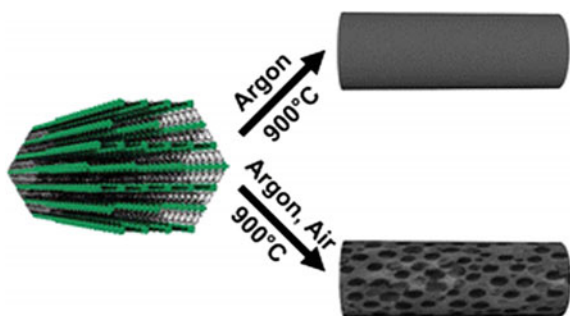


Fig. 4.13 Schematic diagram of the synthesis of **a, b** TIPP-M and **c, d** TEPP-M (M = Fe, Co) monomers, **e, f** porphyrinic conjugated network PCN-FeCo, and **g** thermolysis product PCN-FeCo/C. (FeFe/C and CoCo/C are prepared by the same synthetic route). TIPP = 5,10,15,20-tetrakis(4-iodophenyl) porphyrin and TEPP = 5,10,15,20-tetrakis(4-ethynylphenyl) porphyrin. Reproduced with permission from Ref. [220]. Copyright (2015) John Wiley and Sons

Fig. 4.14 Schematic representation of influence of air impurities on the process of thermolysis of MOF based on copper porphyrin. Reproduced with permission from Ref. [221]. Copyright (2016) American Chemical Society



time, metal ions with a reduction potential below -0.27 V form metal oxide NPs during thermolysis in N_2 (Fig. 4.15). One of the important conditions for using this strategy is the relationship between NP sizes and the distance between secondary building blocks (SBUs) inside the MOF precursors.

The composition of the products formed is also significantly influenced by the environment (N_2 or air) during thermolysis. As a typical example, we consider the thermolysis of Cd-MOF-1 containing the $[CdL(bpy)(H_2O)]$ units, where H_2L = thiophene-2,5-dicarboxylic acid. Since the reduction potential of Cd is -0.4 V, it does not form metal NPs during thermolysis, and the final products of thermolysis are CdO NPs in air and CdS NPs in nitrogen (Fig. 4.16).

It is of interest to synthesize non-hollow (solid) 1D carbon nanorods with dimensions of 20–40 nm (width) and 200–450 nm (length) by self-sacrificial and morphology-preserved thermolysis of MOF-74 [223] in an argon flow with 1D

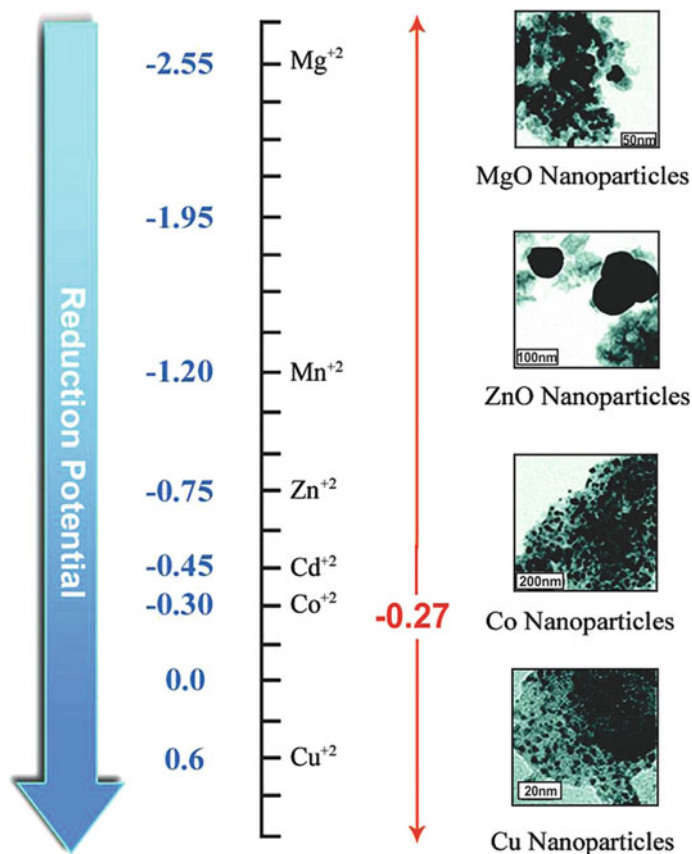


Fig. 4.15 Effect of reduction potential of metal atoms present in the MOFs on the formation of the M–MO NPs. Metals having a reduction potential above -0.27 V undergo thermolysis in an N_2 atmosphere to give pure metal NPs, whereas metals with a reduction potential less than -0.27 V, even in an N_2 atmosphere, produce only MOs. Reproduced with permission from Ref. [17]. Copyright (2012) Royal Society of Chemistry

rod-shaped morphology (MOF-74-Rod), which was obtained at room temperature using a unique modulator-assisted methodology (Scheme 4.7) [155]. Sonochemical treatment of the resulting solid carbon nanorods with subsequent thermal activation at 1073 K results in graphene nanoribbons (50–70 nm wide and 100–150 nm long) with two- to six-layer thickness.

It should be noted the preparation of small Co NPs embedded in the N-doped carbons by simple thermolysis of Co-MOF. It is important that Co NPs are highly dispersed with APS of ca. 7 nm [224]. Similar results were obtained by studying the thermolysis of MOF with $[CoL(L')_{0.5}] \cdot 2DMF \cdot 0.2 H_2O$ unit ($H_2L = 1,4$ -benzene dicarboxylic acid, $L' =$ triethylenediamine) as a sacrificial template using *i*-PrOH as hydrogen-donating solvent [157]. The XRD patterns of the formed Co@C–N–X-T

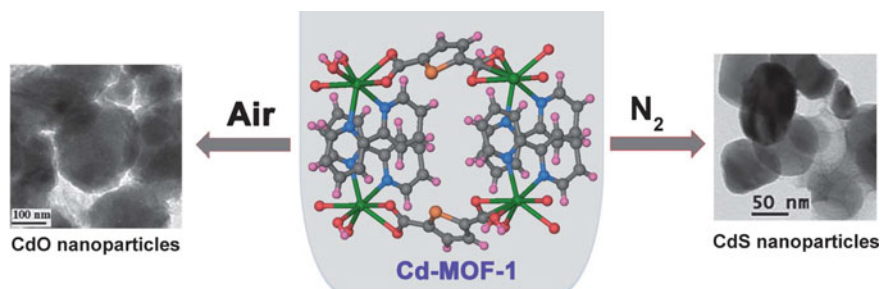
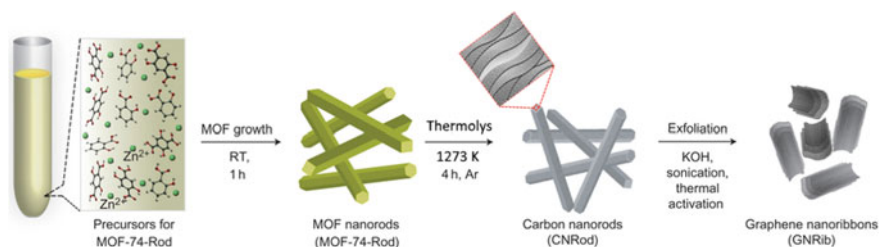


Fig. 4.16 A scheme of the synthesis for CdS/CdO NPs dispersed in a carbon matrix from Cd-MOF-1 after thermolysis in nitrogen and an air environment. Hydrogen atoms and guest molecules are omitted for clarity. Color code: Cd (dark green), N (blue), O (red), C (black). Reproduced with permission from Ref. [17]. Copyright (2012) Royal Society of Chemistry



Scheme 4.7 Scheme of synthesis of MOF-74-Rod, carbon nanorods and graphene nanoribbons. Reproduced with permission from Ref. [223]. Copyright (2006) American Chemical Society

(here X and T represent the temperature and time of thermolysis, respectively) nanomaterials show five diffraction peaks characteristics of metallic Co that have an improved intensity for nanomaterials obtained at higher thermolysis temperatures with longer times due to the higher degree of crystallization of Co. It is important that all Co@C–N nanomaterials exhibit similar particle shapes compared to the original Co-MOF. Elemental mapping (Fig. 4.17) showed a very uniform distribution of Co, C, and N on the surface of Co@C–N nanomaterials.

Co NPs are homogeneously dispersed in Co@C–N nanomaterials (Fig. 4.18), and Co NPs obtained at higher thermolysis temperatures are relatively large. APS varied from 6 to 17 nm with an increase in the thermolysis temperature from 773 to 1173 K.

Solid-state thermolysis of a similar Ni-MOF with $[\text{NiL}(\text{L}')_{0.5}]$ unit (Fig. 4.19a) made it possible to obtain porous Ni/C composites (Fig. 4.19b) [225]. Carrying out thermolysis in the NH_3 atmosphere leads to a significant decrease in the carbon content. For example, in the case of the Ni–Ar sample, the carbon content is more than 30 wt%, whereas for the Ni-0.2 NH_3 sample this value is only 1.22 wt%. A notable feature of the Ni–Ar sample is that it consists of Ni NPs having a diameter of less than 10 nm and uniformly distributed in the carbon matrix

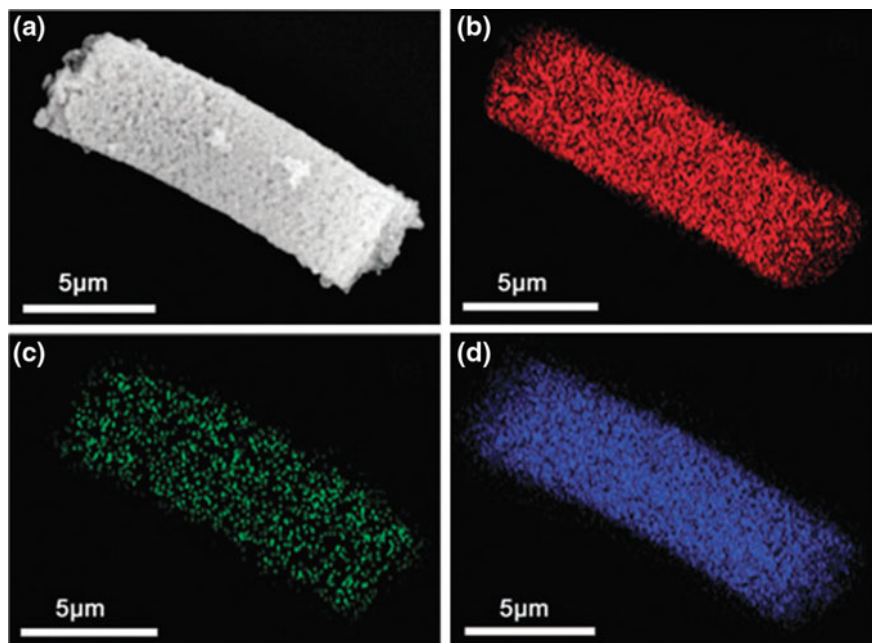


Fig. 4.17 SEM image (a), and elemental mapping of Co@C–N-1173-15 h: C (b), N (c), Co (d). Reproduced with permission from Ref. [157]. Copyright (2015) Royal Society of Chemistry

(Fig. 4.19c). It is interesting that for this sample a graphitic layer is located near Ni NPs, and the carbon matrix is an amorphous mass (Fig. 4.19d). It is important that thermolysis products in NH_3 atmosphere are Ni NPs with a thin layer of carbon, for example, for the Ni-0.2 NH_3 sample, the coating thickness is only 2 nm (Fig. 4.19f), whereas the Ni-0.4 NH_3 sample practically does not contain carbon coating (Fig. 4.19h). Both samples obtained in the NH_3 atmosphere contain Ni NPs about 30–50 nm (Fig. 4.19e, g).

Al-DTPA (DTPA is diethylenetriamine pentaacetic acid) microfibers were used as cost-effective SSPs (Fig. 4.20) for the preparation of nitrogen-doped carbon microfibers (NCF) [226].

The thermolysis of Al-DTPA (Fig. 4.21a) under optimized temperatures and acid-leaching leads to well-defined NCFs with preservation of the microfiber morphology of Al-DTPA (Fig. 4.21b–e). Fibers with a diameter of ~ 500 nm and a length of about 50 mm are formed as a result of Al-DTPA thermolysis at 1173 K (Fig. 4.21b–d). An increase in the thermolysis temperature leads to a slight increase in the graphitization degree of carbon microfibers (Fig. 4.21e, inset). It should be noted that Al-DTPA microfibers can also be used as SSPs for the $\gamma\text{-Al}_2\text{O}_3$ microfibers. After heat treatment of Al-DTPA in air at 1073 K, $\gamma\text{-Al}_2\text{O}_3$ with clearly defined microfiber morphology was observed in SEM images (Fig. 4.21f). There is an obvious shrink in diameter (350 nm) and length (50 mm), in contrast to

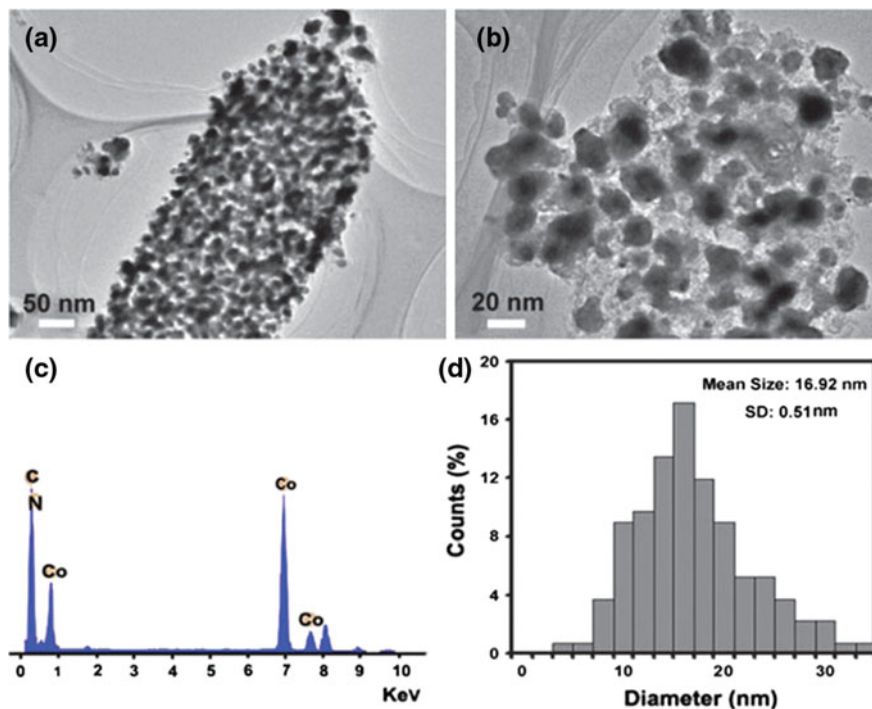


Fig. 4.18 TEM images of Co@C-N-1173-15 h (a, b), EDS (c), and the corresponding size distribution of Co NPs (d). Reproduced with permission from Ref. [157]. Copyright (2015) Royal Society of Chemistry

Al-DTPA microfibers (see Fig. 4.21a). The resulting γ -Al₂O₃ has a smaller BET surface area (50 m² g⁻¹) and a pore size distribution in the range of 2–15 nm.

The total BET surface area of NCF-1023, -1173, and -1173 are 604, 933, and 1072 m² g⁻¹, respectively (Table 4.1). Thus, the NCFs with a uniform fiber morphology, nanoporous structure, and appropriate graphitization degree were successfully obtained by this unique thermolysis of Al-DTPA.

The PMC templates have a number of important advantages associated with their nanoporous architecture, high thermal stability, and the possibility of small molecules penetrating into PMC pores with their subsequent participation in various «ship-in-bottle» reactions [142–144]. These advantages were clearly realized in the production of various nanostructured carbon materials, including the M/MO@C type (Fig. 4.22). The process scheme includes a number of sequential operations: polymerization of small molecules inside the PMC template pores (Fig. 4.22a), thermolysis to obtain the M@C nanocomposite (Fig. 4.22b), and post-thermal processing for conversion from metal to metal oxide NPs (Fig. 4.22c). It is important that parameters, such as the porosity of the carbon matrix and the dimensions of M/MO NPs, can be monitored at each stage of the process. Typical

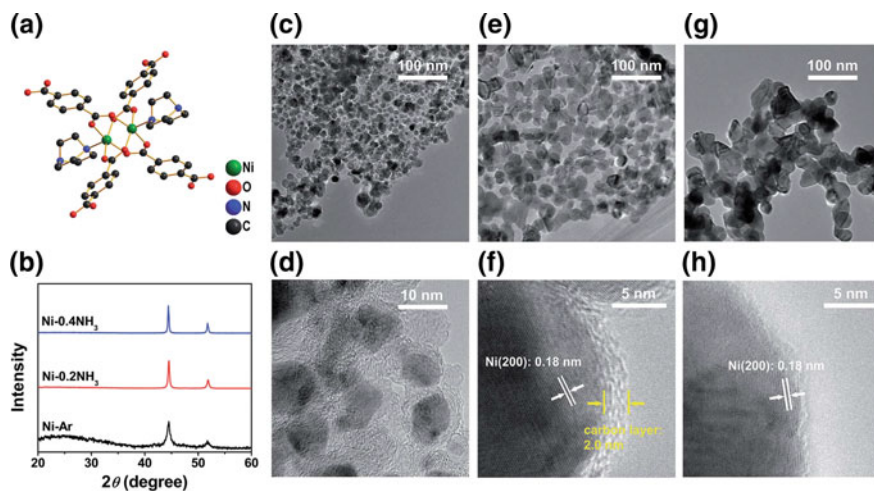


Fig. 4.19 **a** Structure of the Ni coordination environment in $[\text{NiL}(\text{L}')_{0.5}]$, **b** XRD patterns of the Ni-MOF derived NPs, and **c–h** TEM images of the Ni-MOF derived NPs: **c, d** Ni–Ar, **e, f** Ni-0.2NH₃, and **g, h** Ni-0.4NH₃. Reproduced with permission from Ref. [225]. Copyright (2015) Royal Society of Chemistry

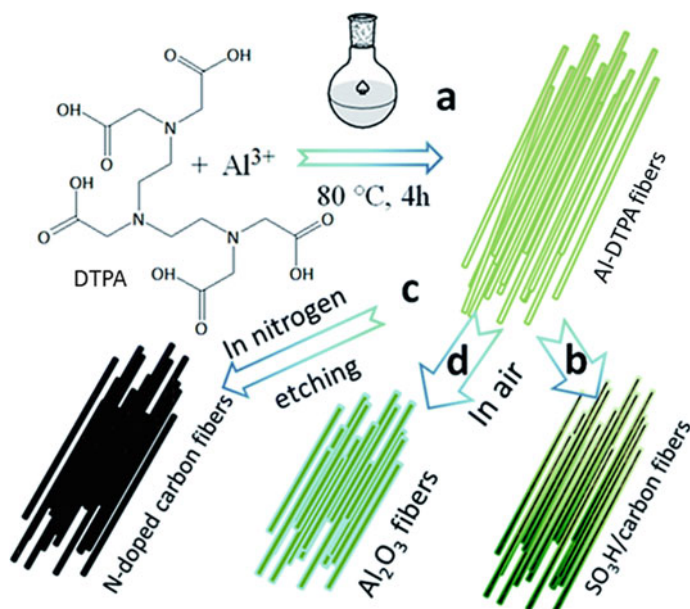


Fig. 4.20 Schematic illustration of the formation process of the nanoporous NCFs and solid acids microfibers. Reproduced with permission from Ref. [226]. Copyright (2015) Royal Society of Chemistry

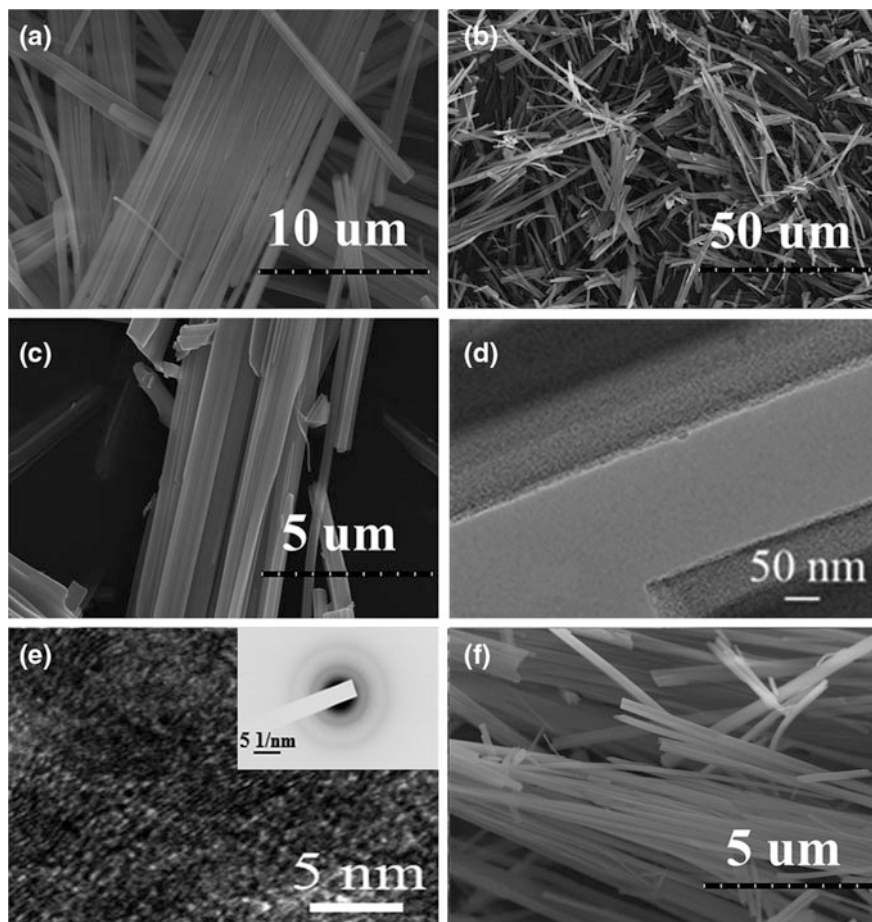


Fig. 4.21 a SEM images of Al-DTPA microfibers; b, c SEM images of NCF-1173; d, e TEM images of NCF-1173. Inset is the corresponding SAED pattern of NCF-1173; f SEM images of γ - Al_2O_3 obtained by heating Al-DTPA at 1073 K in air. Reproduced with permission from Ref. [226]. Copyright (2015) Royal Society of Chemistry

Table 4.1 Textual data of NCFs obtained at 1023, 1173 and 1173 K

Samples	S_{BET} ($\text{cm}^2 \text{g}^{-1}$)	S_{meso} ($\text{cm}^3 \text{g}^{-1}$)	S_{micro} ($\text{cm}^3 \text{g}^{-1}$)	V_{total} ($\text{cm}^3 \text{g}^{-1}$)	$V_{\text{micro}}^{\text{T}}$ ($\text{cm}^3 \text{g}^{-1}$)
1023	604	84	520	0.39	0.28
1173	933	108	825	0.58	0.43
1173	1072	67	1005	0.65	0.55

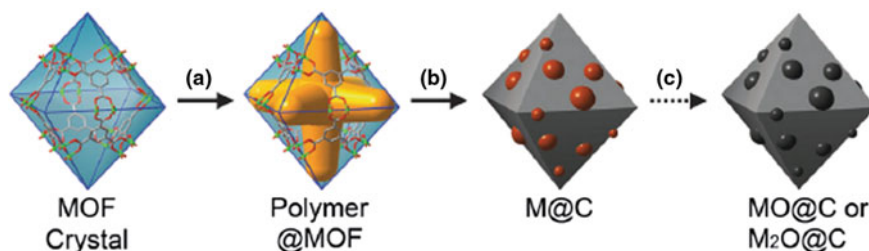
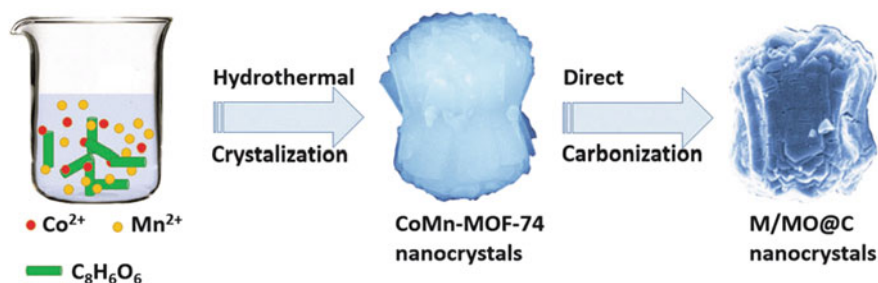


Fig. 4.22 Scheme of the transformation of MOFs in M/MO@C composite. Reproduced with permission from Ref. [227]. Copyright (2010) American Chemical Society



Scheme 4.8 Schematic illustration for the preparation of M/MO@C. Reproduced with permission from Ref. [228]. Copyright (2016) Royal Society of Chemistry

examples include the preparation of Zn@C, ZnO@C [227], and Cu@C, Cu₂O@C or CuO@C nanocomposites [195], preserving the octahedral morphology of the original PMCs. An important feature of the nanomaterials obtained is that the NPs are interconnected by an NPC matrix, and its diffusion properties allow the use of materials in a wide variety of applications.

Of particular interest is the preparation of mixed oxides of cobalt and manganese embedded in the NPC matrix (M/MO@C) by direct thermolysis of binary (CoMn-MOF-74) heterometallic PMC (Scheme 4.8) [228]. It turned out that the optimum temperature of thermolysis is the most important parameter for obtaining such M/MO@C nanomaterial.

The original MOF is characterized by a uniform rod-like structure without any contamination by an amorphous phase (Fig. 4.23a), with one particle built from many nanorods (Fig. 4.23b), and all elements, including Co, Mn, carbon and oxygen, are evenly distributed in the selected area (Fig. 4.23c) [229]. It is important that during the thermolysis the morphology of the CoMn-MOF-74 precursor is practically preserved (Fig. 4.23d–f), while CoO and MnO NPs are homogeneously dispersed in the carbon matrix (Fig. 4.23g). The M/MO NPs, with porous carbon walls outside, are embedded in the carbon framework (Fig. 4.23h–j) [229, 230].

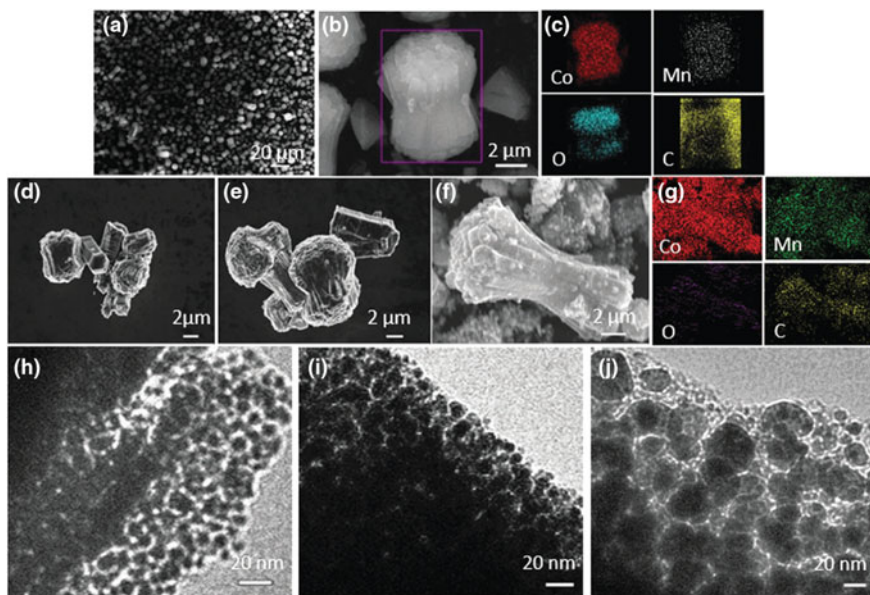
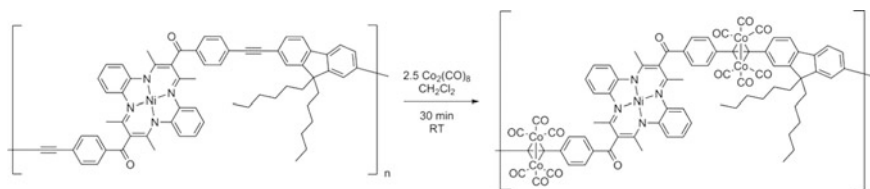


Fig. 4.23 **a** Low-magnification SEM image of CoMn-MOF-74, **b** SEM images of a single particle of CoMn-MOF-74, **c** EDS mappings of each element in CoMn-MOF-74, **d–f** SEM images of M/MO@C, **g** EDS mappings of each element in M/MO@C-1073, **h–j** TEM images of M/MO@C. Reproduced with permission from Ref. [229]. Copyright (2008) American Chemical Society



Scheme 4.9 Synthesis of NiCo-PMC from Ni-PMC. Reproduced with permission from Ref. [231]. Copyright (2016) John Wiley and Sons

It should be also noted the heterobimetallic copolymer precursor NiCo-PMC prepared by the reaction of the presynthesized Ni-PMC with $\text{Co}_2(\text{CO})_8$ in a yield of 95% (Scheme 4.9) [231]. For NiCo-PMC, values of $M_n = 7700$, $M_w = 10,900$ and polydispersity index (PDI) = 1.41 were obtained, and the integrity of the polymer backbone retained after the introduction of carbonyl clusters of cobalt.

Thin films of Ni-PMC and NiCo-PMC (about $5 \mu\text{m}$ thick), created by drop-casting a solution of each polymer in chlorobenzene on a silicon wafer, were thermolyzed at 1173 K (Fig. 4.24). As a result of thermolysis, nanomaterials with poorly defined NPs in a porous matrix were obtained (Fig. 4.24a, b). It is important

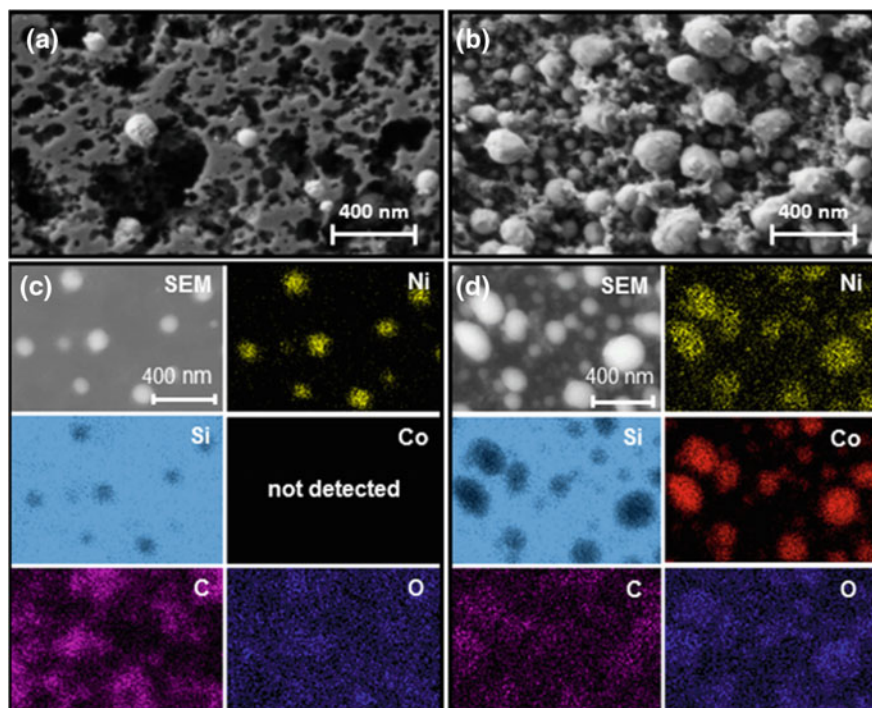


Fig. 4.24 SEMs of the nanomaterials resulting from thermolysis of **a** Ni-PMC and **b** NiCo-PMC. Elemental maps (EDX spectroscopy) of the nanomaterials resulting from the thermolysis of **c** Ni-PMC and **d** NiCo-PMC. Light areas indicate a positive response for the elements in question. Reproduced with permission from Ref. [231]. Copyright (2016) John Wiley and Sons

that NPs are rich in cobalt and nickel, and the cobalt and nickel alloys are more susceptible to oxidation (Fig. 4.24d). In addition, the ratio of cobalt to nickel (about 5.5:1) deviated from the 4:1 ratio of metals present in NiCo-PMC.

Analysis of the available experimental data shows that the combination of a huge selection of metal ions/ligands and the PMC architecture, as well as thermolysis conditions, gives considerable flexibility in the development of the desirable nanomaterials (Fig. 4.25) [232]. Thus, the metal center in PMC can be converted into metal oxides (MO), metal sulfides (MS), single metal carbides (MC) or heterometallic carbides, by changing the composition of MOF or the conditions of the thermolysis process [44, 45, 94, 233–235]. In addition, PMC can be converted to metal-free nanomaterials, such as nitrogen-doped carbons, after metal removal by acid etching or evaporation of metals [38, 124]. The introduction of multiple heteroatom dopants (e.g., N, P, or S) into carbon nanomaterials can be achieved by modifying the parent ligands or adding a second precursor to the MOF pores [148, 236, 237]. Finally, thermolysis of MOF allows to obtaining, under certain conditions, purely carbon nanomaterials that can act as a microporous host for a variety of molecules to expand applications of nanostructured materials [106, 238–241].

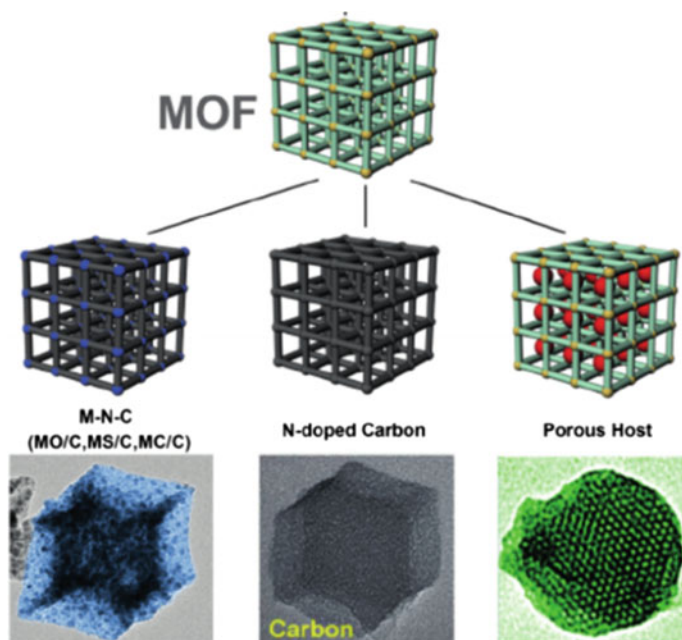


Fig. 4.25 Schematic illustration showing the construction of PMC-derived nanomaterials. Reproduced with permission from Ref. [232]. Copyright (2016) John Wiley and Sons

4.3 Preparation of Metal Oxide Nanomaterials

Synthesis of MO nanomaterials is the subject of intensive research with a special interest in the control of the shape, size, composition, porosity, and surface area of the obtained MO NPs [87, 242–250]. Thermolysis of the PMCs is one of the promising methods for producing MO nanomaterials with the desired properties, since it refers to one-stage, low-cost, well-reproducible, and easily scalable processes [7, 12, 32, 81, 84, 86, 251, 252]. It is important that the morphology and properties of the resulting MO nanomaterials depend on such factors as crystal structure and architecture of the original PMC precursor, the particle size, and the thermolysis conditions (temperature, environment, the presence of a surfactant, etc.) [7, 253–255]. In addition, the structure and properties of synthesized MO nanomaterials can be easily regulated by changing the nature of ligands, metal ions or their stoichiometry [256]. During thermolysis process, the decomposition of organic ligands and the growth of metal nuclei in MO NPs occur spontaneously and the rates of these two processes are the main factors determining textural properties (e.g., morphology, pore size, etc.) of the corresponding MO nanomaterials [11].

However, the forms of MO NPs obtained are often limited by simple spherical topology, which is connected with the difficulty in preparing anisotropic templates [257]. Therefore, PMCs with anisotropic topologies and rigid frameworks

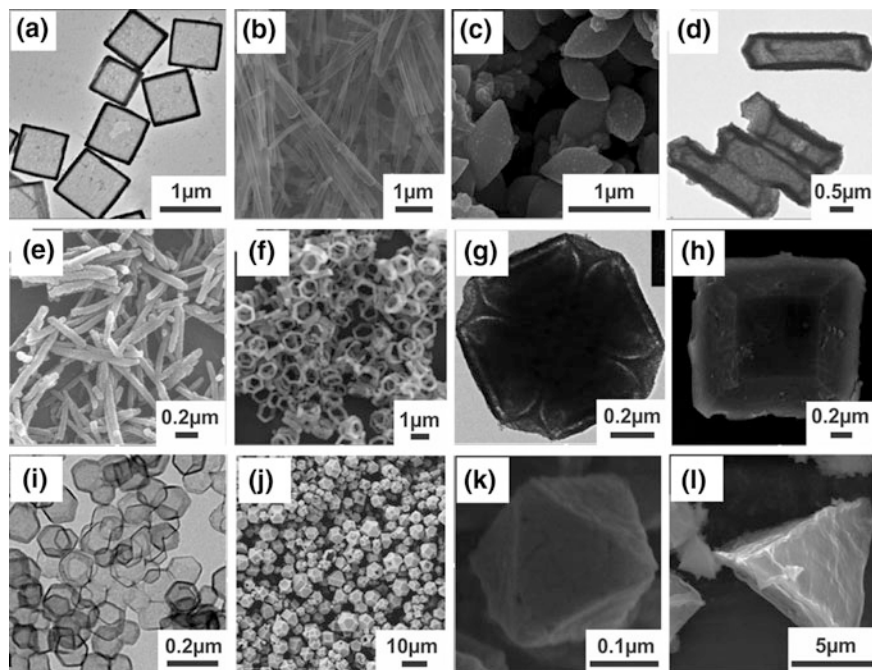


Fig. 4.26 Examples of various PMC-derived MOs with different morphological anisotropy: **a** cubes, **b** quadrate tubular boxes, **c** spindle-like, **d** elongated hexagon-shaped, **e** rod, **f** ring, **g** truncated tetragon, **h** octahedron, **i** rhombic dodecahedron, **j** polyhedrons, **k** octahedron, and **l** tetrahedron. Reproduced with permission from Ref. [11]. Copyright (2017) John Wiley and Sons

[72, 258–265] are promising templates for the production of well-controlled, non-spherical, and highly porous MOs [266]. Among the numerous examples of MOs with different morphological anisotropies based on PMC templates, we note cubic [267, 268], quadrate tubular box [269], spindle-like [40], elongated hexagon-shaped [270], rod [39, 271–275], wires [276–278], needles [279, 280], tubes [281, 282], belts [283–285], hooks [286], cables (i.e., coaxial wires) [287, 288], ribbons [289, 290], fibers [291], tips [292], helices (or spirals) [293, 294], zigzags [294], ring [84], truncated tetragon [295], octahedron [90], rhombic dodecahedron [296], polyhedral [297], octahedron [298], and tetrahedron [299] nanocrystals (Fig. 4.26).

In recent years, the synthetic methodologies of MO NPs, such as ZnO [78, 300–306], Co₃O₄ [79, 307–312], Fe₂O₃ [39, 40, 243, 313, 314], Mn₃O₄ [244, 315], CdO [7], Cu₂O [316, 317], CuO [242, 297, 318–320], Ti₂O₃ [321], PbO [42, 70–72, 85, 322–328], are developed. They are widely studied for the fundamental scientific and technological applications as new class of the nanomaterials. We consider the most common examples.

4.3.1 Transition Metal Oxides

Transition MO NPs are substantial interest due to their different applications and properties [70–72, 242–244, 302–306, 310–312, 315–320, 325].

4.3.1.1 Zinc Oxide

PMC proved to be convenient precursors, which allow regulating the production of ZnO nanocrystals with controlled structures, compositions, and properties [50, 53, 87, 329–335]. Their thermolysis under various conditions, such as different temperatures, precursor concentrations, surfactants, and solvents, was used to control the shape and size of the ZnO nanomaterials [19, 27, 48, 50, 53, 78, 82, 87, 96, 227, 245, 300, 301, 329, 336–355]. In particular, the thermolysis of Zn-PMCs in the presence or absence of air/N₂ leads to ZnO nanomaterials with different morphologies [7, 48, 50, 53, 78, 82, 87, 301, 330, 331, 346, 356–364], including nanowires [365], nanobelts [366], nanorods [367], nanorings [368], nanotubes [369], nanotetrapods [370, 371], nanoflowers [372], nanodisks [373], cones [374], towers [375], hollow spheres [376], nanosprings and nanospirals [377, 378], nanobridges and nanonails [379], nanohelix [380], hierarchical nanostructures [381, 382], and colloidal or arrayed nanocrystals [383–385]. It is important that the shape of the initial MOF is sometimes retained after its thermolysis into the nanomaterials [39, 53, 347, 386–389].

As a typical example, we note the use of thermolysis of infinite rectangular-tubular helices [ZnCl₂L] and [ZnBr₂L], where L is bis(3-pyridyl) cyclotetramethylenesilane, at 773 K to obtain homogeneous hexagonal tubular spire ZnO crystals of $1.2 \times 1.2 \times 4.0 \mu\text{m}^3$ dimensions and spheres, respectively (Fig. 4.27) [390]. Interestingly, for [ZnCl₂L] thermolysis at 773 K leads to the growth process of each ZnO single crystal.

It is of interest to synthesize ZnO NPs by thermolysis of Zn(II) CPs, [ZnL₂(N₃)₂]_n and [ZnL₂(SCN)₂]_n, where L is 2-aminomethylpyridine, at 873 K in

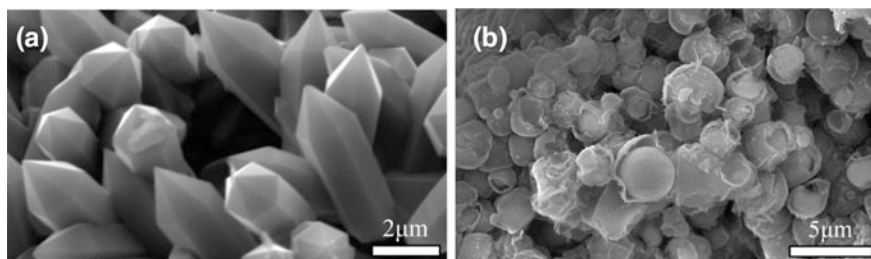


Fig. 4.27 SEM images of thermolysis residue of [ZnCl₂L] (a) and [ZnBr₂L] (b) thermolyzed at 773 K for 2 h. Reproduced with permission from Ref. [390]. Copyright (2015) Royal Society of Chemistry

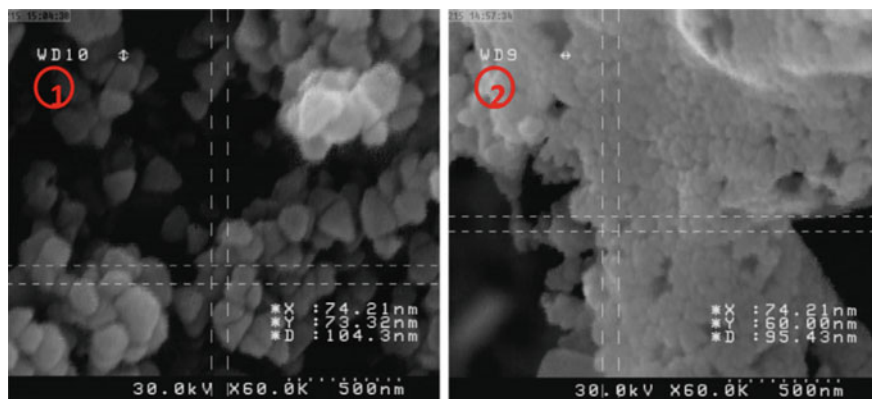


Fig. 4.28 SEM image of ZnO nanostructure prepared by thermolysis of the PMC at 873 K. Reproduced with permission from Ref. [391]. Copyright (2016) Springer Nature

an air atmosphere [391]. The product obtained is hexagonal ZnO with a diameter distribution of 60–70 nm (Fig. 4.28).

The nanorod morphology is characteristic of the thermolysis products of PMC with $[\text{Zn}(4,4'\text{-bipy})\text{Cl}_2]_n$ unit [50], and during the thermolysis of PMC with $[\text{Zn}(\text{ox})(4,4'\text{-bipy})]_n$ unit ZnO nanostructure is formed in radially spaced nanoneedles. In other words, the different framework structure of the initial PMCs affects the final morphology of the ZnO nanostructures formed. It should be noted that the lengths of ZnO nanorods ranged from 1.5 to 2.8 μm , while the diameters were in the range of 80–100 nm and the direction of growth of the nanorod was along [001] direction. At the same time, a typical single nanoneedle has a diameter of 80 nm and the direction of growth of the nanoneedle is also along [001] with a high degree of crystallinity. In this case, the resulting product was composed of assemblies of ZnO nanoneedles with a high content of about 90% and their diameters ranged from 1.5 to 2.2 μm .

Zn(II) CPs $(\text{NH}_4)_n[\text{Zn}(\text{HL})\text{Cl}_2]_n$, $[\text{ZnL}(\text{H}_2\text{O})_2]_n$, $[\text{Zn}(\text{HL})_2]_n \cdot 4n\text{H}_2\text{O}$ (H_2L = iminodiacetic acid) can serve as good SSPs for ZnO NPs at thermolysis at 773 K [392]. In particular, the product based on the first CP has the shape of a regular hexagonal pyramid (Fig. 4.29a). The average diameter and length of the ZnO crystal are about 2.6 and 4.6 μm , respectively, and the aspect (length/width) ratio is about 1.8:1. Regular granular crystallites of ZnO NPs having diameters in the range 25–202 nm were prepared from the second and third CP (Fig. 4.29b). The formation of various shapes and sizes of ZnO crystallites under the same thermolysis conditions is explained by the different network structures of the studied CPs and the presence of the chloride anion. In other words, the nucleation and growth of nanomaterials were influenced by the molecular chemistry of SSPs [393, 394].

It should be noted that N,S-containing ligands were used not only to prepare MS NPs, as expected, but also MO NPs, more thermodynamically stable in air. Thus, the ZnO nanostructure was obtained by direct thermolysis of NPs of Zn(II) CP,

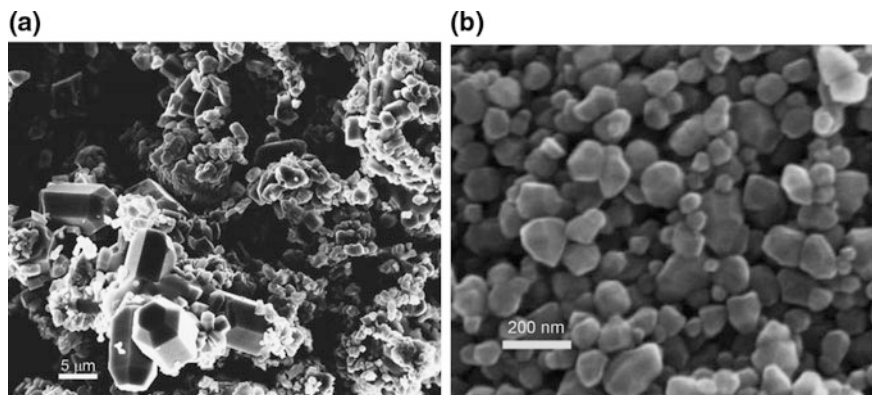


Fig. 4.29 SEM images of: **a** $(\text{NH}_4)_n[\text{Zn}(\text{HL})\text{Cl}_2]_n$ thermolyzed at 773 K for 4 h, **b** $[\text{ZnL}(\text{H}_2\text{O})_2]_n$ and $[\text{Zn}(\text{HL})]_n \cdot 4\text{H}_2\text{O}$ thermolyzed at 773 K for 4 h. Reproduced with permission from Ref. [392]. Copyright (2009) Elsevier

$[\text{ZnL}(\text{CH}_3\text{COO})_2]_n$ ($\text{L} = 2,2'$ -diamino-5,5'-dimethyl-4,4'-bithiazole), at 773 K under the air [395]. In this four-coordinate CP with almost C_2 symmetry, the metal is in a pseudotetrahedral environment and is ligated by two nitrogens of bithiazole rings and oxygen from each of the two monodentate acetates.

ZnO NPs were synthesized from the thermolysis of $[\text{ZnL}_2(\text{H}_2\text{O})_4]_n$, where L is picolinic acid N-oxide, in two different ways (with a surfactant and without a surfactant) and at two temperatures (473 and 873 K) [314]. In the crystal structure of the PMC, Zn(II) is six-coordinate by four oxygen atoms from picolinic acid the N-oxide ligand and two water molecules (Fig. 4.30).

Comparison of SEM images of ZnO NPs obtained by two different methods and at two temperatures (Fig. 4.31) shows that a higher temperature leads to an increase in agglomeration. In particular, small and spherical ZnO NPs with good separation were obtained by thermolysis of the compounds at 473 K and using a surfactant (OA). In addition, the dispersion range size is about 50–60 nm in this method. In both methods, the final product from the PMC is hexagonal ZnO.

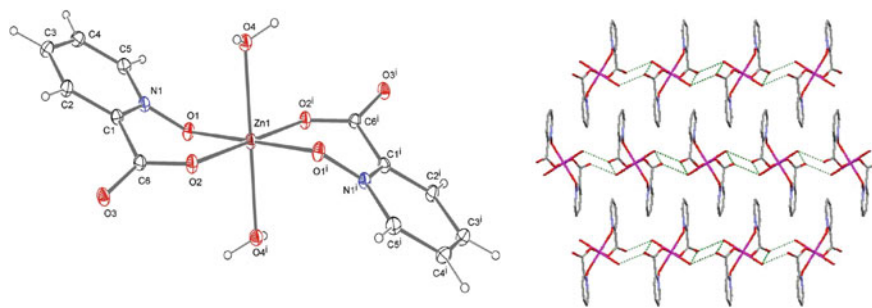


Fig. 4.30 ORTEP diagram (left) and packing diagram (right) of the PMC. Reproduced with permission from Ref. [314]. Copyright (2016) Elsevier

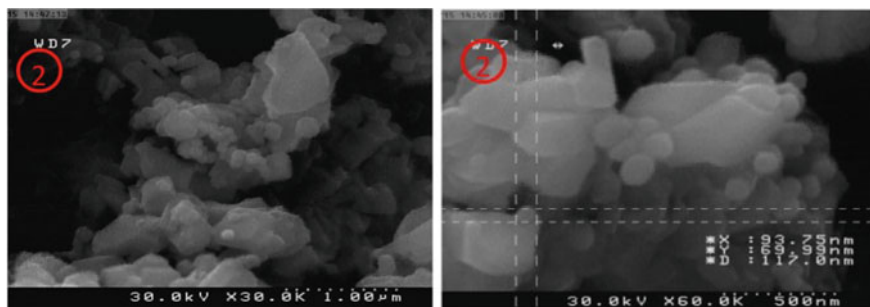


Fig. 4.31 SEM images of ZnO nanostructures prepared by thermolysis of the PMC at 873 K without (left) and with surfactant at 473 K (right). Reproduced with permission from Ref. [314]. Copyright (2016) Elsevier

ZnO NPs were synthesized from the thermolysis of nanocompound $[\text{Zn}(5,5'\text{-di-tert-butyl-bpy})\text{Cl}_2]_n$ at 873 K and the analogous compound, $[\text{Zn}(5,5'\text{-dimethyl-bpy})\text{Cl}_2]_n$, by two different methods (with and without surfactant) [396]. SEM images show that APS of ZnO NPs is 78 and 50 nm for these compounds, respectively.

It should be noted the unique method of manufacturing ZnO hexagonal tubes and rings from Zn-PMC based on two kinds of carboxy-functionalized organic building blocks (salphen ligand N,N' -phenylenebis(salicylideneimine)dicarboxylic acid and 1,4-benzenedicarboxylic acid) in 1:5 molar ratio (Fig. 4.32, left) [84]. In this process, the CPs acted as sacrificial templates for the growth of ZnO hexagonal tubes and rings using thermolysis. This simple method is a new paradigm in preparing the desired MO NPs [84, 329] and was easily extended to other materials [13, 70, 270, 397–404]. At the early stage of the growth process, the reaction product consists exclusively of hexagonal disks (Fig. 4.32, right, a). During heat treatment, a lateral growth of secondary CPs began on the initial disk templates without an apparent change in the disk thickness (Fig. 4.32, right, b). The template-directed growth process upon heating was also accompanied by a gradual dissolution of the templates. The complete removal of the starting templates with polar organic solvents such as DMF in the final stage of particle growth led to the formation of hexagonal rings of CPs with an average internal diameter of 2 mm and a thickness of 1 mm (Fig. 4.32, right, c). Amorphous CP rings can be used to prepare polycrystalline ZnO rings. Conversion to ZnO can be achieved by thermolysis at 823 K (Fig. 4.32, right, d). It is important that the hexagonal ring-shaped crystal morphology is maintained during solid-state thermolysis. The wurtzite structure and elemental composition of the ZnO rings are shown.

2D CP $[\text{ZnLH}_2\text{O}]_n$, where L is the thiodiacetate ligand $\text{S}(\text{CH}_2\text{COO})_2^-$, is thermolyzed at $T > 573$ K to obtain a ZnO sponge with a surface area of $40 \text{ m}^2 \text{ g}^{-1}$, which makes it an attractive SSP for nanoporous ZnO [405–407]. A porous ZnO structure with an extensive connection of thick flakes containing large pores of an

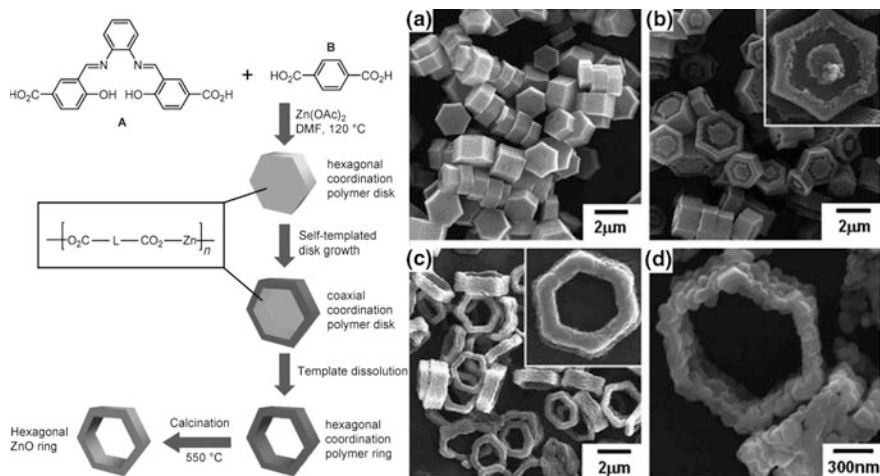
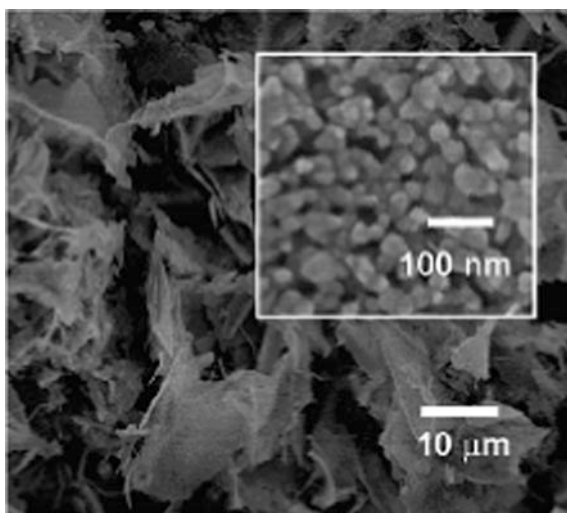


Fig. 4.32 (left) Proposed mechanism for the synthesis of micrometer-sized hexagonal ZnO rings by a combination of template-directed CP growth and thermolysis. $-\text{O}_2\text{C}-\text{L}-\text{CO}_2-$ = deprotonated A or B, (right) **a** SEM image of the hexagonal CP disks formed at the early stage of the particle growth process. **b, c** SEM images of the CP microstructures formed at the later stages of the growth process during heat-up (insets are high-magnification SEM images of the as-synthesized microstructures). **d** High-magnification SEM image of the ZnO rings formed after thermolysis at 823 K. Reproduced with permission from Ref. [84]. Copyright (2009) John Wiley and Sons

Fig. 4.33 SEM image of ZnO from thermolysis at $T > 573$ K. The photograph includes magnified pictures showing the fine structure of ZnO flakes. Reproduced with permission from Ref. [405]. Copyright (2006) American Chemical Society



average diameter of 10 μm is observed (Fig. 4.33). The fine structure of a single flake consists of countless ZnO crystals of an average size of 10 nm (inset of Fig. 4.34). The formation of ZnO flakes may be due to a change in the coordination modes from the octahedral to the tetrahedral environment of the Zn^{2+} cation.

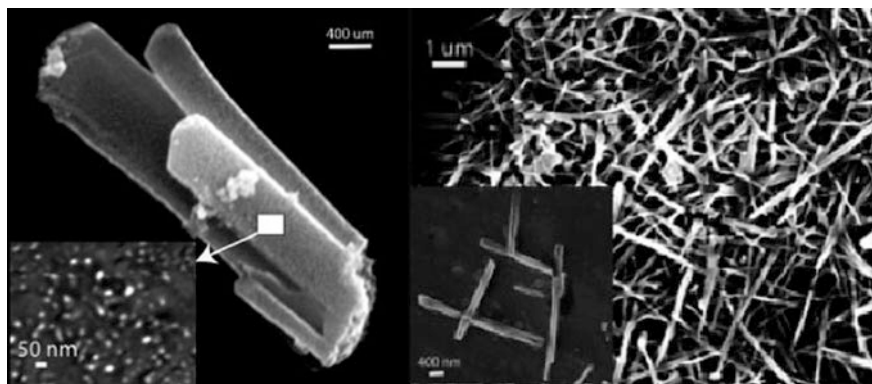
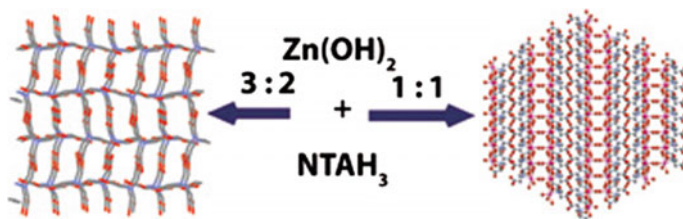


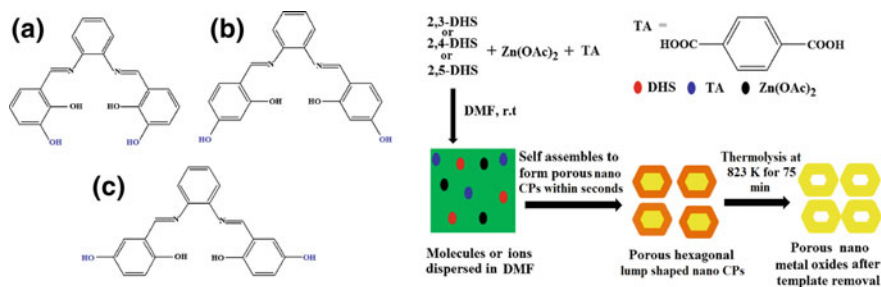
Fig. 4.34 SEM micrographs of microwafers made of ZnO NPs (left) and SEM micrographs of ZnO microwires (right). Reproduced with permission from Ref. [87]. Copyright (2007) John Wiley and Sons



Scheme 4.10 Scheme of synthesis of two different MOFs based on Zn(II) and nitrilotriacetic acid. Reproduced with permission from Ref. [87]. Copyright (2007) John Wiley and Sons

Nitrilotriacetic acid (NTAH_3) reacts in the solid phase with zinc hydroxide to form two different MOFs by changing the metal to ligand ratio (Scheme 4.10) [87]. An infinite array of metallocycles forms interesting ladder and rectangular net-like structures. The first mononuclear PMC contains a 1D zigzag infinite water chain. The stability of the water chain is due to strong H-bond interactions with the carboxylate group and the metal-bound water molecules. The second binuclear PMC contains a very rare μ -oxo carboxylato bridge, where one carboxylate ligand simultaneously binds to three metal centers.

The thermolysis of the first PMC at 973 K for 6 h in a muffle furnace leads to wafers of ZnO with a length of 0.2–1.2 mm. The average size of these wafers remains unchanged with a longer reaction time, up to 14 h. The entire wafer is formed from a homogeneous and densely packed array of ZnO NPs with a diameter of 10–60 nm (Fig. 4.34a). The second PMC decomposes above 773 K to form ZnO microwires with a length of 200 nm to 8 μm (Fig. 4.34b). The average size and shape of these microwires does not change with the thermolysis temperature and time. In both cases, a wurtzite structure of ZnO is formed.



Scheme 4.11 (left) Structure of the dihydroxysalphen (DHS) ligands **a** 2,3-DHS, **b** 2,4-DHS, and **c** 2,5-DHS; (right) Schematic representation of the formation of the hexagonal-shaped hollow Zn (II)-based CPs and corresponding zinc oxides. Reproduced with permission from Ref. [408]. Copyright (2016) Elsevier

Of interest are Zn(II)-based nanoCPs obtained at room temperature from three different isomers of the dihydroxysalphen (DHS) ligand with Zn(OAc)₂·2H₂O and 1,4-benzenedicarboxylic acid in a DMF solvent (Scheme 4.11). Easy thermolysis of PMCs under ambient conditions yields porous ZnO hexagonal nanodisks [408].

The results show that the obtained ZnO have different sizes, surface areas, and porosity. In particular, after the thermolysis of CPs, the shape of the obtained ZnO becomes the type of the hexagonal disk due to the removal of the organic template from the hexagonal-lump PMCs, and the average size of the ZnO nanodisks decreases to ~60–80 nm from that of the hexagonal-lump CP precursor (~80–180 nm). This also fits well with FESEM images (Fig. 4.35). Since the size of 2,4-PMC was the smallest, the size of the corresponding 2,4-ZnO is also smaller (~60 nm) than 2,3- or 2,5-ZnO (~80 nm). It is interesting that the size of all ZnO was almost half of the CP precursors, which is due to ~55% removal of the organic fragment from the CPs. The interplanar distance of 0.31 nm in each sample corresponds to the (220) plane of hexagonal ZnO.

It is of interest to select metal-ion exchange in polymer particles, which was achieved due to the labile nature of interactions between the zinc ion and the Schiff base ligand in the open framework of Zn-PMC structures (Fig. 4.36) [409]. Using this ion-exchange approach, CP nano- and microparticles that contain Cu(II), Mn (II), and Pd(II) ions were deliberately synthesized from a single set of particle precursors in a controlled process. It is interesting that the particle transformation can even be controlled by the naked eye. During thermolysis at elevated temperatures, these composite particles can be converted into hybrid MO NPs with pre-determined morphologies in high yields.

ZnO NPs of different sizes were obtained by thermolysis of PMC [Zn₂L(DMF)₂]_n (L = 1,2,4,5-benzenetetracarboxylate) at 873 K in an air atmosphere. The size and morphology of ZnO NPs are determined by the particles size of the PMC; in particular, the decrease in the PMC particles size leads to a decrease in the particle size of ZnO NPs [359]. A Zn(II) MOF, [Zn₂L(DMF)₂]_n, based on the same ligand, was synthesized using the thermal gradient approach and sonochemical

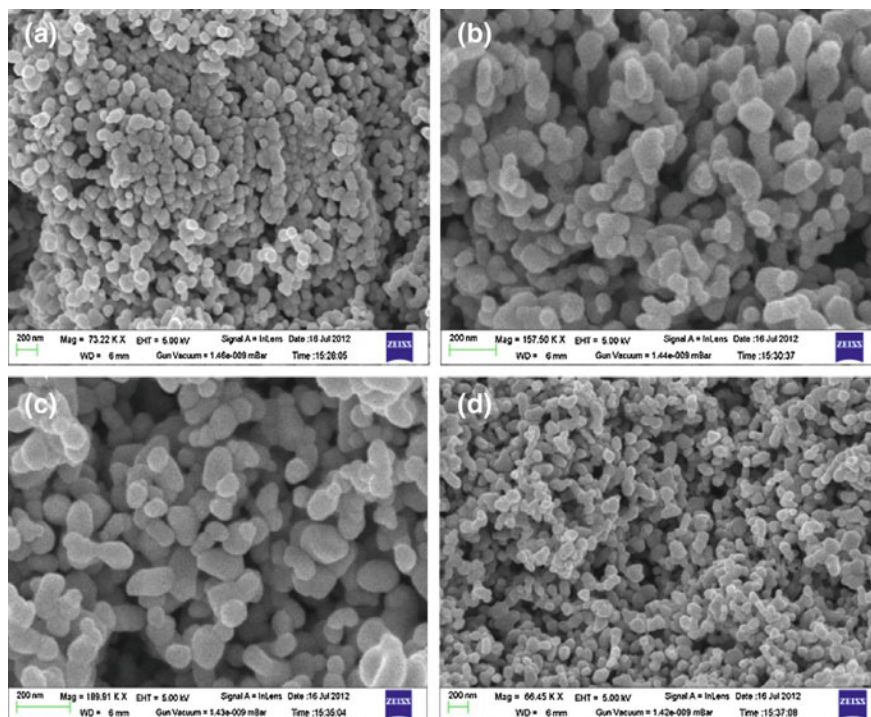


Fig. 4.35 FESEM image of the ZnO **a** 2,3-ZnO, **b**, **c** 2,4-ZnO, and **d** 2,5-ZnO obtained from corresponding CPs after thermolysis at 823 K for 75 min. Reproduced with permission from Ref. [408]. Copyright (2016) Elsevier

irradiation. The SEM image of the product obtained in the direct thermolysis of MOF single crystals at 873 K shows the formation of ZnO NPs (Fig. 4.37, left). The size of ZnO NPs obtained from the direct thermolysis of the MOF nanostructure prepared by the sonochemical process at 873 K is 37 nm (Fig. 4.37, right). These experiments show that the size of the CP precursor correlates with the size particle of the formed ZnO NPs and that the nanoscale precursor produces smaller particles of ZnO.

It should be noted the use of 4'-(4-pyridyl)-2,2':6',2''-terpyridine (L) as a ligand to obtain three Zn(II) CPs, $[\text{ZnL}(\text{OAc})]\text{ClO}_4$, $[\text{ZnL}_2]$, and $[\text{ZnL}_2](\text{ClO}_4)_2(\text{H}_2\text{O})_{2.9}$. The pure phase of ZnO NPs with different sizes and morphology was obtained by direct thermolysis of each SSP [339].

Hexagonal microcrystalline ZnO was prepared using cysteine Zn-PMC $[\text{ZnL}_2\text{L}]_n$ (L = 2-amino-3-mercaptopropionic acid) as SSP by thermolysis at 873 K for 2 h (Fig. 4.38) [410]. It is important that this synthesis method not only gives a good yield, but also does not require high temperatures or high pressures.

Thus, Zn-PMCs can be suitable SSPs for the production of ZnO nanomaterials and it does not need special conditions such as high temperature, long time, and

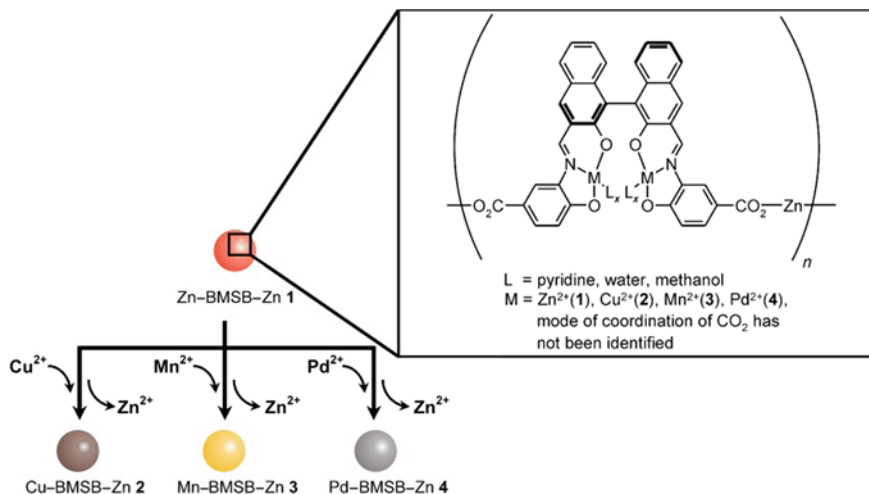


Fig. 4.36 Representation of ion-exchange reaction in Zn-PMC nano- and microparticles. The difference in relative binding strengths means Zn²⁺ ions are readily replaced from the tridentate Schiff base ligand coordination sites (M), but not from the carboxylate sites. BMSB = bimetallic tridentate Schiff base; L = pyridine, water, methanol; M = Zn²⁺ (1), Cu²⁺ (2), Mn²⁺ (3), Pd²⁺ (4). Reproduced with permission from Ref. [409]. Copyright (2006) John Wiley and Sons

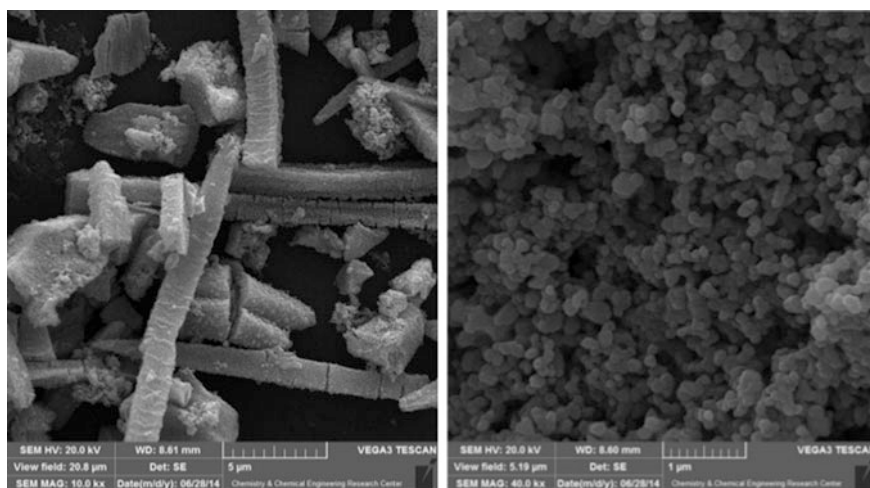


Fig. 4.37 (left) SEM images of ZnO nanostructure prepared by thermolysis of single crystals of MOF at 873 K, (right) SEM image of ZnO nanostructures attained from the direct thermolysis of nanostructure of MOF prepared by sonochemical process at 873 K. Reproduced with permission from Ref. [359]. Copyright (2015) Elsevier

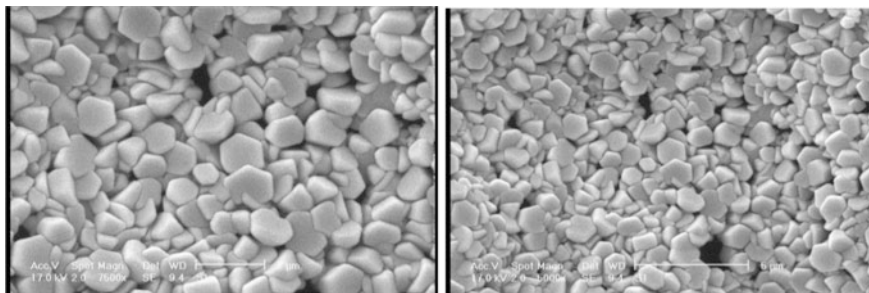


Fig. 4.38 SEM photograph of ZnO (produced by thermolysis of the Zn(II) cysteine complex in air atmosphere) [410]

pressure control [311, 314]. In addition, surfactants are often used to synthesize ZnO nanostructures in order to change the morphology and particle size [19, 20].

4.3.1.2 Cobalt Oxides

The porous Co_3O_4 nano-/microsuperstructures were obtained from the solid-state thermolysis of MOF precursor based on 1,4-benzenedicarboxylic acid at 723 K for 2 h [307]. The Co_3O_4 product consists of 3D superstructures that are actually assembled from hundreds of microscale 2D sheets (Fig. 4.39). The resulting superstructures were assembled by porous microsheet building blocks, which basically consist of homogeneous NPs with a calculated average size of ca. 30 nm.

It should be noted that during MOF thermolysis, an MO nanostructure composed of the same primary particles can be prepared, but with a secondary and tertiary architecture, thus modulating the macroscopic structure of the initial CP. For example, two types of Co_3O_4 nanomaterials with plate-like and rod-like morphology of the NPs, based on the Co-containing plate-shaped ($[\text{Co}_3\text{L}_3(\text{DMF})_4]_n$, *p*-MOF) and rod-shaped ($[\text{CoL}(\text{DMSO})]_n$, *r*-MOF) CPs, consisting of the same constituent units (Co^{2+} and 1,4-benzenedicarboxylate (L)) (Scheme 4.12), were prepared by pseudomorphic transformation [411].

Co_3O_4 NPs were synthesized by thermolysis at 873 K of Co-MOF $\text{Co}_3\text{L}_3(\text{DMF})_4$ (L = 2,6-naphthalenedicarboxylate) [79]. A pure phase of Co_3O_4 with a 250 nm agglomerate structure consisting of smaller primary particles of 25 nm was obtained. The measured low specific surface area ($5.3 \text{ m}^2 \text{ g}^{-1}$) corresponded to a diameter of 250 nm.

$[\text{CoL}(\text{H}_2\text{O})]_n$ polymer, where H_2L is phthalic acid, is introduced as an SSP for the synthesis of Co_3O_4 NPs in the presence of OA and TPP [412]. Injection of organic surfactants, such as OA and TPP, into molecular SSPs gives samples with size control, narrow size distributions, and crystallinity of individual nanocrystals. The NPs with APS of about 20–30 nm are not completely spherical, but each particle is separated from its neighbors by the organic surfactant shell (Fig. 4.40a, b).

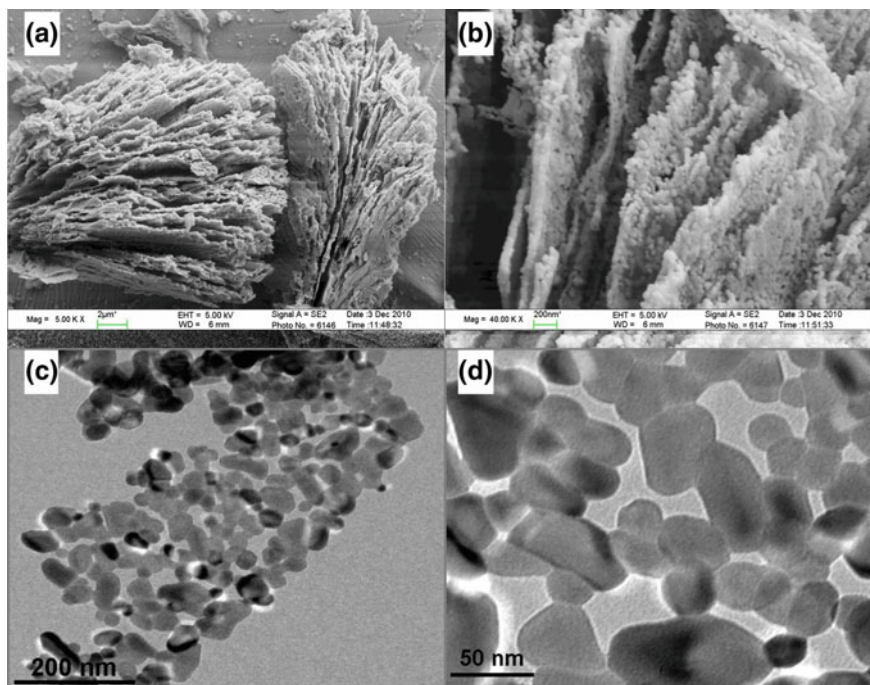
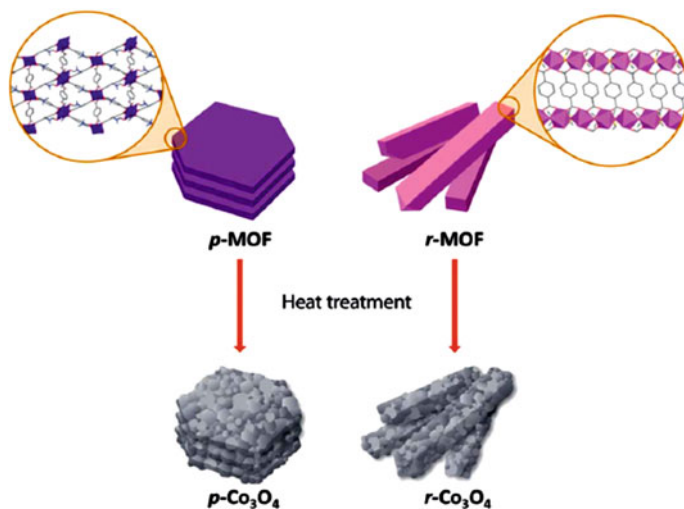


Fig. 4.39 Typical FESEM images (a, b) and TEM images (c, d) of Co_3O_4 nano/microsuperstructures [307]



Scheme 4.12 Scheme of pseudomorphic conversion of Co-based MOFs. Reproduced with permission from Ref. [411]. Copyright (2014) Royal Society of Chemistry

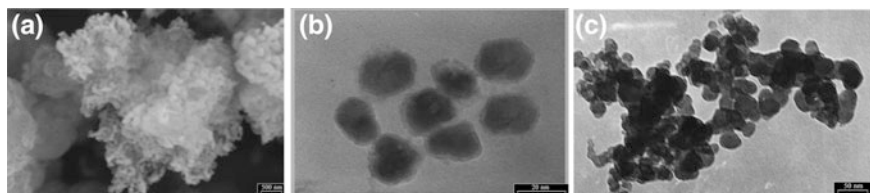
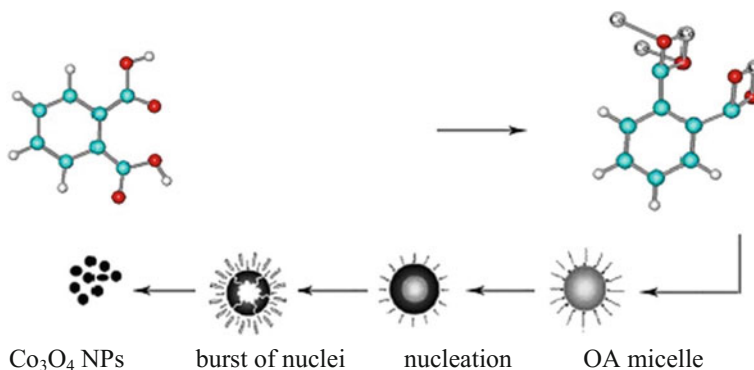


Fig. 4.40 **a** SEM, **b** TEM images of Co_3O_4 NPs obtained in the presence of OA and TPP, and **c** TEM image of Co_3O_4 NPs obtained in the presence of OA without TPP. Reproduced with permission from Ref. [412]. Copyright (2010) Elsevier



Scheme 4.13 Proposed mechanism for preparation of $[\text{CoL}(\text{H}_2\text{O})]_n$ as SSP and Co_3O_4 NPs as final product. Reproduced with permission from Ref. [412]. Copyright (2010) Elsevier

Comparison of NPs obtained in the presence of OA and TPP (Fig. 4.40b) and in the presence of OA without TPP (Fig. 4.40c) shows that the dispersed NPs obtained in the first case are less without any agglomeration.

OA and TPP with a chain length of about 2.0 nm are used as a stabilizer to control particle growth. It is important that OA is coordinated with the surface Co_3O_4 atoms to prevent agglomeration of the NPs. It is believed that $[\text{CoL}]\text{-O}1$ micelles are formed in the presence of OA and during the heat process (408 K for 60 min), Co_3O_4 nucleation occurs (Scheme 4.13).

A simple approach to the preparation of Co_3O_4 NPs based on two hollow-structured CP precursors was developed: CPP-1 prepared in water and CPP-2 obtained in a water/ethanol mixture [413]. Thermolysis of CPP-1 and CPP-2 at 723 K in air leads to the formation of cobalt oxides, namely $\text{Co}_3\text{O}_4\text{-1}$ and $\text{Co}_3\text{O}_4\text{-2}$, respectively. $\text{Co}_3\text{O}_4\text{-1}$ had short rod-like motifs with rough surfaces (Fig. 4.41a, b). The rod-like motifs were porous with a length and width of 100–150 and 30–90 nm separately (Fig. 4.41c, d).

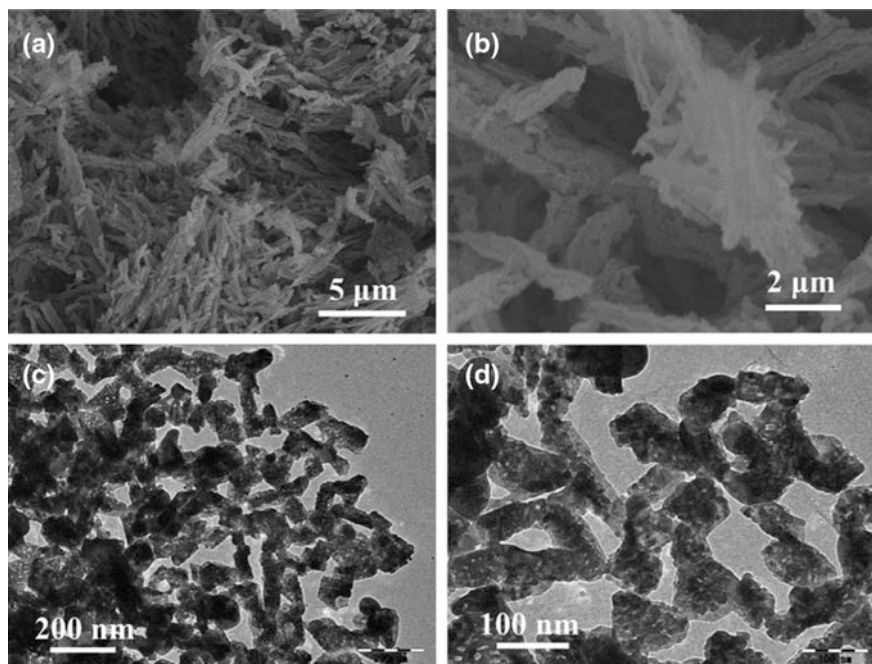


Fig. 4.41 a, b SEM images for the porous Co_3O_4 -1 structure. c, d TEM images show the detailed Co_3O_4 -1 structure NPs clusters to short-rods in comparison with the original precursor CPP-1. Reproduced with permission from Ref. [413]. Copyright (2015) Elsevier

Like Co_3O_4 -1, Co_3O_4 -2 morphology displayed rice-like particles (Fig. 4.42a, b) and was not inherited from their original precursor, CPP-2. Rice-like particles were uneven and arranged in random order with sizes of 5–110 nm (Fig. 4.42c, d).

In addition, thermolysis of CPP-2 under N_2 conditions at 723 K for 30 min may allow the preparation of a carbon/CoO composite. Unlike Co_3O_4 particles, the morphology of C/CoO composite inherited a portion of flake-like shape from the original CPP-2 and these flakes were located in a flower-like motif (Fig. 4.43a). It should be noted that some lamellar structures were parallel, and the others were vertical (Fig. 4.43b).

It is of interest to prepare Co_3O_4 hexagonal nanorings and nanoplates/nanoparticles by thermolysis of Co-MOFs with an organic amine [326]. It was found that the rate of Co(II) release into the reaction system and the spatial hindrance of organic linkers of MOFs determine the final morphology of Co_3O_4 .

4.3.1.3 Iron Oxides

MOFs with various architectures and morphologies were recognized as promising SSPs/templates for the development of porous iron oxides [38, 81, 267, 282, 307,

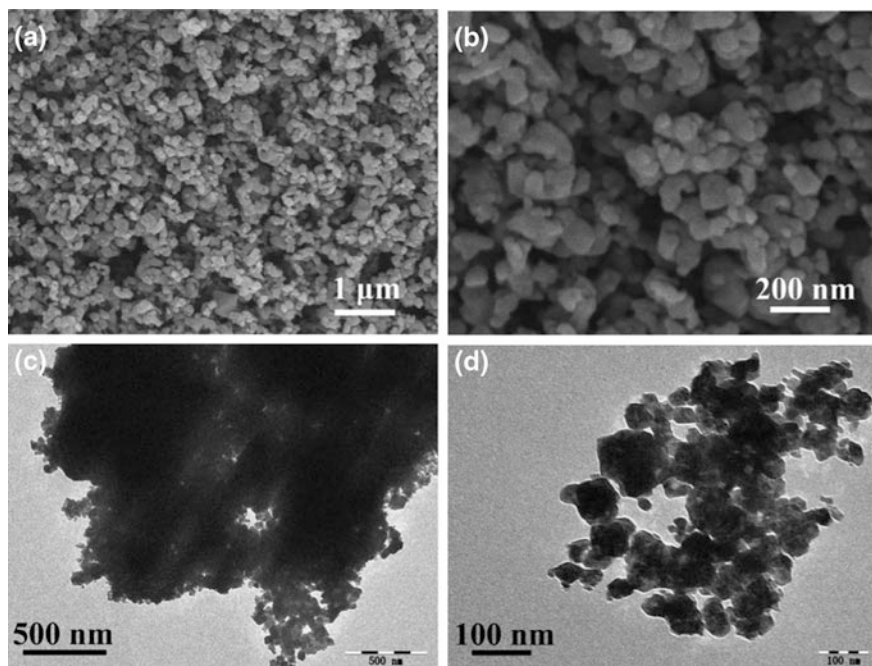


Fig. 4.42 a, b SEM images for the porous $\text{Co}_3\text{O}_4\text{-2}$ structure. c, d TEM images show the $\text{Co}_3\text{O}_4\text{-2}$ particles. Reproduced with permission from Ref. [413]. Copyright (2015) Elsevier

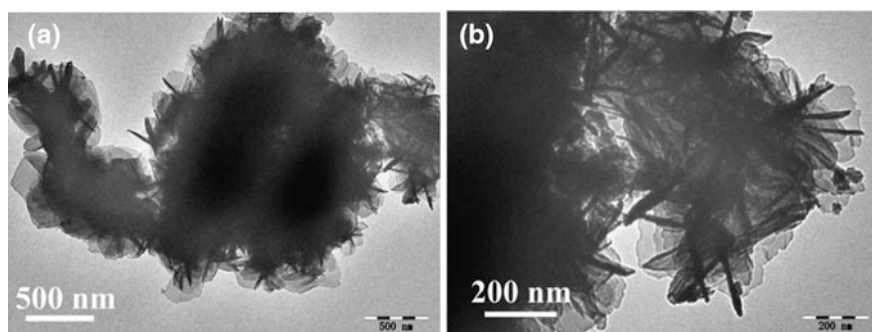


Fig. 4.43 a, b TEM images for C/CoO composites structure which inherited the morphology of CPP-2 precursor. Reproduced with permission from Ref. [413]. Copyright (2015) Elsevier

313, 414–417]. In particular, the $\alpha\text{-Fe}_2\text{O}_3$ and Fe_3O_4 nanorods were obtained by monitoring the thermolysis conditions of MIL-88B [39]. It was demonstrated that thermolysis in air can provide only hematite ($\alpha\text{-Fe}_2\text{O}_3$) by direct thermal transformation of MIL-88B, whereas a two-stage method (thermolysis followed by heating in an inert atmosphere) yields magnetite (Fe_3O_4). The two-step thermolysis

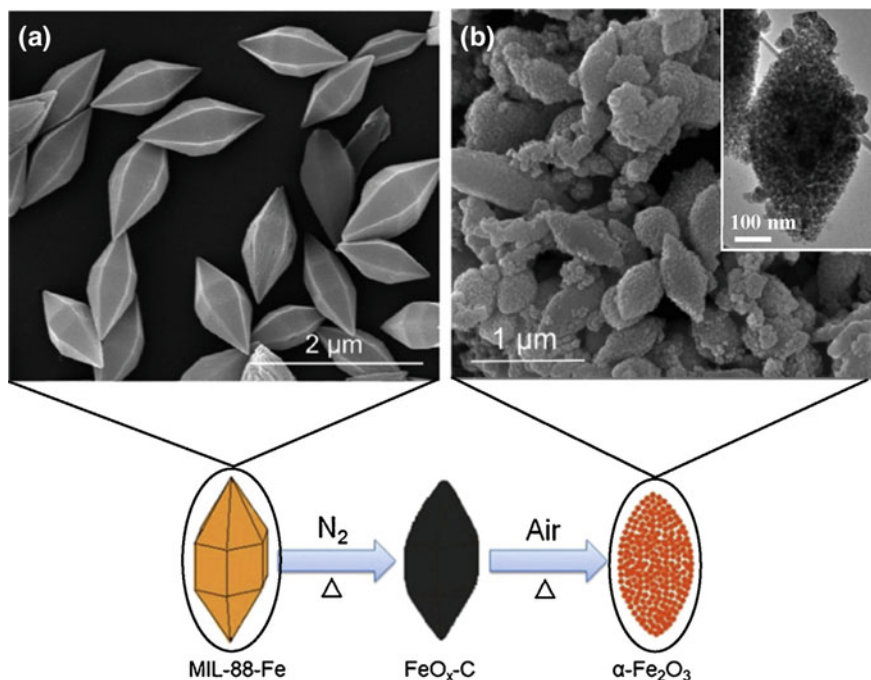


Fig. 4.44 Scheme of the preparation of porous $\alpha\text{-Fe}_2\text{O}_3$ together with the SEM micrographs acquired for **a** the MIL-88-Fe crystals obtained by solvothermal synthesis and **b** the $\alpha\text{-Fe}_2\text{O}_3$ NPs produced after MOF thermolysis in air. *Inset* TEM image of an $\alpha\text{-Fe}_2\text{O}_3$ particle formed by aggregated 20 nm-sized $\alpha\text{-Fe}_2\text{O}_3$ NPs. Reproduced with permission from Ref. [40]. Copyright (2012) American Chemical Society

method of MIL-88(Fe) as a sacrificial template, including thermolysis in N_2 medium and oxidation in air, resulted in the spindle-like mesoporous structures of Fe_2O_3 with a surface area of $75 \text{ m}^2 \text{ g}^{-1}$ [40]. The MOF morphology was retained after thermolysis, and the resulting iron oxide consisted of aggregated 20 nm-sized NPs, between which non-ordered mesopores formed (Fig. 4.44).

Porous $\gamma\text{-Fe}_2\text{O}_3$ NPs were prepared by solid-state thermolysis of a mesoporous Fe(III) carboxylate crystal, MIL-100(Fe) [418]. This nanomaterial has a relatively large specific surface area of $123.5 \text{ m}^2 \text{ g}^{-1}$, which is expected to benefit from a two-step thermolysis of the template MIL-100(Fe). In addition, the pore size distribution shows that most of the pore is concentrated at 10 nm, which indicates that the mesopores are effective for $\gamma\text{-Fe}_2\text{O}_3$. The average size of Fe_2O_3 nanorods obtained from MIL-100(Fe) at temperatures of 623, 823, and 1023 K is 50, 150, and 200 nm, respectively [419]. As a rule, the surface area, pore volume and pore size decrease with increasing thermolysis temperature, which also agrees with the fact that the thermoregulated crystal growth reduces porosity with increasing thermolysis temperature.

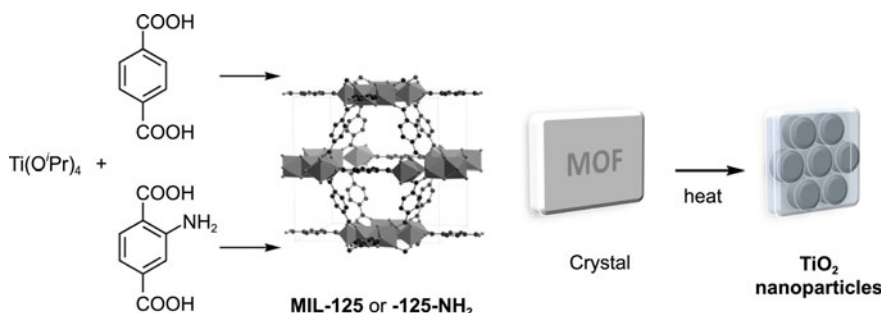
Over the past decade, magnetite (Fe_3O_4) nanostructures have attracted much attention due to their numerous applications in the field of information storage, ferro-fluids, magnetic refrigeration, catalysis, bio-medicine, etc. [420–427]. For these reasons, thermolysis methods have been successfully used to synthesize various 0D, 1D, 2D, and 3D Fe_3O_4 nanostructures with shapes of particles, spheres, polyhedra, belts, tubes, plates, and flowers. For example, iron(III) oxide NPs were obtained by thermolysis of Fe(II) 1D CP, $[\text{FeL}_2](\text{SCN})_2 \cdot \text{MeOH}$, where L is 4'-(4-pyridyl)-2,2':6',2''-terpyridine, in OA (surfactant) at 559 K in an air atmosphere [428]. It turned out that Fe(II) CPs are suitable SSPs for simple one-pot preparation of iron oxide nanomaterials.

4.3.1.4 Titanium Oxides

Thermolysis of Ti-MOFs (MIL-125 and MIL-125- NH_2) at 623 K for 6 h in the air produced TiO_2 NPs of ca. 10 nm in diameter (Scheme 4.14) [429].

The resulting NPs were randomly aggregated in each crystalline particle of their MOF precursors. When MIL-125 and MIL-125- NH_2 were respectively heated at 623 K for 6 h in air, TiO_2 anatase particles (called $\text{TiO}_2(1)$ and $\text{TiO}_2(2)$) were obtained with almost identical particle sizes and shapes (Fig. 4.45a). $\text{TiO}_2(1)$ is formed as thick rectangular plates with ca. 200 nm in size (Fig. 4.45b), whereas $\text{TiO}_2(2)$ particles are sharp rectangles with a large size, ca. 500 nm (Fig. 4.45c). The particle sizes were calculated as ca. 10 nm for $\text{TiO}_2(1)$ and $\text{TiO}_2(2)$ particles.

It is important that each TiO_2 particle is not a single crystal, but an aggregate consisting of randomly oriented ~ 10 nm TiO_2 particles (Fig. 4.46). The lattice fringes of each NP correspond to the d-spacing (0.36 nm) of the (110) crystallographic plane (Fig. 4.46, inset). It is interesting that these ~ 10 nm particles aggregate to form larger particles with well-developed surfaces, which is analogous to their MOF precursor crystals. This means that the formation of TiO_2 NPs occurs within each particle and not with the participation of interparticle reactions. In other



Scheme 4.14 Steps for the production of the aggregated TiO_2 NPs by the thermolysis of MIL-125 or MIL-125- NH_2 crystals. Reproduced with permission from Ref. [429]. Copyright (2014) Korean Chemical Society

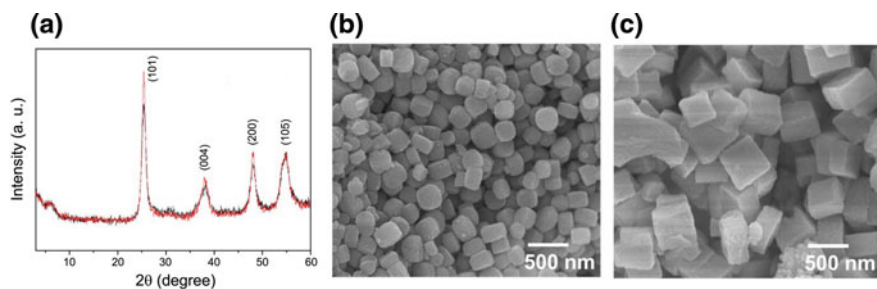


Fig. 4.45 **a** Overlapped power XRD patterns of $\text{TiO}_2(1)$ and **c** $\text{TiO}_2(2)$, and SEM images of **b** $\text{TiO}_2(1)$ and **c** $\text{TiO}_2(2)$. Reproduced with permission from Ref. [429]. Copyright (2014) Korean Chemical Society

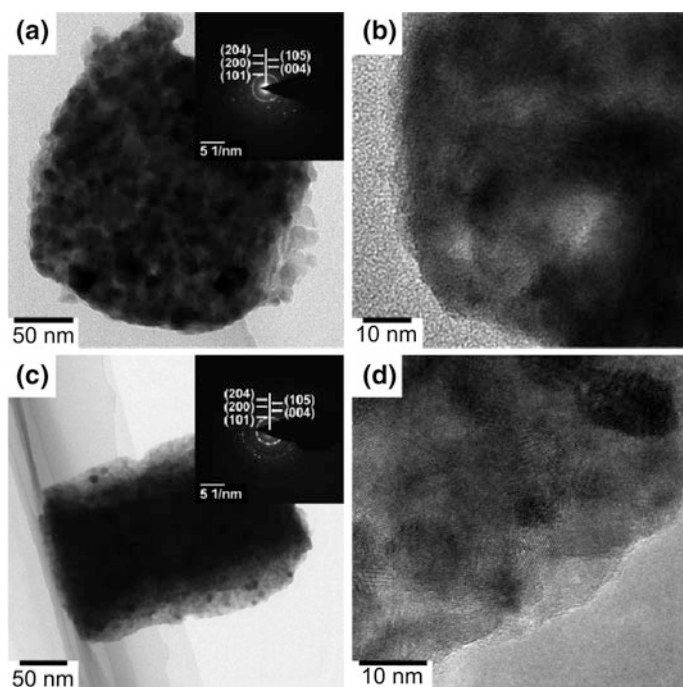


Fig. 4.46 **a, b** TEM images of $\text{TiO}_2(1)$ (*inset* SAED pattern); **c, d** TEM images of $\text{TiO}_2(2)$ (*inset* SAED pattern). The images **b** and **d** show random aggregation of small NPs with about 10 nm domains. Reproduced with permission from Ref. [429]. Copyright (2014) Korean Chemical Society

words, 10 nm TiO_2 NPs are formed in each MOF crystal during thermolysis and become aggregated and stabilized while maintaining the original morphology of the MOF crystal.

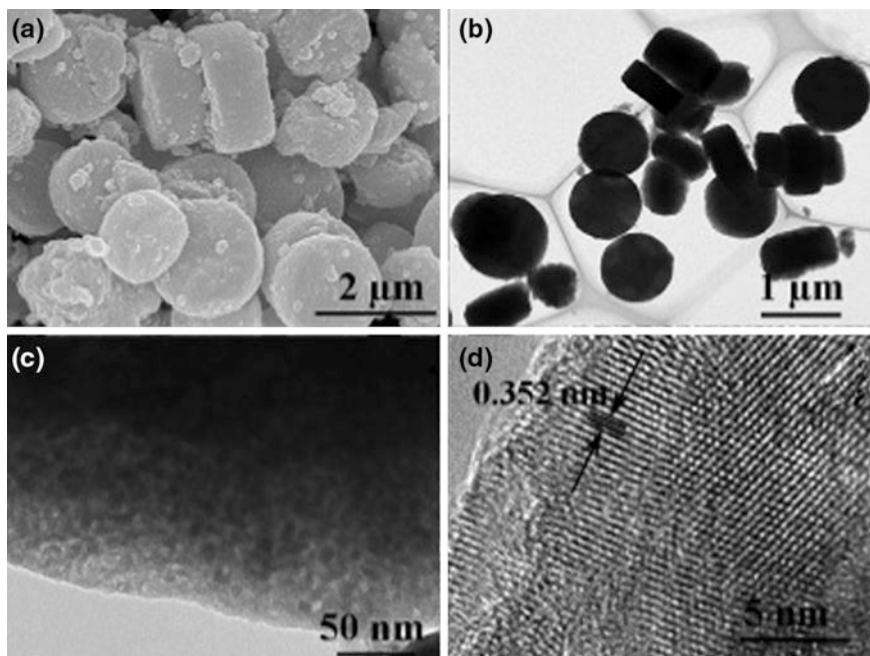
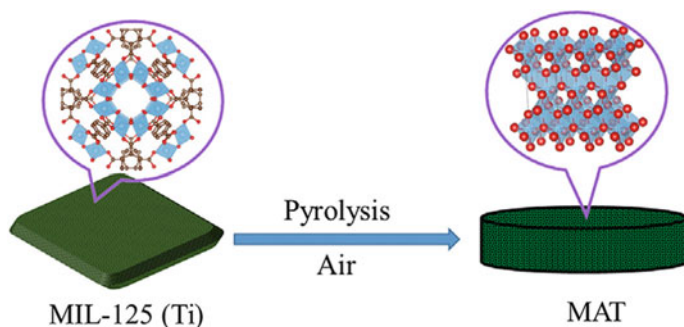


Fig. 4.47 SEM (a), TEM (b, c), and HRTEM (d) images of MAT. Reproduced with permission from Ref. [430]. Copyright (2016) Elsevier

Mesoporous anatase TiO_2 (MAT) with disk-like morphology was prepared by direct thermolysis of MIL-125(Ti) in air [430]. The disk-shaped particles with an average diameter and a thickness of around 1 μm and 400 nm, respectively, are observed (Fig. 4.47a). A porous nature of a material with a pore size of several nanometers was obtained (Fig. 4.47b, c). A single microsize disk-type particle consists of interconnected NPs of ca. 10 nm (Fig. 4.47c). In addition, a lattice fringe width of 0.352 nm corresponds to the interplanar spacing of the anatase $\text{TiO}_2(101)$ plane (Fig. 4.47d).

The mechanism of formation of MAT from high porous MOF (average pore size ~ 1.25 nm) is schematically illustrated in Scheme 4.15 [26]. During the thermolysis of the precursor, Ti^{4+} was converted to TiO_2 , while carbon and other elements were oxidized into gas molecules. The gas was gradually released from the precursor along the micropore channels and, accordingly, the sizes of the secondary particles decreased, which ultimately led to an increase in the micropores in the mesopores.



Scheme 4.15 Schematic illustration of the formation mechanism of MAT. Reproduced with permission from Ref. [430]. Copyright (2016) Elsevier

4.3.1.5 Manganese Oxides

Thermolysis of the MOF precursor in an air-saturated NaOH solution results in the displacement of ligands by oxygen, and γ - MnO_2 nanowire formation with diameters of 20–40 nm grown in the [002] crystalline direction [54].

Temperature is an important parameter controlling the phase composition and morphology of the nanostructures obtained. Thus, the controlled thermolysis of $[\text{Mn}_2\text{L}(\text{DMA})_2]_n$ (L is *meso*-butane-1,2,3,4-tetracarboxylate, DMA is N, N-dimethylacetamide) [395] and $[\text{Mn}_2\text{L}']$ (L' is 2,5-dihydroxyterephthalate) [431] by changing the temperature and the atmosphere results in the formation of a number of nanoporous manganese oxides with different degrees of oxidation: MnO, Mn_3O_4 , Mn_5O_8 , and Mn_2O and maintaining the initial morphology of the original precursor (Fig. 4.48). In addition, a change in the temperature of thermolysis (573–973 K) of $\text{Mn}_2(\text{L}')$ [431] leads to a decrease in lattice defects, increasing the crystallinity degree of the thermolysis products. It is important that rare low-valence oxide MnO and metastable phases of Mn_5O_8 with nanoporous architecture are thus obtained. In other words, MOF thermolysis can significantly enrich the composition, structure, and functional properties of the nanoporous MO materials obtained [41].

A variety of α - Mn_2O_3 nanostructures were obtained from the nitrogen-rich energetic CP $[\text{Mn}(\text{L})(\text{H}_2\text{O})_2]_n$ (L = 1H,1'H-[5,5'-bitetrazole]-1,1'-bis(olate)) by changing the thermolysis atmosphere [432]. The results show that the energetic constituent and thermolysis conditions are the main factors for obtaining completely different morphologies of thermolysis products. In particular, when the thermolysis reaction occurs under N_2 or O_2 , rod-shaped mesoporous α - Mn_2O_3 with a large specific surface of $50.2 \text{ m}^2 \text{ g}^{-1}$ and monodisperse α - Mn_2O_3 with a size of 10–20 nm can be prepared.

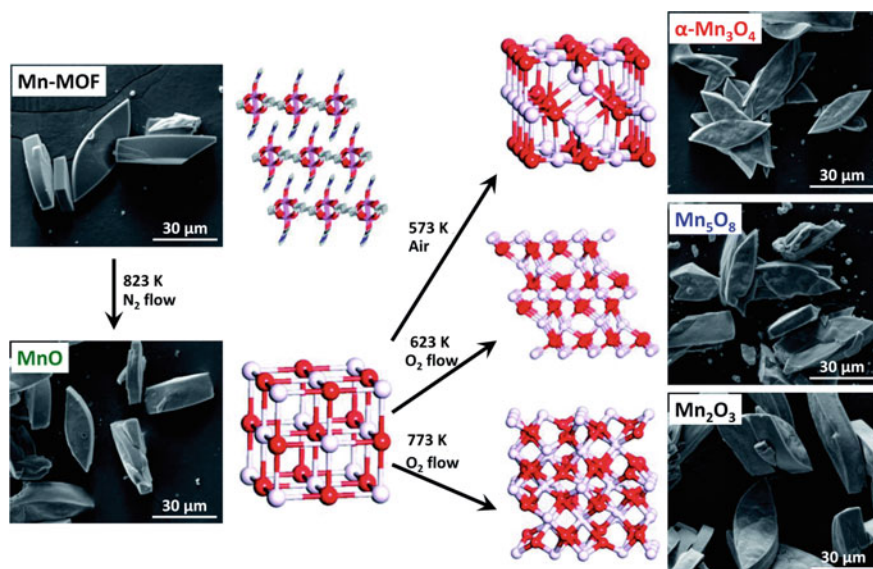


Fig. 4.48 SEM micrographs and diagram of structural transformations of $([Mn_2L(DMA)_2]_n)$ in manganese oxides during thermolysis [395]

4.3.1.6 Cadmium Oxide

Cubic CdO NPs were synthesized from the thermolysis of $[Cd(2,9\text{-dimethyl-phen})(TTA)_2]_n$ in OA at 453 K in air [34]. The bulk powder of the product showed regularly shaped Cd(II) oxide NPs with a diameter of about 35 nm (Fig. 4.49).

It should be noted the preparation of CdO nanowires by thermolysis of Cd CP based on 1,4-benzenedicarboxylic acid, which displays a neutral layered framework along the *ab* plane created of the H-bonding interaction through infinite zigzag chains (Fig. 4.50) [49].

Interestingly, at a higher temperature, the crystal SSP was transformed into homogeneous CdO nanowires (Fig. 4.51a), which indicated an effective and reasonable complex-precursor procedure to obtain 1D crystalline nanomaterials. It can be seen that entangled wires have a high degree of purity, and their diameters range from several to a few ten nanometers, usually about of 20 nm (Fig. 4.51d). In the sample, only Cd and O are present; in addition, the correct stoichiometry of the CdO nanowires is confirmed (Fig. 4.51b). From the morphology of nanowires, it should be noted that some wires in the form of a cluster are assembled by several parts of a single wire (Fig. 4.51c, d).

It is of interest to obtain CdO NPs by the thermolysis of 3D Cd(II) compound, $[CdL_2(H_2O)_2]$ (L^- is 1H-1,2,4-triazole-3-carboxylate), at 923 K in air [433].

Thermolysis of nanoplates of two Cd-MOFs TMU-8 and TMU-9 with V-shaped flexible dicarboxylate ligand 4,4'-oxybis(benzoic acid) and N-donor ligand 1,4-bis(4-pyridyl)-2,3-diaza-1,3-butadiene at 823 K in an air atmosphere yields CdO NPs

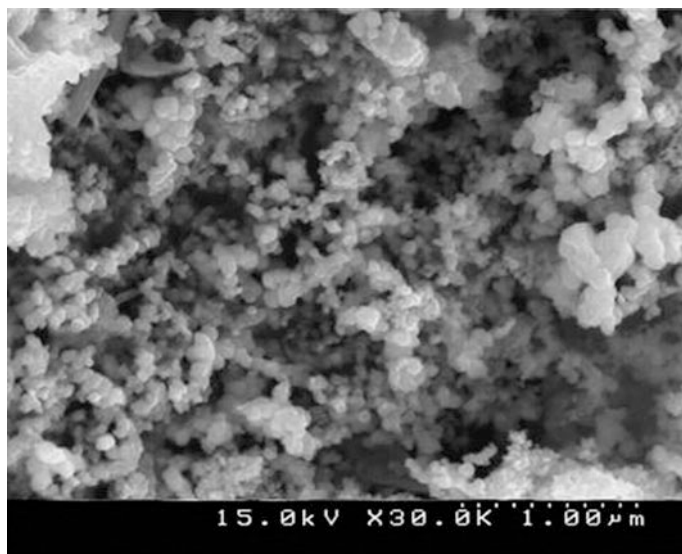


Fig. 4.49 SEM photographs of CdO NPs produced by the thermolysis of CP using OA as the surfactant at 453 K. Reproduced with permission from Ref. [34]. Copyright (2011) Springer Nature

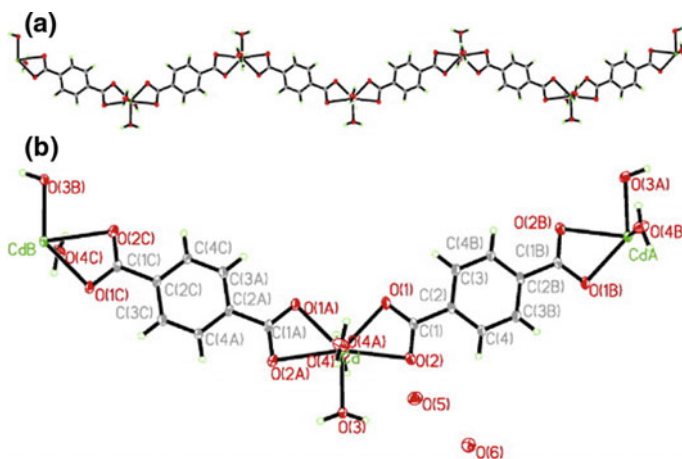


Fig. 4.50 **a** ORTEP diagram of 1D zigzag chain with solvent molecules omitted for clarity and **b** ORTEP diagram of coordination environment of cadmium ion (hydrogen atoms of solvent H_2O were not added). Reproduced with permission from Ref. [49]. Copyright (2008) Elsevier

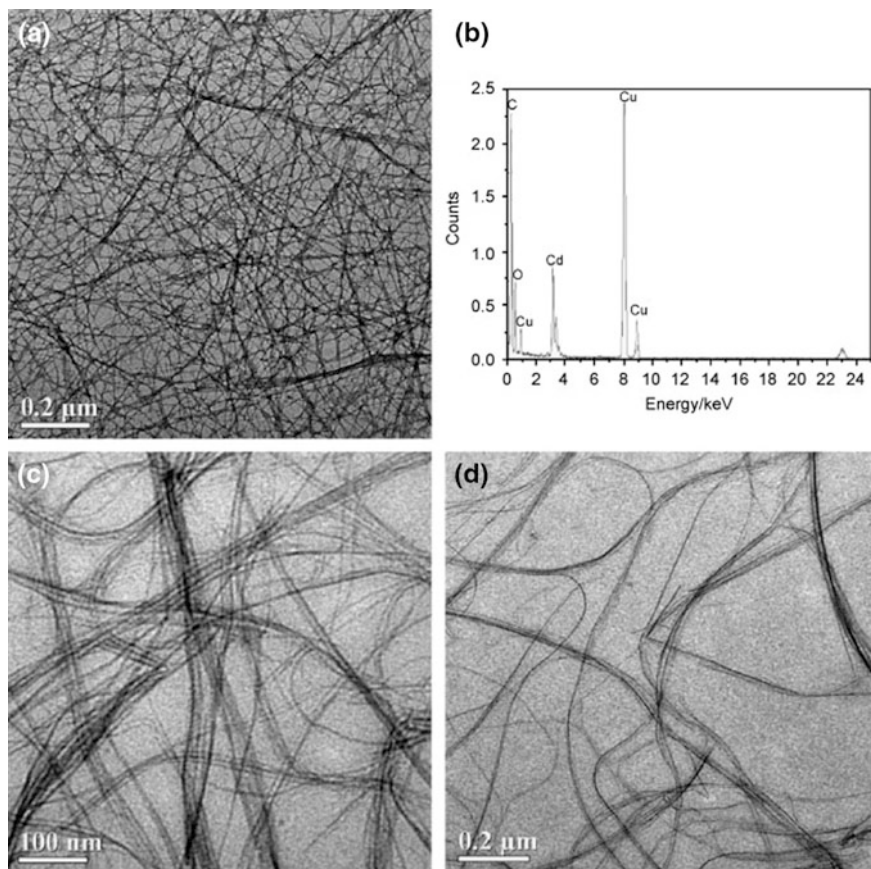


Fig. 4.51 TEM images of (a, c, d) and EDX spectrum (b) obtained from nanowires. Reproduced with permission from Ref. [49]. Copyright (2008) Elsevier

(Fig. 4.52) [434]. The formation of aggregation of CdO NPs in the range of 60–160 nm is observed. It is important that APS of CdO obtained by thermolysis of TMU-9 be less than that of thermolysis of TMU-8, which is related to the structures of these two MOFs that affect the final morphology of CdO NPs [7].

Phase pure CdO NPs were obtained by thermolysis of 3D Cd(II) CP, $[\text{Cd}_2\text{L}(\text{N}_3)_3(\text{CH}_3\text{OH})]_n$ ($\text{L} = 2\text{-pyridinecarbaldehyde isonicotinoylhydrazonate}$), in OA at 453 K in an air atmosphere [435]. It should be also noted CdO NPs synthesized from the thermolysis of Cd(II) CPs, $[\text{CdL}_2(\text{N}_3)_2]_n$ and $[\text{CdL}_2(\text{SCN})_2]_n$ (Fig. 4.53), where L is 2-aminomethylpyridine, at 873 K in air atmosphere for 4 h [435].

The results obtained show that Cd(II) PMCs can be suitable SSPs for the production of nanomaterials and do not need special conditions such as high temperature, long time, and pressure control [13, 314, 342, 434, 436].

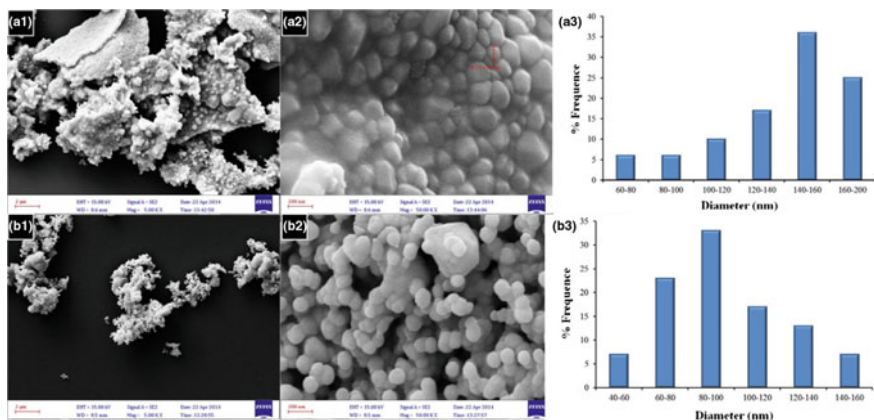


Fig. 4.52 FE-SEM images and the corresponding particle size distribution histogram of CdO NPs prepared by thermolysis of **a** TMU-8 and **b** TMU-9 at 823 K. Reproduced with permission from Ref. [434]. Copyright (2016) Elsevier

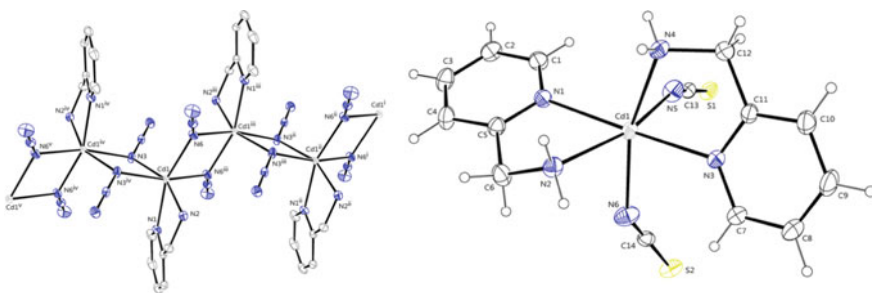


Fig. 4.53 ORTEP diagrams of compounds $[CdL_2(N_3)_2]_n$ and $[CdL_2(SCN)_2]_n$. Reproduced with permission from Ref. [435]. Copyright (2016) American Chemical Society

4.3.1.7 Copper(II) Oxide

1D Copper CP $[Cu(HL)NO_3]_n$ ($H_2L = [2-[1-(2\text{-hydroxy-propylimino})\text{-ethyl}]\text{-phenol}]$) (Fig. 4.54) was used as an SSP to produce single-phase CuO NPs through a solid-state thermolysis procedure [437].

CuO NPs with an average diameter of 40 nm were obtained from direct thermolysis of SSP at 773 K under air (Fig. 4.55).

The thermolysis of nanoscale Cu(II) CP, $[CuL(H_2O)_2]_n$ ($L = 2,6\text{-pyridinedicarboxylate}$), at 773 K under air [438] and MOF $[Cu_3L_2(H_2O)_3]_n$ (where L is benzene-1,3,5-tricarboxylate) gives CuO NPs [415]. In addition, spongy CuO (average diameter varying from 10 to 20 μm) was synthesized [439] by direct thermolysis of microporous MOF $[Cu_3L_2]$ ($L = \text{benzene-1,3,5-tricarboxylate}$) in a horizontal tube furnace in air, in which

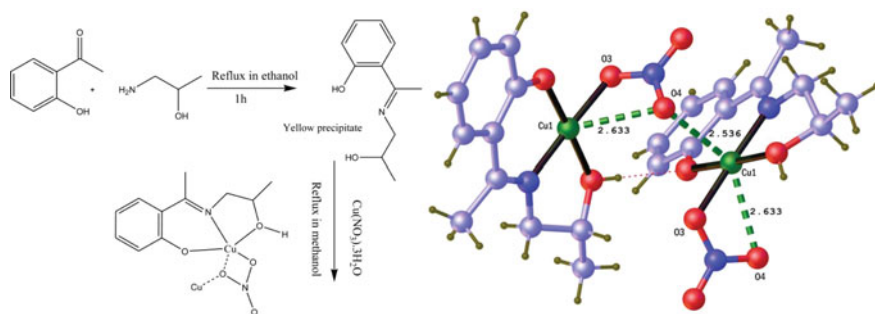


Fig. 4.54 (left) Schematic representation of the synthesis of PMC, and (right) a view of coordination number of Cu. The long Cu–O bonds are indicated by dashed lines. The coordination number of Cu with long Cu–O bonds is 6. Reproduced with permission from Ref. [437]. Copyright (2016) Taylor & Francis

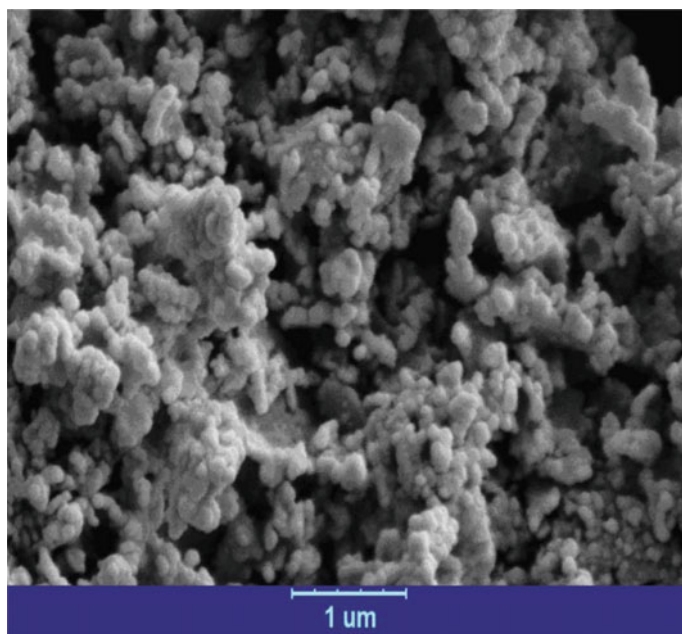


Fig. 4.55 SEM images of CuO NPs prepared by direct thermolysis of Cu(II) CP. Reproduced with permission from Ref. [437]. Copyright (2016) Taylor & Francis

$\text{Cu}_3(\text{L})_2$ was used as a source of Cu and a precursor of the complexing molecule. The thermolysis temperature played a key role in the formation of spongy CuO microstructures. The product consisted of nanosheets with an average edge length of 80–200 nm and a thickness of about 30 nm. The nanostructures of porous CP $\{[\text{Cu}_2(\text{L})_2(\text{dabco})]\text{DMF}\cdot 3\text{H}_2\text{O}\}$ (L = 2-amino-1,4-benzenedicarboxylate, dabco is

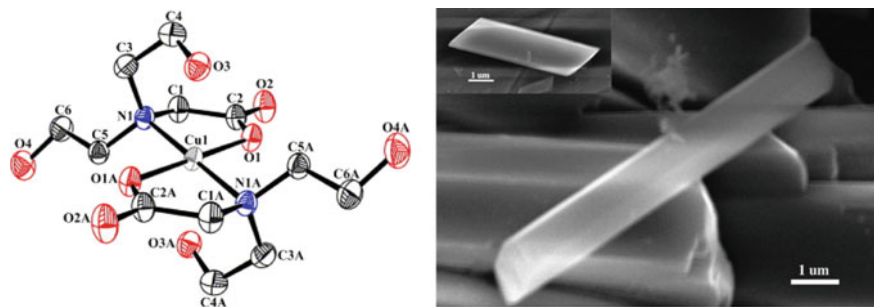


Fig. 4.56 (left) Coordination environment of $[\text{CuL}_2]$. All hydrogen atoms are omitted for clarity, (right) SEM of CuO after thermolysis of **1** at 773 K (6 h). Reproduced with permission from Ref. [440]. Copyright (2007) Elsevier

1,4-diazabicyclo[2.2.2]octane) are thermolyzed at 773 K for 1 h to obtain nanorods and nanotubes of CuO [254].

The blue complex $[\text{CuL}_2]_n$ ($\text{L}^- = \text{N,N-bis(2-hydroxyethyl)glycinate}$) heated to 773 K for 6 h in a muffle furnace leads to the formation of black CuO (tenorite) microplates [440]. The thermolysis product was obtained in the microplate morphology (Fig. 4.56). The length and width of these plates vary from 3 to 12 μm and from 0.5 to 3 μm , respectively. The average size and shape of these plates remain unchanged with a longer thermolysis time, up to 14 h.

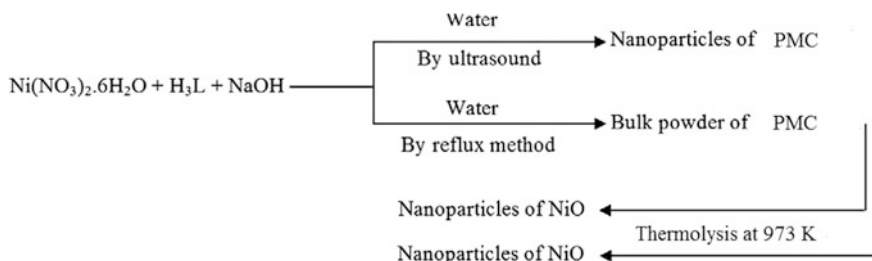
It should be noted that copper oxide NPs have been successfully synthesized by one-step solid-state thermolysis of two MOFs, $[\text{Cu}_3\text{L}_2]$ (**1**) and $[\text{Cu}(\text{L}')(\text{DMF})]$ (**2**), ($\text{L} = \text{benzene-1,3,5-tricarboxylate}$, $\text{L}' = \text{terephthalic acid} = 1,4\text{-benzdicarboxylic acid}$) in an air atmosphere at 673, 773, and 873 K [441]. It is important that the thermolysis temperature plays an important role in the formation of copper oxide NPs.

The conducted studies show that MOFs can be used as the SSPs for obtaining CuO nanomaterials with different and remarkable morphology.

4.3.1.8 Nickel Oxide

Routes of thermolysis [442–444] were studied to obtain nickel oxide NPs. In particular, thermolysis of bulk powder and nanoscale Ni-MOF with cubic building blocks and 1D open channels, in particular, $\{[\text{Na}_{16}(\text{Ni}_8\text{L}_{12})(\text{H}_2\text{O})_{20}(\text{H}_2\text{O})_4](\text{CH}_3\text{CN})(\text{H}_2\text{O})_{18.5}\} \infty$ ($\text{H}_3\text{L} = 4,5\text{-imidazole-dicarboxylic acid}$), at 973 K under air led to NPs with the size and morphology of NiO NPs, depending on the particle size of the parent compound (Scheme 4.16) [445].

The compound $[\text{NiLH}_2\text{O}]_n$, where L is the thiodiacetate ligand $\text{S}(\text{CH}_2\text{COO})_2^{2-}$, was synthesized, and its thermolysis yielded microcrystalline NiS/NiO [363]. The NPs of CP based on 1,4-benzenedicarboxylic acid were thermolyzed at controlled temperature to produce nickel oxide NPs, which have regular multilayered



Scheme 4.16 Materials produced and synthetic methods. Reproduced with permission from Ref. [445]. Copyright (2012) Elsevier

morphology and a high degree of crystallinity [446]. In addition, the NiO NPs had a relatively high BET specific surface area ($112 \text{ m}^2 \text{ g}^{-1}$) and a well-defined pore size (10 nm), and, therefore, showed considerable potential for use in a wide variety of applications.

4.3.1.9 Chromium Oxide

Mesoporous $\text{Cr}_2\text{O}_3/\text{Al}_2\text{O}_3$ with a large specific surface area and a high pore volume was synthesized using MIL-101 as the host matrix and chromium as a precursor along with aluminum isopropoxide as an aluminum precursor [328]. A scalable synthesis strategy for the production of octahedral Cr_2O_3 with a large surface area and porosity was developed by thermolysis synthesis using MIL-101(Cr) as a sacrificial template [298].

4.3.1.10 Palladium Oxide

PdO NPs with a diameter of 5–7 nm were prepared in situ by thermolysis of *meso*-tetrakis(pyridyl)porphyrin and Na_2PdCl_4 in a molar ratio of 1:4 in DMF [447].

4.3.2 Main Group Metal Oxides

Porous In(III) MOF, $[\text{In}_2(\text{OH})_2\text{L}]_n \cdot 2n\text{H}_2\text{O}$ (MIL-60, L = 1,2,4,5-benzenetetracarboxylate) was used to obtain In_2O_3 NPs by direct thermolysis at 723 K under air [448], in which there is no aggregation of particles, and the NPs are clearly different.

It should be noted that indium(III) oxide NPs (50–65 nm) were obtained by thermolysis of $[\text{In}_2(\text{OH})_3(\text{L})_{1.5}]_n$ (L is 1,4-benzenedicarboxylate) at 723 K in air [449]. Also from the thermolysis of the series of In(III) coordination polymer

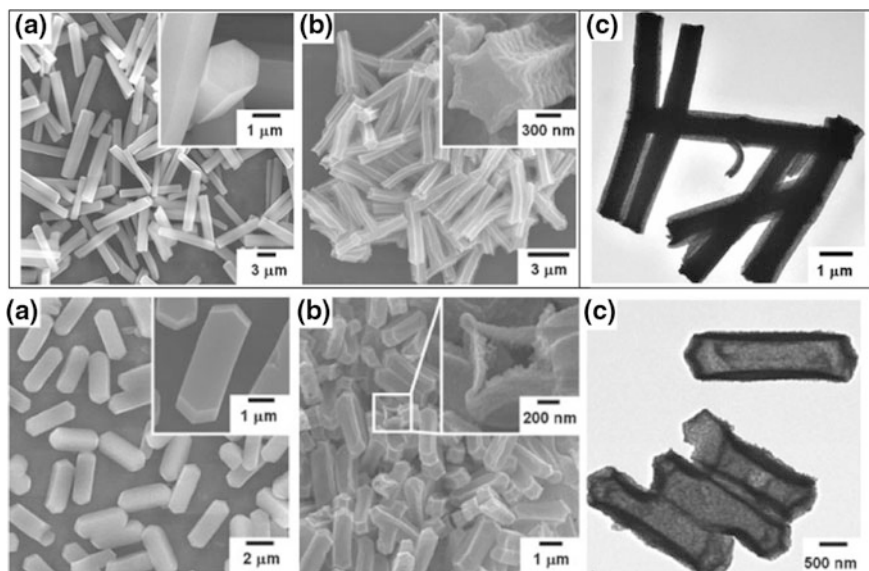


Fig. 4.57 a SEM images of (a-top) hexagonal rod-shaped precursor CPP-1, b (b-top) elongated hexagon-shaped precursor CPP-2. SEM (middle) and TEM (bottom) images of a non-hollow hexagonal rod-shaped In_2O_3 , b hollow elongated hexagon-shaped In_2O_3 . Reproduced with permission from Ref. [80]. Copyright (2009) Royal Society of Chemistry

particles (CPP), CPP-1, CPP-2 [80], CPP-3, CPP-5 [270], CPP-6, CPP-7, and CPP-8 [450], various morphologies of In_2O_3 have been achieved. Hollow and non-hollow In_2O_3 particles with different morphologies can be selectively obtained from PMCs in accordance with their chemical composition and porosity. During thermolysis at 823 K, the hexagonal rod microparticles of the CPP-1 based on 1,4-benzenedicarboxylate and In(III) ions form hexagonal polycrystalline NPs (consisting of ~ 20 nm crystallites) of In_2O_3 in the form of rods whose size is about 35% smaller than the original SSP [80]. A similar character of morphology transformation during thermolysis is shown in the case of CPP-2, consisting of In (III) and 2,6-bis[(4-carboxyanilino) carbonyl] pyridine with the particles in the form of hexagons (Fig. 4.57).

Interesting are porous CPs, CPP-3, and CPP-5 with $[\text{In}(\text{OH})(\text{L})_n]$ unit (L is 1,4-benzenedicarboxylate), which have the same components but have different morphologies, as well as CPP-6, CPP-7, and CPP-8, obtained by the solvothermal reaction of $\text{In}(\text{NO}_3)_3 \cdot x\text{H}_2\text{O}$ and L ligands in which the morphology of compounds changes by simply adding acetonitrile under identical reaction conditions. During thermolysis, the initial PMC precursor morphology was retained [80]. These morphologies include non-hollow microhexagonal rod-shaped, non-hollow hexagonal disk-shaped, hollow microelongated hexagonal-shaped, hollow microellipsoid and rod-shaped, which are polycrystalline In_2O_3 consisting of numerous In_2O_3 NPs with APS of ~ 20 – 40 nm. The difference in composition and

porosity can influence the production of different morphologies of non-hollow and hollow, influenced by the thermolysis mechanism of PMC precursors.

Another MO that can be obtained from PMC thermolysis is lead oxide, which is captivating due to its numerous compositions and phases, such as PbO, Pb₂O, Pb₂O₃, and Pb₃O₄. The use of PMCs as SSPs for the production of PbO has not yet been thoroughly investigated [57, 58, 451–453]. Among the various synthesis methods for the preparation of lead oxide, the thermolysis of lead complexes has advantages due to its relatively low processing costs, much milder processing conditions and the ability to control the grain size. A series of Pb-PMCs was used to form PbO NP [454, 455]. In all cases, PbO obtained from nanoPMCs or using a surfactant has a better morphology or particle size.

Thus, [Pb₂(2,9-dimethyl-phen)₂(μ-N₃)₂(μ-ClO₄)₂]_n [456] was used to obtain PbO NPs. We also note PbO NPs (~25 nm) obtained by thermolysis of plate-shaped nanostructures of 1D Pb(II)-PMC containing the Pb₂(μ-I)₂ motif, [PbLI₂]_n (L = neocuproine or 2,9-dimethyl-phen), at 453 K with OA as a surfactant [457]. The thermolysis of the 3D CP [Pb(phen)(μ-N₃)(μ-NO₃)]_n containing the azide-anion ligand at 453 K with OA as a surfactant gave PbO NPs [458]. The average diameter of the NPs was estimated as 33 nm by the Scherrer equation. 3D Pb(II) CP, [Pb₃(2,9-dimethyl-phen)₂Cl₆]_n (Fig. 4.58, left), obtained by the reaction of PbCl₂ with 2,9-dimethyl-phen was used as SSP for the preparation of PbO NPs by direct thermolysis at 873 K in the air [459]. Diffraction peaks are consistent with the orthorhombic crystalline system. It was found that APS of the NPs is about 70 nm, and the NPs have a narrow size distribution (23–56 nm) and good particle separation (Fig. 4.58, middle). Analysis of the EDX spectrum (Fig. 4.58, right) proved the existence of lead and oxygen in NPs without any impurities, indicating complete removal of the organic part.

NPs of two CPs, [Pb(5,5'-dimethyl-bpy)Cl₂]_n and [Pb(5,5'-dimethyl-bpy)Br₂]_n, were synthesized by ultrasonic at various concentrations [460]. Metal oxide NPs were prepared from CP thermolysis at 873 K in an air atmosphere for 4 h (Fig. 4.59). The formation of lead(II) oxide NPs with an average diameter of about 80 and 90 nm for the first and second CP, respectively, is shown. The XRD pattern corresponds to standard pattern of the orthorhombic PbO structure. It is important that the size of the CP SSP and temperature correlate with the particle size of the resulting lead(II) oxide NPs.

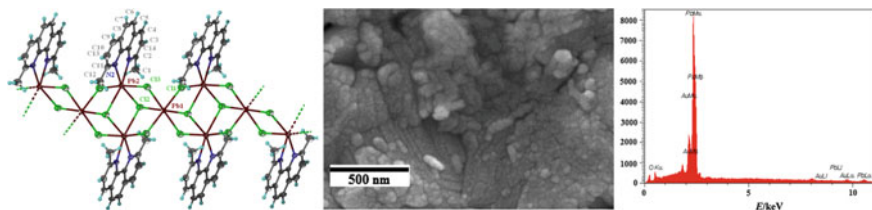


Fig. 4.58 (left) ORTEP diagram of the asymmetric unit of the PMC. Thermal ellipsoids are drawn at 40% probability level; (middle) SEM image, and (right) EDX spectrum of PbO NPs. Reproduced with permission from Ref. [459]. Copyright (2014) Springer Nature

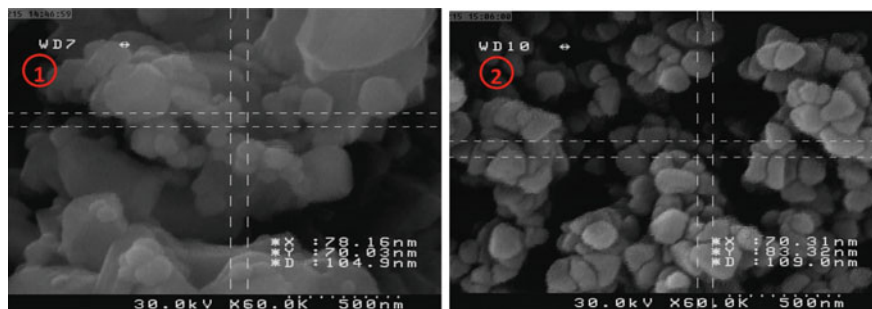


Fig. 4.59 SEM image of PbO nanostructure prepared by thermolysis of first (left) and second CP (right) at 873 K. Reproduced with permission from Ref. [460]. Copyright (2017) Springer Nature

The PMC of Pb(II) nitrate complex with bridging *trans*-1,2-bis(4-pyridyl) ethene (L) ligand, $[\text{Pb}(\mu\text{-NO}_3)_2\text{L}(\text{MeOH})_n]_n$, was used [461] to prepare PbO NPs by two different ways. Nanostructured PbI_2 and PbO were synthesized from Pb(II) CP, $[\text{Pb}(\mu\text{-L})(\mu\text{-I})_2]_n$, where L is pyrazine, by thermolysis with argon and air, respectively [462]. Various N-heterocyclic ligands with carboxyl or carboxamide groups were also used. Thus, after thermolysis of nanobelts of Pb(II) CP, $[\text{Pb}_2]_n$, HL = 3-pyridinecarboxylic acid, a pure phase of nanoscale PbO was obtained at 673 K [386]. The crystalline and nanostructures of two Pb(II) CPs, $[\text{Pb}_2\text{L}_4(\text{MeOH})_n]$ (L = 2-pyrazinecarboxylic acid) and $[\text{Pb}(\text{L}')_2]_n$ (L' = 2-quinolinecarboxylic acid), were heated to 873 K to obtain PbO NPs with different morphology and size [463].

It is of interest to synthesize PbO NPs (~ 30 nm) by thermolysis of the Pb(II) complex, $[\text{Pb}_2\text{L}_2(\text{NO}_3)_4 \cdot \text{MeOH}]_n$, where L is N,N',N''-tris(pyrid-3-ylmethyl)-1,3,5-benzenetricarboxamide, at 453 K with OA as a surfactant [461]. The thermolysis of 2D Pb(II) CPs, $[\text{Pb}_2(\mu_2\text{-L})_2(\text{NO}_3)_4]_n$, where L is 1,6-bis(2-pyridyl)-2,5-diaza-1,5-hexadiene, in OA as a surfactant at 453 and 473 K under air led to PbO particles of about 60 nm [464].

It should be noted the preparation of PbO NPs by thermolysis of 1D Pb(II) CP, $[\text{Pb}_3\text{L}_3(\text{N}_3)_3(\text{NO}_3)_3]_n$ (**1**), (L = pyridin-2-ylmethanamine), at 453 K with OA as a surfactant (Fig. 4.60, top) [465]. The nanostructure of CP was obtained by ultrasonic irradiation in an aqueous methanol solution, and single crystal material was obtained using a heat gradient applied to a solution of the reagents (the “branched tube method”). In these compounds, the three Pb(II) centers have different coordination numbers. In addition, three interesting coordination modes of azide anions (μ_2 -1,1, μ_3 -1,1,3 and terminal azide anions) are observed in the structure. The thermolysis process produces a regular shape of PbO NPs with a diameter of about 20–30 nm (Fig. 4.60, bottom). The final product of PMC thermolysis corresponds to the standard pattern of tetragonal PbO.

PbO NPs can be synthesized from the thermolysis of 1D Pb(II) CP, $[\text{Pb}(\mu\text{-NO}_2)(\mu\text{-L})(\text{H}_2\text{O})_n]_n$ (HL = 2-pyridinecarboxylic acid) under two different conditions with OA and OAm as a bisurfactant (Fig. 4.61a) or OA as a surfactant (Fig. 4.61b) in an

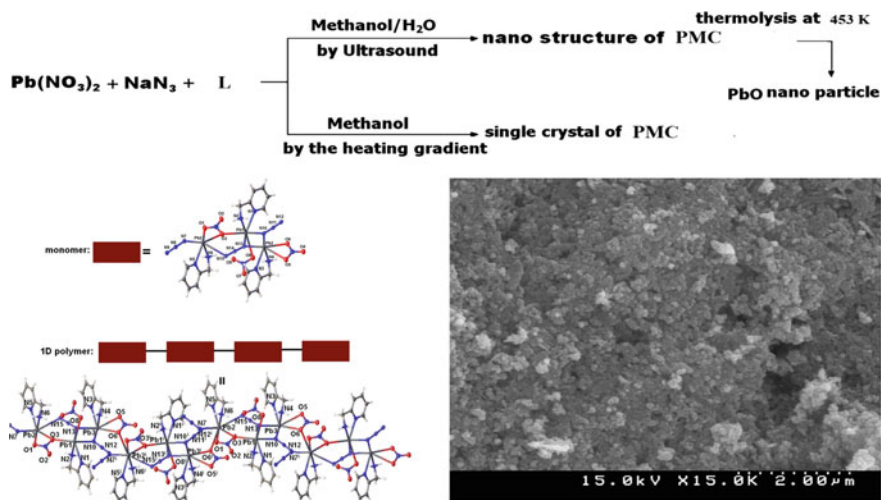


Fig. 4.60 (top) Materials produced and synthetic methods, (bottom, left) From three nuclear building blocks (monomer) to 1D coordination polymer, (bottom, right) SEM photographs of PbO nanopowders (produced by thermolysis of nanoPMC). Reproduced with permission from Ref. [465]. Copyright (2011) Taylor & Francis

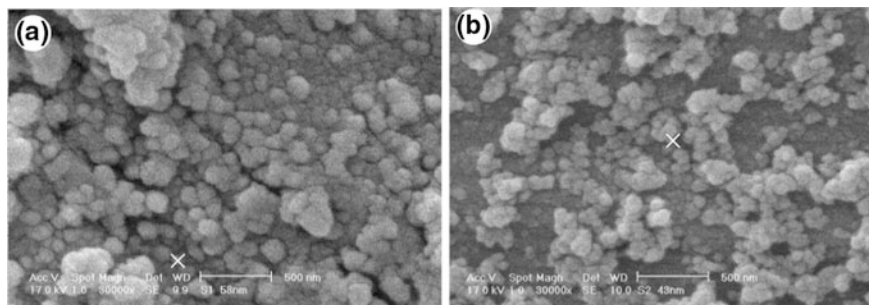


Fig. 4.61 SEM photographs of PbO NPs produced by thermolysis of PMC under two different conditions; **a** using bisurfactant, OA and OAm, and **b** using only OA as a surfactant. Reproduced with permission from Ref. [466]. Copyright (2010) Elsevier

air atmosphere [466]. The final products in the PMC thermolysis are tetragonal PbO NPs of regular shape.

The nanoflower Pb(II) CP, $[\text{PbLN}_3\text{MeOH}]_n$, where L is 2-pyridinecarbaldehyde isonicotinoylhydrazoneate), was synthesized using a sonochemical method, and single crystalline material was obtained using a heat gradient applied to the reagent solution [467]. After thermolysis of CP at 453 K with OA, a pure phase of nanoscale PbO was obtained. At the same time, nanopowders of tetragonal PbO were prepared by thermolysis in an air atmosphere of nanoflowers (Fig. 4.62).

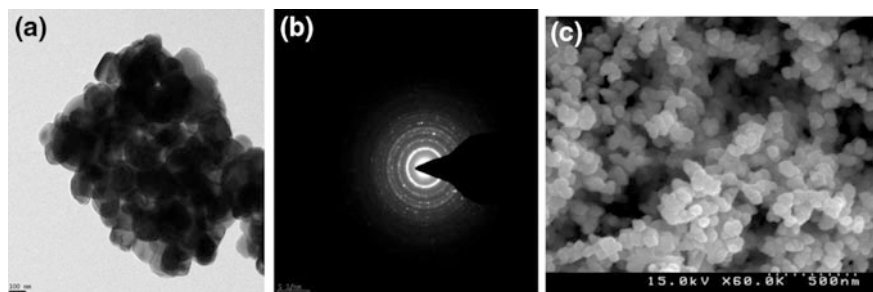


Fig. 4.62 **a** TEM image, **b** SAED pattern, and **c** SEM photographs of PbO nanopowders produced by thermolysis of PMC. Reproduced with permission from Ref. [467]. Copyright (2013) Springer Nature

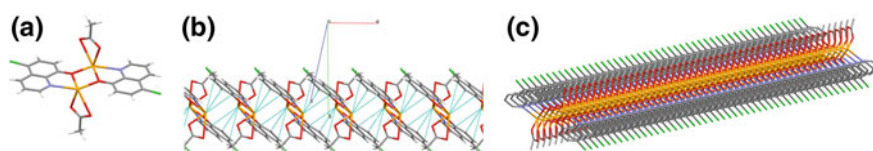


Fig. 4.63 **a** Primary structural building unit of $[Pb_2(L)_2(OAc)_2]_n$, **b** formation of 1D supramolecular polymer as a result of secondary Pb ... C interactions, and **c** another view of this 1D supramolecular polymer, (Pb = orange, O = red, N = blue, C = gray, Cl = green, and H = white). Reproduced with permission from Ref. [468]. Copyright (2017) Elsevier

PMC $[Pb_2L_2(OAc)_2]_n$, (HL = 5-chloroquinolin-8-ol) (Fig. 4.63), synthesized in the presence of MeCN, was used as an SSP to produce PbO NPs by thermolysis in OA [468].

The resulting compounds are PbO NPs (Fig. 4.64a). These NPs have a diameter of 8–27 nm, but the frequency (the number of NPs in each size distribution) of NPs with 10–15 nm diameters is higher than that of others (Fig. 4.64b). In fact, OA forms micelles as nanoreactors, kinetically preventing agglomeration of NPs.

Among the other interesting examples, we note the preparation of PbO from thermolysis of the CPs such as $[Pb_4(\mu-8\text{-hydroxyquinolin})_6(NO_3)_2]_n$ [469], $[Pb(2\text{-quinolincarbaldehyde nicotinohydrazide})(NO_3)_2]_n$ [470], $[Pb(H_2O)(\mu-OAc)(\mu\text{-saccharin})]_n$ [471], $[Pb_3(8\text{-hydroxyquinolin})_2(\mu-Br)_4]_n$ [472], $[Pb(2,3\text{-pyridinedicarboxylic acid})(H_2O)]_n$ [473], $[Pb_2(2\text{-pyridinecarboxylic acid})_2(I)_2]_n$ and $[Pb_2(2\text{-pyridinecarboxylic acid})_2(Br)_2]_n$ [474], $[Pb_2(4\text{-pyridinecarboxylic acid})_2I_2(H_2O)]_n$ and $[Pb(3\text{-pyridinecarboxylic acid})I]_n$ [475], $[Pb(\text{diphenyl acetic acid})_2]_n$ and $[Pb(\text{monophenyl acetic acid})_2]_n$ [62], $[Pb_2(2\text{-Me-8-hydroxyquinolin})_2(\text{MeOH})_2]_n$ [476], and nanostructures of lead(II) oxalate (PbC_2O_4) [477].

As an example of the production of MgO NPs, we note solid-state thermolysis at 923 K of bulk powder and nanosized MOF $\{[Mg(HL)(H_2O)_2 \cdot 1.5H_2O]_n, (H_3L = 4,5\text{-imidazoleedicarboxylic acid})\}$ prepared using two different paths (Fig. 4.65). It is important that the size and morphology of MgO NPs depend on the size and morphology of PMC [478].

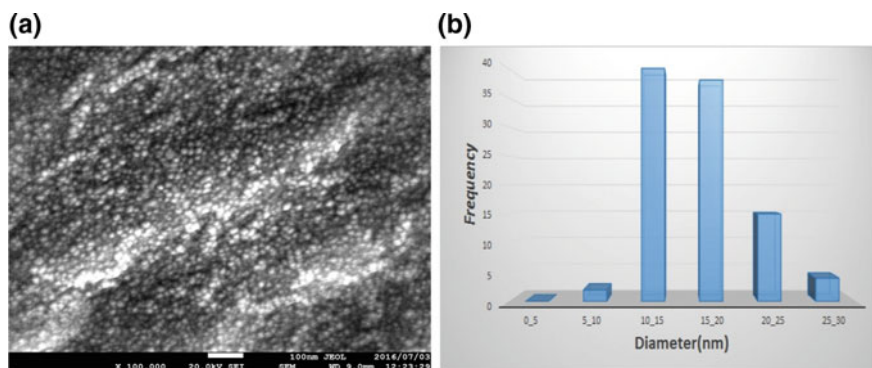


Fig. 4.64 **a** SEM image of PbO NPs synthesized from thermolysis of PMC microrods prepared in 1:1 mixture of MeOH:MeCN as the bulk sample, **b** corresponding histogram of it. Reproduced with permission from Ref. [468]. Copyright (2017) Elsevier

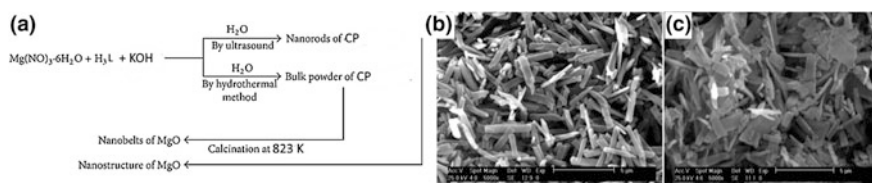


Fig. 4.65 **a** Overview of the methods used for the synthesis of PMC, and SEM images of **b** PMC nanorods prepared by a sonochemical process, and **c** MgO nanostructure prepared by the solid-state thermolysis of the PMC nanostructure at 923 K [478]

It is of interest to prepare mesoporous and nanostructure alumina from Al-MOFs, such as MIL-53, DUT-5, MIL-100, MIL-110, and MIL-96 as SSPs [479, 480]. It is important that the final alumina texture, such as morphology, porosity, and crystallinity, strongly depend on the SBU and the ligand type that was used to construct the MOF [481]. All of the aforementioned MOFs produce amorphous alumina or alumina with a low degree of crystallinity and a low surface area. At the same time, the aluminum fumarate MOFA520 was used as an SSP to produce mesoporous alumina with a high surface area during thermolysis at 1023 K (Fig. 4.66) [482–484]. A well-crystallized mesoporous γ -alumina with a surface area of $205 \text{ m}^2 \text{ g}^{-1}$ and a narrow pore size distribution is observed. In addition, worm-like morphology of MOFA520 was maintained and did not collapse during thermolysis; it is simply compressed and transferred to γ -alumina. It is interesting that 1D fibrous morphology is shown in which fibers, twisted and manufactured scrolls are present.

It should be noted that the sharp bands of MOFA520 after heat treatment at 723 K collapsed, which clearly indicates the destruction of the MOFA520 framework. The brownish color of the material (Fig. 4.67b) confirmed this conclusion.

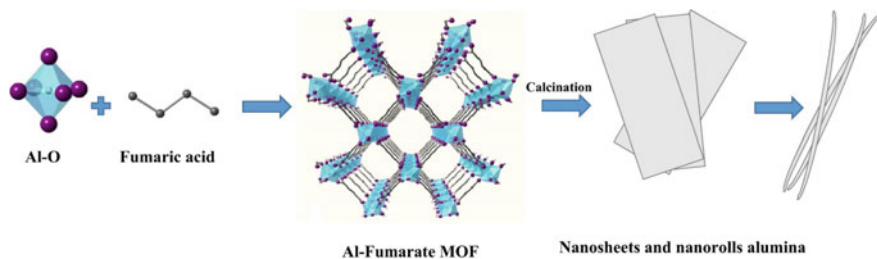


Fig. 4.66 Preparation of MOFA520 and conversion to nanosheet and nanorolls alumina. Reproduced with permission from Ref. [484]. Copyright (2016) Elsevier



Fig. 4.67 MOF A520 as-synthesized (a), A520-723 K (b), A520-823 K (c), A520-923 K (d). Reproduced with permission from Ref. [484]. Copyright (2016) Elsevier

With further heat treatment, the color of the material changed, and in the FTIR spectrum, the valley began to develop between 435 and 1000 cm^{-1} , and after thermolysis at 1023 K , two bands at 738 and 620 cm^{-1} were solved, which were associated with the bending vibrations of Al–O and Al–O–Al of γ -alumina, respectively [32].

4.3.3 Rare Earth Metal Oxides

There are few reports on the synthesis of nanoceria from PMCs [485, 486]. As a typical example, we note the thermolysis of the cerium-based CPs micro/nanostructures such as NPs, nanorods, and microflowers based on three isomers of benzenedicarboxylic acid at a high temperature, leading to ceria with retention of morphology [487]. It is important that the amorphous products were obtained using benzene-1,2-dicarboxylic acid. At the same time, well-crystallized CeO_2 NPs were obtained with the other two isomers by thermolysis at 1073 K for 2.5 h (Fig. 4.68a). Powder XRD pattern of the residue confirmed the formation of CeO_2 (Fig. 4.68b).

NPs of Ce(III) CP, $(\text{NAMH}^+)_2[\text{Ce}_4\text{L}_6(\text{HL})_2(\text{H}_2\text{O})_8]^-8\text{H}_2\text{O}$, ($\text{H}_2\text{L} = 2,6$ -pyridinedicarboxylic acid, NAM = nicotinamide), are synthesized using the sonochemical method [488]. Ceria NPs were obtained by thermolysis of PMC at 1073 K in atmospheric air. In another interesting example, the thermolysis of 2D cerium (III) CP, $[\text{Ce}(\text{L})(\text{HL})(\text{H}_2\text{O})_3]_n$, ($\text{H}_2\text{L} = 2,3$ -pyrazinedicarboxylic acid) at 1073 K in the air atmosphere yields ceria NPs [489].

Thermolysis of monolithic macroporous foams of lanthanide-organic CPs ($\text{Ln} = \text{La}, \text{Ce}, \text{Pr}, \text{Nd}, \text{Sm}, \text{Eu}$) based on L-asparagine as SSPs gives hierarchically mesomacroporous or macroporous monolithic foams of lanthanide oxides (La_2O_3 , CeO_2 , Pr_6O_{11} , Nd_2O_3 , Sm_2O_3 , and Eu_2O_3) [490]. For La_2O_3 , CeO_2 and Pr_6O_{11} foams, macropore walls consist of crystal flakes, aggregation of nanocrystals, and meshwork of crystal Pr_6O_{11} nanorods, respectively, whereas in the case of Sm_2O_3 and Eu_2O_3 foams irregular macropores of different sizes are observed. The mixed-lanthanide oxides and lanthanide transition metal oxides can be obtained using doped lanthanide CP foams [490].

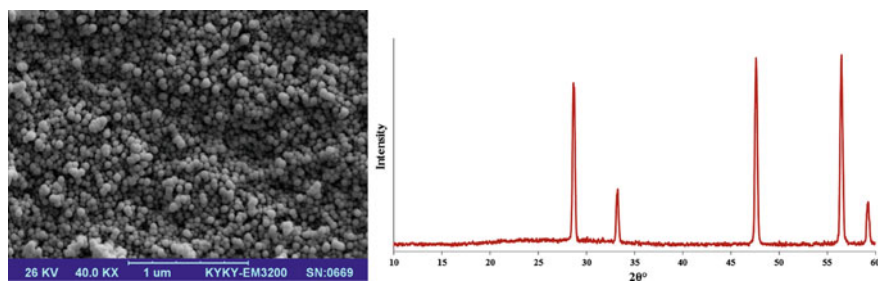


Fig. 4.68 SEM image (left) and XRD pattern (right) of CeO_2 NPs, prepared by thermolysis of PMC at 1073 K . Reproduced with permission from Ref. [487]. Copyright (2017) Taylor & Francis

4.3.4 Preparation of Metal Nanomaterials

There are many ways to generate metallic NPs with different shapes and sizes [491, 492]. However, the solid-phase synthesis of metallic NPs through the precursor complex synthesis is very rare. In particular, the use of silver CPs or silver nanoCPs for the preparation of silver NPs has not been widely studied. As an example, we note the thermolysis of CP chains assembled from Ni(II) hexaazamacrocyclic based on cyclam (1,4,8,11-tetraazacyclotetradecane) and sodium 4,4'-biphenyldicarboxylate, which can be packed to form a porous framework (Fig. 4.69). Nanocomposites of silver NPs and matrices can be obtained by immersing the framework in AgNO_3 solution and the matrix-free silver NPs (≈ 3 nm), isolated by solid treatment with boiling dioctyl ether containing OA [28].

It should be noted that the temperature of thermolysis of two silver(I) CPs, $[\text{Ag}(\text{HQ})(\text{Q})]_n$ and $\{[\text{Ag}(\text{HQ})_2]\text{NO}_3\}_n$, where HQ is 8-hydroxyquinoline, has effect on the formation of silver NPs [18]. Single crystal X-ray analysis showed that CPs have a 3D supramolecular network (Fig. 4.70).

It turned out that with increasing temperature, the tendency toward agglomeration of silver NPs increases (Fig. 4.71).

The thermolysis of the sinusoidal CP $[\text{AgL}](\text{ClO}_4)$, where L is diethylbis(4-pyridyl)silane, at 673 K creates the circle morphology with the evolving burned organics and at 873 K forms network circles consisting of silver(0)/silver chloride (chlorargyrite)/silicon(IV) oxide composite with a microsized convexo-concave surface [493]. In contrast, the thermolysis of $[\text{Ag}(\text{L})](\text{BF}_4)$ crystals at 873 K produces silver(0) materials without silicon(IV) oxide.

The solid-phase grinding of the unique framework-builder bpy with AgNO_3 led to the efficient formation of 2D CP of Ag(I) SSP (Fig. 4.72) [56]. The crystalline SSP is transformed into silver NPs during thermolysis. Supramolecular preorganization of SSP in the solid-state plays a significant role in the formation of Ag NPs. This is an efficient way of synthesis of Ag NPs in solid state in bulk without the use of a reducing agent and a stabilizer. Ag NPs have a uniform size distribution.

Ag NPs were synthesized by thermolysis of crystalline PMC. The SSP was heated to about 823 K in an N_2 atmosphere in a muffle furnace. The formation of

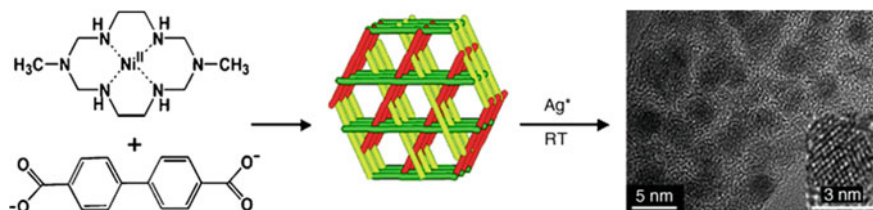


Fig. 4.69 Synthesis of CP based on 4,4'-biphenyldicarboxylate and cyclam, the stacking of the linear chains to generate 1D channel and HRTEM images of the solid isolated after immersion of the desolvated CP in a methanolic solution of AgNO_3 at room temperature for 10 min. Reproduced with permission from Ref. [28]. Copyright (2005) John Wiley and Sons

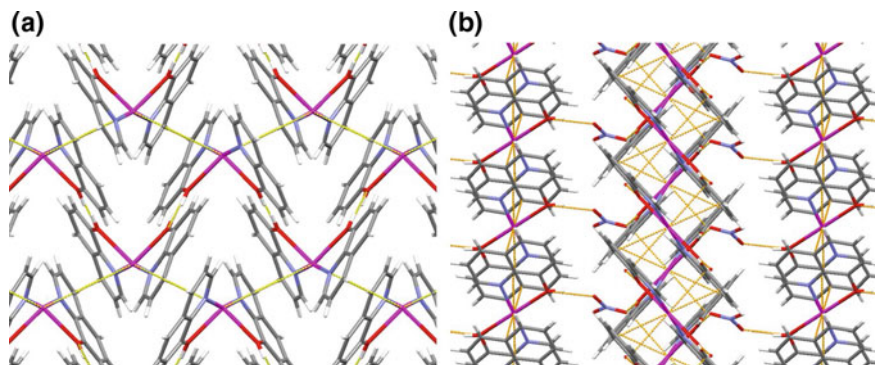


Fig. 4.70 Fragments of supramolecular networks in first (a) and second CP (b), showing the role of secondary Ag ... C and hydrogen bonding interactions in the formation of these polymers, (Ag violet, O red, N blue, C gray, H white). Reproduced with permission from Ref. [18]. Copyright (2016) Springer Nature

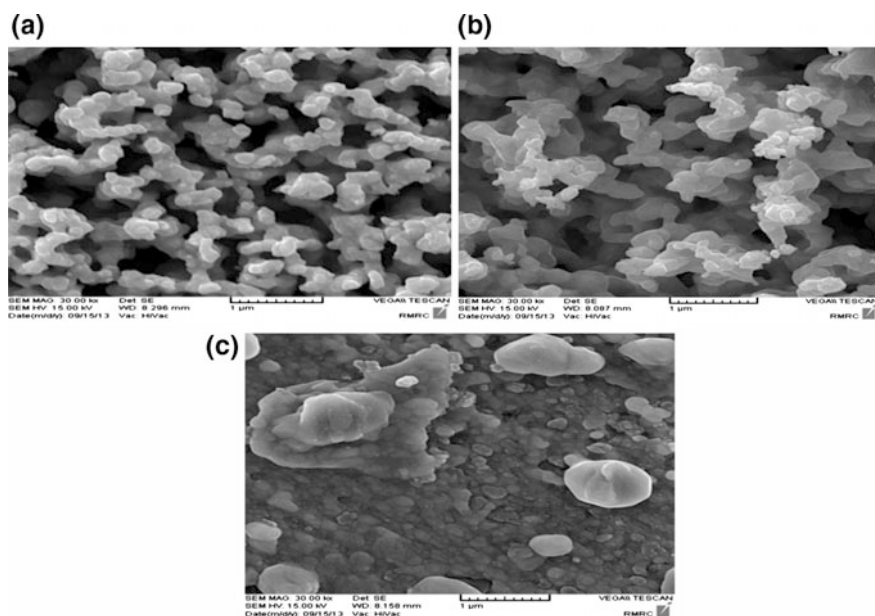


Fig. 4.71 SEM images of silver NPs obtained from the thermolysis of PMC at a 673, b 873, and c 973 K. Reproduced with permission from Ref. [18]. Copyright (2016) Springer Nature

spherical Ag NPs in the prepared sample is shown (Fig. 4.73). There is an accurate size distribution and a well-stabilized Ag NPs with a critical size of 15 nm (Fig. 4.73, inset). These solid NPs are stable for 15 day when stored under N_2 atmosphere at room temperature.

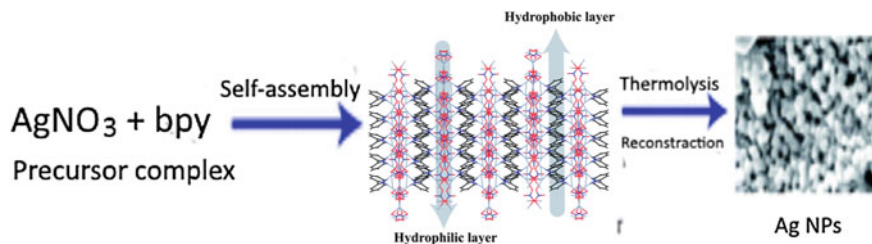


Fig. 4.72 Solid-phase precursor synthesis of Ag NPs. Reproduced with permission from Ref. [56]. Copyright (2010) Royal Society of Chemistry

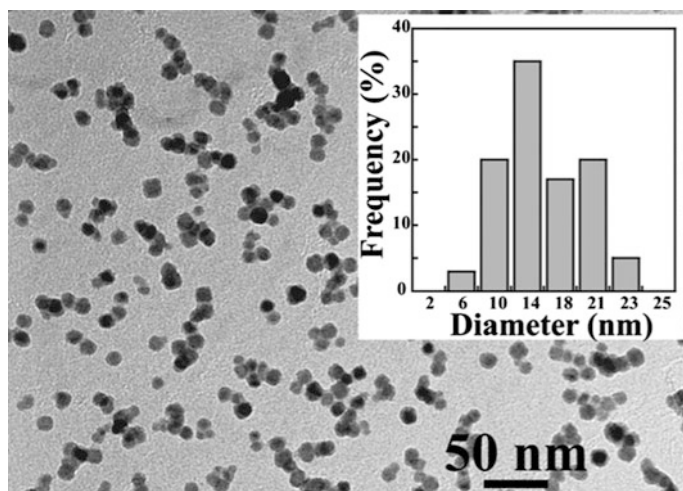


Fig. 4.73 TEM pictures of Ag NPs. *Inset* particle size distributions of the as-prepared Ag NPs. Reproduced with permission from Ref. [56]. Copyright (2010) Royal Society of Chemistry

Two linear silver(I) nitrate CPs with the bitopic ligand 1,1,2,2-tetra(pyrazol-1-yl) ethane were synthesized [494]. In both structures, silver ions are connected through the bridging molecules of the ligand to form polymeric chains with a five-atomic environment. The coordination environment of the central atom corresponds to a distorted trigonal bipyramid with two N atoms of different ligands in apical positions (Fig. 4.74).

Thermolysis of CPs in a reducing atmosphere (H_2/He) leads to the formation of silver NPs with a narrow size distribution. The effect of the atmosphere and the final temperature of thermolysis on the size of product crystallites have been studied for complex **2**. Thermolysis of **2** in a reducing atmosphere showed that parameters such as the thermolysis time and the final temperature do not have a significant effect on the crystallite size of the formed Ag NPs, and in the helium atmosphere such dependence exists. The formation of amorphous carbon obviously has a great

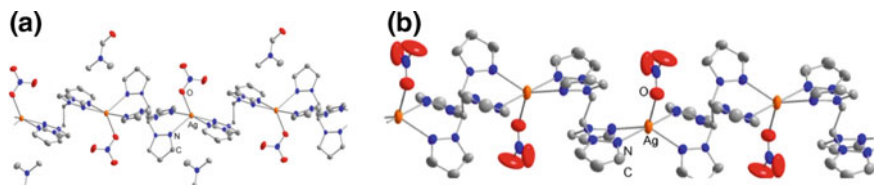


Fig. 4.74 Thermal ellipsoid plots of complexes **1** (a) and **2** (b) showing 50% probability ellipsoids. Hydrogen atoms have been omitted for clarity [494]

Table 4.2 Crystallite size of Ag NPs: final products of PMC (**2**) thermolysis under different conditions [494]

Thermolysis conditions (<i>T</i> , thermolysis time)	Crystallite size range for different atmospheres (nm)	
	He	H ₂ /He (7.2%)
673 K, 0 h	12–23	11–20
673 K, 3 h	–	11–20
673 K, 10 h	17–30	10–20
873 K, 0 h	–	10–21
1073 K, 0 h	26–53	–

influence on the stabilization of the formed silver NPs, and its crystallite size is always in the range of 9–21 nm. On the other hand, the size distribution for NPs formed in the helium atmosphere was wider and reached 12–53 nm (Table 4.2) [494].

The micro- and nanostructures of 1D CP [Ag₂(μ₂-L)₂]_n (HL = 2,4-dichlorophenoxyacetic acid) with corrugated tape chains synthesized as a bulk sample by sonochemical process and from a mechanochemical reaction were used as SSPs for the preparation of silver NPs by direct thermolysis at 573 K and thermolysis in OA as a surfactant at 453 K [73]. It turned out that in the presence of OA less agglomerated nanostructures are formed. It is important that the size, dispersion, morphology, and agglomeration of the original SSP have a direct influence on the size, dispersion, morphology, and agglomeration of metallic silver.

The thermolysis of nanostructures of 1D CP [Ag(HL)(L)]_n (HL = 2-methyl-8-hydroxyquinoline) synthesized by the reaction of HL and AgNO₃ by sonochemical process in OA leads to the formation of a silver nanostructure (Fig. 4.75) [97].

Agglomerated metallic silver with spongy nanostructure from direct thermolysis of nanostructures of 2D CP [Ag(μ₃-HL)]_n (H₂L = maleic acid) was obtained [353].

An interesting strategy is the preparation of symmetrical coralloid Cu 3D superstructures with a surface alternating with clusters of Cu NPs by direct thermolysis of [Cu₃L₂]_n (L = benzene-1,3,5-tricarboxylato) MOF in a one-end-closed horizontal tube furnace [495].

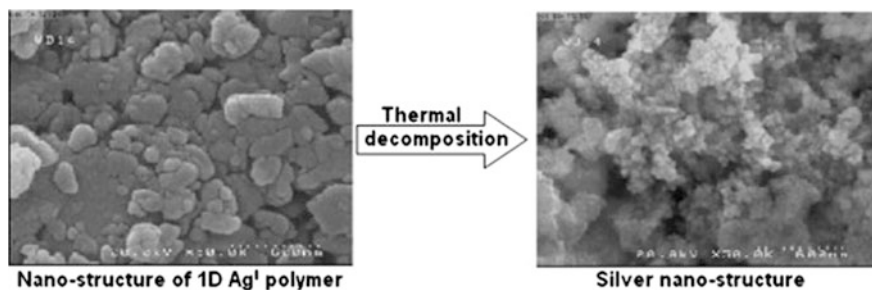


Fig. 4.75 SEM images of CP nanostructure prepared by sonochemical process (left) and silver nanostructure prepared by thermolysis (right). Reproduced with permission from Ref. [97]. Copyright (2014) Elsevier

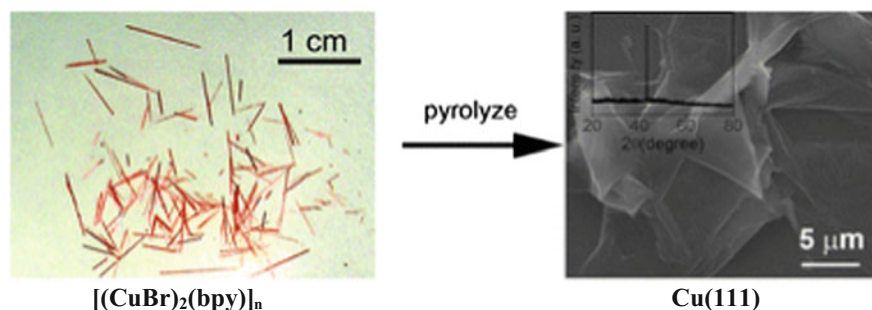


Fig. 4.76 Preparation of Cu(111) flake by thermolysis of $[(\text{CuBr})_2(\text{bpy})]_n$ under N_2 at 1023 K. Reproduced with permission from Ref. [496]. Copyright (2009) Royal Society of Chemistry

The oriented growth of single crystalline Cu(111) flake, which is usually prepared by depositing high-quality metal films (substrates) on the surface, was synthesized by simply thermolysis of the 1D chain-like hybrid CP $[(\text{CuBr})_2(\text{bpy})]_n$ by adjusting the heating procedures (Fig. 4.76) [496]. It is important that thermolysis conditions influence the morphology of the product and provide a simple method for the synthesis of Cu(111) flake.

The SEM image indicates that the sample is a folded flake (Fig. 4.77a) and EDS data (Fig. 4.77b) show that the product contains only Cu, C, and O. The TEM and HRTEM images (Fig. 4.77c, d) show that the Cu flake is a single crystal and corresponds to the [111] zone axis. Together, the data obtained are consistent with the oriented growth of the Cu(111) flakes.

CPs can also be used in the synthesis of certain alloys, which is a rare phenomenon [497]. As an example, we note the synthesis of $\text{GeFe}_{1.4}$ alloy NPs using nano CP, Ge-ox-Fe as SSP, in a reaction involving the solid-phase reduction at H_2 above 1073 K, accompanied by decomposition. The transformed $\text{GeFe}_{1.4}$ NPs demonstrated a unique ferromagnetic behavior [315].

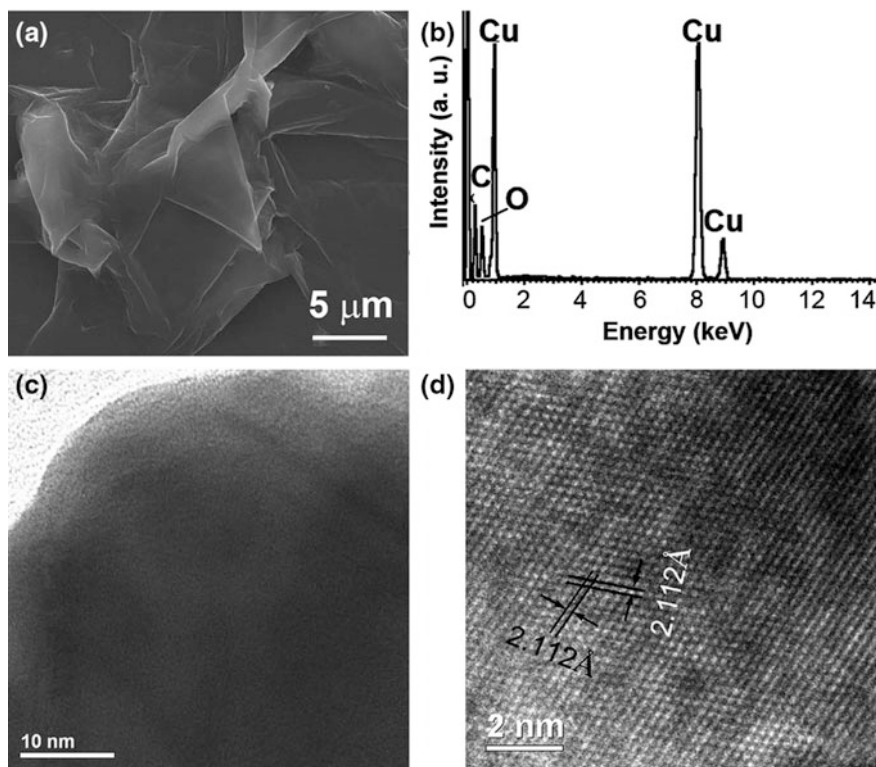


Fig. 4.77 **a** SEM image, **b** EDS spectrum, **c** TEM, and **d** HRTEM images of sample: Cu(111) flake from thermolysis of $[(\text{CuBr})_2(\text{bpy})]_n$ at 1023 K for half an hour with under N_2 . Reproduced with permission from Ref. [496]. Copyright (2009) Royal Society of Chemistry

4.4 Preparation of Mixed-Oxide Nanocomposites

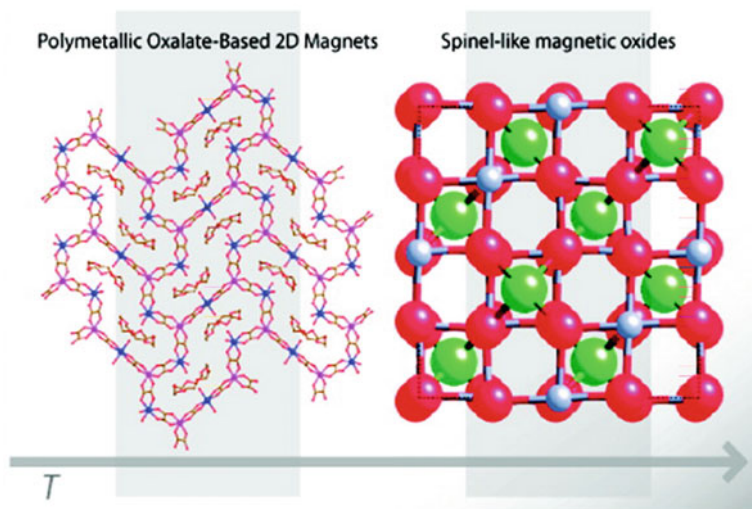
Heterometallic PMCs can be used as SSPs for the synthesis of functional oxide materials (e.g., metal oxide ceramics) because of the existence of various types of metals in the structure. In this case, heterometallic PMCs have the following advantages: the ratio of metal ions is precisely determined, the temperature of solid-phase thermolysis to oxide is relatively low, and the size of the resulting particles can be controlled, which is usually in the nanometer range, changing the thermolysis temperature [498]. It should be noted that heterometallic carboxylate PMCs constitute a significant proportion of such SSPs [499]. Interest in these PMCs is due to their structure: ions of different metals are located relatively close to each other in the molecule [500–502], and carboxylate groups provide a sufficient number of oxygen atoms, which can facilitate the thermolysis to metal oxides. This allows the use of such heterometallic PMCs as SSPs for the thermal synthesis of

mixed oxides [503–505]. It is important that carboxylate PMCs are usually readily available, which is important for large-scale synthesis of oxides.

Spinel ferrite NPs with the formula of MFe_2O_4 ($M = Co, Ni, Zn$, or other metals) have both technological and scientific significance due to their exceptional properties and a wide range of applications in various fields [506–514]. Among spinel ferrites, $CoFe_2O_4$ has a cubic spinel structure and is widely studied because of its high chemical stability, mechanical hardness, and interesting magnetic properties [493]. Several synthesis routes have been developed for the production of cobalt ferrite NPs [515, 516]. The route of synthesis is an important factor affecting the physical and chemical properties of spinel NPs; therefore, a large number of studies on these materials with respect to methods of their preparation have been carried out [511].

Mixed-metal oxalate PMCs were used to obtain bimetallic or mixed-oxide NPs. Thus, a family of 2D polymetallic oxalate-bridged polymeric networks [517] with general formula $[M^{II}(H_2O)_2]_3[M^{III}(ox)_3]_2(18\text{-crown-6})_2$ ($M^{III} = Cr, Fe$; $M^{II} = Mn, Fe, Co, Ni$) exhibiting ferro- (Cr^{3+}) or ferrimagnetic (Fe^{3+}) ordering in the 3.6–20 K interval, depending on the nature of the trivalent metal ion, was used as SSPs to obtain pure phases of mixed oxides of spinel-like structures as $(Mn,Co,Fe)_3O_4$, which behave like a magnet at room temperature (Scheme 4.17).

Mesoporous nickel ferrite ($NiFe_2O_4$) spheres were prepared by aerosol spray pyrolysis method using Pluronic F127 as a structure-directing agent, and metal nitrates were used as inorganic precursors for the oxide [518]. Self-assembly of organic and inorganic species with subsequent decomposition of metal nitrate and



Scheme 4.17 Transformation of polymetallic oxalate-based 2D magnets into spinel-like magnetic oxides by thermolysis. Reproduced with permission from Ref. [517]. Copyright (2016) American Chemical Society

inorganic polymerization was carried out in droplets of ethanol aerosol in N_2 atmosphere at 673 K. It is important that evaporation of the solvent at 323 K in the chamber caused self-assembly between the structure-directing agent and the metal ions. It should be noted that the mesoporous crystalline nickel ferrite spheres were obtained after the spheres were thermolyzed at 573 K in air to remove the structure-directing agent and increase the crystallinity. Mesoporous $NiFe_2O_4$ spheres with a high specific surface area ($278 \text{ m}^2 \text{ g}^{-1}$) with a highly crystalline framework were prepared by adjusting the amount of structure-directing agent and the thermolysis conditions.

It is interesting to use the “escape-by-crafty-scheme” strategy to obtain spinel oxides AMn_2O_4 ($A = \text{Zn}, \text{Co}$ or Ni) by thermolysis of the corresponding MOF SSPs [519]. The synthesis starts from mixed-metal MOFs containing two metal cations using the appropriate metal acetates and perylene-3,4,9,10-tetracarboxylic dianhydride (L) as a ligand. Synthesized MOFs, $ZnMn_2-L$, is a gypsum-flower-like morphology with a size of ca. 3 μm (Fig. 4.78a). In a second step, MOFs are thermally transformed into a structured spinel of $ZnMn_2O_4$ with a morphology inherited from the MOFs precursors. The spinels retained the morphology of the precursor MOFs, showing gypsum-flower-like morphology of 2–3 μm , containing

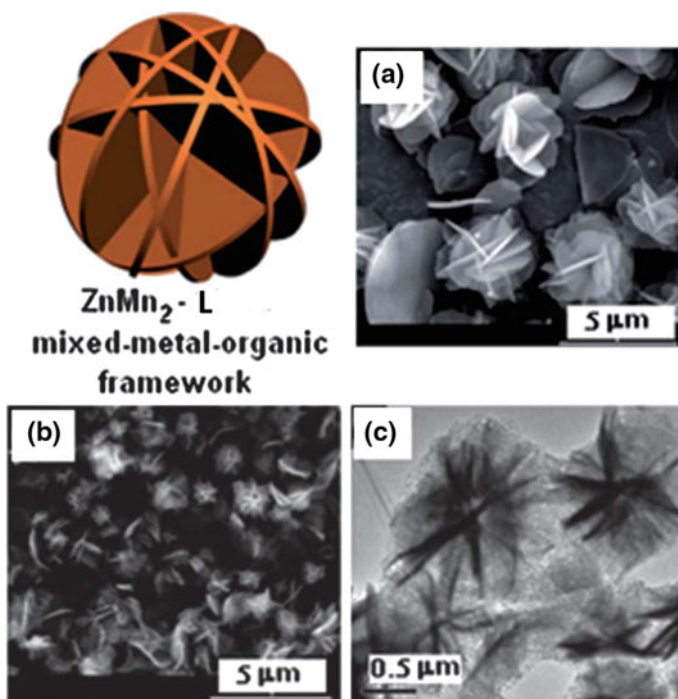
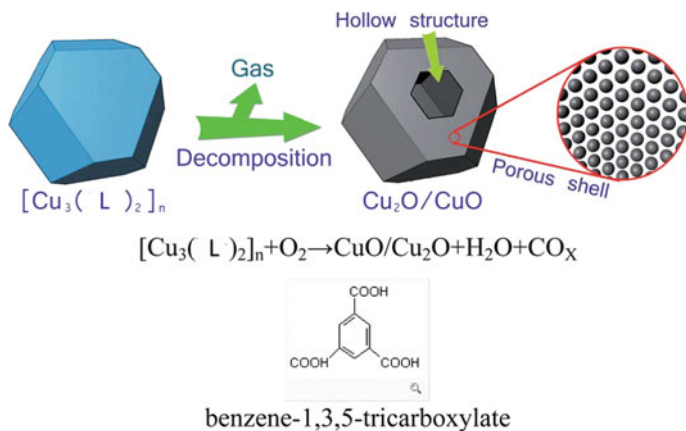


Fig. 4.78 Illustration of the $ZnMn_2$ -PTCDA MOF precursor. **a** SEM image of $ZnMn_2-L$, **b** SEM, and **c** TEM images of $ZnMn_2O_4$. Reproduced with permission from Ref. [573]. Copyright (2012) Royal Society of Chemistry



Scheme 4.18 Schematic illustration of the formation of CuO/Cu₂O hollow polyhedrons with a porous shell. Reproduced with permission from Ref. [397]. Copyright (2006) American Chemical Society

platelets 60 nm in thickness (Fig. 4.78b, c). The ZnMn₂O₄ material has a mesoporous structure and a specific surface area of 42 m² g⁻¹.

Hollow structures of mixed valence metal oxides (CuO/Cu₂O) were obtained from MOF [Cu₃(L)₂]_n (L = benzene-1,3,5-tricarboxylate) by thermolysis at 623 K (Scheme 4.18) [397].

Two types of d-f heterometallic CP SSPs, {Sm[M(ox)₃]₃·nH₂O}_x (M = Fe and Co), were prepared by the reaction of K₃[M(ox)₃]₃·3H₂O with Sm(NO₃)₃·nH₂O in methanol solvent [520]. It was found that oxides of the perovskite type, SmMO₃ (M = Fe and Co), are formed in the temperature range >873 K. The average dimensions of the SmFeO₃ crystallites in the (110) direction, as well as BET specific surface areas of the SmFeO₃ samples thermolyzed at each temperature are shown in Table 4.3 [520]. The estimated average sizes decreased with a decrease in the thermolysis temperature of the heterometallic CP SSP, and the specific surface areas increased with decreasing temperature of thermolysis.

Another typical example of the use of CPs for the production of mixed-metal oxides is the thermolysis of MOF [Gd(H₂O)₃Co(L)₃]_n (L is 2,3-pyridinedi carboxylate) at 673, 973, and 1073 K, which results in the production of GdCoO₃ mixed-metal oxides with APS of 3 ± 2, 12 ± 3, and 200 ± 20 nm, respectively [521].

Comparative study of the thermolysis processes of CPs [BaCuL₂]_n, [BaCuL₂(H₂O)]_n and [Ba₃Cu₃L₆(H₂O)₁₁]_n·2n(H₂O), where H₂L is 1,1-cyclopropanedicarboxylic, 1,1-cyclobutanedicarboxylic, and butylmalonic acid, respectively, showed that dehydration proceeds according to one scheme, and the bonds between structural fragments in anhydrous intermediates become stronger [522]. Thermal destruction of anhydrous CPs occurs above 443 K. It is important that the phase compositions of their solid products are determined by the conditions of

Table 4.3 Average sizes of crystallite and specific surface areas of products thermolyzed at each temperature

Sample	Thermolysis temperature (K)	Crystallite size (nm) ^a	Surface area (m ² g ⁻¹)
Sm[Fe(ox) ₃].3H ₂ O	823	– ^b	– ^c
Sm[Fe(ox) ₃].3H ₂ O	873	22	8.6
Sm[Fe(ox) ₃].3H ₂ O	923	23	– ^c
Sm[Fe(ox) ₃].3H ₂ O	973	25	7.9
Sm[Fe(ox) ₃].3H ₂ O	1073	27	3.3
Sm[Fe(ox) ₃].3H ₂ O	1173	29	– ^c
Sm[Fe(ox) ₃].3H ₂ O	1273	31	1.8
Sm[Co(ox) ₃].8H ₂ O	973	36	3.9

^aThe average sizes of SmFeO₃ and SmCoO₃ crystallites in the (110) and (002) directions, respectively, were evaluated from XRD line broadening using Scherrer's equation

^bNo peaks

^cNot measured

thermolysis, and the formation of BaCuO₂ from the last CP could be realized under softer conditions than the formation from the first two CPs.

It should be noted the isostructural complexes [LnL(acac)₂(H₂O)]_n (Ln = Eu, Gd, Tb, Dy, Ho, Er; L = (η⁵-C₅H₄)Mn(CO)₃) having a polymer structure based on L-bridged {Ln(acac)₂(H₂O)} fragments, which were prepared by the exchange reactions of hydrated Ln acetylacetonates with L in a mixture of CHCl₃-EtOH-H₂O [523]. Thermolysis of CPs in air and in the atmosphere of Ar gives the phases of LnMnO₃.

3D porous CPs [(H₂O)₃(μ-H₂O)₂CuBa(μ₃-L)L]_n and [(μ-H₂O)CuBa(μ₃-L)(μ₄-L)]_n are of interest, where HL is dimethylmalonic acid [524]. Full solid-phase thermolysis of CPs leads to a mixture of BaCuO₂, BaCO₃, and CuO. It is important that the crystalline phase of the pure cubic BaCuO₂ can be obtained using specific conditions. The thermolysis of Ba-Co and Ba-Zn heterometallic 3D CPs [BaM(H₂O)₅L₂]_n based on the same ligand occurs in one step [525]. Crystalline BaCoO_{3-x} and BaZnO₂ are formed as a result of solid-phase thermolysis of the CPs under the following conditions: air flow rate 60 ml min⁻¹, heating rate 10 K min⁻¹ to *t* = 1073 or 1023 K, followed by storage for 12 h at the same temperatures (Fig. 4.79).

The ultrafine powders obtained by thermolysis of the polymeric SSP of the La₂Mo₂O₉ composition were successfully prepared by the in situ polymerizable complex method [526]. The high-temperature cubic phase of La₂Mo₂O₉ can be

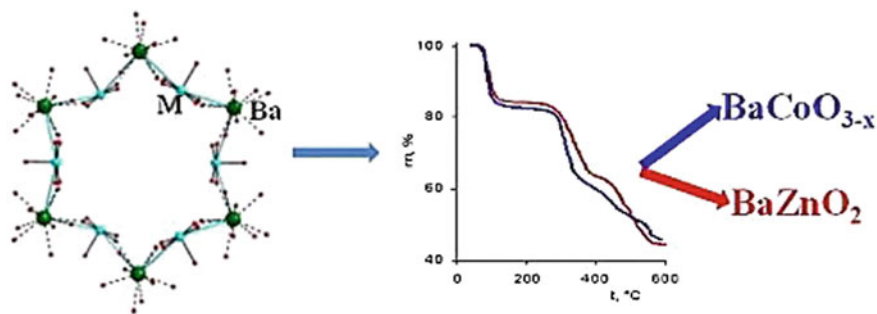


Fig. 4.79 Preparation of crystalline BaCoO_{3-x} and BaZnO_2 as a result of solid-state thermolysis of the CPs. Reproduced with permission from Ref. [525]. Copyright (2015) Elsevier

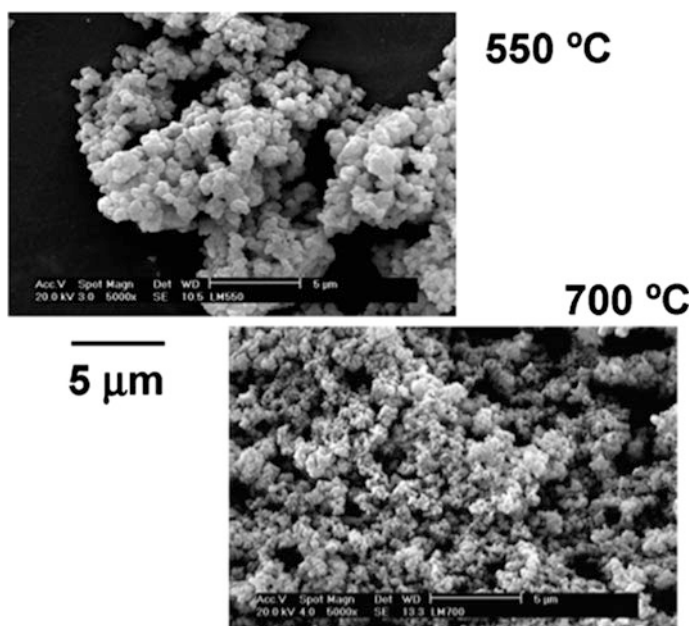


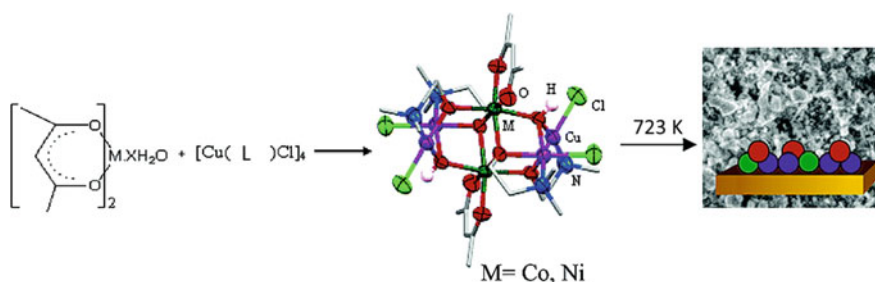
Fig. 4.80 SEM of the phase $\text{La}_2\text{Mo}_2\text{O}_9$ prepared at different temperatures. Reproduced with permission from Ref. [526]. Copyright (2003) American Chemical Society

directly obtained by thermolysis of SSP at relatively low temperatures. The results of TA show that the polymer precursor of $\text{La}_2\text{Mo}_2\text{O}_9$ has a crystallization temperature of about 823 K, and a characteristic behavior of the decomposition compared to the decomposition of individual cationic polymer precursors. SEM demonstrates a different morphology of powder particles after thermolysis at selected temperatures and powder XRD patterns were obtained for identify the phase (Fig. 4.80).

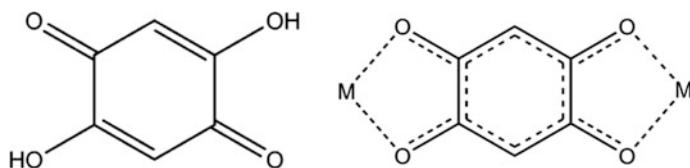
Ni–Fe bimetallic oxide nanotubes with hollow and porous structures were synthesized using MOF thermolysis processes [527]. The Ni/Fe molar ratios in binary MO were rationally developed. As a rule, $\text{Ni}_{0.62}\text{Fe}_{2.38}\text{O}_4$ nanotubes with a tubular shell of about 10 nm have a specific surface area of $134.3 \text{ m}^2 \text{ g}^{-1}$ and consist of nanosized primary particles.

Mixed ceramic oxide materials from isostructural cage-like heterobimetallic molecular SSPs $[\text{Co}_2(\text{acac})_2(\mu\text{-OH})_2\text{Cu}_4(\text{L})_4\text{Cl}_4]$ and $[\text{Ni}_2(\text{acac})_2(\mu\text{-OH})_2\text{Cu}_4(\text{L})_4\text{Cl}_4]$ (HL = N,N-dimethylaminoethanol) were obtained [528]. SSPs for the deposition of mixed-oxide thin films were prepared by the interaction of tetrameric N,N-dimethylaminoethanolato copper(II) chloride, $[\text{Cu}(\text{L})\text{Cl}]_4$ with M (acac) $_2 \cdot x\text{H}_2\text{O}$ (M = Co, Ni) in toluene. Both complexes undergo controlled thermolysis at 723 K to obtain mixed metal oxides (Scheme 4.19). The obtained results indicate the formation of impurity-free crystalline mixed-oxide films with APS in the range from 0.55 to 2.0 μm .

Two types of ternary MO, $\text{MnCo}_2\text{O}_{4.5}$, and MnNi_6O_8 , NPs have been separately synthesized through chemical transformation from the corresponding bimetallic CP particles SSP under high-heating conditions [529]. $\text{MnCo}_2\text{O}_{4.5}$ NPs with different sizes have been firstly fabricated by a straightforward soft template route (using a Mn–Co–CP SSP based on 3-amino-1,2,4-triazole-5-carboxylic acid hemihydrate) followed by high heat treatment at different temperature. The Mn/Co-based ternary oxide NPs (denoted as Mn/Co-673) are then prepared by the thermolysis of the Mn–Co–CP SSP at 673 K for 1 h using a muffle furnace. The structure of Mn/Co-673 displays an irregularly particle-like morphology that originated from the SSP, but APS reduces to nanometers with mean diameter of 65 nm. Increasing the thermolysis temperature to 773 K leads to the morphology of the bimetallic composites, namely Mn/Co-773. Smaller particles with mean diameter of 43 nm gathered together to form a bigger motif. At consequent increasing the heating temperature to 873 K, the particles sizes of the thermolysis sample (denoted as Mn/Co-873) increase from 40 to 200 nm. Similarly, thermolysis of Mn–Ni–CP SSP at 673, 773, and 873 K for 60 min can lead to the formation of ternary oxide Mn/Ni-based nanomaterials. Mn/Ni-673 inherits the morphology from the SSP. Interestingly, each petal still consists of many NPs with a diameter of



Scheme 4.19 Synthesis of SSPs and their thermolysis into mixed metal oxides. Reproduced with permission from Ref. [528]. Copyright (2006) American Chemical Society



Scheme 4.20 A representation of free and coordinated L. Reproduced with permission from Ref. [530]. Copyright (2012) John Wiley and Sons

5–50 nm and these particles are adsorbed together due to high surface energy. At the same time, the external morphology of Mn/Ni-773 changes from flower-like to block-like and the block-like motif is a hybrid of particles and flakes. It should be noted that the structure of Mn/Ni-873 is also a bulk composition of monodisperse particles, in which the particles are chaotic and the size of these particles is larger than that of Mn/Ni-673. Thus, the change in temperature of thermolysis plays a key role in the temperature of thermolysis shape.

A series of bimetallic lanthanide CPs with 2,5-dihydroxy-1,4-benzoquinone (L) as a bridging ligand (Scheme 4.20) is used as SSPs for mixed-oxide synthesis [530]. Thermolysis at 1123 K of the CP readily yielded mixed $\text{Nd}_x\text{Gd}_{(1-x)}$ and $\text{Nd}_x\text{Ce}_{(1-x)}$ oxides in the form of solid solutions in which x varies from 0 to 1. It is important that the morphology of the SSP powders is maintained during thermolysis, which makes it easy to control some of the properties of the oxides at the stage of synthesis of the coordination compound. In particular, BET measurements indicated that the choice of anhydrous reaction conditions for the synthesis of SSP leads to an increase in the specific surface areas of oxides by an order of magnitude. It should be noted that the use of well-characterized CPs as SSPs adds another advantage to the solution route processes, because it allows you to control the sequences of atoms in the chains, the number of coordination bonds, and the dimensionality of the SSP structure.

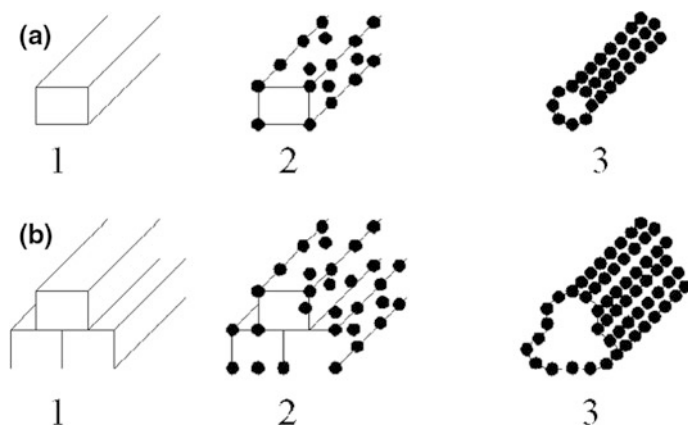
Another example of the preservation of the morphology of SSP during thermolysis to oxides is shown in the example of LnFeO_3 [531]. It should be noted that this is a key step in the process of modulation of the macroscopic properties of ceramics. The morphology of the SSPs, and therefore the oxides, can be modified by selecting suitable synthesis conditions, which in turn are likely to affect such properties as the specific surface area. Thus, a thorough design of the SSP microstructure through fine chemical control can be an efficient tool in engineering ceramics with special macroscopic properties.

It is of interest to synthesize YSZ from Y-doped MOFs by two-step thermolysis in an inert atmosphere and then in oxygen [532]. The resulting YSZ had a large surface area, a crystalline framework and a high conductivity of oxygen ions.

4.5 Preparation of Metal Sulfide Nanomaterials

Metal sulfide nanomaterials are a large class of solid compounds that are not as widely studied as metal oxides [533]. Among the various metal chalcogenides, copper sulfides have been extensively studied in recent years due to their semiconductor and non-toxic nature, which makes them useful in a wide range of applications [534]. In particular, stoichiometric compositions of nanoscale copper sulfides from Cu-rich (Cu_2S) to Cu-deficient (CuS_2) exist with different crystal structures, as well as with phases, which leads to different unique properties. As a typical example, we note nanowires $[\text{Cu}(\text{L})]\text{Cl}\cdot 0.5\text{H}_2\text{O}$ (diameter 100 nm), where L is thiourea, which were synthesized by mixing a solution of CuCl_2 with L [535]. The well-aligned $[\text{Cu}(\text{L})]\text{Cl}\cdot 0.5\text{H}_2\text{O}$ nanowires were self-assembled into a dandelion- or thorn-like architecture, depending on the initial concentrations of L and CuCl_2 . Prepared nanowire SSPs were used to produce black porous CuS nanotubes with good morphological and high chemical purity in an alkaline aqueous solution under ambient conditions. It is important that SSP nanowire architectures influence the morphology of the CuS nanotubes product (Scheme 4.21).

H-bound 1D CP, $\{[\text{Cu}(\text{HSglu})(\text{H}_2\text{O})]\cdot \text{H}_2\text{O}\}_n$, where H_3Sglu is N-(2-hydroxybenzyl)-l-glutamic acid, was used as an SSP and also sacrificial template to synthesize covellite CuS nanomaterials with a predetermined shape [536]. From a detailed study of the effect of experimental conditions on final products, a remarkable correlation was found between the repeating samples of metal atoms in the CP with the preliminary shape of the obtained CuS. In particular, the reaction conditions were optimized to obtain the morphology of the petal bed-like, flower-like, and rice-balls (Fig. 4.81). The mechanism for the formation of the final



Scheme 4.21 Growth mechanisms of the hierarchical nanotubular structures from steps 1–3 using **a** dandelion- and **b** thorn-like $[\text{Cu}(\text{L})]\text{Cl}\cdot 1/2\text{H}_2\text{O}$ nanowires. Reproduced with permission from Ref. [535]. Copyright (2009) American Chemical Society

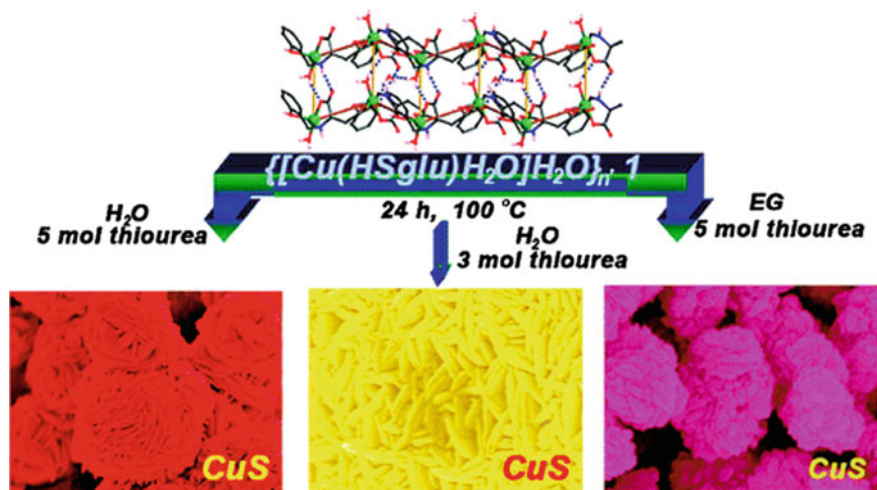


Fig. 4.81 Portion of the 2D sheet-like structure of $[[\text{Cu}(\text{HSglu})(\text{H}_2\text{O})]\text{H}_2\text{O}]_n$. Reproduced with permission from Ref. [536]. Copyright (2009) American Chemical Society

mesostructured product was explained on the basis of the role of the chelating ligand and solvents in the self-assembly process.

The use of a 2D CP based on the trinuclear building block $[\text{Cu}_3(\text{HSser})_3(\text{H}_2\text{O})_2] \cdot 2\text{H}_2\text{O}$, where H_3Sser is *N*-(2-hydroxybenzyl)-*L*-serine, as an SSP in the synthesis of copper sulfide resulted in a hierarchical 3D color structure of CuS and hollow nanospheres (Fig. 4.82) [51]. CuS 3D flower-like mesostructure is an assembly of many plate-like petals, and the hollow spheres of CuS were self-assembled from nanorod/plate particles with a shell thickness of 70 ± 7 nm. The formation of hollow materials is explained by the angular arrangement of Cu(II) atoms and ligands in the crystal lattice.

Dandelion-like architectures of 1D CP Pb-cysteine assembled from well-aligned nanowires in the aqueous solution of *L*-cysteine and $\text{Pb}(\text{OAc})_2$ are of interest. They were converted to spherical and various flower-like microstructures of PbS by ordinary hydrothermal conditions [537].

By thermolysis at 673 K of nanostructures of two Pb(II) 2D CPs, $[\text{Pb}(2\text{-L})(\text{NCS})]_n$ and $[\text{Pb}(3\text{-L})(\text{NCS})]_n$ (HL = pyridinecarboxylic acid), nanorods and nanoplates of PbS were obtained, accordingly [52]. It is important that the dimensions and shapes of the nanostructures are related to the CP structure and various frameworks leading to different morphologies of PbS.

In another interesting example, various types of Bi_2S_3 nanorods were obtained from CP SSPs, $[\text{Bi}_6(\text{L})_8(\text{HL})_2(\text{L}')_8]$ and $\{[\text{Bi}_2(\text{L})_3(\text{L}'')(\text{H}_2\text{O})_2] \cdot 3\text{H}_2\text{O}\}_n$ (HL = 2,6-pyridinedicarboxylic acid, L' is thiourea, L'' is thiosemicarbazide) using various thermolysis methods and conditions (solvent, temperature, and surfactant) [538]. It should be noted that the formation of Bi_2S_3 1D nanostructures in anisotropic growth along the *c* axis can be caused by strong covalent bonds along the

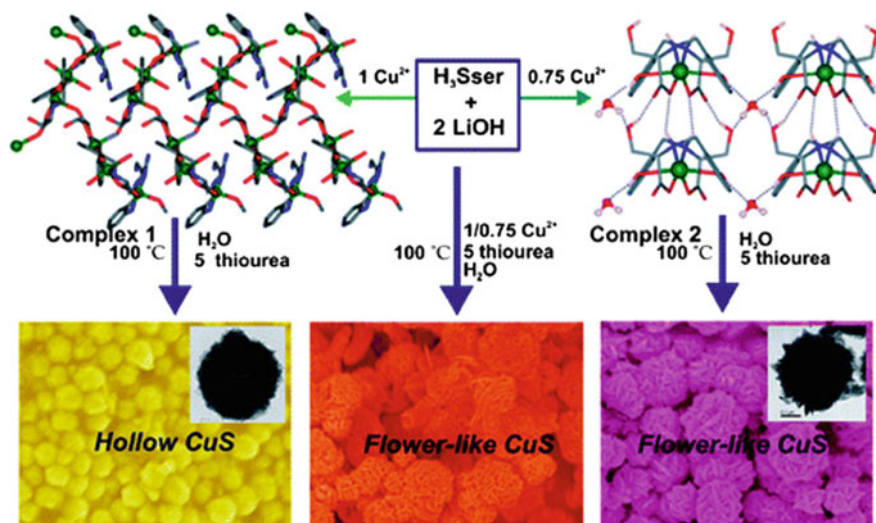


Fig. 4.82 Effect of experimental conditions and the packing patterns of the complexes on the formation mechanism of the morphologically different CuS. Reproduced with permission from Ref. [51]. Copyright (2009) American Chemical Society

c crystallographic axis and by a much weaker van der Waals bonding between chains of CP layered structures. In addition, the capping ability of surfactants plays an important role in the formation of nanorods of various morphologies. Along the lamellar lines in [001] direction, a long-range strain diffraction contrast is observed within individual nanorods, which is better identified at a higher resolution (Fig. 4.83a, lines A–C). HRTEM images (Fig. 4.83b, c) show that this contrast is caused by a number of crystal defects: linear defects (dislocations), planar defects (stacking faults), and atomic distortions (displacements of atoms from their regular positions). This means that the crystal lattice in these areas is under strong stress.

Semiconductor silver sulfide NPs were formed with the same shape as Ag(I)-cysteine nanofiber templates [539]. The resulting NP superstructures appear in chains consisting of individual Ag_2S NPs in the acanthite phase with a diameter of 4–9 nm.

4.6 Preparation of Polymer-Derived Non-oxide Nanocomposites

Si-based advanced ceramics, commonly referred to as polymer-derived ceramics (PDCs), has gained considerable research interest in recent years [540–547]. In contrast to porous nanomaterials based on oxide and carbon, much less research was conducted on porous non-oxide-type ceramics derived from self-assembled

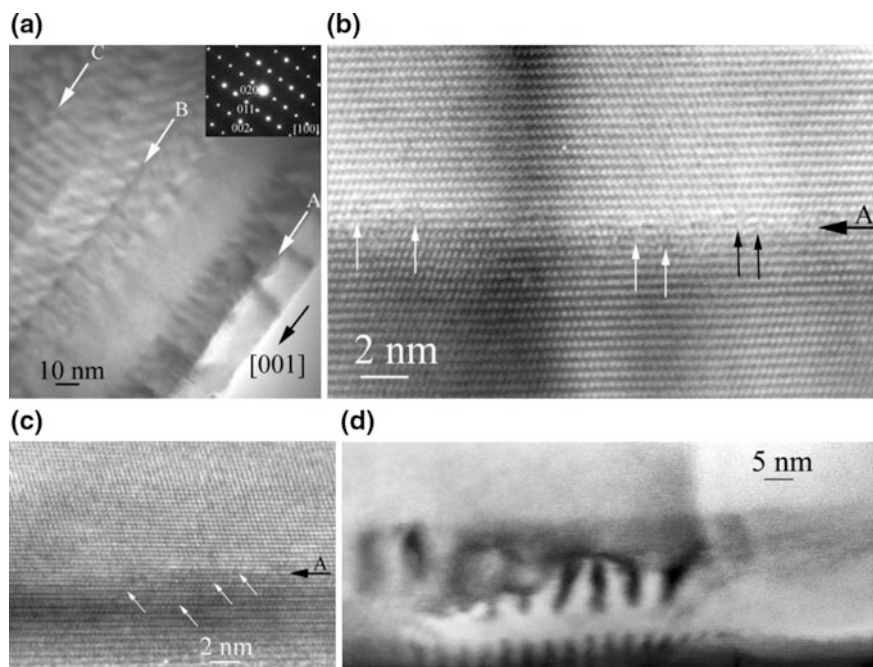


Fig. 4.83 HRTEM images of a Bi_2S_3 NP showing a variety of structural defects. **a** Image showing long-range deformation contrast caused by the presence of defects along the $[001]$ direction (arrows A–C). **b** Black arrows point out dislocations and white arrows atomic distortions. **c** The white arrows indicate planar defects (stacking faults). **d** Image showing the origin of split rods along one of the lines where the defects have collected. Reproduced with permission from Ref. [538]. Copyright (2009) American Chemical Society

composites [548]. High-temperature stability, corrosion resistance, and durability are provided by amorphous SiCN precursor ceramics [549], such as polysiloxane, polycarbosilane, and polysilazane [540, 550]. Because of the molecular path to this ceramic, they are highly tunable and versatile materials [551–558].

The production of porous ceramics from various specialized SSPs suppliers offers advantages in terms of simple processing methodology, low processing cost, and ease of control over porosity and other properties arising from the composition of the resulting ceramics [559, 560]. Particular attention is paid to the discussion of the close relationship between chemistry and structural architecture of the precursor, as well as the structural features and properties of the resulting ceramic nanocomposites [542]. Therefore, studies concerning the relationships between their molecular architecture and the microstructure and properties of the ceramic materials obtained there are of decisive importance [542, 550, 561]. Thermolysis of Si-based preceramic polymers under specific atmosphere conditions and heat treatment is a straightforward and inexpensive additive-free process [550, 562] which allows controlling and regulating the phase composition and microstructure and, consequently, the properties of the ceramic materials.

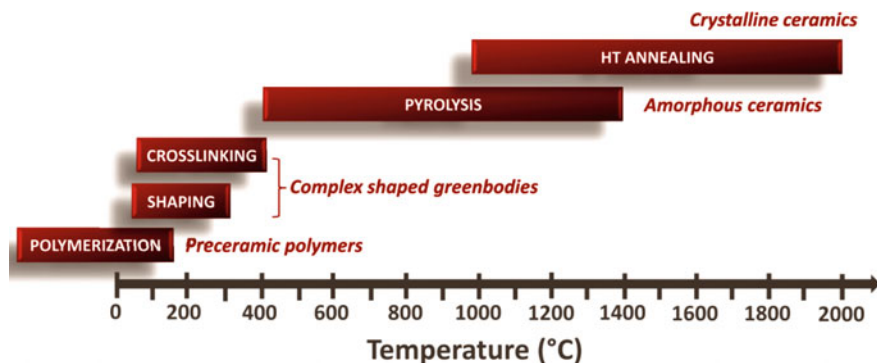


Fig. 4.84 Polymer-to-ceramic transformation of preceramic polymers. Reproduced with permission from Ref. [563]. Copyright (2010) John Wiley and Sons

Controlled thermolysis of silicon-based polymers provides nanostructured ceramics with nanostructures that are strongly determined by chemistry and the architecture of precursors, their technological way and parameters used for their thermolysis (heating rate, reactive or inert atmosphere, and thermolysis time). Depending on the temperature, preceramic polymers undergo various processes during their transformation into ceramics. After polymerization, the molding and cross-linking of the polymer can be easily carried out at moderate temperatures to produce complex-shaped green bodies that can retain their shape during thermolysis to 1673 K, and also during high-temperature annealing up to 2273 K (Fig. 4.84) [563].

The process of transformation of the polymer into ceramics has made it possible to achieve significant technological breakthroughs in ceramic science and technology, such as the development of ceramic fibers, coatings or ceramics that are stable at ultrahigh temperatures (up to 2273 K) with respect to decomposition, crystallization, phase separation, and creep. In recent years, several important achievements have been achieved, such as the discovery of a variety of functional properties associated with the PDCs. Moreover, new views on their structure at the nanoscale level have contributed to a fundamental understanding of the various useful and unique features of PDCs associated with their high chemical resistance or high creep resistance or semiconducting behavior. From a processing point of view, SSPs were used as reactive binders to produce technical ceramics and were processed to ensure the formation of ordered pores in the mesorange. They were tested to combine advanced ceramic components and were processed into bulk or macroporous components. Consequently, the possible applications of the PDCs have significantly expanded due to recent research and development. Several key engineering areas suitable for PDC applications include high-temperature materials (energy materials, automotive, aerospace, etc.), hard materials, chemical engineering (catalyst support, food and biotechnology, etc.), or functional materials in electrical engineering, as well as in micro-/nanoelectronics.

Unlike the classical manufacture of ceramic powders at high temperatures, PDC treatment is a relatively young technology and has several advantages over the conventional method [546]. Using various compounds and different types of reactions, the chemical and physical properties of the SSPs, such as elemental composition, solubility, fusibility and viscosity, are regulated. Expansion of property profiles, such as improving electrical and thermal conductivity, should be achieved by introducing transition metals into the ceramic. In particular, metal chelates allow further polymer modification to produce completely new ceramic materials with a high degree of purity and homogenous distribution of elements. They provide 3D cross-linking with a non-meltable polymer (green body), which is a prerequisite for ceramics. The transformation of a thermoset material into ceramic materials already occurs at relatively low temperatures (1273 K).

As an example, we consider a chemical modification of a commercially available polysilazane (HTT1800) using an aminopyridinato Ni(II) chelate based on (4-methylpyridin-2-yl) trimethylsilylamine, which resulted in the formation of a nanoporous silicon oxycarbonitride ceramics modified by Ni NPs [564]. Amido complexes can be synthesized with good yields on a large-scale and soluble in conventional organic solvents, so a good mixing of the polymer/coordination compound is possible. In addition, they contain the same elements as the precursor polymer, which avoids the penetration of any alien element into the ceramic composites. The amido ligand contributes to the achievement of the ceramic yield by providing Si, C, and N atoms to the ceramic. Ni-polysilazane SSPs are superparamagnetic, indicating the formation of nickel NPs ($\sim 2\text{--}3$ nm). The resulting aminopyridinato nickel chelate modified polysilazane precursors were thermolyzed at 973 K and converted into ceramic nanocomposites, exhibiting a nanoporous structure, revealing a BET surface area of $215\text{ m}^2\text{ g}^{-1}$, a surface area of the micropores of $205\text{ m}^2\text{ g}^{-1}$ and a micropore volume of $0.113\text{ cm}^3\text{ g}^{-1}$. Although Si–C–N–(O) ceramics obtained from native polysilazane is non-porous, the pronounced development of porosity in the Ni/Si–C–N–(O) system is explained by the stabilizing effect of carbosilane bonds, which inhibit the formation of macropores during thermolysis, a reduced barrier for heterogeneous pore nucleation as a result of in situ created nickel NPs, and a decrease in the viscous flow of pores due to the presence of nickel NPs and turbostratic carbon. The formation of turbostratic carbon is associated with the reactions catalyzed by nickel NPs, which leads to the laying of graphene.

Formation in situ of Ni NPs at room temperature during the reaction between poly(vinylmethyl)-*co*-poly(methylhydro)silazane (polysilazane hereafter, Fig. 4.85a, e) and trans-bis(acetato-kO)bis(2-aminoethanol-k²N,O)nickel(II) (Ni(II)-complex hereafter, Fig. 4.85b, f) was reported [565]. This reaction results in a stable dispersion of Ni NPs in THF (Fig. 4.85g). After removal of THF in vacuo, a superparamagnetic material containing well-dispersed Ni NPs is obtained. Formation in situ and stabilization of Ni NPs are achieved by reducing silane groups and formed in situ amphiphilic molecules, respectively.

The reaction between the polysilazane and Ni(II) complex causes the release of certain silazane bonds in the form of ammonia [565].

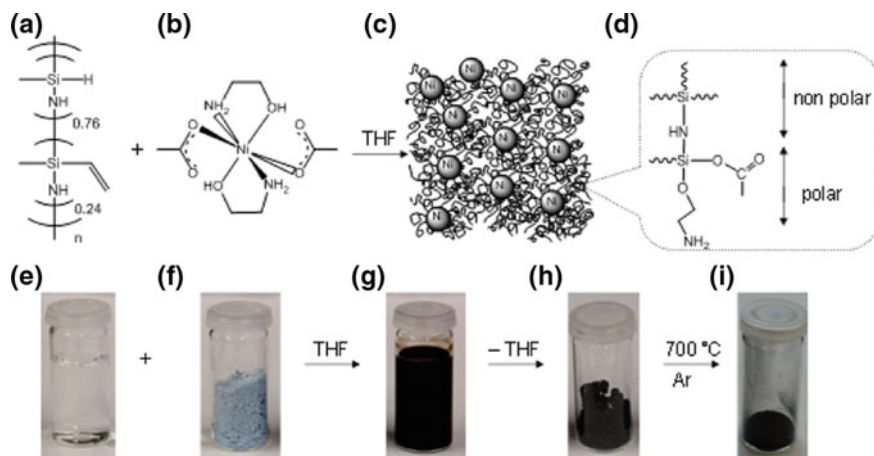


Fig. 4.85 **a, e** Polysilazane reacted with **b, f** 40 wt% Ni(II)-complex to form **c, g, h** superparamagnetic Ni/polysilazane nanocomposite. **d** Nucleophilic substitution of ethanolamine and acetate groups at the Si centers in the polysilazane replaces silazane linkages ($-\text{Si}-\text{NH}-\text{Si}-$) with aminoethoxysilyl ($\text{NH}_2\text{CH}_2\text{CH}_2\text{OSi}-$) and acetoxyethyl ($\text{CH}_3\text{COOSi}-$) groups forming amphiphilic polysilazane molecules. **g** Ni NPs are encapsulated by amphiphilic polysilazane molecules and are sterically stabilized in solution. **g** Dispersion of Ni/polysilazane in THF results in **h** a superparamagnetic elastomer, which after thermolysis at 973 K transforms into **i** a superparamagnetic Ni/SiCNO nanocomposite. Reproduced with permission from Ref. [565]. Copyright (2014) American Chemical Society

Ni NPs in situ are formed at room temperature in the reaction between the Ni(II)-complex and the commercial polysilazane HTT. The transfer of an electron from the negatively charged hydrogen in the silane group ($\text{Si}^{\delta+}-\text{H}^{\delta-}$) in Ni^{2+} in the Ni(II)-complex induces the reduction of Ni^{2+} with the simultaneous nucleophilic substitution of ethanolamine in the Si centers, which leads to the formation of aminoethoxysilyl ($\text{NH}_2\text{CH}_2\text{CH}_2\text{OSi}-$) and acetoxyethyl ($\text{CH}_3\text{COOSi}-$) groups. As a result, Ni NPs become stable in situ by amphiphilic polysilazane molecules, protecting them against agglomeration and growth.

After thermolysis of the Ni/polysilazane nanocomposite at 973 K in the Ar atmosphere, the average size and superparamagnetism of Ni NPs are conserved in the Ni/SiCNO nanocomposite, indicating a higher than expected saturation magnetization.

The nanocomposite (solution) of Ni/polysilazane can be formed to produce various ceramic materials, including a ceramic monolith, a foam, and a membrane.

Superparamagnetic Ni NPs with a diameter of about 3 nm are formed in situ at room temperature in a polysilazane matrix, forming Ni/polysilazane nanocomposite in the reaction between polysilazane and trans-bis(acetokO)bis(2-aminohydroxy)nickel(II) [565]. Thermolysis of the Ni/polysilazane nanocomposite at 973 K in an argon atmosphere results in a microporous superparamagnetic Ni/silicon oxycarbonitride (Ni/SiCNO) ceramic nanocomposite. The growth of Ni NPs

in a ceramic Ni/SiCNO nanocomposite is completely suppressed even after thermolysis at 973 K.

An analysis of the saturation magnetization of Ni NPs in Ni/polysilazane and Ni/SiCNO nanocomposites indicates that the saturation magnetization of Ni NPs is higher than expected values and that Ni NP surfaces are not oxidized. The microporous superparamagnetic Ni/SiCNO nanocomposite has the form of a monolithic and foam plastic. In addition, Ni/SiCNO membranes are manufactured by the dip-coating of tubular alumina in a dispersion of Ni/polysilazane in THF, followed by thermolysis in 973 K under an argon atmosphere.

Similar robust microporous nanocomposites (specific surface area $\approx 400 \text{ m}^2 \text{ g}^{-1}$) containing nickel NPs were synthesized using various and controlled Si:Ni ratios in THF [566]. The amido nickel complex catalyzed the cross-linking of HTT1800 by hydrosilylation at room temperature. In thermolysis at 873 K in an inert atmosphere, nickel NPs and micropores are generated in a concerted process. It is important that a specific surface area, pore volume, and nickel particle size can be adjusted. In addition, the materials demonstrate excellent retention of the shape during pyrolysis, which makes it possible to manufacture monoliths. It is important that, after thermolysis to 873 K in an inert atmosphere, Ni NPs located near the outer surface of the SiCN ceramic and also inside the internal voids were obtained.

By changing character of SSP and using commercial allylhydridopolycarbosilane, Ni-containing SiC ceramics can be synthesized by self-assembly of allylhydridopolycarbosilane-*b*-polyethylene (PE) [567]. The block copolymer was synthesized by Ni complex-catalyzed Si-H dehydrocoupling in allylhydridopolycarbosilane with O-H in hydroxy-terminated PE. The added aminopyridinato nickel complex also catalyzes the cross-linking of the block of allylhydridopolycarbosilane, for example, by dehydrocoupling reactions of Si-H bonds.

During the modification of HTT1800 by aminopyridinato copper complexes, metal is transferred from the complex to the polymer (Fig. 4.86, left) [546]. ^1H and ^{13}C NMR investigations of the reaction showed the release of the free protonated ligand, which indirectly indicates the transfer of the metal to the nitrogen donor atoms of the polymer (Fig. 4.86, right).

The metal-modified polymer was cross-linked using dicumylperoxide and thermolyzed at 1273 K to form copper-containing SiCN (Cu@SiCN). Copper cations bound to a polymer backbone are reduced to a copper metal during the thermolysis stage. The loading of copper can vary in a wide range up to the ratio of Si to Cu 5. The size of the Cu particles found in Cu@SiCN increases with the increase in the loading of the copper complex (Fig. 4.87). Due to the presence of aminopyridinato complexes, this bottom-up approach should be expandable to other transition metals.

Interestingly, a very different behavior was observed for palladium aminopyridinates (compared to copper), which generate intermetallic NPs. In particular, simultaneous chemical modification and cross-linking of polyorganosilazane were achieved using aminopyridinato palladium complex at room temperature [568]. Cross-linking occurs with the evolution of hydrogen, supporting the dehydrocoupling mechanism in parallel with hydrosilylation, which increases the yield of

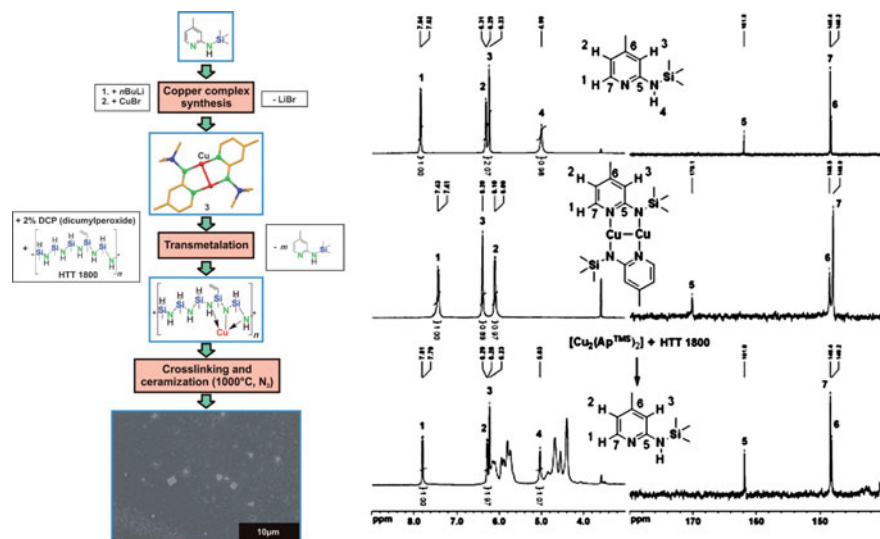


Fig. 4.86 (left) Modification of HTT1800 with an aminopyridinato copper complex leading to Cu-containing SiCN ceramics by thermolysis to 1273 K under nitrogen, (right) ^1H (left) and ^{13}C NMR spectra (right) of ApTMSH (top), $[\text{Cu}_2\text{Ap}_2\text{TMS}]$ (middle), and after its reaction with HTT1800 (bottom). Reproduced with permission from Ref. [546]. Copyright (2012) Royal Society of Chemistry

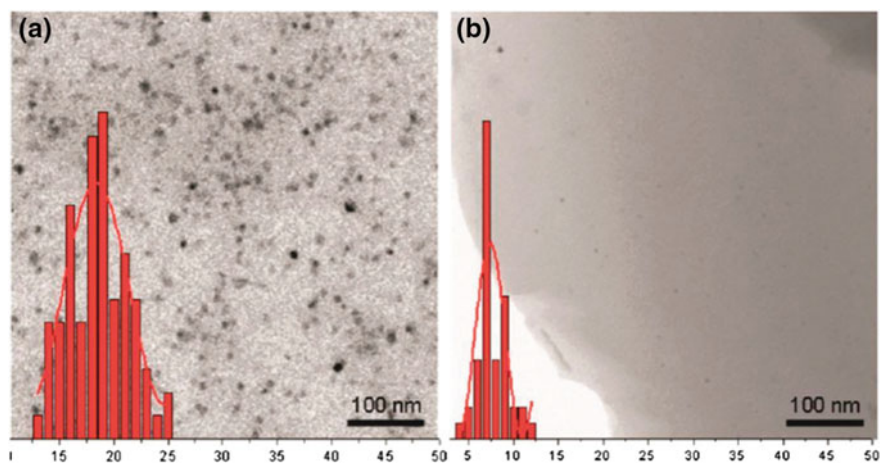


Fig. 4.87 TEM micrographs of Cu@SiCN: **a** Si/Cu = 10 **b** Si/Cu = 100 including particle size distribution statistics. Reproduced with permission from Ref. [546]. Copyright (2012) Royal Society of Chemistry

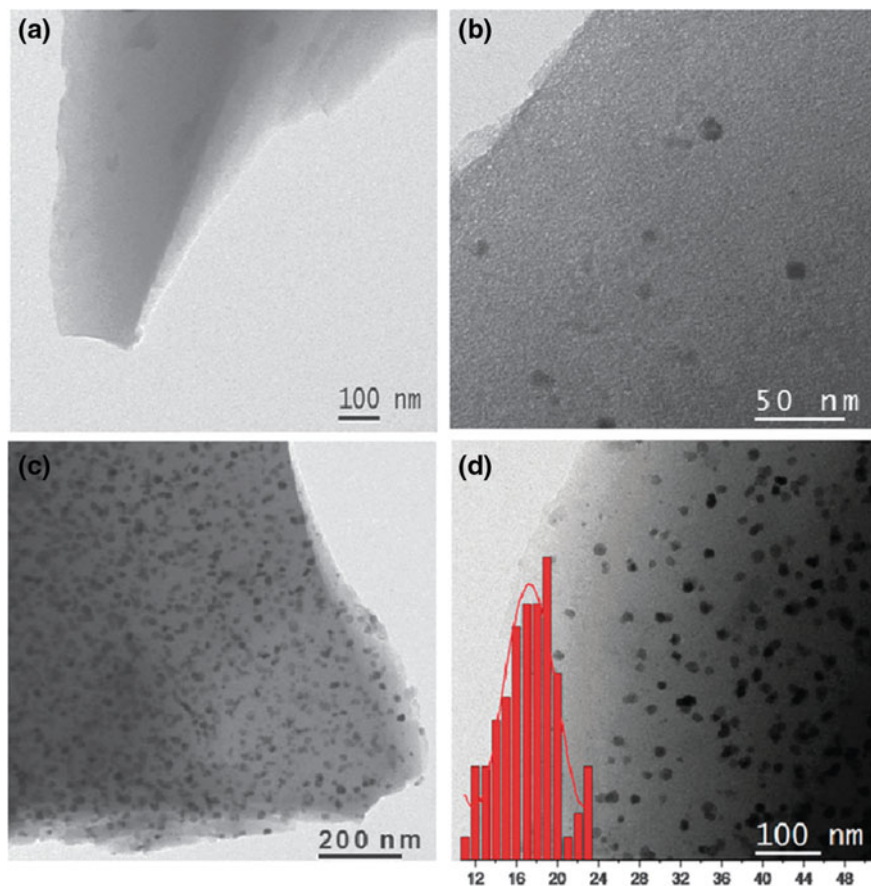


Fig. 4.88 TEM micrographs of ceramic materials. **a** SiCN ceramic without palladium loading does not show any particles; **b** lower loading of palladium (0.2 wt%, Si/Pd ratio 1000) decreases the density of particles keeping their size in the same regime; **c** Pd₂Si particles uniformly distributed over the ceramic support Si/Pd = 20 (8 wt% Pd); **d** particle size distribution for the sample shown in (c). Reproduced with permission from Ref. [568]. Copyright (2011) Royal Society of Chemistry

ceramics due to the retention of carbon and nitrogen atoms. The ceramic yield was even higher than in the case of a pure polyorganosilazane cross-linked by the addition of free radical initiators such as dicumylperoxide. Thermolysis at 1373 K in the N₂ atmosphere provides Pd₂Si@SiCN. Powder XRD studies confirmed the presence of hexagonal phases of Pd₂Si in an amorphous SiCN matrix, and the size of the particles formed depends on the nature of the solvent used in the cross-linking stage. The amount of added palladium complex apparently does not affect the size of the formed particles, but increases their population density (Fig. 4.88).

In an attempt to relate the generation of metal NPs and porosity in SiCN ceramics, the chemical modification of HTT1800 with aminopyridinato metal complexes ($M = \text{Fe}, \text{Co}, \text{Pt}, \text{Cu}, \text{Ag}, \text{Au}$) along with the addition of the sacrificial filler (PE) has been investigated [569]. In the simultaneous process, both porosity (Fig. 4.89) and MWCNT (Figs. 4.89c and 4.90) were generated. Thermolysis of PE leads not only to the formation of open porosity, but also to the reaction in situ of its thermolysis products with metal NPs to form the MWCNT in the pores. During the thermolysis, gaseous hydrocarbons are formed, the decomposition of which leads to the production of MWCNT by a CVD process. It was found that cobalt and iron are more efficient in generating MWCNT than other metals used.

Using higher magnifications, it is clearly seen that the metal particles are located on the top of the MWCNT (Fig. 4.90a). The lattice fringe distance of metal particles could be determined up to 215 pm (Fig. 4.90b), which agrees perfectly with the **hcp**-Co distance. In addition, TEM micrographs allow an approximate calculation

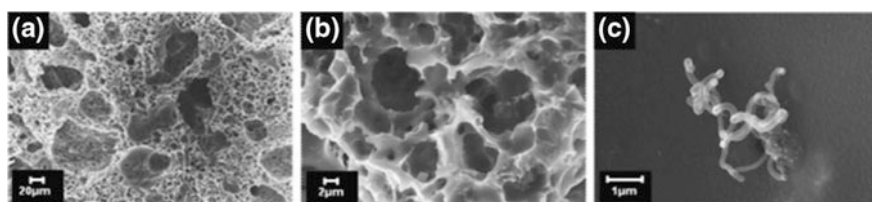


Fig. 4.89 a–c SEM micrographs of an Au@SiCN ceramic (1273 K/N₂; Au:Si = 1:50). Reproduced with permission from Ref. [569]. Copyright (2011) Elsevier

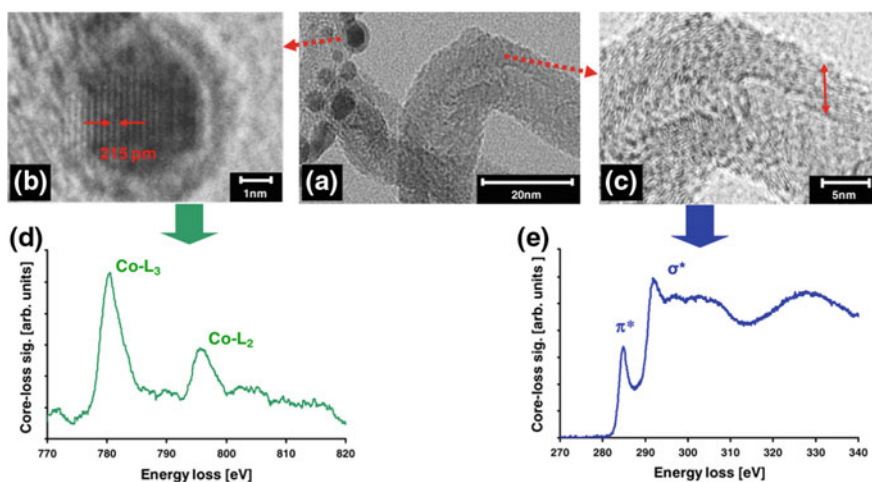


Fig. 4.90 a–c TEM micrographs of a Co@SiCN ceramic (Co:Si = 1:50), **d** core-loss electron energy loss spectroscopy (EELS) of the metal particle, **e** core-loss EELS of the MWCNT. Reproduced with permission from Ref. [569]. Copyright (2011) Elsevier

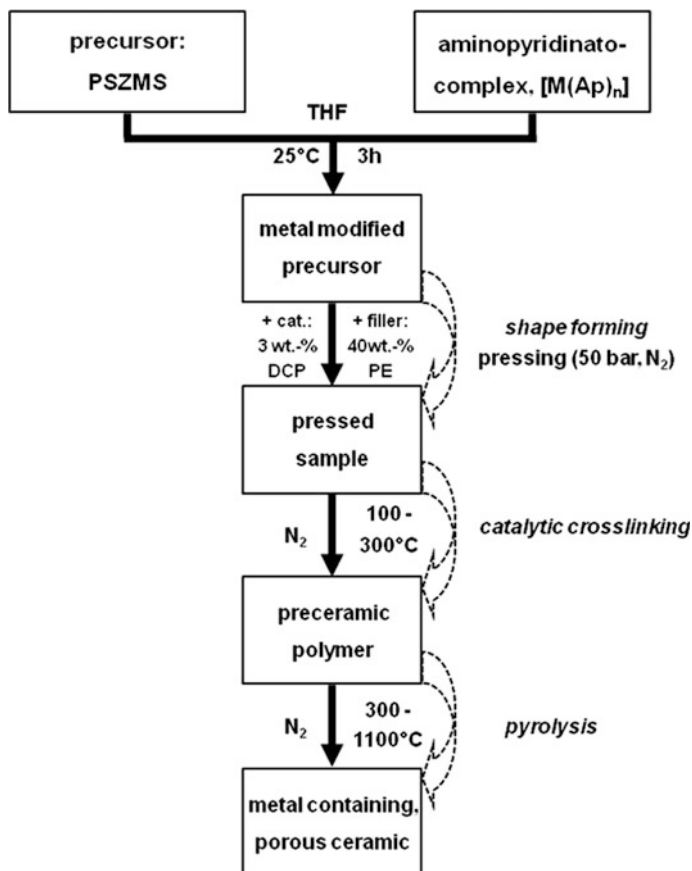


Fig. 4.91 Processing scheme of the porous M@SiCN precursor ceramics (M = Fe, Co, Pt, Cu, Ag, Au). Reproduced with permission from Ref. [569]. Copyright (2011) Elsevier

of the number of carbon sheets of MWCNT. For example, the MWCNT investigated in Fig. 4.90c consists of 13–15 walls (along the red arrow).

An interesting method for the simultaneous formation of catalytically active metal NPs, MWCNTs and/or turbostratic carbon and porous M@SiCN (M = Fe, Co, Pt, Cu, Ag, Au) ceramics during the thermolysis of metal-modified polysilazanes and PE particles as sacrificial filler is described (Fig. 4.91). Thermolysis of PE leads not only to the generation of the porosity, but also to the reduction in situ of metal compounds to metal NPs due to the reducing atmosphere. Depending on the metal, carbon nanotubes, as well as turbostratic carbon, were formed in different amounts because of conditions similar to CVD. The obtained carbon phases, ceramics, and metal NPs were studied, which indicates the presence of carbon phases and metal particles.

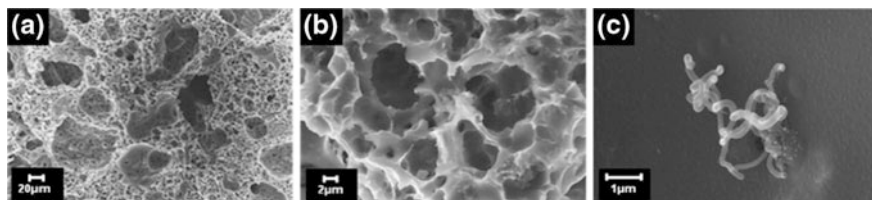


Fig. 4.92 a–c SEM micrographs of the Au@SiCN ceramic (1000 °C/N₂; Au:Si = 1:50). Reproduced with permission from Ref. [569]. Copyright (2011) Elsevier

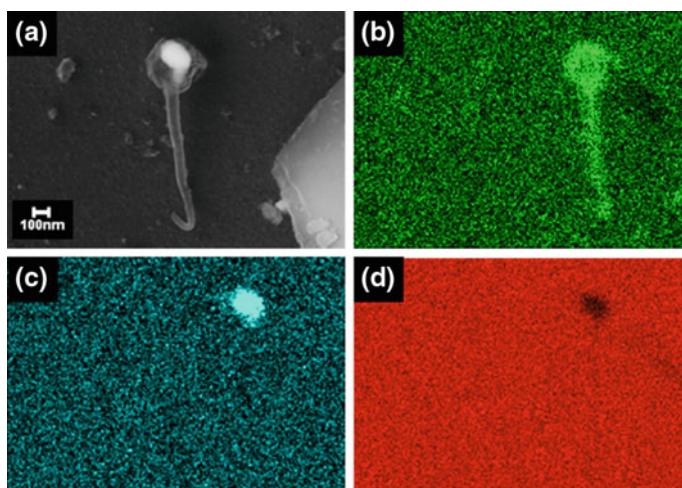


Fig. 4.93 a SEM micrograph of the Cu@SiCN ceramic (1273 K/N₂ Cu:Si = 1:50), b EDS mapping (C–K α), c EDS mapping (Cu–K α), d EDS mapping (Si–K α). Reproduced with permission from Ref. [569]. Copyright (2011) Elsevier

Only a few examples have been described in which the formation of carbon nanotubes and turbostratic carbon in the metal-loaded PDC has been observed in situ. In a unique “one-pot” synthesis, both are formed during the polymer-to-ceramic transformation of polysiloxanes, catalytically active metal particles and carbonic decomposition gases [570–572]. Initially, measurements confirm the presence of an open pore network in ceramic (Fig. 4.92a, b). Using $M = \text{Cu}, \text{Ag},$ and Au , only a few CNTs could be detected in $M@SiCN$ ceramics, as these metals are known to be not very active in the catalytic formation of C–C bonds (Fig. 4.92c).

The elemental composition of this structure was analyzed using an EDS mapping. The study confirms that the tubes consist of pure carbon, which includes catalytically active metal particles at the upper part (Fig. 4.93) or sometimes at their bottom.

References

1. A.D. Pomogailo, A.S. Rozenberg, I.E. Uflyand, *Metal Nanoparticles in Polymers* (Khimiya, Moscow, 2000)
2. A.D. Pomogailo, V.N. Kestelman, *Metallopolymer Nanocomposites* (Springer, Berlin, 2005)
3. A.D. Pomogailo, G.I. Dzhardimalieva, *Monomer and Polymer Metal Carboxylates* (Fizmatlit, Moscow, 2009)
4. A.D. Pomogailo, G.I. Dzhardimalieva, V.N. Kestelman, *Macromolecular Metal Carboxylates and Their Nanocomposites* (Springer, Berlin, 2010)
5. A.D. Pomogailo, G.I. Dzhardimalieva, *Nanostructured Materials Preparation via Condensation Ways* (Springer, Dordrecht, 2014)
6. A.D. Pomogailo, G.I. Dzhardimalieva, *Metallopolymeric Hybrid Nanocomposites* (Nauka, Moscow, 2015)
7. M.Y. Masoomi, A. Morsali, *Coord. Chem. Rev.* **256**, 2921 (2012)
8. B.I. Kharisov, O.V. Kharissova, U.O. Méndez, *J. Coord. Chem.* **66**, 3791 (2013)
9. O. Carp, Materials obtained by solid-state thermal decomposition of coordination compounds and metal-organic coordination polymers, in *Reactions and Mechanisms in Thermal Analysis of Advanced Materials*, ed. by A. Tiwari, B. Raj (Scrivener Publishing LLC, 2015)
10. B.I. Kharisov, H.V. Rasika Dias, O.V. Kharissova, V.M. Jiménez-Pérez, B.O. Pérez, B.M. Flores, *RSC Adv.* **2**, 9325 (2012)
11. H.D. Mai, K. Rafiq, H. Yoo, *Chem. Eur. J.* **23**, 5631 (2017)
12. W.L. Leong, J.J. Vittal, *Chem. Rev.* **111**, 688 (2011)
13. M. Oh, C.A. Mirkin, *Nature* **438**, 651 (2005)
14. A.P. Reverberi, N.T. Kuznetsov, V.P. Meshalkin, M. Salerno, B. Fabiano, *Theor. Found. Chem. Eng.* **50**, 59 (2016)
15. J. You-Moon, H. Jungseok, C.A. Mirkin, *J. Am. Chem. Soc.* **129**, 7480 (2007)
16. G.I. Dzhardimalieva, I.E. Uflyand, *RSC Adv.* **7**, 42242 (2017)
17. R. Das, P. Pachfule, R. Banerjee, P. Poddar, *Nanoscale* **4**, 591 (2012)
18. K. Akhbari, N.B. Bahman, A. Morsali, P. Retailleau, *J. Iran. Chem. Soc.* **13**, 165 (2016)
19. F.S. Shirazi, K. Akhbari, *Inorg. Chim. Acta* **436**, 1 (2015)
20. M. Moeinian, K. Akhbari, *J. Solid State Chem.* **225**, 459 (2015)
21. F. Zou, X. Hu, Z. Li, L. Qie, C. Hu, R. Zeng, Y. Jiang, Y. Huang, *Adv. Mater.* **26**, 6622 (2014)
22. F.S. Shirazi, K. Akhbari, *RSC Adv.* **5**, 50778 (2015)
23. K. Akhbari, A. Morsali, *Z. Anorg. Allg. Chem.* **638**, 692 (2012)
24. M. Ramanathan, S.B. Darling, *Polym. Int.* **62**, 1123 (2013)
25. M. Ramanathan, Y.-C. Tseng, K. Ariga, S.B. Darling, *J. Mater. Chem. C* **1**, 2080 (2013)
26. M. Ramazani, A. Morsali, *Ultrason. Sonochem.* **18**, 1160 (2011)
27. K. Akhbari, A. Morsali, *Inorg. Chim. Acta* **363**, 1435 (2010)
28. H.R. Moon, J.H. Kim, M.P. Suh, *Angew. Chem. Int. Ed.* **44**, 1261 (2005)
29. M. Salavati-Niasari, F. Mohandes, F. Davar, M. Mazaheri, M. Monemzadeh, N. Yavarinia, *Inorg. Chim. Acta* **362**, 3691 (2009)
30. A.D. Pomogailo, A.S. Rozenberg, G.I. Dzhardimalieva, *Russ. Khim. Zh. (Mendeleev Chem. J.)* **53**, 140 (2009)
31. R. Coskun, M. Yigitoglu, M. Sacak, *J. Appl. Polym. Sci.* **75**, 766 (2000)
32. J.J. Vittal, M.T. Ng, *Acc. Chem. Res.* **39**, 869 (2006)
33. M.A. Malik, P. O'Brien, in *Organometallic and Metallo-Organic Precursors for Nanoparticles Precursor Chemistry of Advanced Materials*, ed. by R. Fischer (Springer, Berlin, 2005), p. 173
34. Y. Hanifehpour, B. Mirtamizdoust, S.W. Joo, *J. Inorg. Organomet. Polym.* **22**, 816 (2012)
35. Y. Hanifehpour, S. Mokhtari Asl, B. Mirtamizdoust, S.W. Joo, *J. Inorg. Organomet. Polym.* **22**, 923 (2012)

36. Y. Hanifehpour, B. Mirtamizdoust, S.W. Joo, J. Inorg. Organomet. Polym. **22**, 916 (2012)
37. Y. Hanifehpour, B. Mirtamizdoust, S.W. Joo, J. Inorg. Organomet. Polym. **22**, 549 (2012)
38. B. Liu, H. Shioyama, T. Akita, Q. Xu, J. Am. Chem. Soc. **130**, 5390 (2008)
39. W. Cho, S. Park, M. Oh, Chem. Commun. **47**, 4138 (2011)
40. X. Xu, R. Cao, S. Jeong, J. Cho, Nano Lett. **12**, 4988 (2012)
41. T.K. Kim, K.J. Lee, J.Y. Cheon, J.H. Lee, S.H. Joo, H.R. Moon, J. Am. Chem. Soc. **135**, 8940 (2013)
42. J.-K. Sun, Q. Xu, Energy Environ. Sci. **7**, 2071 (2014)
43. J. Xi, Y. Xia, Y. Xu, J. Xiao, S. Wang, Chem. Commun. **51**, 10479 (2015)
44. A. Kong, Q. Lin, C. Mao, X. Bu, P. Feng, Chem. Commun. **50**, 15619 (2014)
45. S. Ma, G.A. Goenaga, A.V. Call, D.-J. Liu, Chem. Eur. J. **17**, 2063 (2011)
46. Y. Lü, W. Zhan, Y. He, Y. Wang, X. Kong, Q. Kuang, Z. Xie, L. Zheng, ACS Appl. Mater. Interfaces **6**, 4186 (2014)
47. H. Pang, B. Zhang, J. Du, J. Chen, J. Zhang, S. Li, RSC Adv. **2**, 2257 (2012)
48. F. Bigdeli, A. Morsali, Mater. Lett. **64**, 4 (2010)
49. F. Zhang, F.-L. Bei, J.-M. Cao, X. Wang, J. Solid State Chem. **181**, 143 (2008)
50. Z. Li, Y. Xiong, Y. Xie, Nanotechnology **16**, 2303 (2005)
51. M. Nagarathinam, K. Saravanan, W.L. Leong, P. Balaya, J.J. Vittal, Cryst. Growth Des. **9**, 4461 (2009)
52. A. Aslani, A. Morsali, M. Zeller, Solid State Sci. **10**, 1591 (2008)
53. C.Y. Su, A.M. Goforth, M.D. Smith, P.J. Pellechia, H.C. zur Loye, J. Am. Chem. Soc. **126**, 3576 (2004)
54. Y.J. Xiong, Y. Xie, Z.Q. Li, C.Z. Wu, Chem. Eur. J. **9**, 1645 (2003)
55. Y. Xiong, Z. Li, R. Zhang, Y. Xie, J. Yang, C. Wu, J. Phys. Chem. B **107**, 3697 (2003)
56. A. Pramanik, G. Das, CrystEngComm **12**, 401 (2010)
57. S. Khanjani, A. Morsali, J. Mol. Struct. **935**, 27 (2009)
58. S. Khanjani, A. Morsali, J. Coord. Chem. **62**, 3343 (2009)
59. R.K. Sahu, A.K. Ray, T.M.C. Pathak, Cryst. Growth Des. **8**, 3754 (2008)
60. P. Banerjee, S. Kar, A. Bhaumik, G.-H. Lee, S.-M. Peng, S. Goswami, Eur. J. Inorg. Chem. **835** (2007)
61. M. Mohammadi, A. Morsali, Mater. Lett. **63**, 2349 (2009)
62. H. Haddadian, A. Aslani, A. Morsali, Inorg. Chim. Acta **362**, 1805 (2009)
63. N. Soltanzadeh, A. Morsali, Polyhedron **28**, 1343 (2009)
64. S. Khanjani, A. Morsali, J. Coord. Chem. **62**, 3642 (2009)
65. F. Bigdeli, A. Morsali, P. Retailleau, Polyhedron **29**, 801 (2010)
66. N. Soltanzadeh, A. Morsali, Ultrason. Sonochem. **17**, 139 (2010)
67. H. Pang, F. Gao, Q. Chen, R.M. Liu, Q.Y. Lu, Dalton Trans. **41**, 5862 (2012)
68. C.C. Li, L. Mei, L.B. Chen, Q.H. Li, T.H. Wang, J. Mater. Chem. **22**, 4982 (2012)
69. D. Su, H.S. Kim, W.S. Kim, G.X. Wang, Chem. Eur. J. **18**, 8224 (2012)
70. W. Lin, W.J. Rieter, K.M.L. Taylor, Angew. Chem. Int. Ed. **48**, 650 (2009)
71. A. Carne, C. Carbonell, I. Imaz, D. Maspoch, Chem. Soc. Rev. **40**, 291 (2011)
72. A.M. Spokoyiny, D. Kim, A. Sumrein, C.A. Mirkin, Chem. Soc. Rev. **38**, 1218 (2009)
73. Z. Moradi, K. Akhbari, A. Phuruangrat, F. Costantino, J. Mol. Struct. **1133**, 172 (2017)
74. C. Liang, Z. Li, S. Dai, Angew. Chem. Int. Ed. **47**, 3696 (2008)
75. A.J. Amali, J.-K. Sun, Q. Xu, Chem. Commun. **50**, 1519 (2014)
76. L. Radhakrishnan, J. Reboul, S. Furukawa, P. Srinivasu, S. Kitagawa, Y. Yamauchi, Chem. Mater. **23**, 1225 (2011)
77. M. Hu, J. Reboul, S. Furukawa, L. Radhakrishnan, Y. Zhang, P. Srinivasu, H. Iwai, H. Wang, Y. Nemoto, N. Suzuki, S. Kitagawa, Y. Yamauchi, Chem. Commun. **47**, 8124 (2011)
78. H.-Y. Shi, B. Deng, S.-L. Zhong, L. Wang, A.-W. Xu, J. Mater. Chem. **21**, 12309 (2011)
79. B. Liu, X. Zhang, H. Shioyama, T. Mukai, T. Sakai, Q. Xu, J. Power Sources **195**, 857 (2010)
80. W. Cho, Y.H. Lee, H.J. Lee, M. Oh, Chem. Commun. 4756 (2009)
81. W. Cho, Y.H. Lee, H.J. Lee, M. Oh, Adv. Mater. **23**, 1720 (2011)

82. J. Xu, Q. Liu, W.-Y. Sun, *Solid State Sci.* **12**, 1575 (2010)
83. R. Bashiri, K. Akhbari, A. Morsali, *Inorg. Chim. Acta* **362**, 1035 (2009)
84. S. Jung, W. Cho, H.J. Lee, M. Oh, *Angew. Chem. Int. Ed.* **48**, 1459 (2009)
85. Y.H. Song, X. Li, L.L. Sun, L. Wang, *RSC Adv.* **5**, 7267 (2015)
86. K. Wang, X. Ma, Z. Zhang, M. Zheng, Z. Geng, Z.L. Wang, *Chem. Eur. J.* **19**, 7084 (2013)
87. H. Thakuria, B.M. Borah, G. Das, *Eur. J. Inorg. Chem.* 524 (2007)
88. S.H. Yu, J. Yang, Y.T. Qian, M. Yoshimura, *Chem. Phys. Lett.* **361**, 362 (2005)
89. O.C. Monteiro, H.I.S. Nogueira, T. Trindade, *Chem. Mater.* **13**, 2103 (2001)
90. Z. Wang, X. Li, H. Xu, Y. Yang, Y. Cui, H. Pan, Z. Wang, B. Chen, G. Qian, *J. Mater. Chem. A* **2**, 12571 (2014)
91. S.H. Yu, M. Yoshimura, *Adv. Mater.* **14**, 296 (2002)
92. Y.H. Ni, X.F. Cao, G.Z. Hu, Z.S. Yang, X.W. Wei, Y.H. Chen, J. Xu, *Cryst. Growth Des.* **7**, 280 (2007)
93. Z. Ni, R.I. Masel, *J. Am. Chem. Soc.* **128**, 12394 (2006)
94. W. Xia, R.Q. Zou, L. An, D.G. Xia, S.J. Guo, *Energy Environ. Sci.* **8**, 568 (2015)
95. H.R. Moon, D.W. Lim, M.P. Suh, *Chem. Soc. Rev.* **42**, 1807 (2013)
96. F.S. Shirazi, K. Akhbari, *Inorg. Chem. Commun.* **63**, 5 (2016)
97. S. Hojaghani, K. Akhbari, M.H. Sadr, A. Morsali, *Inorg. Chem. Commun.* **44**, 1 (2014)
98. K. Akhbari, A. Morsali, *Polyhedron* **30**, 1456 (2011)
99. K. Akhbari, A. Morsali, *CrystEngComm* **13**, 2047 (2011)
100. K. Akhbari, A. Morsali, *CrystEngComm* **14**, 1618 (2012)
101. K. Akhbari, M. Hemmati, A. Morsali, *J. Inorg. Organomet. Polym.* **21**, 352 (2011)
102. K. Akhbari, A. Morsali, *Mater. Lett.* **141**, 315 (2015)
103. S.S. Dhankhar, M. Kaur, C.M. Nagaraja, *Eur. J. Inorg. Chem.* 5669 (2015)
104. W. Chaikittisilp, K. Ariga, Y. Yamauchi, *J. Mater. Chem. A* **1**, 14 (2013)
105. X. Wang, J. Zhou, H. Fu, W. Li, X. Fan, G. Xin, J. Zheng, X. Li, *J. Mater. Chem. A* **2**, 14064 (2014)
106. W. Xia, J.H. Zhu, W.H. Guo, L. An, D.G. Xia, R.Q. Zou, *J. Mater. Chem. A* **2**, 11606 (2014)
107. W. Chaikittisilp, M. Hu, H. Wang, H.-S. Huang, T. Fujita, K.C.-W. Wu, L.-C. Chen, Y. Yamauchi, K. Ariga, *Chem. Commun.* **48**, 7259 (2012)
108. Y. Sharma, N. Sharma, G.V.S. Rao, B.V.R. Chowdari, *Adv. Funct. Mater.* **17**, 2855 (2007)
109. A. Banerjee, K.K. Upadhyay, D. Puthusseri, V. Aravindan, S. Madhavi, S. Ogale, *Nanoscale* **6**, 4387 (2014)
110. S.-N. Zhao, X.-Z. Song, S.-Y. Song, H.-J. Zhang, *Coord. Chem. Rev.* **337**, 80 (2017)
111. Z. Li, L. Yin, *J. Mater. Chem.* **3**, 21569 (2015)
112. F.S. Shirazi, K. Akhbari, *Ultrason. Sonochem.* **31**, 51 (2016)
113. S. Aghabeygi, L. Hashemi, A. Morsal, *J. Inorg. Organomet. Polym.* **26**, 1 (2016)
114. D.C. Guo, J. Mi, G.P. Hao, W. Dong, G. Xiong, W.C. Li, A.H. Lu, *Energy Environ. Sci.* **6**, 652 (2013)
115. B. Liu, H. Shioyama, H.L. Jiang, X.B. Zhang, Q. Xu, *Carbon* **48**, 456 (2010)
116. P. Simon, Y. Gogotsi, *Nat. Mater.* **7**, 845 (2008)
117. W. Schmitt, J.P. Hill, M.P. Juanico, A. Caneschi, F. Costantino, C.E. Anson, A.K. Powell, *Angew. Chem. Int. Ed.* **44**, 4187 (2005)
118. W. Xia, A. Mahmood, R. Zou, Q. Xu, *Energy Environ. Sci.* **8**, 1837 (2015)
119. K. Shen, X. Chen, J. Chen, Y. Li, *ACS Catal.* **6**, 5887 (2016)
120. H.-L. Jiang, B. Liu, Y.-Q. Lan, K. Kuratani, T. Akita, H. Shioyama, F. Zong, Q. Xu, *J. Am. Chem. Soc.* **133**, 11854 (2011)
121. M. Hu, J. Reboul, S. Furukawa, N.L. Torad, Q. Ji, P. Srinivasu, K. Ariga, S. Kitagawa, Y. Yamauchi, *J. Am. Chem. Soc.* **134**, 2864 (2012)
122. S. Lim, K. Suh, Y. Kim, M. Yoon, H. Park, D.N. Dybtsev, K. Kim, *Chem. Commun.* **48**, 7447 (2012)
123. P. Zhang, F. Sun, Z. Xiang, Z. Shen, J. Yun, D. Cao, *Energy Environ. Sci.* **7**, 442 (2014)
124. A. Aijaz, N. Fujiwara, Q. Xu, *J. Am. Chem. Soc.* **136**, 6790 (2014)

125. A. Almasoudi, R. Mokaya, *J. Mater. Chem.* **22**, 146 (2012)
126. M. O'Keeffe, O.M. Yaghi, *Chem. Rev.* **112**, 675 (2012)
127. S. Horike, S. Shimomura, S. Kitagawa, *Nat. Chem.* **1**, 695 (2009)
128. J.J. Perry IV, J.A. Perman, M.J. Zaworotko, *Chem. Soc. Rev.* **38**, 1400 (2009)
129. K.S. Park, Z. Ni, A.P. Cote, J.Y. Choi, R. Huang, F.J. Uribe-Romo, H.K. Chae, M. O'Keeffe, O.M. Yaghi, *Proc. Natl. Acad. Sci. U. S. A.* **103**, 10186 (2006)
130. A. Comotti, S. Bracco, P. Sozzani, S. Horike, R. Matsuda, J. Chen, M. Takata, Y. Kubota, S. Kitagawa, *J. Am. Chem. Soc.* **130**, 13664 (2008)
131. S.-L. Li, Q. Xu, *Energy Environ. Sci.* **6**, 1656 (2013)
132. P. Pachfule, B.P. Biswal, R. Banerjee, *Chem. Eur. J.* **18**, 11399 (2012)
133. S.J. Yang, C.R. Park, *Adv. Mater.* **24**, 4010 (2012)
134. S.L. James, *Chem. Soc. Rev.* **32**, 276 (2003)
135. S.L. Zhao, H.J. Yin, L. Du, L.C. He, K. Zhao, L. Chang, G.P. Yin, H.J. Zhao, S.Q. Liu, Z.Y. Tang, *ACS Nano* **8**, 12660 (2014)
136. L.J. Zhang, Z.X. Su, F.L. Jiang, L.L. Yang, J.J. Qian, Y.F. Zhou, W.M. Li, M.C. Hong, *Nanoscale* **6**, 6590 (2014)
137. S.T. Meek, J.A. Greathouse, M.D. Allendorf, *Adv. Mater.* **23**, 249 (2011)
138. M. Jahan, Z. Liu, K.P. Loh, *Adv. Funct. Mater.* **23**, 5363 (2013)
139. S. Lim, K. Suh, Y. Kim, M. Yoon, H. Park, D.N. Dybtsev, K. Kim, *Chem. Commun.* **48**, 7447 (2012)
140. D.N. Dybtsev, H. Chun, K. Kim, *Angew. Chem. Int. Ed.* **38**, 5143 (2004)
141. A. Filer, H.-J. Choi, J.-M. Seo, J.-B. Baek, *Phys. Chem. Chem. Phys.* **16**, 11150 (2014)
142. J.P. Paraknowitsch, J. Zhang, D. Su, A. Thomas, M. Antonietti, *Adv. Mater.* **22**, 87 (2010)
143. Y. Wang, J. Zhang, X. Wang, M. Antonietti, H. Li, *Angew. Chem. Int. Ed.* **49**, 3356 (2010)
144. A. Thomas, A. Fischer, F. Goettmann, M. Antonietti, J.O. Müller, R. Schloegl, J.M. Carlssonc, *J. Mater. Chem.* **18**, 4893 (2008)
145. S. Yang, R.E. Bachman, X. Feng, K. Müllen, *Acc. Chem. Res.* **46**, 116 (2013)
146. J. Hu, H. Wang, Q. Gao, H. Guo, *Carbon* **48**, 3599 (2010)
147. S.J. Yang, T. Kim, J.H. Im, Y.S. Kim, K. Lee, H. Jung, C.R. Park, *Chem. Mater.* **24**, 464 (2012)
148. J.S. Li, S.L. Li, Y.J. Tang, K. Li, L. Zhou, N. Kong, Y.Q. Lan, J.C. Bao, Z.H. Dai, *Sci. Rep.* **4**, 5130 (2014)
149. N.L. Torad, M. Hu, Y. Kamachi, K. Takai, M. Imura, M. Naito, Y. Yamauchi, *Chem. Commun.* **49**, 2521 (2013)
150. W. Xia, B. Qiu, D. Xia, R. Zou, *Sci. Rep.* **3**, 1935 (2013)
151. Q. Wang, W. Xia, W. Guo, L. An, D. Xia, R. Zou, *Chem. Asian J.* **8**, 1879 (2013)
152. D. Yuan, J. Chen, S. Tan, N. Xia, Y. Liu, *Electrochem. Commun.* **11**, 1191 (2009)
153. L. Ye, G. Chai, Z. Wen, *Adv. Funct. Mater.* 1606190 (2017)
154. A.J. Amali, H. Hoshino, C. Wu, M. Ando, Q. Xu, *Chem. Eur. J.* **20**, 8279 (2014)
155. P. Pachfule, D. Shinde, M. Majumder, Q. Xu, *Nat. Chem.* **8**, 718 (2016)
156. L. Chen, J. Bai, C. Wang, Y. Pan, M. Scheer, X. You, *Chem. Commun.* 1581 (2008)
157. J.L. Long, Y. Zhou, Y.W. Li, *Chem. Commun.* **51**, 2331 (2015)
158. Q. Tian, Z. Zhang, L. Yang, S. Hirano, *Carbon* **93**, 887 (2015)
159. C.P. Li, J. Chen, C.S. Liu, M. Du, *Chem. Commun.* **51**, 2768 (2015)
160. R. Matsuoka, R. Toyoda, R. Sakamoto, M. Tsuchiya, K. Hoshiko, T. Nagayama, Y. Nonoguchi, K. Sugimoto, E. Nishibori, T. Kawai, H. Nishihara, *Chem. Sci.* **6**, 2853 (2015)
161. A. Béziau, S.A. Baudron, G. Rogez, *Inorg. Chem.* **54**, 2032 (2015)
162. Y. Ye, L. Zhang, Q. Peng, *J. Am. Chem. Soc.* **137**, 913 (2015)
163. L. Zhang, X. Wang, R. Wang, M. Hong, *Chem. Mater.* **27**, 7610 (2015)
164. J.-K. Sun, Q. Xu, *Chem. Commun.* **50**, 13502 (2014)
165. H. Li, M. Eddaoudi, M. O'Keeffe, O.M. Yaghi, *Nature* **402**, 276 (1999)
166. J. Tang, R.R. Salunkhe, J. Liu, N.L. Torad, M. Imura, S. Furukawa, Y. Yamauchi, *J. Am. Chem. Soc.* **137**, 1572 (2015)
167. Q. Zhu, Y. Li, Y. Gao, X. Wang, S.Y. Song, *Chem. Eur. J.* **22**, 6876 (2016)

168. M. Zeng, Y. Liu, F. Zhao, K. Nie, N. Han, X. Wang, W. Huang, X. Song, J. Zhong, Y. Li, *Adv. Funct. Mater.* **26**, 4397 (2016)
169. Y.Z. Chen, C.M. Wang, Z.Y. Wu, Y.J. Xiong, Q. Xu, S.H. Yu, H.L. Jiang, *Adv. Mater.* **27**, 5010 (2015)
170. R.R. Salunkhe, Y. Kamachi, N.L. Torad, S.M. Hwang, Z. Sun, S.X. Dou, J.H. Kim, Y. Yamauchi, *J. Mater. Chem. A* **2**, 19848 (2014)
171. P. Zhang, F. Sun, Z. Shen, D. Cao, *J. Mater. Chem. A* **2**, 12873 (2014)
172. R. Wu, X. Qian, K. Zhou, J. Wei, J. Lou, P.M. Ajayan, *ACS Nano* **8**, 6297 (2014)
173. H.J. Lee, W. Cho, E. Lim, M. Oh, *Chem. Commun.* **50**, 5476 (2014)
174. K. Xi, S. Cao, X. Peng, C. Ducati, R.V. Kumar, A.K. Cheetham, *Chem. Commun.* **49**, 2192 (2013)
175. R.R. Salunkhe, J. Tang, Y. Kamachi, T. Nakato, J.H. Kim, Y. Yamauchi, *ACS Nano* **9**, 6288 (2015)
176. N.L. Torad, M. Hu, S. Ishihara, H. Sukegawa, A.A. Belik, M. Imura, K. Ariga, Y. Sakka, Y. Yamauchi, *Small* **10**, 2096 (2014)
177. G. Wang, L. Zhang, J. Zhang, *Chem. Soc. Rev.* **41**, 797 (2012)
178. G. Yu, X. Xie, L. Pan, Z. Bao, Y. Cui, *Nano Energy* **2**, 213 (2013)
179. M. Zhi, C. Xiang, J. Li, M. Li, N. Wu, *Nanoscale* **5**, 72 (2013)
180. Q. Qu, S. Yang, X. Feng, *Adv. Mater.* **23**, 5574 (2011)
181. C. Nethravathi, C. Rajamathi, M. Rajamathi, X. Wang, U.K. Gautam, D. Golberg, Y. Bando, *ACS Nano* **8**, 2755 (2014)
182. Z.J. Han, D.H. Seo, S. Yick, J.H. Chen, K. Ostrikov, *NPG Asia Mater.* **6**, 140 (2014)
183. M. Mazloumi, S. Shadmehr, Y. Rangom, L.F. Nazar, X. Tang, *ACS Nano* **7**, 4281 (2013)
184. G. Lota, K. Fic, E. Frackowiak, *Energy Environ. Sci.* **4**, 1592 (2011)
185. S. Bose, T. Kuila, A. Mishra, K. Ananta, R. Rajasekar, N.H. Kim, J.H. Lee, *J. Mater. Chem.* **22**, 767 (2012)
186. M.G. Bakker, R.M. Frazier, S. Burkett, J.E. Bara, N. Chopra, S. Spear, S. Pan, C. Xu, *Nanomater. Energy* **1**, 136 (2012)
187. T. Kuila, P. Khanra, N.H. Kim, J.H. Lee, in *Handbook of Carbon Nanomaterials*, vol. 6, ed. by F. D'Souza, K.M. Kadish (World Scientific, Singapore, 2014), pp. 1–49
188. S. Faraji, F.N. Ani, *Renew. Sustain. Energy Rev.* **42**, 823 (2015)
189. H. Jin, J. Wang, D. Su, Z. Wei, Z. Pang, Y. Wang, *J. Am. Chem. Soc.* **137**, 2688 (2015)
190. Y. Liang, H. Wang, J. Zhou, Y. Li, J. Wang, T. Regier, H. Dai, *J. Am. Chem. Soc.* **134**, 3517 (2012)
191. Y. Liang, H. Wang, P. Diao, W. Chang, G. Hong, Y. Li, M. Gong, L. Xie, J. Zhou, J. Wang, *J. Am. Chem. Soc.* **134**, 15849 (2012)
192. H. Jiang, J. Ma, C. Li, *Adv. Mater.* **24**, 4197 (2012)
193. J. Jiang, Y. Li, J. Liu, X. Huang, C. Yuan, X.W. Lou, *Adv. Mater.* **24**, 5166 (2012)
194. W. Chaikittisilp, N.L. Torad, C. Li, M. Imura, N. Suzuki, S. Ishihara, K. Ariga, Y. Yamauchi, *Chem. Eur. J.* **20**, 4217 (2014)
195. W. Bak, H.S. Kim, H. Chun, W.C. Yoo, *Chem. Commun.* **51**, 7238 (2015)
196. A. Pariyar, S. Gopalakrishnan, J. Stansbery, R.L. Patel, X. Liang, N. Gerasimchuk, A. Choudhury, *RSC Adv.* **6**, 38533 (2016)
197. X. Li, Y. Fang, X. Lin, M. Tian, X. An, Y. Fu, R. Li, J. Jin, J. Ma, *J. Mater. Chem. A* **3**, 17392 (2015)
198. M. Lu, K. Zhang, H.S. Chan, J. Wu, *J. Mater. Chem. A* **22**, 1845 (2012)
199. J. Tao, N. Liu, W. Ma, L. Ding, L. Li, J. Su, Y. Gao, *Sci. Rep.* **3**, 2286 (2013)
200. G. Yu, L. Hu, N. Liu, H. Wang, M. Vosgueritchian, Y. Yang, Y. Cui, Z. Bao, *Nano Lett.* **11**, 4438 (2011)
201. Z.S. Wu, D.W. Wang, W. Ren, J. Zhao, G. Zhou, F. Li, H.M. Cheng, *Adv. Mater.* **20**, 3595 (2010)
202. R. Bi, X.L. Wu, F.F. Cao, L.Y. Jiang, Y.G. Guo, L.J. Wan, *J. Phys. Chem. C* **114**, 2448 (2010)

203. S.C. Hong, S. Kim, W.J. Jang, T.H. Han, J.P. Hong, J.S. Oh, T. Hwang, Y. Lee, J.H. Lee, J. D. Nam, *RSC Adv.* **4**, 48276 (2014)
204. J. Zhu, D. Lei, G. Zhang, Q. Li, B. Lu, T. Wang, *Nanoscale* **5**, 5499 (2013)
205. Y. Huang, D. Wu, J. Wang, S. Han, L. Lv, F. Zhang, X. Feng, *Small* **10**, 2226 (2014)
206. Y. Zhang, Z. Hu, Y. Liang, Y. Yang, N. An, Z. Li, H. Wu, *J. Mater. Chem. A* **3**, 15057 (2015)
207. R. Madhu, V. Veeramani, S.M. Chen, A. Manikandan, A.Y. Lo, Y.L. Chueh, *ACS Appl. Mater. Interfaces* **174**, 1104 (2015)
208. Q. Liao, N. Li, S. Jin, G. Yang, C. Wang, *ACS Nano* **9**, 5310 (2015)
209. J. Mu, B. Chen, Z. Guo, M. Zhang, Z. Zhang, P. Zhang, C. Shao, Y. Liu, *Nanoscale* **3**, 5034 (2011)
210. D. Liu, X. Wang, X. Wang, W. Tian, J. Liu, C. Zhi, D. He, Y. Bando, D. Golberg, *J. Mater. Chem. A* **1**, 1952 (2013)
211. B. Sethuraman, K. Purushothaman, G. Muralidharan, *RSC Adv.* **4**, 4631 (2014)
212. C. Guan, J. Liu, Y. Wang, L. Mao, Z. Fan, Z. Shen, H. Zhang, J. Wang, *ACS Nano* **9**, 5198 (2015)
213. D. Zhao, J.L. Shui, L.R. Grabstanowicz, C. Chen, S.M. Commet, T. Xu, J. Lu, D.J. Liu, *Adv. Mater.* **26**, 1093 (2014)
214. Z.-S. Wu, L. Chen, J. Liu, K. Parvez, H. Liang, J. Shu, H. Sachdev, R. Graf, X. Feng, K. Müllen, *Adv. Mater.* **26**, 1450 (2014)
215. Q. Lin, X. Bu, A. Kong, C. Mao, X. Zhao, F. Bu, P. Feng, *J. Am. Chem. Soc.* **137**, 2235 (2015)
216. W. Zhang, T. Cui, L. Yang, C. Zhang, M. Cai, S. Sun, Y. Yao, X. Zhuang, F. Zhang, *J. Colloid Interface Sci.* **497**, 108 (2017)
217. S. Jin, J.P. Hill, Q. Ji, L. Kumar Shrestha, K. Ariga, *J. Mater. Chem. A* **4**, 5737 (2016)
218. S.-Y. Ding, J. Gao, Q. Wang, Y. Zhang, W.-G. Song, C.-Y. Su, W. Wang, *J. Am. Chem. Soc.* **133**, 19816 (2011)
219. Z. Xiang, Y. Xue, D. Cao, L. Huang, J.-F. Chen, L. Dai, *Angew. Chem. Int. Ed.* **53**, 2433 (2014)
220. Q. Lin, X. Bu, A. Kong, C. Mao, F. Bu, P. Feng, *Adv. Mater.* **27**, 3431 (2015)
221. B. Voloskiy, H. Fei, Z. Zhao, S. Lee, M. Li, Z. Lin, B. Papandrea, C. Wang, Y. Huang, X. Duan, *ACS Appl. Mater. Interfaces* **8**, 26769 (2016)
222. D.Y. Chung, M.J. Kim, N. Kang, J.M. Yoo, H. Shin, O.-H. Kim, Y.-E. Sung, *Chem. Mater.* **29**, 2890 (2017)
223. J.L.C. Rowsell, O.M. Yaghi, *J. Am. Chem. Soc.* **128**, 1304 (2006)
224. C.H. Bai, X.F. Yao, Y.W. Li, *ACS Catal.* **5**, 884 (2015)
225. T. Wang, Q. Zhou, X. Wang, J. Zheng, X. Li, *J. Mater. Chem. A* **3**, 16435 (2015)
226. Z. Han, Y. Yu, Y. Zhang, B. Dong, A. Kong, Y. Shan, *J. Mater. Chem. A* **3**, 23716 (2015)
227. L. Zhang, Y.H. Hu, *J. Phys. Chem. C* **114**, 2566 (2010)
228. Y.C. Wang, W.B. Li, L. Zhao, B.Q. Xu, *Phys. Chem. Chem. Phys.* **18**, 17941 (2016)
229. S.R. Caskey, A.G. Wong-Foy, A.J. Matzger, *J. Am. Chem. Soc.* **130**, 10870 (2008)
230. K. Artyushkova, S. Levendosky, P. Atanassov, J. Fulghum, *Top. Catal.* **46**, 263 (2007)
231. J.A. Paquette, J.B. Gilroy, *J. Polym. Sci., Part A: Polym. Chem.* **54**, 3257 (2016)
232. W. Xia, A. Mahmood, Z. Liang, R. Zou, S. Guo, *Angew. Chem. Int. Ed.* **55**, 2650 (2016)
233. D. Zhao, J.-L. Shui, C. Chen, X. Chen, B.M. Reprögle, D. Wang, D.-J. Liu, *Chem. Sci.* **3**, 3200 (2012)
234. M. Seredych, E. Rodriguez-Castellon, T.J. Bandoz, *J. Mater. Chem. A* **2**, 20164 (2014)
235. Y. Hou, T. Huang, Z. Wen, S. Mao, S. Cui, J. Chen, *Adv. Energy Mater.* **4**, 1400337 (2014)
236. X. Zhao, H. Zhao, T. Zhang, X. Yan, Y. Yuan, H. Zhang, H. Zhao, D. Zhang, G. Zhu, X. Yao, *J. Mater. Chem. A* **2**, 11666 (2014)
237. J. Li, Y. Chen, Y. Tang, S. Li, H. Dong, K. Li, M. Han, Y.-Q. Lan, J. Bao, Z. Dai, *J. Mater. Chem. A* **2**, 6316 (2014)
238. Q. Li, P. Xu, W. Gao, S. Ma, G. Zhang, R. Cao, J. Cho, H.L. Wang, G. Wu, *Adv. Mater.* **26**, 1378 (2014)

239. E. Proietti, F. Jaouen, M. LefAvre, N. Larouche, J. Tian, J. Herranz, J.-P. Dodelet, *Nat. Commun.* **2**, 416 (2011)
240. W. Zhang, Z.Y. Wu, H.L. Jiang, S.H. Yu, *J. Am. Chem. Soc.* **136**, 14385 (2014)
241. T.Y. Ma, S. Dai, M. Jaroniec, S.Z. Qiao, *J. Am. Chem. Soc.* **136**, 13925 (2014)
242. B. Folch, J. Larionova, Y. Guari, L. Datas, C. Guerin, *J. Mater. Chem.* **16**, 4435 (2006)
243. L. Zhao, Y. Qiu, J. Yu, X. Deng, C. Dai, X. Bai, *Nanoscale* **5**, 4902 (2013)
244. W. Chen, R.B. Rakhi, L. Hu, X. Xie, Y. Cui, H.N. Alshareef, *Nano Lett.* **11**, 5165 (2011)
245. J. Zhao, M. Li, J. Sun, L. Liu, P. Su, Q. Yang, C. Li, *Chem. Eur. J.* **18**, 3163 (2012)
246. A. Taguchi, F. Schüth, *Micropor. Mesopor. Mater.* **77**, 1 (2005)
247. E. Casbeer, V.K. Sharma, X.-Z. Li, *Sep. Purif. Technol.* **87**, 1 (2012)
248. Y. Yamada, K. Yano, D. Hong, S. Fukuzumi, *Phys. Chem. Chem. Phys.* **14**, 5753 (2012)
249. D. Hong, Y. Yamada, A. Nomura, S. Fukuzumi, *Phys. Chem. Chem. Phys.* **15**, 19125 (2013)
250. S. Fukuzumi, D. Hong, Y. Yamada, *J. Phys. Chem. Lett.* **4**, 3458 (2013)
251. X. Yan, N. Lu, B. Fan, J. Bao, D. Pan, M. Wang, R. Li, *CrystEngComm* **17**, 6426 (2015)
252. E. Mirzadeh, K. Akhbari, *CrystEngComm* **18**, 7410 (2016)
253. L. Hashemi, A. Morsali, *J. Inorg. Organomet. Polym.* **22**, 272 (2012)
254. M.A. Alavi, A. Morsali, S.W. Joo, B.K. Min, *Ultrason. Sonochem.* **22**, 349 (2015)
255. A. Mehrani, A. Morsali, Y. Hanifehpour, S.W. Joo, *Ultrason. Sonochem.* **21**, 1430 (2014)
256. M. Rakibuddin, R. Ananthkrishnan, *RSC Adv.* **5**, 68117 (2015)
257. Z. Wang, L. Zhou, X.W. David Lou, *Adv. Mater.* **24**, 1903 (2012)
258. N. Stock, S. Biswas, *Chem. Rev.* **112**, 933 (2012)
259. M. Sindoro, N. Yanai, A.Y. Jee, S. Granick, *Acc. Chem. Res.* **47**, 459 (2014)
260. H. Wu, Q. Gong, D.H. Olson, J. Li, *Chem. Rev.* **112**, 836 (2012)
261. M.Y. Masoomi, A. Morsali, *RSC Adv.* **3**, 19191 (2013)
262. L.N. Jin, Q. Liu, W.Y. Sun, *CrystEngComm* **16**, 3816 (2014)
263. Y. Ma, Y. Ni, F. Guo, N. Xiang, *Cryst. Growth Des.* **15**, 2243 (2015)
264. J. Cravillon, R. Nayuk, S. Springer, A. Feldhoff, K. Huber, M. Wiebcke, *Chem. Mater.* **23**, 2130 (2011)
265. J. Cravillon, C.A. Schroder, H. Bux, A. Rothkirch, J. Caro, M. Wiebcke, *CrystEngComm* **14**, 492 (2012)
266. L. Hu, Q. Chen, *Nanoscale* **6**, 1236 (2014)
267. L. Zhang, H.B. Wu, S. Madhavi, H.H. Hng, X.W. Lou, *J. Am. Chem. Soc.* **134**, 17388 (2012)
268. L. Zhang, H.B. Wu, X.W. Lou, *J. Am. Chem. Soc.* **135**, 10664 (2013)
269. H. Song, L. Shen, C. Wang, *J. Mater. Chem. A* **2**, 20597 (2014)
270. W. Cho, H.J. Lee, M. Oh, *J. Am. Chem. Soc.* **130**, 16943 (2008)
271. X.D. Wang, C.J. Summers, Z.L. Wang, *Nano Lett.* **4**, 423 (2004)
272. Y.-R. Ma, C.-M. Lin, C.-L. Yeh, R.-T. Huang, *J. Vac. Sci. Technol., B* **23**, 2141 (2005)
273. Y.-R. Ma, C.-C. Tsai, S.F. Lee, K.-W. Cheng, Y. Liou, Y.D. Yao, *J. Magn. Magn. Mater.* **304**, E13 (2006)
274. R.S. Devan, W.-D. Ho, J.-H. Lin, S.Y. Wu, Y.-R. Ma, P.-C. Lee, Y. Liou, *Cryst. Growth Des.* **8**, 4465 (2008)
275. L. Kumari, Y.-R. Ma, C.-C. Tsai, Y.-W. Lin, S.Y. Wu, K.-W. Cheng, Y. Liou, *Nanotechnology* **18**, 115717 (2007)
276. Y.W. Heo, D.P. Norton, L.C. Tien, Y. Kwon, B.S. Kang, F. Ren, S.J. Pearton, J.R. LaRoche, *Mater. Sci. Eng., R* **47**, 1 (2004)
277. J. Zhou, Y. Ding, S.Z. Deng, L. Gong, N.S. Xu, Z.L. Wang, *Adv. Mater.* **17**, 2107 (2005)
278. Z.L. Wang, J. Song, *Science* **312**, 242 (2006)
279. C.J. Park, D.-K. Choi, J. Yoo, G.-C. Yi, C.J. Lee, *Appl. Phys. Lett.* **90**, 083107 (2007)
280. P.M. Rao, X. Zheng, *Nano Lett.* **9**, 3001 (2009)
281. S.M. Liu, L.M. Gan, L.H. Liu, W.D. Zhang, H.C. Zeng, *Chem. Mater.* **14**, 1391 (2002)
282. H.E. Prakasam, K. Shankar, M. Paulose, O.K. Varghese, C.A. Grimes, *J. Phys. Chem. C* **111**, 7235 (2007)

283. Z.W. Pan, Z.R. Dai, Z.L. Wang, *Science* **291**, 1947 (2001)
284. A. Kolmakov, D.O. Klenov, Y. Lilach, S. Stemmer, M. Moskovits, *Nano Lett.* **5**, 667 (2005)
285. W. Wang, B. Zeng, J. Yang, B. Poudel, J. Huang, M.J. Naughton, Z. Ren, *Adv. Mater.* **18**, 3275 (2006)
286. L. Kumari, J.-H. Lin, Y.-R. Ma, *J. Phys.-Condens. Matter* **19**, 406204 (2007)
287. B. Wang, Y.H. Yang, G.W. Yang, *Nanotechnology* **17**, 4682 (2006)
288. O. Kazakova, B. Daly, J.D. Holmes, *Phys. Rev. B* **74**, 184413 (2006)
289. K. Matsui, B.K. Pradhan, T. Kyotani, A. Tomita, *J. Phys. Chem. B* **105**, 5682 (2001)
290. M. Law, X.F. Zhang, R. Yu, T. Kuykendall, P. Yang, *Small* **1**, 858 (2005)
291. I.-D. Kim, A. Rothschild, B.H. Lee, D.Y. Kim, S.M. Jo, H.L. Tuller, *Nano Lett.* **6**, 2009 (2006)
292. Z. Yang, T. Xu, Y. Ito, U. Welp, W.K. Kwok, *J. Phys. Chem. C* **113**, 20521 (2009)
293. X.Y. Kong, Z.L. Wang, *Nano Lett.* **3**, 1625 (2003)
294. S. Tsoi, E. Fok, J.C. Sit, J.G.C. Veinot, *Chem. Mater.* **18**, 5260 (2006)
295. M. Hu, J.-S. Jiang, Y. Zeng, *Chem. Commun.* **46**, 1133 (2010)
296. L. He, L. Li, L. Zhang, S. Xing, T. Wang, G. Li, X. Wu, Z. Su, C. Wang, *CrystEngComm* **16**, 6534 (2014)
297. L. Hu, Y. Huang, F. Zhang, Q. Chen, *Nanoscale* **5**, 4186 (2013)
298. A.A. Voskanyan, C.Y.V. Li, K.Y. Chan, L. Gao, *CrystEngComm* **17**, 2620 (2015)
299. D. Tian, X.L. Zhou, Y.H. Zhang, Z. Zhou, X.H. Bu, *Inorg. Chem.* **54**, 8159 (2015)
300. Z.R. Ranjbar, A. Morsali, *Ultrason. Sonochem.* **18**, 644 (2011)
301. S. Aghabeygi, F. Bigdeli, A. Morsali, *J. Inorg. Organomet. Polym. Mater.* **22**, 526 (2012)
302. B. Messaoudi, S. Joiret, M. Keddad, H. Takenouti, *Electrochim. Acta* **46**, 2487 (2001)
303. B. Djurfors, J. Broughton, M. Brett, D. Ivey, *J. Mater. Sci.* 957 (2003)
304. J. Broughton, M. Brett, *Electrochim. Acta* **49**, 4439 (2004)
305. Y. Xia, Y. Yang, H. Shao, *J. Power Sources* **196**, 495 (2011)
306. L. Li, Y. Li, S. Gao, N. Koshizaki, *J. Mater. Chem.* **19**, 8366 (2009)
307. F. Zhang, L. Hao, L. Zhang, X. Zhang, *Int. J. Electrochem. Sci.* **6**, 2943 (2011)
308. C. Li, X. Yin, L. Chen, Q. Li, T. Wang, *Chem. Eur. J.* **16**, 5215 (2010)
309. F. Zhang, D.-D. Qi, X.-G. Zhang, *Int. J. Electrochem. Sci.* **11**, 189 (2016)
310. J.X. Yang, S.M. Wang, X.L. Zhao, Y.P. Tian, S.Y. Zhang, B.K. Jin, X.P. Hao, X.Y. Xu, X. T. Tao, M.H. Jiang, *J. Cryst. Growth* **310**, 4358 (2008)
311. S.L. Shi, G.Q. Li, S.J. Xu, Y. Zhao, G.H. Chen, *J. Phys. Chem. B* **110**, 10475 (2006)
312. E. Frackowiak, *Phys. Chem. Chem. Phys.* **9**, 1774 (2007)
313. R. Zboril, L. Machala, M. Mashlan, V. Sharma, *Cryst. Growth Des.* **4**, 1317 (2004)
314. F. Marandi, L. Hashemi, A. Morsali, H. Krautscheid, *Ultrason. Sonochem.* **32**, 86 (2016)
315. M. Yamada, R. Ohkawa, M. Miyake, *I.E.E.J. Trans. IEEJ Trans. Electron. Inf. Syst.* **127**, 1342 (2007)
316. Y. Meng, G.-H. Wang, S. Bernt, N. Stock, A.-H. Lu, *Chem. Commun.* **47**, 10479 (2011)
317. Y. Qiu, X. Zhang, S. Yang, *Phys. Chem. Chem. Phys.* **13**, 12554 (2011)
318. T. Tian, L. Ai, J. Jiang, *RSC Adv.* **5**, 10290 (2015)
319. S. Zhang, H. Liu, C. Sun, P. Liu, L. Li, Z. Yang, X. Feng, F. Huo, X. Lu, *J. Mater. Chem. A* **3**, 5294 (2015)
320. K.Q. Ding, *J. Chin. Chem. Soc.* **55**, 543 (2008)
321. M. Moeinian, K. Akhbari, *J. Inorg. Organomet. Polym.* **26**, 1 (2016)
322. L. Aboutorabi, A. Morsali, *Inorg. Chim. Acta* **363**, 2506 (2010)
323. H. Sadeghzadeh, A. Morsali, *J. Coord. Chem.* **63**, 713 (2010)
324. B. Mirtamizdoust, D.C. Bienko, Y. Hanifehpour, E.R.T. Tiepink, V.T. Yilmaz, P. Talemi, S. W. Joo, *J. Inorg. Organomet. Polym.* **26**, 819 (2016)
325. W. Li, K. Xu, G. Song, X. Zhou, R. Zou, J. Yang, Z. Chen, J. Hu, *Cryst. Eng. Commun.* **16**, 2335 (2014)
326. P.P. Su, S.C. Liao, F. Rong, F.Q. Wang, J. Chen, C. Li, Q.H. Yang, *J. Mater. Chem. A* **2**, 17408 (2014)

327. V.P. Santos, T.A. Wezendonk, J.J.D. Jaén, A.I. Dugulan, M.A. Nasalevich, H.-U. Islam, A. Chojecki, S. Sartipi, X.H. Sun, A.A. Hakeem, A.C.J. Koeken, M. Ruitenbeek, T. Davidian, G.R. Meima, G. Sankar, F. Kapteijn, M. Makkee, J. Gascon, *Nat. Commun.* **6**, 6451 (2015)
328. H.H. Zhao, H.L. Song, L.L. Xu, L.J. Chou, *Appl. Catal. A* **456**, 188 (2013)
329. X. Liu, *Angew. Chem. Int. Ed.* **48**, 3018 (2009)
330. Z. Li, Y. Xie, Y. Xiong, R. Zhang, *New J. Chem.* **27**, 1518 (2003)
331. H. Liu, J. Yang, J. Liang, Y. Huang, C. Tang, *J. Am. Ceram. Soc.* **91**, 1287 (2008)
332. O.M. Yaghi, M. O'Keeffe, N.W. Ockwig, H.K. Chae, M. Eddaoudi, J. Kim, *Nature* **423**, 705 (2003)
333. M. Eddaoudi, J. Kim, N.L. Rosi, D. Vodak, J. Wachter, M. O'Keeffe, O.M. Yaghi, *Science* **295**, 469 (2002)
334. A.K. Cheetham, C.N.R. Rao, R.K. Feller, *Chem. Commun.* 4780 (2006)
335. B. Wang, A.P. Cote, H. Furukawa, M. O'Keeffe, O.M. Yaghi, *Nature* **453**, 207 (2008)
336. G.M. Duffy, S.C. Pillai, D.E. McCormack, *Smart Mater. Struct.* **16**, 1379 (2007)
337. K. Akhbari, A. Morsali, *J. Coord. Chem.* **64**, 3521 (2011)
338. A. Abbasi, M. Gharib, M. Najafi, *J. Sci. I. R. Iran* **27**, 217 (2016)
339. A. Mehrani, A. Morsali, P. Ebrahimpour, *J. Coord. Chem.* **66**, 856 (2013)
340. Z.R. Ranjbar, A. Morsali, P. Retailleau, *Inorg. Chim. Acta* **376**, 486 (2011)
341. C. Paraschiv, A. Cucos, S. Shova, A.M. Madalan, C. Maxim, D. Visinescu, B. Cojocaru, V. I. Parvulescu, M. Andruh, *Cryst. Growth Des.* **15**, 799 (2015)
342. F. Molaie, F. Bigdeli, A. Morsali, *J. Ind. Eng. Chem.* **24**, 229 (2015)
343. S. Khullar, S.K. Mandal, *RSC Adv.* **4**, 39204 (2014)
344. K. Liu, H. Liu, L.L. Yang, F.Y. Zhao, Y. Li, W.J. Ruan, *RSC Adv.* **4**, 25160 (2014)
345. Y. Li, Z. Che, X. Sun, J. Douab, M. Wei, *Chem. Commun.* **50**, 9769 (2014)
346. S.J.Y. Yang, J.H. Im, T. Kim, K. Lee, C.R. Park, *J. Hazard. Mater.* **186**, 376 (2011)
347. M.S. Niassari, F. Davar, M. Mazaheri, *Mater. Lett.* **62**, 1890 (2008)
348. Z.P. Qiao, G. Xie, J. Tao, Z.Y. Nie, Y.Z. Lin, X.M. Chen, *J. Solid State Chem.* **166**, 49 (2002)
349. G. Xie, Z.P. Qiao, M.H. Zeng, X.M. Chen, S.L. Gao, *Cryst. Growth Des.* **4**, 513 (2004)
350. P. Roy, S.K. Srivastva, *Cryst. Growth Des.* **6**, 1921 (2006)
351. B. Luo, W.L. Gladfelter, *J. Coord. Chem.* **64**, 82 (2011)
352. Z. Rashidi, A. Ranjbar, *Ultrason. Sonochem.* **18**, 644 (2011)
353. K. Akhbari, A. Morsali, P. Retailleau, *Polyhedron* **29**, 3304 (2010)
354. Y. Song, Y. Chen, J. Wu, Y. Fu, R. Zhou, S. Chen, L. Wang, *J. Alloys Compd.* **694**, 1246 (2017)
355. S. Xu, Z.L. Wang, *Nano Res.* **4**, 1013 (2011)
356. K. Bijanzad, A. Tadjarodi, O. Akhavan, *Chin. J. Catal.* **36**, 742 (2015)
357. K. Okuyama, I.W. Lenggono, *Chem. Eng. Sci.* **58**, 537 (2003)
358. H.-P. Xiao, A. Morsali, *Helvet. Chim. Acta* **88**, 2543 (2005)
359. F.Z. Karizi, V. Safarifard, S.K. Khani, A. Morsali, *Ultrason. Sonochem.* **23**, 238 (2015)
360. M.Y. Masoomi, A. Morsali, P.C. Junk, *RSC Adv.* **4**, 47894 (2014)
361. Z. Wang, H. Zhang, L. Zhang, J. Yuan, S. Yan, C. Wang, *Nanotechnology* **14**, 11 (2003)
362. X. Zhang, J. Qin, R. Hao, L. Wang, X. Shen, R. Yu, S. Limpanart, M. Ma, R. Liu, *J. Phys. Chem. C* **119**, 20544 (2015)
363. J. Xue, S. Ma, Y. Zhou, Z. Zhang, *New J. Chem.* **39**, 1852 (2015)
364. A.A. Tehrani, V. Safarifard, A. Morsali, G. Bruno, H.A. Rudbari, *Inorg. Chem. Commun.* **59**, 41 (2015)
365. L.E. Greene, M. Law, D.H. Tan, M. Montano, J. Goldberger, G. Somorjai, P. Yang, *Nano Lett.* **5**, 1231 (2005)
366. P.X. Gao, Y. Ding, W. Mai, W.L. Hughes, C. Lao, Z.L. Wang, *Science* **309**, 1700 (2005)
367. J.J. Wu, S.C. Liu, *Adv. Mater.* **14**, 215 (2002)
368. X.Y. Kong, Y. Ding, R. Yang, Z.L. Wang, *Science* **303**, 1348 (2004)
369. D.H. Fan, W.Z. Shen, M.J. Zheng, Y.F. Zhu, J.J. Lu, *J. Phys. Chem. C* **111**, 9116 (2007)
370. L. Shen, H. Zhang, S. Guo, *Mater. Chem. Phys.* **114**, 580 (2009)

371. H. Li, Y. Huang, Y. Zhang, J. Qi, X. Yan, Q. Zhang, J. Wang, *Cryst. Growth Des.* **9**, 1863 (2009)
372. P. Li, H. Liu, Y.-F. Zhang, Y. Wei, X.-K. Wang, *Mater. Chem. Phys.* **106**, 63 (2007)
373. F. Li, Y. Ding, P. Gao, X. Xin, Z.L. Wang, *Angew. Chem. Int. Ed.* **43**, 5238 (2004)
374. J. Joo, S.G. Kwon, J.H. Yu, T. Hyeon, *Adv. Mater.* **17**, 1873 (2005)
375. Z. Pan, J.D. Budai, Z.R. Dai, W. Liu, M.P. Paranthaman, S. Dai, *Adv. Mater.* **21**, 890 (2009)
376. Z. Deng, M. Chen, G. Gu, L. Wu, *J. Phys. Chem. B* **112**, 16 (2007)
377. X.Y. Kong, Z.L. Wang, *Appl. Phys. Lett.* **84**, 975 (2004)
378. Y. Ding, X.Y. Kong, Z.L. Wang, *Phys. Rev. B* **70**, 235408 (2004)
379. J.Y. Lao, J.Y. Huang, D.Z. Wang, Z.F. Ren, *Nano Lett.* **3**, 235 (2002)
380. P.-X. Gao, Y. Ding, Z.L. Wang, *Nano Lett.* **9**, 137 (2008)
381. Z.R. Tian, J.A. Voigt, J. Liu, B. McKenzie, M.J. McDermott, M.A. Rodriguez, H. Konishi, H. Xu, *Nat. Mater.* **2**, 821 (2003)
382. T. Zhang, W. Dong, M. Keeter-Brewer, S. Konar, R.N. Njabon, Z.R. Tian, *J. Am. Chem. Soc.* **128**, 10960 (2006)
383. X. Gao, X. Li, W. Gao, J. Qiu, X. Gan, C. Wang, X. Leng, *CrystEngComm* **13**, 4741 (2011)
384. X. Hu, J. Gong, L. Zhang, J.C. Yu, *Adv. Mater.* **20**, 4845 (2008)
385. S. Zou, H. Bai, P. Yang, W. Yang, *Macromol. Chem. Phys.* **210**, 1519 (2009)
386. H. Sadeghzadeh, A. Morsali, *Ultrason. Sonochem.* **18**, 80 (2011)
387. J.J.F. Conley, L. Stecker, Y. Ono, *Nanotechnology* **16**, 292 (2005)
388. X.H. Sun, S. Lam, T.K. Sham, F. Heigl, A. Jürgensen, N.B. Wong, *J. Phys. Chem. B* **109**, 3120 (2005)
389. Z. Li, Y. Ding, Y. Xiong, Q. Yang, Y. Xie, *Chem. Eur. J.* **10**, 5823 (2004)
390. H. Kim, M. Park, H. Lee, O.S. Jung, *Dalton Trans.* **44**, 8198 (2015)
391. F. Marandi, L. Hashemi, A. Morsali, H. Krautscheid, *J. Inorg. Organomet. Polym.* **26**, 962 (2016)
392. L.-B. Ni, R.-H. Zhang, Q.-X. Liu, W.-S. Xia, H. Wang, Z.-H. Zhou, *J. Solid State Chem.* **182**, 2698 (2009)
393. J. Rautio, P. Per, J. Honkamo, H. Jantunen, *Microchem. J.* **91**, 272 (2009)
394. K.S. Cho, J.I. Hong, C.I. Chung, *Polym. Eng. Sci.* **44**, 1702 (2004)
395. J.H. Lee, Y.J. Sa, T.K. Kim, H.R. Moon, S.H. Joo, *J. Mater. Chem. A* **2**, 10435 (2014)
396. M. Hossienifard, L. Hashemi, V. Amani, K. Kalateh, A. Morsali, *J. Inorg. Organomet. Polym.* **21**, 527 (2011)
397. W.J. Rieter, K.M.L. Taylor, H. An, W. Lin, W. Lin, *J. Am. Chem. Soc.* **128**, 9024 (2006)
398. M.P. Suh, H.R. Moon, E.Y. Lee, S.Y. Jang, *J. Am. Chem. Soc.* **128**, 4710 (2006)
399. S. Jung, M. Oh, *Angew. Chem. Int. Ed.* **47**, 2049 (2008)
400. F. Schreder, D. Esken, M. Cokoja, M.W.E. Van den Berg, O.I. Lebedev, G.V. Tendeloo, B. Walaszek, G. Buntkowsky, H.-H. Limbach, B. Chaudret, R.A. Fischer, *J. Am. Chem. Soc.* **130**, 6119 (2008)
401. Y.-M. Jeon, G.S. Armatas, D. Kim, M.G. Kanatzidis, C.A. Mirkin, *Small* **5**, 46 (2009)
402. K.H. Park, K. Jang, S.U. Son, D.A. Sweigart, *J. Am. Chem. Soc.* **128**, 8740 (2006)
403. W.J. Rieter, K.M. Pott, K.M.L. Taylor, W. Lin, *J. Am. Chem. Soc.* **130**, 11584 (2008)
404. K.M.L. Taylor, W.J. Rieter, W. Lin, *J. Am. Chem. Soc.* **130**, 14358 (2008)
405. M.-C. Wu, C.-S. Lee, *Inorg. Chem.* **45**, 9634 (2006)
406. Y. Chen, Y. Zhang, Q.-Z. Yao, G.-T. Zhou, S. Fu, H. Fan, *J. Solid State Chem.* **180**, 1218 (2007)
407. M. Yin, Y. Gu, I.L. Kuskovsky, T. Andelman, Y. Zhu, G.F. Neumark, S. O'Brien, *J. Am. Chem. Soc.* **126**, 6206 (2004)
408. M. Rakibuddin, R. Ananthkrishnan, *Appl. Surf. Sci.* **362**, 265 (2016)
409. M. Oh, C.A. Mirkin, *Angew. Chem. Int. Ed.* **45**, 5492 (2006)
410. M. Ranjbar, N. Shahsavan, M. Yousefi, *Am. Chem. Sci. J.* **2**, 111 (2012)
411. K.J. Lee, T.-H. Kim, T.K. Kim, J.H. Lee, H.-K. Song, H.R. Moon, *J. Mater. Chem. A* **2**, 14393 (2014)
412. F. Mohandes, F. Davar, M. Salavati-Niasari, *J. Magn. Magn. Mater.* **322**, 872 (2010)

413. Z. Xu, B. Lv, X. Shi, L. Chen, K. Wang, *Inorg. Chim. Acta* **427**, 266 (2015)
414. F. Meng, Z. Fang, Z. Li, W. Xu, M. Wang, Y. Liu, J. Zhang, W. Wang, D. Zhao, X. Guo, *J. Mater. Chem. A* **1**, 7235 (2013)
415. N.N. Sheno, A. Morsali, S. Woo Joo, *Mater. Lett.* **117**, 31 (2014)
416. M. Hu, A.A. Belik, M. Imura, K. Mibu, Y. Tsujimoto, Y. Yamauchi, *Chem. Mater.* **24**, 2698 (2012)
417. L. Zhang, H.B. Wu, R. Xu, X.W. Lou, *CrystEngComm* **15**, 9332 (2013)
418. S. Hei, Y. Jin, F. Zhang, *J. Chem.* **2014** (2014), Article ID 546956
419. Z.-M. Liu, S.-H. Wu, S.-Y. Jia, F.-X. Qin, S.-M. Zhou, H.-T. Ren, P. Na, Y. Liu, *Mater. Lett.* **132**, 8 (2014)
420. S. Laurent, D. Forge, M. Port, A. Roch, C. Robic, L. Vander Elst, R.N. Muller, *Chem. Rev.* **108**, 2064 (2008)
421. K. Cheng, S. Peng, C.J. Xu, S.H. Sun, *J. Am. Chem. Soc.* **131**, 10637 (2009)
422. B. Feng, R.Y. Hong, Y.J. Wu, G.H. Liu, L.H. Zhong, Y. Zheng, J.M. Ding, D.G. Wei, *J. Alloys Compd.* **473**, 356 (2009)
423. Z. Li, L. Wei, M.Y. Gao, H. Lei, *Adv. Mater.* **17**, 1001 (2005)
424. S.M. El-Sheikh, F.A. Harraz, K.S. Abdel-Halim, *J. Alloys Compd.* **487**, 716 (2009)
425. S.H. Liu, R.M. Xing, F. Lu, R.K. Rana, J.J. Zhu, *J. Phys. Chem. C* **113**, 21042 (2009)
426. L.Y. Chen, Z.X. Xu, H. Dai, S.T. Zhang, *J. Alloys Compd.* **497**, 221 (2010)
427. E.H. Kim, Y. Ahn, H.S. Lee, *J. Alloys Compd.* **434–435**, 633 (2007)
428. A. Mehrani, A. Morsali, *J. Inorg. Organomet. Polym.* **21**, 476 (2011)
429. J.H. Im, E. Kang, S.J. Yang, H.J. Park, J. Kim, C.R. Park, *Bull. Kor. Chem. Soc.* **35**, 2477 (2014)
430. Z. Xiu, M.H. Alfaruqi, J. Gim, J. Song, S. Kim, P.T. Duong, J.P. Baboo, V. Mathew, J. Kim, *J. Alloys Compd.* **674**, 174 (2016)
431. H. Jiang, C. Wang, H. Wang, M. Zhang, *Mater. Lett.* **168**, 17 (2016)
432. D. Jing, D. Chen, G. Fan, Q. Zhang, J. Xu, S. Gou, H. Li, F. Nie, *Cryst. Growth Des.* **16**, 6849 (2016)
433. V. Safarifard, A. Morsali, *Ultrason. Sonochem.* **19**, 1227 (2012)
434. M.Y. Masoomi, A. Morsali, *Ultrason. Sonochem.* **28**, 240 (2016)
435. G.H. Shahverdizadeh, *Main Group Chem.* **15**, 179 (2016)
436. L. Hashemi, A. Morsali, P. Retailleau, *Inorg. Chim. Acta* **367**, 207 (2011)
437. S. Saeednia, P. Iranmanesh, H.A. Rudbari, L. Saeednia, *J. Macromol. Sci. Part A Pure Appl. Chem.* **53**, 227 (2016)
438. R. Gupta, S. Sanotra, H. Nawaz Sheikh, B. Lal Kalsotra, V. Kumar Gupta, Rajnikant, *J. Coord. Chem.* **65**, 3917 (2012)
439. L. Chen, C. Zhao, Z. Wei, S. Wang, Y. Gu, *Mater. Lett.* **65**, 446 (2011)
440. H. Thakuria, G. Das, *Polyhedron* **26**, 149 (2007)
441. N.N. Sheno, A. Morsali, *Int. J. Nanosci. Nanotechnol.* **8**, 99 (2012)
442. B. Fang, M. Kim, S.Q. Fan, J.H. Kim, D.P. Wilkinson, J. Ko, J.S. Yu, *J. Mater. Chem.* **21**, 8742 (2011)
443. T. Fu, M. Wang, W.M. Cai, Y.M. Cui, F. Gao, L.M. Peng, W. Chen, W.P. Ding, *ACS Catal.* **4**, 2536 (2014)
444. V.I. Merkulov, D.H. Lowndes, Y.Y. Wei, G. Eres, E. Voelkl, *Appl. Phys. Lett.* **76**, 3555 (2000)
445. A. Tahmasian, A. Morsali, *Inorg. Chim. Acta* **387**, 327 (2012)
446. H.D. Mai, G.Y. Sung, H. Yoo, *RSC Adv.* **5**, 78807 (2015)
447. V. Bagchi, D. Bandyopadhyay, *J. Organomet. Chem.* **694**, 1259 (2009)
448. M.S.Y. Parast, A. Morsali, *Inorg. Chem. Commun.* **14**, 450 (2011)
449. M.S.Y. Parast, A. Morsali, *J. Inorg. Organomet. Polym.* **21**, 365 (2011)
450. H.J. Lee, W. Cho, S. Jung, M. Oh, *Adv. Mater.* **21**, 674 (2009)
451. Y. Liu, J. Zhou, A. Larbot, M. Persin, *J. Mater. Process. Technol.* **189**, 379 (2007)
452. Z.R. Ranjbar, A. Morsali, *J. Mol. Struct.* **936**, 206 (2009)
453. H. Ahmadzadi, F. Marandi, A. Morsali, *J. Organomet. Chem.* **694**, 3565 (2009)

454. S.K. Pasha, V.S.V. Satyanarayana, A. Sivakumar, K. Chidambaram, L.J. Kennedy, *Chin. Chem. Lett.* **22**, 891 (2011)
455. A.V. Borhadea, B.K. Uphadeb, D.R. Tope, *J. Chem. Sci.* **125**, 583 (2013)
456. B. Mirtamizdoust, B. Shaabani, A. Khandar, H.-K. Fun, S. Huang, M. Shadman, P. Hojati-Talemi, *Z. Anorg. Allg. Chem.* **638**, 844 (2012)
457. B. Mirtamizdoust, B. Shaabani, A. Khandar, H. Pourradi, Y. Abbasityula, H. Goudarziafshar, D. Viterbo, G. Croce, P. Hojati-Talemi, *J. Inorg. Organomet. Polym.* **22**, 1293 (2012)
458. Y. Hanifehpour, B. Mirtamizdoust, A.R. Farzam, S.W. Joo, *J. Inorg. Organomet. Polym.* **22**, 957 (2012)
459. A. Aliakbari, E. Najafi, M.M. Amini, S.W. Ng, *Monatsh. Chem.* **145**, 1277 (2014)
460. L. Hashemi, F. Marandi, A. Morsali, H. Krautscheid, *J. Iran. Chem. Soc.* **14**, 1271 (2017)
461. L. Hashemi, A. Aslani, A. Morsali, *J. Inorg. Organomet. Polym.* **22**, 867 (2012)
462. A. Aslani, A. Morsali, *Inorg. Chim. Acta* **362**, 5012 (2009)
463. A. Morsali, A. Panjehpour, *Inorg. Chim. Acta* **391**, 210 (2012)
464. G.H. Shahverdizadeh, F. Hakimi, B. Mirtamizdoust, A. Souidi, P. Hojati-Talemi, *J. Inorg. Organomet. Polym.* **22**, 903 (2012)
465. L. Hashemi, A. Morsali, *J. Coord. Chem.* **64**, 4088 (2011)
466. H. Sadeghzadeh, A. Morsali, V.T. Yilmaz, O. Büyükgüngör, *Mater. Lett.* **64**, 810 (2010)
467. H.J. Shin, B.K. Min, *J. Inorg. Organomet. Polym.* **23**, 1305 (2013)
468. Y. Noori, K. Akhbari, A. Phuruangrat, F. Costantino, *Ultrason. Sonochem.* **35**, 36 (2017)
469. M.J.S. Fard, H.S. Naraghi, *J. Mol. Struct.* **1035**, 236 (2013)
470. B. Mirtamizdoust, Z. Trávníček, Y. Hanifehpour, P. Talemi, H. Hammud, S.W. Joo, *Ultrason. Sonochem.* **34**, 255 (2017)
471. A. Aslani, S.J. Musevi, E. Sahin, V.T. Yilmaz, *Appl. Surf. Sci.* **318**, 206 (2014)
472. M.J.S. Fard, F. Rastaghi, *J. Mol. Struct.* **1063**, 289 (2014)
473. M.J.S. Fard, N. Ghanbari, F. Rastaghi, *Inorg. Chim. Acta* **396**, 149 (2013)
474. M.J.S. Fard, F. Rastaghi, N. Ghanbari, *J. Mol. Struct.* **1032**, 133 (2013)
475. H. Sadeghzadeh, A. Morsali, V.T. Yilmaz, O. Büyükgüngör, *Ultrason. Sonochem.* **17**, 592 (2010)
476. H. Sadeghzadeh, A. Morsali, P. Retailleau, *Polyhedron* **29**, 925 (2010)
477. K. Akhbari, A. Morsali, P. Retailleau, *Ultrason. Sonochem.* **20**, 1428 (2013)
478. A. Tahmasian, A. Morsali, S.W. Joo, *J. Nanomaterials* **2013**, 7 (2013), Article ID 313456
479. Y. Liu, S. Liu, Z. Yue, *RSC Adv.* **5**, 31742 (2015)
480. D. Liu, F. Dai, H. Liu, Y. Liu, C. Liu, *Mater. Lett.* **139**, 7 (2015)
481. D. Liu, F. Dai, X. Li, J. Liang, Y. Liu, C. Liu, *RSC Adv.* **5**, 15182 (2015)
482. E. Alvarez, N. Guillou, C. Martineau, B. Bueken, B. Vande Voorde, C. Le Guillouzer, P. Fabry, F. Nouar, F. Taulelle, D. De Vos, J.S. Chang, *Angew. Chem. Int. Ed.* **54**, 3664 (2015)
483. M. Gaab, N. Trukhan, S. Maurer, R. Gummaraju, U. Müller, *Microporous Mesoporous Mater.* **157**, 131 (2012)
484. M. Derakhshani, A. Hashamzadeh, M.M. Aminin, *Ceram. Int.* **42**, 17742 (2016)
485. R. Mohammadinassab, M. Tabatabaee, B.M. Kukovec, H. Aghaie, *Inorg. Chim. Acta* **405**, 368 (2013)
486. Z. Shen, J. Liu, F. Hu, S. Liu, N. Cao, Y. Sui, Q. Zeng, Y. Shen, *CrystEngComm* **16**, 3387 (2014)
487. L. Wang, H. Zou, Y. Li, X. Li, S. Zhong, *Mater. Manufact. Proc.* **32**, 484 (2017)
488. P.G. Derakhshandeh, J. Soleimannejad, *Ultrason. Sonochem.* **31**, 122 (2016)
489. P.G. Derakhshandeh, J. Soleimannejad, J. Janczak, *Ultrason. Sonochem.* **26**, 273 (2015)
490. Z. Shen, G. Zhang, H. Zhou, P. Sun, B. Li, D. Ding, T. Chen, *Adv. Mater.* **20**, 984 (2008)
491. T.K. Sau, A.L. Rogach (eds.), *Complex-Shaped Metal Nanoparticles: Bottom-Up Syntheses and Applications* (Wiley, Weinheim, 2012)
492. K. Gudikandula, S.C. Maringanti, *J. Exp. Nanosci.* **11**, 714 (2016)
493. C. Xuebo, G. Li, *Nanotechnology* **16**, 180 (2005)

494. E. Semitut, V. Komarov, T. Sukhikh, E. Filatov, A. Potapov, *Crystals* **6**, 138 (2016)
495. L. Chen, Y. Shen, J. Bai, C. Wang, *J. Solid State Chem.* **182**, 2298 (2009)
496. Z.-F. Liu, A.-X. Zhu, C.-K. Lam, G.-W. Xie, C.-L. Liang, X.-M. Chen, Z.-P. Qiao, *CrystEngComm* **11**, 1303 (2009)
497. B.M. Muñoz-Flores, B.I. Kharisov, V.M. Jiménez-Pérez, P.E. Martínez, S.T. López, *Ind. Eng. Chem. Res.* **50**, 7705 (2011)
498. D. Ghoshal, T.K. Maji, T. Mallah, T.-H. Lu, G. Mostafa, N.R. Chaudhuri, *Inorg. Chim. Acta* **358**, 1027 (2005)
499. M. Sakamoto, K. Manseki, H. Okawa, *Coord. Chem. Rev.* **219–221**, 379 (2001)
500. E. Coronado, J.R. Galán-Mascaró, C. Martí-Gastaldo, *Inorg. Chem.* **46**, 8108 (2007)
501. Z.-G. Gu, S.C. Sevov, *J. Mater. Chem.* **19**, 8442 (2009)
502. B.-H. Ye, M.-L. Tong, X.-M. Chen, *Coord. Chem. Rev.* **249**, 545 (2005)
503. I.G. Fomina, ZhV Dobrokhotova, G.G. Aleksandrov, M.L. Kovba, V.I. Zhilov, A.S. Bogomyakov, V.M. Novotortsev, I.L. Eremanko, *Russ. Chem. Bull.* **59**, 699 (2010)
504. E.V. Orlova, A.E. Goldberg, M.A. Kiskin, P.S. Koroteev, A.L. Emelina, M.A. Bykov, G.G. Aleksandrov, ZhV Dobrokhotova, V.M. Novotortsev, I.L. Eremanko, *Russ. Chem. Bull.* **60**, 2236 (2011)
505. T.A. Ostomel, Q. Shi, C.-K. Tsung, H. Liang, G.D. Stucky, *Small* **2**, 1261 (2006)
506. M.G. Naseri, E.B. Saion, A.H. Abbastabar, A.H. Shaari, M. Hashim, *J. Nanomater.* **2010** (2010), Article ID 907686
507. L. Chen, Y. Shen, J. Bai, *Mater. Lett.* **63**, 1099 (2009)
508. M. Gharagozlou, *J. Alloys Compd.* **486**, 660 (2009)
509. S.S. Hayrapetyan, H.G. Khachatryan, *Micropor. Mesopor. Mater.* **72**, 105 (2004)
510. A.M. Ibrahim, M.M.A. El-Latif, M.M. Mahmoud, *J. Alloys Compd.* **506**, 201 (2010)
511. M.H. Khedr, A.A. Omar, S.A. Abdel-Moaty, *Colloids Surf. A: Physicochem. Eng. Asp.* **281**, 8 (2006)
512. K. Maaz, A. Mumtaz, S.K. Hasanain, A. Ceylan, *J. Magn. Magn. Mater.* **308**, 289 (2007)
513. H. Shadpour, M. Edrissi, M. Zanjanchi, *J. Mater. Sci., Mater. Electron* **13**, 139 (2002)
514. J.B. Silva, W.D. Brito, N.D.S. Mohallem, *Mater. Sci. Eng., B* **112**, 182 (2004)
515. Y. Wang, D. Su, A. Ung, J.-H. Ahn, G. Wang, *Nanotechnology* **23**, 055402 (2012)
516. M. Veverka, P. Veverka, O. Kaman, A. Lancok, K. Zaveta, E. Pollert, K. Knizek, J. Bohacek, M. Benes, P. Kaspar, E. Duguet, S. Vasseur, *Nanotechnology* **18**, 345704 (2007)
517. E. Coronado, C. Martí-Gastaldo, J.R. Galán-Mascaró, M. Cavallini, *J. Am. Chem. Soc.* **132**, 5456 (2010)
518. D. Hong, Y. Yamada, M. Sheehan, S. Shikano, C.-H. Kuo, M. Tian, C.-K. Tsung, S. Fukuzumi, *ACS Sustain. Chem. Eng.* **2**, 2588 (2014)
519. J. Zhao, F. Wang, P. Su, M. Li, J. Chen, Q. Yang, C. Li, *J. Mater. Chem.* **22**, 13328 (2012)
520. S. Yamaguchi, N. Kimoto, H. Sasagawa, K. Takiguchi, T. Okuwa, M. Asamoto, H. Yahiro, *J. Ceram. Soc. Jpn.* **121**, 84 (2013)
521. P. Mahata, T. Aarathi, G. Madras, S. Natarajan, *J. Phys. Chem. C* **111**, 1665 (2007)
522. Z.V. Dobrokhotova, N.V. Gogoleva, E.N. Zorina-Tikhonova, M.A. Kiskin, V.V. Chernyshev, A.L. Emelina, M.A. Bukov, A.S. Goloveshkin, I.S. Bushmarinov, A.A. Sidorov, A.S. Bogomyakov, M.L. Kovba, V.M. Novotortsev, I.L. Eremanko, *Eur. J. Inorg. Chem.* **2015**, 3116 (2015)
523. A.V. Gavrikov, P.S. Koroteev, Z.V. Dobrokhotova, A.B. Ilyukhin, N.N. Efimov, D.I. Kirdyankin, M.A. Bykov, M.A. Ryumin, V.M. Novotortsev, *Polyhedron* **102**, 48 (2015)
524. N. Zauzolkova, Z. Dobrokhotova, A. Lermontov, E. Zorina, A. Emelina, M. Bukov, V. Chernyshev, A. Sidorov, M. Kiskin, A. Bogomyakov, A. Lytvynenko, S. Kolotilov, Y. Velikodnyi, M. Kovba, V. Novotortsev, I. Eremanko, *J. Solid State Chem.* **197**, 379 (2013)
525. M.A. Ryumin, Z.V. Dobrokhotova, A.L. Emelina, M.A. Bukov, N.V. Gogoleva, K.S. Gavrichev, E.N. Zorina-Tikhonova, L.I. Demina, M.A. Kiskin, A.A. Sidorov, I.L. Eremanko, V.M. Novotortsev, *Polyhedron* **87**, 28 (2015)
526. R.A. Rocha, E.N.S. Muccillo, *Chem. Mater.* **15**, 4268 (2003)

527. Y. Xia, B. Wang, G. Wang, X. Liu, H. Wang, *ChemElectroChem* **3**, 299 (2016)
528. M. Hamid, A.A. Tahir, M. Mazhar, M. Zeller, K.C. Molloy, A.D. Hunter, *Inorg. Chem.* **45**, 10457 (2006)
529. K. Wang, J. Xu, A. Lu, Y. Shi, Z. Lin, *Solid State Sci.* **58**, 70 (2016)
530. T. Demars, M. Boltoeva, N. Vigier, J. Maynadié, J. Ravaux, C. Genre, D. Meyer, *Eur. J. Inorg. Chem.* **2012**, 3875 (2012)
531. J. Maruyama, K. Sumino, M. Kawaguchi, I. Abe, *Carbon* **42**, 3115 (2004)
532. Z.F. Yue, S.C. Liu, Y. Liu, *RSC Adv.* **5**, 10619 (2015)
533. M.R. Harrison, M.G. Francesconi, *Coord. Chem. Rev.* **255**, 451 (2011)
534. P. Roy, S.K. Srivastava, *CrystEngComm* **17**, 7801 (2015)
535. J. Mao, Q. Shu, Y. Wen, H. Yuan, D. Xiao, M.M.F. Choi, *Cryst. Growth Des.* **9**, 2546 (2009)
536. M. Nagarathinam, J. Chen, J.J. Vittal, *Cryst. Growth Des.* **9**, 2457 (2009)
537. X.-F. Shen, X.-P. Yan, *Angew. Chem. Int. Ed.* **46**, 7659 (2007)
538. V. Stavila, K.H. Whitmire, I. Rusakova, *Chem. Mater.* **21**, 5456 (2009)
539. J. Puigmarti-Luis, M. Rubio-Martinez, U. Hartfelder, I. Imaz, D. MasPOCH, P.S. Dittrich, *J. Am. Chem. Soc.* **133**, 4216 (2011)
540. P. Colombo, G. Mera, R. Riedel, G.D. Sorarù, *J. Am. Ceram. Soc.* **93**, 1805 (2010)
541. L.V. Interrante, K. Moraes, Q. Liu, N. Lu, A. Puerta, L.G. Sneddon, *Pure Appl. Chem.* **74**, 2111 (2002)
542. R. Riedel, G. Mera, R. Hauser, A. Klönczynski, *J. Ceram. Soc. Jpn.* **114**, 425 (2006)
543. E. Kroke, Y.-L. Li, C. Konetschny, E. Lecomte, C. Fasel, R. Riedel, *Mater. Sci. Eng., R* **26**, 97 (2000)
544. A. Lukacs, *Am. Ceram. Soc. Bull.* **86**, 9301 (2007)
545. G. Glatz, T. Schmalz, T. Kraus, F. Haarmann, G. Motz, R. Kempe, *Chem. Eur. J.* **16**, 4231 (2010)
546. M. Zaheer, T. Schmalz, G. Motz, R. Kempe, *Chem. Soc. Rev.* **41**, 5102 (2012)
547. A.M. Tsirlin, G.I. Shcherbakova, E.K. Florina, N.A. Popova, S.P. Gubin, E.M. Moroz, R. Riedel, E. Kroke, M. Steen, *J. Eur. Ceram. Soc.* **22**, 2577 (2002)
548. M. Kamperman, A. Burns, R. Weissgraeber, N. van Vegten, S.C. Warren, S.M. Gruner, A. Baiker, U. Wiesner, *Nano Lett.* **9**, 2756 (2009)
549. G. Mera, E. Ionescu, Silicon-containing preceramic polymers, in *Encyclopedia of Polymer Science and Technology* (Wiley, Hoboken, 2013)
550. E. Ionescu, R. Riedel, Polymer processing of ceramics, in *Ceramics and Composites Processing Methods*, ed. by N. Bansal, A. Boccaccini (Wiley, Hoboken, 2012)
551. G. Motz, *Adv. Sci. Technol.* **50**, 24 (2006)
552. G. Motz, T. Kabelitz, G. Ziegler, *Key Eng. Mater.* **264–268**, 481 (2004)
553. G. Motz, J. Hacker, G. Ziegler in *Ceramic Materials for Engines*, ed. by J.G. Heinrich, F. Aldinger (Wiley-VCH, Weinheim, 2001), pp. 581–585
554. G. Motz, G. Ziegler, *Key Eng. Mater.* **206–213**, 475 (2002)
555. G. Motz, J. Hacker, G. Ziegler, in *Ceramic Engineering and Science Proceedings*, vol. 21 (Wiley, New York, 2000), pp. 307–314
556. M. Kamperman, C.B.W. Garcia, P. Du, H.S. Ow, U. Wiesner, *J. Am. Chem. Soc.* **126**, 14708 (2004)
557. I.K. Sung, M. Mitchell, D.P. Kim, P.J.A. Kenis, *Adv. Funct. Mater.* **15**, 1336 (2005)
558. K. Sonnenburg, P. Adelhelm, M. Antonietti, B. Smarsly, R. Noske, P. Strauch, *Phys. Chem. Chem. Phys.* **8**, 3561 (2006)
559. C. Vakifahmetoglu, D. Zeydanli, P. Colombo, *Mater. Sci. Eng. R: Reports* **106**, 1 (2016)
560. G. Mera, M. Gallei, S. Bernard, E. Ionescu, *Nanomaterials* **5**, 468 (2015)
561. G. Mera, R. Riedel, Organosilicon-based polymers as precursors for ceramics, in *Polymer Derived Ceramics: From Nanostructure to Applications*, ed. by P. Colombo, R. Riedel, G.D. Soraru, H.-J. Kleebe (DEStech Publications Inc., Lancaster, 2010)
562. E. Ionescu, H.-J. Kleebe, R. Riedel, *Chem. Soc. Rev.* **41**, 5032 (2012)

563. E. Ionescu, C. Gervais, F. Babonneau, Polymer-to-ceramic transformation, in *Polymer Derived Ceramics: From Nanostructure to Applications*, ed. by P. Colombo, R. Riedel, G.D. Soraru, H.-J. Kleebe (DEStech Publications Inc., Lancaster, 2010)
564. M.S. Bazarjani, H.-J. Kleebe, M.M. Müller, C. Fasel, M.B. Yazdi, A. Gurlo, R. Riedel, *Chem. Mater.* **23**, 4112 (2011)
565. M.S. Bazarjani, M.M. Müller, H.-J. Kleebe, Y. Jüttke, I. Voigt, M.B. Yazdi, L. Alff, R. Riedel, A. Gurlo, *ACS Appl. Mater. Interfaces* **6**, 12270 (2014)
566. M. Zaheer, C.D. Keenan, J. Hermannsdorfer, E. Roessler, G. Motz, J. Senker, R. Kempe, *Chem. Mater.* **24**, 3952 (2012)
567. M. Zaheer, J. Hermannsdorfer, W.P. Kretschmer, G. Motz, R. Kempe, *ChemCatChem* **6**, 91 (2014)
568. M. Zaheer, G. Motz, R. Kempe, *J. Mater. Chem.* **21**, 18825 (2011)
569. T. Schmalz, T. Kraus, M. Guenther, C. Liebscher, U. Glatzel, R. Kempe, G. Motz, *Carbon* **49**, 3065 (2011)
570. M. Scheffler, P. Greil, A. Berger, E. Pippel, J. Woltersdorf, *Mater. Chem. Phys.* **84**, 131 (2004)
571. A. Berger, E. Pippel, J. Woltersdorf, M. Scheffler, P. Cromme, P. Greil, *Phys. Stat. Sol.* **202**, 2277 (2005)
572. H.B. Du, Y.L. Li, F.Q. Zhou, D. Su, F. Hou, *J. Am. Ceram. Soc.* **93**, 1290 (2010)
573. A. Morozaan, F. Jaouen, *Energy Environ. Sci.* **5**, 9269 (2012)

Chapter 5

The Conjugate Thermolysis—Thermal Polymerization of Metal Chelate Monomers and Thermolysis of Polymers Formed In Situ



A common drawback of practically all methods for obtaining metal–polymer nanocomposite materials with “core–shell” structure is the multistage of process, on the one hand, and the formation of polydispersed systems with a wide distribution of particle size, on the other hand. Traditional approaches are rather laborious and include the stage of formation of macromolecular complexes, metal ions reduction reaction to form nano-sized particles, separation of the phase of chemically unbound components [1–7]. In addition, NPs tend to aggregate, and the chemically inert material in the dispersed state becomes even more reactive. This, sometimes, is a big problem.

In this respect, it is of particular interest to find ways to reduce the synthesis stages. In particular, self-regulated systems, in which the synthesis of the polymer matrix and the nucleation and growth of NPs simultaneously proceed, can be useful for solving the problem of stabilizing NPs with polymers and their structural organization. Particularly, promising is the self-stabilization of highly dispersed metal particles or as metal-containing precursors, or in the form of monomers, which are then subjected to polymerization and thermolysis. This approach is based on solid-phase homo- and copolymerization of metal chelate monomers (MCMs) followed by controlled thermolysis of the resulting metal-containing polymers [8–12]. This direction of research is most intensive in recent years.

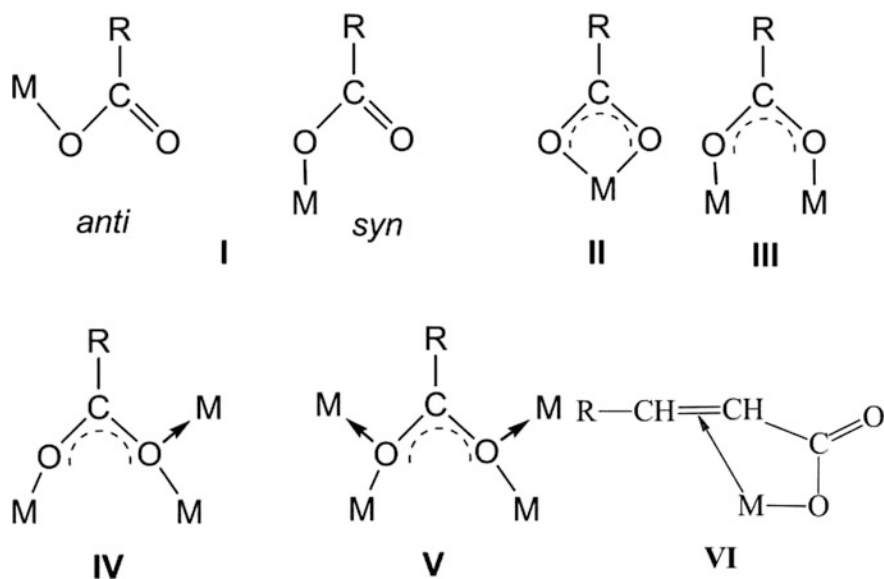
Characteristic features that make it possible to reliably identify MCMs as a special class of chemical compounds are the presence of a chelate cycle and a multiple bond for polymerization or functionalities that can be involved in polycondensation [13, 14]. The undoubted advantage of this method is the possibility of one-step production of polymeric metal chelates (PMCs), in which each chelating fragment contains a metal ion with a certain spatial configuration. Because of the chelate effect, MCM is much more stable than other metal-containing monomers [15]. MCM proved to be convenient for studying a number of theoretical problems, such as the effect of metal on the reactivity of multiple bonds and functionality contained in MCM, as well as the effect of double bonding and functionality on the stereochemistry of the chelate node and the electronic properties of the metal.

5.1 General Characteristics of Metal Chelate Monomers Used in Conjugated Thermolysis

Thermolysis of MCMs is intensively rapidly developing field of research, which may be the best embodiment of the idea of NP stabilization in situ. We consider this process as an example of such an interesting class of MCMs as metal carboxylates of unsaturated mono- and dicarboxylic acids [2–7]. Metal carboxylates are a large group of metal complexes containing a carboxylate functional group with a different type of coordination with the metal atom, including chelation type (Scheme 5.1) [2, 3]. In the most typical cases, the RCOO^- carboxylate group can be coordinated with the metal as a monodentate (I) *anti*- and *syn*-configuration, bidentate cyclic (chelating) (II), bidentate bridging (III), tridentate (IV), and the tetradentate ligand (V). Such a wide variety of possible metal carboxylate compositions and structures in the case of unsaturated analogs can be supplemented by the structural function of multiple bonds, which, as is known, can participate in coordination with the metal atom to form the π -bond (VI).

The simplest representatives of this class of MCMs are metal acrylates (MAcr_n) and methacrylates (MMAcr_n) [3–5].

The synthesis of certain MAcr_n is accompanied by an increase in metal ion nuclearity. Metal acrylates have mono- (NiAcr_2 , CoAcr_2), bi- (CuAcr_2), and trinuclear (FeAcr_3 , CrAcr_3 , VAcr_n) structures. The binuclear structure of CuAcr_2 , $[\text{Cu}_2(\text{Acr})_4(\text{ROH})_2]\text{ROH}$ ($\text{R}=\text{CH}_3$ or C_2H_5), determined by X-ray analysis [16], consists of a binuclear cluster with a Cu–Cu distance of 0.2617 nm. Coordination

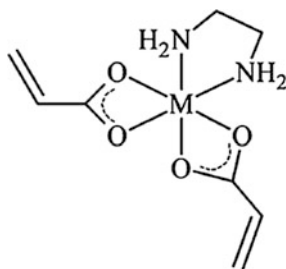


Scheme 5.1 Possible coordination modes of unsaturated carboxylates

of copper atoms is square pyramidal (CuO_5), and four oxygen atoms bounded by two bidentate carboxylate bridges form an almost regular square base of the pyramid. The fifth oxygen atom of the structure is from $\text{C}_2\text{H}_5\text{OH}$ molecule. The Cu–O bond length ranges from 0.1947 to 0.1956 nm.

In addition to acrylate, other donor ligands such as phen [17–21], bpy [18–22], 4,4'-bipyridine [23], en [24], 3-amino-4H-1,2,4-triazole [25], benzimidazole, 2-methyl-, 5-methyl- or 5,6-dimethylbenzimidazole [26–28] are often contained in the metal carboxylate complex.

In particular, it is of interest to study the thermal stability of mixed Acr and en metal complexes $[\text{M}(\text{en})(\text{Acr})_2] \cdot n\text{H}_2\text{O}$ ($\text{M} = \text{Ni}$, $n = 2$; $\text{M} = \text{Cu}$, $n = 0$; $\text{M} = \text{Zn}$, $n = 2$) [24]. After dehydration and elimination of ethylenediamine, the MO product is formed, with the exception of metallic copper originating from the copper complex.



In complexes with mixed ligands of the type $[\text{ML}(\text{Acr})_2]_n \cdot \text{H}_2\text{O}$ ($\text{M} = \text{Mn}$, Co(II) , Ni(II) , Cu(II) , Zn(II) ; $n = 0-4$; $\text{L} = 3\text{-amino-1,2,4-triazole}$), L acts as bridge, whereas Acr is a bidentate ligand, with the exception of the Zn(II) complex, where it is found to be unidentate (Fig. 5.1) [25]. Thermolysis is a complex process involving dehydration, as well as the decomposition of Acr ion and 3-amino-1,2,4-triazole, respectively. The final products of thermolysis are the most stable metal oxides, with the exception of the Cu(II) complex leading to metallic copper.

It should be noted that these complexes have a different structure depending on the metal nature. Thus, in Ni(II) complexes with mixed ligands, Acr ions act both as

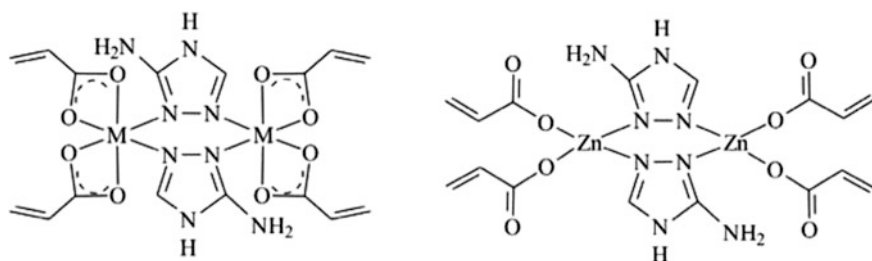


Fig. 5.1 Proposed coordination for complexes; $\text{M} = \text{Mn}$, Co , Ni , Cu . Reproduced with permission from Ref. [25]. Copyright (2009) Springer Nature

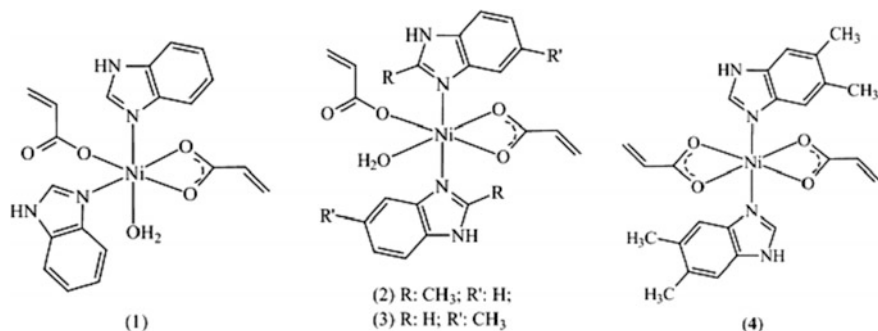


Fig. 5.2 Proposed coordination for Ni(II) complexes (1)–(4). Reproduced with permission from Ref. [25]. Copyright (2009) Springer Nature

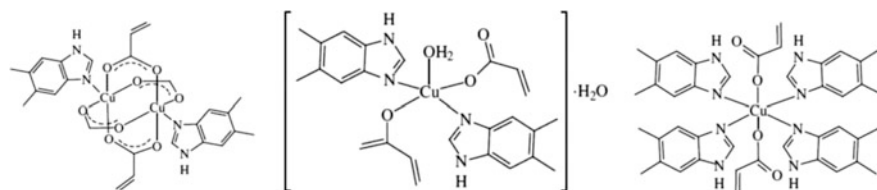


Fig. 5.3 Proposed formulation for Cu(II) complexes. Reproduced with permission from Ref. [27]. Copyright (2013) Springer Nature

a unidentate and chelate ligands in complexes (1)–(3), and in complex (4) it is only a chelating ligand (Fig. 5.2).

At the same time, in the Cu(II) complexes, the Acr ion acts as a uni- or bidentate ligand forming mono- and binuclear compounds (Fig. 5.3) [27].

An X-ray characteristic of the cadmium complex $[\text{Cd}(\text{H}_2\text{O})(\text{Acr})_2(\text{phen})]$ is of interest, where the seven-coordinated Cd atom uses a distorted monocapped octahedral environment formed by two nitrogen atoms of the phen ligand and five oxygen atoms from one aqua ligand and two Acr anion groups with the Acr O2 atom residing at the cap site and the axial apical positions occupied by one aromatic pyridyl atoms (N2) and one Acr O atom (O1) (Fig. 5.4, left) [29]. Changing the pH of the initial solution, the complex $[\text{CdCl}(\text{Acr})(\text{phen})_2]$ was obtained [30]. In this complex, the Cd atoms are pentagonal bipyramidally coordinated by one chloro atom, two oxygen atoms of Acr anion, and four nitrogen atoms of two phen ligands with apical positions occupied by each aromatic pyridyl N3 atom and a chloro atom (Fig. 5.4, right). In addition, three other aromatic pyridyl N atoms and two Acr oxygen atoms are located on the equatorial plane sites.

It should be noted the synthesis of lanthanide-containing (Ln = Eu, Tb, Nd, Gd) MCMs based on acrylic and methacrylic acids [31]. It turned out that the infinite chains of $\text{Eu}(\text{Macr})_3$ molecules are directed along the crystallographic *c*-axis and are connected by van der Waals interactions (Fig. 5.5).

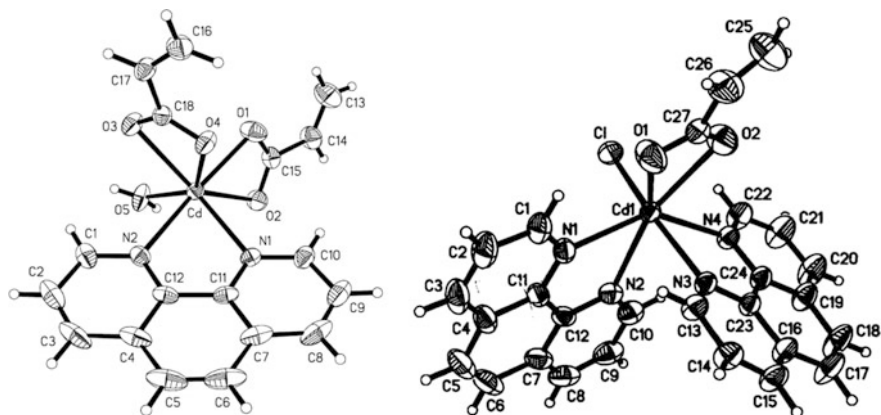


Fig. 5.4 Crystal structure of the complexes $[\text{Cd}(\text{H}_2\text{O})(\text{Acr})_2(\text{phen})]$ (left) [29] and $[\text{CdCl}(\text{Acr})(\text{phen})_2]$ (right) [30]

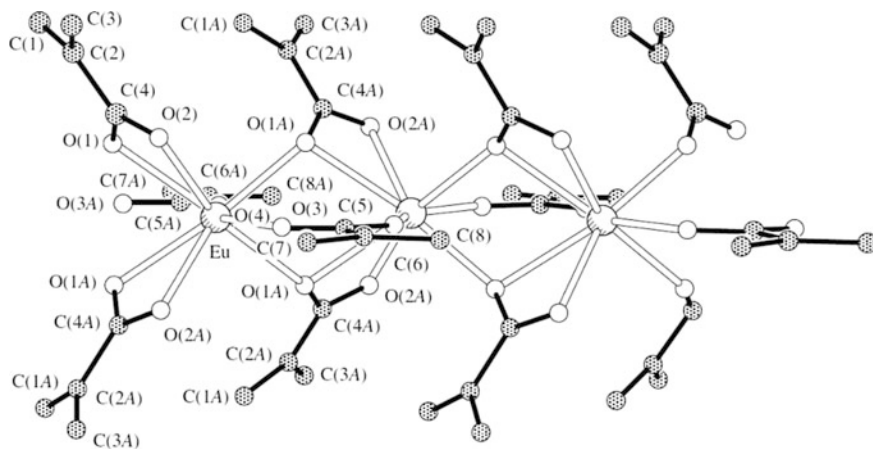
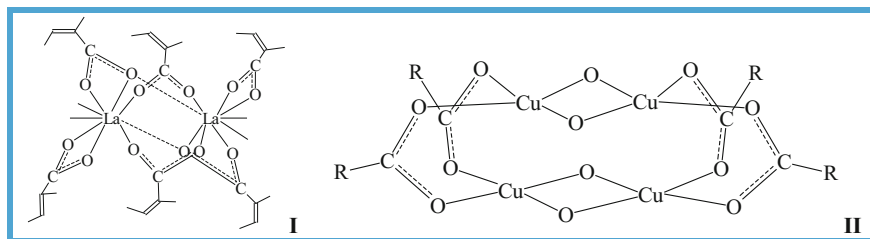


Fig. 5.5 Fragment of the europium methacrylate polymeric chain. Reproduced with permission from Ref. [31]. Copyright (2002) Springer Nature

The formation of four-membered cycles during chelation of carboxyl group requires a large deformation of the valence angles of the metal atom. In compounds of rare earth elements, such a strain does not arise and the probability of bidentate cyclic coordination increases. This is probably facilitated by an increase in the polarity of the M–L bond and the high coordination numbers of the metal. For example, in the heteronuclear Cu_2La_2 - [32, 33] or CoCe - [34] methacrylate complexes, the chelate groups are also located at the lanthanide center together with the bridging groups. Moreover, in the carboxylates of this type, the tridentate coordination of methacrylate groups is not unusual when one of the O atoms of the

carboxyl group forms bonds simultaneously with two metal atoms. In isomorphous binuclear complexes of *trans*-2,3-dimethacrylates La or Gd [M(OOC(CH₃)C(CH₃)CH)₃(phen)]₂, metal atoms are bound by two bridged bidentate and two tridentate carboxylate groups (**I**) [35]. The nature of the magnetic behavior of Cu(II) (meth)acrylate complexes, [Cu(Acr)₂Cu(OH)₂] [36] and [Cu(Macr)₂Cu(OH)₂] [37], is associated with their possible tetrameric structure (**II**).



Complexes of MAcr_n with tetradentate tripod ligands were also synthesized and structurally characterized [38–40]. In particular, in zinc complexes containing a tripod ligand tris(2-benzimidazolylmethyl) amine, the zinc ion is a 5-coordinate with the N₄O ligand set, and the coordination geometry of the zinc ion is best described as a distorted trigonal bipyramid [39].

It should be noted that the complexes carrying Acr and the aromatic amine were synthesized to modulate biological properties; in particular, such complexes show the superoxide dismutase-like activity. However, in these works the stage of polymerization, the feature of thermolysis of such complexes and, consequently, the properties of the resulting NPs are ignored.

Acetylene-type monocarboxylates are attractive because of their propensity for solid-state polymerization, favored by the presence of an infinite chain of short acetylene–acetylene contacts, as well as the energy of the crystal lattice and the absorption cross section of X-ray or γ -rays. Most propiolates of heavy metals meet these structural criteria [41–43]. The distances between the acetylene fragments in lanthanide propynoate complexes [41] are 3.5–3.94 Å; in dimethylthallium propynoate [42] and scandium(III) tripropiolate [42], they are, respectively, 3.454 and 3.79–4.02 Å. It should be noted that the introduction of a more cumbersome ligand into the molecule leads to the fact that the chain of acetylene–acetylene contacts is shortened. For example, when bpy is introduced into the structure of La₂O(OOCC≡CH)₆(H₂O)₄·2H₂O, a complex La₂O(OOCC≡CH)₆(bpy)(H₂O)₂·2(bpy)·4H₂O is formed, where the chain of acetylene–acetylene contacts is reduced to 5–6 [41], which cannot but be reflected in the reactivity in the polymerization transformations.

Among a wide variety of MCMs based on unsaturated carboxylic acids, a special place belongs to complexes of unsaturated dicarboxylic acids, for example maleates (MMal_n), itaconates (MITac_n), fumarates (MFum_n) of metals, which exhibit both unsaturated and carboxylate functions [3–5, 44–50]. The presence of two carboxyl

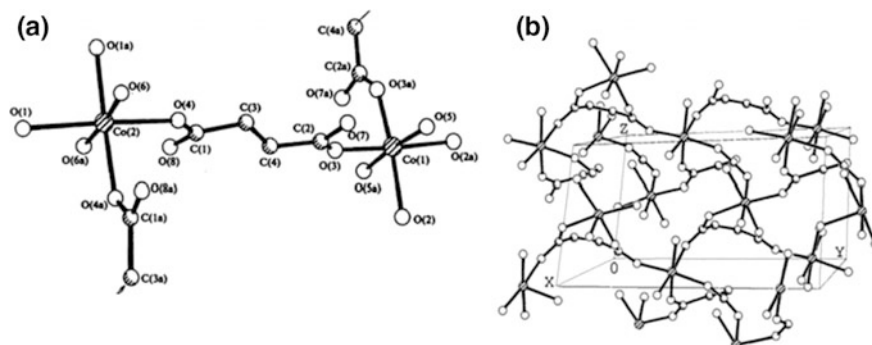
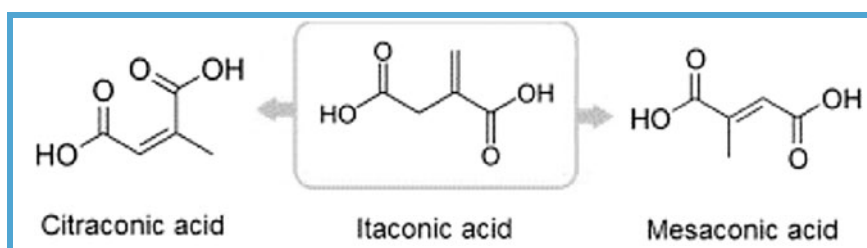


Fig. 5.6 Molecular structure of CPs of CoFum·5H₂O (a) and CoMal·3H₂O (b) [45]

groups in the molecule of dicarboxylic acids increases their functional capabilities as ligands and creates on their basis a variety of monomeric and polymeric structures of metal carboxylates. Synthetic approaches and the structure of prethermolyzed carboxylates of unsaturated dicarboxylic acids differ from those of monocarboxylic acids. First, at the stage of their synthesis (as shown for metal maleates, fumarates, itaconates, acetylenedicarboxylates [45, 51]) coordination polymers (CPs) are formed. Thus, according to X-ray diffraction analysis, unsaturated metal dicarboxylates have both monomeric (Co(II) and Fe(II) hydromaleates, M(HMal)₂·4H₂O) and chain (Co(II) fumarate, CoFum·5H₂O) or 3D (Co(II) malate, CoMal·3H₂O) polymeric structure (Fig. 5.6), the multiple bonds of which are not coordinated with the metal.

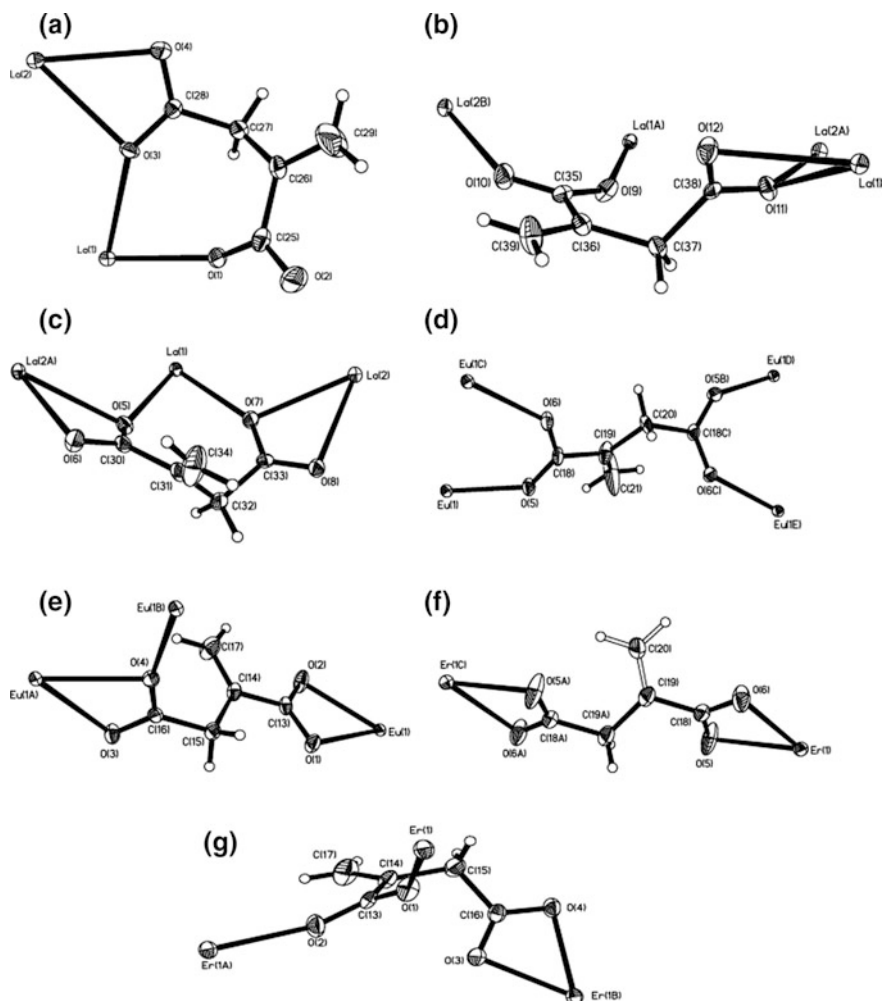
Itaconic acid (H₂Itac) ligands are completely deprotonated and give seven types of coordination modes (Scheme 5.2).

In addition, itaconic acid is easily isomerized to citraconic or mesaconic acid.



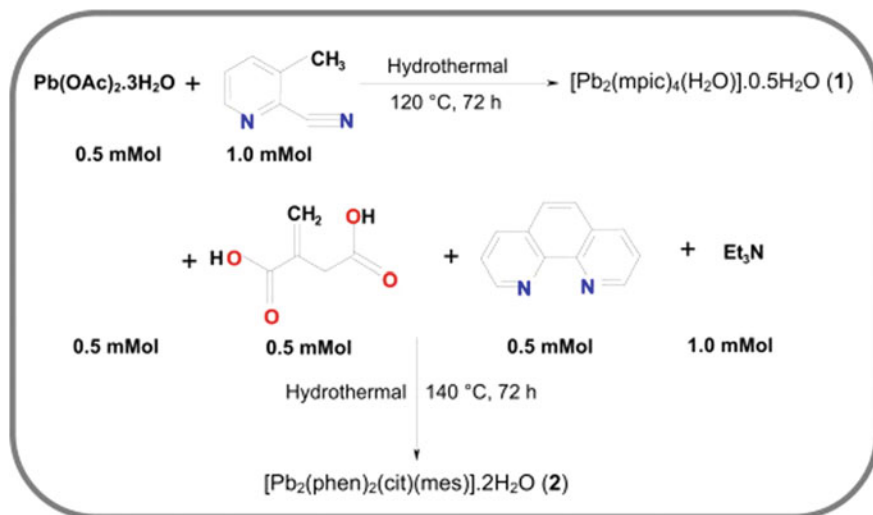
It is known that coordination compounds containing citraconate (2-methylmaleate) or its isomer, mesaconate, have interesting electrical and optical properties [52–56].

It should be noted lanthanide CPs with three different structures: {[La₂(Itac)₃(phen)₂]·2H₂O}_n (**1**), {[Ln(Itac)_{1.5}(phen)]·xH₂O}_n [*x* = 1, Ln = Eu (**2**); *x* = 0.25, Ln = Dy (**3**)], and [Ln(Itac)_{1.5}(phen)]_n [Ln = Er (**4**); Yb (**5**)] [57].



Scheme 5.2 Seven crystallographically established coordination modes of the Itac ligands

Compound **1** contains 1D double chain, which are then assembled into a 3D supramolecular structure through H-bonds and π - π stacks between the phen molecules. In compounds **2** and **3**, there are 2D infinite networks, which are further designed to form 3D supramolecular architectures with a 1D channel by π - π aromatic interactions. Finally, compounds **4** and **5** have 2D layer structures consisting of three types of rings, which are further architected to form 3D supramolecular structures with the help of C-H...O hydrogen bonds. The H₂Itac ligands are completely deprotonated and exhibit tetra-, penta-, and hexadentate coordination modes in complexes.



Scheme 5.3 Reaction scheme. Reproduced with permission from Ref. [55]. Copyright (2013) Elsevier

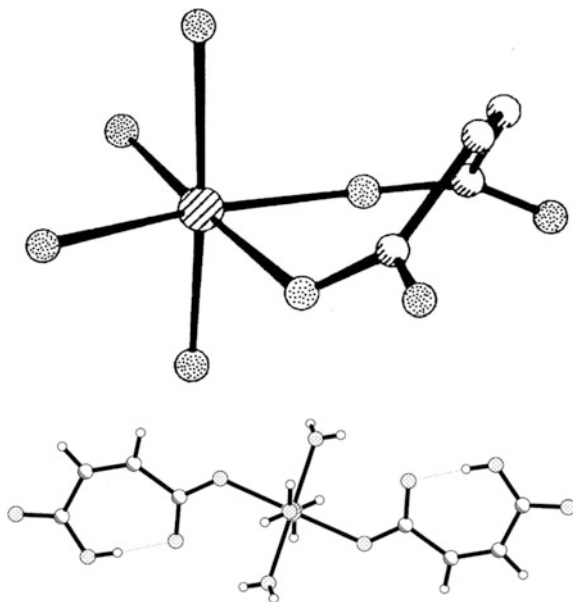
A complex of Cu(II) with nicotinamide (L) and itaconic acid $[\text{Cu}(\text{Itac})_2(\text{L})_2(\text{H}_2\text{O})_2 \cdot 2(\text{H}_2\text{O})]$ is of interest [58]. The octahedral geometry around the copper(II) ion is CuN_2O_4 , consisting of two L molecules acting as a monodentate ligand through the nitrogen atoms, two H_2Itac ligand molecules, and two coordinated water molecules, each coordinated through the oxygen atoms. The structure of the complex showed that infinite chains grow, linking molecules together through strong O–H/O and N–H/O intermolecular H-bonds generating 2D network sheet along the *c*-axis.

It should be noted the synthesis of two lead(II) CPs, $[\text{Pb}_2(\text{mpic})_4(\text{H}_2\text{O})] \cdot 0.5\text{H}_2\text{O}$ (1) and $[\text{Pb}_2(\text{phen})_2(\text{cit})(\text{mes})] \cdot 2\text{H}_2\text{O}$ (2), where mpic = 3-methylpicolinate, H_2cit = citraconic acid, H_2mes = mesaconic acid (Scheme 5.3) [55]. The complexes contain topologically distinct 1D polymer chains stabilized by weak interactions, and both contain tetranuclear Pb_4 units bound by carboxylate groups. In compound 1, 3-methylpicolinic acid is formed in situ from 3-methylpicolinate and mesaconate and citraconate anions were unexpectedly formed from itaconic acid during synthesis of 2.

CP $[\text{Zn}(\text{mesaconate})(\text{L})]_n$ (L = 4,4'-dipyridylamine) was obtained from hydrothermal treatment of zinc chloride, L and itaconic acid [52].

It should be noted that maleic acid (H_2Mal) tends to form an intramolecular H-bond, which leads to a large difference between the dissociation constants [45]. Therefore, H_2Mal can provide only one carboxyl group for substitution, which functions as a monodentate ligand and forms, most often, acid salts. The formation of acid or normal metal salts of carboxylic acids affects the structure of the carboxylate in the condensed phase [44, 45, 48, 59, 60]. In particular, cobalt and nickel

Fig. 5.7 A fragment of coordination polyhedron of normal maleates [M(H₂O)₂(Mal)](H₂O) (M = Co(II), Ni(II)) (top); molecular structure of acid maleates [M(H₂O)₄(HMal)₂] (M = Mn(II), Fe(II), Co(II), Ni(II)) (down). Reproduced with permission from Ref. [61]. Copyright (2014) Springer Nature



hydrogen maleates form a monomeric structure, whereas a normal cobalt maleate exists as a 3D structure (CP) [45, 61]. Both carboxyl groups of H₂Mal participate in the binding of metal in these maleates. The formation of a seven-membered chelate ring is an interesting feature of these structures (Fig. 5.7, left). The coordination polyhedron is a slightly distorted octahedron consisting of four O atoms from two Mal ligands and two O atoms of coordinated water molecules. The third H₂O molecule is crystalline water, which is weakly bound by the structure during thermolysis, apparently providing an infinite chain of alternating coordinated and crystalline H₂O molecules [45]. Acid maleates of Mn(II), Fe(II), Co(II), and Ni(II) have a monomeric chain structure (Fig. 5.7, right) [61]. Two monodentate H₂Mal residues are bound to the metal atom in the centrosymmetrical complex; coordination is supplemented to the octahedral by four oxygen atoms of water molecules.

The structures of the metal carboxylate affect the thermal transformations and properties of the metal-containing nanocomposites formed. Therefore, the study of the influence of intramolecular H-bonding in molecules of unsaturated dicarboxylic acid on the formation of metal carboxylates is of interest for predicting the properties of nanocomposites formed during the thermolysis of carboxylate. For example, the multiple bonds in CuMal do not participate in coordination, which is important for subsequent polymerization transformations of salts based on unsaturated dicarboxylic acids.

It should be noted that all of the unsaturated dicarboxylic acid form cobalt hydrogen carboxylates when synthesized in aqueous solutions [62]. In particular,

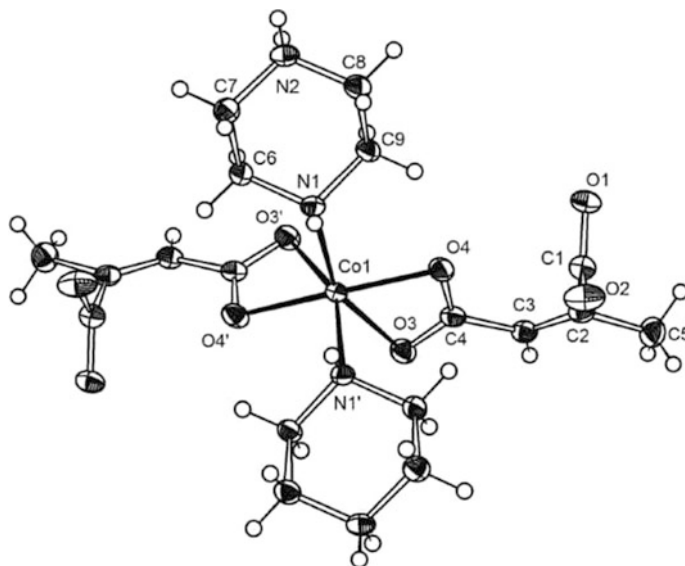


Fig. 5.8 Crystal structure of *trans*-bis(2-methylmaleato- k^2O,O') bis(piperazinium- kN) cobalt(II) trihydrate [65]

the formation of cobalt and nickel acid salts of allylmalonic, itaconic, and *cis,cis*-muconic acids is energetically more favorable than the formation of normal carboxylates [63].

MS and theoretical studies of decarboxylation of anionic lithium complexes of doubly deprotonated dicarboxylic acids, which include succinic acid, L-malic acid, L-mercaptosuccinic acid, L-aspartic acid, and oxaloacetic acid, are interesting [64]. It turned out that decarboxylation reactions of these complexes in the gas phase can take place, and α -substituted groups in dicarboxylic acids such as $-OH$, $-NH_2$, and $-SH$ can promote decarboxylation of the corresponding anionic lithium complexes.

It should be noted the study of the crystal structure of *trans*-bis(2-methylmaleato- k^2O,O') bis(piperazinium- kN) cobalt(II) trihydrate (Fig. 5.8) [65]. It contains discrete cobalt(II) complex fragments and lattice water molecules. The crystallographically unique Co atom is coordinated by four oxygen atoms from two symmetry-related citraconate ligands. The nitrogen atoms of two monoprotonated piperazine ligands in the *trans*-configuration fill the distorted octahedral environment of Co.

It should be also noted trinuclear chromium, iron, and vanadium acrylates, as well as chromium and iron maleates and itaconates [47, 66–69]. In particular, the mass spectra of Cr(III) maleate and itaconate contain peaks with $m/z = 862, 894, 926$ and $946, 978, 1010$ corresponding to $[Cr_3O(Mal)_6]^+$ and $[Cr_3O(Ita)_6]^+$ cationic clusters that are either solvent-free or solvated with one or two methanol molecules, respectively.

Interest in carboxylates with unsaturated ligands of acetylene type depends on their ability to polymerize in the solid state, determined by the short distances

between reaction centers and appearance of short acetylene–acetylene contacts. In addition, complexes of dicarboxylic acids with bidentate carboxylic bridges between paramagnetic centers are efficient magnetically concentrated systems [70]. There is a wide variety of structures, including monomeric salts, linear and 3D CPs, depending on the type of metal. Thus, acetylenedicarboxylic acid (H_2ADC) is a promising candidate for the synthesis of new metal–organic networks with interesting properties. It can be considered as one of the simplest linear bifunctional linker ligands with a rigid carbon backbone, which allows us to investigate the basic mechanisms and interactions that lead to the formation of a specific structural arrangement in the CP.

Up to now, numerous metal compounds with the ADC^{2-} anion have been reported [71–103]. They can be classified into the following three categories. The first of these includes anhydrous CPs, for example PbADC [75], CaADC [76], SrADC [77], and Tl_2ADC [78, 79].

The second group includes a variety of hydrates like $\text{PbADC}\cdot\text{H}_2\text{O}$ [75], $\text{MnADC}\cdot 2\text{H}_2\text{O}$ [76], $\text{BaADC}\cdot\text{H}_2\text{O}$ [77], $\text{Bi}_2\text{ADC}_3\cdot 8\text{H}_2\text{O}$ [78], $\text{K}_2\text{ADC}\cdot\text{H}_2\text{O}$ [79], $\text{Na}_2\text{ADC}\cdot 4\text{H}_2\text{O}$ [79], $\text{La}_2\text{ADC}_3\cdot 8\text{H}_2\text{O}$ [80]. Finally, CPs were obtained that contain ADC^{2-} and additional ligands, such as N-donor ligands or anions such as CO_3^{2-} and NO_3^- [81–87].

All known compounds can be further subdivided into the dimension of the formed polymer network. Anhydrous CPs only create 3D networks, whereas for hydrates 1D, 2D, and 3D networks are detected. The rich structural universality of the ADC^{2-} ligand is further confirmed by the formation of supramolecular networks, such as $[\text{Be}(\text{H}_2\text{O})_4]\text{ADC}$ [88] and $[\text{Co}(\text{NH}_3)_6](\text{ADC})(\text{HADC})\cdot 2\text{H}_2\text{O}$ [89].

It is well known that acetylenedicarboxylic acid as carboxylic acids with short aliphatic chains forms complexes with transition metals such as $\text{Cu}(\text{II})$ [90], $\text{Mn}(\text{II})$ [90, 91], $\text{Ni}(\text{II})$ [11], $\text{Co}(\text{II})$ and $\text{Cd}(\text{II})$ [92–94], $\text{Zn}(\text{II})$ [95], or lanthanide cations [80, 81, 96] either in a single crystal or in the form of a powder. Metal cations are coordinated with both carboxylate groups in the chelating regime, forming metal–organic chains. It is interesting that the triple bond centered between the carboxylate units of acetylenedicarboxylic acid gives new design parameters for the synthesis of new structures. Among the most interesting examples, we note a topochemical reaction between $[\text{Pb}(\text{ADC})]$ and $[\text{Pb}(\text{ADC})(\text{H}_2\text{O})]$ [75] and the crystallization of acentric CPs with the addition of trigonal planar NO_3^- as additional ligand [81]. MOF-type CPs with ADC^{2-} as bridging ligand are also of interest [95, 97].

It should be noted the diamond-like topology of the crystal structure of anhydrous strontium acetylenedicarboxylate $[\text{Sr}(\text{ADC})]$ [72] (Fig. 5.9, left) and the complex $[\text{Zn}(\text{ADC})_2(\text{HTEA})_2]_n$ (HTEA is triethylamine) [95]. Each zinc ion in the latter binds monodently to four different carboxylate bridges, forming two interpenetrating diamond-like networks (Fig. 5.9, right). It is believed that the four carboxylate carbon atoms in each $\text{Zn}(\text{CO}_2)_4$ unit as a tetrahedral unit, occupying the position of the vertex C in the diamond structure, can enlarge and expand the framework, that is, serve as a molecular building block for creating new complex structures. It is noteworthy that $\text{Sr}(\text{C}_4\text{O}_4)$ exhibits extraordinary thermal stability.

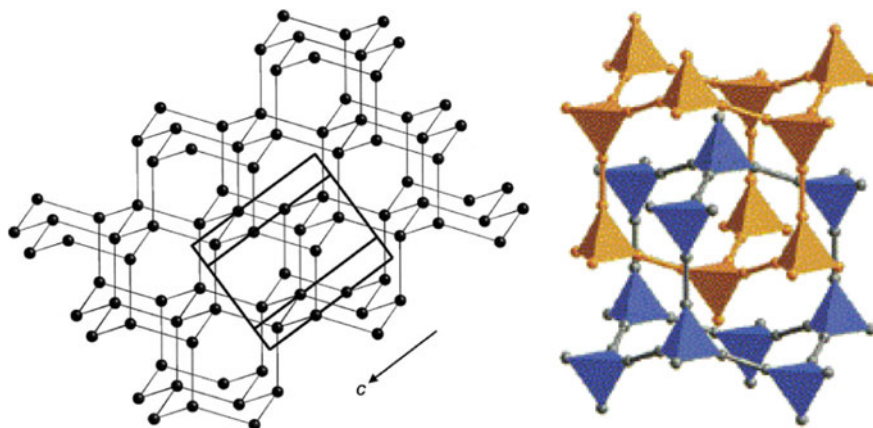


Fig. 5.9 Diamond-like structures in the acetylenedicarboxylates of Sr(II) (left) and Zn(II) (right). Reproduced with permission from Ref. [72]. Copyright (2002) John Wiley and Sons, and reproduced with permission from Ref. [95]. Copyright (2001) American Chemical Society

In air, the decomposition of the complex begins only at 723 K, whereas in argon it begins at 753 K. Of interest is negative thermal expansion in $[\text{Sr}(\text{ADC})]$ [72].

The structural diversity of Mn(II) complexes with ADC^{2-} and hexadentate ancillary ligands should be noted: N,N,N',N' -tetrakis-(2-pyridylmethyl)-1,2-diaminoethane, N,N,N',N' -tetrakis-(2-pyridylmethyl)-1,2-diaminopropane, N,N,N',N' -tetrakis-(2-pyridylmethyl)-1,3-diaminopropane, N,N',N'',N''' -tetrakis-(2-pyridylmethyl)-1,4-diaminobutane, N,N',N'',N''' -tetrakis-(2-pyridylmethyl)-1,5-diaminopentane [98]. It turned out that the length of methylene chain plays a decisive role in coordination architectures. In another interesting example, the Mn ions in the compound $[\text{Mn}(\text{ADC})_2(\text{L})] \cdot \text{H}_2\text{O}$, where L is 1,3-bis(4-pyridyl)propane, are connected by acetylenedicarboxylate to a 1D zigzag chain, which binds to the L ligand to generate a 3D six-bonded structure [99]. The coordination polymers ${}^2_{\infty}[\text{Bi}(\text{ADC})_{2/4}(\text{ADC})_{3/3}(\text{H}_2\text{O})_2] \cdot 2\text{H}_2\text{O}$ and ${}^3_{\infty}[\text{Bi}(\text{ADC})_{2/4}(\text{ADC})_{3/3}(\text{H}_2\text{O})_3] \cdot \text{H}_2\text{O}$ are hydrate isomers with taking into account the central Bi^{3+} ion, which leads to completely different topologies of the resultant CPs [73]. Also of interest are lithium-containing coordination polymers $\text{Li}_2\text{ADC} \cdot 2\text{H}_2\text{O}$ and Li_2ADC , in which LiO_4 tetrahedra are interconnected by ADC^{2-} anions to form a 3D polymeric structure [100].

The specific structural features of metal acetylenedicarboxylates also correspond to the structural criteria of solid-phase polymerization, since in this case the orientation of the MCMs is optimal for the formation of new chemical bonds [101]. For example, carbon-carbon triple bonds in CPs of zinc(II) and cobalt(II) acetylenedicarboxylates are at distances of ~ 3.8 Å from each other, which is most advantageous for solid-state polymerization (Fig. 5.10) [102]. Compound $[\text{Zn}(\text{ADC})(\text{H}_2\text{O})_2]_n$ is a CP formed by Zn^{2+} cations containing four ADC ligands and two water molecules in the nearest environment [51, 102]. Metal ions have a centrosymmetric octahedral environment and are bound by carboxyl groups to form

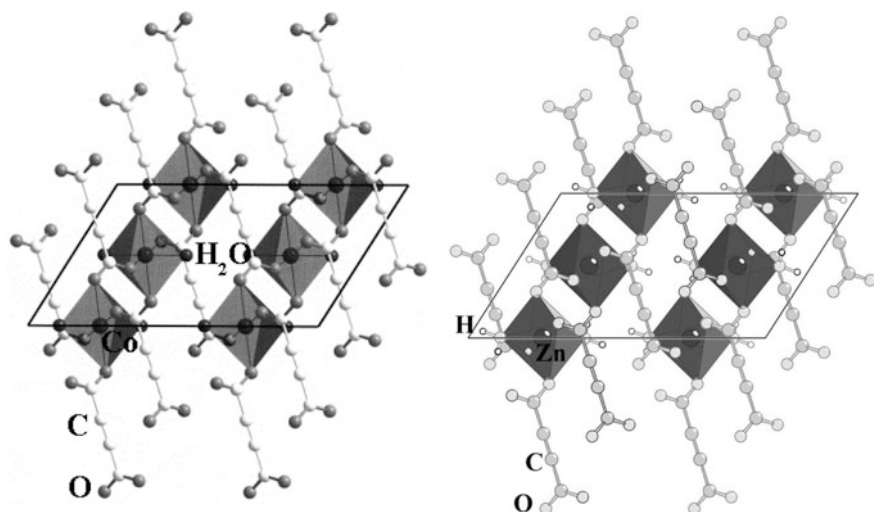


Fig. 5.10 Crystal structures of CoADC (left) and ZnADC (right) [51]

layers parallel to the (011) plane. These layers are bound by the second carboxyl groups of dianions to the 3D coordination structure. The growth of the polymer chain can occur in the plane of building units—parallel close-packed molecules of ZnADC·2H₂O and CoADC·2H₂O. The possibility of carrying out solid-phase polymerization of these compounds has been experimentally confirmed [51].

However, the mechanisms of initiation, polymerization, and thermal transformation of unsaturated carboxylates and, mainly, acetylene-type metal-containing monomers have been poorly understood [51, 59, 93, 103].

5.2 Thermal Polymerization of Metal Chelate Monomers

Most of the metal carboxylates at room temperature are solid substances (crystalline or amorphous). The use of solid-phase polymerization methods makes it possible to reduce the role of a number of side processes that arise in solutions, for example the dissociation of salts in solutions and the limitation of the range of solvents in which sufficiently concentrated solutions of monomers can be obtained. Metal carboxylates are often convenient objects for solid-state polymerization in the structural plan, since the orientation of their molecules is optimal for the formation of chemical bonds between monomers. Growth of chains occurs in the plane of “billets”: parallel to each other densely packed monomer molecules. Such a process is not typical for either a liquid or a gaseous state. The basis of the kinetic scheme of solid-phase polymerization, regardless of the type of initiation, is the almost complete absence of translational diffusion of the reacting particles,

the heterogeneity of the crystal lattice (the place of termination of growing chains), the anisotropy of the reactivity of molecules (determines the direction of chain growth) [104].

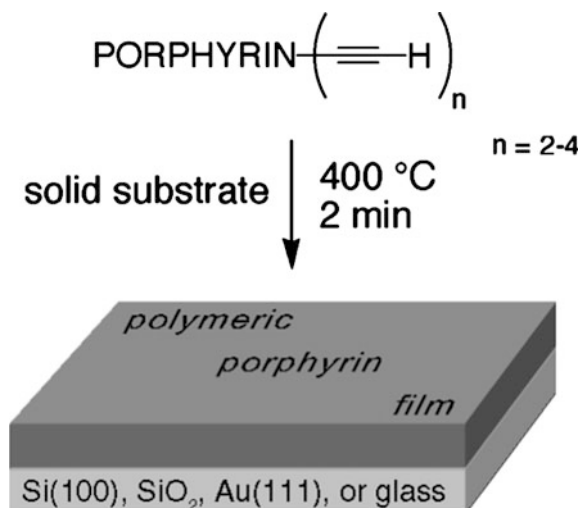
In thermal generation, free radicals arise from the opening of C–C or C–H bonds, or the opening of a double bond (to form biradicals). The polymerization rate increases with increasing temperature.

It should be noted that thermal polymerization of MCM for the production of metal-containing polymers has been poorly studied. Among the most typical examples, we note the use of a thermally induced polymerization process to produce various metal–polymer coatings by depositing an MCM solution on the electrode surface followed by thermal polymerization. The effectiveness of this approach is shown by the example of the polymerization of ethynyl Zn-porphyrin, which has different models of 1–4 ethyne or protected ethyne groups and various non-bonding substituents. These MCMs undergo thermal in situ polymerization on surface, which gives robust M-porphyrin films with a controlled thickness; in particular, films obtained on different surfaces of Si(100), SiO₂, Au(111), or glass have a thickness in the range from tens to hundreds of nm (Scheme 5.4) [105].

In another interesting example, physical vapor deposition polymerization of the MCM was carried out by evaporating the vinyl monomers followed by heat treatment [106]. This method is used to obtain hole-transport and emission layers of organic light-emitting diodes (OLEDs) (Fig. 5.11). In particular, the emission layers were doped with red- or blue-emitting phosphorescent Ir complexes, modified by styryl fragments, and deposition polymerization was very promising for increasing the irradiation efficiency.

It should be noted the thermal solid-state polymerization of zinc diacrylate separately and with additives, such as diphenyl disulfide and thiophenol derivatives and dicumyl peroxide [107]. This polymerization is non-topochemical, and the

Scheme 5.4 Schematic representation of the thermal polymerization of ethynyl Zn-porphyrin. Reproduced with permission from Ref. [105]. Copyright (2005) American Chemical Society



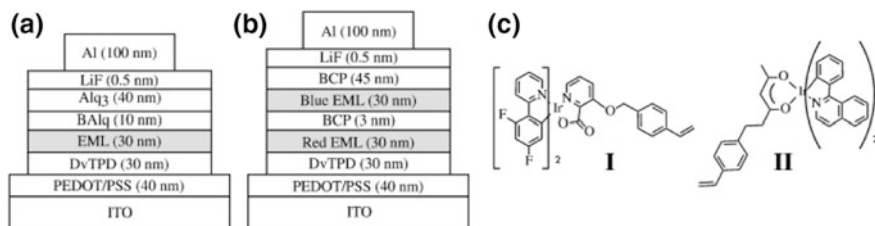


Fig. 5.11 OLED structures having **a** single emissive layers (EML) and **b** double EMLs, including tetraphenyl-diaminobiphenyl (DvTPD), bis(2-methyl-8-quinolino)-4-phenylphenolate aluminum (BAIq), bathocuproine (BCP), poly(3,4-ethylene dioxythiophene)/poly(styrene sulfonate) (PEDOT/PSS), and indium tin oxide (ITO). Chemical structures of synthesized vinyl monomers bis[(4,6-difluorophenyl)pyridinato-N,C²][3-(4-vinylbenzyloxy)picolinato] Ir(III) (**I**) and bis(1-phenylisoquinolino)-6-(4-vinylphenyl)acetylacetonate Ir(III) (**II**) are shown in (c). Reproduced with permission from Ref. [106]. Copyright (2009) Elsevier

main polymer structure is polyacrylate with acrylate or polyacrylate bound by Zn^{2+} , although part of the monomer structure was eliminated during polymerization. The effect of these additives can be explained by the ability of initiation and chain transfer for the radical polymerization of additives.

It is of interest to thermal polymerization of 1:1 mixtures of zinc diacrylate and zinc dialkanoate [108]. The mixtures began to melt at lower temperatures than the melting points of the original components, and the polymerization of the acrylate parts progressed in the molten state at lower temperatures than the thermal polymerization temperature of zinc diacrylate alone. It is found that the accelerated polymerization rate is initiated by ion exchange in which one of the carboxylate anions of zinc diacrylate is exchanged with the alkanoate of zinc dialkanoate, just above the melting point.

It should be noted that data on acetylenedicarboxylate polymerization and the properties of the resulting metallopolymers are insufficient. A typical example is solid-state polymerization of cadmium salt of acetylenedicarboxylic acid [93]. In 1D CP $[Cd(ADC)(H_2O)_3]H_2O$, carbon–carbon triple bonds are in the immediate vicinity (3.27 Å) along the *a*-axis. This causes, when heating, polymerization to form conjugated polycarboxylic chains. EPR data show that either thermal treatment or X-ray irradiation of CP can create long-lived paramagnetic radicals. In all cases, the main component is a radical with *g* about 2.0038 and a line width of about 4.5 G (Fig. 5.12). It delocalizes over a chain fragment that includes alternative carbon bonds and side carboxylates.

It has also been demonstrated that CP of Ln acetylenedicarboxylate tends to undergo thermal solid-state polymerization in situ [80].

However, special approaches are often required in this case, especially for disubstituted acetylene molecules with low reactivity. Regardless of the method for initiating solid-state polymerization, its kinetic scheme includes the following prerequisites: The spatial displacement of growing macroradicals and their collisions with monomer molecules only lead to chain growth events (due to the absence

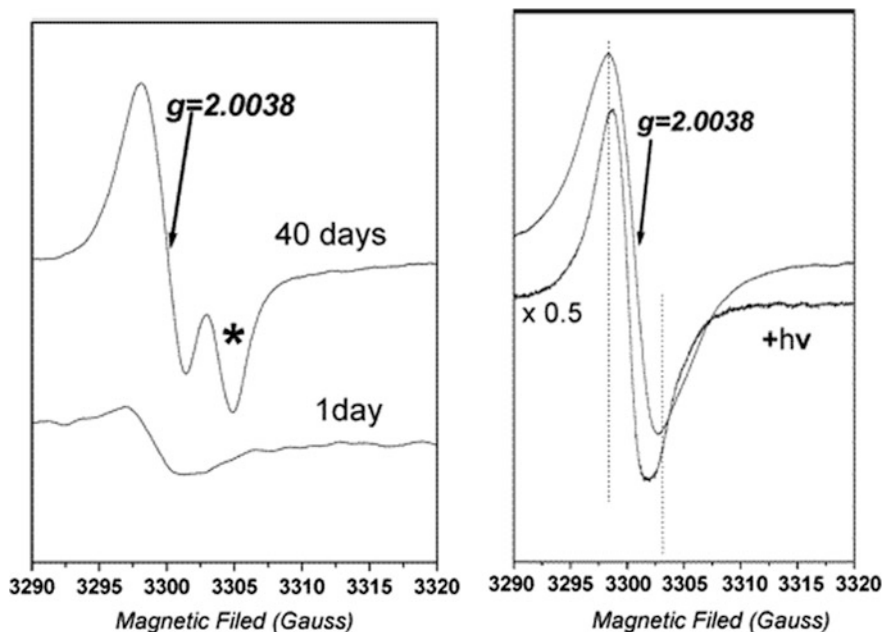


Fig. 5.12 (left) EPR spectrum of CP heated at 363 K for different periods of time; (right) EPR spectra of CP heated at 433 K for 24 h (upper trace), followed by subsequent X-ray irradiation for 6 h (lower trace). Reproduced with permission from Ref. [93]. Copyright (2003) American Chemical Society

of translational diffusion of reacting species); defects of the crystal lattice (dislocations, gaps, vacancies, etc.) cause the chain to terminate; the reactivity of growing macromolecules in the crystal lattice is anisotropic, and consequently, there is a preferred crystallographic axis of their growth. Free radical (less often ionic) solid-state polymerization of unsaturated metal carboxylates can be initiated in different ways. The most frequently used are thermal, photochemical and radiation initiation, and less studied is mechanochemical initiation. As an example, we consider high-pressure polymerization under shear deformation (HP + SD) of ZnADC. It is known that polymerization of many classes of monomers takes place under HP + SD conditions, even if monomers are usually difficult to polymerize (as, for example, with acetylene derivatives). Indeed, ZnADC tends to polymerize when its solid sample is compressed in appropriate equipment such as the Bridgman anvil (Fig. 5.13) under high pressure, combined with shear deformation (pressure 5–10 kbar, rotation angles 100° and 300°): The resulting colored product is rarely soluble in water and insoluble in organic solvents [51].

According to obtained data, the yield of the product increases with increasing pressure (5–10 kbar) and the degree of conversion is generally dependent on the shear deformation expressed in terms of an angle of rotation (100° – 300°). Note that the IR spectrum of the product obtained is similar to the spectra of polymer samples

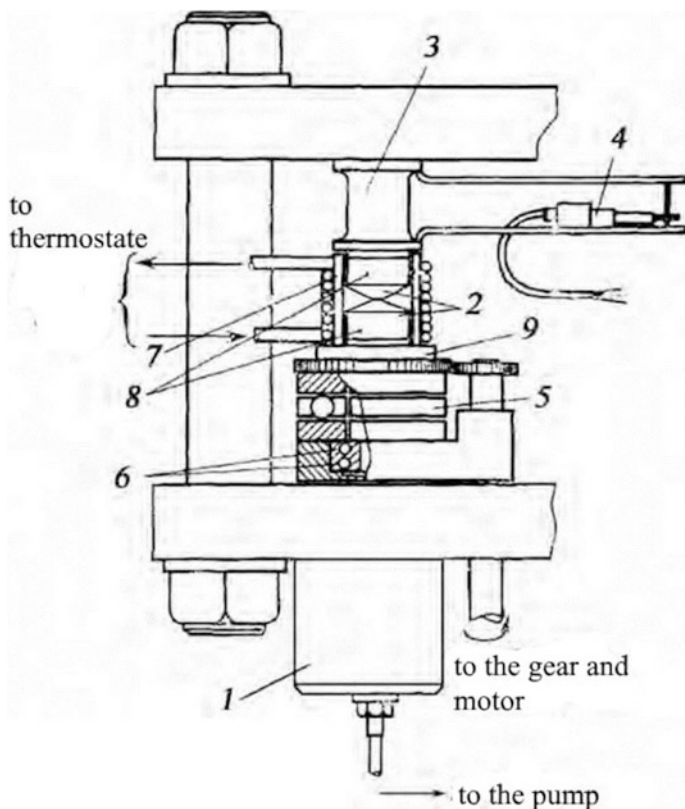
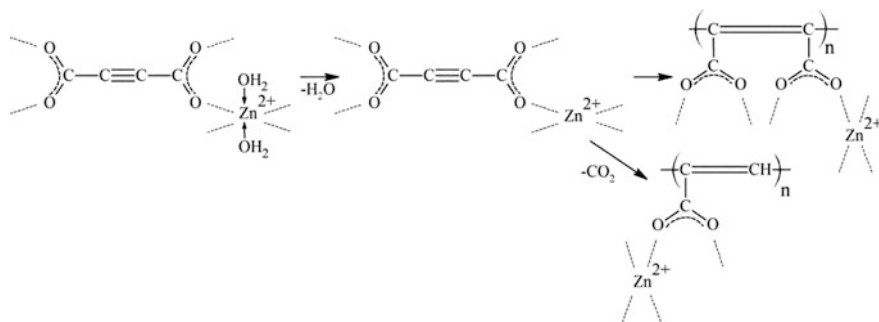


Fig. 5.13 Bridgman's anvil scheme: 1—hydropress cylinder; 2— anvils; 3—elastic element; 4—mechanotrope; 5—thrust ball bearing; 6—the radial ball bearing; 7—thermostatic shirt; 8—places for thermocouples; 9—thrust bearing from heat insulator [51]

synthesized from ZnADC in alternative ways; this suggests their structural similarity.

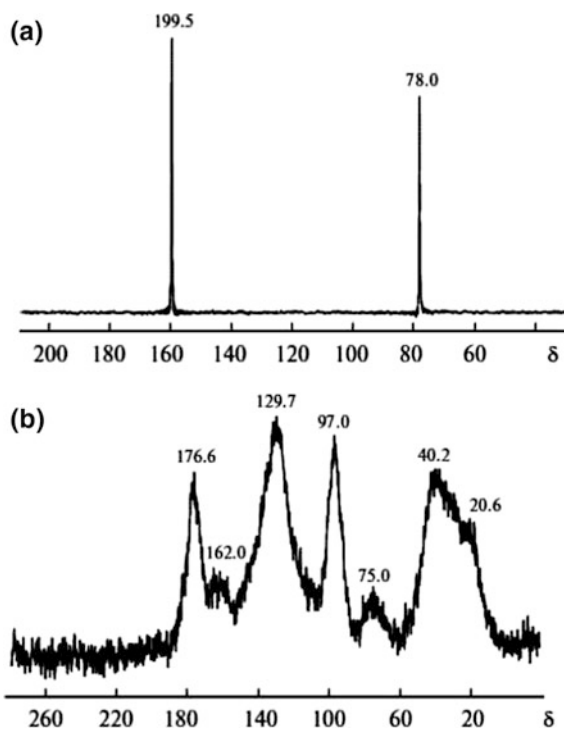
The DSC curve of ZnADC shows an exothermic peak at 187.8 °C due to thermal polymerization (heat effect 180.4 J g⁻¹). According to TGA data, the weight loss at the step immediately preceding the polymerization corresponds to the elimination of water of crystallization and a CO₂ molecule; the polymerization properly entails no changes in the sample weight. Polymerization of ZnADC under isothermal conditions in an inert atmosphere and in vacuum at 150 °C for 2 h yields a colored polymer. The product is insoluble in water or organic solvents and can pass into solution only when 0.1 M HNO₃ is used. The proposed scheme for ZnADC solid-phase polymerization is shown in Scheme 5.5.

In addition, the formation of the polymer is indirectly confirmed by the ¹³C NMR spectra of ZnADC and its polymerization product (Fig. 5.14a). The former spectrum consists of two singlets for two types of carbon atoms in ZnADC:



Scheme 5.5 Scheme of solid-state polymerization of ZnADC [51]

Fig. 5.14 ^{13}C NMR spectra of ZnADC (a) and the product obtained by its thermal polymerization (b) [51]



at δ 159.5 (COO) and 78 (C \equiv C). The latter spectrum (Fig. 5.14b) is strongly broadened, which suggests the polymeric structure of the sample. In addition, the presence of more peaks is characteristic of a more complicated structure that can result from molecular reorganization following fragment elimination of CO and/or CO₂ during the polymerization, e.g., the formation of cyclic structures. The spectrum contains weak peaks at δ 162 (COO) and 75 (C \equiv C) and intense peaks at δ 176 and 40, which can be assigned to the C(O)–C–O and CH₂ fragment.

However, most of the results of investigations of thermal transformations of MCMs are qualitative [109–115].

It should be noted such interesting approach as melt surface graft functionalization of MCMs in polymer matrixes [116–134]. In particular, it was used in situ polymerization of zinc dimethacrylate in poly(oxyethylene) elastomer [135] and calcium di(meth)acrylate divinyl monomers in linear low-density polyethylene [136]. It turned out that the in situ polymerization of zinc dimethacrylate is almost complete at the beginning stage of curing and that substantial cross-linking starts subsequently.

At present, such a promising method of polymerization of metal-containing monomers, such as thermal frontal polymerization (FP), attracts considerable attention [137, 138]. The FP process involves converting the monomer into a polymer in a localized reaction zone that is propagated in a bulk medium. The modern application of FP and the study of its kinetics and dynamics are widely used [139–143]. Among the advantages of frontal polymerization, one can note a high reaction rate, a short reaction time, low energy consumption, and the possibility of polymerization in an environmentally friendly manner without the addition of a solvent. FP provides a significant increase in the homogeneity of the polymer chain composition, despite the higher conversion [144]. The formation and stabilization of the polymerization front are affected by the chemical evolution of heat and its dispersion by thermal conductivity. Therefore, high exothermic reactions are preferred for FP reactions in which the heat of reaction is greater than the heat loss. The use of FP to polymerize metal-containing monomers in the condensed phase was discovered in the early 1980s [145]. In particular, this reaction was found to be characteristic of acrylamide complexes of transition metal nitrates [146]. FP of these monomers is the first example of thermal initiation of a process without chemical initiators. The FP method was used to polymerize CoADC [50] by heating a quartz vessel with CoADC in a tubular furnace. The process was carried out in a vacuum at 473 K and heated for 1 h (the temperature gradually increased, and to reach 473 K it took about an hour and a half). A general concept of mathematical modeling of complex multistage reactions, accompanied by an essentially uneven thermal pattern, is proposed for describing the FP of metal-containing monomers [147]. This concept mainly focuses on the chemical kinetics of the transformations that occur, and a mathematical model of the thermal FP of metal-containing monomers based on the simplest chemical kinetic scheme is constructed in its framework.

5.3 Overall Scheme of Conjugated Thermolysis

Studies of the thermolysis of MCMs in the TA regime in air and in an inert atmosphere give only a qualitative pattern of the transformations that occur during their thermolysis [110, 148]. The most complete information on the influence of various factors on the kinetics and dispersion of the products prepared can be

obtained by isothermal studies of the thermolysis of MCMs in SGA. Thus, thermolysis was studied for a number of unsaturated metal carboxylates, in particular, CuAc_2 [149], CoAc_2 [150], NiAc_2 [10, 107], ScAc_4 [151], polynuclear oxoacrylate FeAc_3 [152], cocrystallizates FeAc_3 and CoAc_2 , FeAc_3 and NiAc_2 with atomic ratio of Fe/Co equal to 1:0.8 (FeCoAc) and 2:1 (Fe_2CoAc) [153], Fe/Ni = 2:1 (Fe_2NiAc), Hf(IV) (meth)acrylate and fumarate derivatives [154, 155], maleates $\text{CoMal}\cdot 2\text{H}_2\text{O}$ [47] and $\text{Fe}_3\text{O}(\text{OH})(\text{Mal})_6\cdot 3\text{H}_2\text{O}$ [156], etc.

In general, the study of MCM thermolysis in TA and SGA regimes showed an overall pattern of the nature of their transformation, consisting in a sequence of three main differing in temperature macrostages [6, 8, 11, 157–160]: dehydration (desolvation) of the original MCMs (403–473 K); solid-phase homo- or copolymerization of dehydrated MCMs (473–573 K); decarboxylation of the resulting metallopolymer into a metal-containing phase; and an oxygen-free polymer matrix at temperatures >523 K (in the case of copper MCMs above 453 K), accompanied by intense gas evolution. A stage mechanism of thermolysis has been also proposed for complex acrylates of the composition of $\text{M}(\text{phen})(\text{Acr})_2(\text{H}_2\text{O})_y$, $\text{M} = \text{Mn}(\text{II})$ ($y = 0$), $\text{Ni}(\text{II})$ ($y = 2$), $\text{Cu}(\text{II})$ ($y = 1$), $\text{Zn}(\text{II})$ ($y = 2$) (TG, DTG, air, 293–1273 K, rate heating 10 deg min^{-1}) [17]. For these acrylates, with the exception of the Zn-complex, all macrostages were exothermic. The solid products are Mn_2O_3 , NiO, CuO, and ZnO, respectively.

The initial decomposition temperatures of acrylates increase in the sequence of metals: $\text{Fe} < \text{Cr} < \text{Ni} < \text{Co} < \text{Mn}$; however, these temperatures are lower than the decomposition temperature of polyacrylic acid. This is probably due the catalytic effect of metal ions or NPs on the destruction of polyacrylate fragments. Preliminary γ -irradiation (200–600 kGy) of Ni(II), Co(II), and Cu(II) polyacrylates and increase in the irradiation dose lead to a decrease in the initial decomposition temperatures [161].

The thermolysis of the Co(II), Ni(II) normal maleates, and Mn(II), Fe(II), Co(II), Ni(II) acid maleates proceeds in three stages [61]. The initial decomposition temperatures for the first and second stages decrease in the series of normal maleates $\text{Co}(\text{II}) \geq \text{Ni}(\text{II})$ and increase in the series of acid maleates $\text{Fe}(\text{II}) < \text{Co}(\text{II}) < \text{Ni}(\text{II}) \approx \text{Mn}(\text{II})$. The temperature of the beginning of the third stage decreases in the series of both the normal maleates $\text{Co}(\text{II}) > \text{Ni}(\text{II})$ and the acid maleates $\text{Mn}(\text{II}) > \text{Fe}(\text{II}) > \text{Co}(\text{II}) > \text{Ni}(\text{II})$. At the same time, the thermolysis of neutral ($[\text{Cu}(\text{H}_2\text{O})(\text{Mal})]$) and acidic ($[\text{Cu}(\text{H}_2\text{O})_4](\text{HMal})_2$) maleates can be divided into four stages: (1) dehydration, (2) polymerization, (3) isomerization of the Mal ion with the simultaneous reduction $\text{Cu}(\text{II}) \rightarrow \text{Cu}(\text{I})$, and (4) decarboxylation of copper(I) fumarate [60]. The third and fourth stages of thermolysis of these salts coincide. The residue after thermolysis of copper(II) maleates in the He stream is a composite consisting of aggregates ranging in size from 50 nm to several microns. Spherical conglomerates (50–200 nm) containing many spherical Cu particles (5–10 nm) are included in the organic polymer matrix of these aggregates.

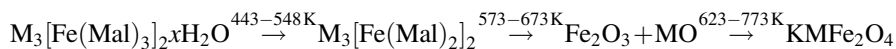
It is of interest to obtain bimetallic NPs containing solid solutions of transition metals with parameters (e.g., conductivity, catalytic activity, and magnetic properties), other than single-metal NPs. As an example, we note the thermolysis of

solid solutions in which one cation is replaced by another in the systems Co(II) hydrogen maleate–Ni(II) hydrogen maleate; Fe(II) hydrogen maleate–Co(II) hydrogen maleate; and Fe(II) hydrogen maleate–Ni(II) hydrogen maleate [162]. When heated, bimetallic NPs embedded in the polymeric matrix of composites obtained by thermolysis of solid solutions of hydrogen maleates undergo a second-order phase transition, which leads to the decomposition of solid metal solutions at the Curie temperature.

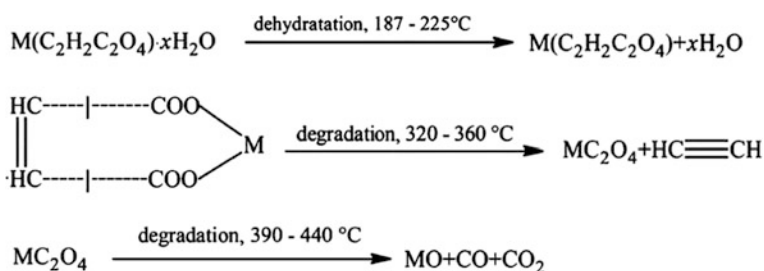
The thermolysis of $M(\text{Mal}/\text{Fum}) \cdot x\text{H}_2\text{O}$ ($M = \text{Mn}, \text{Co}, \text{Ni}, \text{Cu}, \text{Zn}$) has been studied in the static air atmosphere by non-isothermal methods (TGA, DTG, DTA) from ambient to 773 K [163, 164]. After dehydration, anhydrous maleate salts decompose to metal oxalate in a temperature range of 593–633 K, which is subjected to a sharp oxidative thermolysis to oxides at a higher temperature. It was found that the anhydrous fumarate salts are thermolyzed directly into the oxide phase. Comparison of TA shows that fumarates are thermally more stable than maleates.

Based on various TA studies, the following mechanism for the air decomposition of transition metal maleates can be proposed (Scheme 5.6).

In the study of the thermolysis of the ferrimaleates $M_3[\text{Fe}(\text{Mal})_3]_2 \cdot x\text{H}_2\text{O}$ ($M = \text{Mn}, \text{Co}, \text{Ni}, \text{Cu}$), the general characteristics of the decomposition process were established in a static air atmosphere at temperatures up to 873 K [109]. This is a multistep transformation, starting with the dehydration of ferrimaleates to ferrites; after dehydration, the Fe(III) precursor is converted to an intermediate Fe(II) derivative, $M_3[\text{Fe}(\text{Mal})_2]_2$; after this, the degradation of the monomer gives iron(III) oxide and a metal oxide. The formation of ferrite $M\text{Fe}_2\text{O}_4$ can be described by the following reactions:



In the case of non-isothermal decompositions of copper and cobalt itaconate complexes, thermolysis proceeds in three steps: dehydration, formation of the corresponding metal carbonate, and its decomposition to form a metal oxide [165].



Scheme 5.6 A scheme of thermolysis of metal maleates and fumarates in air

It is of interest to study the mechanism of local order near iron atoms during thermolysis of $[\text{Fe}_3\text{O}(\text{Mal})_6]\text{OH}\cdot 3\text{H}_2\text{O}$ as the initial stage of nucleation of NPs in metal–polymer systems using EXAFS spectroscopy [166]. The following processes associated with thermolysis were reported: dehydration with simultaneous rearrangement of the ligand environment, partial removal of maleic acid molecules, and thermal polymerization of the rearranged monomer, while maintaining the coordination of the trinuclear Fe_3O fragment with maleic ligands. The cluster of the metal carboxylate $[\text{Fe}_3\text{OR}_6]$ decomposes without metal–metal binding at the initial stage of decarboxylation, followed by the formation of Fe–O-containing phases. This process can be regarded as the nucleation of NPs in a metal–polymer system.

5.3.1 Dehydration

At low temperatures of thermolysis ($T_{\text{therm}} < 473$ K), dehydration of monomeric crystallohydrates takes place. According to the studies of TG, DTA, and DTG, dehydration of MCMs occurs at $T_{\text{therm}} = 353\text{--}487$ (FeAcr₃), 413–453 (CoAcr₂), 373–473 K (NiAcr₂), 393–433 K (CoMal), and 373–433 K (FeMal). A detailed study of the dehydration of CoAcr₂ under isothermal conditions at $T_{\text{therm}} = 303\text{--}433$ K indicates a reversible process [155]. This was also confirmed by IR spectroscopy. As a result of the dehydration, the absorption bands associated with the crystallization water modes $\nu(\text{O}\text{--}\text{H})$ 3000–3600 cm^{-1} , $\rho_{\omega}(\text{O}\text{--}\text{H}) + \nu(\text{Co}\text{--}\text{OH}_2)$ 880 cm^{-1} disappear. The intensity of the modes due to $\delta(\text{O}\text{--}\text{H}) + \nu(\text{C}=\text{C})$ 1655 cm^{-1} , $\rho_{\omega}(\text{CH}_2) + \delta(\text{Co}\text{--}\text{OH}_2)$ 690 cm^{-1} , $\delta(\text{CH}_2) + \delta(\text{Co}\text{--}\text{OH}_2)$ 595 cm^{-1} decreases simultaneously. In some cases, there are two areas of evaporation. For example, during dehydration of CoAcr₂ under completely isothermal conditions, evaporation at 303–348 K is limited by evaporation of dehydrated water, $P_{\text{H}_2\text{O}}(T_{\text{therm}}) = 1.7 \times 10^7 \exp[-9200/RT]$ kPa, and evaporation heat $\Delta H_{\text{st}}(\text{H}_2\text{O}) = 38.5$ kJ mol⁻¹ is close to the heat of evaporation of H₂O, $\Delta H_{\text{evap}}(\text{H}_2\text{O}) = 43.9$ kJ mol⁻¹ [155]. The evaporation at $T_{\text{therm}} > 348$ K is described by the dependence of $P_{\text{H}_2\text{O}}(T_{\text{therm}}) = 2.7 \cdot 10^4 \exp[-4800/RT]$ kPa and is limited directly by the dehydration of CoAcr₂, $\Delta H_{\text{evap}}(\text{H}_2\text{O}) = 20.1$ kJ mol⁻¹. A similar process of dehydration is observed in the case of thermolysis of CoMal (Fig. 5.15). Endoeffects at 400 and 433 K are associated with a two-step process of dehydration of CoMal and are accompanied by a weight loss of 15.2 wt% (calc. 17.23%).

Thermolysis of Cu(II) and Zn(II) [163] maleates and fumarates was studied by non-isothermal methods (TGA, DTG, DTA) in the temperature range 273–873 K. Dehydration of the complexes showed that the thermal stability of copper and zinc fumarates was higher than stability of the corresponding maleates, dehydrated copper fumarates and maleates were equivalent in stability, and zinc fumarate was more stable than zinc maleate.

The comparative analysis of the thermolysis of geometry isomers (*cis*- and *trans*-) was carried out for Zn(II) and Cu(II) [164] and Mn(II), Co(II), and Ni(II) [163] maleates and fumarates, respectively, to studying the influence of the ligand

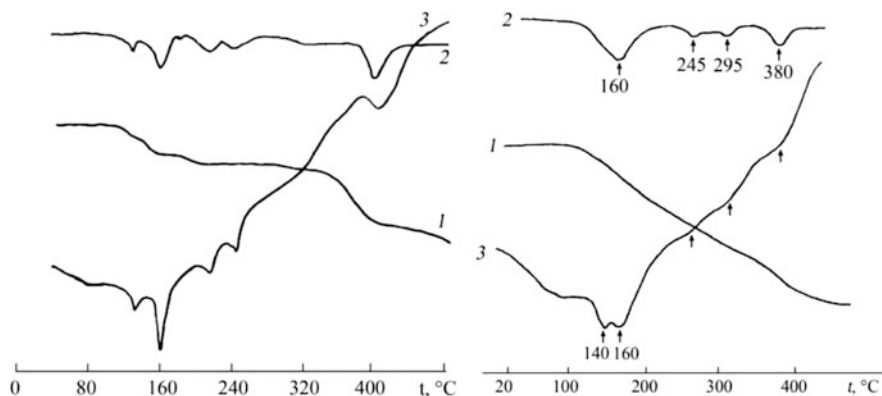


Fig. 5.15 TA curves of the thermolysis of CoMal (left) and FeMal (right): 1—TGA, 2—DTGA, 3—DTA [155]

structure on the thermal stability and the mechanism of thermolysis of the corresponding complexes. In the case of the nickel MCMs, dehydration begins at 403 K and ends at 498 K. The second stage involves a rapid oxidative decomposition (weight loss 69% at 663 K) to NiO. This indicates that the yield product occurs directly from nickel fumarate.

In the first stage of decomposition, Co(II) and Ni(II) normal maleates eliminate one crystal water molecule and the next two coordination water molecules, which are in good agreement with structural data [61]. In the first stage of the decomposition of Mn(II), Fe(II), Co(II), and Ni(II) acid maleates, the coordinated water removal proceeds in two stages, which correlates with the M–O(H₂O) distance in the coordination octahedron containing two water molecules in two different positions. Diffractograms of samples of both normal and acid maleates after the completion of the first stage show that the products obtained are amorphous. As a result of chemical analysis and IR spectroscopy, it was found that no complete removal of H₂O ($\nu(\text{OH}) = 3400 \text{ cm}^{-1}$) took place.

The main weight loss of CoADC (Fig. 5.16) observed in the TG profile was between 433 and 463 K [51]. Probably, the final weight loss, observed in the range of 588–673 K, can be associated with the loss of absorbed water molecules.

During dehydration in vacuum, the crystals of cobalt and zinc acetylenedicarboxylates (CoADC·2H₂O and ZnADC·2H₂O) [101] are stable only up to some minimum content of coordination water, at which there is a sharp release of gaseous products of thermolysis and the formation of reactive residues capable of initiating the solid-phase MCM polymerization. According to quantum chemical calculations (DFT), the dehydration energy of crystallohydrates CoADC·2H₂O and ZnADC·2H₂O is equal to 150–200 kJ mol⁻¹. Such a large amount can lead to mechanochemical activation of crystal decomposition and coordination structures of CoADC·2H₂O and ZnADC·2H₂O during their dehydration. The structural feature of cobalt and zinc acetylenedicarboxylates is important for understanding the

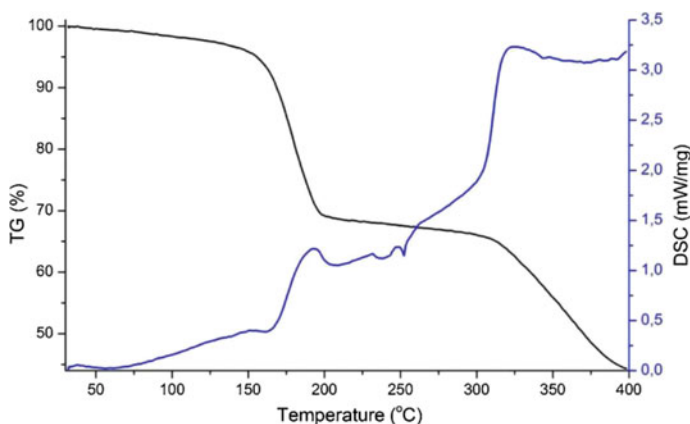


Fig. 5.16 DSC and TGA for CoADC (argon) [51]

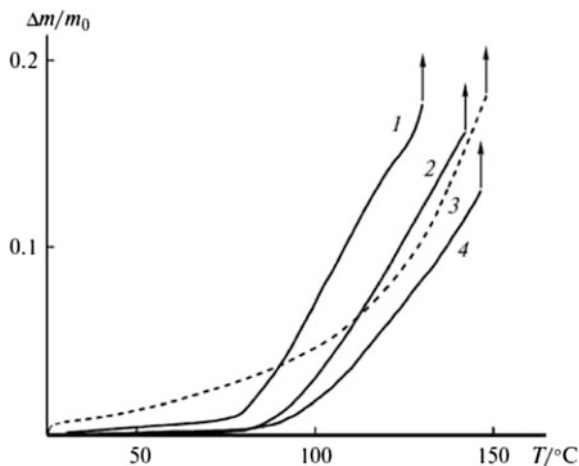
Table 5.1 Thermolysis rate constants (k) and the critical weight loss values $((\Delta m/m_0)_{cr})$ for crystalline hydrates of zinc and cobalt dicarboxylates

Sample	T/K	$k \times 10^4/s^{-1}$	$(\Delta m/m_0)_{cr}$
ZnADC·2H ₂ O	366	1.2	>0.185
	375	2.2	>0.205
	386	2.8	>0.180
	395	5.7	>0.181
	413	7.5	>0.181
CoADC·2H ₂ O	366	3.3	>0.160
	386	3.6	–
	405	–	>0.216

mechanism of solid-phase polymerization. This is the presence of critical conditions for the existence. During dehydration, the test compounds retain stable only up to a certain critical moment corresponding to the minimum content of coordinated water, after which the acetylenedicarboxylate anion undergoes thermolysis accompanied by the accumulation of CO₂ in the solid phase. After reaching the critical (for this temperature) concentration of CO₂, there is a strong release of gaseous products of thermolysis. The kinetic dependences of the weight loss of the sample in the temperature range 366–413 K are satisfactorily described by the first-order reaction equation. The reaction constants derived from this equation are listed in Table 5.1. The temperature dependence of the rate constant of thermolysis for ZnADC·2H₂O obeys the Arrhenius equation. The logarithm of the preexponential factor and the activation energy calculated from this dependence are $2.7 \pm 0.3 \text{ s}^{-1}$ and $51 \pm 7 \text{ kJ mol}^{-1}$, respectively. Low values of activation parameters show that weight loss in this temperature range is most likely related to physical processes, such as dehydration and diffusion.

In addition, in the studies of thermal transformations of ZnADC·2H₂O and CoADC·2H₂O in vacuum (Fig. 5.17), a so-called boiling layer is observed,

Fig. 5.17 Temperature dependences of the relative weight loss for ZnADC·2H₂O (1, 2, and 4) and CoADC·2H₂O (3) in vacuo. The temperature rise rate is 0.8 (1), 1.6 (2), and 2.4 deg min⁻¹ (3, 4) [101]

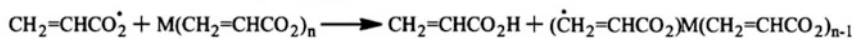
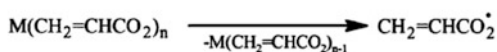


accompanied by a significant entrainment of solid particles from the reactor. This strong evolution of gaseous products upon the destruction of crystalline hydrates was observed irrespective of the conditions used (isothermal, non-isothermal) and the rate of temperature growth. The energetic release of the gaseous products of thermolysis of crystalline hydrates, leading to the boiling of a powdered sample, is not associated with a certain characteristic temperature and occurs even at low heating rates. Thus, at a heating rate of 0.8 deg min⁻¹, this temperature for ZnADC·2H₂O is 403 K and at a heating rate of 1.6 deg min⁻¹, 415 K. At a heating rate of 2.4 deg min⁻¹, the boiling of the zinc salt occurs at 421 K and of the cobalt salt, at 422 K.

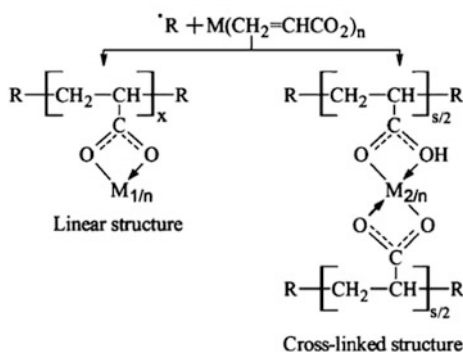
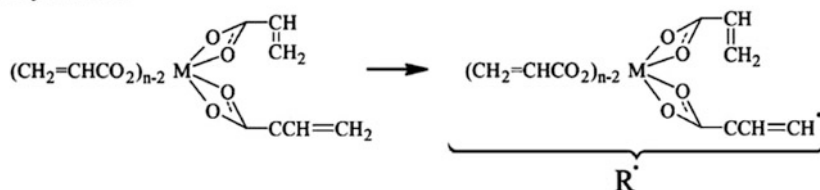
5.3.2 Polymerization

Analysis of chemical transformation pathways shows that the state of a part of Acr ligands can change as a result of MCM dehydration in the temperature range 333–403 K, which causes non-equivalence of the M–O bonds [111, 160]. This leads to the rupture of the weak M–O bond and the formation of the radical $\text{CH}_2=\text{CHCOO}\cdot$, which initiates the formation of polymers with a linear structure (Scheme 5.7). According to the adopted scheme [167], the polymerization of bifunctional acrylic monomers gives a comb-shaped linear polymer, which usually has a conventional structure in the first stage and 3D network in the subsequent stage. It should be noted that changes can be tracked due to the formation of 3D polymer network structure in the system when the chain growth reaction involves the C=C bonds in the side chains of macroradicals. At this stage, the chain grows with a strong steric hindrance and a high level of internal stresses. As was shown earlier [168],

I. Initiation



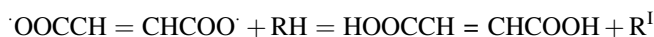
II. Polymerization



Scheme 5.7 Scheme of second step of thermolysis of MCMs

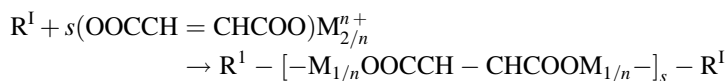
low-frequency IR spectra of polyacrylate in the regions of $-\text{O}-\text{M}-\text{O}-$ vibrations show a broad band at 340 cm^{-1} instead of two narrowband characteristic of MCM.

The mechanism of thermolysis of dicarboxylates is analogous to that of unsaturated monocarboxylic acid salts [111]. It can be assumed that with an increase in the level of thermal vibrations in the lattice of the monomer, the rupture of the weakest $\text{M}-\text{O}$ bonds is most likely. As a result, the biradicals $\cdot\text{OOCCH}=\text{CHCOO}\cdot$ are formed, for example, from maleates. The formed radicals react with the metal-containing maleate fragments to give corresponding acids and H-depleted radical R^I of the M_1 groups according to the following scheme:



Here, $\text{RH} = (\text{CHCOO})_2\text{M}_{2/n}^{n+}$, $\text{RI} = (\text{CCOO})_2\text{M}_{1/n}^{n+}$.

The resulting R^I initiates polymerization to produce linear or network polymers.



Increasing the temperature to $T_{\text{therm}} = 473\text{--}573$ K leads to solid-state polymerization of the dehydrated monomer. Transformation of MCMs under the conditions of TA and SGA showed that in this temperature range there is a small evolution of the gas, as well as a small loss of sample weight ($\ll 10$ wt%). In the case of metal acrylates and maleates, the main contribution is made by CO_2 and vapors of HAc and HMal condensed on the walls of the reactor at room temperature, respectively. This is confirmed by the results of the IR and MS study. According to TA data, typical polymerization temperature ranges (T_{polym}) are as follows: ~ 543 K (CoAcr_2), ~ 563 K (NiAcr_2), ~ 510 K (CuAcr_2), ~ 518 K (FeAcr_3), $488\text{--}518$ K (CoMal), ~ 518 K (FeMal). During the polymerization, the IR absorption spectrum of the dehydrated monomer changes due to a decrease in the absorption intensity of the stretching band of the $\text{C}=\text{C}$ bond and the absorption frequency of stretching of $\text{C}=\text{O}$ bond valence modes resulting in the appearance of a broadened absorption band in the $1540\text{--}1560$ cm^{-1} region (Tables 5.2, 5.3, and 5.4). It is interesting that in the thermolysis of NiAcr_2 ($T_{\text{exp}} = 593$ K) at low degrees of gassing (warm-up time) a regularly band (RB) appears with $\Psi = 1.27$ ($\delta_{\text{C-H}} 830$ cm^{-1} , $\nu_{\text{C-H}} 2930$ cm^{-1}) which disappears with increasing conversion and is not observed at $T_{\text{exp}} = 573$ K. The appearance of RB indicates an ongoing polymerization process that precedes the evolution of the base gas.

According to the results of the TA analysis, when FeMal is thermolyzed, the loss of weight Δm of the sample with the thermal effect of DTA with a maximum at 433 and 518 K is 31.2 and 8.7 wt%, respectively. The first endoeffect (strong enough) is associated with the dehydration process (5.2% for the loss of three water molecules) and, apparently, with the partial elimination of three molecules of maleic acid (36.8% calc.) (Fig. 5.18a). EXAFS study of solid of the product in the initial stage of thermolysis ($T_{\text{term}} = 5$ min at 643 K) also indicates a rearrangement of the FeMal ligand environment during its dehydration and polymerization. As a result, the Fe atoms coordinate the O atoms of both carboxylate groups of the maleate anion (Fig. 5.18b). The second weak endoeffect, accompanied by the loss of weight of the sample, is most likely due to the polymerization of the dehydrated monomer. Finally, Δm in this area is about 40%.

5.3.3 Decarboxylation

At $T_{\text{therm}} > 523$ K (for CuAcr_2 $T_{\text{therm}} > 453$ K), the thermopolymerized samples undergo an intensive evolution of the gas (Scheme 5.8). The kinetics of the process under isothermal conditions and in a SGA was studied [149, 150] for CuAcr_2 ($\langle T_{\text{therm}} \rangle = 363\text{--}513$ K), CoAcr_2 (623–663 K), NiAcr_2 (573–633 K), FeAcr_3 (473–643 K), FeCoAcr (613–633 K), Fe_2CoAcr (613–633 K), Fe_2NiAcr (603–643 K), CoMal (613–643 K), FeMal (573–643 K).

The rate of gas evolution $W = d\eta/dt$ decreases monotonically with increasing degree of conversion, $\eta = \Delta\alpha_{\Sigma, f} / \Delta\alpha_{\Sigma, f}$, where $\Delta\alpha_{\Sigma, t} = \alpha_{\Sigma, t} - \alpha_{\Sigma, 0}$, $\Delta\alpha_{\Sigma, f} = \alpha_{\Sigma, f} - \alpha_{\Sigma, 0}$, $\alpha_{\Sigma, f}$, $\alpha_{\Sigma, t}$, and $\alpha_{\Sigma, 0}$, respectively, the final, current, and initial

Table 5.2 Values of vibration frequencies in the IR spectra of CuAcAc₂, its polymer, and thermolysis products [149]

CuAcAc ₂		Polyacrylate Cu(II)		CuAcAc ₂ thermolysis product	
ν , cm ⁻¹	I_{rel}	Assignment	ν , cm ⁻¹	I_{rel}	Assignment
3100	0.2	ν_{as} C-H (=CH ₂)			
3045	0.10	ν_{as} C-H (=CH-)			
3030sh	0.02				
2950	0.03	ν_s C-H (=CH ₂)	2975	0.06	ν_s C-H(-CH ₂ -)
2930	0.06	ν_s C-H (=CH-)	2925	0.10	ν_s C-H(-CH ₂ -)
2900sh	0.02		2915	0.12	
2850	0.03		2850	0.05	ν (=C-H)
2790	0.02				
2730	0.02				
1945	0.02				
1645	0.49	ν C-C (C=C)	1640	0.08	ν C-C (C=C) _{conc}
1580	1.00	ν_{as} C-O (COO)	1560	1.00	ν_{as} C-O (COO)
1560sh	0.44		1550sh	0.51	
1515	0.33	δ C-H (-CHCH ₂)	1515	0.32	δ C-H (-CHCH ₂)
1440	0.82		1415	0.44	
1370	0.46	ν_s C-O (COO)	1345	0.26	ν_s C-O (COO)
1275	0.34	ρ_t (CH ₂)	1275	0.14	ρ_t (CH ₂)
			1240	0.19	
1065	0.27	ν C-C (=CH-C)	1075	0.19	ν C-C (=CH-C)
995	0.41	π (-CHCH ₂)	980	0.13	π (CH ₂)
975	0.46		940	0.19	
915	0.09	π (-CHCH ₂)			
830	0.50	ρ_w (CH ₂)	815	0.20	ρ_w (CH ₂)
695	0.48	ρ_t (CH ₂)	678	0.20	ρ_t (CH ₂)

Note $I_{rel} = D_\nu/D_\nu^{max}$ is relative intensity; D_ν is absorption at ν frequency. Vibrations: ν stretching, δ bending, ρ_t twisting, ρ_w wagging, ρ_t rocking, π out-of-plane

Table 5.3 Values of vibration frequencies in the IR spectra of Fe₂CoAcr and thermolysis products [111]

Co-crystallite Fe ₂ CoAcr		Fe ₂ CoAcr thermolysis products							
ν (cm ⁻¹)	I_{rel}	Assignment	$\Delta m = 25.1\text{--}27.8\%$		$\Delta m = 37.3\%$		$\Delta m = 42.0\%$		Assignment
			ν (cm ⁻¹)	I_{rel}	ν (cm ⁻¹)	I_{rel}	ν (cm ⁻¹)	I_{rel}	
3000– 3600br		$\nu(\text{OH})$ (H ₂ O)							
3045		$\nu_{as}(\text{CH})$							
2960		$\nu_s(\text{CH})$	2930						
1630	0.74	$\nu(\text{C}=\text{C})$, $\delta(\text{OH})(\text{H}_2\text{O})$	1640	0.35	1680	0.46	1685	0.38	$\nu(\text{CH})$ $\nu(\text{C}=\text{C})$
1575	1.00	$\nu_{as}(\text{COO})$ (Fe cluster)	1555	1.00	1555	1.00	1565	1.00	$\nu_{as}(\text{COO})$ (Fe cluster)
1540	0.80	$\nu_{as}(\text{COO})$ (Co)	1540	0.99	1540	0.99	1550	1.07	$\nu_{as}(\text{COO})$ (Co)
1525	0.77	$\nu_{as}(\text{COO})$ (Fe cluster)	1520	0.92	1520	0.98	1520	0.99	$\nu_{as}(\text{COO})$ (Fe cluster)
1505	0.485	$\nu_{as}(\text{COO})$ (Co)	1505sh	0.715	1498	0.89			$\nu_{as}(\text{COO})$ (Co)
1490sh	0.39	$\delta(\text{CH})$	1490	0.6					$\delta(\text{CH})$
1435	0.92	$\nu_s(\text{COO})$ (Fe cluster)	1435	0.85	1440	1.02	1420	1.23	$\nu_s(\text{COO})$ (Fe cluster), $\nu(\text{OH}_2)$
1420	0.92	$\nu_s(\text{COO})$ (Co)	1415	0.85	1408	1.07			$\nu(\text{OH}_2)$ (-CH ₂ -CHR-) $\nu_s(\text{COO})$ (Co), $\delta(\text{OH}_2)$
1360	0.82	$\nu_s(\text{COO})$ (Fe cluster)	1400	0.97	1395	1.10	1400	1.20	$\delta(\text{OH}_2)$ (H ₂ C-CR-) $\nu_s(\text{COO})$ (Fe cluster), $\delta(\text{OH}_2)$ (CH ₂ =CR-)

(continued)

Table 5.3 (continued)

Co-crystallizate Fe ₂ CoAc		Fe ₂ CoAc thermolysis products						
ν (cm ⁻¹)	I_{rel}	Assignment	$\Delta m = 25.1-27.8\%$		$\Delta m = 37.3\%$		$\Delta m = 42.0\%$	
			ν (cm ⁻¹)	I_{rel}	ν (cm ⁻¹)	I_{rel}	ν (cm ⁻¹)	I_{rel}
1350	0.71		1315	0.57				$\nu_s(\text{COO}) (\text{Co}),$ $\delta(\text{OH})$
1270	0.44	$\rho_t(\text{CH}_2)$	1280sh	0.51	1270sh	0.665	1265	$\rho_t(\text{CH}_2)$ (-CH ₂ -CHR-)
			1185	0.35	1160		1150	$\rho_t(\text{CH}_2)$ (CH ₂ -CH=CH-) trans $\nu(\text{C}-\text{C})$
								(=CH-CHR-)
1120br	0.10							
1068	0.32	$\nu(\text{C}-\text{C})$						
990	0.38	$\pi(\text{CH})$ (-CH=CH ₂)						
965	0.31	$\pi(\text{CH})$ (-CH=CH ₂)						
910	0.07	$\rho(\text{OH}) (\text{H}_2\text{O}),$ $\nu(\text{M}-\text{OH}_2)$	855	0.08	860	0.15	875	$\delta(\text{CH})$ (-CH=CHR)
830	0.61	$\rho_w(\text{CH}_2)$	835	0.09	830	0.10	830	$\rho_w(\text{CH})$ (-CH ₂ -CHR-)
728	0.12		775	0.07	755	0.11	750	
673	0.50	$\rho_t(\text{CH}_2),$ $\delta(\text{M}-\text{OH}_2)$	645br	0.03				$\rho_t(\text{CH})$ (-CH ₂ -CR=CH-) cis, $\delta(\text{CH}_2),$ $\rho_w(\text{CH})$ (-CH=CHR)
598	0.11	$\delta(\text{CH}_2),$ $\delta(\text{M}-\text{OH}_2)$	592	0.02				
545	0.07	$\delta(\text{CH}_2),$ $\delta(\text{M}-\text{OH}_2)$						

Table 5.4 Values of vibration frequencies in the IR spectra of CoAcCr₂, its polymer, and thermolysis products [150]

CoAcCr ₂ ·H ₂ O		Polyacrylate Co(II)		CoAcCr ₂ dehydration products		CoAcCr ₂ thermolysis products		
ν , cm ⁻¹	I_{rel}	ν , cm ⁻¹	I_{rel}	Assignment	I_{rel}	Assignment	I_{rel}	Assignment
3000–3600br	0.24			(3400 cm ⁻¹) νO–H	0.02	(3400 cm ⁻¹) νO–H		
3100	0.03			ν _{as} C–H (=CH ₂)	0.04	ν _{as} C–H (=CH ₂)		
3050	0.03			ν _{as} C–H (=CH–)	0.03	ν _{as} C–H (=CH–)		
3025	0.03			ν _s C–H (=CH ₂)				
2985	0.03							
2925	0.03	2930	0.15	ν _s C–H–CH ₂ –)	0.03	ν _s C–H (=CH ₂)	2940	0.26
2850	0.02	2860	0.06	ν _s C–H(=CH–)	0.03	ν _s C–H(=CH–)	2860	0.175
1975	0.02	1925	0.04	Overtone			2730	0.07
1655	0.63	1655	0.92	ν(C=C) _{conic}	0.50	ν(C=C)	1675sh	0.16
1595	1.00	1595	0.92	ν _{as} C–O (COO)	0.90	ν _{as} C–O (COO)	1565	1.00
1585	1.00	1575	1.00				1535 _{sh}	0.78
		1535sh	0.66					
1450	1.00	1450	0.92	δC–H (–CHCH ₂)	1.00	δC–H (–CHCH ₂)	1435	0.53
		1435sh	0.79				1415	0.63
1370	0.68	1375	0.68	ν _s C–O (COO)	0.675	ν _s C–O (COO)	1385	0.51
1285	0.44	1285	0.49	ρ _t (CH ₂)	0.57	ρ _t (CH ₂)	1260	0.39
1070	0.15	1060	0.14	ν C–C (=CH–C) _{conic}	0.10	ν C–C (=CH–C)	1235	0.375
995	0.31	995	0.21	π(–CHCH ₂)	0.31	π(–CHCH ₂)	1130	0.06
960	0.28	975	0.17		0.28		1080	0.05
880	0.05			ρOH (H ₂ O), ν(M–OH ₂)			1010	0.14
840	0.42	835	0.26	ρ _w (CH ₂)	0.43	ρ _w (CH ₂)	985	0.125
685	0.24	685	0.06	ρ _t (CH ₂), δ(M–OH ₂)	0.195	ρ _t (CH ₂)		
590	0.06			δ(CH ₂), δ(M–OH ₂)	0.032	δ(CH ₂)		

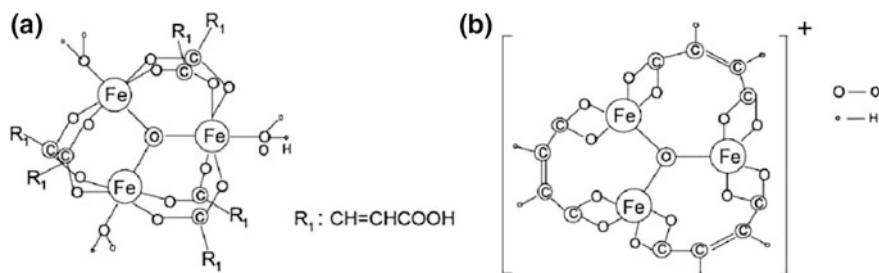
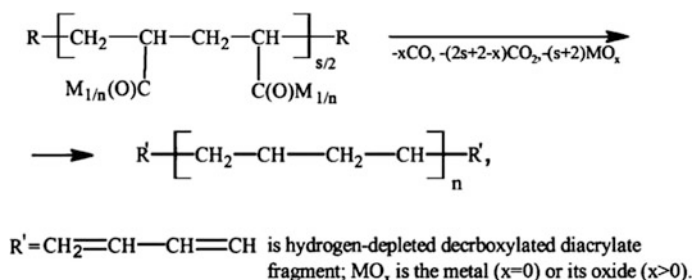


Fig. 5.18 Structure of FeMal (a) and product of its thermolysis (b) at initial stage of thermolysis



Scheme 5.8 Scheme of decarboxylation process

number of moles of gaseous products released per mole of the starting sample at room temperature. The kinetics of the evolution of the gas $\eta(\tau)$ in the general case (up $\eta \leq 0.95$) is satisfactorily approximated by the equation for the two parallel reactions:

$$\eta(\tau) = \eta_{1f} [1 - \exp(-k_1 \tau)] + (1 - \eta_{1f}) [1 - \exp(-k_2 \tau)] \quad (5.1)$$

where $\tau = t - t_0$ (t_0 is the time of heating), $\eta_{1f} = \eta(\tau)|_{k_2 t \rightarrow 0, k_1 t \rightarrow \infty}$, and k_1, k_2 are the effective rate constants. Parameters $k_1, k_2, \eta_{1f}, \Delta\alpha_{\Sigma, f}$ depend on the temperature of the thermolysis (T_{therm}):

$$\eta_{1f}, \Delta\alpha_{\Sigma, f} = A \exp[-E_{a, \text{eff}} / (RT_{\text{therm}})] \quad (5.2)$$

$$k_{\text{eff}} = k_{0, \text{eff}} \exp[-E_{a, \text{eff}} / (RT_{\text{therm}})] \quad (5.3)$$

where A and $k_{0, \text{eff}}$ are preexponential factors and $E_{a, \text{eff}}$ is the effective activation energy.

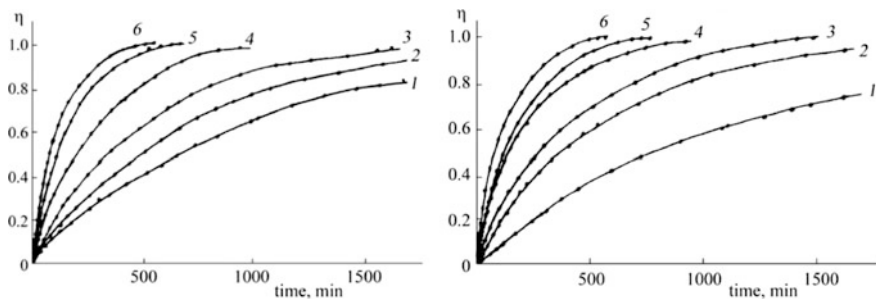


Fig. 5.19 Kinetics of accumulation of gaseous products during thermolysis of cocrystallizates FeCoAcr (left) and Fe₂CoAcr (right). Curves are calculation of Eq. (5.1); points are the experimental values: $T_{\text{exp}} = 613$ (1), 623 (2), 633 (3), 643 (4), 653 (5), 663 K (6); $m_0/V = 1.80 (\pm 0.05), 10^{-3}$ [11, 149, 150]

The initial rate of gas evolution $W_{\tau=0} = W_0$ is

$$W_0 = \eta_{1f}k_1 + (1 - \eta_{1f})k_2 \quad (5.4)$$

Equations (5.1) and (5.4) describe the kinetics of the gas evolution of NiAcr₂, FeCoAcr, Fe₂CoAcr, Fe₂NiAcr, and FeMal (Fig. 5.19) [11, 149, 150].

When $k_2 \approx 0$, $\eta_{1f} \rightarrow 1$

$$\eta(\tau) \approx 1 - \exp(-k_1\tau) \quad (5.5)$$

$$W_0 \approx k_1 \quad (5.6)$$

Equations (5.5) and (5.6) describe the kinetics of the gas evolution during thermolysis of CoAcr₂ and CoMal (Fig. 5.20).

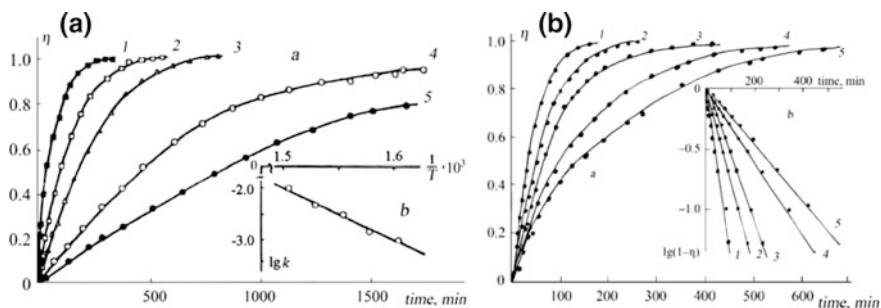
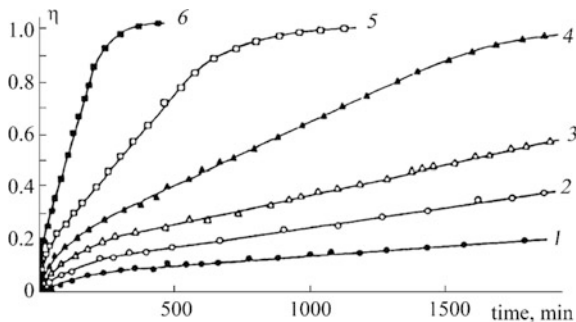


Fig. 5.20 (left) Kinetics of the thermolysis of CoAcr: **a** dependence $\eta(t)$ at various temperatures: 663 (1), 653 (2), 643 (3), 633 (4), 623 K (5); **b** the dependence $\lg k$ versus $1/T$; (right) thermolysis of CoMal in SGA: **a** gas evolution kinetics $\eta(t)$; **b** semilogarithmic anamorphosis [$\lg(1-\eta)$, t]. 1—653, 2—643, 3—633, 4—623, 5—613 K

Fig. 5.21 Dependence $\eta(t)$ during the thermolysis of CuAcCr_2 : 1—463, 2—473, 3—483, 4—493, 5—503, 6—513 K; $m_0/v = 2.45 (\pm 0.1) \times 10^{-3}$



In the case where $\tau \ll 1/k_2$, $k_1 \gg k_2$,

$$\eta(\tau) \approx \eta_{1f}[1 - \exp(-k_1\tau)] + (1 - \eta_{1f})\eta_2\tau \quad (5.7)$$

$$W_0 \approx \eta_{1f}k_1 \quad (5.8)$$

Dependence of η on time (t) during thermolysis of CuAcCr_2 is satisfactorily described by Eq. (5.7) (Fig. 5.21).

Kinetic parameters of gas evolution during MCM thermolysis are presented in Table 5.5.

It should be noted that when the thermopolymerized FeAcCr_3 is heated, two regions of gas evolution are observed (Fig. 5.22) [152]: a low-temperature region ($\langle T_{\text{therm}} \rangle = 473\text{--}573$ K) and a high-temperature region ($\langle T_{\text{therm}} \rangle = 603\text{--}643$ K). Their gas evolution rate is well approximated by Eqs. (5.5 and 5.6), but with different values of k and $\Delta\alpha_{\Sigma, f}$ (see Table 5.5). It is possible that the difference in the kinetic parameters of FeAcCr_3 thermolysis in the low- and high-temperature regions or in the case of the difference of FeCoAcCr , Fe_2CoAcCr , Fe_2NiAcCr at the η_{1f} level at constant values of other kinetic parameters ($\Delta\alpha_{\Sigma, f}$, k_1 , k_2) is due to the presence of two parallel processes of gas evolution.

Using the values of W_0 , the reactivity of metal acrylates in thermolysis can be arranged as follows: $\text{Cu} \geq \text{Fe} > \text{Co} > \text{Ni}$. The values of effective activation energies of the initial gas evolution rate under SGA conditions for CuAcCr_2 ($E_{a, \text{eff}} = 202.7 \text{ kJ mol}^{-1}$), NiAcCr_2 ($E_{a, \text{eff}} = 246.6 \text{ kJ mol}^{-1}$) shown in Table 5.5 are close to the calculated values of $E_{a, \text{eff}}$ for thermolysis in TA regime [10]: 211.1 and 244.1 kJ mol^{-1} . At the same time, $E_{a, \text{eff}} = 238.3 \text{ kJ mol}^{-1}$ of the initial rate for CoAcCr_2 thermolysis in SGA regime is higher than for the corresponding value $E_{a, \text{eff}} = 206.1 \text{ kJ mol}^{-1}$ under TA conditions. Attention is drawn to the difference in the rate constants of gas evolution from cobalt acrylate and maleate thermolysis. The values of the FeMal activation parameters are close to those for FeAcCr_3 , FeCoAcCr , Fe_2CoAcCr , and Fe_2NiAcCr in the same region of T_{therm} .

Table 5.5 Kinetic parameters of gas evolution during thermolysis of metal acrylates and maleates [11, 149, 150, 169]

Sample	$\eta_{1f}, \Delta\alpha_{\Sigma, f} =$ $A \exp[-E_{a, \text{eff}}/(RT_{\text{therm}})]$	A		$E_{a, \text{eff}},$ kJ mol ⁻¹	k	$k_{0, \text{eff}} = k_{0, \text{eff}} \exp$ $[-E_{a, \text{eff}}/(RT_{\text{therm}})]$	$W_0 = k_{0, \text{eff}} \exp$ $[-E_{a, \text{eff}}/(RT_{\text{therm}})]$
		$\eta_{1f},$ $\Delta\alpha_{\Sigma, f}$	$\eta_{1f},$ $\Delta\alpha_{\Sigma, f}$				
CuAct ₂	$\eta_{1f},$ $\Delta\alpha_{\Sigma, f}$	1.8×10^4	48.1	k ₁	9.5×10^{11}	9.5×10^{11}	202.7
	$\eta_{1f},$ $\Delta\alpha_{\Sigma, f}$	3.6	12.5	k ₂	9.2×10^{11}	163.0	202.7
CoAct ₂	$\eta_{1f},$ $\Delta\alpha_{\Sigma, f}$	1.0	0	k ₁	3.0×10^{14}	238.3	238.3
	$\eta_{1f},$ $\Delta\alpha_{\Sigma, f}$	1.55	0	k ₂	0	0	238.3
FeAct ₃ (473–573 K) (573–643 K)	$\eta_{1f},$ $\Delta\alpha_{\Sigma, f}$	1.0	0	k ₁	4.2×10^{21}	246.5	246.5
	$\eta_{1f},$ $\Delta\alpha_{\Sigma, f}$	1.6×10^2	25.5	k ₂	0	0	127.5
	$\eta_{1f},$ $\Delta\alpha_{\Sigma, f}$	1.0	0	k ₁	1.3×10^6	127.5	127.5
	$\eta_{1f},$ $\Delta\alpha_{\Sigma, f}$	1.7×10^2	26.3	k ₂	0	0	127.5
NiAct ₂	$\eta_{1f},$ $\Delta\alpha_{\Sigma, f} < 593 \text{ K}$	2.6	4.6	k ₁	1.7×10^{17}	242.4	247.0
	$\eta_{1f},$ $\Delta\alpha_{\Sigma, f} > 633 \text{ K}$	1.4×10^{11}	125.4	k ₂	7.5×10^8	156.7	247.0
FeCoAct	$\eta_{1f},$ $\Delta\alpha_{\Sigma, f}$	0.45 (663 K)–0.65 (613 K)	10.5	k ₁	2.3×10^{12}	207.0	207.0
	$\eta_{1f},$ $\Delta\alpha_{\Sigma, f}$	5.25×10^2	31.3	k ₂	6.0×10^6	138.0	207.0
Fe ₂ CoAct	$\eta_{1f},$ $\Delta\alpha_{\Sigma, f}$	0.35 (663 K)–0.50 (613 K)	25.1	k ₁	2.6×10^{12}	205.0	205.0
	$\eta_{1f},$ $\Delta\alpha_{\Sigma, f}$	1.5×10^2	75.0	k ₂	6.6×10^5	125.5	205.0
Fe ₂ NiAct	$\eta_{1f},$ $\Delta\alpha_{\Sigma, f}$	4.4×10^7	25.5	k ₁	6.1×10^6	129.5	205.0
	$\eta_{1f},$ $\Delta\alpha_{\Sigma, f}$	6.5×10^2	75.0	k ₂	0.6×10^2	79.4	205.0
CoMal	$\eta_{1f},$ $\Delta\alpha_{\Sigma, f}$	1.0	0	k ₁	1.1×10^6	125.4	125.4
	$\eta_{1f},$ $\Delta\alpha_{\Sigma, f}$	1.3×10^2	23.4	k ₂	0	0	125.4
FeMal	$\eta_{1f},$ $\Delta\alpha_{\Sigma, f} = 4.78 (573 \text{ K})\text{--}7.40 (643 \text{ K})$	0.59×10^2	23.4	k ₁	3.3×10^7	133.8	157.2
	$\eta_{1f},$ $\Delta\alpha_{\Sigma, f}$	7.40 (643 K)	110.8	k ₂	1.0×10^7	110.8	157.2

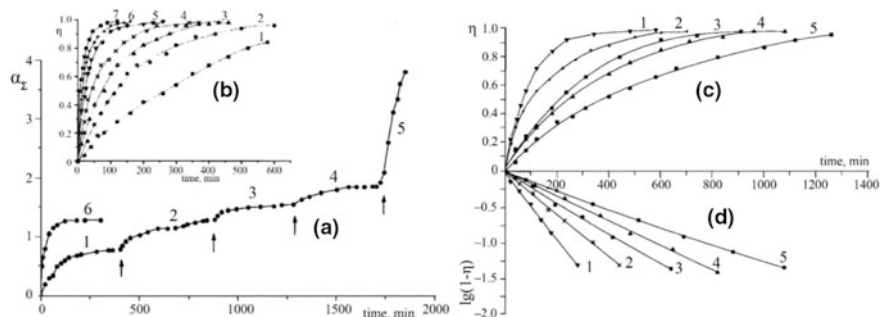
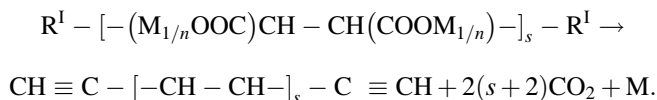


Fig. 5.22 **a** Gas evolution kinetics during FeAcr_3 thermolysis at T_{exp} : 1—488, 2—523, 3—548, 4—573, 5—623, 6—513 K. The arrow shows the moment of temperature increase. **b** Dependence $\eta(T)$ versus T_{exp} : 1—473, 2—478, 3—483, 4—488, 5—493, 6—503, 7—513 K ($m_0/v = 6.7 \times 10^{-3} \text{ g cm}^{-3}$). **c** The dependence $\eta(t)$ versus T_{exp} : 1—643, 2—633, 3—623, 4—613, 5—603 K. **d** Semilogarithmic anamorphosis of the dependence $\eta(t)$ [152]

As the temperature rises, the metal-containing fragments of the formed polymers decompose to produce the metal (or its oxide) and CO_2 .



Polymers obtained as a result of the decarboxylation reaction can be additionally thermopolymerized to form a network with conjugated multiple bonds.

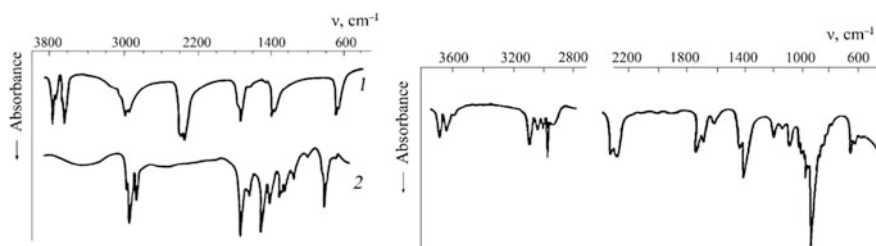
5.4 The Composition of Gaseous and Solid Products of Conjugated Thermolysis

5.4.1 Gaseous and Condensed Products

The main gaseous product of the conversion of the metal acrylates and maleates as well as their cocrystallizates is CO_2 . This confirmed the data of IR spectroscopy and MS. CO (IR, MS), H_2 (MS), condensed at T_{room} H_2O vapor (IR, MS), as well as HAcr (IR, MS) and H_2Mal (IR, MS) ligands, which are thermolysis products of the corresponding MCMs, are evolved in much less amount. Evolution of the main quantity of vapors of the condensed product is observed in the early stages of the evolution of the gas (during the warm-up of the sample $\alpha_{\Sigma,0}$) and is associated with dehydration and solid-state polymerization processes, which are the previous main evolution of the gas. This is indicated by comparing the amount of gaseous products released and the weight loss of the sample. In addition to these gaseous products, CH_4 (IR, MS) was detected in the case of CoAcr_2 (trace amount) and

Table 5.6 Composition of the gaseous and condensable thermolysis products of MCMs [48, 149, 150, 153, 156]

MCM	Products (% o.b.)						
	Condensable at 88 K				Non-condensable at 88 K		
	CO ₂	C ₂ H ₄	Vapor HAcr (H ₂ Mal)	Vapor H ₂ O	H ₂	CO	CH ₄
CoAcr ₂	>90	–	+	+	56.8	34.0	9.2
CuAcr ₂	>90	5–6	+	+	19.4	77.6	3
NiAcr ₂	79		+	+	0.5	~0.5	18.5 from α^Σ
FeAcr ₃	90–93	–	+	2.3	2.7 from α^Σ	–	–
CoMal	90	–	+	+	2–2.5 from α^Σ	2–2.5 from α^Σ	–
FeMal	90	–	+	+	Trace	≤ 10 from α^Σ CO ₂	

**Fig. 5.23** (left) IR absorption spectra of the gaseous products (1) and the product condensed on the walls of the reaction vessel (2) during the thermolysis of CoAcr₂; (right) the IR absorption spectra of the gaseous products of thermolysis of CuAcr₂, non-condensing at 88 K [149]

NiAcr₂ (commensurate with the amount of CO₂) (Table 5.6). C₂H₄ (IR, MS) is formed in the CuAcr₂ conversion products in measurable quantities.

In the IR spectra of gaseous products that condense at 88 K (Fig. 5.23, left), there is a system of characteristic absorption bands in the 3600–3700, 2320–2340, 625–670 cm⁻¹ regions associated with CO₂ oscillations. Absorptions at frequencies of 2990, 2930, 1750sh, 1725, 1630, 1370, 1350 cm⁻¹ with respect to the oscillations of $\nu(\text{C-H})$, $\nu(\text{C=O})$, $\nu(\text{C=C})$, $\delta(\text{C-H})$ are due to the presence of vapor of HAcr. In the case of CuAcr₂, there are also absorption bands of C₂H₄ ($\nu(\text{CH})$ 3106, 3020, 3000, 2970 cm⁻¹ in similar IR spectra; $\nu(\text{C=C})$ 1625 cm⁻¹; $\delta_{\text{as}}(\text{CH}_2)$ 1445 cm⁻¹; $\delta_{\text{s}}(\text{CH}_2)$ 1380 cm⁻¹; $\rho_{\text{w}}(\text{CH}_2)$ 950 cm⁻¹). In the IR spectra of gaseous products that do not condense at 88 K, in the region of 2140 and 2100 cm⁻¹ there are absorption bands associated with CO oscillations (Fig. 5.23, right) [149].

The level of the general evolution of gas at the end of thermolysis (α_Σ , τ) is specific for each compound and increases with T_{therm} (see Table 5.6). At a constant

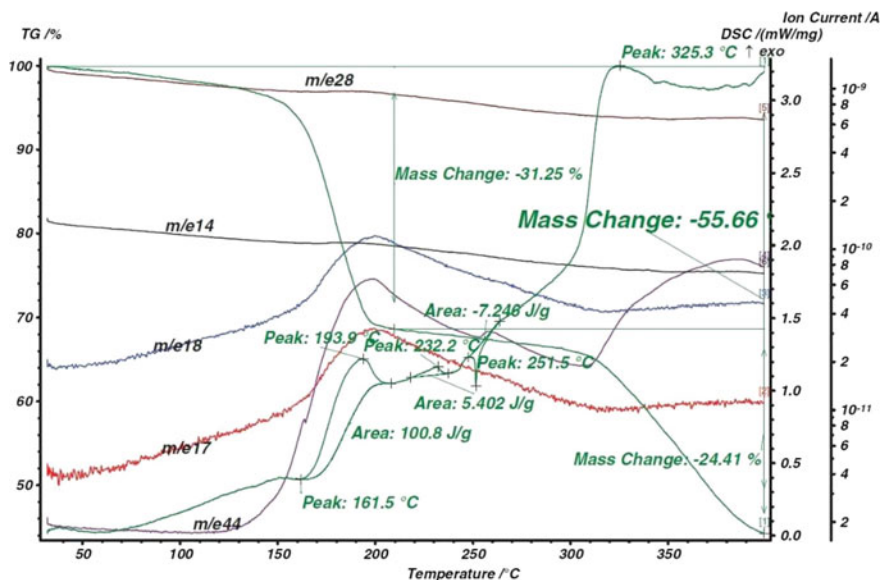


Fig. 5.24 TGA, DSC, and mass spectra of CoADC (heating rate 5 deg min⁻¹, argon) [51]

value of T_{therm} , $\alpha_{\Sigma, f}$ increases with increasing amount of Acr ligands in acrylate monomers. With an increase in T_{therm} , the loss of weight of the sample at the end of the gas evolution also increases, but does not reach the values that could be expected for the decomposition of metal carboxylates onto the metal or its oxide.

The main gaseous products of CoADC thermolysis in the temperature range 413–1223 K are CO₂, C₂H₂, C₆H₆ which can be attributed to the decarboxylation process the polymerization of MCM (Fig. 5.24) [51]. In the temperature range 413–453 K, the rate of gas evolution during the thermolysis of CoADC is satisfactorily approximated by the first-order equation.

$$W = d\eta/dt = k(1 - \eta)$$

where $\eta = (\alpha_t - \alpha_0)/(\alpha_1 - \alpha_0)$ is the degree of transformation and α_t , α_0 , and α_1 are current, initial, and final total amount of gaseous thermolysis products produced per mole of the original CoADC, $k = 1.61015 \exp[-35,800/(RT)]$, s⁻¹.

It was found that the complete decarboxylation of metal-containing fragments of CoADC completes over 673 K, and the complete evolution of the gas n ends at >1073 K. In this case, a significant loss of sample weight (up to 70% at 1223 K) was observed.

5.4.2 The Composition of the Solid-Phase Products

In the thermolysis of MCMs, changes in the IR absorption spectra of solid products of thermolysis are observed with increasing $\alpha_{\Sigma, t}$. They lie in the evolution of the relative intensity of the absorption bands I_{rel} and the shift of the absorption bands. Despite the inherent individuality of each of the compounds studied in the changes in the IR absorption spectrum, there are general regularities connected primarily with the system of mode of C=C and COO bonds:

- (i) At low degrees of gas evolution, including thermolysis of FeAc_3 at low temperatures, the I_{rel} values of the modes $\nu(>\text{C}=\text{C}<)$, $\rho(\text{CH}_2)$, $\nu(\text{C}-\text{C})$, and $\pi(-\text{CH}=\text{CH}_2)$ and the IR spectrum become analogous to the spectrum of the corresponding metal polyacrylates [170] and polymaleates [8, 45]. This is evidenced by the comparison of I_{rel} in the IR spectra of products of thermolysis and individual polyacrylate and polymaleate.
- (ii) An increase in the degree of gas evolution leads to a decrease in the I_{rel} stretching values $\nu(\text{C}(\text{O})-\text{O})$ and the bending of $\delta(\text{C}-\text{O})$ to their complete disappearance. This conclusion indicates the decomposition of carboxylate groups.
- (iii) Simultaneously with the drop in the I_{rel} of the $\text{C}(\text{O})\text{O}$ mode, a shift of the absorption bands of the stretching $\nu(\text{C}-\text{H})$ modes in the high-frequency region is observed, which indicates the strengthening of the C-H bond. This is typical of =CH- fragments.
- (iv) Absorption in the range $1630\text{--}1655\text{ cm}^{-1}$, associated with the vibrations of $\nu(\text{C}=\text{C}-)$ shifted in the high-frequency region $1685\text{--}1720\text{ cm}^{-1}$ with a decrease in I_{rel} . This may be due to the appearance of stretching modes in conjugated C=C- fragments of reaction products.

In general, quantitative monitoring of evolution in the transformation of IR absorption spectra of solid products of thermolysis of carboxylate MCMs suggests decarboxylation of metal-containing fragments and the appearance of conjugated C=C bonds.

The formation of a new phase in the decarboxylation of a metal-containing polymer manifests itself in a stepwise increase in the dielectric losses (the imaginary part of the complex permittivity ε'') by six orders of magnitude at an electric field frequency of 1 Hz and a temperature $T \approx 533\text{ K}$ (Fig. 5.25, surface 1; inset, curve 1) [171]. When CoAc_2 is heated, ε'' varies from 10 to 10^7 , which corresponds to a conductivity change of 10^{-13} to 10^{-7} S cm^{-1} . After cooling and reheating, the achieved dielectric loss remains at the same high level (Fig. 5.25, surface 2; inset, curve 2).

The EM study of the final thermolysis products of CoAc_2 , FeAc_3 , CoMal , Fe_2NiAc , FeCoAc , and Fe_2CoAc showed that they are characterized by a morphologically similar character: There are electron-dense particles in electron-less-dense matrix. Analysis of the data obtained shows that thermolysis of MCMs leads to the formation of metal-polymer nanocomposites that contain NPs of metals and/or oxides and carbides evenly distributed in stabilizing polymer matrices and having different core-shell interfaces (Scheme 5.9). In these systems, NPs are

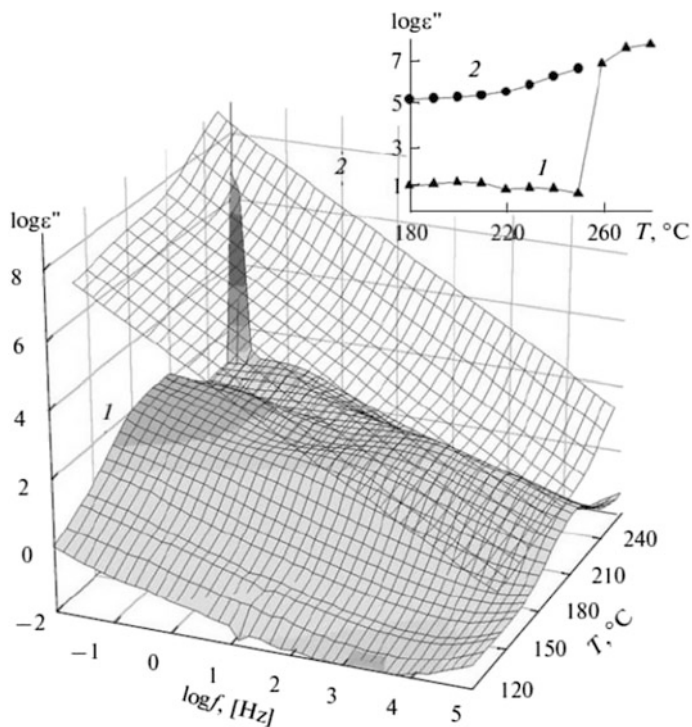
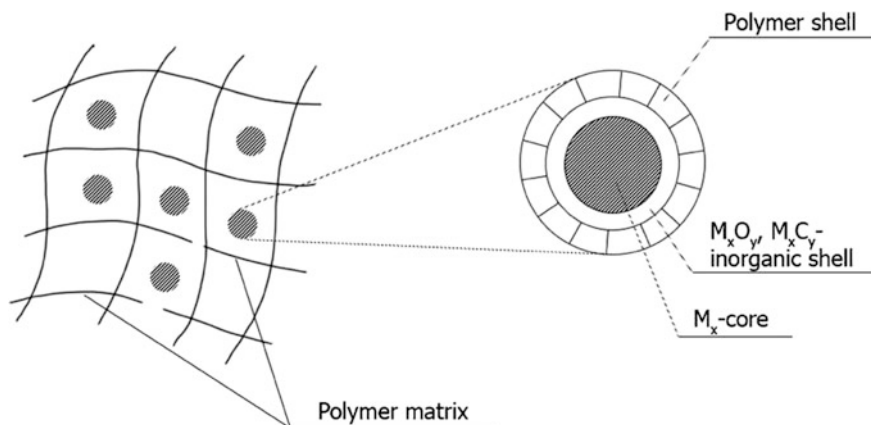


Fig. 5.25 Dependences $\varepsilon''(f, T)$ for CoAcr_2 measured upon (1) first and (2) repeated heating to 533 K. Dependence $\varepsilon''(T)$ at $f = 1$ Hz is presented in inset [171]



Scheme 5.9 Structure of core-shell NPs

characterized by a certain core-shell structure, which contains a metal-containing core and a polymer shell as a surface layer. They are stable over time; i.e., at their long-term storage, there are no changes in the chemical composition, size, and form of the NP.

In the products of thermolysis of carboxylate MCMs, the metal-containing cores contain significant fractions of oxide shells. For example, upon the thermolysis of CoAcr, the CoO fraction in the core reaches 85%; in thermolysis of NiAcr (wt%), NiO \approx 43; NiO \approx 35; and Ni₃C \approx 22, while in the case of thermolysis of its polymer, NiO \approx 75 wt% and NiO \approx 25 wt%. For comparison, the composition of the thermolysis products of Ni(II) polyacrylate, which was obtained by the interaction between polyacrylic acid and Ni(II) acetate and underwent thermolysis under the same conditions, was equal to Ni \approx 84 wt% and NiC \approx 16 wt% [10].

The particles are close to spherical in shape, have a narrow size distribution, and are present either individually or as aggregates of 3–10 particles (Figs. 5.26 and 5.27).

The average particle diameter ($d_{EM,av}$) is shown in Table 5.7.

NPs are distributed fairly evenly in the matrix with an average center-to-center distance of 8–10 nm. In the case of CoMal, along with spherical NPs, relatively large aggregates are also observed in the form of a cubic crystal habitus with dimensions of 10–20 nm. Assuming that the volume of the initial acrylate consumed for the formation of a metal-containing particle MO_x (having a size of d_{MO_x} and a specific density of ρ_{MO_x}), like the initial particle MAcr_n, spherical symmetry, and diameter d_{Acr} , the final product is the decarboxylated matrix (–CH₂–CH=CH–CH₂–)_n– composition with immobilized MO_x molecules in it and has an average density $\bar{\rho}_{prod} \approx 0.5(\rho_{MO_x} + \rho_{Acr})$, where ρ_{Acr} is the density of the initial monomer ($\rho_{Acr} = 1.5 \text{ g cm}^{-3}$). Then, we get the average center-to-center distance d_{prod} between NPs:

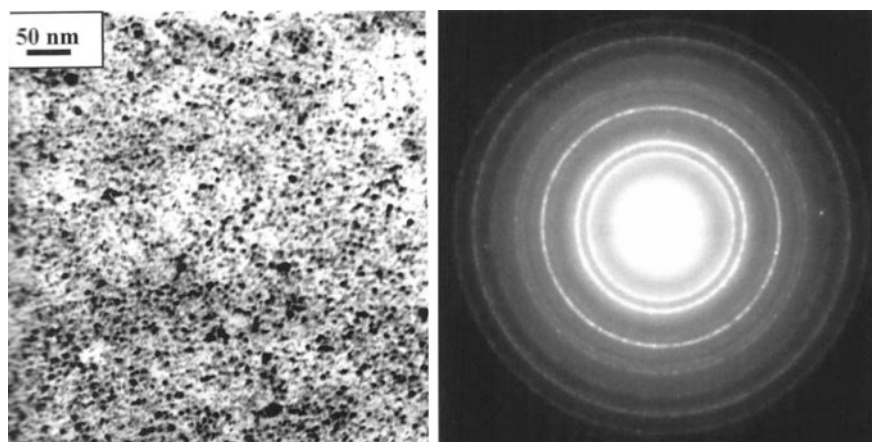


Fig. 5.26 TEM microstructure (left) and electron diffraction (right) of the thermolysis product of CoAcr₂ at 643 K [10]

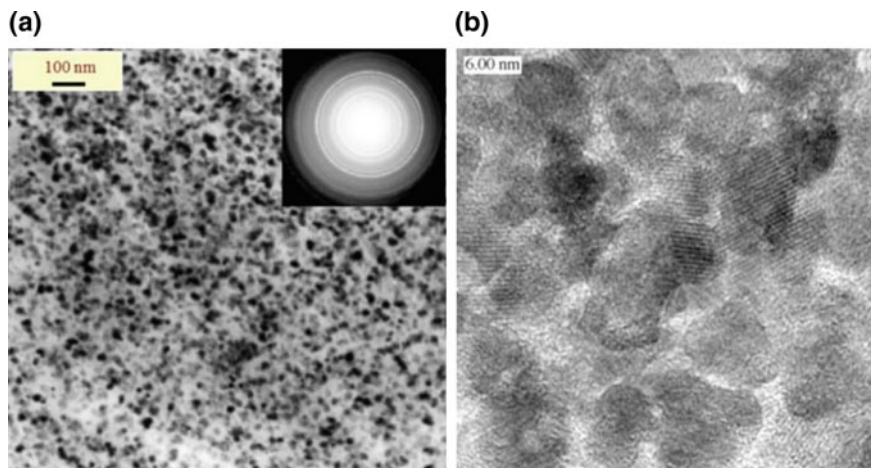


Fig. 5.27 Thermolysis product microstructure of Fe_2CoAcr at 643 K according to the TEM (left) and HRTEM (right) [10]

Table 5.7 Average size of the spherical clusters in decarboxylated matrix

Sample	CoAcr ₂	FeAcr ₃	FeCoAcr	Fe ₂ CoAcr	Fe ₂ NiAcr	CoMal
$d_{\text{EM, av}}$, nm	7	7–9	5–6	5–6	6–8	3–4

$$\bar{d}_{\text{prod}} = \bar{d}_{\text{MO}_x} \xi^{1/3}$$

Here, $\xi = \rho_{\text{MO}_x}(1 + n\mu_2/\mu_1)/\bar{\rho}_{\text{prod}}$, $\mu_1 = \mu_{\text{MO}_x}$ is the molecular weight of MO_x , $\mu_2 = \mu_{\text{CH}_2\text{CH}}$, and n is the number of Acr groups in the original monomer per unit atom M.

For $\rho_{\text{MO}_x} = 5.2 \text{ g cm}^{-3}$ (specific density of Fe_3O_4 or Fe_2CoO_4), $\bar{\rho}_{\text{prod}} = 3.35 \text{ g cm}^{-3}$, $\mu_{\text{MO}_x} = 78$, $\mu_{\text{CH}_2\text{CH}} = 27$, $n = 3$, we obtain $\bar{d}_{\text{prod}} \cong 1.5 \bar{d}_{\text{MO}_x}$. Thus, for $\bar{d}_{\text{MO}_x} = 5.0\text{--}9.0 \text{ nm}$ we have $\bar{d}_{\text{prod}} = 7.5\text{--}13.5 \text{ nm}$, which is close to the interparticle distance in the decarboxylated matrix.

It is important to note that the APS formed during the thermolysis of unsaturated metal carboxylates is lower than that of the products of thermolysis of saturated metal carboxylates (Fig. 5.28) [12].

In chemical reactions of the solid phase, the most important factors affecting the process rate are the morphological characteristics of the starting compounds, such as the dispersity, the specific surface, and topography of the particles. On the one hand, knowledge about the evolution of the morphology of solid-phase products allows one to evaluate the kinetic features of the process. On the other hand, the study of the topography of solid-phase products, in particular, at the end of the thermolysis, allows us to understand physicochemical properties of the materials

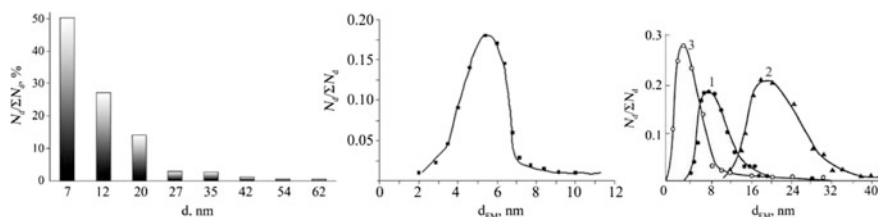


Fig. 5.28 Size distribution of metal-containing particles. Products of thermolysis of metal carboxylates (left): CoAcr₂, (middle) cocrystallite Fe₂CoAcr, and (right) 1—FeAcr₃, 2—Fe(HCOO)₂·2H₂O, 3—CoMal [12]

formed. In this respect, the morphology of metal-containing polymeric nanocomposites obtained, for example, by thermolysis of the corresponding MCMs in the self-organizing regime, has been little studied.

The initial samples of MAcr_n and MMal_n are optically transparent crystal-like porous particles without crystallinity at distances comparable to the transmitted light wavelength. They have a relatively large specific surface area ($S_{sp}^0 = 9\text{--}30\text{ m}^2\text{ g}^{-1}$), which does not change significantly during thermolysis. However, in some cases (for CuAcr₂, CoAcr₂ and several for NiAcr₂), large aggregates are dispersed. As a result, APS decreases, and S_{sp} increases by 2–3 times and then decreases again due to particle sintering [149, 150]. Even in the early stages (during the sample warming up), the particles lose transparency, and their surface becomes sugar-like, probably as a result of desolvation processes, which may indicate a significant contribution of a bulk homogeneous reaction. Thus, the thermolysis of these compounds is a heterogeneous–homogeneous process [10, 151, 154].

APS of decarboxylated metallopolymer (S_{sp} measurement data) is estimated as $\sim 20\text{--}30\text{ nm}$ for CuAcr₂ and $\sim 30\text{--}50\text{ nm}$ for CoAcr₂. Electron microscopy and electron diffraction studies [10, 48] of the microstructure of the sample showed (Fig. 5.29a) a rather narrow particle size distribution, an average particle diameter of 4–9 nm (Fig. 5.29b) and an 8–10 nm average distance between the particles in the matrix. Even distribution of particles in the matrix and a narrow particle size distribution may indicate a high degree of pseudohomogeneity of decarboxylation and the formation of a new phase. It should be noted that the average size of thermolysis products is much higher for salts of saturated carboxylic acids than for the unsaturated acid salts (see Fig. 5.29b).

As can be seen from the results of optical microscopy (OM) studies (Table 5.8), the metal carboxylate powders are characterized by a high and very similar dispersity [11].

It was shown that the starting powders consist of both agglomerates of transparent particles as plates or flat prisms (CoMal) and shapeless glassy particles. Some large crystals had macrodefects, such as deposits and cracks. In many cases, metal powder particles of metal carboxylates did not rotate the polarized plane of transmitted light in crossed polaroids. This means that the particles are amorphous, whose dimensions are comparable to the wavelength of transmitted light.

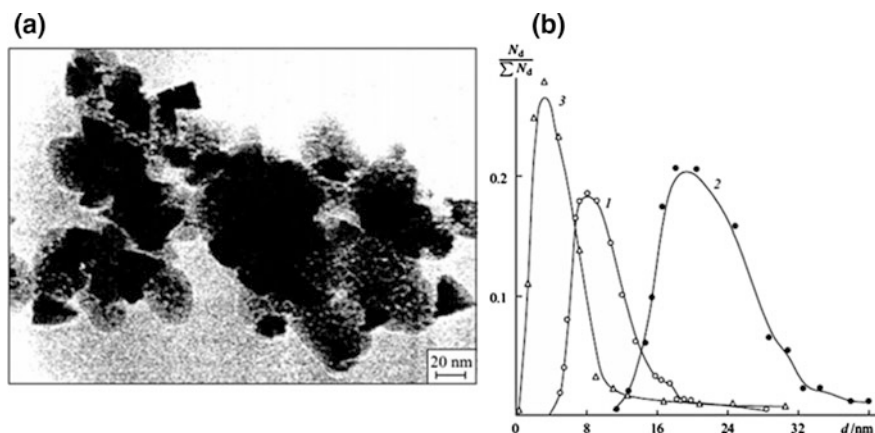


Fig. 5.29 EM image of the thermolysis product of $\text{Co}(\text{Mal})_2\text{H}_2\text{O}$ at 623 K (a) and size distribution of metal-containing particles (b) [36] (1) $\text{Fe}_3\text{O}(\text{OH})(\text{Acr})_6 \cdot 3\text{H}_2\text{O}$, (2) $\text{Fe}(\text{HCOO})_2 \cdot 2\text{H}_2\text{O}$, (3) $\text{Co}(\text{Mal})_2 \cdot \text{H}_2\text{O}$ [10, 48]

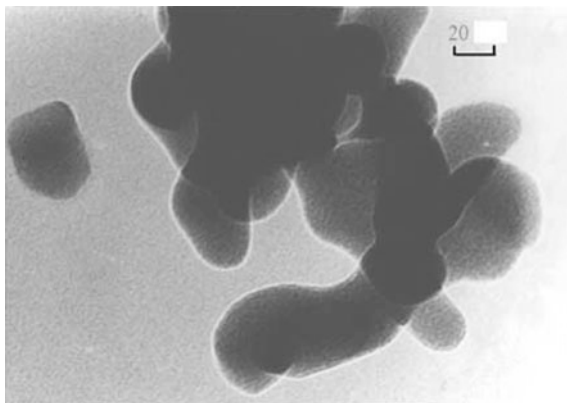
Table 5.8 Dispersity of the initial MCMs and their thermolysis products

MCM	$S_{0,\text{sp}}$ ($\text{m}^2 \text{g}^{-1}$)	$S_{f,\text{sp}}$ ($\text{m}^2 \text{g}^{-1}$)	APS_{OM} (μm)
CuAcr_2	14.7	48.0 (463 K)–53.8 (473 K)–43.8 (503 K)	5–50
CoAcr_2	20.2	24.1 (623 K)–42.1 (663 K)	100–150
FeAcr_3	15.0	15.0	1–5
NiAcr_2	16.0	55.0–60.5	60–100
FeCoAcr	9.0	13.6	5–10
Fe_2CoAcr	8.1	11.3	10–15
Fe_2NiAcr	8.5	13.5	100–200
CoMal	30.0	30.0	5–70
FeMal	24.0	26.0	30–50

The CoMal particles formed two fractions: amorphous particles and crystalline flattened prism particles (in some cases, they were well faceted with an average size of $\sim 50 \times 15 \times 5 \mu\text{m}^3$) that rotated plane-polarized light in crossed polaroids. The estimated weight ratio of the first and second fractions was 1:1. APSs, calculated from $S_{0,\text{sp}}$, are 0.01–0.05 μm (without taking into account the shape factor). This is substantially less than APS_{OM} . Such differences between the values of APS show the high porosity of the original samples, i.e., the block structure with transparent interblock boundaries. Only amorphous particles (the first fraction) were studied by electron microscopy. They demonstrated a homogeneous network of increased electron density with a unit cell size of $\sim 2.0 \text{ nm}$ (Fig. 5.30).

During thermolysis, it was found that specific surface $S_{\text{sp},f}$ of the sample increases in the case of CuAcr_2 , CoAcr_2 , and NiAcr_2 . The main changes occur at the early stage of conversion, and at the end, the value of $S_{\text{sp},f}$ exceeds the value of

Fig. 5.30 Electron micrograph of initial particles of fraction 2 of CoMal [11]



$S_{sp,0}$ by 2–3 times (see Table 5.8). In the case of CuAcCr_2 , the behavior of $S_{sp,f}(T_{\text{term}})$ is peculiar. The first value of $S_{sp,f}$ increases from T_{temp} to 493 K and then decreases. The decrease in $S_{sp,f}$ at $T_{\text{term}} > 493$ K is apparently determined by particle sintering. However, in the thermal conversion of FeAcCr_3 , FeCoAcCr , Fe_2CoAcCr , Fe_2NiAcCr , CoMal , and FeMal , the values of $S_{sp,f}$ do not change substantially.

It should be noted that APS is 6.0–13.0 nm in the case of FeAcCr_6 (based on the electron diffraction data, the main product is Fe_3O_4), 6.0 nm for FeCoAcCr_8 and $\text{Fe}_2\text{CoAcCr}_{14}$ (Fe_3O_4 , CoO , Fe_2CoO_4), and 6 nm for CoMal_2 (CoO) [172]. The formed material consists of NPs uniformly distributed in the polymer matrix.

The composites obtained by thermolysis of unsaturated cobalt hydrogen carboxylates in an argon flow are black powders and, according to XRD data (Fig. 5.31), consist of two structural elements: Co_3O_4 NPs (cubic symmetry) with small CoO impurities (tetragonal symmetry) and metallic cobalt (hexagonal symmetry) in the polymeric shell are embedded in the organic polymer matrix [62]. The black color of the composites is due to the presence of amorphous carbon. The C:H ratio in the synthesized composite is equal to ~ 1 . This indicates that the content of ($=\text{CH}-$) fragments in the formed polymer matrix is very large.

The SEM and TEM studies of the composites show that they consist of aggregates with sizes from 100 nm to 8 μm . The composite prepared by the thermolysis of cobalt hydrogen itaconate exhibits the reflections corresponding to cobalt, oxygen, and carbon. In combination with chemical analysis data, these reflections prove the formation of Co_3O_4 NPs in a polymer shell, which generally consists of ($=\text{CH}-$) moieties. The TEM image processing stages for the composite prepared by the thermolysis of cobalt hydrogen itaconate are illustrated in Fig. 5.32.

According to XRD data (Table 5.9), the thermolysis of nickel(II) itaconate, acetylenedicarboxylate, and allylmalonate leads to the formation of NiO and $\beta\text{-Ni}$, and the composite obtained by thermolysis of nickel glutaconate contains $\alpha\text{-Ni}$ in addition to the listed phases [173]. The nickel maleate and *cis,cis*-muconate thermolysis products contain NiO , $\beta\text{-Ni}$, and impurities of $\alpha\text{-Ni}$.

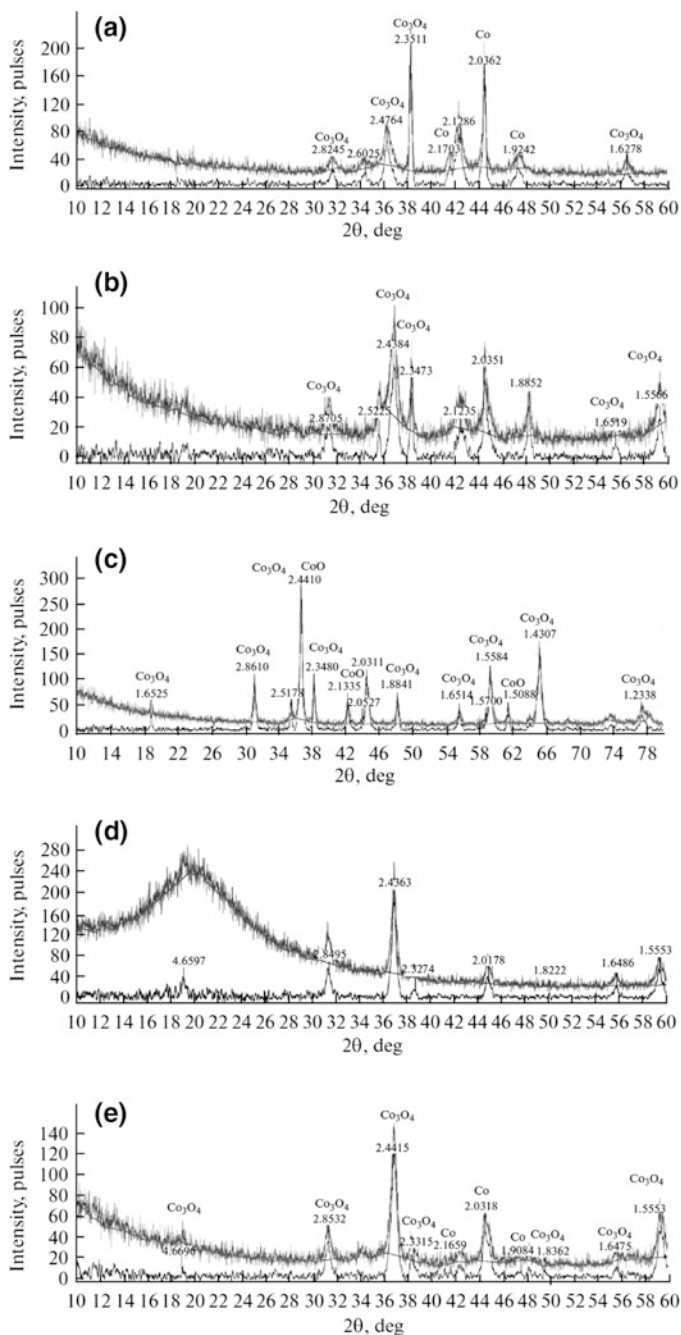


Fig. 5.31 XRD patterns of the composites synthesized from precursors: **a** cobalt hydrogen maleate, **b** cobalt hydrogen allylmalonate, **c** cobalt hydrogen *cis-cis*-muconate, **d** cobalt acetylenedicarboxylate, **e** cobalt hydrogen glutaconate [62]

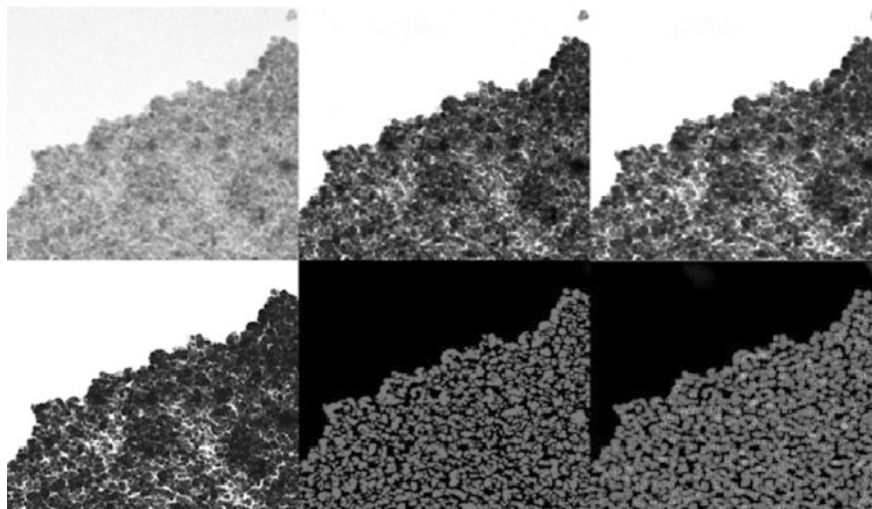
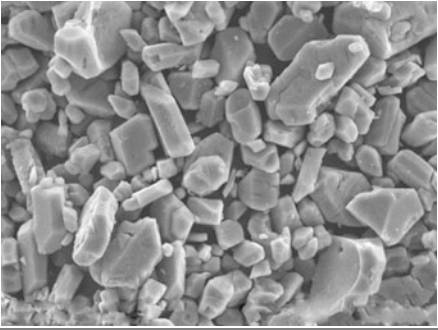
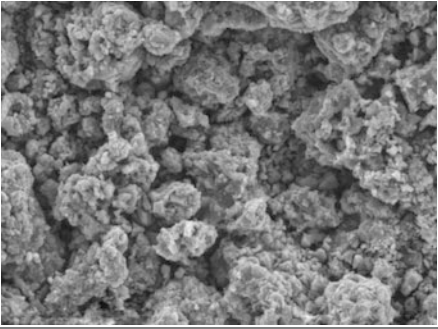
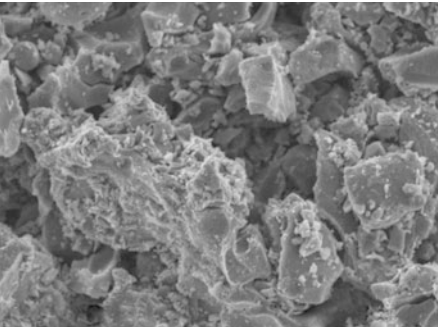


Fig. 5.32 Stages of TEM image processing with the LabVIEW 8.5.1 software for the nanocomposite synthesized by the thermolysis of cobalt hydrogen itaconate [62]

Table 5.9 XRD results for the nickel(II) carboxylate thermolysis products

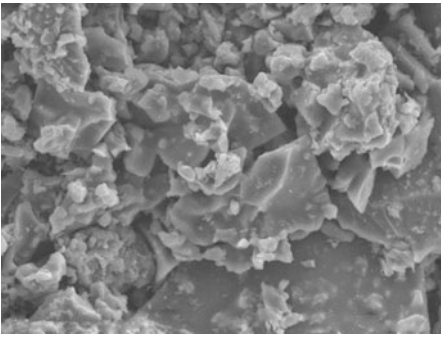
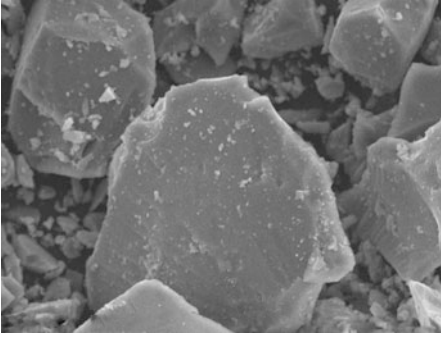
MCM	Phase	Symmetry system	Space group	Unit cell parameters, Å	Content, wt%
Nickel maleate	NiO	Cubic	<i>Fm3m</i>	$a = 4.184$	33.4 ± 0.1
	β -Ni	Cubic	<i>Fm3m</i>	$a = 3.519$	57.3 ± 0.1
	α -Ni	Hexagonal	<i>P63/mmc</i>	–	9.3 ± 0.1
Nickel itaconate	NiO	Cubic	<i>Fm3m</i>	$a = 4.175$	73.3 ± 0.1
		Cubic	<i>Fm3m</i>	$a = 3.523$	26.7 ± 0.1
	α -Ni	Hexagonal	–	–	–
Nickel acetylenedicarboxylate	NiO	Cubic	<i>Fm3m</i>	$a = 4.176$	73.7 ± 0.1
	β -Ni	Cubic	<i>Fm3m</i>	$a = 3.525$	26.3 ± 0.1
	α -Ni	Hexagonal	–	–	–
Nickel allylmalonate	NiO	Cubic	<i>Fm3m</i>	$a = 4.178$	67.8 ± 0.0
	β -Ni	Cubic	<i>Fm3m</i>	$a = 3.522$	32.2 ± 0.0
	α -Ni	Hexagonal	–	–	–
Nickel glutaconate	NiO	Cubic	<i>Fm3m</i>	$a = 4.178$	21.6 ± 0.1
	β -Ni	Cubic	<i>Fm3m</i>	$a = 3.521$	56.8 ± 0.1
	α -Ni	Hexagonal	<i>P63/mmc</i>	$a = 2.485$ $c = 4.093$	21.5 ± 0.1
Nickel <i>cis-cis</i> -muconate	NiO	Cubic	<i>Fm3m</i>	$a = 4.197$	30.0 ± 0.2
	β -Ni	Cubic	<i>Fm3m</i>	$a = 3.517$	66.8 ± 0.2
	α -Ni	Hexagonal	<i>P63/mmc</i>	–	2.9 ± 0.1

Table 5.10 Micrographs and aggregate size for the nickel carboxylate thermolysis products

Nanocomposite precursor	Aggregate size, μm	SEM image
Nickel maleate	5.5–20.5	
Nickel acetylenedicarboxylate	0.6–173	
Nickel allylmalonate	0.6–267	

(continued)

Table 5.10 (continued)

Nanocomposite precursor	Aggregate size, μm	SEM image
Nickel glutaconate	1.4–107	
Nickel <i>cis,cis</i> -muconate	0.3–211	

The SEM and TEM studies of the composites show that they consist of aggregates of 0.3–260 μm in size (Table 5.10).

It is noteworthy that carbon nanotubes are formed in the nanocomposite, which results from the thermolysis of nickel itaconate (Fig. 5.33). As a rule, the growth temperature of carbon nanotubes is usually in the range of 773–1273 K; however, in this case synthesis of nanocomposites was carried out at 608 K.

The residues after the thermolysis (up to 723 K) of salts (both normal and acid) of transition metals with maleic acid are composites comprising two structural

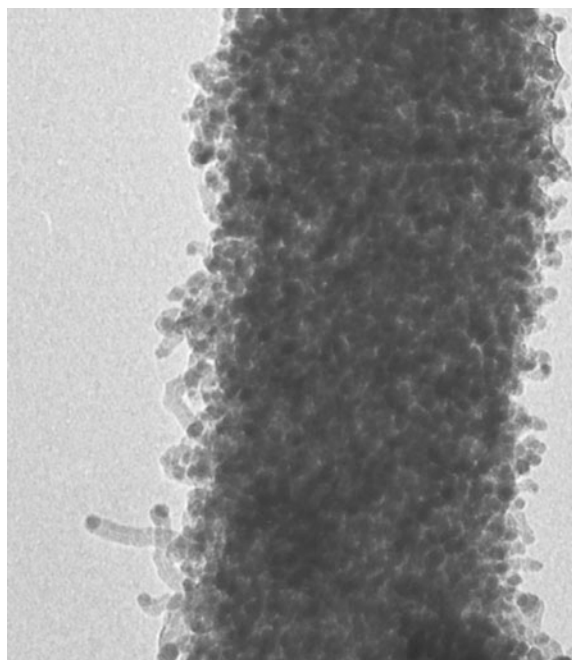


Fig. 5.33 TEM image of the nanocomposite obtained by the thermolysis of NiIta [173]

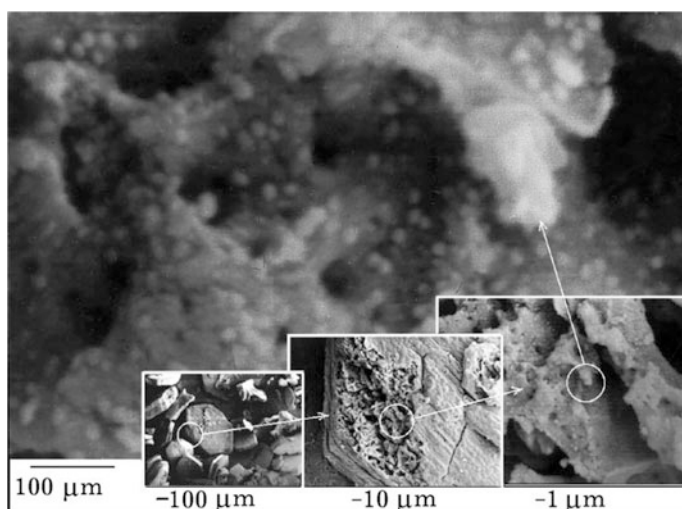


Fig. 5.34 A photograph of the composite synthesized from CuMal [174]

components: an organic polymer matrix and spherical conglomerates of metal grains coated with a polymer (Fig. 5.34) [174].

The composition and monophasic homogeneity of the normal Co(II), Ni(II) maleates and Mn(II), Fe(II), Co(II), Ni(II) acid maleates greatly influence the thermolysis process, which is accompanied by graphitization of the matrix and NPs [61]. The thermolysis conditions (temperature, atmosphere), ligand environment, and the nature of the metal in the precursor favor the decomposition reactions along different paths, with the formation in the solid residue of various NPs: metallic, oxide, carbide embedded in the polymer matrix or incorporated into the carbon-containing shell.

The metallic NPs were embedded into the polymer composite matrix during the thermolysis of normal (Co(II), Ni(II), Cu(II)) and acid (Fe(II), Co(II), Ni(II), Cu(II)) maleates in the He atmosphere, around which there is a negligible small envelope (Fe) matrix together with a polymer (Co) or graphene (Ni) shell containing oxide impurities (only for iron- and cobalt-based composites) [60, 61, 175]. In particular, the polymer matrix of the composite obtained from cobalt maleate contained four types of NPs: α -Co, β -Co and CoO in polymer shells, and Co₃O₄ without a polymer shell. Spherical conglomerates (50–200 nm) with numerous copper spherical particles (5–10 nm) are introduced into the polymer matrix in composites with Cu. After 7-day exposure of copper-based composites in air, they show the oxide phase of Cu₂O in addition to the metallic phase. Longer storage results in almost complete oxidation of copper.

The study of the non-isothermal thermolysis of cadmium itaconate monohydrate Cd(Ita)·H₂O between ambient temperature and 873 K in different dynamic atmospheres of N₂, H₂, and air showed that CdO is the only solid product obtained from thermolysis in air [176]. In N₂, the product solid was dominated by cadmium oxide along with traces of cadmium metal and cadmium hydroxide Cd(OH)₂. However, in the H₂ atmosphere, the cadmium metal was obtained as the main product, which sublimates above 723 K.

It should be noted the preparation of ZnO and CdO NPs with APSs around 13 and 30 nm by thermolysis of the precursor M(L)₂·(N₂H₄)₂ (M = Zn/Cd, L = cinnamic acid) [177]. It is interesting that in the case of Zn-complex, randomly distributed ZnO grains with smaller size are formed, while the products of the thermolysis of Cd complex are rock candy-like CdO structures with agglomeration of particles (Fig. 5.35).

Polymerization of metal acetylenedicarboxylates was accompanied by the formation of polyconjugated chains [51]. The nanocomposites obtained are pyrolyzed polymer matrices with homogeneous distribution of metal-containing NPs

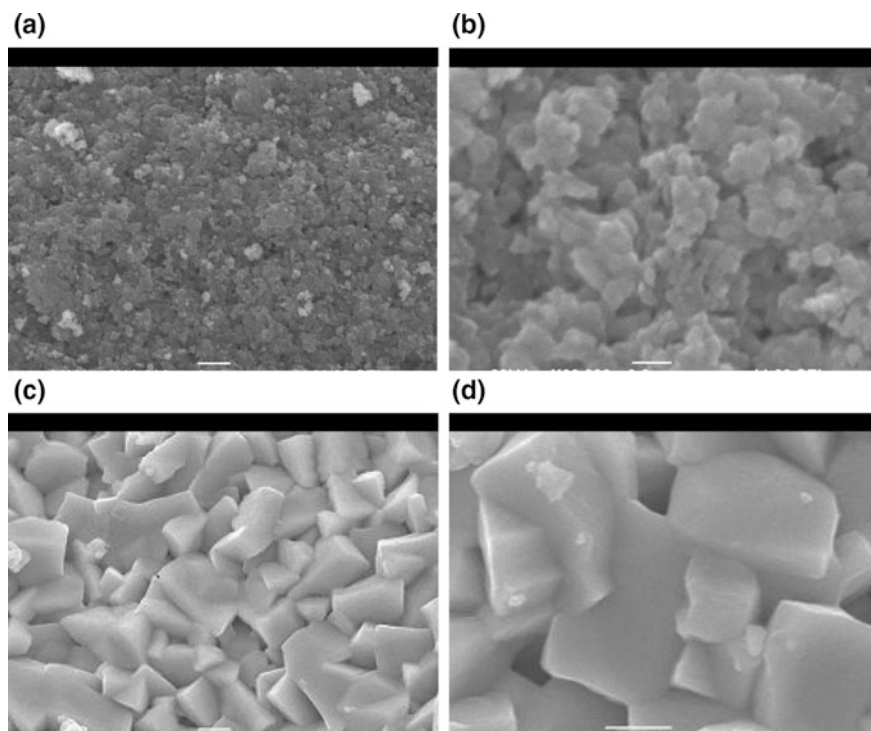


Fig. 5.35 **a** SEM micrograph of ZnO NPs ($\times 10,000$), **b** SEM micrograph of ZnO NPs ($\times 60,000$), **c** SEM micrograph of CdO NPs ($\times 10,000$), **d** SEM micrograph of CdO NPs ($\times 20,000$) [177]

[159, 178]. Iron (<10 nm) and cobalt NPs (10–20 nm) are spherical, while zinc NPs (~ 20 nm) look like plates (Fig. 5.36).

SEM images (Fig. 5.37) demonstrated nanorods with a diameter of 30–60 nm and a length of several micrometers. Image verification shows that the thermolysis of CP Zn(ABDC)(ADC) at 873 K led to the formation of more uniform rods with a longer length (Fig. 5.37c) [179].

Spherical silver NPs embedded in the carbon matrix were synthesized by thermolysis of AgADC. It is important that these NPs, which are formed either by thermolysis at 573 K in an autoclave or by thermolysis in a xylene suspension at reflux temperature, act catalytically for graphite layers [103]. Both reactions

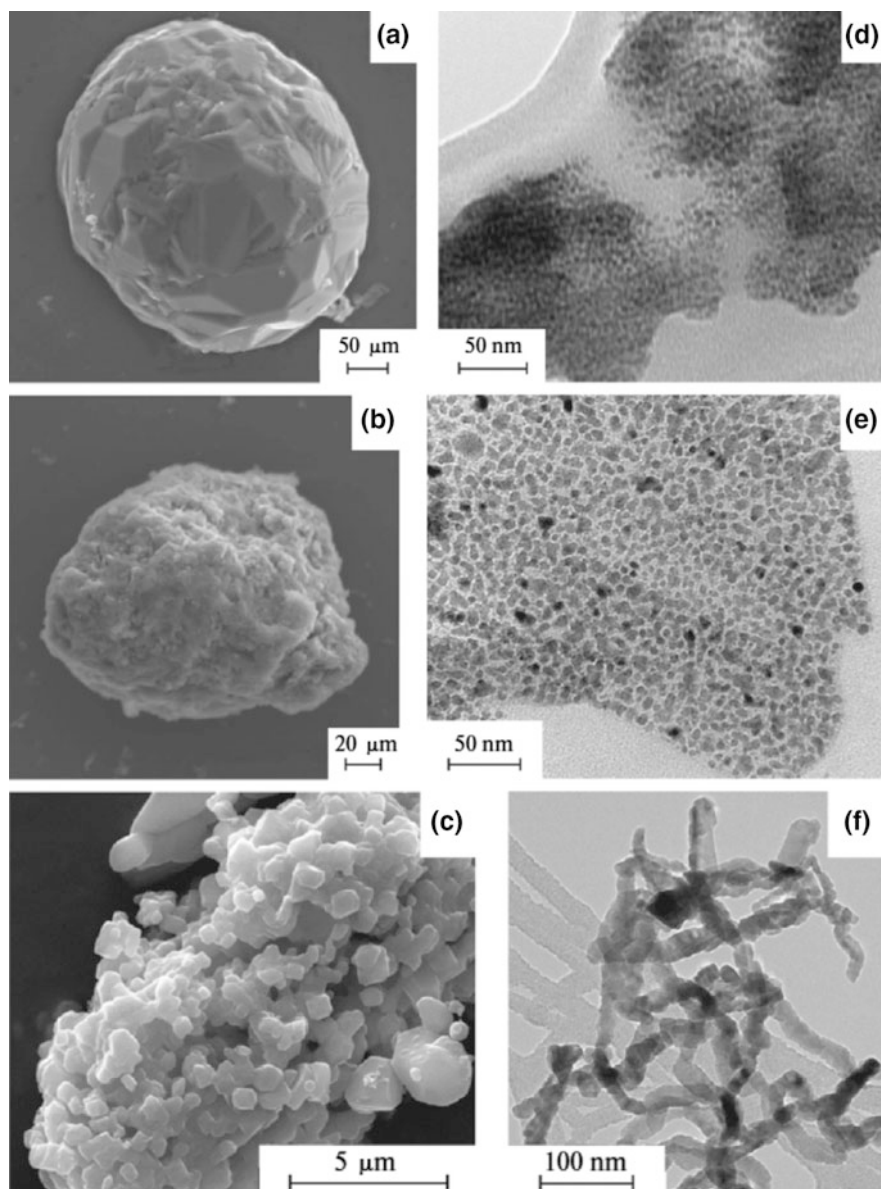


Fig. 5.36 SEM (a–c) and TEM images (d–f) of the thermolysis products of CoADC (a, d), FeADC (b, e), and ZnADC (c, f) [51]

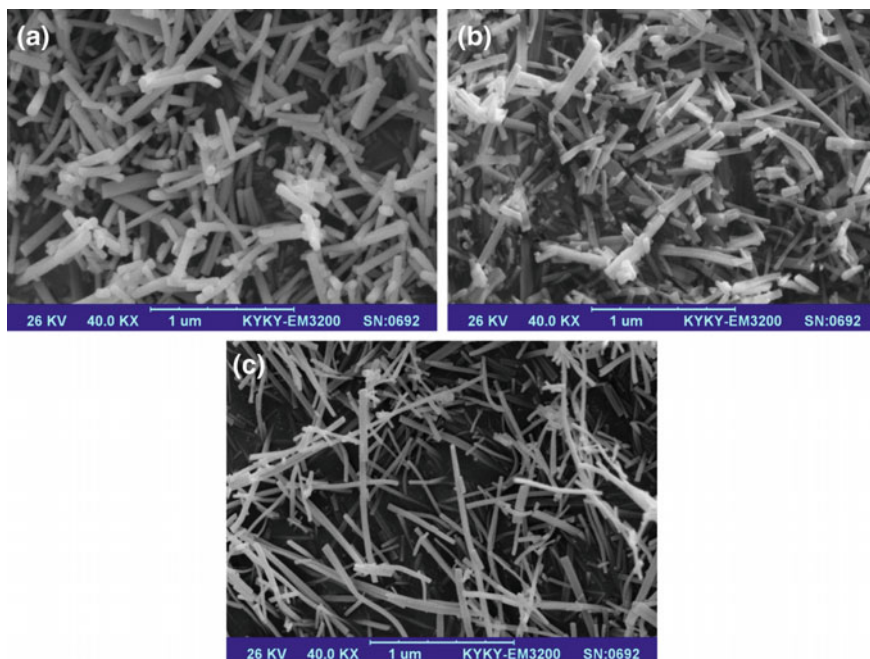


Fig. 5.37 SEM images of ZnO nanorods obtained by thermolysis of Zn(ABDC)(ADC) at **a** 673 **b** 773 and **c** 873 K [178]

proceed through in situ reduction of silver cations and polymerization of the central acetylene triple bonds, and the exact reaction temperature can be monitored by DTA. Interestingly, the thermolysis of this silver salt in xylene partially results in a negligible fraction of quasi-crystalline silver. The graphitic layers covering silver NPs are clearly visible in HRTEM images (Fig. 5.38) and, in addition, are determined by the presence of sp^2 carbon in the Raman spectra of both samples. Silver NPs seem to be the core areas of the composite, which are interconnected by layers of carbon. This corresponds to the reaction steps when the formation of silver NPs is the catalytic stage of polymerization of the central acetylene units.

Thus, during MCM thermolysis, a material consisting of NPs stabilized in a matrix with a narrow size distribution is formed. The phase composition, morphology, and structure of the formed nanocomposites are discussed in more detail below.

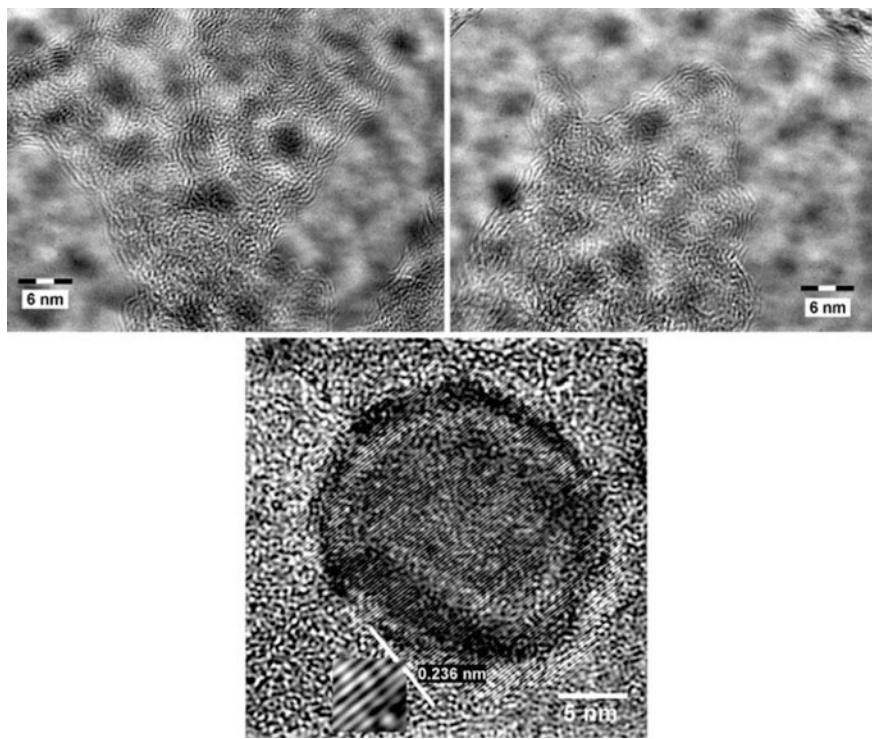


Fig. 5.38 HRTEM images of the Ag/pyr sample. The graphitic layers can be seen surrounding the individual silver NPs, thus forming a carbon matrix where the NPs are encapsulated. In the last image, a single silver NP and its typical interlayer spacing are shown in magnification [103]

5.5 Kinetic Schemes and Reactions of Thermal Transformation of Metal Chelate Monomers

The thermal stability of MCMs can be measured by the relative strength of the M–O and C–O interatomic bonds in its crystallochemical structure. The lengths of M–O and C–O bonds in the coordination polyhedron can vary significantly, which indicates their difference in energy. According to the IR spectroscopy of dehydrated monomers (see Tables 5.2, 5.3 and 5.4), during dehydration the basic unit of the structure of MCMs is usually preserved. But in this case, the denticity of a certain portion of the unsaturated ligands can change and, like the anhydrous carboxylates of unsaturated acids, they begin, simultaneously, to fulfill the role of the ligand and the missing solvate function in the crystal structure. An increase in the ligand denticity leads to a distortion of the oxygen environment of the metal with a corresponding change in the distances of M–O and C–O in the structure and, consequently, a change in their strength. In particular, the difference in the energy of M–OOCCH=CH₂ in FeAcr₃ indicates [66] the dependence of Acr ion

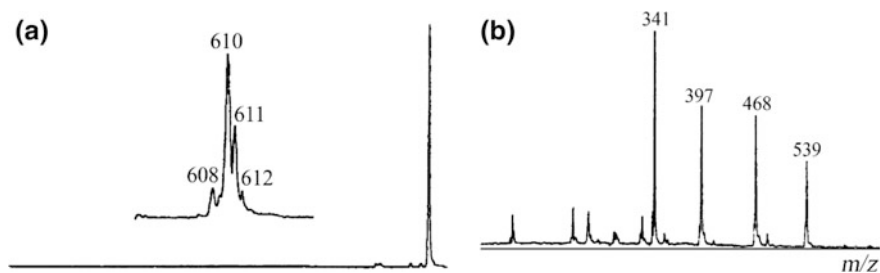


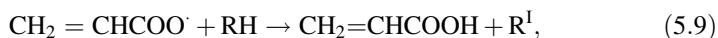
Fig. 5.39 Mass spectra of positive ions extracted from the aqueous alcoholic solution of FeAcAc_3 at $U = 200$ V (a) and 400 V (b) [66]

fragmentation on the accelerating field voltage in MS studies on fragmentation of $[\text{Fe}_3\text{O}(\text{Acr})_6]^+$ ion. The mass spectrum at $U = 400$ V (Fig. 5.39) of ions with $m/z = 539, 468, 397$ corresponds to the evolution of one, two, or three Acr groups, and the ion with $m/z = 341$ corresponds to the evolution of FeAcAc_3 molecules from $[\text{Fe}_3\text{O}(\text{Acr})_6]^+$ molecular ion.

5.5.1 General Kinetic Scheme and Ways of Decomposition of Metal Chelate Monomers

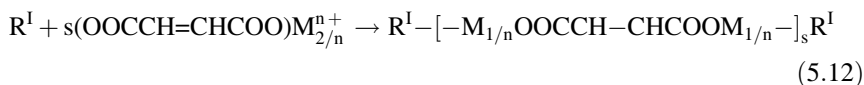
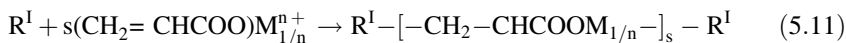
Analysis of the chemical transformation pathways shows that, assuming the energy non-equivalence of the M–O bonds in the unsaturated metal carboxylates, the primary decomposition stage is the formation of the radicals: acrylic ($\text{CH}_2=\text{CHCOO}^\cdot$) and maleic ($^\cdot\text{OOCCH}=\text{CHCOO}^\cdot$) radicals for acrylates and maleates, respectively. Radicals initiate polymerization, followed by decarboxylation of the metal–polymer.

With an increase in the level of thermal vibrations of the lattice of the dehydrated monomer (with increasing temperature), the breakdown of the weakest M–O bonds is, in all probability, mono- or biradicals of the ligands: $\text{CH}_2=\text{CHCOO}^\cdot$ in the case of acrylates and $^\cdot\text{OOCCH}=\text{CHCOO}^\cdot$ if maleates. The interaction of these radicals with metal-containing maleate or acrylate residues leads to the corresponding acids and the radical R^\cdot with the H-depleted acrylate (maleate) group:

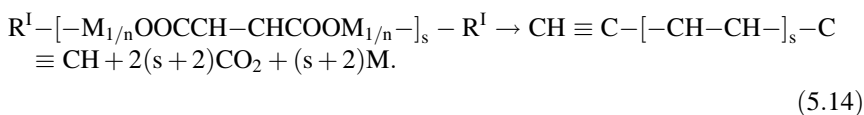
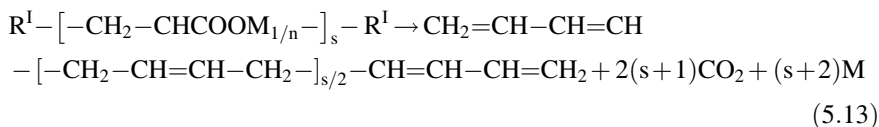


where $\text{RH}=(\text{CH}_2\text{CHCOO})\text{M}_{1/n}^+$, $\text{R}^\cdot=(^\cdot\text{CHCHCOO})\text{M}_{1/n}^+$ (in the case of acrylate) and $\text{RH}=(\text{CHCOO})_2\text{M}_{2/n}^+$, $\text{R}^\cdot=(^\cdot\text{CCOO})_2\text{M}_{1/n}^+$ (in the case of maleate).

The resulting R^\cdot radical participates in the growth and chain termination reaction to form a network polymer or a linear structure:



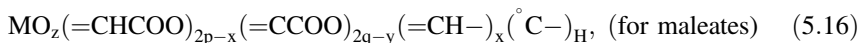
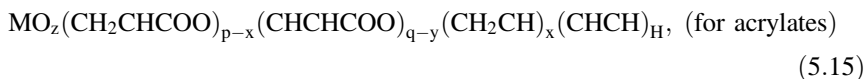
With increasing temperature, the metal-containing groups of the resulting polymer undergo decarboxylation to form a metal and (or) its oxide:



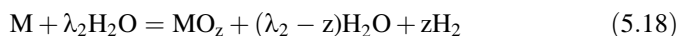
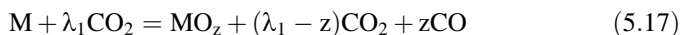
Additional thermal polymerization involving multiple bonds in decarboxylated products is likely to contribute to the creation of a cross-linked network structure, as evidenced by the lack of solubility of the reaction product in organic solvents.

Taking into account the material balance equations and quantitative data on the yields of gaseous and volatile thermolysis products, it was found that the composition of the solid phase changes during the thermolysis. It can be represented by the following balance relationship: for the acrylates $MO_r(CH_2CHCOO)_{p-k}(CH_2CH)_k(CHCHCOO)_{q-1}(CHCH)_1$ and for the maleates $MO_r(=CHCOO)_{2p-k}(=C-)_k(=CCOO)_{2q-1}(=C-)_1$, where before decarboxylation, $r = k = 1 = 0$ ($r \neq 0$ for $FeAc_3$), p and q are the numbers of internal and terminal (hydrogen-depleted) carboxylate groups, respectively.

Thus, in general, a solid thermolytic product composition of metal acrylates and maleates can be represented as a sum of a fraction of a C-H-O fragment:



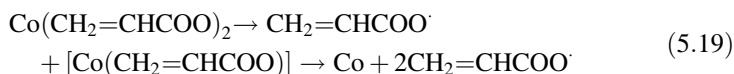
where $x = y = z = 0$ ($z \neq 0$ in the case of $FeAc_3$ and $FeMal$), and p and q are the amounts of intrachain and terminal H-depleted groups ($p + q = 1$), respectively. The most likely way of forming metal oxides is the oxidation reaction.



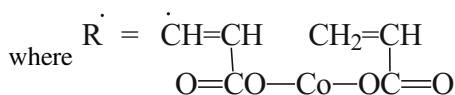
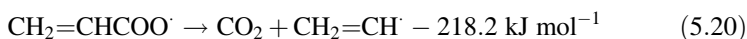
By solving the mass balance equation using quantitative data on the evolution of gas, the weight loss of the sample, low-temperature fractionation, and MS analysis of the composition of the gaseous products, CO₂, H₂, and CO and the yield of the thermolysis product of the complexes under analysis were calculated [149, 150, 152, 153]. Consider this in more detail using the example of CoAcr₂.

5.5.2 Transformation Pathways of Cobalt Acrylate

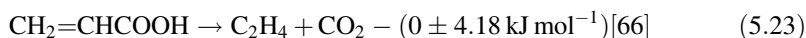
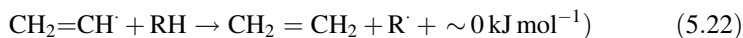
As mentioned above, as a result of dehydration (desolvation), the denticity of the part of Acr ligands changes, which leads to mismatch of M–O bonds. As a result, the breakdown of the weak M–O bond occurs with the formation of the radical CH₂=CHCOO·



The resulting CH₂=CHCOO· radical can then be consumed through the following channels¹:



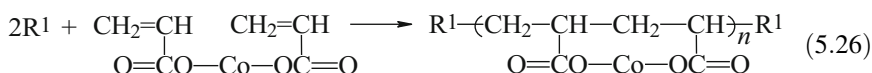
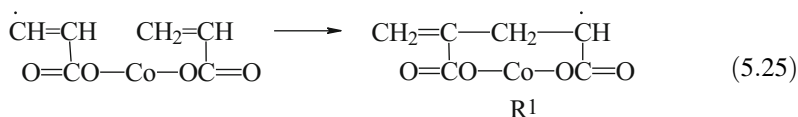
and further²



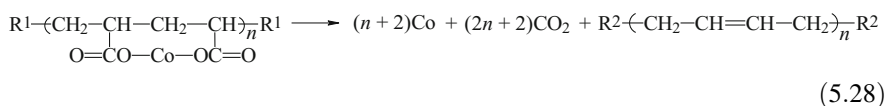
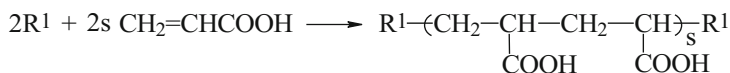
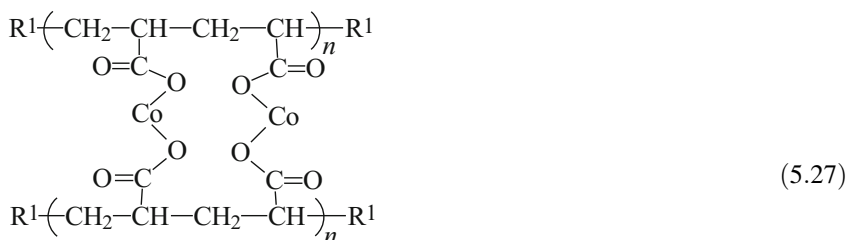
¹It is believed that $E(\text{CH}_2\text{CHCOOH}) (\text{g}) = 461.5 \text{ kJ mol}^{-1}$.

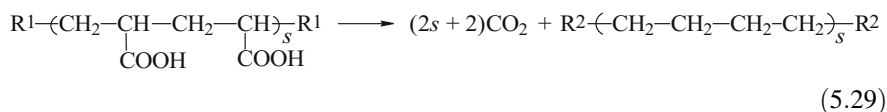
²Estimates of the thermal effects were carried out for a gas-phase reaction using the following data and assumptions: $E(\text{CH}_2\text{CHCOOH}) (\text{g}) = E(\text{MeCOOH}) = 461.5 \text{ kJ mol}^{-1}$, $\Delta H_f^\circ(\text{CH}_2\text{CHCOOH}) (\text{l}) = -384.6 \text{ kJ mol}^{-1}$, $\Delta H_{\text{ev}}(\text{CH}_2\text{CHCOOH}) (\text{l}) = 545.6 \text{ kJ mol}^{-1}$, $\Delta H_f^\circ(\text{CH}_2\text{CHCOOH}) (\text{g}) = 96.2 \text{ kJ mol}^{-1}$, $\Delta H_f^\circ(\text{CH}_2\text{CH} (\text{g})) \approx 271.7 \text{ kJ mol}^{-1}$, $\Delta H_f^\circ(\text{C}_2\text{H}_4(\text{g})) = 52.3 \text{ kJ mol}^{-1}$, $\Delta H_f^\circ(\text{CO}_2(\text{g})) = -393 \text{ kJ mol}^{-1}$.

Since C_2H_4 in the gaseous products of the decomposition of $CoAcr_2$ is not detected (see Table 5.5), it can be assumed that the disappearance of the radical $CH_2=CHCO\cdot$ occurs mainly in the reactions (5.21) and (5.24) in the investigated temperature range of the thermal decomposition of $CoAcr_2$. The radical formed by the reaction (5.21) can participate in the polymerization of the monomeric carboxylate and acrylic acid (5.26) and (5.27) followed by decarboxylation of $COOH$ and $Co(COO)_2$ fragments of the polymer product. It is also likely that these processes are preceded by the intramolecular opening of the double bond in R.



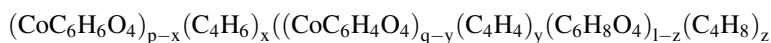
It is assumed that both linear and network structures of the formed polymer are possible:





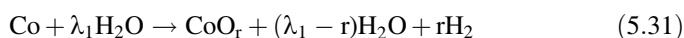
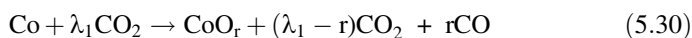
where $R^2 = \text{CH}_2=\text{CH}-\text{CH}=\text{CH}$.

After the transformation, the polymeric product (PP) can have the following composition:



However, with regard to the thermolysis of CoAcr_2 , which occurs at 623–653 K, it is difficult to expect that $(-\text{CH}_2-\underset{\text{COOH}}{\text{CH}}-)$ groups can be present in the PP, since the latter excludes the amount of CO_2 already at 473–488 K [126].

As already noted, in non-condensable at 88 K gaseous products of thermolysis, the main components are H_2 and CO , the appearance of which is most likely due to the oxidation of the metal produced by H_2O and CO_2 vapor:



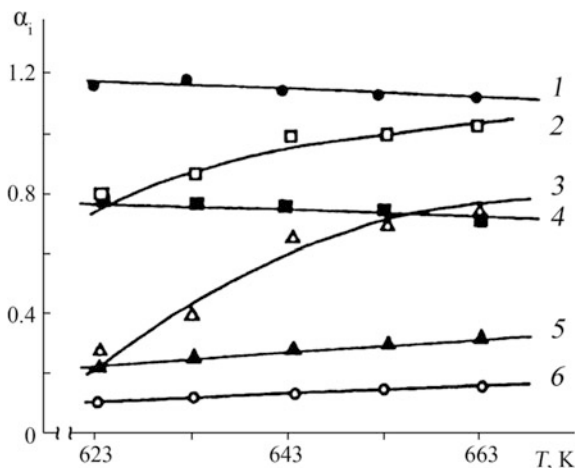
Based on data on gas evolution and weight loss of the sample as a result of the thermolysis CoAcr_2 , the following system of equations is constructed which relates the values of α_i of the decomposition products:

$$\begin{aligned} 6\alpha_{\text{C}_6\text{H}_8\text{O}_4} + 4\alpha_{\text{C}_4\text{H}_8} + 6\alpha_{\text{CoC}_6\text{H}_6\text{O}_4} + 4\alpha_{\text{C}_4\text{H}_6} + 6\alpha_{\text{CoC}_6\text{H}_4\text{O}_4} + 4\alpha_{\text{C}_4\text{H}_4} \\ = 6 - \alpha_{\text{CO}_2} - \alpha_{\text{CO}} - 3\alpha_{\text{C}_3\text{H}_4\text{O}_2} \\ 4\alpha_{\text{C}_6\text{H}_8\text{O}_4} + 4\alpha_{\text{C}_4\text{H}_8} + 3\alpha_{\text{CoC}_6\text{H}_6\text{O}_4} + 3\alpha_{\text{C}_4\text{H}_6} + 2\alpha_{\text{CoC}_6\text{H}_4\text{O}_4} + 2\alpha_{\text{C}_4\text{H}_4} \\ = 4 - \alpha_{\text{H}_2} - \alpha_{\text{H}_2\text{O}} - 2\alpha_{\text{C}_3\text{H}_4\text{O}_2} \\ 4\alpha_{\text{C}_6\text{H}_8\text{O}_4} + 4\alpha_{\text{CoC}_6\text{H}_6\text{O}_4} + 4\alpha_{\text{CoC}_6\text{H}_4\text{O}_4} \\ = 5 - 2\alpha_{\text{CO}_2} - \alpha_{\text{CO}} - 2\alpha_{\text{C}_3\text{H}_4\text{O}_2} - \alpha_{\text{H}_2\text{O}} - r\alpha_{\text{CoO}_r} \\ \alpha_{\text{CoO}_r} + \alpha_{\text{CoC}_6\text{H}_6\text{O}_4} + \alpha_{\text{CoC}_6\text{H}_4\text{O}_4} = 1 \\ \alpha_{\text{H}_2} + \alpha_{\text{CO}} = p = r\alpha_{\text{CoO}_r}, \alpha_{\text{H}_2}/\alpha_{\text{CO}} = \beta \\ \alpha_{\text{H}_2} + \alpha_{\text{H}_2\text{O}} = 1, \alpha_{\text{CO}} + 1.64\alpha_{\text{C}_3\text{H}_4\text{O}_2} = \alpha \end{aligned} \quad (5.32)$$

Here, $\alpha_{\text{CO}_2}, \alpha_{\text{H}_2} + \alpha_{\text{CO}} = p, \alpha = 1/44(\Delta m/n_o - 18 + 16p) - \alpha_{\text{CO}_2}$ is the experimentally determined values (Δm is the weight loss of the sample; n_o is the number of moles in the sample before the experiment).

Assuming that $\alpha_{\text{C}_6\text{H}_8\text{O}_4} = 0, \beta = 2$ (according to the determination of MS), the yield of thermolysis products was calculated and the various options for PP were

Fig. 5.40 Product yield at the thermolysis end of CoAc_2 : 1— α_{CO_2} ; 2— α_{CoO_r} ; 3— α_{Ac_r} ; 4— $\alpha_{\text{H}_2\text{O}}$; 5— α_{H_2} ; 6— α_{CO}



analyzed. Experimental data satisfy the polymer composition $(\text{CoC}_6\text{H}_6\text{O}_4)_{p-x}(\text{C}_4\text{H}_6)_x(\text{C}_4\text{H}_4)_y$.

At higher temperatures (Fig. 5.40), the values of α_{CO_2} , $\alpha_{\text{H}_2\text{O}}$ decrease somewhat, α_{CO} , α_{H_2} , $\alpha_{\text{C}_3\text{H}_4\text{O}_2}$, and α_{CoO_r} increase, and $\alpha_{\text{C}_3\text{H}_4\text{O}_2}$ increases rather strongly:

$$\alpha_{\text{C}_3\text{H}_4\text{O}_2} = 2.5 \cdot 10^8 \exp[-100/(RT)].$$

The ratio $[\text{O}]:[\text{Co}] = r$ is independent of T_{therm} and is 0.43 ± 0.03 , which corresponds to a mixture of metal and its oxide ($\text{Co} + \lambda\text{CoO}$), where λ is 0.75, 0.20, and 0.16 for CoO , Co_2O_3 , and Co_3O_4 , respectively.

The main source of CO_2 in the thermolysis of CoAc_2 appears to be decarboxylation processes, while additional reactions due to the appearance of C_2H_4 and CO_2 [reactions (5.20) and (5.23)] appear in the thermolysis of CuAc_2 .

The absence of polyacrylic acid fragments in PP indicates that the resulting acrylic acid from the reaction zone is faster than the start time of the polymerization.

Table 5.11 Composition of PP $(\text{CoC}_6\text{H}_6\text{O}_4)_{p-x}(\text{C}_4\text{H}_6)_x(\text{C}_4\text{H}_4)_y$ at various T_{therm}

PP composition	623 K	633 K	643 K	653 K	663 K
$\alpha_{\text{CoC}_6\text{H}_6\text{O}_4} = p - x$	0.22 (0.26)	0.16 (0.20)	0.03 (0.04)	0.02 (0.03)	0.01 (0.02)
$\alpha_{\text{C}_4\text{H}_6} = x$	0.51 (0.59)	0.45 (0.56)	0.31 (0.46)	0.28 (0.46)	0.26 (0.41)
$\alpha_{\text{C}_4\text{H}_4} = y$	0.13 (0.15)	0.19 (0.24)	0.33 (0.49)	0.31 (0.51)	0.36 (0.57)
$\alpha_{\text{CoC}_6\text{H}_6\text{O}_4} + \alpha_{\text{C}_4\text{H}_6} = p$	0.73 (0.85)	0.61 (0.76)	0.34 (0.50)	0.30 (0.49)	0.27 (0.43)
$\alpha_{\text{CoC}_6\text{H}_6\text{O}_4} + \alpha_{\text{C}_4\text{H}_6} + \alpha_{\text{C}_4\text{H}_4}$	0.86	0.80	0.67	0.61	0.63
$\alpha_{\text{C}_4\text{H}_6}/\alpha_{\text{CoC}_6\text{H}_6\text{O}_4} = \gamma$	2.32	2.81	10.3	14.0	26.0

Note In parenthesis, the proportion of fragment in the overall composition of the PP is given

The presence of C_4H_4 fragments in the composition of PP as a result of the decarboxylation of $CoC_6H_6O_4$ fragments seems to indicate, as in the case of other carboxylates studied, the low thermal stability of the metal carboxylate units. The ratio of the fragments $CoC_6H_6O_4$, C_4H_6 , and C_4H_4 in PP depends on T_{therm} (Table 5.11).

It is noteworthy that with increasing T_{therm} :

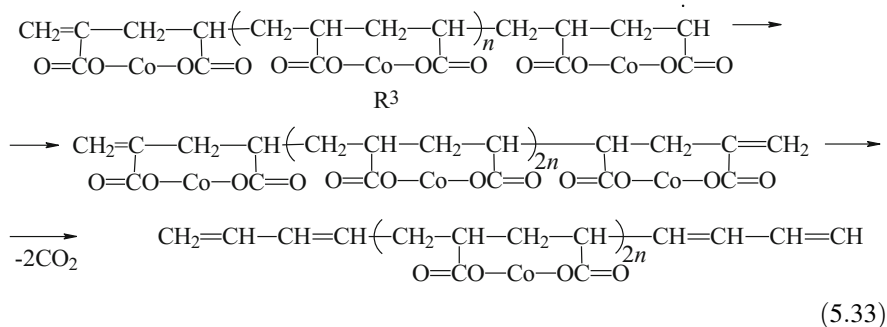
- The total yield of PP ($\alpha_{PP} = \alpha_{CoC_6H_6O_4} + \alpha_{C_4H_6} + \alpha_{C_4H_4}$) falls $\alpha_{PP} = 1.9 \times 10^{-3} \exp[34/(RT)]$.
- The yield $\alpha_{CoC_6H_6O_4}$, $\alpha_{C_4H_6}$ decreases and $\alpha_{C_4H_4}$ increases.
- The ratio $\omega = p/y$ decreases and $\alpha_{C_4H_6}/\alpha_{CoC_6H_6O_4} = \gamma$ increases.

$$\omega = 4.7 \times 10^{-16} \exp[192/(RT)]$$

$$\gamma = 7.1 \times 10^{19} \exp[-238/(RT)]$$

Considering that the fragments of $CoC_6H_4O_4$ (after decarboxylation of C_4H_4) form short polymer chains, a drop of ω can indicate a decrease in the length of chains of Co-polyacrylate in PP with an increase in T_{therm} . While the fragments of $CoC_6H_4O_4$ decarboxylate at $T_{therm} < 623$ K, the $CoC_6H_6O_4$ fragments at 623 K are fairly quite stable (their fraction is $\sim 30\%$), but even at 663 K they are practically absent in PP ($< 4\%$). Compare the effective activation energy of the gas evolution rate constants, and the activation parameter of the temperature dependence $\gamma(T)$ ($E_a = 238.3$ kJ mol $^{-1}$) shows that the decarboxylation reaction of polyacrylate fragments ($CoC_6H_4O_4$) is a rate-limiting step in the evolution of the gas.

Within the framework of the proposed thermolysis scheme, the appearance of fragments $(C_2H_2)_2$ (or C_4H_4) is possible only due to the recombination of polymer radicals R^3 formed from the R^1 radical to form PP and subsequent decarboxylation.



Assuming that the radicals R^3 formed are highly reactive, it can make the assumption that during the thermolysis of $CoAc_2$, the kinetic equilibrium concentration of the growing radicals is established in the reaction zone, and the amount of recombinant radicals R^3 at the end of thermolysis is close to the number of acrylic acid formed. As a result, the value of ω is the ratio of the polymer radical

growth rate (W_P) to the rate of PP formation (recombination rate R^3). Therefore, $W_P \approx W_{PP} \approx k_{PP}\omega[R^3]^2 \approx k_{PP}\omega\alpha_{CH_2CHCOOH}^2 = 0.26 \times 10^2 \exp[-8/(RT)] \cdot k_{PP}$, where k_{PP} is the rate constant of radical R^3 recombination. The yield of acrylic acid is equal to the ratio of the rate of formation of acrylic acid and the rate of consumption of $CoAc_2$:

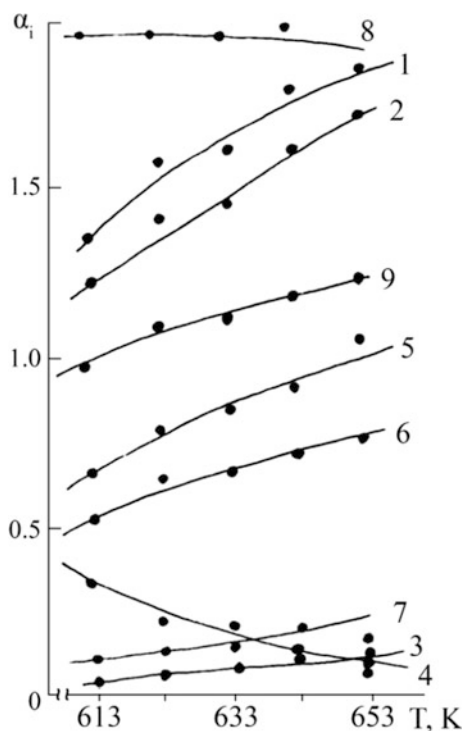
$$\alpha_{CH_2CHCOOH} = \frac{W_{CH_2CHCOOH}}{W_0 + W_{CH_2CHCOOH} + W} = \frac{W_0}{W_0 + W_P}, \quad (5.34)$$

where W_0 is the rate of $CH_2=CHCOO\cdot$ radical formation. Assuming that $W_P \gg W_0$, we get

$$\alpha_{CH_2CHCOOH} = \frac{W_0}{W_P} \approx \frac{W_0}{k_{PP}\omega\alpha_{CH_2CHCOOH}^2} \approx 6.5 \cdot 10^9 \exp[-109/(RT)] \cdot k_{PP} = 6.5 \cdot 10^9 \exp[-(E_a + 109)/(RT)] \cdot k_{PP}^0$$

The effective activation energy for the formation of the radical $CH_2=CHCOO\cdot \approx 109.0 \text{ kJ mol}^{-1}$. Thus, by increasing T_{therm} , the proportion of $CoAc_2$ monomer molecules, immediately subjected to thermolysis, increases with the part that

Fig. 5.41 Dependence of the product yield at the thermolysis end of $CoMal$ from at $T_{therm} (m_0/V) \times 10^3 = 2.04 \text{ g cm}^{-3}$:
 1— $\alpha_{\Sigma f}$, 2— $\alpha_{CO_2 f}$, 3— $\alpha_{H_2 f}$,
 $\alpha_{CO f}$, 4— $\alpha_{(=CHCOO)2f}$,
 5— $10\alpha_{(=CHCOOH)2f} \approx$
 $10\alpha_{(=C^-)2f}$, 6— $\alpha_{(=CH^-)2f}$,
 7— $\alpha_{CO_2 f}$, 8— $\alpha_{H_2O f}$,
 9— $(\Delta m/\pi_0) \times 10^{-2}$
 [48, 156]



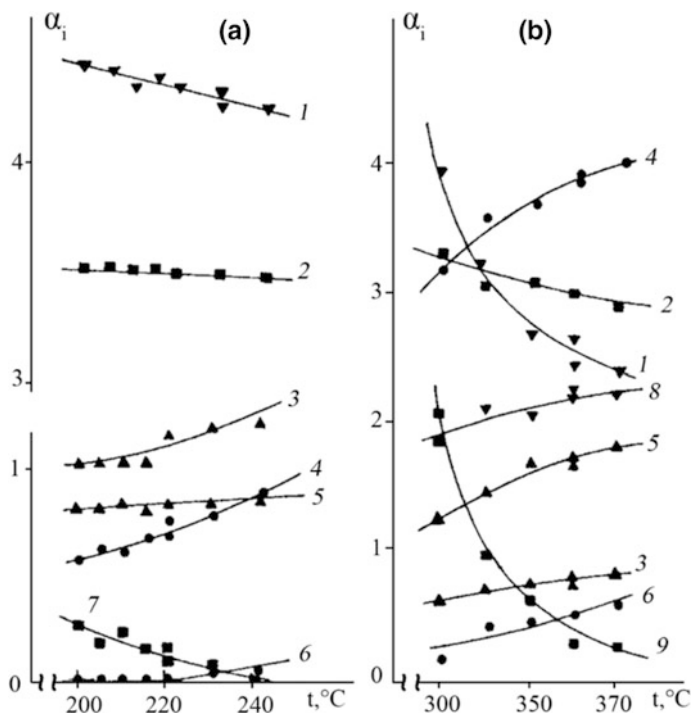


Fig. 5.42 Thermolysis product yield of FeAcAc_3 at 473–513 (a) and 603–643 K (b): $\alpha_{\text{CH}_2=\text{CH}} + \alpha_{\text{CH}_2\text{CH}}$ (1); $\alpha_{\text{H}_2\text{O}}$ (2); $2z(a), z(b)$ (3); α_{CO_2} (4); $\alpha_{\text{CH}_2=\text{CHCOOH}}\alpha_{\text{CHCHCOO}} + \alpha_{\text{CHCH}}$ (5); α_{H_2} (6); $\alpha_{\text{CH}_2\text{CH}}$ (8); $\alpha_{\text{CH}_2\text{CHCOO}}$ (9) [48, 156]

participates in the polymerization process. The composition of the PP and its evolution at higher temperatures show that the end groups of metal carboxylates are much more susceptible to decarboxylation than the $\text{CoC}_6\text{H}_6\text{O}_4$ fragments.

The value of γ , equal to the ratio of the amount of metal carboxylate groups in the polymer chain, including decarboxylated groups, to the number of end groups at the end of the gas evolution ..., decreases with increasing T_{therm} (Figs. 5.41 and 5.42) [48, 156].

The analysis of experimental data and calculation results show the following:

- (i) Polymerization and, accordingly, the formation of HAc and H_2Mal occur significantly at lower temperatures than the characteristic of the main release of gas. In the latter case, most of the condensable at T_{room} products appear at the early stages of thermolysis (the warm-up period in the sample).
- (ii) The formation of radicals ($\text{CH}_2=\text{CHCOO}\cdot$; $\cdot\text{OCOCH}=\text{CHCOO}$) leading to the initiation of polymerization depends on the thermal stability of the M–O bond in the desolvated monomer. For example, investigations of the thermolysis of cocrystallizates FeCoAc and Fe_2CoAc have shown that $\text{CH}_2=\text{CHCOO}\cdot$ radicals formed from Fe-containing cluster monomer that is

less thermally stable than the Co-containing monomer play the main role in initiating the copolymerization process. In this system, at a high T_{therm} , it is possible to exclude two Acr radicals on the dehydrated molecule $[\text{Fe}_3\text{O}(\text{Acr})_6](\text{OH})$.

- (iii) Decarboxylation is a key reaction in the gas evolution process. Thus, H-depleted terminal groups of metal carboxylate are much more susceptible to decarboxylation than the corresponding intrachain ones. This is consistent with the concept of increased energy saturation of terminal groups of long-chain polymers [180]. Thus, during the CuAcr_2 , CoAcr_2 , CoMal thermolysis, the decomposition of the terminal groups of the metal carboxylate already occurs during the test heated sample, the degree of decarboxylation of the intrachain groups of the metal carboxylate at the end of the gas evolution depends on the temperature, and only with high T_{therm} CO_2 release is achieved almost completely. The pattern is very important for the thermolysis of FeAcr_3 . The decomposition of terminal carboxylate groups is the main factor in the evolution of the gas at low temperatures (Fig. 5.42a) against the background of the thermal stability of the corresponding intrachain groups that decompose at high temperatures (Fig. 5.42b).
- (iv) In copolymers based on FeCoAcr and Fe_2CoAcr , unlike improved thermal stability of CoAcr_2 as compared to FeAcr_3 , intrachain and terminal Co-containing carboxylate fragments are thermally less stable than the corresponding Fe-containing ones prior to the elimination of Acr radical.
- (v) The ratio of γ is equal to the amount of metal carboxylate groups in the polymer chain, including decarboxylated groups, to the number of terminal groups at the end of the gas evolution [$\gamma = (\alpha_{\text{CH}_2\text{CHCOO}} + \alpha_{\text{CH}_2\text{CH}})/(\alpha_{\text{CHCHCOO}} + \alpha_{\text{CHCH}})$ for acrylates and $\gamma = (\alpha_{(=\text{CHCOO})_2} + \alpha_{(=\text{CH})_2})/(\alpha_{(=\text{CCOO})_2} + \alpha_{(=\text{C})_2})$ for malates] decreases with increasing T_{therm} . Thus, the level γ is in the range of 5.75 (473 K)/5.0 (513 K) and 2.64 (603 K)/1.4 (643 K) for FeAcr_3 , respectively, in areas with high temperature and low temperature and 12.9 (613 K)/9.2 (653 K) for CoMal . In the case of Fe–Co-cocrystallizates at the same $T_{\text{therm}} = 613\text{--}663$ K, the level of γ is slightly higher than FeAcr_3 and CoAcr_2 , and $\gamma = 7.7/5.0$ (FeCoAcr), 5.5/3.8 (Fe_2CoAcr). The value of 2γ can characterize the effective length of the formed polymer chain, and its change with increasing T_{therm} indicates a change in the ratio of the elimination rate and the reaction zone of the thermo-initiated radical ($\text{CH}_2=\text{CHCOO}\cdot$; $\cdot\text{OOCCH}=\text{CHCOO}$) and the rate of radical polymerization. This is most pronounced when thermolysis of CuAcr_2 and CoAcr_2 for a decrease in γ is also observed with the growth of T_{therm} . However, for CoAcr_2 at $T_{\text{therm}} > 643$ K and for CuAcr_2 in the entire studied T_{therm} range, the value of γ is less than unity. This is probably due to the high concentration of radicals initiating the polymerization in the transformation zone, in particular, to competition of polymerization initiation and radical recombination followed by decarboxylation of the recombination products.
- (vi) The composition of the metal-containing phase in solid products of the conversion of metal carboxylates at the end of the gas evolution depends on the thermolysis temperature (T_{term}). With increasing temperature, the

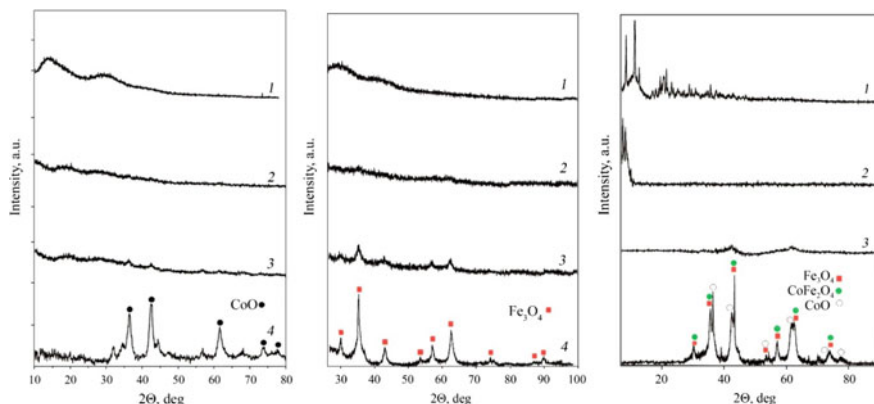


Fig. 5.43 (left) XRD patterns of CoAcCr_2 (1) and the thermolysis products at 643 K and different depths conversion: $\Delta m = 17.5\%$ (2), 26.2% (3), 48.6% (4); (middle) XRD patterns of FeAcCr_3 (1) and the thermolysis products at 663 K and different depths conversion: $\Delta m = 27.4\%$ (2), 33.3% (3), 55.5% (4); (right) XRD patterns of Fe_2CoAcCr (1) and the thermolysis products at 643 K and different depths conversion: $\Delta m = 25.1\%$ (2), 37.3% (3), 42.0% (4)

proportion of the metal oxide phase increases, which is associated with an increase in the rate of oxidation of the reactions (5.17) and (5.18), and is accompanied by an increase in the yield of CO and H_2 . In the case of CuAcCr_2 , a Cu is formed at low temperatures, but at $T_{\text{therm}} > 503$ K copper oxides are found ($z \leq 0.05$). After thermolysis of CoAcCr_2 , the value of z is 0.43 ± 0.03 , which corresponds to a composition of $0.25\text{Co} + 0.75\text{CoO}$ (Fig. 5.43, left). The proportion of the oxide phase in CoMal at the end of thermolysis is less than 15.0 mol% of the total metal content of the starting compound. In the thermolysis of FeAcCr_3 , the metal-containing products are a mixture of $\text{Fe} + \text{FeO}_z$ in T_{therm} over the entire range in the high-temperature region (see Fig. 5.27) $0 < z < 1$. Taking into account that $\text{FeO}_z = \text{Fe}_3\text{O}_4$, we can assume that the value of $\alpha_{\text{Fe}_3\text{O}_4}$ is close to the content Fe atom in Fe_3O_4 (Fig. 5.43, middle), determined by measuring the specific magnetization of solid-phase products. The value of z in MO_z in thermolysis products of FeCoAcCr and Fe_2CoAcCr (where $\text{M} = \text{Fe}_{1-a}\text{Co}_a$) also increases with T_{therm} . At the same time, the yield of ferrite $\alpha_{\text{CoFe}_2\text{O}_4} < 1$, which is lower than the maximum expected for FeCoAcCr and Fe_2CoAcCr (Fig. 5.43, right). The formation of CoFe_2O_4 occurs only in the final stages of thermolysis during decarboxylation of Fe-containing carboxylate groups, as evidenced by the dynamics of the change in the magnetic characteristics of solid-state products: a strong increase in χ_σ , σ_s , H_C due to the appearance of the CoFe_2O_4 phase during thermolysis.

Thus, the thermolysis of MCMs and the study of the properties of products indicate a combining of the synthesis of NPs with simultaneous stabilization of the obtained decarboxylated matrix of controlled thickness («one-pot» process).

References

1. A.D. Pomogailo, A.S. Rozenberg, I.E. Uflyand, *Nanochastitsy metallov v polimerakh (Metal Nanoparticles in Polymers)* (Khimiya, Moscow, 2000)
2. A.D. Pomogailo, G.I. Dzhardimalieva, V.N. Kestelman, *Macromolecular metal carboxylates and their nanocomposites* (Springer, Heidelberg, 2010)
3. G.I. Dzhardimalieva, A.D. Pomogailo, Russ. Chem. Rev. **77**, 259 (2008)
4. A.D. Pomogailo, G.I. Dzhardimalieva, *Monomeric and Polymeric Metal Carboxylates* (Fizmatlit, Moscow, 2009)
5. A.D. Pomogailo, A.S. Rozenberg, G.I. Dzhardimalieva, Russ. Chem. Rev. **80**, 257 (2011)
6. A.D. Pomogailo, G.I. Dzhardimalieva, *Nanostructured Materials Preparation via Condensation Ways* (Springer, Dordrecht, 2014)
7. A.D. Pomogailo, G.I. Dzhardimalieva, *Metallopolymeric Hybrid Nanocomposites* (Nauka, Moscow, 2015)
8. A.D. Pomogailo, G.I. Dzhardimalieva, Macromol. Symp. **317–318**, 198 (2012)
9. A.D. Pomogailo, A.S. Rozenberg, G.I. Dzhardimalieva, Ros. Khim. Zh. (Mendelev Chem. J.) **53**, 140 (2009)
10. A.S. Rozenberg, G.I. Dzhardimalieva, N.V. Chukanov, A.D. Pomogailo, Colloid J. **67**, 57 (2005)
11. A.D. Pomogailo, G.I. Dzhardimalieva, A.S. Rozenberg, D.N. Muraviev, J. Nanoparticle Res. **5**, 497 (2003)
12. A.S. Rozenberg, G.I. Dzhardimalieva, A.D. Pomogailo, Dokl. Akad. Nauk **356**, 66 (1997)
13. G.I. Dzhardimalieva, I.E. Uflyand, J. Inorg. Organomet. Polym. **26**, 1112 (2016)
14. G.I. Dzhardimalieva, I.E. Uflyand, J. Coord. Chem. **70**, 1468 (2017)
15. A.D. Pomogailo, I.E. Uflyand, *Makromolekulayrnye Metallokhelatny (Macromolecular Metal Chelates)* (Khimiya, Moscow, 1991)
16. G.I. Dzhardimalieva, A.D. Pomogailo, V.I. Ponomarev, L.O. Atovmyan, YuM Shulga, A.G. Starikov, Bull. Acad. Sci. USSR, Div. Chem. Sci. **37**, 1352 (1988)
17. M. Badea, R. Olar, D. Marinescu, G. Vasile, J. Therm. Anal. Calorim. **80**, 683 (2005)
18. M. Badea, R. Olar, D. Marinescu, V. Lazar, C. Chifiriuc, G. Vasile, J. Therm. Anal. Calorim. **97**, 781 (2009)
19. I.E. Uflyand, I.V. Kokoreva, A.S. Kuzharov, V.N. Sheinker, in *Advances in Surface Engineering—Processes, Fundamentals and Applications in Corrosion and Wear*, ed. by K.N. Strafford, P.K. Datta, J.S. Gray (Ellis Horwood Ltd., Sussex, Great Britain, 1990)
20. I.E. Uflyand, I.V. Kokoreva, A.G. Starikov, V.N. Sheinker, A.D. Pomogailo, React. Polym. **11**, 221 (1989)
21. I.E. Uflyand, I.V. Kokoreva, V.N. Sheinker, A.S. Kuzharov, Transit. Met. Chem. **17**, 360 (1992)
22. M. Badea, R. Olar, D. Marinescu, G. Vasile, J. Therm. Anal. Calorim. **85**, 285 (2006)
23. M. Badea, R. Olar, D. Marinescu, E. Segal, A. Rotaru, J. Therm. Anal. Calorim. **88**, 317 (2007)
24. M. Badea, R. Olar, D. Marinescu, G. Vasile, J. Therm. Anal. Calorim. **92**, 205 (2008)
25. M. Badea, R. Olar, D. Marinescu, G. Vasile, J. Therm. Anal. Calorim. **92**, 209 (2008)
26. M. Badea, I.D. Vlaicu, R. Olar, M. Constand, C. Bleotu, M.C. Chifiriuc, L. Marutescu, V. Lazar, M.N. Grecu, D. Marinescu, J. Therm. Anal. Calorim. **118**, 1119 (2014)
27. I.D. Vlaicu, M. Constand, R. Olar, D. Marinescu, M.N. Grecu, V. Lazar, M.C. Chifiriuc, M. Badea, J. Therm. Anal. Calorim. **113**, 1369 (2013)
28. R. Olar, I.D. Vlaicu, M.C. Chifiriuc, C. Bleotu, N. Stănică, G.V. Scăețeanu, L. Silvestro, C. Dulea, M. Badea, J. Therm. Anal. Calorim. **127**, 731 (2017)
29. T.-J. Cai, W.-J. Jiang, Z.-S. Peng, Y.-F. Long, Q. Deng, Z. Kristallogr, NCS **221**, 421 (2006)
30. T.-J. Cai, W.-J. Jiang, Z.-S. Peng, Y.-F. Long, Q. Deng, Z. Kristallogr, NCS **221**, 231 (2006)
31. N.V. Petrochenkova, B.V. Bukvetskii, A.G. Mirochnik, V.E. Karasev, Russ. J. Coord. Chem. **28**, 64 (2002)

32. B. Wu, W.-M. Lu, X.-M. Zheng, *Chin. J. Chem.* **20**, 846 (2002)
33. B. Wu, W. Lu, X. Zheng, *Transit. Met. Chem.* **28**, 323 (2003)
34. B. Wu, W. Lu, X. Zheng, *J. Coord. Chem.* **56**, 65 (2003)
35. Y. Lu, W. Lu, B. Wu, L. Wang, *J. Coord. Chem.* **53**, 15 (2001)
36. P.A. Vasiljev, *Zh. Neorg. Khim.* **30**, 1688 (1994)
37. P.A. Vasiljev, A.L. Ivanov, O.N. Rubacheva, A.N. Glebov, *Zh. Neorg. Khim.* **41**, 1747 (1996)
38. H.L. Wu, W. Ying, L. Pen, Y.C. Gao, K.B. Yu, *Synth. React. Inorg.; Met.-Org.; Nano-Met. Chem.* **34**, 1019 (2005)
39. H.L. Wu, Y.C. Gao, K.B. Yu, *Trans. Met. Chem.* **29**, 175 (2004)
40. H.L. Wu, Y.C. Gao, *J. Coord. Chem.* **59**, 137 (2006)
41. J.S. Brodtkin, B.M. Foxman, *Chem. Mater.* **8**, 242 (1996)
42. J.S. Brodtkin, B.M. Foxman, *J. Chem. Soc. Chem. Commun.* 1073 (1991)
43. M.J. Moloney, B.M. Foxman, *Inorg. Chim. Acta* **229**, 323 (1995)
44. L.I. Yudanov, V.A. Logvinenko, L.A. Sheludyakova, N.F. Yudanov, G.N. Chekhova, N.I. Alferova, V.I. Alekseev, P.P. Semyannikov, V.I. Lisoivan, *Russ. J. Inorg. Chem.* **53**, 1459 (2008)
45. N.P. Porollo, Z.A. Aliev, G.I. Dzhardimalieva, I.N. Ivleva, I.E. Uflyand, A.D. Pomogailo, N.S. Ovanesyan, *Russ. Chem. Bull.* **46**, 362 (1997)
46. N.P. Porollo, G.I. Dzhardimalieva, I.E. Uflyand, A.D. Pomogailo, *Russ. Khim. Zh. (Mendeleev Chem. J.)* **40**, 190 (1996)
47. G.I. Dzhardimalieva, A.D. Pomogailo, *Macromol. Symp.* **131**, 19 (1998)
48. A.S. Rozenberg, E.I. Aleksandrova, N.P. Ivleva, G.I. Dzhardimalieva, A.V. Raevskii, O.I. Kolesova, I.E. Uflyand, A.D. Pomogailo, *Russ. Chem. Bull.* **47**, 259 (1998)
49. A.S. Rozenberg, A.A. Rozenberg, A.V. Lankin et al., *Dokl. Akad. Nauk* **393**, 325 (2003)
50. S. Singh, A. Singh, B.C. Yadav, P. Tandon, A. Shukla, V.A. Shershnev, G.I. Dzhardimalieva, N.D. Golubeva, A.D. Pomogailo, *Sens. Actuat. B, Chem.* **192**, 503 (2014)
51. V.A. Shershnev, G.I. Dzhardimalieva, D.P. Kiryuhin, V.A. Zhorin, A.D. Pomogailo, *Russ. Chem. Bull.* **62**, 1649 (2013)
52. K.A. Brown, D.P. Martin, R.L. La Duca, *Cryst. Eng. Comm.* **10**, 1305 (2008)
53. X. Xu, X. Zhang, X. Liu, T. Sun, E. Wang, *Cryst. Growth Des.* **10**, 2272 (2010)
54. M.-S. Wang, G.-C. Guo, W.-Q. Zou, W.-W. Zhou, Z.-J. Zhang, G. Xu, J.-S. Huang, *Angew. Chem. Int. Ed.* **47**, 3565 (2008)
55. A. Rana, S.K. Jana, S. Datta, R.J. Butcher, E. Zangrando, S. Dalai, *J. Solid State Chem.* **207**, 61 (2013)
56. P. Thuéry, *Eur. J. Inorg. Chem.* 4563 (2013)
57. C.-B. Liu, M.-X. Yu, X.-J. Zheng, L.-P. Jin, S. Gao, S.-Z. Lu, *Inorg. Chim. Acta* **358**, 2687 (2005)
58. A.C. Tella, S.O. Owalude, P.A. Ajibade, N. Simon, S.J. Olatunji, M.S.M. Abdelbaky, S. Garcia-Granda, *J. Mol. Struct.* **1125**, 570 (2016)
59. V.A. Logvinenko, L.I. Yudanov, N.F. Yudanov, G.N. Chekhova, *J. Therm. Anal. Calorim.* **74**, 395 (2003)
60. L.I. Yudanov, V.A. Logvinenko, N.F. Yudanov, N.A. Rudina, A.V. Ishchenko, P.P. Semyannikov, L.A. Sheludyakova, N.I. Alferova, *Russ. J. Coord. Chem.* **39**, 415 (2013)
61. L.I. Yudanov, V.A. Logvinenko, L.A. Sheludyakova, N.F. Yudanov, P.P. Semyannikov, S.I. Kozhemyachenko, I.V. Korol'kov, N.A. Rudina, A.V. Ishchenko, *Russ. J. Inorg. Chem.* **59**, 1180 (2014)
62. S.A. Semenov, D.V. Drobot, VYu. Musatova, A.S. Pronin, A.D. Pomogailo, G.I. Dzhardimalieva, V.I. Popenko, *Russ. J. Inorg. Chem.* **60**, 897 (2015)
63. S.A. Semenov, D.V. Drobot, VYu. Musatova, A.S. Pronin, A.D. Pomogailo, G.I. Dzhardimalieva, *Russ. J. Inorg. Chem.* **61**, 59 (2016)
64. X. Zhang, *J. Mol. Struct.* **1015**, 12 (2012)
65. J. Kang, K.M. Ok, J. Do, *Z. Kristallogr. NCS* **231**, 553 (2016)

66. YuM Shulga, O.S. Roshchupkina, G.I. Dzhardimalieva, I.V. Chernushchevich, A.F. Dodonov, YuV Baldokhin, P.Ya. Kolotyrkin, A.S. Rozenberg, A.D. Pomogailo, *Russ. Chem. Bull.* **42**, 1661 (1993)
67. YuM Shulga, I.V. Chernushchevich, G.I. Dzhardimalieva, O.S. Roshchupkina, A.F. Dodonov, A.D. Pomogailo, *Russ. Chem. Bull.* **43**, 983 (1994)
68. G.I. Dzhardimalieva, A.D. Pomogailo, in *Metal-Containing Polymeric Materials*, ed. by C.U. Pittman, Jr., Ch.E. Carraher, Jr., M. Zeldin, J.E. Sheats, B.M. Culbertson (Plenum Press, New York, 1998), pp. 63–80
69. G.I. Dzhardimalieva, A.D. Pomogailo, *Macromol. Symp.* **186**, 147 (2002)
70. S.P. Gubin (ed.), *Magnetic Nanoparticles* (Wiley-VCH, Verlag, 2009)
71. I. Stein, U. Ruschewitz, *Z. Anorg. Allg. Chem.* **636**, 400 (2010)
72. F. Hohn, I. Pantenburg, U. Ruschewitz, *Chem. Eur. J.* **8**, 4536 (2002)
73. A. Askarnejad, A. Morsali, *J. Coord. Chem.* **60**, 1903 (2007)
74. R. Ahlers, U. Ruschewitz, *Solid State Sci.* **11**, 1058 (2009)
75. A. Schuy, I. Stein, U. Ruschewitz, *Z. Anorg. Allg. Chem.* **636**, 1026 (2010)
76. Ch. Robl, S. Hentschel, *Z. Anorg. Allg. Chem.* **591**, 188 (1990)
77. Ch. Robl, S. Hentschel, *Z. Anorg. Allg. Chem.* **596**, 149 (1991)
78. S. Busch, I. Stein, U. Ruschewitz, *Z. Anorg. Allg. Chem.* **638**, 2098 (2012)
79. H. Billetter, I. Pantenburg, U. Ruschewitz, *Z. Naturforsch.* **59b**, 903 (2004)
80. A. Michaelides, S. Skoulika, *Cryst. Growth Des.* **5**, 529 (2005)
81. C. Serre, J. Marrot, G. Férey, *Inorg. Chem.* **44**, 654 (2005)
82. I. Stein, M. Speldrich, H. Schilder, H. Lueken, U. Ruschewitz, *Z. Anorg. Allg. Chem.* **633**, 1382 (2007)
83. S. Khullar, S.K. Mandal, *RSC Adv.* **4**, 39204 (2014)
84. J.-L. Lin, H.-L. Zhu, J. Zhang, J.-M. Zhao, Y.-Q. Zheng, *J. Mol. Struct.* **995**, 91 (2011)
85. D. Hermann, C. Näther, U. Ruschewitz, *Solid State Sci.* **13**, 1096 (2011)
86. A. Schuy, H. Billetter, F. Hohn, I. Pantenburg, U. Ruschewitz, *Z. Kristallogr.* **220**, 250 (2005)
87. S. Khullar, S.K. Mandal, *Dalton Trans.* **44**, 1203 (2015)
88. Ch. Robl, S. Hentschel, *Z. Naturforsch.* **45b**, 1499 (1990)
89. R.W. Seidel, R. Goddard, V. Gramm, U. Ruschewitz, *Z. Naturforsch.* **69b**, 277 (2014)
90. M.X. Li, M. Shao, H. Dai, B.L. An, W.C. Lu, Y. Zhu, C.X. Du, *Chin. Chem. Lett.* **16**, 1405 (2005)
91. M. Shao, M.X. Li, H. Dai, W.C. Lu, B.L. An, *J. Mol. Struct.* **829**, 155 (2007)
92. I. Pantenburg, U. Ruschewitz, *Z. Anorg. Allg. Chem.* **628**, 1697 (2002)
93. S. Skoulika, P. Dallas, M.G. Siskos, Y. Deligiannakis, A. Michaelides, *Chem. Mater.* **15**, 4576 (2003)
94. U. Ruschewitz, I. Pantenburg, *Acta Crystallogr.* **C58**, 483 (2002)
95. J. Kim, B. Chen, T.M. Reineke, H. Li, M. Eddaoudi, D.B. Moler, M. O’Keeffe, O.M. Yaghi, *J. Am. Chem. Soc.* **123**, 8239 (2001)
96. G. Zhang, Q. Wang, Y. Qian, G. Yang, J.S. Ma, *J. Mol. Struct.* **796**, 187 (2006)
97. D.J. Tranchemontagne, J.R. Hunt, O.M. Yaghi, *Tetrahedron* **64**, 8553 (2008)
98. S. Khullar, S.K. Mandal, *Cryst. Growth Des.* **13**, 3116 (2013)
99. H.-L. Zhu, J.-L. Lin, J.-Y. Liu, Y.-Q. Zheng, *Synth. React. Inorg. Metal-org. Nano-Metal Chem.* **43**, 1190 (2013)
100. V.K. Gramm, I. Stein, E. Riesen, U. Ruschewitz, *Z. Anorg. Allg. Chem.* **642**, 1350 (2016)
101. N.N. Volkova, G.I. Dzhardimalieva, B.E. Krisyuk, N.V. Chukanov, V.A. Shershnev, G.V. Shilov, *Russ. Chem. Bull.* **65**, 2025 (2016)
102. I. Stein, U. Ruschewitz, *Acta Crystallogr. Sect. E* **61**, m2680 (2005)
103. P. Dallas, A.B. Bourlinos, P. Komninou, M. Karakassides, D. Niarchos, *Nanoscale Res. Lett.* **4**, 1358 (2009)
104. A.A. Berlin, G.M. Trofimova, L.K. Pakhomova, E.V. Prut, J.M. Barkalov, S.S. Kuzmina, N.S. Enikolopyan, V.I. Goldanskiĭ, *J. Polym. Sci. Part C: Polym. Symp.* **16**, 2323 (1967)

105. Z. Liu, I. Schmidt, P. Thamyongkit, R.S. Loewe, D. Syomin, J.R. Diers, Q. Zhao, V. Misra, J.S. Lindsey, D.F. Bocian, *Chem. Mater.* **17**, 3728 (2005)
106. E. Otsuki, H. Sato, A. Kawakami, H. Taka, H. Kita, H. Usui, *Thin Solid Films* **518**, 703 (2009)
107. J. Tsuchida, Y. Saito, S. Sato, U. Yuki, S. Inayama, Y. Tatewaki, S. Okada, A. Shindo, C. Mikura, K. Fushihara, M. Yamada, *Polym. J.* **45**, 1007 (2013)
108. S. Nakashima, Y. Tatewaki, S. Okada, H. Nagakura, A. Shindo, C. Mikura, K. Shiga, K. Terakawa, M. Yamada, *Polym. J.* **48**, 855 (2016)
109. B.S. Randhawa, K.J. Sweetey, M. Kaur, J.M. Greneche, *J. Therm. Anal. Calorim.* **75**, 101 (2004)
110. Z. Wojtczak, A. Gronowski, *J. Therm. Anal.* **36**, 2357 (1990)
111. A.S. Rozenberg, G.I. Dzhardimalieva, A.D. Pomogailo, *Polym. Adv. Technol.* **9**, 527 (1998)
112. J. Skupiska, H. Wilezura, H. Boniuk, *J. Therm. Anal.* **31**, 1017 (1986)
113. P.A. Vasil'ev, A.L. Ivanov, A.N. Glebov, *Zh. Obshch. Khim.* **68**, 535 (1998)
114. J.M. Filipović, L. Katsicas, I.G. Popović, S.L. Velickovic, T.A. Djakov, D.M. Petrovic-Djakov, *J. Therm. Anal.* **49**, 335 (1997)
115. I.C. McNeill, A. Alston, *Angew. Makromol. Chem.* **261/262**, 157 (1998)
116. J. Zhang, H. Zhang, J. Pang, L. Li, S. Wang, M. Liu, *RSC Adv.* **6**, 104416 (2016)
117. Y. Nie, *J. Polym. Res.* **22**, 2 (2015)
118. A. Shokrzadeh, G. Naderi, G.R. Bakhshandeh, M.J. Zohuriaan-Mehr, E. Esmizadeh, *J. Composite Mater.* **48**, 471 (2014)
119. W. Wu, Y. Zhai, Y. Zhang, W. Ren, *Composites. Part B: Eng.* **56**, 497 (2014)
120. W. Guo, Z. Shen, B. Guo, L. Zhang, D. Jia, *Polymer* **55**, 4324 (2014)
121. S. Wen, Y. Zhou, L. Yao, L. Zhang, T.W. Chan, Y. Liang, L. Liu, *Thermochim. Acta* **571**, 15 (2013)
122. L. Yao, S. Wen, X. Duan, X. Hu, M. Che, W. Jing, H. Liu, L. Liu, *J. Rare Earths* **31**, 1130 (2013)
123. C. Xu, Y. Chen, L. Cao, Y. Wang, X. Zeng, *J. Macromol. Sci. Part B* **52**, 319 (2013)
124. C. Xu, Y. Chen, Y. Wang, X. Zeng, *J. Appl. Polym. Sci.* **128**, 2350 (2013)
125. L. Wang, F. Lang, F. Du, Z. Wang, *J. Macromol. Sci. Part B* **52**, 178 (2013)
126. S. Li, F. Lang, Z. Wang, *Polym.-Plast. Techn. Eng.* **52**, 683 (2013)
127. C. Xu, Y. Chen, X. Zeng, *J. Appl. Polym. Sci.* **125**, 2449 (2012)
128. Z. Wei, Y. Lu, S. Yan, Y. Meng, L. Zhang, *J. Appl. Polym. Sci.* **124**, 288 (2012)
129. C. Xu, Y. Chen, L. Cao, X. Zeng, *Polym. Compos.* **33**, 1244 (2012)
130. U. Basuli, G.B. Lee, S.Y. Jang, J. Oh, J.H. Lee, S.C. Kim, N.D. Jeon, Y.I. Huh, C. Nah, *Elastomers Compos.* **47**, 297 (2012)
131. H.D. Chae, U. Basuli, J.H. Lee, C.I. Lim, R.H. Lee, S.C. Kim, N.D. Jeon, C. Nah, *Polym. Compos.* **33**, 1141 (2012)
132. Y. Chen, C. Xu, *J. Macromol. Sci. Part B* **51**, 1384 (2012)
133. C. Xu, Y. Chen, J. Huang, X. Zeng, J. Ding, *J. Appl. Polym. Sci.* **124**, 2240 (2012)
134. Y. Chen, C. Xu, Y. Wang, *Polym. Compos.* **33**, 967 (2012)
135. Y. Lu, L. Lu, D. Shen, C. Yang, L. Zharg, *Polym. Int.* **53**, 802 (2004)
136. R. Anbarasan, V. Dhanalakshmi, K. Rajasulochana, M. Sudha, T. Jayalakshmi, M. Anusuya, *J. Appl. Polym. Sci.* **115**, 2582 (2010)
137. J.A. Pojman, Frontal Polymerization, in *Polymer Science: A Comprehensive Reference*, Vol. 4, Chap. 4.38, ed. by K. Matyjaszewski, M. Möller (Elsevier, Amsterdam, 2012), pp. 957–980
138. P.M. Goldfeder, V.A. Volpert, V.M. Ilyashenko, A. Khan, J.A. Pojman, S.E. Solovyov, *J. Phys. Chem. B.* **101**, 3474 (1997)
139. A.D. Pomogailo, G.I. Dzhardimalieva, *Polym. Sci. A* **46**, 250 (2004)
140. L.P. Kholpanov, S.E. Zakiev, A.D. Pomogailo, *Polym. Sci. A* **48**, 11 (2006)
141. E. Sowka, M. Leonowicz, J. Kazmierczak, A. Slawska-Waniewska, A.D. Pomogailo, G.I. Dzhardimalieva, *Phys. B* **384**, 282 (2006)
142. A.D. Pomogailo, *Inorg. Mater.* **41**, S47 (2005)

143. A.D. Pomogailo, *Colloid J.* **67**, 658 (2005)
144. A. Tredici, R. Pecchini, M. Morbidelli, *J. Polym. Sci. A: Polym. Chem.* **36**, 1117 (1998)
145. A.D. Pomogailo, V.S. Savostyanov, *Synthesis and Polymerization of Metal-Containing Monomers* (CRC, Boca Raton, FL, 1994)
146. S. Singh, B.C. Yadav, P. Tandon, M. Singh, A. Shukla, G.I. Dzhardimalieva, S.I. Pomogailo, N.D. Golubeva, A.D. Pomogailo, *Sens. Actuators, B* **166–167**, 281 (2012)
147. S.E. Zakiev, G.I. Dzhardimalieva, A.D. Pomogailo, *Polym. Sci. Ser. B* **59**, 210 (2017)
148. A. Gronowski, Z. Wojtczak, *J. Therm. Anal.* **26**, 233 (1983)
149. E.I. Aleksandrova, G.I. Dzhardimalieva, A.S. Rozenberg, A.D. Pomogailo, *Russ. Chem. Bull.* **42**, 259 (1993)
150. E.I. Aleksandrova, G.I. Dzhardimalieva, A.S. Rozenberg, A.D. Pomogailo, *Russ. Chem. Bull.* **42**, 264 (1993)
151. G.I. Dzhardimalieva, S.A. Semenov, E.I. Knerelman, G.I. Davydova, K.A. Kydralieva, *J. Inorg. Organomet. Polym.* **26**, 1441 (2016)
152. A.S. Rozenberg, E.I. Aleksandrova, G.I. Dzhardimalieva, A.N. Titkov, A.D. Pomogailo, *Russ. Chem. Bull.* **42**, 1666 (1993)
153. A.S. Rozenberg, E.I. Aleksandrova, G.I. Dzhardimalieva, N.V. Kiryakov, P.E. Chizhov, V.I. Petinov, A.D. Pomogailo, *Russ. Chem. Bull.* **44**, 858 (1995)
154. A.D. Pomogailo, A.S. Rozenberg, G.I. Dzhardimalieva, A.M. Bochkin, S.I. Pomogailo, N.D. Golubeva, V.M. Grischenko, *Neorg. Mater.* **42**, 164 (2006)
155. A.D. Pomogailo, G.I. Dzhardimalieva, A.S. Rozenberg, V.N. Kestelman, *J. Thermoplast. Compos. Mater.* **20**, 151 (2007)
156. A.T. Shuvaev, A.S. Rozenberg, G.I. Dzhardimalieva, N.P. Ivleva, V.G. Vlasenko, T.I. Nedoseikina, T.A. Lubeznova, I.E. Uflyand, A.D. Pomogailo, *Russ. Chem. Bull.* **47**, 1460 (1998)
157. Y.Y. Wang, Q. Shi, Q.Z. Shi, Y.C. Gao, X. Hou, *Polyhedron* **19**, 891 (2000)
158. Y.Y. Wang, Q. Shi, Q.Z. Shi, *Acta Chim. Sinica* **58**, 675 (2000)
159. A.D. Pomogailo, G.I. Dzhardimalieva, A.S. Rozenberg, V.A. Shershnev, M. Leonovich, *Russ. Chem. Bull.* **60**, 1476 (2011)
160. I.A. Chernov, G.F. Novikov, G.I. Dzhardimalieva, A.D. Pomogailo, *Polym. Sci. Ser. A* **49**, 267 (2007)
161. M. Zulfiqar, R. Hussain, S. Zulfiqar, D. Mohammad, I.C. McNeill, *Polym. Degrad. Stab.* **51**, 167 (1996)
162. L.I. Yudanova, V.A. Logvinenko, L.A. Sheludyakova, A.V. Ishchenko, N.A. Rudina, *Russ. J. Phys. Chem. A* **91**, 136 (2017)
163. B.S. Randhawa, M. Kaur, *J. Therm. Anal. Calorim.* **89**, 251 (2007)
164. P.S. Bassi, B.S. Randhawa, C.M. Khajuria, S. Kaur, *J. Therm. Anal.* **32**, 569 (1987)
165. A.A. El-Bellihi, *J. Therm. Anal.* **41**, 191 (1994)
166. A.D. Pomogailo, V.G. Vlasenko, A.T. Shuvaev, A.S. Rozenberg, G.I. Dzhardimalieva, *Coll. J.* **64**, 472 (2002)
167. V.P. Roshchupkin, B.V. Ozerkovskii, Z.A. Karapetyan, *Vysokomol. Soedin. Ser. A* **19**, 2239 (1977)
168. B.S. Selenova, G.I. Dzhardimalieva, M.V. Tsikalova, et al., *Izv. Akad. Nauk, Ser. Khim.* 500 (1993)
169. A.D. Pomogailo, A.S. Rosenberg, G.I. Dzhardimalieva, *Solid State Phenom.* **94**, 313 (2003)
170. G.I. Dzhardimalieva, A.D. Pomogailo, S.P. Davtyan, V.I. Ponomarev, *Izv. Akad. Nauk. Ser. Khim.* 1531 (1988)
171. G.I. Dzhardimalieva, A.D. Pomogailo, N.D. Golubeva, S.I. Pomogailo, O.S. Roshchupkina, G.F. Novikov, A.S. Rozenberg, M. Leonowicz, *Colloid J.* **73**, 458 (2011)
172. A.D. Pomogailo, G.I. Dzhardimalieva, A.S. Rosenberg, *Acta Phys. Polonica A* **102**, 135 (2002)
173. VYu. Musatova, S.A. Semenov, D.V. Drobot, A.S. Pronin, A.D. Pomogailo, G.I. Dzhardimalieva, V.I. Popenko, *Russ. J. Inorg. Chem.* **61**, 1111 (2016)

174. V.A. Logvinenko, N.F. Yudanov, G.N. Chekhova, Y.G. Kriger, L.I. Yudanova, N.A. Rudina, *Chem. Sustain. Dev.* **8**, 171 (2000)
175. L.I. Yudanova, V.A. Logvinenko, N.F. Yudanov, N.A. Rudina, A.V. Ishchenko, P.P. Semyannikov, L.A. Sheludyakova, N.I. Alferova, A.I. Romanenko, O.B. Anikeeva, *Inorg. Mater.* **49**, 1055 (2013)
176. M.A. Mohamed, S.A. Halawy, *J. Anal. Appl. Pyrol.* **65**, 287 (2002)
177. K. Kalpanadevi, C.R. Sinduja, R. Manimekalai, *ISRN Inorg. Chem.* **2013**, (Article ID 823040) (2013)
178. V.A. Shershnev, G.V. Shilov, G.I. Dzhardimalieva, A.D. Pomogailo, M. Izydorzak, M. Leonowicz, *Macromol. Symp.* **317–318**, 180 (2012)
179. H.Y. Shi, B. Deng, S.L. Zhong, L. Wang, A.W. Xu, *J. Mater. Chem.* **21**, 12309 (2011)
180. N.V. Chukanov, I.V. Kumpanenko, V.V. Losev, N.G. Entelis, *Dokl. Akad. Nauk* **261**, 135 (1981)

Chapter 6

Thermolysis of Metal Chelates in Polymer Matrices



In recent years, nanostructured materials (nanocomposites), consisting of a polymer matrix (thermoplastic, thermosets or elastomers), filled with small amounts of metal or metal oxide NPs, have attracted the considerable attention of researchers [1–7]. Organic matrix, i.e., polymer, forms the basis of such nanocomposites, while NPs are dispersed in the polymer matrix and have a significant and unique influence on its macroscopic properties and are also able to interact with the polymer matrix at the molecular level [8–10]. It is known that the combination of the advantages of simple processing and structural flexibility of polymers with optical properties and stability provided by inorganic material has strong synergistic effects [11, 12]. Nanostructured materials offer many applications because of their diverse physical and chemical properties. They can be adapted in a wide range, using various combinations of materials, morphology, and nanostructure. In particular, nanocomposites attract great interest in the materials of photovoltaic-cell materials, where the combined absorption band of both materials can also collect sunlight better [13–15]. Such devices are known as potential candidates for inexpensive and efficient conversion of solar energy and constitute the so-called solar cells of the third generation. In this new class of photovoltaic devices, the inclusion of oxide and metallic NPs were successfully achieved. Hybrid polymer/NPs devices offer a number of advantages over more traditional polymer/fullerene systems. However, the current efficiency of such devices is much lower than for polymer/fullerene devices. This is mainly due to the fact that achieving a controlled continuous percolation network and a well-defined interface between the NPs and the polymer matrix remains a challenge.

It should be noted that iron oxide NPs localized in the polymer matrix exhibits unique superparamagnetic properties and can be used in various fields of biotechnology, including purification of proteins, viruses, nucleic acids, in biosensors, and immobilization of enzymes. [16–21]. Targeting in vivo of Au NPs, PEG has been recommended as a capping material used to provide Au NP with the required stealth against the reticuloendothelial system, which was an important component of the immune system consisting of phagocytic cells [22]. PEG-coated

Au NPs were successful as image contrast and treatment agents for in vivo targeting [23, 24]. In order for PEG–Au NPs to have practical application in the field as a biomedical agent, they need a synthetic pathway with the possibility of mass production [25]. It is important that the agglomeration of Au NPs significantly alters biological traits and the toxicology of Au NPs as well as limits their application in several areas of human activity, especially in the areas of biomedicine [26–30]. Therefore, PEG is used as an agent for coating Au NPs to increase their stability and further interaction due to its good solubility, biocompatibility, and antifouling property [31–34]. In addition, PEG will help in the protection of colloids that will be absorbed on the surface of Au NPs, which will lead to the separation of colloids from each other and to preventing their agglomeration [35–37].

The properties of nanocomposites depend on the type of polymer matrix, the nature of NPs, their shape, size, and concentration, as well as the intensity of interfacial interactions between the polymer matrix and NPs. The choice of polymer matrix is usually determined by the mechanical and thermal behavior of the polymer, hydrophobic/hydrophilic balance, chemical stability, biocompatibility, optical and/or electronic properties, and chemical functionality (i.e., solvation, template effect, wettability.). It is important that even with extremely low NP loads in polymer matrices, there is a significant change in the properties of the polymer matrix, such as mechanical, chemical, barrier, thermal, electrophysical, magnetic, optical, catalytic, and other [38–42]. It should be noted that the thermal stability of the polymer usually determines its upper limit of operating temperature in the environment, which is related to the kinetic parameters: initial temperature and destruction rate [43]. Knowledge of these parameters is necessary for the application and storage of polymers [44]. Ways thermolysis of polymers is universal [45–50]. In addition, thermolysis of polymers is a complex process involving a number of chemical reactions: destruction, cross-linking, transformation of functional groups, and intramolecular rearrangements. The chemical or physical introduction of metal-containing particles is sometimes used to stabilize the polymer and reduce its reactivity, which allows the production of new materials and composite systems. It should be noted that the introduction of certain types of NPs, such as Ag, Au, and TiO₂, can induce or improve the antimicrobial efficacy of the polymer matrix [51–57]. In the thermolysis stage, various additives can be incorporated into polymers, including those containing a metal, that affect the thermolysis mechanism and lead to a variety of interesting products, for example, polymer derivatives of ceramics. Thus, by thermolysis of polyvinyl alcohol (PVA), a polymer with conjugated bonds like polyacetylene is obtained, and when additives such as lead and bismuth formates are added in the PVA, a doped conjugated polymer is formed [58]. Metallic NPs formed to promote the transfer of electrons between polymer chains and, consequently, increase the conductivity of the polymer. One of the most interesting properties of polymers, which can be influenced by the presence of NPs, is the glass transition temperature (T_g), since changes in T_g correlate with changes in the dynamics of polymer chains and regimes of chain relaxation. The value of T_g depends on the nature and molecular weight of the polymer, the NP content, the thermal history of nanocomposites, interparticle distances, and mainly on the

interfacial interaction between the polymer matrix and NPs. This interaction may be attractive (which leads to a decrease in the dynamics of the polymer chains and an increase in the value of T_g) [59–61] or repulsion (leading to an acceleration in the dynamics of the polymer chains and a decrease in the T_g value) [62–65]. If these interphase interactions are very weak, then NPs practically do not affect the dynamics of polymer chains and the value of T_g will not change [66–69]. The presence of NPs can also have a certain effect on the molecular weight and PDI of the polymer matrix, the degree of the crystallinity of the polymer, etc. [69–73].

The main task in the preparation of nanocomposites is to prevent the aggregation of NPs and the formation of large agglomerates or unwanted assemblies that can arise due to the high interfacial reactivity of NPs and their high surface tension energy. In addition, most polymers are hydrophobic, whereas the NP surface is usually hydrophilic, which leads to NP incompatibility with the polymer, lack of uniform distribution within the polymer matrix, aggregation and extended phase separation between the NPs and the polymer matrix. As a result, nanocomposites will not show the expected improvement in properties. Therefore, effective stabilization and uniform distribution of NPs in the polymer matrix is necessary for polymer nanotechnology to prevent the aggregation of NPs before, during and after their production or to achieve deagglomeration.

There are two choices for the introduction of metal NPs into a polymer matrix: *ex situ* and *in situ* (Fig. 6.1) [74, 75].

In the *classical ex situ approach* (in the second moment), inorganic NPs are synthesized in a first, separate stage, after which they are purified and usually subjected to a ligand exchange reaction. Then they are mixed with the polymer in solution or in a melt or by grinding [38–40, 61–63, 76–79]. Typically, NPs are synthesized using organic capping ligands to stabilize their size and prevent aggregation [80–83]. The starting ligands are usually exchanged for shorter ones, such as pyridine, *n*-butylamine and *tert*-butylthiol [81, 84, 85]. This approach, moreover, requires the use of conventional solvents for NPs and polymer, which can adversely affect the solubility of nanocrystals and the orientation of the polymer chains. Such an approach can also lead to a disruption of the uniformity of the surface quality of the sample [86].

In the *in situ approach*, NPs are formed directly from precursors in the polymer matrix through the thermolysis of the corresponding metal chelate or its conversion products [60, 64, 66–73, 87–94]. As a rule, the polymer matrix affects the rate of decomposition of the thermolyzed compound. However, at low polymer concentrations, when the viscosity of the system is low, the kinetics of the thermolysis of the precursor in the polymer solution and in the solution of the free polymer is the same. To overcome the undesirable effect of ligands, the synthesis of uncapped NPs within the polymer matrix is carried out without the use of surfactants or ligands [90, 91, 95]. Therefore, it is not necessary to exchange the surface ligand during the growth and nucleation of the NPs, since the polymer itself controls the growth of NPs and thus eliminates the need for additional capping agents. The change in the time and temperature of thermolysis of the molecular precursor can control the size of the NP produced. During the reaction, the polymer acts as a capping agent and prevents the extensive growth of the NPs. It should be specially emphasized that in

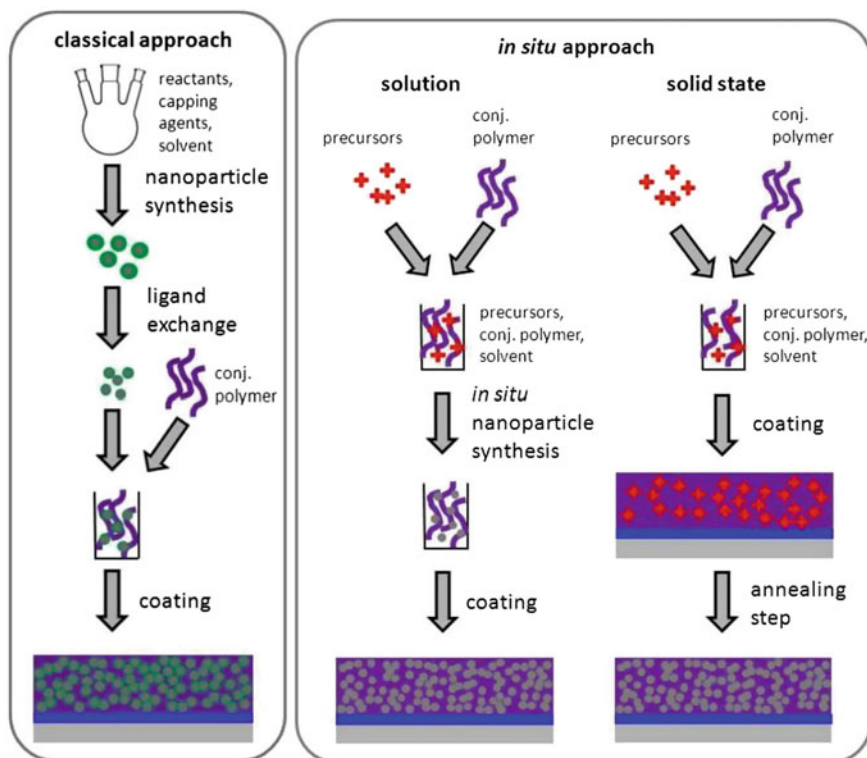
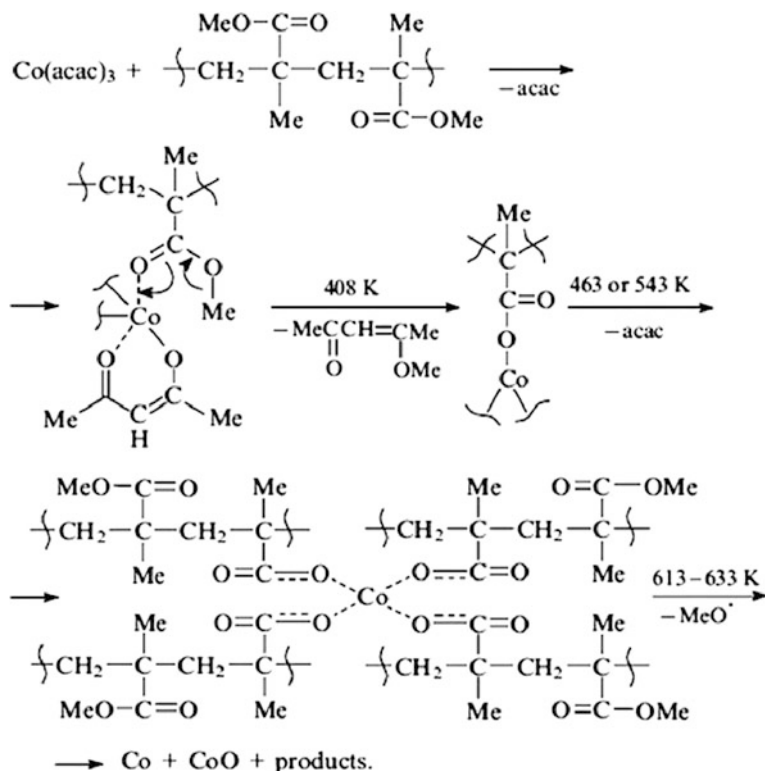


Fig. 6.1 Routes toward the preparation of nanocomposites [74]

recent years, various new in situ approaches have appeared, which enable easier control of the dispersion of NPs and result in a more well-defined structure of nanocomposites [96, 97].

The preparation of in situ nanocomposites can be carried out in solution or without solvent by the solid-state reaction directly in the polymer matrix using various precursors. To develop a suitable in situ route, it is necessary to highlight some general aspects.

1. The precursor should be converted into the desired nanocomposites using experimental conditions compatible with the polymers (low temperatures, no reactions of precursors and by-products with polymer, etc.).
2. The resulting by-products of thermolysis must be removed from the final nanocomposite, so they must be volatile or extractable.
3. The precursor and polymer must be dissolved in the same solvent or mixture of solvents.
4. For industrial use, the precursor itself and its solution with the polymer must be stable, and, of course, the precursor must be easily obtained and cheap.



Scheme 6.1 Mechanism of the thermal destruction in the system of PMMA-Co(acac)₃. Reproduced with permission from Ref. [98]. Copyright (1990) Elsevier

The thermolysis process was studied in detail in M(acac)_n—polymer matrix systems. In particular, it is established that in the process of thermolysis, the metal chelate can perform a dual function. On the one hand, thermolysis of the precursor leads to the formation of metal-containing NPs, on the other hand, it interacts with the matrix, initiating its destruction and depolymerization. As the most interesting examples, we note the thermolysis of the systems Co(acac)₃—poly(methyl methacrylate) (PMMA) and Mn(acac)₃—PMMA in a wide range of M(acac)₃/PMMA ratios (from 1:10 to 1:400) [98, 99]. For the thermolysis of the Co-containing system, the four steps corresponding to the maximum temperatures of 405, 460, 540, and 610–630 K are typical (Scheme 6.1). The first stage is associated with the gradual reduction of Co(acac)₃ and the formation of acetylacetone and Co(acac)₂, which is linked with unsaturated terminal groups of PMMA. The decomposition of this complex is accompanied by the evolution of the monomer, which is the main product of decomposition. The formation of the monomer continues in the second and third stages by continuous reduction of Co (III) to form a complex and subsequent depolymerization of the remaining end

Table 6.1 Thermal stability of PMMA and its complexes with Mn(acac)₃

Polymer	The number of monomer units per Mn(acac) ₃ molecule	<i>T_d</i> (K)	<i>T_{max}</i> (K)
High-molecular-weight PMMA	See ^a	483	623
	50	403	638
	10	398	673
Low-molecular-weight PMMA	See ^a	493	633
	50	403	638
	10	403	673

^aNeat polymer

groups. Simultaneously, Co(acac)₂ can be coordinated with ester groups, accelerating the degradation of the latter and generating methoxy radicals CH₃O, which, in turn, can attack ester groups to form anhydride fragments. The fourth stage is due to the decomposition, characterized by the strongest release of gases, mainly non-condensable gases.

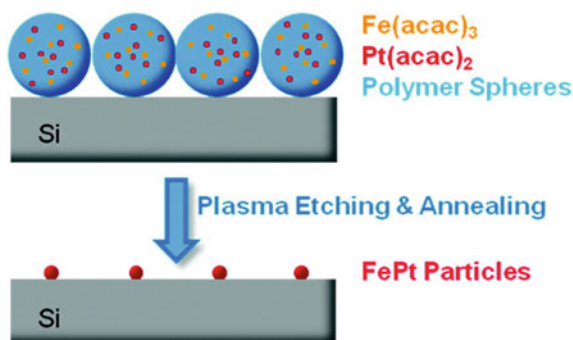
A similar situation is observed in the thermolysis of an Mn-containing system. In particular, the decomposition begins at 395 K (i.e., at a lower temperature than for pure PMMA); however, the main process proceeds at higher temperatures. This conclusion is confirmed by comparing the temperatures of the beginning of the decomposition (*T_d*) and the main decomposition (*T_{max}*), presented in Table 6.1 [99].

It is of interest to thermolysis Rh(acac)₃ in the presence of polyols as reducing agents to form rhodium nanocrystals of various shapes (multipods, cubes, horns, cuboctedra) [100]. Another convenient method for the preparation of these polymer-protected monodisperse rhodium NPs (5–15 nm in size) is the one-step reduction of Rh(acac)₃ rhodium complex in the presence of butane-1,4-diol and poly (vinylpyrrolidone) (PVP) (*M_w* = 55,000) at temperatures of 240–300 K [101]. This process leads to triangular, pentagonal, and hexagonal particles, the cab of which forms Langmuir–Blodgett films on the surface of silicon.

Thus, thermolysis of analyzed systems is a multistage process and usually develops in two main mutually influencing directions: immediate decomposition of the precursor and inhibition of various transformations of the polymer chain (migration of double bonds, depolymerization, cross-linking, degradation, etc.). At the same time, the formed NPs can have a catalytic effect on the processes of carbonization and graphitization of polymers, in particular, at the deep stages of decomposition of organic polymers, the mechanisms of which are not completely clear in most cases. This greatly contributes to the study of such interactions. The only obvious is the tendency: an increase in NP dispersion during thermolysis promotes an increase in the content of the polar group in the polymer [1].

In another interesting example, an experimental approach is presented that makes it possible to obtain deposited on a substrate a hexagonally arranged metallic alloy NPs with a narrow size distribution, clearly defined interparticle distances and

Fig. 6.2 Highly ordered alloy NPs based on precursor-filled latex spheres. Reproduced with permission from Ref. [102]. Copyright (2012) American Chemical Society



controlled chemical composition [102]. In particular, PS and PMMA colloids containing complexes of Fe- and Pt-precursors in a predetermined ratio are deposited on hydrophilic Si/SiO₂ substrates by dip-coating, forming a highly ordered monolayer (Fig. 6.2). After reactive ion etching and thermolysis, hexagonally ordered arrays of crystalline FePt NPs are formed, demonstrating the desired Fe:Pt ratio of 1:1, as determined by a detailed analysis after each production step.

Of interest is a silver NPs/PS nanocomposite prepared by dissolving silver 1,5-cyclooctadiene-hexafluoroacetylacetonate [Ag(hfac)(COD)] in an amorphous PS followed by heating for *ca.* 10 s at a convenient temperature (453 K). Under these conditions, the metal precursor decomposes and forms silver atoms, which diffuse into the polymer matrix and cluster, which leads to the formation of a contact-free dispersion of silver NPs (Fig. 6.3) [103, 104]. Pseudospherical silver NPs with a narrow particle size distribution (average diameter of *ca.* 7 nm) appear to be uniformly distributed in a continuous PS matrix. Interestingly, light-fast color filters (intensely and brightly colored) can be easily prepared by dyeing optical plastics with surface plasmon resonance (SPR) of nanocomposites obtained.

It should be noted the synthetic pathway to inorganic nanoheterostructures with adjustable size and morphology using self-assembled block copolymer mesophase templates PS-*b*-poly-4-vinylpyridine (PS-P4VP, where the molecular weight ratio PS/P4VP was 22,000–22,000 or 40,000/5500) [105]. Two precursors of Fe, tricarbonyl(cyclooctatetraene) iron and Fe(acac)₃ were dissolved together with the Pt precursor, platinum dimethylcyclooctadiene, in a toluene solution containing self-assembled block copolymer and the solution was transferred to a Petri dish (Fig. 6.4a). Different compositions of the copolymers resulted in the generation of two different mesophases (Fig. 6.4b, c). The application of an external magnetic field (10 T) to PS-P4VP composites (40,000/5500) at 453 K led to a phase transition of the P4VP block from spheres into hexagonal cylinders (Fig. 6.4d). After removal of the copolymer by pyrolysis, periodically ordered inorganic nanoheterostructures (spheres, hexagonal cylinders and layers of the hard magnetic phase of FePt) were built into the inorganic matrix of the soft magnetic phase of α -Fe (Fig. 6.4e–g). It is important that the morphology and domain size of nanoheterostructures could be adjusted by controlling the molecular weight and the

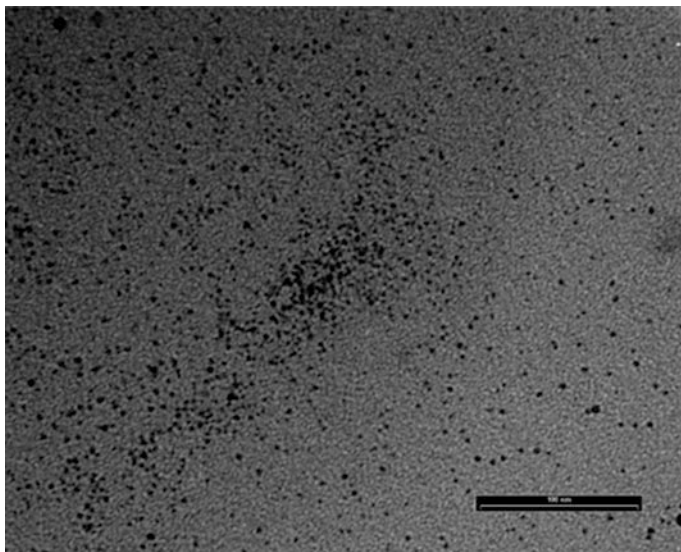


Fig. 6.3 TEM micrograph of a nanocomposite sample (1% by weight of [Ag(hfac)(COD)]). As visible, quite pseudospherical silver particles of narrow particle size distribution are present. Reproduced with permission from Ref. [103]. Copyright (2012) John Wiley and Sons

relative lengths of the block copolymer blocks. Thus, block copolymers exhibiting microphase separation into ordered morphologies, such as lamellar, cylindrical, and spherical microdomains, provide a convenient self-assembled template for the synthesis of nanocomposites. These microdomains are nanoreactors, within which many NPs can be synthesized.

It should be specially emphasized that the adjustment of the process of nucleation with the help of a hosting medium that encapsulates the precursors, dispersing them in separate compartments, improves control over the formation of particles [106]. These inorganic–organic hybrids inherit properties from both organic and inorganic material, whereas the organic component can also introduce specific functionality into particles or prevent their aggregation in water. In other words, the shape and size of the synthesized NPs can to some extent be controlled by the geometry and size of the organic templates used, which can thus be considered as nanometer-scale molds for both porous continuous matrices and suspensions. This approach is especially useful experimentally for synthetic linear polymer templates, since they can possess controlled chemical structures, molecular weights, and molecular weight distributions, which allows to obtain NPs with enhanced colloidal stability and biocompatibility.

It is widely recognized that the main limitation of the thermolysis of $\text{Fe}(\text{CO})_5$ for the production of monodisperse Fe_3O_4 NPs is the high toxicity of the carbonyl precursor. In an attempt to solve this problem, $\text{Fe}(\text{acac})_3$ was used in the one-pot polyol reduction process in an octyl ether and in the presence of a water-soluble

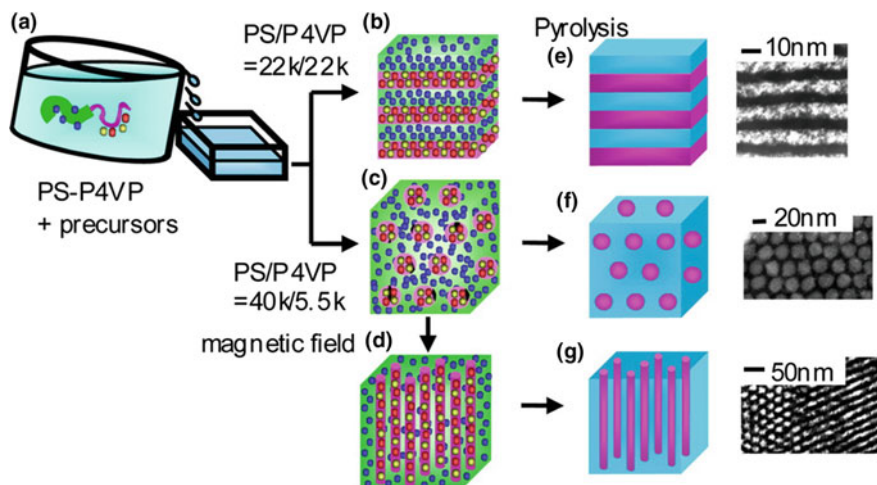


Fig. 6.4 Preparation of periodically ordered inorganic nanoheterostructures from self-assembled block copolymer composites. **a** Dissolution of PS–P4VP block copolymers (PS, green; P4VP, pink) and Fe (brown and blue spheres) and Pt (red spheres) precursors. **b** Self-assembly of a lamellar structure from PS–P4VP (22,000/22,000) and precursors. **c** Self-assembly of a spheres-in-a-matrix structure (P4VP spheres, pink; PS matrix, green) from PS–P4VP (40,000/5500) and precursors. **d** Self-assembly of hexagonal cylinders upon application of a magnetic field to sample shown in panel (c). Pyrolytic formation of periodically ordered nanoheterostructures consisting of (e) layers, (f) spheres, and (g) cylinders (purple) embedded in a matrix (light blue). Reproduced with permission from Ref. [105]. Copyright (2013) American Chemical Society

polymer PVp playing the role of a polymer stabilizer [107]. The obtained PVp-coated monodisperse Fe_3O_4 NPs had a diameter <5 nm and showed a clearly defined superparamagnetic behavior at room temperature with zero H_c .

Interestingly, even water-insoluble cross-linked PS microspheres can serve as hosts for the thermolysis of encapsulated $\text{Fe}(\text{OI})_3$ after swelling of microspheres in an organic solvent (CHCl_3) to facilitate impregnation [108]. Iron oxide NPs were formed in the polymer matrix by thermolysis of trivalent iron oleate (at 573 K, for 0.5 h, nitrogen atmosphere). Almost spherical iron oxide NPs with an average diameter of 11 nm and low size dispersity (standard deviation of 21%) were uniformly distributed within the network serving as a matrix (Fig. 6.5).

It should be noted that the polymer matrix, in turn, can affect the thermal transformation of metal complexes, but information on this issue is limited.

Of interest is a non-hydrolytic method for the synthesis of nanocrystalline magnetite (Fe_3O_4) in the presence of rigid matrices, namely linear ω -sulfonate PS (M_w 5000), ω -thiolated PS (M_w 5000), and ω -carboxylate PS (M_w 39,400) [109]. The thermolysis of iron(III) acetylacetonate is carried out in hexadecane-1,2-diol at 532–537 K. It is important that ω -carboxypolystyrene stabilizes iron NPs more effectively than other PSs; the size of magnetite NPs is 3–10 nm and decreases with

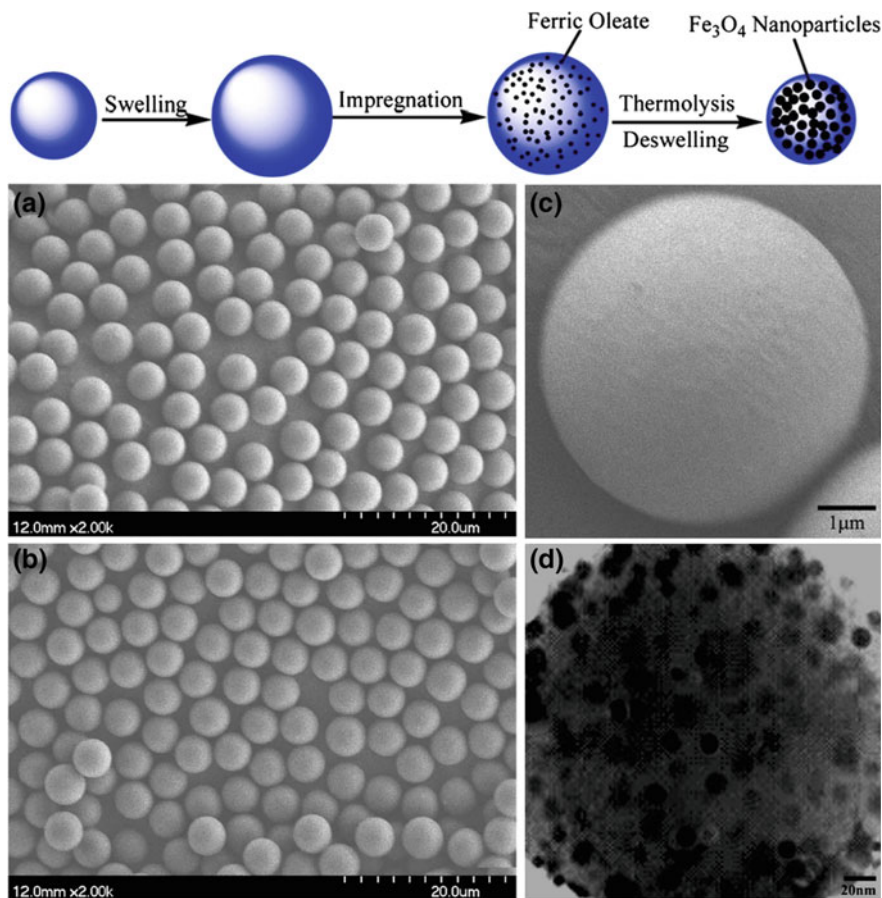


Fig. 6.5 (top) Schematic representation of the preparation of Fe_3O_4 NPs embedded in PS microspheres by thermolysis of $\text{Fe}(\text{O}i)_3$ at 573 K; (down) SEM images for: **a** the polymer seed microspheres prepared by dispersion polymerization; **b** the magnetic polymer microspheres prepared by swelling and thermolysis; **c** the outer surface of magnetic polymer microspheres; and **d** TEM image for the ultramicrotomed magnetic polymer microspheres, showing the location of the iron oxide NPs in the microspheres. Reproduced with permission from Ref. [108]. Copyright (2010) American Chemical Society

increasing polymer content. The resulting magnetic composites with APS less than 10 nm can be easily dissolved in organic solvents, forming stable organosols.

Among other carefully studied precursors, we note the thermolysis of metal acetates in polymer matrices. For example, metal-polymer composites are formed at high-temperature (1273 K) thermolysis of cobalt acetate in the presence of PS, poly (acrylic acid) or poly (methyl vinyl ketone) [110]. Carbonization of the organic polymer gives a material containing metallic cobalt clusters.

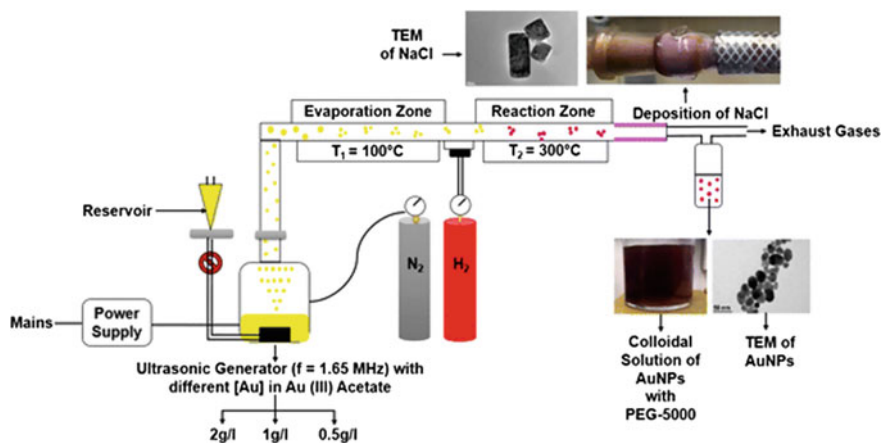


Fig. 6.6 Schematic diagram of experimental setup of USP comprising of ultrasonic generator, evaporation chamber, reaction chamber, quartz transport tubes, and collection bottles for Au NPs. Reproduced with permission from Ref. [111]. Copyright (2017) Springer Nature

In another interesting example, Au NPs were synthesized using the Au(III) acetate precursor in PEG on the USP modular device (Fig. 6.6) [111]. Evaporation and reaction temperatures (373 and 573 K) of USP were selected based on the detected decomposition temperatures of Au(III) acetate with TGA–DT.

It was confirmed (Fig. 6.7a–c) the presence of circular shaped, unagglomerated Au NPs with circularity value range of 0.89–0.92 synthesized at different concentrations of Au acetate of 2, 1 and 0.5 g l^{-1} (Experiments 1, 2, and 3). The average diameters with standard deviation of Au NPs, measured in Experiments 1, 2, and 3, were 26.90 ± 6.40 , 16.90 ± 5.70 , and 14.20 ± 4.50 nm, respectively. This indicates that as the concentration of the Au (III) acetate precursor increases, the size of the Au NPs increases and vice versa (Fig. 6.7d).

It is of interest to use thermolysis of metal chelates in polymer matrices to obtain ZnO and its use in hybrid solar cells [112–115]. One of the alternative strategies in this regard is the deposition of films from polymer solutions, which also contain a soluble precursor. This approach has been studied using soluble zinc chelates that decompose during and after the deposition process by interacting with water from the surrounding atmosphere to produce bicontinuous, interpenetrating ZnO, and polymer networks in the resulting film [113, 116]. Moreover, an impressive power conversion efficiency (PCE) of more than 2% was recorded for the ZnO/polymer solar cells using this production approach [113].

It should be noted that several blocks and grafts copolymers were prepared on the basis of the polythiophene chain serving as an absorber and donor material and poly (zinc methacrylate) chains (Scheme 6.2) [117–119]. The precursor film of active layers obtained from chlorobenzene solutions contains a zinc source coordinated directly to the polymer phase, which leads to a complete homogeneous distribution of zinc in the bulk, but with some predetermined phase separation due

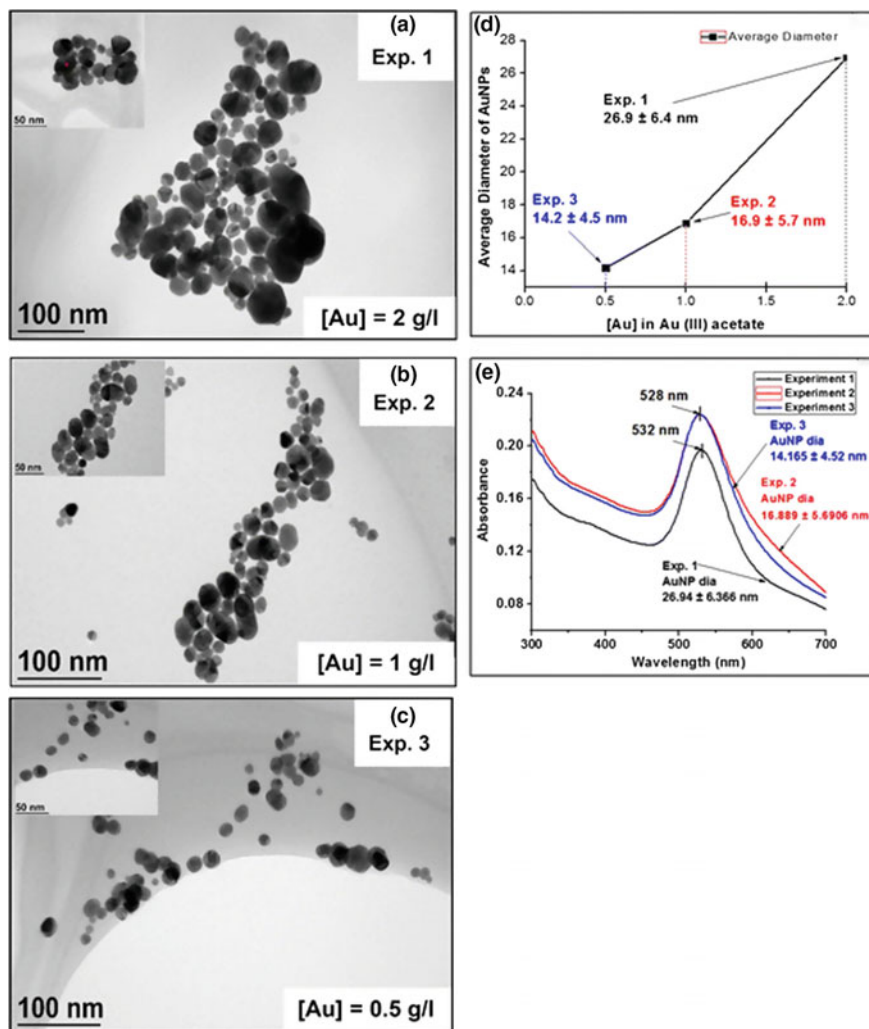
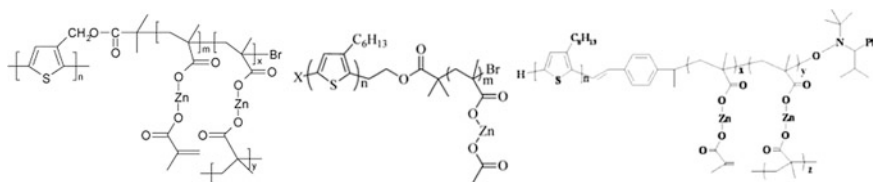


Fig. 6.7 a–c The TEM images of the Au NPs synthesized from Exps. 1, 2, and 3, respectively. **d** The size distribution of Au NPs obtained by TEM characterization and UV–Vis measurement of the Au NPs from Exps. 1, 2, and 3, respectively. Reproduced with permission from Ref. [111]. Copyright (2017) Springer Nature

to the self-assembly properties of such polymers. Using zinc dimethacrylate, already cross-linked polymer structures were obtained in the polymerization process [117, 118], whereas non-cross-linked polymer chains were obtained using asymmetric zinc acetate methacrylate as the monomer [119]. It is important that with this approach, promising PCEs of 0.6% have already been obtained.



Scheme 6.2 Structure of poly(3-hexylthiophene) (P3HT)—Zn-methacrylate copolymers: poly(3-hexylthiophene-*g*-p[Zn(Macr)₂]. Reproduced with permission from Ref. [117]. Copyright (2010) Elsevier; P3HT-*b*-p[Zn(Macr)(OAc)] [119], P3HT-*b*-p[Zn(Macr)₂]. Reproduced with permission from Ref. [118]. Copyright (2012) Elsevier

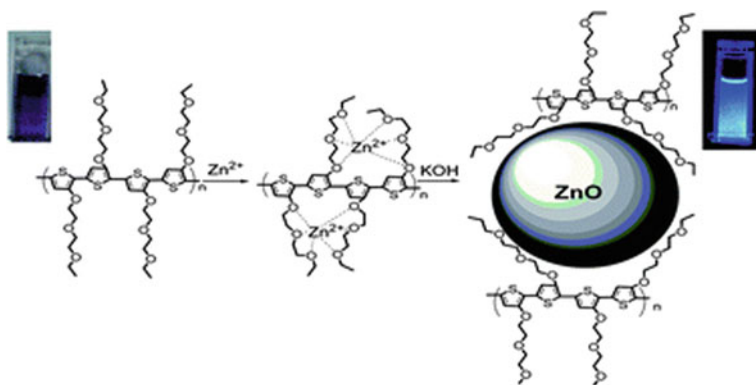


Fig. 6.8 Qualitative illustration of polymer backbone conformation with Zn(II) ion complexation and polymer-ZnO nanocomposite using P3EEET as template. Reproduced with permission from Ref. [120]. Copyright (2009) Royal Society of Chemistry

It is of interest to prepare hybrid ZnO/polymer nanomaterials in a solution in situ approach before the active layer is coated. In this case, the conjugated polymer controls growth and prevents agglomeration and precipitation of the NPs. In particular, functional groups in poly (3-alkylthiophenes), for example, poly(3-[(2'-(2-ethoxy)ethoxy)ethoxy]-thiophene) P3EEET, capable of interacting with ZnO, are favorable for implementing this concept (Fig. 6.8) [120]. Chains with a side alkoxy group can be coordinated with the zinc cations used, controlling growth and interacting also with final ZnO NPs. It is important that this method makes it possible to obtain luminescent nanomaterials.

The growth of ZnO NPs, starting with zinc acetate in a mixture of PVA and poly (*para*-phenylenevinylene) (PPV)-precursor polymer, has been studied [121]. The precursor solution is then cast on the PEDOT:PSS (poly (3,4-ethylenedioxythiophene)/polystyrene sulfonate) layer and during thermolysis at 433 K for 6 h ZnO is formed and at the same time PPV from the PPV precursor. The solar cells obtained with this method show a PCE of 0.026%.

Thermolysis of metal chelates in polymeric matrices proved to be an effective method for the synthesis of metal chalcogenide NPs [122–124]. As an example, we note the synthesis of PbS NPs by thermolysis of a molecular precursor, such as xanthate or carbamate, in PS [122].

To date, various inorganic NPs have been synthesized in situ in the presence of polymers [90, 91, 95, 125–127]. An interesting example is the controlled assembly of PbS nanostructures through oriented attachment of PbS NPs synthesized in the presence of MEH-PPV (MEH is poly (2-methoxy-5-(2'-ethylhexyloxy))) [90]. The lead acetate trihydrate was used as a precursor and was reacted with sulfur in the presence of a polymer in a mixture of DMSO and dichlorobenzene at temperatures from 373 to 451 K. The composite precipitated from the solution by the rapid addition of alcohols, and the aggregation of NPs depended on the polarity of the alcohol. In particular, the use of methanol led to the ordered aggregation of NPs into spherical particles, and precipitation by other alcohols, such as ethanol, propanol, or hexanol, consisted in the formation of nanorods.

A similar synthetic methodology was used in the synthesis of CdS nanostructures with different proportions in the presence of head-to-tail P3HT [92]. The particle geometry and size were monitored by varying the temperature, Cd precursor concentration or time (Fig. 6.9). It is important to note that the choice of solvent affects the conformation of the P3HT chains, which contain the electron donating sulfur functionality, the potential fixation for nucleation and growth of NPs, along with steric hindrances due to long hexyl side chains. For example, a planar P3HT conformation can provide a flat, stacked molecular architecture to guide the growth of CdS NPs in an oriented approach. The aspect ratio of the nanorod obtained can be controlled in accordance with the scale of the length of the P3HT chain, which propagates to the dilution medium and is controlled by a change in the composition of the solvent. Devices prepared using these composites showed a PCE of up to 2.9%.

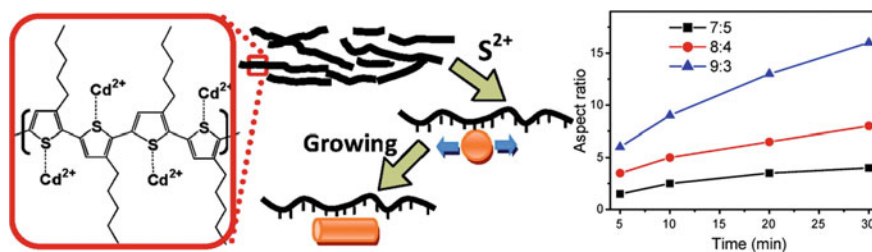


Fig. 6.9 (left) Scheme of the synthesis of P3HT/CdS composites by in situ synthesis of CdS spherical nanocrystals or nanorods via reaction of cadmium acetate dehydrate and sulfur in the presence of the polymer, DMSO, and dichlorobenzene. The Cd^{2+} ions are assumed to be coupled with the unpaired S along the P3HT planar chain network. (right) Average aspect ratio of CdS nanocrystals plotted as a function of the reaction time for the CdS nanorods growth. Reproduced with permission from Ref. [92]. Copyright (2009) American Chemical Society

It should be noted direct synthesis of CdSe QDs in a 1-octadecene solution in the presence of a P3HT polymer [91]. A similar route was used for the synthesis of CdTe NPs in the P3HT matrix, using cadmium acetate dihydrate and tellurium powder in TOP as precursors [95]. It turned out that the ratio of P3HT to the cadmium acetate precursor plays an important role in regulating the size and shape of nanocomposites. In particular, at a low concentration of CdTe, P3HT will have a greater binding ability, which will lead to the formation of some nanorod-shaped particles, and as the concentration of CdTe increases, NP precipitation occurs. It was suggested that the optimal condition happen when both effects are suppressed.

General method for preparation of metal sulfide NPs/polymer films using inexpensive and low-temperature path based on the controlled in situ thermolysis of a solution-processable precursor metal xanthate precursor complex Cd (S_2COEt)₂(Py)₂ in the semiconductor polymer film is interesting (Fig. 6.10c) [93]. Hybrid photoactive layers of CdS/P3HT were prepared by spin casting from a chlorobenzene solution containing a precursor and P3HT (Step 1, Fig. 6.10). The casted solid film P3HT: precursor was heated to 393–433 K to provide the precursor decomposition, and CdS NPs are formed in the polymer matrix (Step 2, Fig. 6.10). It is important that the nanomorphology of such CdS/P3HT films strongly depends on the thermolysis temperature [128].

This approach was extended to the design of polymer/CuInS₂ (CIS) [129, 130] and polymer/Sb₂S₃ nanocomposites [131] and for the deposition of nanocrystalline thin ZnS films hosting CdSe–CdS–ZnS QDs [132], indicating that in situ thermolysis of metal chelates is an attractive and universal way for hybrid inorganic–organic nanocomposites and can be applied to other metal chalcogenides. In particular, in recent years, metal xanthate SSPs has been developed for the solid-phase synthesis

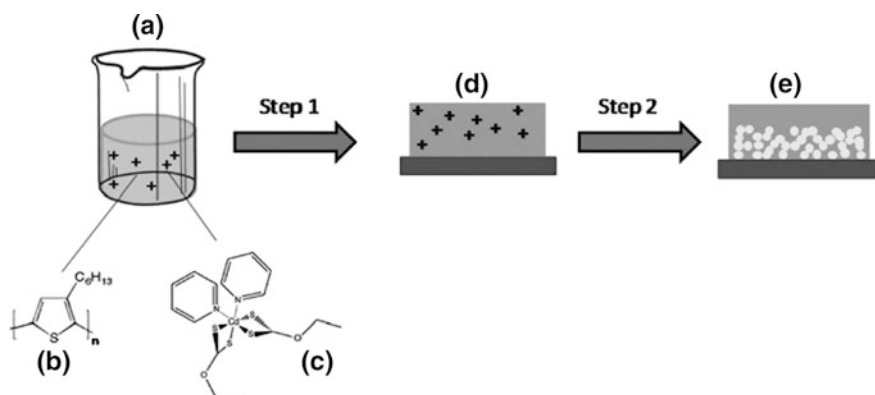


Fig. 6.10 Illustration of the preparation of the CdS/P3HT films from a chlorobenzene mixture **a** of **b** P3HT and **c** cadmium ethylxanthate pyridine [Cd(S₂COEt)₂.2Py]. Deposition of this mixture through spin coating (step 1) results in **d** the formation of a thin film comprising the metal xanthate precursor and the polymer. Upon thermolysis (step 2) a hybrid cadmium sulfide NPs/polymer film **e** is formed. Reproduced with permission from Ref. [93]. Copyright (2010) American Chemical Society

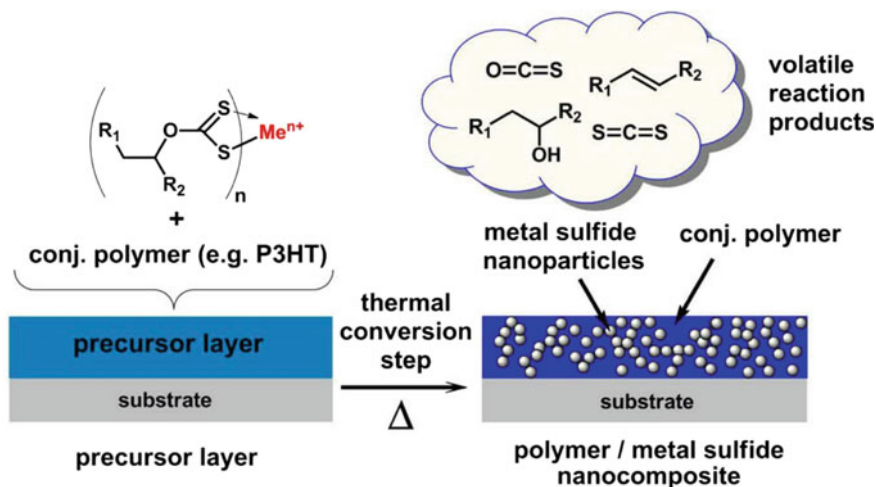


Fig. 6.11 Scheme of the metal xanthate—solid state in situ route (Me: metal ions, Cu, In, Cd; n = oxidation number of the metal; R1, R2: H, alkyl) [74]

of hybrid nanomaterials in situ, which solve problems of solubility and by-products. Through this metal xanthate route the polymer/CdS and polymer/CIS nanocomposites have been prepared (Fig. 6.11) [93, 128, 129]. The advantages of metal xanthates are that they decompose at temperatures well below 473 K and that their solubility can be tuned by changing the alkyl part of the xanthate group. In addition, additional ligands, such as pyridine, can be introduced to optimize the decomposition temperature and solubility. Despite their relatively low decomposition temperatures, they are stable for a long time at room temperature, even in solution.

It should be noted that polymer/NP nanocomposites have been actively studied in recent years in hybrid solar cells because of their promising prospects of combining the advantages of the polymer component, such as high absorption coefficient and simplicity of the solution-based processing [133], with those of inorganic nanoparticulate semiconductors, such as a regulated form (nanodot, nanorod, and tetrapod) [134], tunable absorption properties (quantum confinement effect) [135] and high conductivity [136]. In this respect, it is of interest to use various combinations of polymer/NP as absorbing layers of bulk heterojunction hybrid solar cells [83, 85, 133, 136–142]. As typical examples, we note combinations of conjugated polymers such as polythiophenes, PPVs, or various low band gap polymers with NPs, including CdSe [143], CdS [144], CdTe [145], CIS [129], PbS [146], or ZnO [113]. Currently, the best polymer/NP hybrid solar cells show maximum levels of PCE from 4 to 5.5% [144, 145, 147, 148].

It is of considerable interest in situ to obtain PbS NPs in the presence of a conjugated polymer, MEH-PPV, or P3HT, by heating a solution of $PbAc_2$, elemental sulfur and polymer in a mixture of DMSO and toluene solvents to 433 K for 15 min [125, 149–153]. The removal of excess lead and sulfur ions by precipitation

and re-dissolution followed by coating on the substrates completes the preparation of the nanocomposite layers. The crystalline NPs are not aggregated and well dispersed in the polymer matrix and have high crystallinity. It is important that in situ synthesis makes it possible to control the size and shape of NPs mainly by changing the reaction time and temperature. In addition, the shape of the NPs can be regulated by both precursor materials and solvents or solvent mixtures used for synthesis. For example, using elemental sulfur for the reaction, spherical NPs are obtained, and when H_2S as a source of sulfur is used, cubic nanostructures are formed [149]. It is shown that the controlled formation of PbS NPs in the presence of a conjugated polymer is explained by the steric effects of long polymer chains. The size of NPs was observed to depend on the molecular weight of the polymer: the higher molecular weight of the conjugated polymer resulted in smaller NPs [150].

The influence of the nature of the solvent on the shape of nanostructures was also shown during the synthesis of hybrid CdS/P3HT nanomaterials from Cd $(\text{Ac})_2(\text{H}_2\text{O})_2$ and elemental sulfur [92, 154]. In particular, by using various ratios of dichlorobenzene and DMSO, nanorods with different aspect ratios in the P3HT matrix were obtained. Thus, a higher content of dichlorobenzene in a mixture of solvents led to an increase in the aspect ratio of prepared nanorods (Fig. 6.12).

Instead of elemental sulfur, Na_2S was used to produce CdS NPs with dimensions of 5–6 nm [155], and CdSe NPs were synthesized using Na_2SeO_3 as a source of selenium [156] in the P3HT matrix. The ordered morphology of CdS and CdSe NPs in the presence of a polymer matrix is shown. In particular, the structure and apparent morphology of nanocomposites differ significantly from the structure of the polymer (Fig. 6.13a). For example, in polymers, pores with certain edges with

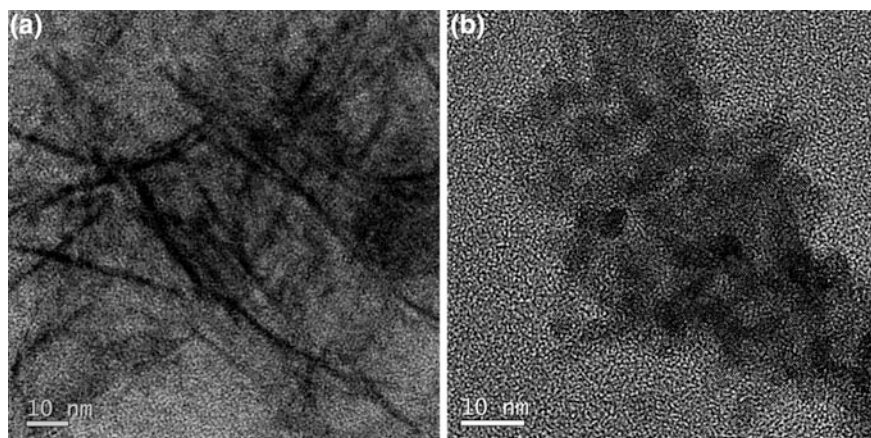


Fig. 6.12 TEM image of CdS nanorods synthesized in P3HT with volume ratios dichlorobenzene-to-DMSO of **a** 9:3 and **b** 7:5. Reproduced with permission from Ref. [92]. Copyright (2009) American Chemical Society

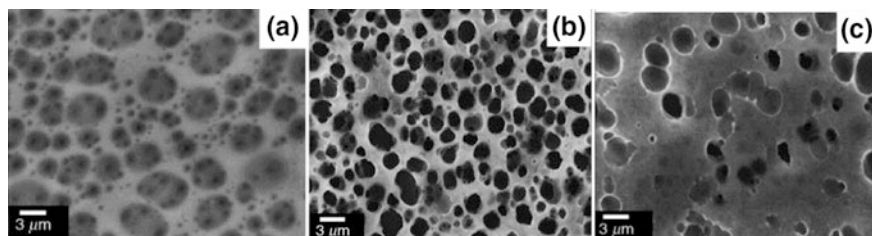


Fig. 6.13 SEM images of **a** P3HT, **b** CdS nanocomposites and **c** CdSe nanocomposites [155]

different distributions are visible, while the CdS/P3HT nanocomposite (Fig. 6.13b) shows identical NPs with a constant interparticle separation. Interestingly, for the CdSe/P3HT sample (Fig. 6.13c), relatively large particles with different separation between the particles are characteristic. Black spots of 1 μm size refer to the formation of clusters within the polymer matrix, which may be due to NP aggregation. The apparent morphology shows NPs/polymer nanocomposites with large dimensions, and these features clearly show the capture of NPs in the polymer matrix.

We also note the use of a not defined cadmium ethyl xanthate complex as a precursor for the preparation of the P3HT/CdS nanocomposite [157].

The in situ synthesis of nanomaterials by thermolysis of metal chelates in polymers gives a potentially shorter path to thin films of bicontinuous phases of inorganic NPs and polymers. The wide range of SSPs and available polymers makes the growth of nanomaterials directly within polymers an attractive route for the synthesis of composite thin films and was used for PbS [158], CdS [93, 128, 159–161], Bi₂S₃ [162], CIS [129, 163–166], Sb₂S₃ [130, 131] in photovoltaic and thermoelectric devices [167].

As a typical example, we note the production of lead sulfide from SSPs in the PS matrix with the formation of PbS NP networks [158]. The treatment is carried out by spin coating a solution containing SSP and PS onto the substrate, followed by heating of the film to decompose the SSP (Fig. 6.14). As SSPs, lead(II) dithiocarbamates, their phen adducts and lead(II) xanthates with different alkyl chain lengths (butyl, hexyl, and octyl) were used. It turned out that xanthates are more promising SSPs, providing control of the size and shape of NPs when changing the length of the alkyl chain. In particular, the lead(II) octylxanthate complex causes anisotropic growth, forming PbS nanowires inside the polymer matrix.

It should be noted that molecular tuning of the metal xanthate precursors has a significant effect on the heterojunction morphology of hybrid P3HT/CdS blends and, as a result, the photochemical processes and the total productivity of in situ prepared hybrid solar cells [159]. It is shown that in situ method gives an increased yield of charge generation and the overall performance of the device as compared to an equivalent device manufactured using the conventional ex situ method of blending NPs with the polymer before thin film formation [168]. The in situ method is also potentially compatible with large-scale production, which is considered critical for the success of solution-processed photovoltaic technologies [169, 170].

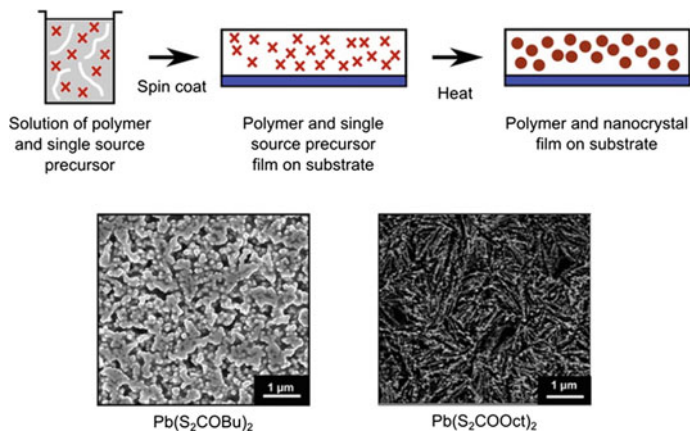


Fig. 6.14 Schematic of the in situ approach employed to fabricate the PbS–polymer films. Reproduced with permission from Ref. [158]. Copyright (2015) American Chemical Society

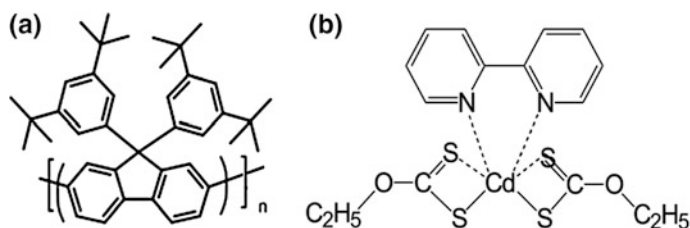


Fig. 6.15 Molecular structure of **a** PBPFO polymer and **b** CdDEX precursor [160]

Although extensive studies on the optimization of charge generation in these systems have been carried out [94, 171], little is known about how to influence the nanomorphology of in situ produced hybrid solar cells and the process of in situ formation of NPs themselves. In particular, it has been suggested that the nanomorphology of the absorber layer will be a key factor in the further optimization of the PCEs of this new type of solar cells [172]. For example, the effect of various NP shapes (spherical, rod-like) [173] or size [174] on the characteristics of the devices was shown.

It is of interest a convenient method for in situ formation of QDs from the nanocomposites of the blue emitting polymer [9,9-bis(3,5-di-*tert*-butylphenyl)-9H-fluorene] (PBPFO) together with the complex of cadmium diethylxanthate and bpy (CdDEX) (Fig. 6.15) [160].

Micrographs with low and high magnification (Fig. 6.16a and b, respectively) before heating the nanocomposite show that the organic–inorganic matrix is uniformly distributed over the carbon film, and no QD aggregates are observed under these conditions. In addition, there are no crystalline particles in the sample, and the observed radial distribution is typical of the polymer (Fig. 6.16c). After the film is heated at 433 K for

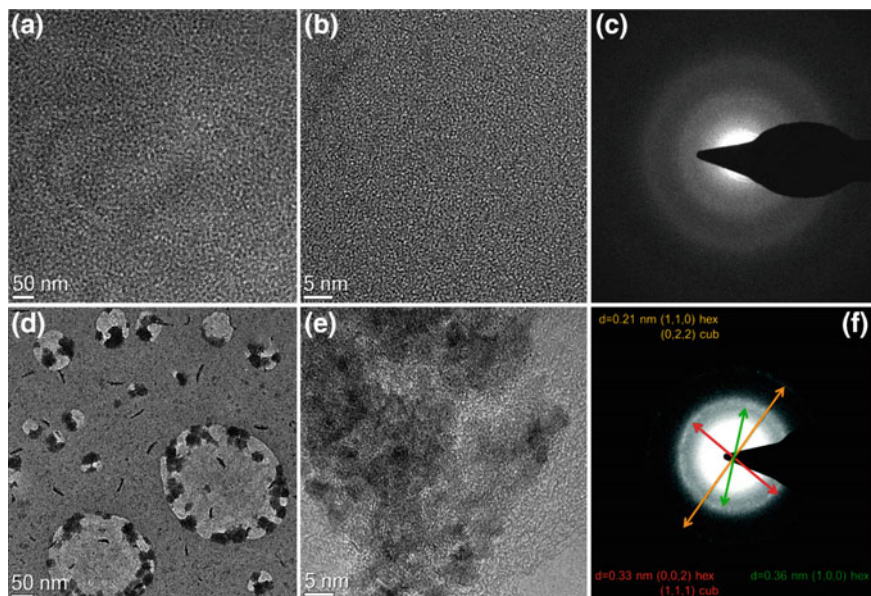


Fig. 6.16 **a** Low magnification and **b** high magnification images of polymer–CdDEX precursor blend before baking **c** SAED image before baking. **d** Low and **e** high magnification images of QDs generated by thermolysis of the polymer–precursor film at 433 K for 10 min; the SAED **f** confirms the presence of crystalline species. The diffraction rings indicated by a red and an orange arrow are compatible with both CdS cubic or hexagonal phase, while the one highlighted in green is typical of the hexagonal phase only [160]

10 min, the formation of nanocrystals occurs in the polymer matrix, and these particles within the polymer tend to aggregate in clusters between 20–60 nm in size (Fig. 6.16d). It is important that the particle size is from 3 to 6 nm (Fig. 6.16e), and the resulting NPs are hexagonal CdS (Fig. 6.16f). However, it is impossible to exclude the cubic phase, because the reflections of the two phases overlap.

Cadmium ethyl xanthate was used as SSP to obtain CdS NPs directly in the P3HT matrix at 393 K [161]. It is important that monodisperse CdS NPs of average size 4 nm are formed and the nanosize can be controlled by the concentration of the polymer additive in the composite. The atom force microscopy (AFM) images of the pure P3HT and P3HT/CdS composite films of 1:1, 1:4, and 1:8 ratios show (Fig. 6.17a–d) that the composite with a high NP content is more rough than the pure P3HT film. In addition, the values of the surface roughness of films increase with increasing content of NPs; in particular, for a pure P3HT film it was 2 nm, but it increased to 3.5 nm for a 1:4 sample and was 11.5 nm for a 1:8 sample. It should be noted that partial aggregation was detected (see Fig. 6.17d) on the surface of a sample containing a large the number of NPs (1:8). The P3HT–CdS nanocomposite is characterized by a homogeneous morphology with small nanocrystallites aggregated to nodule size of 40 nm, so the segregation of NPs or polymer in these composites is not high.

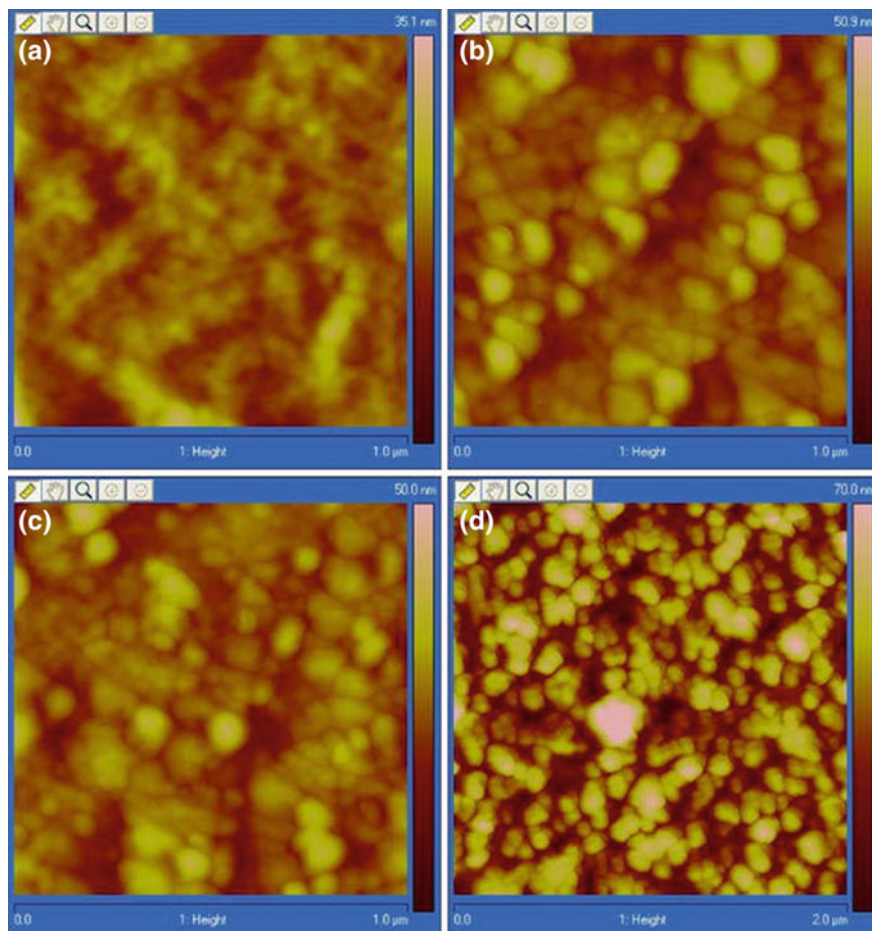


Fig. 6.17 AFM for **a** P3HT, **b** P3HT–CdS 1:2, **c** P3HT–CdS 1:4 **d** P3HT–CdS 1:8. Reproduced with permission from Ref. [161]. Copyright (2013) Springer Nature

Of great interest is the use of bismuth xanthate [bismuth(III) O-3,3-dimethylbutan-2-yl dithiocarbonate] (BiHexXan) to obtain Bi_2S_3 NPs directly within the polymer matrix (PMMA or P3NT) [162]. The bismuth xanthate can be converted to Bi_2S_3 NPs with an orthorhombic crystal structure through a thermally induced solid-state reaction at moderate temperatures below 473 K (Fig. 6.18, left). The polymer forms several large domains with a length of 100 nm (Fig. 6.18, right). In addition, in the Bi_2S_3 –PMMA layers, structures with smaller dimensions of about 50 nm are also visible, which can be attributed to the Bi_2S_3 nanostructures present in the nanocomposite. However, these smaller structures are not observed in the AFM image of the Bi_2S_3 –P3HT hybrid layer.

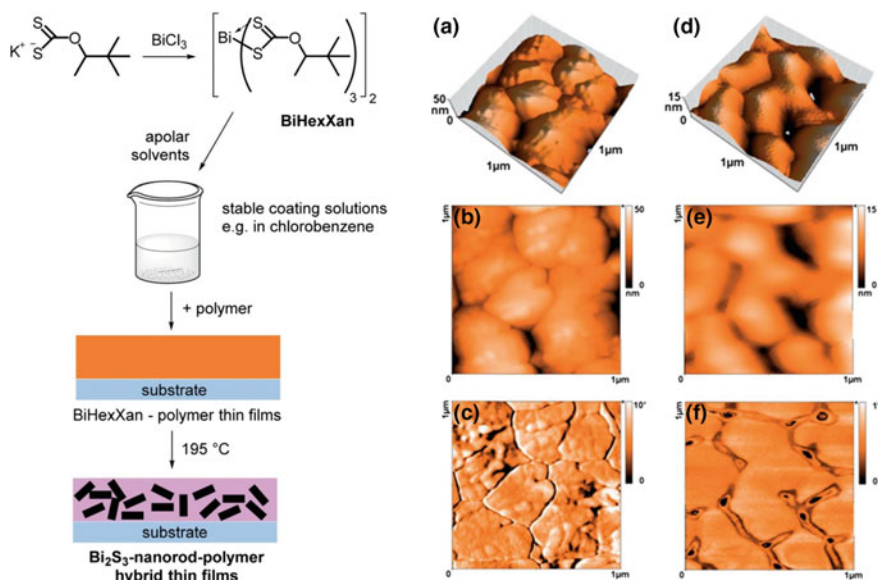


Fig. 6.18 (left) Synthesis of BiHexXan and Bi_2S_3 -polymer hybrid materials; (right) AFM images (a and b topography; c phase contrast) of a Bi_2S_3 -PMMA hybrid layer and a Bi_2S_3 -P3HT layer (d and e topography; f phase contrast) [162]

It should be noted the direct synthetic pathway for the preparation of P3HT/CdS nanocomposites with cadmium acetate dihydrate $[\text{Cd}(\text{OOCCH}_3)_2 \cdot 2\text{H}_2\text{O}]$ used as a source of cadmium, sulfur powder as a source of sulfur, dichlorobenzene and DMSO as co-solvents, phosphonic ester end-functionalized P3HT as a conjugated polymer matrix [175]. It turned out that the size and distribution of CdS NPs were not only temperature-dependent, but also strongly depend on the molar ratio S/Cd. In addition, CdS NPs were evenly dispersed in P3HT/CdS nanocomposites, indicating that the end-functionalized P3HT can be used as a template to prevent effective aggregation of CdS.

CIS NPs were directly synthesized in a P3HT matrix with different concentrations ratio of P3HT and CIS (1:2, 1:4, and 1:8) by decomposition of CIX [176]. In this process, copper indium xanthate and P3HT were homogeneously mixed in *o*-dichlorobenzene, which led to the formation of a CIS NPs by thermolysis of the SSP in situ at temperatures up to 383 K. It is important that CIS nanocrystals are capped by P3HT (Fig. 6.19, left, a), and the size of NPs synthesized in P3HT/CIS nanocomposites of composition 1:4 is ~ 5 –6 nm (Fig. 6.19, left, b). The results obtained (Fig. 6.19, left, c and d) indicate the tetragonal crystal structure of the CIS, clearly showing that in situ growth of NPs in polymer templates controls the dispersion of inorganic NPs in the polymer matrix, thereby providing a large distributed surface area for the charge separation in these nanocomposites. In addition, the decrease in the dominance of the P3HT polymer with increasing CIX

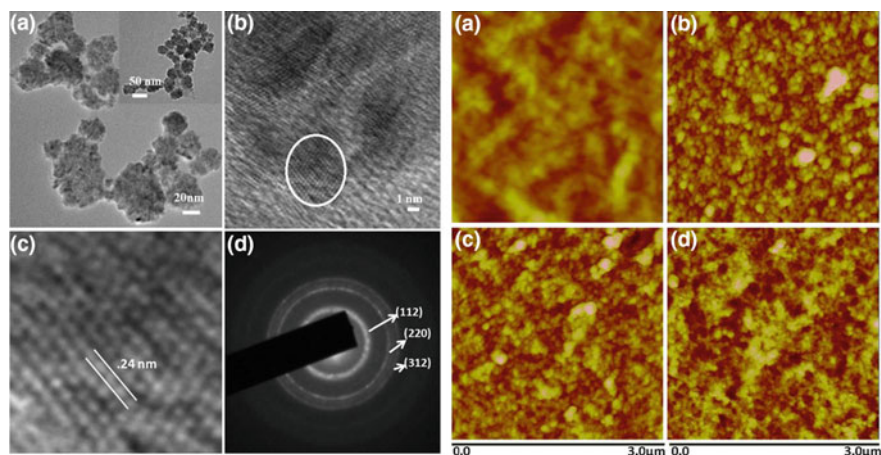


Fig. 6.19 (left) TEM (a) and HRTEM (b) images of P3HT/CIS nanocomposites. Magnified views of circled area (c). Selected area diffraction pattern (SADP) of P3HT/CIS composites (d). (right) AFM images of the films: **a** P3HT, **b** P3HT/CIS (1:2), **c** P3HT/CIS (1:4), and **d** P3HT/CIS (1:8) nanocomposites. Reproduced with permission from Ref. [176]. Copyright (2013) Springer Nature

concentration is shown. For a neat P3HT film, densely packed polymer nodules are characteristic, which results in a surface roughness of 1.67 nm (Fig. 6.19, right, a). At the same time, P3HT/CIS nanocomposites (Fig. 6.19, right, b–d) clearly demonstrate a homogeneous morphology with small NPs without significant segregation of NP or polymeric nodules. Surface roughness values increased from 7 to 12.2 nm with an increase in CIS concentration from 1:2 to 1:8.

It should be also noted the synthesis of lead sulfide NPs in a solution-processable sulfur “inverse vulcanization” polymer thin film matrix during in situ thermolysis of lead(II) *n*-octylxanthate, $[\text{Pb}(\text{S}_2\text{COOct})_2]$ (Fig. 6.20, left) [177]. The “reverse vulcanization” polymer contains a hybrid linker system that exhibits high solubility in organic solvents, which allows the treatment of a sulfur-based polymer solution ideally suited for the formation of thin films. It is important that, beyond a certain concentration of SSPs, the formed NPs were not only inside the film, but also on the surface, which indicated a limiting load in the polymer. Well-defined cubes with random small elongation forming irregular cuboids were obtained (Fig. 6.20, right, a–d) [178]. The size of the NPs did not show a trend with increasing concentration, although all the NPs obtained were less than 80 nm along the edge length. Using 0.1 mmol $[\text{Pb}(\text{S}_2\text{COOct})_2]$, the resulting NPs showed the highest monodispersity and the lowest average size (28.6 nm) (see Fig. 6.20, right, b). In other words, 0.1 mmol $[\text{Pb}(\text{S}_2\text{COOct})_2]$ is the optimum amount of SSP in terms of particle monodispersity.

CdS/PVA nanocomposite thin films on glass substrates were obtained by in situ thermolysis of cadmium acetate and thiourea as initial reagents dispersed in PVA [179]. It is important that the developed synthetic technology does not contain a complexing agent and, therefore, does not require the control of the pH of the solution, as in the case of conventional chemical bath deposition (CBD). CdS NPs

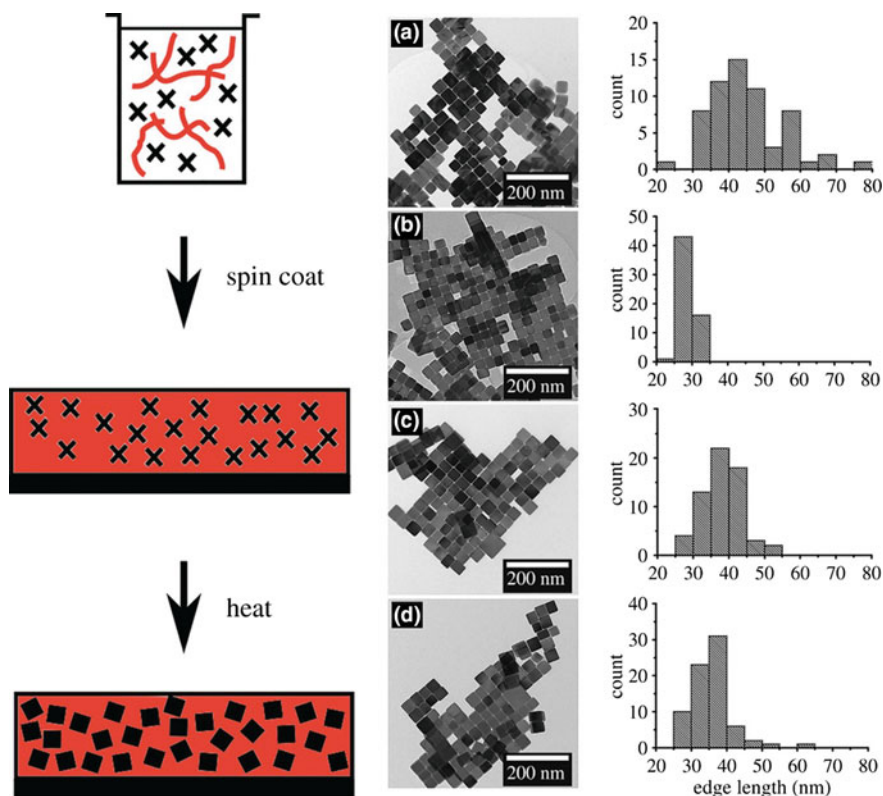


Fig. 6.20 (left) The processing of precursor and polymer to form PbS nanocrystals within the sulfur polymer. (right) TEM images and corresponding size analysis of the extracted PbS nanocrystals formed within the S-polymer when using **a** 0.05 mmol, **b** 0.1 mmol, **c** 0.15 mmol, and **d** 0.2 mmol of $[\text{Pb}(\text{S}_2\text{COOct})_2]$ [177]

with a hexagonal phase are formed in the pores of the PVA matrix and, as the films grow, they become uniform, without visible spots and cracks.

It should be noted that organic–inorganic hybrid solar cells made from a bulk heterojunction between semiconductor NPs and conjugated polymers are a promising type of solution-processable solar cells and have made significant progress in recent years [180]. Despite a number of potential advantages of hybrid solar cells, their efficiency still lags behind those obtained for purely organic solar cells, as well as devices using only NPs as an absorber. However, in situ approach is very promising, bearing in mind that this is a fairly young research topic. Further optimization of the device architecture, as well as, for example, the introduction of adapted interface layers, can lead to an additional improvement in in situ produced hybrid solar cells. Table 6.2 lists important examples of inorganic–organic hybrid solar cells prepared on in situ routes [74].

Table 6.2 Important examples of in situ prepared hybrid solar cells

Inorganic phase	Organic phase	Precursor	Solution/ solid state	I_{SC} (mA cm ⁻²)	V_{OC} (V)	FF (%)	Eff. (%)	Reference
CdS	P3HT	CdAc ₂ ·2H ₂ O, elemental sulfur	Solution	–	–	–	2.95	[155]
CdS	P3HT	CdAc ₂ ·2H ₂ O, elemental sulfur	Solution	9.0	0.64	48	2.9	[92]
CIS	poly[(2,7-silafluorene)- <i>alt</i> -(4,7-di-2-thienyl)-2,1,3-benzothiadiazole]	Xanthates	Solid state	10.3	0.54	50	2.8	[129]
CIS	poly[(2,7-silafluorene)- <i>alt</i> -(4,7-di-2-thienyl)-2,1,3-benzothiadiazole]	Xanthates	Solid state	10.4	0.46	56	2.66	[164]
CdS	P3HT	Xanthates	Solid state	4.85	0.84	53	2.17	[128]
CIS	<i>p</i> -DTS(FBTTh ₂) ^a	Xanthates	Solid state	5.5	0.46	52	1.3	[166]
PbS	MEH-PPV	PbAc ₂ , elemental sulfur	Solution	0.13	1	28	0.7	[152]
CdS	P3HT	Xanthates	Solid state	3.54	0.61	33	0.7	[93]
ZnO	P3HT ^b	p(Zn-Macr ₂)	Solid state	2.9	0.5	43	0.62	[118]
ZnO	P3HT ^b	p(Zn(Macr)(OAc))	Solid state	1.7	0.37	31	0.19	[119]
CdS	poly(3-(ethyl-4-butanate)thiophene)	CdAc ₂ ·2H ₂ O, thiourea	Solid state	0.46	0.51	28	0.06	[188]
ZnO	PPV	Zn(OAc) ₂	Solution/solid state	0.09	0.94	30	0.026	[121]

^aSmall molecule 7,7'-(4,4-bis(2-ethylhexyl)-4H-silolo[3,2-b:4,5-b']dithiophene-2,6-diy)bis(6-fluoro-4-(5'-hexyl[2,2'-bithiophen]-5-yl)benzo[c] [1, 2, 5]thiadiazole)

^bP3HT as part of the copolymer

Another interesting trend in the practical use of thermolysis of metal chelates in polymer matrices was the catalytic curing of an epoxy composite under the action of NPs [181]. In particular, in this process, Cu(I), Pb(II), Sb(III), Zn(II), Cb(III), Zn(II), Cd(II), In(III), Ga(III) xanthates were used, which, when thermolysis at 423 K, give corresponding metal sulfides. It was shown that the order of the curing time at a given temperature and the trend of the decomposition temperature of the metal xanthate were the same. The analysis of the epoxy composite, consisting of metal xanthates cured by thermal annealing, illustrates the generation of metal sulfide in situ in the matrix. More detailed studies of this process were carried out with the example of linear and branched zinc(II) xanthates with different alkyl chain length [182]. The presence of ZnS in situ in the composite matrix was shown, indicating the thermal decomposition of zinc (II) xanthates in situ as a likely mechanism for curing. It is interesting that in the case of linear alkylzinc(II) xanthates with increasing alkyl chain length, both the thermal decomposition temperature and the curing time were increased. In contrast, in the case of branched alkyl chain zinc(II) xanthates, the temperature of the thermal decomposition as well as the curing time decreases with increasing length of the alkyl chain.

It should also be noted the thermolysis of metal chelates in other matrices, for example, reduced graphene oxide (RGO) [183, 184]. As a typical example, we note an efficient approach to the production of porous iron oxide ribbons by controlling the nucleation and growth of the iron precursor (iron acetylacetonate/ethylene glycol) on the surface of RGO and subsequent annealing treatment [185]. The obtained iron oxide ribbons have a large aspect ratio, a porous structure, a thin feature and improved open edges. The general procedure for the synthesis of porous iron oxide ribbons is schematically illustrated in Fig. 6.21. The chemically RGO was first dispersed in an ethylene glycol solution to create a dark suspension with a dispersant, PVp. The suspension was then mixed with iron(II) acetylacetonate by ultrasonic treatment and then heated to 343 K for the heterogeneous nucleation of iron glycolate on the surface of RGO. As soon as the nucleation takes place, the residual iron precursor will further grow around the nucleus to form iron glycolate ribbons of various lengths with an increase in the reaction time from 30 min to 5 h. Subsequent thermal annealing of the resulting ribbons at different temperatures (523–673 K) in air provided iron oxide ribbons.

It is also of considerable interest to synthesize high-performance Cu-based ORR catalysts by pyrolysis of mesoporous KIT-6 silica-supported phthalocyanines at superhigh temperature (1473 K) by grinding-nanocasting technique (Fig. 6.22) [186].

It should be noted an in situ production of Pt NPs incorporated into 1D NPCs via an organometallic precursor-controlled thermolysis approach [187]. In this process, platinum dichloride complex of 3,4-bis(4-dodecynylphenyl)-2,5-bis(4-(2,2'-bipyridyl)phenyl) cyclopentadienone are chosen as SSP for the synthesis of NPCs integrated with Pt NPs (Fig. 6.23, left). The platinum complex is first impregnated into the nanochannels of AAO (anodic alumina oxide) membranes (Fig. 6.23, right). The intermolecular Diels–Alder reaction of these precursor molecules affords the formation of platinum functionalized polyphenylene skeletons. Subsequent

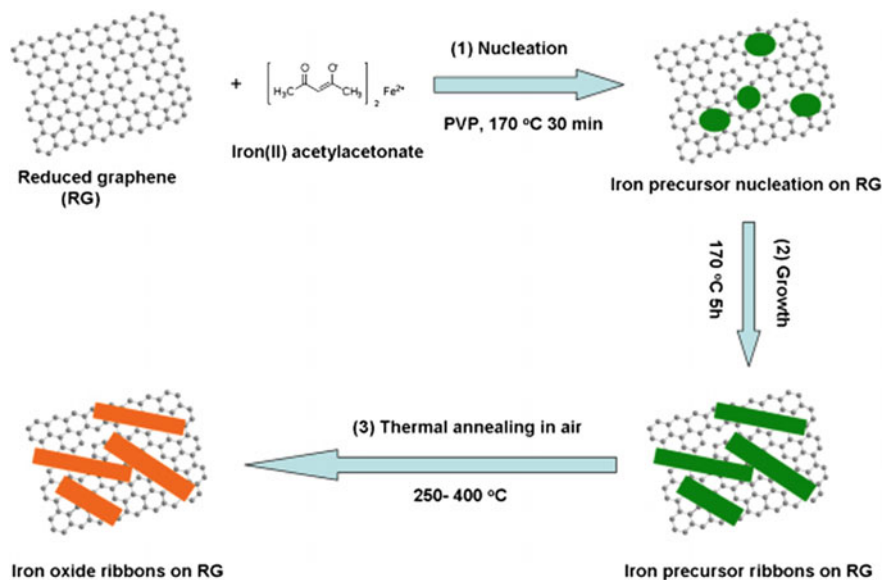


Fig. 6.21 Fabrication of iron oxide ribbons. It includes (1) and (2) controllable nucleation and growth of the iron glycolate onto the surface of the RGO at 443 K, and (3) thermolysis at different temperatures (523–673 K) in air [185]

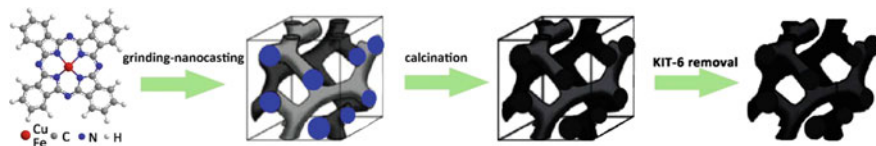


Fig. 6.22 Phthalocyanine-derived mesoporous Cu-based electrocatalysts for oxygen electroreduction. Reproduced with permission from Ref. [186]. Copyright (2017) Elsevier

thermolysis transforms the polyphenylene backbones into 1D NPC frameworks, while the metallic moieties are reduced into Pt NPs. After removal of the AAO template, 1D NPCs/Pt is obtained.

It is important that Pt NPs with an average diameter of 2–6 nm are homogeneously distributed into carbon frameworks (Fig. 6.24a, b), and the metallic phase is composed of Pt single crystals (Fig. 6.24c–e). In accordance with nanoelectron diffraction (NED) patterns (Fig. 6.24f), the only crystalline phase presented in NPCs/Pt is metallic platinum showing high-resolution lattice fringes. The resulting product contains both the C and Pt components (Fig. 6.24g) and additional peaks for Cu and O can be attributed to the underlying copper grid.

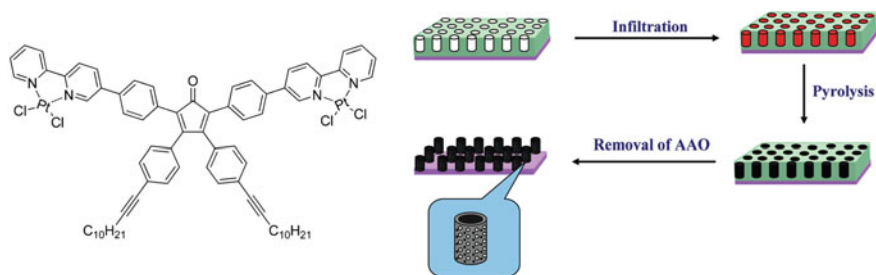


Fig. 6.23 (left) Structure of the SSP. (right) Schematic illustration of the preparation of 1D NPCs/Pt. Reproduced with permission from Ref. [187]. Copyright (2003) American Chemical Society

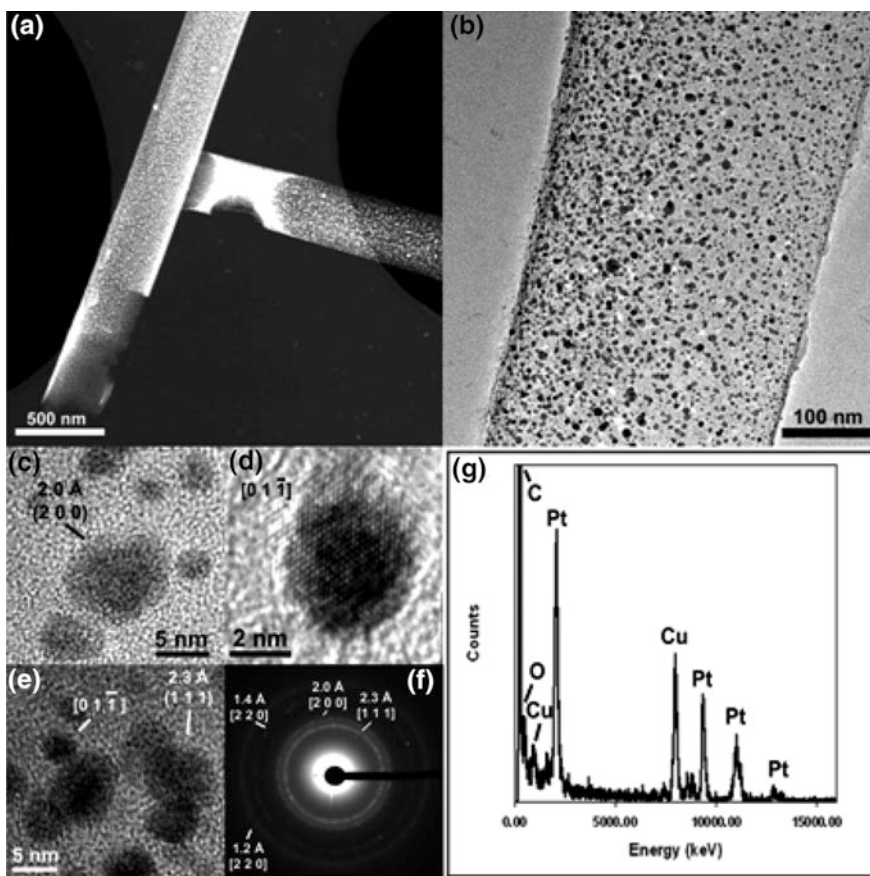


Fig. 6.24 **a** STEM image of NPCs/Pt (dark field) overview shows the typical tubular feature of the carbons. **b** TEM image of NPCs/Pt discloses the homogeneously dispersed platinum NPs on 1D carbon substrates with rounded shape. **c–e** HRTEM images of different oriented platinum NPs demonstrate that each particle is a single crystal. **f** NED patterns show that the only crystalline phase is metallic Pt. **g** EDX reveals both C and Pt peaks and a small O peak possibly coming from the Cu grid. Reproduced with permission from Ref. [187]. Copyright (2003) American Chemical Society

References

1. A.D. Pomogailo, A.S. Rozenberg, I.E. Uflyand, *Nanochastitsy metallov v polimerakh (Metal Nanoparticles in Polymers)* (Khimiya, Moscow, 2000)
2. A.D. Pomogailo, G.I. Dzhardimalieva, V.N. Kestelman, *Macromolecular Metal Carboxylates and their Nanocomposites* (Springer, Heidelberg, 2010)
3. A.D. Pomogailo, G.I. Dzhardimalieva, *Nanostructured Materials Preparation via Condensation Ways* (Springer, Dordrecht, 2014)
4. A.D. Pomogailo, G.I. Dzhardimalieva, *Metallopolymeric Hybrid Nanocomposites* (Nauka, Moscow, 2015)
5. V.V. Vodnik, E.S. Džunuzović, J.V. Džunuzović, Synthesis and characterization of polystyrene based nanocomposites, in *Polystyrene: Synthesis, Characteristics and Applications*, ed. by C. Lynwood (Nova Science Publishers, Inc., New York, 2014)
6. B.C. Sih, M.O. Wolf, Chem. Commun. 3375 (2005)
7. S. Rangelov, A. Pispas, *Polymer and Polymer-Hybrid Nanoparticles: From Synthesis to Biomedical Applications* (CRC, Boca Raton, 2013)
8. L.H. Mancini, C.L. Esposito, *Nanocomposites: Preparation, Properties and Performance* (Nova Science Publication Inc, New York, 2008)
9. G. Carotenuto, L. Nicolais, B. Martorana, P. Perlo, Metal-polymer nanocomposite synthesis: Novel ex situ and in situ approaches, in *Metal-Polymer Nanocomposites*, eds. by L. Nicolais, G. Carotenuto (John Wiley and Sons, Hoboken, New Jersey, 2004), p. 319
10. M.T. Ramesan, K. Suhailath, Role of nanoparticles on polymer composites, in *Micro and Nano Fibrillar Composites (MFCs and NFCs) from Polymer Blends*, eds. by S. Thomas, R. Mishra, N. Kalarikkal (Elsevier, Amsterdam, 2017), pp. 301–326
11. G. Kickelbick, *Hybrid Materials: Synthesis, Characterization, and Applications* (John Wiley & Sons, New York, 2007)
12. K. Du, C.R. Knutson, E. Glogowski, K.D. McCarthy, R. Shenhar, V.M. Rotello, M.T. Tuominen, T. Emrick, T.P. Russell, A.D. Dinsmore, Small **5**, 1974 (2009)
13. R. Liu, Materials **7**, 2747 (2014)
14. J.N. Freitas, A.S. Gonçalves, A.F. Nogueira, Nanoscale **6**, 6371 (2014)
15. T. Dimopoulos, All-oxide solar cells. The future of semiconductor oxides in next-generation solar cells, in *The Future of Semiconductor Oxides in Next-Generation Solar Cells*, ed. by M. Lira-Cantu (Elsevier, Amsterdam, 2017), pp. 439–480
16. R. De Palma, G. Reekmans, C. Liu, R. Wirix-Speetjens, W. Laureyn, O. Nilsson, L. Lagae, Anal. Chem. **79**, 8669 (2007)
17. M. Kuhara, H. Takeyama, T. Tanaka, T. Matsunaga, Anal. Chem. **76**, 6207 (2004)
18. S.L. Lu, G.X. Cheng, H.C. Zhang, X.S. Pang, J. Appl. Polym. Sci. **99**, 3241 (2006)
19. H. Lei, W. Wang, L. Chen, X. Li, B. Yi, L. Deng, Enzyme Microb. Technol. **35**, 15 (2004)
20. H. Qian, Z. Lin, H. Xu, M. Chen, Biotechnol. Prog. **25**, 376 (2009)
21. S. Yang, K. Lien, K. Huang, H. Lei, G. Lee, Biosens. Bioelectron. **24**, 861 (2008)
22. T. Niidome, M. Yamagata, Y. Okamoto, Y. Akiyama, H. Takahashi, T. Kawano, Y. Katayama, Y. Niidome, J. Controlled Release **114**, 343 (2006)
23. D.K. Kim, S.J. Park, J.H. Lee, Y.Y. Jeong, S.Y. Jon, J. Am. Chem. Soc. **129**, 7661 (2007)
24. C.-J. Liu, C.-H. Wang, C.-C. Chien, C.-H. Wang, C.-C. Chien, T.-Y. Yang, S.-T. Chen, W.-H. Leng, C.-F. Lee, K.-H. Lee, Y. Hwu, Y.-C. Lee, C.-L. Cheng, C.-S. Yang, Y.J. Chen, J. H. Je, G. Margaritondo, Nanotechnology **19**, 295104 (2008)
25. S.K. Seol, D. Kim, S. Jung, W.S. Chang, J.T. Kim, J. Nanomater. **6** (2013), Article ID 531760
26. B.D. Warheit, Toxicolog. Sci. **101**, 183 (2008)
27. L. Canesi, C. Ciacci, R. Fabbri, A. Marcomini, G. Pojana, G. Gallo, Marine. Environ. Res. **76**, 16 (2012)
28. A.L. Fernandez, A. Fernandez, J. Blasco, TrAC Trends Anal. Chem. **32**, 40 (2012)
29. T.B. Lee, F.J. Ranville, J. Hazard. Mater. **213–214**, 434 (2012)

30. S. Balog, L.R. Lorenzo, A.C. Monnier, M.R. Obiols, B.R. Rothen, P. Schurtenberger, A.F. Petri, *Nanoscale* **7**, 5991 (2015)
31. Y. Liu, K.M. Shipton, J. Ryan, D.E. Kaufman, S. Franzen, L.D. Feldheim, *Anal. Chem.* **79**, 2221 (2007)
32. V.J. Jokerst, T. Lobovkina, N.R. Zare, S.S. Gambhir, *Nanomedicine* **6**, 715 (2011)
33. J. Manson, D. Kumar, B. Meenan, D. Dixon, *Gold Bull.* **44**, 99 (2011)
34. L.H.T. Nghiem, T.T. Nguyen, E. Fort, P.T. Nguyen, N.M.T. Hoang, Q.T. Nguyen, N.H. Tran, *Adv. Nat. Sci.* **3**, 015002 (2012)
35. H. Bonnemann, R.M. Richards, *Eur. J. Inorg. Chem.* **1434**, 2455 (2001)
36. X. Sun, S. Dong, E. Wang, *Mat. Chem. Phys.* **96**, 29 (2006)
37. L. Persano, A. Camposeo, F. Di Benedetto, R. Stabile, A.M. Laera, E. Piscopiello, L. Tapfer, D. Pisignano, *Adv. Mater.* **24**, 5320 (2012)
38. V.V. Vodnik, J.V. Vuković, J.M. Nedeljković, *Colloid Polym. Sci.* **287**, 847 (2009)
39. T.S. Radoman, J.V. Džunuzović, K.B. Jeremić, A.D. Marinković, P.M. Spasojević, I.G. Popović, E.S. Džunuzović, *Hem. Ind.* **67**, 923 (2013)
40. A.D. Marinković, T. Radoman, E.S. Džunuzović, J.V. Džunuzović, P. Spasojević, B. Isailović, B. Bugarski, *Hem. Ind.* **67**, 913 (2013)
41. A. Laachachi, E. Leroy, M. Cochez, M. Ferriol, J.M. Lopez Cuesta, *Polym. Degrad. Stab.* **89**, 344 (2005)
42. M. Inkyo, Y. Tokunaga, T. Tahara, T. Iwaki, F. Iskandar, C.J. Hogan Jr., K. Okuyama, *Ind. Eng. Chem. Res.* **47**, 2597 (2008)
43. A.J. Gu, G.Z. Liang, *J. Appl. Polym. Sci.* **89**, 3954 (2003)
44. S.M. Pourmortazavi, I. Kohsari, M.B. Teimouri, S.S. Hajimirsadeghi, *Mater. Lett.* **61**, 4670 (2007)
45. E. Themistou, A. Kanari, C.S. Patrickios, *J. Polym. Sci.: Part A: Polym. Chem.* **45**, 5811 (2007)
46. S.H. Kim, F. Nederberg, L. Zhang, C.G. Wade, R.M. Waymouth, J.L. Hedric, *Nano Lett.* **8**, 294 (2008)
47. J.D. Menczel, R.B. Prime (eds.), *Thermal Analysis of Polymers. Fundamentals and Applications* (Wiley, London, 2009)
48. P. Greil, *Adv. Eng. Mater.* **2**, 339 (2000)
49. S. Bernard, M. Weinmann, P. Gerstel, P. Viele, F. Aldinger, *J. Mater. Chem.* **15**, 289 (2005)
50. S. Duperrier, C. Gervais, S. Bernard, D. Cornu, F. Babboneau, C. Balan, P. Miele, *Macromolecules* **40**, 1018 (2007)
51. X. Chen, S. Mao, *Chem. Rev.* **107**, 2891 (2007)
52. V. Ilić, Z. Šaponjić, V. Vodnik, S. Lazović, S. Dimitrijević, P. Jovančić, J.M. Nedeljković, M. Radetić, *Ind. Eng. Chem. Res.* **49**, 7287 (2010)
53. D. Mihailović, Z. Šaponjić, V. Vodnik, B. Potkonjak, P. Jovančić, J.M. Nedeljković, M. Radetić, *Polym. Adv. Technol.* **22**, 2244 (2011)
54. V. Ilić, Z. Šaponjić, V. Vodnik, B. Potkonjak, P. Jovančić, J. Nedeljković, M. Radetić, *Carbohydr. Polym.* **78**, 564 (2009)
55. V. Ilić, Z. Šaponjić, V. Vodnik, D. Mihailović, P. Jovančić, J. Nedeljković, M. Radetić, *Fiber. Polym.* **10**, 650 (2009)
56. M. Radetić, V. Ilić, V. Vodnik, S. Dimitrijević, P. Jovančić, Z. Šaponjić, J.M. Nedeljković, *Polym. Adv. Technol.* **19**, 1816 (2008)
57. V. Ilić, Z. Šaponjić, V. Vodnik, D. Mihailović, P. Jovančić, J.M. Nedeljković, M. Radetić, *J. Serb. Chem. Soc.* **74**, 349 (2009)
58. Y. Prosanov, F.F. Matvienko, *Phys. Solid State* **53**, 824 (2011)
59. V. Ilić, Z. Šaponjić, V. Vodnik, R. Molina, S. Dimitrijević, P. Jovančić, J.M. Nedeljković, M. Radetić, *J. Mater. Sci.* **44**, 3983 (2009)
60. E. Džunuzović, V. Vodnik, K. Jeremić, J.M. Nedeljković, *Mater. Lett.* **63**, 908 (2009)
61. V.V. Vodnik, Z. Šaponjić, J.V. Džunuzović, U. Bogdanović, M. Mitrić, J. Nedeljković, *Mater. Res. Bull.* **48**, 52 (2013)

62. V.V. Vodnik, N.D. Abazović, Z.A. Stojanović, M. Marinović-Cincović, M. Mitrić, M.I. Čomor, *J. Comp. Mater.* **46**, 987 (2012)
63. V. Vodnik, D.K. Božanić, J.V. Džunuzović, I. Vukoje, J. Nedeljković, *Polym. Compos.* **33**, 782 (2012)
64. V.V. Vodnik, D.K. Božanić, E. Džunuzović, J. Vuković, J.M. Nedeljković, *Eur. Polym. J.* **46**, 137 (2010)
65. Ch. Pandis, E. Logakis, A. Kyritsis, P. Pissis, V.V. Vodnik, E. Džunuzović, J.M. Nedeljković, V. Djoković, J.C. Rodriguez Hernandez, J.L. Gomez Ribelles, *Eur. Polym. J.* **47**, 1514 (2011)
66. I.D. Vukoje, V.V. Vodnik, J.V. Džunuzović, E.S. Džunuzović, M.T. Marinović-Cincović, K. Jeremić, J.M. Nedeljković, *Mater. Res. Bull.* **49**, 434 (2014)
67. E.S. Džunuzović, J.V. Džunuzović, T.S. Radoman, M.T. Marinović-Cincović, LjB Nikolić, K.B. Jeremić, J.M. Nedeljković, *Polym. Compos.* **34**, 399 (2013)
68. E. Džunuzović, K. Jeremić, J.M. Nedeljković, *Eur. Polym. J.* **43**, 3719 (2007)
69. E. Džunuzović, M. Marinović-Cincović, K. Jeremić, J. Nedeljković, *Polym. Degrad. Stab.* **94**, 701 (2009)
70. E.S. Džunuzović, J.V. Džunuzović, A.D. Marinković, M.T. Marinović-Cincović, K.B. Jeremić, J.M. Nedeljković, *Eur. Polym. J.* **48**, 1385 (2012)
71. E.S. Džunuzović, M.T. Marinović-Cincović, J.V. Džunuzović, K.B. Jeremić, J.M. Nedeljković, *Hem. Ind.* **64**, 473 (2010)
72. E. Džunuzović, M. Marinović-Cincović, J. Vuković, K. Jeremić, J.M. Nedeljković, *Polym. Compos.* **30**, 737 (2009)
73. E. Džunuzović, M. Marinović-Cincović, K. Jeremić, J. Vuković, J. Nedeljković, *Polym. Degrad. Stab.* **93**, 77 (2008)
74. T. Rath, G. Trimmel, *Hybrid Mater.* **1**, 15 (2013)
75. A.D. Pomogaĭlo, *Ros. Khim. Zh. (Mendeleev Chem. J.)* **46**, 64 (2002)
76. J.Z. Liang, *Polym. Int.* **51**, 1473 (2002)
77. E. Arici, H. Hoppe, F. Schaffler, D. Meissner, M.A. Malik, N.S. Sariciftci, *Appl. Phys. A* **79**, 59 (2004)
78. W. Yue, S. Han, R. Peng, W. Shen, H. Geng, F. Wu, S. Tao, M. Wang, *J. Mater. Chem.* **20**, 7570 (2010)
79. J.J. Wang, Y.Q. Wang, F.F. Cao, Y.G. Guo, L.J. Wan, *J. Am. Chem. Soc.* **132**, 12218 (2010)
80. W.U. Huynh, J.J. Dittmer, A.P. Alivisatos, *Science* **295**, 2425 (2002)
81. W.U. Huynh, J.J. Dittmer, W.C. Libby, G.L. Whiting, A.P. Alivisatos, *Adv. Funct. Mater.* **13**, 73 (2003)
82. D.V. Talapin, J.S. Lee, M.V. Kovalenko, E.V. Shevchenko, *Chem. Rev.* **110**, 389 (2010)
83. A.J. Moule, L. Chang, C. Thambidurai, R. Vidu, P. Stroeve, *J. Mater. Chem.* **22**, 2351 (2012)
84. A.M. Smith, S. Nie, *Acc. Chem. Res.* **43**, 190 (2010)
85. Y. Zhou, M. Eck, M. Kruger, *Energy Environ. Sci.* **3**, 1851 (2010)
86. M.J. Greaney, S. Das, D.H. Webber, S.E. Bradforth, R.L. Brutchey, *ACS Nano* **6**, 4222 (2012)
87. R. Sanz, C. Luna, M. Hernandez-Velez, M. Vazquez, D. Lopez, C. Mijangos, *Nanotechnology* **16**, S278 (2005)
88. S.C. Hsu, W.T. Whang, C.H. Hung, P.C. Chiang, Y.N. Hsiao, *Macromol. Chem. Phys.* **206**, 291 (2005)
89. L.F. Cai, X.B. Huang, M.Z. Rong, W.H. Ruan, M.Q. Zhang, *Macromol. Chem. Phys.* **207**, 2093 (2006)
90. A. Stavrinadis, R. Beal, J.M. Smith, H.E. Assender, A.A.R. Watt, *Adv. Mater.* **20**, 3105 (2008)
91. S. Dayal, N. Kopidakis, D.C. Olson, D.S. Ginley, G. Rumbles, *J. Am. Chem. Soc.* **131**, 17726 (2009)
92. H.C. Liao, S.Y. Chen, D.M. Liu, *Macromolecules* **42**, 6558 (2009)

93. H.C. Leventis, S.P. King, A. Sudlow, M.S. Hill, K.C. Molloy, S.A. Haque, *Nano Lett.* **10**, 1253 (2010)
94. N. Bansal, L.X. Reynolds, A. MacLachlan, T. Lutz, R.S. Ashraf, W. Zhang, C.B. Nielsen, I. McCulloch, D.G. Rebois, T. Kirchartz, M.S. Hill, K.C. Molloy, J. Nelson, S.A. Haque, *Sci. Rep.* **3**, 1531 (2013)
95. M.T. Khan, A. Kaur, S.K. Dhawan, S. Chand, *J. Appl. Phys.* **110**, 044509, 7 (2011)
96. F. Nicolais, G. Carotenuto, *Recent Pat. Mater. Sci.* **1**, 1 (2008)
97. G. Carotenuto, A. Longo, S. De Nicola, F. Nicolais, *Advanced thermochromic plastics for optical temperature sensing*, in *Chromic Materials, Phenomena and Their Technological Applications*, ed. by P.R. Somani (Applied Science Innovation, Pune, India, 2010)
98. I.C. McNeill, J.J. Liggat, *Polym. Degrad. Stabil.* **29**, 93 (1990)
99. I.C. McNeill, J.J. Liggat, *Polym. Degrad. Stabil.* **37**, 25 (1992)
100. S.M. Humphrey, M.E. Grass, S.E. Habas, L. Niesz, G.A. Somorjai, T.D. Tilley, *Nano Lett.* **7**, 785 (2007)
101. Y. Zhang, M.E. Grass, S.E. Habas, F. Tao, T. Zhang, P. Yang, G.A. Somorjai, *J. Phys. Chem. C* **111**, 12243 (2007)
102. A. Manzke, A. Plettl, U. Wiedwald, L. Han, P. Ziemann, E. Schreiber, U. Ziener, N. Vogel, C.K. Weiss, K. Landfester, K. Fauth, J. Biskupek, U. Kaiser, *Chem. Mater.* **24**, 1048 (2012)
103. G. Carotenuto, M. Palomba, L. Nicolais, *Adv. Polym. Technol.* **31**, 242 (2012)
104. G. Carotenuto, M. Palomba, L. Nicolais, *Sci. Eng. Compos. Mater.* **19**, 195 (2012)
105. H. Wakayama, H. Yonekura, Y. Kawai, *ACS Macro Lett.* **2**, 284 (2013)
106. V.T.A. Nguyen, M. Gauthier, O. Sandre, *Nanomaterials* **4**, 628 (2014)
107. H.-L. Liu, S.P. Ko, J.-H. Wu, M.-H. Jung, J.H. Min, J.H. Lee, B.H. An, Y.K. Kim, *J. Magn. Magn. Mater.* **310**, e815 (2007)
108. C. Yang, Q. Shao, J. He, B. Jiang, *Langmuir* **26**, 5179 (2010)
109. L. Jiang, J. Kim, *J. Appl. Polym. Sci.* **101**, 186 (2006)
110. M.C. Alves, G. Tourillon, *J. Phys. Chem.* **100**, 7566 (1996)
111. M. Shariq, P. Majeric, B. Friedrich, B. Budic, D. Jenko, A.R. Dixit, R. Rudolf, *J. Clust. Sci.* **28**, 1647 (2017)
112. W.J.E. Beek, M.M. Wienk, M. Kemerink, X. Yang, R.A.J. Janssen, *J. Phys. Chem. B* **109**, 9505 (2005)
113. S.D. Oosterhout, M.M. Wienk, S.S. van Bavel, R. Thiedmann, L.J.A. Koster, J. Gilot, J. Loos, V. Schmidt, R.A.J. Janssen, *Nat. Mater.* **8**, 818 (2009)
114. T. Gershon, *Mater. Sci. Technol.* **27**, 1357 (2011)
115. J. Boucle, P. Ravirajan, J. Nelson, *J. Mater. Chem.* **17**, 3141 (2007)
116. W. van Beek, R.A.J. Janssen, *Hybrid polymer-inorganic photovoltaic cells*, in *Hybrid Nanocomposites for Nanotechnology*, ed. by L. Merhari (Springer, Boston, 2009), pp. 321–385
117. X. Peng, L. Zhang, Y. Chen, F. Li, W. Zhou, *Appl. Surf. Sci.* **256**, 2948 (2010)
118. K. Yuan, F. Li, L. Chen, Y. Chen, *Thin Solid Films* **520**, 6299 (2012)
119. K. Yuan, F. Li, Y. Chen, X. Wang, L. Chen, *J. Mater. Chem.* **21**, 11886 (2011)
120. C.-H. Lai, W.-F. Lee, I.-C. Wu, C.-C. Kang, D.-Y. Chen, L.-J. Chen, P.-T. Chou, *J. Mater. Chem.* **19**, 7284 (2009)
121. M. Wang, Y. Lian, X. Wang, *Curr. Appl. Phys.* **9**, 189 (2009)
122. P.S. Nair, T. Radhakrishna, N. Revaprasadu, G.A. Kolawole, A.S. Luyt, V.J. Djokovic, *Mater. Sci.* **40**, 4407 (2005)
123. I.J.L. Plante, T.W. Zeid, P. Yang, T. Mokari, *J. Mater. Chem.* **20**, 6612 (2010)
124. S. Shen, Y. Zhang, L. Peng, B.Y. Xu, M. Du, H. Deng, Q. Wang Xu, *Crys. Eng. Commun.* **13**, 4572 (2011)
125. J.H. Warner, A.A.R. Watt, *Mater. Lett.* **60**, 2375 (2006)
126. N.E. Coates, H. Zhou, S. Kramer, L. Li, D. Moses, *Adv. Mater.* **22**, 5366 (2010)
127. E. Maier, T. Rath, W. Hass, O. Werzer, R. Saf, F. Hofer, D. Meissner, O. Volobujeva, S. Bereznev, E. Mellikov, H. Amenitsch, R. Resel, G. Trimmel, *Sol. Energy Mater. Sol. Cells C* **95**, 1354 (2011)

128. S. Dowland, T. Lutz, A. Ward, S.P. King, A. Sudlow, M.S. Hill, K.C. Molloy, S.A. Haque, *Adv. Mater.* **23**, 2739 (2011)
129. T. Rath, M. Edler, W. Haas, A. Fischereder, S. Moscher, A. Schenk, R. Trattinig, M. Sezen, G. Mauthner, A. Pein, D. Meischler, K. Bartl, R. Saf, N. Bansal, S.A. Haque, F. Hofer, E.J. W. List, G. Trimmel, *Adv. Energy Mater.* **1**, 1046 (2011)
130. M. Arar, M. Gruber, M. Edler, W. Haas, F. Hofer, N. Bansal, L.X. Reynolds, S.A. Haque, K. Zojer, G. Trimmel, T. Rath, *Nanotechnology* **24**, 484005 (2013)
131. N. Bansal, F.T.F. O'Mahony, T. Lutz, S.A. Haque, *Adv. Energy Mater.* **3**, 986 (2013)
132. F. Todescato, A.S.R. Chesman, A. Martucci, R. Signorini, J.J. Jasieniak, *Chem. Mater.* **24**, 2117 (2012)
133. M. Helgesen, R. Søndergaard, F.C. Krebs, *J. Mater. Chem.* **20**, 36 (2010)
134. I. Gur, N.A. Fromer, C.-P. Chen, A.G. Kanaras, A.P. Alivisatos, *Nano Lett.* **7**, 409 (2007)
135. C. de Mello, Donegá. *Chem. Soc. Rev.* **40**, 1512 (2011)
136. F. Gao, S. Ren, J. Wang, *Energy Environ. Sci.* **6**, 2020 (2013)
137. R. Zhou, J. Xue, *ChemPhysChem* **13**, 2471 (2012)
138. B.R. Saunders, *J. Colloid Interface Sci.* **369**, 1 (2012)
139. P. Reiss, E. Couderc, J. De Girolamo, A. Pron, *Nanoscale* **3**, 446 (2011)
140. M. Wright, A. Uddin, *Sol. Energy Mater. Sol. Cells* **107**, 87 (2012)
141. L. Zhao, Z. Lin, *Adv. Mater.* **24**, 4353 (2012)
142. E. Martínez-Ferrero, J. Albero, E. Palomares, *J. Phys. Chem. Lett.* **1**, 3039 (2010)
143. K.F. Jeltsch, M. Schädel, J.-B. Bonekamp, P. Niyamakom, F. Rauscher, H.W.A. Lademann, I. Dumsch, S. Allard, U. Scherf, K. Meerholz, *Adv. Funct. Mater.* **22**, 397 (2012)
144. S. Ren, L.-Y. Chang, S.-K. Lim, J. Zhao, M. Smith, N. Zhao, V. Bulović, M. Bawendi, S. Gradecak, *Nano Lett.* **11**, 3998 (2011)
145. Z. Chen, H. Zhang, X. Du, X. Cheng, X. Chen, Y. Jiang, B. Yang, *Energy Environ. Sci.* **6**, 1597 (2013)
146. J. Seo, M.J. Cho, D. Lee, A.N. Cartwright, P.N. Prasad, *Adv. Mater.* **23**, 3984 (2011)
147. R. Zhou, R. Stalder, D. Xie, W. Cao, Y. Zheng, Y. Yang, M. Plaisant, P.H. Holloway, K.S. Schanze, J.R. Reynolds, J. Xue, *ACS Nano* **7**, 4846 (2013)
148. Z. Liu, Y. Sun, J. Yuan, H. Wei, X. Huang, L. Han, W. Wang, H. Wang, W. Ma, *Adv. Mater.* **25**, 5772 (2013)
149. A.A.R. Watt, P. Meredith, J.D. Riches, S. Atkinson, H. Rubinsztein-Dunlop, *Curr. Appl. Phys.* **4**, 320 (2004)
150. A. Watt, E. Thomsen, P. Meredith, H. Rubinsztein-Dunlop, *Chem. Commun.* 2334 (2004)
151. A. Watt, H. Rubinsztein-Dunlop, P. Meredith, *Mater. Lett.* **59**, 3033 (2005)
152. A.A.R. Watt, D. Blake, J.H. Warner, E.A. Thomsen, E.L. Tavenner, H. Rubinsztein-Dunlop, P. Meredith, *J. Phys. D: Appl. Phys.* **38**, 2006 (2005)
153. A. Watt, T. Eichmann, H. Rubinsztein-Dunlop, P. Meredith, *Appl. Phys. Lett.* **87**, 253109-1-3 (2005)
154. A. Stavrinadis, S. Xu, J.H. Warner, J.L. Hutchison, J.M. Smith, A.A.R. Watt, *Nanotechnology* **20**, 445608-1-7 (2009)
155. H.-C. Liao, N. Chantarat, S.-Y. Chen, C.-H. Peng, *J. Electrochem. Soc.* **158**, E67 (2011)
156. P. Sonar, K.P. Sreenivasan, T. Maddanimath, K. Vijayamohan, *Mater. Res. Bull.* **41**, 198 (2006)
157. R.K. Bhardwaj, H.S. Kushwaha, J. Gaur, T. Upreti, V. Bharti, V. Gupta, N. Chaudhary, G. D. Sharma, K. Banerjee, S. Chand, *Mater. Lett.* **89**, 195 (2012)
158. E.A. Lewis, E.A. Lewis, P.D. McNaughtner, Z. Yin, Y. Chen, J.R. Brent, S.A. Saah, J. Raftery, J.A.M. Awudza, M.A. Malik, P. O'Brien, S.J. Haigh, *Chem. Mater.* **27**, 2127 (2015)
159. A.J. MacLachlan, T. Rath, U.B. Cappel, S.A. Dowland, H. Amenitsch, A.-C. Knall, C. Buchmaier, G. Trimmel, J. Nelson, S.A. Haque, *Adv. Funct. Mater.* **25**, 409 (2015)
160. A.K. Bansal, F. Antolini, M.T. Sajjad, L. Stroea, R. Mazzaro, S.G. Ramkumar, K.-J. Kass, S. Allard, U. Scherf, I.D.W. Samuel, *Phys. Chem. Chem. Phys.* **16**, 9556 (2014)
161. V. Agrawal, K. Jain, L. Arora, S. Chand, *J. Nanopart. Res.* **15**, 1697 (2013)

162. V. Kaltenhauser, T. Rath, W. Haas, A. Torvisco, S.K. Müller, B. Friedel, B. Kunert, R. Saf, F. Hofer, G. Trimmel, *J. Mater. Chem. C* **1**, 7825 (2013)
163. C. Fradler, T. Rath, S. Dunst, I. Letofsky-Papst, R. Saf, B. Kunert, F. Hofer, R. Resel, G. Trimmel, *Sol. Energy Mater. Sol. Cells* **124**, 117 (2014)
164. M. Arar, A. Pein, W. Haas, F. Hofer, K. Normman, F.C. Krebs, T. Rath, G. Trimmel, *J. Phys. Chem. C* **116**, 19191 (2012)
165. M. Jäger, R. Trattnig, M. Postl, W. Haas, B. Kunert, R. Resel, F. Hofer, A. Klug, G. Trimmel, E.J.W. List, *J. Polym. Sci. Part B: Polym. Phys.* **51**, 1400 (2013)
166. T. Rath, V. Kaltenhauser, W. Haas, A. Reichmann, F. Hofer, G. Trimmel, *Sol. Energy Mater. Sol. Cells* **114**, 38 (2013)
167. V. Kaltenhauser, T. Rath, M. Edler, A. Reichmann, G. Trimmel, *RSC Adv.* **3**, 18643 (2013)
168. L.X. Reynolds, T. Lutz, S. Dowland, A. MacLachlan, S. King, S.A. Haque, *Nanoscale* **4**, 1561 (2012)
169. F.C. Krebs, N. Espinosa, M. Hösel, R.R. Søndergaard, M. Jørgensen, *Adv. Mater.* **26**, 29 (2014)
170. S.B. Darling, F. You, *RSC Adv.* **3**, 17633 (2013)
171. S.A. Dowland, L.X. Reynolds, A. MacLachlan, U.B. Cappel, S.A. Haque, *J. Mater. Chem. A* **1**, 13896 (2013)
172. W. Chen, M.P. Nikiforov, S.B. Darling, *Energy Environ. Sci.* **5**, 8045 (2012)
173. Y. Zhou, M. Eck, C. Men, F. Rauscher, P. Niyamakom, S. Yilmaz, I. Dumsch, S. Allard, U. Scherf, M. Krüger, *Sol. Energy Mater. Sol. Cells* **95**, 3227 (2011)
174. J. Yang, A. Tang, R. Zhou, J. Xue, *Sol. Energy Mater. Sol. Cells* **95**, 476 (2011)
175. H. Ma, H. Gao, Z. Zhou, W. Xu, F. Ren, *Polym. Polym. Compos.* **23**, 435 (2015)
176. A. Kharkwal, S.N. Sharma, K. Jain, L. Arora, P. Chawla, A.K. Singh, S. Chand, *Colloid Polym. Sci.* **291**, 2607 (2013)
177. P.D. McNaughtner, J.C. Bear, A.G. Mayes, I.P. Parkin, P. O'Brien, *R. Soc. Open Sci.* **4**, 170383 (2017)
178. L. Persano, A. Camposeo, A.M. Laera, F.D. Benedetto, V. Resta, L. Tapfer, D. Pisignano, In situ thermal, photon, and electron-beam synthesis of polymer nanocomposites, in *Synthesis Techniques for Polymer Nanocomposites*, ed. by V. Mittal (Wiley-VCH Verlag GmbH & Co. KGaA, Weinheim, 2014) doi: <https://doi.org/10.1002/9783527670307.ch7>
179. D. Saikia, P.K. Saikia, P.K. Gogoi, M.R. Das, P. Sengupta, M.V. Shelke, *Mater. Chem. Phys.* **131**, 223 (2011)
180. C. Krause, D. Scheunemann, J. Parisi, H. Borchert, *J. Appl. Phys.* **118**, 205501 (2015)
181. T.C. Vagvala, S.S. Pandey, Y. Ogomi, T. Ma, S. Hayase, *Inorg. Chim. Acta* **435**, 292 (2015)
182. T.C. Vagvala, S.S. Pandey, S. Krishnamurthy, S. Hayase, *Z. Anorg. Allg. Chem.* **642**, 134 (2016)
183. A. Jana, E. Scheer, S. Polarz, Beilstein *J. Nanotechnol.* **8**, 688 (2017)
184. S. Yang, R.E. Bachman, X. Feng, K. Müllen, *Acc. Chem. Res.* **46**, 116 (2013)
185. S. Yang, Y. Sun, L. Chen, Y. Hernandez, X. Feng, K. Müllen, *Sci. Rep.* **2**, 427 (2012)
186. A. Chen, A. Kong, X. Fan, X. Yang, C. Li, Z. Chen, Y. Shan, *Int. J. Hydrogen Energy* **42**, 16557 (2017)
187. Y.Y. Liang, M.G. Schwab, L.J. Zhi, E. Mugnaioli, U. Kolb, X.L. Feng, K. Müllen, *J. Am. Chem. Soc.* **132**, 15030 (2010)
188. E. Maier, A. Fischeder, W. Haas, G. Mauthner, J. Albering, T. Rath, F. Hofer, E.J.W. List, G. Trimmel, *Thin Solid Films* **519**, 4201 (2011)

Chapter 7

Application of Nanomaterials Prepared by Thermolysis of Metal Chelates



Nanomaterials obtained by thermolysis of metal chelates are widely used in many promising areas: from catalysis and sensing to energy storage [1–42]. This is achieved by easy fabrication of NPs obtained from metal chelates and other properties, including a large active surface area, optimized porosity, size selectivity, and controlled texture and composition, as well as high photocatalytic activity, high adsorption capacity, good electrocatalytic activity, and outstanding electrochemical performance. These properties have led to applications in many fields, such as the lithium-ion battery (LIB) [43–53], electrochemical capacitors (ECs) [54, 55], sensors [56], catalysis [57–62], adsorption/separation of gases [63]. Nanomaterials obtained by thermolysis of MOFs with chelated units deserve special attention (Table 7.1).

7.1 Fuel Cells

The increase in global energy demand has led to intensive research in the field of storage technologies and conversion of renewable energy sources to replace fossil fuel energy for sustainable development. At present, the development of high-performance storage and energy conversion devices is an important step toward alternative energy technologies [81, 82]. Electrochemical storage of energy is considered one of the most promising ways of storing energy. Among these systems, fuel cells are one of the most promising sources of clean energy as an alternative to traditional fossil fuel technology [83–86]. In these cells, the fuel reacts with oxygen through soft electrochemical processes without combustion, and the overall efficiency of fuel conversion is not limited by the laws of the Carnot cycle. The advantages of fuel cells allowed them to develop into widespread commercial use in the field of transport, as well as in stationary and portable electronics and thus contribute to solving the global energy demand problem [87].

Table 7.1 Metal oxides derived from MOFs and their applications

MOF ^a	Target temperature (K), rate (deg min ⁻¹)	Atmosphere	Product and morphology	Application	References
MOF-5	823, 10	Inert	ZnO QD@C	LIBs	[45]
[(HNTA)(H ₂ O) ₃ Zn] ₂ ·H ₂ O	873, —	—	Microparticle of ZnO	Solar cells	[64]
[(H ₂ O) ₆ Zn]([NTA) ₂ Zn ₂] ₂ ·2H ₂ O	773, —	—	Microwires of ZnO	Solar cells	[64]
ZnMn ₆ -PTCDA MMOFs	723, 5	Air	Spinel ZnMn ₂ O ₄ nanoplates	LIBs	[65]
Cu ₃ (BTC) ₂	873, —	Air	CuO/CeO ₂	CO oxidation	[62]
HKUST-1	673	Air	CuO-Ce ₂ O NPs	CO oxidation	[60]
[Cu ₃ (BTC) ₂] _{2,ln}	823	Air	CuO	LIBs	[51]
[Cu ₃ (BTC) ₂] _{2,ln}	623		CuO/Cu ₂ O composite hollow polyhedrons	LIBs	[44]
[Cu ₃ (BTC) ₂] _{2,ln}	673, 5	N ₂	Cu@C	Sensors	[66]
[Cu ₃ (BTC) ₂] _{2,ln}	573	N ₂ -air	Hollow octahedral CuO	LIBs	[43]
Co ₃ (NDC) ₃ (DMF) ₄	873, 10	Air	Co ₃ O ₄ NPs	LIBs	[48]
TiO ₂ loading MIL-101	823	Air	Fe ₂ O ₃ TiO ₂ nanocomposite	Hydrogen production	[57]
MIL-10	873-1073	N ₂	N-doped graphene/Fe-Fe ₃ C nanocomposite	LIBs	[67]
MIL-53	873	N ₂	Carbon-Fe ₃ O ₄ nanocomposite	Superadsorbent material	[63]
MIL-88-Fe	773	N ₂ -air	Spindle-like mesoporous α-Fe ₂ O ₃	LIBs	[50]
Gd(H ₂ O) ₃ Co	873/973/1073	Air	GdCoO ₃	Photocatalytic degradation of dyes	[68]
[Co ₃ (ABTC) ₃ (bpy) _{1.5} (H ₂ O) ₃] (H ₂ O) ₂	823, 4	Ar	Porous Co ₃ O ₄	Supercapacitors	[54]
In-loading Co-BTC	973	Argon	Co ₃ InC _{0.75}	ORR	[69]

(continued)

Table 7.1 (continued)

MOF ^a	Target temperature (K), rate (deg min ⁻¹)	Atmosphere	Product and morphology	Application	References
Al-loading MIL-101	773/873/973/1073/1173	Air	Cr ₂ O ₃ /Al ₂ O ₃	Isobutane dehydrogenation	[58]
Co-loading MIL-100-Fe	973	Air	CoFe ₂ O ₄	Phenol degradation	[59]
[Co(BDC)(DMF)]	723	–	Co ₃ O ₄ , NPs	LIB	[70]
[Mn(BDC)]	673	–	Mn ₃ O ₄ nanocubes	As a catalyst for the degradation of methylene blue (MB) in wastewater treatment	[71]
MOF-5, [Zn ₄ O(BDC) ₃]	773	–	Octahedral ZnO/ZnFe ₂ O ₄ /C	LIB	[72]
Fe ₂ Ni MIL-88/Fe MIL-88	723	–	NiFe ₂ O ₄ /Fe ₂ O ₃ nanotubes	LIB	[73]
Cr-MIL-101	673	–	Cr ₂ O ₃ @TiO ₂ yolk/shell structure	LIB	[74]
[Mg ₄ (adipate) ₄ (DMA)(H ₂ O) ₅ ·5DMA·2MeOH·4H ₂ O]	773	–	MgO NPs	CO ₂ adsorption	[75]
[Fe ₃ O(BDC) ₃]	823	–	α-Fe ₂ O ₃ nanospindles	Superior lithium storage properties	[76]
Fe ^{III} (OH)(BDC)	623	–	α-Fe ₂ O ₃ needle-like morphology	Methane storage capacity	[77]
[Pb(4-bpdh)(NO ₃)(H ₂ O)] _n	453	–	PbO NPs	Catalyst activity	[78]
[Zr ₆ O ₄ (BDC) ₆]	–	–	Pt NPs@UiO-66 core-shell heterostructure	Electrocatalytic H ₂ O ₂ oxidation	[79]
Ce(BTC)(H ₂ O) ₆ MOF	923	–	CeO ₂	Extraordinarily high pseudocapacitance	[80]

^aH₃ABTC = azobenzene-3,5,4'-tricarboxylic acid; H₃NTA = nitrilotriacetic acid; BTC = 1,3,5-benzene-tricarboxylate; BDC = 1,4-benzenedicarboxylate; NDC = 2,6-naphthalenedicarboxylate; PTCDA = perylene-3,4,9,10-tetracarboxylic dianhydride; DMA = N,N-dimethylacetamide; 4-bpdh = 2,5-bis(4-pyridyl)-3,4-diaza-2,4-hexadiene

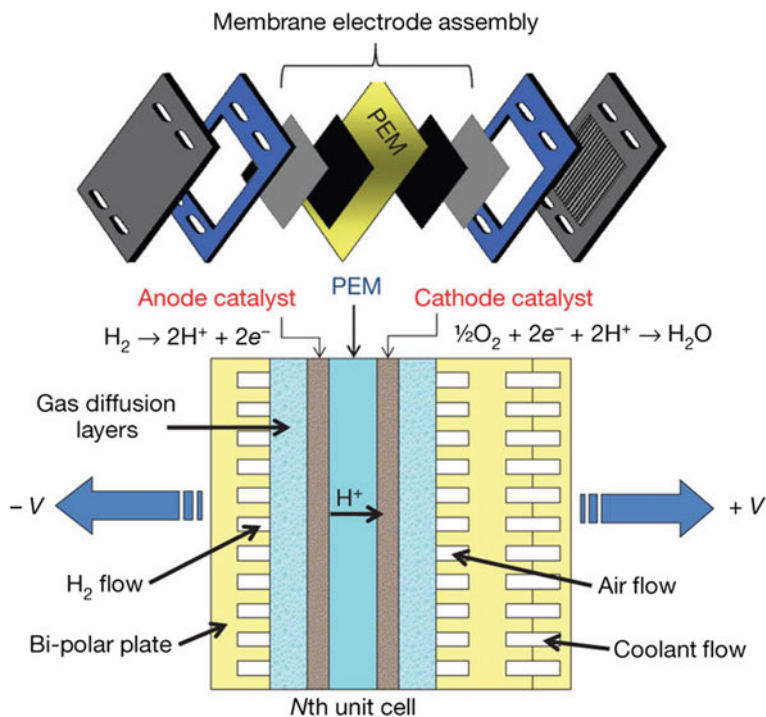
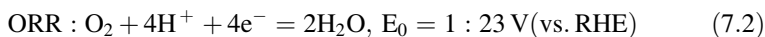
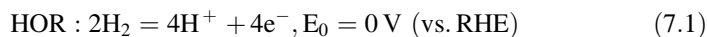


Fig. 7.1 Fuel cell components. Reproduced with permission from Ref. [87]. Copyright (2012) Springer Nature

Among the fuel cells that convert the energy of the chemical reaction into electricity, proton-exchange membrane fuel cells (PEMFCs) are characterized by low operating temperature, high power density, attractive conversion efficiency, low environmental impact, and rapid start-up and are actively developing for supply of future electric vehicles, portable electronics, and other energy-consuming devices [42, 88–97]. They consume fuel (hydrogen, methanol, ethanol, or formic acid) and generate electricity through gentle electrochemical reactions. Each fuel cell consists of an anode, a cathode, and an electrolyte (Fig. 7.1) [87]. In an alkaline fuel cell, the oxygen reagent can be reduced to OH^- with a general reaction of $\text{O}_2 + 2\text{H}_2\text{O} + 4\text{e}^- = 4\text{OH}^-$ from the cathode side. Obtained OH^- anions reach the anode through the electrolyte of the anion-exchange membrane. On the side of the anode, hydrogen (H_2) can interact with OH^- as a fuel and produce H_2O and electrons ($2\text{H}_2 + 4\text{OH}^- = 4\text{H}_2\text{O} + 4\text{e}^-$). Electrons are transferred to the cathode through an external circuit, and hydroxide ions reach the cathode through the electrolyte membrane.

Generally, in typical H_2 – O_2 fuel cells [98–100], the hydrogen oxidation reaction (HOR) at the anode and oxygen reduction reaction (ORR) at the cathode can be simplified as two half-cell reactions [Eqs. (7.1 and 7.2)]:



where RHE is reversible hydrogen electrode.

The kinetics of these two reactions is critical to the output characteristics of the fuel cells. However, in low-temperature fuel cells, both reactions are limited by huge activation energy barriers that can be conquered by catalysts that induce lower energy intermediates [101].

The development of inexpensive, highly active, and durable cathode material is a priority area of research in the commercialization of low-temperature fuel cells [86]. Currently, carbon-supported Pt NPs are widely used as catalysts both at the anode and at the cathode to accelerate the kinetics of the HOR and ORR reactions [102–106]. The reaction rate of HOR on Pt is fast enough, so the required amount of Pt loading at the anode can be less than 0.05 mg cm^{-2} . However, on the cathode, the slow kinetics of the ORR reaction requires a much higher Pt load ($\sim 0.4 \text{ mg cm}^{-2}$) for achieving the appropriate characteristics of fuel cells [107–109]. Pt-based noble metal catalysts still suffer from a number of critical problems such as high cost, low abundance, poor stability, crossover effect, CO poisoning, low selectivity, and harmful environmental effects [110–118]. Moreover, excessive cost and Pt deficiency also limit the commercialization of PEMFCs. These bottlenecks impede the widespread commercialization of fuel cells. Under these conditions, the reduction in the load of Pt or even the study of alternatives for the replacement of the expensive Pt alloy was intensively studied for the creation of high-efficiency inexpensive non-noble metal catalysts.

Great efforts have been made to develop high-efficient, economical, and stable ORR catalysts, including advanced Pt-based catalysts, core–shell structures, heteroatom-doped carbon, and transition metal/metal oxide–carbon composite catalysts (Fig. 7.2) [88, 119–140].

In general, two different approaches (or a combination thereof) can be used to reduce Pt's load in PEFC: (i) the development of the surface structure (i.e., the atomic arrangement) of catalytic Pt NPs and hence the maximization of specific activity [141–144]; and (ii) the inclusion of another less expensive metal (e.g., Ni, Co, Fe, Cu, and Pd, among others) in NPs to create a core–shell or a doped nanostructure and, thus, improve the dispersion of Pt and change its electronic properties [141, 145–148].

As a typical example, we note the synthesis in non-hydrolytic systems of highly homogeneous Pt icosahedra nanocrystals with an edge length of 8.8 nm using the GRAILS method with hot injection [149]. The structural feature of the icosahedron is its surfaces surrounded by {111} faces. This is important for applications in electrocatalysis, since the expanded surface of Pt (111) is nine times more active than the highly active commercial Pt/C catalysts relative to ORR [148]. The electrocatalytic properties of icosahedra, cubes, and 3-nm Pt NPs on carbon were studied using a three-electrode system (Fig. 7.3). The onset potentials for the ORR

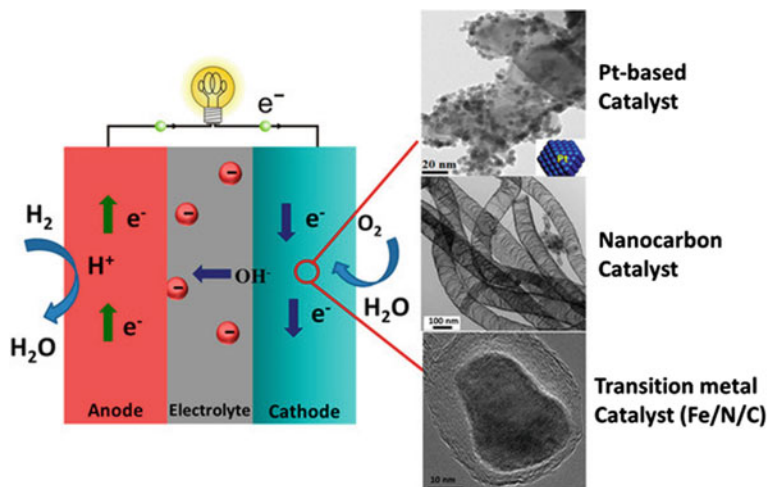
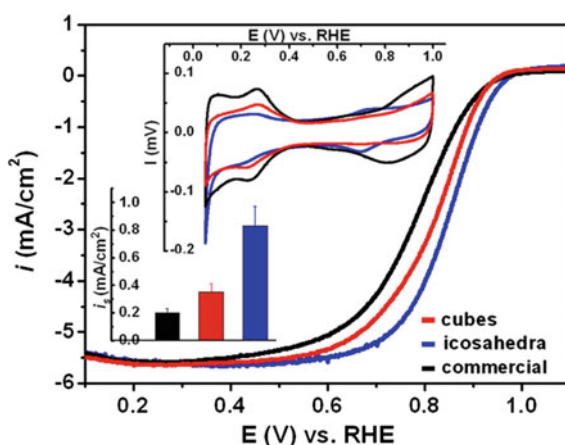


Fig. 7.2 Illustration of typical pathways of oxygen reduction reaction in an alkaline fuel cell and three categories of the cathode catalysts used for ORR [132]

Fig. 7.3 ORR polarization curves for icosahedra (blue), cubes (red), and commercial (black) Pt catalysts. The upper inset shows their corresponding cyclic voltammogram (CV) curves. The inset at the bottom shows their specific-area activities at 0.9 V. Reproduced with permission from Ref. [149]. Copyright (2013) American Chemical Society



polarization curves follow the order of icosahedra > cubes > Pt reference (commercial). The specific surface activity reached $0.83 \pm 0.14 \text{ mA cm}^{-2} \text{ Pt}$ for Pt icosahedra and $0.35 \pm 0.06 \text{ mA cm}^{-2} \text{ Pt}$ for cubes Pt. These results indicate that the intrinsic ORR activity of the (111) surface coated with the Pt-icosahedron was about four times higher than that of the reference Pt/C catalyst ($0.20 \pm 0.03 \text{ mA cm}^{-2} \text{ Pt}$) and about half the value evacuated, expanded single crystal (111) surface of Pt. It should be noted that recent simulations and experimental data suggest that twinning in NPs of Pt and some Pt alloys helps to shift the binding energy of the reacting intermediates due to the surface and deformation

effect of NPs [150–152]. Thus, the significantly improved ORR activity for icosahedral NP catalysts can be attributed to the {111} factor and the presence of double planes in such types of NP electrocatalysts.

It is of interest to investigate inexpensive alternatives with high activity and excellent stability as replacements for Pt catalysts, such as Pt-M alloys (M = Fe, Co, Ni) and Pt-free catalysts [153–156]. In particular, various bimetallic Pt nanocrystals with controlled faces were rationally synthesized and shown with strongly extended activities for ORR [115, 118, 155, 157–162]. Among them, the octahedral NPs of Pt₃Ni have shown the greatest interest in recent years, as a study of the Pt₃Ni (111) single crystal was published in 2007, in which a 90-fold improvement in the specific activity over the commercial Pt/C catalyst was observed. After that, the octahedral NPs Pt-Ni alloys enclosed by {111} faces were successfully obtained [157, 158, 163]. An over sevenfold improvement in area-specific activity in the ORR was achieved by changing from the (100) to (111) Pt₃Ni single crystal surfaces [149]. Therefore, morphology control over Pt alloy nanocrystals has great technological implications [164–166]. However, the highest ORR activity (both specific and Pt mass) obtained from these catalysts was only ten times higher than the commercial Pt/C catalyst, far below the values proposed in the work based on bulk single crystals.

It should be noted the synthesis of homogeneous 9-nm Pt-Ni octahedra using OAm and OA as surfactants and W(CO)₆ as a source of CO, which can promote the formation of {111} faces in the presence of Ni [167]. By removing surfactants with acetic acid, the specific activity was observed 51 times higher than that of the Pt/C catalyst for ORR at 0.93 V together with a record high mass activity of 3.3 A mg_{Pt}⁻¹ at 0.9 V. A significant increase in ORR activity can be explained by the presence of a clean, well-preserved (111) surface for octahedral Pt-Ni (Fig. 7.4).

A wet chemical approach to the production of monodisperse Pt₃Ni nano-octahedra and nanocubes ending in {111} and {100} faces, respectively, is of interest [168]. In particular, it was shown that the ORR activity on Pt₃Ni nano-octahedra is five times higher than for nanocubes with the same size (Fig. 7.5). In addition, a comparison of ORR activity between carbon-supported Pt₃Ni nano-octahedra and commercial Pt/C shows that Pt₃Ni nano-octahedra are highly active electrocatalysts.

The polarization curves of the rotating disk electrode (RDE) show that the cubic and octahedral Pt₃Ni catalysts have more positive onset potentials and, therefore, are more active than Pt (Fig. 7.6a) [156]. It was found that the ORR specific activity at 0.9 V is 0.85 mA cm⁻² Pt for cubic and 1.26 mA cm⁻² Pt for octahedral Pt₃Ni catalysts (Fig. 7.6b). ORR activity increased with the change in shape from cube to octahedron. The mass activity of the octahedral Pt₃Ni catalyst reaches 0.44 A mg_{Pt}⁻¹ (Fig. 7.6c), which is approximately three times the activity of the reference Pt/C and is one of the highest values for Pt₃Ni nanocrystals with a controlled shape [156, 168].

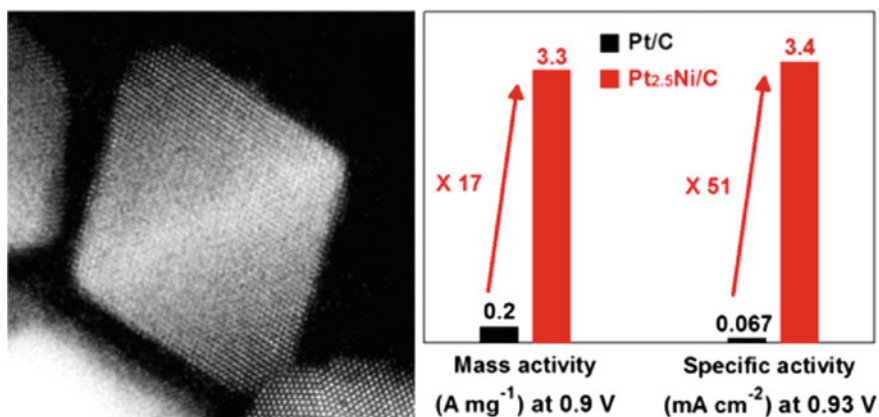


Fig. 7.4 Scanning TEM-high angle annular dark field (STEM-HAADF) image of the as-obtained Pt-Ni octahedron and comparative analysis of mass and specific activity of Pt/C and Pt_{2.5}Ni/C. Reproduced with permission from Ref. [167]. Copyright (2013) American Chemical Society

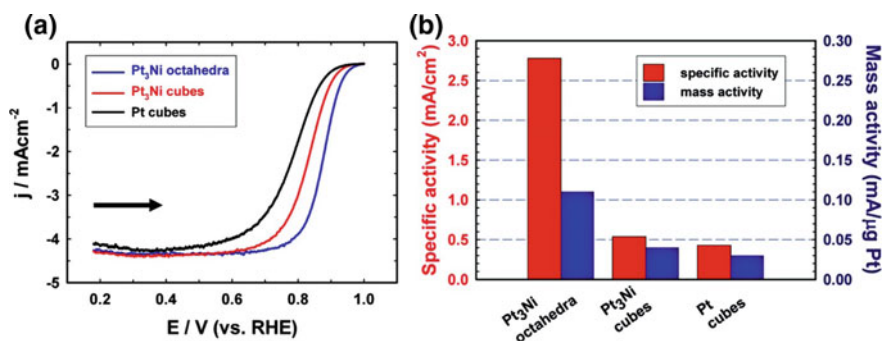


Fig. 7.5 **a** Polarization curves for ORR on Pt₃Ni nano-octahedra, Pt₃Ni nanocubes, and Pt nanocubes supported on a rotating glassy carbon (GC) disk electrode in O₂-saturated 0.1 M HClO₄ solution at 295 K; scan rate, 20 mV s⁻¹; rotation rate, 900 rpm. Catalyst loading in terms of Pt mass: Pt₃Ni octahedra, 3.0 μg; Pt₃Ni cube, 2.0 μg; Pt cube, 1.1 μg. Current density was normalized to the GC geometric surface area (0.196 cm²). The arrow indicates the potential scan direction. **b** Comparison of the ORR activities on the three types of catalysts. Specific activity and mass activity were all measured at 0.9 V vs RHE at 295 K. Reproduced with permission from Ref. [168]. Copyright (2010) American Chemical Society

Studies on the search for efficient and economical electrocatalysts for ORR have led to the appearance of some new competitors, including some porous carbonaceous materials, due to their outstanding advantages, for example, high electrical conductivity, large surface area, and high thermal and chemical stability [169–171]. Nevertheless, carbon itself exhibits low internal activity of ORR [172]. At the same

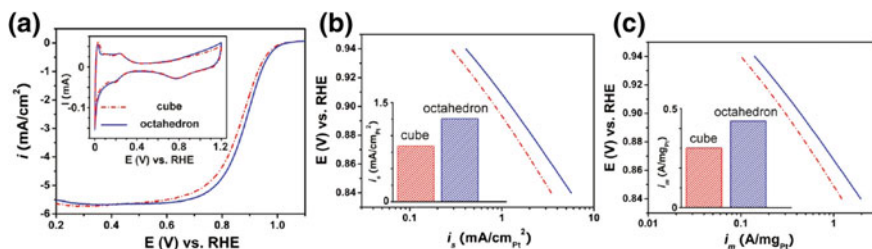


Fig. 7.6 Comparison of electrocatalytic properties of cubic and octahedral Pt₃Ni nanocrystals: **a** ORR polarization and CV (insert) curves, **b** area, and **c** mass specific activities. Reproduced with permission from Ref. [156]. Copyright (2010) American Chemical Society, and reproduced with permission from Ref. [168]. Copyright (2010) American Chemical Society

time, carbon materials obtained by thermolysis of metal chelates are widely used in devices for storing and converting energy [14, 21, 35, 173–182]. It is widely recognized that the inclusion of nitrogen atoms in the carbon lattice can significantly improve the surface polarity and electron-donor tendency of the carbon matrix, leading to advanced electrocatalytic characteristics with respect to ORR [166, 183, 184]. Functional NPC materials doped with a heteroatom are considered promising metal-free electrocatalysts in fuel cells because of their unique physical and chemical characteristics, pronounced electrocatalytic activity, long-term stability, and relatively low costs [89, 185, 186]. Among them, nanocarbon composites (e.g., nanocarbon/carbon nanotubes (CNTs), nanocarbon/graphene) [187–189], as well as single- [190–192] and multidoped nanocarbon [193–200], as effective electrocatalysts in fuel cells were studied. Recent studies have shown that the inclusion of heteroatoms of nitrogen and non-noble transition metals in nanostructured carbon materials can significantly improve the electrocatalytic characteristics [129, 166, 201].

One of the main achievements is the development of metal–nitrogen–carbon catalysts (M–N–C), obtained from the precursors based on macrocyclic complexes of transition metals. Since the discovery of the 1960s that the phthalocyanines of Co catalyze ORR [202], much work has been done using Co and Fe complexes with macrocycles, such as porphyrins and other nitrogen-containing ligands, as catalysts for ORR. Later, it was found that thermolysis products of these compounds, as well as other complexes derived from Co and Fe salts, N-donor ligands, and/or polymers applied to different carbon atoms, exhibit higher activity and stability than their precursor materials, comparable in some cases with a platinum catalyst [203–207]. Among them, special attention was paid to catalysts based on porphyrin polymers with coordinated transition metal [38, 208, 209].

As a typical example, we note a porous Co–N–C catalyst (Fig. 7.7a) with a high specific surface area (1074 m² g⁻¹) [210]. This catalyst showed a high performance in the hydrogen evolution reaction (HER) at all pH values, such as 10 mA cm⁻²,

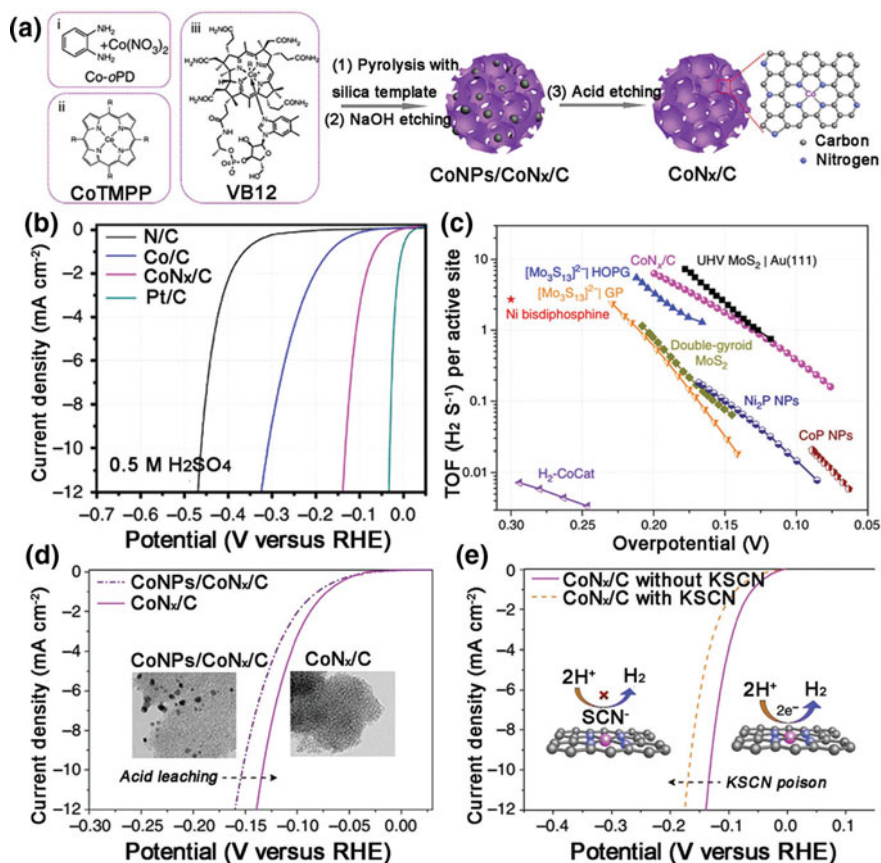


Fig. 7.7 a Schematic illustration of the synthesis of CoNx/C electrocatalysts. b HER polarization plots of CoNx/C, N/C, Co/N and Pt/C catalysts in 0.5 M H_2SO_4 . c Comparison of the TOF of CoNx/C with other catalysts. d Comparison of the HER activity of CoNPs/CoNx/C and CoNx/C catalysts, showing the influence of acid leaching. Insets are TEM images demonstrating that all Co particles were removed by acid leaching. e HER polarization plots of CoNx/C with and without 10 mM KSCN in 0.5 M H_2SO_4 [210]

achieved with 133 mV overpotential in the acid and an unprecedented turnover frequency (TOF), where TOFs per atom Co are 0.39 and 6.5 s^{-1} at an overpotential of 100 and 200 mV, respectively (Fig. 7.7b, c). In addition, thiocyanate ions (SCN^-), which can poison metal-centered catalytic centers in acid, have been adapted to demonstrate that the active sites are CoNx centers (Fig. 7.7d, e).

It should be noted that there are still some disagreements regarding the nature of the active sites on which the ORR occurs. For example, it has been suggested that pyridine nitrogen atoms, in particular those that do not contain metals, are active centers [211]. On the other hand, it was shown that Fe-Nx or Co-Nx groups with coordinated pyridine N atoms correspond to active sites [212–216]. Finally,

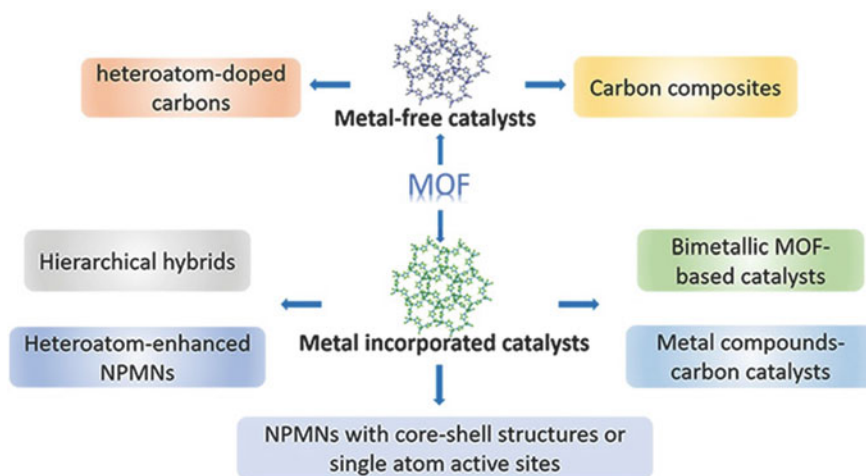
high-activity catalysts based on Fe were found in which no direct coordination of metal-nitrogen was observed [217].

Of interest are carbon-based non-precious metal nanocatalysts with porous structures considered as the class of the most promising ORR catalysts because of the low cost and high availability of their raw materials. They are effective in ORR due to the provision of abundant open active sites, increased availability of reagents, rapid mass transfer, and electron transfer [185, 218, 219]. These properties play an important role in improving the catalytic characteristics. Generally, catalysts with a high surface area, a large percentage of mesopores, and a narrow pore distribution are highly desirable for ORR catalysis. For example, mesoporous Co, N-doped carbon (Co–N–C) and Fe,N-doped carbon (Fe–N–C) catalysts based on vitamin B12 and polyaniline-Fe, respectively, were obtained [220]. Silicon NPs, ordered mesoporous silica SBA-15, and montmorillonite were also used as templates for the preparation of porous structures. Despite the almost identical composition of these three Co–N–C catalysts, a strong correlation was observed between the activity and the BET surface area, demonstrating the importance of the porous structure for ORR. The increased electrocatalytic characteristics of these catalysts were due to the homogeneous distribution of the metal–nitrogen–carbon active centers (M–N–C), the high BET surface area, and the narrow pore distribution. As rigid templates for the synthesis of porous Fe/N-doped carbon catalysts for ORR in the presence of dopant and carbon sources, silica NPs with different diameters were also used [221].

Carbon nanomaterials designed by heteroatoms (e.g., N, B, P, S, and F) have made it possible to achieve a marked improvement in the activity of the catalyzed ORR due to their tunable electronic properties and conductivity [191, 222–228]. In particular, nitrogen-doping in nanocarbon is the easiest-to-implement strategy for the development of Pt-alternative ORR electrocatalysts because of their good performance, high stability, low cost, and environmental friendliness [171, 183, 184, 217, 229–238]. Doping nitrogen atoms into carbon matrices can disrupt the electrical homogeneity of the carbon framework and create active centers of ORR with a higher electron density [88, 157, 239–245]. The additional electron density of nitrogen-doped carbons makes it possible to obtain a larger number of protonic acid sites ($-\text{SO}_3\text{H}$) by sulfonation [220, 246, 247]. As a result, nitrogen-doped carbon materials have high catalytic activity for ORR and can be used as effective carriers for the protonic acid sites [248, 249].

It should be noted that MOF materials have been widely used as templates and/or precursors for the production of porous carbon and related functional nanomaterials that exhibit excellent catalytic activity against ORR or oxygen evolution reaction (OER) and possess composition and morphology-dependent catalytic performances (Scheme 7.1) [81, 123, 221, 250–252].

Due to the subtle design of the MOF precursors, as well as the careful post-processing, the advantages and catalytic activity of MOF materials can be completely inherited by nanomaterials derived from MOF. For example, MOF-derived heteroatom-doped nanocarbon [187–190], transition metal/metal oxide–carbon hybrids, and composites [46, 65, 176, 253–255] with high surface



Scheme 7.1 Non-precious metal nanoparticles (NPMNs) derived from MOFs. Reproduced with permission from Ref. [250]. Copyright (2017) John Wiley and Sons

area and porosity exhibit excellent catalytic activity and stability and also show outstanding bifunctional activity with respect to the ORR and OER. It should be noted that the MOF precursors used in the preparation of the heteroatom-doped nanocarbon can be readily adapted by binding them to a second heteroatom-containing precursor. This duality makes it possible to control both the chemical composition and the porous structure of the final carbon product [172]. In addition, N [44, 166, 256–259], B [222, 260–262], S [263–266], P [265, 267–270], and the halogen atom [270] have been widely used to produce single-, double-, or triple-doped porous carbon atoms to increase ORR activity, especially transition metals (e.g., Fe, Co) containing nitrogen-doped porous carbon materials showed promising results [38, 207, 208, 271, 272]. In particular, the double or triple doping of nitrogen, sulfur, and phosphorus in carbon has been further optimized to improve ORR activity [273]. Theoretical calculations have shown that the S atom is positively charged and is considered an effective catalytic center of the ORR, whereas P-doping can enhance the delocalization of the charge of carbon atoms and lead to carbon structures with increased edge sites.

It should be noted that the inclusion of an ultrathin layer of MOF-derived nanocarbon on graphene oxide sheets can lead to the formation of a nanocarbon/graphene oxide/nanocarbon sandwich-like structure with a high specific surface area and excellent electronic conductivity.

Furthermore, a large cathodic current density (5.06 mA cm^{-2}) was observed, with a value slightly higher than that found for Pt/C (4.76 mA cm^{-2}). Notably, the excellent ORR catalytic performance typically results from the unique heterostructure of N-doped graphite porous nanocarbon (NGPC)/N-doped carbon nanotubes (NCNTs) composite. Based on the fact that the decrease in N content in NGPC/NCNTs does not lead to a proportional drop in ORR activity, the authors

discovered that pyridine-N and pyrrolic-N, located at graphitic plane sites, play a critical role for obtaining high ORR activity [193].

In addition to the graphene carrier, CNTs and NCNTs used in the synthesis of nanocarbon composite materials have also demonstrated enhanced activity and the durability of ORR. In particular, NGPC)/NCNT composites were studied as ORR catalysts operating in alkaline media [223]. The MOF-5, $[\text{Zn}_4\text{O}(\text{BDC})_3]$, in combination with urea and nickel was used as the precursor and catalyst for the development of the NGPC/NCNT composite at 1173 K under N_2 . The resulting NGPC/NCNTs catalyst contains NCNT of *ca.* 30 nm with an outside diameter and in joint length is *ca.* 20 nm (Fig. 7.8). It is important that bamboo-like defects on NCNTs are a typical morphological feature of N-doping and help in creating active sites for ORR. The ORR half-wave potential measured with the NGPC/NCNTs composite catalyst is by *ca.* 8 mV higher than for Pt/C. In addition, a large cathode current density (5.06 mA cm^{-2}) was observed with a value, slightly exceeding the value found for Pt/C (4.76 mA cm^{-2}).

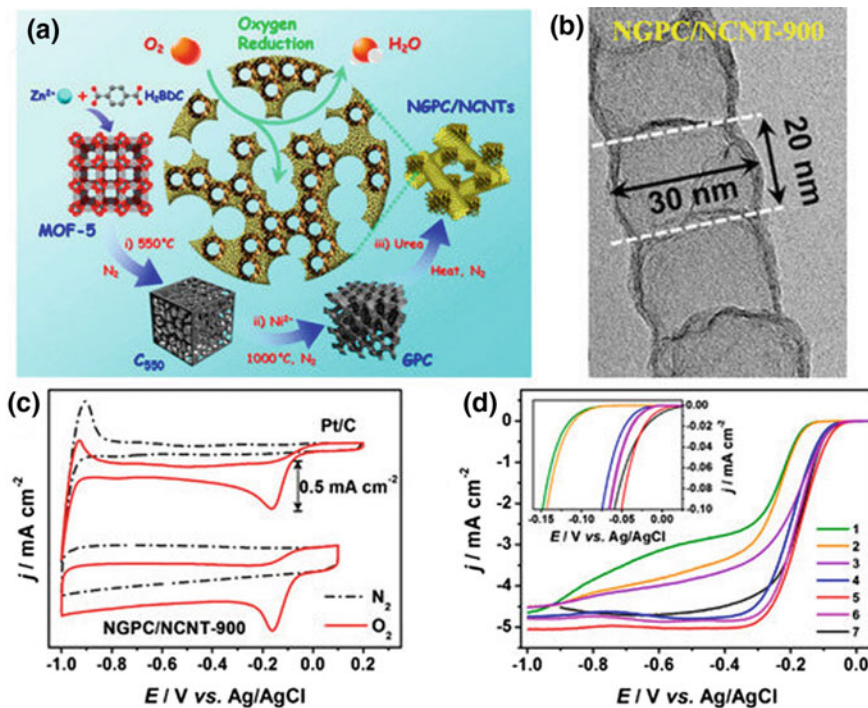


Fig. 7.8 **a** Schematic illustration of the stepwise structural evolution from MOF-5 to NGPC/NCNTs; **b** HRTEM images of NCNTs in NGPC/NCNT-900; **c** CVs of NGPC/NCNT-900 and Pt/C; **d** Linear sweep voltammograms (LSVs) of GPC (trace 1), CMOF-5 (trace 2), NPC (trace 3), NGPC/NCNT-800 (trace 4), NGPC/NCNT-900 (trace 5), NGPC/NCNT-1000 (trace 6), and Pt/C (trace 7) in O_2 -saturated 0.1 M KOH with an electrode rotation speed of 1600 rpm. Reproduced with permission from Ref. [223]. Copyright (2012) American Chemical Society

A reliable and controllable route suitable for the preparation of nitrogen-doped porous carbon with high yields and exceptional quality by Zn-MOF-74 thermolysis is of interest [274]. The prepared NPC demonstrates the advantages of high activity, high durability, and methanol resistance as an effective pH-universal electrocatalyst for ORR, demonstrating comparable or even better activity compared to commercial Pt/C catalysts not only in alkaline media but also in acid and neutral electrolyte. In particular, the CV curves of NPC-1000 (Fig. 7.9a) show that the peak was not observed in the absence of an electrolyte without O₂, whereas in the O₂-saturated electrolyte a distinct peak at 0.828 V was observed, indicating a high catalytic ORR activity of the NPC-1000. An onset potential of the NPC-1000 is 1.02 V, and the potential of a half-wave ($E_{1/2}$) of 0.902 V with a limiting current density is of about -5.85 mA cm^{-2} (Fig. 7.9b). These performance parameters outperform the original Zn-MOF-74. The RDE voltammograms for ORR on the prepared electrode NPC-1000 were run at a rotation speed of 400–2500 rpm (Fig. 7.9c). The Koutecky–Levich (K–L) linear plots assume the kinetics of a first-order reaction with respect to the concentration of dissolved O₂ and a similar number of electron transfer for ORR at different potentials. In addition, the ratio of the undesirable production of H₂O₂ at the NPC-1000 electrode with a low percentage (<10%) is consistent with commercial Pt/C, indicating a high catalytic selectivity of the NPC-1000 (Fig. 7.9d). The NPC-1000 exhibited very slow damping with high current retention of more than 98% after a continuous reaction of 20,000 s, while the Pt/C catalyst showed a decrease in activity of 6.0% in the same state (Fig. 7.9e). Compared to commercial Pt/C and PC-1000, the NPC-1000 demonstrates a noticeable negative shift in the onset potential (0.818 V) and a significant improvement in the diffusion-limiting current density (Fig. 7.9f). This may be due to the protonation of nitrogen atoms and, consequently, adsorbs the SO₄²⁻ anion on the NPC surface to block some active sites [275, 276]. When the ORR is performed in O₂-saturated phosphate buffer, the NPC-1000 showed an onset potential of 1.03 V and $E_{1/2}$ of 0.818 V, which are more positive than those obtained on Pt/C and PC-1000 (Fig. 7.9h). As with the alkaline solution, the NPC-1000 is highly durable and does not contain methanol poisoning under both conditions, whereas the Pt/C demonstrates low stability and low tolerance of methanol under similar conditions (Fig. 7.9g, i).

Nanoporous nitrogen-doped carbon microfibers were easily synthesized by thermolysis of CP microfibers of Al-DTPA [277]. NCF characteristics, including high surface area, nanoporous structure, appropriate degree of graphitization, and abundant nitrogen-doped carbon sites, can allow the use of NCF as efficient ORR electrocatalysts. In the Ar-saturated 0.1 M KOH solution, there appear faceless voltammetric curves for NCFs, while in the 0.1 M KOH solution saturated with O₂, noticeable cathodic ORR peaks are observed at about 0.8 V, which illustrates their effective ORR activity in alkaline media (Fig. 7.10a). NCFs obtained at different temperatures show different ORR activities in terms of their onset ORR potentials and $E_{1/2}$ (Fig. 7.10b). The corresponding K–L plots from the RDE curves (Fig. 7.10c, d) between 0.5 and 0.0 V showed good parallel straight lines, which indicates the order of reaction of one with respect to oxygen in this potential range. The significant

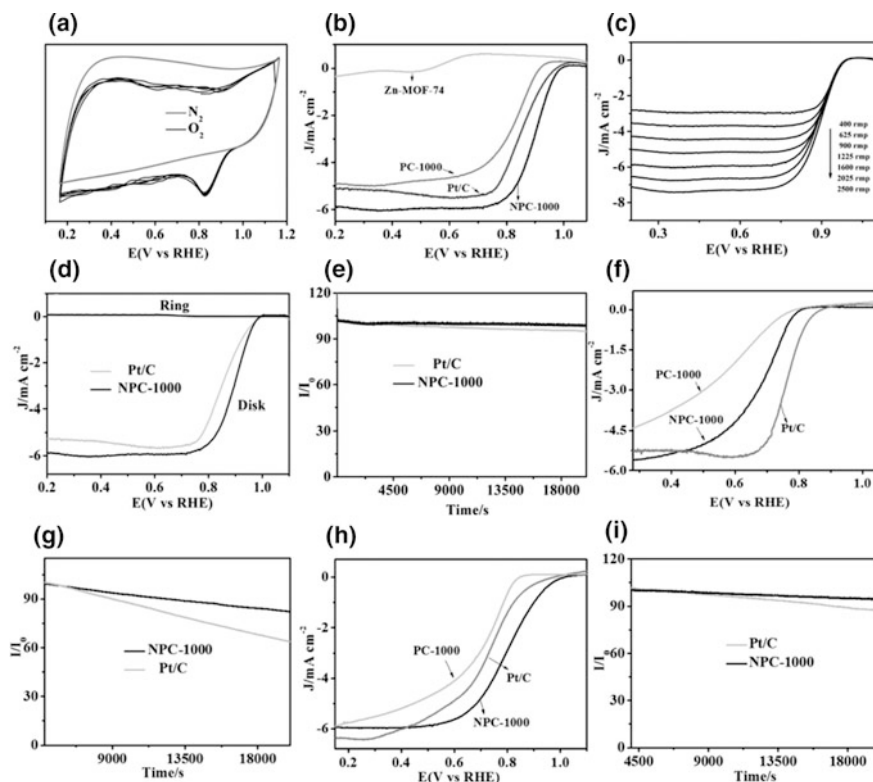


Fig. 7.9 **a** CV of NPC-1000 in N_2 - and O_2 -saturated 0.1 M KOH solution at a scan rate of 50 mV s^{-1} . **b** LSV curves for Zn-MOF-74, NPC-1000, PC-1000, and a benchmark Pt/C at an RDE rotation rate of 1600 rpm with a scan rate of 10 mV s^{-1} . **c** LSV curves of NPC-1000 at different rotating speeds. **d** Rotating ring-disk electrode (RRDE) curve for NPC-1000 for a rotation speed of 1600 rpm. **e** Current–time (*i*–*t*) chronoamperometric response of NPC-1000 and benchmark Pt/C electrodes at 0.56 V in O_2 -saturated 0.1 M KOH at a rotation rate of 1600 rpm. **f** LSV curves for PC-1000, NPC-1000, and Pt/C at an RDE rotation rate of 1600 rpm with a scan rate of 10 mV s^{-1} in O_2 -saturated 0.5 M H_2SO_4 solution. **g** *i*–*t* chronoamperometric response of NPC-1000 and benchmark Pt/C electrodes at 0.62 V in O_2 -saturated 0.5 M H_2SO_4 solution at a rotation rate of 1600 rpm. **h** LSV curves for PC-1000, NPC-1000, and Pt/C at an RDE rotation rate of 1600 rpm with a scan rate of 10 mV s^{-1} in O_2 -saturated 0.1 M buffer. **i** *i*–*t* chronoamperometric response of NPC-1000 and benchmark Pt/C electrodes at 0.25 V in O_2 -saturated 0.1 M buffer solution at a rotation rate of 1600 rpm. Reproduced with permission from Ref. [274]. Copyright (2011) American Chemical Society

effect of methanol on the ORR current density over the Pt/C cathode was observed on the corresponding (*i*–*t*) curve after the addition of methanol (Fig. 7.10e). Moreover, the durability of the NCF-900 during the ORR exceeds the Pt/C materials, and the corresponding *i*–*t* plots of NCF-900 show a relative slow decay (Fig. 7.10f).

However, the electrocatalytic characteristics of most of the developed doped porous carbons are still far beyond modern noble metal catalysts. In addition, although it has been shown that pyridinic-N and graphitic-N are the main catalytic

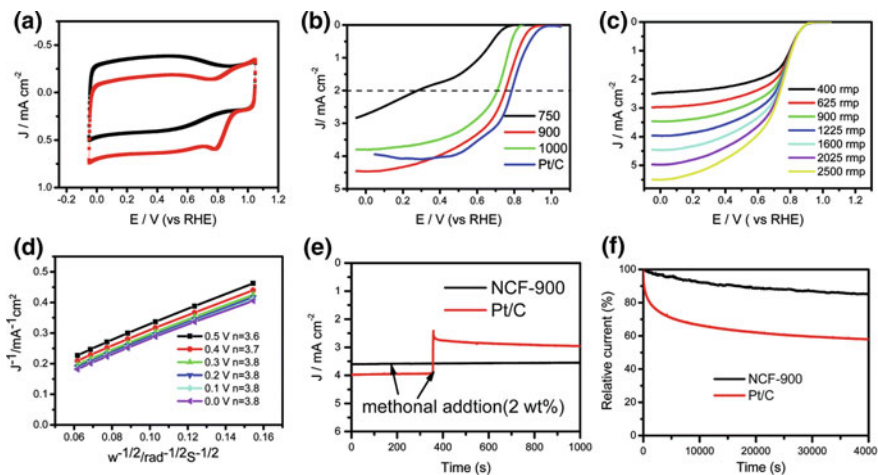


Fig. 7.10 **a** CVs recorded on porous NCF-900 in a Ar- or O₂-saturated 0.1 M KOH solution at a scan rate of 10 mV s⁻¹; **b** RDE voltammograms recorded on porous NCFs obtained at different temperatures and Pt/C (10 wt%) in 0.1 M O₂-saturated KOH solution; **c** RDE voltammograms recorded on porous NCF-900 at different rotation speeds from 400 to 2500 rpm; **d** K–L plots of J⁻¹ versus w^{-1/2} on porous NCF-900 at different potentials; **e** current–time (i–t) plots of NCF-900 and Pt/C at 0.55 V in the presence of methanol; **f** current–time (i–t) plots of NCFs-900 and Pt/C at 0.55 V in O₂-saturated KOH solution [277]

active sites for ORR [166, 183, 249, 278–283], it is difficult to adjust the amount and mode of N-doping in the synthesis of N-doped nanocarbon. More importantly, most N-doped nanocarbon can show comparable ORR catalytic characteristics with Pt-based catalysts only in alkaline electrolyte, while they cannot work well as Pt-based catalysts in acidic and neutral solutions [275, 284–287].

MOF-derived metal-containing NPs are demonstrated to possess great potential in ORR electrocatalysis by serving as catalysts or supports [177, 271, 288, 289]. Among the non-noble metal catalysts, the transition metal/oxide–carbons (e.g., Co/Co₃O₄–C, Co–N_x–C, Fe–N_x–C) have been the main research direction due to their excellent electrocatalytic activity, high stability, and low cost [216, 289–295]. In particular, non-precious metal catalysts made from MOF precursors were investigated and demonstrated a number of advantages due to their high specific surface area, porous structure, and abundantly high distribution of active sites. In addition, the method for manufacturing metal/metal oxide–carbon electrocatalysts from MOF precursors not only offers a promising approach for further enhancing the catalytic activity, but also helps overcome the limitations on the internal activity and conductivity of the existing transition metal/metal oxide NPs. Unfortunately, most of the M–N–C catalysts currently reported are still unlikely to meet the requirements of high activity, strong strength, and low cost.

The main achievements of metal/nanocarbon composite catalysts derived from MOF are the synergistic effect that occurs between loaded transition metal NPs and a nanocarbon matrix, which leads to a significant increase in catalytic activity. To

date, carbon-supported $\text{Co}/\text{Co}_3\text{O}_4$ is one of the most widely studied catalysts for oxygen reduction in fuel cells [39, 294–296]. For example, Co_3O_4 nanocrystals embedded in N-doped mesoporous graphitic carbon layer/MWCNT hybrids are obtained by simplified carbonization and subsequent oxidation process of MWCNT-based MOFs [297]. As a result, in alkaline media, the hybrid material catalyzes OER with an onset potential of 1.50 V (vs. RHE) and overpotential of only 320 mV to achieve a stable current density of 10 mA cm^{-2} for at least 25 h. The same hybrids also exhibit similar catalytic activity, but excellent stability to a commercial 20 wt% Pt/C catalyst for ORR, which makes it a highly effective cheap bi-catalyst for OER and ORR.

The direct growth of MOF precursors on metal substrates for the production of electrodes from porous nanowire arrays is suggested (Fig. 7.11) [298].

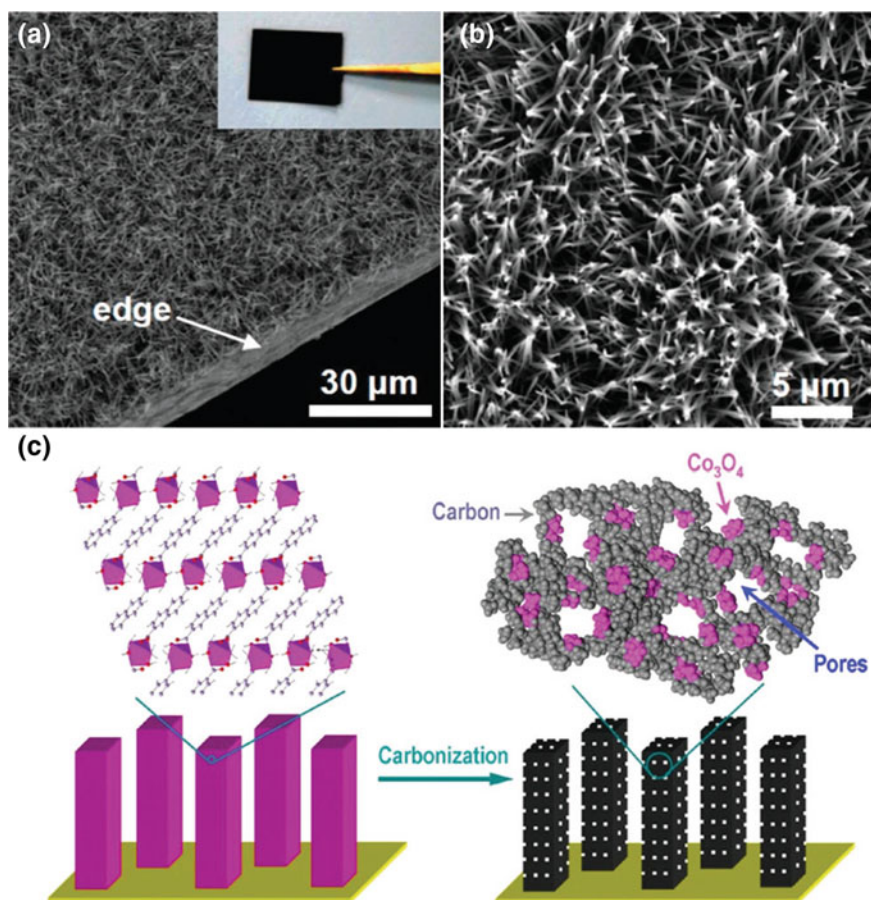


Fig. 7.11 **a** and **b** SEM and [inset in (a)] optical image of Co_3O_4 -C-nanowire arrays. **c** Schematic illustration of Co_3O_4 -C nanowire array formation on Cu foil. Reproduced with permission from Ref. [298]. Copyright (2014) American Chemical Society

The precursor MOF, Co-NDC, was grown directly on a Cu film from a simple hydrothermal reaction at 353 K. MOF was then converted to porous nanowire arrays consisting of strongly interacting Co_3O_4 and carbon by heat treatment in an N_2 atmosphere. The developed electrode with porous nanowire arrays showed abundant active sites, highly improved conductivity and extremely strong stability and therefore excellently performed as an OER electrocatalyst. The original morphology of the nanowire of the parent MOF was retained in the derivative product with the addition of additional micro- and mesopores. $\text{Co}_3\text{O}_4/\text{C}$ nanowires have a smooth surface with no signs of morphologically dissimilar particles, which indicates that all types of Co_3O_4 and C species are well integrated into the nanowire arrays. By combining the distinctive properties of Co_3O_4 with nanocarbon and using their uniform distribution, the obtained $\text{Co}_3\text{O}_4/\text{C}$ -nanowire arrays have improved catalytic characteristics compared to conventional electrode materials. It is remarkable that excellent performance results from a unique nanostructure. First, in situ, the incorporation of nanocarbon in the arrays of $\text{Co}_3\text{O}_4/\text{C}$ provided using MOF as a precursor results in a structure with strongly interacting Co_3O_4 and a nanocarbon matrix. Secondly, the conducting and porous structure is favorable for rapid charge transfer and mass transport, which also ensures a smooth progression of the oxygen reaction.

Co nanomaterials obtained by thermolysis of Co-MOF, CPM-24 $[(\text{CH}_3)_2\text{NH}_2]_{10}[\text{Co}_2(\text{L})_4(\text{Ac})_2][\text{Co}_2(\text{BTC})_2(\text{H}_2\text{O})]_4[\text{Co}_2(\text{OH})(\text{L})_3]_4$ (L = isonicotinic acid), show excellent electrocatalytic activity for ORR with an efficiency comparable to the commercial Pt/C catalyst [299]. A clear cathode peak centered at -0.23 V appeared on the CV curve when the electrolyte was saturated with O_2 , indicating a marked catalytic activity for the cobalt porphyrin-based conjugated mesoporous polymer (CoP-CMP) frameworks CoP-CMP800 for the ORR (Fig. 7.12a). The CoP-CMP800 provided $E_{1/2}$ of -0.18 V, which was more positive than for CoP-CMP (-0.48 V), CoP-CMP600 (-0.26 V), CoP-CMP1000 (-0.23 V), and the CoP-CMP800 showed a highly stable diffusion-limiting current (~ 4.6 mA cm^{-2}), which exceeded CoP-CMP, CoP-CMP600, CoP-CMP1000, and Pt/C (~ 4.5 mA cm^{-2}) (Fig. 7.12b). Measurements of RRDE showed that the electron transfer number (n) of the CoP-CMP800 is 3.83–3.86 at -0.40 to 0.30 V, indicating a preferential four-electron reduction process oxygen (Fig. 7.12c). In contrast, CoP-CMP, CoP-CMP600, CoP-CMP1000, and $\text{H}_2\text{P-CMP800}$ showed significantly smaller values of $n \sim 3.55$, ~ 3.63 , ~ 3.60 , and 3.54 at -0.35 V, respectively (Fig. 7.12d).

It is of interest to use of cobalt oxide NPs for the manufacture of metal oxide-based electrodes. These NPs are obtained by thermolysis of suitable cobalt chelates [300], in particular, $\text{Co}(\text{C}_6\text{H}_5\text{COO})_2(\text{N}_2\text{H}_4)_2$ [301]. It should also be noted cobalt oxides Co_3O_4 (**1**) and (**2**) synthesized by thermolysis of $[\text{Co}(\text{L})]$ and $[\text{Co}(\text{L}')]$ (L^{2-} is {3,4-bis(2-quinoline carboxamido) benzophenone} and $(\text{L}')^{2-}$ is {bis(2-quinolinecarboxamido)-1,2-benzene}), respectively [302]. Oxides **1** and **2** exhibited higher catalytic activity compared to 10 wt% Pt/C and showed lower onset potential and higher current densities at 0.8 V (Fig. 7.13a). In addition, the Tafel slope for oxide **1** was lower, than oxide **2**, i.e., 78 versus 84 mV dec^{-1} ,

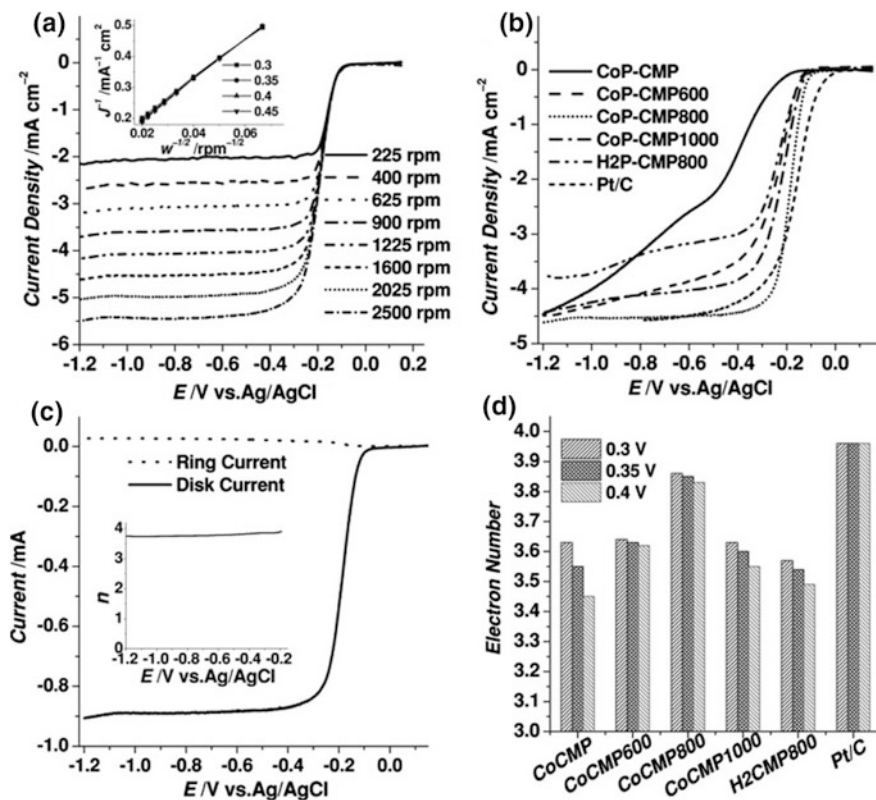


Fig. 7.12 **a** LSV curves for CoP-CMP800 at different rotation rates in O_2 -saturated 0.1 M KOH at 10 mV s^{-1} . The inset shows K–L plot. **b** LSV curves for CoP-CMP, CoP-CMP600, CoP-CMP800, CoP-CMP1000, H_2P -CMP800, and Pt/C in O_2 -saturated 0.1 M KOH at 10 mV s^{-1} at 1600 rpm. **c** RRDE test of the ORR on CoP-CMP800 in O_2 -saturated 0.1 M KOH electrolyte at 1600 rpm. The inset shows the electron transfer number (n) against electrode potential. **d** The n values of CoP-CMP, CoP-CMP600, CoP-CMP800, CoP-CMP1000, H_2P -CMP800, and Pt/C against electrode potential. Reproduced with permission from Ref. [299]. Copyright (2015) Royal Society of Chemistry

respectively (Fig. 7.13b). These results show that the surface of oxides significantly enhances OER, which agrees with the results obtained in the literature [303, 304]. However, the aging tests of the two oxides in OER revealed that oxide 1 is more stable than oxide 2. These results demonstrated that oxide 1 has a superior performance which can be employed in the alkaline water electrolyzer anode.

In addition to Co-containing MOFs, mention should be made of Fe-based MOFs that were used as precursors in the preparation of Fe–N_x–C and N-doped Fe/Fe₃C@C/RGO catalysts, where RGO is reduced graphene oxide, to activate ORR in alkaline media [124, 305–310]. In particular, it was found [306] that Fe-containing MOF, MIL-88B-NH₃, based on 2-aminoterephthalic acid can be used

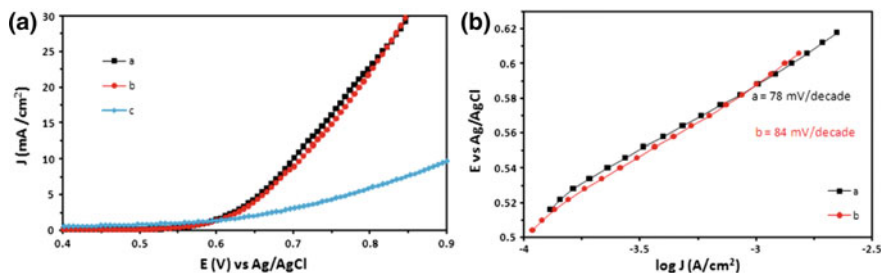


Fig. 7.13 **a** LSV of (a) oxide **1**, (b) oxide **2**, and (c) 10 wt% Pt/C at 5 mV s⁻¹ in 1 M KOH. **b** Corresponding Tafel plots for OER on (a) oxide **1** and (b) oxide **2**. Reproduced with permission from Ref. [302]. Copyright (2017) Springer Nature

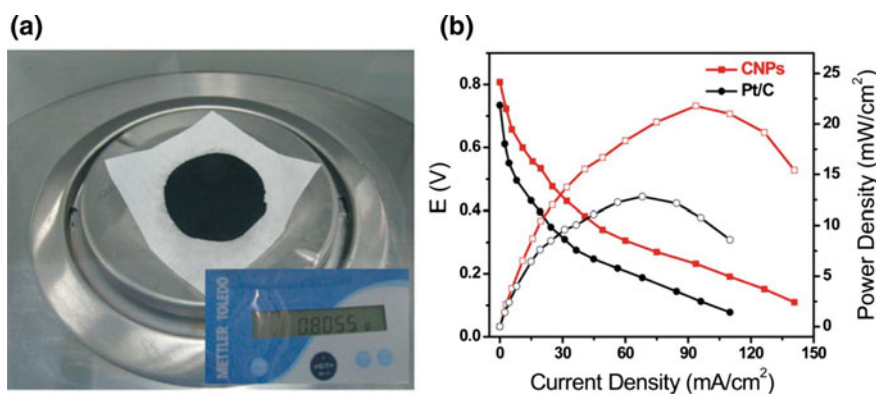


Fig. 7.14 **a** Photograph of CNPs at gram level obtained by one batch synthesis; **b** alkaline direct methanol fuel cell single-cell performance constructed with CNPs and Pt/C catalysts at 333 K under the same condition. The loading amount of both CNPs and Pt/C is set to 3 mg cm⁻². Reproduced with permission from Ref. [306]. Copyright (2014) American Chemical Society

as a template and as thermolysis precursor for the development of the Fe-N_x-C nanostructure as an electrocatalyst. It is established that the onset potential and E_{1/2} of the Fe-N_x-C catalyst for ORR are 1.03 and 0.92 V (vs. RHE) in 0.1 M KOH, respectively. In addition, when using the cathode of the alkaline direct fuel cell, the power density obtained with carbonated NP (CNP) reaches mW cm⁻², which is 1.7 times higher than that of commercial Pt/C catalysts (Fig. 7.14).

It should be noted the rational design of Fe/N-codoped hierarchical porous carbons (HPC-Fe/N-X, X = 700–900) by thermolysis of iron-porphyrin-containing conjugated microporous polymeric sphere with a hollow structure at various temperatures and by etching [311]. The onset potential for HPC-Fe/N-700 was approximately 0.92 V, and the calculated electron transfer number and H₂O₂ concentration were 3.89 and 5.4% at 0.65 versus RHE (Fig. 7.15a) respectively, which indicated a direct conversion of oxygen into water into a four-electron

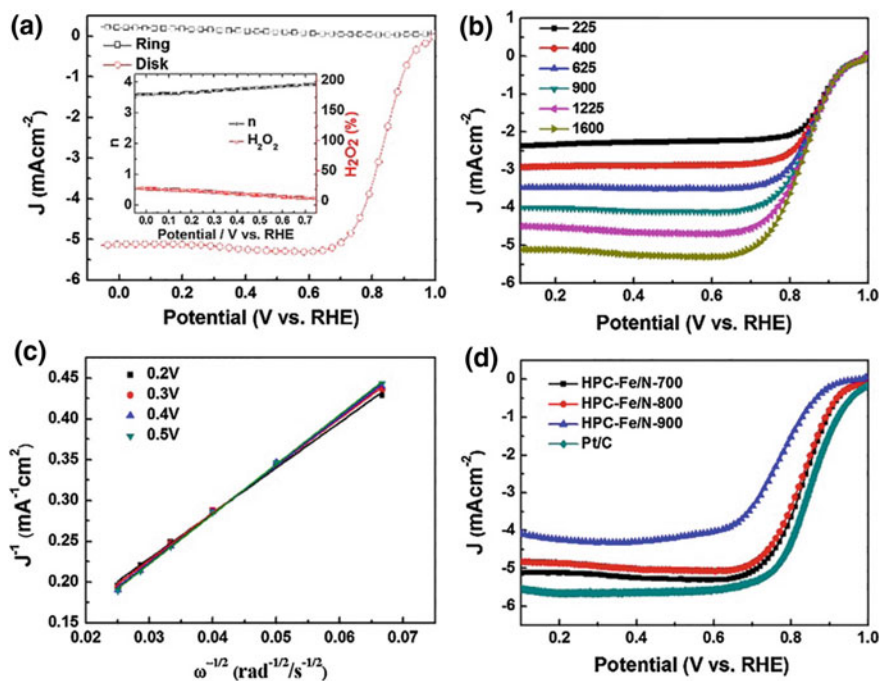


Fig. 7.15 **a** RRDE voltammogram for HPC-Fe/N-700 in 0.1 M KOH solution saturated with O_2 . The electrode rotation rate was 1600 rpm, and the Pt ring electrode was held at 0.5 V (*inset* electron transfer number and percentage of H_2O_2 as a function of potential); **b** RDE voltammograms for HPC-Fe/N-700 in 0.1 M KOH solution saturated with O_2 ; **c** K–L plots obtained from the RDE curves; **d** oxygen reduction polarization curves for HPC-Fe/N-700, HPC-Fe/N-800, HPC-Fe/N-900 and Pt/C at 1600 rpm in 0.1 M KOH. Reproduced with permission from Ref. [311]. Copyright (2017) Elsevier

transfer mechanism. Voltammetric profiles of RDE in O_2 -saturated 0.1 M KOH showed that the current density was increased by increasing the rotation transfer from 225 to 1600 rpm (Fig. 7.15b). The corresponding K–L plots (Fig. 7.15c) show a good linear relationship for HPC-Fe/N-700, indicating the kinetics of the first-order reaction relative to the concentration of dissolved O_2 . The HPC-Fe/N-700 exhibits the lowest onset potential at 0.92 V and the maximum current density to 5.19 mA cm^{-2} , which is slightly lower than for Pt/C (Fig. 7.15d). Thus, due to the high surface area and the Fe/N codoped nature, HPC-Fe/N-700 exhibited excellent electrochemical catalytic characteristics for ORR under alkaline conditions (0.1 M KOH) with a low $E_{1/2}$ (0.84 V), dominant four-electron transfer mechanism, as well as a high diffusion-limiting current density comparable to those of porous ORR carbon-based catalysts with excellent electrochemical characteristics.

It is of interest the class of 2D covalent organic polymers (COPs) comprising a metal (such as Fe, Co, Mn) with precisely controlled locations of nitrogen

heteroatoms and holes obtained from various N-containing organometallic complexes (e.g., metalloporphyrin complexes) by nickel-catalyzed Yamamoto reaction [208]. Subsequent thermolysis of the metal-incorporated COPs led to the formation of COP-based graphene analogues that acted as effective electrocatalysts for ORR in both alkaline and acidic media with good stability and without any methanol crossover/CO poisoning effects. All three electrodes with metal-incorporated C-COP-P-M (M = Fe, Co, or Mn) exhibited remarkably improved electrocatalytic properties compared to the metal-free C-COP-P graphene (Fig. 7.16a). Among them, the C-COP-P-Fe electrode showed a similar onset potential, as in commercially available Pt/C (0.98 V vs. RHE), while the C-COP-P-Co electrode showed a higher limited current than that of the limited Pt/C (Fig. 7.16b). The transfer number of electrons (n) per O₂ molecule for the C-COP-P-Fe and C-COP-P-Co electrodes was calculated from the K–L curves to 3.81 and 3.56, respectively, at 0.35 V (Fig. 7.16c, e), which indicates the almost 4e[−] path for oxygen reduction. In addition, the kinetic-limiting current densities (j_k) of C-COP-P-Co were obtained from the K–L plots as 13.50 mA cm^{−2} at 0.75 V, which are the highest values exceeding the commercial Pt/C of 9 mA cm^{−2} at 0.75 V (Fig. 7.16c). The electron transfer number, calculated from the RRDE measurements (Fig. 7.16d, e), is similar to the number obtained from the K–L plots, which confirms the almost 4e[−] oxygen reduction process. It should be noted that the calculated H₂O₂ yields are less than 16% for the C-COP-P-Fe electrode and below 28% for the C-COP-P-Co electrode in the 0.00–0.80 V potential range (Fig. 7.16e).

It should be noted Fe/Fe₃C-embedded nitrogen-doped carbon obtained by thermolysis of iron-porphyrin-encapsulated mesoporous MOFs PCN-333 (Fe), where “PCN” means “porous coordination network” and TCPP is tetra(carboxyphenyl)porphyrin, at 973 K (Scheme 7.2) [312]. The resulting FeP-P333-700 demonstrated excellent electrocatalytic characteristics for ORR and HER due to the synergistic effect of the active sites Fe/Fe₃C and Fe–N–C active sites.

It is of interest to produce oxide-derived Cu/carbon (OD Cu/C) by the facile thermolysis of MOF (HKUST-1) based on Cu(NO₃)₂ and BTC (Fig. 7.17a) [313]. By selecting a suitable thermolysis temperature, the optimized OD Cu/C-1000, consisting of Cu NPs on a porous carbon framework, retained the morphology and size of the precursor HKUST-1 (Fig. 7.17b, c, d). Due to its useful components, morphology, and structure, OD Cu/C-1000 exhibited high activity and selectivity for the energy conversion reaction, reaching a very low overpotential of ≈190 mV for ethanol formation, as well as high production rates for methanol and ethanol to 12.4 and 13.4 mg L^{−1} h^{−1}, respectively (Fig. 7.17e, f).

A representative metalloporphyrinic MOF, PCN-600-Ni, combined with RGO, was used as a precursor and template to produce a bimetallic iron–nickel phosphide/RGO composite (denoted as Fe–Ni–P/RGO-T; T represents the thermolysis temperature) by thermolysis and the subsequent phosphidation process (Scheme 7.3) [314]. Due to the highly porous structure, the synergistic effect of Fe and Ni elements in the bimetallic phosphide, and the good conductivity provided by RGO, the optimized Fe–Ni–P/RGO-400 exhibits remarkable OER activity in 1 M KOH solution, providing an extremely low overpotential of 240 mV at 10 mA cm^{−2},

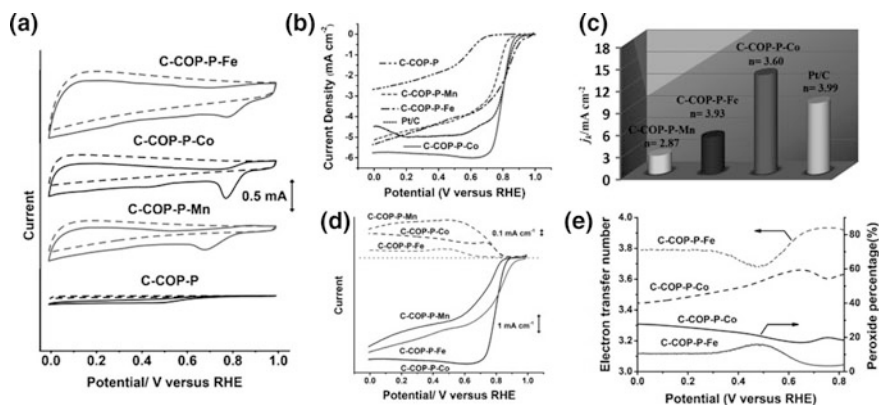
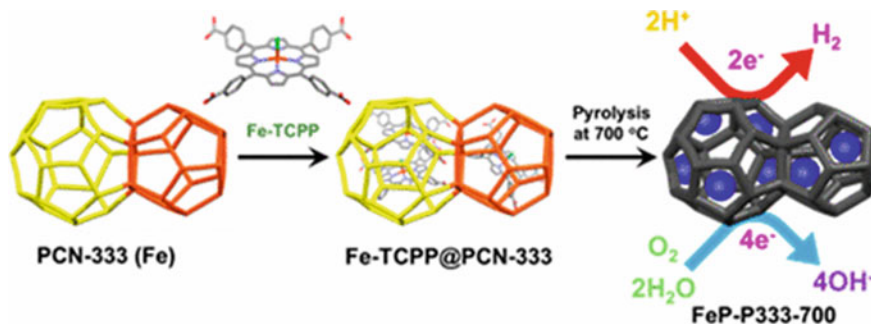


Fig. 7.16 a CV curves of the metal-incorporated and metal-free C-COP-P on GC electrodes in O_2 -saturated (solid line) or N_2 -saturated (dashed line) in 0.1 M KOH at a sweep rate of 10 mV s^{-1} . b LSV curves of metal-incorporated C-COP-P-M in O_2 -saturated 0.1 M KOH at 1600 rpm at a sweep rate of 5 mV s^{-1} . c The comparison of electrochemical activity given as the kinetic-limiting current density (j_k) at 0.75 V (versus RHE) for the metal-incorporated C-COP-P-M. Also included are the calculated electron transfer numbers. d) RRDE voltammograms recorded with the metal-incorporated C-COP-P-M graphene in O_2 -saturated 0.1 M KOH at 1600 rpm. Disk current (I_d) (solid line) is shown on the lower half and the ring current (I_r) (dotted line) is shown on the upper half of the graph. The disk potential was scanned at 5 mV s^{-1} , and the ring potential was constant at 1.5 V versus RHE. e The calculated percentage of peroxide (solid line) and the electron transfer number (n) (dotted line) for the metal-incorporated C-COP-P-M (M = Fe, Co) samples at various potentials, derived from the corresponding RRDE data in (d). Reproduced with permission from Ref. [208]. Copyright (2014) John Wiley and Sons



Scheme 7.2 Synthesis of FeP-P333-700 by thermolysis of Fe-TCPP@PCN-333. Reproduced with permission from Ref. [312]. Copyright (2016) American Chemical Society

which is far superior to commercial IrO_2 and is one of the best in all non-noble metal electrocatalysts.

It should be noted exceptionally active bifunctional catalysts for oxygen electrodes containing Mn_3O_4 and Co_3O_4 NPs embedded in nitrogen-doped carbon obtained by selective pyrolysis and subsequent soft calcination of N4 macrocyclic

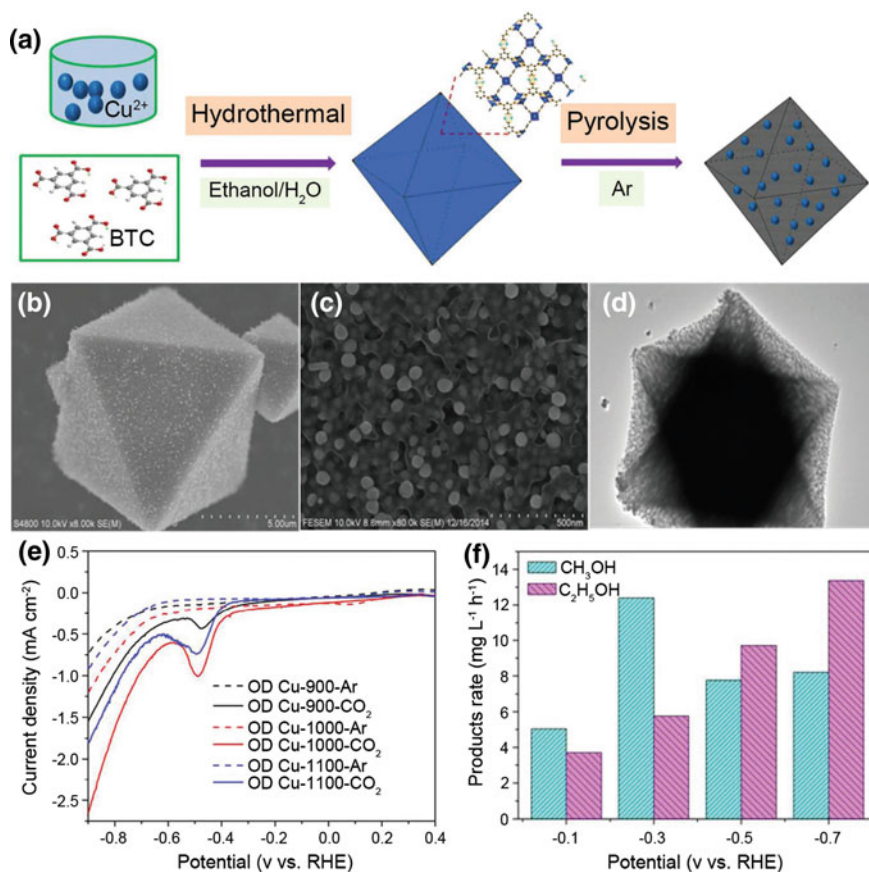
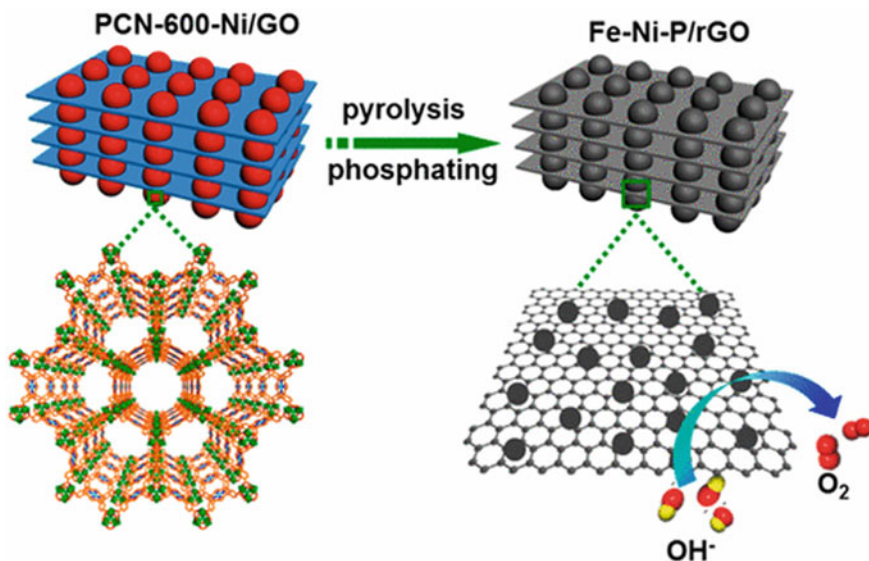


Fig. 7.17 **a** Schematic illustration of the synthesis process of oxide-derived Cu/carbon catalysts. **b**, **c** SEM and **d** TEM images of the OD Cu/C-1000. **e** LSV curves of OD Cu/C materials in Ar- or CO₂-saturated solution with a scan rate of 5 mV s⁻¹. **f** Methanol and ethanol production rate of OD Cu/C-1000 for electrochemical CO₂ reduction (applied potential from -0.1 to -0.7 versus RHE and electrolyte concentration 0.1 m KHCO₃). Reproduced with permission from Ref. [313]. Copyright (2017) American Chemical Society

complexes of manganese and cobalt [315]. In particular, Mn_xO_y/NC, where NC is nitrogen-doped carbon, clearly shows a higher oxygen evolution current for all potentials compared to conventional manganese oxides (Fig. 7.18a). In addition, the catalysts give significantly lower reversible overpotentials in KOH (0.1 M) than the catalysts RuO₂, IrO₂, Pt, NiO, Mn₃O₄, and Co₃O₄ (Fig. 7.18b). It is interesting to note that this method also works very well for the synthesis of the corresponding cobalt catalysts, Co_xO_y/NC (Fig. 7.18c) and nickel Ni_xO_y/NC (Fig. 7.18d), which exceed Co₃O₄ and NiO, respectively, for both ORR and OER.

It is well known that the overvoltage between ORR and OER leads to a decrease in efficiency and, therefore, is a very important parameter for evaluating the



Scheme 7.3 Synthesis of Fe-Ni-P/rGO by thermolysis of PCN-600-Ni and subsequent phosphating. Reproduced with permission from Ref. [314]. Copyright (2017) American Chemical Society

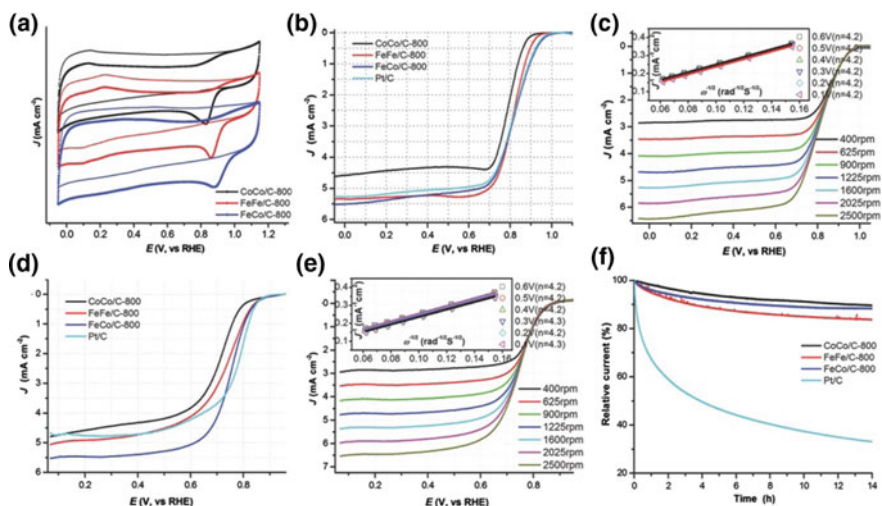


Fig. 7.18 LSVs showing the electrocatalysis of oxygen reduction and water oxidation by **a** Mn_xO_y/NC and commercial manganese oxides, **b** Mn_xO_y/NC and Pt/C, IrO₂, and RuO₂, **c** Co_xO_y/NC compared with Co₃O₄ and **d** Ni_xO_y/NC compared with NiO, in oxygen saturated KOH (0.1 M) at a scan rate of 10 mV s⁻¹ and rotation of 1600 rpm. Reproduced with permission from Ref. [315]. Copyright (2014) John Wiley and Sons

bifunctional electrocatalytic activity of the test catalyst. It turned out that a low overvoltage between ORR and OER using bifunctional catalysts $\text{Co}_x\text{O}_y/\text{NC}$, $\text{Mn}_x\text{O}_y/\text{NC}$, and $\text{Ni}_x\text{O}_y/\text{NC}$ instead of Pt/C will result in energy savings of at least 80, 70, and 10 mV, respectively [316].

The metallic-constituent-controllable metallomultiporphyrin porous conjugated networks, denoted as PCN-MM (MM = FeCo, FeFe, CoCo), whose thermolysis leads to heterometalloporphyrin carbon PCN/C, are of interest [198]. The well-defined cathodic peaks appear in all CV curves of three samples in a solution saturated with O_2 (Fig. 7.19a). Compared to the pure cobalt-containing sample PCN-CoCo/C (peak potential ≈ 0.83 V versus RHE), Fe-incorporated PCN-FeFe/C showed much more positive ORR potentials (0.86 V). In particular, the peak potential of the double-doped Fe and Co electrode (PCN-FeCo/C) reached 0.88 V. It was found that PCN-FeCo/C exhibits a more positive onset potential (1.00 V) than the PCN-FeFe/C (0.97 V), and PCN-CoCo/C (0.92 V) (Fig. 7.19b). In addition, the heterometallic product gives $E_{1/2}$ of 0.85 V, comparable to the Pt/C potential (0.84 V). PCN-FeCo/C showed a very stable diffusion-limiting current, superior to monometallic analogs and even comparable to Pt/C . Based on the RDE polarization curves at different rotational rates, the electron transfer number (n) of PCN-FeCo/C was calculated as 4.2 ± 0.1 at 0.1–0.6 V (Fig. 7.19d). In addition to

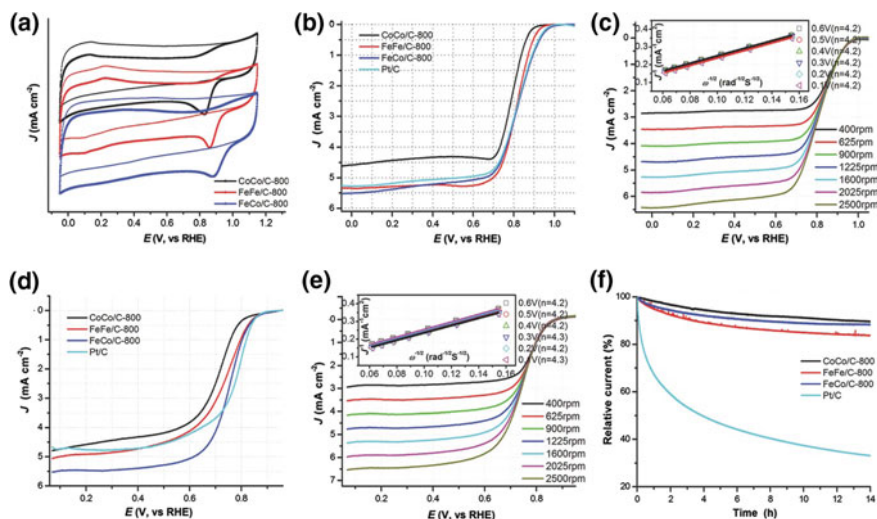


Fig. 7.19 **a** CV and **b** RDE polarization curves (at rotation rate of 1600 rpm) on PCN/C and 20% Pt/C in 0.1 M KOH solution. **c** RDE polarization curves on PCN-FeCo/C at different rotation rates, inset K–L plot of J^{-1} versus ω^{-1} . **d** RDE polarization curves at 1600 rpm on PCN/C and 20% Pt/C in 0.1 M HClO_4 solution. **e** RDE polarization curves on PCN-FeCo/C at different rotation rates, inset K–L plot of J^{-1} versus ω^{-1} . **f** Current versus time (i - t) chronoamperometric response of the PCN/C and Pt/C at 0.5 V (vs. RHE) in O_2 -saturated 0.1 M HClO_4 at 1600 rpm, respectively. Reproduced with permission from Ref. [198]. Copyright (2014) American Chemical Society

high activity, nanocomposites obtained from PCN also have high stability (Fig. 7.19f). Among them, the current density of PCN-FeCo/C decreases only by 10% after 14 h that indicates a much longer durability in acid solution than Pt/C.

Cubic zirconium-porphyrin frameworks, CPM-99 (H_2 , Zn, Co, Fe), were synthesized by a molecular-configuration-guided strategy [272]. The rigid template effect of the Zr_6 -polyoxo-cluster and uniformly embedded (metallo)-porphyrin centers affords CPM-99 with highly desirable properties as precursors for ORR catalysts. Thermolysis products not only retain the microcubic morphology of the parent CPM-99, but also possess porphyrinic active sites, hierarchical porosity, and highly conducting networks. The electrocatalytic activity of CPM-99X/C has the following order: $\text{Fe} > \text{Co} > \text{Zn} \approx \text{H}_2$ (Fig. 7.20a). The CPM-99Fe/C shows the best ORR activity among the electrodes obtained from the CPM-99, showing the onset and half-wave potentials (0.950 and 0.802 V) close to those (0.978 and 0.818 V) of the 20 wt% Pt/C (Fig. 7.20b). These results show that CPM-99Fe/C has ORR catalytic activity comparable to commercial Pt/C catalyst. In addition, the

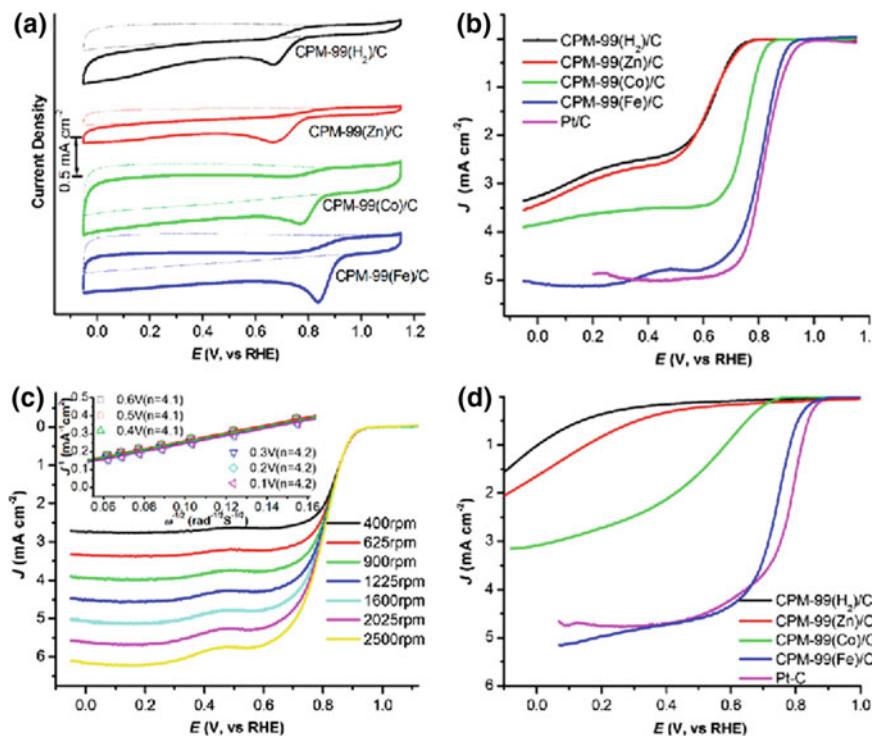


Fig. 7.20 **a** CVs and **b** RDE polarization curves on CPM-99X/C and 20% Pt/C in 0.1 M KOH solution. **c** RDE polarization curves on CPM-99Fe/C at different rotation rates. *Inset* K–L plot of J^{-1} versus ω^{-1} at different potentials. **d** RDE polarization curves on CPM-99X/C and 20% Pt/C in 0.1 M HClO_4 solution. The scan rate is 10 mV s^{-1} . Reproduced with permission from Ref. [209]. Copyright (2015) American Chemical Society

K–L plots from the RDE polarization curves (Fig. 7.20c) for CPM-99Fe/C between 0.6 and 0.1 V showed good parallel straight lines and the number of electrons transferred was 4.1 ± 0.1 , which means that CPM-99Fe/C catalyzed four-electron ORR in a 0.1 M solution of KOH. The CPM-99Fe/C electrode showed better electrocatalytic activity among four samples with an onset potential (0.875 V) comparable to Pt/C (0.880 V), while CPM-99Co/C, CPM-99Zn/C and CPM-99H₂/C electrodes showed a much lower onset potential and current density (Fig. 7.20d).

To increase the efficiency of electricity-to-hydrogen conversion, effective electrocatalysts for the HER are required. As an ordinary inexpensive alternative to Pt in many catalytic reactions, Ni-based electrodes are widely used in modern commercial alkaline cells. In particular, controlled thermolysis of MOFs is an effective method to prepare highly efficient noble metal-free HER catalysts. As a typical example, we noted thermolysis of a Ni-based MOF in NH₃, which yields Ni NPs with surface nitridation together with thin carbon coating layers [317]. Such subtle surface modification significantly improves the catalytic performance for the HER. The surface-modified Ni NPs show a low overpotential of only 88 mV at a current density of 20 mA cm⁻², which is one of the most efficient HER catalysts based on metallic Ni. It is noteworthy that the Ni-0.2NH₃ sample demonstrates very high HER activity, which is characterized by a low overvoltage at a certain current density j ($h_{10} = 61$ mV and $h_{20} = 88$ mV) (Fig. 7.21a). However, the efficiency of HER is very sensitive to the partial pressure of NH₃ during thermolysis; in particular, the performance of the Ni-0.4NH₃ sample is lower ($h_{20} = 112$ mV). At the same time, the Ni-Ar sample is rather inactive ($h_{20} = 390$ mV). In addition, catalysts derived from Ni-MOF also have different HER mechanisms that can be derived from the Tafel plots (Fig. 7.21b). The Tafel slope for catalysts obtained in NH₃ is in the range of 71–83 mV per decade, suggesting a mixed Volmer and Heyrovsky mechanism for HER; that is, the HER rate is determined by both the evolution of H₂O and the desorption of H₂ from the catalyst surface. For the Ni-Ar catalyst, the Tafel slope is

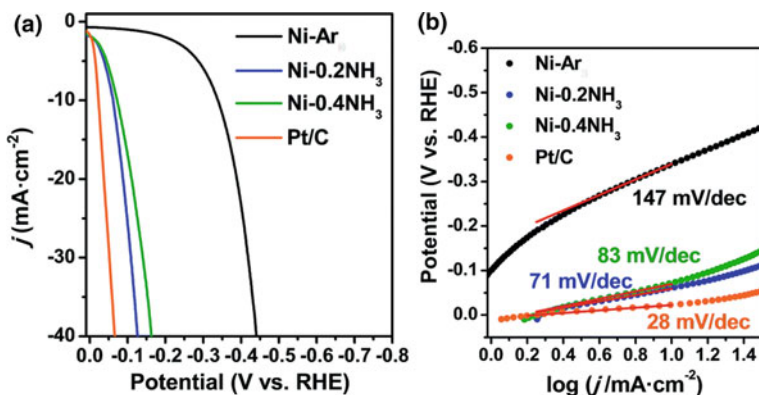


Fig. 7.21 a LSVs and b Tafel plots of the MOF-derived catalysts in 1 M KOH solution. Reproduced with permission from Ref. [317]. Copyright (2015) Royal Society of Chemistry

much higher (147 mV per decade), which indicates that the Volmer mechanism dominates in the HER; i.e., it is determined by the evolution of H_2O .

7.2 Supercapacitors

Supercapacitors, also called “electrochemical capacitors” (ECs), have recently attracted much attention for energy storage than conventional batteries or capacitors due to their fast charging/discharging, high power density, moderate energy density, safe operation, and long life cycle [20, 96, 103, 107, 124, 249, 318–327]. Depending on the charge–discharge mechanism, ECs can be divided into two types: an electric two-layer capacitor (EDLC) and Faradic pseudocapacitors (or redox supercapacitors) [16, 30, 96, 327]. EDLC consists of two activated carbon electrodes that are impregnated with a non-aqueous or aqueous electrolyte and separated by a porous membrane separator (Fig. 7.22a) [30]. EDLC stores electrical energy directly by forming an electrical double layer (EDL) on the surface of each electrode that diffuses very quickly, thereby providing a very fast discharge and, hence, giving higher power densities. The most important parameters that influence the capacitance characteristics of EDLC are the surface area, pore size distribution, pore volume, and size of electrolyte ions in solvated and desolvated shells [328–332]. Pseudocapacitors include active redox species, for example, transition metal oxides [54, 333] or electroactive polymers [334], using a reversible Faradaic reaction for storing charges [319, 335, 336]. This class of materials showed significantly higher capacitive capabilities, which improve the energy density, at least by an order of magnitude. Pseudocapacitance of materials strongly depends on the size

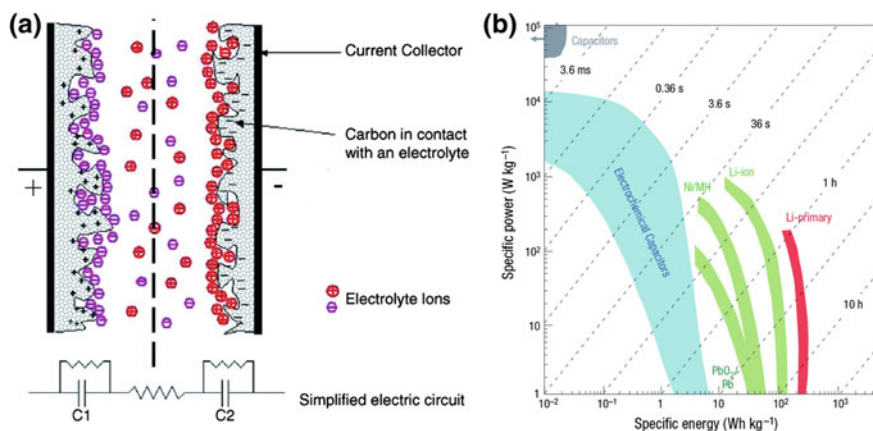


Fig. 7.22 **a** Schematic representation of an EDLC (in its charged state) and **b** Ragone plot for various electrical energy storage devices. Reproduced with permission from Ref. [30]. Copyright (2016) Royal Society of Chemistry

of active redox species, porosity (to ensure quick access to the electrolyte), crystallinity (optimization of deep diffusion of electrolyte), and surface area of electrode materials.

The breakthrough in electrode materials is the key to improving the characteristics of the supercapacitor. Up to now, improved carbon materials, including activated carbon, CNTs, and carbon foams, have been mainly studied as a supercapacitor electrode because of their remarkable advantages such as a large surface area, excellent chemical stability, relatively low cost, a controlled pore structure, and the desired electrical conductivity [205, 337–355]. In general, EDLC can demonstrate high power density up to 10^5 W kg^{-1} and a long life cycle in millions of cycles. However, the tortuous microporosity and non-graphitic structure of the carbon walls in the activated carbons lead to long diffusion distances with a relatively high ion resistance, in addition to low electronic conductivity, which do not satisfy the need for high energy density of ECs at high power output (Fig. 7.22b) [30]. In addition, carbon-based supercapacitors often have low specific capacitance and energy density [206, 356], since the capacitance of carbon materials is due to the separation of electrostatic charges at the electrode–electrolyte interface based on double-layer capacitors, and several electrochemical reactions occur between the carbon electrode and electrolyte.

Therefore, lately attention has been focused on increasing the EDLC energy density, to improve which it is necessary either to increase the specific capacitance of the electrodes, or to increase the operating voltage in the cells [319, 323, 357, 358]. Currently, the main strategy is the development of pseudocapacitive electrodes based on fast redox reactions on electrode surfaces or inside nanodomains [334, 336, 359–368]. Nevertheless, it remains a huge problem to increase the energy density of supercapacitors without sacrificing the most valuable EDLC characteristics, high power density, and long life cycle. In this regard, it is of interest to obtain carbon materials with improved electrochemical characteristics by thermolysis of MOF with chelated units [369]. Table 7.2 shows different types of carbon from MOFs with their respective surface areas and capacitive characteristics.

Table 7.2 Surface area and capacitances of carbon derived from different MOF precursors^a

Precursor	<i>T</i> (K)	<i>S</i> _{BET} (m ² g ⁻¹)	<i>V</i> (cm ³ g ⁻¹)	<i>C</i> (F g ⁻¹)	References
MOF-5	1273	2872	2.06	204 @ 5 mV s ⁻¹	[370]
MOF-5	1223	2587	3.14	344 @ 50 mA g ⁻¹	[371]
MOF-5	773	2222	1.14	271 @ 2 mV s ⁻¹	[372]
MOF-5	873	1521	1.48	100 @ 5 mV s ⁻¹	[373]
MOF-2	1273	1378	–	165 @ 10 mV s ⁻¹	[374]
IRMOF-3	1223	553	0.34	239 @ 5 mV s ⁻¹	[375]
Al-PCP	1073	1103	1.04	174 @ 1 A g ⁻¹	[376]
HKUST-1	1073	50	1.46	83 @ 1 A g ⁻¹	[376]

^a*C* = specific capacitance; *T* = thermolysis temperature; *V* = pore volume

MOFs have recently begun to be used as precursors to produce highly disperse NPC materials for supercapacitors due to structural diversity, large specific surface areas, and porous properties [369, 370, 377–380]. MOF-derived NPC materials had a high capacitance comparable to the highest values obtained for supercapacitors with carbon electrodes, probably due to high surface areas and optimal micropore diameters [173]. Despite extensive research on synthesis, the rational design of supercapacitive electrodes that can meet the requirements of high capacity, high energy density, and outstanding stability remains a serious problem. As a typical example, we note the production of NPCs by direct thermolysis of HKUST-1, MOF-5, and Al-PCP without additional carbon precursors [376]. It turned out that the MOF-5- and Al-PCP-derived carbons showed the ideal behavior of the capacitors, whereas the HKUST-1-derived carbon had poor capacitive behavior at different sweep rates and current densities. In addition, Al-PCP-derived carbons exhibited the highest specific capacity (232.8 F g^{-1}) in a 30% KOH solution at a current density of 100 mA g^{-1} .

Of interest is the analysis of the usability of carbon nanorods and graphene nanocarbons from rod-shaped MOF-74 in a two-electrode symmetric supercapacitor cell using $1.0 \text{ M H}_2\text{SO}_4$ as the electrolyte (Fig. 7.23a) [20]. In steady-state CVs for graphene nanocarbons, conventional rectangular shapes without any redox peaks show excellent capacitive behavior (Fig. 7.23d). The specific capacitance for nanocarbons reaches 193 F g^{-1} at 10 mV s^{-1} , which decreases to 123 F g^{-1} at 400 mV s^{-1} , indicating a 35% drop in capacitance with an increase in sweep rate (Fig. 7.23c). In addition, in galvanostatic charge–discharge measurements, typical triangular profiles confirm the excellent electrochemical capacitive properties of these nanoribbons (Fig. 7.23g). The specific capacitance for carbon nanorods is 164 F g^{-1} at a sweep rate of 10 mV s^{-1} , which decreases to 116 F g^{-1} at 400 mV s^{-1} , which shows a $\sim 33\%$ drop in capacitance with an increase in sweep rate (Fig. 7.23c, e). The specific capacitances calculated from charge–discharge curves at current densities of 50 and 100 mA g^{-1} are 187 and 174 F g^{-1} , respectively (Fig. 7.23g). Compared to carbon nanorods, lower capacitances (110 F g^{-1} at 10 mV s^{-1} and 71 F g^{-1} at 400 mV s^{-1}) for microporous carbon (MPC) are observed, but with the same capacitance decrease (Fig. 7.23f). Lower specific capacitance values (120 F g^{-1} at 50 mA g^{-1} and 114 F g^{-1} at 100 mA g^{-1}) have also been obtained for the MPC from the charge–discharge curves (Fig. 7.23g). The reason for the low performance of the supercapacitor for MPCs can be a noticeable presence of microporosity and its lower electrical conductivity (Fig. 6.23b). On the Nyquist plots, especially in the inset in Fig. 7.23h, there are observed effects of improving the transport of ion and electronic conductivity in a small semicircle (first segment), the Warburg diffusion line (second segment), and the capacitive line (third segment). The Bode plot (phase angle as a function of frequency) shows a phase angle of $\sim 90^\circ$ with a frequency of 0.1 Hz for nanoribbons and nanorods, which indicates \sim ideal capacitive behavior (Fig. 7.23i).

It is worth noting the production of NPCs by the polymerization of an additional carbon source (furfuryl alcohol) located in MOF-5 followed by thermolysis of the product obtained [373]. NPC samples obtained at temperatures above 873 K as

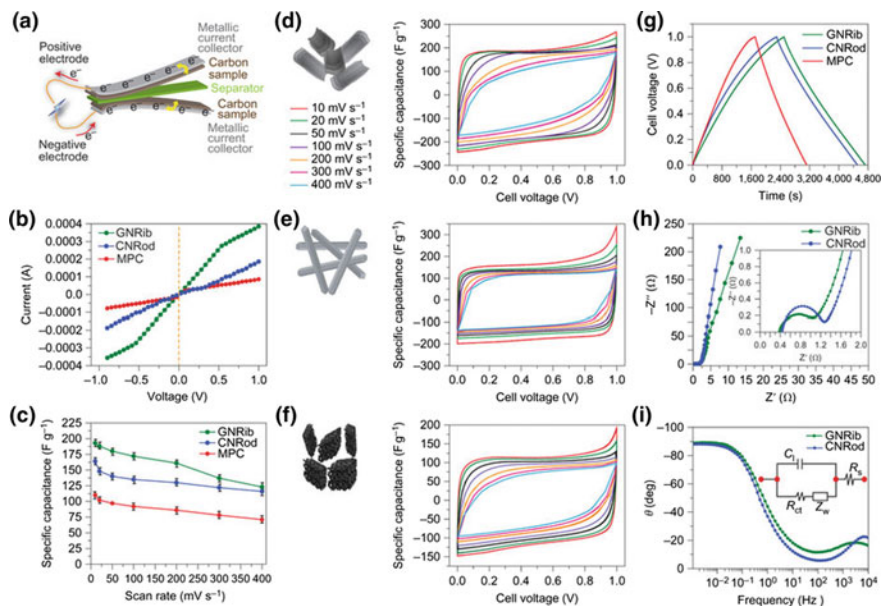


Fig. 7.23 Applications of graphene nanoribbons and carbon nanorods for electrochemical energy storage. **a** Schematic of a simple supercapacitor cell. Electrolyte presentation is omitted for clarity. **b** Comparative current–voltage characteristics of graphene nanoribbons (GNRib), carbon nanorods (CNRod), and MPC showing improved conductivity for GNRib due to unraveling and annealing. **c** Representation of specific capacitance as a function of scan rate for GNRib, CNRod, and MPC. **d** Morphological demonstration of GNRib and CVs at different sweep rates using GNRib as an electrode material. **e** Morphological illustration of CNRod and CVs at different sweep rates using CNRod as an electrode material. **f** Morphological representation of MPC and CVs at different sweep rates using MPC as an electrode material. **g** Comparative galvanostatic charge–discharge curves for GNRib, CNRod and MPC at a current density of 50 mA g^{-1} , showing the better performance for GNRib. **h** Nyquist plots for GNRib and CNRod, showing the imaginary part versus the real part of the impedance. *Inset* impedance data in the high-frequency range showing the lower electrochemical series resistance values for GNRib. **i** Bode phase plots for GNRib and CNRod showing the phase angle (θ) close to 90° . *Inset* Equivalent circuit for the electrode–solution interface. C_i , double-layer capacitance. The Faradic impedance includes Z_w (the Warburg impedance) and R_{ct} (the charge-transfer resistance). R_s , spreading resistance. Reproduced with permission from Ref. [20]. Copyright (2016) Springer Nature

electrode materials for a supercapacitor demonstrate the ideal behavior of capacitors and give an almost constant specific capacitance (above 100 F g^{-1} at 5 mV s^{-1}) at different sweep rates, which is due to their mesoporous characteristics. However, the NPC sample with the highest BET surface area ($3040 \text{ m}^2 \text{ g}^{-1}$) obtained by thermolysis at 803 K gives an unusually low capacitance (12 F g^{-1} at 5 mV s^{-1}), which can be attributed to poor conductivity of NPC due to low thermolysis temperature.

It has recently been demonstrated that, among doped carbons, nitrogen-doped carbonaceous materials allow improving the capacitance through surface faradaic

reactions without sacrificing high rate capability and long life cycle. Due to the high electronic conductivity and improved hydrophilic properties, along with their easy synthesis, low cost, and the possibility of broad functionalization, N-doped carbons showed great potential in applications for energy storage and conversion [30, 367]. MOFs can ensure the inherent presence of nitrogen atoms in the ligands that will be retained in the resulting product during thermolysis, thereby providing N-doped carbonaceous material (Table 7.3).

In particular, the thermolysis of a nitrogen-rich MOF with an IRMOF-3-like structure at 1223 K resulted in the formation of N-rich carbonaceous materials [381]. This N-doped carbon with a 3D structure exhibited a high capacity of 239 F g⁻¹ with a scan rate of 5 mV s⁻¹ (Fig. 7.24).

Investigation of electrode materials for ECs with improved energy density has also been directed to many other materials, such as nano-sized MO, conducting polymers and heteroatom-doped (such as B, P, O and S) carbons, which are capable

Table 7.3 Nitrogen-doped carbons for supercapacitors

N content (wt%)	Surface area (m ² g ⁻¹)	Electrolyte	Capacitance (F g ⁻¹)	E (W h kg ⁻¹)	P (W kg ⁻¹)	References
–	720	H ₂ SO ₄	130 at 50 mV s ⁻¹	–	–	[369]
3.3	553	H ₂ SO ₄	239 at 0.5 A g ⁻¹	–	–	[381]
10.6	1276	H ₂ SO ₄	270 at 2 A g ⁻¹	–	–	[183]
0.98	2188	H ₂ SO ₄	307 at 1 A g ⁻¹	–	–	[382]
–	2264	H ₂ SO ₄	168 at 5 mV s ⁻¹	–	–	[378]
–	943	H ₂ SO ₄	238 at 20 mV s ⁻¹	19.6/11.0	700/22 900	[383]

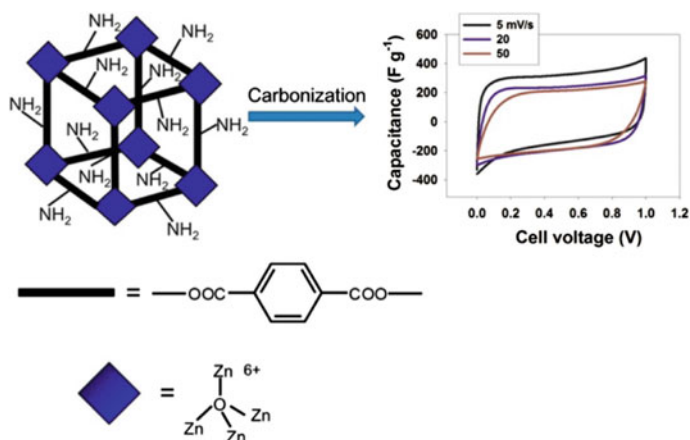


Fig. 7.24 Supercapacitor application of a nitrogen-containing MOF (IRMOF-3)-derived carbon product. Reproduced with permission from Ref. [381]. Copyright (2014) American Chemical Society

of providing a high specific capacity and energy density by means of a storage mechanism based on reversible faradaic redox reactions [139, 384–386].

It should be noted that transition metal oxides attracted considerable attention for energy storage applications, such as supercapacitors, because of their good electrical conductivity, high electrochemical reaction (by providing the Faradaic reaction), low production costs, and easy processability [387, 388]. For example, 1D MO nanomaterials are excellent candidates for supercapacitors because of their large surface area and prominent capillary paths, which gives them a good charge storage capacity and high specific capacity [31]. The schematic diagram of a supercapacitor based on the MO nanostructure, which consists of 1D MO materials, electrolyte solution, a separator, and two indium tin oxide (ITO) thin-film electrodes, is shown in Fig. 7.25.

In recent years, the MOF has received considerable attention as precursors or templates for the production of porous metal oxide nanostructures and nanocomposites for supercapacitor applications of the next generation (Table 7.4).

Fig. 7.25 Schematic diagram of a 1D MO nanostructure-based supercapacitor. Reproduced with permission from Ref. [31]. Copyright (2012) John Wiley and Sons

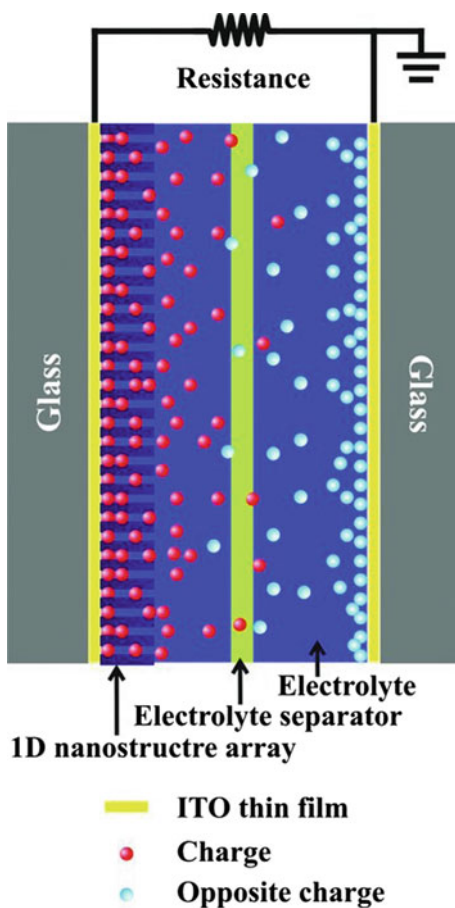


Table 7.4 Comparison of the performance of various nanostructures synthesized from MOF precursors as supercapacitors

Materials	Doping	Original MOF	Specific surface area ($\text{m}^2 \text{g}^{-1}$)	Mass normalized current (A g^{-1})	Specific capacitance (F g^{-1})	Cycle numbers	References
NiCo ₂ S ₄	Sulfur, nickel	Co-MOF	72	10	765.6	10,000	[389]
Co/MnO/CoO/C	–	CoMn-MOF-74	242.4	1	800	1000	[390]
NiO	–	Ni ₃ (HCOO) ₆	34	1	324	1000	[391]
Ni@Graphitic C	–	Ni-BDC	140	1	886	1000	[392]
CeO ₂	–	Ce-BTC	205	1	779	10,000	[393]
Cr ₂ O ₃	Carbon	MIL-101	438	0.25	291	3000	[394]

Co_3O_4 has been extensively researched as the electrode material for pseudocapacitors [395–400]. As a typical example, we note a simple thermolysis in air to convert Co-based MOF based on BDC to obtain Co_3O_4 nanomaterials for capacitive energy storage [401]. The resulting nanomaterials exhibited a specific capacitance of 208 F g^{-1} at a current density of 1 A g^{-1} and a specific capacitance retention of *ca.* 97% after 1000 continuous charge–discharge cycles in 6.0 M aqueous KOH solution (vs. SCE), suggesting their potential applications for supercapacitors. In another interesting example, a straightforward approach has been developed to fabricate Co_3O_4 nanostructures (**1** and **2**) by thermolysis of hollow-structured coordination polymer particles (CPP-1 and CPP-2) based on 3,5-diaminobenzoic acid, which have been synthesized in different solvent systems $\text{H}_2\text{O}/\text{DMF}$ and $\text{H}_2\text{O}/\text{EtOH}$, respectively [402]. It turned out that the porous Co_3O_4 rods have less charge-transfer resistance and a higher ion diffusion rate compared to Co_3O_4 particles and exhibit better cyclic properties at a charge–discharge intensity of 3 A g^{-1} . The CV curves (Fig. 7.26a, b) are almost symmetrical and show two pairs of redox peaks. Wide redox reaction peaks originating from the redox processes of $\text{Co}_3\text{O}_4/\text{CoOOH}/\text{CoO}_2$ are characteristic of electrochemical pseudocapacitors from reversible faradaic redox reactions occurring in electroactive materials [403, 404]. It is important that porous oxide **1** can provide fast ion and electron transfer, which is advantageous for electrochemical characteristics (Fig. 7.26c). The shapes of the charge–discharge curves show the characteristics of the pseudocapacitor (Fig. 7.26d), which are consistent with the result of the CV curves. Both samples represent two ranges of variation during the charging and discharging steps, and the increase in charging time is a higher capacity of oxide **1** rods.

High-grade Co_3O_4 nanomaterials were also obtained from Co-MOF with a relatively smaller pore distribution having a capacitance of up to 150 F g^{-1} at a discharge rate of 1 A g^{-1} [54].

It should be especially noted that MOF composites with highly conducting substrates lead to further improvement in the characteristics of electrode materials by decorating the MO with porous carbon or graphene. In particular, highly porous composites Fe_2O_3 -3DGN (3DGN is three-dimensional graphene network) were obtained from composites Fe-MOF with RGO followed by annealing (Fig. 7.27) [405]. The composite provided a high capacity of 864 mA h g^{-1} at 200 mA g^{-1} even after 50 cycles.

Mixed cobalt and manganese oxides embedded in the nanoporous carbon framework (M/MO@C), which were obtained by direct carbonization of the binary mixed-metal organic framework (CoMn-MOF-74) [390], are of considerable interest. The obtained carbon materials M/MO@C retained the basic morphology of CoMn-MOF-74 and showed homogeneous dispersibility of Co, MnO, and CoO NPs in the carbon matrix and, therefore, significantly increased the conductivity of M/MO@C materials. In particular, a remarkable specific capacitance of 800 F g^{-1} was obtained using the M/MO@C-700 sample at a current density of 1 A g^{-1} in 6 M KOH electrolyte (Fig. 7.28a). The CV curves, which are completely different from the ideal rectangular shape of the electric double-layer capacitance, contain redox peaks, suggesting that the main mechanism of charge storage is pseudocapacitive (Fig. 7.28b).

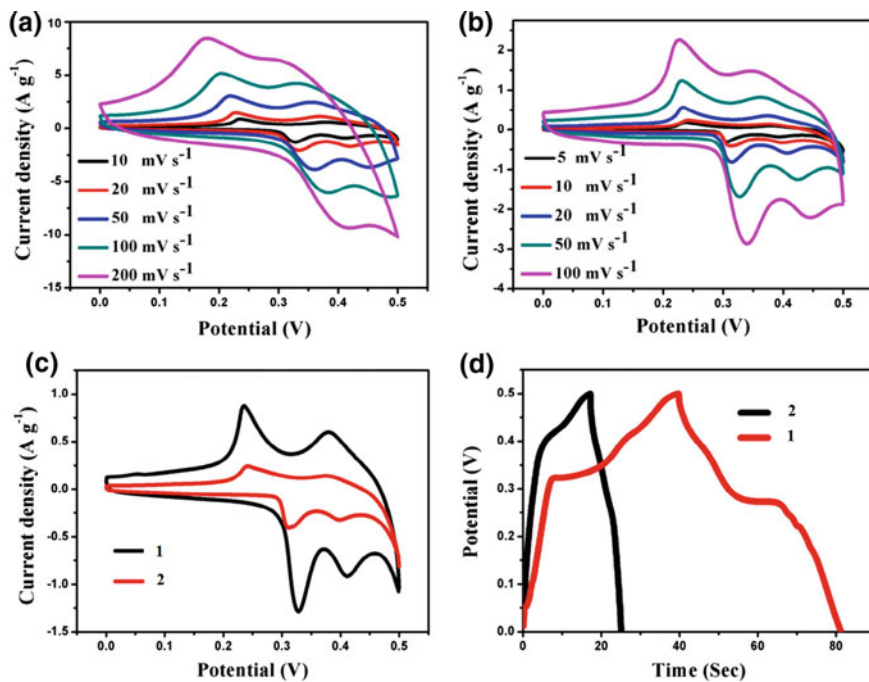


Fig. 7.26 **a** and **b** CV curves of **1** and **2** at various scan rates of 5–200 mV s⁻¹. **c** CV curves for **1** and **2** at scan rate of 10 mV s⁻¹. **d** Charge–discharge curves for **1** and **2** at the same current density of 1 A g⁻¹. Reproduced with permission from Ref. [402]. Copyright (2015) Elsevier

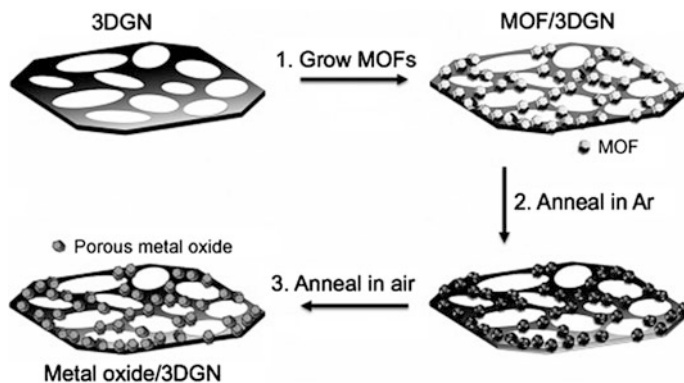


Fig. 7.27 **a** Schematic illustration of the process used for the synthesis of MO-3DGN composites. **b**, **c** Rate capacity of electrodes composed of the Fe₂O₃-3DGN composite (**b**) and Fe₂O₃ (**c**). Square and triangle symbols indicate the discharge and charge specific capacities, respectively. Reproduced with permission from Ref. [405]. Copyright (2014) John Wiley and Sons

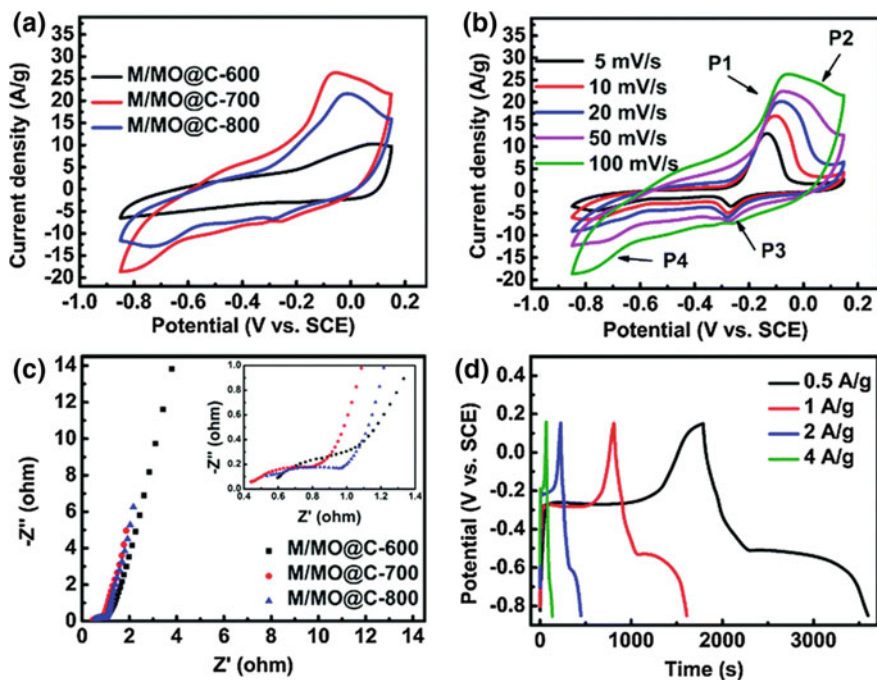


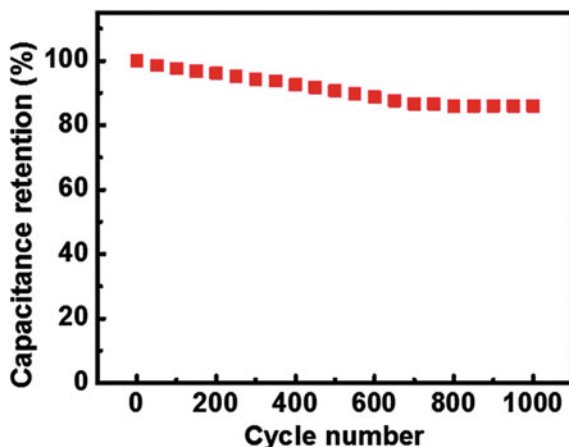
Fig. 7.28 **a** CV curves of M/MO@C at a scanning rate of 100 mV s^{-1} , **b** CV curves of M/MO@C-700 at various scanning rates, **c** electrochemical impedance spectroscopy (EIS) of all three samples, **d** galvanostatic charge–discharge curves of M/MO@C-700 at different current densities. Reproduced with permission from Ref. [390]. Copyright (2016) Royal Society of Chemistry

In addition, the sample M/MO@C showed good cycling stability with capacitance retention of 85% after 1000 cycles. It is important that the optimized carbonization temperature is a critical parameter for obtaining a nanoporous carbon framework M/MO@C with the best capacitive characteristics (Fig. 7.29). A specific capacitance change of the M/MO@C-700 between -0.85 and 0.15 V with a scanning rate of 20 mV s^{-1} in the 6 M KOH electrolyte was obtained.

At present, ternary transition metal oxides, such as MgCo_2O_4 , NiCo_2O_4 , ZnCo_2O_4 , CuCo_2O_4 , MnCo_2O_4 , have been extensively studied as electrode materials for the EC because of the combined advantages over other EC materials in terms of low cost, availability, and high theoretical capacity [280, 407–415]. In addition, it has been shown that the introduction of the secondary metal element into the ternary transition metal oxides can contribute to their electrochemical characteristics due to increased electronic conductivity and electrochemical activity and the coupling effect of the two metal particles that provide rich sites of redox reactions.

As a typical example, we note two types of ternary MOs, $\text{MnCo}_2\text{O}_{4.5}$ and MnNi_6O_8 NPs, synthesized by thermolysis of the corresponding precursors, bimetallic CP particles [416]. It turned out that the $\text{MnCo}_2\text{O}_{4.5}$ structure, especially

Fig. 7.29 CV cycling stability of M/MO@C-700. Reproduced with permission from Ref. [390]. Copyright (2016) Royal Society of Chemistry



Mn/Co-600, has a much higher capacitance than MnNi_6O_8 NPs, showing that the $\text{MnCo}_2\text{O}_{4.5}$ electrode is more suitable for use in a neutral electrolyte system. The Mn/Co-600 electrode has a specific capacitance of 158 F g^{-1} at 5 mV s^{-1} , a good rate capability of 53.8% with a 20-fold increase in current density, good cycle performance (92.9% of capacity retention after 1000 cycles), and high power density (a specific power of 5760 W kg^{-1} at 4.0 A g^{-1}) with a low charge-transfer resistance of 1.8 Ω .

It has been found that MO-C nanocomposites are very interesting for supercapacitor applications with performances above 1000 F g^{-1} due to the presence of active redox substances. However, until now a very limited number of MO-C composites from MOF for the application of supercapacitors have been reported [35]. In this respect, it is of interest to use nanoscale metal particles with a carbon coating [416, 417] or decorate them on a high-conductivity substrate [368, 418–420]. Carbon coating on metallic species is important to prevent agglomeration of particles during the charge–discharge process and increase the electrical conductivity of the composite.

7.3 Lithium-Ion Batteries

Lithium-ion battery (LIBs) have developed tremendously in recent years due to their high reversible capacity, light weight, small volume, high energy density, long life span, environmental friendliness, lack of memory effects, and widespread use in various portable electronic devices (e.g., electric cars, laptops, smartphones) [72, 405, 421–433]. Primitive LIBs used graphite and lithium cobalt oxide (LiCoO_2) as anode and cathode materials, respectively [434]. However, in our time, their practical application is seriously hampered by the low theoretical capacity (372 mA h g^{-1} for graphite and 148 mA h g^{-1} for LiCoO_2). These primitive electrode materials were replaced by lithium alloys, which significantly improved

capacities, but were accompanied by large volume changes that caused damage to the electrode and ultimately affected the performance. In this regard, a significant number of studies have been devoted to the search for alternative electrode materials that can provide better performance and rate of lithium storage in order to meet the ever-growing demands of all kinds of electronic equipment.

In particular, nanostructured electrodes have been developed, such as NP, nanowires, or nanotubes, or hybrid composites with an inactive matrix such as carbon that mechanically buffers against volume changes [426, 435–439]. The most common and practical method is to use MOFs as sacrificial precursors in the formation of transition MO NPs, which are often used as LIB anode materials. Because of their high surface area and nanoporosity, MOFs provide ideal sacrificial templates for the production of nanoporous MO or metal sulfides with a high surface area for LIB (Table 7.5) [439–445].

Considering natural abundance, non-toxicity, low cost, and environmental friendliness, nanoscale ZnO has attracted universal attention as an alternative anode material for LIB [457–459]. In addition, its specific capacity (981 mA h g^{-1}) is higher than that of commercial graphite (372 mA h g^{-1}) [50, 460]. However, ZnO NPs usually suffer from severe aggregation caused by extensive volume deformation during the lithiation/delithiation process, which inevitably leads to electrode collapse, a sharp loss of capacity, and inferior cycling stability. Taking into account these shortcomings, it is very limited in its practical application. To further increase the electrochemical properties of ZnO, the researchers focused on the coating of ZnO with carbon and doping ZnO by graphene (Table 7.6).

In particular, Zn-based MOF, IRMOF-1, was used to produce hierarchically porous carbon-coated ZnO QDs ($\sim 3.5 \text{ nm}$) with a high surface area [45]. It was found that the temperature and duration of thermolysis play a decisive role in determining the characteristics of the product. Thermolysis of IRMOF-1 at $550 \text{ }^\circ\text{C}$ resulted in the formation of carbon-coated ZnO QDs without agglomeration, which have a high capacity of $>1200 \text{ mA h g}^{-1}$ at 75 mA g^{-1} and excellent charge storage reversibility (capacity retention $>100\%$ after 50 cycles). It should also be noted the synthesis of ZnO@ZnO QDs/C core-shell nanorod arrays derived from MOF grown on flexible carbon cloth, as an anode for LIB, which combine the advantages of the ZnO/C core-shell architecture and unique 3D nanorod arrays [433]. Despite these huge successes, rational design and simple synthesis of excellent ZnO-based anode materials are still very complex. Hybrid hollow porous ZnO/C nanocages with high surface areas of $256 \text{ m}^2 \text{ g}^{-1}$ and a high carbon content of about 50%, obtained by thermolysis of the hollow MOF-5 material both as a precursor and as a self-sacrificial template in the N_2 atmosphere, are of interest [446]. The hollow porous ZnO/C nanocages showed an initial discharge capacity of 1928 mA h g^{-1} at a current density of 100 mA g^{-1} and retained a high reversible capacity of 750 mA h g^{-1} after 100 cycles. In addition, they had a good rate capability of 351 mA h g^{-1} at a relatively high current density of 2 A g^{-1} . It is important that these excellent electrochemical characteristics are mainly due to the special nanostructures of the materials produced.

Table 7.5 Comparison of the performance of various nanostructures synthesized from MOF precursors as negative materials for LIBs

Materials	Doping	Original MOF	Pore size (nm)	Mass normalized current (mA g ⁻¹)	Reversible capacity (mA h g ⁻¹)	Cycle numbers	References
ZnO(QD)@C	-	MOF-5	35	75	1200	50	[445]
Hollow ZnO@C	-	MOF-5	-	100	750	100	[446]
Co-ZnO@C	Cobalt	MOF-5	-	100	725	50	[447]
ZnO@C	-	Zn ₃ (HCOO) ₆	30	100	955	50	[448]
ZnO/ZnFe ₂ O ₄ /C	-	MOF-5	7	500	1060	60	[72]
ZnCo ₂ O ₄	Zinc	MOF-74	~18	100	1243	80	[449]
Co ₃ O ₄ nanorings	-	Co-NTCDA Co-PTCDA	-	100	1370	30	[450]
FeS ₂ @S-doped C	Sulfur	MIL-88-Fe	3-10	100	1336.5	200	[451]
NiP ₂ @C	Phosphorus	Ni-MOF-74	4-30	50	656	50	[452]
SnO ₂ @C	Tin (Sn)	Cu-BTC	100	100	880	200	[453]
CuO/3DGN	-	Cu-BTC	16	100	409	50	[454]
CuO	-	Cu-BTC	-	100	470	100	[43]
Anatase TiO ₂	-	MIL-125	~1.25	10,000	127	1100	[455]
Anatase TiO ₂	-	MIL-125	~1.9	1000	166	500	[456]

Table 7.6 Comparison of the performance of ZnO-based materials as anode materials for LIBs

Active material	Current density mA g ⁻¹	Reversible capacity (Nth) mA h g ⁻¹	References
ZnO/porous carbon	100	653 (100)	[461]
C/Cu/ZnO	50	818 (100)	[462]
Cobalt-doped ZnO@C	100	725 (50)	[447]
ZnO@ZnO QDs/C	500	615 (100)	[433]
ZnO/RGO	200	360 (200)	[463]
ZnO/graphene	100	610 (500)	[464]
Porous carbon-ZnO	100	706 (100)	[465]
ZnO nanospheres	450	400 (30)	[466]
ZnO QD/graphene	100	960 (50)	[467]
Hollow ZnO/C	100	750 (100)	[446]

Porous hollow Co₃O₄ parallelepipeds synthesized by thermolysis of a parallelepiped Co-MOF ([Co₃(HCOO)₆]₂·DMF) crystal template were used as an anode material for LIBs [468]. Interestingly, the product obtained demonstrates an improved reversible capacity, excellent cyclic stability (1115 mA h g⁻¹ at 100 mA g⁻¹ after 50 cycles), and good rate capability.

It should be noted the use of agglomerated Co₃O₄ NPs, obtained from Co₃(NDC)₃(DMF)₄ MOF, as a Li-ion battery material [48]. At the first discharge process (Fig. 7.30a), a high discharge capacity (1118 mA h g⁻¹) was obtained. The capacity shows a gradual increase in subsequent cycles to a peak value of 965 mA h g⁻¹ at the 50th cycle (Fig. 7.30b), which is 86% of the initial capacity. The cycle performance at a higher current density of 100 mA shows similar behavior with the measured at a current density of 50 mA g⁻¹ (Fig. 7.30c, d). The capacity in the first discharge cycle is 1090 mA h g⁻¹, 730 mA h g⁻¹ of which remains above 100 cycles with a maximum value of 824 mA h g⁻¹ in the 39th cycle (Fig. 7.30d).

An effective approach for the production of porous iron oxide ribbons is interesting by controlling the nucleation and growth of the iron precursor Fe(acac)₃ on the graphene surface followed by annealing treatment. The resulting iron oxide ribbons exhibit a high reversible capacity and excellent cycle stability for lithium storage [436]. In particular, a high first discharge capacity of 1426 mA is shown for ribbons (Fig. 7.31a). It is important that the reversible charge capacity can be maintained almost 100% after 130 cycles (Fig. 7.31b), which is an excellent retention property. The influence of the annealing temperature on the electrochemical characteristics of FeO ribbons was studied, because it can effectively adapt the nanostructure, including the porous structure and crystal size in FeO ribbons. In particular, when the annealing temperature rises from 523 to 623 K, the storage capacity retention decreases significantly, although their first reversible capacity is similar (about 1000 mA h g⁻¹) (Fig. 7.31c). More importantly, the rate capabilities of iron oxide ribbons depend strongly on the annealing temperature (Fig. 7.31d).

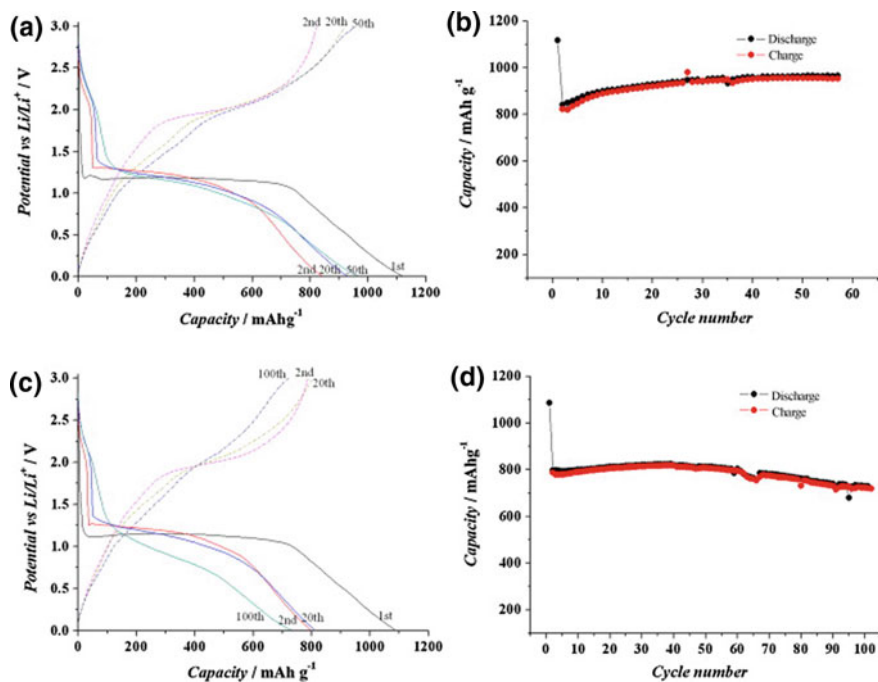


Fig. 7.30 a Charge–discharge curves and b cycle performance at a current density of 50 mA g^{-1} and c charge–discharge curves and (d) cycle performance at a current density of 100 mA g^{-1} for the as-prepared $\text{Co}_3\text{O}_4/\text{Li}$ half-cell cycled between 3.0 and 0.01 V. Only the mass of Co_3O_4 was considered in calculating the specific capacity. Reproduced with permission from Ref. [48]. Copyright (2010) Elsevier

Anatase TiO_2 is a promising alternative anode for LIB because of its high volumetric and gravimetric energy densities [469, 470]. In addition, TiO_2 is an abundant, cheap, environmentally friendly material that is sufficiently safe to use at a higher lithium extraction potential of 1.6 V compared to Li/Li^+ [471–473]. However, due to poor electronic conductivity and slow diffusion of lithium ions, it is practically impossible to use TiO_2 in systems with high output power [474]. Therefore, nanostructured materials constructed by NPs have been developed which have excellent rate capabilities as anode materials in the LIB because of their greater electrode–electrolyte contact area and shorter lengths of Li^+ and e^- transport (Table 7.7) [475–480].

As a typical example, we note the mesoporous anatase TiO_2 (MAT) with disc-shaped morphology obtained by direct thermolysis of titanium MOF [MIL-125 (Ti)] in air [455]. When used as an anode material for LIBs, the prepared MAT electrode showed excellent lithium storage properties with a slight capacity loss at high charge–discharge rates. At a rate of 10C, the prepared electrode still fed a high reversible capacity of 127 mA h g^{-1} after 1100 cycles (Fig. 7.32a). The first discharge–charge capacities are 265/228 (0.1C), 185/180 (1C), 176/173 (2C),

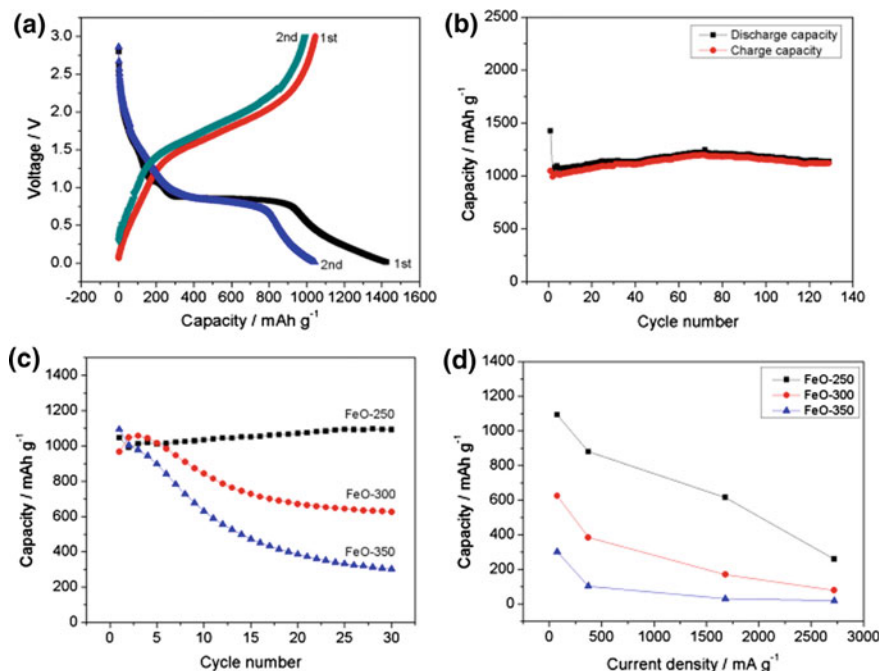


Fig. 7.31 Electrochemical properties of the iron oxide ribbons for lithium storage. **a** First two discharge–charge curves and **b** cycle performance of FeO-250 ribbons at a current density of 74 mA g⁻¹. **c** Comparisons of the cycle performance of FeO-250, FeO-300 and FeO-350 ribbons during 30 cycles, as well as **d** rate capabilities of FeO-250, FeO-300 and FeO-350 ribbons at the current densities of 74, 372, 1680 and 3720 mA g⁻¹ after 30 cycles [436]

Table 7.7 Comparison of the electrochemical performance of the porous TiO₂ electrodes

Sample	Capacity/C-rate (mA h g ⁻¹)	Cycling stability	References
Porous TiO ₂	170/1C	3.2, 22.4 and 50% capacity loss after 500 cycles at 1C, 5C and 10C, respectively	[456]
	140/5C		
	110/10C		
Porous TiO ₂ wires	152.1/1C	31.7% capacity loss after 51 cycles at 0.625C	[481]
	139.7/2C		
	116.1/5C		
Nanoporous TiO ₂ mesocrystals	164.9/1C	25.8% capacity loss after 60 cycles at 1.2C	[482]
	151.7/2C		
Mesoporous TiO ₂ microspheres	175/0.6C	3.8% capacity loss after 50 cycles at 1.2C	[483]
	156/1.2C		
Mesoporous TiO ₂ microdisc	122/10C	No obvious capacity loss after 1100 cycles	[455]

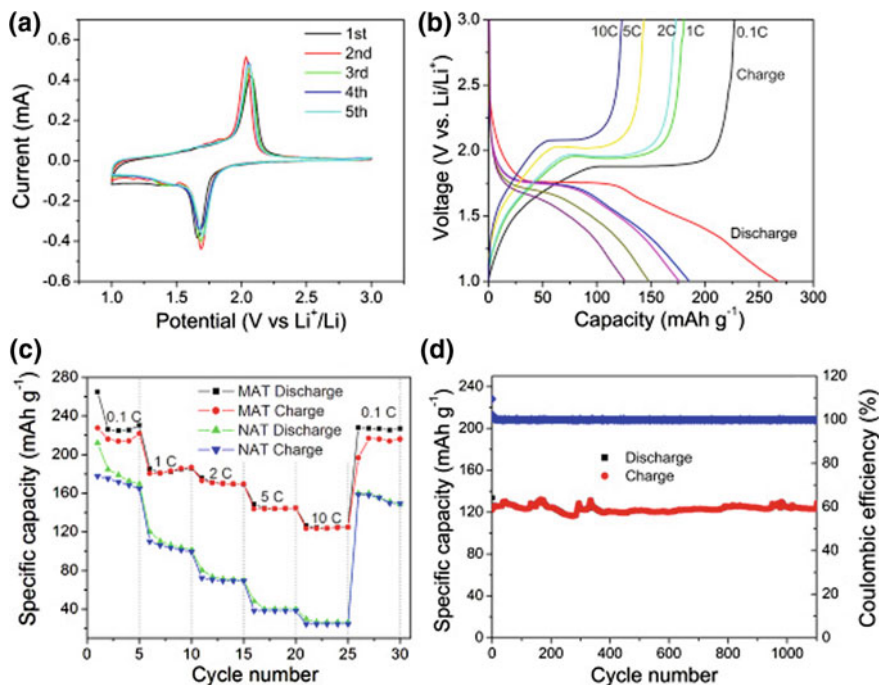
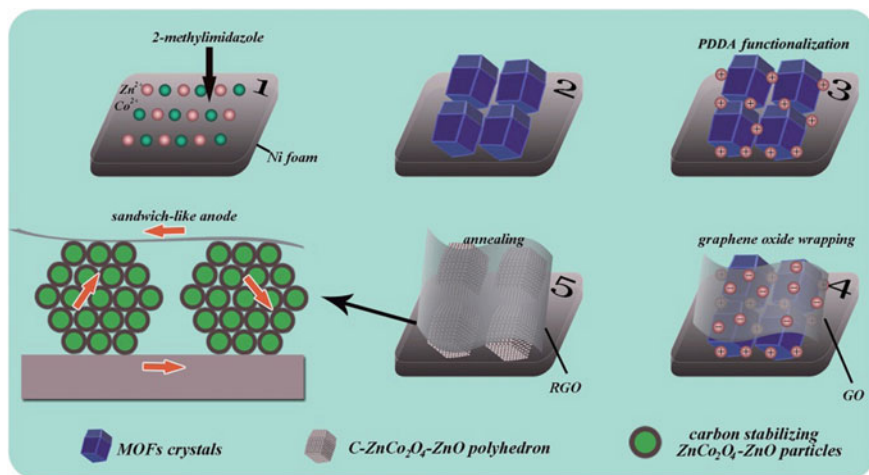


Fig. 7.32 **a** CV of the MAT electrode at a scan speed of 0.1 mV s^{-1} . **b** First discharge–charge voltage profiles of the MAT electrode at different rates ($1\text{C} = 168 \text{ mA g}^{-1}$). **c** Rate-dependent cycling performance of the MAT electrode and the NAT electrode. **d** Cycle performance of the MAT electrode at 10C with corresponding CEs. Reproduced with permission from Ref. [455]. Copyright (2016) Elsevier

149/144 (5C), and 126/123 (10C) mA h g^{-1} , respectively (Fig. 7.32b). It is of interest to compare the rate characteristics of the MAT electrode with the nanoporous anatase (NAT) electrode (Fig. 7.32c). It turned out that the rate capacities of the MAT electrode are much higher than those of the NAT electrode. In addition to excellent rate characteristics, the MAT electrode also exhibits high cycle stability (Fig. 7.32d).

It should be noted the use of mixed-metal oxides (such as spinel oxides) for LIBs with improved characteristics, in particular spinel-structured ternary cobalt-based oxides (ZnCo_2O_4 [430, 484], NiCo_2O_4 [485, 486], MnCo_2O_4 [487, 488], etc.), in which Co is partially replaced by less expensive and environmentally friendly metals. A promising method of increasing the efficiency of such materials is the production of composites with a conducting buffer matrix, for example, carbon materials, which lead to a remarkable improvement in electrochemical characteristics. As a typical example, we note a ZnMn_2O_4 /carbon aerogel composite, which demonstrated a significant increase in electrochemical performance compared to pure ZnMn_2O_4 [489]. Carbon materials can not only greatly facilitate the transfer of



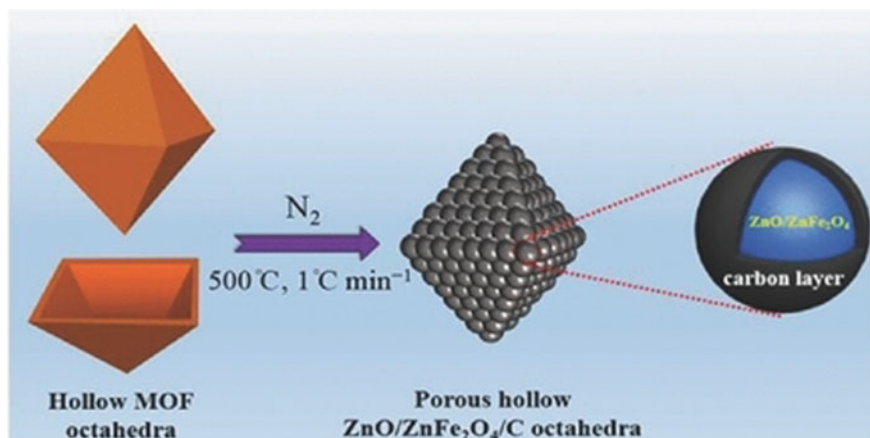
Scheme 7.4 Schematic illustration of the formation of the sandwich-like RGO/ZnCo₂O₄-ZnO-C/Ni electrode. Reproduced with permission from Ref. [490]. Copyright (2015) Royal Society of Chemistry

charge, but also serve as a cushion layer for changing the buffer volume, which leads to a marked enhancement in electrochemical characteristics.

Of interest is a sandwich-like structure with RGO-wrapped MOF-derived ZnCo₂O₄-ZnO-C polyhedrons on nickel foam as an anode for high-productivity LIBs obtained by simply growing MOF on Ni foam and wrapping GO nanosheets on MOFs, and then annealing in the atmosphere N₂ (Scheme 7.4) [490]. When tested as anodes for LIBs, they have superior Coulomb efficiency (CE), excellent cycling stability, and rate capability. The in situ formed carbon layers outside of ZnCo₂O₄-ZnO act as both a conductive substrate and a buffer layer for volume change. Open pores in ZnCo₂O₄-ZnO-C polyhedrons provide sufficient electrolyte and also serve as a cushion space for further softening of volume changes. RGO nanosheets act as a flexible protector for firmly fix polyhedrons on Ni foam, as well as a conductive substrate for joining all polyhedra. The interconnected carbon layers and two high-conductivity substrates (RGO and Ni foams) together form an unobstructed backbone for charge transfer during discharge–charge processes, promising good electrochemical characteristics.

It should be noted a unique hollow octahedral nanoarchitecture consisting of 3D-interconnected, porous carbon-stabilized ZnO/ZnFe₂O₄ networks, proposed for storage of lithium ions (Scheme 7.5) [72].

At the first cathode scan, two distinct peaks can be observed at 0.75 and 0.2 V (Fig. 7.33a). The CV profiles remain steady after the first cycle, since they do not change significantly with further sweeps, which indicates highly reversible



Scheme 7.5 Schematic illustration for the preparation process of porous hollow ZnO/ZnFe₂O₄/C octahedral. Reproduced with permission from Ref. [72]. Copyright (2014) John Wiley and Sons

electrochemical reactions. The initial discharge–charge capacities are 1385 and 1047 mA h g⁻¹, respectively (Fig. 7.33b), and the initial value of CE is 75.6% (Fig. 7.33c). It is important to note that the porous ZnO/ZnFe₂O₄/C electrode has excellent cycling characteristics at a much higher current density of 2 A g⁻¹, and it is capable of delivering a capacity of 988 mA h g⁻¹ after 100 discharge–charge cycles (Fig. 7.33d). The resulting hybrid demonstrates excellent capacity retention at different rates (Fig. 7.33e). Figure 7.33f shows the current-rate dependence of the discharge capacitance of the ZnO/ZnFe₂O₄/C electrode.

2D CP based on the trinuclear building block [Cu₃(HSer)₃(H₂O)₂]₃2H₂O was used as a precursor for the preparation of CuS nanospheres with hollow interiors [491]. The electrochemical behavior (Fig. 7.34) of these nano-sized CuS mesoassemblies (CuS-1) as a cathode material for LIBs has shown that the reaction proceeds through the insertion and deinsertion mechanisms, and the CuS with a hollow interior is more efficient and has good cyclability in comparison with that with flower-like morphology (CuS-2). The electrochemical storage behavior of nanostructured CuS (hollow and flower-like) in the first cycle is very similar to those described previously on commercially available bulk CuS. In particular, during the first discharge, the plateau at 2.09 V corresponds to the insertion of Li⁺ ion into the covellite CuS lattice, which forms a homogeneous Li_xCuS phase. Further insertion of lithium leads to a transformation reaction, forming Cu and Li₂S nanocomposite.

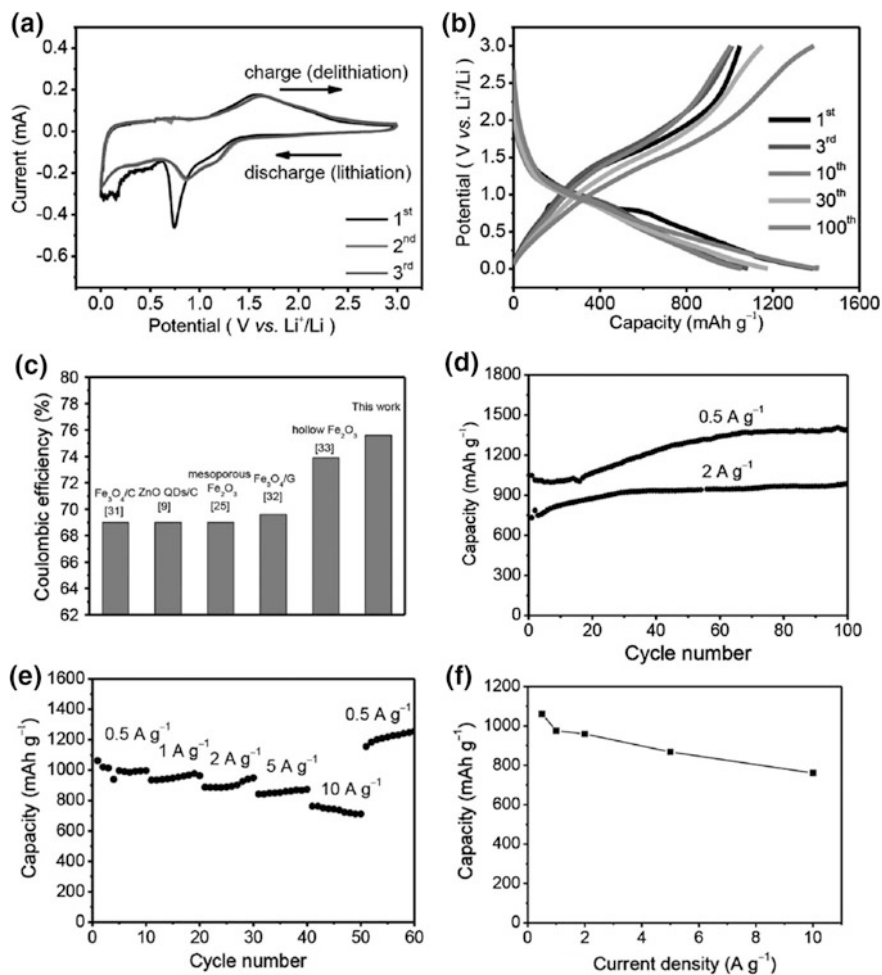
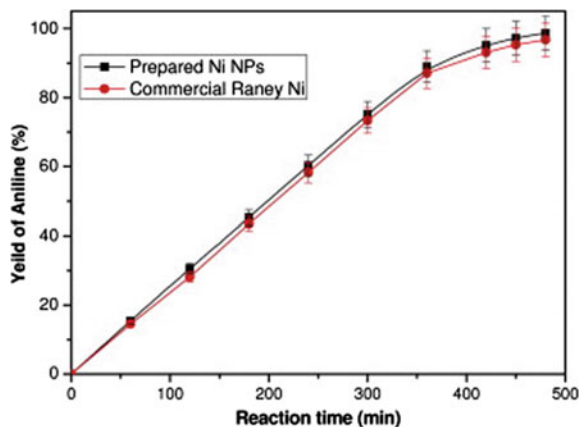


Fig. 7.33 Electrochemical performances of the electrode made of the as-formed porous ZnO/ZnFe₂O₄/C hollow octahedra: **a** representative CVs at a scan rate of 0.2 mV s⁻¹ for the first, second, and third cycles; **b** charge-discharge profiles at a current density of 0.5 A g⁻¹; **c** comparison of initial CE; **d** cycling performance at current densities of 0.5 and 2 A g⁻¹; **e** rate capability at current densities of 0.5, 1, 2, 5, 10 A g⁻¹; **f** current-rate dependence of charge capacities. All the measurements were carried out in the potential range of 0.005–3 V versus Li⁺/Li. Reproduced with permission from Ref. [72]. Copyright (2014) John Wiley and Sons

Fig. 7.34 a, b Galvanostatic cycling of CuS-1 and CuS-2; c cycle number versus capacity plots of CuS-1 and CuS-2; d CVs of hollow CuS-1. Reproduced with permission from Ref. [491]. Copyright (2009) American Chemical Society



7.4 Nanocatalysis

The current interest in NPs for catalysis (the so-called nanocatalysis) is high, since with small dimensions the catalytic properties of particles are significantly improved in terms of efficiency, catalyst recovery, and minimization of contamination by ions and metal particles [27, 35, 81, 492, 493]. At present, a large number of nanocatalysts have been developed, appropriate theoretical concepts have been developed, and nanocatalysis technologies have been substantiated. Nanocatalysts have well-defined structures and are monodisperse in nature, which retains the advantage of homogeneous catalysts under conditions of rapid kinetic behavior, easy flexibility, and rationalization. Nanocatalysts can be easily removed from the reaction mixture by precipitation, membrane or nanofiltration methods because of their large dimensions compared to products, which increases the benefits of heterogeneous catalysts. In addition, the catalytic properties of nanocatalysts can be precisely regulated by changing their structure, size, shape, chemical functionality, and solubility. The properties of NPs also depend on the shape, like nanorods, nanowires, nanocubes, nanoplates, nano-octahedra/tetrahedra, nanoplates and nanoflowers or nanostars differ in their properties (including catalytic ones) [165, 494]. For example, it was found that the Pd and Pt nanoflowers are excellent for catalysis of the reduction of ferricyanide by thiosulfate [495] and electro-oxidation of methanol [496]. It should be noted that the NPs fixed on the carrier [497–500] are many times more effective for catalysis. In addition, metal or MO NPs are often introduced into the carbonaceous shell, which makes them excellent candidates for catalysis [48, 296, 299, 377, 501–504]. Composites of the nanostructures and carbon materials, such as carbon nanotubes, nanorods, and graphenes, increase the stability and activity of catalysts [505, 506]. Thus, nanomaterials have been proposed to bridge the gap between homogeneous and heterogeneous catalysis, and nanocatalysts can approach catalysts that have high activity, selectivity, stability, and easy separation.

7.4.1 Catalytic Hydrogenation

As a typical example, we note the performances of Ni NPs synthesized by thermolysis of nickel chelate with 2,3-bis-[(3-ethoxy-2-hydroxybenzylidene)amino]but-2-enedinitrile Schiff base ligand and commercial Raney Ni as catalysts for the hydrogenation of nitrobenzene without any catalyst prereluction (Fig. 7.35) [507]. Linear conversion of nitrobenzene with time from the beginning of the reaction clearly indicates the stability of Ni NPs. The catalytic activity of synthesized Ni NPs showed high selectivity for aniline (98%). In addition, the catalytic efficiency of prepared Ni NPs is slightly higher compared to commercial Ni Raney, which may be due to the large surface area, large pore volume, and small pore radius of prepared Ni NPs. It is important that no other intermediate products were found during the reduction of nitrobenzene and the magnetic behavior of the prepared Ni NPs provides a simple way to remove the catalyst from the reaction medium by applying an external magnetic field.

In another interesting example, the catalytic activities of Co@C-N-X-T materials obtained after Co-MOF thermolysis (here X and T represent the thermolysis temperature and time, respectively) were tested in the transfer hydrogenation of acetophenone to phenethanol as a model process [508]. It turned out that nanomaterials obtained at longer times of thermolysis and at higher temperatures show higher activity and selectivity. Ethylbenzene was the main by-product obtained in this reaction. It was shown that Co@C-N-900-15 h is the best catalyst among the materials studied in terms of conversion and selectivity to phenethanol. There is no noticeable loss of conversion or selectivity up to four runs. A study of the transfer hydrogenation of different unsaturated chemicals, including aldehydes, ketones, nitro compounds, nitriles, and alkenes (Table 7.8), has demonstrated the general applicability of this catalytic system. Since the basic sites were present in the synthesized Co@C-N materials, it was suggested that they could play a similar role with base additives to facilitate proton transfer in Co NPs to form Co metal hydrides, thereby contributing to the desired hydrogenation products.

Fig. 7.35 Performance of Ni NPs as a catalyst in the hydrogenation of nitrobenzene without prereluction. Reproduced with permission from Ref. [507]. Copyright (2014) Elsevier

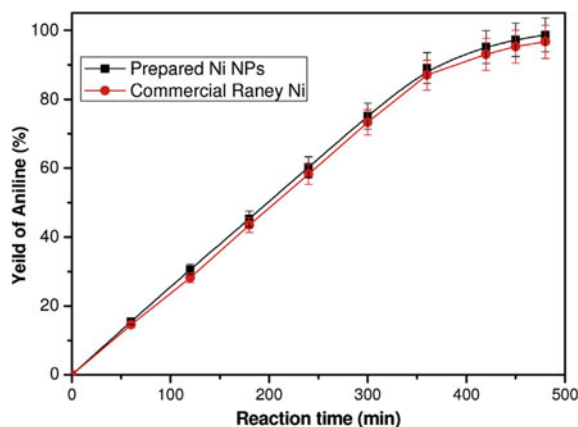
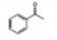
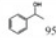
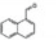
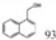
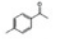
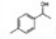
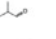
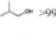
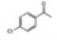
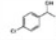
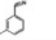
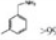
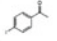
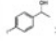
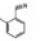
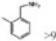

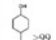
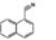
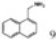
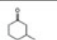
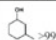
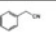
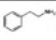
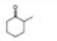
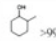
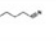
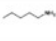
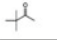
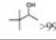
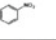
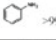
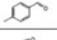
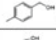
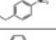
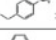
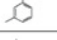
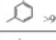


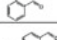
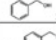


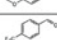
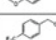

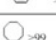
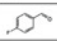
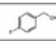


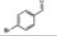
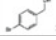


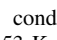
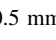


Table 7.8 Transfer hydrogenation of various substrates with isopropanol^a

Entry	Substrate	Time (h)	Con.(%)	Sel. (%)	Entry	Substrate	Time (h)	Con.(%)	Sel. (%)
1		17	99	 95	16 ^b		36	>99	 93
2		12	>99	 >99	17		30	>99	 >99
3		30	>99	 >99	18 ^c		50	>99	 >99
4		30	>99	 >99	19 ^c		46	>99	 >99
5 ^b		24	>99	 >99	20 ^{b,c}		40	>99	 90
6 ^b		24	>99	 >99	21 ^{b,c}		46	>99	 >99
7 ^b		24	>99	 >99	22 ^{b,c}		24	>99	 90
8 ^b		60	95	 >99	23 ^d		80	80	 >99
9		34	>99	 >99	24 ^b		50	>99	 >99
10		40	>99	 >99	25 ^b		50	>99	 >99
11		45	>99	 >99	26 ^d		60	95	 >99
12		40	>99	 >99	27 ^d		50	98	 >99
13		45	>99	 >99	28		20	>99	 >99
14		35	>99	 >99	29		20	>99	 >99
15 ^b		35	>99	 >99					

^aReaction conditions: substrate (0.5 mmol), Co@C-N-900-15 h (Co 10 mol%), isopropanol (2 mL), 353 K

^b373 K

^cIsopropanol (1 mL)

^dCatalyst (Co 20 mol%), 423 K

SiCN catalysts containing palladium silicide (Pd₂Si@SiCN) were used for the selective hydrogenation of aromatic ketones [509]. The selectivity of the reaction with respect to alcohol products remained very high and did not change with the content of palladium or with the amount of catalysts added. Importantly, the conversion increased with both the reaction temperature and the amount of catalyst used, while it decreased with increasing alkyl chain length and branching at α -carbon. Catalysts showed appreciable reusability and no loss in catalyst activity were observed up to six consecutive catalytic runs (Fig. 7.36).

The chemical catalytic activity of Pt dendritic nanocubes (DNCs) was studied using alkenes, alkynes, and nitrobenzene as substrates [510]. It turned out that styrene, *p*-methylstyrene, and *p*-methoxystyrene were completely converted to form a single C–C bond for 1 h using 0.5 mol% of the catalyst (Table 7.9). In the case of hydrogenation of alkynes, 1-ethynylbenzene, *p*-methyl-, and *p*-methoxyethynylbenzene provided 100% conversion to the corresponding ethyl benzene

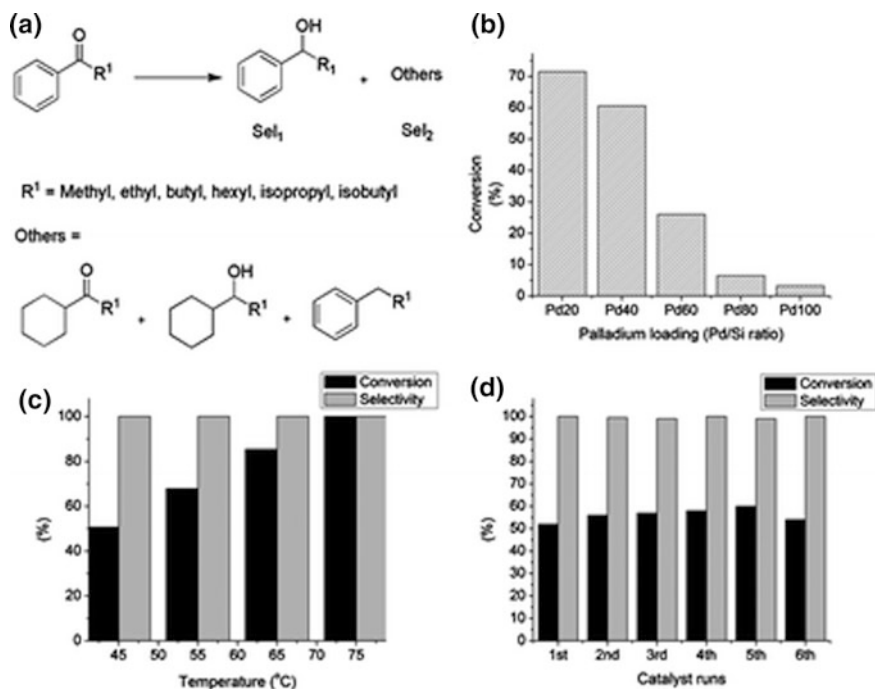
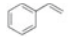
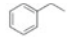
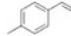
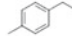
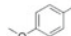
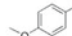
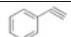
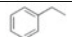
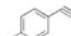
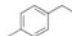

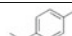
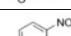
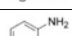
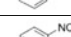
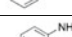
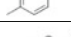
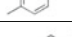


Fig. 7.36 **a** Schematic representation of catalytic hydrogenation of ketones to different products; **b** hydrogenation of acetophenone with catalyst at 348 K under 20 bar hydrogen for 24 h. The conversion decreases with decrease in the amount of palladium contained by the ceramics; **c** hydrogenation of acetophenone using catalyst under 20 bar hydrogen pressure for 24 h. The conversion increases with temperature keeping the selectivity constant; **d** hydrogenation of acetophenone with the catalyst under 20 bar hydrogen pressure at 348 K for 24 h. The figure shows reusability of the catalyst up to six catalyst runs. Reproduced with permission from Ref. [509]. Copyright (2011) Royal Society of Chemistry

products, respectively. In addition, with Pt DNCs catalysts, nitrobenzene, *p*-methyl- and *p*-methoxy-nitrobenzene were converted into the corresponding aniline products in 3 h.

When used in the hydrogenation of glucose, nickel catalysts obtained using a complex of nickel with ethylenediamine show almost no nickel leaching compared to the commercial Ni/SiO₂ catalyst (Ni70S), but they are slightly less active (TOF: 2 to 10 × 10⁻³ s⁻¹) than the commercial catalyst (TOF: 14 × 10⁻³ s⁻¹), and showed a lower yield of sorbitol (3–42% compared to 60%) [511]. Interestingly, the catalytic results depend on the pretreatment conditions performed. In particular, with preliminary calcination of the catalysts, a higher conversion (19–45%) and sorbitol selectivity (81–92%) are obtained than with the catalyst without preliminary calcination (conversion: 10–16% and sorbitol selectivity: 21–59%) after 5 h reaction time, respectively (Fig. 7.37). The difference was due to the fact that complete decomposition of the precursor of nickel ethylenediamine was achieved only with the preliminary calcination.

Table 7.9 Hydrogenation of olefin, alkynes, and nitrobenzene over Pt DNCs^a

Enter	Substrate	Product	Yield ^b , %	Time (h)
1			>99	1
2			>99	1
3			>99	1
4			>99	1
5			>99	3
6			>99	3
7			>99	3
8			>99	3
9			>99	3

^aAll reactions were carried out with 1 mg Pt DNCs, 1.0 mmol substrates and 2 mL methanol at 323 K in hydrogen balloon condition. ^bGas chromatography yield

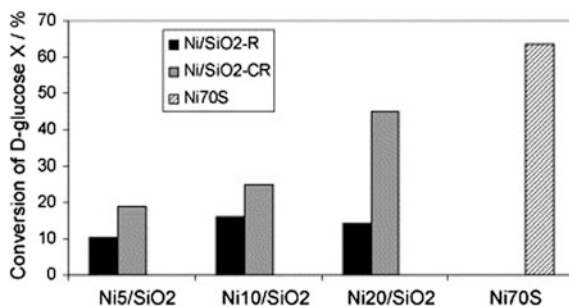
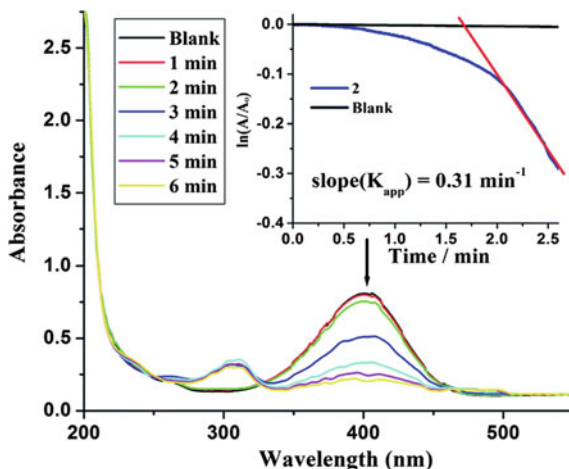


Fig. 7.37 Conversion of glucose for the Ni/SiO₂ catalysts with 5, 10, and 20 wt% nickel activated by reduction treatment only (Ni/SiO₂-R) and by calcination and reduction treatments (Ni/SiO₂-CR) as well as for the commercial catalyst (thermally treated and reduced) (reaction conditions: 493 K, 120 bar, 5 h, 20 wt% aqueous glucose solution). Reproduced with permission from Ref. [511]. Copyright (2007) Elsevier

Carbon-embedded **fcc** cobalt NP composites, Co@C, prepared by thermolysis of the 1D polymeric cobalt(II) coordination complex $[\text{Co}(\text{L})(\text{L}')_2]_n$, H_2L = benzenedicarboxylic acid; L' = N-methylimidazole), show excellent catalytic activity in the reduction of nitrophenol to aminophenol, studied as a model reaction [512]. Preliminary reaction of *p*-nitrophenol with 5 mol% of catalyst using 20 eq. NaBH₄ (catalyst: *p*-nitrophenol: NaBH₄ = 1: 20: 400) in H₂O at 293 K gave quantitative conversion to *p*-aminophenol (Fig. 7.38). The slope of near-linear fit plot of the natural log of absorbance at 400 nm versus time (the inset in Fig. 7.38,

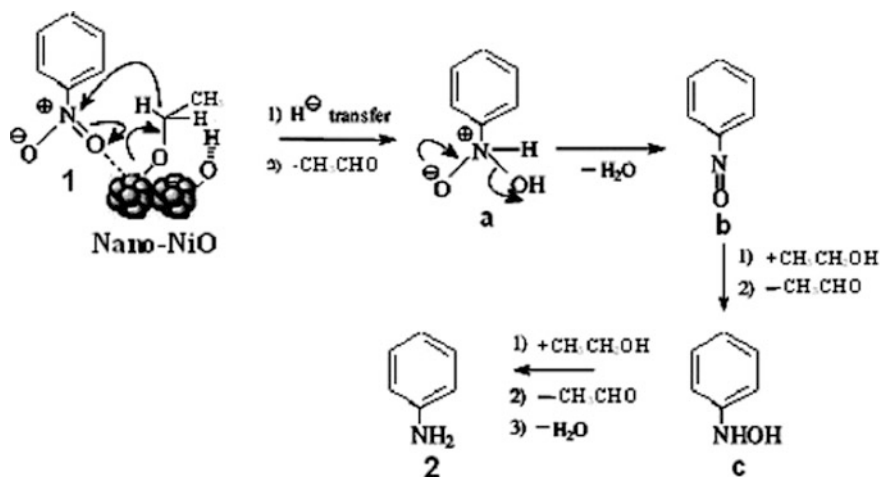
Fig. 7.38 Catalytic reduction of *p*-nitrophenol studied by UV-Vis with increment of time. *Inset* plot of natural log of A/A_0 versus time showing the apparent rate constant marked by red line. Reproduced with permission from Ref. [512]. Copyright (2016) Royal Society of Chemistry



the red line) gives an apparent rate constant ($K_{app} = 0.31 \pm 0.02 \text{ min}^{-1}$). It was found that the induction period is independent of the NaBH_4 concentration and strongly depends on the *p*-nitrophenol concentration, indicating that the *p*-nitrophenol restructuring over the active catalytic center dictates the induction period. The activation energy, measured between 293 and 323 K for the catalytic process, is calculated to be $24.97 \text{ kJ mol}^{-1}$, which is relatively lower than reported for Co/Ni NPs ($25.7\text{--}27.8 \text{ kJ mol}^{-1}$) [513, 514], but relatively higher than the Pt cubes (12 kJ mol^{-1}) [515–518].

NiO NPs with an average size of 12 nm and a high specific surface of $88.5 \text{ m}^2 \text{ g}^{-1}$ obtained by thermolysis of the $\text{Ni}(\text{dmgH})_2$ complex were used as a heterogeneous catalyst for the reduction of nitroarenes into their corresponding amines [519]. Effective and selective reduction was observed using ethanol as a hydrogen-donor (reducing agent) and KOH as a promoter under microwave irradiation. This highly regio- and chemoselective method is fast, simple, inexpensive, high-performance, pure, and compatible with several sensitive functional groups such as halogens, $-\text{OH}$, $-\text{OCH}_3$, $-\text{CHO}$, $-\text{COCH}_3$, $-\text{COOH}$, $-\text{COOEt}$, $-\text{CONH}_2$, $-\text{CN}$, $-\text{CH}=\text{CH}_2$, and $-\text{NHCOCH}_3$. It is important that the method is suitable for large-scale preparation of various substituted anilines, as well as other arylamines. It should be emphasized that the catalytic activity of nano-sized NiO is higher than that of a bulk sample. As shown in Scheme 7.6, the formation of aniline from nitrobenzene occurs by the formation of nitrosobenzene (b) and *N*-phenylhydroxylamine (c) as intermediates. Since the nitro group can remove electrons from the aromatic ring more strongly than other functional groups, it can be readily adsorbed on the surface of the catalyst, resulting in amine products. This may be the reason for the chemoselective reduction of the nitro group in front of the carbonyl group.

Monolithic microporous Ni@SiCN materials were selective hydrogenation catalysts for the conversion of phenylacetylene to styrene (selectivity $\geq 89\%$ and conversion $\geq 99\%$) [520]. By changing the nature of the PDC phase (SiC), the micro-, meso-, and hierarchically porous Ni@SiC catalysts obtained can be active



Scheme 7.6 Plausible pathway for the reduction of nitrobenzene over the nano-sized NiO catalyst. Reproduced with permission from Ref. [519]. Copyright (2011) Elsevier

and highly selective in the selective hydrogenolysis of aromatic carbon–oxygen (C–O) bonds [521]. In particular, the most active catalysts were the hierarchically structured Ni@SiC materials.

7.4.2 Oxidation Reactions

Depending on the nature of the metal, the resulting metal-containing PDC nanocomposites can be used for heterogeneous catalysis for reactions under harsh conditions due to the robust nature of the non-oxide ceramic such as SiC and SiCN, the differences in polarity and acidic properties in comparison with oxide ceramics, their inertness, and chemical resistance [522]. As a proof-of-principle experiments, the catalytic activity and thermal stability of the highly porous and hierarchically ordered SiCN ceramics combining well-dispersed Pt NPs were tested in the total oxidation (combustion) of methane (Fig. 7.39) [523]. Carbon dioxide was the only product detected, indicating complete oxidation of methane under experimental conditions.

Copper-containing silicon carbonitride ceramics (Cu@SiCN) using silylaminopyridinate complexes were used as a robust, efficient, heterogeneous, and recyclable catalyst with respect to the oxidation of cycloalkanes with air as an oxidant [524]. It has been demonstrated that selectivity problems can be solved by adapting the copper content and the nature of the metal loading into the polymer. In particular, with increasing copper content in the ceramic, the selectivity rises gradually up to 80% for the mono-oxygenation product cyclooctanone (Fig. 7.40). It is important that the catalysts showed no loss of activity up to four consecutive catalytic runs.

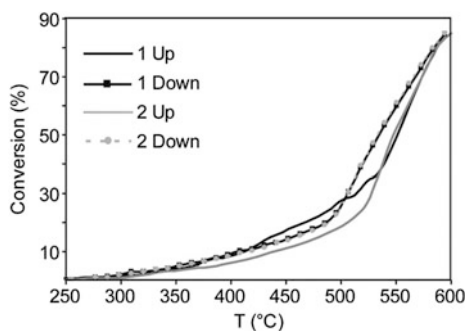


Fig. 7.39 Methane conversion (activity) of highly porous and hierarchically ordered SiCN ceramics that integrate well-dispersed Pt NPs as a function of the reaction temperature during two heating/cooling cycles. Reproduced with permission from Ref. [523]. Copyright (2009) American Chemical Society

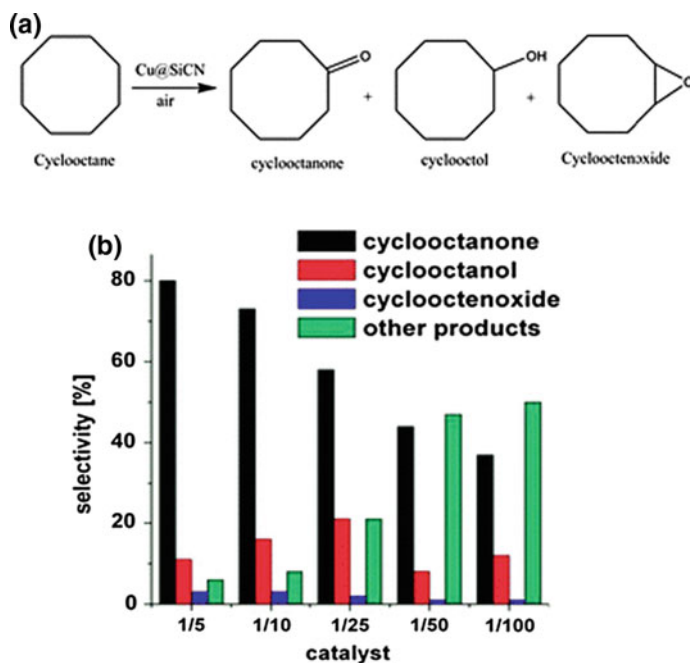
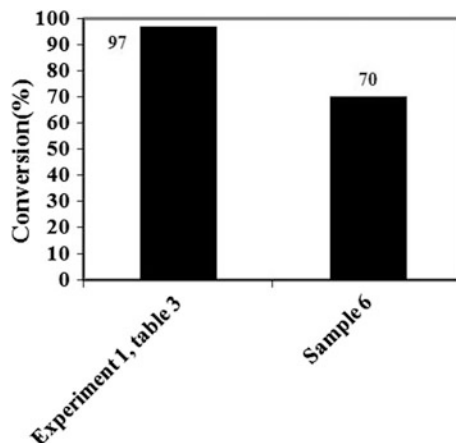


Fig. 7.40 Scheme showing the formation of different products obtained by the oxidation of cyclooctane using Cu@SiCN as catalyst (a). Selectivities (%) of different catalysts (b). The copper to silicon ratios vary from 1:5 to 1:100. Reproduced with permission from Ref. [524]. Copyright (2010) John Wiley and Sons

Fig. 7.41 Trichloroethylene conversion over CoCr_2O_4 samples prepared by optimized thermolysis procedure and conventional coprecipitation method at weight hourly space velocities: $60 \text{ L g}^{-1} \text{ h}^{-1}$ [526]



Catalysts based on $\text{Pt/CeO}_2/\text{SiC}$ composites showed good catalytic activity and stability with respect to methane oxidation, which was explained by the presence of nano-sized platinum and cerium particles [525]. It is important that the catalytic activity decreases both with a decrease in the specific surface area and in the amount of cerium oxide contained in the catalysts.

It is of interest to investigate the oxidation of trichloroethylene over CoCr_2O_4 nanocrystallite (Fig. 7.41) [526]. It was found that CoCr_2O_4 NPs, obtained in accordance with the thermolysis procedure (average particle size is 4.1 nm), showed a higher conversion (97%) than the sample (particle size in the range of 30–60 nm) obtained by the conventional coprecipitation method, which gave a 70% conversion. Comparison of the catalytic activity and the crystallite size of the samples confirmed that the catalyst with a smaller crystallite size gives more favorable active sites for the decomposition of trichloroethylene.

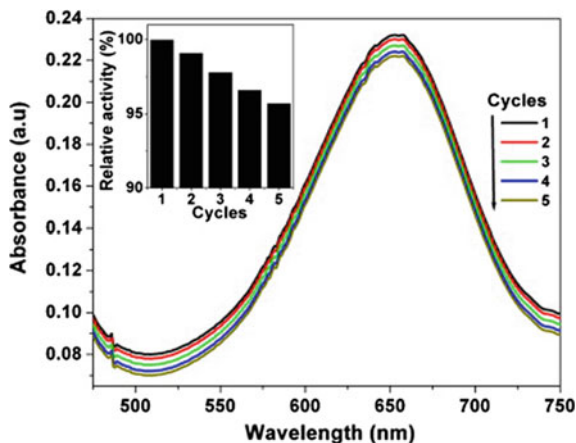
It should be noted CoFe_2O_4 nanocomposite particles, synthesized using the template MOF and precursors, which retained the morphology of the template [59]. Using potassium peroxydisulfate as an oxidant, the nanomaterials obtained showed relatively high catalytic characteristics for the oxidation degradation of phenol. In particular, after 120 min of degradation, the phenol concentration was reduced by about 95%, and the regenerated catalysts showed high catalytic performance in successive runs.

Among other catalytic nanomaterials, we also note CuO-CeO_2 NP catalysts for CO oxidation [62].

It is of interest to investigate the intrinsic peroxidase-like activity of CdS NPs with respect to peroxidase substrates 3,3',5,5'-tetramethyl benzidine and hydrogen peroxide [527]. Catalysis by CdS NPs shows the typical Michaelis–Menten kinetics, and the synthesized CdS NPs exhibit higher catalytic characteristics with higher binding affinity for the substrate than horseradish peroxidase and other nanomimetics. Optimized catalytic conditions are approximately equal to pH 4.0 and a temperature of 313 K. A slight decrease in the intensity of absorption is

Fig. 7.42 Catalytic activity of CdS NPs in five successive recycles. *Inset* relative activity versus number of cycles.

Reproduced with permission from Ref. [527]. Copyright (2012) Elsevier



observed after five consecutive cycles (Fig. 7.42), showing that CdS NPs are stable and have excellent reproducibility during the cycling process.

7.4.3 Ullmann-Type Amination Coupling Reaction

Uniform Cu_2O -coated Cu NPs, obtained from the thermolysis of copper acetylacetonate and subsequent oxidation in air, were used as catalysts for Ullmann-type amination coupling reactions of aryl chlorides [528]. When coupling reactions using aryl bromides, such as 2-bromopyridine and 4-bromoacetophenone, were carried out in DMSO at 423 K, the reactions proceeded to the completion. High yields were obtained in the case of the Ullmann-type amination reactions of imidazole with various aryl chlorides having electron-withdrawing groups using Cu_2O -coated copper NPs as catalysts (entries 1–8 in Table 7.10). This high catalytic activity of the catalysts is apparently due to the high surface area derived from the NPs. In addition, coordination of OAm on the NPs can affect catalytic activity.

Table 7.10 Catalytic reactions using Cu_2O -coated Cu NPs for Ullmann coupling of imidazole with various aryl chlorides^a

Entry	Reactant	Product	Yield(%) ^b	Entry	Reactant	Product	Yield(%) ^b
1			95	6			69
2			91	7			86
3			90	8			88
4			85	9			0
5			97	10			0

^a5 mol% Cu_2O -coated Cu NPs and 2 eq. imidazole used, Cs_2CO_3 , DMSO, 523 K, 18 h

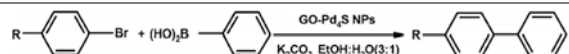
^bIsolated yield

It should be noted that commercially available bulk Cu_2O powder showed only a 16% conversion for 4-chloroacetophenone under the same conditions. In the case of non-activated aryl chlorides, such as chlorobenzene and 4-methoxychlorobenzene, it was not possible to isolate any coupled product (entries 9 and 10 in Table 6.10). As expected, the single imidazole coupled product, 4-chloroimidazolylbenzene, is selectively obtained in 69% yield (entry 6 in Table 7.10). Freshly prepared Cu NPs also showed good activity for this Ullmann-type amination (95% isolated yield for 4-chlorofluorobenzene).

7.4.4 Suzuki–Miyaura Coupling Reaction

It is known that some reactions of formation of carbon–carbon bonds, for example, Suzuki coupling based on Pd(0) or its compounds, are associated with NPs [529–531]. Thus, the nanoflowers and nanospheres of Pd_4S NPs obtained by thermolysis at 468 K of the SSP, $[\text{PdCl}_2(\text{PhS}-\text{CH}_2\text{CH}_2\text{CH}_2-\text{NH}_2)]$, were investigated individually and as composites with GO for the catalysis of Suzuki–Miyaura coupling reactions [532]. It turned out that the flower-shaped NPs exceed the spherical for this catalysis in aqueous ethanol, and the catalytic efficiency increases when grafting the nanoflowers/spheres onto the GO. The conversion was $\sim 99\%$ (after 5 h, at 353 K) for GO composite with Pd_4S nanoflowers (Pd: 0.2 mol%). The catalytic efficiency corresponds to the order of the GO- Pd_4S -nanoflowers > GO- Pd_4S -nanospheres > Pd_4S nanoflowers > Pd_4S nanospheres. Recyclability of the GO- Pd_4S nanoflower catalyst in the fourth run turned out to be $\sim 46\%$ even after increasing the reaction time to 12 h. The scope of the Suzuki–Miyaura reaction with GO- Pd_4S nanoflowers/spheres as a catalyst was investigated using various substrates (Table 7.11) with optimum conditions. It has been found that the

Table 7.11 Suzuki–Miyaura coupling reactions catalyzed with GO- Pd_4S nanoflowers and nanospheres



S. No.	Aryl halide	Yield (%)	
		GO- Pd_4S nanoflower	GO- Pd_4S nanosphere
1	4-Bromobenzaldehyde	~ 99	36
2	1-Bromo-4-nitrobenzene	~ 99	58
3	4-Bromobenzonitrile	80	26
4	4-Bromoacetophenone	~ 99	42
5	4-Bromobenzoic acid	93	45
6	Bromobenzene	91	19
7	4-Bromotoluene	73	17

Reaction conditions: aryl bromide, 1.0 mmol; phenylboronic acid, 1.2 equiv.; K_2CO_3 , 2.0 equiv.; GO- Pd_4S 0.2 mol% Pd, time 5 h; EtOH- H_2O (3:1), TBAB 1.0 mmol, temperature 353 K; yield: NMR % yield

performance of a composite catalyst based on Pd₄S nanosphere is better than that of a Pd₄S nanosphere in comparable experimental conditions. The higher catalytic activity of nanoflowers compared to nanospheres can be attributed to the flower surface structure, which leads to catalytically active Pd atoms along the edges or corners and a large number of reaction sites.

7.4.5 Fischer–Tropsch Synthesis

Modern technologies for the conversion of natural gas into liquid products are carried out by the formation of carbon monoxide and hydrogen (syn-gas), which is then converted to higher products through the Fischer–Tropsch chemistry. As a typical example, we note the use of CoO nanocrystals with tunable particle sizes obtained by thermolysis of cobalt (II) acetate in various long-chain alkylamines for the synthesis of a supported catalyst that showed higher catalytic activity in the Fischer–Tropsch reaction demonstrating that nanocrystals are active precursors [533]. The TOF of CO on a catalyst prepared from CoO nanocrystals is ~ 1.5 times higher than for a conventional catalyst with the same particle size, indicating that the introduction of CoO nanocrystals with a narrow size distribution can be used to obtain more active sites.

It should be noted the strategy of obtaining highly dispersed iron carbides embedded in the matrix of porous carbon, Fe@C catalysts, which were tested in the Fischer–Tropsch synthesis (Fig. 7.43a) [254]. Regardless of the method of preparation, all materials showed very high conversion levels, ranging from 72 to 77% after 90 h on stream. The selectivity to olefins (C₂–C₅) ranges from 14.6 to 15.5%. The striking stability of Fe@C catalysts is explained by the fact that most Fe NPs are less than 9 nm and to the spatial limitation created by encapsulated carbon. Conversion profiles and product distributions of the 38-Fe@C catalysts, promoted with 0.6, 0.7 and 1.0 wt% of K, are shown in Fig. 7.43b, c, respectively. Among the promoted samples, an optimum amount of K 0.6 wt% was found. The higher activity of the catalyst is associated with an increase in the water gas shift functionality and the higher ratio of olefins to paraffin with modulation of the hydrogenation ability, as a direct consequence of the promotion of K.

7.4.6 Enantioselective Catalysis

Enantioselective catalysis is crucial for the industrial production of many biologically active compounds and presents an interesting problem in terms of developing a basic-molecular-level understanding of issues that control selectivity in heterogeneous catalysis [534]. One successful approach included the modification of conventional NPs by adsorption of chiral molecules [535]. The adsorption geometry of a chiral ligand on a metal surface is crucial for observing asymmetric

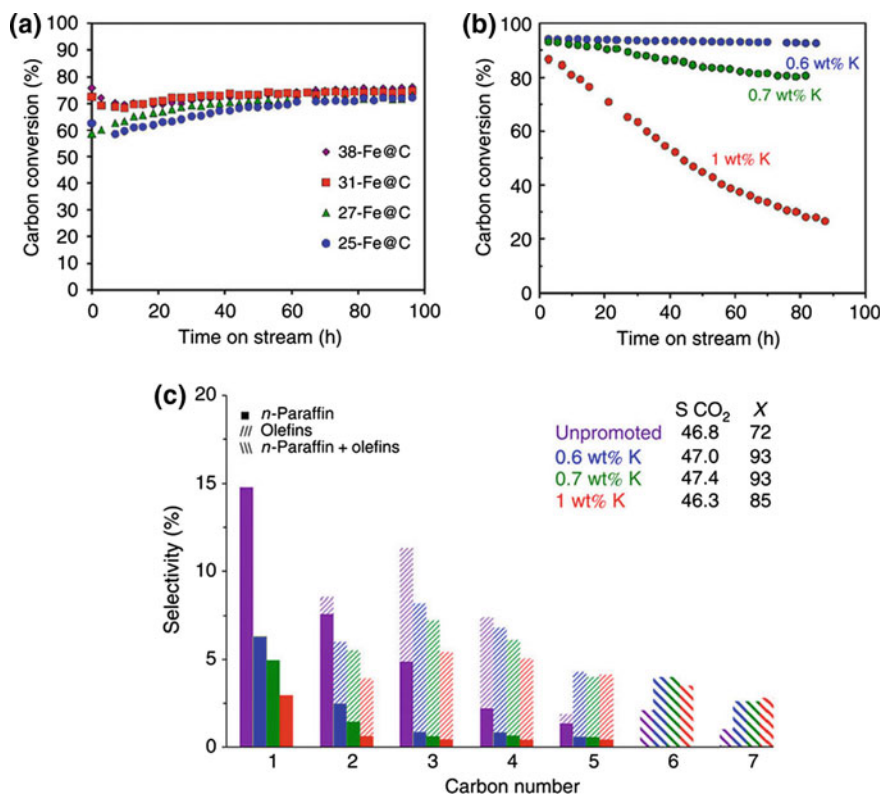


Fig. 7.43 **a** Time-on-stream evolution of CO conversion for the unpromoted Fe@C catalysts. **b** Time-on-stream evolution of CO conversion for K-promoted 38-Fe@C catalysts. **c** Product distribution after 10 h TOS for the unpromoted and promoted 38-Fe@C catalysts. Reaction conditions: 613 K, 20 bar, H₂/CO = 1, and GHSV of 30,000 h⁻¹ (space velocity based on catalyst bed volume). Reproduced with permission from Ref. [254]. Copyright (2015) Springer Nature

induction. Enantioselection can be strongly influenced not only by the interaction of the substrate–modifier–metal, but also by the interactions of substrate–substrate, substrate–solvent and product–modifier [536].

As a typical example, we note the use of chiral xylofuranoside diphosphites-modified Pd NPs in the allylic alkylation of *rac*-3-acetoxy-1,3-diphenyl-1-propene with dimethyl malonate [537]. These NPs showed high selectivity, mainly the reaction proceeded with one enantiomer of the substrate with enantiomeric excess (ee) > 95%, which demonstrated a very high degree of kinetic resolution. These systems depend both on ligands and substrates in a much more dramatic manner than the corresponding molecular systems. In another interesting example, Pd NPs stabilized with chiral mono- and bisphosphine ligands, for example, the 2,2'-bis(diarylphosphino)-1,1'-binaphthyl (BINAP), 5,5'-bis(diphenylphosphino)-4,4'-bi-1,3-benzodioxole (SEGPLHO), and 2,3-*O*-isopropylidene-2,3-dihydroxy-

1,4-bis(diphenylphosphino)butane (DIOP) derivatives, are active nanocatalysts in the Suzuki–Miyaura cross-coupling reactions. Depending on the ligand, enantioselectivity varied up to 58% ee [538, 539]. It should also be noted magnetic FePd magnetic NPs modified with chiral BINAP, which acted as a recoverable catalyst for the same asymmetric coupling reaction [540]. In general, nanocatalysts are much more sensitive to regulation between a metal, a ligand, and a substrate than the corresponding molecular catalysts and can resemble enzymatic systems.

7.4.7 Photocatalysis

Numerous studies have been devoted to the study of the photocatalytic activity of nanomaterials obtained by thermolysis of metal chelates. As a typical example, we note a study of the photocatalytic activity of a porous ZnO nanostructure obtained by the thermolysis of hollow microblocks $[\text{Zn}(\text{L})_2]$, where HL is 2-aminonicotinic acid, to remove Congo red (CR), as a typical toxic azo dye, from an aqueous solution [541]. It turned out that the nanomaterial can be used as an effective photocatalyst for wastewater treatment with high degradation efficiency. In particular, the maximum CR removal efficiency after 3 h of illumination was 96%, which confirms the excellent performance of the synthesized ZnO NPs in the photodegradation of CR under light illumination in a short time. In addition, the highest CR removal efficiency occurs at pH 6, which is close to neutral pH.

In another interesting example, the photocatalytic activity of porous hexagonal ZnO nanodisks with different sizes, surface areas, and porosities obtained by thermolysis of $[\text{Zn}(\text{DHS})(\text{L})]\cdot n\text{H}_2\text{O}$ (DHS are three different isomers of dihydroxylphen ligand and L is 1,4-benzenedicarboxylic acid) was studied [542]. In particular, in the presence of UV illumination, the degradation of methylene blue (MB) reaches up to 95% in 1 h for the 2,4-ZnO (Fig. 7.44). Interestingly, the

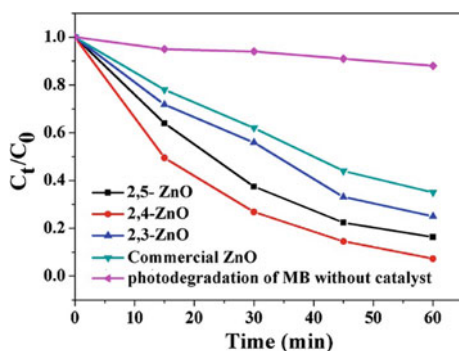
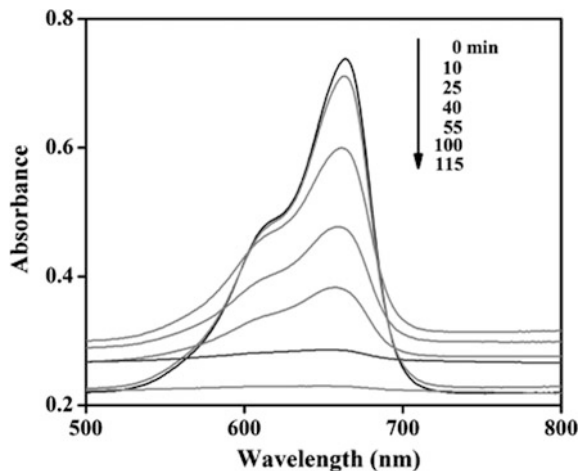


Fig. 7.44 Comparative MB degradation kinetic plot (C_t/C_0 vs. time) of the prepared ZnOs photocatalyst. Reproduced with permission from Ref. [542]. Copyright (2016) Elsevier

Fig. 7.45 Time-dependent UV/Vis absorption spectra for the degradation of MB with ZnO-C nanocomposite. Reproduced with permission from Ref. [543]. Copyright (2015) John Wiley and Sons



photocatalytic activity is significantly reduced to 75% in 1 h for 2,3-ZnO, whereas 2,5-ZnO exhibits moderate photocatalytic activity (85% in 1 h). Importantly, commercial ZnO showed relatively low photocatalytic activity (65% in 1 h) than nano-CPs-derived ZnO. The ZnO surface areas followed the order 2,4-ZnO > 2,5-ZnO > 2,3-ZnO > commercial ZnO, which is in good agreement with the photocatalytic activity. Accordingly, MO with a lower surface area will have poor photocatalytic activity.

It should be noted ZnO-C nanocomposite, obtained by solid-state conversion of $[\text{Zn}(\text{L})(\text{L}')_{0.5}]\cdot\text{H}_2\text{O}$ [L = 4,4'-(hexafluoroisopropylene)bis(benzoic acid); L' = 1,4-bis(4-pyridyl)-2,3-diaza-1,3-butadiene] [543]. The synthesized nanomaterial shows good photocatalytic activity for degradation of MB in aqueous solution under UV irradiation (Fig. 7.45). For example, as the irradiation time increases, the concentration of MB decreases, and after 100 min, the degree of degradation of MB was 89%. At the same time, the estimated value of the k_{app} constant for degradation of MB was lower than that of pure ZnO NPs and may be due to the large amount of carbon present in the sample.

ZnO NPs and ZnO@C hybrid composites derived from MOF-5 under several heating and atmospheric (air or nitrogen) conditions showed relatively high photocatalytic decomposition activity and significantly enhanced the adsorption capacity for the organic pollutant Rhodamine-B (RhB) under UV irradiation [544]. It turned out that the commercial TiO_2 materials P25 and ST01 decomposed 98 and 83% of the RhB, respectively, after irradiation with UV light for 12 h (Fig. 7.46a). Interestingly, sample 600A has an activity comparable to that of P25 with increased activity compared to ST01. In addition, 600A 3 h and 700A samples showed slightly higher activity than ST01. Samples (600N and 600N 3 h) obtained under a nitrogen atmosphere showed relatively low activity due to the large amount of porous carbon present in the samples. It should be noted that photodegradation of RhB obeys first-order kinetics (Fig. 7.46b), and the slope of the graphs provides

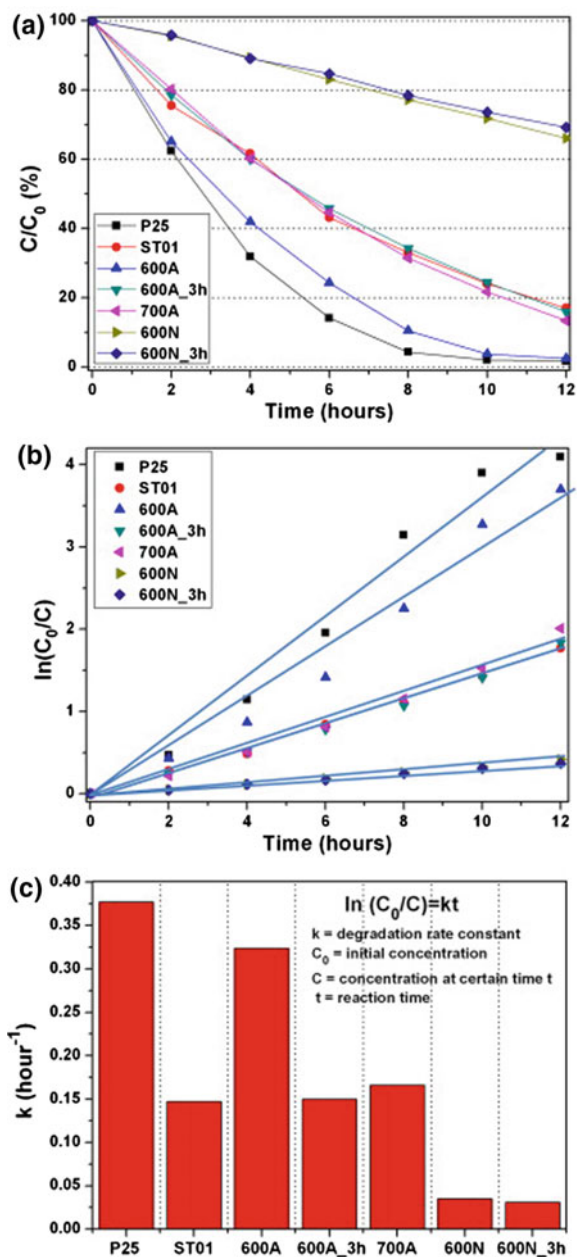
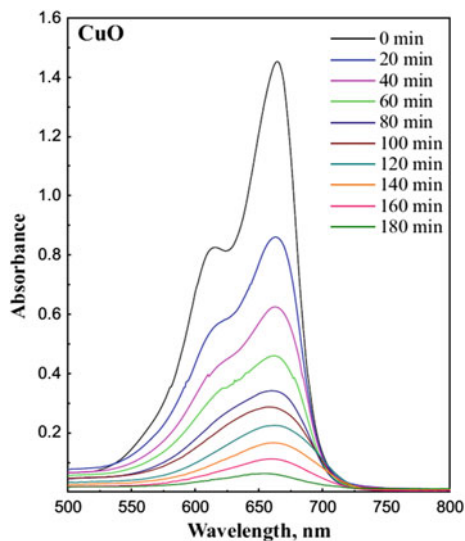


Fig. 7.46 a Photodegradation of RhB as a function of UV irradiation time in the presence of the prepared nanomaterials. b Linear-log plot of (a). c Degradation rate constants of the products. Reproduced with permission from Ref. [544]. Copyright (2011) Elsevier

Fig. 7.47 Absorbance of MB at regular intervals during photocatalytic degradation using CuO NPs. Reproduced with permission from Ref. [546]. Copyright (2017) Springer Nature



quantitative estimates for the photocatalytic activity of the samples (Fig. 7.46c). In particular, the slope showed that the choice of the samples obtained can provide ZnO-based photocatalysts to remove organic pollutants from the wastewater.

Hexagonal ZnO nanomaterials obtained by thermolysis of the complex $[\text{ZnL}]_n$ ($\text{H}_2\text{L} = 4\text{-}[(1\text{H-imidazol-4-yl)methylamino}]benzoic\text{ acid}$) have photocatalytic properties, and ZnO formed at a lower thermolysis temperature has a higher photocatalytic activity [545]. It was found that SSP and the resulting ZnO can photocatalytically degrade RhB, since the intensity of the absorption peak at 552 nm corresponding to RhB decreases in the presence of SSP and ZnO. Furthermore, it can be seen that SSP showed the weakest photocatalytic ability, while ZnO thermolyzed at 773 K, showed the strongest one. In addition, the intensity of the absorption peak of RhB rapidly decreases with increasing irradiation time, which indicates that the C–N bond of the dye is vulnerable to attack.

Photocatalytic activity of CuO NPs obtained by thermolysis of Cu(II) complexes of copper(II) salts (Cl^- , Br^- , CH_3COO^- , and SO_4^{2-}) with 2-(3-amino-4,6-dimethyl-1H-pyrazolo[3,4-b]pyridin-1-yl)acetohydrazide was evaluated by MB dye degradation (Fig. 7.47) [546]. The bleaching reaction follows a pseudo-first-order reaction, and the results showed an efficiency of 97% at a degradation rate of 0.018 min^{-1} .

The degradation of MB dye over CuO obtained by thermolysis of the Cu(II) complex with 3-ethyl-4-amino-5-mercapto-1,2,4-triazole was studied, under UV illumination in the presence of H_2O_2 to investigate the photocatalytic activity via photo-Fenton reaction [547]. The intensity of absorption of the dye solution gradually decreases with increasing exposed time, indicating a decrease in the concentration of MB dye, which means, therefore, an effective photodegradation of the dye using a CuO catalyst under UV illumination in the presence of H_2O_2

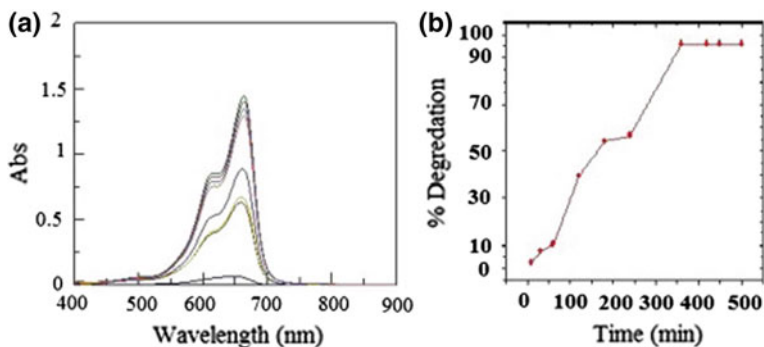
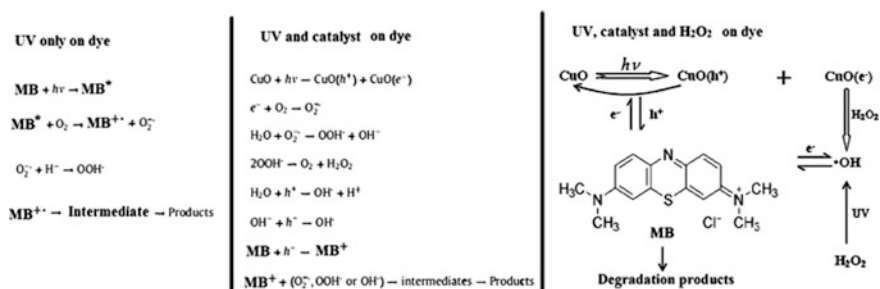


Fig. 7.48 a Photocatalytic degradation of MB dye using CuO and b % degradation versus time. Reproduced with permission from Ref. [547]. Copyright (2015) Elsevier



Scheme 7.7 Proposed reactions for the photodegradation of MB dye in the presence of UV only, (catalyst + UV), and (UV + catalyst + H_2O_2). Reproduced with permission from Ref. [547]. Copyright (2015) Elsevier

(Fig. 7.48a, b). Almost 96.18% of the MB dye decomposes under UV illumination in the presence of H_2O_2 for 6 h.

The mechanism of the photodegradation reaction in the presence of only UV (catalyst + UV) and (UV + catalyst + H_2O_2) was clarified in Scheme 7.7. After absorbing only UV radiation, the excited MB reduces O_2 to O_2^- , which in turn reacts with the proton (from the autoprotolysis of the solvent water) to produce OOH^- . In general, the cationic radical of the dye degrades to carbon dioxide, water, and mineral acids through intermediate. Photocatalytic degradation of MB dye in the presence of (catalyst + UV) usually involves the separation of electron-hole pairs and subsequent redox reactions under UV irradiation, and electrons and holes are generated on the CuO surface. Electrons absorbed by the adsorbed molecular oxygen species, and holes trapped in water or adsorbed MB molecules.

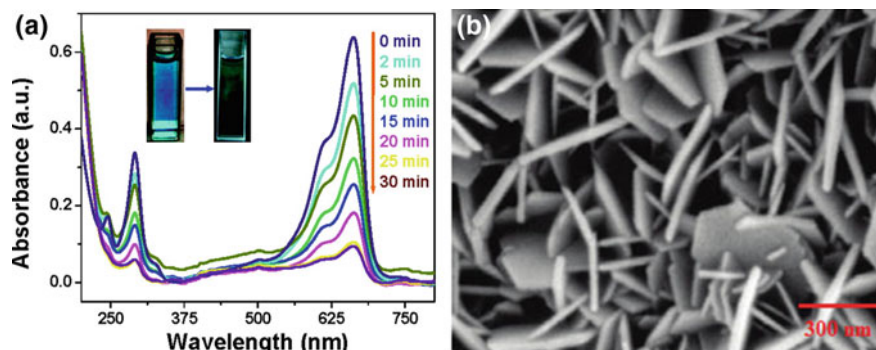


Fig. 7.49 **a** Photodegradation of MB dye in visible light, plot of absorbance (A) versus wavelength and the inset image indicates the decolorization reaction. **b** FESEM image of CuS NPs. Reproduced with permission from Ref. [548]. Copyright (2010) American Chemical Society

The addition of H_2O_2 in the presence of a catalyst and UV increases the photodegradation rate of the MB dye, since the direct decomposition of H_2O_2 under UV light produces OH^- , which directly oxidizes the MB dye.

Due to strong absorption in the visible region and excellent skeletal stability under various pH conditions, the dyes can be used to study their photodegradation by CuS. In the case of MB, a decrease in the absorbance at 663 nm (Fig. 7.49a) was scanned for the photocatalytic activity of rod-shaped CuS NPs obtained by thermolysis of $\text{Cu}(\text{acac})_2$ in the presence of thioacetamide (Fig. 7.49b) [548]. It is important that the photoreaction becomes faster with increasing catalyst concentration, and the change in the rate of degradation of the dye can be explained from the CuS–dye interaction, and it was stated that hydroxyl ions are present on the CuS surface that encompasses cationic dye molecules with electrostatic attraction and facilitates electron transfer. The most suitable for catalytic activity are adsorption and desorption on the catalyst surface. The high specific surface area of the nanocatalyst leads to the appearance of more unsaturated surface sites of coordination that are exposed to the reactants.

The photocatalytic activity of CdS NPs of various shapes and sizes (rods and spheres) synthesized by thermolysis of the precursor complex $[\text{Cd}(\text{SOCPh})_2\text{Lut}_2]$ was evaluated by degradation of the Rose Bengal (RB) dye in an aqueous solution under white light illumination [549]. CdS NPs have an excellent photocatalytic activity compared to the commercial TiO_2 . As can be seen from the time-dependent UV–Vis absorption curves of the RB solution catalyzed by CdS NPs (Fig. 7.50), the absorption intensity of RB at 554 nm rapidly decreases and disappears

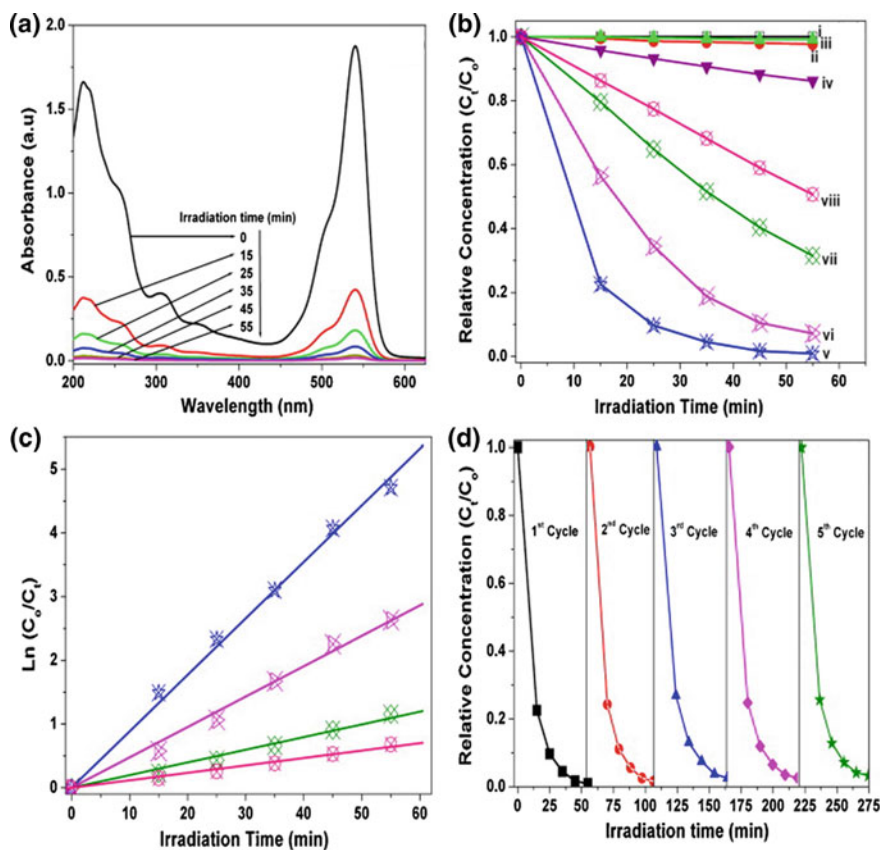


Fig. 7.50 **a** Time-dependent UV-Vis absorption spectral changes of aqueous RB solution catalyzed by CdS NPs under light irradiation, **b** degradation of RB in terms of relative concentration versus time plots under different conditions, **c** kinetic plots for the photodegradation process of RB catalyzed by CdS NPs and **d** cyclic run for the catalytic decomposition of RB with CdS NPs. Reproduced with permission from Ref. [549]. Copyright (2012) Elsevier

completely after 55 min. A study of the mechanism of photocatalytic degradation of RB in the presence of CdS NPs showed that photogenerated holes are the predominant active species.

It should also be noted the study of the photocatalytic activity of nanocrystalline cobalt ferrite for the degradation of a representative pollutant, MB, and visible light as an energy source [550]. The results showed that approximately 92% of MB degradation can be achieved in 7 h of visible light irradiation. The resulting catalyst demonstrated rather good photochemical properties.

References

1. A.D. Pomogailo, A.S. Rozenberg, I.E. Uflyand, *Nanochastitsy metallov v polimerakh (Metal Nanoparticles in Polymers)* (Khimiya, Moscow, 2000)
2. A.D. Pomogailo, G.I. Dzhardimalieva, V.N. Kestelman, *Macromolecular Metal Carboxylates and Their Nanocomposites* (Springer, Heidelberg, 2010)
3. A.D. Pomogailo, G.I. Dzhardimalieva, *Nanostructured Materials Preparation via Condensation Ways* (Springer, Dordrecht, 2014)
4. A.D. Pomogailo, G.I. Dzhardimalieva, *Metallopolymeric Hybride Nanocomposites* (Nauka, Moscow, 2015)
5. G.I. Dzhardimalieva, I.E. Uflyand, RSC Adv. **7**, 42242 (2017)
6. B.I. Kharisov, O.V. Kharissova, U.O. Méndez, J. Coord. Chem. **66**, 3791 (2013)
7. O. Carp, Materials Obtained by Solid-State Thermal Decomposition of Coordination Compounds and Metal-Organic Coordination Polymers, in *Reactions and Mechanisms in Thermal Analysis of Advanced Materials*, eds. by A. Tiwari, B. Raj (Scrivener Publishing LLC, Salem, Massachusetts, 2015)
8. M.A. Malik, P. O'Brien, *Organometallic and Metallo-Organic Precursors for Nanoparticles* (Precursor Chemistry of Advanced Materials (Springer, Berlin, Heidelberg, 2005)
9. B.I. Kharisov, H.V. Rasika Dias, O.V. Kharissova, V.M. Jiménez-Pérez, B.O. Pérez, B.M. Flores, RSC Adv. **2**, 9325 (2012)
10. H.B. Wu, X.W. Lou, Sci. Adv. **3**, eaap9252 (2017)
11. B.I. Kharisov, O.V. Kharissova, U.O. Méndez, Nanomaterials on the Basis of Chelating Agents, Metal Complexes, and Organometallics for Environmental Purposes, in *Nanomaterials for Environmental Protection*, eds. by B.I. Kharisov, O.V. Kharissova, H. V.R. Dias (Wiley Inc, Hoboken, NJ, 2014) doi:10.1002/9781118845530.ch7
12. U. Shamraiz, R.A. Hussain, A. Badshah, J. Solid State Chem. **238**, 25 (2016)
13. P. Roy, S.K. Srivastava, CrystEngComm **17**, 7801 (2015)
14. K. Shen, X. Chen, J. Chen, Y. Li, ACS Catal. **6**, 5887 (2016)
15. Y. Cao, S. Mao, M. Li, Y. Chen, Y. Wang, ACS Catal. **7**, 8090 (2017)
16. S.-N. Zhao, X.-Z. Song, S.-Y. Song, H.-J. Zhang, Coord. Chem. Rev. **337**, 80 (2017)
17. Q. Gao, N. Liu, S. Wang, Y. Tang, Nanoscale **6**, 14106 (2014)
18. M. Zaheer, T. Schmalz, G. Motz, R. Kempe, Chem. Soc. Rev. **41**, 5102 (2012)
19. C. Su, J. Hazard. Mater. **322**, 48 (2017)
20. P. Pachfule, D. Shinde, M. Majumder, Q. Xu, Nat. Chem. **8**, 718 (2016)
21. E. Mirzadeh, K. Akhbari, CrystEngComm **18**, 7410 (2016)
22. A.-H. Lu, E.L. Salabas, F. Schüth, Angew. Chem. Int. Ed. **46**, 1222 (2007)
23. W. Liu, Q. Shao, G. Ji, X. Liang, Y. Cheng, B. Quan, Y. Du, Chem. Eng. J. **313**, 734 (2017)
24. D. Ling, T. Hyeon, Small **9**, 1450 (2013)
25. K.D. Gilroy, A. Ruditskiy, H.-C. Peng, D. Qin, Y. Xia, Chem. Rev. **116**, 10414 (2016)
26. C. Amiens, D. Ciuculescu-Pradines, K. Philippot, Coord. Chem. Rev. **308**, 409 (2016)
27. Y. Song, X. Li, L. Sun, L. Wang, RSC Adv. **5**, 7267 (2015)
28. A. Chen, C. Ostrom, Chem. Rev. **115**, 11999 (2015)
29. C. Coughlan, M. Ibáñez, O. Dobrozhan, A. Singh, A. Cabot, K.M. Ryan, Chem. Rev. **117**, 5865 (2017)
30. Y. Deng, Y. Xie, K. Zou, X. Ji, J. Mater. Chem. A **4**, 1144 (2016)
31. R.S. Devan, R.A. Patil, J.-H. Lin, Y.-R. Ma, Adv. Funct. Mater. **22**, 3326 (2012)
32. J. Liu, Z. Wu, Q. Tian, W. Wu, X. Xiao, CrystEngComm **18**, 6303 (2016)
33. H.D. Mai, K. Rafiq, H. Yoo, Chem. Eur. J. **23**, 5631 (2017)
34. L. Wu, A. Mendoza-Garcia, Q. Li, S. Sun, Chem. Rev. **116**, 10473 (2016)
35. W. Xia, A. Mahmood, R. Zou, Q. Xu, Energy Environ. Sci. **8**, 1837 (2015)
36. C. Yang, J. Wu, Y. Hou, Chem. Commun. **47**, 5130 (2011)
37. Q. Li, S. Sun, Nano Energy **29**, 178 (2016)

38. K. Liu, H. Zhong, F. Meng, X. Zhang, J. Yan, Q. Jiang, *Mater. Chem. Front.* **1**, 2155 (2017)
39. J. Liu, D. Zhu, C. Guo, A. Vasileff, S.-Z. Qiao, *Adv. Energy Mater.* 1700518 (2017)
40. G. Prieto, H. Tüysüz, N. Duyckaerts, J. Knossalla, G.-H. Wang, F. Schüth, *Chem. Rev.* **116**, 14056 (2016)
41. D. Wang, D. Astruc, *Chem. Soc. Rev.* **46**, 816 (2017)
42. W. Xia, A. Mahmood, Z. Liang, R. Zou, S. Guo, *Angew. Chem. Int. Ed.* **55**, 2650 (2016)
43. R. Wu, X. Qian, F. Yu, H. Liu, K. Zhou, J. Wei, Y. Huang, *J. Mater. Chem. A* **1**, 11126 (2013)
44. L. Hu, Y. Huang, F. Zhang, Q. Chen, *Nanoscale* **5**, 4186 (2013)
45. S.J. Yang, S. Nam, T. Kim, J.H. Im, H. Jung, J.H. Kang, S. Wi, B. Park, C.R. Park, *J. Am. Chem. Soc.* **135**, 7394 (2013)
46. L. Zhang, H.B. Wu, S. Madhavi, H.H. Hng, X.W. Lou, *J. Am. Chem. Soc.* **134**, 17388 (2012)
47. N. Yan, L. Hu, Y. Li, Y. Wang, H. Zhong, X. Hu, X. Kong, Q. Chen, *J. Phys. Chem. C* **116**, 7227 (2012)
48. B. Liu, X. Zhang, H. Shioyama, T. Mukai, T. Sakai, Q. Xu, *J. Power Sources* **195**, 857 (2010)
49. L. Hu, N. Yan, Q. Chen, P. Zhang, H. Zhong, X. Zheng, Y. Li, X. Hu, *Chem. Eur. J.* **18**, 8971 (2012)
50. X. Xu, R. Cao, S. Jeong, J. Cho, *Nano Lett.* **12**, 4988 (2012)
51. A. Banerjee, U. Singh, V. Aravindan, M. Srinivasan, S. Ogale, *Nano Energy* **3**, 1158 (2013)
52. L. Hu, B. Qu, C. Li, Y. Chen, L. Mei, D. Lei, L. Chen, Q. Li, T. Wang, *J. Mater. Chem. A* **1**, 5596 (2013)
53. D. Xie, Q. Su, Z. Dong, J. Zhang, G. Du, *CrystEngComm* **15**, 8314 (2013)
54. F. Meng, Z. Fang, Z. Li, W. Xu, M. Wang, Y. Liu, J. Zhang, W. Wang, D. Zhao, X. Guo, *J. Mater. Chem. A* **1**, 7235 (2013)
55. S.J. Yang, J.H. Im, T. Kim, K. Lee, C.R. Park, *J. Hazard. Mater.* **186**, 376 (2011)
56. H.D. Mai, G.Y. Sung, H. Yoo, *RSC Adv.* **5**, 78807 (2015)
57. K.E. de Krafft, C. Wang, W. Lin, *Adv. Mater.* **24**, 2014 (2012)
58. H. Zhao, H. Song, L. Xu, L. Chou, *Appl. Catal. A* **456**, 188 (2013)
59. F.-X. Qin, S.-Y. Jia, Y. Liu, X. Han, H.-T. Ren, W.-W. Zhang, J.-W. Hou, S.-H. Wu, *Mater. Lett.* **101**, 93 (2013)
60. J.M. Zamaro, N.C. Pérez, E.E. Miro, C. Casado, B. Seoane, C. Tellez, J. Coronas, *Chem. Eng. J.* **195–196**, 180 (2012)
61. W. Wang, Y. Li, R. Zhang, D. He, H. Liu, S. Liao, *Catal. Commun.* **12**, 875 (2011)
62. F. Zhang, C. Chen, W.-M. Xiao, L. Xu, N. Zhang, *Catal. Commun.* **26**, 25 (2012)
63. A. Banerjee, R. Gokhale, S. Bhatnagar, J. Jog, M. Bhardwaj, B. Lefez, B. Hannoyer, S. Ogale, *J. Mater. Chem.* **22**, 19694 (2012)
64. H. Thakuria, B.M. Borah, G. Das, *Eur. J. Inorg. Chem.* **2007**, 524 (2007)
65. J. Zhao, F. Wang, P. Su, M. Li, J. Chen, Q. Yang, C. Li, *J. Mater. Chem.* **22**, 13328 (2012)
66. H. Tan, C. Ma, L. Gao, Q. Li, Y. Song, F. Xu, T. Wang, L. Wang, *Chem. Eur. J.* **20**, 16377 (2014)
67. Y. Tan, K. Zhu, D. Li, F. Bai, Y. Wei, P. Zhang, *Chem. Eng. J.* **258**, 93 (2014)
68. P. Mahata, T. Aarathi, G. Madras, S. Natarajan, *J. Phys. Chem. C* **111**, 1665 (2007)
69. A. Kong, Q. Lin, C. Mao, X. Bu, P. Feng, *Chem. Commun.* **50**, 15619 (2014)
70. Ch. Li, T. Chen, W. Xu, X. Lou, L. Pan, Q. Chen, B. Hu, *J. Mater. Chem.* **3**, 5585 (2015)
71. L. Peng, J. Zhang, Z. Xue, B. Han, J. Li, G. Yang, *Chem. Commun.* **49**, 11695 (2013)
72. F. Zou, X. Hu, Z. Li, L. Qie, C. Hu, R. Zeng, Y. Jiang, Y. Huang, *Adv. Mater.* **26**, 6622 (2014)
73. G. Huang, F. Zhang, L. Zhang, X. Du, J. Wang, L. Wang, *J. Mater. Chem.* **2**, 8048 (2014)
74. B. Wang, Z. Wang, Y. Cui, Y. Yang, Zh Wang, B. Chen, *Microporous Mesoporous Mater.* **203**, 86 (2015)
75. T. Kim, K.J. Lee, J.Y. Cheon, J.H. Lee, S.H. Joo, H.R. Moon, *J. Am. Chem. Soc.* **135**, 8940 (2013)

76. A. Banerjee, V. Aravindan, S. Bhatnagar, D. Mhamane, S. Mahdavi, S. Ogale, *Nano Energy* **2**, 890 (2013)
77. K. Akhbari, A. Morsali, *Mater. Lett.* **141**, 315 (2015)
78. L. Hashemi, A. Morsali, V. Yilmaz, O. Buyukgungor, H.R. Khavasi, F. Ashouri, M. Bagherzadeh, *J. Mol. Struct.* **102**, 260 (2014)
79. Zh Xu, L. Yang, C. Xu, *Anal. Chem.* **87**, 343 (2015)
80. S. Maiti, A. Pramanik, S. Mahanty, *Chem. Commun.* **50**, 11717 (2014)
81. J.-K. Sun, Q. Xu, *Energy Environ. Sci.* **7**, 2071 (2014)
82. S. Chu, A. Majumdar, *Nature* **488**, 294 (2012)
83. Y. Wang, X. Liu, Z. Li, Y. Cao, Y. Li, Y. Zhao, *ChemNanoMat* **3**, 58 (2017)
84. X. Liu, J. Yang, W. Zhao, Y. Wang, Z. Li, Z. Lin, *Small* **12**, 4077 (2016)
85. X. Liu, J. Iocozzia, Y. Wang, X. Cui, Y. Chen, S. Zhao, Z. Li, Z. Lin, *Energy Environ. Sci.* (2017). <https://doi.org/10.1039/C6EE02265K>
86. B. Sørensen, *Renewable Energy: Physics, Engineering, Environmental Impacts, Economics and Planning*, 4th edn. (Academic Press Elsevier, Amsterdam, 2010)
87. M.K. Debe, *Nature* **486**, 43 (2012)
88. Y. Nie, L. Li, Z.D. Wei, *Chem. Soc. Rev.* **44**, 2168 (2015)
89. C.Z. Zhu, H. Li, S.F. Fu, D. Du, Y.H. Lin, *Chem. Soc. Rev.* **45**, 517 (2016)
90. D.P. Wilkinson, J. Zhang, R. Hui, J. Fergus, X. Li, *Proton Exchange Membrane Fuel Cells Materials Properties and Performance* (CRC Press Taylor & Francis Group, 2010)
91. C.-H. Cui, S.-H. Yu, *Acc. Chem. Res.* **46**, 1427 (2013)
92. Z. Zhang, J. Liu, J. Gu, L. Su, L. Cheng, *Energy Environ. Sci.* **7**, 2535 (2014)
93. C.-J. Zhong, J. Luo, P.N. Njoki, D. Mott, B. Wanjala, R. Loukrakpam, S. Lim, L. Wang, B. Fang, Z. Xu, *Energy Environ. Sci.* **1**, 454 (2008)
94. N. Cheng, M.N. Banis, J. Liu, A. Riese, X. Li, R. Li, S. Ye, S. Knights, X. Sun, *Adv. Mater.* **27**, 277 (2015)
95. N. Cheng, M.N. Banis, J. Liu, A. Riese, S. Mu, R. Li, T.-K. Sham, X. Sun, *Energy Environ. Sci.* **8**, 1450 (2015)
96. M. Winter, R.J. Brodd, *Chem. Rev.* **104**, 4245 (2004)
97. B.C.H. Steele, A. Heinzl, *Nature* **414**, 345 (2001)
98. P. Du, R. Eisenberg, *Energy Environ. Sci.* **5**, 6012 (2012)
99. L. Trotochaud, J.K. Ranney, K.N. Williams, S.W. Boettcher, *J. Am. Chem. Soc.* **134**, 17253 (2012)
100. S.M. Barnett, K.I. Goldberg, J.M. Mayer, *Nat. Chem.* **4**, 498 (2012)
101. D. Merki, X. Hu, *Energy Environ. Sci.* **4**, 3878 (2011)
102. S. Guo, S. Zhang, S. Sun, *Angew. Chem. Int. Ed.* **52**, 8526 (2013)
103. I.E.L. Stephens, A.S. Bondarenko, U. Gronbjerg, J. Rossmeisl, I. Chorkendorff, *Energy Environ. Sci.* **5**, 6744 (2012)
104. M.G. Walter, E.L. Warren, J.R. McKone, S.W. Boettcher, Q. Mi, E.A. Santori, N.S. Lewis, *Chem. Rev.* **110**, 6446 (2010)
105. W. Vielstich, A. Lamm, H.A. Gasteiger, *Handbook of Fuel Cells—Fundamentals, Technology and Applications* (Wiley, Chichester, U.K., 2003)
106. M.L. Perry, T.F. Fuller, *J. Electrochem. Soc.* **149**, S59 (2002)
107. C. Sealy, *Mater. Today* **11**, 65 (2008)
108. A. Rabis, P. Rodriguez, T.J. Schmidt, *ACS Catal.* **2**, 864 (2012)
109. Z.H. Xia, A. Li, P.K. Chen, D.G. Xia, *Adv. Energy Mater.* **6**, 1600458 (2016)
110. N. Cheng, S. Mu, M. Pan, P.P. Edwards, *Electrochem. Commun.* **11**, 1610 (2009)
111. Z.-Z. Jiang, Z.-B. Wang, Y.-Y. Chu, D.-M. Gu, G.-P. Yin, *Energy Environ. Sci.* **4**, 2558 (2011)
112. G.L. Tian, M.Q. Zhao, D. Yu, X.Y. Kong, J.Q. Huang, Q. Zhang, F. Wei, *Small* **10**, 2251 (2014)
113. S.H. Sun, G.X. Zhang, D.S. Geng, Y.G. Chen, R.Y. Li, M. Cai, X.L. Sun, *Angew. Chem. Int. Ed.* **50**, 422 (2011)
114. S. Zhang, Y.Y. Shao, G.P. Yin, Y.H. Lin, *J. Mater. Chem. A* **1**, 4631 (2013)

115. M. Shao, *Electrocatalysis in Fuel Cells. A Non- and Low-Platinum Approach* (Springer-Verlag, London, 2013)
116. J. Duan, S. Chen, S. Dai, S.Z. Qiao, *Adv. Funct. Mater.* **24**, 2072 (2014)
117. F.T. Wagner, B. Lakshmanan, M.F. Mathias, *J. Phys. Chem. Lett.* **1**, 2204 (2010)
118. H.A. Gasteiger, S.S. Kocha, B. Sompalli, F.T. Wagner, *Appl. Catal. B* **56**, 9 (2005)
119. N. Jung, D.Y. Chung, J. Ryu, S.J. Yoo, Y.-E. Sung, *Nano Today* **9**, 433 (2014)
120. Y.-J. Wang, N. Zhao, B. Fang, H. Li, X.T. Bi, H. Wang, *Chem. Rev.* **115**, 3433 (2015)
121. A. Morozan, B. Josselme, S. Palacin, *Energy Environ. Sci.* **4**, 1238 (2011)
122. F. Jaouen, E. Proietti, M. Lefèvre, R. Chenitz, J.-P. Dodelet, G. Wu, H.T. Chung, C.M. Johnston, P. Zelenay, *Energy Environ. Sci.* **4**, 114 (2011)
123. M.B. Zakaria, C. Li, Q. Ji, B. Jiang, S. Tominaka, Y. Ide, J.P. Hill, K. Ariga, Y. Yamauchi, *Angew. Chem.* **55**, 8426 (2016)
124. E. Proietti, F. Jaouen, M. Lefevre, N. Larouche, J. Tian, J. Herranz, J.P. Dodelet, *Nat. Commun.* **2**, 416 (2011)
125. H.T. Chung, J.H. Won, P. Zelenay, *Nat. Commun.* **4** (2013)
126. Y. Li, W. Zhou, H. Wang, L. Xie, Y. Liang, F. Wei, J.-C. Idrobo, S.J. Pennycook, H. Dai, *Nat. Nanotechnol.* **7**, 394 (2012)
127. B. Winther-Jensen, O. Winther-Jensen, M. Forsyth, D.R. MacFarlane, *Science* **321**, 671 (2008)
128. F. Cheng, J. Shen, B. Peng, Y. Pan, Z. Tao, J. Chen, *Nat. Chem.* **3**, 79 (2010)
129. Y. Liang, Y. Li, H. Wang, J. Zhou, J. Wang, T. Regier, H. Dai, *Nat. Mater.* **10**, 780 (2011)
130. J. Suntivich, H.A. Gasteiger, N. Yabuuchi, H. Nakanishi, J.B. Goodenough, Y. Shao-Horn, *Nat. Chem.* **3**, 546 (2011)
131. R. Cao, R. Thapa, H. Kim, X. Xu, M.G. Kim, Q. Li, N. Park, M. Liu, J. Cho, *Nat. Commun.* **4**, 2076 (2013)
132. Z. Song, N. Cheng, A. Lushington, X. Sun, *Catalysts* **6**, 116 (2016)
133. S.J. Guo, S. Zhang, L.H. Wu, S.H. Sun, *Angew. Chem. Int. Ed.* **51**, 11770 (2012)
134. P. Chen, T.Y. Xiao, H.H. Li, J.J. Yang, Z. Wang, H.B. Yao, S.H. Yu, *ACS Nano* **6**, 712 (2012)
135. Y. Zheng, Y. Jiao, M. Jaroniec, Y.G. Jin, S.Z. Qiao, *Small* **8**, 3550 (2012)
136. M. Sun, H. Liu, Y. Liu, J. Qu, J. Li, *Nanoscale* **7**, 1250 (2015)
137. M.J. Liu, J.H. Li, *Electrochim. Acta* **154**, 177 (2015)
138. M.J. Liu, J.H. Li, *ACS Appl. Mater. Interfaces* **8**, 2158 (2016)
139. S.Q. Ma, G.A. Goenaga, A.V. Call, D.J. Liu, *Chem. Eur. J.* **7**, 2063 (2011)
140. C. Wang, H. Daimon, Y. Lee, J. Kim, S. Sun, *J. Am. Chem. Soc.* **129**, 6974 (2007)
141. Y.G. Liu, Y.G. Wang, J.Y. Zhang, S.L. Shi, P. Feng, T.H. Wang, *Catal. Commun.* **10**, 1244 (2009)
142. N. Tian, Z.-Y. Zhou, S.-G. Sun, Y. Ding, Z.L. Wang, *Science* **316**, 732 (2007)
143. T. Yu, D. Kim, H. Zhang, Y. Xia, *Angew. Chem. Int. Ed.* **50**, 2773 (2011)
144. V.R. Stamenkovic, B.S. Mun, K.J.J. Mayrhofer, P.N. Ross, N.M. Markovic, J. Rossmeisl, J. Greeley, J.K. Nørskov, *Angew. Chem. Int. Ed.* **45**, 2897 (2006)
145. J. Greeley, I.E.L. Stephens, A.S. Bondarenko, T.P. Johansson, H.A. Hansen, T.F. Jaramillo, J. Rossmeisl, I. Chorkendorff, J.K. Nørskov, *Nature Chem.* **1**, 552 (2009)
146. B. Lim, M. Jiang, P.H.C. Camargo, E.C. Cho, J. Tao, X. Lu, Y. Zhu, Y. Xia, *Science* **324**, 1302 (2009)
147. M.K. Carpenter, T.E. Moylan, R.S. Kukreja, M.H. Atwan, M.M. Tessema, *J. Am. Chem. Soc.* **134**, 8535 (2012)
148. V.R. Stamenkovic, B. Fowler, B.S. Mun, G. Wang, P.N. Ross, C.A. Lucas, N.M. Marković, *Science* **315**, 493 (2007)
149. W. Zhou, J. Wu, H. Yang, *Nano Lett.* **13**, 2870 (2013)
150. S.J. Guo, D.G. Li, H.Y. Zhu, S. Zhang, N.M. Markovic, V.R. Stamenkovic, S.H. Sun, *Angew. Chem. Int. Ed.* **52**, 3465 (2013)
151. C. Chen, Y.J. Kang, Z.Y. Huo, Z.W. Zhu, W.Y. Huang, H.L.L. Xin, J.D. Snyder, D.G. Li, J. A. Herron, M. Mavrikakis, M. Chi, K.L. More, Y. Li, N.M. Markovic, G.A. Somorjai, P. Yang, V.R. Stamenkovic, *Science* **343**, 1339 (2014)

152. S.J. Guo, S. Zhang, D. Su, S.H. Sun, *J. Am. Chem. Soc.* **135**, 13879 (2013)
153. J. Wu, H. Yang, *Nano Res.* **4**, 72 (2011)
154. J. Wu, L. Qi, H. You, A. Gross, J. Li, H. Yang, *J. Am. Chem. Soc.* **134**, 11880 (2012)
155. L. Qi, J. Li, *J. Catal.* **295**, 59 (2012)
156. J. Wu, J. Zhang, Z. Peng, S. Yang, F.T. Wagner, H. Yang, *J. Am. Chem. Soc.* **132**, 4984 (2010)
157. J. Wu, A. Gross, H. Yang, *Nano Lett.* **11**, 798 (2011)
158. C. Cui, L. Gan, H.-H. Li, S.-H. Yu, M. Heggen, P. Strasser, *Nano Lett.* **12**, 5885 (2012)
159. S.-I. Choi, R. Choi, S.W. Han, J.T. Park, *Chem. Eur. J.* **17**, 12280 (2011)
160. S.-I. Choi, S.-U. Lee, W.Y. Kim, R. Choi, K. Hong, K.M. Nam, S.W. Han, J.T. Park, *ACS Appl. Mater. Interfaces* **4**, 6228 (2012)
161. Y. Kang, C.B. Murray, *J. Am. Chem. Soc.* **132**, 7568 (2010)
162. H. Zhang, M. Jin, J. Wang, W. Li, P.H.C. Camargo, M.J. Kim, D. Yang, Z. Xie, Y. Xia, *J. Am. Chem. Soc.* **133**, 6078 (2011)
163. Y. Wu, S. Cai, D. Wang, W. He, Y. Li, *J. Am. Chem. Soc.* **134**, 8975 (2012)
164. Z.M. Peng, H. Yang, *Nano Today* **4**, 143 (2009)
165. Y. Xia, Y.J. Xiong, B. Lim, S.E. Skrabalak, *Angew. Chem. Int. Ed.* **48**, 60 (2009)
166. G.A. Somorjai, H. Frei, J.Y. Park, *J. Am. Chem. Soc.* **131**, 16589 (2009)
167. S.-I. Choi, S. Xie, M. Shao, J.H. Odell, N. Lu, H.-C. Peng, L. Protsailo, S. Guerrero, J. Park, X. Xia, J. Wang, M.J. Kim, Y. Xia, *Nano Lett.* **13**, 3420 (2013)
168. J. Zhang, H. Yang, J. Fang, S. Zou, *Nano Lett.* **10**, 638 (2010)
169. K. Gong, F. Du, Z. Xia, M. Durstock, L. Dai, *Science* **323**, 760 (2009)
170. T.C. Nagaiah, A. Bordoloi, M.D. Sanchez, M. Muhler, W. Schuhmann, *ChemSusChem* **5**, 637 (2012)
171. Y. Zhao, R. Nakamura, K. Kamiya, S. Nakanishi, K. Hashimoto, *Nat. Commun.* **4**, 2390 (2013)
172. Y. Shao, J. Sui, G. Yin, Y. Gao, *Appl. Catal. B* **79**, 89 (2008)
173. W. Chaikittisilp, K. Ariga, Y. Yamauchi, *J. Mater. Chem. A* **1**, 14 (2013)
174. S.-L. Li, Q. Xu, *Energy Environ. Sci.* **6**, 1656 (2013)
175. Q.L. Zhu, Q. Xu, *Chem. Soc. Rev.* **43**, 5468 (2014)
176. S. Li, F. Huo, *Nanoscale* **7**, 7482 (2015)
177. A. Morozan, F. Jaouen, *Energy Environ. Sci.* **5**, 9269 (2012)
178. A. Mahmood, W. Guo, H. Tabassum, R. Zou, *Adv. Energy Mater.* **6**, 1600423 (2016)
179. D.F. Wu, Z.Y. Guo, X.B. Yin, Q.Q. Pang, B.B. Tu, L.J. Zhang, Y.G. Wang, Q.W. Li, *Adv. Mater.* **26**, 3258 (2014)
180. K.M. Choi, H.M. Jeong, J.H. Park, Y.B. Zhang, J.K. Kang, O.M. Yaghi, *ACS Nano* **8**, 7451 (2014)
181. R. Bendi, V. Kumar, V. Bhavanasi, K. Parida, P.S. Lee, *Adv. Energy Mater.* **6**, 1501833 (2016)
182. L. Wang, X. Feng, L.T. Ren, Q.H. Piao, J.Q. Zhong, Y.B. Wang, H.W. Li, Y.F. Chen, B. Wang, *J. Am. Chem. Soc.* **137**, 4920 (2015)
183. J. Tang, R.R. Salunkhe, J. Liu, N.L. Torad, M. Imura, S. Furukawa, Y. Yamauchi, *J. Am. Chem. Soc.* **137**, 1572 (2015)
184. R. Liu, D. Wu, X. Feng, K. Müllen, *Angew. Chem.* **122**, 2619 (2010); *Angew. Chem. Int. Ed.* **49**, 2565 (2010)
185. W. Yang, T. Feller, M. Antonietti, *J. Am. Chem. Soc.* **133**, 206 (2010)
186. L. Dai, Y. Xue, L. Qu, H.-J. Choi, J.-B. Baek, *Chem. Rev.* **115**, 4823 (2015)
187. D.S. Su, S. Perathoner, G. Centi, *Chem. Rev.* **113**, 5782 (2013)
188. L. Jiao, Y.-X. Zhou, H.-L. Jiang, *Chem. Sci.* **7**, 1690 (2016)
189. J. Wei, Y. Hu, Y. Liang, B. Kong, J. Zhang, J. Song, Q. Bao, G.P. Simon, S.P. Jiang, H. Wang, *Adv. Funct. Mater.* **25**, 5768 (2015)
190. L. Ge, Y. Yang, L. Wang, W. Zhou, R. De Marco, Z. Chen, J. Zou, Z. Zhu, *Carbon* **82**, 417 (2015)
191. L. Zhang, Z. Su, F. Jiang, L. Yang, J. Qian, Y. Zhou, W. Li, M. Hong, *Nanoscale* **6**, 6590 (2014)

192. D. Geng, Y. Chen, Y. Chen, Y. Li, R. Li, X. Sun, S. Ye, S. Knights, *Energy Environ. Sci.* **4**, 760 (2011)
193. L. Zhang, X. Wang, R. Wang, M. Hong, *Chem. Mater.* **27**, 7610 (2015)
194. Z.-W. Liu, F. Peng, H.-J. Wang, H. Yu, W.-X. Zheng, J. Yang, *Angew. Chem. Int. Ed.* **50**, 3257 (2011); *Angew. Chem.* **123**, 3315 (2011)
195. H. Li, H. Liu, Z. Jong, W. Qu, D. Geng, X. Sun, H. Wang, *Int. J. Hydrog. Energy* **36**, 2258 (2011)
196. X. Wang, R. Liu, M.M. Waje, Z. Chen, Y. Yan, K.N. Bozhilov, P. Feng, *Chem. Mater.* **19**, 2395 (2007)
197. J. Li, Y. Chen, Y. Tang, S. Li, H. Dong, K. Li, M. Han, Y.-Q. Lan, J. Bao, Z. Dai, *J. Mater. Chem. A* **2**, 6316 (2014)
198. S. Zhao, J. Liu, C. Li, W. Ji, M. Yang, H. Huang, Y. Liu, Z. Kang, *ACS Appl. Mater. Interfaces* **6**, 22297 (2014)
199. W. Yang, X. Yue, X. Liu, J. Zhai, J. Jia, *Nanoscale* **7**, 11956 (2015)
200. X. Gong, S. Liu, C. Ouyang, P. Strasser, R. Yang, *ACS Catal.* **5**, 920 (2015)
201. Y. Fu, Y. Huang, Z. Xiang, G. Liu, D. Cao, *Eur. J. Inorg. Chem.* **2016**, 2100 (2016)
202. P. Chen, T.-Y. Xiao, Y.-H. Qian, S.-S. Li, S.-H. Yu, *Adv. Mater.* **25**, 3192 (2013)
203. R. Jasinski, *Nature* **201**, 1212 (1964)
204. J.H. Zagal, F. Bedioui, *Electrochemistry of N4 Macrocyclic Metal Complexes*, 2nd edn. (Springer International Publishing Group, Switzerland, 2016)
205. M. Lefevre, E. Proietti, F. Jaouen, J.P. Dodelet, *Science* **324**, 71 (2009)
206. R. Bashyam, P. Zelenay, *Nature* **443**, 63 (2006)
207. Z.S. Wu, L. Chen, J. Liu, K. Parvez, H. Liang, J. Shu, H. Sachdev, R. Graf, X. Feng, K. Mullen, *Adv. Mater.* **26**, 1450 (2014)
208. Z. Xiang, Y. Xue, D. Cao, L. Huang, J.F. Chen, L. Dai, *Angew. Chem. Int. Ed.* **53**, 2433 (2014)
209. Q. Lin, X. Bu, A. Kong, C. Mao, X. Zhao, F. Bu, P. Feng, *J. Am. Chem. Soc.* **137**, 2235 (2015)
210. H.-W. Liang, S. Brueller, R. Dong, J. Zhang, X. Feng, K. Muellen, *Nat. Commun.* **6**, 7992 (2015)
211. J.D. Wiggins-Camacho, K.J. Stevenson, *J. Phys. Chem. C* **115**, 20002 (2011)
212. J. Li, S. Ghoshal, W. Liang, M.-T. Sougrati, F. Jaouen, B. Halevi, S. McKinney, G. McCool, C. Ma, X. Yuan, Z.-F. Ma, S. Mukerjee, Q. Jia, *Energy Environ. Sci.* **9**, 2418 (2016)
213. K. Artyushkova, A. Serov, S. Rojas-Carbonell, P. Atanassov, *J. Phys. Chem. C* **119**, 25917 (2015)
214. U.I. Kramm, M. Lefèvre, N. Larouche, D. Schmeisser, J.-P. Dodelet, *J. Am. Chem. Soc.* **136**, 978 (2014)
215. A. Zitolo, V. Goellner, V. Armel, M.-T. Sougrati, T. Mineva, L. Stievano, E. Fonda, F. Jaouen, *Nat. Mat.* **14**, 937 (2015)
216. Q. Jia, N. Ramaswamy, U. Tylus, K. Strickland, J. Li, A. Serov, K. Artyushkova, P. Atanassov, J. Anibal, C. Gumeci, S.C. Barton, M.-T. Sougrati, F. Jaouen, B. Halevi, S. Mukerjee, *Nano Energy* **29**, 65 (2016)
217. K. Strickland, E. Miner, Q. Jia, U. Tylus, N. Ramaswamy, W. Liang, M.-T. Sougrati, F. Jaouen, S. Mukerjee, *Nat. Commun.* **6**, 7343 (2015)
218. J. Tang, J. Liu, C.L. Li, Y.Q. Li, M.O. Tade, S. Dai, Y. Yamauchi, *Angew. Chem. Int. Ed.* **54**, 588 (2015)
219. V. Malgras, Q.M. Ji, Y. Kamachi, T. Mori, F.K. Shieh, K.C.-W. Wu, K. Ariga, Y. Yamauchi, *Bull. Chem. Soc. Jpn* **88**, 1171 (2015)
220. H.W. Liang, W. Wei, Z.S. Wu, X.L. Feng, K. Mullen, *J. Am. Chem. Soc.* **135**, 16002 (2013)
221. S. Lee, D.H. Kwak, S.B. Han, Y.W. Lee, J.Y. Lee, I.A. Choi, H.S. Park, J.Y. Park, K.W. Park, *ACS Catal.* **6**, 5095 (2016)
222. Y. He, D. Gehrig, F. Zhang, C. Lu, C. Zhang, M. Cai, Y. Wang, F. Laquai, X. Zhuang, X. Feng, *Adv. Funct. Mater.* **26**, 8255 (2016)
223. C.H. Choi, S.H. Park, S.I. Woo, *ACS Nano* **6**, 7084 (2012)
224. T.C. Nagaiah, S. Kundu, M. Bron, M. Muhler, W. Schuhmann, *Electrochem. Commun.* **12**, 338 (2010)

225. C. Zhang, N. Mahmood, H. Yin, F. Liu, Y. Hou, *Adv. Mater.* **25**, 4932 (2013)
226. Z.P. Jin, H.G. Nie, Z. Yang, J. Zhang, Z. Liu, X.J. Xu, S.M. Huang, *Nanoscale* **4**, 6455 (2012)
227. Y.Z. Dong, J.H. Li, *Chem. Commun.* **51**, 572 (2015)
228. M. Hu, J. Reboul, S.H. Furukawa, N.L. Torad, Q.M. Ji, P. Srinivasu, K. Ariga, S. Kitagawa, Y. Yamauchi, *J. Am. Chem. Soc.* **134**, 2864 (2012)
229. Y. Xin, J.G. Liu, X. Jie, W. Liu, F. Liu, Y. Yin, J. Gu, Z. Zou, *Electrochim. Acta* **60**, 354 (2012)
230. Q. Li, R.G. Cao, J. Cho, G. Wu, *Adv. Energy Mater.* **4**, 1301415 (2014)
231. Z.Y. Liu, G.X. Zhang, Z.Y. Lu, X.Y. Jin, Z. Chang, X. Sun, *Nano Res.* **6**, 293 (2013)
232. R.W. Chen, J. Yan, Y. Liu, J.H. Li, *J. Phys. Chem. C* **119**, 8032 (2015)
233. J. Hou, C. Cao, F. Idrees, *ACS Nano* **9**, 2556 (2015)
234. S. Gao, H. Liu, K. Geng, *Nano Energy* **12**, 785 (2015)
235. K. Sakaushi, T.P. Fellinger, M. Antonietti, *ChemSusChem* **8**, 1156 (2015)
236. J. Zhang, Z. Zhao, Z. Xia, *Nat. Nanotechnol.* **10**, 444 (2015)
237. Z. Ma, S. Dou, A. Shen, *Angew. Chem.* **127**, 1908 (2015)
238. L. Hao, S. Zhang, R. Liu, *Adv. Mater.* **27**, 3190 (2015)
239. E.F. Holby, C.D. Taylor, *Sci. Rep.* **5**, 9286 (2015)
240. W. Yuan, J. Li, A. Xie, *Electrochim. Acta* **165**, 29 (2015)
241. J. Shui, M. Wang, F. Du, *Sci. Adv.* **1**, e1400129 (2015)
242. H. Watanabe, S. Asano, S. Fujita, *ACS Catal.* **5**, 2886 (2015)
243. H.W. Liang, Z.Y. Wu, L.F. Chen, *Nano Energy* **11**, 366 (2015)
244. Y. Gong, H. Fei, X. Zou, *Chem. Mater.* **27**, 1181 (2015)
245. X. Liu, Y. Zhou, W. Zhou, *Nanoscale* **7**, 6136 (2015)
246. Y.A. Zehab, K. Chizari, A. Jalilov, *ACS Nano* **9**, 5833 (2015)
247. E. Haque, M.M. Islam, E. Pourazadi, *RSC Adv.* **5**, 30679 (2015)
248. Y. Chen, R. Ma, Z. Zhou, *Adv. Mater. Interfaces* **9**, 5833 (2015)
249. G.A. Ferrero, M. Sevilla, A.B. Fuertes, *Carbon* **88**, 239 (2015)
250. S. Fu, C. Zhu, J. Song, D. Du, Y. Lin, *Adv. Energy Mater.* **7**, 1700363 (2017)
251. A.K. Diaz-Duran, F. Roncaroli, *Electrochim. Acta* **251**, 638 (2017)
252. H. Zhang, H. Osgood, X. Xie, Y. Shao, G. Wu, *Nano Energy* **31**, 331 (2017)
253. Y. Qian, I.A. Khan, D. Zhao, *Small* **13**, 1701143 (2017)
254. V.P. Santos, T.A. Wezendonk, J.J.D. Jaén, A.I. Dugulan, M.A. Nasalevich, H.-U. Islam, A. Chojecki, S. Sartipi, X. Sun, A.A. Hakeem, A.C.J. Koeken, M. Ruitenbeek, T. Davidian, G. R. Meima, G. Sankar, F. Kapteijn, M. Makkee, J. Gascon, *Nat. Commun.* **6**, 6451 (2015)
255. R. Das, P. Pachfule, R. Banerjee, P. Poddar, *Nanoscale* **4**, 591 (2012)
256. Z.S. Wu, L. Chen, J. Liu, K. Parvez, H. Liang, J. Shu, H. Sachdev, R. Graf, X. Feng, K. Mullen, *Adv. Mater.* **26**, 1450 (2014)
257. G.J. Tao, L.X. Zhang, L.S. Chen, X.Z. Cui, Z.L. Hua, M. Wang, J.C. Wang, Y. Chen, J.L. Shi, *Carbon* **86**, 108 (2015)
258. S. Chen, J. Bi, Y. Zhao, L. Yang, C. Zhang, Y. Ma, Q. Wu, X. Wang, Z. Hu, *Adv. Mater.* **24**, 5593 (2012)
259. N. Alexeyeva, E. Shulga, V. Kisand, I. Kink, K. Tammeveski, *J. Electroanal. Chem.* **648**, 169 (2010)
260. S. Ratso, I. Kruusenberg, M. Vikkisk, U. Joost, E. Shulga, I. Kink, T. Kallio, K. Tammeveski, *Carbon* **73**, 361 (2014)
261. G. Jo, S. Shanmugam, *Electrochem. Commun.* **25**, 101 (2012)
262. X. Zhuang, D. Gehrig, N. Forler, H. Liang, M. Wagner, M.R. Hansen, F. Laquai, F. Zhang, X. Feng, *Adv. Mater.* **27**, 3789 (2015)
263. L. Yang, S. Jiang, Y. Zhao, L. Zhu, S. Chen, X. Wang, Q. Wu, J. Ma, Y. Ma, Z. Hu, *Angew. Chem. Int. Ed.* **50**, 7132 (2011)
264. Z. Yang, Z. Yao, G. Li, G. Fang, H. Nie, Z. Liu, X. Zhou, X. Chen, S. Huang, *ACS Nano* **6**, 205 (2012)
265. X. Zhuang, F. Zhang, D. Wu, N. Forler, H. Liang, M. Wagner, D. Gehrig, M.R. Hansen, F. Laquai, X. Feng, *Angew. Chem. Int. Ed.* **52**, 9668 (2013)
266. Z. Liu, H. Nie, Z. Yang, J. Zhang, Z. Jin, Y. Lu, Z. Xiao, S. Huang, *Nanoscale* **5**, 3283 (2013)

267. Y. Su, Z. Yao, F. Zhang, H. Wang, Z. Mics, E. Cánovas, M. Bonn, X. Zhuang, X. Feng, *Adv. Funct. Mater.* **26**, 5893 (2016)
268. D.S. Yang, D. Bhattacharjya, S. Inamdar, J. Park, J.S. Yu, *J. Am. Chem. Soc.* **134**, 16127 (2012)
269. J. Wu, Z. Yang, X. Li, Q. Sun, C. Jin, P. Strasser, R. Yang, *J. Mater. Chem. A* **1**, 9889 (2013)
270. J. Wu, Z. Yang, Q. Sun, X. Li, P. Strasser, R. Yang, *Electrochim. Acta* **127**, 53 (2014)
271. T. Ishizaki, Y. Wada, S. Chiba, S. Kumagai, H. Lee, A. Serizawa, O.L. Li, G. Panomsuwan, *Phys. Chem. Chem. Phys.* **18**, 21843 (2016)
272. Q. Lin, X. Bu, A. Kong, C. Mao, F. Bu, P. Feng, *Adv. Mater.* **27**, 3431 (2015)
273. N.M. Cantillo, G.A. Goenaga, W. Gao, K. Williams, C.A. Neal, S. Ma, K.L. More, T.A. Zawodzinski, *J. Mater. Chem. A* **4**, 15621 (2016)
274. J. Herranz, F. Jaouen, M. Lefèvre, U.I. Kramm, E. Proietti, J.P. Dodelet, P. Bogdanoff, S. Fiechter, I.A. Wurmbach, P. Bertrand, T.M. Arruda, S. Mukerjee, *J. Phys. Chem. C* **115**, 16087 (2011)
275. S.J. You, M. Ma, W. Wang, D.P. Qi, X.D. Chen, J.H. Qu, N.Q. Ren, *Adv. Energy Mater.* **6**, 1501497 (2016)
276. J. Liang, Y. Jiao, M. Jaroniec, S.Z. Qiao, *Angew. Chem. Int. Ed.* **51**, 11496 (2012)
277. Z. Han, Y. Yu, Y. Zhang, B. Dong, A. Kong, Y. Shan, *J. Mater. Chem. A* **3**, 23716 (2015)
278. D. Yu, Q. Zhang, L. Dai, *J. Am. Chem. Soc.* **132**, 15127 (2010)
279. S. Yang, X. Feng, X. Wang, K. Mullen, *Angew. Chem. Int. Ed.* **50**, 5339 (2011)
280. P. Zhang, F. Sun, Z.H. Xiang, Z.G. Shen, J. Yun, D.P. Cao, *Energy Environ. Sci.* **7**, 442 (2014)
281. P. Chen, L.K. Wang, G. Wang, M.R. Gao, J. Ge, W.J. Yuan, Y.H. Shen, A.J. Xie, S.H. Yu, *Energy Environ. Sci.* **7**, 4095 (2014)
282. Z.S. Wu, S.B. Yang, Y. Sun, K. Parvez, X.L. Feng, K. Müllen, *J. Am. Chem. Soc.* **134**, 9082 (2012)
283. J. Liang, Y. Zheng, J. Chen, J. Liu, D. Hulicova-Jurcakova, M. Jaroniec, S. Zhang, Qiao, *Angew. Chem. Int. Ed.* **51**, 3892 (2012)
284. J. Zhu, C. He, Y. Li, S. Kang, P.K. Shen, *J. Mater. Chem. A* **1**, 14700 (2013)
285. Y.Y. Liang, H.L. Wang, J.G. Zhou, Y.G. Li, J. Wang, T. Regier, H.J. Dai, *J. Am. Chem. Soc.* **134**, 3517 (2012)
286. H.L. Wang, Y.Y. Liang, Y.G. Li, H.J. Dai, *Angew. Chem. Int. Ed.* **50**, 10969 (2011)
287. L.Y. Feng, Y.Y. Yan, Y.G. Chen, L.J. Wang, *Energy Environ. Sci.* **4**, 1892 (2011)
288. A. Aijaz, N. Fujiwara, Q. Xu, *J. Am. Chem. Soc.* **136**, 6790 (2014)
289. D. Zhao, J.L. Shui, L.R. Grabstanowicz, C. Chen, S.M. Commet, T. Xu, J. Lu, D.J. Liu, *Adv. Mater.* **26**, 1093 (2014)
290. L. Shang, H.J. Yu, X. Huang, T. Bian, R. Shi, Y.F. Zhao, G.I.N. Waterhouse, L.Z. Wu, C.H. Tung, T.R. Zhang, *Adv. Mater.* **28**, 1668 (2016)
291. B.Y. Xia, Y. Yan, N. Li, H.B. Wu, X.W.D. Lou, X. Wang, *Nat. Energy* **1**, 15006 (2016)
292. J. Liang, R.F. Zhou, X.M. Chen, Y.H. Tang, S.Z. Qiao, *Adv. Mater.* **26**, 6074 (2014)
293. Q. Wang, Z.Y. Zhou, Y.J. Lai, Y. You, J.G. Liu, X.L. Wu, E. Terefe, C. Chen, L. Song, M. Rauf, N. Tian, S.G. Sun, *J. Am. Chem. Soc.* **136**, 10882 (2014)
294. X. Li, Y. Fang, X. Lin, M. Tian, X. An, Y. Fu, R. Li, J. Jin, J. Ma, *J. Am. Chem. Soc.* **136**, 13925 (2014)
295. W. Xia, R. Zou, L. An, D. Xia, S. Guo, *J. Mater. Chem. A* **3**, 17392 (2015)
296. W. Chaikittisilp, N.L. Torad, C. Li, M. Imura, N. Suzuki, S. Ishihara, K. Ariga, Y. Yamauchi, *Chem. Eur. J.* **20**, 4217 (2014)
297. X. Li, Y. Fang, X. Lin, M. Tian, X. An, Y. Fu, R. Li, J. Jin, J. Ma, *Mater. Chem. A* **3**, 17392 (2015)
298. T.Y. Ma, S. Dai, M. Jaroniec, S.Z. Qiao, *J. Am. Chem. Soc.* **136**, 13925 (2014)
299. A. Kong, C. Mao, Q. Lin, X. Wei, X. Bu, P. Feng, *Dalton Trans.* **44**, 6748 (2015)
300. R.K. Gupta, A.K. Sinha, B.N. Raja Sekhar, A.K. Srivastava, G. Singh, S.K. Deb, *Appl. Phys. A Mater. Sci. Process.* **103**, 13 (2011)
301. K. Thangavelu, K. Parameswari, K. Kuppasamy, Y. Haldorai, *Mater. Lett.* **65**, 1482 (2011)
302. S. Meghdadi, M. Amirnasr, M. Zhiani, F. Jallili, M. Jari, M. Kiani, *Electrocatalysis* **8**, 122 (2017)

303. D.Y. Lee, S.J. Yoon, N.K. Shrestha, S.-H. Lee, H. Ahn, S.-H. Han, *Microporous Mesoporous Mater.* **153**, 163 (2012)
304. A.D. Roberts, X. Li, H. Zhang, *Chem. Soc. Rev.* **43**, 4341 (2014)
305. J. Shui, C. Chen, L. Grabstanowicz, D. Zhao, D.J. Liu, *Proc. Natl. Acad. Sci. U.S.A.* **112**, 10629 (2015)
306. S. Zhao, H. Yin, L. Du, L. He, K. Zhao, L. Chang, G. Yin, H. Zhao, S. Liu, Z. Tang, *ACS Nano* **8**, 12660 (2014)
307. J.-S. Li, S.-L. Li, Y.-J. Tang, M. Han, Z.-H. Dai, J.-C. Bao, Y.-Q. Lan, *Chem. Commun.* **51**, 2710 (2015)
308. Y. Hou, T. Huang, Z. Wen, S. Mao, S. Cui, J. Chen, *Adv. Energy Mater.* **4**, 1400337 (2014)
309. M. Jahan, Q. Bao, K.P. Loh, *J. Am. Chem. Soc.* **134**, 6707 (2012)
310. Y. Wang, X. Chen, Q. Lin, A. Kong, Q.G. Zhai, S. Xie, P. Feng, *Nanoscale* **9**, 862 (2017)
311. W. Zhang, T. Cui, L. Yang, C. Zhang, M. Cai, S. Sun, Y. Yao, X. Zhuang, F. Zhang, *J. Coll. Interface Sci.* **497**, 108 (2017)
312. J. Park, H. Lee, Y.E. Bae, K.C. Park, H. Ji, N.C. Jeong, M.H. Lee, O.J. Kwon, C.Y. Lee, *ACS Appl. Mater. Interfaces* **9**, 28758 (2017)
313. K. Zhao, Y. Liu, X. Quan, S. Chen, H. Yu, *ACS Appl. Mater. Interfaces* **9**, 5302 (2017)
314. X. Fang, L. Jiao, R. Zhang, H.-L. Jiang, *ACS Appl. Mater. Interfaces* **9**, 23852 (2017)
315. J. Masa, W. Xia, I. Sinev, A. Zhao, Z. Sun, S. Grützke, P. Weide, M. Muhler, W. Schuhmann, *Angew. Chem. Int. Ed.* **53**, 8508 (2014)
316. Y. Gorlin, T.F. Jaramillo, *J. Am. Chem. Soc.* **132**, 13612 (2010)
317. T. Wang, Q. Zhou, X. Wang, J. Zheng, X. Li, *J. Mater. Chem. A* **3**, 16435 (2015)
318. A.S. Arico, P. Bruce, B. Scrosati, J.-M. Tarascon, W. Van Schalkwijk, *Nat. Mater.* **4**, 366 (2005)
319. G. Wang, L. Zhang, J. Zhang, *Chem. Soc. Rev.* **41**, 797 (2012)
320. D. Yu, A.O. Yazaydin, J.R. Lane, P.D.C. Dietzel, R.Q. Snurr, *Chem. Sci.* **4**, 3544 (2013)
321. G. Wu, K.L. More, C.M. Johnston, P. Zelenay, *Science* **332**, 443 (2011)
322. J. Tian, A. Morozan, M.T. Sougrati, M. Lefevre, R. Chenitz, J.P. Dodelet, D. Jones, F. Jaouen, *Angew. Chem. Int. Ed.* **52**, 6867 (2013)
323. L.L. Zhang, X.S. Zhao, *Chem. Soc. Rev.* **38**, 2520 (2009)
324. P. Simon, Y. Gogotsi, *Nat. Mater.* **7**, 845 (2008)
325. B.E. Conway, *Electrochemical Supercapacitors: Scientific Fundamentals and Technological Applications* (Kluwer Academic/Plenum Publishers, New York, 1997)
326. C. Liu, F. Li, L.P. Ma, H.M. Cheng, *Adv. Mater.* **22**, E28 (2010)
327. Y. Lv, F. Zhang, Y. Dou, Y. Zhai, J. Wang, H. Liu, Y. Xia, B. Tu, D. Zhao, *J. Mater. Chem.* **22**, 93 (2012)
328. L.Z. Fan, Y.S. Hu, J. Maier, P. Adelhelm, B. Smarsly, M. Antonietti, *Adv. Funct. Mater.* **17**, 3083 (2007)
329. C. Largeot, C. Portet, J. Chmiola, P.-L. Taberna, Y. Gogotsi, P. Simon, *J. Am. Chem. Soc.* **130**, 2730 (2008)
330. H. Zhang, G. Cao, Y. Yang, Z. Gu, *Carbon* **46**, 30 (2008)
331. D.E. Jiang, Z.H. Jin, D. Henderson, J. Wu, *J. Phys. Chem. Lett.* **3**, 1727 (2012)
332. L. Zhang, X. Yang, F. Zhang, G. Long, T. Zhang, K. Leng, Y. Zhang, Y. Huang, Y. Ma, M. Zhang, Y. Chen, *J. Am. Chem. Soc.* **135**, 5921 (2013)
333. S. Xiong, C. Yuan, X. Zhang, B. Xi, Y. Qian, *Chem. Eur. J.* **15**, 5320 (2009)
334. R. Ramya, R. Sivasubramanian, M.V. Sangaranarayanan, *Electrochim. Acta* **101**, 109 (2013)
335. Y. Zhang, H. Feng, X. Wu, L. Wang, A. Zhang, T. Xia, H. Dong, X. Li, L. Zhang, *Int. J. Hydrogen Energy* **34**, 4889 (2009)
336. V. Augustyn, P. Simon, B. Dunn, *Energy Environ. Sci.* **7**, 1597 (2014)
337. L. Hao, X. Li, L. Zhi, *Adv. Mater.* **25**, 3899 (2013)
338. D.H. Seo, Z.J. Han, S. Kumar, K.K. Ostrikov, *Adv. Energy Mater.* **3**, 1316 (2013)
339. Y. Zhao, C. Hu, Y. Hu, H. Cheng, G. Shi, L. Qu, *Angew. Chem. Int. Ed.* **51**, 11371 (2012)
340. L. Hou, L. Lian, D. Li, G. Pang, J. Li, X. Zhang, S. Xiong, C. Yuan, *Carbon* **64**, 141 (2013)
341. A.G. Pandolfo, A.F. Hollenkamp, *J. Power Sources* **157**, 11 (2006)
342. E. Frackowiak, F. Beguin, *Carbon* **39**, 937 (2001)

343. M.X. Liu, J.S. Qian, Y.H. Zhao, D.Z. Zhu, L.H. Gan, L.W. Chen, *J. Mater. Chem. A* **3**, 11517 (2015)
344. M. Inagaki, H. Konno, O. Tanaike, *J. Power Sources* **195**, 7880 (2010)
345. Y. Zhai, Y. Dou, D.Y. Zhao, P.F. Fulvio, R.T. Mayes, S. Dai, *Adv. Mater.* **23**, 4828 (2011)
346. H.J. Choi, S.M. Jung, J.M. Seo, D.W. Chang, L.M. Dai, J.B. Baek, *Nano Energy* **1**, 534 (2012)
347. M. Sevilla, R. Mokaya, *Energy Environ. Sci.* **7**, 1250 (2014)
348. K.N. Wood, R. O'Hayre, S. Pylypenko, *Energy Environ. Sci.* **7**, 1212 (2014)
349. N. Mahmood, C.Z. Zhang, H. Yin, Y.L. Hou, *J. Mater. Chem. A* **2**, 15 (2014)
350. H.B. Wang, T. Maiyalagan, X. Wang, *ACS Catal.* **2**, 781 (2012)
351. W.Z. Shen, W.B. Fan, *J. Mater. Chem. A* **1**, 999 (2013)
352. K. Xie, X. Qin, X. Wang, Y. Wang, H. Tao, Q. Wu, L. Yang, Z. Hu, *Adv. Mater.* **24**, 347 (2012)
353. M. Noked, S. Okashy, T. Zimrin, D. Aurbach, *Angew. Chem.* **124**, 1600 (2012)
354. H.Y. Jung, M.B. Karimi, M.G. Hahm, P.M. Ajayan, Y.J. Jung, *Sci. Rep.* **2**, 773 (2012)
355. J.P. Dodelet, in *N4-Macrocyclic Metal Complexes*, eds. by J.H. Zagal, F. Bedioui, J. P. Dodelet (Springer, New York, 2006), pp. 83–147
356. A. Ghosh, Y.H. Lee, *ChemSusChem* **5**, 480 (2012)
357. Y.W. Zhu, S. Murali, M.D. Stoller, K.J. Ganesh, W.W. Cai, P.J. Ferreira, A. Pirkle, R.M. Wallace, K.A. Cychosz, M. Thommes, D. Su, E.A. Stach, R.S. Ruoff, *Science* **332**, 1537 (2011)
358. F. Bèguin, V. Presser, A. Balducci, E. Frackowiak, *Adv. Mater.* **26**, 2219 (2014)
359. S.L. Candelaria, Y.Y. Shao, W. Zhou, X.L. Li, J. Xiao, J.G. Zhang, Y. Wang, J. Liu, J.H. Li, G.Z. Cao, *Nano Energy* **1**, 195 (2012)
360. C. Sassoey, C. Laberty, H. Le Khanh, S. Cassaigne, C. Boissiere, M. Antonietti, C. Sanchez, *Adv. Funct. Mater.* **19**, 1922 (2009)
361. E. Raymundo-Pinero, M. Cadek, F. Beguin, *Adv. Funct. Mater.* **19**, 1032 (2009)
362. B. Xu, S.F. Yue, Z.Y. Sui, X.T. Zhang, S.S. Hou, G.P. Cao, Y.S. Yang, *Energy Environ. Sci.* **4**, 2826 (2011)
363. J. Han, L.L. Zhang, S. Lee, J. Oh, K.-S. Lee, J.R. Potts, J. Ji, X. Zhao, R.S. Ruoff, S. Park, *ACS Nano* **7**, 19 (2013)
364. J.P. Paraknowitsch, A. Thomas, *Energy Environ. Sci.* **6**, 2839 (2013)
365. W.S.V. Lee, M. Leng, M. Li, X.L. Huang, J.M. Xuen, *Nano Energy* **12**, 250 (2015)
366. Y.Y. Wen, B. Wang, C.C. Huang, L.Z. Wang, D. Hulicova-Jurcakova, *Chem. Eur. J.* **21**, 80 (2015)
367. Z.B. Yang, J. Ren, Z.T. Zhang, X.L. Chen, G.Z. Guan, L.B. Qiu, Y. Zhang, H.S. Peng, *Chem. Rev.* **115**, 5159 (2015)
368. J. Jiang, Y. Li, J. Liu, X. Huang, C. Yuan, X.W. Lou, *Adv. Mater.* **24**, 5166 (2012)
369. W. Chaikittisilp, M. Hu, H. Wang, H.-S. Huang, T. Fujita, K.C.W. Wu, L.-C. Chen, Y. Yamauchi, K. Ariga, *Chem. Commun.* **48**, 7259 (2012)
370. B. Liu, H. Shioyama, T. Akita, Q. Xu, *J. Am. Chem. Soc.* **130**, 5390 (2008)
371. D. Yuan, J. Chen, S. Tan, N. Xia, Y. Liu, *Electrochem. Commun.* **11**, 1191 (2009)
372. J. Hu, H. Wang, Q. Gao, H. Guo, *Carbon* **48**, 3599 (2010)
373. B. Liu, H. Shioyama, H. Jiang, X. Zhang, Q. Xu, *Carbon* **48**, 456 (2010)
374. H.B. Aiyappa, P. Pachfule, R. Banerjee, S. Kurungot, *Cryst. Growth Des.* **13**, 4195 (2013)
375. J.W. Jeon, R. Sharma, P. Meduri, B.W. Arey, H.T. Schaefer, J.L. Lutkenhaus, J.P. Lemmon, P.K. Thallapally, M.I. Nandasiri, B.P. McGrail, S.K. Nune, *A.C.S. Appl. Mater. Interfaces* **6**, 7214 (2014)
376. X. Yan, X. Li, Z. Yan, S. Komarneni, *Appl. Surf. Sci.* **308**, 306 (2014)
377. H.-L. Jiang, B. Liu, Y.-Q. Lan, K. Kuratani, T. Akita, H. Shioyama, F. Zong, Q. Xu, *J. Am. Chem. Soc.* **133**, 11854 (2011)
378. Q. Wang, W. Xia, W. Guo, L. An, D. Xia, R. Zou, *Chem. Asian J.* **8**, 1879 (2013)
379. S. Mo, Z. Sun, X. Huang, W. Zou, J. Chen, D. Yuan, *Synth. Met.* **162**, 85 (2012)
380. P. Su, L. Jiang, J. Zhao, J. Yan, C. Li, Q. Yang, *Chem. Commun.* **48**, 8769 (2012)

381. J.W. Jeon, R. Sharma, P. Meduri, B.W. Arey, H.T. Schaefer, J.L. Lutkenhaus, J.P. Lemmon, P.K. Thallapally, M.I. Nandasiri, B.P. McGrail, S.K. Nune, *ACS Appl. Mater. Interfaces* **6**, 7214 (2014)
382. F. Hao, L. Li, X.H. Zhan, J. Chen, *Mater. Res. Bull.* **66**, 88 (2015)
383. N.L. Torad, R.R. Salunkhe, Y. Li, H. Hamoudi, M. Imura, Y. Sakka, C.C. Hu, Y. Yamauchi, *Chem. Eur. J.* **20**, 7895 (2014)
384. F. Jaouen, M. Lefevre, J.P. Dodelet, M. Cai, *J. Phys. Chem. B* **110**, 5553 (2006)
385. M.B. Sassin, C.N. Chervin, D.R. Rolison, J.W. Long, *Acc. Chem. Res.* **46**, 1062 (2012)
386. X. Lang, A. Hirata, T. Fujita, M. Chen, *Nat. Nanotechnol.* **6**, 232 (2011)
387. R.R. Salunkhe, Y.V. Kaneti, Y. Yamauchi, *ACS Nano* **11**, 5293 (2017)
388. M.H. Yap, K.L. Fow, G.Z. Chen, *Green Energy Environ.* **2**, 218 (2017)
389. B.Y. Guan, L. Yu, X. Wang, S. Song, X.W. Lou, *Adv. Mater.* **29**, 1605051 (2017)
390. Y.C. Wang, W.B. Li, L. Zhao, B.Q. Xu, *Phys. Chem. Chem. Phys.* **18**, 17941 (2016)
391. Y. Han, S. Zhang, N. Shen, D. Li, X. Li, *Mater. Lett.* **188**, 1 (2017)
392. M.-S. Wu, W.-H. Hsu, *J. Power Sources* **274**, 1055 (2015)
393. G. Zeng, Y. Chen, L. Chen, P. Xiong, M. Wei, *Electrochim. Acta* **222**, 773 (2016)
394. S. Ullah, I.A. Khan, M. Choucair, A. Badshah, I. Khan, M.A. Nadeem, *Electrochim. Acta* **171**, 142 (2015)
395. H. Pang, F. Gao, Q. Chen, R.M. Liu, Q.Y. Lu, *Dalton Trans.* **41**, 5862 (2012)
396. M.B. Zheng, J. Cao, S.T. Liao, J.S. Liu, H.Q. Chen, Y. Zhao, W.J. Dai, G.B. Ji, J.M. Cao, J. Tao, *J. Phys. Chem. C* **113**, 3887 (2009)
397. R.B. Rakhi, W. Chen, M.N. Hedhili, D. Cha, H.N. Alshareef, *ACS Appl. Mater. Interfaces* **6**, 4196 (2014)
398. S.G. Kandalkar, C.D. Lokhande, R.S. Mane, S.H. Han, *Appl. Surf. Sci.* **253**, 3952 (2007)
399. Y.G. Li, B. Tan, Y.Y. Wu, *Nano Lett.* **8**, 265 (2008)
400. X.W. Lou, D. Deng, J.Y. Lee, J. Feng, L.A. Archer, *Adv. Mater.* **20**, 258 (2008)
401. F. Zhang, L. Hao, L.J. Zhang, X.G. Zhang, *Int. J. Electrochem. Sci.* **6**, 2943 (2011)
402. Z. Xu, B. Lv, X. Shi, L. Chen, K. Wang, *Inorg. Chim. Acta* **427**, 266 (2015)
403. G.L. Wang, D.X. Cao, C.L. Yin, Y.Y. Gao, J.L. Yin, L. Cheng, *Chem. Mater.* **21**, 5112 (2009)
404. S. Palmas, F. Ferrara, A. Vacca, M. Mascia, A.M. Polcaro, *Electrochim. Acta* **53**, 400 (2007)
405. X. Cao, B. Zheng, X. Rui, W. Shi, Q. Yan, H. Zhang, *Angew. Chem. Int. Ed.* **53**, 1404 (2014)
406. Y.C. Wang, W.B. Li, L. Zhao, B.Q. Xu, *Phys. Chem. Chem. Phys.* **18**, 17941 (2016)
407. W. Xia, J. Zhu, W. Guo, L. An, D. Xia, R. Zou, *J. Mater. Chem. A* **2**, 11606 (2014)
408. W. Xia, R.Q. Zou, L. An, D.G. Xia, S.J. Guo, *Energy Environ. Sci.* **8**, 568 (2015)
409. H.X. Zhong, J. Wang, Y.W. Zhang, W.L. Xu, W. Xing, D. Xu, Y.F. Zhang, X.B. Zhang, *Angew. Chem. Int. Ed.* **53**, 14235 (2014)
410. W. Zhang, Z.Y. Wu, H.L. Jiang, S.H. Yu, *J. Am. Chem. Soc.* **136**, 14385 (2014)
411. S.G. Krishnan, M.V. Reddy, M. Harilal, B. Vidyadharan, I.I. Misnon, M.H.A. Rahim, J. Ismail, R. Jose, *Electrochim. Acta* **161**, 312 (2015)
412. H. Chen, J. Jiang, L. Zhang, T. Qi, D. Xia, H. Wan, *J. Power Sources* **248**, 28 (2014)
413. G. Zhou, J. Zhu, Y. Chen, L. Mei, X. Duan, G. Zhang, L. Chen, T. Wang, B. Lu, *Electrochim. Acta* **123**, 450 (2014)
414. A. Pendashteh, M.S. Rahmanifar, R.B. Kaner, M.F. Mousavi, *Chem. Commun.* **50**, 1972 (2014)
415. J. Gomez, E.E. Kalu, *J. Power Sources* **230**, 218 (2013)
416. K. Wang, J. Xu, A. Lu, Y. Shi, Z. Lin, *Solid State Sci.* **58**, 70 (2016)
417. H. Li, H. Zhou, *Chem. Commun.* **48**, 1201 (2012)
418. J. Wang, X. Sun, *Energy Environ. Sci.* **5**, 5163 (2012)
419. J. Jiang, Y. Li, J. Liu, X. Huang, *Nanoscale* **3**, 45 (2011)
420. Z.-S. Wu, G. Zhou, L.-C. Yin, W. Ren, F. Li, H.-M. Cheng, *Nano Energy* **1**, 107 (2012)
421. B. Dunn, H. Kamath, J.-M. Tarascon, *Science* **334**, 928 (2011)
422. P.G. Bruce, B. Scrosati, J.-M. Tarascon, *Angew. Chem. Int. Ed.* **47**, 2930 (2008)

423. J.B. Goodenough, Y. Kim, *Chem. Mater.* **22**, 587 (2009)
424. Y. Ding, Y.F. Yang, H.X. Shao, *Electrochim. Acta* **56**, 9433 (2011)
425. Y.F. Deng, Q.M. Zhang, S.D. Tang, L.T. Zhang, S.N. Deng, Z.C. Shi, G.H. Chen, *Chem. Commun.* **47**, 6828 (2011)
426. Y. Ren, Z. Ma, P.G. Bruce, *Chem. Soc. Rev.* **41**, 4909 (2012)
427. M.N. Obrovac, V.L. Chevrier, *Chem. Rev.* **114**, 11444 (2014)
428. Z. Wan, J. Shao, J. Yun, H. Zheng, T. Gao, M. Shen, Q. Qu, H. Zheng, *Small* **10**, 4975 (2014)
429. N. Du, H. Zhang, B. Chen, J. Wu, X. Ma, Z. Liu, Y. Zhang, D. Yang, X. Huang, J. Tu, *Adv. Mater.* **19**, 4505 (2007)
430. G. Gao, H.B. Wu, B. Dong, S. Ding, X.W.D. Lou, *Adv. Sci.* **2**, 1400014 (2015)
431. S. Yang, R.E. Bachman, X. Feng, K. Müllen, *Acc. Chem. Res.* **46**, 116 (2013)
432. F. Zheng, Y. Yang, Q. Chen, *Nat. Commun.* **5**, 5261 (2014)
433. G. Zhang, S. Hou, H. Zhang, W. Zeng, F. Yan, C.C. Li, H. Duan, *Adv. Mater.* **27**, 2400 (2015)
434. H. Buqa, D. Goers, M. Holzapfel, M.E. Spahr, P. Novak, *J. Electrochem. Soc.* **152**, A474 (2005)
435. X.S. Zhou, L.J. Wan, Y.G. Guo, *Adv. Mater.* **25**, 2152 (2013)
436. S. Yang, Y. Sun, L. Chen, Y. Hernandez, X. Feng, K. Müllen, *Sci. Rep.* **2**, 427 (2012)
437. C. Ban, Z. Wu, D.T. Gillaspie, L. Chen, Y. Yan, J.L. Blackburn, A.C. Dillon, *Adv. Mater.* **22**, E145 (2010)
438. J.S. Zhou, H. Song, X. Chen, L. Zhi, S. Yang, J. Huo, W. Yang, *Chem. Mater.* **21**, 2935 (2009)
439. W. Zhou, L. Lin, W. Wang, L. Zhang, Q. Wu, J. Li, L. Guo, *J. Phys. Chem. C* **115**, 7126 (2011)
440. S.B. Yang, X.L. Feng, K. Müllen, *Adv. Mater.* **23**, 3575 (2011)
441. C.Z. Wu, P. Yin, X. Zhu, C.Z. Ouyang, Y. Xie, *J. Phys. Chem. B* **110**, 17806 (2006)
442. E. Kang, Y.S. Jung, A.S. Cavanagh, G.-H. Kim, S.M. George, A.C. Dillon, J.K. Kim, J. Lee, *Adv. Funct. Mater.* **21**, 2430 (2011)
443. Z.Y. Wang, D.Y. Luan, S. Madhavi, C.M. Li, X.W. Lou, *Chem. Commun.* **47**, 8061 (2011)
444. W.M. Zhang, X.L. Wu, J.S. Hu, Y.G. Guo, L.J. Wan, *Adv. Funct. Mater.* **18**, 3941 (2008)
445. G.M. Zhou et al., *Chem. Mater.* **22**, 5306 (2010)
446. Y. Song, Y. Chen, J. Wu, Y. Fu, R. Zhou, S. Chen, L. Wang, *J. Alloys Compd.* **694**, 1246 (2017)
447. H. Yue, Z. Shi, Q. Wang, Z. Cao, H. Dong, Y. Qiao, Y. Yin, S. Yang, *ACS Appl. Mater. Interfaces* **6**, 17067 (2014)
448. S. Gao, R. Fan, B. Li, L. Qiang, Y. Yang, *Electrochim. Acta* **215**, 171 (2016)
449. M. Du, D. He, Y. Lou, J. Chen, *J. Energy Chem.* **26**, 673 (2017)
450. P. Su, S. Liao, F. Rong, F. Wang, J. Chen, C. Li, Q. Yang, *J. Mater. Chem. A* **2**, 17408 (2014)
451. H. Pang, W. Sun, L.-P. Lv, F. Jin, Y. Wang, *J. Mater. Chem. A* **4**, 19179 (2016)
452. G. Li, H. Yang, F. Li, J. Du, W. Shi, P. Cheng, *J. Mater. Chem. A* **4**(24), 9593 (2016)
453. M. Wang, H. Yang, X. Zhou, W. Shi, Z. Zhou, P. Cheng, *Chem. Commun.* **52**, 717 (2016)
454. D. Ji, H. Zhou, Y. Tong, J. Wang, M. Zhu, T. Chen, A. Yuan, *Chem. Eng. J.* **313**, 1623 (2017)
455. Z. Xiu, M.H. Alfaruqi, J. Gim, J. Song, S. Kim, P.T. Duong, J.P. Baboo, V. Mathew, J. Kim, *J. Alloys Compd.* **674**, 174 (2016)
456. Z. Wang, X. Li, H. Xu, Y. Yang, Y. Cui, H. Pan, Z. Wang, B. Chen, G. Qian, *J. Mater. Chem. A* **2**, 12571 (2014)
457. W. Wei, S.B. Yang, H.X. Zhou, I. Lieberwirth, X.L. Feng, K. Mullen, *Adv. Mater.* **25**, 2909 (2013)
458. L. Zhou, H.Y. Xu, H.W. Zhang, J. Yang, S.B. Hartono, K. Qian, J. Zou, C.Z. Yu, *Chem. Commun.* **49**, 8695 (2013)
459. N. Stock, S. Biswas, *Chem. Rev.* **112**, 933 (2012)

460. Y.M. Sun, X.L. Hu, W. Luo, F.F. Xia, Y.H. Huang, *Adv. Funct. Mater.* **23**, 2436 (2013)
461. X. Shen, D. Mu, S. Chen, B. Wu, F. Wu, *ACS Appl. Mater. Interfaces* **5**, 3118 (2013)
462. Y. Wang, X. Jiang, L. Yang, N. Jia, Y. Ding, *ACS Appl. Mater. Interfaces* **6**, 1525 (2014)
463. J. Wu, C. Chen, Y. Hao, C. Wang, *ColloidS. Surf., A* **468**, 17 (2015)
464. M. Yu, D. Shao, F. Lu, X. Sun, H. Sun, T. Hu, G. Wang, S. Sawyer, H. Qiu, J. Lian, *Electrochem. Commun.* **34**, 312 (2013)
465. R. Guo, W. Yue, Y. An, Y. Ren, X. Yan, *Electrochim. Acta* **135**, 161 (2014)
466. F. Li, L. Yang, G. Xu, H. Xiaoqiang, X. Yang, X. Wei, Z. Ren, G. Shen, G. Han, *J. Alloys Compd.* **577**, 663 (2013)
467. X. Sun, C. Zhou, M. Xie, H. Sun, T. Hu, F. Lu, S.M. Scott, S.M. George, J. Lian, *J. Mater. Chem. A* **2**, 7319 (2014)
468. Y. Han, M. Zhao, L. Dong, J. Feng, Y. Wang, D. Li, X. Li, *J. Mater. Chem. A* **3**, 22542 (2015)
469. D.V. Bavykin, J.M. Friedrich, F.C. Walsh, *Adv. Mater.* **18**, 2807 (2006)
470. G.N. Zhu, Y.G. Wang, Y.Y. Xia, *Energy Environ. Sci.* **5**, 6652 (2012)
471. M. Mancini, F. Nobili, R. Tossici, M. Wohlfahrt-Mehrens, R. Marassi, *J. Power Sources* **196**, 9665 (2011)
472. C. Lai, G.R. Li, Y.Y. Dou, X.P. Gao, *Electrochim. Acta* **55**, 4567 (2010)
473. Y. Zhang, H. Zheng, G. Liu, V. Battaglia, *Electrochim. Acta* **54**, 4079 (2009)
474. D. Wang, D. Choi, J. Li, Z. Yang, Z. Nie, R. Kou, D. Hu, C. Wang, L.V. Saraf, J. Zhang, I. A. Aksay, J. Liu, *ACS Nano* **3**, 907 (2009)
475. H. Han, T. Song, E.K. Lee, A. Devadoss, Y. Jeon, J. Ha, Y.C. Chung, Y.M. Choi, Y.G. Jung, U. Paik, *ACS Nano* **6**, 8308 (2012)
476. J. Liang, X. Han, Y. Li, K. Ye, C. Hou, K. Yu, *New J. Chem.* **39**, 3145 (2015)
477. Y. Li, J. Luo, X. Hu, X. Wang, J. Liang, K. Yu, *J. Alloys Comp.* **651**, 685 (2015)
478. L.J. Fu, T. Zhang, Q. Cao, H.P. Zhang, Y.P. Wu, *Electrochem. Commun.* **9**, 2140 (2007)
479. A. Yu, R. Frech, *J. Power Sources* **104**, 97 (2002)
480. H.G. Jung, S.W. Oh, J. Ce, N. Jayaprakash, Y.K. Sun, *Electrochem. Commun.* **11**, 756 (2009)
481. H.E. Wang, Z.G. Lu, L.J. Xi, R.G. Ma, C.D. Wang, J.A. Zapien, I. Bello, *ACS Appl. Mater. Interfaces* **4**, 1608 (2012)
482. J. Ye, W. Liu, J. Cai, S. Chen, X. Zhao, H. Zhou, L. Qi, *J. Am. Chem. Soc.* **133**, 933 (2011)
483. J. Wang, Y. Zhou, Y. Hu, R. O'Hayre, Z. Shao, *J. Phys. Chem. C* **115**, 2529 (2011)
484. L. Guo, Q. Ru, X. Song, S. Hu, Y. Mo, *J. Mater. Chem. A* **3**, 8683 (2015)
485. L. Shen, L. Yu, X.Y. Yu, X. Zhang, X.W. Lou, *Angew. Chem. Int. Ed.* **54**, 1868 (2015)
486. L. Shen, Q. Che, H. Li, X. Zhang, *Adv. Funct. Mater.* **24**, 2630 (2014)
487. C. Fu, G. Li, D. Luo, X. Huang, J. Zheng, L. Li, *ACS Appl. Mater. Interfaces* **6**, 2439 (2014)
488. A.K. Mondal, D. Su, S. Chen, A. Ung, H.S. Kim, G. Wang, *Chem. Eur. J.* **21**, 1526 (2015)
489. L. Yin, Z. Zhang, Z. Li, F. Hao, Q. Li, C. Wang, R. Fan, Y. Qi, *Adv. Funct. Mater.* **24**, 4176 (2014)
490. Z. Li, L. Yin, *J. Mater. Chem. A* **3**, 21569 (2015)
491. M. Nagarathinam, K. Saravanan, W.L. Leong, P. Balaya, J.J. Vittal, *Cryst. Growth Des.* **9**, 4461 (2009)
492. R.J. White, R. Luque, V.L. Budarin, J.H. Clark, D.J. Macquarrie, *Chem. Soc. Rev.* **38**, 481 (2009)
493. D. Astruc, F. Lu, J.R. Aranzas, *Angew. Chem. Int. Ed.* **44**, 7852 (2005)
494. C. Burda, X. Chen, R. Narayanan, M.A. El-Sayed, *Chem. Rev.* **105**, 1025 (2005)
495. M.A. Mahmoud, C.E. Tabor, M.A. El-Sayed, Y. Ding, Z.L. Wang, *J. Am. Chem. Soc.* **130**, 4590 (2008)
496. Z. Yin, H. Zheng, D. Ma, X. Bao, *J. Phys. Chem. C* **113**, 1001 (2009)
497. D. Obermayer, A.M. Balu, A.A. Romero, W. Goessler, R. Luque, C.O. Kappe, *Green Chem.* **15**, 1530 (2013)
498. J.A. Farmer, C.T. Campbell, *Science* **329**, 933 (2010)
499. H. Lee, S.E. Habas, G.A. Somorjai, P. Yang, *J. Am. Chem. Soc.* **130**, 5406 (2008)

500. M. Pang, J. Hu, H.C. Zeng, *J. Am. Chem. Soc.* **132**, 10771 (2010)
501. N.L. Torad, M. Hu, S. Ishihara, H. Sukegawa, A.A. Belik, M. Imura, K. Ariga, Y. Sakka, Y. Yamauchi, *Small* **10**, 2096 (2014)
502. H.B. Wu, B.Y. Xia, L. Yu, X.Y. Yu, X.W. Lou, *Nat. Commun.* **6**, 6512 (2015)
503. N.L. Torad, M. Hu, Y. Kamachi, K. Takai, M. Imura, M. Naitoa, Y. Yamauchi, *Chem. Commun.* **49**, 2521 (2013)
504. F. Wei, J. Jiang, G. Yu, Y. Sui, *Mater. Lett.* **146**, 20 (2015)
505. M.H. Kim, J.Y. Choi, H.K. Choi, S.M. Yoon, O.O. Park, D.K. Yi, S.J. Choi, H.J. Shin, *Adv. Mater.* **20**, 457 (2008)
506. Y. Xiong, J.M. McLellan, J. Chen, Y. Yin, Z.Y. Li, Y. Xia, *J. Am. Chem. Soc.* **127**, 17118 (2005)
507. E.S. Aazam, W.A. El-Said, *Bioorg. Chem.* **57**, 5 (2014)
508. J. Long, Y. Zhou, Y. Li, *Chem. Commun.* **51**, 2331 (2015)
509. M. Zaheer, G. Motzm, R. Kempe, *J. Mater. Chem.* **21**, 18825 (2011)
510. R. Xie, Y. Pan, H. Gu, *RSC Adv.* **5**, 16497 (2015)
511. S. Schimpf, C. Louis, P. Claus, *Appl. Catal. A* **318**, 45 (2007)
512. A. Pariyar, S. Gopalakrishnan, J. Stansbery, R.L. Patel, X. Liang, N. Gerasimchuk, A. Choudhury, *RSC Adv.* **6**, 38533 (2016)
513. N. Sahiner, H. Ozay, O. Ozay, N. Aktas, *Appl. Catal. A* **385**, 201 (2010)
514. N. Sahiner, H. Ozay, O. Ozay, N. Aktas, *Appl. Catal. B* **101**, 137 (2010)
515. M.A. Mahmoud, B. Snyder, M.A. El-Sayed, *J. Phys. Chem. Lett.* **1**, 28 (2010)
516. K. Kuroda, T. Ishida, M. Haruta, *J. Mol. Catal. A: Chem.* **298**, 7 (2009)
517. S. Saha, A. Pal, S. Kundu, S. Basu, T. Pal, *Langmuir* **26**, 2885 (2010)
518. S. Arora, P. Kapoor, M.L. Singla, *React. Kinet. Mech. Catal.* **99**, 157 (2010)
519. S. Farhadi, M. Kazem, F. Siadatnasab, *Polyhedron* **30**, 606 (2011)
520. M. Zaheer, C.D. Keenan, J. Hermannsdorfer, E. Roessler, G. Motz, J. Senker, R. Kempe, *Chem. Mater.* **24**, 3952 (2012)
521. M. Zaheer, J. Hermannsdorfer, W.P. Kretschmer, G. Motz, R. Kempe, *ChemCatChem* **6**, 91 (2014)
522. G. Mera, M. Gallei, S. Bernard, E. Ionescu, *Nanomaterials* **5**, 468 (2015)
523. M. Kamperman, A. Burns, R. Weissgraeber, N.V. Vegten, S.C. Warren, S.M. Gruner, A. Baiker, U. Wiesner, *Nano Lett.* **9**, 2756 (2009)
524. G. Glatz, T. Schmalz, T. Kraus, F. Haarmann, G. Motz, R. Kempe, *Chem. Eur. J.* **16**, 4231 (2010)
525. L. Hu, J. Peng, W. Wang, Z. Xia, J. Yuan, J. Lu, X. Huang, W. Ma, H. Song, W. Chen, Y.-B. Cheng, J. Tang, *ACS Photon.* **1**, 547 (2014)
526. M. Edrissi, A.R. Keshavarz, *Nano-Micro Lett.* **4**, 83 (2012)
527. S.K. Maji, A.K. Dutta, S. Dutta, D.N. Srivastava, P. Paulc, A. Mondal, B. Adhikary, *Appl. Catal. B* **126**, 265 (2012)
528. S.U. Son, I.K. Park, J. Park, T. Hyeon, *Chem. Commun.* 778 (2004)
529. Y. Li, X. Fan, J. Qi, J. Ji, S. Wang, G. Zhang, F. Zhang, *Nano Res.* **3**, 429 (2010)
530. A. Kumar, G.K. Rao, S. Kumar, A.K. Singh, *Organometallics* **33**, 2921 (2014)
531. B. Lim, M. Jiang, J. Tao, P.H.C. Camargo, Y. Zhu, Y. Xia, *Adv. Funct. Mater.* **19**, 189 (2009)
532. V.V. Singh, U. Kumar, S.N. Tripathi, A.K. Singh, *Dalton Trans.* **43**, 12555 (2014)
533. S. Lv, X. Zhao, G. Xia, C. Jin, L. Wang, W. Yang, Y. Zhang, J. Li, *Chem. Phys. Lett.* **667**, 32 (2017)
534. A.J. Gellman, W.T. Tysoc, F. Zaera, *Catal. Lett.* **145**, 220 (2015)
535. C.J. Beddeley, T.E. Jones, A.G. Trant, K. Wilson, *Top. Catal.* **54**, 1348 (2011)
536. E. Schmidt, C. Bucher, G. Santarossa, T. Mallat, R. Gilmour, A. Baiker, *J. Catal.* **289**, 238 (2012)

537. S. Jansat, M. Gómez, K. Philippot, G. Muller, E. Guiu, C. Claver, S. Castellón, B. Chaudret, *J. Am. Chem. Soc.* **126**, 1592 (2004)
538. K. Sawai, R. Tatumi, T. Nakahodo, H. Fujihara, *Angew. Chem. Int. Ed.* **47**, 6917 (2008)
539. R. Tatumi, T. Akita, H. Fujihara, *Chem. Commun.* **31**, 3349 (2006)
540. K. Mori, Y.T. Kondo, H. Fujihara, *Phys. Chem. Chem. Phys.* **11**, 8949 (2009)
541. K. Bijanzad, A. Tadjarodi, O. Akhavan, *Chin. J. Catal.* **36**, 742 (2015)
542. M. Rakibuddin, R. Ananthakrishnan, *Appl. Surf. Sci.* **362**, 265 (2016)
543. S.S. Dhankhar, M. Kaur, C.M. Nagaraja, *Eur. J. Inorg. Chem.* 5669 (2015)
544. S.J. Yang, J.H. Im, T. Kim, K. Lee, C.R. Park, *J. Hazard. Mater.* **186**, 376 (2011)
545. J. Xu, Q. Liu, W.-Y. Sun, *Solid State Sci.* **12**, 1575 (2010)
546. Y.K. Abdel-Monem, S.M. Emam, H.M.Y. Okda, *J. Mater. Sci.: Mater. Electron.* **28**, 2923 (2017)
547. H.M. Aly, M.E. Moustafa, M.Y. Nassar, E.A. Abdelrahman, *J. Mol. Struct.* **1086**, 223 (2015)
548. M. Basu, A.K. Sinha, M. Pradhan, S. Sarkar, Y. Negishi, T. Pal, *Environ. Sci. Technol.* **44**, 6313 (2010)
549. S.K. Maji, A.K. Dutta, S. Dutta, D.N. Srivastava, P. Paulc, A. Mondal, B. Adhikary, *Appl. Catal. B* **126**, 265 (2012)
550. J. Tavana, M. Edrisi, *Mater. Res. Expr.* **3**, 035009 (2016)

Conclusions and Future Prospects

As the content of this book shows, the preparation of nanomaterials by thermolysis of metal chelates is an intensively developing field of materials science and coordination chemistry, which has its own objects and methods of research, and is based on its design principles and methodological approaches. Information in this area is constantly accumulating, gathering facts that previously seemed strange, and ending with the logical structuring of new ways of obtaining nanomaterials with high marketing potential.

We can say with confidence that the current stage in the development of this interesting field of chemistry has reached its peak in the accumulation of experimental facts, their theoretical interpretation and generalization, although this is only the tip of the iceberg in terms of their potential applications and methods of synthesis. Many new types of NPs will appear as a research topic. The advantages of this environmentally friendly technology, the possibility of mass production and low costs can make these materials promising for future industrial applications. Nevertheless, until now, unfortunately, it is impossible to find correlations between the composition, structural features, and properties of nanomaterials obtained by this method, which in many respects hinders the development of a scientifically grounded approach to structuring these materials and predicting their promising properties.

How do we see the development of this interesting field of modern chemistry?

First, special attention will be paid to metrological research of new nanomaterials obtained by thermolysis of metal chelates: the development of subtle methods of monitoring, analysis, increasing sensitivity, the accuracy of methods, increasing their express performance, and reliability of new measurement equipment containing a modern electronic component base.

The promising way will be further development of new metal chelate precursors, the use of which can be useful and will open a new way for preparing nanomaterials with favorable properties. The processes of thermolysis will be studied on the basis of combined roles of chelating ligands during the thermolysis process, which determines its suitability as a capping agent, reductant, and also its ease of

decomposition. Ultimately, the shape and the size of the obtained NPs can be tailored by careful choice of chelating ligands and metal chelates based on them. On the other hand, there are superior potential applications for the resulting NPs in a number of different fields, included applying in drug delivery, gene therapy, etc., which would remarkably increase the value of thermolysis method in the near future. The use of structurally characterized precursors based on metals for the formation of nanomaterials gives an idea of the relationships between the structural features of the precursors and the morphology of the materials. In this context, a comprehensive approach, involving synthetic chemistry, physical chemistry, and chemical engineering, is of considerable interest for materials science.

Despite advances in chemistry and the application of these fascinating metal chelate precursors, some areas have yet to be explored further. For example, the development of heterometallic SSPs for bimetallic nanomaterials is one of those areas that need to be investigated further because of their potential applications. Some recent publications highlight the advantages of these SSPs over homometallic precursors. It should also be noted that precursors based on metal chelates can also be used in a polymer matrix to produce transparent nanocomposite films for various applications (e.g., scratch-resistant lenses, laser optics, and waveguide amplifiers).

The use of PMCs as precursors for the production of nanomaterials, such as metals, metal oxides, metal sulfides, carbon, is a method with interesting advantages. However, this process entails complex stages associated with the preparation of precursors based on polymer ligands. Most likely, the mechanism of formation of the final morphology in nanomaterials depends on various intermediates controlled by internal and external forces in the process of formation. Finally, the main task in this area is to find precise and clear mechanisms for the transformation of PMCs into the necessary nanomaterials. Thus, future research should focus on describing and explaining the mechanisms of nanomaterial formation and defining rules that determine the relationship between influential factors and final morphologies. This can be achieved through the targeted use of various PMCs with different compositions and structural varieties, for example, 1D, 2D, 3D, as well as porous and non-porous structures. In addition, the design of novel PMCs with different particles sizes and structures may be an effective way to improve the properties of the derived materials.

Index

A

Acids

- acetic, 306, 465
- acetylenedicarboxylic, 362, 366
- acrylic, 354
- azobenzene-3,5,4'-tricarboxylic, 461
- folic, 7
- itaconic, 357, 359
- methacrylic, 5, 354
- nitrilotriacetic, 281
- oleic, 4
- polyacrylic, 392, 412

Acrylates

- metal, 352, 361, 371, 386, 407, 408, 416
- thermal polymerization, 15, 365, 366, 368, 369, 408

Aerosol assisted chemical vapor, 187

Anode, 462, 463, 477, 497, 498, 500, 501, 504

Agent

- chain transfer, 7
- reducing, 12, 77, 114, 120, 127, 167, 216, 217, 224, 226, 227, 310, 430, 512
- stabilizing, 2, 3, 13, 77, 107, 115, 128, 132

Agglomeration, 5, 106, 132, 139, 165, 171, 184, 207, 209, 278, 287, 306, 310, 313, 329, 402, 426, 437, 497, 498

Aggregates, 83, 99, 101, 109, 156, 182, 371, 392, 394, 396, 400, 443

Alloy, 90, 156, 219–221, 230, 273, 314, 430, 431, 463–465, 497

Atom Transfer Radical Polymerization (ATRP), 4, 5, 7

B

2,2'-Bipyridine (bpy), 72, 138

4,4'-Bipyridine (4,4'-bpy), 139, 353

Bonds

- coordination, 11, 322
- covalent, 11, 324
- hydrogen, 358, 359
- Van-der-Waals, 325, 354

Bourdon pressure gauge, 33, 34

Brunauer–Emmett–Teller (BET), 161, 268, 301, 318, 322, 328, 469, 490

C

Carbon

- doped, 469, 490
- hierarchical porous, 478
- microporous, 489
- multi-walled nanotube, 253, 333, 334, 475
- nanoporous, 248, 494, 496
- nanotube, 215, 253, 255, 334, 335, 400, 467, 507
- nitrogen-doped, 251, 263, 267, 273, 469, 472, 480–482, 491

Cathode, 462–464, 471, 472, 476, 478, 497, 504, 505

Cell

- fuel, 459, 462–464, 467, 475, 478

Ceramics

- stabilized yttrium-zirconium (YSZ), 47, 322

Chalcogenides, 323, 439

Chelate

- Chelate (*cont.*)
 effect, 11, 156
 node, 351
- Chelation
 mechanism, 50
 metal, 11, 12, 15, 28, 30, 32, 45, 49, 50, 52, 55, 71, 72, 105, 107, 127, 130, 133, 135, 138, 139, 143, 151–153, 155–157, 161, 163, 165, 168
 process, 163
- Chemistry
 coordination, 11–13, 179, 543
- Clusters, 4, 42, 115, 156, 171, 193, 258, 272, 288, 313, 361, 393, 434, 442, 444
- Coatings, 5, 7, 202, 327, 365
- Combustion, 41, 42, 459, 513
- Complex
 macrocyclic, 11, 467, 482
 metal, 11, 35, 36, 39, 71, 97, 134, 161, 175, 192, 202, 232, 333, 352, 353, 433
 polymer, 330, 426
- Computer modelling, 25, 28, 39
- Copolymer, 4, 60, 61, 272, 330, 416, 431, 435, 449
- Current
 density, 466, 470–472, 475, 479, 481, 485, 486, 489, 490, 494, 495, 497, 498, 500–502, 505, 506
- Curie temperature, 372
- 1,5-Cyclooctadiene (COD), 256, 431, 432
- D**
- Dabco, 299
- Decomposition, 9, 11, 12, 27–29, 31, 33, 35, 37, 38, 42, 50, 51, 72, 73, 76, 84, 99–104, 133, 140, 143, 152, 156, 177, 182, 185, 197, 198, 202, 274, 314, 316, 320, 327, 333, 335, 353, 363, 371, 372, 374, 389, 390, 402, 407, 410, 411, 416, 427, 429, 430, 435, 439, 440, 446, 450, 510, 515, 521, 525, 526, 544
- Dendrimer, 3, 13
- Deposition, 44, 439
- E**
- Electrical Double Layer (EDL), 487
- Electrochemical Capacitor (EC), 459, 487
- Electrode
 reversible hydrogen, 463, 466, 475, 478, 480–482, 484
 rotating disc, 465
 rotating ring-disk, 473
- Equation
 Arrhenius, 39, 49, 375
 Avrami–Erofeev, 99
 Coats–Redfern, 52, 54, 55
- Ethylenediamine, 140, 141, 156, 353, 510
- Ethylene glycol, 101, 202, 450
- F**
- Forces
 repulsive, 6, 13, 167, 427
 Van-der-Waals, 354
- Fourier Transformation Infrared Spectroscopy (FTIR), 36–38, 309
- Frontal Polymerization (FP), 370
- G**
- Glassy Carbon (GC), 466, 481
- Grafting, 4–7, 517
- Graphene
 nanoribbons, 253, 265, 266, 490
 oxide, 178, 470
- Growth, 2, 3, 12, 13, 42, 45, 47, 71, 73, 75, 76, 83, 90, 100, 106, 114, 117, 124, 143, 161, 181, 182, 187, 190, 195, 197, 221, 274, 276, 277, 279, 280, 287, 290, 314, 323, 324, 329, 364, 366, 376, 400, 407, 414, 416, 427, 437, 438, 442, 446, 450, 451, 475, 500
- H**
- Heating
 hydrothermal, 9, 87, 171, 175, 359, 476
 microwave, 10, 47, 512
- Hexadecylamine, 77, 184
- High-frequency, 39, 390, 490
- Histogram, 87, 119, 199, 225, 298, 307
- 8-Hydroxyquinoline, 310, 313
- I**
- Interactions
 π - π -, 358
 energy, 321, 359, 362, 426, 519
 intermolecular, 105
- L**
- Ligand
 chelating, 11–13, 28, 71, 134, 150, 171, 175, 179, 202, 205, 209, 324, 354, 543, 544
 macrocyclic, 11, 12
 monodentate, 11, 107, 359
 polydentate, 11

- Lithium-ion battery, 459, 497
Luminescence, 437
- M**
- Macrokinetics, 37, 50
Macromolecule, 3, 59, 367
Magnetism, 1, 14
Magnetite, 7, 75, 86, 87, 97, 99, 114, 289, 291, 433
Maleate, 356, 360, 361, 371–374, 377, 378, 385–387, 402, 407, 408, 416
Matrix
 polymer, 104, 370, 371, 396, 402, 425–428, 431, 433, 439, 441, 442, 444–446, 544
Mechanism
 thermolysis, stages, 32, 35, 49, 52, 73, 138, 156, 303, 426
Membrane, 33, 329, 330, 450, 462, 487, 507
Metal
 carbides, 155, 273
 carbonyls, 10, 34
 compound, 7, 15, 25, 33, 156, 334, 362
 ion, 11, 13, 14, 32, 35, 62, 63, 105, 107, 133, 202, 250, 253, 264, 273, 274, 315–317, 352, 363, 371, 440
 oxide, 3, 6, 7, 14, 35, 36, 40, 42, 45, 107, 248, 255, 261, 263, 264, 268, 273, 274, 276, 301, 303, 309, 315, 318, 321, 323, 353, 372, 408, 417, 425, 460, 474, 487, 492, 496, 503, 544
 sulfide, 7, 14, 155, 180–182, 248, 323, 439, 450, 498, 544
 thiolate, 433
Metal chelate
 low molecular weight, 15, 71
 monomer, 15, 262, 352, 364, 406, 407
 polymeric, 13, 15, 247
Metal-containing monomers, 364, 370
Metal–Organic Frameworks (MOFs), 14, 248
Methods
 absorption spectroscopic, 28
 atomic force microscopy (AFM), 187, 444–447
 differential scanning calorimetry (DSC), 26, 31
 differential thermal analysis (DTA), 26, 28
 differential thermogravimetry (DTG), 371–373
 electron ionization mass spectrometry (EI-MS), 193
 electrospray mass spectrometry, 193
 Fourier transformation infrared spectroscopy (FTIR), 36–38, 309
 gas chromatography-mass spectrometry (GC-MS), 185, 193
 isothermal, 25, 33, 49, 60, 73, 100, 101, 368, 371, 373, 376, 378
 non-isothermal, 25, 27, 34, 51, 101, 372, 373
 scanning electron microscopy (SEM), 80
 thermogravimetric, TG, TGA, 27
 thermomechanical analysis (TMA), 26
 volumetric, 25, 33
 X-ray analysis, 310, 352
 X-ray photoelectron spectrometer (XPS), 261
Molecular dynamics, 369
- N**
- Nanocomposite
 hybrid organic-inorganic, 439, 448
 layered, 441
 polymer, definition, 3, 440, 442
 self-assembling, 79
Nanocrystals, 40, 77–79, 81, 84–87, 89, 94, 107, 111, 112, 120, 130–132, 167, 171, 181, 185, 188, 192, 197–199, 201, 213, 219, 220, 228–231, 275, 276, 285, 309, 427, 430, 438, 444, 446, 448, 463, 465, 467, 475, 518
Nanomaterial, 1–3, 7–9, 11–15, 34, 40–42, 44, 45, 47, 71, 72, 105, 107, 109, 128, 129, 152, 156, 167, 175, 180, 182, 197, 208, 247–250, 252, 253, 255–257, 260–263, 266, 271–276
Nanoparticles
 bimetallic, 465
 carbonated, 478
 rods, 7, 92, 96, 100, 128, 143, 175, 177, 180–184, 192, 194, 196, 198, 199, 201, 202, 205, 213, 230, 248, 265, 266, 271, 276, 277, 289, 290, 300, 302, 307, 309, 324, 325, 403, 405, 438, 441, 489, 490, 507
 self-organized, 156
 sheets, 168, 180, 182, 183, 204, 253, 299, 504
 spherical, 73, 77, 83, 88, 89, 107, 112, 115, 125, 127, 132, 143, 147, 161, 167, 194, 204, 392, 441
 star-like, 78, 79, 83, 93
 tetrapod-like, 276
 triangular, 121, 430, 489
Nanostructure, 3, 13, 14, 78, 105, 121, 130, 138, 160, 170, 182, 248, 252, 276, 277, 283, 291, 294, 303, 306, 313, 324, 327,

- 425, 438, 463, 476, 492, 493, 499, 500, 507, 520
- Nanowire, 77, 175, 181, 230, 233, 248, 294, 295, 323, 324, 475, 476, 507
- Networks, 262, 311, 358, 362, 435, 484, 504
- Nitrogen-doped Carbon Microfibers (NCF), 267, 469, 480, 481
- Nucleation, 2–4, 13, 73, 83, 120, 121, 150, 229, 277, 373, 432, 450, 500
- O**
- Oleate, 10, 84, 86, 88, 90, 433
- Oleylamine, 4
- Oxalate, 10, 97–99, 101, 141, 306, 316, 372
- Oxide
- indium-tin, 366, 492
 - metal, 6, 36, 40, 248, 255, 268, 274, 303, 315, 321, 408, 469, 544
- P**
- Phenanthroline, 72
- Photocatalysis, 249, 520
- Phthalocyanine, 263, 450, 467
- Polyacrylic acid, 371, 392, 412
- Polyethylene
- low density, LDPE, 370
- Polymer
- brushes, 7
 - chain, 4, 13, 14, 359, 370, 416, 426, 427, 436, 441
 - covalent organic, 479
 - metal-containing, 3, 14, 25, 250, 360, 365, 371, 389, 392, 394, 407, 474
 - shell, 4, 12, 392, 402
- Polymerization
- atom transfer radical, ATRP, 4, 7
 - conditions, 5
 - frontal, FP, 370
 - functionalization, 5, 370, 491
 - grafted, 4, 143, 178
 - initiator, 4
 - in situ*, 366
 - living radical, 4
 - nitroxide-mediated, 7
 - reversible addition-fragmentation chain transfer, 7
 - ring-opening, 4
 - solid-state, 14, 52, 97, 106, 156, 163, 209, 266, 290, 306, 310, 363, 366, 378
 - topochemical, 362, 365
- Porphyrin, 256, 257, 260–262, 264, 301, 467, 480, 485
- Potential
- redox, 487, 489, 492, 494, 496, 524
- Precursor
- single-source, 12, 71, 72, 75–77, 95, 108, 109, 111, 112, 117, 122, 128, 132, 133, 138, 143, 145, 147, 151, 152, 154, 156, 160, 161, 163, 168, 171, 173–175, 177, 179, 180, 182–185, 187, 189, 192, 195–197, 199, 201–216, 279, 283, 285, 287, 295, 298, 302, 303, 306, 307, 310, 313, 314, 318–324, 330
- Processes
- aerosol, 2, 40
 - flame pyrolysis, 75
 - graphitization, 253, 254, 268, 430, 472
 - redox, 494
- Pyridine, 138, 192, 284, 302, 427, 439, 468
- Pyrolysis
- linear (LP), 37
- Q**
- Quantum dots, 82
- R**
- Reaction
- center, 362
 - decarboxylation, 361, 387, 413
 - electrochemical, 462, 488, 492, 505
 - faradaic, 487, 491, 492, 494
 - hydrogen evolution, 467
 - hydrogen oxidation, 462
 - oxygen evolution, 469
 - oxygen reduction, 462, 464
 - rate, 50, 57, 107, 370, 463
 - topochemical, 362, 365
- Reaction under Autogenic Pressure at Elevated Temperature (RAPET), 34
- Reduction, 27, 98, 122, 138, 143, 218, 229, 230, 263–265, 329, 405, 429, 432, 462, 463, 476, 480, 482, 507, 508, 511–513
- Rhodamine-B, 521
- S**
- Salen, 30, 156, 160, 214
- Salphen, 161, 279
- Schiff bases, 35, 54, 213, 508
- Secondary Building Unit (SBU), 307
- Self-Generated Atmosphere (SGA), 33
- Self-organization, 156, 394
- Sensors, 1, 3, 249, 459
- Sonochemistry, 147

- Specific conductivity, 13, 71, 232, 250, 254, 285, 317, 393, 417, 465, 470, 489, 492, 494, 498
- Specific surface, 74, 151, 173, 228, 232, 254, 259, 290, 301, 317, 318, 321, 322, 330, 395, 467, 474, 515, 525
- Spin coating, 132, 439, 442
- Spinel, 87, 99, 135, 217, 224, 227, 316, 317, 503
- Spray-pyrolysis, 40–42, 228, 316
- Structure
- core-shell, 156
 - diamond-like, 363
 - hybrid, 4
 - spinel, 114, 159, 316
 - three-dimensional, 494
 - turbostratic, 140, 328, 334
- Supercapacitor, 249, 487–489, 491, 492, 497
- Superparamagnetic Iron Oxides (SPIOs), 84, 88
- Supersaturation, 40
- Surface
- area, 40, 96, 159, 173, 204, 232, 250, 251, 253, 254, 260, 268, 279, 290, 301, 307, 319, 322, 328, 446, 466, 469, 470, 472, 479, 488–490, 493, 498, 516, 521
- Surfactant, 3, 6, 12, 34, 75, 77, 82, 92, 101, 102, 105–107, 112, 127, 139, 168, 181, 206, 218, 221, 224, 226, 278, 285, 303–305, 427, 465
- Synthesis
- flame spray-pyrolysis, 40, 41, 228
 - hydrothermal, 9, 171, 182
 - microwave–polyolic, 10, 47
 - solvothermal, 290
 - sonochemical, 135, 138, 146, 168, 232, 265, 283, 305, 309, 313
- T**
- 2,2': 6',2''-Terpyridine, 283, 291
- Temperature
- Curie, 372
 - decomposition, 11
 - thermolysis, 14, 49, 60, 130, 171, 221, 262
- Templates, 34, 247, 250, 254, 259, 274, 275, 279, 325, 432, 446, 469, 492, 498
- Tetrahydrofuran, 328, 329, 330
- Tetrahydroquinoline, 185
- Thermolysis
- isothermal, 402
 - kinetics, 25, 33
 - non-isothermal, 101, 372, 376, 402
 - products, 37, 73, 75, 156, 202, 209, 252, 267, 294, 333, 380, 382, 387, 389, 392, 395, 398, 404, 411, 417, 485
 - stage, 36, 54, 330, 426
- Tri-*n*-octylphosphine oxide, 168
- Turnover Frequency (TOF), 468
- V**
- Voltammogram
- cyclic, 472, 474, 479, 481
 - linear-sweep, 471
- W**
- Wavelength, 394
- X**
- X-ray analysis, 310, 352
- Z**
- Zeolite, 9, 14, 248